

Book of Abstracts



**13th International Conference on Mathematical
and Numerical Aspects of Wave Propagation**

University of Minnesota, Twin Cities
May 15–19, 2017

TABLE OF CONTENTS

Local absorbing boundary condition for multiple scattering of time-harmonic waves in two dimensions (<u>Acosta/ Villamizar</u>)	1
On the preconditioning of the hypersingular operator via a dual Haar basis in the stabilization of the electric field integral equation (<u>Adrian/ Andriulli/ Eibert</u>).....	3
Solving the homogeneous isotropic linear elastodynamics equations using potentials. The case of the free surface boundary condition (<u>Albella/ Imperiale/ Joly</u>)	5
3D metric-based anisotropic mesh adaptation for the fast multipole accelerated boundary element method in acoustics (<u>Amlani/ Chaillat/ Groth/ Loseille</u>).....	7
A Fourier continuation-based solver for 3D elastic wave propagation (<u>Amlani/ Bruno</u>)	9
Optoelectronic finite-element simulations of thin-film solar cells (<u>Anderson/ Lakhtakia/ Mackay</u>)	11
An energy based discontinuous Galerkin method for Hamiltonian systems (<u>Appelö/ Hagstrom/ Semenova</u>)	13
Measuring electromagnetic chirality (<u>Arens/ Hagemann/ Hettlich</u>)	15
Low-rank separable expansion for the Helmholtz fundamental solution with absorption (<u>Arter/ Graham/ Spence</u>)	17
Efficient forward and inverse algorithms for guided wave inversion (<u>Astaneh/ Guddati</u>)	19
A two-level domain decomposition method for Helmholtz equation (<u>Astaneh/ Guddati</u>)	21
Generalized sampling method with noisy measurements (<u>Audibert</u>)	23
OpenHmX, an open-source H-Matrix toolbox in Matlab (<u>Aussal</u>)	25
Full determination of the characteristics of elastic scatterers from some FFP measurements (<u>Azpiroz/ Barucq/ Diaz/ Djellouli</u>)	27
Promise and progress of millihertz gravitational-wave astronomy (<u>Baker</u>)	29
Shear waves in prestrained poroelastic media (<u>Nazari/ Barbone</u>)	31
Elastic waves in a soft electrically conducting solid in a strong magnetic field (<u>Gendin/ Barbone</u>)	33
The generation of inertial-Alfvén waves in planetary cores (<u>Bardsley/ Davidson</u>).....	35
Regional computation of acoustic waves propagating from the near surface of the Sun (<u>Barucq/ Chabassier/ Duruflé/ Gizon/ Leguèbe</u>).....	37
On the well-posedness of Goldstein's equations for aeroacoustics in recirculating flows (<u>Bensalah/ Mercier/ Joly</u>).....	39
A continuation method for building large invisible obstacles in waveguides (<u>Bera/ Bonnet-Ben Dhia/ Chesnel/ Nazarov</u>)	41
Waves in solids with slow dynamics: an internal-variable model (<u>Berjamin/ Lombard/ Chiavassa/ Favrie</u>)	43
Stable and unstable Airy-related caustics and beams (<u>Berry</u>).....	45
Reprogrammable nonlinear phononic metamaterials (<u>Bilal/ Foehr/ Daraio</u>).....	47
Discontinuous Galerkin discretizations for Maxwell's equations in nonlinear Kerr media with linear Lorentz dispersion (<u>Bokil/ Cheng/ Jiang/ Li</u>)	49
Hybridizable discontinuous Galerkin methods for modelling 3D seismic wave propagation in harmonic domains (<u>Bonasse-Gahot/ Calandra/ Diaz/ Lanteri</u>)	51

Solvability of volume integral equations for elastodynamic scattering (<u>Bonnet</u>).....	53
Formulation of invisibility in waveguides as an eigenvalue problem (Bera/ <u>Bonnet-Ben Dhia</u> / Chesnel/ Nazarov/ Pagneux)	55
Homogenization of the spectrum of the Poincaré -Neumann operator (<u>Bonnetier</u> / Dapogny/ Triki).....	57
Normal modes and internal wave attractors (<u>Booker</u> / Bokhove/ Walkley).....	59
A mixed quasi-reversibility approach to identify obstacles in an acoustic waveguide (<u>Bourgeois</u> / Recoquillay)	61
High order accurate solution of the wave equation by compact finite differences and difference potentials (<u>Britt</u> / Turkel/ Tsynkov)	63
Semidiscrete evolution of elastic waves in a piezoelectric solid (<u>Brown</u> / Sánchez-Vizuet/ Sayas)	65
Gravitational wave astronomy and astrophysics (<u>Brown</u>)	67
A sparsity regularization and total variation based computational framework for the inverse medium problem in scattering (<u>Bürgel</u> / Kazimierski/ Lechleiter).....	69
The detection of defects at the interface between two materials (<u>Cakoni</u> / de Teresa/ Haddar/ Monk).....	71
Electromagnetic Stekloff eigenvalues in inverse scattering (<u>Camañ</u> o/ Lackner/ Monk).....	73
Local analysis of near fields in acoustic scattering (<u>Carvalho</u> / Khatri/ Kim).....	75
Imaging polarizable dipoles (<u>Cassier</u> / Guevara Vasquez)	77
A well-conditioned weak coupling between interior and exterior domains for harmonic electromagnetic scattering (<u>Caudron</u> / Antoine/ Geuzaine)	79
Nonlinear hysteretic propagation of torsional waves in a granular chain (<u>Cebrecos</u> / Béquin/ Theocharis/ Gusev/ Tournat).....	81
Weight-adjusted discontinuous Galerkin methods for wave propagation in arbitrary heterogeneous media (<u>Chan</u> / Hewett/ Warburton).....	83
BVP And BIE formulations for scattering by fractal screens (<u>Chandler-Wilde</u> / Hewett)	85
Invisibility and perfect reflectivity in waveguides with finite length branches (<u>Chesnel</u> / Nazarov/ Pagneux)	91
Second kind boundary integral equation for multi-subdomain diffusion problems (<u>Claeys</u> / Hiptmair/ Spindler)	93
Topological derivatives of leading- and second-order homogenized coefficients in bi-periodic media (<u>Bonnet</u> / <u>Cornaggia</u> / Guzina).....	95
High order DG overlapping solution FEM for the Helmholtz equation (<u>Coyle</u>)	97
An efficient semi-analytical scheme for determining the reflection of Lamb waves in a semi-infinite waveguide (<u>Davey</u> / Assier/ Abrahams/ Hewitt)	99
Mathematical studies of the Kuznetsov equation (<u>Dekkers</u> / Rozanova-Pierrat).....	101
On the local approximate rank of Helmholtz Green's kernel (Abboud/ <u>Delamotte</u> / Lafitte).....	103
On DGTD-Lawson exponential time integrators for time-domain electromagnetics (<u>Descombes</u> / Lanteri/ Wang/ Xu/ Li)	105
E.M. waves in magnetic plasmas (Campos-Pinto/ <u>Després</u>)	107
A combined Bayesian optimization-finite element approach for isoperimetric inequalities (<u>Dominguez</u> / Nigam/ Shahriari)	111
On a three parameter family of Boussinesq systems for internal waves (Dougalis/ <u>Durán</u> / Mitsotakis)	113

A new discontinuous Galerkin spectral element method for elastic waves with physically motivated numerical fluxes (<u>Duru</u> / Gabriel/ Igel)	115
Efficient boundary element schemes for the solution of high-frequency convex scattering problems (Ecevit/ Boubendir/ Souad).....	117
Geo-inspired mechanical metamaterials (<u>Elbanna</u> / Rao/ Ma)	119
Non-equilibrium magnetosonic wave motion (<u>Ellermeier</u>)	121
Uncertainty quantification of velocity models and seismic imaging (<u>Ely</u> / Poliannikov/ Malcolm/ Nicholls)	123
The application of discontinuous Petrov-Galerkin space-time discretizations and inexact Newton methods to seismic imaging (<u>Ernesti</u> / Wieners).....	125
Uncertainty quantification for inverse problems with a weak wave-equation constraint (<u>Fang</u> / Silva/ Kuske/ Herrmann)	127
Modeling the multimodal radiation from an open-ended waveguide (<u>Félix</u> / Doc/ Boucher)	129
Minnaert resonances for acoustic waves in bubbly media (Ammari/ <u>Fitzpatrick</u> / Gontier/ Lee/ Zhang)....	131
Transparent boundary conditions for general waveguide problems (Bonnet Ben-Dhia/ <u>Fliss</u> / Tonnour)....	133
Domain evolution kinetics of mechanical, phase-transforming structures (<u>Frazier</u> / Kochmann).....	135
Wave stability and invariance in nonlinear periodic media (<u>Fronk</u> / Leamy).....	137
Elastic full waveform inversion of reflection seismic data: migration based formulation (<u>Gadylshin</u> / Chavent/ Tcheverda).....	139
Modal expansion in elastic open waveguides with perfectly matched layers (<u>Gallezot</u> / Treyssède/ Laguerre)	141
Coercivity and iterative solvers for a class of preconditioned wave propagation models (<u>Ganesh</u> / Morgenstern)	143
Resonant activation of optoacoustic functionalities in phononic crystals (<u>Ganesh</u> / Gonella)	145
Diffuse acoustic waves in a randomly stratified flow (<u>Gay</u> / Savin/ Garnier)	147
Identification of a time-dependent potential in a wave equation (<u>Gerken</u> / Lechleiter)	149
Recent advances in optimized Schwarz domain decomposition methods for time-harmonic wave problems (<u>Geuzaine</u>)	151
Stable implementation of embedding formulae for computation of far field patterns (<u>Gibbs</u> / Langdon/ Moiola).....	157
Effective dielectric tensor of a two-dimensional periodic medium in the low-frequency approximation (<u>Godin</u> / Vainberg)	159
Resolution control in half-space time-reversal wave focusing (<u>Goh</u> / Koo/ Kallivokas)	161
Adaptive eigenspace method for inverse scattering problems in the frequency domain (<u>Graff-Kray</u> / Grote/ Nahum).....	163
Domain decomposition with local impedance condition for the Helmholtz equation (<u>Graham</u> / Chung/ Spence/ Vainikko/ Zou).....	165
Convergence analysis of energy conserving explicit local time-stepping methods for the wave equation (<u>Grote</u> / Mehlin/ Sauter)	167
Impedance-preserving discretization for modeling unbounded domains (<u>Guddati</u>)	169
A numerical scheme for the wave kinetic equation and its application to cross-polarization scattering in turbulent plasmas (<u>Guidi</u> / Maj/ Weber/ Köhn/ Snicker/ Poli)	171

Low-wavenumber expansion of Willis' effective constitutive relations in periodic media (Meng/ <u>Guzina</u>)	173
Extensions of complete radiation boundary conditions to dispersive waves (<u>Hagstrom</u>)	175
Faraday cages, homogenized boundary conditions and resonance effects (<u>Hewett/ Hewitt</u>)	177
Strongly nonlinear elastic wave dispersion in 1D homogenous media and metamaterials (Khajehtourian/ <u>Hussein</u>)	179
Generalized plane waves, variable amplitude and vector valued equations (<u>Imbert-Gérard</u>).....	181
Fourth order explicit scheme for dissipative wave problems based on modified equation technique (Chabassier/ Diaz/ Ha/ <u>Imperiale</u>)	183
Acoustic metamaterials in moving inhomogeneous media (<u>Jeon</u> / Ryoo).....	185
Wave diffraction by random surfaces: uncertainty quantification via sparse tensor boundary elements (Escapil-Inchauspé/ <u>Jerez-Hanckes</u>)	187
Nonlinear models of lasers, noise, and the SALT equations (<u>Johnson</u>)	189
Transparent boundary condition for the wave propagation in fractal trees (<u>Joly</u> / Kachanovska/ Semin) ...	191
A discontinuous Galerkin difference discretization of the wave equation (<u>Juhnke</u> / Hagstrom).....	193
Analytic solutions to the extended Korteweg – de Vries equation (<u>Karczewska</u> / Rozmej/ Infeld/ Rowlands)	195
High frequency acoustic scattering in isogeometric analysis (<u>Khajah</u> / Antoine/ Bordas).....	197
Complete radiation boundary conditions for the Helmholtz equation in waveguides (<u>Kim</u>).....	199
On the efficiency of an ADI splitting combined with a discontinuous Galerkin discretization (Hochbruck/ <u>Köhler</u>)	201
Application of the Floquet-transform to scattering problems from locally perturbed bi-periodic structures in R^3 (<u>Konschin</u> / Lechleiter).....	203
Wave energy delivery to multiple subsurface targets using time-reversal method (<u>Koo</u> / Kallivokas).....	205
Sobolev-dG: a class of dG methods with tame CFL numbers (Appelö/ Hagstrom/ <u>Kornelus</u>)	207
Estimating the error distribution of recovered changes in Earth properties with full-waveform inversion (<u>Kotsi</u> / Malcolm)	209
Modelling and design of nano-structures: multilayer nanoplasmatics configurations (<u>Kurkcu</u>)	211
Sparse modal spectral-element methods for binary neutron stars (<u>Lau</u>).....	213
Inverse random source scattering problems (Bao/ Chen/ <u>Li</u>)	215
Numerical study of fracture connectivity effect on seismic wave propagation (Novikov/ <u>Lisitsa</u>)	217
Numerical modeling of a time-fractional Burgers equation (<u>Lombard</u> / Matignon).....	219
Modeling gravitational waves with numerical-relativity simulations (<u>Lousto</u> / Campanelli/ Zlochower) ...	221
Scattering from a row of aligned cylinders of arbitrary cross-section; tail-end asymptotics for efficient evaluation of the periodic Green's function (<u>Lynott</u> / Parnell/ Abrahams/ Simon).....	223
Adaptive finite-element simulation of surface-plasmon polaritons on 2D materials (<u>Maier</u> / Margetis/ Luskin)	225
An algorithm for vector data full waveform inversion (Akrami/ <u>Malcolm</u>)	227
Discrete exterior calculus for electromagnetic scattering by massive particle clusters (Räbinä/ Mönkölä/ Rossi/ <u>Markkanen</u> / Penttilä/ Muinonen)	229

Acoustic scattering by spheres and spheroids in the time domain (<u>Martin</u>)	231
Transmission conditions for non-overlapping Schwarz domain decomposition methods applied to time-harmonic elastic waves (<u>Mattesi</u> / Darbas/ Geuzaine).....	233
A dispersion optimized mimetic finite difference method for Maxwell's equations in metamaterials (Bokil/ Gyrya/ <u>McGregor</u>).....	235
Time harmonic acoustic radiation in a circular flow (<u>Mercier</u> / Bensalah/ Joly).....	237
Stochastic boundary integral equations in electromagnetic scattering (<u>Michielsen</u>)	239
A nodal discontinuous Galerkin method with high-order absorbing boundary conditions and corner/edge compatibility (<u>Modave</u> / Atle/ Chan/ Warburton)	241
Time dependent inverse scattering in a waveguide (<u>Monk</u> / Selgas).....	243
Asymptotic stability of the linearised Euler equations with long-memory impedance boundary condition (<u>Monteghetti</u> / Matignon/ Piot/ Pascal).....	245
Gravitational waves from core-collapse supernovae (<u>Müller</u>).....	247
DPG methodology for wave phenomena in optical fibers (<u>Nagaraj</u> / Demkowicz/ Grosek).....	249
Two scale Hardy space infinite elements (<u>Nannen</u> / Halla).....	251
Existence and computation of a weak solution to the Hasegawa-Mima equation in periodic Sobolev spaces (Nassif/ Karakazian)	253
A-stable high-order implicit time schemes (Barucq/ Duruflé/ <u>N'Diaye</u>).....	255
Electromagnetic wave diffraction of perfect electric conducting wedges with arbitrary linear polarization (<u>Nethercote</u> / Assier/ Abrahams)	257
Reconstructing the geometry of a local perturbation in periodic layers (<u>Nguyen</u> / Haddar)	259
An efficient Monte Carlo transformed field expansion method for electromagnetic wave scattering by random rough surfaces (Feng/ Lin/ <u>Nicholls</u>).....	261
Singular solutions of cold plasma Maxwell's equations (Campos-Pinto/ Després/ <u>Nicolopoulos</u>)	263
Eigenvalue computation with the boundary element method and the contour integral method for periodic boundary value problems for Helmholtz' equation in 3D (Yamamoto/ <u>Niino</u> / Nishimura)	265
Performances of the boundary integral equations for transmission problems and the distributions of the complex fictitious eigenvalues (Misawa/ <u>Nishimura</u>)	267
Dispersive quantization of linear and nonlinear waves (<u>Olver</u>).....	269
Computational complexity of artificial boundary conditions for Maxwell's equations in the FDTD method (<u>Osintcev</u> / Tsynkov)	275
Using gravitational waves to understand the physics of neutron stars (<u>Owen</u>)	277
Spectral analysis of cavities partially filled with a negative-index material (<u>Paolantoni</u> / Hazard).....	279
Imaging with intensities only (<u>Papanicolaou</u>)	281
An efficient flux-lumped discontinuous Galerkin scheme for the 3D Maxwell equations on nonconforming Cartesian grids (<u>Patrizio</u> / Fornet/ Mouysset/ Ferrieres)	283
Acoustic scattering by inhomogeneous media with piecewise smooth material properties (<u>Paul</u> / Kumar/ Anand).....	285
Gravitational waves from inflation at interferometer scales (<u>Peloso</u>).....	287
Bounds on the Helmholtz equation in heterogeneous and random media (<u>Pemberry</u> / Graham/ Spence)....	289
Reliable and efficient a posteriori error estimate for EFIE in electromagnetism (Bakry/ <u>Pernet</u> / Collino) .	291

A hybrid method combining boundary elements and ray tracing for high frequency diffraction. Application to NDT (Bonnet/ Collino/ Demaldent/ Imperiale/ <u>Pesudo</u>)	293
An adaptive DPG method for high frequency time-harmonic wave propagation problems (<u>Petrides</u> / Demkowicz).....	295
A study of the numerical robustness of single-layer method with Fourier basis for multiple obstacle scattering in homogeneous media (Barucq/ Chabassier/ <u>Pham</u> / Tordeux)	297
Generalized linear sampling method for active imaging of subsurface fractures (<u>Pourahmadian</u> / Guzina/ Haddar).....	299
Adiabatically propagating phase boundaries in non-linear chains with twist and stretch (<u>Purohit</u>)	301
Imaging defects in an elastic waveguide using time-dependent surface data (Baronian/ Bourgeois/ <u>Recoquillay</u>)	303
Localized time-periodic solutions of nonlinear wave equations (<u>Reichel</u>).....	305
Non-linear Tikhonov regularization for inverse scattering from anisotropic media (<u>Rennoch</u> / Lechleiter)	307
Searching for a stochastic background of gravitational radiation (<u>Romano</u> / Cornish)	309
Adiabatic invariants of the Extended KdV equation (<u>Rozmej</u> / Karczewska/ Infeld/ Rowlands)	311
Mathematical analysis of plasmonic nanoparticles (Ammari/ Millien/ Romero/ <u>Ruiz</u> / Zhang)	313
Wave attenuation along a rough floating elastic beam (<u>Rupprecht</u> / Bennetts/ Peter).....	315
Coupling high-frequency methods and boundary element techniques for scattering problems with several obstacles (Lenoir/ Lunéville/ <u>Salles</u>)	317
FEM-BEM coupling for transient acoustic scattering by thermoelastic obstacles (<u>Sánchez-Vizuet</u> / Hsiao/ Sayas/ Weinacht).....	319
BEM with variable time step size for absorbing boundary conditions (Sauter/ <u>Schanz</u>).....	321
Inverse scattering with iterative determination of the regularization parameter (<u>Schenkels</u> / Vanroose)....	323
The unified transform method in dispersive quantization (<u>Sheils</u> / Olver).....	325
Timelike surfaces and the wave equation (<u>Shipman</u> / Shipman)	327
Robin spectrum of quantum trees and orthogonal polynomials (<u>Shipman</u> / Wang)	329
Trefftz-DG approximation for elasto-acoustics (<u>Shishenina</u> / Barucq/ Calandra/ Diaz)	331
On the dynamic features of discrete lattices with nonlinear local resonators (<u>Silva</u> / Kouznetsova/ Geers) .	333
Uncertainty quantification for electromagnetic scattering by 1D perfect electric conducting gratings (Aylwin/ Fay/ Jerez-Hanckes/ <u>Silva-Oelker</u>).....	335
Low-rank properties in Schur complements of discretized Helmholtz equations (<u>Solovyev</u> / Gander).....	337
Domain decomposition preconditioning for high-frequency Helmholtz and Maxwell problems with absorption (<u>Spence</u> / Bonazzoli/ Dolean/ Graham/ Tournier/ Vainikko).....	339
Boundary elements with mesh refinements for the wave equation (Gimperlein/ Meyer/ Oezdemir/ <u>Stark</u> / Stephan).....	341
Upwind discontinuous Galerkin space discretization and locally implicit time integration for Maxwell's equations (Hochbruck/ <u>Sturm</u>).....	343
Surface water waves over bathymetry (Craig/ <u>Sulem</u>)	345
Polarized uncertainty principles for the inverse source problem (<u>Sylvester</u>)	351
Local time-stepping for the solution of the Helmholtz equation via controllability methods (Grote/ <u>Tang</u>)	353

Accuracy and pollution errors of HDG methods for the Helmholtz equation involving point sources (<u>Taus</u> / <u>Zepeda-Núñez</u> / <u>Demanet</u>).....	355
The half-space matching method for the diffraction by polygonal scatterers (<u>Bonnet-Ben Dhia</u> / <u>Fliss</u> / <u>Tjandrawidjaja</u> / <u>Tonnoir</u>).....	357
Analysis of an observers strategy for initial state reconstruction in unbounded domains (<u>Fliss</u> / <u>Impériaile</u> / <u>Moireau</u> / <u>Tonnoir</u>)	359
A Trefftz method whose shape functions are constructed thanks to a high-order DG finite element method (<u>Barucq</u> / <u>Bendali</u> / <u>Diaz</u> / <u>Tordueux</u>)	361
Vector solitons for elastic waves in architected soft solids (<u>Deng</u> / <u>Raney</u> / <u>Tournat</u> / <u>Bertoldi</u>)	363
An efficient numerical algorithm for the 3D wave equation in domains of complex shape (<u>Petropavlovsky</u> / <u>Tsynkov</u> / <u>Turkel</u>)	365
High-order numerical solution of the Helmholtz equation for domains with reentrant corners (<u>Magura</u> / <u>Petropavlovsky</u> / <u>Tsynkov</u> / <u>Turkel</u>)	367
The doppler effect for SAR (<u>Gilman</u> / <u>Tsynkov</u>).....	369
Boundary integral equations for scattering problems with mixed boundary conditions (<u>Turc</u> / <u>Bruno</u>)	371
Solution of the focusing Davey-Stewartson equations and the reconstruction of complex-valued conductivities (<u>Lakshtanov</u> / <u>Vainberg</u>).....	373
Breathers and passive wave redirection in forced ordered granular networks (<u>Zhang</u> / <u>Moore</u> / <u>McFarland</u> / <u>Vakakis</u>)	375
Parallel preconditioned boundary element methods for wave scattering problems (<u>van't Wout</u>)	377
Minimum-uncertainty squeezed states for the simple harmonic oscillator (<u>Vega Guzmán</u>)	379
Criteria for opening band gaps in periodic media (<u>Lipton</u> / <u>Viator Jr.</u>)	381
Detecting low-frequency gravitational waves with pulsar timing arrays (<u>Vigeland</u> / The NANOGrav Collaboration).....	383
High order farfield expansions absorbing boundary condition coupled with high order finite difference methods (<u>Villamizar</u> / <u>Rojas</u> / <u>Acosta</u>).....	385
Approximate models for transmission problems between homogeneous and homogenized half-planes (<u>Claeys</u> / <u>Fliss</u> / <u>Vinoles</u>)	387
An energy based discontinuous Galerkin method for acoustic-elastic waves (<u>Appelö</u> / <u>Wang</u>)	389
Discrete resonances of the complex scaled Helmholtz equation (<u>Wess</u> / <u>Nannen</u>)	391
Probing extreme gravity with gravitational waves from binary black hole coalescences (<u>Yagi</u> / <u>Yunes</u> / <u>Pretorius</u>)	393
Shape reconstruction of nanoparticles from plasmonic resonances (<u>Ammari</u> / <u>Putinar</u> / <u>Ruiz</u> / <u>Yu</u> / <u>Zhang</u>) .	395
Quasi-stable dynamics of a mode-locked laser (<u>Yu</u> / <u>Moore</u>)	397

Local Absorbing Boundary Condition for Multiple Scattering of Time-Harmonic Waves in Two Dimensions

Sebastian Acosta^{1,*}, **Vianey Villamizar**²

¹Department of Pediatrics–Cardiology, Baylor College of Medicine, Houston TX, USA ²Department of Mathematics, Brigham Young University, Provo UT, USA

*Email: sacosta@bcm.edu

Abstract

We formulate a local absorbing boundary condition (ABC) for multiple scattering of time-harmonic waves in two dimensions. We start from the framework used in Grote–Kirsch [2] to decompose the scattered field as the superposition of purely outgoing wave fields in the exterior of appropriate artificial boundaries. Then following our approach from [1], we employ a truncated Karp’s expansion (with its recursive equations) as an evaluation formula for the scattered field in the exterior region to the artificial boundaries. By matching the Cauchy data of the exterior scattered field with the interior field at the artificial boundaries, we obtain a local ABC for multiple scattering. Including more terms from Karp’s expansion increases the order of approximation of the proposed ABC. The formulation is completely local, requiring only second order tangential derivatives on the artificial boundary.

Keywords: Multiple scattering, nonreflecting boundary conditions, Helmholtz equation.

1 Introduction

This work is concerned with the formulation of appropriate ABCs on artificial boundaries needed to truncate unbounded domains and apply numerical methods for wave scattering problems. Sometimes the scatterer may be formed by several obstacles that could be distant from each other. Choosing an artificial boundary, large enough to enclose all the scatterers, leads to an unnecessarily large computational domain and non-optimal use of computational resources.

In this work, we derive a new local ABC for multiple scattering of time-harmonic waves in two dimensions. As our first step in the derivation process, we adopt a technique, first introduced by Grote–Kirsch [2]. This consists of defining artificial boundaries that only enclose the immediate vicinity of each obstacle. Then, ABCs are imposed at each artificial boundary

which leads to a dramatic reduction of the discretization region. As a consequence, the computational cost is greatly reduced. In [2], they imposed a nonlocal DtN-type condition on each artificial boundary. The DtN approach provides an exact analytical formula to evaluate fields outside of the computational domain in order to propagate the waves from one sub-domain to another. However, a disadvantage of this approach is that the matrix that results from the discretization is partially dense at boundary points due to the nonlocal nature of the DtN-map.

Our local ABC is obtained by representing the purely-outgoing fields in terms of the Karp’s expansion [3] which avoids the nonlocal eigenfunction representation from [2]. Using Karp’s representation, we can evaluate wave fields semi-analytically at a distance in order to match the Cauchy data of the scattered field across the artificial boundaries. As a result, we obtain a new local ABC, which effectively accounts for the outgoing behavior of the scattered field, as well as its interaction between the obstacles. The matrix that results from applying discretizations to the scattering problem is sparse, contrary to the partially dense matrix obtained using the DtN approach. Also, improving the order of approximation of the local ABC is simple. It only requires to incorporate as many terms of the Karp’s expansion as needed to reach the desired order.

2 Statement of the problem

We consider J disjoint obstacles each occupying a bounded domain with boundary Γ_j . The unbounded region in the exterior of Γ_j is denoted by Ω_j . Now, we assume that the obstacles are sufficiently separated from each other as to enclose each one with disjoint artificial boundaries \mathfrak{B}_j for $j = 1 \dots J$. These artificial boundaries are assumed to be circles. We define the computational sub-domains Ω_j^- as the region bounded internally by the obstacle boundary Γ_j and ex-

ternally by the artificial boundary \mathfrak{B}_j . The unbounded region in the exterior of \mathfrak{B}_j is denoted by Ω_j^+ so that \mathfrak{B}_j is precisely the interface between Ω_j^- and Ω_j^+ . Also consider the following definitions,

$$\begin{aligned}\Omega &= \bigcap_{j=1}^J \Omega_j, & \Omega^- &= \bigcup_{j=1}^J \Omega_j^-, \\ \Omega^+ &= \bigcap_{j=1}^J \Omega_j^+ & \text{and} & \Gamma = \bigcup_{j=1}^J \Gamma_j.\end{aligned}$$

For sake of simplicity, we assume a Dirichlet condition $u_{\text{sc}} = -u_{\text{inc}}$ on Γ , where u_{inc} is an incident field, and u_{sc} is a radiating solution to the Helmholtz equation in Ω . For clarity, we replace the BVP for u_{sc} by an equivalent interface problem where the artificial surfaces \mathfrak{B}_j become the interfaces. By defining $u_{\text{sc}}^- = u_{\text{sc}}|_{\Omega^-}$ and $u_{\text{sc}}^+ = |_{\Omega^+}$, we arrive to the following interface problem,

$$\Delta u_{\text{sc}}^- + k^2 u_{\text{sc}}^- = 0 \quad \text{in } \Omega^-, \quad (1)$$

$$\Delta u_{\text{sc}}^+ + k^2 u_{\text{sc}}^+ = 0 \quad \text{in } \Omega^+, \quad (2)$$

$$u_{\text{sc}}^- = -u_{\text{inc}} \quad \text{on } \Gamma, \quad (3)$$

$$\lim_{r \rightarrow \infty} r^{1/2} (\partial_r u_{\text{sc}}^+ - ik u_{\text{sc}}^+) = 0, \quad (4)$$

with the interface conditions,

$$u_{\text{sc}}^- = u_{\text{sc}}^+, \quad \text{and} \quad \partial_\nu u_{\text{sc}}^- = \partial_\nu u_{\text{sc}}^+ \quad (5)$$

on $\bigcup_{j=1}^J \mathfrak{B}_j$.

3 The local ABC for multiple scattering

Our derivation of the multiple absorbing condition rests upon the following fundamental decomposition theorem of u_{sc}^+ for multiple scattering problems.

Theorem 1 *Let u_{sc}^+ solve the above interface BVP. Then, u_{sc}^+ can be uniquely decomposed in Ω^+ into purely-outgoing wave fields u_j for $j = 1, 2, \dots, J$ such that $u_{\text{sc}}^+ = \sum_{j=1}^J u_j$ in Ω^+ , where u_j is a wave field in Ω_j^+ radiating from \mathfrak{B}_j .*

We note that by *purely-outgoing* field u_j , we mean a radiating solution to Helmholtz equation in all of Ω_j^+ , including the interior of all the other obstacles. This suggests a representation of u_j in Ω_j^+ as described in the next theorem.

Theorem 2 (Karp [3]) *Let u_j for $j = 1, 2, \dots, J$ be the purely-outgoing wave fields defined in Theorem 1. Then,*

$$\begin{aligned}u_j(x) &= H_0(k|x_j|) \sum_{n=0}^{\infty} \frac{F_{j,n}(\hat{x}_j)}{|x_j|^n} \\ &\quad + H_1(k|x_j|) \sum_{n=0}^{\infty} \frac{G_{j,n}(\hat{x}_j)}{|x_j|^n},\end{aligned}$$

where $x_j = x - c_j$ and c_j is the center of \mathfrak{B}_j , and $\hat{x}_j = x_j/|x_j|$. Here H_0 and H_1 are the Hankel functions of the first kind of order zero and one, resp. Moreover, the coefficients $F_{j,n}$ and $G_{j,n}$ satisfy the following recursive relations ,

$$2nG_{j,n} = (n-1)^2 F_{j,n-1} + d_\theta^2 F_{j,n-1},$$

$$2nF_{j,n} = -n^2 G_{j,n-1} - d_\theta^2 G_{j,n-1},$$

for $n \geq 1$. Also $F_{j,0}(\hat{x}_j) = F_{j,0}(-\hat{x}_j)$ (podal) and $G_{j,0}(\hat{x}_j) = -G_{j,0}(-\hat{x}_j)$ (antipodal).

The numerical computation requires to use only a finite number N of terms from Karp's series. We obtain the proposed local ABC by replacing this truncated series in our interface problem (1)–(5) along with the recursive formulas from Theorem 2 and the fact that $F_{j,0}/G_{j,0}$ is podal/antipodal.

We note that by truncating Karp's expansion at N terms, an error is introduced. This truncation error can be easily controlled by including more terms in the series. The new unknowns introduced also satisfy the recursive formula from Theorem 2 which leads to a well-determined system of equations. In other words, this extended BVP provides enough equations to fully determine the unknowns: u_{sc}^- , $F_{j,n}$, $G_{j,n}$ for $j = 1, \dots, J$ and $n = 0, 1, \dots, N-1$. In the presentation, we will discuss our numerical results for various shapes and configurations of multiple obstacles.

References

- [1] V. Villamizar, S. Acosta, B. Dastrup, High order local absorbing boundary conditions for acoustic waves in terms of farfield expansions, *J. Comput. Phys.* Accepted (2016).
- [2] M. Grote, C. Kirsch, Dirichlet-to-Neumann boundary conditions for multiple scattering problems, *J. Comput. Phys.* **201** (2004), pp. 630–650.
- [3] S.N. Karp, A convergent farfield expansion for two-dimensional radiation functions, *Comm. Pure Appl. Math.* **14** (1961), pp. 427–434.

On the Preconditioning of the Hypersingular Operator via a Dual Haar Basis in the Stabilization of the Electric Field Integral Equation

Simon Adrian^{1,*}, Francesco P. Andriulli¹, Thomas F. Eibert²

¹Ecole Nationale Supérieure Mines-Telecom Atlantique, Brest, France

²Technical University of Munich, Munich, Germany

*Email: simon.adrian@imt-atlantique.fr

Abstract

It is well-known that generalized Haar wavelets can precondition the single layer operator. This means that these functions are suitable for regularizing the scalar potential part of the electric field integral equation (EFIE). Unfortunately, however, a dual Haar basis is not regular enough to regularize the vector potential part of the EFIE if used in a naive way. In this work, we address this issue by leveraging on an explicit inverse of the dual Haar wavelet transformation matrix and on the scalar Calderón identity. We can prove that this strategy gives rise to a quasi-optimal preconditioner, i.e., the condition number grows polylogarithmically in the number of unknowns. Numerical results demonstrate the effectiveness of our approach.

Keywords: Integral equations, Haar wavelets, preconditioning

1 Introduction

Integral operators such as the single layer, the hypersingular operator, or the electric field integral equation (EFIE) operator used for the formulation of acoustic and electromagnetic problems give rise to ill-conditioned systems when discretized with a singlescale basis, that is, the condition number of the system matrix grows when the average mesh size h is decreased.

Multiscale bases are a well-known remedy for the ill-conditioning that have been successfully applied in the past [1–4]. When piecewise constant basis functions are admissible as singlescale basis (e.g., for the single layer operator), multiscale bases can be constructed for any mesh (a typical example are Haar wavelets shown in [5]). When a minimum of piecewise linear regularity is required for the singlescale basis, multiscale bases have only been shown for structured meshes, that is, meshes that are obtained by refining an initial mesh structuredly [2] (e.g., a structured refinement is obtained by connecting the midpoints of the edges of the tri-

angles of a mesh). Disadvantages of this strategy are that the condition number is at least as large as the condition number obtained from a discretization of the operator on the initial mesh, which can still be prohibitively large, and that a structured refinement does not allow to reduce the geometrical modelling error.

In this work, we show that Haar wavelets can be applied to the hypersingular operator, which requires at least piecewise linear basis functions for its discretization. To this end, we construct dual Haar wavelets using black-box graph partitioning schemes (such as METIS [6]), which differently from primal Haar wavelets are constructed on the dual mesh. For the hypersingular operator, the preconditioner is obtained by using an explicit inverse Haar wavelet transformation matrix and the Calderón identities. We can show that in the case of the hypersingular operator the condition number has a $\mathcal{O}(\log^2(1/h))$ behavior. Using a combination of primal and dual Haar wavelets, we can obtain a preconditioner for the EFIE [7].

2 Formulation

Let Γ describe the surface of a closed domain Ω . We define the single layer operator

$$\mathcal{V}\phi = \int_{\Gamma} \frac{1}{4\pi|\mathbf{r} - \mathbf{r}'|} \phi(\mathbf{r}') dS(\mathbf{r}') \quad (1)$$

and the hypersingular operator

$$\mathcal{W}\lambda = \hat{\mathbf{n}}_{\mathbf{r}} \cdot \nabla \times \int_{\Gamma} \frac{1}{4\pi|\mathbf{r} - \mathbf{r}'|} \nabla' \times \hat{\mathbf{n}}_{\mathbf{r}'} \lambda(\mathbf{r}') dS(\mathbf{r}'), \quad (2)$$

where $\hat{\mathbf{n}}_{\mathbf{r}}$ denotes the surface normal at \mathbf{r} . For simplification, we consider the modified hypersingular operator $\hat{\mathcal{W}} : H^{1/2} \rightarrow H^{-1/2}$ defined by the bilinear form

$$\left(v, \hat{\mathcal{W}}w \right)_{L^2} := (v, \mathcal{W}w)_{L^2} + (1, w)_{L^2} (1, v)_{L^2} \quad (3)$$

for all $w, v \in H^{1/2}(\Gamma)$.

Let $\tilde{p}_i \in X_p$ denote the dual piecewise constant functions (i.e., these functions are defined on the cells of the dual mesh) and $\lambda_i \in X_\lambda$ denote primal piecewise linear functions. Using a Galerkin approach we obtain the system matrix $[\tilde{\mathbf{V}}]_{ij} = (\tilde{p}_i, \mathcal{V}\tilde{p}_j)_{L^2}$ and $[\hat{\mathbf{W}}]_{ij} = (\lambda_i, \hat{\mathcal{W}}\lambda_j)_{L^2}$.

Let \mathbf{H} be the transformation matrix that maps the expansion coefficients of a function represented by Haar wavelets to the expansion coefficients of a function represented by \tilde{p}_i functions, and we define the diagonal rescaling matrix $[\mathbf{D}]_{ii} = 2^{-l(i)/2}$, where $l(i)$ returns the level on which the associated Haar function is defined. Then following [5], we have

$$\text{cond}(\mathbf{D}\mathbf{H}^T \mathbf{V} \mathbf{H} \mathbf{D}) \lesssim \log^2(1/h), \quad (4)$$

where $a \lesssim b$ means that there is a constant C independent from h such that $a \lesssim Cb$ holds.

We define the mixed Gram matrix $[\mathbf{G}_{\lambda\tilde{p}}]_{ij} = (\lambda_i, \tilde{p}_j)_{L^2}$. Then we can show the following proposition.

Proposition 1 *We find that*

$$\begin{aligned} \text{cond}(\mathbf{D}^{-1} \mathbf{H}^{-1} \mathbf{G}_{\lambda\tilde{p}}^{-1} \hat{\mathbf{W}} \mathbf{G}_{\lambda\tilde{p}}^{-T} \mathbf{H}^{-T} \mathbf{D}^{-1}) \\ \lesssim \log^2(1/h) \end{aligned} \quad (5)$$

holds.

This statement can be proven after some manipulation starting from the discretized scalar Calderón identity [8]

$$\mathbf{x}^T \tilde{\mathbf{V}} \mathbf{x} \asymp \mathbf{x}^T \mathbf{G}_{\lambda\tilde{p}}^T \hat{\mathbf{W}}^{-1} \mathbf{G}_{\lambda\tilde{p}} \mathbf{x}, \quad \forall \mathbf{x} \in \mathbb{R}^{N_{\text{Vertices}}}. \quad (6)$$

We notice that \mathbf{H}^{-1} is a sparse matrix that can be computed as

$$\mathbf{H}^{-1} = (\mathbf{H}^T \mathbf{G}_{\tilde{p}\tilde{p}} \mathbf{H})^{-1} \mathbf{H}^T \mathbf{G}_{\tilde{p}\tilde{p}} \quad (7)$$

in quasilinear complexity, with the Gram matrix $[\mathbf{G}_{\tilde{p}\tilde{p}}]_{ij} = (\tilde{p}_i, \tilde{p}_j)_{L^2}$ since the Haar wavelets are compactly supported and wavelets from different levels are orthogonal so that $\mathbf{H}^T \mathbf{G}_{\tilde{p}\tilde{p}} \mathbf{H}$ is block diagonal. For the EFIE, one would rather precondition \mathbf{W} than $\hat{\mathbf{W}}$. In this case, one would eliminate the constant Haar wavelet, which spans the entire geometry, so that \mathbf{H} becomes a rectangular matrix. Still, the right hand side in (7) can be used to obtain a pseudo-inverse.

Using a combination of primal Haar wavelets and the proposed dual inverse Haar wavelet transformation, we can also obtain a preconditioner for the EFIE as it will be shown during the talk [7].

References

- [1] P. Oswald, *Multilevel Finite Element Approximation*. Teubner, 1994.
- [2] R. Stevenson, “Piecewise Linear (pre-) Wavelets on Non-Uniform Meshes,” *Multigrid Methods V*, pp. 306–319, 1997.
- [3] H. Harbrecht, U. Kähler, and R. Schneider, “Wavelet Galerkin BEM on Unstructured Meshes,” *Computing and Visualization in Science*, vol. 8, no. 3-4, pp. 189–199, 2005.
- [4] F. P. Andriulli, A. Tabacco, and G. Vecchi, “Solving the EFIE at Low Frequencies with a Conditioning That Grows Only Logarithmically with the Number of Unknowns,” *IEEE Transactions on Antennas and Propagation*, vol. 58, no. 5, pp. 1614–1624, May 2010.
- [5] P. Oswald, “Multilevel Norms for $H^{-1/2}$,” *Computing*, vol. 61, no. 3, pp. 235–255, Sep. 1998.
- [6] G. Karypis and V. Kumar, “A Fast and High Quality Multilevel Scheme for Partitioning Irregular Graphs,” *SIAM Journal on Scientific Computing*, vol. 20, no. 1, pp. 359–392, 1998.
- [7] S. Adrian, F. Andriulli, and T. Eibert, “A Hierarchical Preconditioner for the Electric Field Integral Equation on Unstructured Meshes Based on Primal and Dual Haar Bases,” *Journal of Computational Physics*, vol. 330, pp. 365–379, Feb. 2017.
- [8] O. Steinbach and W. L. Wendland, “The Construction of Some Efficient Preconditioners in the Boundary Element Method,” *Advances in Computational Mathematics*, vol. 9, no. 1-2, pp. 191–216, 1998.

**Solving the Homogeneous Isotropic Linear Elastodynamics Equations Using Potentials.
The Case of the Free Surface Boundary Condition**

Jorge Albellal^{1,*}, Sébastien Imperiale², Patrick Joly³

¹Department of Applied Mathematics - Universidade de Santiago de Compostela

²M3DISIM - Inria and Paris-Saclay University

³POEMS - Inria and Paris-Saclay University, CNRS, ENSTA

*Email: jorge.albellal@usc.es

Abstract

We consider the numerical solution of 2D elastodynamics isotropic equations using the decomposition of the displacement fields into potentials. This appears as a challenge for finite element methods. We address here the particular question of free boundary conditions. A stable (mixed) variational formulation of the evolution problem is proposed based on a clever choice of Lagrange multipliers.

Keywords: Elastic waves, Numerical schemes.

1 Motivation and model problem

Two types of waves propagate in an isotropic elastic material: pressure waves, with velocity V_P and shear waves, with velocity $V_S < V_P$. We wish to solve numerically elastodynamics equations using scalar potentials: this is expected to be efficient when $V_S \ll V_P$ since one can adapt the discretization to each type of waves.

The case of rigid boundary conditions was treated in [1] but surprisingly, the naive extension of the method led to severe time instabilities. We propose below a solution to this problem.

Let $\Omega \subset \mathbb{R}^2$ with $\partial\Omega = \Gamma_D \cup \Gamma_N$ with Γ_N is parametrized by a curvilinear abscissa τ . Define

$$V = \{\mathbf{v} \in H^1(\Omega)^2, \mathbf{v}|_{\Gamma_D} = \mathbf{0}\}.$$

Let \mathcal{A} be the elasticity operator (curl (resp. curl) is the scalar (resp. vector) rotational)

$$\mathcal{A}\mathbf{u} = -V_P^2 \nabla \operatorname{div} \mathbf{u} + V_S^2 \operatorname{curl} \operatorname{curl} \mathbf{u}.$$

We search $\mathbf{u} \in C^1(\mathbb{R}^+; V) \cap C^0(\mathbb{R}^+; D(\mathcal{A}))$ with

$$D(\mathcal{A}) = \{\mathbf{u} \in V, \mathcal{A}\mathbf{u} \in L^2(\Omega)^2, \sigma(\mathbf{u})\mathbf{n}|_{\Gamma_N} = \mathbf{0}\}$$

with $\sigma(\mathbf{u})\mathbf{n} := (V_P^2 - 2V_S^2) \operatorname{div} \mathbf{u} \mathbf{n} + 2V_S^2 \varepsilon(\mathbf{u}) \mathbf{n}$ and $\varepsilon(\mathbf{u})$ the strain tensor.

The evolution problem reads

$$\partial_t^2 \mathbf{u} + \mathcal{A}\mathbf{u} = \mathbf{0}, \quad (1)$$

completed with initial data $(\mathbf{u}_0, \mathbf{u}_1)$.

2 Potential Formulation

We define $\phi = (\varphi_P, \varphi_S)^t$ such that

$$\partial_t \varphi_P := V_P^2 \operatorname{div} \mathbf{u} \quad \text{and} \quad \partial_t \varphi_S := -V_S^2 \operatorname{curl} \mathbf{u},$$

so that it results from (1) that

$$\partial_t \mathbf{u} = \nabla \varphi_P + \operatorname{curl} \varphi_S \text{ in } \Omega \times \mathbb{R}^+. \quad (2)$$

Taking the div and curl of (2), we get

$$\partial_t^2 \varphi_P - V_P^2 \Delta \varphi_P = 0 \text{ in } \Omega \times \mathbb{R}^+, \quad (3)$$

$$\partial_t^2 \varphi_S - V_S^2 \Delta \varphi_S = 0 \text{ in } \Omega \times \mathbb{R}^+. \quad (4)$$

Moreover from equation (2) we see that

$$\phi(t) = (\varphi_P(t), \varphi_S(t))^t,$$

should be looked for in (below $\psi = (\psi_P, \psi_S)^t$)

$$W = \{ \psi \in L^2(\Omega)^2, \nabla \psi_P + \operatorname{curl} \psi_S \in L^2(\Omega)^2$$

i.e. $W = H(\operatorname{div}; \Omega) \cap H(\operatorname{curl}; \Omega)$, which is a Hilbert space equipped with its natural norm.

Theorem 1 *The field $\phi \in C^1(\mathbb{R}^+; W^0)$, where*

$$W^0 = \{ \psi \in W, \int_{\Gamma_N} \psi \times \mathbf{n} d\tau = \int_{\Gamma_N} \psi \cdot \mathbf{n} d\tau = 0 \},$$

is a closed subspace of W and ϕ satisfies,

$$\frac{d^2}{dt^2} m(\phi(t), \psi) + a(\phi(t), \psi) = 0, \quad \forall \psi \in W^0, \quad (5)$$

with $a(\phi, \psi)$ the symmetric positive bilinear form

$$a(\phi, \psi) = \int_{\Omega} [\nabla \varphi_P + \operatorname{curl} \varphi_S] \cdot [\nabla \psi_P + \operatorname{curl} \psi_S]$$

and $m(\phi, \psi)$ the symmetric bilinear form

$$m(\phi, \psi) = m_{\Omega}(\phi, \psi) + m_N(\phi, \psi)$$

$$\text{with } m_{\Omega}(\phi, \psi) = V_P^{-2} \int_{\Omega} \varphi_P \psi_P + V_S^{-2} \int_{\Omega} \varphi_S \psi_S,$$

$$\text{and } m_N(\phi, \psi) = \frac{1}{2V_S^2} [\langle \phi, \psi \rangle_N + \langle \psi, \phi \rangle_N] \text{ where}$$

$$\langle \phi, \psi \rangle_N := \int_{\Gamma_N} \left(\int_0^\tau \phi \cdot \mathbf{n} \right) \times \mathbf{n} d\tau.$$

The major problem with the variational problem (5) is that $m(\cdot, \cdot)$ has indefinite sign in W^0 . This explains why natural Galerkin discretizations lead to the instabilities observed in [1].

3 A well-posed variational formulation

In order to get a stabilized version of (5), it appears sufficient to restrict the space in which the solution ϕ is sought to an adequate subspace of W^0 . To characterize this subspace we introduce the operator

$$\begin{aligned} \mathcal{T}: \quad W^0 &\longrightarrow W^0 \\ (\varphi_P, \varphi_S)^t &\mapsto (V_P^2 \operatorname{div} \mathbf{v}, -V_S^2 \operatorname{curl} \mathbf{v})^t \end{aligned}$$

with $\mathbf{v} \in D(\mathcal{A})$ the unique solution of the elastostatic problem $-\mathcal{A}\mathbf{v} = \nabla\varphi_P + \operatorname{curl} \varphi_S$.

Lemma 2 \mathcal{T} is a bounded linear projector, i.e. $\mathcal{T}^2 = \mathcal{T}$ and one has the decomposition

$$W^0 = W_N^0 \oplus \operatorname{Ker} \mathcal{T}, \quad W_N^0 = \operatorname{Ker}(\mathcal{I} - \mathcal{T}).$$

Note that in the result below the decomposition is not orthogonal for the natural scalar product in W^0 (see however lemma 6). The space W_N^0 plays a special role because of the following results.

Lemma 3 The potentials satisfy $\partial_t \phi \in W_N^0$.

This lemma allows us to prove that

Theorem 4 The problem (5) is equivalent to

$$\begin{aligned} \text{Find } \phi \in C^1(\mathbb{R}^+; W_N^0) / \forall \psi \in W_N^0, \\ \frac{d^2}{dt^2} m(\phi(t), \psi) + a(\phi(t), \psi) = 0. \end{aligned} \tag{6}$$

Finally, the fact that (6) is now a nice well-posed variational problem results from the

Lemma 5 There exists $c > 0$ such that

$$c \|\psi\|_{L^2(\Omega)^2}^2 \leq m(\psi, \psi), \quad \forall \psi \in W_N^0.$$

4 Numerical approximation

Lemma 5 guarantees the stability of any Galerkin approximation of (6). The problem from a numerical point is that it is difficult to build a good Galerkin approximation space (such as a finite element space) of W_N^0 . Therefore the approach we suggest is to look for ϕ in W^0 , which admits nice approximation finite element spaces, and to enforce that the solution belongs

to W_N^0 by introducing an appropriate Lagrange multiplier. This strategy is based on the following result which says that the decomposition of lemma 6 is “orthogonal” with respect to the bilinear form $m(\cdot, \cdot)$:

Lemma 6 If $(\phi, \psi) \in W_N^0 \times \operatorname{Ker} \mathcal{T}$, $m(\phi, \psi) = 0$. Furthermore, if $\phi \in W^0$ is such that

$$\forall \psi \in \operatorname{Ker} \mathcal{T}, \quad m(\phi, \psi) = 0,$$

then $\phi \in W_N^0$.

As a consequence, the variational problem (6) is equivalent to the mixed variational problem : find $(\phi(t), \lambda(t)) : \mathbb{R}^+ \rightarrow W^0 \times \operatorname{Ker} \mathcal{T}$ such that for any $(\psi, \mu) \in W^0 \times \operatorname{Ker} \mathcal{T}$

$$\left\{ \begin{array}{l} \frac{d^2}{dt^2} m(\phi(t), \psi) + a(\phi(t), \psi) \\ \quad + m(\lambda(t), \psi) = 0, \\ m(\phi(t), \mu) = 0. \end{array} \right. \tag{7}$$

One is thus reduced to find a good approximation space for $\operatorname{Ker} \mathcal{T}$, which is easier than for W_N^0 thanks to the following

Lemma 7 The space $\operatorname{Ker} \mathcal{T}$ is isomorphic to $H^{-1/2}(\partial\Omega)$. Moreover the isomorphism is known explicitly and easy to approximate with finite elements.

As a consequence, one constructs a basis for a Galerkin subspace of $\operatorname{Ker} \mathcal{T}$ from the basis of a standard finite element approximation space for $H^{-1/2}(\partial\Omega)$.

The implementation of the corresponding numerical method is in progress. Numerical results will be presented at the conference.

References

- [1] A. Burel, Contributions à la simulation numérique en élastodynamique : découplage des ondes P et S, modèles asymptotiques pour la traversée de couches minces, Thèse de doctorat, 2014.

3D metric-based anisotropic mesh adaptation for the fast multipole accelerated boundary element method in acoustics

F. Amlani^{1,*}, S. Chaillat¹, S.P. Groth¹, A. Loseille²

¹POEMS, ENSTA, Université Paris-Saclay, Palaiseau, France

²Project Team Gamma, INRIA Paris-Saclay, Palaiseau, France

*Email: faisal.amlani@ensta.fr

Abstract

We introduce a metric-based anisotropic mesh adaptation strategy for the fast multipole accelerated boundary element method (FM-BEM) applied to exterior boundary value problems of the three-dimensional Helmholtz equation. The present methodology is independent of discretization technique and iteratively constructs meshes refined in size, shape and orientation according to an “optimal” metric reliant on a reconstructed Hessian of the boundary solution. The resulting adaptation is anisotropic in nature and numerical examples demonstrate optimal convergence rates for domains that include geometric singularities such as corners and ridges.

Keywords: acoustic scattering, boundary element methods, anisotropic mesh adaptation, fast multipole method

1 Introduction

We consider the scattering of an incident acoustic field $u^i(\mathbf{x})$ (characterized by the wavenumber k) by a bounded domain $\Omega \subset \mathbb{R}^3$ with boundary $\Gamma = \partial\Omega$ and unit normal \mathbf{n} outward to Ω . The corresponding scattered field $u^s(\mathbf{x})$ exterior to the obstacle is a solution to the time-harmonic scalar wave equation

$$\nabla^2 u^s + k^2 u^s = 0 \quad \mathbf{x} \in \mathbb{R}^3 \setminus \Omega \quad (1)$$

satisfying either Dirichlet (i.e. $u^s = -u^i$) or Neumann (i.e. $\partial u^s / \partial \mathbf{n} = -\partial u^i / \partial \mathbf{n}$) boundary conditions on Γ , as well as the Sommerfeld radiation condition at infinity. Problems can be formulated as boundary integral equations (BIEs) whose corresponding numerical solutions are constructed by boundary element methods (BEMs). The main advantages of BEMs is that their formulations exactly account for the radiation conditions and restrict the discretization of the domain to that of the boundary alone. Standard BEMs, however, lead to dense and (possibly) nonsymmetric linear systems whose solutions become prohibitively expensive for large-scale

problems. Fast multipole methods (FMM) overcome this drawback by enabling drastic reduction in solution time and memory requirements.

Further improvements of accuracy and computation time can be made by employing adapted meshes. Such strategies optimize the placement of the degrees of freedom to better capture solutions with anisotropic features as well as discontinuities in the acoustic field near geometric singularities such as corners or ridges. Fewer studies on these strategies have been made for BEMs, and most current BEM adaptation strategies, like those relying on Dörfler marking, have been confined to isotropic techniques. These methods are unable to recover optimal orders of accuracy and have been restrictive to Galerkin discretization techniques as well as the particular underlying equations. The focus of this work is to introduce and extend an anisotropic mesh adaptivity strategy [3] in the context of FM-BEM that addresses these issues by using a metric-based error estimator whose effectiveness has been demonstrated for volumetric (finite element) methods but not for BEMs.

2 Metric-based mesh adaptation

To find an optimal mesh that achieves a desired level of accuracy and convergence we use the following iterative procedure:

Coarse initialization step. Generate an initial uniform mesh $\mathcal{T}_i = \mathcal{T}_0$ with $N_i = N_0$ vertices for the surface Γ . The parameter N_0 can be chosen, for example, by requiring elements to have widths of approximately $\lambda/2$ (where $\lambda = 2\pi/k$).

Step 1. Compute a BEM approximation $u_{N_i}^s$ on the mesh with boundary element basis functions $\{\psi_j\}_{j=1}^{N_i}$.

Step 2. Associate with \mathcal{T}_i a Riemannian metric space $\mathbf{M} = (\mathcal{M}(\mathbf{x}))_{\mathbf{x} \in \Gamma}$, where \mathcal{M} is the metric tensor whose value at each vertex dictates the size and orientation of adjacent elements upon adaptation. Defining \hat{u}^s to be the second-

order Taylor expansion of the exact solution u^s around a mesh vertex, $\Pi_N u^s$ the linear interpolant of u^s on the mesh \mathcal{T}_i with elements K , we extend to the use of boundary solutions the results of [3] so that the total interpolation error

$$\sum_{K \in \mathcal{T}_i} \|\hat{u}^s - \Pi_N u^s\|_{L^2(K)} \leq 2 \int_{\Gamma} \text{trace} \left(\mathcal{M}^{-\frac{1}{2}} H \mathcal{M}^{-\frac{1}{2}} \right) d\Gamma \quad (2)$$

is minimized by a mesh generated by the metric

$$\mathcal{M}_{L^2} = N \left(\int_{\Gamma} \det(|H|)^{\frac{1}{3}} \right)^{-1} \det(|H|)^{-\frac{1}{6}} |H|. \quad (3)$$

Here, H is a symmetric matrix representing the Hessian of u^s and is computed at a vertex from the approximate solution u_N^s by the expression

$$(H)_{ij} = -\frac{3}{|K|} \sum_{K \in \mathcal{T}_i} \left(\frac{\partial u_N^s}{\partial x_i} \right)_K \int_K \frac{\partial \psi_{k \in K}}{\partial x_j} dx. \quad (4)$$

Step 3. Construct a new mesh \mathcal{T}_{i+1} with vertices $N_{i+1} = 2N_i$ that is *quasi-unit* with respect to the optimal metric computed from (3), i.e. seek triangles K with edges $\{\mathbf{e}_i\}_{i=1}^3$ such that $\frac{1}{\sqrt{2}} \leq \|\mathbf{e}_i\|_{\mathcal{M}} \leq \sqrt{2}$, $i = 1, 2, 3$ and $|K|_{\mathcal{M}} \simeq \frac{\sqrt{3}}{4}$.

Step 4. Iterate over Steps 1-4 until a specified maximum number of vertices N is surpassed.

3 Validation of the adaptive mesh strategy with numerical examples

The proposed strategy constructs adapted meshes that can recover optimal convergence rates for domains with corners and ridges. Figure 1 shows a mesh after four adapting iterations—with clear refinement at the edges—for the exterior Dirichlet problem of the scattering of an incident plane-wave ($k = 5$) by a cube with a cavity. The Hessian and metric tensor of Step 2 are computed by METRIX [3] and the mesh construction of Step 3 by the AMG library [4]. The approximate solution in Step 1 employs a \mathbb{P}_1 -element discretization for a BEM whose efficient solution is facilitated by the fast multipole method [5]. The relative L^2 -errors for the scattered field with varying degrees of freedom, depicted in Figure 2, indicate a reduced convergence order for a uniform refinement due to edge singularities of the obstacle. On the other hand, the anisotropic refinement is shown to recover the optimal convergence rate of $\mathcal{O}(n^{-1})$.

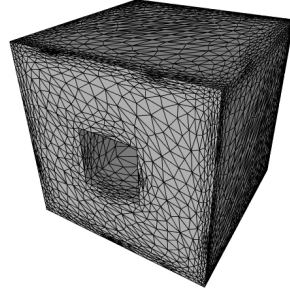


Figure 1: Adapted mesh at the fourth step of adaptation for the cube with cavity.

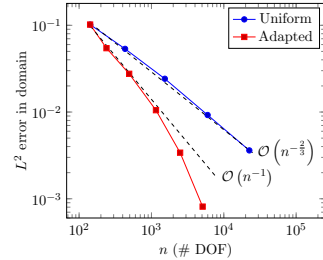


Figure 2: Relative L^2 -errors for uniform and anisotropic refinement of the example.

References

- [1] M. Aurada, S. Ferraz-Leite and D. Praetorius, Estimator reduction and convergence of adaptive BEM, *Applied Numerical Mathematics* **62** (2012), pp. 787-801.
- [2] S. Ferraz-Leite and D. Praetorius, Simple a posteriori error estimators for the h-version of the boundary element method, *Computing* **83** (2008), pp. 135-162.
- [3] A. Loseille and F. Alauzet, Optimal 3D highly anisotropic mesh adaptation based on the continuous mesh framework, *Proc. in 18th International Meshing Roundtable, Salt Lake City, USA, Oct 2009*, pp. 575-594
- [4] A. Loseille and R. Löhner, Adaptive anisotropic simulations in Aerodynamics, *48th AIAA Aerospace Sciences Meeting, Orlando, USA, Jan 2010*.
- [5] E. Darve, The fast multipole method: Numerical implementation, *J. Comput. Physics* **160** (2000), pp. 195-240.

A Fourier Continuation-based solver for 3D elastic wave propagation

F. Amlani^{1,*}, O. Bruno²

¹POEMS, ENSTA, Université Paris-Saclay, Palaiseau, France

²Computing & Mathematical Sciences, California Institute of Technology (Caltech), Pasadena, USA

*Email: faisal.amlani@ensta.fr

Abstract

We present a spectral numerical algorithm for the fast solution of elastodynamics problems in general 3D domains based on a FFT-speed Fourier Continuation (FC) approximation for accurate Fourier expansion of non-periodic functions. The high-order methodology yields physically correct solutions including those with traction conditions on curved boundaries. The approach is essentially without dispersion errors; entails mild CFL constraints; runs at a cost scaling linearly with discretization size; and can be efficiently parallelized for computing clusters.

Keywords: Fourier Continuation, elastic wave equation, high-performance numerical methods

1 Introduction

This work considers the propagation of elastic waves in a linear, isotropic, possibly heterogeneous medium contained in a general domain $\Omega \in \mathbb{R}^3$ and governed by the Navier equation

$$\begin{aligned} \rho(\mathbf{x})\mathbf{u}_{tt}(\mathbf{x}, t) = \nabla \cdot [\mu(\mathbf{x}) (\nabla \mathbf{u}(\mathbf{x}, t) + \nabla \mathbf{u}^T(\mathbf{x}, t)) \\ + \lambda(\mathbf{x}) (\nabla \cdot \mathbf{u}(\mathbf{x}, t)) I] + \mathbf{f}(\mathbf{x}, t) \end{aligned} \quad (1)$$

for position and displacement vectors \mathbf{x} and \mathbf{u} ; Lamé parameters $\mu(\mathbf{x}), \lambda(\mathbf{x})$; density $\rho(\mathbf{x})$; and a given vector of body forces $\mathbf{f}(\mathbf{x}, t)$. Initial conditions $\mathbf{u}(\mathbf{x}, t_0), \mathbf{u}_t(\mathbf{x}, t_0)$ are prescribed at initial time $t = t_0$, and the boundary $\partial\Omega$ is partitioned as a union $\partial\Omega = \Gamma_D \cup \Gamma_T$ of two surfaces Γ_D and Γ_T upon which boundary displacements and boundary tractions,

$$\begin{aligned} \mathbf{u} = \mathbf{c}(\mathbf{x}, t) &\quad \text{on } \Gamma_D \quad \text{and} \\ \boldsymbol{\sigma} \cdot \mathbf{n} = \mathbf{d}(\mathbf{x}, t) &\quad \text{on } \Gamma_T, \end{aligned}$$

are prescribed, where \mathbf{n} is the inward unit normal and $\boldsymbol{\sigma}$ is the (symmetric) stress tensor for an isotropic medium.

2 Methodology

Accelerated FC(Gram). The FC method [1, 2] enables high-order convergence of Fourier series

approximations of non-periodic functions by solving the Gibbs “ringing” effect, extending the applicability of classical Fourier-based PDE solvers (together with their inherent qualities, e.g. limited dispersion, high-order accuracy and mild CFL conditions) to problems with general domains and boundary conditions. Given point values $f(x_i)$ of a function $f : [0, 1] \rightarrow \mathbb{R}$ on a uniform grid $x_i = i/(N - 1)$, $i = 0, \dots, N - 1$, the FC method produces a rapidly-convergent interpolating Fourier series representation $f^c : [0, b] \rightarrow \mathbb{R}$ on a region $[0, b]$ larger than the physical domain $[0, 1]$ as

$$f^c(x) = \sum_{k=-M}^M a_k e^{\frac{2\pi i k x}{b}} \quad \text{s.t. } f^c(x_i) = f(x_i), \quad (2)$$

for suitably chosen FC-parameters M (bandwidth) and $b > 1$ (interval length). The b -periodic continuation function f^c is an approximate *periodic extension* of f that closely approximates f in $[0, 1]$. Derivatives for a PDE solver can be then produced with high-order accuracy by term-wise differentiation. We base the construction of (2) on a “biased-order” technique [1] that uses numbers d_ℓ and d_r of function values near the left and right endpoints 0 and 1, together with projections of the corresponding vectors of function values onto a Gram polynomial basis—whose continuations are precomputed by means of high-precision linear algebra methods. This is then extended to a form suitable for use in traction conditions [2].

Geometry and parallelization. Physically realistic configurations with curved geometries are treated by an overset method [3] that decomposes Ω into a union $\Omega = \bigcup_j \Omega_j$ of a finite number of overlapping, boundary-conforming curvilinear patches—endowed with uniform Cartesian-like discretizations—within each one of which a curvilinear formulation of (1) is evolved. Information is exchanged via interpolation, and sharp corners and edges are approximated by rounded patches. Further decomposition of each patch Ω_j into mutually disjoint sub-patches, to-

gether with the use of certain “line-segmented” FC operators (which produce very efficient calculation of the corresponding optimally-sized discrete Fourier transforms), enables a parallelization for distributed-memory computing environments that achieves excellent scalability [2].

3 Numerical experiments

These examples utilize an explicit fourth-order Adams-Bashforth scheme (AB4) in time and a fixed number of 25 discrete points in the periodic extension to construct continuations for fourth-order Gram polynomials ($d_\ell, d_r = 5$). Further parameters and studies are detailed in [2].

A convergence study. A solid cylinder composed of two patches is prescribed with body forces and traction boundary conditions corresponding to a known solution (see [2]). The table below reports the max errors in displacement over all time and space, where fifth-order accuracy can be appreciated.

N (patch Ω_1)	N (patch Ω_2)	L_{err}^∞	$O(L_{\text{err}}^\infty)$
27,000	72,000	2.82e-03	—
216,000	576,000	8.29e-05	5.09
729,000	1,944,000	9.37e-06	5.38
1,728,000	4,608,000	2.00e-06	5.37

A parallel performance study. The table below reports errors and CPU-seconds per million unknowns (denoted S) for propagation in a 3D aluminum plate with a circular hole modeled by six different curvilinear patches. Nearly perfect scalability is achieved as the number of cores is increased for a fixed number of grid points.

# grid pts	# cores	L_{err}^∞	S
3,033,360	240	7.89e-3	1.51 sec
—	360	7.98e-3	1.55 sec
—	480	8.32e-3	1.45 sec

A dispersion study. Plane-waves of various numbers W of wavelengths are advanced through a 3D aluminum plate with traction boundary conditions. Figure 1 shows the max errors over all space and over one full temporal cycle (defined as the time required for any one crest to travel the length of the plate) of the solution for increasing W . For each fixed number of points-per-wavelength (PPW), the accuracy of the FC solver remains essentially constant, suggesting that the use of large numbers of sub-domains and sub-patches does not give rise to significant dispersion (up to 512 cores are employed for the highest values of W).

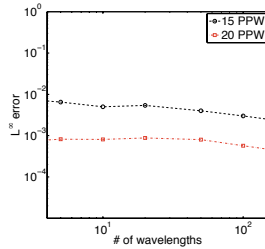


Figure 1: Errors over a cycle for varying W .

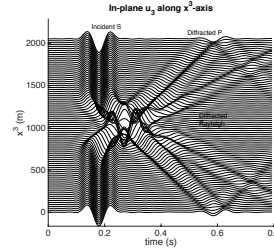


Figure 2: Simulated response of an earthquake.

A classical seismology problem. Wave amplification by a 180m hill in a 3D region impacted by an incident shear (S-)wave is depicted in the seismogram of Figure 2 using the FC-based elasticity solver and a traction-free boundary condition at the surface. The high-definition solutions are constructed in 58 seconds on 96 cores of a high-performance cluster using just shy of 150,000 volumetric discretization points—significantly coarser than a high-order spectral element method (4,935,953 points) and a stable difference method (109,808,412 points) [2].

References

- [1] N. Albin and O.P. Bruno, A spectral FC solver for the compressible Navier-Stokes equations in general domains I: Explicit time-stepping, *J. Comput. Physics* **230** (2011), pp. 6248-6270.
- [2] F. Amlani and O.P. Bruno, An FC-based spectral solver for elastodynamic problems in general three-dimensional domains, *J. Comput. Physics* **307** (2016), pp. 333-354.
- [3] W.D. Henshaw and D. Schwendeman, Parallel computation of three-dimensional flows using overlapping grids with adaptive mesh refinement, *J. Comput. Physics* **227** (2008), pp. 7469-7502.

Optoelectronic finite-element simulations of nonhomogeneous thin-film solar cells

Tom H. Anderson¹, Akhlesh Lakhtakia², Tom G. Mackay^{2,3}

¹University of Delaware, Department of Mathematical Sciences, 501 Ewing Hall, Newark, DE 19716, USA

²Pennsylvania State University, Department of Engineering Science and Mechanics, NanoMM—Nanoengineered Metamaterials Group, 212 EES Building, University Park, PA 16802, USA

³University of Edinburgh, School of Mathematics and Maxwell Institute for Mathematical Sciences, Edinburgh EH9 3FD, UK

Abstract

A two-dimensional COMSOL model was developed to simulate the optoelectronic properties of amorphous silicon, thin-film, *p-i-n* junction, solar cells. The *i*-layers were periodically nonhomogeneous in the thickness direction, while the *p*-layer was backed by a periodically corrugated metallic back reflector. The charge carrier generation rate was calculated using the frequency-domain Maxwell postulates. Steady-state drift-diffusion equations were solved to calculate the current density-voltage curve. Use of a periodically corrugated back reflector and the inclusion of a periodic bandgap profile increased total efficiency by up to 17% compared to solar cell without these features.

Keywords: COMSOL modelling, Hydrogenated Amorphous Silicon, Nonhomogeneous, Optoelectronic, Periodic Grating, p-i-n Junction, Solar Cell, Surface Plasmon-Polariton, Thin Film, Simulation

1 Background

A periodic back reflector (PBR) [1] can couple incident light to surface-plasmon-polariton (SPP) waves [2] and waveguide modes [3] in solar cells. If the solar cell has periodically varying dielectric properties in the thickness direction, multiple SPP waves and waveguide modes can be excited at a multitude of free-space wavelengths [4]. This phenomenon can increase photonic absorption and, therefore, electron-hole-pair generation.

By changing the amount of carbon or germanium included, hydrogenated amorphous silicon (a-Si:H) alloys with a bandgap $E_g \in (1.3, 1.95)$ can be produced. The bandgap can be related to a complex-valued optical permittivity spectrum via function that is Kramers-Kronig consistent [5]. A bandgap that is periodically non-

homogeneous may also facilitate charge-carrier extraction and reduce electron-hole recombination [6].

A two-dimensional optoelectronic model [7] was developed in COMSOL [8] to simulate the total efficiency of these a-Si:H, *p-i-n* junction, solar cells. First, the optical charge-carrier generation profile is calculated by employing the frequency-domain Maxwell postulates. Next, steady-state drift-diffusion equations are solved to calculate the current density-voltage characteristics.

2 Model Design

The solar cell design presented in this paper comprises a nonhomogeneous a-Si:H *p-i-n* junction between an aluminium zinc oxide (AZO) window and a PBR made from silver and AZO. The PBR is periodic along the *x* axis, while the *z* axis is aligned with the thickness direction of the solar cell. The thicknesses of the *n*- and *p*-layers were fixed at $L_n = L_p = 15$ nm, while several different configurations for *i* layer of thickness L_i were investigated. The AZO window thickness $L_w = 100$ nm was chosen to reduce optical reflection, while the PBR parameters were chosen to maximize total efficiency. A PBR with a duty cycle of 0.5, a maximum thickness of 120 nm, a minimum thickness of 100 nm, a period of 400 nm, and a grating relief of 80 nm, is known to improve photonic absorption in the solar spectrum [1].

Wide bandgaps of 1.95 eV were chosen for the *n*- and *p*-layers to aid photonic absorption [6]. The bandgap profile in the *i*-layer was given by

$$E_g(z) = E_{g0} + A \left\{ \frac{1}{2} \left[\sin \left(2\pi K \frac{z - L_p}{L_i} - 2\pi\psi \right) + 1 \right] \right\}^\alpha,$$

where E_{g0} is the minimum bandgap in the *i* layer, A is the amplitude of the perturbation from the

homogeneous case, $\psi \in [0, 1)$ is a phase shift, K is the number of periods of the perturbation, and $\alpha > 0$ is a shaping parameter.

3 Results

From a series of studies [7], we concluded that $\alpha = 5$, $E_{g0} = 1.6$ eV, $K = 2$, and $\psi = 0.75$ enhance total efficiency. The most efficient a-Si:H *p-i-n* junction solar cell studied, with total efficiency $\eta \approx 12.1\%$, has $L_i = 200$ nm and $A = 0.35$ eV. This is 17% higher than an analogous solar cell without these features. The relative total efficiency increases monotonically for $L_i \in \{500, 80\}$ nm. For thinner solar cells, total efficiency is initially seen to decrease as A increases, before ultimately improving efficiency in all cases for sufficiently large A .

As demonstrated through our model, the coupled optical and electronic performance of the solar cell must be rigorously considered. Furthermore, the facility to accommodate periodic nonhomogeneity in the *i*-layer allows for potential efficiency gains associated with increased electron-hole pair generation due to excitation of multiple guided-wave modes. Although a substantial increase in efficiency was found to be attributable to the presence of a PBR and a nonhomogeneous *i* layer, the solar-cell design studied and the materials used were not optimized for efficiency. Higher efficiencies may be anticipated for optimized solar-cell designs, but this remains a matter for future investigation.

References

- [1] M. Solano, M. Faryad, A. S. Hall, T. E. Mallouk, P. B. Monk, and A. Lakhtakia, “Optimization of the absorption efficiency of an amorphous-silicon thin-film tandem solar cell backed by a metallic surface-relief grating,” *Appl. Opt.* **52** (2013), pp. 966–979; errata: **54** (2015), pp. 398–399.
- [2] J. A. Polo Jr., T. G. Mackay, and A. Lakhtakia, *Electromagnetic Surface Waves: A Modern Perspective*, Elsevier, Waltham, MA, USA, 2013.
- [3] T. Khaleque and R. Magnusson, “Light management through guided-mode resonances in thin-film silicon solar cells,” *J. Nanophoton.* **8** (2014), art. no. 083995.
- [4] M. Faryad and A. Lakhtakia, “Enhancement of light absorption efficiency of amorphous-silicon thin-film tandem solar cell due to multiple surface-plasmon-polariton waves in the near-infrared spectral regime,” *Opt. Eng.* **52** (2013), art. no. 087106; errata: **53** (2014), art. no. 129801.
- [5] A. S. Ferlauto, G. M. Ferreira, J. M. Pearce, C. R. Wronski, and R. W. Collins, “Analytical model for the optical functions of amorphous semiconductors from the near-infrared to ultraviolet: Applications in thin film photovoltaics,” *J. Appl. Phys.* **92** (2002), pp. 2424–2436.
- [6] M. I. Kabir, S. A. Shahahmadi, V. Lim, S. Zaidi, K. Sopian, and N. Amin, “Amorphous silicon single-junction thin-film solar cell exceeding 10% efficiency by design optimization,” *Int. J. Photoenergy* (2012), art. no. 460919.
- [7] T. H. Anderson, M. Faryad, T. G. Mackay, A. Lakhtakia, and R. Singh, “Combined optical-electrical finite-element simulations of thin-film solar cells with homogeneous and nonhomogeneous intrinsic layers,” *J. Photon. Energy* **6** (2016), art. no. 025502.
- [8] “COMSOL Multiphysics (V5.1)” www.comsol.com (accessed 19 January 2017).

An Energy Based Discontinuous Galerkin Method for Hamiltonian Systems

Daniel Appelö^{1,*}, Thomas Hagstrom², Anastassiya Semenova¹

¹Department of Mathematics and Statistics, University of New Mexico, Albuquerque, USA

²Department of Mathematics, Southern Methodist University, Dallas, USA

*Email: appelo@math.unm.edu

Abstract

We present a new energy based discontinuous Galerkin method for Hamiltonian systems. Numerical experiments illustrating the properties of the method when applied to Kortevég de Vries equation are also presented.

Keywords: Discontinuous Galerkin, Hamiltonian systems.

1 Introduction

Fundamental to many models in physics is the Hamiltonian $\mathcal{H}[u] = \int H[u]dx$, where the solution u is governed by the equation:

$$\frac{\partial u}{\partial t} = J \frac{\delta \mathcal{H}}{\delta u}.$$

Here J is a skew-adjoint Poisson operator, for example i , the imaginary number in Schrödinger's equation, or simply the spatial derivative $\frac{\partial}{\partial x}$ in the case of the scalar transport equation $u_t = u_x$. The notation $\frac{\delta \mathcal{H}}{\delta u}$ denotes the functional derivative of the Hamiltonian.

Perhaps the most prominent characteristics of a Hamiltonian system is the conservation of \mathcal{H} in time. Assuming homogenous boundary conditions we find

$$\frac{d}{dt} \int H[u]dx = \int \frac{\delta \mathcal{H}}{\delta u} \frac{\partial u}{\partial t} dx = \int \frac{\delta \mathcal{H}}{\delta u} J \frac{\delta \mathcal{H}}{\delta u} dx = 0.$$

Inspired by our formulation of energy based discontinuous Galerkin (dG) methods for wave equations in second order form, [1], we propose the dG discretization defined by the variational equations (3)-(5) on an element.

In (3)-(5) lowercase letters denote approximations to the solution u and the auxiliary variables \dot{u}, r . Upper case letters denote test functions: U, \dot{U}, R from the same space (typically piecewise polynomials). The variational equations are constructed so that if one replaces the test functions with the solution and auxiliary variables the following energy identity is obtained after canceling cross terms

$$\int_{\Omega_j} \frac{\partial H}{\partial u_x} \frac{\partial u_x}{\partial t} + \frac{\partial H}{\partial u} \frac{\partial u}{\partial t} - r J r dx = \left[\frac{\partial H}{\partial u_x} (\dot{u}^* - \dot{u}) + \dot{u} \frac{\partial H^*}{\partial u_x} + r F(r^*) \right]_{\partial \Omega_j} \quad (1)$$

To obtain an energy conserving method the numerical fluxes must be chosen. The specific choice depends on the Hamiltonian and the Poisson operator but are typically either of central or alternating type, similar to those used for second order systems in [1].

2 Application to Korteweg de Vries

As an example we consider the Korteweg-de Vries (KdV) equation

$$u_t + uu_x + \varepsilon^2 u_{xxx} = 0. \quad (2)$$

There is no unique choice for the Hamiltonian and Poisson operator for KdV but one possible option is the Hamiltonian

$$\mathcal{H}[u] = \int_{\Omega} \frac{u^3}{6} - \frac{(\varepsilon u_x)^2}{2} dx,$$

and the simple Poisson operator $J = -\frac{\partial}{\partial x}$.

$$\int_{\Omega_j} \left(-\frac{\partial}{\partial x} \frac{\partial H[U]}{\partial U_x} + \frac{\partial H[U]}{\partial U} \right) \left(\frac{\partial u}{\partial t} - \dot{u} \right) dx = \left[\frac{\partial H[U]}{\partial U_x} \left(\dot{u}^* - \frac{\partial u}{\partial t} \right) \right]_{\partial \Omega_j}, \quad (3)$$

$$\int_{\Omega_j} \dot{U} r - \dot{U}_x \frac{\partial H[u]}{\partial u_x} - \dot{U} \frac{\partial H[u]}{\partial u} = \left[\dot{U} \left(\frac{\partial H[u]}{\partial u_x} \right)^* \right]_{\partial \Omega_j}, \quad (4)$$

$$\int_{\Omega_j} R(\dot{u} - Jr) = [RF(r^*)]_{\partial \Omega_j}. \quad (5)$$

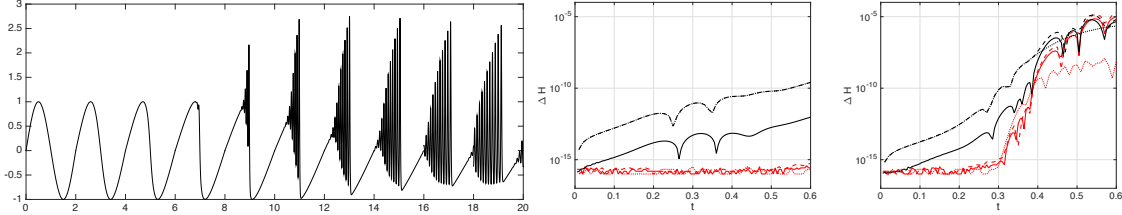


Figure 1: **Left:** Snapshots of the formation of a dispersive shock in KdV. Each snapshot is 2 units wide and are taken at times $t = 0, 0.1, 0.2, \dots$. As the initial cosine wave breaks a dispersive shock forms. **Right:** Conservation of the the Hamiltonian \mathcal{H} (in black) and $\|u\|_2^2$ (in red). The results to the left / right are for $\varepsilon = 0.033 / 0.011$ and for 6 (dashed) and 7 (dotted) elements and 60 time steps and for 6 elements and 120 time steps (solid).

With this choice we can take the numerical fluxes for equations (3) and (4) as the average between the inside and outside state, and the numerical flux in (5) as the outside state

$$\left(\frac{\partial H[u]}{\partial u_x} \right)^* = \{\{u_x\}\}, \quad \dot{u}^* = \{\{\dot{u}\}\}, \quad r^* = r^+.$$

With these numerical fluxes and upon an integration by parts for half of the term rJr the contribution to the right hand side in (1) vanishes. At first the sequence of approximations $u_t \approx \dot{u} \approx J_r \approx J \frac{\delta \mathcal{H}}{\delta u}$ may appear overly complex but it is necessary to make the volume cross terms cancel, ensuring that equality (1) holds.

3 A Numerical Example

To illustrate the method we consider eq. (2) on $x \in [0, 2]$ with periodic boundary conditions and with the initial data $u(x, 0) = \cos(\pi(x - 1/2))$.

The quadratic nonlinear term causes the cosine wave to steepen but before the wave breaks the dispersive term regularizes the shock by creating multiple narrower waves that carries energy away from the shock front, see for example the thesis of Baldwin [3]. A smaller ε results in more and narrower waves running away from the shock. We consider two values for ε , 0.011 and 0.033.

To approximate the solution on each element we project it into a sum of Chebyshev polynomials $T_n(z) = \cos(n \arccos(x))$. For the computations here we take $n = 0, \dots, 75$.

To evolve the solution in time we use a sixth order diagonally implicit symmetric symplectic Runge-Kutta method [2]. In Figure 1 we display snapshots of the $\varepsilon = 0.011$ solution (displaced by multiples of 2 along the x -axis) at

times $t = 0, 0.1, \dots, 1.0$. We also display the conservation of the Hamiltonian and the square of the L_2 norm of the solution for two time steps sizes, $\Delta t = 0.01$ and 0.005 and for 6 and 7 elements.

4 Extensions

Extensions to the non-linear Schrödinger equation in one and two dimensions will be presented in the talk.

Acknowledgement

DA was supported in part by NSF Grant DMS-1319054. TH was supported in part by NSF Grant DMS-1418871. AS was supported in part by NSF Grant ECCS-1231046. Any conclusions or recommendations expressed in this paper are those of the author and do not necessarily reflect the views of NSF.

References

- [1] D. Appelö and T. Hagstrom. A new discontinuous Galerkin formulation for wave equations in second order form. *SIAM Journal On Numerical Analysis*, 53(6):2705–2726, 2016.
- [2] C. Jiang and Y. Cong. A sixth order diagonally implicit symmetric and symplectic Runge-Kutta method for solving Hamiltonian systems. *Journal of Applied Analysis and Computation*, 5(1):159–167, 2015.
- [3] D. E. Baldwin. Dispersive shock wave interactions and two-dimensional ocean-wave soliton interactions. *PhD Thesis*, University of Colorado, Boulder, 2013.

Measuring Electromagnetic Chirality

Tilo Arens^{1,*}, Felix Hagemann¹, Frank Hettlich¹

¹Department of Mathematics, Karlsruhe Institute of Technology, Germany

*Email: tilo.ahrens@kit.edu

Abstract

We present a novel definition of chirality for electromagnetic wave scattering problems. We show that this definition captures both geometric aspects of chirality as well as those caused by optical activity. The definition also makes it possible to define a measure of chirality. Scatterers of relative maximal measure of chirality are those invisible to fields of one helicity.

Keywords: Electromagnetic Scattering Problem, Measuring Chirality

1 Introduction

An optically active material will produce a response to an electromagnetic wave propagating through it that depends on the circular polarization state of the wave, i.e. on its *helicity*. On the other hand, chirality may also be caused simply by the geometry of an individual scatterer. Recently, a novel definition of chirality was proposed in the Physics literature [1] for scattering of electromagnetic waves that includes both aspects and moreover allows to measure *how chiral* a given scatterer is. We will discuss this definition and some of its consequences in the mathematical framework of time-harmonic wave propagation and incident Herglotz wave pairs.

2 Electromagnetic Chirality

A Herglotz wave pair

$$(E, H) = \int_{\mathbf{S}^2} (A(d), d \times A(d)) e^{ikd \cdot x} ds(d)$$

is characterized by its amplitude density $A \in L_t^2(\mathbf{S}^2)$. Circularly polarized Herglotz wave functions (i.e. fields of one helicity) can be characterized as eigenfunctions for the eigenvalues ± 1 of the operator $\mathcal{C} : A \mapsto i d \times A(d)$ in $L_t^2(\mathbf{S}^2)$. This space is hence seen to be the direct sum of the corresponding orthogonal eigenspaces

$$L_t^2(\mathbf{S}^2) = V^+ \oplus V^-.$$

A scattering problem in this framework is fully described by the *far field operator* $\mathcal{F} : L_t^2(\mathbf{S}^2) \rightarrow$

$L_t^2(\mathbf{S}^2)$ mapping the amplitude function to the far field pattern of the scattered electric field. Using the orthogonal projections \mathcal{P}^\pm onto V^\pm , contributions due to different helicities can be identified by setting

$$\mathcal{F}^{pq} = \mathcal{P}^p \mathcal{F} \mathcal{P}^q, \quad p, q \in \{+, -\}.$$

Hence $\mathcal{F} = \sum_{p,q \in \{+, -\}} \mathcal{F}^{pq}$. Translating the definition in [1] into this framework yields the following definition.

Definition 1 *The scatterer D is called electromagnetically achiral (em-achiral) if there exist unitary operators $\mathcal{U}^{(j)}$ in $L_t^2(\mathbf{S}^2)$ with $\mathcal{U}^{(j)} \mathcal{C} = -\mathcal{C} \mathcal{U}^{(j)}$, $j = 1, \dots, 4$, such that*

$$\mathcal{F}^{++} = \mathcal{U}^{(1)} \mathcal{F}^{--} \mathcal{U}^{(2)}, \quad \mathcal{F}^{-+} = \mathcal{U}^{(3)} \mathcal{F}^{+-} \mathcal{U}^{(4)}.$$

If this is not the case, we call the scatterer D em-chiral.

We first relate this new notion of chirality to geometric chirality of the scatterer. Consider a bounded Lipschitz domain in $D \subseteq \mathbb{R}^3$ with connected exterior. We assume that there exists $x_0 \in \mathbb{R}^3$ and an orthogonal matrix $J \in \mathbb{R}^{3 \times 3}$ with $\det J = -1$ such that $D = x_0 + JD$. We call such a D *geometrically chiral*.

As a typical example of a scattering problem, consider a perfect conductor boundary condition. In the magnetic field formulation, the problem is

$$\begin{aligned} \operatorname{curl} \operatorname{curl} H - k^2 H &= 0 && \text{in } \mathbb{R}^3 \setminus \overline{D}, \\ (\operatorname{curl} H) \times \nu &= 0 && \text{on } \partial D. \end{aligned}$$

Additionally, we assume the scattered field

$$H^s = H - H^i[A]$$

to satisfy the Silver-Müller radiation condition. The field H^i is assumed to be the magnetic component of the Herglotz wave function with density $A \in L_t^2(\mathbf{S}^2)$. For this case we prove the following theorem:

Theorem 2 *If the perfect conductor D is geometrically achiral then it is also em-achiral.*

A similar theorem also holds for scattering by an inhomogeneous medium.

3 A Measure of Chirality

Following the idea in [1], a *measure of chirality* can be defined via singular systems for the operators \mathcal{F}^{pq} . Denoting by $(\sigma_j^{pq}, G_j^{pq}, H_j^{pq})$ a singular system of \mathcal{F}^{pq} for a scatterer D , we set

$$\begin{aligned}\chi(\mathcal{F}) = & \left(\|(\sigma_j^{++}) - (\sigma_j^{--})\|_{\ell^2}^2 \right. \\ & \left. + \|(\sigma_j^{+-}) - (\sigma_j^{-+})\|_{\ell^2}^2 \right)^{1/2}.\end{aligned}$$

Also using a singular system (σ_j, G_j, H_j) for \mathcal{F} , define the *total interaction cross section* of D by

$$C_{int}(\mathcal{F}) = \sum_j \sigma_j^2.$$

Theorem 3 *For any scatterer*

$$\chi(\mathcal{F})^2 \leq C_{int}(\mathcal{F}).$$

If the scatterer does not scatterer fields of one helicity, then $\chi(\mathcal{F})^2 = C_{int}(\mathcal{F})$.

This result means that scatterers invisible to fields of one helicity always have maximal measure of chirality among all scatterers with the same total interaction cross section. The reverse of this statement also holds true, if a reciprocity relation holds for the scattering problem under consideration.

Theorem 4 *If the scatterer is reciprocal and $\chi(\mathcal{F})^2 = C_{int}(\mathcal{F})$ holds, then the scatterer is invisible to incident fields of one helicity.*

4 Relations to Models for Chiral Media

A frequently used model for chiral materials is the Drude-Born-Fedorov model, introducing the chirality β of the material as an additional parameter. The equations governing propagation of the magnetic field inside a region B filled with chiral material then take the form

$$\begin{aligned}\operatorname{curl} \operatorname{curl} H - \frac{2\kappa^2\beta}{1-\kappa^2\beta^2} \operatorname{curl} H \\ - \frac{\kappa^2}{1-\kappa^2\beta^2} H = 0 \quad \text{in } B.\end{aligned}$$

Consider the scattering of a Herglotz wave function at B in the case where B is a ball. The field

equations need to be supplemented by transmission boundary conditions

$$\begin{aligned}H \times \nu|_+ &= H \times \nu|_- \\ (\operatorname{curl} H) \times \nu|_+ &= \frac{1}{\epsilon_r} \left[(1 - \kappa^2 \beta^2) (\operatorname{curl} H) \times \nu \right. \\ &\quad \left. - \kappa^2 \beta H \times \nu \right]|_-\end{aligned}$$

Using results from [2] on analytic representations of solutions to this problem, the singular values of the far field operator for this problem can be worked out in detail. The results shows, as expected, that the chiral material model gives rise to an electromagnetic chiral scatterer in the sense of the definition above. Hence this definition indeed captures the complete range of chirality for electromagnetic wave scattering problems.

Future research will be aimed at getting an improved understanding of this notion of chirality. In particular, the proposed measure of chirality is to be used to obtain scatterers close to invisible to one helicity by using shape optimization techniques.

Acknowledgements

We gratefully acknowledge financial support by the Deutsche Forschungsgemeinschaft (DFG) through CRC 1173.

References

- [1] I. Fernandez-Corbaton, M. Fruhnert and C. Rockstuhl, *Objects of maximum electromagnetic chirality*, Phys. Rev. X **6** (2016), 031013, doi: 10.1103/PhysRevX.6.031013.
- [2] S. Heumann, *The Factorization Method for Inverse Scattering from Chiral Media*, PhD thesis, Karlsruhe Institute of Technology, 2012.

Low-Rank Separable Expansion for the Helmholtz Fundamental Solution with Absorption

Elizabeth A. Arter^{1,*}, **Ivan G. Graham**¹, **Euan A. Spence**¹

¹Department of Mathematics, University of Bath, UK

*Email: E.A.Arter@bath.ac.uk

Abstract

We present new results on the existence of low-rank separable expansions for the Helmholtz fundamental solution when absorption is added to the wavenumber. Part of the motivation for these new results is to rigorously justify the choice of absorption added into sweeping-type preconditioners. (Recall that this idea of absorption comes from the so-called ‘‘Shifted-Laplacian’’ preconditioner.)

Keywords: Helmholtz, low-rank expansion, absorption, sweeping preconditioner, Shifted-Laplacian preconditioner

1 Low-Rank Properties of Fundamental Solutions of Linear Elliptic PDEs

Low-rank properties of fundamental solutions of linear-elliptic PDEs have important implications for the numerical solution of linear systems arising from discretising these PDEs. Recall that the fundamental solution of the Laplace equation admits a separable expansion on domains that satisfy an admissibility condition. This result is given by the theory of asymptotically smooth functions; in essence this theory states that if a function’s derivatives satisfy certain bounds, then the function is well approximated by polynomial interpolants, which provide the separable expansion [2]. However, when we apply the same theory to the fundamental solution of the Helmholtz equation, $(\Delta + k^2)u = 0$, the constants in the definition of asymptotically smooth grow with k (since taking a derivative incurs a power of k) and thus the quality of the approximation deteriorates as k increases. However, if certain directionality assumptions are imposed, in addition to the admissibility condition, the fundamental solution can have a low-rank separable expansion with rank that’s independent of k or only weakly dependent upon k [3, 10]. An example of such a theorem is given in [10]:

Theorem 1 ([4, Theorem 2.4] due to Rokhlin and Martinsson [10]) Let $d > 0$. There exists

$C(d)$ such that, for all $b > 0$, for all $\varepsilon > 0$ and a such that $ka > C(d)|\log \varepsilon|$ there exists a constant p such that $p \leq \log(2kb)|\log \varepsilon|^2$ and functions $\{\phi_j, \chi_j\}_{j=1}^p$ such that

$$\left| H_0(k\|x - y\|) - \sum_{j=1}^p \phi_j(x)\chi_j(y) \right| \leq \varepsilon \quad (1)$$

for all $x \in [a, b] \times [-d/2, d/2]$ and $y \in [-b, -a] \times [-d/2, d/2]$. [Note that it is implicitly assumed that $d < b - a$ so that the domains are relatively long and thin.]

In general, however, Helmholtz fundamental solutions can’t be expected to have such a low-rank separable expansion independent of k or weakly dependent upon k [6].

2 Sweeping-Style Preconditioners

An important application of this theory is in motivating sweeping-style preconditioners. The first of these was Engquist and Ying’s Sweeping Preconditioner [4]. This is based on an LDL^T -factorisation of the system matrix and depends on off-diagonal blocks of Schur complements that arise in the factorisation admitting a good low-rank separable expansion. These off-diagonal blocks correspond to evaluating a discrete half-space Green’s function on a grid, with source and target in collinear slender boxes like those in Theorem 1. Many other preconditioners have been introduced since then that have all recently been put into a common framework with Engquist and Ying’s Sweeping Preconditioner by Gander and Zhang [9].

3 Adding Absorption

The idea of adding absorption has become popular following the introduction of the so-called ‘‘Shifted-Laplacian’’ preconditioner in [7] and Engquist and Ying state ‘‘it is more effective to generate the factorization for the matrix ... associated with the modified Helmholtz equation’’ $(\Delta + k^2(x))u(x) = f(x)$ where $k(x) = (\omega +$

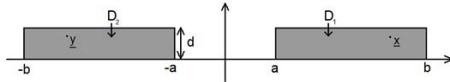


Figure 1: Domains of our new low-rank result

$i\alpha)/c(x)$ “where... α is an $\mathcal{O}(1)$ positive constant” [5, p694]. In particular, the iterative counts for Engquist and Ying’s Sweeping Preconditioner grow more slowly with k when a small amount of absorption is added, even in the homogeneous case (although it might seem counterintuitive), see [11, Tables 5.1-2, 5.7-8, 5.10]. The more absorption we add, the more we expect the Helmholtz fundamental solution to behave like that of $\Delta - k^2$, the Yukawa/modifed Helmholtz operator. In particular, $k \mapsto k + ik$ means both fundamental solutions decay at the same rate and this level of absorption is sufficient to gain near-linear (i.e. near-optimal) complexity in a classical \mathcal{H} -matrix approximation [1, Remark 5.7].

4 Contribution of the Talk

We present several new results explaining how adding absorption affects the Rokhlin and Martinsson low-rank result above. One such result is the following theorem, showing how the quality of the approximation increases with absorption.

Theorem 2 New Low-Rank Result for the Hankel Function *Let $k = k_R + ik_I$ with $0 \leq k_I \leq k_R$. For domains as in Figure 1 with $d \leq b - a$, assume that for some constant $\eta > 0$, $\eta a > b - a$, and $h \sim k_R^{-\mu}$ for $1 \leq \mu \leq 2$, and $d \sim h$ and $a \sim h^\nu$ with $0 \leq \nu \leq 1$. If $\nu < 2 - 1/\mu$, then for k_R sufficiently large there exist functions $\{\phi_j, \chi_j\}_{j=1}^p$ where*

$$p = C_2(\eta) \max \left\{ 1, \log^2 \left(\frac{C_3(\eta)}{\varepsilon} \right) \right\}$$

and where C_2 and C_3 depend only on η , such that

$$\left| H_0(k\|x - y\|) - \sum_{j=1}^p \phi_j(x)\chi_j(y) \right| \leq \varepsilon \exp(-k_I a)$$

for all $x \in D_1, y \in D_2$.

Another result we will present describes how the domains can get “fatter” (i.e. d can be larger) when absorption is added; we expect

this will ultimately be able to justify the variant on the sweeping preconditioner of sweeping several lines at once. We will also discuss using these low-rank results in the hierarchical matrix framework. The end goal of these results is to use them in conjunction with [8] and prove a theorem that rigorously establishes (at least in the case of constant wavenumber) the low iteration counts of the Engquist and Ying sweeping preconditioner seen in practice (with the next step then to extend these results to other sweeping-style preconditioners).

References

- [1] L. Banjai. *SIAM J. Sci. Comput.*, 32(5):2964–2994, 2010.
- [2] M. Bebendorf. *Hierarchical matrices: A Means to Efficiently Solve Elliptic Boundary Value Problems*. Springer, 2008.
- [3] B. Engquist and L. Ying. *SIAM Journal on Scientific Computing*, 29(4):1710–1737, 2007.
- [4] B. Engquist and L. Ying. *Communications on Pure and Applied Mathematics*, 64(5):697–735, May 2011.
- [5] B. Engquist and L. Ying. *Multiscale Modeling & Simulation*, 9(2):686–710, Jun 2011.
- [6] B. Engquist and H. Zhao. Approximate Separability of Green’s Function for High Frequency Helmholtz Equations. Technical report, University of California, Los Angeles, 2014.
- [7] Y. Erlangga, C. Vuik, and C. Oosterlee. *Applied Numerical Mathematics*, 50(3):409–425, 2004.
- [8] M. J. Gander, I. G. Graham, and E. A. Spence. *Numerische Mathematik*, 131(3):567–614, 2015.
- [9] M. J. Gander and H. Zhang. *arXiv:1610.02270 [math.NA]*, 2016.
- [10] P. G. Martinsson and V. Rokhlin. *Journal of Computational Physics*, 221(1):288–302, 2007.
- [11] J. D. Shanks. *Robust solvers for large indefinite systems in seismic inversion*. PhD thesis, University of Bath, 2014.

Efficient Forward and Inverse Algorithms for Guided Wave Inversion

Ali Vaziri Astaneh¹, Murthy N. Guddati^{2,*}

¹Institute for Computational Engineering and Sciences, UT Austin, Austin, TX 78712, USA

²Department of Civil Engineering, North Carolina State University, Raleigh, NC 27695, USA

*Email: murthy.guddati@ncsu.edu

Abstract

Guided waves are widely utilized for estimating the medium properties through inversion of the dispersion curves. This paper presents improved methodologies for computing both dispersion curves and their derivatives, the two main ingredients of guided wave inversion. Specifically, a novel discretization approach, named complex-length finite element method (CFEM), is developed for the computation of dispersion curves, which requires much fewer elements than existing methods. Similarly, a new formulation is developed to compute the derivatives of the dispersion curves without resorting to finite difference approximation, leading to better accuracy and efficiency. As confirmed by synthetic and real-life inversion examples, these algorithms result in more accurate estimates of the medium characteristics than the traditional methods, at a small fraction of computational effort.

Keywords: optimal grids, dispersion analysis, near-surface imaging

1 Introduction

Propagation characteristics of guided waves in stratified media can be exploited for obtaining the structure information in a wide range of applications. Rayleigh and Love waves in layered half-spaces are widely employed in the areas of near surface geophysical imaging as well as pavement and geotechnical site characterization. Lamb waves are utilized for nondestructive evaluation of beams, slabs, composite laminates and pipelines.

Guided wave inversion requires computation of (a) dispersion curves and (b) their gradients. In this work, we introduce improvements for in both venues, and illustrate that the resulting approach estimates the medium properties more accurately, and at a fraction of the cost of existing methods.

2 Forward problem: dispersion curves

Consider a two-dimensional layered *elastic* waveguide in Fig. 1. Each layer is homogeneous and horizontally infinite. The equation representing in-plane wave propagation for the harmonic waves can be written as,

$$-\nabla_s^T \sigma - \rho \omega^2 \mathbf{u} = \mathbf{0}, \quad (1)$$

where \mathbf{u} is the in-plane displacement vector, and σ is the stress vector. Applying Fourier transform on (1) in x direction and using finite element discretization along the z direction results in frequency-wavenumber representation of system stiffness:

$$\mathbf{K}(\omega, k) = k^2 \mathbf{A} + ik \mathbf{B} + \mathbf{C}(\omega), \quad (2)$$

where ω is the temporal frequency and k is the horizontal wavenumber. The dispersion relation is defined as the nontrivial solutions of the eigenvalue problem $\mathbf{K}(\omega, k)\phi = \mathbf{0}$. This can equivalently be viewed as the phase velocities $c_p = \omega/k$ plotted as a function of frequency. This would result in multiple *theoretical* dispersion curves shown in Fig. 2.

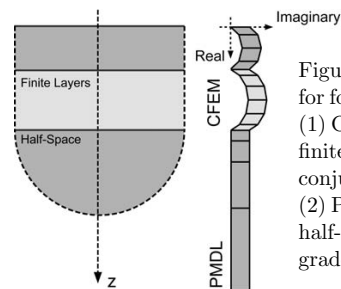


Figure 1: Proposed methods for forward modeling:
(1) CFEM discretization of finite layers with complex conjugate depths.
(2) PMDL discretization of half-space with drastically graded mesh.

For discretization of finite depth layers, instead of using conventional finite or spectral elements, we introduce a novel discretization called Complex-length FEM (CFEM) leading to large reduction in computational cost [1]. This discretization involves *midpoint-integrated linear finite elements with specially chosen complex-valued lengths*. CFEM has several key ingredients that lead to exponential convergence: (a) impedance preserving property associated with

midpoint integration, which is linked to (b) rational approximation of the propagator matrix, and (c) Padé approximants that guide the choice of special (complex) element lengths required for exponential convergence. The resulting mesh is schematically shown in Fig. 1.

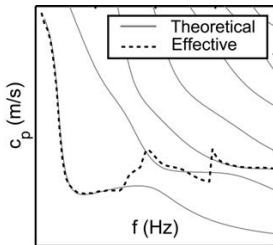


Figure 2: Theoretical (multimodal) dispersion curves, and the effective dispersion curve observed by using 12 transducers.

The unbounded half-space at the bottom is simulated by the Perfectly Matched Discrete Layer (PMDL), which uses midpoint integrated linear elements to preserve the impedance even after discretization. Due to this, PMDL has the ability to represent the half-space with drastically graded mesh with just 2-4 finite elements (again, see Fig. 1).

3 Inverse Problem

The objective of guided wave inversion is to estimate the unknown layer properties from observed dispersion curves computed from measured surface displacements. Due to limited signal-to-noise ratio, not all the modes computed from Eq. 2 are recovered from experiments. Instead the so-called *effective* dispersion curve is recovered from experiments, which results from superposition of various modes in the surface displacement; example effective dispersion curve is shown in Fig. 2. Inversion of the effective dispersion curve requires computing its gradients with respect to layer properties. As illustrated in Fig. 2, the effective curve jumps across the theoretical curves making it difficult to perform analytical differentiation. On the other hand, finite difference approach is expensive and tends to be unstable due to the jumps between various theoretical dispersion curves. To overcome these limitations, we have developed an approximate analytical differentiation formula that is shown to be highly effective, and takes the form [2]:

$$\frac{\partial k^{\text{eff}}}{\partial m_j} = - \frac{\mathbf{P}^T \mathbf{K}^{-1} (\partial \mathbf{K} / \partial m_j) \mathbf{K}^{-1} \mathbf{P}}{\mathbf{P}^T \mathbf{K}^{-1} (\partial \mathbf{K} / \partial k) \mathbf{K}^{-1} \mathbf{P}}, \quad (3)$$

where k^{eff} is the effective wavenumber and m_j

is the j -th model parameter and \mathbf{P} is an arbitrary non-zero load vector. The gradients computed from our approach match with the finite difference gradients, but without the large oscillations present in the finite difference derivatives.

4 Validation with real experiment

We have verified the proposed methods by inverting the synthetic data, and validated with real experimental data. Here we provide a validation example of inverting geophysical data for the borehole profile shown in Fig. 3. A 14-layer subsurface structure is used for inversion of the experimental dispersion curve, by considering the layers' shear wave velocities and thicknesses as the model parameters. Fig. 3 shows that proposed gradient results in a better match with borehole data in comparison with the FDM approach.

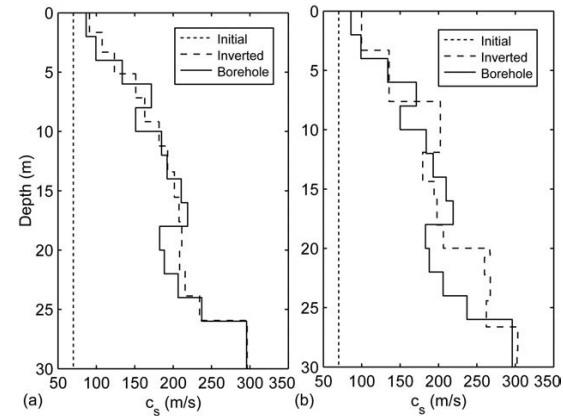


Figure 3: Inverted and borehole profiles using (a) the proposed gradient and (b) FDM gradient.

The associated computational cost is compared in Table 1 which shows a significant improvement by using CFEM and PMDL (almost 400 fold increase in efficiency).

Table 1 Computational cost comparison.

Iterations	CPU Time	Iterations	CPU Time
FDM diff.	FEM+FDM	Anl. diff.	CFEM+ Analytic.

14 5192.2 s 8 13.5 s

References

- [1] Vaziri Astaneh A, Guddati MN, *Meth. Appl. Mech. Eng.* **300** (2016), pp. 27-46.
- [2] Vaziri Astaneh A, Guddati MN, *Geophys. J. Int.* **206** (2016), pp. 1410-1423.

A Two-Level Domain Decomposition Method for Helmholtz Equation

Ali Vaziri Astaneh¹, Murthy N. Guddati^{2,*}

¹Institute for Computational Engineering and Sciences, UT Austin, Austin, TX 78712, USA

²Department of Civil Engineering, North Carolina State University, Raleigh, NC 27695, USA

*Email: murthy.guddati@ncsu.edu

Abstract

A new and efficient two-level, non-overlapping domain decomposition (DD) method is developed for the Helmholtz equation in the two Lagrange multiplier (2LM) framework. To accelerate the convergence, the transmission conditions are designed by utilizing perfectly matched discrete layers (PMDLs), which are more accurate than the polynomial approximations used in the optimized Schwarz method (OSM). Another important ingredient affecting the convergence of a DD method, namely the coarse space augmentation, is also revisited. Specifically, the widely successful approach based on plane waves is modified to that based on interface waves, defined directly on the subdomain boundaries, hence ensuring linear independence and facilitating the estimation of the optimal size for the coarse problem. The effectiveness of both PMDL-based transmission conditions and interface-wave based coarse space augmentation is illustrated with an array of numerical experiments that include comprehensive scalability studies with respect to frequency, mesh size and the number of subdomains.

Keywords: preconditioning, non-overlapping, absorbing interface condition, coarse spaces

1 Introduction

Domain decomposition methods (DDM) have attracted significant interest for numerical solution of partial differential equations; however, there are still open challenges for Helmholtz-type equations.

Designing an accurate interface conditions has significant influence on the convergence and scalability of non-overlapping DDMs. In this work we focus on two Lagrange multiplier fields (2LM) methods that facilitate imposition of more advanced interface (transmission) conditions between the subdomains.

We propose a new 2LM method [1] which is based on utilizing perfectly matched discrete layers (PMDL) to approximate the nonlocal trans-

mission operator using rational approximations, rather than the polynomial approximation used in the Optimized Schwarz Method (OSM) [2]. The resulting PMDL-2LM method is shown to have superior convergence properties compared to OSM.

Separate from this, we introduce a new way of forming the coarse space, based on the interface waves. The new approach automatically guarantees linearly independent bases, thus eliminates the need to filter the redundant bases, a necessary process for building plane-wave based coarse spaces.

2 Two Lagrange multiplier fields (2LM) framework

Consider the exterior Helmholtz problem,

$$-\nabla^2 u - (\omega/c)^2 u = f \quad (1)$$

where u is the pressure, c is the wave velocity and ω is the temporal frequency. We partition the computational domain into arbitrary non-overlapping subdomains. Then the original problem is reduced to a problem involving only the interface nodes, solving the smaller interface problem first, followed by solving on each subdomain. The resulting interface system of equations that will be solved iteratively (and in parallel) takes the form:

$$\mathbf{F}_{2\text{LM}} \lambda = \mathbf{d}, \quad (2)$$

$$\begin{cases} \mathbf{F}_{2\text{LM}} = (\mathbf{S}_{\text{out}} \mathbf{M} - \mathbf{G} \mathbf{S}_{\text{out}})(\mathbf{S}_{\text{in}} + \mathbf{S}_{\text{out}})^{-1} + \mathbf{G}, \\ \mathbf{d} = -(\mathbf{S}_{\text{out}} \mathbf{M} - \mathbf{G} \mathbf{S}_{\text{out}})(\mathbf{S}_{\text{in}} + \mathbf{S}_{\text{out}})^{-1} \mathbf{g}, \end{cases}$$

where λ is vector of Lagrange multipliers over the interfaces and \mathbf{M} , \mathbf{G} are the jump and average matrix operator. The block diagonal matrix \mathbf{S}_{in} is the assembly of subdomain stiffness matrices in terms of interface variables (inner Schur complement) and \mathbf{g} is the corresponding right hand side. Similarly the block diagonal matrix \mathbf{S}_{out} is the assembly of subdomains exterior stiffness matrices (outer Schur complement), which essentially is the Dirichlet to Neumann (DtN) map of the rest of the domain for

each subdomain.

Iterative solution of (2) has optimal convergence if the exact outer Schur complement \mathbf{S}_{out} is substituted. Thus, approximation of the DtN map (interface condition) significantly affects the number of iterations.

3 PMDL-based 2LM method

In the context of wave propagation problems, the effect of the rest of the domain reflecting in \mathbf{S}_{out} , is in some sense wave absorption. Thus, Robin boundary conditions representing viscous damper has been first used and later refined by using second order absorbing boundary conditions in OSM. However, adopting higher order rational approximations, a more accurate transmission condition can be obtained. Thus, we propose to utilize the rational approximation introduced in a recent absorbing boundary using PMDL layers, which are midpoint integrated linear elements that preserve the impedance even after discretization.

Due to impedance preserving property, it can be shown that using only two PMDLs (one with real and one with imaginary length), gives a convergence factor square that of OSM. Fig. 1 (a) shows the two PMDL layers around the subdomain. Note that there is only one line of auxiliary variables that introduces minimal computational overhead compared to OSM.

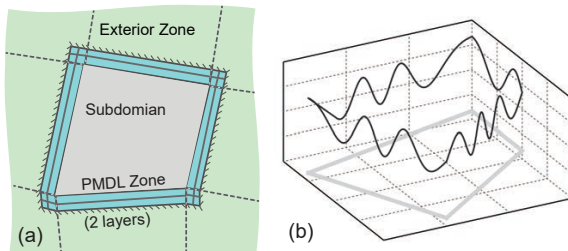


Figure 1 (a) Exterior stiffness using PMDLs and (b) sine component of an interface wave.

4 Coarse space using interface waves

Using plane wave bases for constructing the coarse space for DDMs is a widely used approach given that it captures the oscillating nature of the solution. Unfortunately, the traces of the plane waves on the interface do not form linearly independent bases, necessitating an intermediate step of filtering the redundant bases. To avoid the additional step, we suggest defining the coarse space directly on the interface, ensuring linear

independence while capturing the oscillating nature of the solution. Such a space can in fact be built with the help of Fourier series directly defined on the subdomain boundaries; the basis functions can be chosen as $\{\cos(\omega_j x) \sin(\omega_j x)\}$, with $\omega_j = 2j\pi/L$ where x is the distance along the subdomain boundary and L is the total length of the subdomain boundary (see Fig. 1(b)). Given that they are Fourier bases, interface waves are naturally orthogonal. Therefore, unlike the case of plane waves, no further orthogonalization is necessary.

5 Numerical example: heterogeneous subsurface problem

We have investigated the performance of PMDL-2LM and OSM methods in various examples. Here we only present a single example with the heterogeneous half-space with a scatterer inside as shown in Fig. 2 (a).

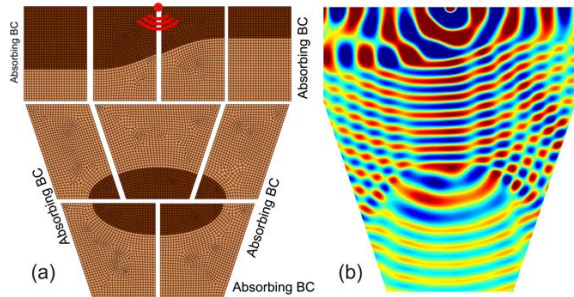


Figure 2 (a) Partitioning of the subsurface (b) real part of the solution.

Results of the frequency scalability study are reported in Table 1 and the converged solution for $\omega = 30\pi$ is shown in Fig. 2 (b). It can be seen that PMDL-2LM converges in roughly half the number of iterations required for OSM and shows a better scalability with respect to frequency.

Table 1. Frequency scalability study.

$1/h$	ω	OSM	PMML
100	10π	37	21
200	20π	41	22
300	30π	44	22
400	40π	45	22

References

- [1] Vaziri Astaneh A, Guddati MN, *Int. J. Numer. Methods Eng.* **107** (2016), pp. 74-90.
- [2] Gander MJ, et al., *SIAM J. Sci. Comput.* **24** (2002), pp. 38-60.

Generalized Sampling Method with noisy measurements

Lorenzo Audibert^{1,*}

¹EDF R&D and INRIA DEFI, Chatou, France

*Email: lorenzo.audibert@edf.fr

Abstract

Qualitative methods are a class of methods that try to retrieve the geometrical support of an obstacle from multistatic data. Recently introduced the Generalized Linear Sampling Method (GLSM) is the extension of the well known Linear Sampling Method (LSM). This extension provides a theoretical justification for the LSM and exhibit better numerical results. The GLSM was introduced for both perfect and noisy data but in the latter case an important ingredient was missing. The proper set up of the weight of regularization with respect to the noise level and ultimately an a priori rules such as Morozov principles. This paper aims at filling this gap under certain constraint on the type of obstacle.

Keywords: Qualitative Method, Sampling Method, Inverse Scattering

1 Introduction

Sampling methods arise in the late nineties in the field of inverse scattering. They aim at reconstructing the support of an obstacle of any type (i.e. penetrable, sound soft, sound hard ...). One of them is the Linear Sampling Method [2] which has a large range of applicability but lack theoretical justification. In order to fill this gap the Factorization Method (FM) and more recently the Generalized Linear Sampling Method (GLSM) [1] have been introduced. These methods use multi static data (multi source and multi measurement data) to form the scattering operator. In the well known case of plane wave source and farfield measurement the operator is the farfield operator. The analysis of sampling methods is based on factorization and range property of this operator. There is a large literature on the properties of the farfield operator depending of the type of obstacle and on the applicability of either the GLSM or the FM. When it is applicable the GLSM relies on regularization theory to invert the compact farfield operator. In the theory associated to this method the noisy case is treated in a non constructive way in the sense that the regularization param-

eter is not link to the noise level. In this paper we focus on setting an explicit link between the regularization parameter of the GLSM and the noise level and derive a priori rules inspired by the Morozov discrepancy principle. We do so in the case of a normal farfield operator. We will discuss potential extension to the non normal case and illustrate our results by numerical simulation.

2 Generalized Linear Sampling Method

We consider the case of penetrable obstacle with index of refraction n and D is the support of $n - 1$. For an incident plane wave $u^i(x, \theta) = e^{ikx \cdot \theta}$ we measure the farfield, $u^\infty(\cdot, \theta)$ associated to the scattered field $u^s(\cdot, \theta)$ that solves:

$$\Delta u^s + k^2 n u^s = k^2(1-n)u^i$$

and the Sommerfeld radiation condition. The farfield operator is defined from $L^2(\mathbb{S}^{d-1})$ to $L^2(\mathbb{S}^{d-1})$ by

$$Fg = \int_{\mathbb{S}^{d-1}} u^\infty(\cdot, \theta) g(\theta).$$

The GLSM method relies on the factorization, $F = GH$ [2] and the fact that the range of G characterize the support of D . H is the well known Herglotz operator defined by

$$Hg = \int_{\mathbb{S}^{d-1}} u^i(\cdot, \theta) g(\theta).$$

When n is real and either strictly less or greater than 1, one could choose to introduce the following cost functional:

$$J_\alpha(g, \phi) = \alpha \left\| (F^* F)^{1/4} g \right\|^2 + \| Fg - \phi \|^2$$

in order to apply the abstract framework of the GLSM to characterize the range of G . The hypothesis on n also implies that F is normal [2], we introduce its singular value decomposition

$$Fg = \sum_i \lambda_i \langle \psi_i, g \rangle \psi_i.$$

Under this setting one can prove the following theorem

Theorem 1 We introduce :

$$g_\alpha = \sum_i \frac{\bar{\lambda}_i}{|\lambda_i|^2 + \alpha\lambda_i} \langle \psi_i, \phi_z^\infty \rangle \psi_i$$

We have the following range characterization, $\phi_z^\infty \in \mathcal{R}(G)$ iff $\lim_{\alpha \rightarrow 0} \|(F^*F)^{1/4}g_\alpha\| < \infty$. Moreover Hg_α converges strongly in $L^2(D)$ to the solution v of the interior transmission problem.

Where the interior transmission problem (ITP) is defined by (for ϕ_z the fundamental solution)

$$\begin{cases} \Delta u + k^2 nu = 0 & \text{in } D, \\ \Delta v + k^2 v = 0 & \text{in } D, \\ (u - v) = \phi_z & \text{on } \partial D, \\ \frac{\partial}{\partial \nu}(u - v) = \frac{\partial}{\partial \nu}\phi_z & \text{on } \partial D, \end{cases} \quad (1)$$

3 A regularized version with explicit choice of the parameter

Even in the noise free case the cost functional J is not easy to handle as it only involves compact operator. In order to avoid this complication we can add a regularization term to ensure the existence of a minimizer:

$$J_\alpha^\beta(g, \phi) = \alpha \|(F^*F)^{1/4}g\|^2 + \beta \|g\|^2 + \|Fg - \phi\|^2.$$

The difficulty is now to obtain a proper balance between α and β in order to keep the range characterization given in theorem 1.

Using this singular value decomposition we are able to prove the following theorem

Theorem 2 The minimizer of J_α^β is

$$g_\alpha^\beta = \sum_i \frac{\bar{\lambda}_i}{|\lambda_i|^2 + \alpha\lambda_i + \beta} \langle \psi_i, \phi \rangle \psi_i.$$

We have that if $\phi \in \mathcal{R}(G)$, $\|(F^*F)^{1/4}(g_\alpha^\beta - g_\alpha)\|$ is bounded and therefore g_α can be substitute by g_α^β in the range characterization of theorem 1. Moreover if $\beta/\alpha^2 \rightarrow 0$ we have that Hg_α^β strongly converges to the solution of the ITP.

4 Application to noisy data

In the case of noisy measurement we consider F_δ instead of F with $\|F_\delta - F\| \leq \delta$ and we have

$$J_{\alpha,\delta}^\beta(g, \phi) = \alpha \|(F_\delta^*F_\delta)^{1/4}g\|^2 + \beta \|g\|^2 + \|F_\delta g - \phi\|^2.$$

We have the following inequality that relates the noisy case and the noise free regularized case :

$$J_{\alpha,\delta}^\beta(g_\alpha^\beta, \phi) \leq J_{\alpha,\delta}^\beta(g_\alpha^\beta, \phi) \leq J_\alpha^\beta(g_\alpha^\beta, \phi) + (\alpha\delta + \delta^2) \|g_\alpha^\beta\|^2$$

Theorem 3 If δ^2/β and $\alpha\delta/\beta$ remains bounded we have that $\phi \in \mathcal{R}(G)$ iff $\lim_{\alpha,\delta,\beta \rightarrow 0} \|(F_\delta^*F_\delta)^{1/4}g_\alpha^\beta\|^2 + \beta/\alpha \|g_\alpha^\beta\|^2 \leq \infty$. Moreover if $\beta/\alpha^2 \rightarrow 0$ and $\delta\alpha/\beta \rightarrow 0$ we have that Hg_α^β converges to the solution of the ITP.

Moreover if we assume that it is possible for δ small enough to ensure

$$(\alpha\delta + \delta^2) \|g_\alpha^\beta\|^2 = \alpha \|(F_\delta^*F_\delta)^{1/4}g_\alpha^\beta\|^2 + \|F_\delta g_\alpha^\beta - \phi\|^2$$

then the range characterization of theorem 3 is verified.

References

- [1] L. Audibert and . Haddar, A generalized formulation of the linear sampling method with exact characterization of targets in terms of farfield measurements, *Inverse Problems* **30** (2014), pp. 035011.
- [2] F. Cakoni, D. Colton and H. Haddar, *Inverse Scattering Theory and Transmission Eigenvalues*, SIAM publications, CBMS Series, 2016.

OpenHmX, an open-source \mathcal{H} -Matrix toolbox in Matlab

Matthieu Aussal^{1,*}

¹CMAP - Ecole Polytechnique, Université Paris-Saclay, Route de Saclay, 91128, Palaiseau Cedex, France.

*Email: matthieu.aussal@polytechnique.edu

Abstract

For many applications in numerical physics, fast convolutions with a Green kernel on unstructured grids are needed to compute in a reasonable time the matrix-vector products. To this aim, many methods have been developed in the last decades. They are divided in two major classes, those which use analytical approximation of the Green kernel [1, 2, 4] and those based on algebraic compression [3, 5]. Associated to this paper, we provide a new open-source Matlab toolbox named *OpenHmX* [6] for the second class of compression.

Keywords : \mathcal{H} -Matrix, open source, green kernel convolution, hierarchical tree, ACA, SVD

1 Context

As a generic example, the case of boundary element formulations for tri-dimensional acoustics is considered, associated to the single layer potential expression :

$$\mathcal{S}\lambda(\mathbf{x}) = \int_{\Gamma} G(\mathbf{x}, \mathbf{y})\lambda(\mathbf{y})d\Gamma_y, \quad \forall \mathbf{x} \in \mathbb{R}^3,$$

where $G(\mathbf{x}, \mathbf{y})$ is the Green kernel :

$$G(\mathbf{x}, \mathbf{y}) = \frac{e^{ik|\mathbf{x}-\mathbf{y}|}}{4\pi|\mathbf{x}-\mathbf{y}|}, \quad (1)$$

and Γ the boundary. Using a discrete quadrature of Γ , this convolution product needs a fast computation of discrete sums as :

$$G * f(\mathbf{x}) \sim \sum_{n=1}^N G(\mathbf{x}, \mathbf{y}_n)f_n, \quad (2)$$

where the potential $(f_n)_{1 \leq n \leq N}$ is known for all \mathbf{y}_n . Since each particle \mathbf{x} interacts with each particle \mathbf{y} , numerical implementation of equation (2) naturally leads to the computation of a dense matrix-vector product. However, thanks to local rank defaults, algebraic compression with *divide and conquer* process can be used to approximate accurately many parts of the full matrix with low rank pieces (\mathcal{H} -Matrix based methods [3, 5]).

2 Overview of *OpenHmX*

OpenHmX [6] is an open-source toolbox for \mathcal{H} -Matrix computations, natively written in Matlab language. This library builds the compressed matrix representation of equation (2) in three steps.

Firstly, two independent binary trees are computed for the tri-dimensional clustering of the particles \mathbf{x} and \mathbf{y} respectively. These trees try to keep a well balanced spatial distribution with any spatial configuration. To do so, it uses both geometric and median cutting, dealing with the best way for all particle groups encountered at each depth of the tree. The cutting of the particles is carried on until the number of particles in the leaf reaches the value :

$$N_{leaf} \approx \log(N)^{\frac{3}{2}}. \quad (3)$$

Secondly, from the binary trees associated to particles \mathbf{x} and \mathbf{y} , the allowed block interactions for algebraic compression is constructed hierarchically (fig. 2, left). In order to proceed, for each block defined by the sets of particles $(\mathbf{x}_i)_{i \in I}$ indexed by I and $(\mathbf{y}_j)_{j \in J}$ indexed by J , we use the admissibility condition :

$$D(\mathbf{x}_I, \mathbf{y}_J) > \max(d(\mathbf{x}_I), d(\mathbf{y}_J)), \quad (4)$$

where $D(\mathbf{x}_I, \mathbf{y}_J)$ is the distance between the centres of the two boxes surrounding each set of particles, and $d(\mathbf{x}_I)$ and $d(\mathbf{y}_J)$ are respectively the diameters of theses boxes.

Finally, an Adaptive Cross Approximation [3] is done for admissible interactions, completed by the standard full computation for close interactions, both with Matlab parallel computation. To do, we use a new criterion in order to evaluate the convergence of the ACA algorithm, instead of the classic one. We evaluate the distances between each set of particles $(\mathbf{x}_i)_{i \in I}$ and $(\mathbf{y}_j)_{j \in J}$, from their projections on the axis defined by the two centres of each dataset. We then compute exactly the Green kernel for some representative interactions, indexed by $I_0 \subset I$ and

N	Cores	τ	k	Direct (s)	\mathcal{H} -Matrix (s)	Memory (Mo)	L^2 error for 10^3 values
10^3	1	10^{-3}	0	0.52	0.71	6.9	$7.6 \cdot 10^{-5}$
10^4	1	10^{-3}	0	5.4	7.5	130	$1.1 \cdot 10^{-4}$
10^5	1	10^{-3}	0	-	74	$2.2 \cdot 10^3$	$1.2 \cdot 10^{-4}$
10^6	1	10^{-3}	0	-	783	$4.2 \cdot 10^4$	$1.2 \cdot 10^{-4}$
10^3	8	10^{-3}	0	0.18	0.31	7.1	$7.1 \cdot 10^{-5}$
10^4	8	10^{-3}	0	1.1	1.5	130	$1.1 \cdot 10^{-4}$
10^5	8	10^{-3}	0	-	11	$2.2 \cdot 10^3$	$1.0 \cdot 10^{-4}$
10^6	8	10^{-3}	0	-	120	$4.1 \cdot 10^4$	$1.1 \cdot 10^{-4}$
10^4	8	10^{-6}	0	1.1	2.4	243	$7.1 \cdot 10^{-8}$
10^4	8	10^{-9}	0	1.1	3.4	379	$2.7 \cdot 10^{-11}$
10^4	8	10^{-12}	0	1.1	4.4	520	$2.2 \cdot 10^{-14}$
10^3	8	10^{-3}	5	0.19	0.41	8.4	$1.8 \cdot 10^{-4}$
10^4	8	10^{-3}	10	1.6	1.8	183	$5.5 \cdot 10^{-4}$
10^5	8	10^{-3}	20	-	22	$3.3 \cdot 10^3$	$5.1 \cdot 10^{-4}$
10^6	8	10^{-3}	30	-	260	$6.2 \cdot 10^4$	$5.2 \cdot 10^{-4}$

FIGURE 1 – Numerical results for a random spherical distribution

$J_0 \subset J$. With an user fixed threshold τ , the stopping criterion can now be driven numerically by the condition :

$$\|G(\mathbf{x}_{I_0}, \mathbf{y}_{J_0}) - A_{I_0}B_{J_0}\| < \tau. \quad (5)$$

3 Numericals results and conclusion

In this last section, we present few numerical results from *OpenHmX*, computed with Matlab R2013 on a 8 cores CPU at 2.7 GHz with 128 Go memory. To do, we simply consider a random spherical repartition of N particles both for \mathbf{x} and \mathbf{y} (fig. 2, right). We use the standard Helmholtz Green kernel (1), with various wave numbers k and thresholds τ . All results are given in figure 1.

To conclude, we propose in this paper a new open source Matlab library for \mathcal{H} -Matrix computation. Some noticeable details enrich standard approaches proposed in the state of the art, and numerical test provide good performances, accuracies and paralelization speed-up factors. In the future, we plan to focus on the memory cost and the high frequency problem.

Références

- [1] Alouges, F., & Aussal, M. (2015). The sparse cardinal sine decomposition and its application for fast numerical convolution. *Numerical Algorithms*, 70(2), 427-448.
- [2] Aussal, M. (2014). Méthodes numériques pour la spatialisation sonore, de la simulation à la synthèse binaurale. *Doctoral dissertation, Palaiseau, Ecole polytechnique*.
- [3] Bebendorf, M., & Rjasanow, S. (2003). Adaptive low-rank approximation of collocation matrices. *Computing*, 70(1), 1-24.
- [4] Greengard, L., & Rokhlin, V. (1997). A new version of the fast multipole method for the Laplace equation in three dimensions. *Acta numerica*, 6, 229-269.
- [5] Hackbusch, W. (1999). A sparse matrix arithmetic based on cal h-matrices. part i : Introduction to \mathcal{H} -matrices. *Computing*, 62(2), 89-108.
- [6] <http://www.cmap.polytechnique.fr/~aussal/>

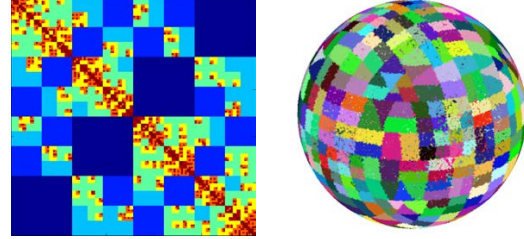


FIGURE 2 – Left : hierarchical interactions from far (blue) to close (red). Right : leaves of the binary hierarchical tree for a spherical distribution of particles.

Full determination of the characteristics of elastic scatterers from some FFP measurements

Izar Azpiroz^{1,*}, Hélène Barucq¹, Julien Diaz¹, Rabia Djellouli²

¹INRIA Project-Team Magique 3D, Université de Pau, France

²Department of Mathematics & IRIS, California State University Northridge, USA

*Email: izar.azpiroz-iragorri@inria.fr

Abstract

The goal is to retrieve the shape of an elastic scatterer along with its material parameters from the knowledge of some far field pattern measurements. To this end, we employ a multi-stage strategy based on Tikhonov iterative-like method. Numerical reconstructions for various two-dimensional scatterers will be presented.

Keywords: Elasto-acoustic Scattering problem, Fréchet derivative, Far-Field Pattern

1 Introduction

The main goal of this work is the development of an efficient computational procedure for determining the shape of the surface along with its characteristics of an elastic obstacle from the knowledge of some elasto-acoustic far-field patterns (FFP). To the best of our knowledge, this is the first time where the problem of simultaneously determining the shape and the material properties is considered. This class of inverse problems is very important to many applications, including earthquake engineering, geophysical exploration, medical imaging, non-destructive testing, underwater acoustics, and electromagnetics. Due to the different nature and scales of the shape and material parameters, we propose a multi-stage solution methodology based on a regularized Newton-type method. Numerical results will be presented to illustrate the salient features of this computational methodology and highlight its performance characteristics. We also suggest practical guidelines to achieve both convergence and acceptable accuracy level.

2 Forward problem

The scattering of a time-harmonic acoustic wave by an elastic obstacle Ω^s embedded in a homogeneous medium Ω^f can be formulated as the following boundary value problem (BVP) :

$$\left\{ \begin{array}{ll} \nabla \cdot \sigma(u) + \omega^2 \rho_s u = 0 & \text{in } \Omega^s \quad (\text{a}) \\ \Delta p + k^2 p = 0 & \text{in } \Omega^f \quad (\text{b}) \\ \sigma(u) \cdot \nu = -p\nu - p^{inc}\nu & \text{on } \Gamma \quad (\text{c}) \\ \omega^2 \rho_f u \cdot \nu = \frac{\partial p}{\partial \nu} + \frac{\partial p^{inc}}{\partial \nu} & \text{on } \Gamma \quad (\text{d}) \\ \lim_{r \rightarrow +\infty} \sqrt{r} \left(\frac{\partial p}{\partial r} - ikp \right) = 0 & \quad (\text{e}) \end{array} \right.$$

where the pair (u, p) represents the elasto-acoustic scattered field vector. p is the scalar-valued fluid pressure in Ω^f , whereas u is the vector-valued displacement field in Ω^s . $p^{inc} = e^{i\omega/c_f x \cdot d}$ corresponds to the given incident plane wave. ω is the circular frequency and c_f is the speed of sound in the fluid Ω^f . ω and c_f are associated with the wavenumber k by $k = \omega/c_f$. ρ_f (resp. ρ_s) is a positive real number denoting the density of the fluid Ω_f (resp. the scatterer Ω_s). σ is the stress tensor related to the strain tensor ϵ by Hooke's law: $\sigma = C \cdot \epsilon$; C being the elastic tensor [1]. We consider here the case of an isotropic medium, and assume σ to be invariant under rotations and reflections [1]. We recall that the scattering amplitude p_∞ of the acoustic scattered field p that is the solution of BVP is defined on the unit sphere S^1 and is obtained from the asymptotic behavior of p [2]:

$$p(x) = \frac{e^{ikr}}{\sqrt{r}} \left(p_\infty \left(\frac{x}{r} \right) + \mathcal{O} \left(\frac{x}{r} \right) \right), \quad r = \|x\|_2 \longrightarrow +\infty$$

Observe that the direct problem BVP contains the standard exterior Helmholtz problem given by Eqs. (b) and (e), and the Navier's equation given by Eq. (a) governing the equilibrium of an elastic scatterer. These equations are coupled via the transmission conditions given by Eqs. (c) and (d). The first one is a dynamic interface condition whereas the second one is a kinematic interface condition [1].

3 Inverse Problem

BVP defines an operator $F : (\rho_s, C, \Gamma) \rightarrow p_\infty$ which maps the solid density ρ_s , the elastic ten-

sor C , and the boundary Γ of the scatterer Ω^s onto p_∞ . Therefore, the simultaneous determination of the shape and the material properties of a given elastic scatterer from some FFPs measurements can be formulated as the following inverse problem:

Given a set of measured FFP for one or several incident plane waves, that differ from the incident direction and/or the frequency regime, find the parameters ρ_s and C , and the shape Γ such that

$$F(\rho_s, C, \Gamma)(\hat{x}) = p_\infty(\hat{x}); \quad \hat{x} \in S \subseteq S^1$$

As stated earlier, the shape and the material parameters are of different nature and scales, and therefore their variations have different effects on the scattered field. For this reason, we propose to employ in a multi-stage fashion a Tikhonov iterative-type method. More specifically, we propose to use a prediction/correction type approach in which, at each stage, a set of parameters remains “frozen” while the set of the “free” parameters is updated.

4 Sensitivity Analysis

We have investigated the dependence of the FFP response with respect to the scatterer characteristics. Due to space limitations, we present here the results of two experiments illustrating the effect of only the shape and the Lamé coefficients. To this end, we consider a disk-shaped scatterer made of steel surrounded by water. We set $r_s = 5\text{mm}$, $k = 100\text{m}^{-1}$, $\lambda = 76\text{GPa}$, $\mu = 97\text{GPa}$, $\rho_s = 2700\text{kg/m}^3$, $\rho_f = 1000\text{kg/m}^3$. In the first experiment, we compare the pointwise values of the FFP intensity by doubling the radius of the scatterer while the Lamé coefficients values remain fixed (see Figure 1(a)), whereas in the second experiment, the radius value is fixed and we double the values of the Lamé coefficients (see Figure 1(b)). The results reported in Figure 1 reveal that the effect of the shape on the FFP is about two order of magnitude higher than the effect of the Lamé coefficients.

5 Numerical Recovery

The results depicted in Figure 2 correspond to the determination of the shape parameters and the Lamé coefficients in the case of an elliptical-shaped obstacle made of steel surrounded by water. Its characteristics are: $r_1 = 10\text{mm}$, $r_2 =$

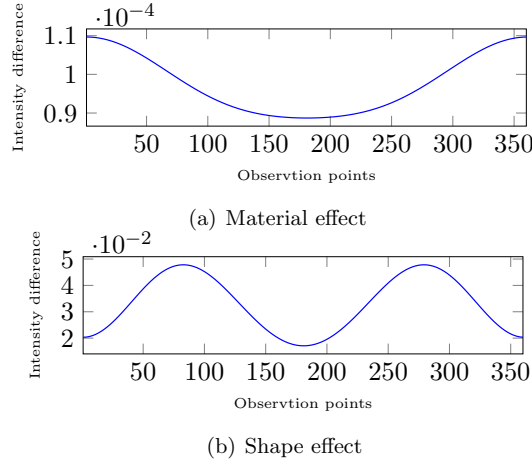


Figure 1: Sensitivity of the FFP to the shape and material parameters. Case of a disk shaped scatterer with $r = 5\text{mm}$, $\lambda = 76\text{GPa}$, $\mu = 97\text{GPa}$, $\rho_s = 2700\text{kg/m}^3$, $\rho_f = 1000\text{kg/m}^3$, and $k = 100\text{m}^{-1}$.

5mm , $\lambda = 76\text{GPa}$, $\mu = 97\text{GPa}$, $k = 267\text{m}^{-1}$, $\rho_s = 2700\text{kg/m}^3$, $\rho_f = 1000\text{kg/m}^3$. The given data are noise free full aperture measurements. Figure 2 indicates that the proposed computational procedure is applied outside the pre-asymptotic convergence region (the relative residual is over 100%) and converges after 9 steps to a relative residual of about 0.02%. Note that each step requires at most 4 iterations. At convergence, the relative error on the reconstructed Lamé parameters is 3% whereas the exact values of the shape parameters are delivered.

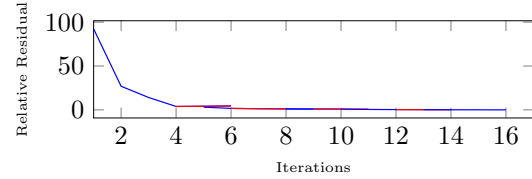


Figure 2: Convergence history

References

- [1] Junger, M. C., & Feit, D. (1986). *Sound, structures, and their interaction* (Vol. 225). Cambridge, MA: MIT press.
- [2] Colton, D., & Kress, R. (2012). *Inverse acoustic and electromagnetic scattering theory* (Vol. 93). Springer Science & Business Media.

Promise and progress of millihertz gravitational-wave astronomy

John G. Baker^{1,*}

¹Gravitational Astrophysics Laboratory, NASA-Goddard Space Flight Center, Greenbelt, MD USA

*Email: john.g.baker@nasa.gov

Abstract

Extending the new field of gravitational wave (GW) astronomy into the millihertz band with a space-based GW observatory is a high-priority objective of international astronomy community. This paper summarizes the astrophysical promise and the technological groundwork for such an observatory, concretely focusing on the prospects for the proposed Laser Interferometer Space Antenna (LISA) mission concept.

Keywords: Gravitational Waves, Time-domain Astronomy, Astrophysics

1 Introduction

Just over a century ago Einstein first described our current theory of gravity, general relativity, and quickly recognized that his theory might imply the existence of gravitational waves. It wasn't until decades later that scientists began to realize that observing GWs could be a practical possibility and may provide especially detailed information about strong-gravity systems inaccessible to electromagnetic astronomy.

Last year the Laser Interferometric Gravitational wave Observatory (LIGO) opened this new field of GW astronomy by announcing the first direct GW observations, simultaneously providing direct observations of a binary black hole systems and revealing a number of relatively large stellar black holes. This should be just the beginning of many years of exciting astronomical observations in the roughly 10-1000 Hz band.

An important upcoming step for the nascent field of GW astronomy is extending the GW window into the promising millihertz band, from roughly 0.01 to 1000 mHz, via a space-based observatory. These observations should expose a great and distinct wealth of astronomical information.

2 Gravitational waves: a new probe of the universe

Gravitational dynamics are described in general relativity by Einstein's equations, which relate

the spacetime curvature tensor to the stress energy tensor describing forces, motion and distribution of matter. Energy and momentum conservation prevents monopole and dipole variation so GWs can only be generated by the time variation of quadropole or higher moments. Where the motion of objects is small compared to the speed of light, GW emissions are tiny, typically scaling with $(v/c)^5$.

Spacetime geometry is mathematically encoded in the metric tensor field \mathbf{g} , which may be treated by linear perturbations for the propagation of GWs far from sources. In this limit with suitable (gauge) choice of coordinates $\mathbf{x} = \{t, x, y, z\}$, metric perturbations are governed by a simple linear wave equation, a solution for waves propagating in the z direction can be written as

$$\mathbf{g} = \begin{bmatrix} -1 & 0 & 0 & 0 \\ 0 & 1 + h_+(\mathbf{x}) & h_\times(\mathbf{x}) & 0 \\ 0 & h_\times(\mathbf{x}) & 1 - h_+(\mathbf{x}) & 0 \\ 0 & 0 & 0 & 1 \end{bmatrix}. \quad (1)$$

Here $h_{+,\times}(\mathbf{x})$ are the two GW polarization modes. A great distance r from a the source, the solution is can be written $h_{+,\times}(\mathbf{x}) = \hat{h}_{+,\times}(t-z)/r$, where the functions $\hat{h}_{+,\times}(t_{\text{ret}})$ encode infomation about the source and its motion.

The special features of GWs as a new messenger of astronomical information include:

- **Clean strong-gravity sources.** Where GWs are measurable, gravity often dominates other forces. Assuming we understand gravity, the simple parameters describing the emission physics may be inferred from observation with unusual precision. To achieve the required velocities, significant GWs can only be emitted by the highest density astronomical objects such as black holes, neutron stars, and white dwarfs.
- **Clean propagation.** Because of their weak coupling to matter, the universe should be mainly transparent to GWs, this enables observation of otherwise obscure sources.

- **Coherent emission and detection.** Unlike light, GW wavelengths are larger than the size of the source yielding a monolithic coherent signal with an amplitude falling off as $1/r$. The signals must also be measured by amplitude, not power, with the same scaling. This makes it relatively easy to observe signals from great cosmological scale distances by GWs.

3 Millihertz GW astronomy

At a given mass, GW emissions are strongest and most likely to be detectable higher frequencies (higher v/c). Then they carry vast energies away from their sources, implying a short lifetime that scales with mass. There is an exact time scaling of GW signals with overall source mass. LIGO band GW astronomy is limited to the rare and short-lived last moments of stellar scale systems ranging up to a few hundred solar masses. The millihertz band provides a sweet spot between rare events with the strongest gravity and more numerous slightly weaker-gravity systems.

Opening the millihertz band [1], exposes the giant signals from mergers of massive black holes up to from $\sim 10^4$ to $\sim 10^8$ solar masses. The signals are so loud that we are likely limited by rate not signal strength even for distant events occurring at the earliest likely cosmological times. These observations will show how these massive black holes at galactic centers form and merge over the epoch of galactic formation and assembly into the large galaxies we see today. Over several years we might expect hundreds of these events.

At the other extreme, millihertz GW observations should also reveal a much larger population of nearby lower velocity binaries. These would include the LIGO binaries, years before merger, as well as somewhat lower density sources including white dwarf binaries in the Milkyway. Such an observatory might individually pick out more than 10,000 of these objects, while a millions more would aggregate into a stochastic foreground signal.

Another expected class of millihertz sources bridges these regimes involving stellar scale objects falling into massive black holes in the relatively recent history of the universe. These events can reveal presently obscured details about stellar remnant populations in the deep hearts

of galaxies while also providing precision information about the spacetime geometry near massive black holes.

4 The LISA concept

Astrophysically plausible GWs yield extremely small relative motion ($\lesssim 10^{-21}$ fractional displacement) in free-falling objects. Observing them requires overcoming two main technical challenges: 1) isolating the objects from any other forces which may cause motion at this level, and 2) measuring the motion. Terrestrial motion seems to preclude surmounting the former of these challenges on the ground. Fortunately they are each facilitated by a space-based instrument where large empty space is easy to come by and ambient forces are much quieter.

The LISA concept includes three spacecraft each following internally isolated free-floating test masses on elliptical solar orbits forming nearly rigid triangle a few million kilometers across. Changes in separation between the testmasses is measured by laser interferometry.

The international science community has honed this concept through many years of science studies and technology development, with a key achievement being the successful demonstration, last year, of key novel technologies in space by the European Space Agency's LISA Pathfinder mission. Building on this success, ESA, with NASA as a junior partner, now plans to launch a millihertz-band gravitational-wave observatory in the early 2030s.

References

- [1] *eLISA Consortium: Seoane, P. A. et al, Whitepaper selected as ESA L3 mission science theme*, arXiv:1305.5720 (2013).
- [2] *LISA Assessment Study Report*. European Space Agency (2011).

Shear waves in prestrained poroelastic media

Navid Nazari¹, Paul E. Barbone^{2,*}

¹Department of Biomedical Engineering, Boston University, Boston, US

²Department of Mechanical Engineering, Boston University, Boston, US

*Email: barbone@bu.edu

Abstract

Shear wave elastography measures shear wave speed in soft tissues for diagnostic purposes. In [1], shear wave speed was shown to depend on prestrain, but not necessarily prestress, in a perfused canine liver. We model this phenomenon by examining incremental waves in a pressurized poroelastic medium with incompressible phases. The analysis suggests novel restrictions on the strain energy functions for soft tissues.

Keywords: incremental waves, poroelasticity, elastography, strain energy function

1 Introduction

Elastic shear wave propagation in soft tissues is of current interest in the field of elastography. Shear wave speed serves as a surrogate for tissue modulus, and is used for diagnosis of various pathologies. Therefore, understanding those parameters which can lead to variations in shear wave speed *in vivo* is necessary. Here the focus is on dependence of shear wave speed on pore pressure, when modeling the soft tissue as a poroelastic solid.

We present a mathematical model for the experimental observations of [1]. In that experiment, a canine liver was re-perfused and submerged in a bath. Pore pressure within the liver was controlled by maintaining pressure in the portal vein. The bath was maintained in two conditions: a constrained condition in which the container was completely sealed; an unconstrained condition in which the container was open to the atmosphere. In each condition, the pressure in the portal vein was controlled, and the shear wave speed was measured as a function of portal vein pressure.

Below we model the liver as a nonlinear poroelastic continuum. We derive a quasistatic solution for the pressurized equilibrium configuration of the medium in both the constrained and unconstrained cases. Then we consider small amplitude shear waves superimposed on the pres-

surized configuration, and derive a formula for the shear wave speed.

2 Nonlinear poroelasticity model

We use equations governing a poroelastic continuum with incompressible phases, following the beautiful paper [2]. We assume the intrinsic mass density of the fluid and solid phases to be equal:

$$\rho = \rho_f = \rho_s = \text{const} \quad (1)$$

The constitutive assumptions on stress are as follows:

$$\boldsymbol{\sigma} = \boldsymbol{\sigma}^s + \boldsymbol{\sigma}^f \quad (2)$$

$$\boldsymbol{\sigma}^f = -\phi^f p_f \mathbf{I} \quad (3)$$

$$\boldsymbol{\sigma}^s = \boldsymbol{\sigma}^{\text{elastic}} - \phi^s p_f \mathbf{I} \quad (4)$$

Equation (4) assumes that the intrinsic pressure in the solid phase is equal to the intrinsic pressure in the fluid phase. This is consistent with the incompressibility assumption. The elastic stress in the solid matrix, $\boldsymbol{\sigma}^{\text{elastic}}$, is given in terms of the derivative of a strain energy function.

2.1 Problem formulation

We consider a poroelastic material submerged in a fluid bath. The fluid-solid interface between the poroelastic solid and fluid bath is denoted Γ_{fs} . On an interior boundary of the poroelastic solid, Γ_p , the pore fluid is assumed to be in contact with a second reservoir, in which the pressure can be controlled. Thus the boundary conditions are assumed to be:

$$\mathbf{t}^s = -p_{\text{bath}} \mathbf{n} \quad \text{on } \Gamma_{fs} \quad (5)$$

$$\mathbf{q} \cdot \mathbf{n} = 0 \quad \text{on } \Gamma_{fs} \setminus \Gamma_p \quad (6)$$

$$p_f = p_0 \quad \text{on } \Gamma_p \quad (7)$$

Here we consider p_0 to be a given constant.

Conservation of fluid volume in the incompressible fluid bath and equation (6) give:

$$\int_{\Omega^s} J dV = \Delta V_f. \quad (8)$$

Here, $J = \lambda^3$ is the relative volume change of the poroelastic solid.

We consider two different conditions on the fluid bath. In one case, the fluid bath surrounding the poroelastic solid is in a sealed container. In this, the constrained case, $\Delta V_f = 0$. In a second case, the unconstrained case, the container is unsealed and open to the atmosphere, and hence $p_b = 0$ in this case.

2.2 Solution for quasistatic expansion

For a given (positive) p_0 , the quasistatic fields for both the constrained and unconstrained cases are given as follows.

Deformation:

$$\mathbf{x} = \lambda \mathbf{X} \quad (9)$$

Mixture stress:

$$\boldsymbol{\sigma} = \sigma_o(\lambda) \mathbf{I} - p_f \mathbf{I} \quad (10)$$

Boundary conditions:

$$\Gamma_p : \quad p_f = p_0 \quad (11)$$

$$\Gamma_{fs} : \quad \sigma_o(\lambda) - p_f = -p_{bath} \quad (12)$$

$$\Delta \text{ Volume} : \quad (\lambda^3 - 1)V_0 = \Delta V_f \quad (13)$$

Now we consider the two cases. For the constrained case, $\Delta V_f = 0 \implies \lambda = 1$. Hence:

$$p_f = p_{bath} = p_0. \quad (14)$$

For the unconstrained case, $p_{bath} = 0$, thus we find:

$$\sigma_o(\lambda) = +p_f = +p_0. \quad (15)$$

We emphasize the point that in the unconstrained case, the elastic matrix is in isotropic *tension*, which counteracts the isotropic pressure in the pore fluid. The stretch of the solid matrix, $\lambda > 1$, is determined by the solution of equation (15), for any given strain energy function W .

3 Incremental waves superposed on dilatation

To consider incremental waves superposed on the quasistatic deformation, we now consider ($\nabla \mathbf{u} \ll 1$):

$$\mathbf{x} = \lambda \mathbf{X} + \mathbf{u}(\mathbf{x}, t) \quad (16)$$

Then, using the results of [3] leads to the following expression for the shear wave speed:

$$\frac{c^2}{c_0^2} = \frac{(W_1(\lambda) + W_2(\lambda)\lambda^2)}{\lambda(W_1(1) + W_2(1))} \quad (17)$$

Here, $W_\alpha = \frac{\partial W}{\partial I_\alpha}$, where W is the strain energy function, and I_α is an invariant of the Cauchy-Green strain tensor [3].

4 Discussion

Equation (17) is our main result, and has several implications regarding the behavior of the shear wave speed and its dependence on the strain energy function.

- The shear wave speed depends on λ , independent of the pore pressure p_f . *In this case, the wave speed is independent of the applied pressure.*
- For the constrained case, $\lambda \equiv 1$. In this case, the shear wave speed is unchanged by a changing pore pressure.
- For the unconstrained case, $\lambda > 1$, and hence the shear wave speed changes with increasing pore pressure.
- For W_1, W_2 positive constants, then shear wave speed increases with increasing λ at most as $\sqrt{\lambda}$. For the further special case $W_2 = 0$, the shear wave speed *decreases* with increasing λ .

References

- [1] V. Rotemberg, B. Byram, M. Palmeri, M. Wang, K. Nightingale, Ultrasonic characterization of the nonlinear properties of canine livers by measuring shear wave speed and axial strain with increasing portal venous pressure, *Journal of Biomechanics* 46 (11) (2013) 1875–1881. doi:10.1016/j.jbiomech.2013.04.027.
- [2] R. M. Bowen, Incompressible porous media models by use of the theory of mixtures, *International Journal of Engineering Science* 18 (9) (1980) 1129–1148. doi:10.1016/0020-7225(80)90114-7.
- [3] M. Shams, M. Destrade, R. W. Ogden, Initial stresses in elastic solids: Constitutive laws and acoustoelasticity, *Wave Motion* 48 (7) (2011) 552–567. doi:10.1016/j.wavemoti.2011.04.004.

Elastic waves in a soft electrically conducting solid in a strong magnetic field

Daniel Gendin¹, Paul E. Barbone^{2,*}

¹Department of Mechanical Engineering, Boston University, Boston, US

²Department of Mechanical Engineering, Boston University, Boston, US

*Email: barbone@bu.edu

Abstract

Shear wave motion of a soft, electrically-conducting solid in the presence of a strong magnetic field excites eddy currents in the solid. These, in turn, give rise to Lorentz forces that resist the wave motion. We derive a mathematical model for linear elastic wave propagation in a soft electrically conducting solid in the presence of a strong magnetic field. The model reduces to an effective anisotropic dissipation term resembling an anisotropic viscous foundation. The application to magnetic resonance elastography, which uses strong magnetic fields to measure shear wave speed in soft tissues for diagnostic purposes, is considered.

Keywords: magnetoelasticity, eddy current, magnetic resonance elastography

1 Introduction

Elastic shear wave propagation in soft tissues is of current interest in the field of elastography. Shear wave speed serves as a surrogate for tissue modulus, and is used for diagnosis of various pathologies. Therefore, understanding those parameters which can lead to variations in shear wave speed *in vivo* is necessary. Here the focus is on dependence of shear wave speed and attenuation in the presence of a strong magnetic field. We note that Lorentz force has been used to generate shear waves in soft tissues [1].

Equations of motion for stressed and unstressed magnetoelastic solids have been studied extensively, c.f. [2]. Equations for incremental waves are presented in [3], though the focus there is largely on materials that are magnetoelastic and non-electrically conducting. Electrically conducting materials are considered in [4]. The focus of the present work is on small amplitude waves in a non-magnetoelastic but electrically conducting solid.

2 Electromagnetic modeling

We begin by recalling Maxwell's equations [5]:

$$\nabla \cdot \mathbf{E} = \frac{q_f}{\varepsilon_0} \quad (1)$$

$$\nabla \cdot \mathbf{B} = 0 \quad (2)$$

$$\nabla \times \mathbf{E} = -\frac{\partial \mathbf{B}}{\partial t} \quad (3)$$

$$\nabla \times \mathbf{B} = \mu_0 \mathbf{J} \quad (4)$$

Here \mathbf{E} is the electric field, \mathbf{B} is the magnetic field, \mathbf{J} is the current density (current per unit area), q_f is the free charge density, μ_0 is the permeability of free space and ε_0 is the permittivity of free space. In Ampere's law, (4), we neglect the term $\mu_0 \varepsilon_0 \frac{\partial \mathbf{E}}{\partial t} \approx 0$, consistent with an electromagnetic quasistatic approximation.

Assuming Ohm's law holds within the material gives us

$$\mathbf{J} = \sigma \frac{\mathbf{F}}{q} = \sigma(\mathbf{E} + \mathbf{v} \times \mathbf{B}). \quad (5)$$

Here, σ is the conductivity. Taking the curl of both sides of (5) and using Maxwell's Equations yields

$$\nabla^2 \mathbf{B} - \sigma \mu_0 \left(\frac{\partial \mathbf{B}}{\partial t} - \nabla \times (\mathbf{v} \times \mathbf{B}) \right) = 0. \quad (6)$$

Equation (6) is our main field equation for the magnetic field within the conducting solid.

3 Magneto-elasticity model

We start with the linear momentum equation in a continuum:

$$\nabla \cdot \boldsymbol{\tau} - \rho \ddot{\mathbf{u}} + \mathbf{f} = 0. \quad (7)$$

Here $\boldsymbol{\tau}$ is the stress, \mathbf{u} is the displacement, and \mathbf{f} is the body force per unit volume. We take \mathbf{f} to be the Lorentz body force, given by

$$\mathbf{f} = \mathbf{J} \times \mathbf{B} \quad (8)$$

$$\text{by (4): } \mathbf{f} = \frac{1}{\mu_0} (\nabla \times \mathbf{B}) \times \mathbf{B} \quad (9)$$

Substituting (9) into (7) gives:

$$\nabla \cdot (\mathbf{C} : \nabla \mathbf{u}) - \rho \ddot{\mathbf{u}} + \left(\frac{1}{\mu_0} (\nabla \times \mathbf{B}) \times \mathbf{B} \right) = 0 \quad (10)$$

4 Linearization and scaling

We consider shear wave propagation at frequency ω_0 , which determines our time scale. We choose to nondimensionalize space with respect to $L_{mech} = \frac{c_{mech}}{\omega_0}$. Two non-dimensional ratios arise in the analysis. These are:

$$\beta = \frac{L_{mech}}{L_{mag}} = c_{mech} \sqrt{\frac{\sigma \mu_0}{\omega_0}} \ll 1 \quad (11)$$

$$\gamma = \frac{B_0^2}{\mu_0 \rho c_{mech}^2} \gg 1 \quad (12)$$

We now assume that the magnetic field is a small perturbation of a strong static field, $\mathbf{B}_0 = B_0 \mathbf{m}$:

$$\mathbf{B} = B_0(\mathbf{m} + \beta^2 \mathbf{h}), \quad \beta^2 \mathbf{h} \ll 1. \quad (13)$$

We thus obtain to leading order:

$$\nabla^2 \mathbf{h} + \nabla \times (\frac{\partial \mathbf{u}}{\partial t} \times \mathbf{m}) = 0 \quad (14)$$

$$\nabla \cdot (\tilde{\mathbf{C}} : \nabla \mathbf{u}) - \frac{\partial^2 \mathbf{u}}{\partial t^2} + \gamma \beta^2 ((\nabla \times \mathbf{h}) \times \mathbf{m}) = 0 \quad (15)$$

Here, $\tilde{\mathbf{C}} = \frac{1}{\rho c_{mech}^2} \mathbf{C}$ is the nondimensional elasticity tensor.

5 Time-harmonic waves

We assume traveling wave solutions for displacement and magnetic field:

$$\mathbf{u} = \mathbf{A} \exp(i\kappa \hat{\mathbf{n}} \cdot \mathbf{x} - it), \quad (16)$$

$$\mathbf{h} = \mathbf{d} \exp(i\kappa \hat{\mathbf{n}} \cdot \mathbf{x} - it). \quad (17)$$

Substituting into (14) and (15), and eliminating \mathbf{d} leads to the following effective dispersion equation for the mechanical wavefield amplitude, \mathbf{A} :

$$(\mathbf{n} \cdot [(\kappa^2 \tilde{\mathbf{C}} + i\gamma \beta^2 \mathbf{D}) \cdot \mathbf{n} - \mathbf{I}]) \mathbf{A} = 0. \quad (18)$$

Here, $\mathbf{D}(\mathbf{m})$ is the non-dimensional tensor:

$$\mathbf{D}_{ijkl} = m_i m_l \delta_{jk} - m_j m_l \delta_{ik} - m_i m_k \delta_{jl} + \delta_{ij} \delta_{kl}. \quad (19)$$

This tensor, $\gamma \beta^2 \mathbf{D}(\mathbf{m})$, may be interpreted as a non-dimensional damping tensor.

6 Discussion

Equations (18) and (19) are our main results, and have several implications regarding the behavior of elastic waves in the presence of a strong magnetic field.

- The dominant effect of the strong magnetic field and the medium conductivity is wave damping through eddy currents.

- The magnitude of the eddy current damping effect is proportional to

$$\gamma \beta^2 = \frac{\sigma B_0^2}{\rho \omega_0}. \quad (20)$$

- The magnitude of the effect is the same for both P-Waves and S-Waves.
- For soft tissues [6,7] the effect is negligible at all practical frequencies.

References

- [1] P. Grasland-Mongrain, R. Souchon, F. Cartellier, A. Zorgani, J. Chapelon, C. Lafon, S. Catheline, Imaging of Shear Waves Induced by Lorentz Force in Soft Tissues, *Physical Review Letters* 113 (3) (2014) 038101.
- [2] A. C. Eringen, Mechanics of continua /2nd edition/, Krieger, Huntington, NY, 1980.
- [3] R. W. Ogden, Incremental elastic motions superimposed on a finite deformation in the presence of an electromagnetic field, *International Journal of Non-Linear Mechanics* 44 (5) (2009) 570–580.
- [4] L. Knopoff, The interaction between elastic wave motions and a magnetic field in electrical conductors, *Journal of Geophysical Research* 60 (4) (1955) 441–456.
- [5] D. J. Griffiths, *Introduction to Electrodynamics*, Prentice Hall, 1999.
- [6] H. C. Burger, R. v. Dongen, Specific Electric Resistance of Body Tissues, *Physics in Medicine and Biology* 5 (4) (1961) 431.
- [7] T. J. C. Faes, H. A. v. d. Meij, J. C. d. Munck, R. M. Heethaar, The electric resistivity of human tissues (100 Hz-10 MHz): a meta-analysis of review studies, *Physiological Measurement* 20 (4) (1999) R1.

The Generation of Inertial-Alfvén Waves in Planetary Cores

O. P. Bardsley^{1,*}, P. A. Davidson¹

¹Department of Engineering, University of Cambridge

*Email: ob275@cam.ac.uk

Abstract

We consider the generation of incompressible waves in a rapidly-rotating, electrically conducting, Boussinesq fluid stirred by buoyant anomalies, a situation thought to arise in many planetary cores. In the absence of a magnetic field, the dispersion of energy from a localised source is known to be dominated by low-frequency inertial waves, which have wavevectors approximately orthogonal to the rotation axis. We study the modification to this process by a large-scale ambient magnetic field consistent with that found in the outer core of the Earth. We find that the response is again dominated by wavevectors normal to the rotation axis, but these now take the form of hybrid “inertial-Alfvén waves”. These propagate along the rotation axis at half the speed of conventional low-frequency inertial waves, but also dispatch energy along magnetic field lines at the Alfvén velocity. We demonstrate their significance via a simple model problem.

Keywords: Rapidly-rotating flows, magnetohydrodynamics, planetary interiors

1 Introduction - inertial waves

A rapidly rotating fluid can support inertial waves through the action of the Coriolis force. These have a group velocity which is perpendicular to their wavevector, so all wavevectors \mathbf{k} in the plane normal to the rotation vector $\boldsymbol{\Omega}$ carry energy along the axis. Such waves are low-frequency, since the relevant dispersion relation is $\varpi = \pm 2\boldsymbol{\Omega} \cdot \mathbf{k}/k$, and automatically focussing since the energy from a large area of \mathbf{k} -space (the horizontal plane) is distributed over a narrow region of real space (the rotation axis) [1]. This means, in the non-magnetic case, that the dispersion of energy from a localised source is dominated by waves which have \mathbf{k} horizontal and $\varpi \approx 0$. Motivated by short-timescale dynamics in planetary cores, we wish to explore how this paradigm is affected by the addition of a mean magnetic field.

2 Rapidly-rotating MHD waves

We consider the ideal linearised momentum and induction equations for the solenoidal velocity and perturbed magnetic fields, \mathbf{u} and \mathbf{b} :

$$\frac{\partial \mathbf{u}}{\partial t} = (\mathbf{B}_0 \cdot \nabla) \mathbf{b} + (2\boldsymbol{\Omega} \cdot \nabla) \mathbf{c}, \quad (1)$$

$$\frac{\partial \mathbf{b}}{\partial t} = (\mathbf{B}_0 \cdot \nabla) \mathbf{u}. \quad (2)$$

Here, \mathbf{B}_0 is the constant ambient magnetic field, taken to be horizontal, $\boldsymbol{\Omega}$ is the background rotation, taken vertical, and \mathbf{c} is the solenoidal vector potential for \mathbf{u} . The density and magnetic permeability are taken to be unity, giving the magnetic field units of an Alfvén velocity. A search for plane wave solutions of frequency ϖ yields the quartic dispersion relation

$$\varpi^2 \mp \varpi_\Omega \varpi - \varpi_B^2 = 0, \quad (3)$$

where $\varpi_\Omega = 2\boldsymbol{\Omega} \cdot \mathbf{k}/k$ and $\varpi_B = \mathbf{B}_0 \cdot \mathbf{k}$ are the inertial-wave and Alfvén frequencies respectively. It is common in the geophysical literature to then exploit the fact that rotation is dominant over the magnetic field, as measured by the Lehnert number $Le = 2B_0/\Omega\ell$ for some lengthscale ℓ . ($Le \sim 0.1$ is thought typical of small scales in the Earth.) For small Le , one might expect $|\varpi_\Omega| \gg |\varpi_B|$, giving (3) two pairs of well-separated roots,

$$\varpi_I \approx \pm \varpi_\Omega, \quad \varpi_M \approx \mp \varpi_B^2/\varpi_\Omega, \quad (4)$$

identified as weakly-modified inertial waves and the much slower *magnetostrophic* waves. However, this ansatz ignores the significance of self-focussing $\varpi_\Omega \approx 0$ solutions in the non-magnetic case. Making the converse assumption $|\varpi_\Omega| \ll |\varpi_B|$ gives roots

$$\varpi \approx (\pm)\varpi_B \pm \varpi_\Omega/2 \approx (\pm)\varpi_B \quad (5)$$

with a group velocity

$$c_g \approx (\pm)\mathbf{B}_0 \pm \boldsymbol{\Omega}/k, \quad (6)$$

demonstrating dispersion along both the rotation axis and magnetic field lines; these are our

“inertial-Alfvén waves”. We now show by example that, contrary to common wisdom, this second regime probably best describes the radiation of waves from localised sources in planetary cores.

3 A model problem

We present the model problem considered in [2] more fully. A buoyant anomaly of Gaussian structure, with a density perturbation $\rho' \propto \exp\{-2x^2/\ell^2\}$, is introduced spontaneously into a quiescent, boussinesq, conducting fluid. The background rotation, ambient magnetic field, and gravitational acceleration are taken to be mutually orthogonal; this might resemble conditions in the equatorial regions of a planet. We do not solve for the evolution of the buoyancy field, but concern ourselves instead with the rather more rapid waves it emits. This initial value problem is solved by taking the spatial Fourier transform, solving in k -space, then evaluating the inverse numerically. An example dispersion pattern, for the case $Le = 0.1$, is shown in Figure 1. We observe significant radiation vertically on the fast inertial-wave timescale, with a more gradual spreading along field lines at the Alfvén velocity.

It is possible to perform diagnostic tests on the dispersion of energy to show that the dominant structures do indeed propagate according to the group velocity expression (6). These results are by no means unique to the specific case studied here, which suggests that small scale dynamics in planetary cores may be governed by inertial-Alfvén waves, rather than the more commonly proposed combination of inertial and magnetostrophic waves.

References

- [1] Davidson, P. A., Staplehurst, P. J. and Dalziel, S. B., On the evolution of eddies in a rapidly rotating system, *J. Fluid Mech.* **557** (2006), pp. 135–144.
- [2] Bardsley, O. P. and Davidson, P. A., Inertial-Alfvén waves as columnar helices in planetary cores, *J. Fluid Mech. (rapids)* **805** (2016).

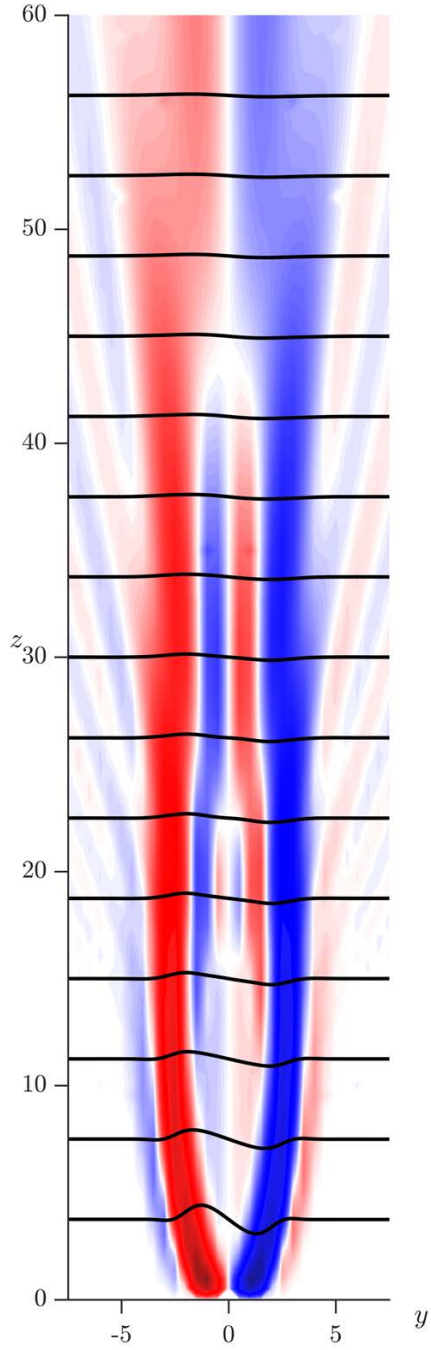


Figure 1: Radiation from a buoyant blob at $\Omega t = 50$ for $Le = 0.1$. Rotation is vertical, magnetic field horizontal, and gravity acts into the page. Colouring shows axial velocity (red positive, blue negative) and field lines are overlaid in black.

Regional computation of acoustic waves propagating from the near surface of the Sun

Hélène Barucq¹, Juliette Chabassier¹, Marc Duruflé², Laurent Gizon and Michael Leguèbe³

¹Magique-3D INRIA Bordeaux Sud-Ouest, LMA-UPPA, Pau, France

²Magique-3D INRIA Bordeaux Sud-Ouest, IMB, Bordeaux, France

³Max Planck Institute for Solar System Research, Goettingen, Germany

Abstract

The numerical simulation of acoustic waves propagating from the near surface of the Sun can be performed by solving a Helmholtz equation whose main feature is having a coefficient that is exponentially decaying into the atmosphere of the Sun. Using high-order finite element methods, there is a need in truncating the computational domain by introducing a boundary surrounding the Sun. We propose a family of Radiation Boundary Conditions that are derived first from the factorization of the Helmholtz equation. When the Sun is approximated by a sphere, the corresponding mixed problem is well-posed and a series of numerical experiments allows to identify a second-order condition that gives accurate simulations at any frequency. The condition can be used for regular boundaries including the sphere but not only which makes it useful for any application involving a Helmholtz equation set into a heterogeneous medium.

Keywords: Helmholtz equation; heterogeneous medium

1 General setting

Acoustic waves are propagating in the near surface of the Sun. They can be represented as the solution to the Helmholtz problem:

$$-\frac{\omega^2}{\rho c^2} u - \operatorname{div} \left(\frac{1}{\rho} \nabla u \right) = f \quad \text{in } \Omega. \quad (1)$$

where ω denotes the pulsation, ρ is the density of the propagation medium and c stands for the wave velocity. The propagation medium is infinite defined *a priori* as the whole space including the Sun. The pulsation is a complex number incorporating a damping parameter γ :

$$\omega = \sqrt{1 + \frac{2i\gamma}{\omega_0}} \omega_0$$

The real pulsation ω_0 is given as $\omega_0 = 2\pi f_0$, where f_0 is the frequency. The density ρ and

the velocity c behave differently regarding they represent the Sun or its exterior [2]. In the near surface of the Sun, the parameters are collapsing to define a region which is called the atmosphere of the Sun. In general, they are represented as radial functions:

$$\begin{cases} \rho(r) = \rho^-(r), c(r) = c^-(r) & \text{if } r \leq R_S \\ \rho(r) = \rho^-(R_S) e^{-\alpha(r-R_S)} \\ ,c(r) = c^-(R_S) & \text{if } r > R_S \end{cases}$$

The volume source f is compactly supported. In the following, we derive conditions that are used to truncate the atmosphere.

2 Radiation conditions

We consider the homogeneous equation set in the atmosphere ($r \geq R_S$). Using separation of variables in spherical coordinates, we seek the solution u under the form

$$u(r, \theta, \phi) = \sum_{\ell=0}^L \sum_{m=-\ell}^{\ell} u_{\ell}^m(r) Y_{\ell}^m(\theta, \phi)$$

where Y_{ℓ}^m are the spherical harmonics and P_{ℓ}^m are the associated Legendre polynomials. L is the maximal degree of spherical harmonics used in the expression of u . The equation satisfied by u_{ℓ}^m is then

$$-\frac{\omega^2 r^2}{\rho c^2} u_{\ell}^m - \frac{\partial}{\partial r} \left(\frac{r^2}{\rho} \frac{\partial u_{\ell}^m}{\partial r} \right) + \frac{\ell(\ell+1)}{\rho} u_{\ell}^m = 0$$

Supposing that the density ρ is smooth enough and introducing α is given by : $\alpha(r) = -\frac{\rho'(r)}{\rho(r)}$, we end up with

$$\left(\frac{\partial}{\partial r} + \left(\frac{1}{r} + \frac{\alpha}{2} \right) \right)^2 u_{\ell}^m = - \frac{\omega^2}{c^2} - \frac{\omega_{c,\ell}^2}{c^2} u_{\ell}^m$$

where $\omega_{c,\ell}(r)$ is a cut-off frequency given by

$$\frac{\omega_{c,\ell}^2(r)}{c^2} = -\frac{1}{r^2} + \left(\frac{1}{r} + \frac{\alpha}{2} \right)^2 + \frac{\ell(\ell+1)}{r^2}$$

We then have, since α is constant, Expression (2) makes it possible to extract the principal part of the Dirichlet-to-Neumann operator governing outgoing and ingoing waves for a given surface. For that purpose, we see that to select propagating waves, we have to consider pulsations ω that are larger than the cut-off frequency. Then we get:

$$\left(\frac{\partial}{\partial r} + \left(\frac{1}{r} + \frac{\alpha}{2} \right) \right) u_\ell^m = \pm i \sqrt{\frac{\omega^2}{c^2} - \frac{\omega_{c,\ell}^2}{c^2}} u_\ell^m$$

where the sign $=$ means *equals modulo a zero-order operator*. Actually the factorization may not be exact because the factoring acts on a noncommutative ring. To select the relation which represents outgoing waves, we consider the equation which ensures the real part of the symbol of $i \partial_r$ to be negative ([3]). We then have: for r and ℓ fixed, if $\omega \geq \omega_{c,\ell}(r)$ out-going waves u_ℓ^m are formally represented as the waves that satisfy

$$\left(\frac{\partial}{\partial r} + \left(\frac{1}{r} + \frac{\alpha}{2} \right) \right) u_\ell^m = i \sqrt{\frac{\omega^2}{c^2} - \frac{\omega_{c,\ell}^2(r)}{c^2}} u_\ell^m \quad (2)$$

From a practical point of view, this condition is not well-suited for axisymmetrical cases since its dependency in ℓ is involved inside the square-root. Nevertheless, the squareroot can be replaced by a Taylor approximation using $\frac{\ell(\ell+1)}{\omega^2}$ as variable. We then get a second radiation condition given by:

$$\begin{aligned} \frac{\partial u_\ell^m}{\partial r} &= - \left(\kappa + \frac{\alpha}{2} \right) u_\ell^m + \frac{i\omega}{c} \sqrt{1 - \frac{c^2}{\omega^2} \left(\kappa\alpha + \frac{\alpha^2}{4} \right)} u_\ell^m \\ &+ \frac{c}{2i\omega} \frac{\ell(\ell+1)}{R^2} u_\ell^m \end{aligned} \quad (3)$$

3 Performance assessments

We have performed a large series of numerical experiments along with different boundary conditions. We have considered both toy problems for which we have reference solutions and a more realistic case based upon the so-called Model S (see [1]). We have studied how the different parameters may impact on the simulation accuracy. They are the value of the frequency f_0 , the value of α , the distance of truncation. It

turns out that in each case, condition (2) outperforms the other ones, followed very closely by (3). Figure 1 provides an illustration of the performance of the conditions. We see that for two very different values of α , the two conditions perform very well for any frequency, as compared to the standard Sommerfeld condition and to Dirichlet condition.

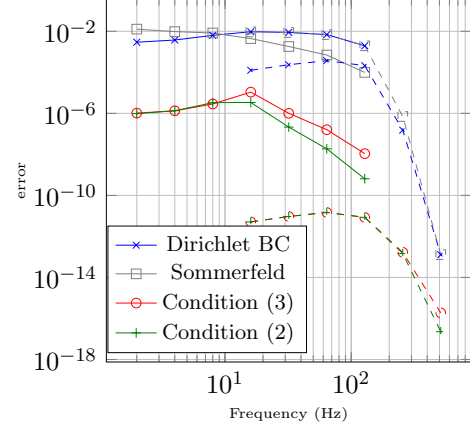


Figure 1: Relative L2 error. Solid line : $\alpha = 50$, Dashed line : $\alpha = 5 \times 10^3$.

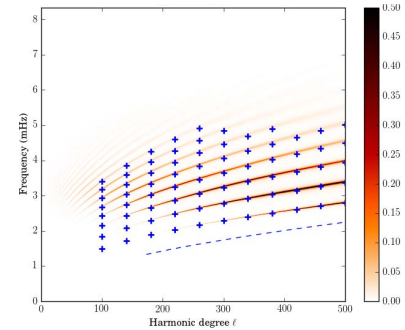


Figure 2: Power Spectrum obtained with Model S data and condition (2) compared with experimental data of the Sun (+).

References

- [1] Christensen-Dalsgaard et al. The current state of solar modeling. *Science*, vol 272, pp 1286 - 1292, 1996.
- [2] Schunker et al. Constructing and Characterising Solar Structure Models for Computational Helioseismology. *Solar Physics*, vol 271, pp 1–26, 2011.
- [3] Taylor Pseudodifferential operators. ISBN 978-1-4757-4189-6, 1996.

On the well-posedness of Goldstein's equations for aeroacoustics in recirculating flows

Antoine Bensalah^{1,*}, Jean-Francois Mercier², Patrick Joly²

¹ Airbus Group Innovations, 12 rue Pasteur, 92150 Suresnes, France

² POEMS (CNRS-INRIA-ENSTA), ENSTA ParisTech, 828 Boulevard des Maréchaux, 91762 Palaiseau Cedex, France

*Email: antoine.bensalah@ensta.fr

Abstract

We study the propagation of small time-harmonic acoustic perturbations of a stationary fluid flow. We use the Goldstein equations, coupling the acoustic phenomena to the vortices transport. On a simple toy geometry, allowing explicit calculations, we show the existence of resonant frequencies for recirculating flows, corresponding to an ill-posed problem for the transport of vortices. We prove that far enough from these resonances, the Goldstein model is well-posed under a coercivity condition. We determine numerically the frequency validity domain of this condition.

Keywords: aeroacoustics, harmonic transport equation, resonance, Fredholm alternative

1 Introduction

We consider an air flow of density and velocity ρ_0 and \mathbf{v}_0 , which satisfy the stationary Euler equations. We are interested in the time-harmonic acoustic perturbations $\rho(\mathbf{x})e^{-i\omega t}$ and $\mathbf{v}(\mathbf{x})e^{-i\omega t}$ of this carrier flow, at given frequency $\omega > 0$. They are solutions of the linearized Euler equations and we choose an equivalent model, Goldstein's equations [1], because lower computational cost is expected.

When the base flow is potential, meaning that $\boldsymbol{\omega}_0 := \text{curl}(\mathbf{v}_0) = \mathbf{0}$, the Goldstein equations reduce to a scalar convected Helmholtz equation, governing the acoustic potential φ defined by $\nabla\varphi = \mathbf{v}$. In a general flow, $\boldsymbol{\omega}_0 \neq \mathbf{0}$, acoustic perturbations are no longer potential and the Goldstein equations of unknowns φ and $\boldsymbol{\xi} = \mathbf{v} - \nabla\varphi$ are, for an acoustic source term f :

$$\begin{cases} D_\omega \left(\frac{1}{c_0^2} D_\omega \varphi \right) - \frac{1}{\rho_0} \nabla \cdot (\rho_0 (\nabla \varphi + \boldsymbol{\xi})) = f, \\ D_\omega \boldsymbol{\xi} + (\boldsymbol{\xi} \cdot \nabla) \mathbf{v}_0 - \nabla \varphi \times \boldsymbol{\omega}_0 = \mathbf{0}, \end{cases} \quad (1a, 1b)$$

where $D_\omega := -i\omega + \mathbf{v}_0 \cdot \nabla$ is the harmonic convective derivative, c_0 the speed of sound.

A great interest of Goldstein's model is that it can be seen as a perturbation of the scalar

convected Helmholtz equation. Following this remark, our general strategy to study the well-posedness of the Goldstein equations is to first show that the transport equation (1b) is well-posed, to express $\boldsymbol{\xi}$ as a function of φ and to control its L^2 norm with a positive constant C :

$$\|\boldsymbol{\xi}\|_{L^2} \leq C \|\nabla\varphi \times \boldsymbol{\omega}_0\|_{L^2}. \quad (2)$$

With the estimation (2), we show that Goldstein's equations, with suitable boundary conditions, are well-posed in the H^1 framework if

$$1 - \|\mathbf{v}_0/c_0\|_\infty^2 - C\|\boldsymbol{\omega}_0\|_\infty > 0. \quad (3)$$

Therefore the key point is to establish the estimation (2). We have shown that it is always possible in the case of unclosed streamlines with no stopping point. In presence of closed streamlines, the Goldstein equations may be ill-posed because of possible resonances. To clarify this last case, we focus here on a simple geometry, adapted to cartesian coordinates, for which we are able to fully determine the resonant frequencies of the transport equation. Moreover we are able to study the impact of these resonances on the full coupled Goldstein model.

2 A toy model in a simple geometry

We consider a rectangle $\Omega = (0, L) \times (0, h)$ and the shear flow $\mathbf{v}_0(x, y) = v_0(y)\mathbf{e}_x$, $v_0 > 0$, as shown on Fig. 1. To mimic a recirculating flow, we suppose that Ω is periodic in the x -direction.

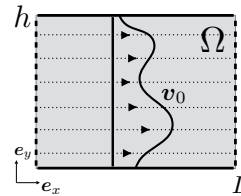


Figure 1: Domain Ω periodic in x -direction

3 Transport equation and its resonances

In Ω , the transport equation (1b) simplifies: noting $\mathbf{g} = \nabla\varphi \times \boldsymbol{\omega}_0$, $\boldsymbol{\xi} \in L^2(\Omega)^2$ satisfies

$$D_\omega \boldsymbol{\xi} + \begin{pmatrix} 0 & v'_0 \\ 0 & 0 \end{pmatrix} \boldsymbol{\xi} = \mathbf{g}, \quad \boldsymbol{\xi}(\cdot, y) \text{ } L\text{-per.} \quad (4)$$

We have proved that Eq. (4) is well-posed if and only if the frequency ω is not in the resonant set

$$\mathcal{W}_{res} := \bigcup_{n \in \mathbb{Z}} \frac{2\pi n}{L} \left[\min v_0, \max v_0 \right],$$

and outside this set we have the estimation

$$\|\boldsymbol{\xi}\|_{L^2} \leq \underbrace{\tilde{C} \sqrt{2(1 + \tilde{C}^2)}}_{C_0} \|\mathbf{g}\|_{L^2}, \quad (5)$$

$$\text{with, } \tilde{C} := \sup_{y \in (0, h)} \left| \frac{L/v_0(y)}{2 \sin(\omega L/v_0(y))} \right|.$$

In other words, to each streamline $\{y = y^*\}$ corresponds a discrete family of resonant frequencies, $2\pi/Lv_0(y^*)\mathbb{Z}$, to avoid to be well-posedness.

4 Fredholm alternative outside \mathcal{W}_{res}

Outside the resonant set i.e. $\omega \notin \mathcal{W}_{res}$, the *a priori* estimation (5) enables us to prove that the Goldstein problem is of Fredholm type if

$$C(\omega) := 1 - \|v_0/c_0\|_\infty^2 - \|v'_0\|_\infty C_0 > 0. \quad (6)$$

We represent on Fig. 2, for a linear velocity profile $v_0(y) = ay + b$, the set \mathcal{W}_{res} in red and the constant C versus ω . If the blue curve is above the dashed red line, (6) holds. This figure illustrates that ω has not only to be outside \mathcal{W}_{res} but has to be far enough, as shows in particular the part of the blue curve around $\omega = 30$, remaining below 0. Moreover, there is no resonance at low frequencies, at least in $(0, 2\pi \min v_0/L)$ and the spectrum becomes continuous above a threshold, here $\omega \approx 31$.

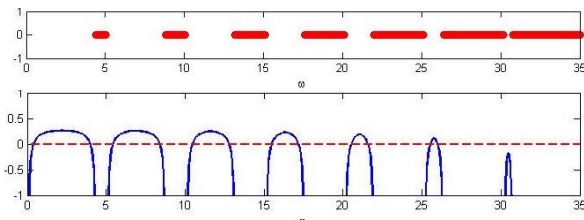


Figure 2: In red: resonant set; in blue: $C(\omega)$, Goldstein's equations are well-posed iff $C(\omega) > 0$

5 Unicity : Fourier analysis

Applying Fredholm theory, we deduce well-posedness by proving the unicity of solution. Given the following Fourier decompositions

$$\varphi = \sum_{n \in \mathbb{Z}} \varphi_n(y) e^{i\beta_n x}, \quad \boldsymbol{\xi} = \sum_{n \in \mathbb{Z}} \boldsymbol{\xi}_n(y) e^{i\beta_n x},$$

where $\beta_n = 2n\pi/L$, Goldstein's equations and associated boundary conditions reduce to a family of scalar boundary value problems on φ_n :

$$-\frac{d^2\varphi_n}{dy^2} + p_n \varphi_n = 0, \quad (7a)$$

$$\frac{d\varphi_n}{dy}(h) = \left(i\omega - \frac{\alpha'_n}{\alpha_n} \right) \varphi_n(h) \quad (7b)$$

$$\frac{d\varphi_n}{dy}(0) = -\frac{\alpha'_n}{\alpha_n} \varphi_n(0) \quad (7c)$$

where $p_n := \beta_n^2 - \alpha_n^2 - \frac{\alpha''_n}{\alpha_n} + 2 \left(\frac{\alpha'_n}{\alpha_n} \right)^2$, and $\alpha_n := -\omega + \beta_n v_0$. $\boldsymbol{\xi}_n$ are then deduced from

$$\xi_{x,n} = \frac{i}{\beta_n} \frac{\alpha'_n}{\alpha_n} \left(\frac{\alpha'_n}{\alpha_n} + \frac{d}{dy} \right) \varphi_n, \quad \xi_{y,n} = \frac{\alpha'_n}{\alpha_n} \varphi_n. \quad (8)$$

The study of the variational formulation associated with (7) shows that only 0 is solution.

6 Going further: with resonant lines

When ω is a resonant frequency, the transport equation is ill-posed in the sense that it has no solution in $L^2(\Omega)^2$. To look for solutions in larger spaces, let us notice that resonant frequencies correspond to the vanishing of the coefficient α_n , making p_n a singular function. Moreover, given φ_n , Eq. (8) shows that the components of $\boldsymbol{\xi}_n$ are singular at the resonant lines located at $\{y^* : \alpha_n(y^*) = 0\}$. Therefore solutions at resonance frequencies should be looked for in more singular spaces. Similar results have been obtained in plasma [2] and we have started to adapt the approach to aeroacoustics. The idea is to introduce absorption and to look how the solutions degenerate as it goes to 0.

References

- [1] M. E. Goldstein, Unsteady vortical and entropic distortion of potential flows round arbitrary obstacles, *J. Fluid Mech.* **89**(3), 433-468 (1978)
- [2] Bruno Desprès, Lise-Marie Imbert-Gérard, Olivier Lafitte. Singular solutions for the plasma at the resonance. 2014. [<hal-01097364>](https://hal-01097364)

A continuation method for building large invisible obstacles in waveguides

Antoine Bera^{1,*}, Anne-Sophie Bonnet-Ben Dhia¹, Lucas Chesnel², Sergei Nazarov³

¹POEMS (CNRS-INRIA-ENSTA ParisTech-Université Paris Saclay), Palaiseau, France

²INRIA, CMAP (Ecole Polytechnique-Université Paris Saclay), Palaiseau, France

³Institute of Problems of Mechanical Engineering, Russian Academy of Sciences, St.Petersburg, Russia

*Email: antoine.bera@ensta-paristech.fr

Abstract

In previous papers [1, 2], a method has been proposed to prove the existence of invisible perturbations in waveguides. The method is constructive and has been validated numerically. But the drawback is that it is limited to small perturbations. In the present work, we show that the previous idea can be combined with a continuation method, in order to get larger invisible perturbations.

Keywords: waveguides, invisibility, continuation method

1 The model problem

We consider a 2D acoustic waveguide occupying the domain $\Omega = \{(x, y); x \in \mathbb{R} \text{ and } 0 < y < 1\}$. In presence of a bounded penetrable obstacle \mathcal{O} and in harmonic regime of angular frequency ω , the acoustic pressure p satisfies the equations

$$\begin{cases} \Delta p + k^2(1 + \chi_{\mathcal{O}}\rho)p = 0 & \text{in } \Omega \\ \frac{\partial p}{\partial y} = 0 & \text{on } \partial\Omega \end{cases} \quad (1)$$

where $k = \omega/c$ (c is the acoustic waves velocity), $\chi_{\mathcal{O}}$ is the characteristic function of \mathcal{O} and $\rho \in L^\infty(\mathcal{O})$.

We suppose that $k < \pi$, so that there is only one propagative mode in the waveguide, which is the piston mode $e^{\pm ikx}$. The scattering of this mode, coming from the left, by the perturbation \mathcal{O} leads to a solution p of (1) such that:

$$p = \begin{cases} e^{ikx} + Re^{-ikx} + \tilde{p}(x, y) & x < 0 \\ Te^{ikx} + \tilde{p}(x, y) & x > 0 \end{cases} \quad (2)$$

where \tilde{p} is a superposition of evanescent modes which decay exponentially at infinity. Due to conservation of energy, the complex reflection and transmission coefficients R and T are such that

$$|R|^2 + |T|^2 = 1. \quad (3)$$

We say that the obstacle (\mathcal{O}, ρ) is *invisible* if $T = 1$ (which implies $R = 0$ by (3)). An obstacle such that $R = 0$ is called *non-reflective*. By (3), it satisfies $|T| = 1$, but not necessarily $T = 1$: there may be a phase shift of the transmitted wave. In the sequel, we focus our attention to build non-reflective obstacles. One can proceed similarly to get invisible perturbations.

2 Building small non-reflective obstacles

Let us first show how to build small non-reflective obstacles. We fix the support of the heterogeneity $\overline{\mathcal{O}}$. Giving some small parameter ε , we look for a function $\mu \in L^\infty(\mathcal{O})$ satisfying

$$R(\varepsilon\mu) = 0. \quad (4)$$

Since $R(0) = 0$ (no obstacle produces no reflection), the Taylor expansion of $R(\varepsilon\mu)$ takes the form:

$$R(\varepsilon\mu) = \varepsilon dR(0)\mu + \varepsilon^2 \tilde{R}(\varepsilon, \mu)$$

where $dR(0)$, the differential of R at 0, has the following expression:

$$dR(0)\mu = \frac{ik}{2} \int_{\mathcal{O}} \mu(x, y) e^{2ikx} dx dy.$$

The idea is then to choose some real valued functions μ_0, μ_1 and μ_2 such that

$$dR(0)\mu_0 = 0, \quad dR(0)\mu_1 = 1 \quad \text{and} \quad dR(0)\mu_2 = i$$

and to look for a solution μ of (4) of the form

$$\mu = \mu_0 + \tau_1\mu_1 + \tau_2\mu_2 \quad (5)$$

where the τ_j are real parameters to determine. Inserting (5) in the Taylor expansion of $R(\varepsilon\mu)$, we get the following fixed-point equation for $\tau = \tau_1 + i\tau_2 \in \mathbb{C}$:

$$\tau = -\varepsilon \tilde{R}(\varepsilon, \mu_0 + \tau_1\mu_1 + \tau_2\mu_2). \quad (6)$$

We can prove that, for ε small enough, the function (of the variable τ) on the right hand side of (6) is a contraction on any given closed ball of \mathbb{C} . This yields the following result.

Theorem 1 *For ε small enough, there is a unique solution μ of the form (5) to equation (4).*

3 The continuation method

To build non-reflective obstacles of larger amplitude, the idea (given in section 3 of [3]) is to iterate the previous technique. More precisely, at iteration n , we denote by $\rho^{(n)}$ a solution of $R(\rho^{(n)}) = 0$. To build the next iterate, we introduce $\mu_0^{(n)}$, $\mu_1^{(n)}$ and $\mu_2^{(n)}$ such that $dR(\rho^{(n)})\mu_0^{(n)} = 0$, $dR(\rho^{(n)})\mu_1^{(n)} = 1$ and $dR(\rho^{(n)})\mu_2^{(n)} = i$. Then we prove that, for $\varepsilon^{(n)}$ small enough, there exists a unique solution

$$\rho^{(n+1)} = \rho^{(n)} + \varepsilon^{(n)}(\mu_0^{(n)} + \tau_1^{(n)}\mu_1^{(n)} + \tau_2^{(n)}\mu_2^{(n)})$$

of $R(\rho^{(n+1)}) = 0$ with $(\tau_1^{(n)}, \tau_2^{(n)})$ in \mathbb{R}^2 . One difficulty is that the existence of $\mu_1^{(n)}$ and $\mu_2^{(n)}$ is ensured if and only if the differential $dR(\rho^{(n)})$ is onto, which cannot be easily proved from its expression:

$$dR(\rho^{(n)})\mu = \frac{ik}{2} \int_{\mathcal{O}} \mu(x, y)p^{(n)}(x, y)e^{ikx}dxdy$$

where $p^{(n)}$ denotes the solution of (1) of the form (2) for $\rho = \rho^{(n)}$. Concerning the choice of the $\mu_j^{(n)}$, we explore two strategies.

First strategy: we choose the $\mu_j^{(n)}$ for all n in the same 3D space $V = \text{span}(\mu_0, \mu_1, \mu_2)$. The advantage is that this leads to a large non-reflective perturbation described by only three real parameters. For instance, using piecewise constant μ_j , we obtain the following curve in the space V (note the very small scale of the vertical coordinate).

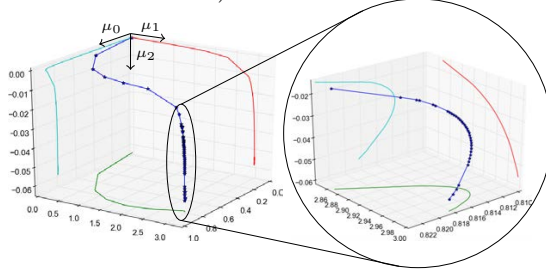


Figure 1: Solutions of $R(\rho) = 0$ in V . Each dot corresponds to a non-reflective ρ .

The non-reflective obstacle at the end of the curve (depicted on Figure 2 top) has an amplitude which is 4 times larger than the one obtained at the first iteration. The algorithm is almost blocked at this point because of the presence of a very small radius of curvature of the curve, which imposes to ε to be less than 10^{-5} to ensure the convergence of the fixed-point algorithm.

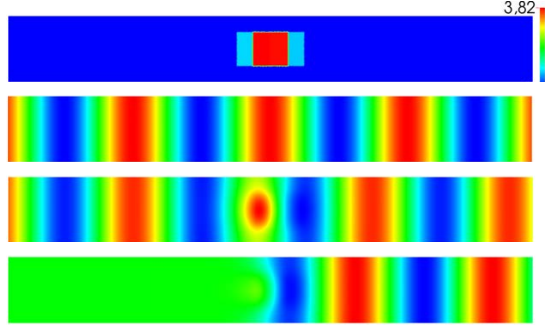


Figure 2: From top to bottom: non-reflective obstacle, incident field, total field and scattered field at the end of the curve of Figure 1.

Second strategy: we choose the $\mu_j^{(n)}$ in a space V of dimension $N \gg 3$. $\mu_0^{(n)}$ is built by an extrapolation of the previous points, $\mu_1^{(n)}$ and $\mu_2^{(n)}$ are obtained by using a pseudo-inverse of $dR(\rho^{(n)})$. Compared to the first one, this strategy is supposed to give access to larger obstacles. The counterpart is that the contrast function ρ is described by a large number of parameters, so that it could be difficult to realize in practice.

Acknowledgement: we thank the DGA for its financial support.

References

- [1] A.-S. Bonnet-Ben Dhia and S. Nazarov, Obstacles in acoustic waveguides becoming “invisible” at given frequencies, *Acoustical Physics*, 59(6), (2013) pp. 633-639.
- [2] A.-S. Bonnet-Ben Dhia, E. Lunéville, Y. Mbeutcha and S. Nazarov, A method to build non-scattering perturbations of two-dimensional acoustic waveguides, *Math. Meth. in the Appl. Sci.*, (2015).
- [3] A.-S. Bonnet-Ben Dhia, J. Taskinen and S. Nazarov, Underwater topography invisible for surface waves at given frequencies, *Wave Motion*, 57, (2015) pp. 129-142.

Waves in solids with slow dynamics: an internal-variable model

Harold Benjamin¹, Bruno Lombard^{1,*}, Guillaume Chiavassa², Nicolas Favrie³

¹Aix-Marseille Univ, CNRS, Centrale Marseille, LMA, Marseille, France

²Centrale Marseille, CNRS, Aix-Marseille Univ, M2P2 UMR 7340, 13451 Marseille Cedex 20, France

³Aix-Marseille Univ, UMR CNRS 7343, IUSTI, Polytech Marseille, 13453 Marseille Cedex 13, France

*Email: lombard@lma.cnrs-mrs.fr

Abstract

Rocks and concrete have a strong nonlinear behavior. Moreover, the speed of sound diminishes slowly under a dynamic loading. To reproduce this behavior, an internal-variable model of continuum is proposed. It is composed of a constitutive law for the stress and an evolution equation for the internal variable. Qualitatively, the model reproduces the experiments.

Keywords: acoustoelasticity, softening, continuum mechanics

1 Introduction

In dynamic acoustoelastic testing, the speed of sound measured locally decreases in time. This softening occurs over a time scale larger than the period of the dynamic loading, which highlights the phenomenon of *slow dynamics*. Moreover, the evolution of this speed with respect to the strain presents an hysteresis curve. All these phenomena are accentuated when the strain amplitude is increased [1].

Several models, such as Preisach-Mayergoyz, have been designed to mimic the hysteresis. The soft-ratchet model [2] by Vakhnenko et al. results from a different approach. A variable g , interpreted as a concentration of activated defects, is introduced in order to modify the elastic modulus. Also, an evolution equation for g is provided. The soft-ratchet model was developed in one space dimension and does not generalize straightforwardly to higher dimensions.

We propose a new model based on thermodynamics with internal variables. Here too, a variable g is introduced to describe the softening, as well as an evolution equation for g . The model satisfies the principles of thermodynamics by construction, which is not the case of the soft-ratchet model. For the sake of simplicity, only the 1D case is presented here. In a particular case, the equations are solved analytically. Qualitatively, the three expected phenomena are reproduced. The general 3D case is

detailed in a future publication [3].

2 Governing equations

We consider an elastic solid, which is vibrating longitudinally. In classical Green elasticity, the internal energy per unit volume is $\rho_0 e = W(\varepsilon)$, where e is the internal energy per unit mass and ρ_0 is the mass density in the reference (undeformed) configuration. The strain energy density W is a function of the axial strain $\varepsilon = \partial u / \partial x$, where u denotes the axial displacement. In the Lagrangian representation of motion, elastodynamics write [2]

$$\begin{cases} \frac{\partial \varepsilon}{\partial t} = \frac{\partial v}{\partial x}, \\ \rho_0 \frac{\partial v}{\partial t} = \frac{\partial \sigma}{\partial x}, \end{cases} \quad (1)$$

where v denotes the particle velocity. The Cauchy stress is deduced from the strain energy density according to $\sigma = W'(\varepsilon)$, where the ' denotes the derivative.

Now, an internal variable g is introduced to describe the softening of the material. We define the internal energy per unit volume of material as follows:

$$\rho_0 e = \phi_1(g) W(\varepsilon) + \phi_2(g). \quad (2)$$

The functions ϕ_1 and ϕ_2 are smooth functions of the internal variable g , typically

$$\phi_1(g) = 1 - g, \quad (3)$$

$$\phi_2(g) = \frac{1}{2} \gamma g^2, \quad (4)$$

where $\gamma > 0$ is an energy per unit volume. An evolution equation for g and a constitutive law for σ are added to the equations of elastodynamics (1):

$$\begin{cases} \sigma = \phi_1(g) \bar{\sigma}(\varepsilon), \\ \frac{\partial g}{\partial t} = -\frac{\phi'_1(g) W(\varepsilon) + \phi'_2(g)}{\tau_1}, \end{cases} \quad (5)$$

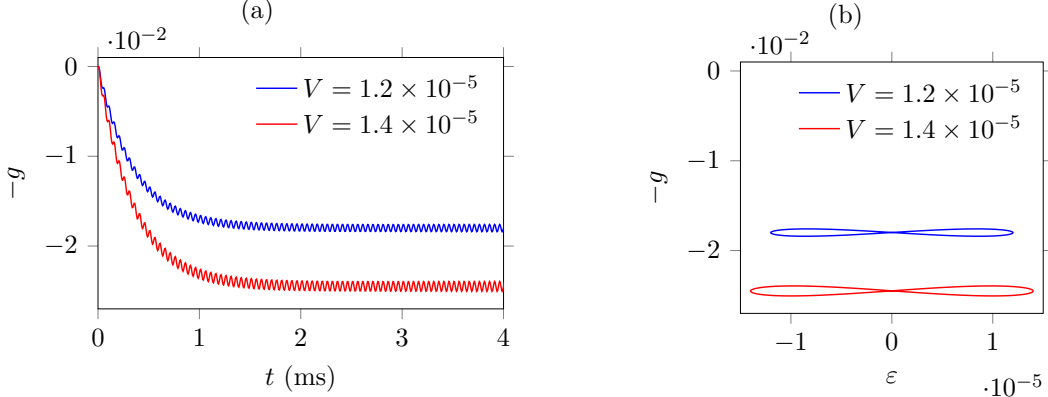


Figure 1: (a) Softening of the material for several strain amplitudes (7). (b) Hysteresis curves in steady state ($t \gg \tau_\gamma$ in (7)).

where $\tau_1 > 0$ is a given parameter. The stress $\bar{\sigma}(\varepsilon) = W'(\varepsilon)$ is derived from the strain energy density function, as in classical Green elasticity. By construction, the constitutive laws (5) satisfy the principles of thermodynamics.

3 Example

With the functions ϕ_1 and ϕ_2 from (3)-(4), the evolution equation in (5) becomes

$$\frac{\partial g}{\partial t} + \frac{g}{\tau_\gamma} = \frac{W(\varepsilon)}{\tau_1}, \quad (6)$$

where $\tau_\gamma = \tau_1/\gamma$. In the case of Hooke's law, the strain energy density is $W(\varepsilon) = \frac{1}{2}E\varepsilon^2$, where E is the Young's modulus. If the strain is imposed, equation (6) can be solved analytically. For instance, the solution of (6) with the initial condition $g(0) = 0$ is

$$g(t) = \frac{EV^2}{4\gamma} \left(1 - \frac{(2\omega_c\tau_\gamma)^2}{1 + (2\omega_c\tau_\gamma)^2} e^{-t/\tau_\gamma} - \frac{\cos(2\omega_c t) + 2\omega_c\tau_\gamma \sin(2\omega_c t)}{1 + (2\omega_c\tau_\gamma)^2} \right), \quad (7)$$

in the case of a sinusoidal strain $\varepsilon = V\sin(\omega_c t)$. According to the expression of the stress in (5), the relative variation in elastic modulus with respect to a linear-elastic solid is

$$\frac{\Delta M}{M} = \frac{\partial \sigma / \partial \varepsilon - E}{E} = -g. \quad (8)$$

On figure 1, we represent the variation in elastic modulus (8) deduced from (7). The parameters are issued from table 1 and the angular frequency is $\omega_c = 2\pi \times 10^4$ rad/s.

Table 1: Physical parameters.

E (GPa)	γ (J.m^{-3})	τ_1 ($\text{J.m}^{-3}.\text{s}$)
10	20	7×10^{-3}

4 Conclusion

A thermodynamically admissible 1D model of solid with slow dynamics has been developed. In a simplified case, the model is shown to reproduce qualitatively the experimental observations. Furthermore, the model adds only one scalar evolution equation to the classical equations of elastodynamics, with a reduced number of new parameters. Extension to 3D geometries is described in a future publication [3].

References

- [1] J. Rivière, G. Renaud, R. A. Guyer and P. A. Johnson, Pump and probe waves in dynamic acousto-elasticity: Comprehensive description and comparison with nonlinear elastic theories. *J. Appl. Phys.* **114** (2013), p. 054905.
- [2] N. Favrie, B. Lombard and C. Payan, Fast and slow dynamics in a nonlinear elastic bar excited by longitudinal vibrations. *Wave Motion* **56** (2015), pp. 221–238.
- [3] H. Benjamin, B. Lombard, G. Chiavassa and N. Favrie, Nonlinear waves in solids with slow dynamics: an internal-variable model. Submitted (2016).

Stable and unstable Airy-related caustics and beams

Michael Berry^{1,*}

¹H H Wills Physics Laboratory, University of Bristol, UK

<https://michaelberryphysics.wordpress.com>

*Email: asymptotico@bristol.ac.uk

Abstract

Accelerated beams (Airy and Airy-related) correspond to curved caustics of the underlying geometrical rays. The connections will be explained in detail, concentrating on beams associated with the stable caustics classified by catastrophe theory. Some such beams, including the simplest Airy beam in three-dimensional space, are unstable in the mathematical sense: under a symmetry-breaking perturbation, they break up into caustics that are stable. In the Airy case, this is a hyperbolic umbilic catastrophe. Associated with the stable caustics are a variety of exact solutions of the paraxial wave equations.

Reprogrammable nonlinear phononic metamaterials

Osama R. Bilal^{1,*}, André Foehr², Chiara Daraio³

¹Department of Physics, ETH Zürich, Zürich, Switzerland

²Department of Mechanical and Process Engineering, ETH Zürich, Zurich, Switzerland

³Division of Engineering and Applied Science, California Institute of Technology, Pasadena, USA

*Email: bilalo@ethz.ch

Abstract

A major challenge in materials design is to engineer matter that has the ability to change its mechanical properties in a predetermined manner within a practical time frame. Most of these mechanical properties are inscribed in materials' frequency dispersion spectrum, ranging from material stiffness at zero frequency to its thermal conductivity at much higher frequencies. In this work, we harness geometric and magnetic nonlinearities to tune the dispersion characteristics of matter in real-time. As a demonstration of principle, we program our nonlinear metamaterials to change the frequency range of its subwavelength band gap, where mechanical waves don't propagate, in real-time. Using numerical modeling and experiments, we realize a meta-plate that can be re-programmed at the unit cell level (i.e., element wise) to guide elastic energy in arbitrary directions in space within fractions of a second. The realized concept can inspire the design of advanced functioning materials.

Keywords: metamaterial, geometric & magnetic nonlinearity , shape changing materials

Phononic metamaterials are material systems with the ability to manipulate mechanical (i.e., phononic) waves in desired fashions as they can present peculiar properties, for example, negative effective density and stiffness [1]. These properties can be engineered to guide, focus and cloak elastic waves. Moreover, they have the potential to shield objects, ranging from nano & micro-scale devices to buildings from thermal and seismic energy (for a complete list of applications consult the recent reviews in [1] and the references within).

The basic principle of operation in phononic metamaterials is local resonance at the unit cell (the basic building block that tessellates in space) level. These resonances hybridize with the material transmission bands creating narrow frequency ranges where mechanical waves can't

propagate (band gaps). Such resonance hybridization is shown to break the mass-density law of sound transmission by more than an order of magnitude at subwavelength frequencies [2]. However, these resonance-induced band gaps are typically narrow, which impose a hard limit on the material functionality in practical applications such as seismic shielding. A logical step to overcome this hurdle is to utilize materials with tunable properties. Such tunability can be achieved by means of piezo shunting, cell symmetry relaxation, static loading, granular contacts and acoustic trapping [3]. However, most of the methods reported in the literature are not tunable in real-time, require continuous consumption of energy or need direct contact with the material.

Here, we present a new avenue to material tunability by means of geometrically nonlinear metamaterial [4], which can change its shape from flat "two dimensional" to extruded "three dimensional" form as in figure 1a. The realized metamaterial retains a subwavelength band gap in its flat configuration, which can be systematically reduced by extruding the unitcell vertically until the band gap closes, as shown in the numerically obtained dispersion diagrams of both flat and extruded unit cells in figure 1b.

In order to engineer a shape change in our material in real-time, we exploit magnetic nonlinearities by embedding a permanent magnet at the center of the metamaterial unit cell. By changing the intensity of an external magnetic field underneath the metamaterial, we are able to "program" it in real-time to change shape, therefore changing its phononic properties at a given frequency from propagation to attenuation and vice-versa. To verify our numerical prediction, we excite the system harmonically using a mechanical shaker and measure the transmitted wave signal, using a laser Doppler vibrometer, before and after the programming (figure 2).

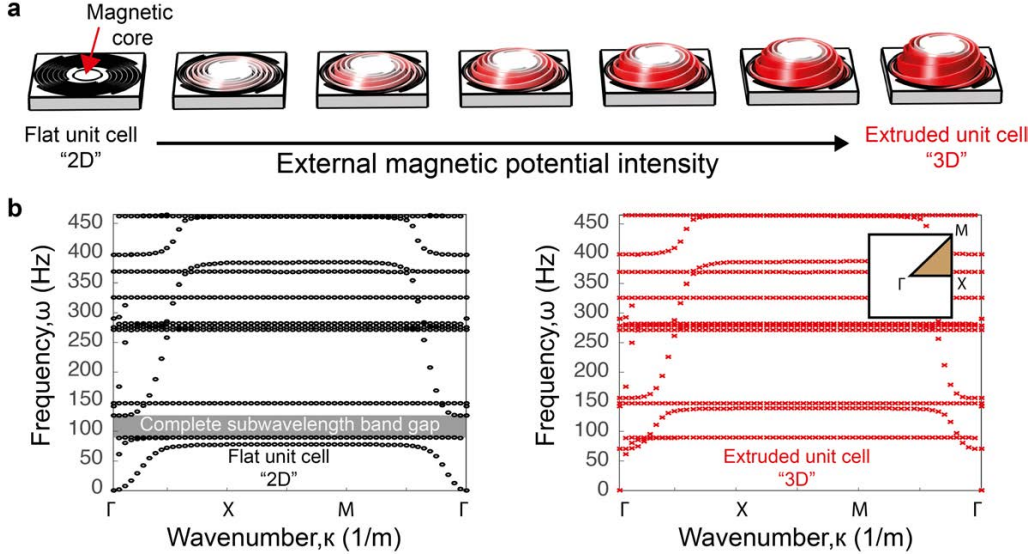


Figure 1: (a) The geometric evolution of the metamaterial unit cell during programming; as the intensity of the external magnetic field increases, the metamaterial transforms from two to three-dimensions. (b) Dispersion curves for a unit cell made of polycarbonate by means of additive manufacturing with in-plane Floquet boundary conditions. The lattice constant is 12.5 mm and the thickness is 2 mm. When the unit cell is flat “2D” there exist a complete band gap between 89 and 126 Hz. The band gap closes completely in the extruded case “3D” (right). The inset in figure b left highlights the irreducible Brillouin zone of the unit cell.

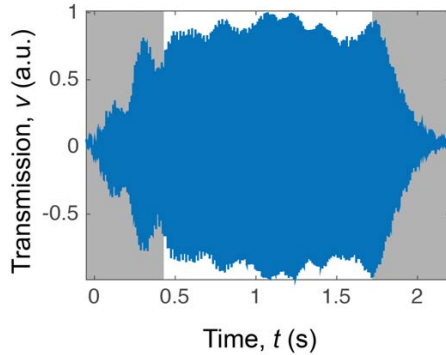


Figure 2: Experimentally acquired time signal at $\omega = 96$ Hz in the center of a meta-plate composed of (28x20) unit cells with fixed corners. The time periods spanned in programming from 2D to 3D and vice-versa are highlighted in gray.

This work presents a realization of a programmable phononic metamaterial with band gap tunability. We harness nonlinearities of both geometry and magnets providing a non-invasive element-wise control methodology. Our metamaterial can have impact in the design of ad-

vanced functional materials, programmable matter and transducers for acoustic imaging.

References

- [1] M. Hussein, M. Leamy and M. Ruzzene *Appl. Mech. Rev.* **66** (2014): 040802. S. Cummer, C. A. Johan, and A. Alu, *Nature Reviews Materials* **1** (2016): 16001.
- [2] Z. Liu, *et.al.*, *Science* **289** (2000): 1734.
- [3] Z. Hou, and B. M Assouar, *Appl. Phys. Lett.*, **106** (2015):251901. P. Celli and S. Gonella, *Appl. Phys. Lett.*, **106** (2015):091905. P. Wang, *et. al.*, *Phys. Rev. Lett.*, **113** (2014):014301. N. Boehler G. Theocharis and C. Daraio *Nat. mat.*, **10**, (2011):665–668. M. Caleap and B. Drinkwater, *PNAS*, **111**, (2014):6226–6230.
- [4] O. R. Bilal, A. Foehr and C. Daraio, *Under review* (2016). & *In preparation* (2017).

Discontinuous Galerkin Discretizations for Maxwell's equations in Nonlinear Kerr Media with Linear Lorentz Dispersion

Vrushali A. Bokil^{1,*}, Yingda Cheng², Yan Jiang², Fengyan Li³

¹Department of Mathematics, Oregon State University, Corvallis, OR, USA

²Department of Mathematics, Michigan State University, East Lansing, MI, USA

³Department of Mathematical Sciences, Rensselaer Polytechnic Institute, Troy, NY, USA

*Email: bokilv@math.oregonstate.edu

Abstract

In this talk, we consider a nonlinear, dispersive, Maxwell model in its first order form, where the nonlinearity comes from the *instantaneous electronic Kerr response* together with the *single resonance linear Lorentz dispersion*. We design high order Discontinuous Galerkin (DG) discretizations in space for this model, and prove that the resulting semi-discrete and fully-discrete methods, based on leap-frog and implicit trapezoidal temporal schemes, are energy stable.

Keywords: Maxwell's equations, Kerr nonlinearity, linear Lorentz dispersion.

1 Introduction

In this talk, we consider the numerical simulation of electromagnetic (EM) pulse propagation in nonlinear optical materials. The model is Maxwell's equations along with ordinary differential equations (ODE) for the electric polarization that comprises of a linear material response, modeled by a Lorentz dispersion, while the nonlinear response has an instantaneous part governed by the Kerr effect [1].

We construct DG methods for the nonlinear Maxwell model in one spatial dimension. When the numerical fluxes are chosen to be central or alternating, the solutions to the semi-discrete DG methods satisfy an energy decay just as the exact solutions do, hence the methods are stable, even in the presence of the Kerr effect. We propose a novel strategy to discretize the nonlinear terms within the commonly used leap-frog and implicit trapezoidal temporal discretization. The resulting fully discrete methods are proved to be stable. More specifically, the leap-frog DG method is conditional stable under an expected CFL condition, while the fully implicit method with the trapezoidal discretization in time is unconditionally stable. In both cases, the ODE part of the model system is discretized implicitly. *In this talk, the methods*

and numerical verification will be presented for the model in one dimensions, and extensions to two spatial dimensions as well as the inclusion of a nonlinear retarded response (stimulated Raman scattering) will be presented.

2 Nonlinear Maxwell Model in 1D

We consider Maxwell's equations in a non magnetic, non-conductive, linear dispersive medium with a Kerr type nonlinearity. In one spatial dimension, the model is given as

$$\mu_0 \frac{\partial H}{\partial t} = \frac{\partial E}{\partial x}, \quad \frac{\partial D}{\partial t} = \frac{\partial H}{\partial x}, \quad (1)$$

$$\frac{\partial P}{\partial t} = J, \quad \frac{\partial J}{\partial t} = -\frac{1}{\tau}J - \omega_0^2 P + \omega_p^2 E, \quad (2)$$

along with the constitutive law

$$D = \epsilon_0(\epsilon_\infty E + P + aE^3). \quad (3)$$

In the above, the variables E and D are the electric field and electric displacement, respectively. The variable H is the magnetic field. The variables P and J are the electric polarization, and its current density, respectively, that describe the linear Lorentz dispersion model. The parameters ω_0 , ω_p and $\frac{1}{\tau}$ are the resonance and plasma frequencies, and damping constant, respectively, of the linear Lorentz model. The parameters ϵ_∞ , ϵ_0 , μ_0 are the infinite frequency relative permittivity, free space permittivity and permeability, respectively, while a is a third order coupling constant associated to the cubic Kerr term. Model (1)-(3) admits the following energy decay.

Theorem 1 *Under the assumption of periodic boundary conditions, the energy $\mathcal{E} = \mathcal{E}(t)$ of the system (1)-(3), defined as*

$$\begin{aligned} \mathcal{E}(t) = & \int_{\Omega} \left(\frac{\mu_0}{2} H^2(t) + \frac{\epsilon_0 \epsilon_\infty}{2} E^2(t) + \frac{\epsilon_0}{2\omega_p^2} J^2(t) \right. \\ & \left. + \frac{\epsilon_0 \omega_0^2}{2\omega_p^2} P^2(t) + \frac{3\epsilon_0 a}{4} E^4(t) \right) dx, \end{aligned}$$

satisfies $\frac{d}{dt}\mathcal{E}(t) = -\frac{\epsilon_0}{\omega_p^2 \tau} \int_{\Omega} J^2(t) dx \leq 0$.

3 Semi-discrete Discontinuous Galerkin Method

We assume periodic boundary conditions in the x direction. We define finite dimensional discrete spaces which consist of piecewise polynomials of degree up to k with respect to a given mesh, and formulate semi-discrete DG methods for the system (1) - (3). The constitutive law (3) is imposed via the L^2 projection. Numerical fluxes for the electric and magnetic fields are introduced that are either central fluxes (CF), or a pair of two different types of alternating fluxes (AFI, AF II). Finally, we establish stability of the semi-discrete DG schemes which are consistent with the energy stability of the PDE-ODE system (1)-(3) given in Theorem 1.

4 Fully discrete DG schemes

Common temporal discretizations such as the second order leap frog (LF) or implicit trapezoidal (IT) method cannot yield provable stability results unlike in the case of linear models [2]. We design novel modifications of LF and the IT methods to design fully discrete DG schemes for (1)-(3). The schemes are second order accurate and with the special treatment for the Kerr terms, fully discrete energy stability can be proved. We show that the LF scheme satisfies a corresponding energy decay under a CFL condition, while the IT method is unconditionally stable.

5 Kink and Anti-Kink Solutions

As shown in [3] with no damping ($1/\tau = 0$), we can find a traveling wave solution $E(x, t) = E(\xi)$, where $\xi = x - vt$, and similarly for other variables. Here, we consider the problem on $x \in [0, 6]$ with periodic boundary condition. A traveling kink and anti-kink wave can be obtained numerically. Here, the approximate solution with 160000 grid points is used as the initial condition (Figure 1). And it can be extended periodically on R with period 6. Numerical results are tested at $t = 6/v$, at which time the wave moves back to the same position as the initial condition. To obtain the high order accuracy, we choose $\Delta t = CFL \times h^{(k+1)/2}$, with appropriate Courant numbers.

With alternating fluxes, the schemes achieve the optimal $(k + 1)$ -th order. However, when using the central flux and leap-frog scheme, the order of accuracy will be sub-optimal for odd

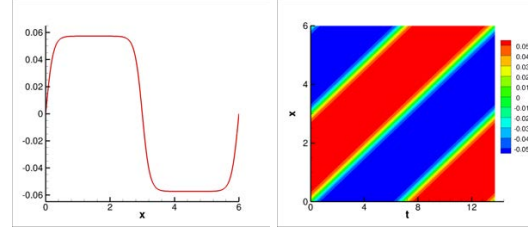


Figure 1: A traveling kink and anti-kink wave: the electric field $E(x, t)$. (Left) Initial Condition (Right) Reference Solution

k [4]. We list the errors and orders of accuracy of E for leap-frog in Table 1 with $k = 3$.

Table 1: A traveling kink and anti-kink wave: errors and orders of accuracy of E . $k = 3$.

	N_x	Leap-frog scheme			
		L_2 errors	order	L_∞ error	order
CF	100	5.68E-06	–	2.59E-05	–
	200	3.62E-07	3.97	1.73E-06	3.91
	400	2.27E-08	4.00	1.09E-07	3.98
	800	1.55E-09	3.87	9.04E-09	3.60
AF I	100	5.60E-06	–	2.30E-05	–
	200	3.53E-07	3.99	1.44E-06	4.00
	400	2.19E-08	4.01	8.97E-08	4.00
	800	1.37E-09	4.00	5.61E-09	4.00

References

- [1] L. GILLES, S. HAGNESS, AND L. VÁZQUEZ, *Comparison between staggered and unstaggered finite-difference time-domain grids for few-cycle temporal optical soliton propagation*, JCP, 161 (2000), pp. 379–400.
- [2] S. LANTERI AND C. SCHEID, *Convergence of a discontinuous Galerkin scheme for the mixed time-domain Maxwell's equations in dispersive media*, IMA J. Numer. Anal., 33 (2013), pp. 432–459.
- [3] M. P. SØRENSEN, G. M. WEBB, M. BRIO, AND J. V. MOLONEY, *Kink shape solutions of the Maxwell-Lorentz system*, Phys. Rev. E, 71 (2005), p. 036602.
- [4] V. A. BOKIL, Y. CHENG, Y. JIANG AND F. LI, *Fully Discrete Energy Stable Discontinuous Galerkin Methods for Maxwell's Equations in Nonlinear Polarization Media*, In preparation, 2017.

Hybridizable Discontinuous Galerkin Methods for modelling 3D seismic wave propagation in harmonic domains.

Marie Bonnasse-Gahot^{1,*}, **Henri Calandra**², **Julien Diaz**¹, **Stephane Lanteri**³

¹Magique 3D project-team, INRIA Bordeaux-Sud-Ouest

²Total Exploration and Production

³Nachos project-team, INRIA Sophia-Antipolis-Méditerranée

*Email: marie.bonnasse-gahot@inria.fr

Abstract

In time domain geophysics context, Discontinuous Galerkin (DG) methods are widely studied and used for the simulation of waves propagation. They can be applied to harmonic problems too but their main drawback is that the linear system to solve becomes very huge. Indeed, the number of degrees of freedom is really large as compared to classical finite element methods. We address this issue by considering a new class of DG methods, the hybridizable discontinuous Galerkin (HDG) method. We have formulated and studied the HDG method applied to 2D and 3D elastic waves propagation equations. Then, to be able with realistic 3D geophysical problems, we compare different solvers, a direct one (Mumps) and an hybrid one (Maphys) that combines direct and iterative solvers by using an algebraic domain decomposition method.

Keywords: seismic imaging, elastic waves equations, harmonic domain, discontinuous Galerkin methods, hybridizable discontinuous Galerkin methods, direct solvers, hybrid solvers

Introduction

As the drilling is expensive, the petroleum industry is interested by methods able to produce accurate images of the intern structures of the Earth before the drilling. One of the most popular seismic imaging methods is the full wave inversion (FWI) method which is an iterative procedure based on an inversion process. The main steps of the FWI method are, starting from an initial velocity model, **a**) to compute the solution of the wave equation for the N sources of the seismic acquisition campaign; **b**) to evaluate, for each source, a residual defined as the difference between the wavefields recorded at receivers on the top of the subsurface during the acquisition campaign and the numerical wavefields; **c**) to compute the solution of the wave equation using the residuals as sources; **d**) to

update the velocity model by cross correlation of images produced at steps **a**) and **c**). Finally, the different steps **a**) to **d**) are repeated until convergence of the velocity model is achieved. We then have to solve $2N$ wave equations at each iteration. The number of sources, N , is usually large (about 1000) and the efficiency of the inverse solver is thus directly related to the efficiency of the numerical method used to solve the wave equation.

Seismic imaging can be performed in the time domain or in the frequency domain regime. We focus here on the second setting. The drawback of time domain is that it requires to store the solution at each time step of the forward simulation. The difficulties related to frequency domain inversion lie in the solution of huge linear systems, which cannot be achieved today when considering realistic 3D elastic media, even with the progress of high-performance computing. In this context, the goal is to develop new forward solvers that reduce the number of degrees of freedom without hampering the accuracy of the numerical solution.

Hybridizable Discontinuous Galerkin method

We consider discontinuous Galerkin (DG) methods formulated on fully unstructured meshes, which are more convenient than finite difference methods on Cartesian grids to handle the topography of the subsurface. Moreover, DG methods are more adapted than continuous Galerkin (CG) methods to deal with hp -adaptivity. This last characteristics is crucial to adapt the mesh to the different regions of the subsurface which is generally highly heterogeneous. Nevertheless, the main drawback of classical DG methods is that they are expensive because they require a large number of degrees of freedom as compared

to CG methods on a given mesh (see figs. 1-2).

We have chosen to consider a new class of DG method, the hybridizable DG (HDG) method (see [1] for more details). They have been introduced by B.Cockburn, J. Gopalakrishnan and R. Lazarov in 2009 for the resolution of second order elliptic problems (see [2]).

Instead of solving a linear system involving the degrees of freedom of all volumic cells of the mesh, the principle of HDG consists in introducing a Lagrange multiplier representing the trace of the numerical solution on each face of the mesh. Hence, it reduces the number of unknowns of the global linear systems and the volumic solution is recovered thanks to a local computation on each element (see fig. 3).

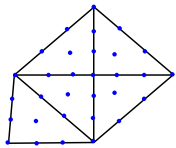


Figure 1: Distribution of the global degrees of freedom (dof) for the FEM with an interpolation order of 3

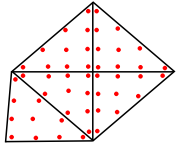


Figure 2: Distribution of the global dof for the DG method with an interpolation order of 3

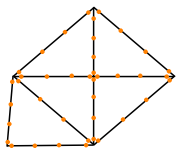


Figure 3: Distribution of the global dof for the HDG method with an interpolation order of 3

HDG methods have been considered in some recent works, for example, for the solution of the elastodynamic equations the time domain [3] and for Maxwell's equations [4]. We have compared the performances of the HDG method with those of classical nodal DG methods like the Internal Penalty Discontinuous Galerkin (IPDG) method. Using a direct solver (Mumps), we

have shown that the memory comsumption, which is the main bottleneck of harmonic problems, is, for example, divided by 4 using HDG methods, and that the computational time is divided by 9 for a same interpolation order $p = 3$. We have been also able to reduce the memory consumption by designing a symmetric HDG formulation for the elastic waves equations obtained by using the compliance tensor which can be viewed as the inverse of the elasticity tensor.

In order to be able to tackle realistic 3D geo-physical media we have also focused on the solver part. We have coupled our method with an hybrid solver (Maphys) that combines direct and iterative solver using an algebraic domain decomposition method. We have shown that Maphys allows for a division of the memory consumption by 0.8 when compared to Mumps, without hampering neither the computational time nor the accuracy of the solution. The next step is the implementation of a multi-right hand side features in Maphys, in order to handle the thousands of sources required by an inverse problem solver.

Acknowledgements

The authors acknowledge the support by the Inria-Tot al strategic action DIP (Depth Imaging Partnership, dip.inria.fr), the Brazilian and European project HPC4E (High Performance Computing for Energy, hpc4e.eu) and the European project GEAGAM (Geophysical Exploration using Advanced Galerkin Methods, sites.google.com/site/geagamnetwork/).

References

- [1] R.M. Kirby, S.J. Sherwin and B. Cockburn, *J.Sci.Comput.* **51** (2012), pp. 183–212.
- [2] B. Cockburn, J. Gopalakrishnan and R. Lazarov, *SIAM J. Numer. Anal.* **47** (2009), pp. 1319–1365.
- [3] N.C. Nguyen, J. Peraire and B. Cockburn, *J. Comput. Phys.*, **230** (2011), pp. 3695–3718.
- [4] S. Lanteri, L. Li and R. Perrussel, *Int.J.Comput.Math.Electr.Electron.Eng.*, **32** (2013), pp. 1112–1138.

Solvability of volume integral equations for elastodynamic scattering

Marc Bonnet¹

¹Poems (UMR 7231 CNRS-INRIA-ENSTA), Palaiseau, France (mbonnet@ensta.fr)

Abstract We establish the well-posedness of volume integral equations (VIEs) for elastodynamic scattering. Such VIEs are known to be compact perturbations of elastostatic VIEs. We derive a modified version of the latter, which is shown to be unconditionally solvable by Neumann series. The modified VIE is also found to extend the range of applicability of fixed-point (iterated Born) methods.

Keywords: volume integral equation, elastodynamic scattering, fixed point, Born approximation.

1. Scattering problem. We consider the scattering of time-harmonic elastic waves by an elastic inhomogeneity (with compact support $D_1 \subset \mathbb{R}^3$) embedded in an unbounded background elastic medium $D_0 := \mathbb{R}^3 \setminus \overline{D_1}$. The (possibly anisotropic) elastic properties in D_0 and D_1 are respectively characterized by the fourth-order real-valued elasticity tensors $\mathcal{C}^0, \mathcal{C}^1$, while the corresponding mass densities are ρ^0, ρ^1 .

The (strongly elliptic) time-harmonic elastodynamic partial differential operator \mathcal{B}_ℓ associated to medium ℓ ($\ell = 0, 1$) is defined by $\mathcal{B}_\ell \mathbf{w} = -\operatorname{div}(\mathcal{C}^\ell : \boldsymbol{\varepsilon}[\mathbf{w}]) - \rho^\ell \omega^2 \mathbf{w}$, where $\boldsymbol{\varepsilon}[\mathbf{w}] := \frac{1}{2}(\nabla \mathbf{w} + \nabla \mathbf{w}^T)$ is the linearized strain tensor associated with a displacement \mathbf{w} . Besides, let $\mathbf{t}_\ell[\mathbf{w}] := (\mathcal{C}^\ell : \boldsymbol{\varepsilon}[\mathbf{w}]) \cdot \mathbf{n}$ denotes the traction vector (i.e. elastic conormal derivative) operator relative to medium ℓ . For a given incident displacement field \mathbf{u}_I satisfying $\mathcal{B}_0 \mathbf{u}_I = \mathbf{0}$ in \mathbb{R}^3 , the total displacement fields $\mathbf{u}_0, \mathbf{u}_1$ in D_0, D_1 satisfy (a) the field equations

$$\mathcal{B}_0(\mathbf{u}_0) = \mathbf{0} \quad \text{in } D_0, \quad \mathcal{B}_1(\mathbf{u}_1) = \mathbf{0} \quad \text{in } D_1,$$

(b) the transmission conditions

$$\mathbf{u}_1 = \mathbf{u}_0, \quad \mathbf{t}_1[\mathbf{u}_1] = \mathbf{t}_0[\mathbf{u}_0] \quad \text{on } \Gamma,$$

(c) a radiation condition at infinity on $\mathbf{u}_0 - \mathbf{u}_I$ (see [1] for the case of anisotropic background).

2. Volume integral equation. Define the volume vector potential \mathbf{V}_ω with density $\mathbf{g} \in L^2(D_1; \mathbb{C}^3)$ and the volume vector potential \mathbf{W}_ω with density $\mathbf{h} \in L^2(D_1; \mathbb{C}^{3 \times 3})$ by

$$\mathbf{V}_\omega[\mathbf{g}](\mathbf{x}) = \int_{D_1} \mathbf{G}_\omega(\mathbf{x} - \mathbf{y}) \cdot \mathbf{g}(\mathbf{y}) d\mathbf{y}, \quad (1)$$

$$\mathbf{W}_\omega[\mathbf{h}](\mathbf{x}) = \int_{D_1} \nabla \mathbf{G}_\omega(\mathbf{x} - \mathbf{y}) : \mathbf{h}(\mathbf{y}) d\mathbf{y}, \quad (2)$$

where \mathbf{G}_ω denotes the full-space elastodynamic fundamental tensor (i.e. the radiating solution of $-\mathcal{B}_0 \mathbf{G}_\omega = \delta \mathbf{I}$ in \mathbb{R}^3), and then the volume integral operator $\mathcal{L}_\omega : \mathbf{H}^1(D_1) \rightarrow \mathbf{H}^1(D_1)$ by

$$\begin{aligned} \mathcal{L}_\omega[\mathbf{w}](\mathbf{x}) &= \mathbf{W}_\omega[\Delta \mathcal{C} : \boldsymbol{\varepsilon}(\mathbf{w})](\mathbf{x}) \\ &\quad + \omega^2 \mathbf{V}_\omega[\Delta \rho \mathbf{w}](\mathbf{x}), \quad \mathbf{x} \in D_1, \end{aligned}$$

having set $\Delta \mathcal{C} := \mathcal{C}^1 - \mathcal{C}^0$ and $\Delta \rho := \rho^1 - \rho^0$. The total field \mathbf{u}_1 solving in D_1 the scattering problem defined by requirements (a), (b), (c) satisfies the volume integral equation (VIE)

$$(\mathcal{I} - \mathcal{L}_\omega)\mathbf{u}_1(\mathbf{x}) = \mathbf{u}_I(\mathbf{x}) \quad (\mathbf{x} \in D_1), \quad (3)$$

with \mathcal{I} denoting the identity operator. Then, \mathbf{u}_0 is given explicitly in terms of \mathbf{u}_1 by the integral representation formula

$$\begin{aligned} \mathbf{u}_0(\mathbf{x}) &= \mathbf{u}_I(\mathbf{x}) + \mathbf{W}_\omega[\Delta \mathcal{C} : \boldsymbol{\varepsilon}(\mathbf{u}_1)](\mathbf{x}) \\ &\quad + \omega^2 \mathbf{V}_\omega[\Delta \rho \mathbf{u}_1](\mathbf{x}) \quad (\mathbf{x} \in D_0). \end{aligned} \quad (4)$$

We address here the solvability of the VIE (3), which has received scant attention so far.

3. Solvability of VIE (3). Consider the corresponding zero-frequency (elastostatic) VIE

$$(\mathcal{I} - \mathcal{L})\mathbf{v}(\mathbf{x}) = \mathbf{u}_I(\mathbf{x}) \quad (\mathbf{x} \in D_1), \quad (5)$$

where $\mathcal{L}[\mathbf{w}] := \mathbf{W}[\Delta \mathcal{C} : \boldsymbol{\varepsilon}(\mathbf{w})]$ and the potential \mathbf{W} is defined by (2) with \mathbf{G}_ω replaced by the full-space elastostatic fundamental tensor \mathbf{G} . Since the kernels $\mathbf{x} \mapsto \mathbf{G}_\omega(\mathbf{x})$ and $\mathbf{x} \mapsto \nabla(\mathbf{G}_\omega - \mathbf{G})(\mathbf{x})$ are weakly singular and bounded, respectively, at $\mathbf{x} = \mathbf{0}$, the operator $(\mathcal{I} - \mathcal{L}_\omega) - (\mathcal{I} - \mathcal{L}) = \mathcal{L} - \mathcal{L}_\omega : H^1(D_1; \mathbb{R}^3) \rightarrow H^1(D_1; \mathbb{R}^3)$ is compact.

Elastostatic VIE. The background elasticity tensor admits the decomposition $\mathcal{C}^0 = \mathcal{B} : \mathcal{B}$, where the fourth-order tensor \mathcal{B} is positive definite and has the same major and minor symmetries as \mathcal{C}^0 . Applying the operator $\mathcal{B}^{-1} : \Delta \mathcal{C} : \boldsymbol{\varepsilon}$ recasts the VIE (5) as a second-kind singular VIE for the new unknown $\mathbf{h}^* := \mathcal{B}^{-1} : \Delta \mathcal{C} : \boldsymbol{\varepsilon}[\mathbf{v}]$:

$$\mathcal{A}[\mathbf{h}^*] = \Delta \mathcal{C} : \boldsymbol{\varepsilon}[\mathbf{u}_I] \quad \text{in } D_1, \quad (6)$$

with $\mathcal{A} : L^2(D_1; \mathbb{R}_{\text{sym}}^{3 \times 3}) \rightarrow L^2(D_1; \mathbb{R}_{\text{sym}}^{3 \times 3})$ defined by

$$\mathcal{A}[\mathbf{h}] = (\mathcal{I} - \Delta \mathcal{C} : \varepsilon[\mathbf{W}])[\mathbf{B} : \mathbf{h}],$$

The following factorization of \mathcal{A} is then found by inspection to hold:

$$\mathcal{A} = \frac{1}{2} \mathbf{B} : (\tilde{\mathcal{C}}^1 + \mathcal{I}) : (\mathcal{I} - \mathcal{Q}_1 : \mathcal{Q}_2)$$

where $\tilde{\mathcal{C}}^1 := \mathbf{B}^{-1} : \mathcal{C}^1 : \mathbf{B}^{-1}$ and the operators $\mathcal{Q}_1, \mathcal{Q}_2 : L^2(\mathbb{R}^3; \mathbb{R}_{\text{sym}}^{3 \times 3}) \rightarrow L^2(\mathbb{R}^3; \mathbb{R}_{\text{sym}}^{3 \times 3})$ are defined by

$$\mathcal{Q}_1 = (\tilde{\mathcal{C}}^1 + \mathcal{I})^{-1} : (\tilde{\mathcal{C}}^1 - \mathcal{I}),$$

$$\mathcal{Q}_2 = \mathcal{I} + 2 \mathbf{B} : \varepsilon[\mathbf{W}] : \mathbf{B}.$$

This yields a modified form of the singular VIE (6):

$$(\mathcal{I} - \mathcal{Q}) \mathbf{h}^* = 2(\tilde{\mathcal{C}}^1 + \mathcal{I})^{-1} : \mathbf{B}^{-1} : \Delta \mathcal{C} : \varepsilon[\mathbf{u}]. \quad (7)$$

Lemma 1 *The operators $\mathcal{Q}_1, \mathcal{Q}_2$ are bounded and satisfy $\|\mathcal{Q}_1\| < 1$, $\|\mathcal{Q}_2\| = 1$. Consequently, $\mathcal{Q} = \mathcal{Q}_1 : \mathcal{Q}_2$ is a contraction: $\|\mathcal{Q}\| < 1$.*

Unlike (6), the modified singular VIE (7) is therefore solvable by Neumann series for any inhomogeneity configuration $(D_1, \Delta \mathcal{C})$, which in turn gives:

Proposition 1 *Assume that both elasticity tensors \mathcal{C} and \mathcal{C}^1 are strongly elliptic and bounded. Then, the integral operator $\mathcal{I} - \mathcal{L} : H^1(D_1; \mathbb{R}^3) \rightarrow H^1(D_1; \mathbb{R}^3)$ is invertible with bounded inverse.*

Elastodynamic VIE. Proposition 1 and compactness of $\mathcal{L}_\omega - \mathcal{L}$ imply that the operator $\mathcal{I} - \mathcal{L}_\omega$ is Fredholm with index 0. Its bounded invertibility follows from known uniqueness results for scattering problems (see [1] if \mathcal{C}^0 is anisotropic) and the Fredholm alternative.

Theorem 1 *Assume that both elasticity tensors \mathcal{C} and \mathcal{C}^1 are strongly elliptic and bounded. Then, the integral operator $\mathcal{I} - \mathcal{L}_\omega : H^1(D_1; \mathbb{R}^3) \rightarrow H^1(D_1; \mathbb{R}^3)$ is invertible with bounded inverse. The solution $(\mathbf{u}_0, \mathbf{u}_1)$ to the original scattering problem is found by solving (3) for \mathbf{u}_1 and invoking the representation formula (4).*

4. Consequences on fixed-point methods. In the elastodynamic case ($\omega > 0$) with $\Delta \mathcal{C} \neq \mathbf{0}, \Delta \rho = 0$, using the modified singular VIE (7) (with \mathbf{W} replaced by \mathbf{W}_ω) has useful implications on fixed-point methods, due to the following lemmas verified by $\varepsilon[\mathbf{W}_\omega]$ as a (bounded) $L^2(D_1; \mathbb{R}_{\text{sym}}^{3 \times 3}) \rightarrow L^2(D_1; \mathbb{R}_{\text{sym}}^{3 \times 3})$ operator:

Lemma 2 *There exists a constant $C_1 > 0$, independent of ω and D_1 , such that*

$$\|\mathbf{B} : \varepsilon[\mathbf{W}_\omega] : \mathbf{B}\| \geq C_1.$$

Lemma 3 *Assume that $D_1 \subset B_R$, where B_R is the ball of radius R . There exists a constant $C_2 > 0$, independent of ω and R , such that*

$$\|\mathbf{B} : \varepsilon[\mathbf{W}_\omega - \mathbf{W}] : \mathbf{B}\| \leq C_2(kR)^2,$$

where $k = \omega/c$ with c a characteristic wave velocity for the background medium.

Then, let $\lambda_1, \dots, \lambda_6$ be the (strictly positive, non-dimensional) eigenvalues of $\tilde{\mathcal{C}}^1$ treated as a $\mathbb{R}_{\text{sym}}^{3 \times 3} \rightarrow \mathbb{R}_{\text{sym}}^{3 \times 3}$ linear operator, and define $\lambda_m := \arg \min |\lambda_i - 1|$ and $\lambda_M := \arg \max |\lambda_i - 1|$.

Proposition 2

- (a) *Fixed-point iterations applied to the singular VIE (6) diverge if $|\lambda_m - 1|C_1 > 1$;*
- (b) *Fixed-point iterations applied to the singular VIE (7) converge if $C_2(kR)^2 < \frac{1}{2}(\frac{\lambda_M+1}{|\lambda_M-1|} - 1)$.*

For any inhomogeneity contrast $\tilde{\mathcal{C}}^1 - \mathcal{I}$ large enough to verify $|\lambda_m - 1|C_1 > 1$ (and hence to cause divergence of fixed-point iterations applied to the classical VIE (6)), we see that there exist values of kR such that fixed-point iterations applied to the modified VIE (7) converge. In other words, the latter equation extends the range of applicability (in terms of frequency and scatterer characteristics) of fixed-point (iterated Born) methods (while any elastostatic inhomogeneity problem can be solved by fixed-point iterations by virtue of Prop. 1).

5. Remarks. Similar results are obtained for the VIE governing acoustic scattering problems and the associated zero-frequency problems involving conducting inhomogeneities [3].

The well-posedness of VIEs such as (3) is for instance useful for the justification of small-inhomogeneity solution asymptotics.

References

- [1] BONNET, M. Solvability of a volume integral equation formulation for anisotropic elastodynamic scattering. *J. Integral Eq. Appl.*, **28**:169–203 (2016).
- [2] BONNET, M. A modified volume integral equation for anisotropic elastic or conducting inhomogeneities. Unconditional solvability by Neumann series. *J. Integral Eq. Appl.* (to appear).
- [3] MARTIN, P. A. Acoustic scattering by inhomogeneous obstacles. *SIAM J. Appl. Math.*, **64**:297–308 (2003).
- [4] POTTHAST, R. Electromagnetic scattering from an orthotropic medium. *J. Integral Eq. Appl.*, **11**:197–215 (1999).

Formulation of invisibility in waveguides as an eigenvalue problem

Antoine Bera¹, Anne-Sophie Bonnet-Ben Dhia^{1,*}, Lucas Chesnel², Sergei Nazarov³, Vincent Pagneux⁴

¹POEMS (CNRS-INRIA-ENSTA ParisTech-Université Paris Saclay), Palaiseau, France

²INRIA, CMAP (Ecole Polytechnique-Université Paris Saclay), Palaiseau, France

³Institute of Problems of Mechanical Engineering, Russian Academy of Sciences, St.Petersburg, Russia

⁴LAUM (CNRS, Université du Maine), Le Mans, France

*Email: anne-sophie.bonnet-bendhia@ensta-paristech.fr

Abstract

A scatterer placed in an infinite waveguide may be *invisible* at particular discrete frequencies (that are called here invisibility frequencies). We consider two different definitions of invisibility: no reflection (but possible conversion or phase shift in transmission) or perfect invisibility (the scattered field is exponentially decaying at infinity). Our objective is to show that the invisibility frequencies can be characterized as eigenvalues of some spectral problems. Two different approaches will be used for the two different definitions of invisibility, leading to non-selfadjoint eigenvalue problems. Concerning the non-reflection case, our approach based on an original use of PMLs allows to extend to higher dimension the results obtained in [1] on a 1D model problem.

Keywords: waveguides, invisibility, trapped modes, perfectly matched layers, \mathcal{PT} -symmetry

1 Introduction

We consider for simplicity a 2D acoustic waveguide occupying the domain $\Omega = \{(x, y); x \in \mathbb{R} \text{ and } 0 < y < 1\}$. In presence of a bounded penetrable obstacle \mathcal{O} and in harmonic regime, the acoustic pressure p satisfies the equations

$$\begin{aligned} \Delta p + k^2(1 + \chi_{\mathcal{O}}\rho)p &= 0 & (\Omega) \\ \frac{\partial p}{\partial y} &= 0 & (\partial\Omega) \end{aligned} \quad (1)$$

where $k = \omega/c$ (c is the acoustic waves velocity and ω the angular frequency), $\chi_{\mathcal{O}}$ is the characteristic function of \mathcal{O} and $\rho \in L^\infty(\mathcal{O})$. Taking as incident field a linear combination of propagative modes

$$p_i = \sum_{n < k/\pi} a_n \cos(n\pi y) e^{i\beta_n x},$$

with $\beta_n = \sqrt{k^2 - n^2\pi^2}$, we consider the scattering problem where the total field $p = p_i + p_s$

is a solution of (1) and the scattered field p_s is outgoing. It is well-known that this problem is well-posed, except when there exists a trapped mode, that is a non trivial solution $p \in L^2(\Omega)$ of (1). We say that the obstacle (\mathcal{O}, ρ) is *non-reflective* at the frequency k if there exists an incident wave p_i such that p_s is exponentially decaying when $x \rightarrow -\infty$. And we say that the obstacle is *invisible* to this incident wave p_i if the corresponding scattered field p_s is exponentially decaying both at $\pm\infty$.

In the sequel, we denote by \mathcal{K}_{TM} (resp. \mathcal{K}_{NR}) the set of all values of $k \in \mathbb{R}^+$ corresponding to trapped modes (resp. the set of all frequencies $k \in \mathbb{R}^+$ where the obstacle is non-reflective).

2 The case of no reflection

Suppose that the obstacle \mathcal{O} is located in $|x| < L$. If there are no reflections, the total field p is ingoing for $x < -L$ and outgoing for $x > L$. As a consequence, it can be extended analytically to complex values of x . More precisely, we define for $(x, y) \in \Omega$ and $0 < \theta < \pi/2$:

$$p_\theta(x, y) = \begin{cases} p(x, y) & \text{for } |x| < L \\ p(\pm(L + (|x| - L)e^{\pm i\theta}), y) & \text{for } \pm x > L \end{cases}$$

Note that there is a main difference with the classical complex scaling (or PMLs [2]): here we must use *conjugate PMLs* on both sides of the perturbation because p is ingoing and not outgoing at the left of the perturbation. As usual, the interest of the analytic dilation is that contrary to p , p_θ belongs to $L^2(\Omega)$. Moreover p_θ satisfies the following equation in Ω :

$$\alpha_\theta(x) \frac{\partial}{\partial x} \left(\alpha_\theta(x) \frac{\partial p_\theta}{\partial x} \right) + \frac{\partial^2 p_\theta}{\partial y^2} + k^2(1 + \chi_{\mathcal{O}}\rho)p_\theta = 0$$

with $\alpha_\theta(x) = 1$ for $|x| < L$ and $e^{\pm i\theta}$ for $\pm x > L$. Defining the unbounded operator of $L^2(\Omega)$:

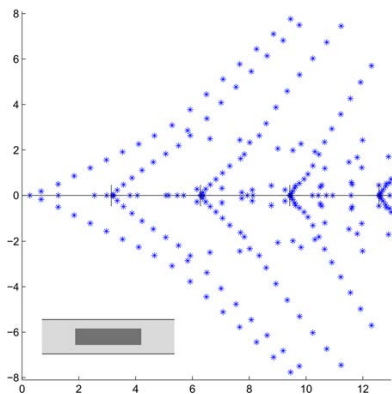
$$A_\theta p_\theta = \frac{-1}{1 + \chi_{\mathcal{O}} \rho} \left(\alpha_\theta \frac{\partial}{\partial x} \left(\alpha_\theta \frac{\partial p_\theta}{\partial x} \right) + \frac{\partial^2 p_\theta}{\partial y^2} \right)$$

with domain

$$\{p_\theta \in H^1(\Omega); A_\theta p_\theta \in L^2(\Omega), \frac{\partial p_\theta}{\partial y} = 0 \text{ on } \partial\Omega\},$$

we can prove the

- Theorem 1** 1. k^2 is a real eigenvalue of A_θ iff $k \in \mathcal{K}_{TM} \cup \mathcal{K}_{NR}$.
 2. The essential spectrum of A_θ is given by $\sigma_{ess}(A_\theta) = \bigcup_{n \in \mathbb{N}} \{n^2\pi^2 + te^{\pm i\theta}; t \in \mathbb{R}^+\}$
 3. If the obstacle is symmetric with respect to $x = 0$, A_θ is \mathcal{PT} -symmetric and its spectrum is stable by complex conjugation.



We have represented on the figure the square root of the spectrum of A_θ obtained by a finite element discretization. The continuous spectrum is discretized and deformed, far from the real axis. Concerning the discrete spectrum, in addition to real eigenvalues corresponding to trapped modes and to non-reflective frequencies, we obtain some complex eigenvalues, similar to leaky modes, have to be investigated further.

3 The case of invisibility

Suppose now that the obstacle is invisible to some incident wave p_i at the frequency k . Then p_s is exponentially decaying at infinity, so that $p_s \in H^1(\Omega)$ and satisfies in Ω the equation

$$\Delta p_s + k^2(1 + \chi_{\mathcal{O}} \rho)p_s = -k^2 \chi_{\mathcal{O}} \rho p_i$$

A priori, this does not look like an eigenvalue problem, due to the presence of the non-homogeneous right-hand side. However, if we choose ρ and p_i satisfying the following normalization:

$$\int_{\mathcal{O}} \rho |p_i|^2 = 1,$$

we prove after several simple integrations by parts that $p_s \in H^1(\Omega)$ satisfies the following homogeneous variational formulation:

$$\int_{\Omega} \nabla p_s \cdot \nabla \bar{q}_s = k^2 b(k; p_s, q_s) \quad \forall q_s \in H^1(\Omega) \quad (2)$$

with

$$b(k; p_s, q_s) = \int_{\Omega} (1 + \chi_{\mathcal{O}} \rho) p_s \bar{q}_s - \int_{\mathcal{O}} \rho p_s \bar{p}_i \int_{\mathcal{O}} \rho q_s \bar{p}_i$$

Note that contrary to the previous one, it is a *non-linear* eigenvalue problem since the bilinear form $b(k; p_s, q_s)$ depends on k through p_i .

Theorem 2 For $k \in \mathbb{R}$, problem (2) admits solutions $p_s \neq 0$ iff either $k \in \mathcal{K}_{TM}$ or the obstacle is invisible to the incident wave p_i .

An additional difficulty is that eigenvalues are embedded in the continuous spectrum which covers \mathbb{R}^+ . Again PMLs can be used to rotate this continuous spectrum and reveal the discrete eigenvalues. Note finally that, if p_i is chosen as one propagative mode, the problem can be rewritten as a quadratic eigenvalue problem in k by the change of unknown $\tilde{p}_s = p_s \bar{p}_i$. For instance, if we choose $p_i = (\int_{\mathcal{O}} \rho)^{-1/2} e^{ikx}$, we get the following problem: $\forall \tilde{q}_s \in H^1(\Omega)$

$$\int_{\Omega} \nabla \tilde{p}_s \cdot \nabla \bar{\tilde{q}}_s + ik \left(\tilde{p}_s \frac{\partial \bar{\tilde{q}}_s}{\partial x} - \frac{\partial \tilde{p}_s}{\partial x} \bar{\tilde{q}}_s \right) = k^2 b(\tilde{p}_s, \tilde{q}_s)$$

with

$$b(\tilde{p}_s, \tilde{q}_s) = \int_{\Omega} (1 + \chi_{\mathcal{O}} \rho) p_s \bar{q}_s - \int_{\mathcal{O}} \rho \tilde{p}_s \int_{\mathcal{O}} \rho \tilde{q}_s$$

Acknowledgement: we thank the DGA for its financial support.

References

- [1] H. Hernandez-Coronado, D. Krejcirik and P. Siegl, Perfect transmission scattering as a \mathcal{PT} -symmetric spectral problem, *Physics Letters A*, 375(22), (2011) pp.2149-2152.
- [2] E. Bécache, A.-S. Bonnet-BenDhia and G. Legendre, Perfectly matched layers for the convected Helmholtz equation, *SINUM*, (42), (2004) pp 409–433.

Homogenization of the spectrum of the Poincaré-Neumann operator

Eric Bonnetier^{1,*}, Charles Dapogny¹, Faouzi Triki¹

¹Laboratoire Jean Kuntzmann, Université Grenoble Alpes, France

*Email: Eric.Bonnetier@imag.fr

Abstract

We study the spectrum of the Neumann-Poincaré operator K_ε^* of a periodic collection of smooth inhomogeneities, as the period $\varepsilon \rightarrow 0$. Under the assumption that the pattern of inhomogeneity is strictly included in the periodicity cell, we show that the limit set $\lim_{\varepsilon \rightarrow 0} \sigma(K_\varepsilon^*)$ is the union of a Bloch spectrum and of a boundary spectrum, associated with eigenfunctions which are not too small (as functions in H^1) near the boundary.

Keywords: Potential theory, homogenization, Bloch waves.

1 Introduction

The Neumann Poincaré operator has been recently a subject of great interest, as it naturally appears in questions involving metamaterials, such as cloaking and plasmonic resonances, since it allows the representation of solutions to transmission problems in media with piecewise constant coefficients. In this work, Ω denotes a smooth bounded domain in \mathbb{R}^d , $Y = (0, 1)^d$, and we let $\omega \subset\subset Y$ be a proper subset of Y with C^2 boundary. We consider ε -periodic collections

$$\begin{aligned}\omega_\varepsilon &= \bigcup_{\xi \in \Xi_\varepsilon} Y_\varepsilon^\xi, \quad Y_\varepsilon^\xi := \varepsilon(\xi + Y), \\ \Xi_\varepsilon &= \{\xi \in \mathbb{Z}^2, Y_\varepsilon^\xi \subset \Omega\},\end{aligned}$$

of smooth metallic inclusions distributed in Ω . The associated Neumann-Poincaré operator $K_\varepsilon^* : L^2(\partial\omega_\varepsilon) \longrightarrow L^2(\partial\omega_\varepsilon)$ is defined by

$$K_\varepsilon^* \varphi(x) = \int_{\partial\omega_\varepsilon} \frac{\partial P}{\partial \nu_x}(x, y) \varphi(y) d\sigma(y),$$

where P is the Poisson Kernel associated to Ω , i.e., the unique solution to

$$\begin{cases} \Delta_y P(x, y) &= \delta_x, \quad y \in \Omega, \\ P(x, y) &= 0, \quad y \in \partial\Omega, \end{cases}$$

and where ν_x denotes the outward normal.

For a given ε , K_ε^* is compact and self-adjoint on the space of single-layer potentials [4]. Its

spectrum consists of a sequence of eigenvalues, with $\lambda = 0$ as unique accumulation point. If the set ω_ε is regarded as a collection of particles with complex conductivity, the eigenvalues of K_ε^* would correspond to the plasmonic resonances of these particles in the quasistatic limit [3]. We are interested in studying the limit of the spectrum of $\sigma(K_\varepsilon^*)$ as $\varepsilon \rightarrow 0$.

Since K_ε^* is an integral operator supported on the boundary of the components of ω_ε , which changes as ε varies, we study instead the operator T_ε associated to the so-called Poincaré variational problem: For $u \in H_0^1(\Omega)$, $T_\varepsilon u$ is defined by

$$\forall v \in H_0^1(\Omega), \int_{\Omega} (\nabla T_\varepsilon u) \cdot \nabla v = \int_{\omega_\varepsilon} \nabla u \cdot \nabla v,$$

for which one can show that $\sigma(K_\varepsilon^*) = 1/2 - \sigma(T_\varepsilon)$.

2 The limit spectrum $\lim_{\varepsilon \rightarrow 0} \sigma(T_\varepsilon)$

The operators T_ε only converges weakly as $\varepsilon \rightarrow 0$, so that it is not possible to infer anything concerning the spectra $\sigma(T_\varepsilon)$ from this convergence. To capture the microscopic behavior of the T_ε 's and what it induces on their spectrum, we introduce a 2-scale formulation of the Poincaré variational problem over the periodicity cell Y . We construct a 2-scale limiting operator T_0 defined on $L^2(\Omega, H_\#^1(Y)/\mathbb{C})$, so that $T_\varepsilon \rightarrow T_0$ strongly in the sense of the 2-scale convergence ($H_\#^1(Y)$ is the closure of the space of periodic C^∞ functions for the H^1 norm). As noted in [1], whose analysis we closely follow, we may infer from this strong convergence that $\sigma(T_0) \subset \lim_{\varepsilon \rightarrow 0} \sigma(T_\varepsilon)$. We can repeat this process, by considering 2-scale convergence with respect to blocks of K^d periodic cells and define associated limiting operators T_0^K . Using a discrete Bloch transform, the spectrum of each T_0^K splits as

$$\sigma(T_0^K) = \bigcup_{j=(j_1, \dots, j_K), 0 \leq j_i \leq K-1} \sigma(T_{\eta_j})$$

where $\eta_j = j/K \in \overline{Y}$ and where T_{η_j} is a quasi-periodic operator defined on the periodicity cell Y . It follows that

Theorem 1 *The set $\lim_{\varepsilon \rightarrow 0} \sigma(T_\varepsilon)$ contains the Bloch spectrum σ_{Bloch} defined as*

$$\sigma_{\text{Bloch}} = \bigcup_{j=1}^{\infty} [\min_{\eta \in Y} \lambda_j(\eta), \max_{\eta \in Y} \lambda_j(\eta)],$$

where $\lambda_j(\eta)$ denotes the j^{th} eigenvalue of the operator T_η .

As for the remainder of $\lim_{\varepsilon \rightarrow 0} \sigma(T_\varepsilon)$ we show the following

Theorem 2 *The limit spectrum decomposes as*

$$\lim_{\varepsilon \rightarrow 0} \sigma(T_\varepsilon) = \{0, 1\} \cup \sigma_{\text{Bloch}} \cup \sigma_{\partial\Omega},$$

where the boundary layer spectrum $\sigma_{\partial\Omega}$ is defined as the set of λ 's for which there exists a sequence of eigenvalues λ_ε , and a sequence of associated eigenvectors u_ε , such that $\lambda_\varepsilon \rightarrow \lambda$, and such that for all $s > 0$

$$\lim_{\varepsilon \rightarrow 0} \varepsilon^{1-1/d+s} \|\nabla u_\varepsilon\|_{L^2(\mathcal{U}_\varepsilon)} = +\infty,$$

where \mathcal{U}_ε is the tubular neighborhood of $\partial\Omega$ of width ε .

3 Consequences for the homogenization of certain composites made with metamaterials

Here, we assume that the set ω_ε represents inclusions made of a metamaterial with complex conductivity a , while $\Omega \setminus \overline{\omega_\varepsilon}$ is filled with a dielectric medium of conductivity 1. We denote A_ε the associated conductivity map. Given a source term $f \in H^{-1}(\Omega)$, we seek the voltage potential u_ε^a solution to

$$\begin{cases} -\operatorname{div}(A_\varepsilon \nabla u_\varepsilon^a) = f & \text{in } \Omega \\ u_\varepsilon^a = 0 & \text{on } \partial\Omega. \end{cases} \quad (1)$$

It is well known that when the conductivity a is real and strictly positive, the solutions u_ε of the above PDE converge weakly in $H_0^1(\Omega)$ to the solution of the homogenized problem, whose effective conductivity A_* is given in terms of the solutions χ_j^a ($j = 1, \dots, d$) of the following cell problems: for any $v \in H_\#^1(Y)$

$$\int_Y A_1(y) \nabla(\chi_j^a(y) + y_j) \cdot \nabla v \, dy = 0.$$

When a takes complex values, we introduce the Poincaré variational operator $T_0^\# : H_\#^1(Y)/\mathbb{C} \rightarrow H_\#^1(Y)/\mathbb{C}$. The cell problems are solvable provided $\frac{1}{1-a} \notin \sigma(T_0^\#) \setminus \{0, 1\}$. We show the following (see also [2])

Theorem 3 *Assume that ω is smooth and that $\omega \subset\subset Y$. There exists constants $\alpha > 0$, such that, if the conductivity a inside the inclusion lies in $(-\infty, -1/\alpha) \cup (-\alpha, 0)$, then*

- (i) *For $\varepsilon > 0$, the PDE (1) has a unique solution u_ε^a , which depends continuously on f .*
- (ii) *The homogenized tensor A^* is elliptic (i.e. positive definite) and the homogenized equation is well-posed.*
- (iii) *For any $f \in H^{-1}(\Omega)$ the solutions u_ε^a to (1) converge weakly in $H^1(\Omega)$ to the solution of the homogenized equation, with source f .*
- (iv) *For large contrast, the convergence of u_ε^a to the homogenized solution u_* is uniform:*

$$\lim_{\varepsilon \rightarrow 0} \sup_{a \in (-\infty, \alpha) \cup (\alpha, \infty)} \|u_\varepsilon^a - u_*\| = 0.$$

References

- [1] G. Allaire and C. Conca, Bloch wave homogenization and spectral asymptotic analysis, *J. Math. Pures et Appli.* **77** (1998), pp.153–208.
- [2] R. Bunoiu and K. Ramdani, Homogenization of materials with sign changing coefficients, *preprint* (2015).
- [3] D. Grieser, The plasmonic eigenvalue problem, *Rev. Math. Phys.* **26** (2014), 1450005.
- [4] D. Khavinson, M. Putinar and H.S. Shapiro, On Poincaré's variational problem in potential theory, *Arch. Rational Mech. Anal.* **185** (2007), pp. 143–184.

Normal modes and internal wave attractors

William Booker^{1,*}, Onno Bokhove², Mark Walkley³

¹Centre for Doctoral Training in Fluid Dynamics, University of Leeds, LS2 9JT Leeds, UK

²School of Mathematics, University of Leeds, LS2 9JT Leeds, UK

³School of Computing, University of Leeds, LS2 9JT Leeds, UK

*Email: scwb@leeds.ac.uk

Abstract

Confined internal gravity wave systems in asymmetric domains can lead to the evolution of a spatial singularity called a wave attractor. The existence of this singularity is the result of wave energy focusing, that is wave energy becomes localised on small spatial scales. It has been observed that ocean ridges, such as the Luzon strait, can support such energy localisation and a study of this mechanism will lead to a better understanding of ocean mixing in these areas. Simulations of wave attractors have been shown to match laboratory observations, despite being derived from an inviscid, ideal fluid model. We utilise a non-dissipative discontinuous finite element method that preserves the Hamiltonian structure of internal wave systems. By conserving discrete energy our numerical method allows for accurate long time modelling of wave attractors. We extend previous work by considering body forces in our numerical model to allow closer comparison to experimental results.

Keywords: Internal gravity waves, wave attractors, discontinuous Galerkin method

1 Introduction

Internal gravity waves have their maximum displacement in the interior of the fluid. They play an important role in the transport of energy and momentum in the ocean, as they allow for the vertically transport of such quantities. Internal waves can only exist in a stably stratified fluid. In nature fluids are frequently stratified by depth variations in their salt or temperature concentration.

Internal gravity waves propagate at a fixed angle with respect to gravity. Waves of a given frequency will preserve this propagation angle upon reflection from any boundary. If wave beams are enclosed by sloping boundaries, then this results in focusing onto a limit orbit, called a wave attractor [5]. As many wave beams are focused onto the same wave attractor, there is

a fine localisation of energy at this structure. In the vicinity of the wave attractor we expect large shearing motion. Wave attractors have been observed in experiments [6] and in numerical simulations [1]. Van Oers et al. [1] developed a numerical method that preserved the Hamiltonian structure of the mathematical model for internal waves. By discretising the Hamiltonian structure, the resulting numerical method has discrete analogues to all conserved variables in the continuous case.

In this paper we expand the work of Van Oers et al. by including external body forcing in the numerical model. This changes the nature of the wave attractors we can model. Forced wave attractors are a closer approximation to what is generated in experiments, and in nature. This body forcing can, for example, be used to model tidal forcing.

Previous work on internal wave attractors has only considered the incompressible Euler-Boussinesq model in their simulations. However by observing the dispersion relation of the compressible model we know that these internal gravity waves also exist when we relax these assumptions. This enables our computational model to be closer to reality as the ocean is weakly compressible. In the compressible model we can see internal gravity, Lamb and acoustic modes. The acoustic modes are high frequency, and could act as sufficient noise that would disrupt the formation of an internal wave attractor. Thus we filter out these acoustic modes numerically.

2 Stratified Fluids

Linear compressible fluids in a stratified background can be modeled by the scaled Euler equations:

$$\frac{\partial(\rho_0 \underline{u})}{\partial t} = -\nabla p - \rho g \hat{z} + \underline{F}(\underline{x}, t), \quad (1)$$

$$\frac{\partial \rho}{\partial t} = -\nabla \cdot (\rho_0 \underline{u}), \quad (2)$$

$$Ma^2 \frac{\partial p}{\partial t} = Ma^2 \rho_0 g w - c_0^2 \rho_0 \nabla \cdot \underline{u}, \quad (3)$$

where c_0^2 is the scaled linearised speed of sound, Ma is the Mach number, \underline{F} is the body force, and $\rho_0 = \rho_0(z)$ a hydrostatic background.

Internal gravity waves are frequently modeled by applying two approximations to this model. The first is an incompressible constraint that filters out acoustic waves by taking $Ma \rightarrow 0$. The second simplification is the Boussinesq approximation where we assume that the background density can be split into a constant mean and a small perturbation.

We discretise in space using a discontinuous Galerkin finite element method with a non-dissipative flux. By considering the Hamiltonian structure of our governing equations while deriving our numerical method, we ensure that the Hamiltonian structure is preserved discretely. This leads to discrete conservation of any conserved variable of the continuous system. We use a symplectic time integrator, the implicit midpoint rule [4], to preserve the conserved variables in time. Our numerical method was implemented using the finite element package Firedrake [2].

3 Results

In experiments, internal wave attractors are generated by applying periodic forcing to the wave tank. Our domain is a unit square that is rotated 20° to produce a slope with respect to gravity. We consider a divergence free body force [3]

$$\underline{F} = \nabla \times \underline{a} = F_0 \cos(\omega_0 t).$$

Internal wave beam angles can be controlled by varying the stratification and the forcing frequency. Acoustic modes are filtered by considering a numerical dispersion relation $\Delta t \geq 2\pi/N^2$, where N^2 is the buoyancy frequency. We can choose a timestep that would then under-resolve the acoustic modes. We note here that numerical stability will be preserved as we have used an implicit time integrator. In figure 1 we

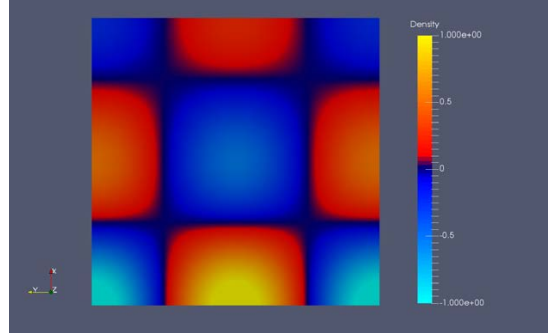


Figure 1: Density field of a normal mode solution of incompressible stratified Euler equations. 128 quadratic elements were taken in each direction. $dt = 1/NxNz$.

show a normal mode solution at a half wave period. The solution showed no long term drift in energy.

References

- [1] A van Oers, L Maas, and O Bokhove, Hamiltonian discontinuous Galerkin FEM for linear, stratified (in)compressible Euler equations: internal gravity waves. *J. Comp. Phys.* To appear (2016).
- [2] F Rathgeber, D Ham, L Mitchell, M Lange, F Luporini, A McRae, G-T Bercea, G Markall and P Kelly, Firedrake: automating the finite element method by composing abstractions. *Subm. ACM TOMS* <http://arxiv.org/abs/1501.01809> (2015).
- [3] L Jouve, and G Ogilvie, Direct numerical simulations of an inertial wave attractor in linear and nonlinear regimes. *J. Fluid Mech.* 745 (2014): 223-250.
- [4] E Hairer, C Lubich, and G Wanner, Geometric numerical integration: structure-preserving algorithms for ordinary differential equations. *Springer* 31 (2016).
- [5] L Maas, and A Frans-Peter, Geometric focusing of internal waves. *J. Fluid Mech.* 300 (1995): 1-41.
- [6] L Maas, D Benielli, J Sommeria and F-P Lam, Observation of an internal wave attractor in a confined, stably stratified fluid. *Nature* 388.6642 (1997): 557-561.

A mixed quasi-reversibility approach to identify obstacles in an acoustic waveguide

Laurent Bourgeois^{1,*}, Arnaud Recoquillay²

¹Laboratoire POEMS, ENSTA ParisTech, Palaiseau, France

²CEA, LIST, Gif-sur-Yvette, France

*Email: laurent.bourgeois@ensta.fr

Abstract

We consider an inverse obstacle problem in an acoustic waveguide using a single incident wave, which we solve with the help of an “exterior approach” coupling a mixed formulation of quasi-reversibility and a simple level set method.

Keywords: acoustic waveguide, inverse obstacle problem, quasi-reversibility, level set

1 Introduction

We consider a smooth 2D/3D waveguide $W = \Sigma \times \mathbb{R}$, where Σ is a 1D/2D bounded domain and x_3 is the coordinate in the infinite direction. Let us consider a smooth domain D such that $\overline{D} \subset W$, referred to as the obstacle. For some wavenumber $k > 0$, a distribution $g \in H^{-1/2}(\partial W)$ of compact support in the bounded domain $\Gamma \subset \partial W$ and $f \in H^{1/2}(\Gamma)$, the inverse obstacle problem consists in finding a domain D and a function $u \in H_{\text{loc}}^1(W \setminus \overline{D})$ such that

$$\left\{ \begin{array}{ll} (\Delta + k^2)u = 0 & \text{in } W \setminus \overline{D} \\ (u, \partial_\nu u) = (f, g) & \text{on } \Gamma \\ u = 0 & \text{on } \partial D \\ (RC), \end{array} \right. \quad (1)$$

where ν is the outward unit normal and (RC) is a radiation condition. Can we identify the defect D from a single pair of Cauchy data (f, g) ? Uniqueness for this problem is unknown in general, only a local uniqueness result is known. When so few data are available, a Linear Sampling type method, inspired by [1] and adapted to the acoustic waveguide in [2], cannot be applied. In order to solve the problem, we propose an “exterior approach” coupling a quasi-reversibility method and a level set method, introduced in [3] in the case of the Laplacian. In such iterative approach, for a given defect \tilde{D} we update the solution \tilde{u} with the help of a mixed formulation of quasi-reversibility while for a given solution \tilde{u} we update the defect \tilde{D} with the help of a level set method based on a Poisson problem.

2 A new formulation of quasi-reversibility

We first consider an abstract framework. Let us consider three Hilbert spaces V , M and H , $A : V \rightarrow H$ a continuous onto operator. For some $f \in H$, we consider the affine space $V_f = \{u \in V, Au = f\}$. For a continuous sesquilinear form b on $V \times M$ and an antilinear form ℓ on M , let us consider the weak formulation: find $u \in V_f$ such that for all $\mu \in M$,

$$b(u, \mu) = \ell(\mu). \quad (2)$$

We assume that the sesquilinear form b does not satisfy the inf – sup condition on $V_0 \times M$, which from the Brezzi-Necas-Babuska theorem implies that the problem (2) is in general ill-posed for a given ℓ . However, b satisfies the following uniqueness property: if $u \in V_0$ and $b(u, \mu) = 0$, for all $\mu \in M$, then $u = 0$. A regularized formulation of problem (2) is the following: for $\varepsilon > 0$, find $(u_\varepsilon, \lambda_\varepsilon) \in V_f \times M$ such that for all $(v, \mu) \in V_0 \times M$,

$$\left\{ \begin{array}{l} \varepsilon(u_\varepsilon, v)_V + b(v, \lambda_\varepsilon) = 0 \\ b(u_\varepsilon, \mu) - (\lambda_\varepsilon, \mu)_M = \ell(\mu). \end{array} \right. \quad (3)$$

We have the following theorem.

Theorem 1 *For any $f \in H$ and $\ell \in M'$, the problem (3) is well-posed. For some $f \in H$ and $\ell \in M'$ such that (2) has a (unique) solution $u \in V_f$, then the solution $(u_\varepsilon, \lambda_\varepsilon) \in V_f \times M$ satisfies $(u_\varepsilon, \lambda_\varepsilon) \rightarrow (u, 0)$ in $V \times M$ when $\varepsilon \rightarrow 0$.*

Let us denote by B the subpart of W delimited by some transverses sections Σ_\pm that surround Γ . Now let us consider, for a known obstacle D , the following ill-posed problem in the bounded domain $\Omega = B \setminus \overline{D}$: for $(f, g) \in H^{1/2}(\Gamma) \times (H^{1/2}(\Gamma))'$, find $u \in H^1(\Omega)$ such that

$$\left\{ \begin{array}{ll} (\Delta + k^2)u = 0 & \text{in } \Omega \\ (u, \partial_\nu u) = (f, g) & \text{on } \Gamma \\ \pm \partial_{x_3} u = T_\pm u & \text{on } \Sigma_\pm, \end{array} \right. \quad (4)$$

where the last equation is equivalent to the radiation condition and involves the Dirichlet-to-

Neumann operators T_{\pm} on the transverse sections Σ_{\pm} . We can directly apply the above abstract framework to the regularization of problem (4), which is equivalent to problem (2) with $V = H^1(\Omega)$, $M = \{\mu \in H^1(\Omega), \mu|_{\partial D} = 0\}$, $H = H^{1/2}(\Gamma)$, while A is the trace operator on Γ and for $(v, \mu) \in V \times M$,

$$\begin{aligned} b(v, \mu) &= \int_{\Omega} (\nabla v \cdot \nabla \bar{\mu} - k^2 v \bar{\mu}) \, dx \\ &- \int_{\Sigma_{\pm}} (T_{\pm} v) \bar{\mu} \, ds, \quad \ell(\mu) = \int_{\Gamma} g \bar{\mu} \, ds, \end{aligned}$$

where the surface integrals have the meaning of pairing between $H^{1/2}$ and its dual space.

3 A simple level set method

For a defect D and a solution u satisfying the inverse obstacle problem (1) for Cauchy data (f, g) , let us consider a function $V \in H^1(B)$ such that $V = |u|$ in Ω and $V \leq 0$ in D and a distribution $f \in H^{-1}(B)$ such that $f - \Delta V \geq 0$. For some open domain $\omega \subset B$ and $g \in H^{-1}(B)$, let us define by $v_{g, \omega}$ the solution $v \in H_0^1(\omega)$ of the Poisson problem $\Delta v = g$ in ω . We now define a sequence of open domains D_n by following induction. We first consider an open domain D_0 such that $D \subset D_0 \Subset B$. The domain D_n being given, we define

$$D_{n+1} = D_n \setminus \text{supp}(\sup(\phi_n, 0)),$$

where (supp denotes the support of a function)

$$\phi_n = V + v_{g, D_n}, \quad g = f - \Delta V. \quad (5)$$

Since the open domains D_n form a decreasing sequence, it converges in the sense of Hausdorff distance to some open domain D_{∞} . Furthermore we prove that $D \subset D_{\infty}$. Lastly, the following convergence theorem justifies the method.

Theorem 2 *If we assume that the sequence of functions v_{g, D_n} converge in $H_0^1(B)$ to the function $v_{g, D_{\infty}}$ and if k^2 is not a Dirichlet eigenvalue of operator $-\Delta$ in $D_{\infty} \setminus \overline{D}$, then $D_{\infty} = D$.*

4 The “exterior approach”

We propose the following algorithm inspired by theorems 1 and 2:

1. Choose an initial guess D_0 such that $D \subset D_0 \Subset B$.

2. Step 1: for a given D_n , compute the quasi-reversibility solution u_n of system (3) associated with problem (4) in Ω_n for sufficiently small ε , where $\Omega_n := B \setminus \overline{D_n}$.

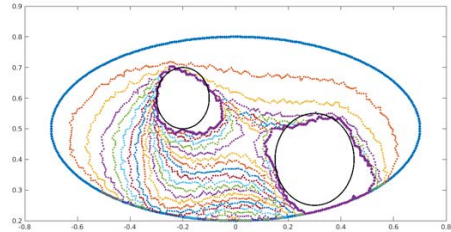
3. Step 2: for a given u_n in Ω_n , compute $V_n(x) = |u_n|$ in Ω_n and the solution ϕ_n to problem (5) for sufficiently large f , which simply reads for smooth D_n :

$$\begin{cases} \Delta \phi_n = f & \text{in } D_n \\ \phi_n = V_n & \text{on } \partial D_n. \end{cases}$$

Compute $D_{n+1} = \{x \in D_n, \phi_n(x) < 0\}$.

4. Go back to step 1 until some stopping criterion is satisfied.

We show on the figure a numerical test of the above algorithm (with the intermediate steps D_n starting from an elliptic initial guess D_0) when D is the union of two spheres, from uncorrupted Cauchy data (f, g) coming from a forward scattering simulation, $d = 1$ and $k = 5$.



References

- [1] D. Colton and A. Kirsch, A simple method for solving inverse scattering problems in the resonance region, *Inverse Problems* **12** (1996), pp. 383–393.
- [2] V. Baronian, L. Bourgeois and A. Recoquillay, Imaging an acoustic waveguide from surface data in the time domain, *Wave Motion* **66** (2016), pp. 68–87.
- [3] L. Bourgeois and J. Dardé, A quasi-reversibility approach to solve the inverse obstacle problem, *Inverse Problems and Imaging* **4/3** (2010), pp. 351–377.

High order accurate solution of the wave equation by compact finite differences and difference potentials

Steven Britt^{1,*}, Eli Turkel², Semyon Tsynkov³

¹Fulbright Postdoctoral Scholar, Tel Aviv University, Tel Aviv, Israel

²School of Mathematical Sciences, Tel Aviv University, Tel Aviv, Israel

³Department of Mathematics, North Carolina State University, Raleigh, NC, USA

*Email: dsbritt@ncsu.edu

Abstract

High order numerical methods exhibit dramatic gains in efficiency over low order methods by providing better accuracy on coarse grids, and therefore the computation time needed to obtain a desired level of accuracy in simulations is greatly reduced. In addition to the increased convergence rate, it has been shown that high order methods result in smaller dispersion errors than low order methods. In order to fit the needs of physical problems, high order methods must exhibit several capabilities, such as handling variable coefficient operators, realistic geometries, and different types of boundary conditions. We demonstrate a flexible approach that efficiently solves second order hyperbolic PDEs with high order accuracy through the combined methodology of compact high order finite differences and difference potentials.

Keywords: high order accuracy, non-conforming boundaries, time-dependent waves, variable wave speed

1 Introduction

Consider the wave equation

$$u_{tt} = c^2 \Delta u + F(x, y, t), \quad (1)$$

where F is an inhomogeneous term and the wave-speed c may vary in space but not in time. Time discretization by the θ -method with $\theta = \frac{1}{12}$ yields a temporally fourth order implicit scheme. At each time step, one must solve an elliptic spatial equation in the form of the modified Helmholtz equation,

$$\Delta u - Ku = G, \quad (2)$$

where G depends on the inhomogeneous term F as well as the solution at two previous time steps, and $K = \frac{1}{\theta c^2 h_t^2}$ where h_t is the time step. When $\theta = \frac{1}{12}$, the scheme is conditionally stable and fourth order accurate in time, while

choosing $\theta \geq \frac{1}{4}$ yields an unconditionally stable scheme which is only second order in time. At each time step, equation (2) can be interpreted as a steady-state equation. We propose to solve it by compact high order finite differences and the method of difference potentials [4]. This is a distinctly different approach than that of [3], where the method of difference potentials is applied directly to the unsteady wave equation in 3+1 dimensional space-time.

2 Compact finite differences

Finite difference schemes on regular structured grids are a straightforward and efficient way to achieve high order accuracy for variable coefficient equations such as (2). Compact schemes enable high order accuracy without increasing the stencil size, and this simplifies the treatment of boundary conditions since the stencil will not extend beyond the boundary at the near-boundary nodes, see Figure 1. Compact

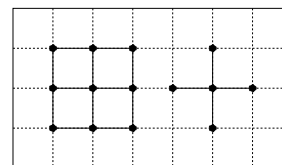


Figure 1: 2D compact (left) and five-point (right) stencils.

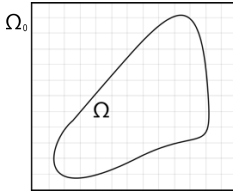
schemes also yield matrices with lower bandwidths than those resulting from wider stencils, and this reduced bandwidth improves the efficiency of solving the resulting linear system. A major limitation of conventional or compact finite differences is that they lose accuracy on domains which do not coincide with the discretization grid, and we address this by the method of difference potentials [4].

A compact 4th order Cartesian scheme for the Helmholtz equation (2) with variable K can be found in [5], and its efficiency in solving the wave equation (1) on conforming domains is examined in [1].

3 Difference potentials

The method of difference potentials incorporates a given finite difference scheme to solve problems efficiently on nonconforming geometries while maintaining the design convergence rate. For a general domain Ω , we embed the problem within an auxiliary domain Ω_0 which is a simple shape (e.g., a square, as in Figure 2). The shape of Ω_0 along with its boundary condi-

Figure 2: Domain for the method of difference potentials.



tions should be chosen so that the PDE on Ω_0 is well-posed, but otherwise can be chosen for convenience. The key feature of the method of difference potentials is that the original problem on Ω is reformulated as an equivalent set of problems on the auxiliary domain Ω_0 with different right-hand sides.

4 Time marching with difference potentials on each step

After discretizing the wave equation (1) in time, at time t_n we solve the modified Helmholtz equation (2) with $K = \frac{1}{\theta c^2 h_t^2}$ on Ω by difference potentials, where the right-hand side $G = G(x, y, t_n)$ on Ω is given. In 2D, the auxiliary problem is given by the modified Helmholtz equation (2) on the auxiliary domain Ω_0 which is a square with homogeneous Dirichlet boundary conditions.

Three finite difference solves on the auxiliary domain Ω_0 are required at each time step to produce the solution on the nonconforming domain Ω with high order accuracy, with the right-hand sides determined by the method of difference potentials. The solutions of the resulting finite difference problems on Ω_0 can be computed efficiently by iterative methods.

Fourth order convergence in both space and time for Dirichlet and Neumann problems has been demonstrated using $\theta = \frac{1}{12}$ for variable wave speeds on a nonconforming disk centered at the origin in 2D (Figure 3).

Acknowledgement

This work was supported by the US ARO under grant # W911NF-16-1-0115, by the US-Israel

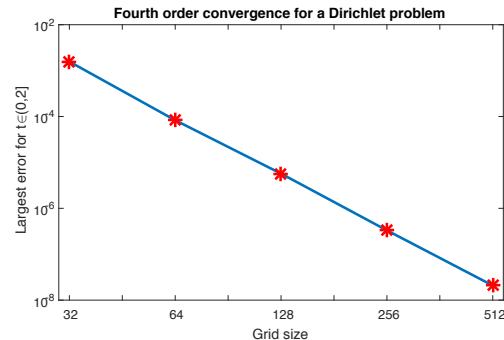


Figure 3: Variable wave speed $c(r) = \frac{r}{4} + 1$ on a nonconforming disk with $CFL = 0.6$. Error is measured from the test solution $u = \cos(5x) \cos(2y) \cos(4t)$.

BSF under grant # 2014048, as well as the United States International Education Foundation and the Raymond and Beverly Sackler Post-Doctoral Scholarship.

References

- [1] S. Britt, S. V. Tsynkov, and E. Turkel. *In submission, Journal of Computational Physics*, 2016.
- [2] S. Britt, S. V. Tsynkov, and E. Turkel. *SIAM Journal on Scientific Computing* 35:A2255–A2292, 2013.
- [3] S. V. Petropavlovsky, S. V. Tsynkov, and E. Turkel. *WAVES 2017, to appear*.
- [4] V. S. Ryaben'kii, *Method of Difference Potentials and Its Applications*, Springer-Verlag, Berlin, 2002.
- [5] I. Singer and E. Turkel. *Computational Methods Applied Mechanical Engineering* 163(1-4):343–358, 1998.

Semidiscrete evolution of elastic waves in a piezoelectric solid

Thomas Brown^{1,*}, Tonatiuh Sánchez-Vizuet², Francisco-Javier Sayas¹

¹Department of Mathematical Sciences, University of Delaware, Newark, DE , USA

²Courant Institute of Mathematical Sciences, New York University, New York, USA

*Email: tsbrown@udel.edu

Abstract

We consider a model problem of the propagation of elastic waves which are coupled with an electric field inside a piezoelectric solid as well as the discretization of this problem in space. The stress tensor in the solid combines the effect of a linear dependence of strains with the influence of an existing electric field. The system is closed using Gauss's law for the associated electric displacement. We use a first order in time and space differential system to study the well-posedness of both problems. This requires the use of an elliptic lifting operator. In the semidiscrete case we formulate the problem corresponding to an abstract Finite Element discretization in the electric and elastic fields.

Keywords: Piezoelectricity, finite elements, elastic wave propagation

1 Introduction

We consider a solid occupying a bounded region of space $\Omega \subset \mathbb{R}^3$. At positive time an elastic wave is triggered in the solid. Formally the equations we consider are the following

$$\begin{aligned}\rho \mathbf{u}_{tt} &= \operatorname{div} \boldsymbol{\sigma} + \mathbf{f} & \Omega \times [0, \infty), \\ \operatorname{div} \mathbf{D} &= 0 & \Omega \times [0, \infty),\end{aligned}$$

where \mathbf{u} represents the elastic displacement, $\boldsymbol{\sigma}$ the stress, \mathbf{D} the electric displacement, ρ the mass density, and \mathbf{f} any source terms. Expressing the electric field through an electric potential, ψ , the piezoelectric behavior of the solid is expressed in two ways. The first is through the definition of stress as the combination of an instantaneous linear operator, \mathcal{C} , acting on strain (Hooke's Law) and the effect of electric fields in the solid:

$$\boldsymbol{\sigma} := \mathcal{C} \varepsilon(\mathbf{u}) + \mathbf{e} \nabla \psi, \quad (1)$$

where $\varepsilon(\mathbf{u})$ is the symmetric strain tensor and \mathbf{e} is the third-order piezoelectric tensor. We can also see the piezoelectricity through definition of the electric displacement for which we imposed

Gauss' Law above,

$$\mathbf{D} := \mathbf{e}^\top \varepsilon(\mathbf{u}) - \kappa \nabla \psi, \quad (2)$$

where κ is the dielectric tensor. We consider two partitions of the boundary $\Gamma = \partial \Omega$ into relatively open sets such that

$$\Gamma_{ds} \cap \Gamma_{tr} = \Gamma_{pt} \cap \Gamma_{fl} = \emptyset,$$

and

$$\Gamma = \overline{\Gamma_{ds}} \cup \overline{\Gamma_{tr}} = \overline{\Gamma_{pt}} \cup \overline{\Gamma_{fl}}.$$

The partitions are independent of one another. We consider the following boundary conditions as part of our model problem:

$$\begin{aligned}\gamma \mathbf{u} &= \mathbf{g} & \Gamma_{ds} \times [0, \infty), \\ \sigma \boldsymbol{\nu} &= \mathbf{h} & \Gamma_{tr} \times [0, \infty), \\ \gamma \psi &= \mu & \Gamma_{pt} \times [0, \infty), \\ \mathbf{D} \cdot \boldsymbol{\nu} &= \eta & \Gamma_{fl} \times [0, \infty).\end{aligned}$$

Here γ represents the trace operator and $\boldsymbol{\nu}$ the outward pointing unit normal vector on Γ . Finally we require the initial conditions

$$\mathbf{u} = \mathbf{u}_t = \mathbf{0} \quad t = 0,$$

which signifies that at the initial time the solid is at rest. We will treat this system in the way of abstract evolution equations where our unknowns are mappings in the time variable to the appropriate Hilbert space, which is where we deal with the space differentiation. In this way we can consider our unknowns $\mathbf{u}(t)$ and $\psi(t)$ to be elements of subsets of $H^1(\Omega)^3$ and $H^1(\Omega)$ respectively, for each $t \geq 0$.

2 Semidiscrete formulation

The semidiscrete version of the problem will be formulated with the intention of using finite elements to solve for the elastic displacement and electric potential. To this end we set finite dimensional subspaces $\mathbf{V}_h \subset H^1(\Omega)^3$ and $W_h \subset H^1(\Omega)$ to be our generic finite element spaces. We also consider the spaces

$$\begin{aligned}\mathbf{V}_h^0 &:= \{\mathbf{u}^h \in \mathbf{V}_h : \gamma \mathbf{u}^h = 0 \text{ on } \Gamma_{ds}\}, \\ W_h^0 &:= \{\psi^h \in W_h : \gamma \psi^h = 0 \text{ on } \Gamma_{pt}\},\end{aligned}$$

and interpolation operators

$$\begin{aligned}\mathbf{I}_h : H^{1/2}(\Gamma_{\text{ds}})^d &\longrightarrow \gamma \mathbf{V}_h|_{\Gamma_{\text{ds}}}, \\ I_h : H^{1/2}(\Gamma_{\text{pt}}) &\longrightarrow \gamma W_h|_{\Gamma_{\text{pt}}}.\end{aligned}$$

Using parentheses to represent the $L^2(\Omega)^3$ and $L^2(\Omega)^{3 \times 3}$ inner products and angle brackets to represent the duality pairings of $H^{-1/2}$ and $H^{1/2}$ on appropriate parts of the boundary Γ we state the semidiscrete problem in variational form as looking for $(\mathbf{V}_h \times W_h)$ -valued (\mathbf{u}^h, ψ^h) which for all $t \geq 0$ satisfy

$$\begin{aligned}(\rho \mathbf{u}_{tt}^h, \mathbf{w}) + (\sigma^h, \varepsilon(\mathbf{w})) &= (\mathbf{f}, \mathbf{w}) + \langle \mathbf{h}, \gamma \mathbf{w} \rangle_{\Gamma_{\text{tr}}} \\ \forall \mathbf{w} \in \mathbf{V}_h^0, \\ (\mathbf{D}^h, \nabla \phi) &= \langle \eta, \gamma \phi \rangle_{\Gamma_{\text{fl}}} \quad \forall \phi \in W_h^0, \\ \gamma \mathbf{u}^h &= \mathbf{I}_h \mathbf{g} \quad \text{on } \Gamma_{\text{ds}}, \\ \gamma \psi^h &= I_h \mu \quad \text{on } \Gamma_{\text{pt}},\end{aligned}$$

where for brevity we have used the symbols σ^h and \mathbf{D}^h which are defined in terms of the semidiscrete unknowns \mathbf{u}^h and ψ^h exactly as in (1) and (2).

3 First Order Form

The mathematical analysis of both the continuous and semidiscrete problems is undertaken by rewriting them into a first order system of the form

$$\begin{aligned}\dot{\mathbf{U}}(t) &= A_* \mathbf{U}(t) + \mathbf{F}(t), \\ B \mathbf{U}(t) &= \xi(t), \\ \mathbf{U}(0) &= 0,\end{aligned}$$

for a certain operator A_* that involves first order in space differential operator and the inverse of an elliptic operator and boundary operator B . The unknowns collected in \mathbf{U} are related to displacement, purely elastic stress and electric field, while the terms collected in \mathbf{F} correspond to source terms and Neumann boundary conditions and ξ to Dirichlet boundary conditions. In this form, we follow the template of [2] to arrive at stability bounds and error estimates in the time domain. This technique yields sharper estimates than the Laplace domain technique found in [4] for a similar problem, which also includes acoustic coupling across Γ .

4 Extensions

With the introduction of an incident acoustic wave in Ω^c , we can extend the problem outlined above into the a wave-structure interaction problem, where in addition to solving for

the elastic displacement and electric potential, we look for a scattered acoustic field outside the solid. In this case, the problem is formulated as in [1]. When solving for the acoustic unknowns, we use a retarded potential representation and discretize using boundary elements. Another easy extension of this problem arises when we note that in Ω , the tensor \mathbf{e} serves to couple the quantities \mathbf{u} and ψ . If we take $\mathbf{e} \equiv 0$, the system is reduced to a wave-structure interaction problem (if we include acoustics) with a purely elastic solid. The stability and error analysis we obtain for the piezoelectric problem also apply to this problem and can be compared to their Laplace domain counterparts in [3].

References

- [1] J.-F. Deü, W. Larbi, and R. Ohayon, Variation formulations of interior structural-acoustic vibration problems, in *Computational Aspects of Structural Acoustics and Vibration*, pp. 1-21, Springer Vienna, 2009.
- [2] M. Hassell, T. Qiu, T. Sánchez-Vizuet, and F.-J. Sayas, A new and improved analysis of the time domain boundary integral operators for acoustics, *To appear in the J. Integral Equations Appl.*
- [3] G. Hsiao, T. Sánchez-Vizuet, and F.-J. Sayas, Boundary and coupled boundary-finite element methods for transient wave-structure interaction, *IMA J. Numer. Anal.*, May 2016. doi:10.1093/imanum/drw009.
- [4] T. Sánchez-Vizuet and F.-J. Sayas, Symmetric boundary-finite element discretization of time dependent acoustic scattering by elastic obstacles with piezoelectric behavior, *J. Sci. Comput.*, Sep. 2016. doi: 10.1007/s10915-016-0281-y.

Gravitational Wave Astronomy and Astrophysics

Duncan Brown^{1,*}

¹Physics Department, Syracuse University, Syracuse, USA

*Email: dabrown@syr.edu

Abstract

Gravitational waves were predicted in 1916 by Einstein when he discovered wave solutions to the linearized field equations of General Relativity. The first direct gravitational-wave detection was made by the Advanced Laser Interferometer Gravitational Wave Observatory (LIGO) on September 14, 2015. This discovery marked the culmination of a century-long quest to understand the physical nature of these waves and to build instruments sensitive enough to detect them. LIGO's detections mark the beginning of an entirely new form of observational astronomy. Gravitational waves will allow us to explore the nature of gravity and to observe astrophysical processes that are inaccessible to electromagnetic wave observations. I will review the science of gravitational waves and LIGO's discoveries, the key results from LIGO's first observing run, which was conducted September 2015–January 2016, and discuss future directions for the field of gravitational-wave astronomy.

Keywords: Gravitational Waves, Black Holes, General Relativity.

Gravitational Waves and LIGO

The direct detection of gravitational waves by the Advanced Laser Interferometer Gravitational-wave Observatory (LIGO) [1] has established the new field of gravitational-wave astronomy. Advanced LIGO has confirmed a one-hundred-year-old prediction of Einstein [2] by directly detecting gravitational waves for the first time. Gravitational waves are transverse waves of spatial strain that travel at the speed of light, generated by time variations of the mass quadrupole moment of the source [2,3]. LIGO uses laser interferometry to measure the relative length of two $L = 4$ km long arms and measure the incident strain. The physical effect of these wave is to induce a strain $h = \Delta L/L$, where h is the gravitational-wave strain amplitude projected onto the detector. Fundamental noise sources in the detectors (seismic motion, thermal noise,

and quantum-mechanical noise) limit LIGO's sensitivity to astrophysical sources. The first observing run of the Advanced LIGO detectors took place from September 12, 2015, to January 19, 2016. On September 14, 2015 at 09:50:45 UTC the LIGO Hanford, WA, and Livingston, LA, observatories detected a signal from the binary black hole merger GW150914 [4]. A second binary black hole merger signal, GW151226, was observed on December 26, 2015 at 03:38:53 UTC [5]. Both of these signals were observed with a significance greater than 5σ . A third candidate event, LVT151012, was observed on October 12, 2015 at 09:54:43 UTC with a significance of $\lesssim 2\sigma$ [6]. The emitted signals depend upon the strong field dynamics of general relativity and have been used to constrain deviations from General Relativity [7].

Observed Black Hole Mergers

The GW150914 signal was strong enough to be apparent without using any waveform model in minimally filtered detector strain data. Digital matched filtering [8] was required to detect GW151226 since the signal has a smaller strain amplitude and the detectable signal energy is spread over a longer time interval than GW150914. The candidate LVT151226 is consistent with a binary black hole merger [7] but is not significant enough to claim as a detection.

GW150914 was observed in both LIGO detectors with a time-of-arrival difference of 7 ms, which is less than the 10 ms inter-site propagation time, and a combined matched-filter signal to noise ratio (SNR) of 24. At this SNR, the false alarm rate of the is estimated to be less than 1 event per 203 000 years, equivalent to a significance greater than 5.1σ . The basic features of the GW150914 signal point to it being produced by the coalescence of two black holes. Over 0.2 s, the signal increases in frequency and amplitude in about 8 cycles from 35 to 150 Hz, where the amplitude reaches a maximum. For two objects of masses m_1 and m_2 , we can use Newton's laws of motion, New-

ton's universal law of gravitation, and Einstein's quad-rupole formula for the gravitational-wave luminosity of a system to derived a simple relating the frequency f and frequency derivative $\dot{f} = df/dt$ of emitted gravitational waves to the chirp mass $\mathcal{M} = (m_1 m_2)^{3/5}/(m_1 + m_2)^{1/5}$ [9],

$$\mathcal{M} = \frac{c^3}{G} \left[\left(\frac{5}{96} \right)^3 \pi^{-8} f^{-11} \dot{f}^3 \right]^{\frac{1}{5}}. \quad (1)$$

It is possible to estimate f and \dot{f} by directly from the LIGO data by counting the time between zero-crossings of the strain data $h(t)$ (see e.g. Fig. 1 of Ref. [4]) giving a chirp mass of $\mathcal{M} \approx 30 M_{\odot}$. We can therefore deduce that the total mass of the system is $M = m_1 + m_2 \gtrsim 70 M_{\odot}$ in the detector frame. This bounds the sum of the Schwarzschild radii of the binary components to $2GM/c^2 \gtrsim 210$ km. To reach an orbital frequency of 75 Hz (half the gravitational-wave frequency) the objects must have been very close and very compact; equal Newtonian point masses orbiting at this frequency would be only ≈ 50 km apart. A pair of neutron stars, while compact, would not have the required mass, while a black hole neutron star binary with the deduced chirp mass would have a very large total mass, and would thus merge at much lower frequency. This leaves binary black holes as the only known objects compact enough to reach an orbital frequency of 75 Hz without contact.

Bayesian parameter estimation using fully general-relativistic waveform models has been used to measure the source-frame masses of the black holes. For GW150914 the masses are $m_1 = 36.2^{+5.2}_{-3.8}$ and $m_2 = 29.1^{+3.7}_{-4.4}$. For GW151226 the masses are $m_1 = 14.2^{+8.3}_{-3.7}$ and $7.5^{+2.3}_{-2.3}$. The observed events begin to reveal a population of stellar-mass black hole mergers. Using these signals to constrain the rates of binary black hole mergers in the universe, we find that the 90% range of allowed merger rates has been updated to is $9\text{--}240 \text{ Gpc}^{-3} \text{ yr}^{-1}$. All our observations are consistent with the predictions of general relativity, and the final black holes formed after merger are all predicted to have high spin values with masses that are larger than any black hole measured in x-ray binaries. The measured rates give confidence that current and future observing runs will observe many more binary black holes.

References

- [1] B. P. Abbott et al. (The LIGO Scientific Collaboration and the Virgo Collaboration). GW150914: The Advanced LIGO Detectors in the Era of First Discoveries. *Phys. Rev. Lett.*, 116(13):131103, 2016.
- [2] A. Einstein. Approximative Integration of the Field Equations of Gravitation. *Preuss. Akad. Weiss. Berlin*, page 688, 1916.
- [3] A. Einstein. On Gravitational Waves. *Preuss. Akad. Weiss. Berlin*, page 154, 1918.
- [4] B. P. Abbott et al. (The LIGO Scientific Collaboration and the Virgo Collaboration). Observation of Gravitational Waves from a Binary Black Hole Merger. *Phys. Rev. Lett.*, 116(6):061102, 2016.
- [5] B. P. Abbott et al. (The LIGO Scientific Collaboration and the Virgo Collaboration). GW151226: Observation of Gravitational Waves from a 22-Solar-Mass Binary Black Hole Coalescence. *Phys. Rev. Lett.*, 116(24):241103, 2016.
- [6] B. P. Abbott et al. GW150914: First results from the search for binary black hole coalescence with Advanced LIGO. *Phys. Rev.*, D93(12):122003, 2016.
- [7] B. P. Abbott et al. (The LIGO Scientific Collaboration and the Virgo Collaboration). Binary Black Hole Mergers in the first Advanced LIGO Observing Run. *Phys. Rev.*, X6:041015, 2016.
- [8] Bruce Allen, Warren G. Anderson, Patrick R. Brady, Duncan A. Brown, and Jolien D. E. Creighton. FINDCHIRP: An algorithm for detection of gravitational waves from inspiraling compact binaries. *Phys. Rev.*, D85:122006, 2012.
- [9] Benjamin P. Abbott et al. The basic physics of the binary black hole merger GW150914. *Annalen Phys.*, 2016.

A Sparsity Regularization and Total Variation Based Computational Framework for the Inverse Medium Problem in Scattering

Florian Bürgel^{1,*}, Kamil S. Kazimierski², Armin Lechleiter¹

¹Center for Industrial Mathematics, University of Bremen, Germany.

²Institute of Mathematics and Scientific Computing, University of Graz, Austria.

*Email: fbuerger@uni-bremen.de

Abstract

We consider inverse medium scattering in two or three dimensions modeled by the Helmholtz equation. To this end, we set up an efficient minimization-based inversion scheme that follows on the one hand the paradigm to, roughly speaking, minimize the discrepancy but on the other hand takes into account various structural a-priori information via suitable penalty terms. This allows for instance to combine sparsity-promoting with total variation-based regularization, while at the same time respecting physical bounds for the inhomogeneous medium. The flexibility of our approach is due to a primal-dual algorithm that we employ to minimize the corresponding Tikhonov functional. We show feasibility and performance of the resulting inversion scheme via reconstructions from synthetic and measured data.

Keywords: Inverse scattering problem, Sparsity regularization, Total variation, Primal-dual algorithm.

1 The Direct Scattering Problem

We consider time-harmonic inverse scattering of incident electromagnetic or acoustic waves u^i with time-dependence $e^{-i\omega t}$ from inhomogeneous media $D \subset \mathbb{R}^d$, $d = 2, 3$, e.g. incident point sources or plane waves. For a wave number $k > 0$ the incident wave u^i solves the Helmholtz equation $\Delta u^i + k^2 u^i = 0$. Let $q: \mathbb{R}^d \rightarrow \mathbb{C}$ be the contrast with $\text{supp}(q) = \overline{D}$. Then the total field u^t solves

$$\Delta u^t + k^2(1+q)u^t = 0 \quad \text{in } \mathbb{R}^d. \quad (1)$$

Further the scattered wave

$$u^s = u^t - u^i \quad (2)$$

satisfies Sommerfeld's radiation condition

$$\lim_{|x| \rightarrow \infty} |x|^{(d-1)/2} \left(\frac{\partial}{\partial |x|} - ik \right) u^s(x) = 0, \quad (3)$$

uniformly in all directions $\hat{x} = x/|x|$.

The direct scattering problem is to find a u^s that solves (1)–(3), see [3]. Unique solvability of the scattering problem holds for $q \in L^p(D)$, $p > d/2$.

We denote by Φ the radiating fundamental solution of the Helmholtz equation and define the radiating volume potential

$$V(f)(x) := \int_D \Phi(x, y)f(y) dy, \quad x \in \mathbb{R}^d.$$

Then the direct scattering problem can be reformulated as an integral equation: u^s solves the Lippmann-Schwinger equation

$$u^s - k^2 V(qu^s) = k^2 V(qu^i) \quad \text{in } D. \quad (4)$$

2 The Inverse Scattering Problem

Taking into account (4) a non-linear operator \mathcal{F} maps the discretized contrast $q \in \mathbb{C}^{N \times N}$ onto near or far field measurements $F_{\text{meas}} \in \mathbb{C}^{N_s \times N_i}$, where N_s is the number of receivers and N_i the number of transmitters. We seek q such that $\mathcal{F}(q)$ matches the measured data F_{meas} .

For noisy measurements $F_{\text{meas}}^\varepsilon$ with relative noise level ε we have to regularize, e.g. by minimizing the Tikhonov functional

$$f(q) := \frac{1}{2} \|\mathcal{F}(q) - F_{\text{meas}}^\varepsilon\|_F^2 + \mathcal{P}(q) \quad (5)$$

with a Frobenius norm $\|\cdot\|_F$, and penalty terms in the convex functional \mathcal{P} .

3 Penalty Terms

To take into account several a-priori information, $\mathcal{P}(q)$ is the sum of the following penalty terms.

First, we assume that the contrast of the scatterer is sparse, i.e. described by few non-zero coefficients, in pixel basis. This is taken into account by a penalty term weighted by regularization parameter $\alpha > 0$,

$$\alpha \|q\|_1.$$

Second, we suppose that the scattering object has sharp edges. Therefore we add a penalty term with total variation semi-norm weighted by regularization parameter $\beta > 0$,

$$\beta \|\nabla q\|_1.$$

Third, we respect physical bounds by adding $\delta(q)$, where δ equals infinity if one entry of q is outside a reasonable physical interval and zero otherwise.

To sum up,

$$\mathcal{P}(q) = \alpha \|q\|_1 + \beta \|\nabla q\|_1 + \delta(q).$$

4 Numerical Minimization Techniques

To apply the primal-dual algorithm, see [4], we linearize \mathcal{F} . Instead of the discrepancy

$$d(q_n) := \|\mathcal{F}(q_n) - F_{\text{meas}}^{\varepsilon}\|_F$$

we hence regard the corresponding discrepancy

$$d_{q_n}(h) := \|\mathcal{F}'(q_n)[h] + \mathcal{F}(q_n) - F_{\text{meas}}^{\varepsilon}\|_F$$

to extend the Tikhonov functional (5) to

$$f_{q_n}(h) := \frac{1}{2}[d_{q_n}(h)]^2 + \mathcal{P}(q_n + h). \quad (6)$$

Scheme to minimize $f_{q_n}(h)$: For a fixed contrast q_n we minimize $f_{q_n}(h)$ with respect to h with the primal-dual algorithm given in [4]. We call this *inner iteration*. Afterwards our *outer iteration* is the update $q_{n+1} := q_n + h$ before we minimize $f_{q_n}(h)$ with respect to h again. Modifying the functional (6) enables us to deal with complex-valued contrasts.

Stopping strategies: The outer iteration is stopped by the discrepancy principle, i.e. if $d(q_n) \leq \tau\varepsilon$ with $\tau > 1$. To stop the inner iteration, that minimizes (6) instead of (5), we have two strategies:

- (S1) After the inner iteration is finished we compare $d_{q_n}(h)$ and $d(q_n + h)$. If they are similar, we increase the number of inner iterations, otherwise we decrease it.
- (S2) Inside the inner iteration we stop by comparison of $d_{q_n}(h)$ and $d(q_n)$. (We follow an inexact stopping rule for a Newton-like method, see [5].)

5 Numerical Results

To show feasibility and performance of our inversion algorithm we reconstruct a tripod in 3D (with different contrast values for each arm) as well as two dielectrics from experimentally measured data in 2D using (S1) and discrepancy principle, see Figure 1. In both cases the computational domain is discretized by $N = 256$ points in every dimension.

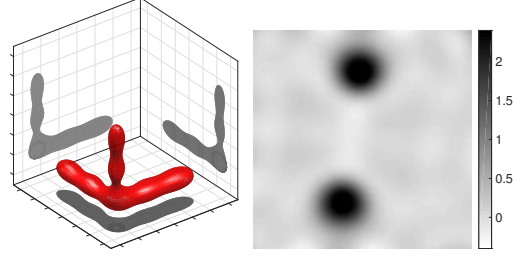


Figure 1: Left: Real part of reconstruction of tripod from synthetic data perturbed with 1% Gaussian noise. Right: Real part of reconstruction of two dielectrics from data measured by the Institute Fresnel at 5 GHz, see [1]; we estimate the noise to 25%. The number of transmitters/receivers is 50/50 and 36/49. Run-time and error are 4.4 h, 60.6% as well as 1.6 min, 51.3%, see [2].

References

- [1] K. Belkebir and M. Saillard. Special section on testing inversion algorithms against experimental data. *Inverse Problems*, 17(6):1565–1571, 2001.
- [2] F. Bürgel, K. S. Kazmierski, and A. Lechleiter. A sparsity regularization and total variation based computational framework for the inverse medium problem in scattering. *Journal of Computational Physics*, 339:1–30, 2017.
- [3] D. Colton and R. Kress. *Inverse Acoustic and Electromagnetic Scattering Theory*. Springer, New York, 2013.
- [4] A. Chambolle and T. Pock. A first-order primal-dual algorithm for convex problems with applications to imaging. *Journal of Mathematical Imaging and Vision*, 40(1):120–145, 2011.
- [5] A. Rieder. On convergence rates of inexact Newton regularizations. *Numerische Mathematik*, 88(2): 347–365, 2001.

The Detection of Defects at the Interface Between Two Materials

Fioralba Cakoni^{1,*}, Irene de Teresa², Houssem Haddar³, Peter Monk⁴

¹Department of Mathematics, Rutgers University Piscataway, NJ 08854-8019, USA

²Department Mathematical Sciences, University of Delaware, Newark, Delaware 19716, USA

³INRIA, Ecole Polytechnique, Université Paris Saclay, Route de Saclay, 91128 Palaiseau, France

⁴Department Mathematical Sciences, University of Delaware, Newark, Delaware 19716, USA

*Email: fc292@math.rutgers.edu

Abstract

We consider the problem of detecting delamination of interfaces in composite materials using acoustic waves or separation between integrated circuit components using electromagnetic waves.

Keywords: Nondestructive testing, inverse problem, linear sampling method, asymptotic methods.

1 Introduction

For sake of presentation, in this report we discuss our problem for the case of acoustic waves [1]. We consider two materials that should have a coincident boundary (in the undamaged or background state) and we wish to detect if there is a part of the common boundary where the two materials have separated. In particular we want to determine the size and position of the delamination. More precisely, we denote by $\Omega \subset \mathbb{R}^m$, $m = 2, 3$ the support of the inhomogeneity to be tested which in absence of delamination is composed of two different materials adjacent to one another with constitutive material properties μ_+ , n_+ and μ_- , n_- . We denote their bounded support by Ω_+ and Ω_- , respectively, and the shared interface by $\Gamma := \partial\Omega_-$ (i.e. $\Omega = \Omega_- \cup \Omega_+$). Both the outer boundary $\partial\Omega_+$ of the domain Ω_+ and the boundary $\partial\Omega_-$ of the simply connected domain Ω_- are assumed to be piece-wise smooth, unless mentioned otherwise, and ν denotes the unit normal always oriented outwards to the region bounded by the curve. Furthermore, we assume that along a part of the interface, denoted here by $\Gamma_0 \subset \Gamma$, these two materials have detached (delaminated) and we model this fact with the appearance of an opening with support Ω_0 and material properties μ_0 , n_0 (see Fig. 1 left). Note that $\Gamma_0 = \Omega_0 \cap \Gamma$. The material properties (possibly complex valued) in each of the domains are assumed to be smooth, i.e. $\mu_+, n_+ \in C^1(\Omega_+)$,

$\mu_-, n_- \in C^1(\Omega_-)$ and $\mu_0, n_0 \in C^1(\Omega_0)$ (however note that across the interfaces there are discontinuities in the material properties). As-

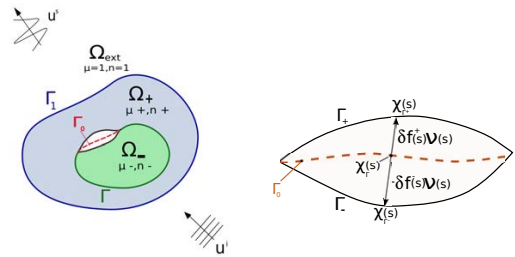


Figure 1: Layered media with a thin delamination at the interface of two layers Ω_- and Ω_+ .

suming now time harmonic fields, the total field $u^{ext} = u^s + u^i$ in Ω_{ext} , where u^s is the scattered field, and the fields u^+ , u^- and U inside Ω_+ , Ω_- and Ω_0 , respectively, satisfy

$$\Delta u^{ext} + k^2 u^{ext} = 0 \quad \text{in } \Omega_{ext} \quad (1)$$

$$\nabla \cdot \left(\frac{1}{\mu_+} \nabla u^+ \right) + k^2 n_+ u^+ = 0 \quad \text{in } \Omega_+ \quad (2)$$

$$\nabla \cdot \left(\frac{1}{\mu_-} \nabla u^- \right) + k^2 n_- u^- = 0 \quad \text{in } \Omega_- \quad (3)$$

$$\nabla \cdot \left(\frac{1}{\mu_0} \nabla U \right) + k^2 n_0 U = 0 \quad \text{in } \Omega_0. \quad (4)$$

Across the interfaces the fields on either side and their conormal derivatives are continuous

$$u^{ext} = u^+, \quad \frac{\partial u^{ext}}{\partial \nu} = \frac{1}{\mu_+} \frac{\partial u^+}{\partial \nu} \quad \text{on } \Gamma_1 \quad (5)$$

$$u^+ = u^-, \quad \frac{1}{\mu_+} \frac{\partial u^+}{\partial \nu} = \frac{1}{\mu_-} \frac{\partial u^-}{\partial \nu} \quad \text{on } \Gamma \setminus \Gamma_0 \quad (6)$$

$$U = u^+, \quad \frac{1}{\mu_0} \frac{\partial U}{\partial \nu} = \frac{1}{\mu_+} \frac{\partial u^+}{\partial \nu} \quad \text{on } \Gamma_+ \quad (7)$$

$$U = u^-, \quad \frac{1}{\mu_0} \frac{\partial U}{\partial \nu} = \frac{1}{\mu_-} \frac{\partial u^-}{\partial \nu} \quad \text{on } \Gamma_-. \quad (8)$$

The scattered field u^s satisfies the Sommerfeld radiation condition uniformly in $\hat{x} = x/|x|$

$$\lim_{r \rightarrow \infty} r^{\frac{m-1}{2}} \left(\frac{\partial u^s}{\partial r} - iku^s \right) = 0. \quad (9)$$

Here we consider plane waves as incident fields which are given by $u^i := e^{ikx \cdot d}$ where the unit

vector d is the incident direction. The goal of this study is to propose an algorithm for detecting the delaminated region using remote measurements of acoustic waves scattered by the structure. In practice, the thickness of the opening is much smaller than both the interrogating wave length in free space $\lambda = \frac{2\pi}{k}$ and the thickness of the layers of background material. We take advantage of the small scale of the thickness δ and, using an asymptotic method from [3], we derive an approximate model of the delaminated structure where the opening Ω_0 is replaced by new jump relations for u^+ and u^- across the delaminated part Γ_0 that account for the presence of the opening (see Fig. 1 right).

2 An approximate asymptotic model

For simplicity of presentation assume that $m = 2$ and, focusing our attention on a neighborhood of the opening Ω_0 , we use formal asymptotic analysis to derive an approximate model that takes into account the thin opening Ω_0 . In the approximate model the equations (1-3) and the transmission conditions (5) and (6) remain the same, (4) disappears and (7)-(8) are replaced by

$$\begin{aligned} [u] &= \alpha \left\langle \frac{1}{\mu} \frac{\partial u}{\partial \nu} \right\rangle && \text{on } \Gamma_0 \\ \left[\frac{1}{\mu} \frac{\partial u}{\partial \nu} \right] &= (-\nabla_\Gamma \cdot \langle \beta f \rangle \nabla_\Gamma + \gamma) \langle u \rangle && \text{on } \Gamma_0 \end{aligned}$$

where $\alpha = 2\delta \langle f(\mu_0 - \mu) \rangle$, $\beta^\pm = 2\delta \left(\frac{1}{\mu_0} - \frac{1}{\mu^\pm} \right)$ and $\gamma = 2\delta k^2 \langle f(n - n_0) \rangle$, recalling that $[w] = w^+ - w^-$ and $\langle w \rangle = (w^+ + w^-)/2$. Next we analyze the well-posedness of the approximate model. To this end, we introduce the space

$$\mathcal{H} := \left\{ u \in H^1(B_R \setminus \overline{\Gamma_0}), \sqrt{f^\pm} \nabla_\Gamma \langle u \rangle \in L^2(\Gamma_0) \right\}$$

equipped with the natural norm. Then we prove that the direct approximate model has a unique solution $u \in \mathcal{H}$, provided that $\Re \left(\frac{1}{\mu^\pm} \right) \geq \epsilon_1 > 0$ and $\Re \left(\frac{1}{\mu_0} - \frac{1}{\mu^\pm} \right) \geq \epsilon_2 > 0$, $0 \leq \Im(n^\pm) \leq \Im(n_0)$ and $0 \leq \Im(\mu^\pm) \leq \Im(\mu_0)$, and finally f^\pm go to zero at the boundary of Γ_0 in Γ such that $1/\langle f(\mu_0 - \mu) \rangle \in L^t(\Gamma_0)$ for $t = 1 + \epsilon$ in \mathbb{R}^2 and $t = 7/4 + \epsilon$ in \mathbb{R}^3 for arbitrary small $\epsilon > 0$.

3 The inverse problem of reconstructing the delaminated part Γ_0

Our reconstruction method is a modified Linear Sampling Method, adapted to our problem

where we already know the interface Γ and only look for the delaminated part Γ_0 [1]. The *inverse problem* we consider here is to determine the delaminated portion Γ_0 of the boundary Γ from a knowledge of the far field pattern $u_\infty(\hat{x}, d)$ for \hat{x} and d on the unit sphere \mathbb{S}^{m-1} . We remark that our inversion algorithm can also be justified and implemented for limited aperture data as well as for near field data. The inversion method is based on the far field equation

$$\int_{\mathbb{S}^{m-1}} (u^\infty(\hat{x}, d) - u_b^\infty(\hat{x}, d)) g(d) ds_d = \phi_L^\infty(\hat{x})$$

where $u^\infty(\hat{x}, d)$ is the measured data and $u_b^\infty(\hat{x}, d)$ is the computed far field pattern for the healthy material, and for some $\alpha_L, \beta_L \in C_0^\infty(L)$,

$$\phi_L^\infty = \int_L \alpha_L(y) G_b^\infty(\cdot, y) + \beta_L(y) \frac{1}{\mu} \frac{\partial G_b^\infty(\cdot, y)}{\partial \nu(y)} ds(y)$$

with $L \subset \Gamma$ and $G_b^\infty(x, y)$ the far field pattern of the radiating Green's function of the background media (i.e. in the absence of delamination). Then we show that roughly the regularized solution of the far field equation has different behavior if $L \subset \Gamma_0$ as opposed to when $L \not\subset \Gamma_0$. We refer to [1] for more details.

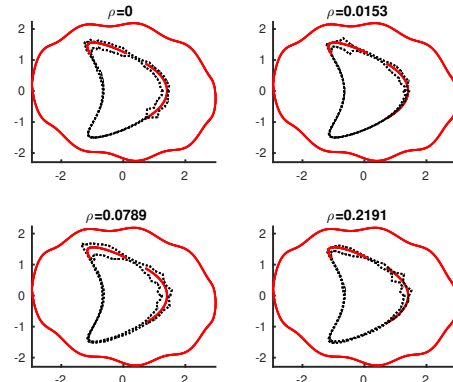


Figure 2: Reconstruction of two delaminated parts $\Gamma_0^1 \cup \Gamma_0^2$ for four levels of noise ρ .

References

- [1] F. Cakoni, I. de Teresa, H. Haddar and P. Monk, *SIAM J. Appl. Math.* **76** (2016), pp. 2306 – 2332.
- [2] B. Delourme, H. Haddar, and P. Joly, *J. Math. Pures Appl.* **98** (2012) pp. 28 – 71.
- [3] H. Haddar, P. Joly, and H. M. Nguyen, *Models and Methods in Applied Sciences* **18** (2005) pp. 1273 – 1300.

Electromagnetic Stekloff Eigenvalues in Inverse Scattering

Jessika Camaño^{1,*}, Christopher Lackner², Peter Monk³

¹Departamento de Matemática y Física Aplicadas, Universidad Católica de la Santísima Concepción and CI²MA, Universidad de Concepción, Concepción, Chile

²TU Vienna

³Department of Mathematical Sciences, University of Delaware, Newark, EEUU.

*Email: jecamano@ucsc.cl

Abstract

This paper investigates the use of Stekloff eigenvalues for Maxwell's equations to detect changes in a scatterer using remote measurements of the scattered wave. Because the Stekloff eigenvalue problem for Maxwell's equations is not a standard eigenvalue problem for a compact operator, we propose a modified Stekloff problem that restores compactness. In order to measure the modified Stekloff eigenvalues of a domain from far field measurements we perturb the usual far field equation of the Linear Sampling Method by using the far field pattern of an auxiliary impedance problem related to the modified Stekloff problem. We show existence of modified Stekloff eigenvalues, well-posedness of the corresponding auxiliary exterior impedance problem and provide theorems that support our claim to be able to detect modified Stekloff eigenvalues from far field measurements. Preliminary numerical results are reported.

Keywords: Stekloff eigenvalues, inverse problem, non-destructive testing, Herglotz wave function.

1 Introduction

In a recent paper [1] it was suggested to use Stekloff eigenvalues for the Helmholtz equation as a novel “target signature” for non-destructive testing via inverse scattering. In particular it was shown that it is possible to measure Stekloff eigenvalues for a bounded inhomogeneous scatterer by solving a sequence of modified far field equations. In this paper we shall continue this research program by considering the determination of Stekloff eigenvalues from far field data for Maxwell's equations.

As is well known, the Stekloff eigenvalue problem for the Helmholtz equation for a bounded domain is equivalent to the determination of eigenvalues of the corresponding Neumann-to-Dirichlet map. For the Helmholtz equation the

compactness of this map allowed the authors of [1] to verify the existence of Stekloff eigenvalues for the Helmholtz equation even in the case of an absorbing medium where the problem is not self adjoint. In our case, for Maxwell's equations, compactness of the corresponding electric current to magnetic current map (still referred to as the Neumann-to-Dirichlet or NtD map here) is unlikely as we shall show. However there is no need for us to use the “natural” NtD map because it is only used as an auxiliary problem for modifying the far field operator. So we propose a new modified Stekloff eigenvalue problem that does give rise to a compact and self adjoint eigenvalue problem in a dielectric medium. We now describe the standard forward scattering problem that is the basis of our study. Suppose D is a bounded domain containing the origin such that $\mathbb{R}^3 \setminus \overline{D}$ is connected and such that the boundary of D denoted ∂D is smooth. The forward electromagnetic scattering problem is to find the electric field $\mathbf{E} \in \mathbf{H}_{\text{loc}}(\mathbf{curl}, \mathbb{R}^3 \setminus \overline{D})$ and the magnetic field $\mathbf{H} \in \mathbf{H}_{\text{loc}}(\mathbf{curl}, \mathbb{R}^3 \setminus \overline{D})$ such that

$$\mathbf{curl}\mathbf{E} - i\kappa\mathbf{H} = \mathbf{0}, \quad \mathbf{curl}\mathbf{H} + i\kappa\epsilon_r\mathbf{E} = \mathbf{0} \quad (1)$$

in \mathbb{R}^3 where the wavenumber κ is real, positive and it is fixed so that the method is applicable to data at a single frequency. The relative permittivity ϵ_r is assumed to be piecewise smooth. The total fields \mathbf{E} and \mathbf{H} are given by

$$\mathbf{E} = \mathbf{E}^i + \mathbf{E}^s, \quad \mathbf{H} = \mathbf{H}^i + \mathbf{H}^s,$$

where $(\mathbf{E}^s, \mathbf{H}^s)$ is the scattered field satisfying the Silver–Müller radiation condition

$$\lim_{r \rightarrow \infty} (\mathbf{H}^s \times \mathbf{x} - r\mathbf{E}^s) = \mathbf{0}$$

uniformly in $\hat{\mathbf{x}} := \mathbf{x}/|\mathbf{x}|$ where $r = |\mathbf{x}|$. The incident field $(\mathbf{E}^i, \mathbf{H}^i)$ is assumed to be a plane

wave given by

$$\begin{aligned}\mathbf{E}^i(\mathbf{x}) &= \frac{i}{\kappa} \operatorname{curl} \operatorname{curl} \mathbf{p} e^{-i\kappa \mathbf{x} \cdot \mathbf{d}}, \\ \mathbf{H}^i(\mathbf{x}) &= \operatorname{curl} \mathbf{p} e^{-i\kappa \mathbf{x} \cdot \mathbf{d}}.\end{aligned}$$

Here \mathbf{d} is a unit vector giving the direction of propagation of the plane wave and \mathbf{p} is the polarization vector assumed real and non zero. The scattered field has the following asymptotic expansion in r [2]:

$$\begin{aligned}\mathbf{E}^s(\mathbf{x}) &= \frac{e^{-i\kappa r}}{r} \mathbf{E}_\infty(\hat{\mathbf{x}}, \mathbf{d}; \mathbf{p}) + \mathcal{O}\left(\frac{1}{r^2}\right), \quad r \rightarrow \infty, \\ \mathbf{H}^s(\mathbf{x}) &= \frac{e^{-i\kappa r}}{r} \mathbf{H}_\infty(\hat{\mathbf{x}}, \mathbf{d}; \mathbf{p}) + \mathcal{O}\left(\frac{1}{r^2}\right), \quad r \rightarrow \infty,\end{aligned}$$

where \mathbf{E}_∞ (respectively \mathbf{H}_∞) is called the far field pattern of the scattered wave \mathbf{E}^s (respectively \mathbf{H}^s) depending, as indicated, on the measurement direction $\hat{\mathbf{x}}$, the incident direction \mathbf{d} , and the polarization \mathbf{p} .

Let $\mathbb{S}^2 = \{\mathbf{x} \in \mathbb{R}^3 \mid |\mathbf{x}| = 1\}$. Now we can state the inverse problem we wish to solve: given the far field pattern for all $\hat{\mathbf{x}} \in \mathbb{S}^2$, $\mathbf{d} \in \mathbb{S}^2$ and $\mathbf{p} \in \mathbb{R}^3$, $\mathbf{p} \neq \mathbf{0}$, we wish to compute approximations of modified Stekloff eigenvalues for a domain B such that either $B = D$ (in non-destructive testing we may know the shape of the object and wish to monitor its interior for changes in ϵ_r) or B is a ball containing D in its interior (for example if the shape of D is not a priori known).

2 The Standard Stekloff Boundary Condition

Following the ideas in [1], we are interested in studying the inverse problem by considering a modified far field operator whose kernel is the difference between the measured far field pattern due to the scattering object and the far field pattern of an auxiliary scattering problem involving a Stekloff boundary condition on the boundary of a domain B containing D (possibly $B = D$). After some analysis, we see that this modified far field operator is injective if λ is not a Stekloff eigenvalue and $\lambda = \lambda(k)$ is called a Stekloff eigenvalue if the following problem:

$$\begin{aligned}\operatorname{curl} \operatorname{curl} \mathbf{w} - \kappa^2 \epsilon_r \mathbf{w} &= \mathbf{0} \quad \text{in } B, \\ \boldsymbol{\nu} \times \operatorname{curl} \mathbf{w} - \lambda \mathbf{w}_T &= \mathbf{0} \quad \text{on } \partial B,\end{aligned}\tag{2}$$

has a nontrivial solution \mathbf{w} . We consider the NtD map for the analysis of this eigenvalue prob-

lem. A priori, we hope that the NtD operator is self-adjoint and compact. However, after some computations we observe that for the sphere the NtD map cannot be compact which defeats an easy proof of the existence of Stekloff eigenvalues in this case (and presumably in general). Notice that we have arrived to the problem (2) from an auxiliary problem which was introduced with the aim of studying the inverse electromagnetic scattering problem. We are thus free to choose a different auxiliary problem.

3 Modified Stekloff Boundary Condition

In this section we proceed as in Section 2 but changing the auxiliary scattering problem for a convenient one. Repeating the argument given in the last section concerning injectivity of the far field operator, we arrive to the following modified Stekloff eigenvalue problem: Find $\mathbf{w} \neq \mathbf{0}$ such that

$$\begin{aligned}\operatorname{curl} \operatorname{curl} \mathbf{w} - \kappa^2 \epsilon_r \mathbf{w} &= \mathbf{0} \quad \text{in } B, \\ \boldsymbol{\nu} \times \operatorname{curl} \mathbf{w} - \lambda \mathbf{S} \mathbf{w}_T &= \mathbf{0} \quad \text{on } \partial B,\end{aligned}\tag{3}$$

where the linear operator \mathbf{S} is defined as follows:

$$\begin{aligned}\mathbf{S} : \mathbf{H}^{-1/2}(\operatorname{curl}_{\partial B}, \partial B) &\longrightarrow \mathbf{H}^{1/2}(\operatorname{div}_{\partial B}^0, \partial B) \\ \boldsymbol{\mu} &\longmapsto \mathbf{S} \boldsymbol{\mu} := \operatorname{curl}_{\partial B} \boldsymbol{\mu},\end{aligned}$$

where $\boldsymbol{\mu} \in \mathbf{H}^{1/2}(\operatorname{div}_{\partial B}^0, \partial B)$ if and only if $\boldsymbol{\mu} \in \mathbf{H}_t^{1/2}(\partial B)$ and $\operatorname{div}_{\partial B} \boldsymbol{\mu} = 0$ and $q \in H^1(\partial B)/\mathbb{C}$ is the solution of the problem $\Delta_{\partial B} q = \operatorname{curl}_{\partial B} \boldsymbol{\mu}$. Finally, we prove that modified Stekloff eigenvalues exist.

Theorem 1 *When ϵ_r is real, a countable discrete set of modified Stekloff eigenvalues (eigenvalues of (3)) exist. They are real and accumulate at ∞ .*

References

- [1] F. Cakoni, D. Colton, S. Meng and P. Monk, Stekloff eigenvalues in inverse scattering, to appear in SIAM J. Appl. Math. (2016).
- [2] D. Colton and R. Kress, *Inverse Acoustic and Electromagnetic Scattering Theory*, 3rd edition, Springer-Verlag, New York, 2012.

Local analysis of near fields in acoustic scattering

C. Carvalho^{1,*}, S. Khatri¹, A.D. Kim¹

¹ Applied Math Unit, University of California Merced, Merced, USA

*Email: ccarvalho3@ucmerced.edu

Abstract

We compute near fields using boundary integral equation methods for 2D acoustic scattering by an obstacle with an analytic boundary. Accurate computation of near fields is needed for optical scattering by nanostructures and for other related problems. A classical method to approximate the solution everywhere consists of using the same quadrature rule (Nyström method) used to solve the underlying boundary integral equation. It is established that this method incurs an $O(1)$ error for a fixed number of quadrature points. Our goal is, for a fixed number of quadrature points and without using high-order Nyström methods, to develop a method to address this $O(1)$ error. Similar to numerical method for approximating singular integrals, we subtract from the associated kernel the asymptotic expansion that captures the nearly singular behavior.

Keywords: boundary integral equation, close evaluation, local analysis

1 Problem setting

We consider the following scattering problem by a sound-soft obstacle $D \subset \mathbb{R}^2$ with ∂D an analytic, closed curve:

$$\Delta u + k^2 u = 0 \quad \text{in } \mathbb{R}^2 \setminus \overline{D}, \quad (1a)$$

$$u = f \quad \text{on } \partial D, \quad (1b)$$

$$\partial_r u - ik u = o(r^{-1/2}), \quad r \rightarrow \infty, \quad (1c)$$

where k denotes the wavenumber and f is an analytic function that gives the field incident on the obstacle. The solution of (1) may be represented as a single- and double-layer potential (see [5]): for all $x \in \mathbb{R}^2 \setminus \overline{D}$,

$$u(x) = \int_{\partial D} [\partial_{n_y} G(x, y) - ikG(x, y)] \mu(y) d\sigma_y. \quad (2)$$

The fundamental solution of (1a) is

$$G(x, y) = \frac{i}{4} H_0^{(1)}(k|x - y|), \quad (3)$$

where $H_0^{(1)}$ is the Hankel function of first kind, and the density μ satisfies the boundary integral equation for all $y' \in \partial D$,

$$\begin{aligned} \frac{1}{2}\mu(y') + \int_{\partial D} \partial_{n_y} G(y', y) \mu(y) d\sigma_y \\ - ik \int_{\partial D} G(y', y) \mu(y) d\sigma_y = f(y'). \end{aligned} \quad (4)$$

Since ∂D is a closed, analytic curve, and G exhibits a log-singular behavior, (4) can be solved numerically with spectral accuracy using Kress' Nyström method [5, Chapter 12] (for Laplace we consider the periodic trapezoid rule [1]). Using the same Nyström method to evaluate (2) incurs an $O(1)$ error for points in $\mathbb{R}^2 \setminus \overline{D}$ that are close to ∂D . This is due to the fact that the kernel $K := \partial_{n_y} G - ikG$ is nearly singular, in the sense that K is sharply peaked when $|x - y| \rightarrow 0^+$, and will not be well resolved for fixed quadrature points. In fact, the error made in evaluating (2) exhibits a boundary layer with thickness $O(1/N)$ where N is the number of quadrature points, leading to a $O(1)$ error as x approaches ∂D [1]. It is necessary to accurately predict these near fields for optical scattering by nanostructures, for instance in plasmonics.

2 Local analysis and numerical results

To address the $O(1)$ error associated with the near-field evaluation problem, we treat nearly singular integrals in a similar fashion to methods developed for singular integrals [3]. We subtract K^{ns} the nearly singular behavior of the kernel K appearing in (2) and write the solution, for all $x \in \mathbb{R}^2 \setminus \overline{D}$, as

$$\begin{aligned} u(x) = & \int_{\partial D} (K(x, y) - K^{ns}(x, y)) \mu(y) d\sigma_y \\ & + \int_{\partial D} K^{ns}(x, y) \mu(y) d\sigma_y. \end{aligned} \quad (5)$$

In (5) the first integral is smooth, and therefore easier to approximate, whereas the second one is evaluated analytically. K^{ns} is found as a linear combination of the asymptotic expansions of the single- and double-layer potentials. Let

δ denote the separation distance between the evaluation point x in $\mathbb{R}^2 \setminus \overline{D}$ and the boundary ∂D : then $x = y^* + \delta n_{y^*}$ with $y^* \in \partial D$. Defining $\mathbf{Y} := \frac{y^* - y}{\delta}$, one can rewrite K as a non-uniform expansion $K(x, y) = K(\delta\mathbf{Y}, \delta)$, then K^{ns} is found as the inner expansion of $K(\delta\mathbf{Y}, \delta)$ as $\mathbf{Y} \rightarrow 0^+$. It is well-known that G has the same singular behavior as G^L , the fundamental solution of Laplace's equation [5]:

$$G = G^L + \text{cst} + O(\delta^2 \log \delta), \quad (6)$$

with $\text{cst} := \frac{i}{4} - \frac{1}{2\pi} \left(\log \frac{k}{2} + C \right)$, and C denoting Euler's constant. Therefore, the leading order of K^{ns} can be found as the inner expansion of $K^L := \partial_{n_y} G^L - ik(G^L + \text{cst})$, with

$$\begin{aligned} G^L(\delta\mathbf{Y}, \delta) &= -\frac{1}{2\pi} \log \delta \\ &\quad - \frac{1}{4\pi} \log(1 + |\mathbf{Y}|^2 - 2n_{\mathbf{Y}^*} \cdot \mathbf{Y}), \end{aligned} \quad (7)$$

$$\partial_{n_y} G^L(\delta\mathbf{Y}, \delta) = -\frac{1}{2\pi\delta} \frac{n_{\mathbf{Y}} \cdot \mathbf{Y} + n_{\mathbf{Y}} \cdot n_{\mathbf{Y}^*}}{1 + |\mathbf{Y}|^2 - 2n_{\mathbf{Y}^*} \cdot \mathbf{Y}}. \quad (8)$$

Using the parametrization $\mathbf{Y}(t) = \frac{y(t^*) - y(t)}{\delta}$, $t, t^* \in [0, 2\pi]$, one can express K^{ns} as a rational trigonometric function of the form

$$\begin{aligned} K^{ns}(t, t^*; \delta) &= \frac{A_0 + A_1 \cos(t - t^*)}{1 + B_1 \cos(t - t^*)} \\ &\quad - ik(\log(C_0 + C_1 \cos(t - t^*)) + D), \end{aligned} \quad (9)$$

where $A_0, A_1, B_1, C_0, C_1, D$ are constants, in particular depending on δ and the curvature of the boundary at y^* . The integral operator with K^{ns} can be computed spectrally using its Fourier series representation [4]. We can then compute (5) efficiently and accurately. Results in Fig. 1 show a gain of at least 3 orders of precision close to boundary. Electrostatic cases ($k = 0$) have shown a gain of at least 6 orders. Since $K \sim K^L$ is valid for $k|x - y|$ sufficiently small, we are performing a sub-wavelength correction (i.e. $k\delta \ll 1$). A new scaling taking into account k will be required to tackle high frequency scattering problems [1].

3 Future works

These results show the advantage of incorporating asymptotic analysis into the numerical evaluation of near-fields. The asymptotic Nyström method with sub-wavelength correction can be

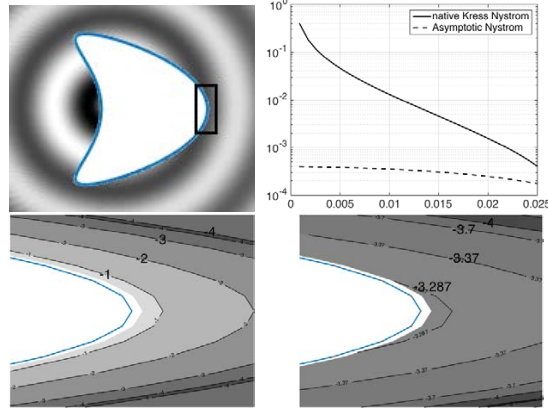


Figure 1: Top left: real part of the solution of (2) given by $u(x) = \frac{i}{4} H_0^{(1)}(k|x - x_0|)$, with $k = 5$, $x_0 = (-0.8, 0.2) \in D$, with $N = 300$. Top right: error (log-scale) with respect to δ for $t^* = \frac{29}{30} 2\pi$. Bottom: contour errors (log-scale) for (2) at the rectangle indicated in the top left figure, using native Nyström method (left), and the asymptotic Nyström method with sub-wavelength correction (right).

improved further using the outer expansion of K (i.e. $\mathbf{Y} \rightarrow \infty$) and using a subtraction method applied to the density μ [3]. Further details will be given in [2]. Extensions to 3D configurations will be considered, and we will apply these techniques for scattering problems in plasmonic structures.

References

- [1] A. H. Barnett, Evaluation of layer potentials close to the boundary for Laplace and Helmholtz problems on analytic planar domains, *SIAM J. Sci. Comput.* **36** (2014), pp. A427–A451.
- [2] C. Carvalho, S. Khatri, A. D. Kim, Local analysis for close evaluation of layer potentials, *in preparation*.
- [3] L. M. Delves, J. L. Mohamed, *Computational Methods for Integral Equations*, Cambridge University Press, 1985.
- [4] J. F. Geer, Rational trigonometric approximations using Fourier series partial sums, *Journal of Scientific Computing*, **10** (1995), pp. 325–356.
- [5] R. Kress, Boundary integral equations in time-harmonic acoustic scattering, *Math. Comput. Model.* **15** (1991), pp. 229–243.

Imaging polarizable dipoles

Maxence Cassier^{1,*}, Fernando Guevara Vasquez¹

¹Department of Mathematics, University of Utah, Salt Lake City, United States

*Email: cassier@math.utah.edu

Abstract

We consider the problem of imaging electric dipoles in a homogeneous medium from measurements of all three components of the electric field at an array of receivers. We show that an electromagnetic version of Kirchhoff migration can be used to recover the position and the orientation of the dipoles in the Fraunhofer asymptotic regime. We prove that the resolution estimates for the position are as in the acoustic case and provide error estimates for the dipole orientation. We extend these results to the case where the dipoles behave as passive sources, that is to say diffracting obstacles. In this setting, one wants to recover both the position and the polarizability tensor of each dipole in the medium.

Keywords: Electromagnetism, Imaging dipoles, Kirchhoff imaging, Fraunhofer asymptotic regime.

1 Introduction

Many chemical molecules (such as biomolecules like proteins) are polarized, in other words, they can be model as electric dipoles. Knowing both the position and the polarization of this dipole is very useful for chemists since it contains information about the geometry and the properties of the molecule. Toward this goal, we study the inverse problem consisting in reconstructing the positions and polarization vectors of a family of electrical radiating dipoles from their emitted electric field.

2 Formulation of the problem

We consider here a homogeneous dielectric medium filling the whole space \mathbb{R}^3 of permittivity ε and permeability μ . We assume that this medium contains N electric dipoles (or antennas) for which one wants to recover both the polarization vectors $\mathbf{p}_1, \dots, \mathbf{p}_N \in \mathbb{C}^3$ and the positions $\mathbf{y}_i \in \mathbb{R}^3$. These dipoles are assumed radiative, that is to say able to emit an electric field (at

the frequency ω) of the form:

$$\mathbf{E}(\mathbf{x}, k) = \sum_{j=1}^N \mu \omega^2 \mathbb{G}(\mathbf{x}, \mathbf{y}_j; k) \mathbf{p}_j$$

where $k = \omega/c = \omega/\sqrt{\varepsilon\mu}$ is the wave number and $\mathbb{G}(\mathbf{x}, \mathbf{y}_j; k)$ the dyadic Green tensor associated to the dielectric medium [2]. We assume that one can measure this electrical field on an array \mathcal{A} (supposed to be continuous, bounded and localized in the plane $z = 0$). Our goal is to use these measurements (up to the factor $\mu \omega^2$):

$$\boldsymbol{\Pi}(\mathbf{x}_r; k) = \sum_{j=1}^N \mathbb{G}(\mathbf{x}_r, \mathbf{y}_j; k) \mathbf{p}_j$$

collected on each point $\mathbf{x}_r \in \mathcal{A}$ to construct an imaging function from which one can extract the positions \mathbf{y}_i of the antennas, but also their orientations \mathbf{p}_i .

In acoustic imaging, in the Fraunhofer regime, the so-called Kirchhoff imaging functional has proved its efficiency. Thus, we chose to look at the properties of its electromagnetic analogous $\mathcal{I}(\mathbf{y}) : \mathbb{R}^3 \rightarrow \mathbb{C}^3$ defined by:

$$\mathcal{I}_k(\mathbf{y}) = \int_{\mathcal{A}} \overline{\mathbb{G}(\mathbf{x}_r, \mathbf{y}; k)} \boldsymbol{\Pi}(\mathbf{x}_r, k) d\tilde{\mathbf{x}}_r, \quad (1)$$

for $\mathbf{x}_r = (\tilde{\mathbf{x}}_r, 0) \in \mathcal{A}$.

3 Summary of results

We first establish the Fraunhofer asymptotics of the dyadic Green function to derive the asymptotics of the imaging function (1). Secondly, we used this asymptotic to study not only the resolution of our image to recover the position \mathbf{y}_i , but also to find a linear system whose solution would give a stable reconstruction of the polarization vector $\mathbf{p}_i \in \mathbb{C}^3$.

Suppose that one wants to recover the position $\mathbf{y}_i = (\tilde{\mathbf{y}}_i, z_i)$ and polarization $\mathbf{p}_i = (\tilde{\mathbf{p}}_i, p_{z,i})$ of the i -th dipole. Like in acoustics, we decompose this work in two steps: first, we study the resolution of $\mathcal{I}_k(\mathbf{y})$ in the cross-range, that is the plane $z = z_i$ and then we integrate the image $\mathcal{I}_k(\mathbf{y})$ over a frequency band ΔB to derive

its range resolution, that is its resolution on the axis transverse to the array which contains \mathbf{y}_i .

Step one: cross-range resolution

In the plane $z = z_i$, we establish, based on stationary phase arguments, that the infinity norm of the image: $\|\mathcal{I}_k(\mathbf{y})\|_\infty$ has, like in acoustic [1], a resolution of order $L/(ak)$. In other words, the ratio $\|\mathcal{I}_k(\mathbf{y})\|_\infty / \|\mathcal{I}_k(\mathbf{y}_i)\|_\infty$ becomes small when the distance $|\tilde{\mathbf{y}} - \tilde{\mathbf{y}}_i|$ between \mathbf{y}_i and a point \mathbf{y} of its cross-range is large with regards to $L/(ak)$. Then using this result, we prove that one obtains a good image of the two first components $\tilde{\mathbf{p}}_i$ of the polarization vector by solving the following linear system:

$$\left[\int_A \overline{\mathbb{G}(\mathbf{x}_r, \mathbf{y}; k)} \mathbb{G}(\mathbf{x}_r, \mathbf{y}; k) d\mathbf{x}_r \right] \mathbf{p} = \mathcal{I}_k(\mathbf{y}), \quad (2)$$

of unknown $\mathbf{p} = (\tilde{\mathbf{p}}, p_z) \in \mathbb{C}^3$ for points \mathbf{y} in the cross-range of \mathbf{y}_i . More precisely, the study of the condition number of (2) shows that it is ill-posed in the sense that one cannot recover in the Fraunhofer regime the component $p_{z,i}$ of \mathbf{p}_i . However, the 2×2 subsystem associated with the components $\tilde{\mathbf{p}} = (p_x, p_y)$ of \mathbf{p} has a condition number close to 1. Furthermore, we prove then that using the magnitude of the solution $\tilde{\mathbf{p}}$ of this subsystem leads to a stable image of the cross-range position $\tilde{\mathbf{y}}_i$ which has the same resolution $L/(ak)$ as the Kirchhoff imaging functional. Moreover, we provide error estimates on $|\tilde{\mathbf{p}} - \tilde{\mathbf{p}}_i|$ at $\mathbf{y} = \mathbf{y}_i$ which involves the distances between the dipoles and the Rayleigh number $L/(ak)$.

Step two: range resolution

We show, by integrating the imaging functional $\mathcal{I}_k(\mathbf{y})$ over a frequency band ΔB , that one gets a depth resolution $c/\Delta B$ (identical to the one in acoustic [1]) of the range position z_i as soon as the frequency band ΔB is sufficiently wide. In addition, the integration of the system (2) over this frequency band leads to a good image (up to a phase term) of \mathbf{p}_i in depth.

Finally, we confirm all these results by a numerical study. More numerical results will be presented in the talk. In figures 2, the position of the two dipoles are represented by a white cross, the polarization vectors that one wants to recover with white arrows, the reconstructed vectors with blue arrows, the color scale indicates the magnitude of $\tilde{\mathbf{p}}$ and λ_0 stands for the

central wavelength of ΔB . Note that we reconstruct the polarization vectors $\tilde{\mathbf{p}}_i$ up to a phase, which is fixed by imposing $\text{Im}(p_x) = 0$.

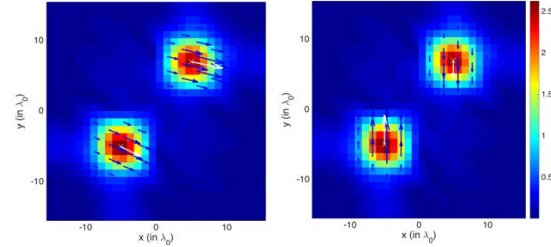


Figure 1: Image of $|\tilde{\mathbf{p}}|$, $\text{Re}(\tilde{\mathbf{p}})$ (left) and $\text{Im}(\tilde{\mathbf{p}})$ (right) in the cross-range plane $z = L$.

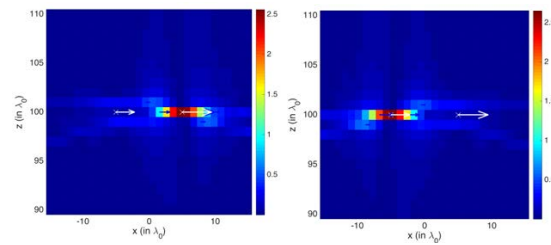


Figure 2: Image of $|\tilde{\mathbf{p}}|$, p_x in the range of the first dipole (left) and p_x in the range of the second dipole (right).

We have extended these results to the case where the dipoles are not radiating but behave as diffracting obstacles. In this setting, the diffraction of an electromagnetic wave by a dipole is governed by a 3×3 matrix: the polarizability tensor (see [2]). The objective is here to find both the position and the polarizability tensor of each dipole in the medium. We establish that one recovers their position with a cross-range resolution: $L/(ka)$ and a range resolution $c/\Delta B$. Furthermore, we show that one can reconstruct only the first 2×2 block of the polarizability tensor since the information about the other blocks is lost in the Fraunhofer regime.

References

- [1] L. Borcea, G. Papanicolaou and C. Tsogka, Adaptive interferometric imaging in clutter and optimal illumination, *Inverse Problems* **22** (4) (2006), p. 1405.
- [2] L. Novotny and B. Hecht, *Principles of nano-optics*, Cambridge university press (2012).

A well-conditioned weak coupling between interior and exterior domains for harmonic electromagnetic scattering

Boris Caudron^{1,*}, Xavier Antoine¹, Christophe Geuzaine²

¹Institut Elie Cartan de Lorraine, Université de Lorraine, UMR CNRS 7502, France

²University of Liège, Department of Electrical Engineering and Computer Science, Belgium

*Email: boris.caudron@univ-lorraine.fr

Abstract

A new weak coupling between the boundary element method and the finite element method for solving harmonic electromagnetic scattering problems is introduced. This method is inspired by domain decomposition techniques. Using suitable approximations of Magnetic-to-Electric operators to build proper transmission conditions allows for good convergence properties.

Keywords: time-harmonic electromagnetic scattering, BEM/FEM coupling, domain decomposition methods, microlocal operators

1 Introduction

The aim of this ongoing work is to numerically solve time-harmonic electromagnetic (EM) scattering problems for which the scatterer is dielectric and inhomogeneous. A standard approach consists in combining integral equations for the exterior domain and a weak formulation for the interior domain resulting in a formulation coupling the boundary element method (BEM) and the finite element method (FEM). A drawback of this strong coupling is that it is not possible to easily combine two pre-existing solvers, one FEM solver for interior domains and one BEM solver for exterior domains, to construct a global solver for the original problem. We present here a weak BEM/FEM coupling, based on a domain decomposition approach, allowing a simple construction of such a solver.

2 The EM scattering problem

We denote by Ω_- the scatterer, Ω_+ the exterior domain, Γ the surface of the scatterer and \mathbf{n} the outward-pointing unit normal vector to Ω_- . The scattered field and the one within the scatterer satisfy in Ω_\pm :

$$\operatorname{rot} \mathbf{E}_\pm - ik_\pm Z_\pm \mathbf{H}_\pm = \mathbf{0}, \quad (1)$$

$$\operatorname{rot} \mathbf{H}_\pm + ik_\pm Z_\pm^{-1} \mathbf{E}_\pm = \mathbf{0}, \quad (2)$$

where k_\pm and Z_\pm are respectively the wave numbers and the impedances of the problem. Note

that the scattered field, as any exterior field, should also satisfy the Silver-Müller radiation condition. Finally, the interface conditions on Γ are:

$$\mathbf{E}_- \wedge \mathbf{n} = \mathbf{E}_+ \wedge \mathbf{n} + \mathbf{E}_i \wedge \mathbf{n}, \quad (3)$$

$$\mathbf{H}_- \wedge \mathbf{n} = \mathbf{H}_+ \wedge \mathbf{n} + \mathbf{H}_i \wedge \mathbf{n}, \quad (4)$$

where $(\mathbf{E}_i; \mathbf{H}_i)$ is an incident plane wave.

3 Reformulating the problem

Introducing two operators \mathbf{T}_\pm , referred to as the transmission operators, problem (1)-(4) can be equivalently recast as:

$$(\mathbf{Id} - \mathbf{S}_\pi) \begin{pmatrix} \mathbf{g}_- \\ \mathbf{g}_+ \end{pmatrix} = \mathbf{B}, \quad (5)$$

where the right-hand side \mathbf{B} is defined through $(\mathbf{E}_i; \mathbf{H}_i)$ and \mathbf{T}_\pm , and:

$$\mathbf{S}_\pi = \begin{pmatrix} 0 & \mathbf{S}_+ \\ \mathbf{S}_- & 0 \end{pmatrix},$$

$$\mathbf{S}_\pm = \mathbf{Id} \pm (\mathbf{T}_+ + \mathbf{T}_-) \mathbf{R}_\pm,$$

The functions \mathbf{g}_\pm should be understood in terms of traces on Γ :

$$\mathbf{g}_\pm = (\mathbf{H}_\pm \wedge \mathbf{n}) \mp \mathbf{T}_\pm (\mathbf{E}_\pm \wedge \mathbf{n}).$$

Finally, \mathbf{R}_\pm are resolution operators defined as:

$$\mathbf{R}_\pm \mathbf{g} = \tilde{\mathbf{E}}_\pm \wedge \mathbf{n},$$

where $(\tilde{\mathbf{E}}_\pm; \tilde{\mathbf{H}}_\pm)$ are the solutions of the following boundary-value problems:

$$\operatorname{rot} \tilde{\mathbf{E}}_\pm - ik_\pm Z_\pm \tilde{\mathbf{H}}_\pm = \mathbf{0} \text{ in } \Omega_\pm,$$

$$\operatorname{rot} \tilde{\mathbf{H}}_\pm + ik_\pm Z_\pm^{-1} \tilde{\mathbf{E}}_\pm = \mathbf{0} \text{ in } \Omega_\pm,$$

$$(\tilde{\mathbf{H}}_\pm \wedge \mathbf{n}) \mp \mathbf{T}_\pm (\tilde{\mathbf{E}}_\pm \wedge \mathbf{n}) = \mathbf{g} \text{ on } \Gamma.$$

The resolution operators \mathbf{R}_\pm should be understood as the pre-existing FEM solver for the interior domain and BEM solver for the exterior domain, as mentioned in the introduction.

4 Solving the reformulation

To solve (5), the GMRES method is employed. As a result, the solvers for the interior and exterior domains are repeatedly and independently called. For this reason, the weak coupling can be interpreted in a domain decomposition method (DDM) framework. Moreover, solving (5) using a fixed point method is equivalent to a standard Jacobi-type DDM method:

$$\begin{aligned}\operatorname{rot} \mathbf{E}_{\pm}^{n+1} - ik_{\pm} Z_{\pm} \mathbf{H}_{\pm}^{n+1} &= \mathbf{0} \text{ in } \Omega_{\pm}, \\ \operatorname{rot} \mathbf{H}_{\pm}^{n+1} + ik_{\pm} Z_{\pm}^{-1} \mathbf{E}_{\pm}^{n+1} &= \mathbf{0} \text{ in } \Omega_{\pm},\end{aligned}$$

the interface conditions on Γ being:

$$\begin{aligned}(\mathbf{H}_{\pm}^{n+1} \wedge \mathbf{n}) \mp \mathbf{T}_{\pm}(\mathbf{E}_{\pm}^{n+1} \wedge \mathbf{n}) &= (\mathbf{H}_{\mp}^n \wedge \mathbf{n}) \\ \mp \mathbf{T}_{\pm}(\mathbf{E}_{\mp}^n \wedge \mathbf{n}) \mp \mathbf{H}_i \wedge \mathbf{n} + \mathbf{T}_{\pm} \mathbf{E}_i \wedge \mathbf{n}. &\end{aligned}$$

5 Choosing the transmission operators

The choices for \mathbf{T}_{\pm} impact the convergence of the GMRES method. Choosing proper Magnetic-to-Electric (MtE) operators as transmission operators ensures that \mathbf{S}_{π} vanishes rendering (5) trivial to solve. It is therefore natural to use approximations of MtE operators as transmission operators. Accurate approximations typically involve the principal part of the MtE operators:

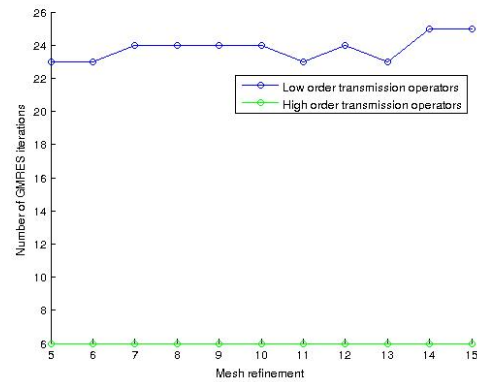
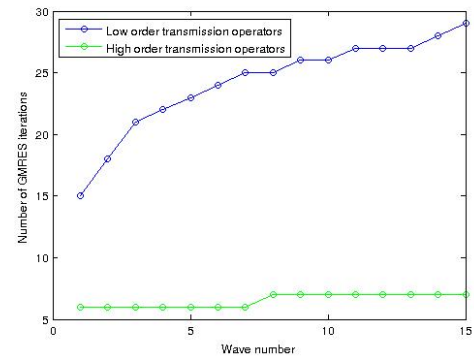
$$\frac{1}{Z_{\pm}} \left(\mathbf{Id} + \frac{\Delta_{\Gamma}}{\tilde{k}_{\pm}^2} \right)^{-\frac{1}{2}} \left(\mathbf{Id} - \frac{1}{\tilde{k}_{\pm}^2} \operatorname{rot}_{\Gamma} \operatorname{rot}_{\Gamma} \right) (\cdot \wedge \mathbf{n}),$$

where $\tilde{k}_{\pm} = k_{\pm} + i\epsilon_{\pm}$, $\epsilon_{\pm} > 0$. Although nonlocal, the above operators can be localized using complex Padé approximants. Such transmission operators have already been successfully used for DDM, resulting in fast GMRES with a convergence only slightly dependent on the mesh refinement and wave number [1]. For the weak coupling, some numerical/analytical tests have been conducted in the case of the sphere, for which the eigenvalues of all the involved operators are known analytically, suggest that it should also be the case for the GMRES convergence of (5).

6 Numerical results

To test formulation (5), we consider a toy problem: a unit transparent sphere (meaning that $k_- = k_+$ and $Z_- = Z_+$) solved by coupling two BEM solutions, i.e. a BEM/BEM DDM. The GMRES-convergence is promising as shown below (the GMRES tolerance is fixed to 10^{-4}).

In this case, high order transmission operators refer to principal parts of MtE operators with Padé approximation whereas low order transmission operators refer to a simple impedance operator (zeroth order Taylor expansion): $\frac{1}{Z_{\pm}}(\cdot \wedge \mathbf{n})$. The mesh parameters h are defined as fractions of the wave length λ : $h = \frac{\lambda}{l} = \frac{2\pi}{kl}$. For the first figure, $l = 5$. For the second one, the wave number is equal to 5. In addition, we will explain how to construct well-conditioned and efficient iterative BEM solvers for the interior and exterior problems.



Acknowledgment

This work was supported by Thales Systèmes Aéroportés SAS.

References

- [1] M. El Bouajaji, B. Thierry, X. Antoine, C. Geuzaine, A Quasi-Optimal Domain Decomposition Algorithm for the Time-Harmonic Maxwell's Equations, *Journal of Computational Physics* **294** (1) (2015), pp. 38–57.

Nonlinear hysteretic propagation of torsional waves in a granular chain

**Alejandro Cebrecos^{1,*}, Philippe Béquin¹, Georgios Theocharis¹, Vitalyi Gusev¹,
Vincent Tournat^{1,*}**

¹LAUM UMR-CNRS 6613, Université du Maine, Av. O. Messiaen, 72085 Le Mans, France

*Email: vincent.tournat@univ-lemans.fr, alejandro.cebreco@univ-lemans.fr

Abstract

The propagation of torsional waves in a 1D granular chain made of self-hanged magnetic beads is considered in this work. Due to the torsional coupling between beads, the propagation medium is purely nonlinear hysteretic, providing the opportunity to study the phenomenon of nonlinear dynamic hysteresis in the absence of other types of material nonlinearities. Specifically, we consider the propagation of large amplitude signals, reaching a strongly nonlinear regime, beyond the limits of the quadratic hysteretic approximation. In this regime, total torsional sliding at the contacts may be observed and strong saturation effects are expected. These results could be of fundamental interest but may also find potential applications in nonlinear wave control devices.

Keywords: Nonlinear torsional waves, hysteresis, torsional sliding, granular phononic crystals.

Nonlinear hysteresis in micro-inhomogeneous materials, i.e. complex or mesoscopic solids, is inherently different from the classical nonlinearity which originates from the expansion of smooth nonlinear stress-strain relationship and geometric nonlinearity. Non-classical nonlinearity is known to be responsible for phenomena like nonlinear softening [1], nonlinear attenuation [2], memory [3] and slow dynamics [4, 5]. The shear coupling between two elastic spheres was one of the first observation of mechanical hysteresis [6]. The first analytical approaches to define the hysteretic behavior in a system formed by two elastic spheres in contact rotating relative to each other were provided by Lubkin [7] and Deresieczwicz [8]. A chain of magnetic beads, where pure rotational waves can propagate due to the torsional coupling at bead contacts, is a physical system of fundamental interest as it constitutes a purely nonlinear hysteretic system, without the presence of other types of nonlinearity. This feature al-

lows the observation of phenomena that have been previously predicted such as pulse distortion [9,10] or frequency mixing [11]. While some of these phenomena have been already observed experimentally [12], the experimental observation of several predicted effects, such as frequency mixing or total torsional sliding, remains a challenge to be achieved. In Ref. [12], the first results on the purely nonlinear hysteretic propagation of rotational waves in a one-dimensional granular chain were presented. The basis of the theory describing the nonlinear pulse distortion by quadratic hysteretic torsional coupling at the contact was established. This description is in agreement with the experimental results obtained in a granular magnetic chain configuration and provided a quantitative estimate of the hysteretic nonlinear parameter. This model configuration is fairly well characterized and allows for the study of a wide variety of nonlinear effects in a purely hysteretic medium. In this work we focus on the study of hysteretic nonlinearity for relatively larger amplitudes than previously, reaching a strongly nonlinear regime, beyond the limits of the quadratic hysteretic approximation. This large relative rotation between beads leads to total torsional sliding at the contacts, and strong saturation effects are observed.

At first, we consider a system composed of only two spherical beads where the contact force between them is of a magnetic nature. Considering a torsional harmonic excitation of increasing amplitude, the relation between the relative angle between beads and torque transmitted to the second bead is measured, as shown in Fig. 1(a). Setting a certain value for the hysteretic parameter, close to the one estimated in Ref. [12], the experimentally measured torque-angle relationship can be well fitted by the theoretical prediction from Ref. [7]. A similar behavior is then observed between the first two beads of a 70 bead-long chain using a sinusoidal pulsed signal as the excitation. As a result of

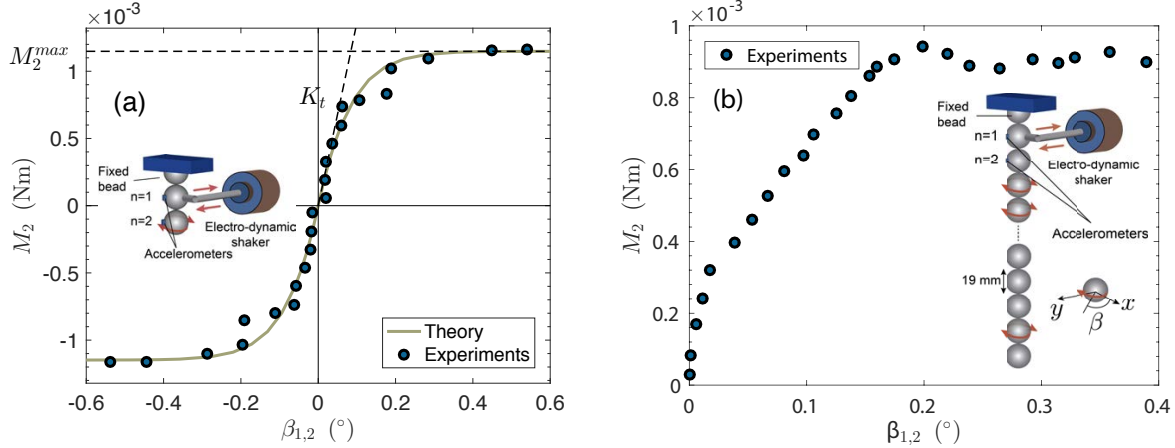


Figure 1: Total torsional sliding experimental results for (a) two bead system, (b) granular chain composed of 70 beads.

the sliding between the first two beads of the system, the amplitude of the rotation along the chain is strongly saturated despite a continuously increasing driving amplitude. These results could be of fundamental interest but also could help in the future design of wave devices based on nonlinear elastic metamaterials.

References

- [1] R. A. Guyer and P. A. Johnson, *Nonlinear mesoscopic elasticity*. Wiley-VCH, 2009.
- [2] V. E. Nazarov, L. A. Ostrovsky, I. A. Soutova, and A. M. Sutin, “Nonlinear acoustics of micro-inhomogeneous media,” *Phys. Earth Planet. Inter.*, vol. 50, no. 1, pp. 65–73, 1988.
- [3] K. McCall and R. Guyer, “Equation of state and wave propagation in hysteretic nonlinear elastic materials,” *J. Geophys. Res.*, vol. 99, no. B12, pp. 23887–23897, 1994.
- [4] J. A. Ten Cate and T. J. Shankland, “Slow dynamics in the nonlinear elastic response,” *Geophys. Res. Lett.*, vol. 23, no. 21, pp. 3019–3022, 1996.
- [5] P. Johnson and A. Sutin, “Slow dynamics and anomalous nonlinear fast dynamics in diverse solids,” *J. Acoust. Soc. Am.*, vol. 117, no. 1, pp. 124–130, 2005.
- [6] K. L. Johnson and K. L. Johnson, *Contact Mechanics*. Cambridge Univ. Press, 1987.
- [7] J. L. Lubkin, “The torsion of elastic spheres in contact,” *J. Appl. Mech. Trans. ASME*, vol. 73, pp. 183–187, 1951.
- [8] H. Deresiewicz, “Contact of elastic spheres under an oscillating torsional couple,” *ASME J. Appl. Mech.*, vol. 21, pp. 52–56, 1954.
- [9] V. Gusev, “Propagation of acoustic pulses in material with hysteretic nonlinearity,” *J. Acoust. Soc. Am.*, vol. 107, no. 6, pp. 3047–3058, 2000.
- [10] V. Gusev, “Propagation of acoustic pulses in a medium with hysteretic nonlinearity prepared by preloading,” *Acta Acust. United. Ac.*, vol. 89, no. 3, pp. 445–450, 2003.
- [11] V. Aleshin, V. Gusev, and V. Yu. Zaitsev, “Propagation of acoustics waves of non-simplex form in a material with hysteretic quadratic nonlinearity: Analysis and numerical simulations,” *J. Comput. Acoust.*, vol. 12, no. 03, pp. 319–354, 2004.
- [12] J. Cabaret, P. Béquin, G. Theocharis, V. Andreev, V. Gusev, and V. Tournat, “Nonlinear hysteretic torsional waves,” *Phys. Rev. Lett.*, vol. 115, no. 5, p. 054301, 2015.

Weight-adjusted discontinuous Galerkin methods for wave propagation in arbitrary heterogeneous media

Jesse Chan^{1,*}, Russell J. Hewett², T. Warburton³

¹Department of Computational and Applied Mathematics, Rice University, Houston, TX

²TOTAL E&P Research and Technology USA, Houston, TX

³Department of Mathematics, Virginia Tech, Blacksburg, VA

*Email: jesse.chan@caam.rice.edu

Abstract

Efficient implementations of high order discontinuous Galerkin (DG) methods on hexahedral meshes can incorporate both local variations in heterogeneous media using mass lumping techniques. However, because the extension of such techniques to simplicial elements is less straightforward, high order DG methods on triangular and tetrahedral meshes typically assume piecewise constant models of heterogeneous media.

We present an alternative to mass-lumping techniques using weight-adjusted approximations to weighted L^2 inner products, resulting in an energy stable, high order accurate, and low-storage method for acoustic and elastic wave propagation in arbitrary heterogeneous media and curvilinear meshes.

Keywords: discontinuous Galerkin, tetrahedral meshes, heterogeneous media, mass lumping

1 Introduction

The inversion of weighted mass matrices in discontinuous Galerkin methods is required in the presence of curvilinear meshes and heterogeneous media with local variations. However, at high orders of approximation, the pre-computation of factorizations significantly increases storage costs, while the on-the-fly construction and inversion of such matrices is expensive and difficult to adapt to the fine grain parallelism of modern many-core architectures.

These costs can be avoided through the use of mass lumping techniques on hexahedral meshes; however, extensions of mass-lumping techniques to tetrahedral meshes are non-trivial to construct for high orders of approximation. As a result, most efficient implementations of DG on tetrahedral meshes assume piecewise constant approximations of media and non-curved meshes.

2 Weight-adjusted mass matrices

To avoid increasing storage costs associated with weighted mass matrices on tetrahedral meshes, we approximate weighted L^2 inner products with a weight-adjusted inner product. Let $0 < w_{\min} \leq w(\mathbf{x}) \leq w_{\max} < \infty$ be a positive weight which varies over an element \widehat{D} , and define T_w^{-1} through

$$\int_{\widehat{D}} w T_w^{-1} u v = \int_{\widehat{D}} u v, \quad u, v \in P^N(\widehat{D}).$$

By noting that $T_w^{-1} u$ approximates u/w , we can approximate a weighted L^2 inner product as follows

$$\int_{\widehat{D}} w u v \approx \int_{\widehat{D}} T_{1/w}^{-1} u v.$$

This approximation generates an L^2 equivalent norm on $P^N(\widehat{D})$

$$w_{\min} \|u\|_{L^2(\widehat{D})}^2 \leq \int_{\widehat{D}} (T_{1/w}^{-1} u) u \leq w_{\max} \|u\|_{L^2(\widehat{D})}^2$$

with equivalence constants identical to those of the weighted L^2 norm [3]. Additionally, this approximation is high order accurate as follows:

Theorem 1 (Theorem 5 in [3]) *Let D^k be quasi-regular with representative size $h = \text{diam}(D^k)$. For $N \geq 0$ and sufficiently regular u, w*

$$\begin{aligned} \|u w - T_{1/w}^{-1} u\|_{L^2(D^k)} &\leq C_w h^{N+1} \|u\|_{W^{N+1,2}(D^k)} \\ C_w &= C \|w\|_{L^\infty(D^k)} \left\| \frac{1}{w} \right\|_{L^\infty(D^k)} \|w\|_{W^{N+1,\infty}(D^k)}. \end{aligned}$$

The use of a weight-adjusted inner product results also approximates the weighted mass matrix \mathbf{M}_w by a weight-adjusted mass matrix

$$\begin{aligned} \mathbf{M}_w &\approx \mathbf{M} \mathbf{M}_{1/w}^{-1} \mathbf{M} \\ \mathbf{M}_w^{-1} &\approx \mathbf{M}^{-1} \mathbf{M}_{1/w} \mathbf{M}^{-1}. \end{aligned}$$

Since $\mathbf{M}_{1/w}$ can be applied in a matrix-free fashion (using, for example, quadrature) using only matrix-vector multiplications, weighted mass matrix inverses can be approximated in a low-storage fashion suitable for fine-grain parallelism.

3 Weight-adjusted DG methods

For appropriate boundary conditions, the acoustic wave equation with spatially varying wavespeed $c^2(\mathbf{x})$

$$\frac{1}{c^2(\mathbf{x})} \frac{\partial p}{\partial t} = \nabla \cdot \mathbf{u}, \quad \frac{\partial \mathbf{u}}{\partial t} = \nabla p$$

is energy stable such that

$$\frac{\partial}{\partial t} \sum_k \left(\int_{D^k} \frac{1}{c^2(\mathbf{x})} p^2 + \int_{D^k} |\mathbf{u}|^2 \right) = 0.$$

Weight-adjusted DG (WADG) methods reproduce this stability at the discrete level. For example, the formulation

$$\begin{aligned} & \sum_k \int_{D^k} T_{c^2}^{-1} p v + \mathbf{u} \mathbf{q} + \int_{D^k} \nabla \cdot \mathbf{u} v + \nabla p \mathbf{q} \\ & + \sum_k \int_{D^k} \frac{1}{2} \int_{\partial D^k} (\tau_p [\![p]\!] - [\![\mathbf{u}]\!] \cdot \mathbf{n}) v \\ & + \sum_k \int_{D^k} \frac{1}{2} \int_{\partial D^k} (\tau_u [\![\mathbf{u}]\!] \cdot \mathbf{n} - [\![p]\!]) \mathbf{q} \cdot \mathbf{n} = 0 \end{aligned}$$

results in a discrete energy stability

$$\begin{aligned} & \frac{\partial}{\partial t} \sum_k \left(\int_{D^k} (T_{c^2}^{-1} p) p + \int_{D^k} |\mathbf{u}|^2 \right) \\ & \leq - \sum_k \int_{\partial D^k} \tau_p [\![p]\!]^2 + \tau_u [\![\mathbf{u}]\!]^2 \leq 0. \end{aligned}$$

WADG methods also preserve high order accuracy, admitting *a-priori* estimates which depend on the regularity of $c^2(\mathbf{x})$. Figure 1 shows a comparison of solutions obtained for heterogeneous media with both smooth local variations and a discontinuity. The DG solution inverts a weighted mass matrix over each element, while the WADG solution uses a weight-adjusted approximation to this inverse. The solutions are visually identical.

Finally, we will discuss the extension of weight-adjusted DG methods both curvilinear meshes [4] and matrix-valued weights, which appear in linear elastic wave propagation in heterogeneous media [5].

References

- [1] E.D. Mercerat, and N. Glinsky. “A nodal high-order discontinuous Galerkin method for elastic wave propagation in arbitrary heterogeneous media.” Geophysical Journal International 201.2 (2015): 1101-1118.

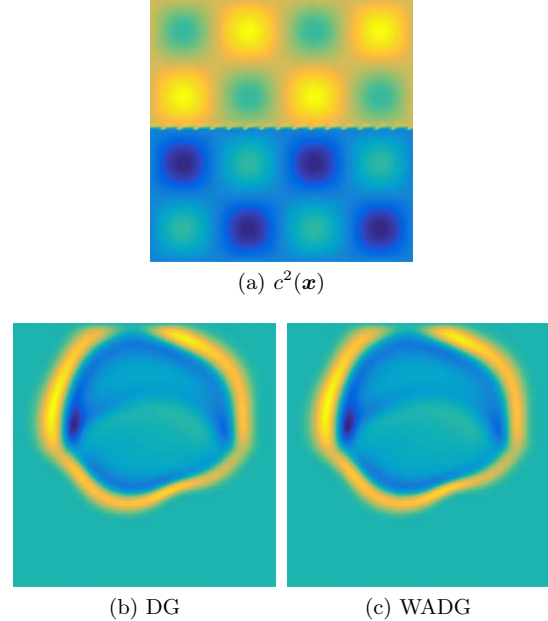


Figure 1: Acoustic wave propagation using DG with weighted mass matrices and the weight-adjusted approximation of WADG.

- [2] A. Klöckner, T. Warburton, J. Bridge, and J. Hesthaven. “Nodal discontinuous Galerkin methods on graphics processors.” Journal of Computational Physics 228.21 (2009): 7863-7882.
- [3] J. Chan, R. J. Hewett, and T. Warburton. “Weight-adjusted discontinuous Galerkin methods: wave propagation in heterogeneous media.” arXiv preprint arXiv:1608.01944 (2016).
- [4] J. Chan, R. J. Hewett, and T. Warburton. “Weight-adjusted discontinuous Galerkin methods: curvilinear meshes.” arXiv preprint arXiv:1608.03836 (2016).
- [5] J. Chan. “Weight-adjusted discontinuous Galerkin methods: matrix-valued weights and elastic wave propagation in heterogeneous media.” arXiv preprint arXiv:1701.00215 (2017).

BVP and BIE Formulations for Scattering by Fractal Screens

Simon N. Chandler-Wilde^{1,*}, David P. Hewett²

¹Department of Mathematics and Statistics, University of Reading, Reading, UK

²Department of Mathematics, University College London, London, UK

*Email: s.n.chandler-wilde@reading.ac.uk

Abstract

There are various formulations as BVPs or BIEs (boundary integral equations) for screen scattering problems in acoustics, all equivalent when the screen occupies a bounded open Lipschitz subset of the plane. Motivated by applications in electromagnetics and ultrasonics we explore what happens when the screen is less regular, in particular fractal or with fractal boundary. The standard formulations divide into an infinite family of well-posed BVP and equivalent BIE formulations, with infinitely many distinct solutions. We use “limiting geometry” arguments to select physically appropriate solutions, and illustrate numerically the surprising new effects that arise.

Keywords: Fractal, Helmholtz Equation, scattering

1 Introduction

We consider time-harmonic acoustic scattering problems modelled by the Helmholtz equation

$$\Delta u + k^2 u = 0, \quad (1)$$

where $k > 0$. Our focus is on scattering by thin planar screens in \mathbb{R}^n ($n = 2$ or 3), so that the domain in which (1) holds is $D := \mathbb{R}^n \setminus \bar{\Gamma}$, where Γ , the *screen*, is a bounded subset of the hyperplane $\Gamma_\infty := \{\mathbf{x} = (x_1, \dots, x_n) \in \mathbb{R}^n : x_n = 0\}$, and the compact set $\bar{\Gamma}$ is its closure. As usual, the complex-valued function u can be interpreted physically as the (total) acoustic pressure field, and we write u as $u = u^i + u^s$, where u^i is the incident field chosen to be the plane wave

$$u^i(\mathbf{x}) = \exp(i k \mathbf{d} \cdot \mathbf{x})$$

where \mathbf{d} is a unit vector, the direction of incidence. The *scattered field* $u^s := u - u^i$ is assumed to satisfy (1) and the standard Sommerfeld radiation condition. For brevity we restrict attention to *sound-hard* boundary conditions, assuming that

$$\frac{\partial u}{\partial \mathbf{n}} = 0 \quad (2)$$

on the screen in some appropriate sense, where \mathbf{n} is the unit normal pointing in the x_n direction. (For generalisations to other incident fields and a treatment of sound soft scattering see [4].)

This is a long-standing scattering problem, its mathematical study dating back at least to [10], and it is well-known [4, 14] that, for arbitrary bounded $\Gamma \subset \Gamma_\infty$, this problem is well-posed (and the solution depends only on the closure $\bar{\Gamma}$) if the boundary condition is understood in the standard weak sense that $u \in W_2^{1,\text{loc}}(D)$ and

$$\int_D (v \Delta u + \nabla v \cdot \nabla u) \, dx = 0, \quad v \in W_2^{1,\text{comp}}(D). \quad (3)$$

In the standard case that Γ is a (relatively) open subset of Γ_∞ that is Lipschitz or smoother, the alternative, *classical formulation*, dating to the late 40s [1], imposes the boundary conditions (2) in a classical sense, and additionally imposes “edge conditions” requiring locally finite energy, that u and ∇u are square integrable in some neighbourhood of $\partial\Gamma$. Equivalently, one can formulate a BVP for u^s in a Sobolev space setting, seeking $u^s \in W_2^{1,\text{loc}}(D)$ satisfying (1) and the radiation condition, and imposing the boundary condition (2) in a trace sense, requiring that the Neumann traces on Γ_∞ , $\partial_{\mathbf{n}}^\pm u^s$, satisfy $(\partial_{\mathbf{n}}^\pm u^s)|_\Gamma = g \in H^{-1/2}(\Gamma)$, where $g := -(\partial_{\mathbf{n}}^\pm u^i)|_\Gamma$ (see, e.g., [11]). Finally, it is well-known (e.g. [11]) that for Lipschitz Γ one can reformulate this BVP as the BIE

$$T[u] = g. \quad (4)$$

In this equation the unknown is the jump across the screen in u , $[u] \in \tilde{H}^{1/2}(\Gamma)$, and the isomorphism $T : \tilde{H}^{1/2}(\Gamma) \rightarrow H^{-1/2}(\Gamma)$ is a hypersingular boundary integral operator (BIO). Here $\tilde{H}^s(\Gamma) \subset H^s(\Gamma_\infty)$, for $s \in \mathbb{R}$, denotes the closure in $H^s(\Gamma_\infty)$ of $C_0^\infty(\Gamma)$. As pointed out in [3], (4) is well-posed for arbitrary open Γ . The total field u is given in terms of $[u]$ by

$$u(\mathbf{x}) = u^i(\mathbf{x}) + \mathcal{D}[u](\mathbf{x}), \quad \mathbf{x} \in D, \quad (5)$$

where $\mathcal{D} : H_{\bar{\Gamma}}^{1/2} \rightarrow C^2(D) \cap W_2^{1,\text{loc}}(D)$ is the standard double-layer potential operator, and $H_{\bar{\Gamma}}^{1/2} \subset H^{1/2}(\Gamma_\infty)$ is the closed subspace of those $\phi \in H^{1/2}(\Gamma_\infty)$ that are supported in $\bar{\Gamma}$. We note that $\tilde{H}^{1/2}(\Gamma) \subset H_{\bar{\Gamma}}^{1/2}$, that these spaces coincide if Γ is sufficiently regular, in particular if Γ is a C^0 open set, but that in general these spaces are distinct.

In this paper we explore what happens when the screen Γ is irregular, in particular fractal or with fractal boundary, this motivated by the use of planar screens with precisely these structures as antennae in electromagnetics and ultrasonics (e.g., [8, 9, 12]). We will see in §2 that the standard classical/Sobolev spaces formulations can be ill-posed, or if well-posed have solution different to the standard weak formulation. In §3 we will see that there exists, when the screen is sufficiently irregular, a whole family of well-posed BVP and BIE formulations with infinitely many distinct solutions. In §4 we discuss the selection of a correct solution by taking limits with respect to the geometry. In the last two sections we explore theoretically, illustrated by numerical computations, wave penetration through a zero-surface-area fractal “hole” in a sound hard screen.

We use throughout the notation S° to denote the (relative) interior of $S \subset \Gamma_\infty$. For Borel $S \subset \Gamma_\infty$ we will denote by $m(S)$ the $(n-1)$ -dimensional (surface) Lebesgue measure of S , and by $\text{cap}(S)$ the n -dimensional capacity of S defined as in [4]. For $s \in \mathbb{R}$ we will say that S is s -null if the only $\phi \in H^s(\Gamma_\infty)$ with $\text{supp}(\phi) \subset S$ is $\phi = 0$. Importantly, it holds that S is $-1/2$ -null if and only if $\text{cap}(S) = 0$, and that $\text{cap}(S) > 0$ if $\dim_H(S) > n-2$, while $\text{cap}(S) = 0$ if $\dim_H(S) < n-2$, where $\dim_H(S)$ denotes the Hausdorff dimension of S . For proofs of these statements and other characterisations of s -nullity see [7].

2 Equivalence and well-posedness (or not) of standard formulations

As we have observed above, the weak formulation of the scattering problem, with the boundary condition imposed in the sense (2), is well-posed for every bounded $\Gamma \subset \Gamma_\infty$. The (equivalent) classical and Sobolev space formulations above equation (4), however, are only well-posed for sufficiently regular Γ . Precisely:

Theorem 1 [4] *The classical and Sobolev space problems formulations are well-posed if and only if $\tilde{H}^{1/2}(\Gamma^\circ) = H_{\bar{\Gamma}}^{1/2}$ and $\partial\Gamma$ is $-1/2$ -null. In particular, these formulations are well-posed if Γ is a Lipschitz open set, or if Γ is C^0 except at a countable set of points that has only finitely many limit points, provided also $\partial\Gamma \subset \cup_{j=1}^\infty \partial\Omega_j$, with each $\Omega_j \subset \Gamma_\infty$ a Lipschitz open set. But these formulations are not well-posed if $\text{cap}(\partial\Gamma) > 0$, in particular if $\dim_H(\partial\Gamma) > n-2$. If these formulations are well-posed then they are equivalent to the weak formulation.*

Figure 1 illustrates this theorem for $n = 3$ with a (non-Lipschitz, indeed non- C^0) example of a screen for which the classical/Sobolev space formulations are well-posed, and an example (the Koch snowflake) where these formulations are not well-posed (because $\dim_H(\partial\Gamma) = \log 4 / \log 3 > 1$).

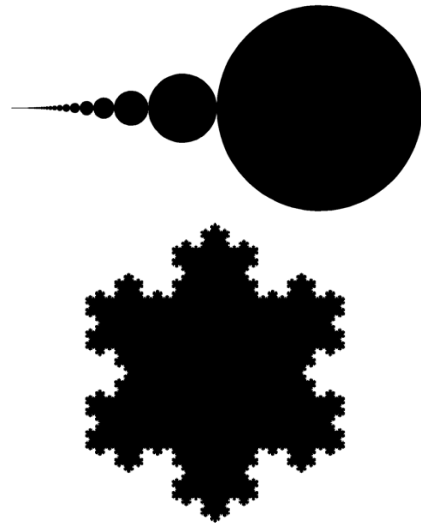


Figure 1: Example sound hard screens for which the classical/Sobolev space formulations are well-posed (top) and not well-posed (bottom).

The solution to the weak formulation always satisfies the classical and Sobolev space formulations, so that when well-posedness of these latter formulations fails it is because the standard edge conditions are insufficient to ensure uniqueness if the screen is sufficiently irregular. But these formulations become well-posed if the standard edge conditions are supplemented by the conditions in the following theorem.

Theorem 2 [4] *The classical and Sobolev space problems formulations, supplemented by the additional requirements that: a) $[u] \in \tilde{H}^{1/2}(\Gamma)$; b) $[\partial_{\mathbf{n}} u] = 0$; are well-posed for every bounded open $\Gamma \subset \Gamma_\infty$.*

If $\tilde{H}^{1/2}(\Gamma) \not\subseteq H_{\bar{\Gamma}}^{1/2}$, which holds in particular if $\dim_H(\bar{\Gamma}^\circ \setminus \Gamma^\circ) > n - 2$ [2, 4], then the equivalent classical/Sobolev space formulations supplemented by the additional constraints a) and b) are well-posed, but [4] their unique solution is different from the solution to the weak formulation, for almost all incident wave directions \mathbf{d} . Indeed, we will see in the next section that when $\tilde{H}^{1/2}(\Gamma) \not\subseteq H_{\bar{\Gamma}}^{1/2}$ there exists an infinite family of well-posed BVPs, intermediate between the weak and classical formulations.

3 An infinite family of BVP and BIE formulations

Recall that $H^{-1/2}(\Gamma_\infty)$ is (a unitary realisation of) the dual space of $H^{1/2}(\Gamma_\infty)$ through the duality pairing $\langle \cdot, \cdot \rangle$ on $H^{-1/2}(\Gamma_\infty) \times H^{1/2}(\Gamma_\infty)$ that extends the $L^2(\Gamma_\infty)$ inner product. Let V be a closed subspace of $H^{1/2}(\Gamma_\infty)$, in particular we will be interested in subspaces satisfying

$$\tilde{H}^{1/2}(\Gamma^\circ) \subset V \subset H_{\bar{\Gamma}}^{1/2}. \quad (6)$$

Let $V^a := \{\phi \in H^{-1/2}(\Gamma_\infty) : \langle \phi, \psi \rangle = 0 \text{ for all } \psi \in V\}$ be the annihilator of V , and let $V^* := (V^a)^\perp \subset H^{-1/2}(\Gamma_\infty)$, so that V^* is the natural unitary realisation of the dual space of V through the duality pairing that is the restriction of $\langle \cdot, \cdot \rangle$ to $V^* \times V$ [2]. Let $P : H^{-1/2}(\Gamma_\infty) \rightarrow V^*$ be orthogonal projection. Explicitly, $V^* = (\tilde{H}^{-1/2}((\bar{\Gamma})^c))^\perp$ if $V = H_{\bar{\Gamma}}^{1/2}$, where c denotes complement in Γ_∞ . Similarly, $V^* = (H_{(\Gamma^\circ)^c}^{-1/2})^\perp$ if $V = \tilde{H}^{1/2}(\Gamma^\circ)$.

We can associate to each $V \subset H_{\bar{\Gamma}}^{1/2}$ a formulation $SN(V)$ of the scattering problem, this a physically sensible mathematical model if V is constrained by (6), and interesting as a numerical approximation when V is finite-dimensional. In this formulation \mathcal{D}_1 denotes the set of those $\chi \in C_0^\infty(\Gamma_\infty)$ that are = 1 in some neighbourhood of $\bar{\Gamma}$

Scattering Problem SN(V): *Find $u \in C^2(D) \cap W_2^{1,\text{loc}}(D)$ such that: i) (1) holds in D ; ii) $u^s := u - u^i$ satisfies the Sommerfeld radiation condition; iii) $[u] \in V$; iv) $[\partial_{\mathbf{n}} u] = 0$; v) the*

boundary condition (2) holds on Γ in the sense that $P(\chi \partial_{\mathbf{n}}^\pm u) = 0$, for every $\chi \in \mathcal{D}_1$.

The choice of V in $SN(V)$ plays two roles: the larger V is the larger the space in which we constrain $[u]$ to lie, and simultaneously the stronger the sense in which we impose the boundary condition (2). In particular [4]: a) if $V = H_{\bar{\Gamma}}^{1/2}$ then $SN(V)$ is equivalent to the weak formulation with the boundary condition understood in the sense (3); and b), for every V satisfying (6) the boundary condition in the sense v) implies that $(\partial_{\mathbf{n}}^\pm u)|_{\Gamma^\circ} = 0$, indeed is equivalent to this condition if $V = \tilde{H}^{1/2}(\Gamma^\circ)$.

Theorem 3 [4] *$SN(V)$ has exactly one solution, and this solution is a solution to the classical/Sobolev space formulation above (4) if V satisfies (6), indeed $SN(V)$ is equivalent to the classical/Sobolev space formulation augmented by the conditions iii) and iv) if $V = \tilde{H}^{1/2}(\Gamma^\circ)$. If $V = H_{\bar{\Gamma}}^{1/2}$ then the solution to $SN(V)$ coincides with the solution to the weak formulation with boundary condition in the sense (3). If $\tilde{H}^{1/2}(\Gamma^\circ) = H_{\bar{\Gamma}}^{1/2}$ then there is only one formulation $SN(V)$ satisfying (6), but if $\tilde{H}^{1/2}(\Gamma^\circ) \not\subseteq H_{\bar{\Gamma}}^{1/2}$ there are infinitely many (with cardinality that of the continuum) distinct formulations, and for almost all incident wave directions these formulations have infinitely many distinct solutions.*

To each $V \subset H_{\bar{\Gamma}}^{1/2}$ we can also associate a unique BIE formulation. To define the associated BIO, choose any bounded open set $\Gamma_\dagger \supset \bar{\Gamma}$, let $T_\dagger : \tilde{H}^{1/2}(\Gamma_\dagger) \rightarrow H^{-1/2}(\Gamma_\dagger)$ be the standard hypersingular BIO on $\tilde{H}^{1/2}(\Gamma_\dagger) \supset H_{\bar{\Gamma}}^{1/2} \supset V$, and define the hypersingular operator $T_V : V \rightarrow V^*$ by

$$T_V \phi = PET_\dagger \phi, \quad \phi \in V,$$

where $E : H^{-1/2}(\Gamma_\dagger) \rightarrow H^{-1/2}(\Gamma_\infty)$ is the operator of minimum norm extension.

Theorem 4 [4] *For every $V \subset H_{\bar{\Gamma}}^{1/2}$ the hypersingular operator $T_V : V \rightarrow V^*$ is an isomorphism. Further, u satisfies $SN(V)$ if and only if (5) holds and $[u] \in V$ and satisfies, for some $\chi \in \mathcal{D}_1$,*

$$T_V[u] = -P(\chi \partial_{\mathbf{n}}^\pm u^i). \quad (7)$$

Moreover, (7) can be written equivalently in variational form as

$$\langle T_V[u], v \rangle = -\langle \chi \partial_{\mathbf{n}}^\pm u^i, v \rangle, \quad v \in V.$$

4 Limiting geometry principles

If $\tilde{H}^{1/2}(\Gamma^\circ) = H_{\bar{\Gamma}}^{1/2}$ the formulations $SN(V)$ that satisfy (6) collapse to a single formulation, equivalent to the standard weak formulation with boundary condition (3). So there is a single unique solution in this case. We note that $\tilde{H}^{1/2}(\Gamma^\circ) = H_{\bar{\Gamma}}^{1/2}$ if Γ is a C^0 open set, and also if Γ is C^0 except at countably many points on $\partial\Gamma$, as long as this set has only finitely many limit points [2] (an example is the screen at the top of Figure 1).

On the other hand, if $\tilde{H}^{1/2}(\Gamma^\circ) \subsetneq H_{\bar{\Gamma}}^{1/2}$, there are infinitely many distinct solutions to the formulations $SN(V)$ by Theorem 3. We propose to select physically appropriate solutions by thinking of the screen Γ as $\lim_{j \rightarrow \infty} \Gamma_j$, with convergence in some appropriate sense and with each bounded $\Gamma_j \subset \Gamma_\infty$ satisfying $\tilde{H}^{1/2}(\Gamma_j^\circ) = H_{\Gamma_j}^{1/2}$. If the (well-defined) solution u_j , for scattering by Γ_j , converges to a limit u which satisfies $SN(V)$ for some V satisfying (6), we will say that $SN(V)$ is the correct formulation for scattering by Γ in this limit. This approach for selecting the correct formulation, which we term a *limiting geometry principle*, seems natural for the many fractal scatterers defined as the limit of a sequence of regular prefractals, and dates back, in the context of potential theory, to Wiener [13].

Given a bounded screen $\Gamma \subset \Gamma_\infty$ there are many different possible approximating sequences Γ_j , and many different senses in which Γ_j may converge to Γ , and correspondingly we expect many different formulations $SN(V)$ to be appropriate as particular limiting geometry solutions (LGSs) [4]. We will focus here on the following particular cases:

Definition 5 (LGS for an Open Screen) *If $\Gamma \subset \Gamma_\infty$ is bounded and open, we call the total field u a LGS for the open screen Γ if there exists a sequence $(\Gamma_j)_{j \in \mathbb{N}}$ of open subsets of Γ_∞ such that: (i) $\Gamma_1 \subset \Gamma_2 \subset \dots$ and $\Gamma = \cup_{j=1}^\infty \Gamma_j$; (ii) for $j \in \mathbb{N}$, $\tilde{H}^{1/2}(\Gamma_j) = H_{\Gamma_j}^{1/2}$, so that the formulations $SN(V)$ satisfying (6) collapse to a single formulation with a well-defined unique solution u_j ; (iii) for $\mathbf{x} \in D = \mathbb{R}^n \setminus \bar{\Gamma}$, $u(\mathbf{x}) = \lim_{j \rightarrow \infty} u_j(\mathbf{x})$.*

Definition 6 (LGS for a Closed Screen) *If $\Gamma \subset \Gamma_\infty$ is compact, call the total field u a LGS*

for the closed screen Γ if there exists a sequence $(\Gamma_j)_{j \in \mathbb{N}}$ of compact subsets of Γ_∞ such that: (i) $\Gamma_1 \supset \Gamma_2 \supset \dots$ and $\Gamma = \cap_{j=1}^\infty \Gamma_j$; (ii) for $j \in \mathbb{N}$, $\tilde{H}^{1/2}(\Gamma_j^\circ) = H_{\Gamma_j}^{1/2}$, so that the formulations $SN(V)$ satisfying (6) collapse to a single formulation with a well-defined unique solution u_j ; (iii) for $\mathbf{x} \in D = \mathbb{R}^n \setminus \Gamma$, $u(\mathbf{x}) = \lim_{j \rightarrow \infty} u_j(\mathbf{x})$.

The following characterises these LGSs in terms of the formulations $SN(V)$.

Theorem 7 [4] *For every bounded open screen Γ there exists a unique LGS u , and this is the unique solution of $SN(V)$ with $V = \tilde{H}^{1/2}(\Gamma)$. Similarly, for every compact screen Γ there exists a unique LGS u , and this is the unique solution of $SN(V)$ with $V = H_{\bar{\Gamma}}^{1/2}$.*

5 What differences between formulations are detectable in the scattered field?

Our first result is concerned with whether the incident field “sees” the screen, i.e., for which Γ and u^i it holds that $u^s \neq 0$.

Theorem 8 [4] *Suppose that u satisfies $SN(V)$ for some $V \subset H_{\bar{\Gamma}}^{1/2}$. Then $u = u^i$ (so that $u^s = 0$) if $\bar{\Gamma}$ is 1/2-null. If $\bar{\Gamma}$ is not 1/2-null, i.e., $H_{\bar{\Gamma}}^{1/2} \neq \{0\}$, and $\{0\} \neq V \subset H_{\bar{\Gamma}}^{1/2}$, then $u \neq u^i$ for almost all incident directions \mathbf{d} .*

$\bar{\Gamma}$ is 1/2-null if $m(\bar{\Gamma}) = 0$, and clearly not 1/2-null if Γ° is non-empty. There exist screens with $\Gamma^\circ = \emptyset$ and $m(\bar{\Gamma}) > 0$ with $\bar{\Gamma}$ not 1/2-null [4, Example 9.3].

In the interesting case that $\Gamma^\circ = \emptyset$ and $\bar{\Gamma}$ is not 1/2-null, the above result implies that $SN(V_1)$ and $SN(V_2)$ have distinct solutions for almost all incident directions if $V_1 = H_{\bar{\Gamma}}^{1/2}$ and $V_2 = \tilde{H}^{1/2}(\Gamma^\circ) = \{0\}$. The following theorem implies results of the same flavour for general screens Γ .

Theorem 9 [4] *Suppose that V_1 and V_2 are subspaces satisfying (6) and that u_j is the solution to $SN(V_j)$, for $j = 1, 2$. Then $u_1 = u_2$ if $\tilde{H}^{1/2}(\Gamma^\circ) = H_{\bar{\Gamma}}^{1/2}$, while $u_1 \neq u_2$ for almost all incident directions \mathbf{d} if $\tilde{H}^{1/2}(\Gamma^\circ) \neq H_{\bar{\Gamma}}^{1/2}$ and $V_1 \neq V_2$. Further, $\tilde{H}^{1/2}(\Gamma^\circ) \neq H_{\bar{\Gamma}}^{1/2}$ if $\bar{\Gamma} \setminus \Gamma^\circ$ is 1/2-null or if $\Gamma^\circ \setminus \bar{\Gamma}$ is -1/2-null, in particular if $\dim_H(\bar{\Gamma} \setminus \Gamma^\circ) > n - 2$.*

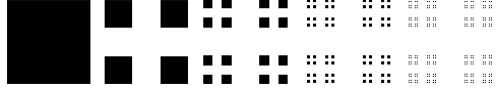


Figure 2: The first five prefractal approximations to the standard two-dimensional middle-third Cantor set (or Cantor dust).

6 Fractal apertures in a sound hard screen: theory and numerical results

As an illustration of the above results (cf. [2, Remark 4.6], [4, Example 9.5]) suppose that $n = 2$ or 3 and let

$$C_j := \{(\tilde{\mathbf{x}}, 0) : \tilde{\mathbf{x}} \in E_{j-1}^{n-1}\} \subset \Gamma_\infty,$$

with $\mathbb{R} \supset E_0 \supset E_1 \supset \dots$ the standard recursive sequence generating the “middle- λ ” Cantor set, for some $0 < \lambda < 1$ [5, Example 4.5]. Where $\alpha = (1 - \lambda)/2 \in (0, 1/2)$, explicitly $E_0 = [0, 1]$, $E_1 = [0, \alpha] \cup [1 - \alpha, 1]$, $E_2 = [0, \alpha^2] \cup [\alpha - \alpha^2, \alpha] \cup [1 - \alpha, 1 - \alpha + \alpha^2] \cup [1 - \alpha^2, 1]$, ..., so that $E_j \subset \mathbb{R}$ is the closure of a Lipschitz open set that is the union of 2^j open intervals of length α^j , while $E_j^2 \subset \mathbb{R}^2$ is the closure of a Lipschitz open set that is the union of 4^j squares of side-length α^j . The limit $C := \cap_{j=1}^\infty C_j$ is the middle- λ Cantor set for $n = 2$, the corresponding Cantor dust for $n = 3$, with [5] $\dim_H(C) = 2^{n-2} \log(2)/\log(1/\alpha)$. Figure 2 visualises E_0^2, \dots, E_4^2 (i.e., C_1, \dots, C_5 for $n = 3$) in the classical “middle third” case $\alpha = \lambda = 1/3$.

Let $\Gamma_0 := C_1^o$, and, for $j \in \mathbb{N}$, let $\Gamma_j := \Gamma_0 \setminus C_j$, so that Γ_j is a Lipschitz open set. Let $\Gamma := \cup_{j=1}^\infty \Gamma_j = \Gamma_0 \setminus C$. Let u_0 denote the total field for scattering by the screen Γ_0 (just the unit interval for $n = 2$, a unit square for $n = 3$) which we compare with scattering by Γ , which is Γ_0 with the fractal “hole” C removed. Let u_j denote the solution for scattering by Γ_j and u the LGS for the open set Γ in the sense of Definition 5 which, by Theorem 7, is the solution to $SN(V)$ with $V = \tilde{H}^{1/2}(\Gamma)$. Then $u_j \rightarrow u$ as $j \rightarrow \infty$ pointwise, and also [4] locally in W_2^1 norm on compact subsets of D .

Whether the “hole” C has an effect, i.e., whether $u \neq u_0$, depends on the dimension and on λ . The total fields u_0 and u are the solutions to the formulations $SN(V_1)$ and $SN(V_2)$, respectively, with $V_1 = H_{\overline{\Gamma}}^{1/2} = H_{\overline{\Gamma}_0}^{1/2} = \tilde{H}^{1/2}(\Gamma_0)$ and $V_2 = \tilde{H}^{1/2}(\Gamma)$. Thus, by Theorem 9, for

almost all incident wave directions, $u \neq u_0$ if $\dim_H(\Gamma_0 \setminus \Gamma) = \dim_H(C) > n - 2$, which holds if $n = 2$ or if $n = 3$ and $\alpha > 1/4$, so the hole has an effect in these cases. More detailed analysis [4] shows that $u = u_0$, i.e., the hole has no effect, if $n = 3$ and $\alpha \leq 1/4$.

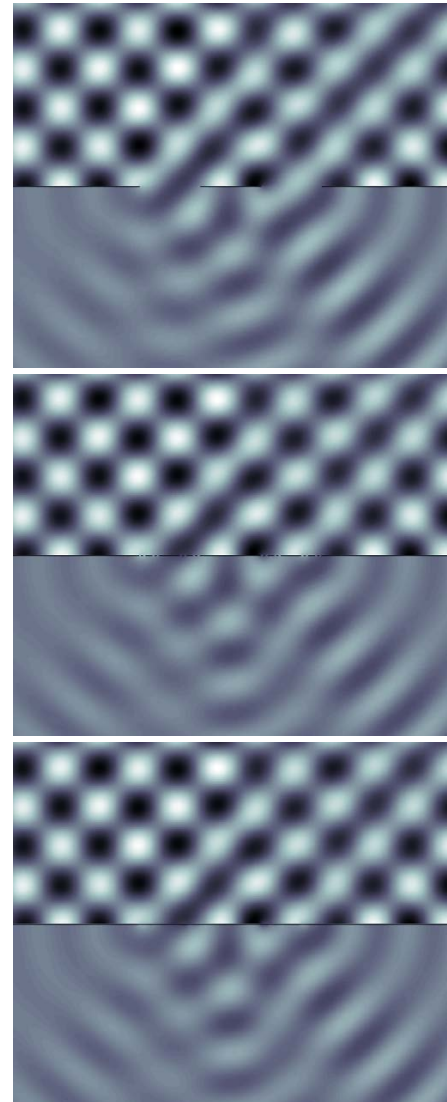


Figure 3: Reflection and transmission by a prefractal Cantor set aperture C_j in a sound hard screen: $j = 2$ (top); $j = 5$ (middle); $j = 8$ (bottom).

Figure 3 shows numerical results for $n = 2$ and $\alpha = \lambda = 1/3$ for a slightly modified problem of scattering by the fractal “hole” or aperture C in an infinite sound hard screen, which can be reduced to a (sound soft) screen scatter-

ing problem by a Babinet principle (e.g., [6]). Shown is $\Re u_j$, computed accurately by a BEM for $j = 2, 5, 8$, where u_j is the total field when $\mathbf{d} = (1, -1)/\sqrt{2}$ and the incident field has wavelength 0.3, so that $k = 20\pi/3 \approx 20.94$, and with the fractal hole C replaced by its prefractal approximation C_j . Our theoretical results predict that u_j approaches a limit that is different from the solution for a screen with no hole, i.e., a limit with a finite non-zero scattered field in the lower half-plane. This indeed seems to be the case, even though in this limit the hole has vanishing size: the total length of the components of C_j is $(2/3)^{j-1}$, which tends to zero as $j \rightarrow \infty$ and is ≈ 0.059 for $j = 8$.

References

- [1] C. J. Bouwkamp, Diffraction Theory, *Reports of Progress in Physics*, **17** (1954), pp. 35–100.
- [2] S. N. Chandler-Wilde, D. P. Hewett, and A. Moiola, Sobolev Spaces on non-Lipschitz Subsets of \mathbb{R}^n with Application to Boundary Integral Equations on Fractal Screens, to appear in *Integral Equations and Operator Theory*. Preprint at arXiv:1607.01994
- [3] S. N. Chandler-Wilde and D. P. Hewett, Wavenumber-Explicit Continuity and Coercivity Estimates in Acoustic Scattering by Planar Screens, *Integral Equations and Operator Theory*, **82** (2015), pp. 423–449.
- [4] S. N. Chandler-Wilde and D. P. Hewett, Well-posed PDE and Integral Equation Formulations for Scattering by Fractal Screens, submitted for publication. Preprint at arXiv:1611.09539
- [5] K. Falconer, *Fractal Geometry: Mathematical Foundations and Applications*, 3rd edition, Wiley, 2014.
- [6] D. P. Hewett, S. Langdon, and S. N. Chandler-Wilde, A Frequency-Independent Boundary Element Method for Scattering by Two-Dimensional Screens and Apertures, *IMA Journal of Numerical Analysis*, **35** (2015), pp. 1698–1728.
- [7] D. P. Hewett and A. Moiola, On the Maximal Sobolev Regularity of Distributions Supported by Subsets of Euclidean Space, *Analysis and Applications*, published online (2016), doi: 10.1142/S021953051650024X.
- [8] A. J. Mulholland and A. J. Walker, Piezoelectric Ultrasonic Transducers with Fractal Geometry, *Fractals*, **19** (2011), pp. 469–479.
- [9] C. Puente-Baliarda, J. Romeu, R. Pous, and A. Cardama, On the Behavior of the Sierpinski Multiband Fractal Antenna, *IEEE Transactions on Antennas and Propagation*, **46** (1998), pp. 517–524.
- [10] J. W. S. Rayleigh, *The Theory of Sound, Volume II*, 2nd edition, Macmillan, 1896.
- [11] E. P. Stephan, Boundary Integral Equations for Screen Problems in \mathbb{R}^3 , *Integral Equations and Operator Theory*, **10** (1987), pp. 236–257.
- [12] D. H. Werner and S. Ganguly, An Overview of Fractal Antenna Engineering Research, *IEEE Antennas and Propagation Magazine*, **45** (2003), pp. 38–57.
- [13] N. Wiener, Certain Notions in Potential Theory, *Journal of Mathematics and Physics*, **3** (1924), pp. 24–51.
- [14] C. H. Wilcox, *Scattering Theory for the d'Alembert Equation in Exterior Domains*, Springer, 1975.

Invisibility and perfect reflectivity in waveguides with finite length branches

Lucas Chesnel^{1,*}, Sergei A. Nazarov², Vincent Pagneux³

¹INRIA/CMAP, École Polytechnique, Université Paris-Saclay, Palaiseau, France

²IPME, Russian Academy of Sciences, St. Petersburg, Russia

³Laboratoire d'Acoustique de l'Université du Maine, Le Mans, France

*Email: Lucas.Chesnel@inria.fr

Abstract

We study a time-harmonic waves problem in a 2D waveguide. The geometry is symmetric with respect to an axis orthogonal to the direction of propagation of waves. Moreover, the waveguide contains one branch of finite length L . We analyse the behaviour of the complex scattering coefficients \mathcal{R} , \mathcal{T} as L goes to $+\infty$ and we exhibit situations where non reflectivity ($\mathcal{R} = 0$, $|\mathcal{T}| = 1$), perfect reflectivity ($|\mathcal{R}| = 1$, $\mathcal{T} = 0$) or perfect invisibility ($\mathcal{R} = 0$, $\mathcal{T} = 1$) hold.

Keywords: waveguides, invisibility, scattering matrix, asymptotic analysis

1 Introduction

In recent articles [1, 2], an approach has been proposed to construct acoustic waveguides different from the reference (straight) geometry where the incident waves produce only exponentially decaying scattered fields. The idea is to perturb the walls of the reference domain in a clever way mimicking the proof of the implicit function theorem. In this work, we wish to obtain a similar result following a different path.

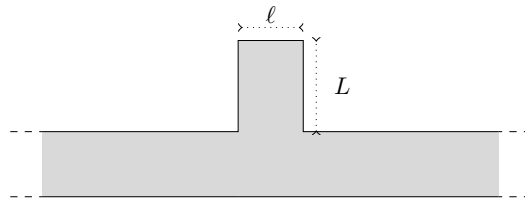


Figure 1: Geometry of Ω_L .

Consider some $\ell > 0$. For $L > 0$, set

$$\Omega_L := \{(x, y) \in \mathbb{R} \times (0; 1) \cup (-\frac{\ell}{2}; \frac{\ell}{2}) \times [1; 1+L]\}.$$

Propagation of acoustic waves in the waveguide Ω_L with sound hard walls leads to study the problem

$$\begin{cases} \Delta v + k^2 v = 0 & \text{in } \Omega_L \\ \partial_n v = 0 & \text{on } \partial\Omega_L. \end{cases} \quad (1)$$

We assume that $k \in (0; \pi)$ so that only two waves $w^\pm(x, y) = e^{\pm ikx}/\sqrt{2k}$ can propagate in Ω_L . The scattering of the wave w^+ coming from the left yields a solution of (1) such that

$$v = \begin{cases} w^+ + \mathcal{R}w^- + \dots, & \text{for } x < -\ell \\ \mathcal{T}w^+ + \dots, & \text{for } x > \ell. \end{cases} \quad (2)$$

Here the dots correspond to a superposition of modes which are exponentially decaying at $\pm\infty$. In (2), the reflection coefficient $\mathcal{R} \in \mathbb{C}$ and transmission coefficient $\mathcal{T} \in \mathbb{C}$ are uniquely defined. Moreover, energy conservation writes

$$|\mathcal{R}|^2 + |\mathcal{T}|^2 = 1. \quad (3)$$

In the following, we explain how to find ℓ , L such that $\mathcal{R} = 0$, $|\mathcal{T}| = 1$ (non reflectivity); $|\mathcal{R}| = 1$, $\mathcal{T} = 0$ (perfect reflectivity); or $\mathcal{R} = 0$, $\mathcal{T} = 1$ (perfect invisibility). To get such particular values, we will use the symmetry of the geometry with respect to the (Oy) axis.

2 Half-waveguide problems

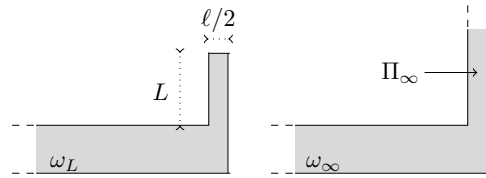


Figure 2: Domains ω_L (left) and ω_∞ (right).

Set $\omega_L := \{(x, y) \in \Omega_L \mid x < 0\}$. Introduce the problem with Neumann boundary conditions

$$\begin{cases} \Delta u + k^2 u = 0 & \text{in } \omega_L \\ \partial_n u = 0 & \text{on } \partial\omega_L \end{cases} \quad (4)$$

and the one with mixed boundary conditions

$$\begin{cases} \Delta U + k^2 U = 0 & \text{in } \omega_L \\ \partial_n U = 0 & \text{on } \partial\omega_L \cap \partial\Omega_L \\ U = 0 & \text{on } \{0\} \times (0; L). \end{cases} \quad (5)$$

Problems (4) and (5) respectively admit the solutions $u = w^+ + r w^- + \dots$ and $U = w^+ + R w^- + \dots$ where $r, R \in \mathbb{C}$ are uniquely defined and where the dots stand for terms which are exponentially decaying at $-\infty$. Due to conservation of energy, one has

$$|r| = |R| = 1. \quad (6)$$

Besides, a simple analysis shows that the coefficients \mathcal{R}, \mathcal{T} appearing in (2) are such that

$$\mathcal{R} = \frac{r + R}{2} \quad \text{and} \quad \mathcal{T} = \frac{r - R}{2}. \quad (7)$$

3 Non reflection and perfect reflection

Now, we study the asymptotic behaviour of \mathcal{R}, \mathcal{T} as $L \rightarrow +\infty$. To proceed, we use (7) and work with r, R . The behaviours of r, R as $L \rightarrow +\infty$ depend on the properties of the equivalents of Problems (4), (5) set in the limit geometry ω_∞ obtained from ω_L making formally $L \rightarrow +\infty$ (see Figure 2, right). In particular, the number of propagating waves existing in the vertical branch Π_∞ of ω_∞ plays a crucial role.

* Assume that $\ell \in (0; \pi/k)$ ($\ell/2$ is the width of Π_∞). Then for Problem (5) set in ω_∞ , propagative modes in Π_∞ do not exist. Due to this property, we can show that $R = R_\infty + \dots$ where $R_\infty \in \mathbb{S} := \{z \in \mathbb{C} \mid |z| = 1\}$ is a constant. Here the dots correspond to a remainder which is exponentially small as $L \rightarrow +\infty$. For Problem (4) (with Neumann boundary condition) set in ω_∞ , one propagative mode exists in Π_∞ . And because of the reflection of this mode on the wall at $y = L$, the coefficient r does not converge as $L \rightarrow +\infty$. More precisely, we can prove that it admits the expansion $r = r_{\text{asy}}(L) + \dots$ where $r_{\text{asy}}(L)$ is a term whose dependence with respect to L can be obtained explicitly and which runs periodically on \mathbb{S} as $L \rightarrow +\infty$. Again the dots stand for an exponentially small remainder.

Imagine that we want to have $\mathcal{R} = 0$ (non reflectivity). According to (7), we must impose $r = -R$. Relations (6) guarantee that for all $L > 0$, both r and R are located on the unit circle \mathbb{S} . But R tends to a constant $R_\infty \in \mathbb{S}$ while r runs continuously on \mathbb{S} as $L \rightarrow +\infty$. This proves the existence of L such that $r = -R$ and so $\mathcal{R} = 0$. This also shows that there are some L such that $r = R$ and so $\mathcal{T} = 0$ (perfect reflec-

tivity). Numerics of Figure 3 confirm these results. To obtain perfect invisibility, *i.e.* $\mathcal{T} = 1$, we must impose both $r = 1$ and $R = -1$. This requires a bit more work but can be achieved.

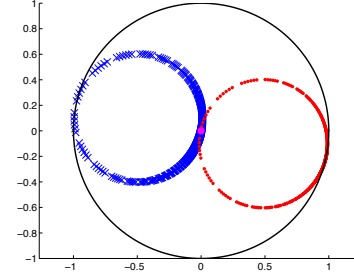


Figure 3: Numerical approximations of \mathcal{R} (blue crosses) and \mathcal{T} (red dots). We take $k = 3$, $\ell = 1$ and $L \in (1; 9)$. As predicted, we obtain circles of radius $1/2$ passing through zero.

* When $\ell \in (\pi/k; 2\pi/k)$, both for Problem (5) and (4) set in ω_∞ , one propagative mode exists in Π_∞ . Then, we can prove that $R = R_{\text{asy}}(L) + \dots$ and $r = r_{\text{asy}}(L) + \dots$ where $R_{\text{asy}}(L), r_{\text{asy}}(L)$ are explicitly known coefficients which run periodically on \mathbb{S} with different speeds V, v . This is enough to conclude that $\mathcal{R} = 0$ or $\mathcal{T} = 0$ for an infinite number of L . However, compared to the case $\ell \in (0; \pi/k)$, the behaviour of \mathcal{R} and \mathcal{T} can be much more complex, especially when v/V is not a rational number (see Figure 4).

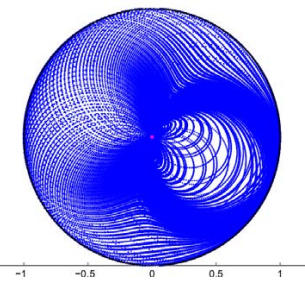


Figure 4: Numerical approximation of \mathcal{R} for $k = 3$, $\ell = 1.7$ and $L \in (1; 99)$.

References

- [1] A.-S. Bonnet-Ben Dhia, L. Chesnel and S.A. Nazarov, Perfect transmission invisibility for waveguides with sound hard walls, *arXiv:1304.4788*, (2016).
- [2] A.-S. Bonnet-Ben Dhia and S.A. Nazarov, Obstacles in acoustic waveguides becoming “invisible” at given frequencies, *Acoustical Physics*, 59(6), (2013) pp. 633-639.

Second Kind Boundary Integral Equation for Multi-Subdomain Diffusion Problems

Xavier Claeys^{1,*}, Ralf Hiptmair², Elke Spindler²

¹Laboratoire Jacques-Louis Lions/INRIA Alpines, Université Pierre-et-Marie Curie Paris 6, France

²Seminar for Applied Mathematics, Swiss Federal Institute of Technology, Zurich, Switzerland

*Email: claeys@ann.jussieu.fr

Abstract

We study elliptic boundary value problems where coefficients are piecewise constant with respect to a partition of space into Lipschitz subdomains, focusing on the case of jumping coefficients arising in the principal part of the partial differential operator. We propose a boundary integral equation of the second kind posed on the interfaces of the partition, and involving only one unknown trace function at each interface. We provide a detailed analysis of the corresponding integral operator, proving well-posedness. We also present numerical results that exhibit a systematically stable condition number for the associated Galerkin matrices, so that GMRES seems to enjoy fast convergence independent of the mesh resolution.

Keywords: integral equations, diffusion problem, second kind, multi-domain

1 Introduction

In the context of second order elliptic boundary value problems with coefficients that are piecewise constant with respect to a Lipschitz partition of the computational domain, boundary element methods are now a well established numerical approach that reduces the problem to an equation posed only at interfaces between subdomains.

In the case of geometrical configurations involving junctions i.e. points adjacent to at least three subdomains, all established boundary integral formulations such as Boundary Element Tearing and Interconnecting (BETI) [1], or Multi-Trace Formulations (MTF) [2] yield, after discretisation, fully populated ill conditionned matrices that require a preconditionner. Only recently in [3–6], integral equations of the second kind that systematically lead to well conditionned matrices have been proposed for geometries with junctions.

So far, such equations had been derived for Helmholtz equations with heterogeneities com-

ing into play only in the effective wave number i.e. the compact part of the partial differential operator. The present contribution derives such an integral equation, focusing on a diffusion problem where heterogeneities come into play in the principal part of the operator, namely

$$\begin{cases} u \in H_{\text{loc}}^1(\mathbb{R}^3) \text{ and} \\ -\operatorname{div}(\mu \nabla u) = f \text{ in } \mathbb{R}^3 \\ \limsup_{|\mathbf{x}| \rightarrow \infty} |\mathbf{x} u(\mathbf{x})| < +\infty \end{cases} \quad (1)$$

where $f \in L^2(\mathbb{R}^3)$ has bounded support. The coefficient $\mu : \mathbb{R}^3 \rightarrow (0, +\infty)$ is piecewise constant, satisfying $\mu(\mathbf{x}) = \mu_j$ for $\mathbf{x} \in \Omega_j$, where

$$\mathbb{R}^3 = \bigcup_{j=0}^n \overline{\Omega}_j \quad (2)$$

is a decomposition of the whole space into Lipschitz subdomains such that $\Omega_j \cap \Omega_k = \emptyset$ for $j \neq k$, and Ω_j is bounded for $j \neq 0$.

Compared to pre-existing works, an integral formulation of the second kind for Problem (1) leads to more challenging analysis because heterogeneities induce non-compact perturbations of the corresponding integral operators. In addition, although we deal with pure diffusion problems, similar results and techniques still apply for Helmholtz type equations sharing the same principal part (e.g. acoustic media with piecewise-uniform mass density), since such equations differ from (1) by a compact perturbation.

2 Reformulation as a system of coupled boundary integral equations

Let us introduce \mathfrak{J} as the set of pairs of integers $J = (j_+, j_-)$ such that $j_\pm \in \{0, \dots, n\}$, $j_+ > j_-$ and the interface $\partial\Omega_{j_+} \cap \partial\Omega_{j_-}$ consists in a non-trivial Lipschitz manifold with boundary. The elements of \mathfrak{J} are the edges of the adjacency graph of the partition (2). Then for $J = (j_+, j_-) \in \mathfrak{J}$, denote

$$\Gamma_J := \partial\Omega_{j_+} \cap \partial\Omega_{j_-}$$

and let \mathbf{n}_J refer to the vector field normal to Γ_J pointing from Ω_{j+} toward Ω_{j-} . Finally introduce the double layer integral operator

$$K_{J,Q}(p)(\mathbf{x}) := \lim_{\epsilon \rightarrow 0} \int_{\Gamma_Q \setminus B_\epsilon(\mathbf{x})} \frac{\mathbf{n}_J(\mathbf{x}) \cdot (\mathbf{y} - \mathbf{x})}{4\pi|\mathbf{y} - \mathbf{x}|^3} p(\mathbf{y}) d\sigma(\mathbf{y})$$

for all $J, Q \in \mathcal{I}$, $\mathbf{x} \in \Gamma_J$. The above formula makes $K_{J,Q}$ a continuous operator mapping $H^s(\Gamma_J)$ to $H^s(\Gamma_Q)$ for all $s \in (-1/2, +1/2)$. In the present talk we will show how Problem (1) can be reformulated as an integral equation of the form

$$\begin{cases} \text{Find } p_J \in H^{-s}(\Gamma_J), J \in \mathcal{I} \text{ such that} \\ p_J - \sum_{Q \in \mathcal{I}} \frac{[\mu_Q]}{\{\mu_Q\}} K_{J,Q}(p_Q) = g_J \quad \forall J \in \mathcal{I} \end{cases} \quad (3)$$

where we set $[\mu_Q] := \mu_{q_+} - \mu_{q_-}$ and $\{\mu_Q\} := (\mu_{q_+} + \mu_{q_-})/2$ for $Q = (q_+, q_-) \in \mathcal{I}$. In these integral equations the right hand sides g_J admit explicit expressions in terms of the datum f appearing in (1).

We prove that the integral operator of (3) is an isomorphism. Besides, since $|s| < 1/2$ in this formulation, it can be discretised by Galerkin procedures based on discontinuous shape functions. We shall also present numerical results exhibiting systematic good conditionning of the corresponding matrices. Further details can be found in [7].

References

- [1] U. Langer and O. Steinbach, Boundary Element Tearing and Interconnecting methods, *Computing*, 71 (2003), no.3, 205-228.
- [2] X. Claeys, R. Hiptmair and C. Jerez-Hanckes, Multitrace boundary integral equations. *Direct and inverse problems in wave propagation and applications*, 51-100, Radon Ser. Comput. Appl. Math., 14, De Gruyter, Berlin, 2013.
- [3] E. Spindler, Second Kind Single-Trace Boundary Integral Formulations for Scattering at Composite Objects, PhD thesis, diss. no. 23620, Seminar of Applied Mathematics, ETH Zürich, 2016.
- [4] X. Claeys, A single trace integral formulation of the second kind for acoustic scattering, technical report 2011-14, Seminar of Applied Mathematics, ETH Zürich, 2011.
- [5] X. Claeys, R. Hiptmair and E. Spindler, A Second-Kind Galerkin Boundary Element Method for Scattering at Composite Objects, *BIT Numer. Math.* 55 (2015), no.1, 33–57.
- [6] L. Greengard and J.-Y. Lee, Stable and accurate integral equation methods for scattering problems with multiple material interfaces in two dimensions. *J. Comput. Phys.* 231 (2012), no. 6, 2389-2395.
- [7] X. Claeys, R. Hiptmair and E. Spindler, Second Kind Boundary Integral Equation for Multi-Subdomain Diffusion Problems, to appear in *Adv. Comput. Math.*, 2017.

Topological derivatives of leading- and second-order homogenized coefficients in bi-periodic media

Marc Bonnet¹, Rémi Cornaggia^{2,*}, Bojan Guzina³

¹Poems (UMR 7231 CNRS-INRIA-ENSTA), Palaiseau, France

²IRMAR, Université Rennes 1, Rennes, France

³CEGE, University of Minnesota, Minneapolis, USA

*Email: remi.cornaggia@univ-rennes1.fr

Abstract We derive the topological derivatives of the homogenized coefficients associated to a periodic material, with respect of the small size of a penetrable inhomogeneity introduced in the unit cell that defines such material. In the context of antiplane elasticity, this work extends existing results to (i) time-harmonic wave equation and (ii) second-order homogenized coefficients, whose contribution reflects the dispersive behavior of the material.

Keywords: homogenization, topological derivatives.

Introduction Consider an elastic material occupying a 2D domain and characterized by periodic shear modulus μ and density ρ . The unit cell Y has characteristic length ℓ . Under time-harmonic conditions, the antiplane displacement u satisfies the wave equation:

$$\nabla \cdot (\mu \nabla u) + \omega^2 \rho u = 0$$

For long-wavelength configurations (i.e. $\ell \ll \lambda$), two-scale periodic homogenization of this equation in terms of $\varepsilon = \ell/\lambda$ [4] leads to the equation satisfied by the mean field U :

$$\begin{aligned} \boldsymbol{\mu}^0 : \nabla^2 U + \omega^2 \rho^0 U \\ = -\varepsilon^2 [\boldsymbol{\mu}^2 : \nabla^4 U + \omega^2 \boldsymbol{\rho}^2 : \nabla^2 U] + O(\varepsilon^4), \end{aligned}$$

where the leading-order and second-order homogenized coefficients $(\boldsymbol{\mu}^0, \rho^0, \boldsymbol{\mu}^2, \boldsymbol{\rho}^2)$ are constant tensors and $\nabla^k U$ stands for the k -th gradient of U .

This study considers a periodic perturbation of this material, whereby a penetrable inhomogeneity B_a , of size a and shape \mathcal{B} , characterized by contrasts $(\Delta\mu, \Delta\rho)$ is introduced at point $\mathbf{z} \in Y$ (Fig. 1). Then, the leading-order expansion coefficients of $(\boldsymbol{\mu}^0, \rho^0, \boldsymbol{\mu}^2, \boldsymbol{\rho}^2)$ w.r.t. a , namely their topological derivatives, are computed, as in [3] for in-plane elastostatics.

Leading-order coefficients Let $\langle \cdot \rangle = \frac{1}{|Y|} \int_Y \cdot$ denote an average on the unit cell. The homogenized density ρ^0 is defined by $\rho^0 = \langle \rho \rangle$, so that

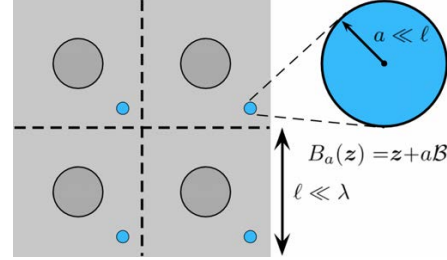


Figure 1: Perturbed periodic material

the perturbed coefficient ρ_a^0 and the topological derivative $\mathcal{D}\rho^0$ are exactly given by:

$$\rho_a^0 = \rho^0 + a^2 |Y|^{-1} \mathcal{D}\rho^0; \quad \mathcal{D}\rho^0 = |\mathcal{B}| \Delta\rho.$$

The homogenized shear modulus $\boldsymbol{\mu}^0$ is defined by $\boldsymbol{\mu}^0 = \langle \mu(\mathbf{I} + \nabla \mathbf{P}) \rangle^S$, where \mathbf{I} is the identity tensor, the first *cell function* \mathbf{P} [4] is the Y -periodic and zero-mean vector-valued solution of:

$$\nabla \cdot (\mu(\mathbf{I} + \nabla \mathbf{P})) = \mathbf{0} \quad (1)$$

and the superscript $.^S$ means symmetrization w.r.t. all index permutations. Consequently, $\boldsymbol{\mu}_a^0$ is computed as:

$$\boldsymbol{\mu}_a^0 = \boldsymbol{\mu}^0 + \langle \mu \nabla \mathbf{p}_a \rangle^S + \langle \chi_{B_a} \Delta\mu(\mathbf{I} + \nabla \mathbf{P}_a) \rangle^S$$

where $\mathbf{p}_a := \mathbf{P}_a - \mathbf{P}$ is the perturbation of \mathbf{P} . The analysis of this perturbation is done by reformulating problem (1) and its perturbed counterpart using domain integral equations [2]. With the help of the adjoint state method, it leads to the following leading-order expansion:

$$\boldsymbol{\mu}_a^0 = \boldsymbol{\mu}^0 + a^2 |Y|^{-1} \mathcal{D}\boldsymbol{\mu}^0(\mathbf{z}) + o(a^2 |Y|^{-1}), \quad (2)$$

with the topological derivative $\mathcal{D}\boldsymbol{\mu}^0$ given by:

$$\mathcal{D}\boldsymbol{\mu}^0(\mathbf{z}) = [(\mathbf{I} + \nabla \mathbf{P}) \cdot \mathbf{A} \cdot (\mathbf{I} + \nabla \mathbf{P})^T](\mathbf{z})$$

and $\mathbf{A}(\mathbf{z}) = \mathbf{A}(\mathcal{B}, \mu(\mathbf{z}), \Delta\mu)$ is the polarization tensor [1] associated to shape \mathcal{B} and moduli $\mu(\mathbf{z})$ and $\mu(\mathbf{z}) + \Delta\mu$. Under notational adjustments, this result is similar to [3]. For homogeneous background materials, in which case $\mathbf{P} = \mathbf{0}$, it reduces to $\mathcal{D}\boldsymbol{\mu}^0 = \mathbf{A}$ as shown by [1].

Second-order coefficients The second-order homogenized density is defined by $\rho^2 = \langle \rho \mathbf{Q} \rangle^S$, where the *second cell function* \mathbf{Q} is the Y -periodic, zero-mean, tensor-valued solution of:

$$\begin{aligned} \nabla \cdot (\mu(\mathbf{P} \otimes \mathbf{I} + \nabla \mathbf{Q})) \\ = -\mu(\mathbf{I} + \nabla \mathbf{P}) + (\rho/\rho^0)\mu^0 \end{aligned} \quad (3)$$

Relying on the same integral equation framework, and with careful analysis of the influence of the source terms involving \mathbf{P}_a when addressing the perturbed cell function \mathbf{Q}_a , we show that ρ_a^2 has an expansion of the same form as (2), with its topological derivative $\mathcal{D}\rho^2$ given by:

$$\begin{aligned} \mathcal{D}\rho^2(z) = & \left[(\mathbf{I} + \nabla \mathbf{P}) \cdot \mathbf{A} \cdot \left(\beta \mathbf{I} + \nabla \hat{\mathbf{X}}[\beta] \right)^T \right. \\ & - (\mathbf{P} \otimes \mathbf{I} + \nabla \mathbf{Q}) \cdot \mathbf{A} \cdot \nabla \beta \\ & - (\mathcal{D}\mu^0 - (\mathcal{D}\rho^0/\rho^0)\mu^0) \langle \rho(\beta/\rho^0) \rangle \\ & \left. - \mathcal{D}\rho^0 ((\beta/\rho^0)\mu^0 - \mathbf{Q}) \right]^S(z). \end{aligned} \quad (4)$$

The above expression features (i) various combinations of the previously computed cell solutions and topological derivatives and (ii) two new *adjoint fields* β and $\hat{\mathbf{X}}[\beta]$ defined as the (Y -periodic, zero-mean) solutions of:

$$\begin{aligned} \nabla \cdot (\mu \nabla \beta) = -(\rho - \rho^0) \\ \text{and } \nabla \cdot (\mu(\beta \mathbf{I} + \nabla \hat{\mathbf{X}}[\beta])) = -\mu \nabla \beta. \end{aligned}$$

In particular, all the fields involved in (4) solve problems posed on the *unperturbed* cell.

The second-order homogenized shear modulus is defined by $\mu^2 = \langle \mu(\mathbf{Q} \otimes \mathbf{I} + \nabla \mathbf{R}) \rangle^S$ in terms of \mathbf{Q} and a third cell function \mathbf{R} . Once again, an analysis of the problems satisfied by \mathbf{R} and \mathbf{R}_a is conducted. As a result, μ_a^2 is found to have an expansion similar to (2), and its topological derivative $\mathcal{D}\mu^2$ (not shown here for brevity) is expressed in terms of the cell solutions $(\mathbf{P}, \mathbf{Q}, \mathbf{R})$ and the previously determined topological derivatives $(\mathcal{D}\rho^0, \mathcal{D}\mu^0, \mathcal{D}\rho^2)$.

Perspectives. The obtained expansions of the homogenized coefficients are useful on their own right, e.g. for computing quickly an approximation of the properties of a perturbed periodic material for several trial inhomogeneity locations \mathbf{z} without solving the new cell problems. As an example, an approximation of μ_a^0 is obtained by neglecting the remainder in (2), as illustrated on Fig. 2 for a chessboard-like cell.

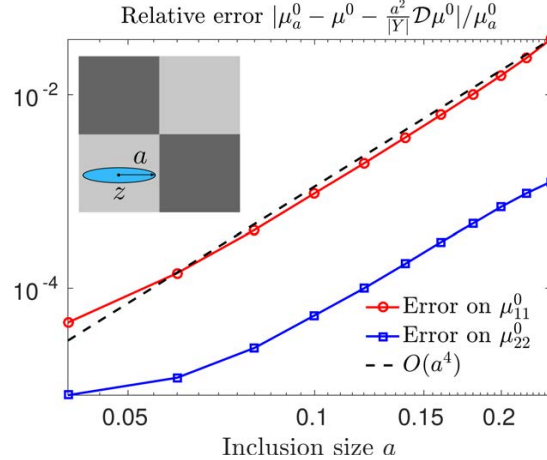


Figure 2: Relative error on shear modulus μ_a^0 approximated by expansion (2) for an ellipsoidal inhomogeneity of semi-axes $(a, 0.2a)$ placed at $\mathbf{z} = (0.25, 0.25)$ in a chessboard-like cell $Y = [0, 1]^2$. In this case, since the medium is locally homogeneous around \mathbf{z} , the remainder can be shown to be in $O(a^4)$ as observed.

However, as already intended in [3], the main usefulness of such expansions occurs for optimizing a periodic structure towards some desirable property. Since they address the time-harmonic case and the second-order homogenized coefficients, our results should notably allow to tune the dispersive properties of the homogenized material, in particular the so-called *band-gaps* (forbidden frequencies for which no wave propagates through the structure).

References

- [1] H. Ammari, H. Kang, and K. Touibi. Boundary layer techniques for deriving the effective properties of composite materials. *Asymptot. Anal.*, 41:119–140, 2005.
- [2] M. Bonnet. Higher-order topological sensitivity for 2-d potential problems. application to fast identification of inclusions. *Int. J. Solids Struct.*, 46:2275–2292, 2009.
- [3] S. M. Giusti, A. A. Novotny, and E. A. de Souza Neto. Sensitivity of the macroscopic response of elastic microstructures to the insertion of inclusions. *Proc. Roy. Soc. London. Series A.*, 2010.
- [4] A. Wautier and B. B. Guzina. On the second-order homogenization of wave motion in periodic media and the sound of a chessboard. *J. Mech. Phys. Solids*, 78:382–404, 2015.

High Order DG Overlapping Solution FEM for the Helmholtz Equation

Joe Coyle^{1,*}

¹Department of Mathematics, Monmouth University, West Long Branch, NJ, U.S.A.

*Email: jcoyle@monmouth.edu

Abstract

The overlapping solution finite element method [1, 2] relies on an integral representation of the scattered field [3] as part of the boundary conditions. In particular, the variational form and modified integral representation of the scattered field on the artificial boundary are given in the context of a discontinuous Galerkin method. Numerical evidence of convergence is presented for uniform high order L^2 -conforming basis functions.

Keywords: Helmholtz, Discontinuous Galerkin, High Order

Scattering Problem

Consider a bounded scatterer D with smooth boundary Γ and set Ω to be the unbounded complement of \overline{D} in \mathbb{R}^2 . The scattering problem considered is to determine the total field u satisfying

$$\Delta u + k^2 u = 0 \quad \text{in } \Omega, \quad (1)$$

$$u = 0 \quad \text{on } \Gamma, \quad (2)$$

$$\lim_{r \rightarrow \infty} \sqrt{r} \left(\frac{\partial u^s}{\partial r} - iku^s \right) = 0, \quad (3)$$

$$u = u^i + u^s, \quad (4)$$

where (3) is the Sommerfeld radiation condition. In (4), u^s is the scattered field and $u^i = e^{ik\mathbf{x} \cdot \mathbf{d}}$ is the incident plane wave with direction \mathbf{d} , $|\mathbf{d}| = 1$.

DG Setup

Denote by $\widehat{\Omega}$ the part of Ω truncated by a piecewise Lipschitz curve, Σ and set F to be a curve inside $\widehat{\Omega}$ where $\Sigma \cap F \neq \emptyset$. Given a triangular partition, \mathcal{P} , of $\widehat{\Omega}$, (Figure ??) identify the edges that coincide with Σ , F and the interior by \mathcal{E}^Σ , \mathcal{E}^F and \mathcal{E}^0 , respectively. Define

$$V_p(K) = \{v \in L^2(K) : \deg(v) \leq p\}.$$

In what follows, define the following usual averages

$$\{u\} = \frac{1}{2}(u^+ + u^-), \quad \{\boldsymbol{\sigma}\} = \frac{1}{2}(\boldsymbol{\sigma}^+ + \boldsymbol{\sigma}^-)$$

and jumps

$$[u]_N = u^+ \mathbf{n}^+ + u^- \mathbf{n}^-, \quad [\boldsymbol{\sigma}]_N = \boldsymbol{\sigma}^+ \cdot \mathbf{n}^+ + \boldsymbol{\sigma}^- \cdot \mathbf{n}^-$$

for $u \in V_p(\mathcal{P})$ and $\boldsymbol{\sigma} \in V_p(\mathcal{P})^2$ where

$$V_p(\mathcal{P}) = \{v \in L^2(\Omega) : v|_K \in V_p(K) \text{ for all } K \in \mathcal{P}\}.$$

Given $\mathbf{x} \in \Sigma$ and \mathbf{n} the unit outward normal to F , the scattered field is represented by

$$\mathcal{I}[u, \Phi](\mathbf{x}) = \sum_{\gamma \in \mathcal{E}^F} \int_{\gamma} \left(\{u^s\} \frac{\partial \Phi}{\partial \mathbf{n}_{\mathbf{y}}} - [\nabla u^s]_N \Phi \right) ds_{\mathbf{y}}$$

where Φ is the appropriate fundamental solution. Define the boundary operator on Σ as

$$\mathcal{L}(u) := \left. \left(\frac{\partial u}{\partial \mathbf{n}} - i\lambda u \right) \right|_{\Sigma}, \quad (5)$$

where $\lambda \neq 0$ and define $\mathcal{I}_{\mathcal{L}}[u, \Phi]$ to be \mathcal{L} applied to $\mathcal{I}[u, \Phi]$. The first order system associated with (1) - (4) is

$$ik\boldsymbol{\sigma} = \nabla u \text{ in } \Omega \quad (6)$$

and

$$\nabla \cdot \boldsymbol{\sigma} = iknu \text{ in } \Omega \quad (7)$$

with the condition on the boundary given by

$$ik\boldsymbol{\sigma} \cdot \mathbf{n} - i\lambda u - \mathcal{I}_{\mathcal{L}}[u, \Phi] = \mathcal{L}(u^i) \text{ on } \Sigma. \quad (8)$$

The fluxes on interior edges (see [4]) are

$$\boldsymbol{\sigma}_f = \frac{1}{ik} \{\nabla_h u\} - \alpha [u]_N$$

and

$$u_f = \{u\} - \beta \frac{1}{ik} [\nabla_h u]_N.$$

On Σ , set

$$ik\boldsymbol{\sigma}_f = i\lambda u \mathbf{n} + I_{\mathcal{L}}^R[u, \Phi] \mathbf{n} + \mathcal{L}(u^i) \mathbf{n}$$

and $u_f = u_p$. Finally, on Γ set

$$\boldsymbol{\sigma}_f = \frac{1}{ik} \nabla_h u - \alpha u \mathbf{n}$$

and to weakly enforce (2), $u_f = 0$.

Variational Form

The variational form is to determine $u \in V_p(\mathcal{P})$ such that

$$A(u, v) = l(v) \quad (9)$$

for all $v \in V_p(\mathcal{P})$ where

$$\begin{aligned} A(u, v) &= \int_{\Omega} (\nabla \bar{v} \cdot \nabla u - k^2 u \bar{v}) dA \\ &- \sum_{\gamma \in \mathcal{E}^\Sigma} \int_{\gamma} (i\lambda u + \mathcal{I}_{\mathcal{L}}[u, \Phi]) \bar{v} ds + ik \sum_{\gamma \in \Gamma} \int_{\gamma} \alpha u \bar{v} ds \\ &+ ik \sum_{\gamma \in \mathcal{E}^0} \int_{\gamma} \left(\beta [\![\nabla u]\!]_N [\![\nabla \bar{v}]\!]_N + \alpha [\![u]\!]_N \cdot [\![v]\!]_N \right) ds \\ &- \sum_{\gamma \in \mathcal{E}^0} \int_{\gamma} \left(\{\!\{ \nabla u \}\!\} \cdot [\![\bar{v}]\!]_N + [\![u]\!]_N \{\!\{ \nabla \bar{v} \}\!\} \right) ds \\ &- \sum_{\gamma \in \mathcal{E}^\Gamma} \int_{\gamma} \left(u (\nabla \bar{v} \cdot \mathbf{n}) ds + (\nabla u \cdot \mathbf{n}) \bar{v} \right) ds \end{aligned}$$

and

$$l(v) = - \sum_{\gamma \in \mathcal{E}^\Sigma} \int_{\gamma} \mathcal{L}(u^i) \bar{v} ds.$$

Numerical Results

Convergence is illustrated in the following example where the boundary of the scatterer is the unit circle, $k = 2\pi$, and $\alpha = \beta = 1/4$. The error is measured with the norm given by

$$\begin{aligned} \|\|u\|\|^2 &= \sum_{K \in \mathcal{P}} \left(\|u\|_{0,K}^2 + \|\nabla u\|_{0,K}^2 \right) \\ &+ \sum_{\gamma \in \mathcal{E}^0} \left(k^{-1} \|\beta^{1/2} [\![\nabla u]\!]_N\|_{0,\gamma}^2 + k \|\alpha^{1/2} [\![u]\!]_N\|_{0,\gamma}^2 \right) \\ &+ \sum_{K \in \mathcal{E}^\Sigma \cup \mathcal{E}^\Gamma} \|u\|_{0,\gamma}^2. \end{aligned}$$

The plots showing the log of the number of degrees of freedom versus the relative error for increasing values of p are given in Figure 2.

Mesches \mathcal{M}_1 to \mathcal{M}_3 are each a refinement of the previous one. Lagrangian basis functions [5] are used throughout.

References

- [1] J. Coyle and P. Monk, Scattering of time-harmonic electromagnetic waves by anisotropic inhomogeneous scatterers or impenetrable obstacles, *SIAM J. Numer. Anal.* **37** (2000), pp. 1590–1617.
- [2] J. Coyle, Overlapping solution finite element method—higher order approximation and implementation, *Appl. Numer. Math.* **62** (2012), pp. 1910–1924.
- [3] C. Hazard and M. Lenoir, On the solution of time-harmonic scattering problems for Maxwell's equations, *SIAM J. Math. Anal.* **27** (1996), pp. 1597–1630.
- [4] R. Hiptmair, A. Moiola and I. Perugia, Plane Wave Discontinuous Galerkin Methods for the 2D Helmholtz Equation: Analysis of the p-Version, *SIAM J. Numer. Anal.* **49** (2011), pp. 264–284.
- [5] S. C. Brenner and L. R. Scott, *The mathematical theory of finite element methods*, 3rd edition, Springer, New York, 2008.

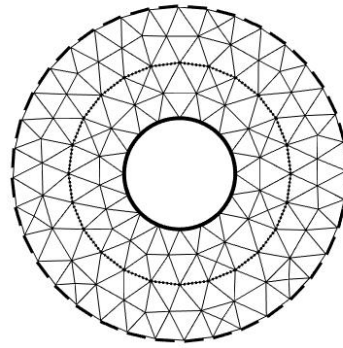


Figure 1: Initial triangular partition denoted by \mathcal{M}_1 . Σ is the outer dashed curve and F is the inner dotted curve.

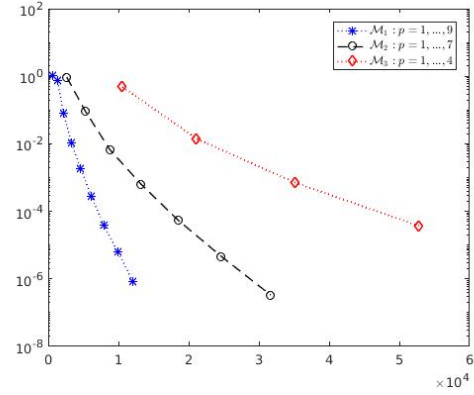


Figure 2: The log of the number of degrees of freedom versus the relative error are shown for increasing values of p for meshes \mathcal{M}_1 to \mathcal{M}_3 .

An Efficient Semi-Analytical Scheme for Determining the Reflection of Lamb Waves in a Semi-Infinite Waveguide

Robert Davey^{1,*}, Raphaël Assier¹, David Abrahams², Rich Hewitt¹

¹School of Mathematics, University of Manchester, United Kingdom

²Isaac Newton Institute, University of Cambridge, United Kingdom

*Email: robert.davey@postgrad.manchester.ac.uk

Abstract

The reflection of Lamb waves from a free edge perpendicular to an elastodynamic plate is studied. It is known that extant methods for finding the reflected field have poor convergence due to irregular behaviour near corners. The form of the irregularity for an elastodynamic corner is derived asymptotically. A new method for incorporating this form of the corner behaviour is then implemented. Results are presented showing this new method improves convergence in the reflection problem.

Keywords: Elasticity, Lamb Waves, Corner Behaviour, Reflection

1 Introduction

We consider the reflection of an incoming linearly-elastic wave in a semi-infinite elastic waveguide, as shown in Figure 1. The waves associated with two dimensional elastic wave guides were first studied by Lamb almost one hundred years ago [1], and are still an active area of research due to their wide range of applications in nondestructive testing. In addition these waves have interesting mathematical features such as the structure of the dispersion relation [2].

It is well known that the corners present in this model have irregular behaviour, this is caused by having three boundary conditions at the intersection of the free edges. The local behaviour of corners at the intersection of two traction free edges is known to be singular if the angle is greater than π and bounded for angles less than π [3]. In this problem with two corners of angle $\pi/2$, we therefore know the local behaviour is bounded, however this work may also be applied to singular corners.

It has also been known for some time that the solution to our test problem in terms of a modal expansion of Lamb waves has extremely poor convergence [4]. This is due to the irregular behaviour of the corners, similarly to how approximating irregular behaviour by Fourier

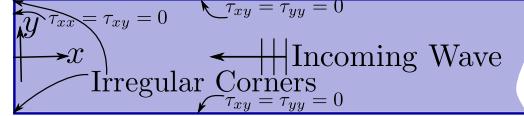


Figure 1: The model we wish to study. There are two corners with locally irregular behaviour at the intersections of the traction free surfaces. A propagating Lamb wave is incoming from the right and we wish to determine the resulting scattered field.

series results in Gibbs phenomena. In the same way that the convergence of Fourier series can be improved by removing the problematic behaviour, we seek to isolate the irregular corner terms from our Lamb wave expansion. To do this we will introduce new modes that accurately represent the behaviour near the corners and so free the Lamb modes to represent the stress field in the rest of the plate where they provide a useful description.

2 Corner Behaviours

We must first find the behaviour that we wish to isolate in our corner modes. To do so we use asymptotic expansions on the solutions of the Navier-Lamé equations in potential form. This enables us to write the corner behaviours as a series of modes. Each mode is known up to a multiplicative constant and has leading order behaviour for all stresses as $\tau \sim \rho^{\gamma_m} - 1$, where ρ is the distance from the corner, γ_m is a solution of the compatibility condition $\sin(\gamma_m \xi) \pm \gamma_m \sin(\xi) = 0$ and $\Re[\gamma_m] > 0$. We now wish to introduce the irregular behaviour of these modes into our expansion.

3 Virtual Plates

In the neighbourhood of the corner, $\rho \ll 1$, we know that the solution will be accurately represented by the corner modes. We can use this in our solution; however, we cannot directly add the corner modes to a modal expansion as they

automatically satisfy the boundary conditions. We will instead use our knowledge that the behaviour near the corner in all directions will be dominated by the corner modes, including in an extended ‘virtual’ domain. As such we know the forms of the behaviour of the stresses on the ‘virtual’ boundaries $y = \pm 1/2$ for $x < 0$, as shown in Figure 2. Here s , p , q and r are the

$$\begin{aligned} \tau_{xy} &= s \quad \tau_{yy} = p \\ \tau_{xy} &= q \quad \tau_{yy} = r \end{aligned}$$

Virtual Plate Physical Plate

Figure 2: The problem we wish to use to implement corner modes. The shaded physical plate has traction free conditions on top and bottom but the condition on the surface $x = 0$ will be applied later. The dashed lines denote the extended ‘virtual’ plate where we are imposing the local form of the stresses resulting from the corners.

functions that describe the local behaviour of a corner and are expressed as a series of corner modes.

We can solve this problem by use of Fourier transform methods. In doing so we find that the Fourier transformed stress fields have dependence on each of the corner modes in addition to having poles at the zeroes of the regular dispersion relation for Lamb waves. When taking the inverse Fourier transform we will find that the contribution from the poles yields the well known forms of Lamb waves up to an unknown constant. We will additionally find that the contour, which must be chosen to be consistent with the number of Lamb waves in the expansion, will generate a series of modes that represent the corner dependence. We may write this as a modal expansion given by

$$\tau_{xx} = \sum_{n=1}^N \zeta_n t_x^n(x, y) + \sum_{m=1}^M \eta_m s_x^m(x, y), \quad (1)$$

$$\tau_{xy} = \sum_{n=1}^N \zeta_n t_y^n(x, y) + \sum_{m=1}^M \eta_m s_y^m(x, y), \quad (2)$$

where t^n is the stress field of the n th Lamb mode and s^m is the stress field of the m th corner mode. Here ζ_n and η_m are as yet undetermined constants.

4 Results

We have found that in using the addition modes we have implemented we have much improved

convergence, Figure 3 shows that the error in the stress field is smaller when using a small number of corner and Lamb modes when compared to a large number of Lamb modes only.

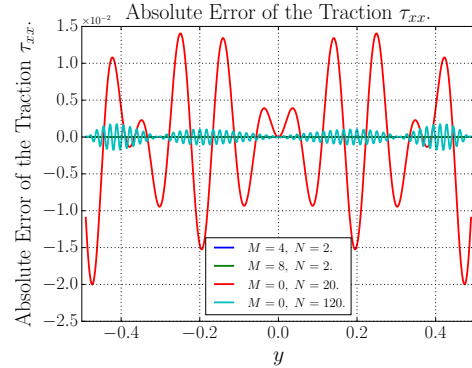


Figure 3: The absolute errors in the tractions generated by various truncations. In generating these plots the transverse free space wave number of the material was $k_t = 1$ and the Poisson ratio was $\nu = 0.3$.

References

- [1] H. Lamb. On waves in an Elastic Plate. *Proceedings of the Royal Society of London*, 1917.
- [2] M. L. Williams. Surface singularities resulting from various boundary conditions in angular corners of plates in extension. *Journal of Applied Mechanics, ASME*, 1952.
- [3] J. B. Lawrie and J. Kaplunov. Edge waves and resonance on elastic structures: An overview. *Mathematics and Mechanics of Solids*, 2012.
- [4] R. D. Gregory and I. Gladwell. The reflection of a symmetric Rayleigh-Lamb wave at the fixed or free edge of a plate. *Journal of Elasticity*, 1983.

Mathematical Studies of the Kuznetsov Equation

Adrien DEKKERS^{1,*}, Anna ROZANOVA-PIERRAT¹

¹Laboratoire MICS, CentraleSupélec, Châtenay-Malabry, France

*Email: adrien.dekkers@centralesupelec.fr

Abstract

We consider the Cauchy problem for the Kuznetsov equation (a model of non-linear acoustics) and we prove local and global well-posedness results both with and without viscosity. Using these results, we also prove that the solutions of the Kuznetsov equation are approximations of the isentropic Navier-Stokes system solutions.

Keywords: Kuznetsov equation, Navier-Stokes system, derivation, well-posedness, approximation.

Introduction

A usefull model of non-linear acoustics in thermo-viscous elastic media, is the Kuznetsov equation [5]. This equation describes the evolution of the velocity potential. It can be derived from a compressible isentropic Navier-Stokes system using small perturbations of the density and of the velocity characterized by a small parameter $\varepsilon > 0$. It reads

$$\begin{cases} u_{tt} - c^2 \Delta u - \frac{\nu}{\rho_0} \varepsilon \Delta u_t = \frac{\gamma-1}{c^2} \varepsilon u_t u_{tt} \\ \quad + 2\varepsilon \nabla u \nabla u_t, \\ u(0) = u_0, \quad u_t(0) = u_1, \end{cases} \quad (1)$$

where c , ρ_0 , γ , ν are the velocity of the sound, the density, the ratio of the specific heats and the viscosity of the medium respectively.

For $\nu > 0$ and without non-linear terms, Eq. (1) becomes the known strongly damped wave equation, which has a global solution the energy of which decreases in time [2]. However, in the non-viscous case $\nu = 0$, there is a blow-up formation for a finite time [1].

Well-posedness for the non viscous case

We study the problem given by Eq. (1) with $\nu = 0$. The local well-posedness of this equation follows from [3]:

Theorem 1 Let $s > \frac{n}{2} + 1$ and $\nu = 0$. For $u_0 \in H^{s+1}(\mathbb{R}^n)$, $u_1 \in H^s(\mathbb{R}^n)$, and $\|u_1\|_{L^\infty} \leq \frac{c^2}{2(\gamma-1)\varepsilon}$, there exists $T > 0$ such that there exists

a unique u solution of the problem (1) with

$u \in X = C^r([0, T], H^{s+1-r}(\mathbb{R}^n))$ for $0 \leq r \leq s$, and $(u_0, u_1) \mapsto (u(t, .), \partial_t u(t, .))$ is continuous in the topology of $H^{s+1} \times H^s$ uniformly on $t \in [0, T]$.

In order to estimate the maximum existence time T^* of such a solution, we use *a priori* estimates leading to introduce the following energy:

Definition 2 We define for $N \in \mathbb{N}$

$$E_N[u](t) = \|\nabla u(t)\|_{H^N}^2 + \sum_{i=1}^{N+1} \|\partial_t^i u(t)\|_{H^{N+1-i}}^2.$$

Theorem 3 Let $\nu = 0$. For $N \geq N_0 = [\frac{n}{2} + 2]$ there exist constants $C_n > 0$ and $C_{N_0} > 0$ such that for any $u_0 \in H^{N+1}(\mathbb{R}^n)$ and $u_1 \in H^N(\mathbb{R}^n)$, satisfying $\sqrt{E_N[u](0)} \leq \frac{C_n c^2}{(\gamma-1)\varepsilon}$, on an interval $[0, T^*]$ with $T^* \geq \frac{C_{N_0}}{\varepsilon \sqrt{E_{N_0}[u](0)}}$ there exists a unique solution $u \in X \cap C^{N+1}([0, T^*], L^2(\mathbb{R}^n))$ of the problem (1) with $E_N[u](t) \leq C < +\infty$.

For $n \geq 4$ the methods used in Ref. [4] allow us to obtain $T^* = +\infty$ for a new energy:

Definition 4 For $\mu = \frac{1}{2}(n^2+3n+2)$, let $\Gamma_1, \dots, \Gamma_\mu$ be the generalized derivatives (see [4]), which are the generators of the group of linear transformations preserving the homogeneous waves equation. Then, with the notation

$$\begin{aligned} \Gamma^A &= (\Gamma_0)^{A_0} \dots (\Gamma_\mu)^{A_\mu} \text{ for a multi-index} \\ A &= (A_0, \dots, A_\mu), \text{ we define for } N \in \mathbb{N} \\ E_{1,N}[u](t) &= \sum_{|A| \leq N} (\|\Gamma^A \partial_t u\|_{L^2}^2 + \|\Gamma^A \nabla u\|_{L^2}^2)(t). \end{aligned}$$

Theorem 5 Let $N \geq N_1 = n + 9$, and $\nu = 0$. For all $u_0 \in H^{N+1}(\mathbb{R}^n)$ and $u_1 \in H^N(\mathbb{R}^n)$, such that by Theorem 1 there exists a unique solution $u \in X$ of the problem (1), the energy $E_{1,N}[u](0) < \infty$ is well-defined. Then there exists $\rho_N > 0$ such that if $\sqrt{E_{1,N}[u](0)} < \varepsilon \rho_N$, then for $n = 2$ there exists $C_2 > 0$ such that $T^* \geq \frac{C_2}{\varepsilon^2}$; for $n = 3$ there exists $C_3 > 0$ such that $T^* \geq C_3 \exp(\varepsilon^{-1})$; for $n \geq 4$, $T^* = \infty$ and the global solution u is such that

$$\forall t \in \mathbb{R}^+, \quad E_{1,N}[u](t) \leq C < +\infty.$$

Actually, S. Alinhac in Ref. [1] proved the blow-up of $\|u_{tt}\|_{L^\infty}$ at such T^* for $n = 2$ and $n = 3$.

Well-posedness for the viscous case

Firstly, we show the local well-posedness in \mathbb{R}^n .

Theorem 6 *Let $T > 0$ and $N \geq [\frac{n}{2} + 3]$. If $u_0 \in H^N(\mathbb{R}^n)$ and $u_1 \in H^N(\mathbb{R}^n)$, then there exists $\rho > 0$ such that if $\|u_0\|_{H^N} + \|u_1\|_{H^N} < \rho$, the problem (1) admits a unique solution $u \in Y_N = H^2(0, T; H^{N-2}(\mathbb{R}^n)) \cap H^1(0, T; H^N(\mathbb{R}^n))$.*

Now, we extend the local existence to a global well-posedness.

Definition 7 *For an even $N \in \mathbb{N}$ we define*

$$E_{2,N}[u](t) = \|\nabla u(t)\|_N^2 + \sum_{i=1}^{\frac{N}{2}+1} \|\partial_t^i u(t)\|_{H^{N-2(i-1)}}^2.$$

Theorem 8 *Let $N \in \mathbb{N}$ be even and $N \geq [\frac{n}{2} + 3]$. For $u_0 \in H^{N+1}(\mathbb{R}^n)$ and $u_1 \in H^N(\mathbb{R}^n)$, satisfying the condition of Theorem 6, there exists a unique solution $u \in Y_N$ of the problem (1) and the energy $E_{2,N}[u](0) < \infty$ is well-defined. Then there exists $\rho > 0$ such that $E_{2,N}[u](0) \leq \rho$ implies that the solution u is global with $\forall t \in \mathbb{R}^+, E_{2,N}[u](t) \leq C < +\infty$.*

Approximation of the solutions of the isentropic Navier-Stokes system

Knowing that the Kuznetsov equation can be derived from the following compressible isentropic Navier-Stokes system [5]:

$$\begin{aligned} F(\rho_\varepsilon, v_\varepsilon) &\equiv \partial_t \rho_\varepsilon + \operatorname{div}(\rho_\varepsilon v_\varepsilon) = \varepsilon \frac{\rho_0}{c^2} \left[\partial_t^2 u - c^2 \Delta u \right. \\ &\quad \left. - \varepsilon \partial_t \left((\nabla u)^2 + \frac{\gamma-1}{2c^2} (\partial_t u)^2 + \frac{\nu}{\rho_0} \Delta u \right) \right] + \varepsilon^3 R_1 = 0, \\ G(\rho_\varepsilon, v_\varepsilon) &\equiv \rho_\varepsilon [\partial_t v_\varepsilon + (v_\varepsilon \cdot \nabla) v_\varepsilon] + \nabla p(\rho_\varepsilon) - \varepsilon \nu \Delta v_\varepsilon \\ &= \varepsilon \nabla \left[\rho_1 - \frac{\rho_0}{c^2} \partial_t u \right] + \varepsilon^2 \nabla \left[c^2 \rho_2 + \frac{\rho_0(\gamma-2)}{2c^2} (\partial_t u)^2 \right. \\ &\quad \left. + \frac{\rho_0}{2} (\nabla u)^2 + \nu \Delta u \right] + \varepsilon^3 \vec{R}_2 = 0, \end{aligned}$$

with $p(\rho_\varepsilon) = p_0 + c^2(\rho_\varepsilon - \rho_0) + \frac{(\gamma-1)c^2}{2\rho_0}(\rho_\varepsilon - \rho_0)^2$, using the ansatz

$$\begin{cases} \rho_\varepsilon(x, t) = \rho_0 + \varepsilon \rho_1(x, t) + \varepsilon^2 \rho_2(x, t), \\ v_\varepsilon(x, t) = -\varepsilon \nabla u(x, t), \end{cases}$$

we calculate the remainder terms R_1 and \vec{R}_2 . If u is a solution of Eq. (1), then all terms of the order less than 3 on ε are equal to 0, and we obtain the approximated system $F(\bar{\rho}_\varepsilon, \bar{v}_\varepsilon) = \varepsilon^3 R_1$ and $G(\bar{\rho}_\varepsilon, \bar{v}_\varepsilon) = \varepsilon^3 \vec{R}_2$. Denoting respectively by $U_\varepsilon = (\rho_\varepsilon, \rho_\varepsilon v_\varepsilon)^t$ and $\bar{U}_\varepsilon = (\bar{\rho}_\varepsilon, \bar{\rho}_\varepsilon \bar{v}_\varepsilon)^t$ solutions of the exact and the approximated Navier-Stokes systems, we consider the case $n = 3$,

when the Navier-Stokes system is globally well-posed [6]. Knowing the existence results for the two problems, we validate the approximation of U_ε by \bar{U}_ε following [7].

Theorem 9 *Let $n = 3$. For $u_0 \in H^5(\mathbb{R}^3)$, $u_1 \in H^4(\mathbb{R}^3)$, and $\bar{U}_\varepsilon(0) = U_\varepsilon(0)$, there exists $k > 0$ such that $\|u_0\|_{H^5} + \|u_1\|_{H^4} < k$ implies the global existence of U_ε and \bar{U}_ε . Moreover, there exists $C_1 > 0$, $C_2 > 0$ such that for all $t \leq \frac{C_1}{\varepsilon} \ln(\frac{1}{\varepsilon})$ $\|(U_\varepsilon - \bar{U}_\varepsilon)(t)\|_{L^2} \leq C_2 \varepsilon$.*

References

- [1] S. Alinhac, A minicourse on global existence and blowup of classical solutions to multidimensional quasilinear wave equations, in *Équations aux Dérivées Partielles*, Univ. Nantes (2003) Exp. No. I, 33.
- [2] R. Ikehata, and G. Todorova, and B. Yordanov, Wave equations with strong damping in Hilbert spaces, in *J. Differential Equations* **254** (2013), pp 3352–3368.
- [3] T.J.R. Hughes, and T. Kato, and J.E Marsden, Well-posed quasi-linear second order hyperbolic systems with applications to nonlinear elastodynamics and general relativity, in *Arch. Rational Mech. Anal.* **63** (1977), pp 273–294.
- [4] F. John, *Nonlinear wave equations, formation of singularities* Vol. 2, AMS, Providence, RI, 1990.
- [5] A. Rozanova-Pierrat, Approximation of a compressible Navier-Stokes system by non-linear acoustical models, in *Proc. of the Int. Conference "Days on Diffraction 2015", St. Petersburg, Russia* pp 270–276.
- [6] A. Matsumura, and T. Nishida, The initial value problem for the equations of motion of viscous and heat-conductive gases, in *J. Math. Kyoto Univ.* **20** (1980), pp 67–104.
- [7] A. Rozanova-Pierrat, On the Derivation and Validation of the Khokhlov-Zabolotskaya-Kuznetsov (KZK) Equation for Viscous and Nonviscous Thermoelastic Media, in *Commun. Math. Sci.*, **7**, No. 3, (2009), pp. 679–718.

On the Local Approximate Rank of Helmholtz Green's Kernel

ABBOUD Toufic¹, DELAMOTTE Kieran^{1,*}, LAFITTE Olivier²

¹IMACS, XTEC, École Polytechnique, 91128 Palaiseau CEDEX, FRANCE

²Institut Galilée, Université Paris 13, 99 av. Jean-Baptiste Clément, 93430 Villetaneuse, FRANCE

*Email: delamotte@imacs.polytechnique.fr

Abstract

Keywords: \mathcal{H} -matrices, Directional approximation, Helmholtz kernel

1 \mathcal{H} -matrices

We seek an efficient approximation of a BEM discretization matrix whose coefficients are

$$M_{ij} = \int_{\Gamma} \int_{\Gamma} G(x, y) \Phi_i^t(x) \Phi_j(y) d\Gamma(x) d\Gamma(y),$$

where $G(x, y)$ is the Helmholtz kernel, Φ_i^t and Φ_j are test and basis functions. The \mathcal{H} -matrix method [1] is based on the low-rank approximation of a block representing far-field interactions i.e. whenever $x \in B_s$ and $y \in B_t$ are sufficiently separated. For the Laplace kernel, Hackbusch has introduced the following admissibility condition $\min(\text{diam}(B_t), \text{diam}(B_s)) \leq \eta \text{dist}(B_t, B_s)$.

Based on the geometric distance, the clustering regroups the unknowns as a binary tree. A matrix partition is obtained with the block-clustering step which is the product of two cluster trees for rows and columns. The admissibility condition acts then as a stopping criterion in the block clustering recursion and produces low-rank subblocks. Computing the low-rank approximation is known as the compression step and can be done either algebraically or analytically. The HCA-2 method from [2] is a reliable and efficient method to compress an admissible block with a 3D-interpolation scheme.

2 Kernel expansion

Let \mathbb{S}_X and \mathbb{S}_Y be two spheres of diameter D spaced apart from one another by a distance of R . Let u_3 be the unit vector defining the direction of the spheres centers and (u_1, u_2, u_3) an orthonormal basis of \mathbb{R}^3 . In this basis the Helmholtz kernel reads as

$$G(x, y) = \frac{e^{ikR}}{|x - y|} e^{ik(x_3 - y_3)} e^{ik \frac{[(x_1 - y_1)^2 + (x_2 - y_2)^2]}{2R}} e^{i\Phi},$$

with $\Phi = \mathcal{O}(k \frac{D^3}{R^2})$.

One remarks that this expression is composed of three different parts. The first part is a Laplace term that is well known from the \mathcal{H} -matrix literature and is associated with the previous static condition $D/R \leq \text{cst}$. The second part is the plane wave terms of unit rank used to approximate the oscillating part of the kernel through the Fraunhofer condition:

$$(kD) \frac{D}{R} \leq \text{cst}. \quad (1)$$

The condition (1) gives a frequency-independent rank but is too restrictive for big radii. Our contribution is to describe the oscillating part with the second order term which is a tensor product in the transverse directions u_1 and u_2 only. Oscillations in the u_3 direction are caught thanks to the plane waves and the Fresnel condition is:

$$\sqrt{kD} \frac{D}{R} \leq \text{cst}. \quad (2)$$

Whenever (2) is satisfied the distance R is smaller than in the Fraunhofer case for a fixed diameter D and the rank is still small. The dominant term of the phase is the second order one which is a product of two 1D Fourier operators (up to conjugation). The rank of the Helmholtz kernel in the Fresnel admissibility zone is bounded by the product of the ranks of each 1D operator.

3 A rank estimate

We define the normalized Fresnel (or Fox-Li) operator by:

$$F_c : \lambda \mapsto [F_c \lambda](x) = \int_{-1}^1 e^{icxt} \lambda(t) dt, \quad x \in [-1, 1]$$

where $c > 0$ is called the bandwidth. This operator has been studied extensively in several scientific areas such as laser theory or signal theory mostly by Slepian, Pollak and Landau in the 1960's (see for instance [3]).

The singular values of F_c are the eigenvalues of $F_c^* F_c$ so we define the self-adjoint and

compact operator $Q_c = \frac{c}{2\pi}[F_c^* F_c]$ and remark that

$$[Q_c \phi](x) = \frac{1}{\pi} \int_{-1}^1 \frac{\sin(c(x-t))}{(x-t)} \phi(t) dt.$$

This integral operator acts as a low-pass filter and the normalization ensures that the eigenvalues are positive and smaller than one. The following result from Landau and Widom [4] links the spectrum of Q_c to the bandwidth c .

Theorem 1 (Landau-Widom) *For all $c > 0$ and $0 < \alpha < 1$, $N(c, \alpha)$ is the number of eigenvalues of Q_c larger than α . It holds,*

$$N(c, \alpha) = \frac{2c}{\pi} + \frac{1}{\pi^2} \log\left(\frac{1-\alpha}{\alpha}\right) \log(c) + o(\log(c))$$

Applying this result to the approximation of the Helmholtz kernel with $\alpha = \varepsilon^2$ gives the ε -rank of F_c :

$$\varepsilon - \text{rank}(F_c) \simeq \frac{2c}{\pi} + \frac{2}{\pi^2} |\log(\varepsilon)| \log(c), \quad (3)$$

where $c = kD^2/4R$. In the static admissibility zone the bandwidth in each transverse direction u_1, u_2 is $c = \mathcal{O}(kD)$ whereas $c = \mathcal{O}(\sqrt{kD})$ in the Fresnel zone. The rank of the Helmholtz kernel is eventually at most linear with the frequency in the Fresnel zone for a non-planar 3D geometry. Plus, the numerical rank estimate (3) gives a good interpolation order in each transverse direction for a HCA-2 scheme. The interpolation order in the longitudinal direction is independent of the frequency as oscillations are described by the plane wave terms. That results in a robust and reliable HCA-2 type algorithm ensuring a compressed precision-controlled assembly of a Fresnel-admissible block.

4 Numerical results

We test the interaction of two opposing plates with a maximal and non-planar cross-section. The memory needed for the \mathcal{H} -matrix approximation is represented for the static and Fresnel criteria according to the frequency. As predicted by (3) the Fresnel condition ensures a linear growth whereas the Hackbusch static one leads to a quadratic growth.

References

- [1] W. Hackbusch, A Sparse Matrix Arithmetic Based on H-Matrices Part I., in *Computing*, **62** (1999), pp. 89–108.

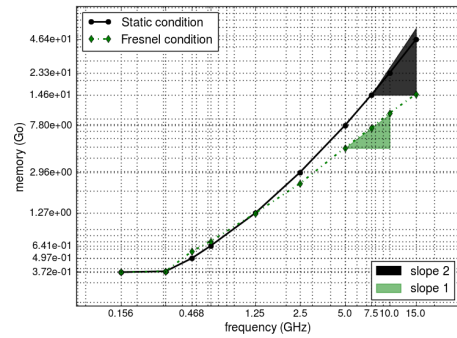


Figure 1: Memory growth (logscale) for different admissibility conditions.

- [2] S. Börm and L. Grasedyck, Hybrid Cross Approximation for Integral Operators, in *Numerische Mathematik*, (2005).
- [3] D. Slepian and H. O. Pollak, Prolate Spheroidal Wave Functions, Fourier Analysis and Uncertainty-I, in *The Bell System Technical Journal*, (1961).
- [4] H. J. Landau and H. Widom, Eigenvalue Distribution of Time and Frequency Limiting, in *Journal of Mathematical Analysis and Applications*, **77** (1980), pp. 469–481.

On DGTD-Lawson exponential time integrators for time-domain electromagnetics

Stéphane Descombes^{1,*}, Stéphane Lanteri², Hao Wang³, Li Xu³, Bin Li³

¹Université Côte d'Azur, CNRS, Inria, LJAD, France

²Université Côte d'Azur, Inria, CNRS, LJAD, France

³School of Physical Electronics, UESTC, China

*Email: stephane.descombes@univ-cotedazur.fr

Abstract

The objective of this work is to design an efficient and accurate time integration strategy based on exponential integrators and explicit time advancing schemes for the system of time-domain Maxwell equations discretized in space with a high order discontinuous Galerkin scheme formulated on locally refined unstructured meshes.

Keywords: Maxwell's equations, discontinuous Galerkin time-domain method, Lawson methods

1 Introduction

For electromagnetic problems with heterogeneous media or complex geometries, adaptive mesh refinement is an attractive technique for the efficient numerical solution of Maxwell's equations. Local mesh refinement however imposes a severe stability constraint on explicit time integration since the maximal time step is determined by the smallest elements in the mesh. A first natural way to limit the impact of this problem is to use a multi-level local time-stepping approach like the one proposed in [1] and a second is to adopt an unconditional implicit time integration. This last approach is very expensive and even infeasible, especially in 3D, since a large global matrix system needs to be solved in each time step. To overcome this resource consumption, various implicit-explicit (IMEX) schemes have been proposed by Piperno [2] or Descombes, Lanteri and Moya [3, 4] (based on the work of Verwer [5]) where implicit schemes are used only for the small refined elements and efficient explicit schemes are used for the remaining elements. These schemes combine unconditional stability properties with ability to produce a very accurate solution even for relatively large time step sizes but are limited so far to order 2. In this work, a new family of IMEX scheme based on exponential time integration is designed for the 3D time-domain Maxwell's

equations discretized by a high order discontinuous Galerkin (DG) scheme formulated on locally refined unstructured meshes.

We consider the system of 3D time-domain Maxwell's equations on a bounded polyhedral domain $\Omega \subset \mathbb{R}^3$

$$\begin{cases} \varepsilon \partial_t \mathcal{E} - \mathbf{curl} \mathcal{H} = 0, & \text{in } \Omega \times [0, T], \\ \mu \partial_t \mathcal{H} + \mathbf{curl} \mathcal{E} = 0, & \text{in } \Omega \times [0, T], \end{cases} \quad (1)$$

where T is the final time, $\mathcal{E}(\mathbf{x}, t)$ and $\mathcal{H}(\mathbf{x}, t)$ are the electric and magnetic fields, ε and μ are the dielectric permittivity and the magnetic permeability. The boundary of Ω is defined as $\partial\Omega = \Gamma_m \cup \Gamma_a$ with $\Gamma_m \cap \Gamma_a = \emptyset$. Introducing $(\mathcal{E}^{\text{inc}}, \mathcal{H}^{\text{inc}})$ a given incident field, the boundary conditions are chosen as

$$\begin{cases} \mathbf{n} \times \mathcal{E} = 0, & \text{on } \Gamma_m \times [0, T], \\ \mathbf{n} \times \mathcal{E} + \sqrt{\frac{\mu}{\varepsilon}} \mathbf{n} \times (\mathbf{n} \times \mathcal{H}) = \mathbf{g}^{\text{inc}}, & \text{on } \Gamma_a \times [0, T], \end{cases} \quad (2)$$

where \mathbf{n} denotes the unit outward normal to $\partial\Omega$ and

$$\mathbf{g}^{\text{inc}} = \mathbf{n} \times \mathcal{E}^{\text{inc}} + \sqrt{\frac{\mu}{\varepsilon}} \mathbf{n} \times (\mathbf{n} \times \mathcal{H}^{\text{inc}})$$

Finally, the system is supplemented with initial conditions: $\mathcal{E}_0(\mathbf{x}) = \mathcal{E}(\mathbf{x}, 0)$ and $\mathcal{H}_0(\mathbf{x}) = \mathcal{H}(\mathbf{x}, 0)$. After a discretization in space by a DG method the global semi-discrete system is usually rewritten as

$$\begin{cases} \partial_t \mathbf{E} = \mathbf{M}^{-\varepsilon} \mathbf{K} \mathbf{H}, \\ \partial_t \mathbf{H} = -\mathbf{M}^{-\mu} \mathbf{K} \mathbf{E}. \end{cases} \quad (3)$$

Gathering electric and magnetic unknowns in a single vector, we can rewrite the global semi-discrete system (3) as follows

$$\partial_t \mathbf{U} = \mathbf{A} \mathbf{B} \mathbf{U}, \quad (4)$$

where

$$\mathbf{U} = \begin{pmatrix} \mathbf{E} \\ \mathbf{H} \end{pmatrix}, \quad \mathbf{A} = \begin{pmatrix} \mathbf{M}^{-\varepsilon} & 0 \\ 0 & \mathbf{M}^{-\mu} \end{pmatrix}$$

and

$$\mathbb{B} = \begin{pmatrix} 0 & \mathbb{K} \\ -\mathbb{K} & 0 \end{pmatrix}.$$

Let $\mathbb{C} = \mathbb{A}\mathbb{B}$, we have

$$\partial_t \mathbf{U} = \mathbb{C}\mathbf{U},$$

we outline below the Lawson [6] procedure in the particular context that we aim at considering in this study. We split the unknowns according to the decomposition of the mesh

$$\mathbf{U} = \mathbb{P}\mathbf{U} + (\mathbb{I} - \mathbb{P})\mathbf{U},$$

where \mathbb{P} is a diagonal matrix with diagonal entries equal to zero or one, to identify the unknowns associated with the locally refined region; \mathbb{I} is the identity matrix. Introducing

$$\mathbb{C}_f = \mathbb{C}\mathbb{P}, \quad \mathbb{C}_c = \mathbb{C}(\mathbb{I} - \mathbb{P}),$$

we have

$$\partial_t \mathbf{U} = \mathbb{C}_f \mathbf{U} + \mathbb{C}_c \mathbf{U}. \quad (5)$$

Let

$$\mathbf{V}(t) = e^{-t\mathbb{C}_f} \mathbf{U}(t),$$

we have

$$\partial_t \mathbf{V} = e^{-t\mathbb{C}_f} \mathbb{C}_c e^{t\mathbb{C}_f} \mathbf{V} = f(t, \mathbf{V}(t)). \quad (6)$$

The transformed system (6) can be integrated in time using an explicit Runge-Kutta scheme or another high order accurate explicit time integration technique. The result is then back transformed to provide an approximation in the \mathbf{U} variable. For example we obtain for the forward Euler scheme

$$\begin{aligned} \mathbf{U}_{n+1} &= e^{\Delta t \mathbb{C}_f} \mathbf{U}_n + \Delta t e^{\Delta t \mathbb{C}_f} \mathbb{C}_c \mathbf{U}_n \\ &= e^{\Delta t \mathbb{C}_f} [\mathbf{U}_n + \Delta t \mathbb{C}_c \mathbf{U}_n]. \end{aligned} \quad (7)$$

We use in this work other explicit schemes of several orders and show how to compute quickly the exponential of the matrix. Numerical simulations show the efficiency of these methods comparing to classical schemes.

References

- [1] J. Diaz, M. Grote, Multi-level explicit local time-stepping methods for second-order wave equations. *Comput. Methods Appl. Mech. Engrg.* **291** (2015), 240–265.
- [2] S. Piperno, Symplectic local time-stepping in non-dissipative DGTD methods applied to wave propagation problems, *M2AN Math. Model. Numer. Anal.* **40** (2006), no. 5, 815–841 (2007).
- [3] S. Descombes, S. Lanteri, L. Moya, Locally implicit time integration strategies in a discontinuous Galerkin method for Maxwell's equations, *J. Sci. Comput.* **56** (2013), no. 1, 190–218.
- [4] S. Descombes, S. Lanteri, L. Moya, Locally implicit discontinuous Galerkin time domain method for electromagnetic wave propagation in dispersive media applied to numerical dosimetry in biological tissues. *SIAM J. Sci. Comput.* **38** (2016), no. 5, A2611–A2633.
- [5] J. Verwer, Component splitting for semi-discrete Maxwell equations. *BIT* **51** (2011), no. 2, 427–445.
- [6] J.D. Lawson, Generalized Runge-Kutta processes for stable systems with large Lipschitz constants. *SIAM J. Numer. Anal.* **4** (1967) 372–380.

E.M. waves in magnetic plasmas

Martin Campos-Pinto^{1,*}, Bruno Després^{2,*}

¹CNRS, UMR 7598, Laboratoire Jacques-Louis Lions, F-75005, Paris, France

²Sorbonne Universités, UPMC Univ Paris 06, UMR 7598, LJLL, F-75005, Paris, France and Institut universitaire de France (IUF)

*Email: despres@ann.jussieu.fr

Abstract

Time harmonic waves in plasmas receive increasing interests [16] due to their scientific importance for the heating of magnetic fusion plasma [11]. Recent progresses are reported on the development of a convenient mathematical theory for time harmonic waves in plasmas near the hybrid resonance. After presenting the cold-plasma dielectric tensor, a basic analytic solution is constructed that captures the essential singularity of the problem. This information is used to construct manufactured solutions in the context of the limit absorption principle. Manufactured solutions have the ability to capture the singular limit in a non singular way. Numerical applications are shown in the companion paper [12]. In dimension two, manufactured solutions exhibit an additional highly oscillating behavior. The modeling of non linear boundary conditions is evoked.

Keywords: Maxwell equations, magnetic plasma, cold plasma tensor.

1 Introduction

Let $\Omega \subset \mathbb{R}^d$ be a bounded domain in dimension $1 \leq d \leq 3$. The boundary $\Gamma = \partial\Omega$ is smooth with outgoing normal $\mathbf{n} = \mathbf{n}(\mathbf{x})$ for $\mathbf{x} \in \Gamma$. The generic model problem consists of the time harmonic ($\partial_t = -i\omega$, $i^2 = -1$) Maxwell equations with a non standard dielectric tensor

$$\nabla \times \nabla \times \mathbf{E} - \underline{\varepsilon} \mathbf{E} = 0, \quad \mathbf{x} \in \Omega$$

plus a boundary condition which is supposed to be a standard dissipative one. With an abuse of notation $\mathbf{B} = \nabla \times \mathbf{E}$ will be called the magnetic field. The mathematical theory is comprehensive for standard dielectric tensors [10, 13] and for coercive equations [4]. Our interest is in non standard differentiable dielectric tensors coming from the physics [15] $\underline{\varepsilon} = \underline{\varepsilon}^* \in [W^{q,\infty}(\Omega)]^{3 \times 3}$ with $q \geq 1$. An example is the cold plasma tensor [1, 3, 9] which models the coupling with a

density of electrons inside a bulk magnetic field \mathbf{B}_0 as in Tokamaks [11]

$$\underline{\varepsilon}(\nu) = \begin{pmatrix} 1 - \frac{\tilde{\omega}\omega_p^2}{\omega(\tilde{\omega}^2 - \omega_c^2)} & i\frac{\omega_c\omega_p^2}{\omega(\tilde{\omega}^2 - \omega_c^2)} & 0 \\ -i\frac{\omega_c\omega_p^2}{\omega(\tilde{\omega}^2 - \omega_c^2)} & 1 - \frac{\tilde{\omega}\omega_p^2}{\omega(\tilde{\omega}^2 - \omega_c^2)} & 0 \\ 0 & 0 & 1 - \frac{\omega_p^2}{\omega\tilde{\omega}} \end{pmatrix}. \quad (1)$$

The parameters of the dielectric tensor are the frequency shifted in the complex plane $\tilde{\omega} = \omega + i\nu$, the cyclotron frequency $\omega_c = \frac{e|\mathbf{B}_0|}{m_e}$ and the plasma frequency $\omega_p = \sqrt{\frac{e^2 N_e}{\epsilon_0 m_e}}$ which depends on the electronic density N_e . The shift $\nu > 0$ is the friction of electrons over a bath of static ions. It can be very small in fusion plasmas. So it is justified to analyze the problem at the limit $\nu \rightarrow 0^+$ in the context of the limit absorption principle.

Convenient mathematical simplifications are possible. For example the hybrid resonance may be studied by considering only the 2×2 block diagonal part of $\underline{\varepsilon}(0)$, written ($\mathbf{x} = (x, y, z)$)

$$\underline{\varepsilon}(0) = \begin{pmatrix} \alpha(x) & i\delta(x) \\ -i\delta(x) & \alpha(x) \end{pmatrix} \in [C^\infty(\Omega)]^{2 \times 2}.$$

At $x = 0$, we note that the extra-diagonal part dominates the diagonal part. This is the X-mode or T.E. equations. For plasma parameters corresponding to $\alpha(x) = -x$ and $\delta(x) = \sqrt{1 - x/4 + x^2}$, and with $\nu = 0$, an elementary analytic solution is obtained which explains some of the main difficulties

$$\begin{aligned} \left\{ \begin{array}{lcl} B_3 & -(E_2)' & = 0, \\ xE_1 & -i\delta E_2 & = 0, \\ -B'_3 & +i\delta E_1 & +xE_2 = 0, \end{array} \right. \\ \iff \left\{ \begin{array}{lcl} B_3 & -E'_2 & = 0, \\ -B'_3 & +(1/4 - 1/x)E_2 & = 0, \\ & & \end{array} \right. \\ \iff -E''_2 + (1/4 - 1/x)E_2 = 0. \end{aligned} \quad (2)$$

The last equation is the Whittaker equation. The case with more general coefficients can be

addressed with confluent hypergeometric functions. But (2) has (miraculously) 2 simple analytical solutions. The first one is explicit

$$u(x) = xe^{-x/2}.$$

The second one is obtained through the variation of the constant $v(x) = u \int \frac{dx}{u^2}$

$$v(x) = e^{x/2} - \left(\log|x| + \int_1^x \frac{e^y - 1}{y} dy \right) xe^{-x/2}.$$

Therefore one can express the solution E_2 as a linear combination of u and v , but separately for $x < 0$ and for $x > 0$ because the equation is singular at the origin. One obtains $E_2 = au + bv \in C^0$, $B_3 = au' + bv' = -b\log|x| + \dots$ which shows a mild logarithmic singularity and

$$E_1 = i \frac{\sqrt{1 - x/4 + x^2}}{x} (au + bv) = ib \frac{1}{x} + \dots \quad (3)$$

which shows a strong singularity. Note that E_1 is even not integrable a priori (for $b \neq 0$).

In this context our strategy is to use the limit absorption principle to obtain a correct definition of the solution. On physical grounds, one takes $\tilde{\omega}$ instead of ω , as in (1). On mathematical grounds, it is sufficient to correct the dielectric tensor $\underline{\epsilon}(0)$ with a term $i\nu I$ (with I the identity matrix). A recent progress in this direction is [8] where singular integral techniques show that $E_1^+ = \lim_{0+} E_1^\nu$ is a Dirac mass plus a principal value. A simpler method proposed in [7] uses a stretching function and an eikonal equation. But unfortunately these theoretical techniques are restricted to dimension one, do not offer possibilities to investigate higher dimensions and explain nothing about the numerical approximation of such problems.

2 Manufactured solutions

An interesting question in view of the use of standard numerical methods is to develop a L^2 based approach which takes into account the singularity. A recent answer is based on manufactured solutions [6]. The idea of manufactured solution consists to define quasi-solutions which have the same singularity as the original problem, but which are easier to handle. Consider for example ($r = \alpha'(0) \neq 0$)

$$F_1^\nu = -\frac{1}{rx + i\nu}, \quad F_2^\nu = \frac{1}{\delta(0)}$$

and

$$C_3^\nu = -i \frac{\delta(0)}{r} \log(rx + i\nu)$$

where \log denotes the principal value of the logarithm in the complex plane. Let us define

$$\begin{cases} C_3^\nu - (F_2^\nu)' &= q_3^\nu, \\ -(\alpha + i\nu)F_1^\nu - i\delta F_2^\nu &= g_1^\nu, \\ -(C_3^\nu)' - i\delta F_1 + (\alpha(x) + i\nu)F_2 &= g_2^\nu. \end{cases}$$

One can check that $q_3^\nu \in L_{\text{loc}}^2(\mathbb{R})$ and $g_2^\nu \in L_{\text{loc}}^2(\mathbb{R})$ with bounds uniform with respect to ν . One has

$$g_1^\nu = \frac{\alpha(x) + i\nu}{rx + i\nu} - \delta(x).$$

Define the spaces $L_{1/x}^2(\Omega) = \{u \mid \frac{1}{x}u \in L^2(\Omega)\}$ and $L_x^2(\Omega) = \{u \mid xu \in L^2(\Omega)\}$. In view (3), we should take $E_1^+ \in L_x^2(\Omega)$. The function g_1^ν admits a limit in $L_{1/x}^2(\Omega)$ as ν tends to zero. Indeed

$$g_1^\nu = \left(\frac{\alpha + i\nu}{rx + i\nu} - 1 \right) - \left(\frac{\delta}{\delta(0)} - 1 \right).$$

Both terms are in $L_{1/x}^2(\Omega)$ with a uniform bound, and they admit a limit in $L_{1/x}^2(\Omega)$.

There is a Poynting-like equality which is

$$(E_2^\nu C_3^\nu - F_2^\nu B_3^\nu)' = B_3^\nu q_3^\nu - E_1^\nu g_1^\nu - E_2^\nu g_2^\nu$$

where all products are composed of terms which are naturally in dual spaces. Therefore one can pass to the limit and obtain formally the integral relation

$$\begin{aligned} & \int_{\Omega} (F_2^+ B_3^+ - E_2^+ C_3^+) \varphi' dx \quad (4) \\ &= \int_{\Omega} (B_3^+ q_3^+ - E_1^+ g_1^+ - E_2^+ g_2^+) \varphi dx. \end{aligned}$$

The central term in the right hand side can also be written as $\int_{\Omega} (xE_1^+) (\frac{1}{x}g_1^+) \varphi dx$ where both terms between parentheses are in $L^2(\Omega)$. We define the space $H_{0,0}^1(\Omega) = \{u \in H_0^1(\Omega), u(0) = 0\}$ and consider the problem below.

Problem 1 Find $(e_1, e_2, b_3) \in L_x^2(\Omega) \times L^2(\Omega) \times L^2(\Omega)$ which satisfy three conditions:

i) they satisfy the weak formulations

$$\begin{cases} \int_{\Omega} (b_3 \varphi_1 + e_2 \varphi'_1) dx = 0, & \forall \varphi_1 \in H_0^1(\Omega), \\ \int_{\Omega} (\alpha e_1 + i\delta e_2) \phi dx = 0, & \forall \phi \in L^2(\Omega), \\ \int_{\Omega} (b_3 \varphi'_2 + i\delta e_1 \varphi_2 - \alpha e_2 \varphi_2) dx = 0, \\ & \forall \varphi_2 \in H_{0,0}^1(\Omega), \end{cases}$$

- ii) they satisfy dissipative boundary conditions in the sense of distributions,
- iii) they satisfy the integral relation (4) for one test function $\varphi \in H_0^1(\Omega)$ with $\varphi(0) \neq 0$.

The fundamental result which explains the interest of this formalization is the following.

Theorem 1 (Refer to [6]) *There exists a unique (e_1, e_2, b_3) solution to Problem 1 and it coincides with the limit solution (E_1^+, E_2^+, B_3^+) obtained with the limit absorption principle.*

This result admits various variants and has been used to design efficient numerical methods.

3 Singularities in multi dimensions

It is possible to develop the theory of manufactured solutions in higher dimension. The singularity appears to be in some cases "more singular" than in the one-dimensional case. One gets

$$F_1^+(x, y) = \left(\frac{1}{r(y)x} \right) (r(y)x + i0^+)^{i\sigma'(y)}$$

where $\alpha(0, y) = 0$, $r(y) = \partial_x \alpha(0, y) \neq 0$ and $\sigma(y) = \delta(0, y)$. In case $\sigma'(y) \neq 0$, it shows oscillations in the direction tangential to the line of resonance. This is illustrated in Figure 1.

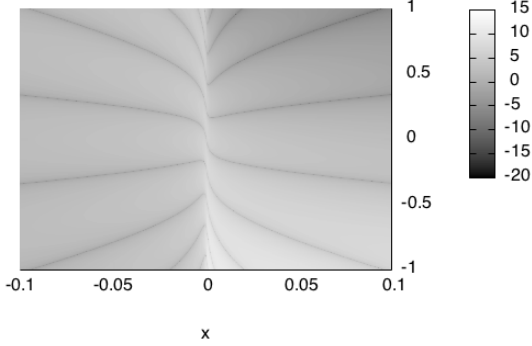


Figure 1: Logarithm of $|\text{real } F_1^+(x, y)|$, with $\alpha(x, y) = -x$ and $\delta(x, y) = y^2 + 1$.

4 An open problem: sheath boundary conditions

Usual boundary conditions at metallic wall are modified in a plasma due to sheaths [5,14] and it completely changes the mathematical structure. A sheath is a boundary layer where a charge

imbalance arises and the models become non-linear. This phenomenon is observed in standard plasmas. We refer to [2] for a recent study at the microscopic scale. It is challenging to derive an equivalent sheath condition for macroscopic modeling in electromagnetic numerical codes. This topic is the subject of continuous and recent research in the plasma physics community and has not received enough mathematical attention. A typical example is the following. It writes with non dimensional variables

$$\begin{cases} \pm \partial_n E + \Delta_\Gamma V = 0, \\ E = \mp \frac{V}{V_0^{\frac{3}{4}}}, \\ V_0 = V_f + \log I_0(|V|). \end{cases}$$

where E is the normal part of the electric field (aligned with the bulk magnetic field), $\Delta_\Gamma V$ is the Laplace-Beltrami operator applied to V , V_f is the sheath potential (given in tables, see also [2]), $I_0(z) = \frac{1}{\pi} \int_0^\pi e^{z \cos \theta} d\theta \leq 1$ is the modified Bessel function or zeroth order and $\log I_0(|V|)$ is the time harmonic rectification. This local model corresponds to a local vanishing conduction current. In the limit where V is asymptotically large, one has $I_0(z) \approx \frac{e^z}{\sqrt{2\pi z}}$ for $z \gg 1$. It yields a non linear boundary condition

$$\partial_n E - \Delta_\Gamma |E|^3 E = 0, \quad x \in \Gamma.$$

The mathematical theory of time Maxwell equations with such non linear boundary conditions is completely open.

References

- [1] A. Back, T. Hattori, S. Labrunie, J.R. Roche, P. Bertrand. Electromagnetic wave propagation and absorption in magnetised plasmas: variational formulations and domain decomposition. *ESAIM: M2AN* 49 (2015) 1239-1260.
- [2] M. Badsi, M. Campos-Pinto and B. Després, A minimization formulation of a bi-kinteic sheath, *Kinetic and Related Models*, AIMS, 2016, 9 (4).
- [3] F.F. Chen and R.B. White. Amplification and Absorption of Electromagnetic Waves in Overdense Plasmas, *Plasma Phys.* 16565 (1974); anthologized in *Laser Interaction with Matter, Series of Selected Papers in Physics*, ed. by C. Yamanaka, *Phys. Soc. Japan*, 1984

- [4] P. G. Ciarlet, Linear and Nonlinear Functional Analysis with Applications, SIAM, 2013.
- [5] L. Colas and al, Self-consistent radio-frequency wave propagation and peripheral direct current plasma biasing: Simplified three dimensional non-linear treatment in the "wide sheet" asymptotic regime, *Phys. Plasmas* 19, 092505 (2012).
- [6] B. Després and M. Campos-Pinto, Constructive formulations of resonant Maxwell's equations, to appear in Siam Journal Math. Anal., preprint online at <https://hal.archives-ouvertes.fr/hal-01278860/document>.
- [7] B. Després, L.-M. Imbert-Gérard and O. Lafitte, Solutions to the cold plasma model at resonances 4 (2017), 177-222 .
- [8] B. Després, L.-M. Imbert-Gérard and R. Weder, Hybrid resonance of Maxwell's equations in slab geometry, Volume 101, Issue 5, 2014, p. 623-659.
- [9] J. P. Freidberg, Plasma physics and fusion energy, Cambridge university press, 2007.
- [10] R. Hiptmair, A. Moiola and I. Perugia, Stability results for the time-harmonic Maxwell equations with impedance boundary conditions. *Math. Models Methods Appl. Sci.*, 21 (2011), no. 11, 2263-2287.
- [11] Iter international web page on "Plasma Heating", <https://www.iter.org/sci/plasmaheating>.
- [12] A. Nicolopoulos, B. Després, M. Campos-Pinto, Singular solutions of cold plasma Maxwell's equations, Waves 2017.
- [13] P. Monk, Finite element methods for Maxwell's equations. Numerical Mathematics and Scientific Computation. Oxford University Press, New York, 2003.
- [14] J.R. Myra and D.A. D'Ippolito, Slow wave propagation and sheath interaction in the ion-cyclotron frequency range, *Plasma Phys. Control Fus.*, 52, 015003, 2010.
- [15] D.G. Swanson, Plasma Waves, Bristol Philadelphia, Institute of Physics Pub., 2003.
- [16] Mini-symposium "Waves in Plasmas", Waves 2015, <http://waves2015.math.kit.edu/program-booklet.pdf>.

A combined Bayesian optimization-finite element approach for isoperimetric inequalities

Sebastian Dominguez^{1,*}, Nilima Nigam¹, Bobak Shahriari²

¹Department of Mathematics, Simon Fraser University, Burnaby, Canada

²Department of Computer Science, The University of British Columbia, Vancouver, Canada

*Email: domingue@sfu.ca

Abstract

The aim of this work is to introduce a novel numerical strategy to study problems arising in Spectral Geometry. We investigate a well-known conjecture by Pólya-Szegö [3] by combining numerical strategies to approximate the eigenvalues and to find local optima of them.

Keywords: Dirichlet eigenvalue problem, Finite Element method, Bayesian optimization.

1 Introduction

Pólya-Szegö [3] stated the following conjecture concerning the first eigenvalue of the Laplacian with Dirichlet boundary conditions: *Of all polygons of n sides with fixed area, the regular polygon of n sides has the smallest eigenvalue.* They also proved this conjecture for $n \in \{3, 4\}$ using Steiner symmetrization. However, to the best of our knowledge, no theoretical results have been shown for $n > 4$. To investigate this optimization problem, we combine the Finite element method (FEM) to approximate the eigenvalue of a given polygon and Bayesian optimization (BO) to find the critical points of this problem.

2 Optimization of Eigenvalues

For fixed $n \in \mathbb{N}$, let $\Omega \in \mathcal{P}_n$, with \mathcal{P}_n the collection of all polygons in \mathbb{R}^2 . Consider the Dirichlet eigenvalue problem: find $\lambda \in \mathbb{R}$ and $u \in H_0^1(\Omega)$, such that

$$-\Delta u = \lambda u \quad \text{in } \Omega, \quad u = 0 \quad \text{on } \partial\Omega. \quad (1)$$

Define the function $F(\Omega) := |\Omega|\lambda_1(\Omega)$, $\forall \Omega \in \mathcal{P}_n$. $|\Omega|$ denotes the area of Ω and $\lambda_1 = \lambda_1(\Omega)$ is the first eigenvalue of (1). We are interested in the following problem:

$$\operatorname{argmin}_{\Omega \in \mathcal{P}_n} F(\Omega). \quad (2)$$

The following result allows us to restrict domains in \mathcal{P}_n within a compact subset S of \mathbb{R}^2 .

Lemma 1 *Function F is invariant under rotations, translations and scalar factors.*

Although we can leverage these properties to simplify (2), the facts that we do not know a closed form for F and that F is expensive to evaluate make the optimization problem challenging. We apply the BO framework, which is designed to handle this type of problems.

3 Methods: FEM and BO

We use FEM to approximate the eigenvalues of (1). Let \mathcal{T}_h be a triangulation of $\bar{\Omega}$. A primal formulation of (1) reads: find $\lambda_h \in \mathbb{R}$ such that

$$(\nabla u_h, \nabla v_h)_\Omega = \lambda_h(u_h, v_h)_\Omega \quad \forall v_h \in H_h.$$

Here H_h is a finite dimensional space. Due to theoretical and computational restrictions within the FEM, we need to avoid some domains in \mathcal{P}_n . Here \mathcal{A}_n will denote the collection of domains in \mathcal{P}_n that are admissible (see Figure 1). Alternatively, we introduce a strategy to find

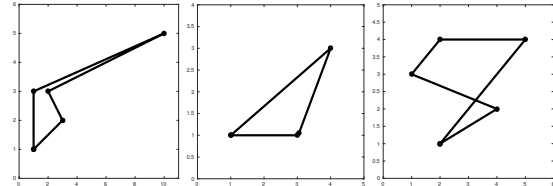


Figure 1: Non admissible domains laying in \mathcal{P}_n but not in \mathcal{A}_n . The first figure (left) shows a pentagon with a very small interior angle which leads to an unstable FEM. The figure in the middle shows a quadrilaterals with one small edge with length smaller than the mesh size h so that we cannot mesh the domain. The last figure (right) shows a non-simple pentagon.

the critical points of F . Let $\Omega \in \mathcal{A}_n$ and let $(x_i, y_i) \in \mathbb{R}^2$ be the vertices of Ω , $i = 1, \dots, n$. We can represent Ω exactly by the vector $\mathbf{x} := (x_1, y_1, \dots, x_n, y_n)^t \in \mathbb{R}^{2n}$ so we can write $F(\mathbf{x})$ instead of $F(\Omega)$. We wish to find the global minimizer

$$\mathbf{x}_{\min} \in \operatorname{argmin}_{\mathbf{x} \in \mathbf{X}} F(\mathbf{x}),$$

where $\mathbf{X} \subseteq \mathbb{R}^{2n}$ is a compact set. For this task, we use BO, which is a global optimization technique that is particularly suited for this objective because it only requires function evaluations (no gradients) while being more efficient than grid search or random search (see [2, 4] for a more detailed description of BO). The two basic ingredients of a BO framework are: (i) a probabilistic model that smoothes the observations to predict evaluations at unobserved inputs along with uncertainty quantification; and (ii) a search strategy that leverages the model predictions and its uncertainty to select the next input to evaluate. In our case we use a Gaussian process as the model which is fully described by a mean function a covariance function (kernel). In particular, since a few properties of F are known, we consider a zero mean and the kernel as a square exponential. Finally, our strategy to obtain the next input to evaluate is based on the optimization of a utility function. We use the Thompson sampling strategy introduced in [5] to construct this function.

4 Results

We parametrize the elements in \mathcal{A}_n to avoid some elements in \mathcal{P}_n . Let (r, θ) be the polar coordinates representation of $\Omega \in \mathcal{A}_n$, $\Omega \subseteq S$. Since F is invariant under scaling factors, we can fix $r \in (0, 1]$. Now let $\delta\theta_i > 0$ such that $\theta_{i+1} = \theta_i + \delta\theta_i$, $i = 1, \dots, n - 1$. We fix $\theta_1 = 0$ and $r_1 = r_2 = 1$, and obtain $\delta\theta_n$ by imposing the constraint: the sum of all $\delta\theta_i$ equals 2π .

We use Lagrange elements and Crouzeix-Raviart (CR) elements to approximate F . It is known that conforming methods give upper bounds for eigenvalues. In turn, it was proved in [1] that the CR elements provide lower bounds of eigenvalues. The conforming calculation is passed to the BO framework to be used as observed data. A run of our method for triangles, quadrilaterals and pentagons gives the results shown in Figure 2. Note that BO finds a minimum within tolerance for triangles and quadrilaterals. For pentagons, BO performs well but it can be improved by adding more iterations.

Conclusion Based on the numerical results we have seen for the Pólya-Szegö conjecture, we believe our proposed framework - combining the use of BO with FEM to compute each instance of the objective function - is a promising ap-

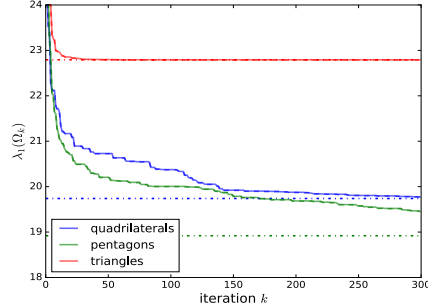


Figure 2: Convergence history of the approximations of λ_1 with conforming and nonconforming P1 elements for triangles, quadrilaterals, and pentagons. The true values are $\frac{4}{\sqrt{3}}\pi^2$ (equilateral triangle), $2\pi^2$ (square) and 18.9191295 (regular pentagon). The latter was approximated with Lagrange elements with $h = 10^{-4}$.

proach to other problems in spectral optimization as well. While there is no current proof that Thompson sampling converges in these settings, the results we present demonstrate the effectiveness of the approach.

Acknowledgements We gratefully acknowledge the support of the Natural Sciences and Engineering Research of Canada (NSERC).

References

- [1] C. Carstensen and J. Gedicke, Guaranteed lower bounds for eigenvalues, *Mathematics of Computation*, **83** (2014), pp. 2605–2629.
- [2] Z. Ghahramani, J. M. Hernández-Lobato and M. W. Hoffman, Predictive Entropy Search for Efficient Global Optimization of Black-box Functions, *Neural Information Processing Systems*, (2014).
- [3] G Pólya and G. Szegö, *Isoperimetric inequalities in mathematical physics*, Princeton University Press, 1951.
- [4] B. Shahriari, K. Swersky, Z. Wang, R. P. Adams and N. de Freitas, Taking the Human Out of the Loop: A Review of Bayesian Optimization, *Proceedings of the IEEE*, **104** (1) (2016), pp. 1–28.
- [5] W. B. Thompson. On the Likelihood that One Unknown Probability Exceeds Another in View of the Evidence of Two Samples, *Biometrika*, **25** (3/4), pp. 285–294, (1933).

On a three parameter family of Boussinesq systems for internal waves

V. A. Dougalis¹, A. Durán^{2,*}, D. E. Mitsotakis³

¹ Department of Mathematics, University of Athens, Athens, Greece

²Department of Applied Mathematics, University of Valladolid, Valladolid, Spain

³ School of Mathematics, Statistics and Operations Research, Victoria University of Wellington,
Wellington, New Zealand

*Email: angel@mac.uva.es

Abstract

A three-parameter family of Boussinesq systems for internal waves derived in [3] is considered. The systems describe the propagation of internal waves in a two-layer interface problem with rigid lid assumption and under the Boussinesq regime for both fluids. After analyzing the well-posedness and the existence of solitary wave solutions, in one and two dimensions, numerical studies concerning the generation and dynamics of the waves will be presented.

Keywords: Boussinesq systems, internal solitary waves

1 Introduction

The idealized model in [3] consists of two inviscid, homogeneous fluids of depths $d_j, j = 1, 2$ and densities $\rho_j, j = 1, 2$ with $\rho_2 > \rho_1$. The upper layer is bounded above by a horizontal rigid lid while the lower layer is bounded below by an impermeable, horizontal, flat bottom. The deviation of the interface, denoted by ζ , is assumed to be a graph over the bottom and surface tension effects are not considered.

The approach in [3] is based on the reformulation of the Euler system with two nonlocal operators. Then, different asymptotic models, consistent with the Euler system, are derived. They are associated to different physical regimes for the layers. The one considered here is the so-called Boussinesq-Boussinesq (B/B) regime, for which the interfacial deformations are assumed to be of small amplitude for both the upper and lower fluid domains and, additionally, the flow has a Boussinesq structure with respect to the two layers, with the nonlinear and dispersive effects of the same size for both fluids.

The B/B regime is modeled by the following

three parameter family of differential systems

$$\begin{aligned} (1 - b\Delta)\zeta_t + \frac{1}{\gamma + \delta}\nabla \cdot \mathbf{v}_\beta &= (1 - d\Delta)(\mathbf{v}_\beta)_t + (1 - \gamma)\nabla\zeta \\ &+ \left(\frac{\delta^2 - \gamma}{(\delta + \gamma)^2}\right)\nabla \cdot (\zeta\mathbf{v}_\beta) + a\nabla \cdot \Delta\mathbf{v}_\beta = 0 \\ &+ \left(\frac{\delta^2 - \gamma}{2(\delta + \gamma)^2}\right)\nabla|\mathbf{v}_\beta|^2 + (1 - \gamma)c\Delta\nabla\zeta = 0, \end{aligned} \quad (1)$$

where ∇, Δ stand, respectively, for the gradient and Laplace operator, $\gamma = \rho_1/\rho_2 < 1$, $\delta = d_1/d_2$ are, respectively, the density and depth ratios, and β is a nonnegative parameter. The variable \mathbf{v} is essentially the gradient of the trace of the velocity potential of the upper fluid layer at the interface and $\mathbf{v}_\beta = (I - \beta\Delta)^{-1}\mathbf{v}$ provides the systems a nonlocal character. The constants a, b, c, d can be made dependent on the parameters γ, δ or, alternatively, on three modeling parameters $\alpha_1 \geq 0, \beta \geq 0, \alpha_2 \leq 1$ in such a way that, [3]

$$\begin{aligned} a &= \frac{(1 - \alpha_1)(1 + \gamma\delta) - 3\delta\beta(\delta + \gamma)}{3\delta(\gamma + \delta)^2}, \\ b &= \alpha_1 \frac{1 + \gamma\delta}{3\delta(\gamma + \delta)}, \\ c &= \beta\alpha_2, \quad d = \beta(1 - \alpha_2). \end{aligned}$$

This leads to the relation

$$(\delta + \gamma)a + b + c + d = \frac{1 + \gamma\delta}{3\delta(\gamma + \delta)}$$

When $\gamma = 0, \delta = 1$, (1) reduces to the known family of Boussinesq systems for surface water waves, derived and analyzed in [1, 2].

2 Main goals

Our purpose is two-fold. First we study some mathematical properties of the system in one and two dimensions. The results are mainly concerned with well-posedness and the existence of solitary wave solutions. Then a computational study on the generation and dynamics of these waves will be carried out.

References

- [1] J. L. Bona, M. Chen and J.-C. Saut, Boussinesq equations and other systems for small-amplitude long waves in nonlinear dispersive media: I. Derivation and linear theory, *J. Nonlin. Sci.* **12** (2002), pp. 283-318.
- [2] J. L. Bona, M. Chen, J.-C. Saut, Boussinesq equations and other systems for small-amplitude long waves in nonlinear dispersive media: II. The nonlinear theory, *Nonlinearity* **17** (2004), pp. 925-952.
- [3] J.L. Bona, D. Lannes and J.-C. Saut, Asymptotic models for internal waves, *J. Math. Pures Appl.*, **89** (2008), pp. 538-566.

A new discontinuous Galerkin spectral element method for elastic waves with physically motivated numerical fluxes

Kenneth Duru^{1,*}, Alice-Agnes Gabriel¹, Heiner Igel¹

¹Department of Geophysics, Ludwig-Maximilian University, Munich, Germany

*Email: kenneth.duru@geophysik.uni-muenchen.de

Abstract

The discontinuous Galerkin spectral element method (DGSEM) [1] is now an established method for computing approximate solutions of partial differential equations in many applications. Unlike continuous finite element methods, in DGSEM, numerical fluxes [2] are used to enforce internal and external physical boundary conditions. This has been successful for many problems. However, for certain problems such as elastic wave propagation in complex media, where several wave types and wave speeds are simultaneously present, a standard numerical flux [2] may not be compatible with physical boundary conditions. For example if surface or interface waves are present, this incompatibility can lead to numerical instabilities. We present a provably stable and arbitrary order accurate DGSEM for elastic waves with physically motivated numerical fluxes. Our numerical flux is compatible with all well-posed physical boundary conditions, including linear and nonlinear friction laws for modeling fracture and dynamic earthquake rupture. By construction our choice of penalty parameters yield an upwind scheme and a discrete energy estimate analogous to the continuous energy estimate.

Keywords: elastodynamics, discontinuous Galerkin, spectral method, boundary conditions, stability

1 Model problem

Consider the 1D elastic wave equation, in

$$\rho(x) \frac{\partial v}{\partial t} = \frac{\partial \sigma}{\partial x}, \quad \frac{1}{\mu(x)} \frac{\partial \sigma}{\partial t} = \frac{\partial v}{\partial x}, \quad t > 0, x > 0, \quad (1)$$

with $(v(x, 0), \sigma(x, 0)) = (v^0(x), \sigma^0(x))$. Define the left-going p , and the right-going q characteristics $p(v, \sigma) = \frac{1}{2}(Z_s v + \sigma)$, $q(v, \sigma) = \frac{1}{2}(Z_s v - \sigma)$, $Z_s = \rho c_s$. At the boundary, $x = 0$, we impose the general linear well-posed boundary conditions: $B(v, \sigma) := q - rp = 0$, having

$$B(v, \sigma) := \frac{Z_s}{2} (1 - r)v - \frac{1+r}{2}\sigma = 0, \quad x = 0, \quad (2)$$

where r is real and $|r| \leq 1$. At internal boundaries, we consider the linear coupling condition

$$\sigma^- = \sigma^+ = \sigma, \quad \sigma = \alpha[v], \quad 0 \leq \alpha \leq \infty, \quad (3)$$

with $[v] := v^+ - v^-$, and the superscripts $-/+$ denote fields at the negative and positive sides of the interface. The parameter $\alpha \geq 0$ models the frictional strength of the interface, and captures some difficulties that could arise for nonlinear friction laws. Note that there are two limiting values, a locked interface: $\alpha \rightarrow \infty \iff [v] \rightarrow 0$, and a frictionless interface: $\alpha \rightarrow 0 \iff \sigma \rightarrow 0$. Introduce the mechanical energy $E(t) = \frac{1}{2} \int_{\Omega} (\rho|v|^2 + \frac{1}{\mu}|\sigma|^2) dx$, we have $\frac{dE(t)}{dt} = -\sigma[v] - v(0, t)\sigma(0, t)$. This energy loss through the boundaries is what the numerical method should mimic.

Our primary objective is to construct a provably stable inter-element procedure for the DGSEM approximation of (1) using the physical interface condition (3). The procedure is designed in a unified manner such that numerical flux functions are compatible with the general linear boundary condition (2). Furthermore, our approach avoids numerical stiffness, for all $0 \leq \alpha \leq \infty$.

We will now reformulate the boundary condition (2) and interface condition (3) by introducing transformed (hat-) variables so that we can simultaneously construct boundary/interface data. The hat-variables preserve the amplitude of the outgoing characteristics and satisfy the physical boundary/interface conditions (2) and (3) exactly. The hat-variables, \hat{v}_0 , $\hat{\sigma}_0$, for the boundary at $x = 0$ have the exact solution $\hat{v}_0 = \frac{(1+r)}{Z_s} p(v, \sigma)$, $\hat{\sigma}_0 = (1 - r_0)p(v, \sigma)$. Next we construct interface data \hat{v}^- , $\hat{\sigma}^-$, \hat{v}^+ , $\hat{\sigma}^+$: $\hat{\sigma}^- = \hat{\sigma}^+$, $\hat{\sigma} = \frac{\alpha}{\eta+\alpha} \Phi$, $[\hat{v}] = \frac{1}{\eta+\alpha} \Phi$, $\hat{v}^- = \frac{1}{Z_s^+} (2p^+ - \hat{\sigma}^+) - [\hat{v}]$, $\hat{v}^+ = \frac{1}{Z_s^-} (2q^- + \hat{\sigma}^-) + [\hat{v}]$, where $\Phi = \eta \left(\frac{2}{Z_s^+} p^+ - \frac{2}{Z_s^-} q^- \right)$, $\eta = \frac{Z_s^- Z_s^+}{Z_s^+ + Z_s^-}$. The data is exact and consistent at the limit: $\alpha \rightarrow \infty \iff [\hat{v}] \rightarrow 0$, $\alpha \rightarrow 0 \iff \hat{\sigma} \rightarrow 0$.

2 The DGSEM

We now formulate the DGSEM for the IBVP (1), (2). We discretize $[0, L]$ with K elements. In a reference element $x \in [x_k, x_{k+1}] \leftrightarrow \xi \in [-1, 1]$, with $\Delta x_k = x_{k+1} - x_k$ and test functions $(\phi_v(\xi), \phi_\sigma(\xi)) \in \mathbb{L}^2(-1, 1)$, the elemental weak form reads

$$\frac{\Delta x_k}{2} \int_{-1}^1 \rho^k(\xi) \phi_v(\xi) \frac{\partial v^k(\xi, t)}{\partial t} d\xi = \int_{-1}^1 \phi_v(\xi) \frac{\partial \sigma^k(\xi, t)}{\partial \xi} d\xi - \phi_v(-1) F^k(-1, t) - \phi_v(1) G^k(1, t), \quad (4)$$

$$\frac{\Delta x_k}{2} \int_{-1}^1 \frac{1}{\mu^k(\xi)} \phi_\sigma(\xi) \frac{\partial \sigma^k(\xi, t)}{\partial t} d\xi = \int_{-1}^1 \phi_\sigma(\xi) \frac{\partial^k(\xi, t)}{\partial \xi} d\xi + \frac{\phi_\sigma(-1)}{Z_s^k(-1)} F^k(-1, t) - \frac{\phi_\sigma(1)}{Z_s^k(1)} G^k(1, t). \quad (5)$$

The superscript k denotes a polynomial approximation within the element, eg. $v^k(\xi, t) = \sum_{j=1}^{N+1} v_j^k(t) \mathcal{L}_j(\xi)$ where $\mathcal{L}_j(\xi)$ are the interpolating polynomials of degree N and $v_j^k(t)$ are the degrees of freedom to be evolved. To couple solutions across the element boundaries, we penalize data against incoming characteristics at the boundary. That is $F^k(-1, t) := q(v^k - \hat{v}^k, \sigma^k - \hat{\sigma}^k)|_{\xi=-1}$, $G^k(1, t) := p(v^k - \hat{v}^k, \sigma^k - \hat{\sigma}^k)|_{\xi=1}$.

The integrals in (4)-(5) are evaluated using Gauss quadrature rules, $\sum_{i=1}^{N+1} f(\xi_i) w_i \approx \int_{-1}^1 f(\xi) d\xi$, that are exact for all polynomial integrand $f(\xi)$ of degree $\leq 2N - 1$. We denote the elemental semi-discrete energy:

$$\mathcal{E}^k(t) = \frac{\Delta x_k}{2} \sum_{j=1}^{N+1} \left(\frac{\omega_j}{2} \left(\rho_j^k |v_j^k(t)|^2 + \frac{1}{\mu_j^k} |\sigma_j^k(t)|^2 \right) \right).$$

The semi-discrete approximation satisfies the energy equation,

$$\frac{d}{dt} \mathcal{E}(t) = - \sum_{k=1}^K \left(\text{IT}^k + \hat{\sigma}^k [\hat{v}^k] \right) - \frac{1-r^2}{Z_s} p^2(v^1, \sigma^1)|_{\xi=-1},$$

with $\mathcal{E}(t) = \sum_{k=1}^K \mathcal{E}^k(t)$, and $\text{IT}^k = |F^k(-1, t)|^2 + |G^k(1, t)|^2$, and $\hat{\sigma}^k [\hat{v}^k]|_{\xi=\pm 1} = \frac{\alpha^k}{(\eta^k + \alpha^k)^2} |\Phi^k|^2|_{\xi=\pm 1}$. Since $\text{IT}^k \geq 0$, $\hat{\sigma}^k [\hat{v}^k] \geq 0$, then $\frac{d}{dt} \mathcal{E}(t) \leq 0$.

We have generated numerical data in a manner that is consistent with physical laws and enforced element boundary data using characteristics. Note that $\hat{\sigma} [\hat{v}] = \frac{\alpha}{(\eta + \alpha)^2} |\Phi|^2 \rightarrow 0$, for $\alpha \rightarrow \infty$ or $\alpha \rightarrow 0$. This implies that the spectral radius of the discrete operator has an upper bound which is independent of $\alpha \geq 0$. If we had used characteristics to directly enforce the physical condition (3), we will have $\sigma [v] = \alpha [v]^2$. The semi-discrete approximation yields an energy estimate, however, it will potentially introduce artificial numerical stiffness, for $\alpha \gg 1$, which will require implicit time integration.

3 Numerical tests

We present numerical experiments to demonstrate stability and accuracy, and extensions to

high space dimension. All inter-element boundaries are locked, $[v] \rightarrow 0$, and we use nodal Lagrange basis, with Gauss-Legendre-Lobatto (GLL) and Gauss-Legendre (GL) quadrature rules, separately. We have chosen initial and boundary data to match the exact solution

$v(x, t) = \frac{1}{2} (\sin(2\pi(x + c_s t)) + \sin(2\pi(x - c_s t)))$. We propagate the solution for 10 s and record the time-history of the numerical error in figure 1. We have performed experiments for different

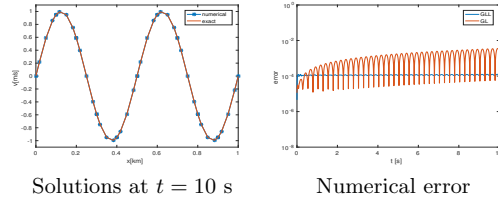


Figure 1: Solutions at $t = 10$ s and time history of the numerical error using $N = 4$ polynomial degree and $K = 10$ number of elements

resolutions and polynomial degree $N \leq 12$. The errors converge spectrally to zero at the rate $N + 1$. In figure 2 we demonstrate extensions of our method to higher space dimensions and make comparisons with the Rusanov flux.

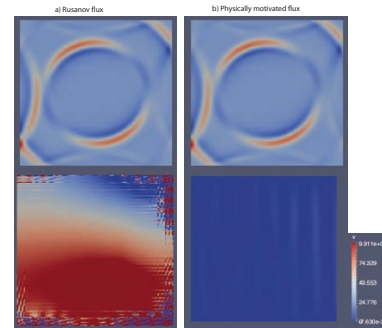


Figure 2: A 2D example. a) The Rusanov flux showing numerical instabilities from boundaries. b) The physically motivated flux showing stable solutions. The top panel are snapshots at $t = 0.2$ s and lower panel are at $t = 10$ s.

References

- [1] J. Hesthaven and T. Warburton, *Nodal Discontinuous Galerkin Methods: Algorithms, Analysis, and Applications*, Springer, New York, 2008.
- [2] V. V. Rusanov, Calculation of interaction of non-stationary shock waves with obstacles, *J. Comput. Math. Phys. USSR*, **1** (1961), pp. 267–279.

Efficient boundary element schemes for the solution of high-frequency convex scattering problems

Fatih Ecevit^{1,*}, Yassine Boubendir², Lazergui Souad³

¹Department of Mathematics, Boğaziçi University, Istanbul, Turkey

²Department of Mathematical Sciences, New Jersey Institute of Technology, Newark, USA

³Department of Pure and Applied Mathematics, University of Mostaghanem, Mostaghanem, Algeria

*Email: fatih.ecevit@boun.edu.tr

Abstract

In this paper we propose efficient boundary element schemes for the solution of high-frequency convex scattering problems. Our approach is based on frequency dependent changes of variables in forming Galerkin approximation spaces and newly developed asymptotic expansions of the normal derivative of the total field.

Keywords: high-frequency, asymptotic expansions, Galerkin method

1 Introduction

We consider numerical solution of the soundsoft scattering problem

$$\begin{cases} \Delta u + k^2 u = 0, & \text{in } \mathbb{R}^2 \setminus K \\ u = -u^{\text{inc}}, & \text{on } \partial K \\ \lim_{|x| \rightarrow \infty} |x|^{1/2} (\partial_{|x|} - ik) u(x) = 0 \end{cases} \quad (1)$$

in the exterior of a smooth, compact, and strictly convex obstacle K illuminated with a plane-wave $u^{\text{inc}}(x) = e^{ik\alpha \cdot x}$ ($|\alpha| = 1$).

As is well known, the computational cost associated with classical schemes for the solution of problem (1) increases at least linearly with increasing k , and this limits their applicability when $k \gg 1$ (see e.g. [2]). To overcome this difficulty, current hybrid integral equation methodologies 1) transform the problem to the determination of the normal derivative of the total field $\eta = \partial_n(u + u^{\text{inc}})$ through the single-layer representation of the scattered field u , 2) utilize the factorization

$$\eta(x) = e^{ik\alpha \cdot x} \eta^{\text{slow}}(x), \quad x \in \partial K$$

to further reduce the problem to the computation of the slowly varying envelope η^{slow} , and 3) use the Melrose-Taylor asymptotics [7]

$$\eta^{\text{slow}}(x) \sim \sum_{p,q \geq 0} a_{p,q}(x) \quad (2)$$

with $a_{p,q} = k^{2/3-2p/3-q} b_{p,q}(x) \Psi^{(p)}(k^{1/3} Z(x))$ for the efficient discretization of integral equations

$$\mathcal{R}_k \eta = f \quad \text{in } L^2(\partial K). \quad (3)$$

Earlier algorithms [1–5] based on the aforementioned prescriptions have displayed the capability of producing solutions to equation (3) in frequency independent computational times. However, the only rigorous algorithms that require an increase of $\mathcal{O}(k^\epsilon)$ (for any $\epsilon > 0$) in the number of degrees of freedom to obtain frequency independent accuracies and that provide highly accurate solutions including the shadow regions are Galerkin boundary element methods we have recently developed [4]. Here we present two improvements of our algorithms based on 1) Galerkin boundary element methods that depend on frequency dependent changes of variables around shadow boundaries, and 2) the alternative form of the asymptotic expansion (2) we have recently derived [6].

2 Galerkin boundary element methods based on changes of variables

Let γ be the arc length parametrization of ∂K in counterclockwise direction with $\alpha \cdot \mathbf{n}(\gamma(0)) = 1$ so that if $0 < t_1 < t_2 < P = |\partial K|$ are the pre-images of the shadow boundary points, that is $\gamma(\{t_1, t_2\}) = \partial K^{SB} = \{\alpha \cdot \mathbf{n}(x) = 0\}$, then the illuminated region $\partial K^{IL} = \{\alpha \cdot \mathbf{n}(x) < 0\}$ and shadow region $\partial K^{SR} = \{\alpha \cdot \mathbf{n}(x) > 0\}$ are given respectively by $\gamma((t_1, t_2))$ and $\gamma((t_2, t_1 + P))$.

For $j = 1, 2$, chose $\xi_j, \xi'_j, \zeta_j, \zeta'_j > 0$ so that

$$\begin{aligned} t_1 + \xi_1 &\leq t_1 + \xi'_1 = t_2 - \xi'_2 \leq t_2 - \xi_2 \\ t_2 + \zeta_2 &\leq t_2 + \zeta'_2 = P + t_1 - \zeta'_1 \leq P + t_1 - \zeta_1, \end{aligned}$$

and, for $k > 1$, define the *illuminated transition*

and *shadow transition* intervals as

$$\begin{aligned} I_{IT_1} &= [t_1 + \xi_1 k^{-1/3}, t_1 + \xi'_1] \\ I_{IT_2} &= [t_2 - \xi'_2, t_2 - \xi_2 k^{-1/3}] \\ I_{ST_1} &= [t_1 - \zeta'_1, t_1 - \zeta_1 k^{-1/3}] \\ I_{ST_2} &= [t_2 + \zeta_2 k^{-1/3}, t_2 + \zeta'_2] \end{aligned}$$

and the *shadow boundary* intervals as

$$\begin{aligned} I_{SB_1} &= [t_1 - \zeta_1 k^{-1/3}, t_1 + \xi_1 k^{-1/3}] \\ I_{SB_2} &= [t_2 - \xi_2 k^{-1/3}, t_2 + \zeta_2 k^{-1/3}]. \end{aligned}$$

Given $d \in \mathbb{Z}_+$, the $6(d+1)$ dimensional *Galerkin approximation space based on algebraic polynomials and frequency dependent changes of variables* is then defined as [3]

$$\mathcal{A}_d^C = \bigoplus_{j=1}^6 \mathbb{1}_{[a_j, b_j]} e^{ik\alpha_j \gamma} \hat{\mathbb{P}}_j^C \quad (4)$$

where, writing \mathbb{P}_d for the space of algebraic polynomials of degree at most d , we have set $\hat{\mathbb{P}}_j^C = \mathbb{P}_d \circ \phi^{-1}$ if $[a_j, b_j]$ is a transition region, and $\hat{\mathbb{P}}_j^C = \mathbb{P}_d$ otherwise. Here ϕ is the change of variables specified on I_{IT_1} by

$$\phi(s) = t_1 + \varphi(s) \exp\left(-\frac{1}{3} \frac{b_1 - s}{b_1 - a_1} \log k\right),$$

with $\varphi(s) = \xi_1 + (\xi'_1 - \xi_1) \frac{s-a_1}{b_1-a_1}$, and defined similarly in the remaining transition intervals.

Theorem 1 [3] Suppose the sesquilinear form $\mathcal{B}_k(\mu, \eta) = \langle \mu, \mathcal{R}_k \eta \rangle$ associated with the operator \mathcal{R}_k is continuous with a continuity constant C_k and coercive with a coercivity constant c_k for all $k > k_0 \geq 1$. Then, for $d \in \mathbb{Z}_+$ & $0 \leq n \leq d+1$,

$$\frac{\|\eta - \hat{\eta}\|_{L^2(\partial K)}}{\|\eta\|_{L^2(\partial K)}} \leq C_{n,k_0} \frac{C_k}{c_k} \frac{(\log k)^{n+1/2}}{d^n} \quad (5)$$

where $\hat{\eta}$ is the solution of the Galerkin equation

$$B_k(\hat{\mu}, \hat{\eta}) = F_k(\hat{\mu}), \quad \text{for all } \hat{\mu} \in \mathcal{A}_d^C.$$

The estimate (5) can then be used to show that [3] the number of degrees of freedom necessary to obtain any given accuracy independent of frequency needs to increase only as $\mathcal{O}(k^\varepsilon)$ for any $\varepsilon > 0$. Furthermore, if the leading term in the expansion (2) is incorporated into the integral equations (3), then this dependency reduces to $\mathcal{O}(1)$ [2].

3 Galerkin boundary element methods based on new asymptotic expansions

As we have recently shown [6], the factors $b_{p,q}$ of $a_{p,q}$ appearing in the asymptotic expansion (2) can be replaced by

$$(1 - \alpha \cdot \nu(x)) c_{p,q}(x) - \frac{\kappa(x)}{2} d_{p,q}(x) \quad (6)$$

which give rise to an alternative asymptotic expansion of η^{slow} . The benefit of this new expansion is its ability to incorporate the decay of the solution in the deep shadow region. This, in return, allows for the alternative definition of Galerkin approximation spaces (4) simply by weighting them with the terms in (6). Our preliminary numerical tests show improvement in the efficiency of the numerical method in terms of the number of degrees of freedom.

References

- [1] Bruno, O. P., Geuzaine, C., Monro J. A., Reitich, F.: *Prescribed error tolerance within fixed computational times for scattering problems of arbitrarily high frequency: the convex case*, Phil. Trans. Roy. Soc. London 362 (2004), 629-645.
- [2] Ecevit, F.: *Freq. ind. solvability of surface scattering problems*, submitted (2016).
- [3] Ecevit, F., Eruslu, H.H.: *Efficient Galerkin schemes for high-frequency scattering problems based on frequency dependent changes of variables*, ArXiv (2016).
- [4] Ecevit, F., Özen, H.C.: *Frequency-adapted Galerkin boundary element methods for convex scattering problems*, Numer. Math. (2016). doi:10.1007/s00211-016-0800-7
- [5] Huybrechs, D., Vandewalle, S.: *A sparse discretization for integral equation formulations of high frequency scattering problems*, SIAM J. Sci. Comput. 29 (2007), no. 6, pp. 2305–2328.
- [6] Lazergui, S., Boubendir, Y.: *Asymptotic expansions of the Helmholtz equation solutions using approximations of the Dirichlet to Neumann operator*, ArXiv (2016).
- [7] Melrose, R.B., Taylor, M.: *Near peak scattering and the corrected Kirchhoff approximation for a convex obstacle*, Adv.in Math. 55 (1985), 242–315.

Geo-Inspired Mechanical Metamaterials

Ahmed E. Elbanna^{1,*}, Yuyang Rao¹, Xiao Ma¹

¹Department of Civil and Environmental Engineering, University of Illinois at Urbana-Champaign, Urbana, US

*Email: elbanna2@illinois.edu

Abstract

Friction is regarded as a source of energy dissipation. Crustal faults, however, leverage friction to grow instabilities, and localize energy. Earthquakes is the pinnacle of such phenomenon. The class of friction laws of relevance here is that in which the steady state friction force decreases with sliding velocity. Such friction may be realized on corrugated surfaces, due to flash melting of contact asperities, or during fast shearing of saturated porous media. We present a mechanical model of a chain of masses connected with linear springs and sliding on a rate weakening frictional interface. We show that the system enables the propagation of solitary waves whose characteristics are tunable by the level of the system prestress. The system is also asymmetric with respect to the direction of excitation. We discuss the implications of these observations on designing new materials that harness friction to generate unique nonlinear wave propagation features.

Keywords: Friction, Slip pulses, Tunable nonlinear waves

Introduction

Friction and fracture are fascinating nonlinear, and often dynamic, phenomena that span multiple spatial and temporal scales. An extreme example integrating both phenomena is earthquake. Our current understanding suggests that earthquakes nucleate as frictional instabilities on pre-existing faults in the crust under slow tectonic loading. Once they outgrow their nucleation region, they generally propagate as shear fractures with a rupture speed close to the shear wave speed (known as subshear ruptures) but sometimes they even exceed the shear wave speed (supershear ruptures) and propagate in the intersonic regime (limited by the pressure wave speed).

For earthquakes to grow spontaneously under the slow tectonic loading, the steady state friction on the fault must decrease with increasing slip or slip rate [1]. Linear stability analysis show that steady frictional sliding is unstable for long wave length perturbations under these conditions [3]. Of special interest, here, is what Heaton [2] suggested, based on multiple seismological observations, that earthquake ruptures propagate as slip pulses. That is, the slip duration at any given point on the fault surface is small compared to the overall duration of

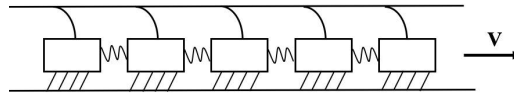


Figure 1: The spring block slider model. A chain of N blocks of identical masses (m) interconnected by coil springs of stiffness (k_c) is driven by a loading plate moving at a very low velocity (v). The blocks feel the effect of the loading plate through a series of leaf springs of stiffness (k_l). Any block is stuck to the interface as long as the total elastic force acting on it is less than the static friction threshold. Once the static friction is exceeded, a sliding block experiences a dynamic friction force g that varies inversely with the block sliding velocity. The blocks are subjected to an initial stress distribution by stretching or compressing the coil springs relative to their natural length. As a block moves, it transfers stresses into neighboring blocks causing them to subsequently move if the static friction level is exceeded.

the earthquake event. Later, Zheng and Rice [1] established that if the friction coefficient decreases with increasing slip rate and the crustal prestress was small enough, then the compact slip pulse solution emerges as a possible candidate for the elastodynamic equations.

In recent years, there has been a surge of interest in nonlinear wave phenomena in mechanical systems. Here, inspired by the above geophysical observations, we show that it is possible to leverage nonlinear friction in an otherwise linear elastic system to generate solitary waves. We demonstrate that these solitary wave solutions are tunable by the level of prestress, the system elasticity and the rate dependence of strength of the sliding interface.

Model setup

We study a simple 1D spring-block-slider model [4] with a setup shown in Fig.1. The equation of motion of the i^{th} block is given by:

$$m_i \ddot{u}_i = k_c(u_{i+1} - 2u_i + u_{i-1}) + k_l(vt - u_i) + \sigma_{oi} - f_{ig}(\dot{u}_i) \quad (1)$$

Where σ_{oi} is the initial traction at the position of the i^{th} block, u_i is the block displacement and all other parameters are explained in Fig. 1. The dynamic friction force g varies inversely with the block sliding

velocity. We use a second order accurate predictor-corrector scheme for time integration. The time step is controlled by the ratio of leaf spring stiffness to coil spring stiffness as well as the rate of frictional weakening. We rewrite Eqn. 1 in non-dimensional form by introducing the following dimensionless quantities:

$$r = \frac{k_c}{k_l} \quad D = \frac{f}{k_l} \quad \omega^2 = \frac{k_c}{m} \quad \tau = \omega t \quad U = \frac{u}{D} \quad (2)$$

Then we have:

$$\ddot{U}_i = r(U_{i+1} - 2U_i + U_{i-1}) + (\bar{v}\tau - U_i) - g(\dot{U}_i, v_c) \quad (3)$$

We are particularly interested in friction laws in which the friction decreases with the slip rate. For that purpose, we adopt the simplified Carlson-Langer friction law:

$$g = \frac{1}{1 + (\dot{U}/v_c)} \quad (4)$$

Results

We integrate Eqn. 1 for number of blocks = 100 and different values of relative stiffness r , frictional weakening parameter v , and prestress level. A snapshot of the solution for $r = 5$ and $v = 0.1$ at $t = 268$ (non-dimensional time) is shown in Fig. 2. After an initial transient, the slip (blocks displacement) evolves into a constant value and the particle velocity distribution is compactly supported and the displacement solution assumes a kink-like form.

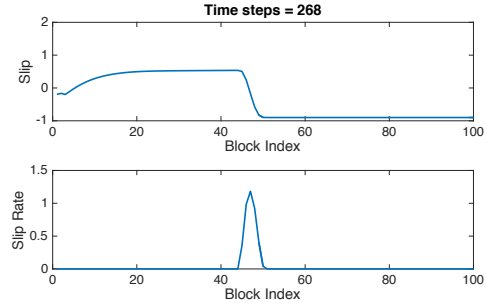


Figure 2: Snapshot of the solution to Eq. 1 for a system with $N = 100$, $r = 5$ and $v_c = 0.2$. The velocity distribution is compactly supported and the displacement solution assumes a kink-like form.

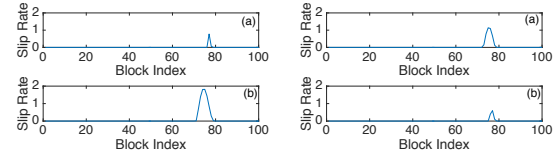


Figure 3: Tunability of the slip pulse solution. [Left] Effect of the stiffness ratio r . (a) low stiffness ratio, (b) high stiffness ratio. [Right] Effect of the rate of weakening v_c . (a) Strong rate weakening (small v_c), (b) small rate weakening (large v_c)

leading to propagating kinks. The slip pulse amplitude and width are tunable by the level of prestress in the chain of springs, by varying the ratio of the coil to leaf springs stiffness and by the strength of the rate weakening friction. Future extension of this work includes study of 2D and 3D systems in which the interplay between friction and system elasticity may lead to interesting localization and energy flow phenomena.

References

- [1] Rice, J.R., Constitutive relations for fault slip and earthquake instabilities, *Pure and Applied Geophysics* **121** (1983), pp. 443–475.
- [2] Heaton, T.H., Evidence for and implications of self-healing pulses of slip in earthquake rupture, *Phys. Earth Planet. Inter.* **121** (1983), pp. 443–475.
- [3] Rice, J. R., N. Lapusta, and K. Ranjith, Rate and state dependent friction and the stability of sliding between elastically deformable solids *J. Mech. Phys. Solids* **49** (2001), pp. 1,865–1,898.
- [4] Carlson, J.M. and J.S. Langer, Mechanical model of an earthquake fault *Phys. Rev. A* **40** (2001), pp. 6470–6484.

Conclusion

In this paper, we showed that it is possible to leverage rate weakening friction to generate nonlinear wave phenomena in an otherwise linear elastic system. The rate weakening nature of friction leads to growth of perturbations, focuses energy in localized traveling waves and balances dispersive effects

Non-Equilibrium Magnetosonic Wave Motion

Wolfgang F. Ellermeier^{1,*}

¹Department of Physics, TU Darmstadt, Darmstadt, Germany

*Email: ellermeier@fkp.tu-darmstadt.de

thermodynamic relaxation, magnetohydrodynamics,piston analogy

Abstract

In ideal compressible hydrodynamics there is an isomorphism between spatially one-dimensional unsteady and two-dimensional steady supersonic flow called piston analogy [7]. This notice shows that this is also true for non-equilibrium magnetosonic flow under alignment of undisturbed flow and magnetic field in case of steady flow. An example for two generic problems, i.e. the signal problem of radiation into a half space and steady flow along a kinked wall bounding a half space, is given.

Keywords: thermodynamic relaxation, magnetohydrodynamics, piston analogy

1 Basic Equations

The MHD equations of motion for a thermodynamically relaxing fluid of infinite electrical conductivity and a single non-equilibrium process comprise the equation of mass, the momentum equation, the induction equation, the energy balance equation, the relaxation equation and the thermodynamic equations of state. They are written, in respective order, see [5]:

$$\dot{\varrho} + \nabla \cdot (\varrho \vec{V}) = 0, \quad (1)$$

$$\varrho(\dot{\vec{V}} + (\vec{V} \cdot \nabla) \vec{V}) = -\nabla p + \frac{1}{\mu_0}(\nabla \times \vec{B}) \times \vec{B},$$

$$\dot{\vec{B}} = \nabla \times (\vec{V} \times \vec{B}), \quad (2)$$

$$\varrho(\dot{h} + \vec{V} \cdot \nabla h) - \dot{p} - \vec{V} \cdot \nabla p = 0, \quad (3)$$

$$\dot{\xi} + \vec{V} \cdot \nabla \xi = -\frac{\xi - \tilde{\xi}(p, \varrho)}{\tau(p, \varrho, \xi)}, \quad (4)$$

$$h = \hat{h}(p, \varrho, \xi). \quad (5)$$

The field variables are mass density ϱ , flow velocity \vec{V} , pressure p , magnetic field \vec{B} , and specific enthalpy h . The thermodynamic state function is \hat{h} , the relaxation time τ is a strictly positive function of state [3]. The inner variable ξ with its equilibrium value $\tilde{\xi}$ describes either the degree of reaction in a single chemical reaction (ionization-recombination) or a vibrational non-equilibrium process in the plasma [4]. Plane magnetosonic relaxing flow is specified by

$$\vec{V} = u(x, y, t) \vec{e}_x + v(x, y, t) \vec{e}_y, \quad (6)$$

$$\vec{b} = a(x, y, t) \vec{e}_x + b(x, y, t) \vec{e}_y, \quad (7)$$

$$\vec{B}_0 = A_0 \vec{e}_x + B_0 \vec{e}_y, \quad (8)$$

with the background magnetic field in the x, y -plane at an angle $\arctan(B_0/A_0)$ between \vec{B}_0 and the x -axis, orthonormal unit vectors \vec{e}_x, \vec{e}_y along the coordinate axes are used.

2 Unsteady one-dimensional flow

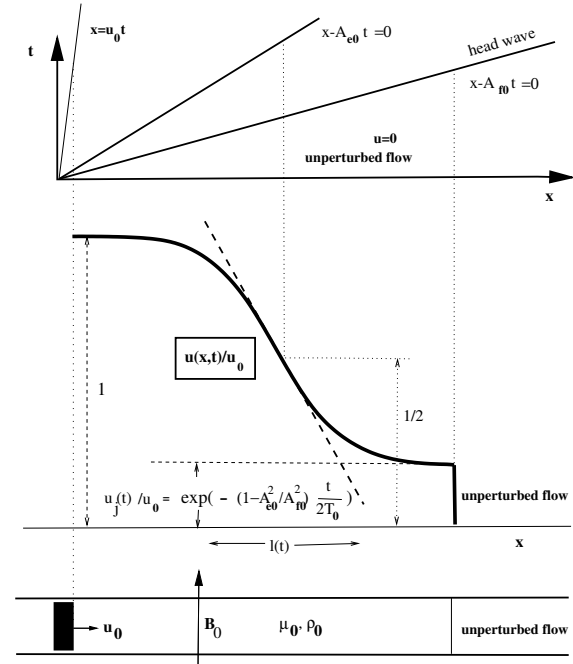


Figure 1: Partially dispersed wave in relaxing MHD flow, unsteady velocity-wave moving from left to right with decaying front discontinuity invading thermodynamic equilibrium state to the right of discontinuity; the front height decays exponentially in time according to eq. (42) as it moves to the right. Both, s-shape and front discontinuity travel faster with increase of the background magnetic field B_0 regardless of upwards or downwards orientation. The flow is realized in a shock tube with the piston at one end suddenly put to constant speed u_0 and the magnetic field transverse to the tube axis.

For $A_0 = 0, v \equiv 0, a \equiv 0, b = b(x, t), u = u(x, t)$, i.e. $\partial/\partial y \equiv 0$ one derives from eq. (13),

$$T_0(\ddot{u} - A_{f0}^2 u_{xx}) + \ddot{u} - A_{e0}^2 u_{xx} = 0, \quad (9)$$

where definitions according to

$$A_{f_0,e_0}^2 := \frac{B_0^2}{\mu_0 \varrho_0} + a_{f_0,e_0}^2, \quad (10)$$

$$a_{f_0}^2 := \frac{\hat{h}_{\varrho_0}}{\varrho_0^{-1} - \hat{h}_{p_0}}, \quad a_{e_0}^2 := \frac{\hat{h}_{\varrho_0} + \hat{h}_{\xi_0} \tilde{\xi}_{\varrho_0}}{\varrho_0^{-1} - \hat{h}_{p_0} - \hat{h}_{\xi_0} \tilde{\xi}_{p_0}},$$

$$T_0 := \tau(p_0, \varrho_0, \xi_0) \frac{\hat{h}_{\varrho_0}}{\hat{h}_{\varrho_0} + \hat{h}_{\xi_0} \tilde{\xi}_{\varrho_0}},$$

are employed. The specification of initial and boundary conditions completes the mathematical formulation:

$$u(0, t) = u_0 H(t), \quad u(x, 0) = 0, \quad (11)$$

with $H(t)$ denoting the Heaviside jump.

3 Steady two-dimensional flow for aligned fields

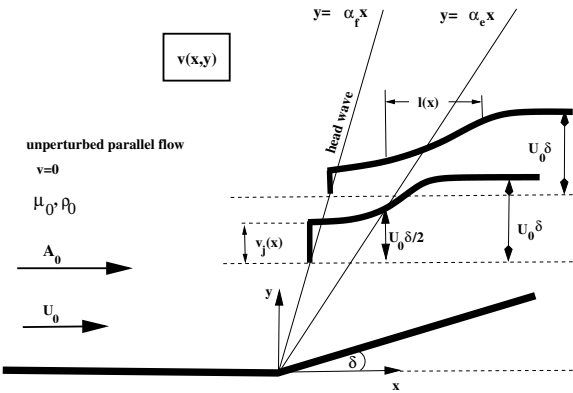


Figure 2: Distribution of $v(x, y)$ in steady flow of a relaxing fluid along kinked wall bounding a half space with aligned magnetic background field. Upstream of head wave there is undisturbed parallel flow, in the far field away from the wall the flow approaches uniform flow with $v \rightarrow U_0 \delta, u \rightarrow U_0$.

For $B_0 = 0, u \rightarrow U_0 + u(x, y), v = v(x, y), p = p(x, y), b = b(x, y), a \rightarrow A_0 + a(x, y), \partial/\partial t = U_0 \partial/\partial x$ and definitions for the constant coefficients, i.e. the frozen and equilibrium Mach numbers $M_{f,e}$ and the Alven-Mach number M_a , i.e.

$$\alpha_{f,e}^2 := \frac{M_a^2 - 1 + M_{f,e}^2}{(M_a^2 - 1)(M_{f,e}^2 - 1)}, \quad (12)$$

$$M_{f,e} := \frac{U_0}{a_{f_0,e_0}}, \quad M_a := \frac{U_0}{A_0 / \sqrt{\mu_0 \varrho_0}}, \quad (13)$$

one obtains the following governing equation for $v(x, y)$ from eq. (13):

$$T_0 U_0 \frac{M_f^2 - 1}{M_e^2 - 1} (v_{xx} - \alpha_f^2 v_{yy})_x + v_{xx} - \alpha_e^2 v_{yy} = 0. \quad (14)$$

The boundary conditions to eq. (30) (with $H(x)$ Heaviside jump) are

$$v(x, 0) = H(x) U_0 \delta. \quad (15)$$

For the case $M_f > 1$, so that $M_e > 1$ as well and $M_a > 1$ so that the flow velocity is supersonic w.r.t. all three wave speeds $a_{f_0,e_0}, A_0 / \sqrt{\varrho_0 \mu_0}$ there is equivalence between the signal problem according to eqs. (19,21) and the steady flow problem by eqs. (30,32) with for instance $u_0 \hat{=} \delta U_0, u \hat{=} v$; for the piston analogy to hold true the wall has to turn into the stream so that the material is compressed rather than expanded, i.e. $0 < \delta (<< 1)$. As a consequence one can immediately describe the solution for the kinked wall problem by reinterpretation of the partially dispersed wave problem and vice versa.

A qualitative representation of the result is depicted in Fig. 2 showing a jump in $v_j(x) = U_0 \delta e^{\frac{-x}{L(M_f,e,a)}}$, decaying away from the wall downstream of the wall kink along the head wave. The s-shaped spreading zone behind the discontinuity is governed by

$$v(x, y) \sim \frac{U_0 \delta}{2} \left(1 - \phi \left(\frac{y - \alpha_e x}{l(x)} \right) \right), \quad (16)$$

with ϕ denoting the error function as in the unsteady case and

$$l(x) := \sqrt{2 T_0 U_0 \frac{M_a^2}{M_a^2 - 1} \frac{M_e^2 - M_f^2}{(M_e^2 - 1)^2} x}. \quad (17)$$

A full description of this contribution can be found in [ArXiv \[9\]](#).

References

- [1] Vincenti, W. G., C.H. Kruger jr., Introduction to Physical Gas Dynamics, Wiley, 1967
- [2] E. Becker: Gasdynamics, Academic Press, 1968
- [3] S.R.deGroot, P.Mazur, Non-Equilibrium Thermodynamics, Dover, 1984
- [4] M.A. Liberman, A. L. Velikovich, Physics of Ionizing Shock Waves in Magnetic Fields, Physics Reports, 84 No.1 (1982), pp.1-84, North-Holland Publ.
- [5] O.P.Bhutani, R.Sharma, General Three-Dimensional Wave Propagation in Non-Equilibrium Magnetogasdynamics, Journal of Mathematical Analysis and Applications 18,(1967), pp 199-217,
- [6] G.B. Whitham, Linear and Nonlinear Waves, Wiley 1974
- [7] H.W. Liepmann, A. Roshko, Elements of Gasdynamics, chap. 4.6, Dover 2001
- [8] E.L.Resler, J.E.McCune, Electromagnetic Interaction With Aerodynamic Flow, in D. Bershadier (ed.), The Magnetohydrodynamics of Conducting Fluids, Stanford University Press, 1959
- [9] <https://arxiv.org/abs/1704.03763>

Uncertainty Quantification of Velocity Models and Seismic Imaging

Gregory Ely^{1,*}, Oleg V. Poliannikov¹, Alison Malcolm², David Nicholls³

¹Department of Geophysics, Massachusetts Institute of Technology

²Memorial University of Newfoundland

³University of Illinois at Chicago

*Email: elyg@mit.edu

Abstract

In this paper we present a two-step framework for uncertainty quantification of estimated seismic images and velocity models. First, we combine the adaptive Metropolis-Hastings algorithm with a fast Helmholtz solver to provide uncertainty estimates of a velocity model based on raw waveform data. Second, this error estimate is propagated through an imaging operator to ask meaningful questions about the error. We demonstrate several methods for presenting this uncertainty in a manageable and useful manner.

Keywords: Uncertainty Quantification, Seismic Imaging, Markov Chain Monte Carlo

1 Introduction

Seismic inverse problems are highly ill-posed and ill-conditioned. Current physics based methods, such as full waveform inversion, generally employ expensive forward solvers that require the use of gradient based techniques that provide only a single realization of the subsurface and provide no error bounds. This conventional work-flow makes it impossible to tell what features in a seismic image are real or to bound quantities of interest.

Uncertainty quantification of seismic images is rarely preformed due to the computational expense and the large dimensionality of seismic velocity models. A modest 128x128 velocity model described by a Gaussian distribution, would have a covariance matrix with 2.7 million entries and be impossible to visualize. In addition, finite difference solvers would likely be too slow for the large number (100,000) of iterations needed for non-parametric uncertainty quantification techniques such as Markov Chain Monte Carlo (MCMC). MCMC methods also require relatively few degrees of freedom that are incompatible with a pixel by pixel description of the distribution.

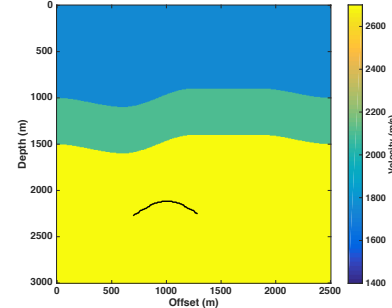


Figure 1: True seismic velocity model with embedded anticline reflector.

2 Model Uncertainty Quantification

To reduce the dimensionality of the seismic velocity model we constrain the model to consist of a series of perturbed layers as shown in Figure 1. This parametrization allows us to use the field expansion method [1] to rapidly calculate a predicted wavefield at given frequency in a given velocity model. This fast forward solver and the reduced degrees of freedom allow us to run the tens of thousands of iterations needed to calculate the uncertainty of the velocity model with MCMC methods.

To determine the posterior velocity model distribution given observed data, $p(\mathbf{m}|\mathbf{d}_{obs})$, we assume that the misfit between the observed data \mathbf{d}_{obs} and the true data, $f(\mathbf{m})$ is entirely due to Gaussian measurement noise with covariance matrix Σ . Under this assumption the likelihood function is given by,

$$p(\mathbf{d}|\mathbf{m}_*) = e^{-\frac{1}{2}\mathbf{r}^t \Sigma^{-1} \mathbf{r}} \quad (1)$$

$$\mathbf{r} = f(\mathbf{m}_*) - \mathbf{d}_{obs}$$

where \mathbf{m}_* is a hypothetical velocity model. Calculating Equation 1 requires a single forward solve but does not directly yield an expression for the posterior distribution of velocity models given data. In order to estimate the posterior distribution we make use of the adaptive Metropolis-Hastings algorithm that allows for the estimation of the posterior distribution through numerous evaluations of the likelihood

function for hypothetical velocity models \mathbf{m}_* as described in [2].

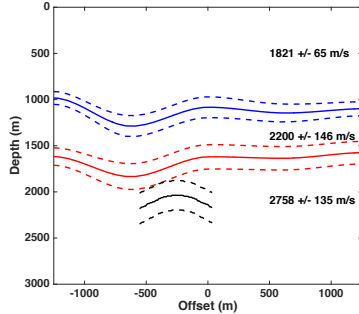


Figure 2: Depth uncertainty of individual interfaces and layer velocities. The strong correlation between the uncertain interface depth is captured but not visualized.

3 Migration Under Model Uncertainty

We ran the adaptive Metropolis-Hastings algorithm on the velocity and reflector model shown in Figure 1 for 100,000 iterations with the first 50,000 evaluations discarded for burn in. Figure 2 shows the standard deviation of the layer boundaries and velocities within each layer for the posterior distribution. This representation of uncertainty does not fully convey the full error in the velocity model and does a particularly poor job of showing correlated error. Instead viewing a few representative samples from the posterior distribution better illustrates this error as shown in Figure 3. From these six random samples we see that the shape of the anticline is well constrained, but its depth is not.

Instead of attempting to visualize the uncertainty of the velocity model it is more useful to observe how this uncertainty affects quantities of interest that heavily depend on velocity model uncertainty such as estimating the area and depth of a migrated anticline. We apply zero-offset migration with the velocity model distribution to determine these quantities. More sophisticated migration methods such as MAP migration, described in [3] can also be used. Figure 4 shows a histogram of anticline relative height and absolute depth and demonstrates that depth uncertainty is greater than relative height uncertainty.

4 Conclusion

Calculating and conveying uncertainty of seismic velocity models and subsequent migrated images pose numerous computational and visu-

alization challenges. In this paper we demonstrated a framework for both calculating and presenting this uncertainty in a meaningful manner.



Figure 3: Six distinct samples from the posterior distribution for the recovery of the model shown in Figure 1 from noisy data.

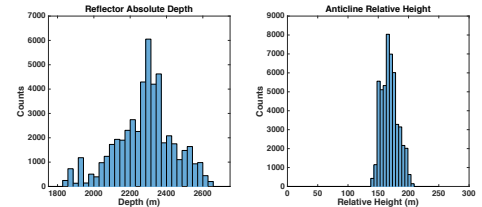


Figure 4: Relative depth uncertainty (170 ± 14 m) is much smaller than absolute depth uncertainty (2300 ± 160 m).

5 Acknowledgments

This material is based upon work supported by the NSF under Grant DGE-0806676, MIT's Earth Resources Laboratory, Chevron and with grants from the NSERC of Canada Industrial Research Chair Program, the Research and Development Corporation of Newfoundland and Labrador, and the Hibernia Management & Development Corporation.

References

- [1] Ely, Malcolm, and Nicholls. "Combining global optimization and boundary integral methods to robustly estimate subsurface velocity models." 2015 SEG Annual Meeting, 2015.
- [2] Haario et. al "An adaptive Metropolis algorithm." Bernoulli (2001): 223-242.
- [3] Poliannikov, and Malcolm. "The effect of velocity uncertainty on migrated reflectors: Improvements from relative-depth imaging." Geophysics 81, no. 1 (2015): S21-S29.

**The application of discontinuous Petrov-Galerkin space-time discretizations
and inexact Newton methods to seismic imaging**

Johannes Ernesti^{1,*}, Christian Wieners²

¹KIT, Institute of Applied and Numerical Mathematics, Karlsruhe, Germany

²KIT, Institute of Applied and Numerical Mathematics, Karlsruhe, Germany

*Email: johannes.ernesti@kit.edu

Abstract

We introduce a weakly conforming discontinuous Petrov-Galerkin method in space and time for the acoustic wave equation in heterogeneous media. The fully implicit high-order discretization is a minimal residual method for the first-order system with discontinuous test spaces on a decomposition of the space-time cylinder and with trace degrees of freedom on the skeleton of this decomposition.

This is applied to a problem in seismic inversion, where the permeability is recovered approximately from measurements of the scattered wave at sampling points. The ill-posed problem in seismic imaging is regularized by an inexact Newton method, where every increment is evaluated by a conjugate gradient iteration. In every iteration step, the residual is computed solving the wave equation, and for the gradient the adjoint wave equation with a right-hand side depending on the full space-time solution is approximated. The efficiency of the method is demonstrated by numerical examples in two space dimensions.

Keywords: Nonconforming finite elements in space and time, acoustic wave equation, inexact Newton methods, seismic imaging

1 The space-time discretization

We consider approximations of the linear acoustic wave equation

$$\rho \partial_t^2 p = \nabla \cdot (\kappa \nabla p)$$

in the space-time cylinder

$$Q = \Omega \times (0, T) \subset \mathbb{R}^D \times \mathbb{R}$$

depending on a density distribution $\rho > 0$ and permeability $\kappa > 0$.

Therefore, we consider the first-order differential operator

$$L(p, \mathbf{v}) = \begin{pmatrix} \rho \partial_t p + \nabla \cdot \mathbf{v} \\ \kappa^{-1} \partial_t \mathbf{v} + \nabla p \end{pmatrix}$$

in the Hilbert space

$$\begin{aligned} H(L, Q) &= \{(p, \mathbf{v}) \in L_2(Q, \mathbb{R} \times \mathbb{R}^D) : \\ &\quad L(p, \mathbf{v}) \in L_2(Q, \mathbb{R} \times \mathbb{R}^D) \end{aligned}$$

with norm $\|(p, \mathbf{v})\|_{L, Q}^2 = \|(p, \mathbf{v})\|_Q^2 + \|L(p, \mathbf{v})\|_Q^2$. For homogeneous initial and boundary conditions in a subspace $V \subset H(L, Q)$ and right-hand side $(f, \mathbf{g}) \in L_2(Q, \mathbb{R} \times \mathbb{R}^D)$ a unique solution $(p, \mathbf{v}) \in V$ of $L(p, \mathbf{v}) = (f, \mathbf{g})$ exists and can efficiently be approximated with a space-time discontinuous Petrov-Galerkin method [2].

Based on a decomposition of Q into space-time cells $Q_h = \bigcup R$, this is extended to a hybrid method by introducing skeleton variables $(\hat{p}, \hat{\mathbf{v}}_n)$ and the bilinear form

$$\begin{aligned} b((p, \mathbf{v}, \hat{p}, \hat{\mathbf{v}}_n), (\delta p, \delta \mathbf{v})) &= \sum_R -((p, \mathbf{v}), L(\delta p, \delta \mathbf{v}))_R \\ &\quad + \langle (\hat{p}, \hat{\mathbf{v}}_n), (\delta p, \delta \mathbf{v} \cdot \mathbf{n}) \rangle_{\partial R} \end{aligned}$$

satisfying the identity

$$b((p, \mathbf{v}, p, \mathbf{v} \cdot \mathbf{n}), (\delta p, \delta \mathbf{v})) = (L(p, \mathbf{v}), (\delta p, \delta \mathbf{v}))_Q.$$

For given $\ell(\delta p, \delta \mathbf{v}) = ((f, \mathbf{g}), (\delta p, \delta \mathbf{v}))_Q$, an approximation $(p^h, \mathbf{v}^h, \hat{p}^h, \hat{\mathbf{v}}_n^h)$ is computed by minimizing the residual

$$\rho(p^h, \mathbf{v}^h, \hat{p}^h, \hat{\mathbf{v}}_n^h) = \sup_{(\delta p, \delta \mathbf{v}) \in \prod V_{h,R}} \frac{b((p^h, \mathbf{v}^h, \hat{p}^h, \hat{\mathbf{v}}_n^h), (\delta p, \delta \mathbf{v})) - \ell(\delta p, \delta \mathbf{v})}{\|(\delta p, \delta \mathbf{v})\|_{L, Q_h}}$$

with $V_{h,R} \subset H(L, R)$, see [1]. This can be reduced to a symmetric positive definite system [7] and can be solved efficiently in parallel in time and space simultaneously, see Fig. 1 for an example. Selecting variable polynomial degrees in $V_{h,R}$ allows for adaptivity with respect to the space-time cone for point sources and receivers.

Furthermore, the full solution in space and time is required for the computation of the gradient in inverse applications.

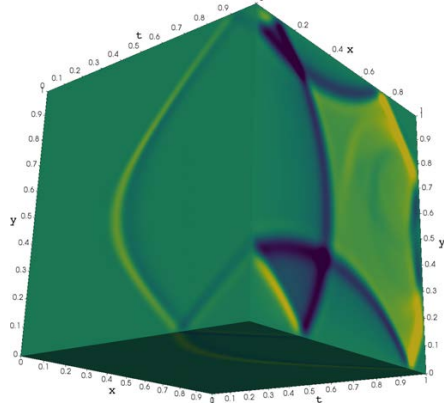


Figure 1: Space-time solution of a single scattered wave front initiated from a point source.

2 The inexact Newton method

The parameter-to-solution operator in seismic tomography is locally ill-posed [3] and Fréchet-differentiable [4] in a suitable Banach space setting. We select a parameter set

$$\mathcal{P} \subset L_\infty(\Omega) \times L_\infty(\Omega) \times L_2(\Omega, \mathbb{R} \times \mathbb{R}^D),$$

where $(\rho, \kappa, f, g) \in \mathcal{P}$ are the unknown material parameters and (f, g) is the unknown right-hand side corresponding to a wave initiated by a point source. The discrete parameter-to-solution operator

$$F_h: \mathcal{P} \longrightarrow V_h$$

is defined by the space-time discretization approximating the forward problem for the material parameters (ρ, κ) . The observation operator

$$\Phi: V_h \longrightarrow \mathbb{R}^N$$

is determined by measurements of the pressure

$$(p(\xi_n, t_n))_{n=1, \dots, N}$$

at sample points $(\xi_n, t_n) \in Q$ in the space-time cylinder.

This defines the problem in seismic imaging as follows: Given an observation $w \in \mathbb{R}^N$ and a noise level $\varepsilon > 0$, find parameters (ρ, κ, f, g) in \mathcal{P} such that

$$\|\Phi \circ F(\rho, \kappa, f, g) - w\| \leq \varepsilon.$$

The inverse problem is regularized by an inexact Newton method, where every increment is approximated by conjugate gradient iterations up

to a relaxed accuracy depending on the residual and the noise level [6]. Variants of this scheme without introducing a noise level are frequently used in seismic imaging [5].

In every step of the cg iteration, the residual is evaluated by solving the wave equation, and for the evaluation of the conjugated gradient the adjoint wave equation with a right-hand side depending on the full space-time solution is approximated.

The full method combining high-order weakly conforming space-time discontinuous Petrov-Galerkin discretizations and the inexact Newton method is realized in parallel, and the convergence of the overall scheme is demonstrated by numerical examples in two space dimensions.

References

- [1] T. BUI-THANH, L. DEMKOWICZ, AND O. GHATTAS, *A unified discontinuous Petrov–Galerkin method and its analysis for Friedrichs’ systems*, SIAM J. on Numer. Anal. **51**:4 (2013), 1933–1958.
- [2] W. DÖRFLER, S. FINDEISEN, AND C. WIENERS, *Space-time discontinuous Galerkin discretizations for linear first-order hyperbolic evolution systems*, Comput. Methods Appl. Math. **16**:3 (2016), 409–428.
- [3] A. KIRSCH AND A. RIEDER, *Seismic tomography is locally ill-posed*, Inverse Problems **30**:12 (2014), 125001.
- [4] A. KIRSCH AND A. RIEDER, *Inverse problems for abstract evolution equations with applications in electrodynamics and elasticity*, Inverse Problems **32**:8 (2016), 085001.
- [5] L. MÉTIVIER, R. BROISSIER, J. VIRIEUX, AND S. OPERTO, *Full waveform inversion and the truncated newton method*, SIAM Journal on Scientific Computing **35**:2 (2013), B401–B437.
- [6] A. RIEDER, *Inexact Newton regularization using conjugate gradients as inner iteration*, SIAM Journal on Numerical Analysis **43**:2 (2005), 604–622.
- [7] C. WIENERS AND B. WOHLMUTH, *Robust operator estimates and the application to substructuring methods for first-order systems*, ESAIM: M²AN **48** (2014), 161–175.

Uncertainty quantification for inverse problems with a weak wave-equation constraint

Zhilong Fang^{1,*}, Curt D. Silva¹, Rachel Kuske², Felix J. Herrmann¹

¹Department of EOAS, University of British Columbia, Vancouver, Canada

²Department of Mathematics, University of British Columbia, Vancouver, Canada

*Email: fzlong88@gmail.com

Abstract

In this work, we present a new posterior distribution to quantify uncertainties in solutions of wave-equation based inverse problems. By introducing an auxiliary variable for the wave-fields, we weaken the strict wave-equation constraint used by conventional Bayesian approaches. With this weak constraint, the new posterior distribution is a bi-Gaussian distribution with respect to both model parameters and wave-fields, which can be directly sampled by the Gibbs sampling method.

Keywords: Uncertainty, wave-equation

1 Introduction

In wave-equation based inverse problems, the goal is to infer the unknown model parameters from the observed data using the wave-equation as a constraint. Conventionally, the wave-equation is treated as a strict constraint in a Bayesian inverse problem. After eliminating this constraint, the problem involves the following forward modeling operator mapping model to predicted data:

$$f(\mathbf{m}) = \mathbf{P}\mathbf{A}(\mathbf{m})^{-1}\mathbf{q}, \quad (1)$$

where the vectors $\mathbf{m} \in \mathbb{R}^{n_{\text{grid}}}$ and $\mathbf{q} \in \mathbb{C}^{n_{\text{grid}}}$ represent the discretized n_{grid} -dimensional unknown model parameters and known source term, respectively. The matrix $\mathbf{A} \in \mathbb{C}^{n_{\text{grid}} \times n_{\text{grid}}}$ represents the discretized wave-equation operator and the operator $\mathbf{P} \in \mathbb{R}^{n_{\text{recv}} \times n_{\text{grid}}}$ projects the solution of the wave-equation $\mathbf{u} = \mathbf{A}(\mathbf{m})^{-1}\mathbf{q}$ onto the n_{recv} receivers.

In the Bayesian framework, the solution of an inverse problem given observed data \mathbf{d} is a posterior probability density function (PDF) $\rho(\mathbf{m}|\mathbf{d})$ expressed as [1]:

$$\rho(\mathbf{m}|\mathbf{d}) \propto \rho(\mathbf{d}|\mathbf{m})\rho(\mathbf{m}), \quad (2)$$

where the likelihood PDF $\rho(\mathbf{d}|\mathbf{m})$ describes the probability of observing data \mathbf{d} given model parameters \mathbf{m} and the prior PDF $\rho(\mathbf{m})$ describes

one's prior knowledge about the model parameters. Under the assumption that the noise in the data is Gaussian with zero mean and covariance matrix Γ_n , and the prior distribution is also Gaussian with a mean model $\tilde{\mathbf{m}}$ and covariance matrix Γ_p , the posterior PDF can be written as:

$$\rho(\mathbf{m}|\mathbf{d}) \propto \exp\left(-\frac{1}{2}(\|f(\mathbf{m}) - \mathbf{d}\|_{\Gamma_n^{-1}}^2 + \|\mathbf{m} - \tilde{\mathbf{m}}\|_{\Gamma_p^{-1}}^2)\right). \quad (3)$$

Due to the non-linear map $f(\mathbf{m})$ and the high dimensionality of the model parameters ($n_{\text{grid}} \geq 10^5$), applying Markov chain Monte Carlo (McMC) methods to sample the posterior PDF (3) faces a difficult challenge of constructing a proposal PDF that provides a reasonable approximation of the target density with reasonable computational costs [1].

2 Posterior PDF with weak constraint

As the exact constraint $A(\mathbf{m})\mathbf{u} = \mathbf{q}$ leads to the difficulty of studying the corresponding posterior PDF, we weaken the constraint and arrive at a more generic posterior PDF with an auxiliary variable – wavefields \mathbf{u} as follows:

$$\rho(\mathbf{m}, \mathbf{u}|\mathbf{d}) \propto \rho_1(\mathbf{d}|\mathbf{u})\rho_2(\mathbf{u}|\mathbf{m})\rho(\mathbf{m}), \text{ with}$$

$$\rho_1(\mathbf{d}|\mathbf{u}) \propto \exp\left(-\frac{1}{2}\|\mathbf{P}\mathbf{u} - \mathbf{d}\|_{\Gamma_n^{-1}}^2\right), \text{ and} \quad (4)$$

$$\rho_2(\mathbf{u}|\mathbf{m}) \propto \exp\left(-\frac{\lambda^2}{2}\|\mathbf{A}(\mathbf{m})\mathbf{u} - \mathbf{q}\|^2\right).$$

Here the penalty parameter λ controls the trade off between the wave-equation and the data-fitting terms. As λ grows, the wavefields are more tightly constrained by the wave-equation. It is readily observed that the posterior PDF (2) is a special case of the posterior PDF (4) with $\rho_2(\mathbf{u}|\mathbf{m}) = 1$ and $\mathbf{A}(\mathbf{m})\mathbf{u} = \mathbf{q}$.

The new posterior PDF (4) has two important properties. First, the conditional PDF $\rho(\mathbf{u}|\mathbf{m}, \mathbf{d})$ of \mathbf{u} on \mathbf{m} is Gaussian. Second, if the matrix $\mathbf{A}(\mathbf{m})$ linearly depends on \mathbf{m} , the conditional PDF $\rho(\mathbf{m}|\mathbf{u}, \mathbf{d})$ of \mathbf{m} on \mathbf{u} is also Gaussian. Therefore, the posterior PDF (4) is bi-Gaussian with respect to \mathbf{u} and \mathbf{m} .

3 Gibbs sampling

The bi-Gaussian property of the posterior PDF (4) provides a straight-forward intuition of applying Gibbs sampling method by alternatively drawing samples \mathbf{u} and \mathbf{m} from the conditional PDFs $\rho(\mathbf{u}|\mathbf{m}, \mathbf{d})$ and $\rho(\mathbf{m}|\mathbf{u}, \mathbf{d})$. At the k^{th} iteration of the Gibbs sampling, starting from the point \mathbf{m}_k , the conditional PDF $\rho(\mathbf{u}|\mathbf{m}_k, \mathbf{d}) = \mathcal{N}(\bar{\mathbf{u}}, \mathbf{H}_u^{-1})$ with the Hessian matrix \mathbf{H}_u and the mean wave-fields $\bar{\mathbf{u}}$ given by:

$$\begin{aligned}\mathbf{H}_u &= \mathbf{P}^\top \Gamma_p^{-1} \mathbf{P} + \lambda^2 \mathbf{A}(\mathbf{m}_k)^\top \mathbf{A}(\mathbf{m}_k), \\ \bar{\mathbf{u}} &= \mathbf{H}_u^{-1} (\mathbf{A}(\mathbf{m}_k)^\top \mathbf{q} + \mathbf{P}^\top \Gamma_p^{-1} \mathbf{d}).\end{aligned}\quad (5)$$

To draw a sample $\mathbf{u}_{k+1} \sim \mathcal{N}(\bar{\mathbf{u}}, \mathbf{H}_u^{-1})$, we first compute the Cholesky factorization of $\mathbf{H}_u = \mathbf{L}_u^\top \mathbf{L}_u$, where \mathbf{L}_u is an upper triangular matrix. Then we apply \mathbf{L}_u to compute $\bar{\mathbf{u}}$ and \mathbf{u}_{k+1} by:

$$\begin{aligned}\bar{\mathbf{u}} &= \mathbf{L}_u^{-1} \mathbf{L}_u^{-\top} (\mathbf{A}(\mathbf{m}_k)^\top \mathbf{q} + \mathbf{P}^\top \Gamma_p^{-1} \mathbf{d}), \\ \mathbf{u}_{k+1} &= \bar{\mathbf{u}} + \mathbf{L}_u^{-1} \mathbf{r}_u, \mathbf{r}_u \sim \mathcal{N}(0, \mathbf{I}).\end{aligned}\quad (6)$$

With \mathbf{u}_{k+1} , the conditional PDF $\rho(\mathbf{m}|\mathbf{u}_{k+1}, \mathbf{d}) = \mathcal{N}(\bar{\mathbf{m}}, \mathbf{H}_m^{-1})$. The mean $\bar{\mathbf{m}} = \mathbf{m}_k - \mathbf{H}_m^{-1} \mathbf{g}_m$ with gradient and Hessian expressed as:

$$\begin{aligned}\mathbf{g}_m &= \mathbf{G}^\top (\mathbf{A}(\mathbf{m}_k) \mathbf{u}_{k+1} - \mathbf{q}) + \Gamma_p^{-1} (\mathbf{m}_k - \tilde{\mathbf{m}}), \\ \mathbf{H}_m &= \mathbf{G}^\top \mathbf{G} + \Gamma_p^{-1},\end{aligned}\quad (7)$$

where $\mathbf{G} = \frac{\partial \mathbf{A}(\mathbf{m}) \mathbf{u}_{k+1}}{\partial \mathbf{m}}$ is the sparse Jacobian matrix. The new sample \mathbf{m}_{k+1} can be computed by:

$$\mathbf{m}_{k+1} = \bar{\mathbf{m}} + \mathbf{L}_m^{-1} \mathbf{r}_m, \mathbf{r}_m \sim \mathcal{N}(0, \mathbf{I}), \quad (8)$$

where $\mathbf{L}_m = \mathbf{H}_m^{1/2}$.

4 Numerical experiment

We apply our proposal method to an inverse problem constrained by the 2D Helmholtz equation. We use single source, single frequency data to invert a 1D gridded squared slowness profile $m(z) = 1/(v_0 + \alpha z)^2$ for values $v_0 = 2000 \text{ m/s}$ and $\alpha = 0.75$. We use frequency increments of 1 Hz, a grid spacing of 50 m, a maximum offset of 10000 m, and a maximum depth of 5000 m. Both source and receivers are located at the surface of the model. Gaussian noise with covariance matrix $\Gamma_n = \mathbf{I}$ is added to the data. The mean model of the prior distribution is selected to have $v_0 = 2000 \text{ m/s}$ and $\alpha = 0.65$. The covariance matrix is set to $\Gamma_p = 2 \times 10^{-8} \mathbf{I}$. We use the Gibbs sampling method to generate 10^6 samples with $\lambda =$

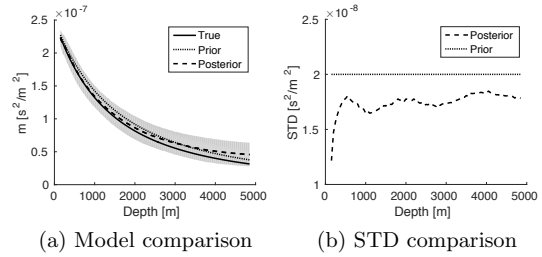


Figure 1: (a) Comparison of true model (solid), mean model of prior PDF (dotted) and posterior PDF (dashed); (b) Comparison of STDs of prior (dotted) and posterior (dashed) PDFs.

10^5 . We compare the true model, the prior mean model, and the posterior mean model in Figure 1a, and the prior and posterior standard deviations (STD) in Figure 1b. The 90% confidence interval of the posterior distribution is also shown in Figure 1a (gray background). Compared to the prior distribution, the posterior mean model has a smaller error in the shallow part but a larger error in the deep part. Meanwhile, the posterior STD in the shallow part has a larger decrease from the prior STD than that in the deep part. Both facts implies that data has a larger influence on the squared slowness in the shallow part than that in the deep part.

5 Conclusion

By weakening the wave-equation constraint in a controlled manner, we arrive at a novel formulation of posterior PDF for wave-equation inversion. This new posterior PDF is bi-Gaussian with respect to model parameters and wave-fields. Numerical experiment demonstrates that this posterior PDF can be successfully and efficiently sampled by the Gibbs sampling method. The computational cost of drawing one sample equals to evaluating one posterior PDF. This allows us to apply the proposed approach to large 2D or 3D problems.

6 Acknowledgements

This research was carried out as part of the SINBAD project with the support of the member organizations of the SINBAD Consortium.

References

- [1] J. Martin, L. C. Wilcox, C. Burstedde, and O. Ghattas, A stochastic newton MCMC method for large-scale statistical inverse problems with application to seismic inversion *SIAM Journal on Scientific Computing* **34** (2012), pp. A1460-A1487

Modeling the multimodal radiation from an open-ended waveguide

Simon Félix^{1,*}, Jean-Baptiste Doc², Matthew Boucher³

¹LAUM, CNRS, Université du Maine, Le Mans, France

²LMSSC, CNAM, Paris, France

³KU Leuven, Department of Mechanical Engineering, Heverlee, Belgium

*Email: simon.felix@univ-lemans.fr

Abstract

Using a multimodal formalism of the guided wave propagation and a complex coordinate stretching (PML), we derive algebraic solutions for the multimodal radiation impedance at the end of a waveguide open on the free space. The basic idea of the method is to turn the original unbounded problem into the problem of a cylindrical waveguide embedded in an infinite waveguide with an annular PML on the inside of its exterior wall. This method makes no assumption on the frequency range and can be applied to any cross-section geometry and wall thickness.

Keywords: waveguide, radiation, impedance, multimodal, PML

1 Introduction

Consider a semi-infinite cylindrical waveguide (denoted WGA, with radius a and wall thickness ea , see Fig. 1), open at its output end (say, $x = 0$, x the axial coordinate) on the free space. For the sake of clarity the cross-section is assumed to be circular and a Neumann condition is assumed at the wall ($r = a$ and $(1 + e)a$), though the same method would apply for other geometries or boundary conditions. The aim of this work is to write a discrete estimate, $Z_A^{(e)}(k)$, of the Neumann-to-Dirichlet operator, $\zeta(k, r)$, satisfying $p(k, 0, r) = \zeta(k, r)\partial_x p(k, 0, r)$, where $p(k, x, r)$ is the solution of the Helmholtz equation $(\Delta + k^2)p e^{i\mu\theta} = 0$, $\mu \in \mathbb{Z}$.¹ The discretization is made by projection on a basis of functions, $\{u_{An}(r)\}$. The choice of this set of functions is naturally not unique, but, for the sake of conciseness, we will restrict to the orthonormal basis of the classical transverse eigenmodes in WGA, such that

$$Z_{Amm}^{(e)} = (u_{Am}, \zeta u_{An})_A \quad (1)$$

¹Owing to the symmetry of the problem, we can restrict to the particular solution with azimuthal dependence $\exp(i\mu\theta)$, without loss of generality.

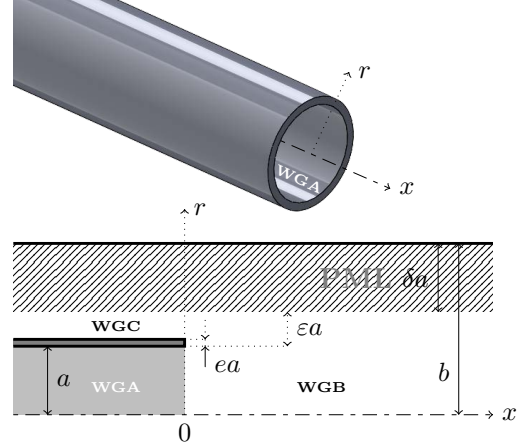


Figure 1: Example of a cylindrical, open-ended, waveguide, and equivalent problem with the semi-infinite “PML-waveguides” WGB and WGC.

with the scalar product $(f, g)_A = \int_0^a \bar{f}g r dr$.

2 General formulation

The basic idea of the proposed method to calculate Z_A is to turn the original unbounded problem into the problem of a waveguide embedded in an infinite cylindrical waveguide with an annular PML on the inside of its exterior wall (Fig. 1). The *perfect matching* and the wave damping in the PML are achieved by means of a complex stretching of the radial coordinate r into

$$\tilde{r}(r) = \int_0^r \alpha(r') dr' \quad (2)$$

with α a complex function filling $\text{Re}[\alpha] > 0$ and $\text{Im}[\alpha] > 0$.

The configuration shown in Fig. 1 actually displays two semi-infinite PML-waveguides: a circular one (WGB), for $x > 0$, and an annular one (WGC), for $x < 0$. In both waveguides, the wavefield satisfies the wave equation

$$\left[\frac{\partial^2}{\partial x^2} + \frac{1}{\tilde{r}} \frac{\partial}{\partial \tilde{r}} \left(\tilde{r} \frac{\partial}{\partial \tilde{r}} \right) - \frac{\mu^2}{\tilde{r}} \right] p = 0. \quad (3)$$

As in WGA, the problem is discretized by projection over bases of functions $\{u_{\eta n}(r)\}$, $\eta = B, C$. We choose the bases of the real, orthonormal solutions of the transverse eigenproblems in the absence of PML, but other choices can be made (complex solutions of the transverse eigenproblem with PML, finite elements, ...).

Then, by writing the exact condition of downward (resp. backward) propagation in the semi-infinite waveguide WGB (resp. WGC), and by writing also the continuity relations, we get the following algebraic solution for the radiation impedance matrix $Z_A^{(e)}$:

$$Z_A^{(e)} = F Z_B (I + G^T Y_C G Z_B)^{-1} F^T, \quad (4)$$

where F and G are matrices of scalar products between the basis functions $u_{\eta n}$, $\eta = A, B, C$, obtained from the continuity relations, and Z_B (resp. Y_C) is the characteristic impedance (resp. admittance) matrix in WGB (resp. WGC).

The limit case of WGA ending in an infinite flange ($e \rightarrow \infty$) is of interest because it is the only case that has been fully solved beyond the low frequency range [1]. The radiation impedance matrix is then simply

$$Z_A^{(\infty)} = F Z_B F^T. \quad (5)$$

3 Results

In order to validate the proposed method, the two limit cases, $e \rightarrow \infty$ and $e \rightarrow 0$, are considered and the results are compared with reference solutions: Zorunski's integral formulation in the first case [1] (Fig. 2) and the low frequency, 1D solution by Levine & Schwinger in the second case [2] (Fig. 3). In each case, four terms of the symmetric impedance matrix $Z_A^{(e)}$ are plotted, showing a excellent agreement. Note that, to allow for comparison with Levine & Schwinger's solution, rather than Z_{A00} , $z_0 = (1 + R_{00})/(1 - R_{00})/ika$ is plotted, where R is the reflexion matrix at $x = 0$, straightforwardly deduced from $Z_A^{(e)}$.

References

- [1] W. E. Zorunski, Generalized radiation impedance and reflection coefficients of circular and annular ducts, *J. Acoust. Soc. Am.* **135** (1973), pp. 1667–1673.
- [2] H. Levine and J. Schwinger, On the radiation of sound from an unflanged circular pipe, *Phys. Rev.* **73** (1948), pp. 383–406.

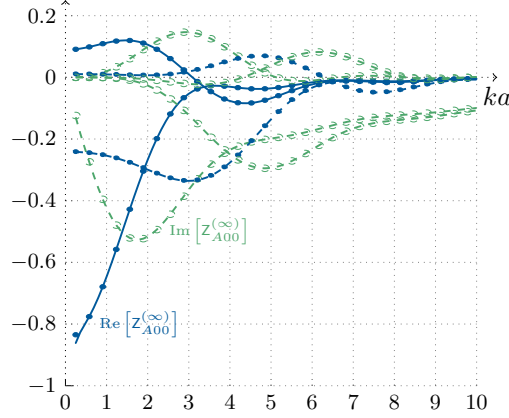


Figure 2: Variation with the frequency of the terms 00, 01, 11 and 12 of the radiation impedance matrix $Z_A^{(\infty)}$ of a waveguide with an infinite flange. Blue: real part, green: imaginary part. Solid and dashed: algebraic solution with PML-waveguides. Dots and circles: Zorunski's integral formulation [1].

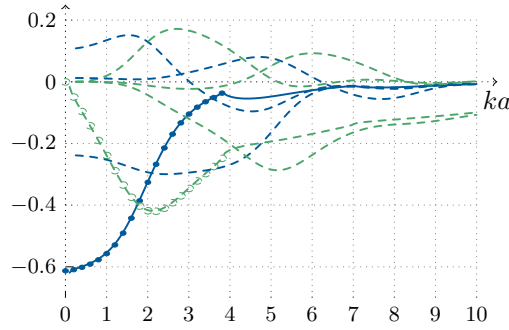


Figure 3: Variation with the frequency of the terms 00, 01, 11 and 12 of the radiation impedance matrix $Z_A^{(e)}$ of an unflanged waveguide ($e \ll 1$). Blue: real part, green: imaginary part. Solid and dashed: algebraic solution with PML-waveguides. Dots and circles: Levine & Schwinger's solution [2].

Minnaert Resonances for Acoustic Waves in Bubbly Media

Habib Ammari¹, Brian Fitzpatrick^{1,*}, David Gontier², Hyundae Lee³, Hai Zhang⁴

¹Seminar for Applied Mathematics, ETH Zurich, Zurich, Switzerland

²CEREMADE, Université Paris-Dauphine, 75775 Paris Cedex 16

³Department of Mathematics, Inha University, 253 Yonghyun-dong Nam-gu, Incheon 402-751, Korea

⁴Department of Mathematics, HKUST, Clear Water Bay, Kowloon, Hong Kong

*Email: brian.fitzpatrick@sam.math.ethz.ch

Abstract

Through the application of layer potential techniques and Gohberg-Sigal theory we derive an original formula for the Minnaert resonance frequencies of arbitrarily shaped bubbles along with providing a mathematical justification for the monopole approximation of scattering of acoustic waves by bubbles at their Minnaert resonant frequency. Our results are complemented by several numerical examples which serve to validate our formula in two dimensions.

Keywords: Acoustic waves, layer potentials, monopole approximation, Minnaert resonance

1 Research focus

Our overall research focus is on developing a mathematical and computational framework for the analysis of Minnaert bubbles. We are interested in characterizing and exploiting the Minnaert resonance frequencies of bubbles in a variety of situations which will allow us to construct a unified theory of acoustic metamaterials [1], phononic crystals [2], and super-focusing of acoustic waves [3].

2 Minnaert resonance for arbitrarily shaped bubbles

A vast assortment of physical works have dealt with systems involving acoustic bubbles and their analysis has been based on the standard Minnaert resonance formula. However, this formula for the resonant frequency of bubbles is only appropriate in the case of spherical bubbles. Determining a Minnaert resonance formula for arbitrarily shaped bubbles has been a longstanding problem. We use layer potential techniques and asymptotic analysis of an operator valued function to obtain a formula for the resonant frequency of arbitrarily shaped bubbles [4].

Assume the bubble occupies a bounded domain D . We denote by ρ_b and κ_b the density and bulk modulus of the air inside the bubble,

respectively. ρ and κ are the corresponding parameters for the background media. The scattering problem can be modelled by the following equations:

$$\left\{ \begin{array}{ll} \nabla \cdot \frac{1}{\rho} \nabla u + \frac{\omega^2}{\kappa} u = 0 & \text{in } \mathbb{R}^3 \setminus D, \\ \nabla \cdot \frac{1}{\rho_b} \nabla u + \frac{\omega^2}{\kappa_b} u = 0 & \text{in } D, \\ u_+ - u_- = 0 & \text{on } \partial D, \\ \frac{1}{\rho} \frac{\partial u}{\partial \nu} \Big|_+ - \frac{1}{\rho_b} \frac{\partial u}{\partial \nu} \Big|_- = 0 & \text{on } \partial D, \\ u^s := u - u^{in} \text{ satisfies the Sommerfeld radiation condition,} \end{array} \right. \quad (1)$$

where u^{in} is the incident wave. The solution of this problem has the representation

$$u(x) = \begin{cases} u^{in} + \mathcal{S}_D^k[\psi], & x \in \mathbb{R}^3 \setminus \bar{D}, \\ \mathcal{S}_D^{k_b}[\psi_b], & x \in D, \end{cases}$$

for some surface potentials $\psi, \psi_b \in L^2(\partial D)$. Using the jump relations for the single layer potential it is straightforward to derive that ψ and ψ_b satisfy the following system of boundary integral equations:

$$\mathcal{A}(\omega, \delta)[\Psi] = F, \quad (2)$$

where

$$\mathcal{A}(\omega, \delta) = \begin{pmatrix} \mathcal{S}_D^{k_b} & -\mathcal{S}_D^k \\ -\frac{1}{2}Id + \mathcal{K}_D^{k_b,*} & -\delta(\frac{1}{2}Id + \mathcal{K}_D^{k,*}) \end{pmatrix},$$

$$\Psi = \begin{pmatrix} \psi_b \\ \psi \end{pmatrix}, \quad F = \begin{pmatrix} u^{in} \\ \delta \frac{\partial u^{in}}{\partial \nu} \end{pmatrix},$$

where $\delta = \frac{\rho_b}{\rho}$ is the contrast parameter, \mathcal{S}_D is the single layer potential, and \mathcal{K}_D^* is the Neumann-Poincaré operator. The resonance of the bubble in the scattering problem (1) can be defined as all the complex numbers ω with negative imaginary part such that there exists a nontrivial solution to the following equation:

$$\mathcal{A}(\omega, \delta)[\Psi] = 0.$$

δ	Relative error
10^{-1}	5.8203%
10^{-2}	0.6727%
10^{-3}	0.0652%
10^{-4}	0.0062%
10^{-5}	0.0030%

Table 1: The relative error between the Minnaert resonance frequency ω_f obtained via the formula and the resonance frequency ω_{num} obtained by direct numerical solution of the system of boundary integral equations in (2).

The Minnaert resonance corresponds to the quasi-static resonance, the resonance frequency at which the size of the bubble is much less than the size of the wavelength of the incident wave outside the bubble. This can be stated formally as follows:

Lemma 2.1 *For any δ , sufficiently small, there exists a characteristic value $\omega_0 = \omega_0(\delta)$ to the operator-valued analytic function $\mathcal{A}(\omega, \delta)$ such that $\omega_0(0) = 0$ and ω_0 depends on δ continuously. This characteristic value is also the quasi-static resonance (or Minnaert resonance).*

We perform asymptotic analysis on the operator $\mathcal{A}(\omega, \delta)$ in order to find an analytic expression for the Minnaert resonance.

Lemma 2.2

$$\begin{aligned} \mathcal{A}(\omega, \delta) := & \mathcal{A}_0 + \mathcal{B}(\omega, \delta) = \mathcal{A}_0 + \omega \mathcal{A}_{1,0} + \omega^2 \mathcal{A}_{2,0} \\ & + \omega^3 \mathcal{A}_{3,0} + \delta \mathcal{A}_{0,1} + \delta \omega^2 \mathcal{A}_{2,1} + O(\omega^4) \\ & + O(\delta \omega^3), \end{aligned} \quad (3)$$

where the terms $\mathcal{A}_{1,0}$, $\mathcal{A}_{2,0}$, $\mathcal{A}_{3,0}$, $\mathcal{A}_{0,1}$, $\mathcal{A}_{2,1}$, and $\mathcal{K}_{D,2}$ can be calculated explicitly.

We show that when the contrast δ is high the Minnaert resonance for the bubble is given by the formula:

$$\begin{aligned} \omega_f(\delta) = & \sqrt{\frac{Cap(D)}{\tau^2 v^2 Vol(D)}} \delta^{\frac{1}{2}} \\ & - i \frac{Cap(D)^2}{8\pi\tau^2 v Vol(D)} \delta + O(\delta^{\frac{3}{2}}), \end{aligned}$$

where $Cap(D)$ is the capacity of the bubble, $\tau = \sqrt{\frac{\rho_b \kappa}{\rho \lambda_b}}$ and $v = \sqrt{\frac{\rho}{\kappa}}$. Table 1 shows that the formula is highly accurate when we are in the high contrast regime.

3 Monopole approximation

Assume that the bubble is excited by the incident wave $u^{in}(x) = e^{ikd \cdot x}$. This corresponds to the bubble being excited by sources in the far field and we have the following result in the regime $\frac{\omega}{\sqrt{\delta}} = O(1)$:

Theorem 3.1 *In the far field, the solution to the scattering problem (1) has the point-wise behaviour:*

$$\begin{aligned} u^s(x) = & g(\omega, \delta, D) (1 + O(\omega) + O(\delta) + o(1)) \\ & \times u^{in}(y_0) G(x, y_0, k), \end{aligned} \quad (4)$$

where y_0 is the center of the bubble and the scattering coefficient g is:

$$g(\omega, \delta, D) = \frac{Cap(D)}{1 - (\frac{\omega_M}{\omega})^2 + i\gamma}, \quad (5)$$

where ω_M is the Minnaert resonance frequency and γ is a damping constant.

References

- [1] M. Lanoy, R. Pierrat, F. Lemoult, M. Fink, V. Leroy, and A. Tourin, Subwavelength focusing in bubbly media using broadband time reversal, *Physical Review B*, 91(22), 224202, 2015.
- [2] H. Ammari, H. Kang, and H. Lee, Asymptotic analysis of high-contrast phononic crystals and a criterion for the band-gap opening, *Archive for rational mechanics and analysis* 193.3: 679-714, 2009.
- [3] H. Ammari, and H. Zhang, Effective medium theory for acoustic waves in bubbly fluids near Minnaert resonant frequency, *arXiv preprint arXiv:1604.08409* 2016.
- [4] H. Ammari, B. Fitzpatrick, D. Gontier, H. Lee, and H. Zhang, Minnaert resonances for acoustic waves in bubbly media, *arXiv preprint*, arXiv:1603.03982, 2016.

Transparent boundary conditions for general waveguide problems

Anne-Sophie Bonnet Ben-Dhia¹, Sonia Fliss^{1,*}, Antoine Tonnoir²

¹POEMS, CNRS-ENSTA ParisTech-INRIA, Université Paris Saclay

²INSA, Rouen, France

*Email: sonia.fliss@ensta-paristech.fr

Abstract

In this work, we propose a construction of transparent boundary conditions which can be used for quite general waveguide problems. Classical Dirichlet-to-Neumann maps used for homogeneous acoustic waveguides can be constructed using separation of variables and the orthogonality of the modes on one transverse section. These properties are also important for the mathematical and numerical analysis of problems involving DtN maps. However this framework does not extend directly to stratified, anisotropic or periodic waveguides and for Maxwell's or elastic equations. The difficulties are that (1) the separation of variables is not always possible and (2) the modes of the waveguides are not necessarily orthogonal on the transverse section. We propose an alternative to the DtN maps which uses two artificial boundaries and is constructed using a general orthogonality property.

Keywords: transparent boundary conditions, waveguides, energy flux

1 The Poynting-to-Neumann map for homogeneous acoustic waveguides

Let us consider a diffraction problem in an acoustic isotropic half-guide $\Omega = S \times]-a, +\infty[$ where $S \subset \mathbb{R}^2$ denotes the bounded cross-section of the guide. We look for the outgoing solution p of

$$\begin{cases} \Delta p + \omega^2 p = f & \text{in } \Omega, \\ \partial_\nu p = 0 & \text{on } \partial\Omega, \end{cases} \quad (1)$$

where ω is the frequency, ν is the exterior normal to $\partial\Omega$ and the source term f is supposed to be compactly supported in $\{z < 0\}$. We denote by p_ℓ (resp. p_∞) the restriction of p to the subdomain $\Omega_\ell = \Omega \cap \{z < \ell\}$ (resp. $\Omega_\infty = \Omega \cap \{z > 0\}$) and we want to derive transparent boundary conditions for p_ℓ on Σ_ℓ . Looking for the outgoing solution, p_∞ admits the following expression

$$p_\infty(x, y, z) = \sum_{k \geq 0} a_k^\infty w_k(x, y, z) \quad (2)$$

involving the right-going modes $w_k(x, y, z) = \varphi_k(x, y) e^{i\beta_k z}$. A finite number (N) of them are propagative ($\text{Im}(\beta_j) = 0$ and $\text{Re}(\beta_j) > 0$) and the rest are evanescent ($\text{Im}(\beta_j) > 0$ and $\text{Re}(\beta_j) = 0$). Here, the sequence $\{\varphi_k, k \in \mathbb{N}\}$ forms an orthonormal basis of $L^2(S)$. The a_k^∞ are the unknown modal amplitudes.

Imposing the two following matching conditions on the boundary Σ_ℓ :

$$p_\ell|_{\Sigma_\ell} = p_\infty|_{\Sigma_\ell} \quad \text{and} \quad \partial_z p_\ell|_{\Sigma_\ell} = \partial_z p_\infty|_{\Sigma_\ell}; \quad (3)$$

using the formula (2) and the orthogonality of the φ_k , one can derive a transparent condition for p_ℓ , involving the classical Dirichlet-to-Neumann operator T_{DtN} :

$$T_{\text{DtN}} p_\ell = \partial_z p_\ell|_{\Sigma_\ell} = \sum_{k \geq 0} i\beta_k (p_\ell, \varphi_k)_{\Sigma_\ell} \varphi_k. \quad (4)$$

However this method to obtain the modal amplitudes thanks to the trace of p_∞ requires the orthogonality of the modes in $L^2(S)$, which does not hold for instance in stratified, anisotropic or periodic waveguides or in (even isotropic) elastic waveguides. So let us explain how to derive some of the modal amplitudes using a more general framework.

Using the expression of w_k , it is easy to see that

$$q(w_j, w_k) = 0 \text{ if } j \neq k$$

$$q(w_j, w_j) = \begin{cases} 0 & \text{for evanescence waves} \\ 2i\beta_j & \text{for propagative waves} \end{cases}$$

where q is a (energy flux) sesquilinear form defined by

$$\forall u, v \in H_{\text{loc}}^2, \quad q(u, v) = \int_{\Sigma_\ell} \partial_z u \bar{v} - u \bar{\partial_z v}.$$

An important property of q is that, due to the Green's formula, $q(u, v)$ is independent of ℓ if u and v are solution of the homogeneous Helmholtz equation let us say in $S \times (0, +\infty)$.

We deduce that, except for the cut-off frequencies (the frequencies for which one β_k vanishes), p_∞ is given by

$$p_\infty = \sum_{k \leq N} \frac{q(p_\infty, w_k)}{2i\beta_k} w_k + p_{\text{evan}}. \quad (5)$$

where p_{evan} is exponentially decreasing at $+\infty$.

Imposing that only the propagative modal amplitudes of p_∞ and p_ℓ match as well as their normal derivative on Σ_ℓ leads to introduce the so-called Poynting-to-Neumann operator T_{PtN} defined by

$$T_{PtN} p_\ell = \sum_{k \leq N} \frac{q(p_\ell, w_k)}{2i\beta_k} \partial_z w_k|_{\Sigma_\ell}. \quad (6)$$

Using the properties of q , we can show that

Theorem 1 *The operator T_{PtN} is compact from V to $H^{-1/2}(\Sigma_\ell)$ where*

$$V = \{p \in H^2(\Omega_\ell \setminus \Omega_0), \quad \Delta p + \omega^2 p = 0\}.$$

and

$$\forall p \in V, \quad \int_{\Sigma_\ell} \bar{p} T_{PtN} p - p \overline{T_{PtN} p} \in i\mathbb{R}^+.$$

The first property gives that the problem

$$\begin{cases} \Delta \tilde{p}_\ell + \omega^2 \tilde{p}_\ell = f & \text{in } \Omega_\ell, \\ \partial_\nu \tilde{p}_\ell = 0 & \text{on } \partial\Omega_\ell \setminus \Sigma_\ell, \\ \partial_z \tilde{p}_\ell = T_{PtN} \tilde{p}_\ell & \text{on } \Sigma_\ell \end{cases} \quad (7)$$

is coercif + compact. From the second property, we can prove that this problem has at most one solution except for a countable set of frequencies. This problem is however not equivalent to the initial one since we have neglected the evanescent part in p_ℓ but by stability of (7), we can show that

$$\|p_\ell - \tilde{p}_\ell\| = \mathcal{O}(e^{-\text{Im}(\beta_{N+1})\ell}).$$

To derive a variational formulation, one question remains : how to understand the normal derivative of \tilde{p}_ℓ in the definition of q ? Because \tilde{p}_ℓ is solution of the homogeneous Helmholtz equation in $\Omega_\ell \setminus \Omega_0$, $q(\tilde{p}_\ell, w_k)$ can be written as an integral on Σ_0 and then the normal derivative of \tilde{p}_ℓ must be understood in the weak sense and can be eliminated by integrating by parts in small volumic domain.

2 The PtN map for more general waveguides

Let us consider now the outgoing solution p of a waveguide problem which is similar to (1) but with Maxwell's or elastic equations in a stratified, anisotropic or periodic media. In this kind of problems, it is impossible to justify the use of a DtN map because the modes does not form necessarily a complete set of $L^2(S)$ and/or they are not necessarily orthogonal in $L^2(S)$.

Suppose that one is able to write that p_∞ (which can be vectorial) is a linear combination of a finite set of the rightgoing modes up to an exponentially decreasing function at $+\infty$

$$p_\infty = \sum_{k \leq N} a_k^+ w_k + p_{\text{evan}}. \quad (8)$$

The rightgoing modes w_k 's are solution of the homogeneous equations far from the perturbations and their energy fluxes are supposed to be positive. More precisely, they verify

$$\begin{cases} q(w_j, w_k) = 0 \text{ if } j \neq k \\ q(w_j, w_j) = i\lambda_j \quad \text{with } \lambda_j \geq 0 \end{cases}$$

where q is a (energy flux) sesquilinear form derived from the Green's formula associated to the problem. To obtain (8), see for instance [1] for scalar problems and [2] devoted to periodic elastic waveguides. Then, except for the cut-off frequencies (the frequencies for which at least one λ_j vanishes) the OtN operator can be derived in the same way than for the isotropic acoustic problem and the properties of the operator remains the same.

In conclusion, to derive transparent boundary conditions using this PtN operator for general waveguide problems, no assumptions on the completeness or the orthogonality of the tranverse modes are required.

References

- [1] Nazarov, Sergey, and Boris A. Plamenevsky. Elliptic problems in domains with piecewise smooth boundaries. Vol. 13. Walter de Gruyter, 1994.
- [2] Nazarov, Sergey. "Umov-Mandelstham radiation conditions in elastic periodic waveguides." Sbornik: Mathematics 205.7 (2014): 953.

Domain Evolution Kinetics of Mechanical, Phase-transforming Structures

Michael J. Frazier¹, Dennis M. Kochmann^{1,*}

¹Graduate Aerospace Laboratories, California Institute of Technology, Pasadena, USA

*Email: kochmann@caltech.edu

Abstract

Multi-welled energy landscapes are key to microstructural pattern formation observed in solids that undergo, e.g., phase transformations, ferroic domain switching, or diffusive phase separation. These processes necessitate the formation and movement of domain walls which separate homogeneous equilibrium states. Here, we present a purely mechanical, size-independent structure (or metamaterial) that exhibits similar domain evolution phenomena, and we demonstrate that the system obeys qualitatively and quantitatively analogous fundamental governing laws but with extreme tunability and experimental accessibility. We thus open a new chapter in mimicking atomic-scale dynamic processes at the observable metamaterial scale.

Keywords: switching, phase transformation, domain evolution

1 Introduction

Nature has inspired the emulation of atomic-scale architectures at the macroscopic, structural level, resulting in, e.g., acoustic metamaterials [1], structural transitions [2], etc. At this level, topological transformations and domain patterning occur as a consequence of structural instability and the associated nonconvex energy landscape. Despite various examples that realized static domain formation through patterning [3], no attempt has been made at exploiting their nonlinear dynamic evolution.

Our mechanical analog translates the atomic-scale polarization found, e.g., in ferroelectrics, into a scalar polarization field that possesses one or two stable equilibria depending on the ambient conditions. We consider a 2D isotropic, centro-symmetric periodic array of elastically-connected bistable elements (Figure 1a) which drive the system towards domains of uniform polarization, while the elastic connections localize domain walls to interpolate between opposing phases. The transition wave results from the stabilized competition between elastic energy release and intrinsic dissipation [4].

2 The Phase-transforming Structures

We consider a network of cylindrical masses of radius R and a single (rotational) degree of freedom φ , the *polarization*. Bistability, arises from an on-site torsional spring and an elastic spring attached eccentrically to the cylinder at one end and to an elevated anchor point at the other. The action of gravity on masses m eccentrically placed on the cylinders creates a torque when the rotation axis and gravity field are not aligned. The energy landscape can be tuned by (*i*) moving the elevated anchor points by a distance $\mathbf{f} = \{f_x, f_y, f_z\}$ and/or (*ii*) tilting the entire system by angles $\boldsymbol{\theta} = \{\alpha, \beta\}$, respectively, about the x - and y -axis.

For a typical cylinder at position \mathbf{x} and connected to n neighbors at $\mathbf{x} + \Delta\mathbf{x}_\gamma$ ($\gamma = 1, \dots, n$) via elastic bands of stiffness k , the governing equation is

$$\begin{aligned} I\ddot{\varphi}(\mathbf{x}) + \eta\dot{\varphi}(\mathbf{x}) + \psi'[\varphi(\mathbf{x}), \boldsymbol{\theta}, \mathbf{f}] \\ = R^2 k \sum_{\gamma=1}^n [\varphi(\mathbf{x} + \Delta\mathbf{x}_\gamma) - \varphi(\mathbf{x})], \end{aligned} \quad (1)$$

with I the total rotational inertia, η the velocity-proportional damping constant, and $\psi(\varphi, \boldsymbol{\theta}, \mathbf{f})$ the on-site, multi-welled energy.

Similar to viewing an atomistic ensemble from greater scale, we observe the dynamic processes in a homogenized sense. Mathematically, this calls for taking the continuum limit as the inter-mass spacing a goes to zero. From (1), we define $\Delta\mathbf{x}_\gamma = a \mathbf{e}^\gamma$ where \mathbf{e}^γ is the unnormalized distance vector. A Taylor expansion of $\varphi(\mathbf{x} + \Delta\mathbf{x}_\gamma)$ (using summation index notation) leads to

$$\begin{aligned} R^2 k \sum_{\gamma=1}^n [\varphi(\mathbf{x} + \Delta\mathbf{x}_\gamma) - \varphi(\mathbf{x})] = \\ \frac{R^2 a^2 k}{2} \varphi_{,ij}(\mathbf{x}) \sum_{\gamma=1}^n e_i^\gamma e_j^\gamma + O(a^3). \end{aligned} \quad (2)$$

For the continuum governing equation and associated solutions remain finite, it is essential that the system parameters obey the correct

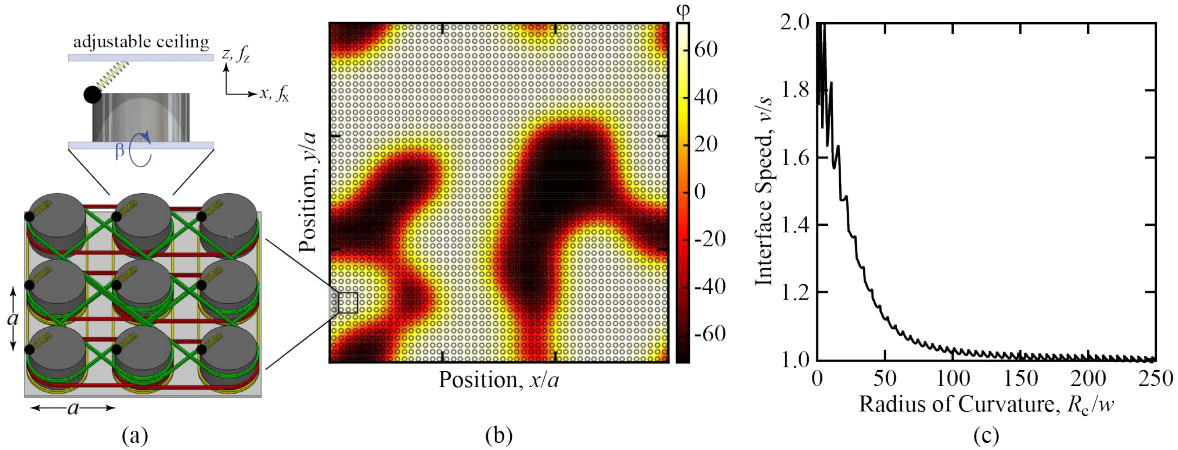


Figure 1: (a) Mechanical, phase-transforming network of rotating cylinders. (b) Domains of opposing polarization φ in the mechanical network. (c) Comparison of predicted v and measured s (from simulation) speeds of a circular domain wall as a function of curvature $\varsigma = 1/R_c$.

scaling. From energy considerations [4], this requires that terms of order $O(a^3)$ and higher vanish. Thus, the continuum governing equation is

$$\rho \ddot{\varphi}(\mathbf{x}) + \nu \dot{\varphi}(\mathbf{x}) = \kappa \Delta \varphi - \psi'[\varphi(\mathbf{x}), \boldsymbol{\theta}, \mathbf{f}], \quad (3)$$

with ρ , ν , and κ , respectively, the inertial density, viscosity, and elasticity coefficient.

In the case of significant damping, we have $|\rho \ddot{\varphi}| \ll |\nu \dot{\varphi}|$ so that (3) reduces to the Allen-Cahn equation of phase separation [5]

$$\nu \dot{\varphi}(\mathbf{x}) = \kappa \Delta \varphi - \psi'[\varphi(\mathbf{x}), \boldsymbol{\theta}, \mathbf{f}]. \quad (4)$$

Although damping can be defined arbitrarily, the linear approximation chosen here worked excellently for our experimentally investigated 1D bistable networks [6]. Linear gradient flow is also the most common kinetic model used in phase field descriptions.

Qualitatively similar to processes in solids, Figure 1b illustrates phase separation within a 150×150 system of rotating cylinders with periodic boundary conditions. With the inertial and coupling conditions satisfied, the kinetics of phase separation within our system is described by (4). For domain boundaries of sufficiently small curvature ς , (4) approximates the local wall speed as $v \approx -\kappa \varsigma / \nu$ [5]. Figure 1c compares the measured speed s of a simulated circular domain in the discrete system following (1) to the speed v predicted by the Allen-Cahn phase field model (4), illustrating further quantitative agreement for $\varsigma \ll 1$ as anticipated.

References

- [1] Y. Chen and L. Wang, Periodic co-continuous acoustic metamaterials with overlapping locally resonant and bragg band gaps *Appl. Phys. Lett.* **105** (2014), p. 191907.
- [2] D. Yang, L. Jin, R. Martinez, K. Bertoldi, G. Whitesides, and Z. Suo, Phase-transforming and switchable metamaterials, *Ext. Mech. Lett.* **6** (2016), pp. 1–9.
- [3] S. Kang, S. Shan, A. Košmrlj, W. Noorduin, S. Shian, J. Weaver, D. Clarke, and K. Bertoldi, Complex ordered patterns in mechanical instability induced geometrically frustrated triangular cellular structures, *Phys. Rev. Lett.* **112** (2014), p. 098701.
- [4] N. Nadkarni, C. Daraio, R. Abeyaratne, and D. M. Kochmann, Universal energy transport law for dissipative and diffusive phase transitions, *Phys. Rev. B* **93** (2016), p. 104109.
- [5] S. Allen and J. Cahn, A microscopic theory for antiphase boundary motion and its application to antiphase domain coarsening, *Acta Metall.* **27** (1979), pp. 1085–1095.
- [6] N. Nadkarni, A. F. Arrieta, C. Chong, D. M. Kochmann, and C. Daraio, Unidirectional transition waves in bistable lattices, *Phys. Rev. Lett.* **116** (2016), p. 244501.

Wave Stability and Invariance in Nonlinear Periodic Media

Matthew D. Fronk¹, Michael J. Leamy^{1,*}

¹George W. Woodruff School of Mechanical Engineering, Georgia Tech, Atlanta, USA

*Email: michael.leamy@me.gatech.edu

Abstract

Higher-order, multiple scales perturbation analyses of nonlinear periodic systems are presented with the goal of predicting invariant waveforms of infinite extent. The multiple scales analysis is also used to study waveform stability, which is shown to be amplitude-dependent. Using example quadratic and cubic chains characterized by dimensionless parameters described herein, numerical studies confirm both amplitude-dependent stability and less temporal growth/decay in spectral content of the predicted waveforms as higher-order approximations are employed.

Keywords: nonlinear wave, perturbation, stability, invariance

1 Introduction

Wave propagation in linear monoatomic, diatomic, and other chains is of contemporary interest due to their non-trivial dispersion, filtering, and frequency bandgap behavior [1]. These model systems may arise in the analysis of one-dimensional waveguides, or in the study of wave propagation in three-dimensional crystals along preferred directions, such as the [100] direction in zincblende crystals (e.g., GaAs and NaCl). The presence of nonlinearities in these systems introduces additional, unique behavior which furthers their functionality and engineering relevance.

Several recent studies have analyzed amplitude-dependent dispersion and other nonlinear behavior of discrete chains [2–4] investigated wave propagation in cubically nonlinear monoatomic and diatomic chains using Lindstedt-Poincaré and the Method of Multiple Scales, respectively, with an emphasis on amplitude-dependent dispersion shifts. Further, they identified wave-based devices which exploit bandgap shifting to enable tunable filtering and wave-guiding. This work builds upon these earlier studies by developing a higher-order multiple scales procedure to inform dispersion, stability, and waveform invariance. Stability is assessed through a local fixed point analysis based on the multiple scales-derived evolution equations. Nondimen-

sionalized chains are numerically simulated to identify and characterize their amplitude-dependent stability and waveform invariance.

2 Wave Invariance and Stability

This section introduces the two systems studied herein, namely weakly nonlinear monoatomic and diatomic chains. For the monoatomic chain, the smallest repeatable subsystem, or unit cell, consists of a single mass and its connecting springs and dampers; the unit cell for the diatomic chain contains two masses and two springs.

For the monatomic chain, a force balance on the j th mass yields its equation of motion,

$$\begin{aligned} m\ddot{x}_j + k_1(2x_j - x_{j+1} - x_{j-1}) - \epsilon k_2(x_{j+1} - x_j)^2 \\ + \epsilon k_2(x_{j-1} - x_j)^2 - \epsilon k_3(x_{j+1} - x_j)^3 \\ - \epsilon k_3(x_{j-1} - x_j)^3 + \epsilon c(2\dot{x}_j - \dot{x}_{j+1} - \dot{x}_{j-1}) \\ = 0 \end{aligned} \quad (1)$$

where $x_j = x(j, t)$ denotes the displacement from equilibrium of the j th mass, m its mass, k_1 , k_2 , and k_3 the linear, quadratic, and cubic stiffnesses, respectively, and c denotes the linear damping coefficient. It is assumed that $\epsilon \ll 1$ such that the nonlinear and damping terms are small. A similar, matrix set of equations governs the response of masses in the j th unit cell of the diatomic system.

A multiple scales analysis approach is chosen for analyzing amplitude-dependent waves in the two weakly nonlinear systems, similar to that carried-out in [4]. Multiple time scales are assumed to exist such that,

$$T_0 \equiv t, T_1 \equiv \epsilon t, T_2 \equiv \epsilon^2 t, \dots, T_n \equiv \epsilon^n t, \quad (2)$$

where t denotes the original time scale and T_n represents the n th time scale. Since $\epsilon \ll 1$, each time scale advances more slowly than its predecessor. In accordance with these time scales, differentiation with respect to time contains multiple orders. This expansion leads to an asymptotic solution approach for x_j of the form $x_j = x_j^{(0)} + \epsilon x_j^{(1)} + \epsilon^2 x_j^{(2)} + \dots + \epsilon^n x_j^{(n)}$ and a series of linear problems whose solution yields higher-order

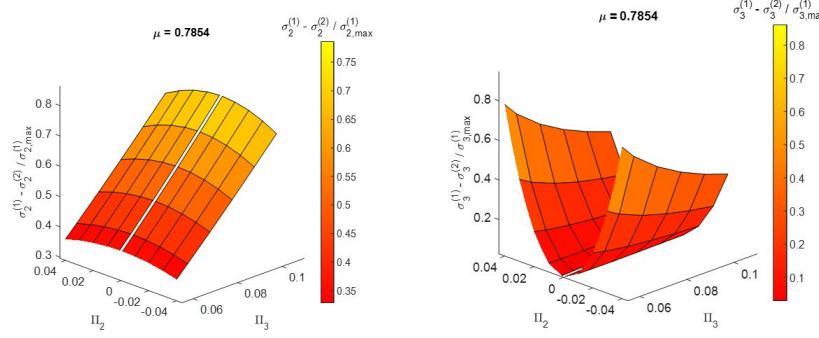


Figure 1: Variance study of monoatomic chains.

dispersion relationships, higher-order waveforms, and evolution equations supporting stability analysis.

Following the multiple time scales procedure, higher-order waveforms are predicted using both homogeneous and particular solutions to the resulting system of linear equations. In the limit as the asymptotic expansions are taken to higher orders, it can be hypothesized that the waveforms should propagate for all space and time without change – i.e., they should be an invariant form. To test this hypothesis, the predicted waveforms are injected into numerical simulations and variance σ is measured as a function of two dimensionless parameters, $\Pi_2 \equiv \frac{\epsilon k_2 \alpha_0}{k_1}$ and $\Pi_3 \equiv \frac{\epsilon k_3 \alpha_0^2}{k_1}$, where α_0 denotes the wave amplitude at the zeroth order. Variance is defined to be the time-averaged growth/decay of each harmonic measured during a simulation. As illustrated in Figure 1 for a monoatomic chain, the harmonic variance of both second and third harmonics (σ_2 and σ_3 , respectively) reduces as one injects waveforms found using 2nd-order approximations (denoted by superscript (2)) over those given 1st-order ones (denoted by superscript (1)). This trend is observed for all Π_2 and Π_3 values in the range illustrated. Similar results can be shown for diatomic chains.

3 Conclusions

Higher-order multiple scales solutions have been described for predicting multi-harmonic plane wave propagation in cubically and quadratically nonlinear monoatomic and diatomic chains. The method yields higher-order waveforms which propagate with decreasing variance as order is increased. Wave stability has also been assessed

through introduction of linear damping and a local stability analysis. The invariance and solution stability suggest these multiharmonic waveforms could inspire devices that rely on the propagation of unaltered harmonic content to relay information over large time and space.

References

- [1] M.I. Hussein, M.J. Leamy, and M. Ruzzene, Dynamics of Phononic Materials and Structures: Historical Origins, Recent Progress, and Future Outlook, *Applied Mechanics Reviews* **66** (2014).
- [2] A. F. Vakakis and M. E. King, Nonlinear Wave Transmission in a Monocoupled Elastic Periodic System, *The Journal of the Acoustical Society of America* **98** (1995), pp. 1534–1546.
- [3] R. K. Narisetti, M.J. Leamy, and M. Ruzzene, A Perturbation Approach for Predicting Wave Propagation in One-Dimensional Nonlinear Periodic Structures, *Journal of Vibration and Acoustics* **132** (2010).
- [4] K. Manktelow, M.J. Leamy, and M. Ruzzene, Multiple Scales Analysis of Wave-Wave Interactions in a Cubically Nonlinear Monoatomic Chain, *Nonlinear Dynamics* **63** (2010), pp. 193–203.

Elastic full waveform inversion of reflection seismic data: migration based formulation

Gadylshin Kirill^{1,*}, Guy Chavent², Vladimir Tcheverda³

¹Institute of Petroleum Geology and Geophysics, SB RAS, Novosibirsk, Russia

²Inria-Rocquencourt Domaine de Voluceau, France

³Institute of Petroleum Geology and Geophysics, SB RAS, Novosibirsk, Russia

*Email: GadylshinKG@ipgg.sbras.ru

Abstract

The paper develops a reliable numerical method to solve inverse dynamical problem of seismic waves propagation on the base of nonlinear least squares formulation which is widely known as Full Waveform Inversion (FWI). The key issue on this way is correct reconstruction of macro-velocity component of the model with input seismic data without time frequencies less than 5 Hz and reasonable source-receivers offsets. To provide correct macro-velocity reconstruction we modify regular nonlinear least squares formulation used in standard versions of FWI by decomposing the model space into two subspaces:

- slowly varying in space functions (propagators p) which do not change direction of propagation of seismic energy, but governs travel times;
- sharply changing in space functions (space reflectivity r) which do not change travel time, but turn propagation direction towards acquisition.

Keywords: elastic fwi, macro-velocity, inverse problem, nonlinear least squares

Introduction

The velocity model building in the depth domain is necessary to guarantee the correct traveltimes of wave propagation and therefore is a crucial element in seismic data processing. As early as the middle of 80's of the last century A. Tarantola introduced the Full Waveform Inversion (FWI) based on the matching of the observed and the synthetic seismograms. The L_2 norm is widely used for such matching, though other criteria are also considered. To minimize the misfit function and to find the elastic parameters of the subsurface, iterative gradient-based algorithms are usually applied. Such approach to FWI proposed originally by Lailly (1983) and Tarantola (1984) has been developed

and studied in a great number of publications (see Virieux and Operto (2009), and the references therein). However, the straightforward application of FWI reconstructs reliably only the reflectivity component of the subsurface but fails to provide a smooth velocity model. The smooth component could not be recovered stably without the presence of extremely low time frequencies. The matter is the shape of the data misfit functional differs a lot with respect to various velocity components – it is nearly quadratic with respect to reflectors, but perturbations of the smooth velocity component (propagator) lead to a very complicated and nonlinear behavior (see e.g. Sirgue, 2006). Heuristically it is explained by the so-called "cycle-skipping" problem when phase shifts between the recorded and synthetic data produce local minima. In the Bunks et al. (1995) authors introduce some new inversion strategy based on the use of increasing time frequencies: they start inversion with the lowest available ones and at each subsequent iteration they increase the frequency and use the results from the previous step as the initial guess. But they perform this inversion in time domain, hence have to use at each step the low-pass band filtering of data in the time domain which reduces the efficiency of this technique. The next step in implementation of the frequency-domain FWI with increasing time frequencies was done by G. Pratt with co-authors in the paper (Pratt et al., 1998). They use minimization in time frequency domain and very naturally proceed sequentially from low to high frequencies. Unfortunately, this approach did not resolve the problem of stable recovery of a macro-velocity when there is a lack of low time frequencies in the data. In contrast, the proposed below modification of the cost function is principally a new approach to the Full Waveform Inversion for reflected waves and stable recovery of the data with reasonable range of time frequencies like 5–25 Hz.

Theory and method

In what follows we are concentrated on application of Full Waveform Inversion in the migration based formulation (Clement, Chavent and Gomez, 2001) to reflection elastic seismic data. Seismic inverse problem can be treated as a nonlinear operator equation:

$$F(m) = d,$$

where $F : M \rightarrow D$ is a nonlinear forward map, which transforms model space M into data space D . Forward map F is associated with elastic waves equation in time-frequency domain of the following form:

$$\begin{aligned} \omega^2 \rho v_x + \frac{\partial}{\partial x} \left[\lambda \left(\frac{\partial v_x}{\partial x} + \frac{\partial v_z}{\partial z} \right) + 2\mu \frac{\partial v_x}{\partial x} \right] \\ + \frac{\partial}{\partial z} \left[\mu \left(\frac{\partial v_z}{\partial x} + \frac{\partial v_x}{\partial z} \right) \right] = 0 \\ \omega^2 \rho v_z + \frac{\partial}{\partial z} \left[\lambda \left(\frac{\partial v_x}{\partial x} + \frac{\partial v_z}{\partial z} \right) + 2\mu \frac{\partial v_z}{\partial z} \right] \\ + \frac{\partial}{\partial x} \left[\mu \left(\frac{\partial v_z}{\partial x} + \frac{\partial v_x}{\partial z} \right) \right] = f(\omega) \delta(x - x_s) \delta(z - z_s) \end{aligned}$$

Data d are solutions to this equation solved at given receiver positions. In contrast to the standard nonlinear least-squares FWI formulation (Tarantola, 1984; Virieux and Operto, 2009), when unknown elastic model

$$\vec{m}(x, z) = (\rho(x, z), \lambda(x, z), \mu(x, z))$$

is searched as the solution to the minimization problem, reflection FWI in migration based formulation uses decomposition of the model \vec{m} in two components (Chavent et. al, 2001):

$$\vec{m} = p + r = p + \mathcal{M}(p)s.$$

Here p - propagator, which describes smooth macro-velocity, r - depth reflector describing rough perturbations of the model. The key moment in this decomposition is propagator-reflector interrelation $r = \mathcal{M}(p)s$, where s is unknown data reflectivity (preimage or inverse image of a depth reflector in data space D for a given propagator p), while $\mathcal{M}(p)$ is true amplitude prestack migration operator with linear reweighting W (true-amplitude imaging):

$$\mathcal{M}(p)s = W \circ \text{Re} \left\{ \left(\frac{\delta F}{\delta \vec{m}}(p) \right)^* s \right\}.$$

Such decomposition of the model leads to the following modified nonlinear least squares FWI formulation:

$$(p^*, s^*) = \text{argmin} ||F(p + \mathcal{M}(p)s) - d||_D^2.$$

The minimization with respect to the new variables (p and s) is done independently by standard local optimization techniques, such as the modified Newton method.

References

- [1] C. Bunks , F.M. Saleck, S. Zaleski and G. Chavent, Multiscale seismic inversion, *Geophysics* **60(5)** (1995), pp. 1457–1473.
- [2] F. Clement, G. Chavent and S. Gomez, Migration-based traveltime waveform inversion of 2-D simple structures *Geophysics* **66** (2001), pp. 845–860.
- [3] P. Lailly, The seismic inverse problem as a sequence of before stack migrations, *Conference on Inverse Scattering: Theory and Application. SIAM*, 1983, pp. 206–220.
- [4] G. Pratt, C. Shin, G.J. Hicks, Gauss-Newton and full Newton methods in frequency-space seismic waveform inversion, *Geophysical Journal International* **133(2)** (1998), pp. 341–362.
- [5] L. Sirgue, The importance of low frequencies and large offset in waveform inversion, *68th EAGE Technical conference and Exhibition, 2006*, A037.
- [6] A. Tarantola, Inversion of seismic reflection data in the acoustic approximation, *Geophysics*, **49(08)** (1984), pp. 1259–1266.
- [7] J. Virieux and S. Operto, An overview of full-waveform inversion in exploration geophysics, *Geophysics* **74(6)** (2009), WCC1–WCC26.

Modal expansion in elastic open waveguides with perfectly matched layers

Matthieu Gallezot^{1,*}, Fabien Treyssède¹, Laurent Laguerre¹

¹LUNAM Université, IFSTTAR, GERS, GeoEND, F-44340 Bouguenais Cedex

*Email: matthieu.gallezot@ifsttar.fr

Abstract

The modal basis of elastic open waveguides contains two continua of radiation modes and a discrete set of trapped modes. A third set also exists: the leaky modes. However, they do not belong to the modal basis as they spatially grow to infinity. Herein, the excitation of elastic open waveguides is investigated. For numerical purpose, the infinite transverse direction is modelled with a truncated perfectly matched layer (PML). Indeed, the PML offers a natural way to reveal the contribution of leaky modes. The PML gives access to the improper Riemann sheets by redefining the branch cuts, yielding two rotated continua of radiation modes (PML modes). The cases of an infinite medium and an open waveguide are considered. It is shown that all sets are necessary for achieving convergence of the modal expansion.

Keywords: modal analysis, open waveguide, leaky modes, perfectly matched layer, Riemann surface

1 Introduction

Numerically, elastic waveguides can be modelled with a cross-section finite element discretization thanks to the so-called Semi-Analytical Finite Element method (SAFE) [1]. For open waveguides, the SAFE can be combined with a PML [2], among various other methods. The PML eigenvalue problem has been studied by way of the convergence of trapped and leaky modes [2, 3]. Yet, the use of these modes and of PML modes in a modal expansion may remain unclear. Besides, a biorthogonality relation must be derived. This talk aims to bring insights on the full modal solution computed with a PML, through numerical and theoretical studies of elastic open waveguides.

2 Numerical modelling

For simplicity, the waveguide has two layers and is axisymmetric. The first layer has a radius $r = a$, and the second layer is infinite. The latter is truncated by a PML of thickness h and

starting from the radial position d . The PML is introduced using an analytic continuation in the radial direction:

$$\tilde{r}(r) = \int_0^r \gamma(\xi) d\xi \quad (1)$$

$\gamma(r)$ is a complex attenuation function ($\text{Im}\gamma > 0$) through the PML ($r > d$). At the end of the PML ($r = d + h$), a Dirichlet condition is applied. Assuming an axial wavenumber and a time-harmonic dependance $e^{j(kz - \omega t)}$, the elastodynamics variational formulation is written on the cross-section. The finite element discretization yields the quadratic eigenvalue problem [2]:

$$(\mathbf{K}_1 + ik(\mathbf{K}_2 - \mathbf{K}_2^T) + k^2 \mathbf{K}_3 - \omega^2 \mathbf{M}) \mathbf{U} = \mathbf{0} \quad (2)$$

\mathbf{K}_1 , \mathbf{K}_3 and \mathbf{M} are symmetric. Because of the PML, all the matrices are complex valued. It has been shown in [1] that the so-called Auld's real orthogonality relationship must be used for modal expansion in waveguides with complex material properties (viscoelastic case). It can be checked that this relation actually still applies with a PML. Then, the total displacement field can be expanded on M positive-going modes as follows:

$$\mathbf{U}(z, \omega) = \sum_{m=1}^M \mathbf{E}_m \mathbf{F}(k_m) e^{ik_m z}. \quad (3)$$

\mathbf{E}_m is the excitability matrix defined in [1], and \mathbf{F} stands for external forces.

3 Numerical results

A homogeneous elastic medium, excited by a unit point load applied at the centre in z direction, is modelled. Figure 1 shows that a good accuracy with respect to analytical results can be achieved within a limited distance range. For a given number of modes, this range increases with the complex thickness $h\hat{\gamma} = \int_d^{d+h} \gamma(\xi) d\xi$. These results are consistent with Olyslager's [5], obtained for Green functions in scalar acoustic waveguides.

In a bilayer open waveguide, leaky modes dominate at small distances. Numerical results

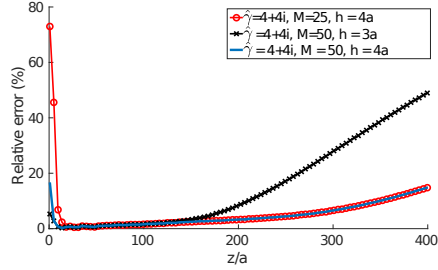


Figure 1: Relative error in an infinite medium on longitudinal displacement at $r = 0$ and at a fixed frequency between numerical and analytical results.

(not presented here for conciseness) show that at great distances, long term diffraction occurs and cannot be properly described by leaky modes but by PML modes that stand for body waves (see section 4). It is noteworthy that a truncated PML enables to compute this phenomenon, while other types of absorbing layers have been proved to be inefficient [4].

4 On the modal decomposition

So far, the M modes included in Eq. (3) have not been precisely defined. First, let us go back to the initial elastic waveguide problem, unbounded and without PML. The key points of the analysis are the definitions of the Riemann surface and of the two branch cuts of the problem, such that outgoing waves in the transverse direction decrease at infinity. The proper Riemann sheet yields two sets of modes. The first one is made of discrete proper poles, including trapped modes. The second one is the branch cuts contribution, yielding two continua of radiation modes. Leaky modes are also poles of the problem, but they lie on the improper Riemann sheets (they grow to infinity in the transverse direction).

With an infinite PML, the proper Riemann sheet is modified. It is shown that both branch cuts are rotated by an angle of $-\arg\gamma$. This gives access to parts of the initial improper Riemann sheets (numbered **2,3,4** - see Figure 2). Hence, the modal basis changes as well. The first set including trapped modes is unchanged. The continua of radiation modes are now defined by the rotated branch cuts. Besides, another discrete set made of revealed leaky modes is now included in the modal decomposition.

For numerical purpose, the PML needs to

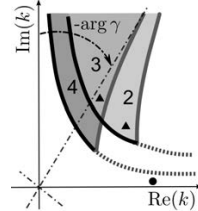


Figure 2: Proper Riemann sheet of a viscoelastic open waveguide with PML: initial branch cuts (black lines) and rotated branch cuts (grey line), trapped modes (circle) and leaky modes (triangle).

be truncated. With a finite PML, the continua of radiation modes become discrete [5]. These modes are called PML modes. Although non intrinsic to the physics (PML modes mainly depend on user-defined PML parameters), they have to be included in the modal expansion to achieve convergence, as mentioned in section 3.

5 Acknowledgements

The authors wish to thank Région Pays de la Loire and the Société Française d'Acoustique for their financial support.

References

- [1] F. Treyyssède and L. Laguerre, Numerical and analytical calculation of modal excitability for elastic wave generation in lossy waveguides, *Journal of the Acoustical Society of America* **133** (2013), pp. 3287–3837.
- [2] F. Treyyssède, K.L. Nguyen, A.-S. Bonnet-BenDhia and C. Hazard, Finite element computation of trapped and leaky elastic waves in open stratified waveguides, *Wave motion* **51** (2014), pp. 1093–1107.
- [3] S. Kim and J. E. Pasciak, The computation of resonances in open systems using a perfectly match layer, *Mathematical of Computation* **78** (2009), pp. 1375–1398.
- [4] J. Hu and C. R. Menyuk, Understanding leaky modes: slab waveguide revisited, *Adv. Opt. Photon.* **1** (2009), pp. 58–106.
- [5] F. Olyslager, Discretization of Continuous Spectra Based on Perfectly Matched Layers, *SIAM Journal on Applied Mathematics* **64** (2004), pp. 1408–1433.

Coercivity and iterative solvers for a class of preconditioned wave propagation models

M. Ganesh^{1,*}, C. Morgenstern¹

¹Department of Applied Mathematics and Statistics, Colorado School of Mines, CO 80401, USA

*Email: mganesh@mines.edu

Abstract

The lack of coercivity of the sesquilinear form in the standard Galerkin problem and associated finite element method (FEM) models is one of the major difficulties for simulating wave propagation models using iterative methods. Practical realization of large-scale/high-frequency preconditioned non-coercive wave propagation models are typically based on Multigrid or domain decomposition methods (MG/DDM). Complete mathematical analysis of the MG/DDM based wave propagation models is still an open problem, and recent efforts in the literature include partially addressing the mathematical challenge for the homogeneous media Helmholtz model. However for coercive diffusion-type MG/DDM models, mathematical analysis have been widely investigated in the literature. A theoretical coercive formulation for the constant coefficient model was developed by Moiola and Spence in 2014. The main focus of this work is on MG/DDM for a new class of preconditioned high-order FEM coercive Helmholtz wave propagation models developed recently by the authors.

Keywords: Helmholtz, Coercive, FEM, Preconditioning

1 Introduction

We consider the Helmholtz acoustic wave propagation model in a bounded media $\Omega \subset \mathbb{R}^d$, $d = 2, 3$, with an inhomogeneous absorbing impedance boundary condition on $\partial\Omega$.

It is well known that the standard Galerkin variational formulation of the Helmholtz partial differential equation (PDE) in $H^1(\Omega)$ is indefinite for large wavenumbers, while the Helmholtz PDE is not indefinite [8]. The lack of coercivity (indefiniteness) of the sesquilinear form in the standard Galerkin problem and associated finite element method (FEM) models is one of the major difficulties for simulating wave propagation models using iterative methods.

A key contribution to tackle the iterative solver difficulty was developed about one decade ago, for the heterogeneous Helmholtz model, by

Erlangga et al. [1] using a multigrid based preconditioner. The preconditioned system in [1] was obtained using a complex-shifted version of the Helmholtz model. Various numerical results suggested that the shift should depend on the wavenumber. The recent mathematical analysis in [2], for homogeneous Helmholtz model, proved that the shift should be chosen proportional to wavenumber to guarantee wavenumber-independent convergence. However, the analysis in [2] does not take into account the multigrid based preconditioner. Indeed recent high-order FEM based multigrid models [3] (and references therein) clearly demonstrate that the shift should be chosen proportional to the square of the wavenumber and that for multigrid based preconditioner the choice proposed in [2] need not result in converging iterates.

While the complex-shifted Helmholtz model based preconditioners are considered to be the best, the MG approach may not be the best option to implement the preconditioner. Indeed, in the recent work [4] we demonstrated that the MGM is not appropriate for a class of high-frequency heterogeneous Helmholtz model, for various shift values include those that work well for the low- and medium-frequency models. Instead, motivated by the work [7], we developed high-order FEM based domain decomposition preconditioning models for high-frequency heterogeneous models in two and three dimensions, and we demonstrated results on non-trivial geometries [4]. The DD preconditioning method and analysis in [7] are restricted to the homogeneous Helmholtz model. It is an open problem to develop analysis for the DDM in [4]. The lack of coercivity in the standard wave propagation models is one of the key difficulties in analyzing the MG/DDM based iterative solvers for wave propagation.

As mentioned in the 2014 SIAM Review article [8], *solving the Helmholtz equation with iterative methods is difficult, and a contributing factor is the sign-indefiniteness of the standard variational formulations.* For the constant coef-

ficient Helmholtz equation case, it was theoretically demonstrated in [8] that a non-standard space approach can produce a sign-definite variational formulation of the wave propagation model in homogeneous media. However, the authors of the theoretical article [8] also questioned the practical use of their coercive sesquilinear formulation for the homogeneous media Helmholtz model.

In our recent work [5], we developed a practical high-order FEM version of the homogeneous formulation in [8], introduced a new shifted preconditioner, showed wavenumber-independent iterations of our new sign-definite preconditioned FEM model, and investigated efficient DD approximations of the preconditioner. Currently [6], we are developing a heterogeneous counterpart of [5], and this includes new formulation with rigorous mathematical analysis. This work [6] does not take into account of the application of the MG/DD for preconditioning. In this work we focus on developing MG/DDM based coercive high-order preconditioned FEM heterogeneous wave propagation models in conjunction with the novel formulation from [6].

1.1 Preliminary Results

Using the classical non-overlapping additive Schwarz preconditioner (see [7] for a description of the algorithm) we efficiently simulate solutions to a heterogeneous media model with the complex non-smooth computational domain geometry from [5] and a spatially varying refractive index $n \notin C^2(\Omega)$. We implement the same high-order FEM from [5] in order to simulate high-frequency problems with non-smooth solutions $u \notin H^2(\Omega)$ and up to 400 wavelengths per diameter of the computational domain. Using a standard BiCGstab iterative solver without preconditioner requires 12,896 iterations for a problem with 200 wavelengths per diameter of the computational domain, but with the classical non-overlapping AS approximation of our novel preconditioner only 74 iterations are required. In this work we investigate several other AS type preconditioners including overlapping and hybrid methods to further increase efficiency and simulate higher-frequency problems with up to 400 wavelengths per diameter of the computational domain.

References

- [1] Erlangga Y, Oosterlee C, Vuik C. A novel multigrid based preconditioner for heterogeneous Helmholtz problems. *SIAM J. Sci. Comput.* 2006; **27**:1471–1492.
- [2] M. GANDER, I. GRAHAM, AND E. SPENCE, *Applying GMRES to the Helmholtz equation with shifted Laplacian preconditioning: what is the largest shift for which wavenumber-independent convergence is guaranteed?*, Numer. Math., 131 (2015), pp. 567–614.
- [3] M. Ganesh and C. Morgenstern. An efficient multigrid algorithm for heterogeneous acoustic media sign-indefinite high-order FEM model. *Numer. Linear Algebra with Applications*, 2017 (to appear, doi:10.1002/nla.2049)).
- [4] M. Ganesh and C. Morgenstern. High-Order FEM Domain Decomposition Models for High-Frequency Wave Propagation in Heterogeneous Media. 2017 (Submitted, http://inside.mines.edu/~mganesh/final_ddmg.pdf).
- [5] M. Ganesh and C. Morgenstern. A sign-definite preconditioned high-order FEM Part-I: Formulation and simulation for bounded homogeneous media wave propagation. *SIAM J Sci Comput*, 2017 (Under Revision, http://inside.mines.edu/~mganesh/final_part1_signdef.pdf).
- [6] M. Ganesh and C. Morgenstern. A sign-definite preconditioned high-order FEM Part-II: Formulation, Analysis and simulation for bounded homogeneous media wave propagation. *Under Preparation*, 2017.
- [7] I. GRAHAM, E. SPENCE, AND E. VAINIKKO, *Domain decomposition preconditioning for high-frequency Helmholtz problems using absorption*, Math. Comp., (2017, to appear), <http://arxiv.org/pdf/1507.02097v2.pdf>.
- [8] A. Moiola and E.A. Spence, Is the Helmholtz equation really sign-indefinite? *SIAM Review*, **56** (2014), pp. 274–312.

Resonant activation of Optoacoustic Functionalities in Phononic Crystals

R. Ganesh^{1,*}, S. Gonella¹

¹Department of Civil, Environmental, and Geo- Engineering, University of Minnesota, Minneapolis, Minnesota, 55455

*Email: ramak015@umn.edu

Abstract

We present a strategy to adaptively manipulate the spatial characteristics of propagating elastic waves in nonlinear phononic crystals. Our approach exploits the interplay of dispersion and nonlinearity to reversibly activate modal characteristics corresponding to higher frequencies even while operating in low-frequency acoustic regimes. This effect, studied here using the well-known nonlinear three-wave resonance mechanism, is demonstrated via numerical simulations for a broad class of phononic crystal architectures exhibiting a wide spectrum of functionality tuning capabilities.

Keywords: Dispersion, Nonlinearity, Modal Mixing, Three-wave resonance

Introduction

Phononic crystals can function as efficient elastic (acoustic) wave manipulators due to their ability to impart frequency-dependent spatial characteristics to harmonic excitations. In this regard, the activation of nonlinear mechanisms in these structures results in the ability to spontaneously alter their response to changes in the operating conditions (e.g., amplitude of excitation). These adaptive characteristics typically result in a significant modification of the spectral and spatial characteristics of propagating wavefields. For tone-burst excitations, the manifestation can be classified into two distinct effects - the modulation of the envelope of the wave packet, and the generation of harmonics in the response [3]. In systems featuring the capability to support multiple modes of deformation, the nonlinearly-generated harmonics display dual spatial characteristics. One of the components, referred to as the forced response, depends on the spatial characteristics of the fundamental excitation, while the characteristics of the other component (referred to as the free response) are solely dependent on the linearized properties of the structure [3]. However, these two components coalesce when phase-matching

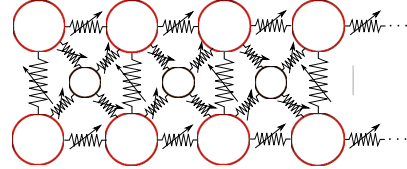


Figure 1: A periodic diatomic spring-mass truss

conditions are satisfied, i.e., the phase velocities of the fundamental and the nonlinearly-generated harmonic are equal in the linearized system [1, 2]. In this work, we focus on the spatial characteristics of phase-matching harmonic generation using the three-wave interaction approach. To this end, we will consider phononic crystals whose behavior can be represented by the following governing equation

$$\mathbf{M}\ddot{\mathbf{u}} + \mathbf{K}\mathbf{u} + \varepsilon\mathbf{f}_{NL}(\mathbf{u}) = 0, \quad (1)$$

where \mathbf{u} represents the vector of displacements in the structure, while \mathbf{M} and \mathbf{K} refer to the mass and linear stiffness matrix. $\mathbf{f}_{NL}(\mathbf{u})$ is a nonlinear force vector whose magnitude is much smaller than the linear terms in the response (represented by the scaling term ε). An example of such a system is shown in fig. 1, where the springs are characterized by a cubic nonlinear potential energy. We constrain wave motion along the horizontal direction, but each mass has two degrees of freedom to accommodate axial and flexural wave motion.

The weakness of the nonlinear terms can be exploited to employ a multiple spatiotemporal scales expansion ($\varepsilon^k n, \varepsilon^k t; k = 0, 1, 2, \dots$), and the leading order solution under the assumption of a multifrequency ansatz can be written as

$$\begin{aligned} \mathbf{u}_n^0 &= A_0(\varepsilon n, \varepsilon t, \varepsilon^2 t) \mathbf{1} \\ &+ \sum_{p=1}^3 A_p(\varepsilon n, \varepsilon t, \varepsilon^2 t) \phi_p e^{i(k_p n - \omega_p t)} + c.c, \end{aligned}$$

where \mathbf{u}_n^0 represents the fundamental solution, and k_p, ω_p and ϕ_p represent the wavenumber,

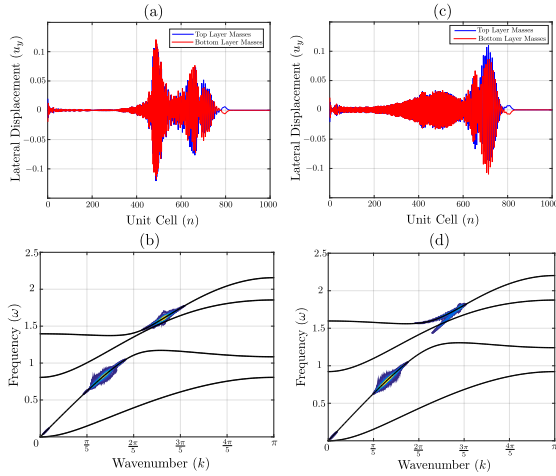


Figure 2: Spatial and spectral wave profile in two diatomic chains for the same excitation. (a,c) Spatial wave profile, (b,d) 2D DFT of the response superimposed to the band diagram evaluated from unit cell analysis.

frequency and modal vector of the eigen solution of the linearized problem. A_0 and A are slowly varying amplitudes whose functional form is determined from the equations obtained at $\mathcal{O}(\varepsilon)$ and higher. Under the assumption $k_3 = k_1 + k_2$ and $\omega_3 = \omega_1 + \omega_2$, the equations governing the evolution of the amplitude envelope A_p can be determined as [1, 2]

$$\begin{aligned} \left(\frac{\partial}{\partial t_1} + c_g^1 \frac{\partial}{\partial n_1} \right) A_1 &= iq_1 \overline{A_2} A_3 \\ \left(\frac{\partial}{\partial t_1} + c_g^2 \frac{\partial}{\partial n_1} \right) A_2 &= iq_2 \overline{A_1} A_3 \\ \left(\frac{\partial}{\partial t_1} + c_g^3 \frac{\partial}{\partial n_1} \right) A_3 &= iq_3 A_1 A_2, \end{aligned} \quad (2)$$

where $n_1 = \varepsilon n$, $t_1 = \varepsilon t$ are the first order spatiotemporal variables, and $c_g^p (= d\omega/dk)$ represents the linear group velocity of the frequency under consideration. The exact solution to these equations can be determined using the inverse scattering transform approach [1].

When $\omega_1 \approx \omega_2$, the above equations degenerate to give rise to the case of second harmonic resonance [2]. Under such conditions, even an initial excitation which consists of only the fundamental harmonic (ω_1) will give rise to a propagating wavefield with an additional second harmonic ($\omega_3 = 2\omega_1$) that resonantly interacts with the fundamental harmonic. This resonant interaction results in the growth of the amplitude of

the second harmonic until the equilibrium conditions of the three-wave interaction are established. Furthermore, the generation of the second harmonic also results in the activation of deformation mechanisms (given by the modal vector ϕ_p) corresponding to the linear solution at twice the excitation frequency. A snapshot of the spatiotemporal evolution of the lateral displacements of the masses under phase-matching conditions is plotted in figs. 2(a-b), where we observe the presence of two coherent wavefields in the response. On the contrary, the spatiotemporal evolution of the same initial excitation in a system that does not satisfy phase-matching conditions (shown in figs. 2(c-d)) features a second harmonic whose amplitude is much smaller, and is also more dispersive due to the presence of two distinct spatial contributions (corresponding to $k(2\omega_1)$ and $2k(\omega_1)$) [3]. Therefore, satisfying phase-matching conditions results in efficient transfer of energy from the fundamental acoustic mode of propagation to an optical mode, whose characteristics are completely described by that of the linear system. As a result, a complete map of the switchable functionalities that can be activated in these structures is entirely determined from linear analysis, which gives rise to virtually endless opportunities for wave manipulation.

Acknowledgements

The authors acknowledge the support of the National Science Foundation (CMMI-1452488).

References

- [1] D. J. Kaup, A. Reiman, and A. Bers, Space-time evolution of nonlinear three-wave interactions. I. Interaction in a homogeneous medium *Reviews of Modern Physics* **51**(1979), pp. 275–309.
- [2] V. V. Konotop, Second-harmonic generation in diatomic lattices, *Physical Review E* **54** (1996), pp. 4266-4270.
- [3] R. Ganesh and S. Gonella, Nonlinear waves in lattice materials: Adaptively augmented directivity and functionality enhancement by modal mixing, *Journal of the Mechanics and Physics of Solids* **99**(2017), pp. 272-298.

Diffuse acoustic waves in a randomly stratified flow

Etienne Gay^{1,*}, Eric Savin¹, Josselin Garnier²

¹Computational Fluid Dynamics Dept., Onera, Châtillon, France

²CMAP, École Polytechnique, Palaiseau, France

*Email: etienne.gay@onera.fr

Abstract

In this communication we develop an integral representation of the acoustic waves emitted by a source and transmitted by a randomly stratified fluid flow. The analysis is carried out in a regime of separation of scales whereby the fluctuations of the flow are much smaller than the source wavelength, which in turn is much smaller than the thickness of the flow—the so-called diffusion regime. Our aim is to subsequently develop coherent interferometric (CINT) imaging algorithms based on cross-correlation functions of the acoustic waves recorded at the bottom of the flow to possibly locate the source above it.

Keywords: Aero-acoustics, Diffusion, Coherent interferometry.

Introduction

The purpose of imaging techniques is to estimate the location of one or more sources and/or reflecting structures with a passive or an active array of receivers. Coherent interferometric (CINT) algorithms [1] have been developed for imaging in cluttered media from the time traces of echoes recorded at a remote array. The main effect of the clutter is to induce large delay spread, or coda, to the recorded time traces in regimes where significant multiple scattering of the acoustic waves occurs. In this work we are more particularly interested in the propagation of acoustic waves in a stratified, heterogeneous flow and the possible localization of sources by these wave fields. CINT imaging is based on the back-propagation of local space-time empirical cross-correlations of the array data, namely the recorded pressure fields at the near free-surface of an half-space or a random slab [3,4]. Our ultimate objective here is to extend CINT imaging techniques to possibly account for the influence of a convecting shear flow.

For that purpose, we study here the acoustic waves emitted by a source and transmitted by a randomly stratified fluid flow. We start

from the earlier works of Garnier *et al.* [3,4] and Borcea *et al.* [2] and consider successively the influence of an homogeneous background flow, and a randomly stratified background flow. The analysis is based on an assumption of separation of scales, whereby the fluctuations of the flow are much smaller than the source wavelength, which in turn is much smaller than the thickness of the flow.

Acoustic waves in an homogeneous flow

We consider the Euler equations for a compressible fluid flow and linearize them about an unperturbed, stationary flow for which the pressure, fluid velocity, and fluid density do not depend on time t . They are denoted by $p_0(\mathbf{r})$, $\mathbf{v}_0(\mathbf{r})$ and $\varrho_0(\mathbf{r})$ respectively, where $\mathbf{r} \in \mathbb{R}^3$ stands for the position, such that:

$$\begin{aligned} (\mathbf{v}_0 \cdot \nabla) \varrho_0 &= -\varrho_0 \nabla \cdot \mathbf{v}_0, \\ (\mathbf{v}_0 \cdot \nabla) \mathbf{v}_0 &= -\frac{1}{\varrho_0} \nabla p_0, \\ (\mathbf{v}_0 \cdot \nabla) p_0 &= c_0^2 (\mathbf{v}_0 \cdot \nabla) \varrho_0. \end{aligned}$$

Here c_0 stands for the sound velocity not influenced by the waves. Linearization consists in assuming that the actual flow is a perturbation $(\varrho', \mathbf{v}', p')$ of the stationary flow generated by a source $\mathbf{f}(t, \mathbf{r})$ per unit mass (neglecting gravity):

$$\delta(t, \mathbf{r}) = \delta_0(\mathbf{r}) + \delta'(t, \mathbf{r}),$$

where $\delta \in \{\varrho, \mathbf{v}, p\}$. The primed quantities p' , \mathbf{v}' and ϱ' are the acoustic pressure, fluid velocity and density, respectively, of which non-linear contributions to the Euler equations above are assumed negligible. We note $\mathbf{r} = (\mathbf{x}, z) \in \mathbb{R}^2 \times \mathbb{R}$ where \mathbf{x} stands for the horizontal coordinates of the position, and z stands for the vertical coordinate. We start with the case where the unperturbed background flow is homogeneous, that is \mathbf{v}_0 and ϱ_0 are non vanishing and constant in a slab $z \in [-L, 0]$. In addition the background flow celerity \mathbf{v}_0 is horizontal, a situation which arises in many instances of real media (oceans,

Earth's crust, atmosphere, jet flows, *etc*). Then the acoustic velocity \mathbf{v}' and pressure p' satisfy:

$$\begin{aligned} (\partial_t + \mathbf{v}_0 \cdot \nabla_{\mathbf{x}}) p' + K_0 \nabla \cdot \mathbf{v}' &= 0, \\ (\partial_t + \mathbf{v}_0 \cdot \nabla_{\mathbf{x}}) \mathbf{v}' + \frac{1}{\varrho_0} \nabla p' &= \mathbf{f}, \end{aligned}$$

where $K_0 = \varrho_0 c_0^2$ is the fluid compressibility, and $\nabla_{\mathbf{x}}$ stands for the gradient in the horizontal plane. With the appropriate Fourier transform (FT) with respect to time t and horizontal coordinates \mathbf{x} , we can solve this system for a source $\mathbf{f}(t, \mathbf{r}) = \mathbf{F}(t, \mathbf{x}) \delta(z - z_s)$ with $z_s \geq 0$ and show that the acoustic pressure below the slab has the integral representation:

$$\begin{aligned} p'(t, \mathbf{x}, -L) &= \frac{1}{16\pi^3} \iint e^{-i\omega(t-\kappa \cdot \mathbf{x} - L\zeta(\kappa))} \\ &\times \left(\frac{\varrho_0 \kappa \cdot \widehat{\mathbf{F}}_{\mathbf{x}}(\omega, \kappa)}{\beta(\kappa)\zeta(\kappa)} - \varrho_0 \widehat{F}_z(\omega, \kappa) \right) \omega^2 d\omega d\kappa, \end{aligned}$$

where $\zeta(\kappa) = (\frac{\beta}{c_0^2} - \frac{\kappa^2}{\beta})^{\frac{1}{2}}$, $\beta = 1 - \mathbf{v}_0 \cdot \kappa$, and $(\widehat{\mathbf{F}}_{\mathbf{x}}(\omega, \kappa), \widehat{F}_z(\omega, \kappa))$ is the FT of the three-dimensional source \mathbf{F} , ω is the circular frequency, and κ is the horizontal slowness vector.

Acoustic waves in a random flow

We now consider the case where the bulk modulus K_0 is randomly varying about an homogenized value $\underline{K} = \varrho_0 \underline{c}^2$ and address the diffusion approximation regime [3], whereby the scale of fluctuations ℓ of the former is much smaller than the typical wavelength λ of the waves, which in turn is much smaller than the depth of the flow L . This scaling is quantified by introducing the small parameter $0 < \varepsilon \ll 1$ such that $\frac{\ell}{\lambda} = \varepsilon$ and $\frac{\ell}{L} = \varepsilon^2$. In this respect, the bulk modulus depends on the depth z in the flow $(-L, 0)$ and is constant outside:

$$\frac{1}{K_0(z)} = \begin{cases} \frac{1}{\underline{K}} \left[1 + \nu \left(\frac{z}{\varepsilon^2} \right) \right] & \text{for } z \in [-L, 0], \\ \frac{1}{\underline{K}} & \text{elsewhere,} \end{cases}$$

where $(\nu(z))_{z \in \mathbb{R}}$ is a zero-mean, second-order stochastic process. Also the source is assumed to vary at the scale ε and is denoted by $\mathbf{F}^\varepsilon(t, \mathbf{x}) = \mathbf{F}(t/\varepsilon, \mathbf{x}/\varepsilon)$. Then the acoustic pressure admits the following integral representation:

$$\begin{aligned} p'_\varepsilon(t, \mathbf{x}, -L) &= \frac{1}{16\pi^3} \iint e^{-\frac{i\omega}{\varepsilon}(t-\kappa \cdot \mathbf{x} - L\underline{\zeta}(\kappa))} T^\varepsilon(\omega, \kappa) \\ &\times \left(\frac{\varrho_0 \kappa \cdot \widehat{\mathbf{F}}_{\mathbf{x}}^\varepsilon(\omega, \kappa)}{\beta(\kappa)\underline{\zeta}(\kappa)} - \varrho_0 \widehat{F}_z^\varepsilon(\omega, \kappa) \right) \omega^2 d\omega d\kappa, \end{aligned}$$

where $\underline{\zeta}(\kappa) = (\frac{\beta}{c_0^2} - \frac{\kappa^2}{\beta})^{\frac{1}{2}}$, and $T^\varepsilon(\omega, \kappa)$ is the transmission coefficient which defines how the acoustic waves cross the slab. Its properties are fully characterized as in [3]. Essentially the main difference between the present situation and the situation addressed in [3] where no background flow is considered lies in the phase ϕ . In the latter situation it is $\phi(t, \mathbf{x}, \kappa) = t - \kappa \cdot \mathbf{x} - \frac{L}{c(\kappa)}$ with $c(\kappa) = \frac{\varepsilon}{\sqrt{1 - \kappa^2 c_0^2}}$, whereas in the situation the celerity $\sqrt{1 - \kappa^2 c_0^2}$ of the background flow has an important influence, as expected: $\phi(t, \mathbf{x}, \kappa) = t - \kappa \cdot \mathbf{x} - L\underline{\zeta}(\kappa)$, with the previous definition of $\underline{\zeta}$.

In future works we shall analyze how this result compares with the existing experiments and numerical simulations reported in the literature [5, 6], and develop a CINT imaging functional of the source \mathbf{f} based on the integral representation established above.

References

- [1] L. Borcea, G. Papanicolaou, C. Tsogka. Coherent interferometric imaging in clutter. *Geophys.* **71**(4), SI165-SI175 (2006).
- [2] L. Borcea, G. Papanicolaou, C. Tsogka. Coherent interferometry in finely layered random media. *Multiscale Model. Simul.* **5**(1), 62-83 (2006).
- [3] J.-P. Fouque, J. Garnier, G. Papanicolaou, K. Sølna. *Wave Propagation and Time Reversal in Randomly Layered Media*. Springer-Verlag, New York NY (2007).
- [4] J. Garnier. Imaging in randomly layered media by cross-correlating noisy signals. *Multiscale Model. Simul.* **4**(2), 610-640 (2005).
- [5] S. Candel, A. Guédel, A. Julianne. Radiation, refraction and scattering of acoustic waves in a free shear flow. In *Proc. 3rd AIAA Aeroacoustics Conf., Palo Alto CA*. AIAA paper 1976-544 (1976).
- [6] I. Bennaceur, D.C. Mincu, I. Mary, M. Terracol, L. Larchevêque, P. Dupont. Numerical simulation of acoustic scattering by a plane turbulent shear layer: Spectral broadening study. *Computers & Fluids* **138**, 83-98 (2016).

Identification of a time-dependent potential in a wave equation

Thies Gerken^{1,*}, Armin Lechleiter¹

¹Center of Industrial Mathematics, University of Bremen, Bremen, Germany

*Email: tgerken@math.uni-bremen.de

Abstract

We augment the classical inhomogeneous wave equation by a zero-order term cu and consider the task of reconstructing c from the solution u . Here c is allowed to be time-dependent, which makes the problem more difficult. We present a suitable existence and uniqueness result for the wave equation and compute the Fréchet derivative of the solution operator. These results allow for the numerical reconstruction of c from artificial data, for which we apply an inexact newton method.

Keywords: parameter identification, dynamic inverse problems, wave equation, Fréchet derivatives, inexact Newton regularization

1 Introduction

For a fixed $f \in L^2([0, T], L^2(\Omega))$ we consider u as the weak solution of the wave equation

$$u'' - \Delta u + cu = f \text{ in } [0, T] \times \Omega, \quad (1)$$

furnished with initial conditions $u(0) = u'(0) = 0$ and homogeneous Dirichlet boundary conditions. Here Ω is a bounded domain of \mathbb{R}^n ($n \in \{1, 2, 3\}$) and $T > 0$. We are interested in the identification of the time- and space dependent parameter c based on knowledge of u .

2 Solution theory

To this end we need a well-defined solution operator $S : \mathcal{D}(S) \subset X \rightarrow L^2([0, T], L^2(\Omega))$, where an open subset $D(S)$ of a Hilbert space X would be ideal. Most existence results require $c \in C^1([0, T] \times \Omega)$, cf. Evans [1]. We expand on the results of Lions and Magenes [2]. Their theory which is based on energy estimates and Galerkin approximation guarantees unique solvability for every $c \in H^2([0, T], L^2(\Omega))$ which is bounded below.

Theorem 1 *There is a radius $\delta > 0$ so that (1) possesses for every $c \in H^2([0, T], L^2(\Omega))$ which satisfies that there are $\tilde{c} \in L^\infty([0, T], L^2(\Omega))$ and $c_0 \in \mathbb{R}$ with $\tilde{c} \geq c_0 \in \mathbb{R}$ a.e. as well as $\|c - \tilde{c}\|_{L^\infty([0, T], L^2(\Omega))} < \delta$ a unique weak solution $u \in L^2([0, T], H_0^1(\Omega))$.*

The set consisting of all those c is an open subset of $H^2([0, T], L^2(\Omega))$.

3 Fréchet derivative

For the numerical inversion of $Sc = u$ we use a Newton approach, which requires the knowledge of the derivative of S . Through formal differentiation of the weak formulation we deduce that $u_h = (S'c)[h]$ solves $u_h'' - \Delta u_h + cu_h = -uh$ with the same initial and boundary conditions as u . To show that u_h is well defined we use the fact that S is locally Lipschitz-continuous and the energy estimates for solutions of the wave equation. These only apply to right hand sides belonging to $L^2([0, T], L^2(\Omega))$, hence we need a bit more spatial smoothness of our searched for parameter, namely

$$c \in H^2([0, T], L^2(\Omega)) \cap L^2([0, T], L^p(\Omega)) =: X$$

with $p > n$.

Theorem 2 *S is Fréchet-differentiable in c . For every $h \in X$ we have $(S'c)[h] = u_h$ as given above.*

4 Ill-posedness

For the discussion of ill-posedness we have the following results.

Lemma 3 *$S' : X \rightarrow \mathcal{L}(X, L^2([0, T], H_0^1(\Omega)))$ is locally Lipschitz-continuous.*

Furthermore $S : X \rightarrow L^\infty([0, T], H_0^1(\Omega))$ and

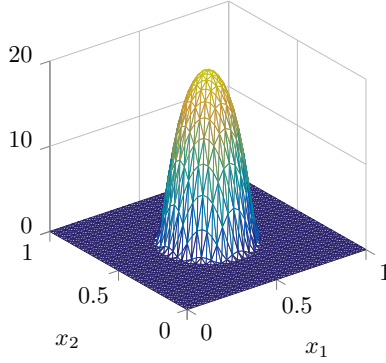
$$S : X \cap H^1([0, T], L^p(\Omega)) \rightarrow L^2([0, T], H_0^1(\Omega))$$

satisfy the tangential cone condition, i.e. for all $c \in \mathcal{D}(S)$ there exist $r > 0$ and $0 < \eta < 1$ so that

$$\|Sv - Sw - (S'w)[v - w]\| \leq \eta \|Sv - Sw\|$$

holds for all $v, w \in B(c, r) \cap \mathcal{D}(S)$.

In the theory of inverse problems in Hilbert spaces these properties would allow us to link the local ill-posedness of the nonlinear equation $Sc = u$ and the local ill-posedness of its linearization. Using compact embeddings we can show that the linearization is indeed ill-posed.

Figure 1: Test parameter at $t = 1.0$.

Lemma 4 If $f \neq 0$ then for every $c \in \mathcal{D}(S)$ the derivative $S'c : X \rightarrow L^2([0, T], L^2(\Omega))$ is a compact operator with infinite dimensional range. In particular its range $\text{Rg}(S'c)$ is not closed in $L^2([0, T], L^2(\Omega))$.

5 Numerical results

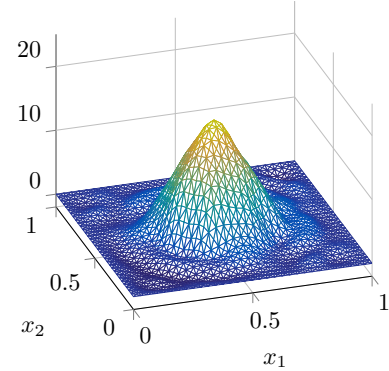
For the discretization of the wave equation we use the finite element method in space and the Crank-Nicolson scheme in time, which we implemented using the C library ALBERTA [4]. For the regularized inversion we applied the inexact newton method CG-REGINN [3], which requires a Hilbert space setting. Because of this we omit the $L^2([0, T], L^p(\Omega))$ part in the definition of X in the numerical discussion. The method further requires not only the derivative of S but its adjoint $(S'c)^*$ as well, for which we have set up a finite difference scheme.

One of our testing parameters in the case $n = 2$ is a ‘hat’, which moves for $t \in [0, 2]$ through the domain $\Omega = (0, 1)^2$, i.e.

$$c(t, x) = 20 h(4 \|x - \frac{1+t}{4}(1, 1)\|)$$

with a smooth function $h : \mathbb{R} \rightarrow \mathbb{R}$ with support in $[-1, 1]$. The inversion algorithm is able to reconstruct this parameter from artificial data with 1% noise, resulting in the approximation in Figure 2. This approximation possesses a $L^2([0, T], L^2(\Omega))$ -error of 45%, which of course depends heavily on the scaling of the parameter.

Motivated by possible applications we also consider the reconstruction from simulated measurements, which yields similar results when using 2000 measurement points in $[0, T] \times \Omega$, which is significantly less than the number of degrees of freedom in the discretized field u .

Figure 2: Reconstruction from data with 1% noise at $t = 1.0$.

References

- [1] Lawrence C. Evans. *Partial differential equations*. 2nd ed. Graduate studies in mathematics. American Mathematical Society, 2010.
- [2] Jacques L. Lions and Enrico Magenes. *Non-homogeneous boundary value problems and applications*. Vol. 1. Die Grundlehren der mathematischen Wissenschaften. Berlin, Heidelberg: Springer, 1972.
- [3] Andreas Rieder. “Inexact Newton regularization using conjugate gradients as inner iteration”. In: *SIAM Journal on Numerical Analysis* 43.2 (2005), pp. 604–622.
- [4] Alfred Schmidt and Kunibert G. Siebert. *Design of adaptive finite element software: The finite element toolbox ALBERTA*. Lecture notes in computational science and engineering. Berlin, Heidelberg: Springer, 2006.

Recent Advances in Optimized Schwarz Domain Decomposition Methods for Time-Harmonic Wave Problems

C. Geuzaine¹

¹University of Liège, Department of Electrical Engineering and Computer Science

Abstract

We present recent advances in domain decomposition methods for high-frequency time-harmonic wave problems, where subproblems of small sizes are solved using sparse direct solvers, and are combined using iterative techniques. We focus on a family of recently proposed quasi-optimal domain decomposition methods based on accurate approximations of the Dirichlet-to-Neumann map, combined with parallel, sweeping-type preconditioners.

Keywords: Optimized Schwarz methods, Finite element methods, Preconditioners

1 Introduction

Solving high-frequency time-harmonic wave problems using finite element techniques is challenging, as such problems lead to very large, complex and possibly indefinite linear systems. Direct sparse solvers do not scale well for such problems, and Krylov subspace iterative solvers can exhibit slow convergence, or even diverge. Domain decomposition methods (DDMs) are currently the most promising approach, where subproblems of smaller sizes are solved using sparse direct solvers, and are combined with iterative Krylov subspace techniques. Among the different families of domain decomposition techniques, optimized Schwarz methods [8] have proved well suited for time-harmonic wave problems. The convergence rate of these methods strongly depends on the transmission condition enforced on the interfaces between the subdomains, the optimal convergence being obtained by using the Dirichlet-to-Neumann (DtN) map related to the complementary of the subdomain of interest. Using the DtN leads to a very expensive numerical procedure in practice, as this operator is non-local. A great variety of techniques based on local transmission conditions have therefore been proposed to build practical algorithms.

In this paper we review a family of quasi-optimal domain decomposition methods obtained by using accurate approximations of the

DtN for acoustic and electromagnetic waves. The transmission conditions are obtained by regularizing the exact half-space DtN and localizing it using complex Padé approximants. The convergence of the resulting algorithm is optimal for the evanescent modes and significantly improved compared to competing approaches for the remaining modes. Even with optimal transmission conditions, however, the number of iterations of Schwarz methods increases with the number of subdomains. To address this issue, we present a sweeping preconditioner that approximates the inverse of the iteration operator for layered decompositions of the domain. The parallel variants of these preconditioners can be advantageously used to solve very large problems with multiple right hand sides, by efficiently exploiting the computational resources of massively parallel computers.

2 Mono-domain Time-Harmonic Wave Problem

A generic time-harmonic wave propagation problem with sources in the domain Ω and homogeneous boundary conditions on Γ can be written in the form

$$\begin{aligned} \mathcal{L}u &= f \quad \text{in } \Omega, \\ \mathcal{B}u &= 0 \quad \text{on } \Gamma, \end{aligned} \tag{1}$$

where \mathcal{L} and \mathcal{B} are linear operators. For example, for an acoustic wave problem with a Sommerfeld radiation condition (the unknown scalar field u denoting the pressure), one would have $\mathcal{L} := (\Delta + k^2)$ (with k the acoustic wavenumber) and $\mathcal{B} := (\partial_{\mathbf{n}} - ik)$. For an electromagnetic wave problem with a Silver-Müller absorbing boundary condition (the unknown vector field u now denoting the electric field), one would have $\mathcal{L} := (\mathbf{curl} \mathbf{curl} - k^2)$ (with k the electromagnetic wavenumber) and $\mathcal{B} := (\gamma_{\mathbf{n}}^t \mathbf{curl} + ik\gamma_{\mathbf{n}}^T)$, with $\gamma_{\mathbf{n}}^t$ and $\gamma_{\mathbf{n}}^T$ respectively the tangential and tangential component trace operators ($\gamma_{\mathbf{n}}^t : \mathbf{v} \mapsto \mathbf{n} \times \mathbf{v}$ and $\gamma_{\mathbf{n}}^T : \mathbf{v} \mapsto \mathbf{n} \times (\mathbf{v} \times \mathbf{n})$). Different sources and more general boundary conditions can be considered without difficulty.

3 Domain Decomposition

We split the domain Ω into N_{dom} sub-domains Ω_i without overlap. Let us denote $\Gamma_i := \Gamma \cap \Omega_i$, $\Gamma_i^\infty := \Gamma^\infty \cap \Omega_i$ and $\Sigma_{i,j} := \overline{\Omega_i \cap \Omega_j}$ the artificial transmission interfaces. The additive Schwarz domain decomposition algorithm can be described as follows, at iteration $k+1$. For $i = 1, \dots, N$, compute $u^{(k+1)}$ solution to

$$\begin{aligned}\mathcal{L}u_i^{(k+1)} &= f && \text{in } \Omega_i, \\ \mathcal{B}u_i^{(k+1)} &= 0 && \text{on } \Gamma_i, \\ \mathcal{B}_{i,j}u_i^{(k+1)} &= g_{i,j}^{(k)} && \text{on } \Sigma_{i,j}.\end{aligned}\quad (2)$$

Then for $i, j = 1, \dots, N$ such that $i \neq j$ and $\Sigma_{i,j} \neq \emptyset$, update the interface unknowns according to:

$$g_{j,i}^{(k+1)} = \mathcal{B}_{j,i}u_i^{(k+1)} \quad \text{on } \Sigma_{j,i}. \quad (3)$$

Detailed expressions for the operators $\mathcal{B}_{i,j}$ in the case of time-harmonic acoustic and electromagnetic wave problems can be found in [12]: they are respectively of the general form $\mathcal{B}_{i,j} = \partial_{\mathbf{n}_i} + \mathcal{S}$ for acoustics and $\mathcal{B}_{i,j} = (\gamma_{\mathbf{n}_i}^t \mathbf{curl} + \mathcal{S})$ for electromagnetics, where \mathcal{S} is called the transmission operator.

Thanks to the general form of the operators $\mathcal{B}_{i,j}$, in the case of non-overlapping decompositions the update relation (3) can be rewritten as

$$g_{j,i}^{(k+1)} = \mathcal{B}_{j,i}u_i^{(k+1)} = -g_{i,j}^{(k)} + 2\mathcal{S}u_i^{(k+1)}, \quad (4)$$

since $\mathbf{n}_i = -\mathbf{n}_j$ on $\Sigma_{i,j} = \Sigma_{j,i}$.

Considering the full vector of unknowns $g = [g_{1,2}, g_{2,1}, g_{2,3}, \dots]^T$ made of all the interface unknowns $g_{i,j}$, one step of the above algorithm can be summarized as:

$$g^{(k+1)} = \mathcal{A}g^{(k)} + b, \quad (5)$$

for some right hand side b . Iteration (5) is a fixed-point iteration, the solution of which solves the linear system:

$$\mathcal{F}g = (\mathcal{I} - \mathcal{A})g = b. \quad (6)$$

In practice (6) is solved using an iterative Krylov subspace method such as GMRES or Orthodir, which only requires the application of the operator \mathcal{F} on a given iterate. This application involves the solution of the subproblems, and is thus usually made ‘‘matrix-free’’, i.e. without explicitly constructing the associated matrix coefficients.

4 Transmission Operators

The homogeneous boundary conditions on the artificial interfaces between the subdomains can be interpreted as impedance-type boundary conditions. For acoustic waves, the lowest order transmission operator on a generic artificial interface Σ reads $\mathcal{S}_{\text{IBC}(\chi)} := (-ik + \chi)$, where χ is a real constant. This is a zeroth-order polynomial approximation of the half-plane DtN, which generalizes the original Després condition [3] ($\chi = 0$). Optimized second-order transmission conditions [9] take the form $\mathcal{S}_{\text{GIBC}(a,b)} := (a + b\Delta_\Sigma)$, where Δ_Σ is the Laplace-Beltrami operator on Σ , and a and b are two complex numbers obtained by solving a min-max optimization problem on the rate of convergence. A rational approximation of the DtN obtained with complex Padé approximants leads to the transmission operator [1]:

$$\begin{aligned}\mathcal{S}_{\text{GIBC}(N_p, \alpha, \varepsilon)} &:= -ikC_0 - ik \sum_{\ell=1}^{N_p} A_\ell \\ \text{div}_\Sigma \left(\frac{1}{k_\varepsilon^2} \nabla_\Sigma \right) \left(I + B_\ell \text{div}_\Sigma \left(\frac{1}{k_\varepsilon^2} \nabla_\Sigma \right) \right)^{-1},\end{aligned}$$

This was shown in [1] to lead to quasi-optimal convergence of the resulting DDM, i.e. to an optimal convergence for evanescent modes, and improved convergence for the other modes. A complexified wave number $k_\varepsilon = k + i\varepsilon$, with ε a real positive constant, allows to regularize the operator for grazing modes on the artificial interfaces. The coefficients C_0 , A_ℓ and B_ℓ are those of a complex Padé approximation of the square root with a rotation α of the branch cut.

For electromagnetic waves, the zeroth-order transmission condition is $\mathcal{S}_{\text{IBC}(0)} := ik\gamma^T$, and optimized second-order transmission conditions take the form [4, 11]:

$$\begin{aligned}\mathcal{S}_{\text{GIBC}(a,b)} &:= ik \left(I + \frac{a}{k^2} \nabla_\Sigma \text{div}_\Sigma \right)^{-1} \\ &\quad \left(I - \frac{b}{k^2} \mathbf{curl}_\Sigma \mathbf{curl}_\Sigma \right) \gamma^T,\end{aligned}$$

where the curl operator is the dual operator of \mathbf{curl} and where a and b are chosen so that an optimal convergence rate is obtained for the TE and TM modes. Quasi-optimal convergence of the DDM can be obtained using a rational ap-

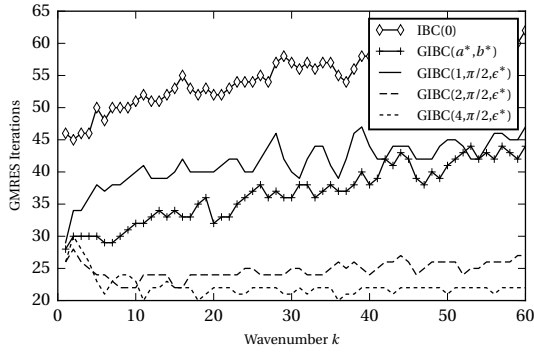


Figure 1: Unit circular cylinder under TE plane wave incidence: number of GMRES iterations vs. wavenumber (5 concentric subdomains, 20 points per wavelength).

proximation of the exact DtN [6, 7]:

$$\begin{aligned} \mathcal{S}_{\text{GIBC}(N_p, \alpha, \varepsilon)} := \\ ik \left(C_0 + \sum_{\ell=1}^{N_p} A_\ell X (I + B_\ell X)^{-1} \right)^{-1} \\ \left(I - \operatorname{curl}_\Sigma \frac{1}{k_\varepsilon^2} \operatorname{curl}_\Sigma \right) \gamma^T, \end{aligned}$$

with $X := \nabla_\Sigma \frac{1}{k_\varepsilon^2} \operatorname{div}_\Sigma - \operatorname{curl}_\Sigma \frac{1}{k_\varepsilon^2} \operatorname{curl}_\Sigma$, and where k_ε , C_0 , A_ℓ and B_ℓ are defined as in the acoustic case. As an example, Figure 1 compares the convergence of the DDM with different transmission conditions when computing the scattered electromagnetic field by a unit radius cylinder illuminated by a plane wave. Similar polynomial or rational approximations of the DtN can also be obtained for elastic waves; current work investigates the properties of the rational approximation of the DtN proposed in [2]. In all cases, transmission conditions based on perfectly matched layers (PMLs) can also be considered, by appending a volume layer to the transmission interface, in which a PML transformation with a given absorption profile is applied.

All these methods are referred to as optimized Schwarz domain decomposition methods. Note that $\text{GIBC}(N_p, \alpha, \varepsilon)$ and PML have in common that they introduce additional unknowns, whereas the other transmission conditions do not. Also, while the polynomial and rational transmission conditions can be formulated explicitly through sparse surface equations, the PML conditions require a volume rep-

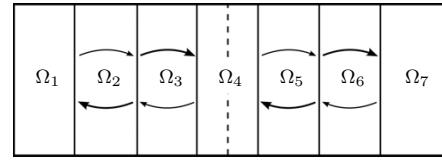


Figure 2: Layered decomposition of the domain, with one cut.

resentation.

5 Sweeping Preconditioners

In order to obtain scalable algorithms in terms of the number subdomains, we consider a layered decomposition of the domain, as depicted in Figure 2 ($\Sigma_{i,j} \neq \emptyset$ if $|i-j| = 1$). We introduce the forward and backward transfer operators \mathcal{B}_i^f and \mathcal{B}_i^b , defined by:

$$\begin{aligned} \mathcal{B}_i^f : g_{i,i-1} &\mapsto -2\mathcal{S}u_i(g_{i,i-1}, 0)|_{\Sigma_{i,i+1}}, \\ \mathcal{B}_i^b : g_{i,i+1} &\mapsto -2\mathcal{S}u_i(0, g_{i,i+1})|_{\Sigma_{i,i-1}}, \end{aligned}$$

where $u_i(g_{i,i-1}, g_{i,i+1})|_\Sigma$ refers to the restriction on Σ of the solution to the subproblem $\mathcal{L}u_i = f$ defined by (2). Notice that the forward and backward transfer operators only involve the solution of subproblems with a nonhomogeneous impedance boundary condition on one side only (left or right), since either $g_{i,i-1}$ or $g_{i,i+1}$ is set to 0. We also define the self-coupling operators \mathcal{E}_i^f and \mathcal{E}_i^b , defined from an interface to itself:

$$\begin{aligned} \mathcal{E}_i^f : g_{i,i-1} &\mapsto g_{i,i-1} - 2\mathcal{S}u_i(g_{i,i-1}, 0)|_{\Sigma_{i,i-1}}, \\ \mathcal{E}_i^b : g_{i,i+1} &\mapsto g_{i,i+1} - 2\mathcal{S}u_i(0, g_{i,i+1})|_{\Sigma_{i,i+1}}. \end{aligned}$$

These operators correspond to the contribution on an interface of the part of a wave that travels through the domain and that is reflected back to its interface of origin.

With these definitions, the matrix corresponding to the Schwarz operator writes:

$$\mathcal{F}(N) = \left[\begin{array}{cc|cc|cc|c} \mathcal{I} & \mathcal{E}_2^f & \mathcal{B}_2^b & & & & & \\ \mathcal{E}_1^b & \mathcal{I} & 0 & 0 & & & & \\ \hline 0 & 0 & \mathcal{I} & \mathcal{E}_3^f & & & & \\ & & \mathcal{B}_2^f & \mathcal{E}_2^b & \mathcal{I} & & & \\ & & & & & \ddots & & \\ & & & & & & \ddots & \\ \hline & & & & & & & \mathcal{B}_{N-1}^b \\ & & & & & & 0 & 0 \\ & & & & & & & \mathcal{I} & \mathcal{E}_N^f \\ & & & & & & & \mathcal{B}_{N-1}^f & \mathcal{E}_{N-1}^b & \mathcal{I} \end{array} \right].$$

Sweeping preconditioners can be constructed by looking for approximate inverses

of this operator. The underlying idea is to look for approximations that would involve the same subproblem solves than for the (direct) iteration operator: this way a fully matrix-free preconditioner can be obtained, whose application is carried out in a similar fashion to the original Schwarz iteration, without any precalculation. Neglecting the self-coupling operators $\mathcal{E}^{\{f,b\}}$ leads to the double-sweep (DS) preconditioner introduced in [13]: the explicit inverse of the Schwarz operator M_{DS}^{-1} can be built and involves two “sweeps” of subproblem solves (forward and backward), which can be done concurrently. Considering the lower and upper triangular parts of the operator without neglecting the self-coupling operators leads to a Symmetric Gauss-Seidel (SGS) preconditioner $M_{\text{SGS}}^{-1} = L_N^{-1}U_N^{-1}$, where both L_N^{-1} and U_N^{-1} also lead to forward and backward sweeps, which must however be done in sequence.

With accurate approximations of the DtN, the number of iterations of the DDM is greatly reduced with the application of these preconditioners, and remains small even for large numbers of subdomains. As each sweep is intrinsically sequential, though, the time-to-solution might not be improved depending on the number of CPUs available. Two avenues can be explored to recover scalability: one the one hand, multiple right hand sides can be pipelined during a sweep; and on the other hand, cuts can be introduced in the sweeping process, in effect resulting in block versions of the preconditioners [14]. Figure 4 illustrates the convergence of the preconditionned DDM on the cobra model depicted in Figure 3, with $N_{\text{dom}} = 100$ subdomains. Short sweeps (over 10 to 25 subdomains) already greatly improve convergence: combined with right hand side pipelining, they allow to efficiently exploit all the available computational power on massively parallel computers.

An open source implementation of all the aforementioned algorithms is available online¹ through the GetDDM package [12], which combines the mesh generator Gmsh [10] and the finite element solver GetDP [5]. All transmission conditions and preconditioners can be readily tested on several examples, scaling from a few thousand to several billion unknowns.

¹<http://onelab.info/wiki/GetDDM>

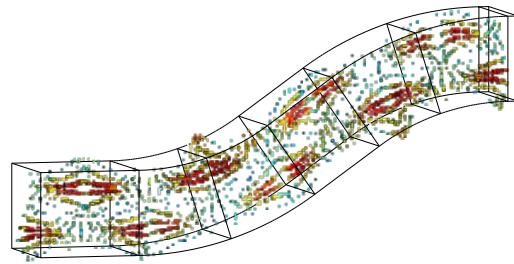


Figure 3: Cross-section of the solution of the cobra model at $k = 30\pi$ (TE21 mode).

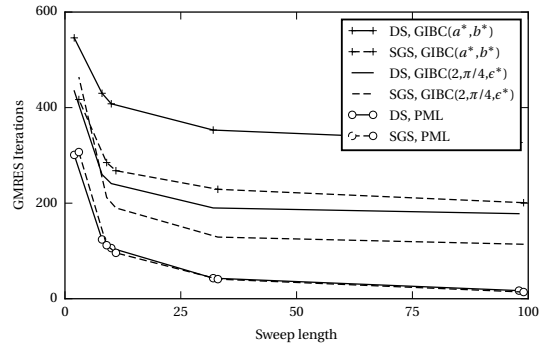


Figure 4: Cobra model: number of GMRES iterations vs. sweep length at $k = 100\pi$ (100 sub-domains, 20 points per wavelength).

References

- [1] Y. Boubendir, X. Antoine, and C. Geuzaine. A quasi-optimal non-overlapping domain decomposition algorithm for the Helmholtz equation. *Journal of Computational Physics*, 231(2):262–280, 2012.
- [2] S. Chaillat, M. Darbas, and F. Le Louer. Approximate local Dirichlet-to-Neumann map for three-dimensional time-harmonic elastic waves. *Computer Methods in Applied Mechanics and Engineering*, 297(1):62–83, 2015.
- [3] B. Després, P. Joly, and J. E. Roberts. A domain decomposition method for the harmonic Maxwell equations. In *Iterative methods in linear algebra (Brussels, 1991)*, pages 475–484, Amsterdam, 1992. North-Holland.
- [4] V. Dolean, M. Gander, S. Lanteri, J.-F. Lee, and Z. Peng. Effective trans-

- mission conditions for domain decomposition methods applied to the time-harmonic curl-curl maxwell's equations. *Journal of Computational Physics*, 280(1):232–247, 2015.
- [5] P. Dular, C. Geuzaine, F. Henrotte, and W. Legros. A general environment for the treatment of discrete problems and its application to the finite element method. *IEEE Transactions on Magnetics*, 34(5):3395–3398, September 1998.
- [6] M. El Bouajaji, X. Antoine, and C. Geuzaine. Approximate local magnetic-to-electric surface operators for time-harmonic Maxwell's equations. *Journal of Computational Physics*, 279(15):241–260, 2014.
- [7] M. El Bouajaji, B. Thierry, X. Antoine, and C. Geuzaine. A quasi-optimal domain decomposition algorithm for the time-harmonic Maxwell's equations. *Journal of Computational Physics*, 294(1):38–57, 2015.
- [8] M. Gander. Optimized schwarz methods. *SIAM Journal on Numerical Analysis*, 44(2):699–731, 2006.
- [9] M. J. Gander, F. Magoulès, and F. Nataf. Optimized Schwarz methods without overlap for the Helmholtz equation. *SIAM Journal on Scientific Computing*, 24(1):38–60, 2002.
- [10] C. Geuzaine and J.-F. Remacle. Gmsh: A 3-D finite element mesh generator with built-in pre- and post-processing facilities. *International Journal for Numerical Methods in Engineering*, 79(11):1309–1331, 2009.
- [11] V. Rawat and J.-F. Lee. Nonoverlapping domain decomposition with second order transmission condition for the time-harmonic Maxwell's equations. *SIAM Journal on Scientific Computing*, 32(6):3584–3603, 2010.
- [12] B. Thierry, A. Vion, S. Tournier, M. El Bouajaji, D. Colignon, N. Marsic, X. Antoine, and C. Geuzaine. GetDDM: An open framework for testing optimized Schwarz methods for time-harmonic wave problems. *Computer Physics Communications*, 203:309–330, 2016.
- [13] A. Vion and C. Geuzaine. Double sweep preconditioner for optimized schwarz methods applied to the Helmholtz problem. *Journal of Computational Physics*, 266(1):171–190, 2014.
- [14] A. Vion and C. Geuzaine. Parallel double sweep preconditioner for the optimized Schwarz algorithm applied to high frequency Helmholtz and Maxwell equations. In *Domain Decomposition Methods in Science and Engineering*, volume 104 of *Lecture Notes in Computational Science and Engineering*, pages 239–247. Springer Berlin Heidelberg, 2016.

Stable implementation of embedding formulae for computation of far field patterns

Andrew Gibbs^{1,*}, Steve Langdon¹, Andrea Moiola¹

¹Department of Mathematics and Statistics, Reading University, UK

*Email: a.j.gibbs@pgr.reading.ac.uk

Abstract

For problems of time harmonic scattering by polygonal obstacles, embedding formulae provide a useful and frequency-independent means of computing the far field pattern for a large class of incident fields, given the far field pattern of a small set of canonical problems. The number of such problems depends only on the geometry of the scatterer. Whilst the formulae themselves are in principle exact, any implementation will inherit numerical error from the method used to solve the canonical problems, leading to relatively large error at certain points. Here we identify the cause of this problem, and present an alternative approach which overcomes this problem.

Keywords: Helmholtz equation, numerical methods, far field pattern, high frequency

1 Problem statement

We consider the two-dimensional acoustic scattering problem, for a time harmonic plane wave

$$u_\alpha^i(\mathbf{x}) := e^{-ik(x_1 \cos \alpha + x_2 \sin \alpha)}, \quad \mathbf{x} := (x_1, x_2) \in \mathbb{R}^2$$

with incident angle $\alpha \in [0, 2\pi)$ and wavenumber $k > 0$, by an N -sided sound-soft polygon Ω_- with boundary Γ . It follows that the total solution $u_\alpha = u_\alpha^i + u_\alpha^s$, where u_α^s denotes the scattered field, satisfies the Helmholtz equation with Dirichlet boundary conditions

$$(\Delta + k^2)u_\alpha = 0 \text{ in } \mathbb{R}^2 \setminus \Omega_- \quad \text{and } u_\alpha = 0 \quad \text{on } \Gamma,$$

whilst u^s must satisfy the Sommerfeld radiation condition (see, e.g. [2, (1.3)]). An object of interest in practical applications is the far-field pattern, which describes the distribution of energy of the scattered field, measured far away from the scatterer. Formally it is defined by

$$u_\alpha^s(\mathbf{x}) \sim D(\theta, \alpha) \frac{e^{i(k|\mathbf{x}| + \pi/4)}}{\sqrt{2\pi k|\mathbf{x}|}}, \quad \text{as } |\mathbf{x}| \rightarrow \infty,$$

where $D(\theta, \alpha)$ is the *far-field coefficient* at observation angle θ , (proportional to [2, (3.63)]).

2 Embedding formulae

Suppose we want to compute the far field coefficient $D(\theta, \alpha)$ for a large range of incident angles $\alpha \in [0, 2\pi)$. Given the solution for a relatively small number of canonical problems, the embedding formulae of [1, (3.4)] can do this for any polygon for which each of the N internal angles are a rational multiple of π . In the (simpler) case where all N internal angles are equal, we choose parameters p and q to be the smallest integers such that $q/p = (N+2)/N$, then solve the problem of §1 and compute $D(\theta, \alpha_m)$ for canonical incident angles $\alpha_1, \dots, \alpha_M$, where $M = N(q-1)$ depends only on the geometry. For a square it follows that $M = 8$, and for an equilateral triangle $M = 12$. For general rational polygons, p , q and M follow from [1, §3.2]. It follows from [1, (3.4)] that

$$D(\theta, \alpha) = \frac{\sum_{m=1}^M B_m(\alpha) \Lambda(\theta, \alpha_m) D(\theta, \alpha_m)}{\Lambda(\theta, \alpha)}, \quad (1)$$

for $(\theta, \alpha) \in [0, \pi)^2$, where $\Lambda(\theta, \alpha) = \cos(p\theta) - (-1)^p \cos(p\alpha)$ and $[B_m]_{m=1}^M \in \mathbb{C}^M$ solves the system of equations

$$\sum_{m=1}^M B_m(\alpha) \hat{D}(\alpha_n, \alpha_m) = (-1)^{p+1} \hat{D}(\alpha, \alpha_n), \quad (2)$$

for $n = 1, \dots, M$, with $\hat{D}(\theta, \alpha) := \Lambda(\theta, \alpha) D(\theta, \alpha)$. As explained in [1], for $(\theta, \alpha) \in [0, 2\pi)^2$ such that $\Lambda(\theta, \alpha) \neq 0$, the representation (1) can be evaluated explicitly to obtain $D(\theta, \alpha)$. One application of L'Hôpital's rule is required for θ in $\Theta_\alpha := \{\theta \in [0, 2\pi) : \Lambda(\theta, \alpha) = 0\}$, with two applications of L'Hôpital's rule for θ in

$$\Theta_* := \left\{ \theta \in \Theta_\alpha : \frac{\partial \Lambda}{\partial \theta}(\theta, \alpha) = 0 \right\}.$$

3 Numerical implementation

In theory, the formula (1) provides a fast method to compute the far field pattern of an incident wave of any angle, given the solution of a small number (dependent only on the geometry) of

canonical problems. We now demonstrate how a naive implementation of (1) can lead to unbounded error at certain points. We denote by $\mathcal{P}D(\cdot, \alpha_m)$ a numerical approximation to $D(\cdot, \alpha_m)$ for $m = 1, \dots, M$, whilst $[b_m]_{m=1}^M \approx [B_m]_{m=1}^M$ solves the system (2) with D replaced by $\mathcal{P}D$. Given the unavoidable error in the numerical approximation of a polygonal scattering problem, the absolute error at a given point $(\theta, \alpha) \in [0, 2\pi)^2$ is

$$\frac{\left| \sum_{m=1}^M \left[B_m(\alpha) \hat{D}(\theta, \alpha_m) - b_m(\alpha) \mathcal{P}\hat{D}(\theta, \alpha_m) \right] \right|}{|\Lambda(\theta, \alpha)|}.$$

This representation shows that even for small numerical error, naive implementation of the embedding formula leads to large relative and absolute error at points $\theta \approx \theta_0 \in \Theta_\alpha$. This is demonstrated by Figure 1, which shows the relative error in the embedding formulae for the problem of scattering by a square of side length $\sqrt{2}$, wavenumber $k = 1$ and incident angle $\alpha = 1$ measured relative to one side of the square, using MPSpack (see [3]) as the numerical solver \mathcal{P} , for a range of degrees of freedom. This numerical instability can be overcome by Taylor expanding around the $\theta_0 \in \Theta_\alpha$ to which θ is closest. Truncating after n_T terms, our approximation reduces to $D(\theta, \alpha) \approx$

$$\frac{\theta - \theta_0}{\Lambda(\theta, \alpha)} \sum_{m=1}^M b_m(\alpha) \sum_{n=1}^{n_T} \frac{(\theta - \theta_0)^{n-1}}{n!} \frac{\partial^n}{\partial \theta^n} \mathcal{P}\hat{D}(\theta, \alpha_m),$$

for which the error is provably bounded, provided θ is not close to $\theta_* \in \Theta_*$. By combining this with a similar approach for the case where θ is close to $\theta_* \in \Theta_*$, one can construct an implementation of the embedding formulae for which the absolute error is bounded on all $(\theta, \alpha) \in [0, 2\pi)^2$. This is demonstrated by Figure 2, which is a correction of Figure 1, solving the same problem.

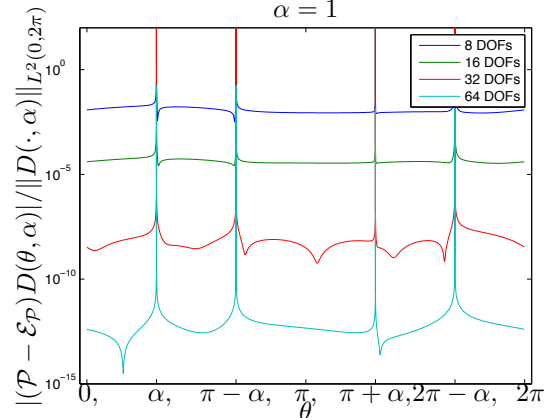


Figure 1: Relative error for naive approach. Here $\mathcal{E}_P D$ denotes the naive approximation..

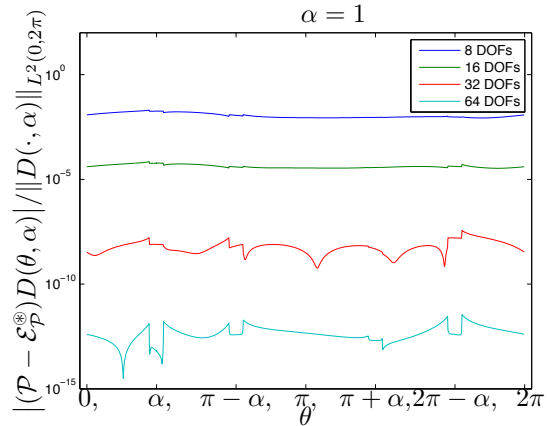


Figure 2: Relative error for the combined approach described in §3, we denote the resulting approximation by $\mathcal{E}_P^* D$.

References

- [1] N. Biggs, A new family of embedding formulae for diffraction by wedges and polygons, *Wave Motion* **43**, (2006), pp. 517–528.
- [2] D. Colton and R. Kress, *Inverse acoustic and electromagnetic scattering theory*, third edition, Springer, New York, (2013).
- [3] A. Barnett and T. Betcke An exponentially convergent nonpolynomial finite element method for time-harmonic scattering from polygons., *SIAM Journal of Scientific Computing*, **32**, (2010), pp. 1417–1441.

Effective dielectric tensor of a two-dimensional periodic medium in the low-frequency approximation

Yuri Godin^{1,*}, **Boris Vainberg**¹

¹Department of Mathematics and Statistics, University of North Carolina at Charlotte, Charlotte NC, USA

*Email: ygodin@uncc.edu

Abstract

We consider transverse propagation of electromagnetic waves through a two-dimensional composite material containing a periodic rectangular array of cylindrical inclusions of radius ρ and calculate the effective dielectric tensor of the medium. We assume that the dimensionless frequency $\nu \ll 1$ while the concentration of the inclusions is small. The approach is based on the expansion of the magnetic field in a power series in terms of a parameter proportional to the quasimomentum q . As a result we obtain an explicit expression of the effective tensor with the accuracy $O(\nu^4 + \rho^4)$.

Keywords: wave propagation, effective tensor, periodic medium

1 Introduction

We consider an infinite periodic rectangular array of parallel cylinders of radius ρ with the periods τ_1 and τ_2 (see Figure 1) embedded in an isotropic medium, and $\ell = \min\{|\tau_1|, |\tau_2|\} = 1$. In dimensionless variables, propagation of the TE mode $\mathbf{H} = (0, 0, u)$ in the xy -plane is described by the equation in the rectangle $ABCD$

$$-\frac{1}{\mu} \nabla \cdot (\varepsilon^{-1} \nabla u(\mathbf{r})) = \nu^2 u(\mathbf{r}), \quad r \neq \rho, \quad (1)$$

where $\mathbf{r} = (x, y)$, $\nu = \frac{\omega}{c}$, with the boundary conditions at $r = \rho$:

$$[u(\mathbf{r})] = 0, \quad \left[\frac{1}{\varepsilon} \frac{\partial u(\mathbf{r})}{\partial n} \right] = 0. \quad (2)$$

Here brackets $[\cdot]$ denote the jump of the enclosed quantity across the interface of the cylinders. In addition, $u(\mathbf{r})$ must satisfy the Floquet-Bloch condition

$$u(\mathbf{r} + \boldsymbol{\tau}) = e^{i\mathbf{q} \cdot \boldsymbol{\tau}} u(\mathbf{r}), \quad (3)$$

where $\boldsymbol{\tau}$ is any of the lattice periods, \mathbf{q} runs the primitive cell of the dual lattice and $\mathbf{q} = q\hat{\mathbf{q}}$ with $\hat{\mathbf{q}} = (\cos \phi, \sin \phi)$ being the unit vector.

For the long waves, $u(\mathbf{r}, \mathbf{q})$ can be represented in terms of a convergent power series in q

$$u(\mathbf{r}, \mathbf{q}) = 1 + qu_1(\mathbf{r}, \hat{\mathbf{q}}) + q^2 u_2(\mathbf{r}, \hat{\mathbf{q}}) + \dots \quad (4)$$

Application of Green's first identity to (1) gives the relation between ν and q

$$\nu^2 = \frac{q^2}{S} \int_S \frac{1}{\varepsilon \mu} |\nabla u_1(\mathbf{r}, \hat{\mathbf{q}})|^2 dS + \dots \quad (5)$$

2 First approximation

Substitution of (4)–(5) into (1) gives a system of recursive equations. For u_1 we have

$$\Delta u_1(\mathbf{r}, \hat{\mathbf{q}}) = 0, \quad r \neq \rho, \quad (6)$$

and conditions (2) and inhomogeneous conditions on the boundary following from (3). Similar to [1] the solution can be found in the form

$$u_1^{in} = \sum_{n=0}^{\infty} [A_n z^{2n+1} + B_n \bar{z}^{2n+1}], \quad (7)$$

$$u_1^{ex} = \alpha_1 z + \beta_1 \bar{z} + \sum_{n=0}^{\infty} \frac{1}{(2n)!} [C_n \zeta^{(2n)}(z) + D_n \zeta^{(2n)}(\bar{z})], \quad (8)$$

where $z = x + iy$ and $\zeta(z)$ is the Weierstrass zeta-function. If we limit ourselves to the first few terms of the above expressions then

$$u_1^{in} = \frac{2\varepsilon_{in}}{\varepsilon_{in} - \varepsilon_{ex}} \alpha (\alpha_1 z + \beta_1 \bar{z}) + O(\rho^3),$$

$$u_1^{ex} = \alpha_1 z + \beta_1 \bar{z} + \alpha \rho^2 (\beta_1 \zeta(z) + \alpha_1 \zeta(\bar{z})) + O(\rho^4),$$

where

$$\alpha_1 = \frac{i}{2} e^{-i\phi} + \alpha \rho^2 \left(\frac{\eta_1}{\tau_1} \cos \phi + \frac{\eta_2}{\tau_2} \sin \phi \right),$$

$$\beta_1 = \frac{i}{2} e^{i\phi} + \alpha \rho^2 \left(\frac{\eta_1}{\tau_1} \cos \phi - \frac{\eta_2}{\tau_2} \sin \phi \right),$$

ϕ is the angle between $\hat{\mathbf{q}}$ and the x -axis, and $\alpha = \frac{\varepsilon^{in} - \varepsilon^{ex}}{\varepsilon^{in} + \varepsilon^{ex}}$, $\eta_1 = \zeta(\frac{1}{2}\tau_1)$, $\eta_2 = \zeta(\frac{1}{2}\tau_2)$, $\tau_k = |\tau_k|$, $k = 1, 2$.

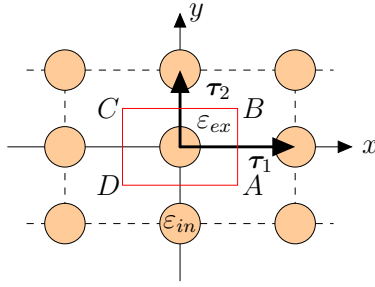


Figure 1: Geometry of rectangular lattice of cylinders of radius ρ and the fundamental cell $ABCD$.

3 Second and third approximations

The second approximation $u_2(\mathbf{r})$ is an even function of z and \bar{z} and does not contribute to the average electric field. The third one $u_3(\mathbf{r})$ should satisfy

$$\Delta u_3(\mathbf{r}) = -u_1(\mathbf{r}), \quad r \neq \rho, \quad (9)$$

conditions (2) and corresponding conditions following from the expansion of (3). The required solution in the whole rectangle $ABCD$ has the form

$$u_3 = -\frac{\alpha_1 z^2 \bar{z}}{8} - \frac{\beta_1 z \bar{z}^2}{8} + \alpha_3 z^3 + \beta_3 \bar{z}^3 + w_3, \quad (10)$$

where $\alpha_3 = -\frac{i}{48} e^{-3i\phi}$, $\beta_3 = -\frac{i}{48} e^{3i\phi}$, and

$$\int_{ABCD} |\nabla w_3| dS = O(\rho^2).$$

4 The effective tensor

We evaluate the electric field \mathbf{E} and dielectric displacement \mathbf{D} by

$$\mathbf{E} = \frac{i}{\nu \varepsilon} (u_y, -u_x), \quad \mathbf{D} = \frac{i}{\nu} (u_y, -u_x). \quad (11)$$

The effective tensor ε^* relates the average values of \mathbf{E} and \mathbf{D} over the rectangle $ABCD$ in Figure 1

$$\langle \mathbf{D} \rangle = \varepsilon^* \langle \mathbf{E} \rangle. \quad (12)$$

Using approximation of the fields u_1 and u_3 we find

$$\begin{aligned} \langle \mathbf{E} \rangle &= \frac{q}{\nu \varepsilon_{ex}} \left[\begin{array}{c} 1 - \alpha f(1 - \gamma) - \sigma q^2, 0 \\ 0, 1 - \alpha f(1 + \gamma) - \sigma q^2 \end{array} \right] \\ &\times \left[\begin{array}{c} \beta_1 - \alpha_1 \\ -i(\alpha_1 + \beta_1) \end{array} \right], \end{aligned} \quad (13)$$

$$\begin{aligned} \langle \mathbf{D} \rangle &= \frac{q}{\nu} \left[\begin{array}{c} 1 + \alpha f(1 + \gamma) - \sigma q^2, 0 \\ 0, 1 + \alpha f(1 - \gamma) - \sigma q^2 \end{array} \right] \\ &\times \left[\begin{array}{c} \beta_1 - \alpha_1 \\ -i(\alpha_1 + \beta_1) \end{array} \right], \end{aligned} \quad (14)$$

From (12)-(14) we derive the effective tensor

$$\varepsilon^* = \varepsilon_{ex} \left[\begin{array}{c} 1 + \alpha f(1 + \gamma) - \sigma q^2, 0 \\ 1 - \alpha f(1 - \gamma) - \sigma q^2, 0 \\ 0, 1 + \alpha f(1 - \gamma) - \sigma q^2 \\ 0, 1 - \alpha f(1 + \gamma) - \sigma q^2 \end{array} \right], \quad (15)$$

where

$$\begin{aligned} \gamma &= \frac{1}{\pi} (i\eta_2 \tau_1 - \eta_1 \tau_2), \quad q^2 = \varepsilon_{ex} \nu^2, \\ \sigma &= \frac{1}{48} [(\tau_1^2 - \tau_2^2) \cos 2\phi + \tau_1^2 + \tau_2^2], \end{aligned}$$

and $f = \pi \rho^2 / \tau_1 \tau_2$ is the volume fraction of the inclusions. Thus, ε^* depends not only on the orientation of the lattice but also on the direction of wave propagation. However, in the case of square lattice when $\tau_1 = \tau_2 = \tau$ and $\gamma = 0$, the effective tensor becomes isotropic in our approximation $\varepsilon_{\square}^* = \varepsilon_{\square} \mathbf{I}$, where

$$\varepsilon_{\square} = \varepsilon_{ex} \frac{1 + \alpha f - \sigma_{\square} \varepsilon_{ex} \nu^2}{1 - \alpha f - \sigma_{\square} \varepsilon_{ex} \nu^2} \quad (16)$$

with $\sigma_{\square} = \frac{\tau^2}{24}$. It should be noticed that our result is somewhat different from that obtained in [2] using a different approach.

References

- [1] Y. A. Godin, Effective complex permittivity tensor of a periodic array of cylinders, *Journal of Mathematical Physics* **54** (2013), p. 053505.
- [2] R. C. McPhedran, C. G. Poulton, N. A. Nicorovici, and A. B. Movchan, Low frequency correction to the static effective dielectric constant of a two-dimensional composite material, *Proceedings of the Royal Society of London A* **452** (1996), pp. 2231–2245.

Resolution Control in Half-space Time-reversal Wave Focusing

Heedong Goh¹, Seungbum Koo¹, Loukas F. Kallivokas^{1,*}

¹Department of Civil, Architectural and Environmental Engineering
The University of Texas at Austin, Austin, Texas, USA

*Email: loukas@mail.utexas.edu

Abstract

In wave focusing subsurface geophysical applications, the recordings at the mirror, situated on the surface of a half-space, may have to be time-reversed while flipping the character of the boundary conditions due to equipment/sensor limitations. For example, the recording sensors at the time-reversal mirror may record Dirichlet data, but the transmitting equipment may be able to accommodate Neumann data only. Under certain conditions, such flipping may worsen the focusing resolution. We study the relation between the wavefields generated by the recording-transmitting pairs D_r -to- D_t and D_r -to- N_t , and propose a filter to improve the resolution imposed by the aforementioned equipment constraints in the D_r -to- N_t case.

Keywords: Time-reversal, wave focusing, half-space, subsurface resolution

1 Introduction

A wave source is located at point $(x_0, 0, 0)$ in a half-space (Fig. 1), and the time-reversal mirror is on the surface of the half-space. The mirror is capable of recording either Dirichlet or Neumann data generated by the wave source at x_0 . We are interested in the time-reversed field ψ generated by time-reversing either the Dirichlet or the Neumann data; the time-reversed field is governed by the Helmholtz equation:

$$\begin{aligned} \operatorname{div}(\mu \operatorname{grad} \psi) + \rho \omega^2 \psi &= 0, \quad \mathbf{x} \in \Omega \text{ and} \\ &= P \text{ or } \mathcal{N}\psi = Q, \quad \mathbf{x} \in \Gamma, \end{aligned} \quad (1)$$

where $\mathcal{N}[\cdot] = \mu \operatorname{grad}[\cdot] \cdot \mathbf{n}$; $\mathbf{x} = (x^1, x^2, x^3)$; μ is shear modulus; ρ is density; and P and Q are the Dirichlet and Neumann prescribed data, respectively (Fig. 1). We are interested in assessing the resolution at the source location x_0 when the recorded Dirichlet data are time-reversed as Dirichlet data (D_r -to- D_t) and when they are time-reversed as Neumann data (D_r -to- N_t). None of the above time-reversals will result in perfect focusing: even the D_r -to- D_t case will result in loss of resolution owing to the incomplete

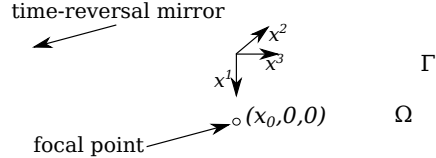


Figure 1: Half-space time-reversal wave focusing problem

time-reversal mirror (or the unboundedness of the physical domain), and the non-reversal of the source (no sink). Of particular interest to geophysical applications is the D_r -to- N_t case, whereby geophones record Dirichlet data and actuators apply Neumann data during the time-reversal phase [1].

2 Resolution in time-reversal focusing

We consider two cases for the time-reversal phase (D_r -to- D_t and D_r -to- N_t), as also proposed in [2] and [3]. Their resolutions, along the depth direction, are of interest. The resolution in the D_r -to- D_t case, defined as the wavefield support above half-maximum strength, is, approximately, 1.1λ (Fig. 2(a)). By comparison, the diffraction limit of a closed cavity problem is $\lambda/2$. As shown in Fig. 2(b), the resolution of the D_r -to- N_t case is fairly poor, amounting to multiple wavelengths. Due to practical applications, the interest is in improving the resolution of the D_r -to- N_t case.

3 Resolution control - filter design

Let g_D and g_N denote the Green's functions for a half-space, corresponding to homogeneous Dirichlet or Neumann surface data, respectively. Furthermore, let p denote the Dirichlet data recorded at the mirror, and let u denote the wavefield generated by time-reversing the p data, i.e., by setting $P = p^*$ in (1), where p^* is the conjugated p . Then, it can be shown that:

$$u = (\mathcal{N}g_D, p^*)_\Gamma \text{ or } \hat{u} = 2\mu \frac{\partial \hat{g}}{\partial x^1} \hat{p}^* \Big|_{\xi^1=0}, \quad (2)$$

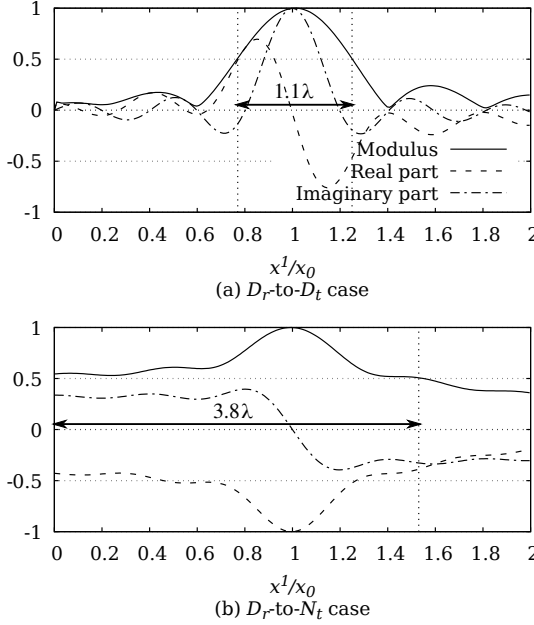


Figure 2: Resolution along the depth direction for cases D_r -to- D_t and D_r -to- N_t ; $\lambda = 0.4$, $x^2 = x^3 = 0$

where a caret is used for the doubly Fourier-transformed function, i.e., $(\hat{\cdot}) = \mathcal{F}_{x_2} \mathcal{F}_{x_3}(\cdot)$; $\hat{g}(\xi^1; x^1) = -\frac{i e^{i \alpha |\xi^1 - x^1|}}{2 \alpha}$, is the full-space Green's function, with $\alpha = \sqrt{(\omega/c)^2 - k^2}$ for $\omega > k$ and $\alpha = i \sqrt{k^2 - (\omega/c)^2}$ for $\omega < k$; $k = \sqrt{k_2^2 + k_3^2}$, and, k_2 and k_3 are the spatial wavenumbers; $c = \sqrt{\frac{\mu}{\rho}}$ is the wave velocity; and $(a, b)_\Gamma = \int_\Gamma ab d\Gamma$.

Similarly, let v denote the wavefield generated by time-reversing the p data, when applied as Neumann data, i.e., $Q = \frac{\mu}{x_0} p^*$. Then:

$$v = - \left(g_N, \frac{\mu}{x_0} p^* \right)_\Gamma \quad \text{or} \quad \hat{v} = -2 \frac{\mu}{x_0} \hat{g} \hat{p}^* \Big|_{\xi^1=0}, \quad (3)$$

In deriving (2) and (3), relations between g_D , g_N and g have been taken into account. Then, with the aid of the translational symmetry of the full-space Green's function g :

$$\mathcal{N}_x [g_N(\mathbf{x}; \xi)] = -\mathcal{N}_\xi [g_D(\mathbf{x}; \xi)], \forall \mathbf{x} \in \Gamma, \quad (4)$$

it follows that:

$$\begin{aligned} -x_0 \frac{\partial}{\partial x^1} v(\mathbf{x}) &= x_0 \frac{\partial}{\partial x^1} \left(g_N, \frac{\mu}{x_0} p^* \right)_\Gamma \\ &= -(\mathcal{N}_x g_N, p^*)_\Gamma = (\mathcal{N}_\xi g_D, p^*)_\Gamma = u(\mathbf{x}). \end{aligned} \quad (5)$$

We would like for the v field (D_r -to- N_t) to have the resolution of the u field (D_r -to- D_t), i.e., a

λ -level resolution quality. Therefore, we require that:

$$-x_0 \left(g_N, \frac{\mu}{x_0} f(p^*) \right)_\Gamma = (\mathcal{N}_D g_D, p^*)_\Gamma = u, \quad (6)$$

where $f(\cdot)$ is the sought filter to be applied on the Dirichlet data prior to being time-reversed as Neumann data. Using $(\frac{\partial}{\partial x^1} - i\alpha) \hat{g} = 0$ and (5), it can be shown that:

$$\begin{aligned} \hat{u} &= -x_0 \frac{\partial}{\partial x^1} \left(-2 \frac{\mu}{x_0} \hat{g} \hat{p}^* \right)_{\xi^1=0} = 2\mu \hat{g}(i\alpha) \hat{p}^*|_{\xi^1=0} \\ &\Rightarrow f(p^*) = \mathcal{F}_{x_2}^{-1} \mathcal{F}_{x_3}^{-1} [-i\alpha \mathcal{F}_{x_2} \mathcal{F}_{x_3} p^*]. \end{aligned} \quad (7)$$

The filter's (7) effect, when applied to the D_r -to- N_t case, is shown in Fig. 3.

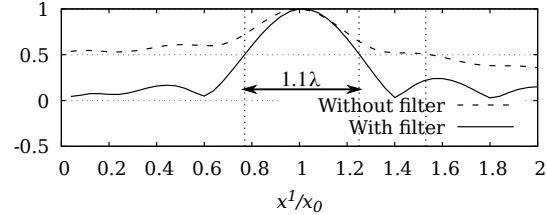


Figure 3: Resolution along the depth direction for case D_r -to- N_t with and without filter; $\lambda = 0.4$, $x^2 = x^3 = 0$

4 Conclusions

A resolution-improving filter was derived that can be applied in certain time-reversal wave focusing applications when equipment limitations enforce a flipping in the character of the boundary conditions between the recording and the time-reversal phases. The filter is capable of rendering resolution of order λ .

References

- [1] S. Koo, P.M. Karve, and L.F. Kallivokas, A comparison of time-reversal and inverse-source methods for the optimal delivery of wave energy to subsurface targets, *Wave Motion* **67** (2016), pp. 121-140.
- [2] D. Cassereau and M. Fink, Focusing with plane time-reversal mirrors: An efficient alternative to closed cavities, *The Journal of the Acoustical Society of America* **94**(4) (1993), pp. 2373–2386.
- [3] A.C. Fannjiang, On time reversal mirrors, *Inverse Problems* **25**(9) (2009), 095010.

Adaptive Eigenspace Method for Inverse Scattering Problems in the Frequency Domain

Marie Graff-Kray^{1,*}, Marcus J. Grote², Uri Nahum³

¹Department of Earth, Ocean and Atmospheric Sciences, University of British Columbia, Vancouver BC, Canada

²Department of Mathematics and Computer Science, University of Basel, Basel, Switzerland

³Department of Biomedical Engineering, University of Basel, Basel, Switzerland

*Email: mgraff@eoas.ubc.ca

Abstract

A nonlinear optimization method is proposed for the solution of inverse scattering problems in the frequency domain, when the scattered field is governed by the Helmholtz equation. The time-harmonic inverse medium problem is formulated as a PDE-constrained optimization problem and solved by an inexact truncated Newton-type iteration [1]. Instead of a grid-based discrete representation, the unknown wave speed is projected to a particular finite-dimensional basis of eigenfunctions [2], which is iteratively adapted during the optimization. Truncating the adaptive eigenspace (AE) basis at a (small and slowly increasing) finite number of eigenfunctions effectively introduces regularization into the inversion and thus avoids the need for standard Tikhonov-type regularization. Both analytical and numerical evidence underpins the accuracy of the AE representation. Numerical experiments demonstrate the efficiency and robustness to missing or noisy data of the resulting adaptive eigenspace inversion (AEI) method.

Keywords: inverse problems, Helmholtz equation, adaptive eigenspace, regularization

1 Inverse problem

We consider a time-harmonic scattering problem in unbounded space from a penetrable inhomogeneity located inside a bounded convex domain $\Omega \subset \mathbb{R}^d$, $d \leq 3$. Outside Ω , the wave speed $c = c_0$ is known and may vary. Inside Ω , we perform N_s illuminations of the medium with source terms $f = f_\ell$, $\ell = 1, \dots, N_s$, and the corresponding scattered field y_ℓ satisfies the Helmholtz equation at the frequency ω together with a Sommerfeld radiation condition at the boundary $\Gamma = \partial\Omega$, for simplicity:

$$\begin{cases} -\omega^2 y_\ell - \nabla \cdot (c^2 \nabla y_\ell) = f_\ell & \text{in } \Omega, \\ \frac{\partial y_\ell}{\partial n} - i \frac{\omega}{c_0} y_\ell = 0 & \text{on } \Gamma. \end{cases} \quad (1)$$

Given the measurements y_ℓ^{obs} on Γ , we seek to reconstruct the squared wave speed $u = c^2$ inside Ω such that every solution y_ℓ of (1) coincides on Γ with the measurements y_ℓ^{obs} . We formulate now the inverse medium problem as a PDE-constrained optimization problem by considering the reduced-space misfit functional [3]

$$\mathcal{F}[u] = \frac{1}{2} \sum_{\ell=1}^{N_s} \|y_\ell(u) - y_\ell^{obs}\|_{L^2(\Gamma)}^2. \quad (2)$$

2 Adaptive eigenspace basis

Usually the unknown u is described by grid-based point values and hence expanded in a nodal basis. Here, we instead expand the parameter u in a basis of global eigenfunctions $\{\phi_m\}_{m \geq 1}$ [2, 4] as

$$u(x) = u_0(x) + \sum_{m=1}^K \beta_m \phi_m(x), \quad (3)$$

where ϕ_m are the first K eigenfunctions of

$$\begin{cases} -\nabla \cdot (\mu(x) \nabla \phi_m) = \lambda_m \phi_m & \text{in } \Omega, \\ \phi_m = 0 & \text{on } \Gamma, \end{cases} \quad (4)$$

and the “background” u_0 satisfies

$$\begin{cases} -\nabla \cdot (\mu(x) \nabla u_0) = 0 & \text{in } \Omega, \\ u_0 = c_0^2 & \text{on } \Gamma, \end{cases} \quad (5)$$

with, in both (4) and (5),

$$\mu(x) = \frac{1}{\sqrt{|\nabla u(x)|^2 + \varepsilon^2}}, \quad \forall x \in \Omega, \varepsilon > 0. \quad (6)$$

Note that μ depends on the unknown parameter u . In practice, we compute μ from the previous parameter u during the iterative process, – see Algorithm below.

We remark that μ essentially coincides with the gradient of the penalized total variation (TV) regularization term [5]. Instead of adding a

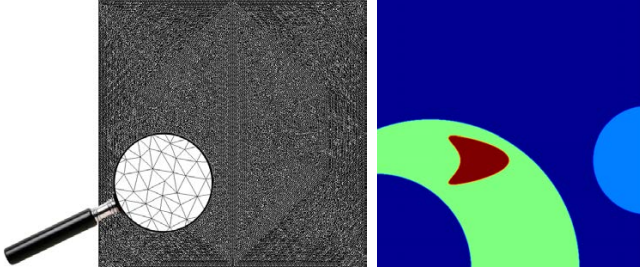


Figure 1: Left: uniform starting FE mesh with 30,534 vertices. Right: exact profile u

Tikhonov regularization term to the objective functional, the AEI approach projects u to the basis of eigenfunctions of the gradient of the penalized TV-regularization functional; hence, the AE basis inherits similar properties. The choice of K is crucial to regularize the optimization problem: at higher eigenvalues λ_m , the AE basis functions ϕ_m become increasingly oscillatory and no longer carry useful information about u , thus truncating the expansion at K builds regularization into the AEI approach.

3 AEI Algorithm

To solve the optimization problem, we use truncated Newton-type methods together with stop criteria [6] and frequency stepping. At each frequency, the eigenfunctions basis is adapted together with the finite element (FE) mesh.

Algorithm

Input: initial guess $u = 1$, observations y_ℓ^{obs}

1. Choose $K \geq 1$
2. Compute ϕ_m (4) and u_0 (5) with $\mu \equiv 1$
3. For $\omega = \omega_1, \dots, \omega_{end}$ do
 - (a) Solve optimization problem

$$u := \underset{v \in u_0 + \text{span}\{\phi_m\}}{\operatorname{argmin}} \mathcal{F}[v]$$
 - (b) Set μ from (6) with current ∇u
 - (c) Update K and the FE mesh
 - (d) Update ϕ_m (4) and u_0 (5)

Output: last updated u

4 Numerical results

We consider the true profile u , shown in Fig. 1, which mimics a layered material with regions of different wave speed. The receivers are located on the four lateral boundaries of $\Omega = (0, 1) \times (0, 1)$. Moreover, nine Gaussian sources are located at $(0.1, 0.8), \dots, (0.9, 0.8)$. We use a 200×200 FE mesh, see Fig. 1, and set the initial profile $u = 1$. To avoid any inverse crime, we

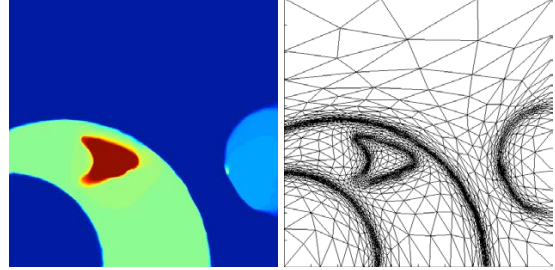


Figure 2: Left: reconstruction of u with 20% noise (L^2 -error = 5.22%). Right: corresponding adapted FE mesh with 2,783 vertices

compute the reference solution on a finer different FE mesh. Starting at the lowest frequency $\omega = 8$, we use frequency stepping at the frequencies $\omega = 10, 12, 14, \dots, 90$.

The reconstructed profile with only $K \leq 360$ control variables and the automatically determined adaptive FE mesh at the end of the adaptation process is shown in Fig. 2 for 20% multiplicative noise on the measurement data. The AEI approach applies regardless of the underlying optimization or discretization method used.

References

- [1] R. S. Dembo, T. Steihaug. Truncated-Newton Algorithms for Large-Scale Unconstrained Optimization. *Math. Progr.* **26** (1983), pp. 190–212.
- [2] M. de Buhan, M. Kray. A new approach to solve the inverse scattering problem for waves: combining the TRAC and the Adaptive Inversion methods. *Inv. Probl.* **29** (2013), pp. 085009.
- [3] E. Haber, U. Ascher and D. Oldenburg. On Optimization Techniques for Solving Nonlinear Inverse Problems. *Inv. Probl.* **16** (2000), pp. 1263–1280.
- [4] M. J. Grote, M. Kray, U. Nahum. Adaptive Eigenspace Method for Inverse Scattering Problems in the Frequency Domain. *Inv. Problems* **33** (2017), pp 025006.
- [5] C. R. Vogel and E. Oman. Iterative methods for total variation denoising. *SIAM J. Sci. Comput.* **17** (1996), pp. 227–238.
- [6] S. C. Eisenstat and H. F. Walker. Choosing the forcing terms in an inexact Newton method. *SIAM J. Sci. Comput.* **17** (1996), 16–32.

Domain decomposition with local impedance condition for the Helmholtz equation

Ivan G. Graham^{1,*}, Eric Chung², Euan A. Spence³, Eero Vainikko⁴, Jun Zou⁵

¹Department of Mathematical Sciences, University of Bath, Bath BA2 7AY, UK

²Chinese University of Hong Kong, Shatin N.T., Hong Kong

³Department of Mathematical Sciences, University of Bath, Bath BA2 7AY, UK

⁴Institute of Computer Science, University of Tartu, Estonia

⁵Chinese University of Hong Kong, Shatin N.T., Hong Kong

*Email: I.G.Graham@bath.ac.uk

Abstract

We describe the theory and practice of Schwarz-type domain decomposition preconditioners with local impedance or PML boundary conditions for solving discretisations of the high-frequency Helmholtz problem. Preconditioners for the pure Helmholtz problem can be constructed by applying the Schwarz algorithm to nearby absorptive problems. We present a new theory which shows that nearly optimal performance for the pure Helmholtz problem can be obtained by solving local impedance problems on the absorptive problem, provided these are combined with suitable restriction and prolongation operators and provided the absorption parameter is properly tuned. We also investigate numerically the benefits of combining these methods with suitable coarse grid problems.

Keywords: Helmholtz equation, high frequency, domain decomposition, local impedance condition, PML

Details of talk

We describe the construction of preconditioners for Helmholtz-type problems of the form:

$$-\Delta u - (k^2 + i\varepsilon)u = f, \quad \text{on } \Omega \quad (1)$$

on a bounded domain Ω with impedance boundary condition

$$\frac{\partial u}{\partial n} - i\eta u = g \quad \text{on } \Gamma, \quad (2)$$

where Γ is the boundary of Ω , $\varepsilon \in \mathbb{R}$ is an absorption parameter and η may depend on ε . Our aim is to solve the “pure Helmholtz problem” with $\varepsilon = 0$ using, as preconditioner, some (hopefully) cheap approximation of the absorptive problem ($\varepsilon \neq 0$), for some carefully chosen ε . Ideally we seek a robust method for the pure Helmholtz equation, where the number of GMRES iterations is bounded with respect to k .

A similar strategy is used in the “shifted Laplace” preconditioner [3], where the chosen approximation of the absorptive problem is the multigrid V -cycle. Here, in order to make the multigrid method work well for the absorptive problem, a rather large choice of ε (typically $\varepsilon \sim k^2$) is usually made. This choice is in a certain sense necessary [2] and it guarantees that the absorptive problem is uniformly coercive independent of k (see, e.g. [5]). However this choice also means the underlying absorptive problem supplying the preconditioner is quite far away from the pure Helmholtz problem which is being preconditioned. In fact, for the absorptive problem (without approximation) to be a good preconditioner for the pure Helmholtz problem we require $\varepsilon \sim k$ [4]. Substantial improvement of the robustness of the shifted Laplace preconditioner has been obtained by applying deflation techniques [8].

An advantage of domain decomposition problems is that elliptic technology (like classical multigrid or Schwarz methods using local Dirichlet problems) can be replaced by more wave-friendly techniques (using various types of absorptive boundary conditions), and there is a large literature on these methods (e.g. [7]). In the talk we present a new theory for additive Schwarz domain decomposition methods on overlapping subdomains where local problems are taken to have impedance (first order absorbing) boundary conditions. An important ingredient is the use of global to local restriction operators obtained by the action of a suitable partition of unity. We shall show that this method yields a robust preconditioner for the absorptive problem when the absorption is of the form $\varepsilon \sim k^{1+\beta}$ with $\beta > 0$, but β can be taken arbitrarily small. Thus, combining this with the results in [4] we have a near robust solver for the pure Helmholtz equation. The details of this new theory will be

in [1].

The subdomains in this near robust solver can get quite large. We combine the local solves with various choices of multilevel approximation and investigate the best combination of methods to yield good parallel efficiency. Related experiments are in [6].

References

- [1] E.T. Chung, I.G. Graham, E.A. Spence, J. Zou, Domain decomposition with local impedance conditions for the Helmholtz equation, in preparation (2017).
- [2] P-H. Cocquet and M.J. Gander, On the minimal shift in the shifted Laplacian preconditioner for multigrid to work, *Domain Decomposition Methods in Science and Engineering XXII*, LNCSE, Springer-Verlag, pp. 137-145 (2016).
- [3] Y. A. Erlangga, C. W. Oosterlee, and C. Vuik. A novel multigrid based preconditioner for heterogeneous Helmholtz problems. *SIAM J. Sci. Comp.*, 27:1471–1492, 2006.
- [4] M.J. Gander, I.G. Graham, E.A. Spence, Applying GMRES to the Helmholtz equation with shifted Laplacian preconditioning: What is the largest shift for which wavenumber-independent convergence is guaranteed? *Numerische Mathematik* **131** (2015), pp 567–614, .
- [5] I.G. Graham, E.A. Spence and E. Vainikko, Domain decomposition preconditioning for high-frequency Helmholtz problems using absorption. *Math. Comp.* (2017), to appear. <https://arxiv.org/abs/1507.02097>
- [6] I.G. Graham, E.A. Spence and E. Vainikko, Recent Results on Domain Decomposition Preconditioning for the High-frequency Helmholtz Equation using Absorption, To appear in: *Modern Solvers for Helmholtz problems*, edited by D. Lahaye, J. Tang and C. Vuik, Springer Geosystems Mathematics series (2016). <http://arxiv.org/abs/1606.07172>
- [7] J.-H. Kimn and M. Sarkis, Restricted overlapping balancing domain decomposition methods and restricted coarse problems for the Helmholtz problem, *Computational Methods in Applied Mechanics and Engineering* 196: 1507-1514, 2007.
- [8] A. H. Sheikh, D. Lahaye, and C. Vuik. On the convergence of shifted Laplace preconditioner combined with multilevel deflation. *Numerical Linear Algebra with Applications*, 20:645–662, 2013.

Convergence Analysis of Energy Conserving Explicit Local Time-stepping Methods for the Wave Equation

Marcus J. Grote^{1,*}, Michaela Mehlin², Stefan A. Sauter³

¹Institute of Mathematics, University of Basel, Basel, Switzerland

²Institute of Applied and Numerical Analysis, KIT, Karlsruhe, Germany

³Institute for Mathematics, University of Zurich, Zurich, Switzerland

*Email: marcus.grote@unibas.ch

Abstract

Local adaptivity and mesh refinement are key to the efficient simulation of wave phenomena in heterogeneous media or complex geometry. Locally refined meshes, however, dictate a small time-step everywhere with a crippling effect on any explicit time-marching method. In [1] a leap-frog (LF) based explicit local time-stepping (LTS) method was proposed, which overcomes the severe bottleneck due to a few small elements by taking small time-steps in the locally refined region and larger steps elsewhere. Here convergence (in the PDE sense) of the LTS-LF method is proved when combined with a standard conforming finite element method (FEM) in space. Numerical results further illustrate the usefulness of the LTS-LF Galerkin FEM in the presence of corner singularities.

Keywords: finite element, leap-frog, multirate methods, local time-stepping

1 Introduction

We consider the classical wave equation

$$u_{tt} - \nabla \cdot (c^2 \nabla u) = f \quad \text{in } \Omega \times (0, T) \quad (1)$$

$$u|_{t=0} = u_0 \quad u_t|_{t=0} = v_0 \quad \text{in } \Omega, \quad (2)$$

where Ω denotes a bounded domain in \mathbb{R}^d , f a (known) source and u_0, v_0 prescribed initial conditions. The speed of propagation, $c = c(x)$, is assumed piecewise smooth and strictly positive. At the boundary, we impose appropriate boundary conditions for well-posedness.

For the spatial discretization of (1), we consider a conforming finite element (FE) method with mass-lumping. For the time discretization, we opt for the leap-frog based local time-stepping (LTS-LF) method to circumvent the bottleneck caused by the overly stringent CFL condition in the presence of local refinement [1–3]. Hence we split the mesh into a "coarse" and a "fine" sub-region with mesh size h and

h_f , respectively. During each time-step Δt inside the "coarse" region, we use p time-steps of smaller size $\Delta\tau = \Delta t/p$ inside the "fine" region, where $p \simeq h/h_f$ — see [1] for details.

Despite the many different explicit LTS methods that were proposed and successfully used for wave propagation in recent years – see [4] and references therein –, a rigorous space-time convergence theory (in the PDE sense) is still lacking.

To develop a general convergence theory for explicit LTS methods, we first define finite-dimensional restriction operators to the "fine" grid and formulate the leap-frog (LF) based LTS method from [1] in a Galerkin conforming finite element setting. Next, we prove continuity and coercivity estimates for the LTS operator that are robust with respect to the number of local time-steps p , provided a genuine CFL condition is satisfied. Here, new estimates on the coefficients that appear when rewriting the LTS-LF scheme in "leap-frog manner" play a key role. Those estimates pave the way for the stability estimate of the time iteration operator, for which we then prove a stability bound independently of p .

Due to the local restriction, however, a judicious splitting of the iteration operator and its inverse is required to avoid negative powers of h via inverse inequalities. By combining our analysis of the semi-discrete formulation, which takes into account the effect of local time-stepping, with classical error estimates, we eventually obtain optimal space-time convergence rates.

Let u_h denote the fully discrete Galerkin solution with continuous piecewise polynomial finite elements of order ℓ . Under standard smoothness assumptions on the solution u of (1)–(2), we rigorously prove that for $\Delta t, h \rightarrow 0$:

$$\|u - u_h\|_{L^\infty([0, T]; L^2(\Omega))} \leq C(1 + T)(h^{\ell+1} + \Delta t^2),$$

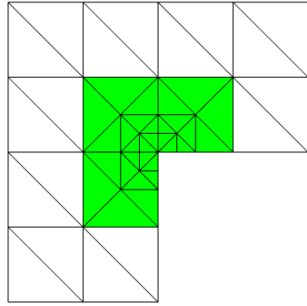


Figure 1: Computational mesh with two levels of local refinement. The "fine" region (in green) always corresponds to the innermost 30 elements.

where the constant C depends only on u , but not on h , Δt , p or T .

2 Numerical experiment

We consider (1)–(2) in an L-shaped domain Ω , shown in Fig. 1, and set $c = 1$, $f = 0$ and the final time $T = 1$. Next, we impose homogeneous Neumann conditions on the boundary. For the spatial discretization we opt for \mathcal{P}^2 continuous finite elements with mass lumping.

First, we partition Ω into equal triangles of size h_{init} . Towards the re-entrant corner, we then locally refine the mesh by subdividing twice the three elements nearest to the corner – see Fig. 1. Hence the mesh refinement ratio, that is the ratio between smallest elements in the "coarse" and the "fine" regions, in the resulting mesh is 4:1. We therefore choose a four times smaller time-step $\Delta\tau = \Delta t/p$ with $p = 4$ inside the "fine" region.

Clearly, this time-stepping strategy, albeit local, is not optimal as the region of local mesh refinement itself contains a sub-region of even smaller elements. Thus, any local time-step will again be overly restricted due to even smaller elements inside the "fine" region. To remedy the repeated bottleneck caused by hierarchical mesh refinement, multi-level local time-stepping methods were proposed in [2, 3], which permit the use of the appropriate time-step at every level of mesh refinement. For simplicity, however, we restrict ourselves here to the original (two-level) LTS-LF scheme from [1].

In Fig. 2 we compare the runtime of the

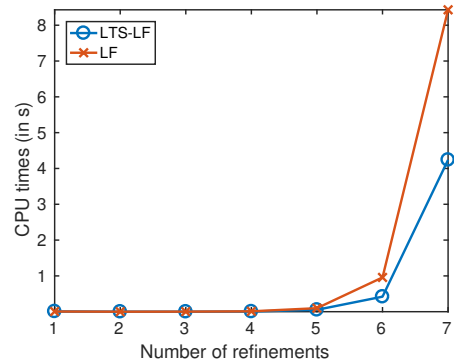


Figure 2: Comparison of run times between LTS-LF and standard LF vs. number of global refinements, with constant coarse/fine mesh size ratio $p = 4$.

LTS-LF method on a sequence of meshes with the runtime of a standard LF scheme with a time-step $\Delta t/4$ throughout the entire domain. As expected, the LTS-LF method is faster than the standard LF scheme, in fact increasingly so, as the number of refinement levels increases. Indeed, as the number of degrees of freedom inside the "coarse" region grows much faster than in the "fine" region, the use of local time-stepping becomes increasingly beneficial.

References

- [1] J. Diaz and M.J. Grote, Energy Conserving Explicit Local Time-stepping for Second-order Wave Equations, *SIAM J. Sci. Comp.* **31** (2009) pp. 1985–2014.
- [2] J. Diaz and M.J. Grote, Multilevel Explicit Local Time-stepping For Second-order Wave Equations, *Comp. Meth. Appl. Mech. Engin.* **291** (2015) pp. 240–265.
- [3] M. Rietmann, M.J. Grote, D. Peter and O. Schenk, Newmark Local Time Stepping on High-Performance Computing Architectures, *J. Comp. Phys.*, **334** (2017) pp. 308–326.
- [4] M.J. Grote, M. Mehlin and T. Mitkova, Runge-Kutta Based Explicit Local Time-Stepping Methods for Wave Propagation, *SIAM J. Sc. Comp.* **37** (2015) pp. A747–A775.

Impedance-Preserving Discretization for Modeling Unbounded Domains

Murthy N. Guddati^{1,*}

¹Department of Civil Engineering, North Carolina State University, Raleigh, NC 27695, USA

*Email: murthy.guddati@ncsu.edu

Abstract

The talk will contain an exposition of the work over the past decade by the author and his collaborators on modeling wave propagation in unbounded domains. Key to the effectiveness of many developed methods is the special property of midpoint integration completely eliminating the discretization error in half-space impedance that arises from linear finite element discretization. Impedance preserving discretization complements the method of perfectly matched layers, where impedance preservation is central to its effectiveness. In this talk, we briefly explain the idea of impedance preserving discretization, and show that the midpoint integration is also critical to developing absorbing boundary conditions for more complicated situations with differing signs of phase and group velocities, e.g. anisotropic and periodic media.

Keywords: Absorbing Boundary Conditions, Perfectly Matched Layers, Impedance Matching

1 Introduction

The idea of perfectly matched layers (PML), introduced first by Berenger in 1994 and reinterpreted in terms of complex coordinate stretching by Chu and coworkers, has transformed the way unbounded domain modeling has been performed. While related sponge/damping layer methods took a backseat to the methods based on rational approximations till that time, the elegant idea of matching the impedance solved the crucial problem of the reflections at the interface of interior and the damping layers. Unfortunately, numerical discretization of PML resulted in loss of perfect impedance matching, requiring care with respect to the choice of the decay functions and discretization.

The impedance preserving discretization introduced by the author and coworkers has mitigated this limitation, facilitating efficient discretization of PML. Specifically, we have shown that a simple midpoint integration can completely eliminate the discretization error introduced by linear finite element discretization in

capturing the half-space impedance. Thus, the PML region is perfectly matched even after discretization, leading to the name perfectly matched discrete layers (PMDL).

Interestingly, PMDL is shown to result in rational approximation of the half-space impedance, making the link to a large class of absorbing boundary conditions (ABCs) built on many innovative ideas over the past four decades. In fact, we have shown that PMDL is intimately linked to Higdon's multidirectional absorbers, which were already shown to be optimal rational approximants of half-space impedance.

2 Impedance preserving discretizations

Consider the differential equation,

$$-\mathcal{A} \frac{d^2 u}{dx^2} + \mathcal{C} u = 0. \quad (1)$$

The exact impedance, or equivalently the dynamic stiffness relation can be derived as,

$$\mathcal{A} \frac{du}{dx} = \sqrt{\mathcal{A}\mathcal{C}} u = K_{\text{exact}} u. \quad (2)$$

Now consider the half-space discretized with linear finite elements of equal length L . The stiffness of the discretized half-space can be derived by noting that adding a single finite element to the discretized half-space results in a composite half-space identical to the original half-space. This results in a recursive relation,

$$\begin{Bmatrix} K_{\text{disc}} u_0 \\ 0 \end{Bmatrix} = \begin{bmatrix} A & B \\ B & A + K_{\text{disc}} \end{bmatrix} \begin{Bmatrix} u_0 \\ u_1 \end{Bmatrix}, \quad (3)$$

where, $[A, B; B, A]$, is the 2×2 stiffness of the single finite element. The discretized impedance is thus given by,

$$K_{\text{disc}} = \sqrt{A^2 - B^2}. \quad (4)$$

Linear finite element discretization of (2) followed by exact integration results in,

$$A = \mathcal{A}/L + \mathcal{C}L/3, \quad B = \mathcal{A}/L + \mathcal{C}L/6, \quad (5)$$

which in turn results in an approximation of the exact half-space stiffness in (3), with the error that is second order in L , as expected from

linear finite element discretization.

Now consider a simple modification of the above procedure. If the element stiffness matrix is computed not with exact integration, but with approximate midpoint integration, we get,

$$A = \mathcal{A}/L + \mathcal{C}L/4, \quad B = \mathcal{A}/L + \mathcal{C}L/4. \quad (6)$$

When (6) is substituted in (4), we get,

$$K_{\text{disc}} = \sqrt{\mathcal{A}\mathcal{C}} = K_{\text{exact}}. \quad (7)$$

In other words, the error introduced by approximate midpoint integration exactly nullifies the error due to the finite element discretization. This simple observation led to significant improvements in unbounded domain modeling as outlined in the remainder of the summary.

3 Consequences of midpoint integration

Firstly, we note that while impedance preserving discretization is illustrated with the help of a simple differential equation (1), the idea is applicable to situations where \mathcal{A}, \mathcal{C} are complicated differential operators [1]. Thus the idea of impedance preserving discretizations is formally applicable to complicated media including elastic, viscoelastic and anisotropic media. It must however be noted that the idea applies only when \mathcal{A}, \mathcal{C} are independent of x , indicating that the material properties must be invariant in the direction of the unboundedness.

The effectiveness of PMDL was easily realized for Helmholtz equation and time-domain wave equation in a relatively straightforward manner, requiring only some attention to time-stepping schemes [2-4]. In fact, PMDL is shown to be effective not only for rectangular corner regions, but also for any convex computational boundaries [4]. Similar success is achieved for homogeneous elastic full- and half-spaces. In fact, given its equivalence to rational ABCs, PMDL provided an effective way of deriving and implementing high order rational ABCs for more complicated wave equations and to corner regions.

Care however must be exercised when analyzing more complicated media due to the presence of back propagating wave modes that have opposing signs of phase and group velocities. These include anisotropic acoustic and elastic media, as well as isotropic elastic media with layering. Back propagating waves are well-known to be problematic in the context of PML given

that they result in artificial growth in PML region. Development of rational ABCs for these cases have been sparse.

It turns out that PMDL offers solutions to the some of the difficult cases of back propagating waves. Two ideas play a central role in this regard, both hinged on the choice of PMDL lengths: (a) choosing the lengths such that the decay of the reflected waves in the PMDL region is stronger than the growth of the incident wave – such choice appears to be effective in modeling elliptic anisotropic media, both acoustic and elastic [5]; (b) pairwise choice of PMDL parameters that seem to be effective in significantly more complicated case of non-elliptic anisotropy [6]. It appears that both these ideas are effective only if midpoint integration is utilized. Any disruption of impedance preservation appears to lead to numerical instabilities.

Another contribution facilitated by PMDL is that impedance preservation is made possible for periodic media, where regular PML ideas are no longer applicable. In such cases, we developed the concept of equivalent impedance matching continuous media, where PMDL ideas can be effectively used [7], although care must be exercised to ensure stability of resulting schemes.

References

- [1] Guddati MN, *Comp. Meth. App. Mech. Engr.*, **195** (2006), pp. 65-93.
- [2] Guddati MN, Tassoulas J, *J. Comp. Acoustics*, **8** (2000), pp. 139-156.
- [3] Asvadurov S, et al., *SIAM J. Num. Anal.*, **41** (2003), pp. 287-305.
- [4] Guddati MN, Lim KW *Int. J. Num. Meth. Engr.*, **66** (2006), pp. 949-977.
- [5] Savadatti S, Guddati MN, *J. Comp. Phys.*, **231** (2012), pp. 7584-7607.
- [6] Savadatti S, Guddati MN, *J. Comp. Phys.*, **231** (2012), pp. 7608-7625.
- [7] Guddati MN, Thirunavukkarasu S, *J. Comp. Phys.*, **228** (2009), pp. 8112-8134.

**A numerical scheme for the wave kinetic equation
and its application to cross-polarization scattering in turbulent plasmas**

L. Guidi^{1,*}, O. Maj¹, H. Weber¹, A. Köhn¹, A. Snicker¹, E. Poli¹

¹Max-Planck-Institute for Plasmaphysics, Garching, Germany

*Email: lguidi@ipp.mpg.de

Abstract

In this paper we present a numerical scheme for the wave kinetic equation, based on the theory of jump Markov processes. The scheme is implemented in **WKBeam**, a code which describes electromagnetic wave beams in realistic nuclear fusion devices, accounting in particular for the effect of density fluctuations due to plasma turbulence.

Keywords: wave kinetic equation, jump Markov process, turbulent plasma

Introduction

For the specific case of wave beams, the wave kinetic equation (WKE) [1–3] takes the form

$$\{H_\alpha, w_\alpha\} = -2\gamma_\alpha w_\alpha + \mathcal{S}_\alpha(\{w_\beta\}), \quad (1)$$

$$H_\alpha w_\alpha = 0, \quad (2)$$

$$w_\alpha|_{\Sigma} = w_\alpha^0, \quad (3)$$

which can be derived from Maxwell equations in the semiclassical limit $\kappa = \omega L/c \rightarrow \infty$ [4]. Here ω is the frequency of the beam, L the characteristic length of variation of the medium and c the speed of light. In order for the equation to hold, the medium has to be weakly dissipative and the Born scattering approximation must be valid. The equation is defined in the geometrical optics phase-space $(x, N) \in \mathbb{R}^3 \times \mathbb{R}^3$, with x the position and N the refractive index vector, and its solution is the Wigner function of the wave electric field $w = \{w_\alpha\}$, decomposed on the polarization basis.

The Poisson brackets on the left-hand side of (1) are defined as $\{u, v\} = \partial_N u \partial_x v - \partial_x u \partial_N v$, and H_α are the geometrical optics Hamiltonians. From (2) we deduce that a non-trivial solution of (1)-(3) is supported on the dispersion surface $\{H_\alpha = 0\}$, which is a closed set, and therefore (1) must be posed in weak sense. More specifically, we look for measure-valued solutions, that have the meaning of a phase-space energy density of the wave. Equation (3) provides boundary conditions on a hypersurface

Σ . On the right-hand side of (1), the first term accounts for dissipation, while the operator \mathcal{S}_α describes scattering due to fluctuations of the medium, and it reads:

$$\mathcal{S}_\alpha\{w_\beta\} = \sum_\beta S_{\alpha\beta} w_\beta - \Sigma_\alpha w_\alpha,$$

where the operator $S_{\alpha\beta}$ acts on measures as

$$S_{\alpha\beta} w_\beta = \int_{\mathbb{R}^d} \sigma_{\beta\alpha}(x, N', dN) w_\beta(dx, dN'),$$

and $\Sigma_\alpha(x, N) = \sum_\beta \int_{\mathbb{R}^d} \sigma_{\alpha\beta}(x, N, dN')$. In particular, the cross section $\sigma_{\alpha\beta}(x, N, dN')$ is related to the probability of transition from the state (x, N, α) to the state (x, N', β) .

In order to solve (1)-(3), we look for weak solutions of the auxiliary Cauchy problem

$$\begin{cases} \frac{\partial u_\alpha}{\partial t} + \{H_\alpha, u_\alpha\} = -2\gamma_\alpha u_\alpha + \mathcal{S}_\alpha\{u_\beta\}, \\ u_\alpha|_{t=0} = u_\alpha^0, \end{cases} \quad (4)$$

with initial condition u_α^0 chosen such that, at least formally, $w_\alpha = \int u_\alpha dt$ satisfies (1)-(3).

Relevant stochastic process

We consider a jump Markov process

$$\{X(t), \mathcal{N}(t), a(t); t \geq 0\} \subseteq \mathbb{R}^d \times \mathbb{R}^d \times E,$$

where E is a finite set. In the proposed application X , \mathcal{N} and a represent the position, momentum (refractive index) and polarization mode, respectively. To characterize the process we need:

- *A bounded and positive-definite function $\lambda : \mathbb{R}^d \times \mathbb{R}^d \times E \rightarrow \mathbb{R}$;*
- *A family of probability measures*

$$\{\Pi(x, N, \alpha; dN', \beta), (x, N, \alpha) \in \mathbb{R}^d \times \mathbb{R}^d \times E\}.$$

We extract then a sequence $0 \leq T_0 < T_1 < \dots < T_n$ of “times of jump” from a Poisson distribution of parameter $\bar{\lambda} = \sup \lambda$, and evolve

the particles as follows:

- Between two jumps $a(t)$ is constant and

$$\left(\dot{X}(t), \dot{\mathcal{N}}(t) \right) = b(X(t), \mathcal{N}(t), a(t));$$

- At the times of jump the variables $\mathcal{N}(t)$ and $a(t)$ are modified, according to the transition semigroup

$$Q_t = e^{-\lambda t} \sum_{n>0} \frac{(\lambda t)^n}{n!} \Pi^n,$$

where Π^n denotes the n -fold convolution of the measure Π .

Theorem 1 *The infinitesimal generator of the described process acts on $f \in C_b^1(\mathbb{R}^d \times \mathbb{R}^d \times E)$ as $\mathcal{A}f = b \cdot \nabla f + \lambda [\mathcal{J}f - f]$, where*

$$\begin{aligned} \mathcal{J}f(x, N, \alpha) &= \sum_{\beta \in E} \int_{\mathbb{R}^d} f(x, N', \beta) \\ &\quad \times \Pi(x, N, \alpha; dN', \beta). \end{aligned}$$

By standard results [5], we know that the probability density $u(t, dx, dN, \alpha)$ of the process satisfies the Fokker-Planck equation (in weak form)

$$u(t, f) = u_0(f) + \int_0^t u(s, \mathcal{A}f) ds, \quad \forall f \in C_b^1. \quad (5)$$

We denote by $\mathcal{A}^*f = -\nabla \cdot (bf) + \mathcal{J}(\lambda f) - \lambda f$ the formal adjoint of \mathcal{A} . When u is absolutely continuous with respect to the Lebesgue measure, and its Radon-Nikodym derivative p is C^1 , (5) is equivalent to $\partial_t p + \mathcal{A}^*p = 0$.

Application to the WKE

For a measure-valued solution, the Cauchy problem (4) can be written in the form (5), where $u(t, dx, dN, \alpha) = u_\alpha(t, dx, dN)$, $f(t, x, N, \alpha) = f_\alpha(t, x, N)$ and:

- *Advection field*

$$b(x, N, \alpha) = (\partial_N H_\alpha(x, N), -\partial_x H_\alpha(x, N))^t.$$

- *Total cross-section* $\lambda(x, N, \alpha) = \Sigma_\alpha(x, N);$
- *Probability measures*

$$\Pi(x, N, \alpha; dN', \beta) = \frac{\sigma_{\alpha\beta}(x, N, dN')}{\Sigma_\alpha(x, N)}.$$

If u_α is absolutely continuous with respect to the Lebesgue measure, $\mathcal{A}^*u_\alpha = -\{H_\alpha, u_\alpha\} + \mathcal{S}_\alpha\{u_\beta\}$, which can be compared with (1). As a

consequence of the specific form of $\sigma_{\alpha\beta}$ encountered in the physics modeling, condition (2) is automatically satisfied.

The interpretation of the WKE as a Fokker-Planck equation allows us to build the following numerical scheme: A number N_m of markers $\{X_i(0), \mathcal{N}_i(0), a_i(0)\}_{i=1,\dots,N_m}$ are sampled according to (2) and (3); markers are evolved according to the described procedure. This provides a solution of (4) for $\gamma_\alpha = 0$. Absorption is then introduced by weighting each marker with the weight $\exp(-2 \int_0^t \gamma_\alpha dt')$. Convergence of the scheme was verified in a $1d \times 1d$ test model, before implementing it in **WKBeam** [4, 6], a code which describes beams in turbulent plasmas accounting for realistic tokamak parameters. An example of application is shown in Figure 1.

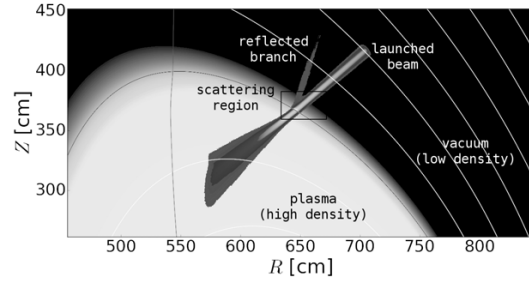


Figure 1: Scattered beam in a tokamak (ITER), poloidal plane zoom. Plasma electron-density fluctuations determine a severe broadening of the beam, and the formation of an undesired reflected branch.

References

- [1] L. Ryzhik, G. Papanicolaou and J. B. Keller, *Wave Motion* **24** (1996), pp. 327–370.
- [2] S. W. McDonald, *Physics Reports* **158** (1988), pp. 337–416.
- [3] S. W. McDonald, *Phys. Rev. A* **43** (1991), pp. 4484–4499.
- [4] H. Weber, O. Maj and E. Poli, *EPJ Web of Conferences* **87** 01002 (2015).
- [5] B. Lapeyre, E. Pardoux and R. Sentis, *Introduction to Monte Carlo Methods for Transport and Diffusion Equations*, Oxford University Press, 2003.
- [6] H. Weber, *IPP Report* **5/134** (2003).

Low-wavenumber expansion of Willis' effective constitutive relations in periodic media

S. Meng¹, B. Guzina²

¹Institute for Mathematics and its Applications, University of Minnesota

²Department of Civil, Environmental, & Geo- Engineering, University of Minnesota

Abstract

Willis [3] proposed effective constitutive relations applicable to the mean wave motion in composites with periodic microstructure. The focus of this work is to represent Willis' (effective) constitutive relations using an eigensystem approach and to explore its asymptotic behavior within the first Brioullin zone.

Keywords: Effective constitutive relations, periodic media, wave dispersion

1 Introduction

Consider the time-harmonic scalar wave equation

$$-\omega^2 \rho(x) u - \nabla \cdot (G(x) \nabla u) = f \quad \text{in } \mathbb{R}^d$$

where $d = 1, 2, 3$, while $G(x)$ and $\rho(x)$ are the shear modulus and mass density that are real-valued L^∞ functions bounded below away from zero. In what follows, $G(x)$ and $\rho(x)$ are taken to be Y -periodic with $Y = \{x_j : 0 \leq x_j < \ell_j; j = \overline{1, d}\}$.

Next, consider the Bloch-wave solutions of the form $u(x) = \tilde{u}(x)e^{-ik \cdot x}$, where \tilde{u} is Y -periodic and depends implicitly on \mathbf{k} and ω which are hereon assumed to be fixed. If further the excitation of a medium is taken in the form of (i) plane-wave body force $f(x) = \tilde{f}(x)e^{-ik \cdot x}$ and (ii) eigenstrain field $\boldsymbol{\gamma} = \tilde{\gamma}(x)e^{-ik \cdot x}$ [3] where both \tilde{f} and $\boldsymbol{\gamma}$ are Y -periodic, one has

$$-\omega^2 \rho(x) \tilde{u} - \nabla_{\mathbf{k}} \cdot (G(x) (\nabla_{\mathbf{k}} \tilde{u} - \tilde{\gamma})) = \tilde{f} \quad \text{in } Y, \quad (1)$$

where $\nabla_{\mathbf{k}} = \nabla + i\mathbf{k}$. In this case the relations between stress, momentum, strain and velocity read

$$\tilde{\boldsymbol{\epsilon}} = (\nabla + i\mathbf{k}) \tilde{u}, \quad \tilde{p} = -i\omega \rho \tilde{u}, \quad (2)$$

$$\tilde{\boldsymbol{\sigma}} = G(\tilde{\boldsymbol{\epsilon}} - \tilde{\gamma}), \quad \tilde{v} = -i\omega \tilde{u}. \quad (3)$$

The scalar wave equation (1) can then be written as $\nabla_{\mathbf{k}} \cdot \tilde{\boldsymbol{\sigma}} + \tilde{f} = -i\omega \tilde{p}$. Averaging over Y yields the effective equation

$$i\mathbf{k} \cdot \langle \tilde{\boldsymbol{\sigma}} \rangle + \langle \tilde{f} \rangle = -i\omega \langle \tilde{p} \rangle, \quad (4)$$

where $\langle \cdot \rangle$ denotes the average of an $L^1(Y)$ function in Y . In this setting, the goal is to obtain the counterpart of (2) and (3) in terms of the mean fields and to expose their asymptotic behavior when $|\mathbf{k}|$ and ω are small.

2 Eigensystem representation of effective constitutive relations

To derive Willis' effective constitutive relations, one may conveniently assume [3] that \tilde{f} and $\tilde{\gamma}$ in (1) are constants. Next, let $\{\tilde{\phi}_n, \tilde{\lambda}_n\}$ denote the eigensystem that satisfies

$$-\nabla_{\mathbf{k}} \cdot (G(x) \nabla_{\mathbf{k}} \tilde{\phi}_n) = \tilde{\lambda}_n \rho \tilde{\phi}_n \quad \text{in } Y,$$

where $\{\tilde{\phi}_n\}$ are complete and orthonormal in $L^2_\rho(Y)$. In this section, we assume that $\tilde{\lambda}_n \neq \omega^2$.

The effective fields can be shown to satisfy

$$\begin{bmatrix} \langle \tilde{\boldsymbol{\sigma}} \rangle \\ \langle \tilde{p} \rangle \end{bmatrix} = \begin{bmatrix} \tilde{\mathbf{C}}^e & -\tilde{\mathbf{S}}^{e*} \\ \tilde{\mathbf{S}}^e & \tilde{\rho}^e \end{bmatrix} \begin{bmatrix} \langle \tilde{\boldsymbol{\epsilon}} - \tilde{\gamma} \rangle \\ \langle \tilde{v} \rangle \end{bmatrix}, \quad (5)$$

where $\tilde{\mathbf{C}}^e = \tilde{\mathbf{C}}^{e*}$, $\tilde{\rho}^e = \tilde{\rho}^{e*}$ and

$$\begin{aligned} \tilde{\mathbf{C}}^e &= \langle G(\nabla_{\mathbf{k}} \otimes \tilde{\mathbf{A}} + \mathbf{I}) \rangle, \\ \tilde{\mathbf{S}}^e &= \langle -i\omega \rho \tilde{\mathbf{A}} \rangle, \\ \tilde{\rho}^e &= \langle \rho - i\omega \rho \tilde{\mathbf{B}} \rangle. \end{aligned}$$

Here $\tilde{\mathbf{A}}$ and $\tilde{\mathbf{B}}$ are represented by (provided $\sum_{n=1}^{\infty} \tilde{a}_n \langle \tilde{\phi}_n \rangle \neq 0$)

$$\begin{aligned} \tilde{\mathbf{A}} &= \sum_{n=1}^{\infty} \tilde{a}_n \frac{\sum_{n=1}^{\infty} \tilde{\mathbf{b}}_n \langle \tilde{\phi}_n \rangle}{\sum_{n=1}^{\infty} \tilde{a}_n \langle \tilde{\phi}_n \rangle} - \tilde{\mathbf{b}}_n \Bigg) \tilde{\phi}_n, \\ \tilde{\mathbf{B}} &= -\frac{1}{i\omega} \Big(\sum_{n=1}^{\infty} \frac{\tilde{a}_n}{\sum_{n=1}^{\infty} \tilde{a}_n \langle \tilde{\phi}_n \rangle} \tilde{\phi}_n - i\mathbf{k} \cdot \tilde{\mathbf{A}} - 1 \Big), \end{aligned}$$

where

$$\tilde{a}_n = \frac{(1, \tilde{\phi}_n)}{\tilde{\lambda}_n - w^2}, \quad \tilde{\mathbf{b}}_n = \frac{(G, \nabla_{\mathbf{k}} \tilde{\phi}_n)}{\tilde{\lambda}_n - w^2}.$$

$\tilde{\mathbf{C}}^e$ and $\tilde{\rho}^e$ are respectively the effective elasticity tensor and mass density in the Fourier (\mathbf{k}, ω) space, and $\tilde{\mathbf{S}}^e$ is the corresponding coupling vector – which together via (5) specify the

non-local constitutive relationship in \mathbb{R}^d . Note that the effective field equation (4) and Willis constitutive relations (5) yield

$$\tilde{Z}^e \langle \tilde{u} \rangle = \tilde{f} - i\mathbf{k} \cdot (\tilde{\mathbf{C}}^e \langle \tilde{\gamma} \rangle) - i\omega \tilde{\mathbf{S}}^e \cdot \langle \tilde{\gamma} \rangle$$

where the effective impedance is given by

$$\tilde{Z}^e = -i\mathbf{k} \cdot (\tilde{\mathbf{C}}^e i\mathbf{k}) + i\mathbf{k} \cdot (\tilde{\mathbf{S}}^e + \tilde{\mathbf{S}}^{e*}) i\omega - \omega^2 \tilde{\rho}^e,$$

and it can be represented by

$$\tilde{Z}^e = \sum_{n=1}^{\infty} \frac{(1, \tilde{\phi}_n) \langle \tilde{\phi}_n \rangle}{\tilde{\lambda}_n - \omega^2} \Bigg)^{-1}.$$

3 Properties of effective constitutive relations and effective impedance

When the eigenvalue $\tilde{\lambda}_n$ has multiplicity one, one can conveniently study the effective constitutive relations as $\omega^2 \rightarrow \tilde{\lambda}_n$.

a. *Non-degenerate case:* $\langle \tilde{\phi}_n \rangle \neq 0, \forall n$. If $\tilde{\lambda}_n \neq \omega^2$, then all effective properties are well-defined. If $\omega^2 \rightarrow \tilde{\lambda}_n$, a direct calculation shows that the effective constitutive relations are well-defined provided $\langle \tilde{\phi}_n \rangle \neq 0, \forall n$.

b. *Exceptional case:* $\langle \tilde{\phi}_n \rangle = 0$. If $\langle \tilde{\phi}_n \rangle \neq 0$ for given n and fixed \mathbf{k} , then $\tilde{Z}^e \rightarrow 0$ as $\omega^2 \rightarrow \tilde{\lambda}_n$. Hence the effective impedance captures the Bloch pair $(\mathbf{k}, \tilde{\lambda}_n)$. On the other hand if $\langle \tilde{\phi}_n \rangle = 0$ for given n , then the effective impedance fails to capture the Bloch pair $(\mathbf{k}, \tilde{\lambda}_n)$, see also [1]. In particular, if $\langle \tilde{\phi}_n \rangle = 0$, then the Bloch eigenfunction $\tilde{\phi}_n$ has zero mean. It is not possible to observe this Bloch pair when one is only capable of capturing the mean motion a physical experiment.

If the eigenvalue $\tilde{\lambda}_n$ has multiplicity more than one, one is still able to study the exceptional and non-degenerate cases as $\omega^2 \rightarrow \tilde{\lambda}_n$ but in a rather complicated form.

4 Asymptotics of effective impedance and effective constitutive relations

We consider the long-wavelength, low-frequency asymptotics of the effective impedance. We assume that $\omega = \epsilon\hat{\omega}$ and $\mathbf{k} = \epsilon\hat{\mathbf{k}}$, where $\epsilon \ll 1$ and $\hat{\mathbf{k}}$ is a fixed Bloch wave vector.

In particular, one can show that

$$\tilde{Z}^e = \tilde{Z}_4^e + O(\epsilon^5),$$

where the $O(\epsilon^4)$ approximation \tilde{Z}^e of the effective impedance satisfies

$$\begin{aligned} \tilde{M}_4^e \tilde{Z}_4^e &= \rho_0 \omega^2 + \boldsymbol{\mu}_0 : (i\mathbf{k} \otimes i\mathbf{k}) + \omega^2 \boldsymbol{\rho}_1 \cdot i\mathbf{k} \\ &+ \boldsymbol{\mu}_1 : (i\mathbf{k} \otimes i\mathbf{k} \otimes i\mathbf{k}) + \omega^2 \boldsymbol{\rho}_2 : (i\mathbf{k} \otimes i\mathbf{k}) \\ &+ \boldsymbol{\mu}_2 : (i\mathbf{k} \otimes i\mathbf{k} \otimes i\mathbf{k} \otimes i\mathbf{k}), \end{aligned}$$

where the coefficient ρ_0 , vector $\boldsymbol{\rho}_1$, and tensors $\boldsymbol{\mu}_0, \boldsymbol{\mu}_1, \boldsymbol{\mu}_2$ and $\boldsymbol{\rho}_2$ are exactly the same as their counterparts in [2] obtained via the multiple-scales homogenization approach, while \tilde{M}_4^e is a polynomial in (\mathbf{k}, ω) . This implies that one will have to modify the body force in the second order homogenized wave equation in order to bear physical relevance.

The leading-order expansions of $\tilde{\rho}^e$, $\tilde{\mathbf{C}}^e$ and $\tilde{\mathbf{S}}^e$ read

$$\begin{aligned} \tilde{\rho}^e &= \rho_0 + O(\epsilon), \\ \tilde{\mathbf{C}}^e &= \boldsymbol{\mu}_0 + O(\epsilon), \\ \tilde{\mathbf{S}}^e &= O(\epsilon). \end{aligned}$$

Higher order expansions of effective density, effective moduli and effective couplings can be obtained similarly.

5 The case of constant mass density

In the case that the mass density ρ is a constant, the effective mass density and effective coupling are constants, in particular

$$\tilde{\rho}^e = \rho, \quad \tilde{\mathbf{S}}^e = \mathbf{0}.$$

6 Discussion

To bear physical relevance, we consider Willis effective constitutive relations for pairs (\mathbf{k}, ω) where \mathbf{k} lies in the first Brillouin zone and ω is limited to the acoustic branch. In principle, however, the eigenfunction expansion approach adopted here has an advantage in that it can be also applied to (higher-frequency) optical branches.

References

- [1] A. N. Norris, A. L. Shuvalov and A. A. Kutsenko, *Proc. R. Soc. A* (2012) **468**, 1629–1651.
- [2] A. Wautier and B. Guzina, *J. Mech. Phys. Solids* (2015) **78**, 382–414.
- [3] J. Willis, *Proc. R. Soc. A* (2011) **467**, 1865–1879.

Extensions of Complete Radiation Boundary Conditions to Dispersive Waves

Thomas Hagstrom^{1,*}

¹Department of Mathematics, Southern Methodist University, Dallas TX, USA

*Email: thagstrom@smu.edu

Abstract

Complete radiation boundary conditions (CRBC) are local boundary condition sequences optimized for models related to the scalar wave equation, such as Maxwell's equations in nondispersive dielectrics. Here we consider their generalization to electromagnetic waves in dispersive media governed by Lorentz models. If only the permittivity is frequency-dependent, parameters can be chosen to guarantee rapid convergence with increasing order. For metamaterials, on the other hand, where both the permittivity and the permeability are frequency-dependent, so-called reverse modes exist and parameters for the standard CRBC cannot be chosen to guarantee convergence. Here we show how to modify the formulation so that convergence can be restored.

Keywords: Radiation conditions, dispersion

Introduction

As the radiation of energy to the far field is typical in wave propagation problems, efficient numerical simulation tools require accurate and reliable techniques for truncating the computational domain. Complete radiation boundary conditions (CRBC), introduced in [1], provide such a technique for the scalar wave equation and related systems, including Maxwell's equations in isotropic dielectric media. Central to the formulation of CRBC is the evolution of a sequence of auxiliary fields, ϕ_j , defined implicitly by recursions:

$$\begin{aligned} a_{2j-1} \frac{\partial \phi_{j-1}}{\partial t} + c \frac{\partial \phi_{j-1}}{\partial n} + \sigma_{2j-1} \phi_{j-1} &= \\ a_{2j} \frac{\partial \phi_j}{\partial t} - c \frac{\partial \phi_j}{\partial n} + \sigma_{2j} \phi_j, \end{aligned}$$

where the parameters a_j , σ_j , are chosen to optimize an error bound.

Introducing the dimensionless parameter $\eta = \frac{\delta}{cT}$, where δ is the separation of any sources or scatterers from the radiation boundary and T is the simulation time, we prove that parameters can be chosen so that the reflection error can be made less than any tolerance τ using

$P \propto \ln \tau \cdot \ln \eta$ auxiliary fields. Optimal parameters are easily computed using the Remez algorithm. A library of implementations of CRBC for Maxwell's equations called `rbcpack`¹ is being released. As of now it contains a module for the Yee scheme [2], but implementations using discontinuous Galerkin and high order difference methods have been tested and will be made available in future versions.

Dispersive Models

Now consider Maxwell's equations in an isotropic dispersive medium:

$$\begin{aligned} \epsilon_0 (1 + \mathcal{K}_e *) \frac{\partial E}{\partial t} &= \nabla \times H, \\ \mu_0 (1 + \mathcal{K}_m *) \frac{\partial H}{\partial t} &= -\nabla \times E. \end{aligned}$$

Here we assume Lorentz models for the temporal convolutions; precisely with s the Laplace transform variable dual to time we suppose

$$\hat{\mathcal{K}}_e = \frac{\omega_e^2}{s^2 + \gamma_e s + \Omega_e^2}, \quad \hat{\mathcal{K}}_m = \frac{\omega_m^2}{s^2 + \gamma_m s + \Omega_m^2}.$$

The Drude model has $\Omega_e = \Omega_m = 0$, and dissipation is absent if $\gamma_e = \gamma_m = 0$.

The analysis and optimization of the CRBC parameters is performed in the Fourier-Laplace domain. Take k dual to the transverse spatial variables and s dual to time with $\Re s = T^{-1}$. Error estimates on this contour up to time T follow from Parseval's Theorem. Outgoing waves are proportional to:

$$e^{-\lambda x}, \quad \lambda = \left(\frac{s^2}{c_0^2} (1 + \hat{\mathcal{K}}_e) (1 + \hat{\mathcal{K}}_m) + |k|^2 \right)^{1/2},$$

where the branch is chosen so that $\Re \lambda > 0$, encoding group velocity of the correct sign. The error is then controlled by the scaled reflection coefficient

$$\rho = e^{-\lambda \delta} \prod \frac{a_j s + \sigma_j - c_0 \lambda}{a_j s + \sigma_j + c_0 \lambda}$$

¹www.rbcpack.org

Consider first $\hat{\mathcal{K}}_m = 0$. Then there are no reverse modes, corresponding to the condition $\Im s \cdot \Im \lambda \geq 0$. Choosing a_j, σ_j nonnegative each of the factors determining ρ has modulus below 1, which allows us to achieve rapid convergence. To compute parameters in general we have, as a first try, solved an ad hoc optimization problem for an average value of $|\rho|^2$, estimated on a mapped frequency domain,

$$(\Im s, k) = ((1+z)/(1-z))(\cos \theta, \sin \theta),$$

using a Gaussian quadrature rule with 100×100 nodes in (z, θ) , and MATLAB's **fmincon** to determine the parameters. As an example, setting $\delta = 0.1$ and $T = 20$ with $c_0 = 1$, we take $P = 4, 6, 8$. We consider a nondissipative Drude model $\omega_e^2 = 4$, which can be optimized directly with the Remez algorithm, add dissipation, $\gamma_e = 10^{-3}$, and a nondissipative Lorentz model setting $\Omega_e^2 = 2$. For the Drude models $\bar{\rho}$ varies from 2.1×10^{-3} to 3.9×10^{-4} , with very little difference in the dissipative and nondissipative cases. Results show some degradation in accuracy for the Lorentz model, $\bar{\rho}$ varying from 6.0×10^{-3} to 1.5×10^{-3} , but clearly the CRBC is still quite efficient in that case. We do find substantial differences in the optimal parameters between the Drude and Lorentz models.

We now consider a metamaterial where both the permittivity and the permeability are governed by the Drude model. The material has a negative index of refraction for frequencies where both $1 + \hat{\mathcal{K}}_e$ and $1 + \hat{\mathcal{K}}_m$ are negative. For such frequencies there are reverse modes. It is well-known that in such circumstances the standard construction of Perfectly Matched Layers (PML) fails [3], while for CRBC we are unable to ensure that the imaginary parts of the denominators in the definition of ρ are larger than those in the denominator, spoiling convergence.

In [4] the authors show how to modify PML to regain stability and accuracy. Their idea is to alter the sign in the so-called complex grid stretching to conform to the sign of the group velocity. Here we adapt their idea to CRBC; in Laplace variables this corresponds to multiplying a_j by a term with certain sign properties. In real space the recursions become:

$$\begin{aligned} a_{2j-1} (1 + \mathcal{K}_c*) \frac{\partial \phi_{j-1}}{\partial t} + c \frac{\partial \phi_{j-1}}{\partial n} + \sigma_{2j-1} \phi_{j-1} &= \\ a_{2j} (1 + \mathcal{K}_c*) \frac{\partial \phi_j}{\partial t} - c \frac{\partial \phi_j}{\partial n} + \sigma_{2j} \phi_j. \end{aligned}$$

To ensure $|\rho| < 1$ we require for $\Re s > 0$

$$\Re(s(1 + \hat{\mathcal{K}}_c)) > 0, \quad \Im(s(1 + \hat{\mathcal{K}}_c)) \cdot \Im \lambda \geq 0.$$

For the Drude models these conditions are satisfied if we make the simple choice $\hat{\mathcal{K}}_c = \frac{\omega_e \omega_m}{s^2}$.

We carried out the optimization procedure for the same cases as above with $\omega_e^2 = 4$, $\omega_m^2 = 3$. Here we found that $\bar{\rho}$ varied from 1.8×10^{-3} to 4.9×10^{-4} . These accuracies are similar, and in some cases better, than in the standard case. We also find that the optimal parameters bear greater similarities to the Drude model, but still are substantially different.

In summary, we have shown how CRBCs can be generalized to various dispersive models for electromagnetic waves. Clearly, much work remains. In particular we need to consider alternatives to the ad hoc optimization used here, and most importantly develop a method for rapid precomputation of good parameters. In addition we need to develop and test various implementations.

Acknowledgements

This work was supported in part by NSF grant DMS-1418871. Any opinions, findings, and conclusions or recommendations expressed in this material are those of the author and do not necessarily reflect the views of the NSF.

References

- [1] T. Hagstrom and T. Warburton, Complete radiation boundary conditions: minimizing the long time error growth of local methods, *SIAM J. Numer. Anal.* **47** (2009), pp. 3678–3704.
- [2] J. Lagrone and T. Hagstrom, Double absorbing boundaries for finite-difference time-domain electromagnetics, *J. Comput. Phys.* **326** (2016), pp. 650–665.
- [3] E. Bécache, S. Fauqueux, and P. Joly, Stability of perfectly matched layers, group velocities, and anisotropic waves, *J. Comput. Phys.* **188** (2003), pp. 399–433.
- [4] E. Bécache, P. Joly, and V. Vinoles, On the analysis of perfectly matched layers for a class of dispersive media and applications to negative index metamaterials, hal-01327315 (2016).

Faraday cages, homogenized boundary conditions and resonance effects

David P. Hewett^{1,*}, Ian J. Hewitt²

¹Department of Mathematics, University College London, London, UK

²Mathematical Institute, University of Oxford, Oxford, UK

*Email: d.hewett@ucl.ac.uk

Abstract

We study electromagnetic shielding by a cage of perfectly conducting wires - the ‘Faraday cage effect’. In the limit as the number of wires tends to infinity we derive continuum models for the shielding, involving homogenized boundary conditions on an effective cage boundary. For wires of sufficiently large radius there are resonance effects: at wavenumbers close to the natural resonances of the equivalent solid shell, the cage actually amplifies the incident field, rather than shielding it. By modifying the continuum model we can calculate the wavenumbers giving the largest response, along with the associated peak amplitudes.

Keywords: Electromagnetic shielding, homogenization, multiple scales, resonance.

Introduction

The Faraday cage effect is a well-known phenomenon whereby electromagnetic waves can be blocked by a wire mesh ‘cage’. Somewhat surprisingly, until recently there was apparently no widely-known mathematical analysis quantifying the effectiveness of the shielding as a function of basic parameters, such as the geometry of the cage, and the thickness, shape and spacing of the wires in the mesh from which it is constructed. The recent publications [1, 3] provide such an analysis for the two-dimensional case where the cage comprises a large number of equally-spaced perfectly-conducting ‘wires’ of the same shape and radius. Our analysis in [1, 3] uses homogenized boundary conditions derived by the method of multiple scales and matched asymptotic expansions, as employed in [2, 4] to study similar problems.

For brevity we consider here only TE polarization, requiring the study of a scalar field satisfying the Helmholtz equation and zero Dirichlet boundary conditions on the wires. The TM case can be treated similarly [3].

Let Ω_- be a bounded simply connected open subset of the plane with smooth boundary Γ =

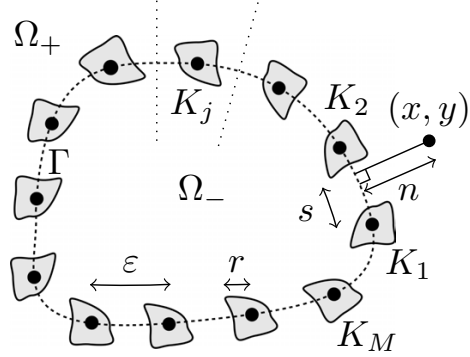


Figure 1: Faraday cage geometry

$\partial\Omega_-$ and let $\Omega_+ := \mathbb{R}^2 \setminus \overline{\Omega}_-$ denote the complementary exterior domain. We consider a ‘cage’ of M non-intersecting wires $\{K_j\}_{j=1}^M$ (compact subsets of the plane, of identical radius r , shape and orientation relative to Γ) distributed along Γ with constant arc length separation

$$\varepsilon = |\Gamma|/M,$$

where $|\Gamma|$ is the total length of Γ , see Figure 1. We set $D := \mathbb{R}^2 \setminus \left(\bigcup_{j=1}^M K_j \right)$. Given an incident wave ϕ^i (e.g. a plane wave or point source) we seek a scattered field ϕ satisfying

$$\begin{aligned} (\nabla^2 + k^2)\phi &= 0, && \text{in } D, \\ \phi &= -\phi^i, && \text{on } \partial D, \end{aligned}$$

and an outgoing radiation condition at infinity.

Homogenization for $\varepsilon \rightarrow 0$

In the limit as $\varepsilon \rightarrow 0$ ($M \rightarrow \infty$) we look for outer approximations in Ω_\pm of the form

$$\phi = \phi_0^\pm + \varepsilon \phi_1^\pm + O(\varepsilon^2) \quad \text{in } \Omega_\pm.$$

The rapid variation close to Γ is modelled by a boundary layer of width $O(\varepsilon)$. Here we look for a solution in multiple-scales form

$$\phi(n, s) = \Phi(N, S; s),$$

where (n, s) are normal and tangential coordinates (see Figure 1), (N, S) are rescaled versions

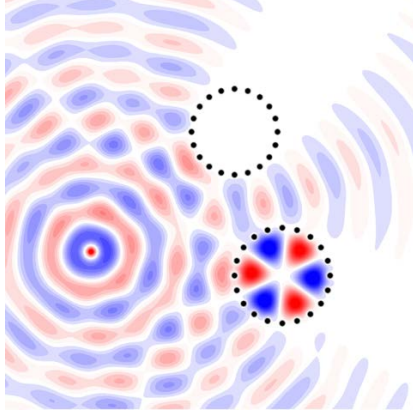


Figure 2: Resonance effects. Two slightly different sized cages of identical circular wires irradiated by a point source. The smaller cage is shielding while the larger cage is amplifying.

defined by $(n, s) = (\varepsilon N, \varepsilon S)$, and $\Phi(N, S; s)$ is assumed 1-periodic in the fast tangential variable S , satisfying an appropriate cell problem. Asymptotic matching gives homogenized boundary conditions for ϕ_j^\pm on Γ , the nature of which depend on the thickness of the wires.

For ‘thin’ wires (radius $r \ll \varepsilon$) the two-term approximation $\phi_0 + \varepsilon\phi_1$ is continuous across Γ but undergoes a jump in normal derivative with

$$\left[\frac{\partial \phi_0}{\partial n} + \varepsilon \frac{\partial \phi_1}{\partial n} \right]_+^+ = \alpha (\phi_0 + \varepsilon\phi_1) \quad \text{on } \Gamma,$$

where

$$\alpha = \frac{|\Gamma|}{\varepsilon \log(\varepsilon/(r|\Gamma|)) + a_0} = \frac{M}{\log(1/(rM)) + a_0},$$

and a_0 is a constant depending on the wire shape. (Specifically, a_0 can be expressed in terms of the logarithmic capacity of the scaled wire $(1/r)K_j$.) The distinguished scaling in which $\alpha = O(1)$ occurs when $r = O(\varepsilon e^{-c/\varepsilon})$ for some $c > 0$.

For ‘thick’ wires (radius $r = O(\varepsilon)$) the leading order approximation satisfies

$$\phi_0^+ = \phi_0^- = 0 \quad \text{on } \Gamma. \quad (1)$$

The $O(\varepsilon)$ corrections ϕ_1^\pm satisfy inhomogeneous Dirichlet boundary conditions involving $\partial\phi_0^\pm/\partial n$ and constants extracted from the boundary layer cell problem. For non-resonant k , the homogeneous boundary condition (1) implies that $\phi_0^- \equiv 0$ in Ω_- , so we predict a shielding effect, with $\phi = O(\varepsilon)$ in Ω_- .

However, if k is resonant, i.e. k^2 is a Dirichlet eigenvalue of the negative Laplacian in Ω_- , then the problem for ϕ_0^- is ill-posed and our approximation breaks down. In practice, close to resonance one observes a large excitation inside Ω_- ; the cage *amplifies* the field rather than shielding from it, see Figure 2. For $k \approx k_*$ (a resonant wavenumber) we modify our ansatz to

$$\phi^-(x, y) = \frac{1}{\varepsilon} \phi_{-1}^- + \phi_0^- + \varepsilon \phi_1^- + O(\varepsilon^2) \quad \text{in } \Omega_-.$$

Matching then reveals that

$$\phi_{-1}^- = C_{-1}\psi^*,$$

where ψ^* is the eigenmode corresponding to k^* (in general a superposition of eigenmodes), and solvability conditions for ϕ_0^- and ϕ_1^- give

$$|C_{-1}| = A_1 \left(1 + \frac{k - \tilde{k}^*}{\varepsilon^2 A_2} \right)^2^{-1/2},$$

where A_1, A_2, \tilde{k}^* are constants depending on Γ (the cage geometry) and the wire shape/size (for details see [3]). The maximum amplitude occurs not at $k = k^*$ but rather at the shifted value \tilde{k}^* ; in [3] we derive a three-term expansion $\tilde{k}^* = k^* + \varepsilon \tilde{k}_1^* + \varepsilon^2 \tilde{k}_2^*$, with explicit formulas for \tilde{k}_1^* and \tilde{k}_2^* . We also demonstrate the excellent agreement between these asymptotic approximations and full numerical simulations.

References

- [1] S. J. Chapman, D. P. Hewett and L. N. Trefethen, Mathematics of the Faraday cage, *SIAM Review* **57**(3) (2015), 398–417.
- [2] B. Delourme, H. Haddar and P. Joly, Approximate models for wave propagation across thin periodic interfaces, *J. Math. Pures Appl.* **98** (2012), 28–71.
- [3] D. P. Hewett and I. J. Hewitt, Homogenized boundary conditions and resonance effects in Faraday cages, *Proc. Roy. Soc. A* **472** (2016), 2189.
- [4] C.L. Holloway, E.F. Kuester and A. Dienstfrey, A homogenization technique for obtaining generalized sheet transition conditions for an arbitrarily shaped coated-wire grating, *Radio Sci.* **49**(10) (2014), 813–850.

Strongly Nonlinear Elastic Wave Dispersion in 1D Homogenous Media and Metamaterials

Romik Khajehtourian¹, Mahmoud I. Hussein^{1,*}

¹Department of Aerospace Engineering Sciences, University of Colorado Boulder, Boulder, Colorado

*Email: mih@colorado.edu

Wave motion lies at the heart of many disciplines in the physical sciences and engineering. For example, problems and applications involving light, sound, heat or fluid flow are all likely to involve wave dynamics at some level. In this extended abstract, we present our recent work on large-deformation elastic waves in solids, focusing on both homogeneous media and metamaterials.

Specifically, we examine the propagation of a large-amplitude wave in an elastic one dimensional medium that is undeformed at its nominal state. In this context, our focus is on the effects of inherent nonlinearities on the dispersion relation. Considering a thin rod, where the thickness is small compared to the wavelength, we present an exact formulation for the treatment of a nonlinearity in the strain-displacement gradient relation. As an example, we consider Green Lagrange strain. The ideas presented, however, apply generally to other types of geometric nonlinearities, such as Hencky strain, and also to material nonlinearities regardless of type or order. The only limitation is that the nonlinearity has to be expressed analytically and be integrable. Furthermore, a thick rod may be considered by simply accounting for lateral inertial in the model.

The derivation starts with an implementation of Hamilton's principle and terminates with an expression for the finite-strain dispersion relation in closed form [1]. The derived relation is then verified by direct time-domain simulations, examining both instantaneous dispersion (by direct observation) (see Figure 1) and short-term, pre-breaking dispersion (by Fourier transformations), as well as by perturbation theory. The results establish a perfect match between theory and simulation and reveal that an otherwise linearly nondispersive elastic solid may exhibit dispersion solely due to the presence of a nonlinearity. The same approach is also applied to flexural waves in an Euler Bernoulli beam, demonstrating qualitatively different nonlinear disper-

sive effects compared to longitudinal waves. Finally, we present a method for extending this analysis to a continuous thin rod with periodically embedded local resonators, i.e., an elastic metamaterial (see Figure 2) [2]. The method, which is based on a standard transfer matrix augmented with a nonlinear enrichment at the constitutive material level, yields an approximate band structure that accounts for the finite wave amplitude. The effects of the nonlinearity on the subwavelength band gap are also high-

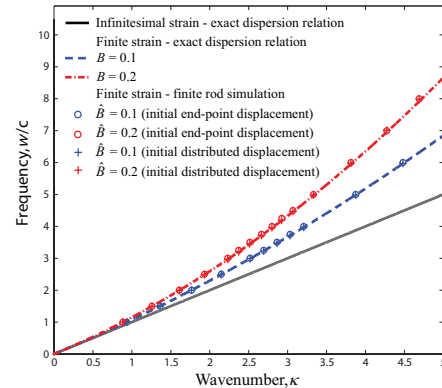


Figure 1: Finite-strain dispersion curves for a thin homogeneous rod [1]

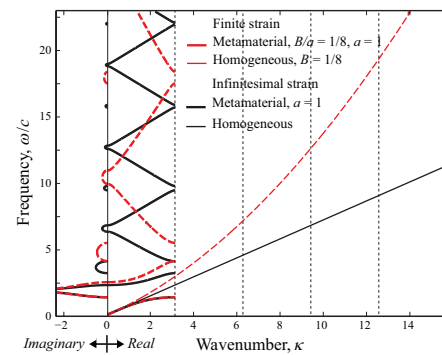


Figure 2: Finite-strain dispersion curves for a thin homogeneous rod with periodically attached local resonators [2]

lighted, among other intriguing outcomes.

The present theory is not limited by the strength of the nonlinearity, unlike perturbation-based analysis which is commonly used in the literature for weakly non-linear waves. A validated dispersion relation for a strongly nonlinear problem provides new understanding of the physics of nonlinear waves in general. This result is relevant to the study of waves in both natural and engineered problems, and in principle is applicable to a range of topics including dislocation and crack dynamics, geophysical and seismic waves, material nondestructive evaluation, biomedical imaging, elastic metamaterial engineering, nanoscale thermal transport, among others.

References

- [1] M. H. Abedinnasab and M. I. Hussein, Wave dispersion under finite deformation, *Wave Motion* **50** (2013), pp. 374–388.
- [2] R. Khajehtourian and M. I. Hussein, Dispersion characteristics of a nonlinear elastic metamaterial, *AIP Advances* **4** (2014), 124308.

Generalized Plane Waves, variable amplitude and vector valued equations

Lise-Marie Imbert-Gérard^{1,*}

¹Courant Institute, New York University, New York, USA

*Email: imbertgerard@cims.nyu.edu

Abstract

The need for approximated solutions to a vector valued equation in electro-magnetic wave propagation raises the question of the amplitude, or polarization, of the approximated function. In this work we propose to incorporate geometric optics expansions into the design process of Generalized Plane Waves in order to take into account variable amplitudes.

Keywords: generalized plane waves, variable amplitude, geometric optics

1 Introduction

Generalized Plane Waves (GPWs) were introduced in [4] as approximated solutions to a variable coefficient equation. These functions were introduced in the framework of wave-based numerical methods to address wave propagation in inhomogeneous media, and in [5] we proved the convergence of a numerical method coupling GPWS with a Trefftz formulation for the variable coefficient Helmholtz equation. The design process for GPWs depends on the coefficients of a given partial differential operator \mathcal{L} , and introduces the parameter q as the order of approximation of the homogeneous equation $\mathcal{L}u = 0$.

In references [4, 5], the operator considered was the variable coefficient Helmholtz operator $\mathcal{L}_H = -\Delta - \kappa^2 n(\mathbf{x})$. The design process was later extended to a wide range of linear partial differential operators, see [2], but only to scalar valued operators. The present work presents a first attempt to design GPWs for the case of vector valued equations. The main specificity in this case, with respect to the scalar valued case, is the need to consider a polarization instead of a constant amplitude.

2 Generalized Plane Waves for a scalar equation

In the framework of wave-based numerical methods to address wave propagation in homogeneous media, the numerical solution is sought in a space of local exact solutions of the equation. That is to say that, if the equation considered is

the constant coefficient equation $\mathcal{L}u = 0$, every basis function φ satisfies $\mathcal{L}\varphi = 0$. In the case of \mathcal{L}_H several options have been considered in the literature, such as classical plane waves or Bessel functions.

In the case of a variable coefficient operator \mathcal{L} , there are in general no such exact solutions. To overcome this fact, GPWs were introduced as local approximated solutions of the equation: a GPW is a function $\varphi = \exp P$ where the polynomial P is designed to ensure that the lowest order terms in the Taylor expansion of $\mathcal{L}[\exp P]$ are zero. Canceling the terms of the Taylor expansion provides a non linear system which unknowns are the coefficients of P . However this system can be split into a hierarchy of linear invertible subsystems, with explicit solutions. Therefore the design process provides an analytic formula to compute each coefficient of the polynomial P .

3 Towards vector valued equations

Now consider the case of a vector valued equation. In homogeneous media, the numerical solution is sought in a space of local solution of the equation. These basis functions have a constant polarization, and the different components oscillate at the same frequency. Such a basis function can then be written as $\mathbf{f}(\mathbf{x}) = \mathbf{p} \exp i\kappa \mathbf{k} \cdot \mathbf{x}$, where \mathbf{p} is a constant polarization vector depending on the operator, κ the wave number and \mathbf{k} the direction of propagation satisfies $|\mathbf{k}| = 1$.

In the case of a variable coefficient vector valued operator \mathbf{L} , the most natural idea would be to use a constant polarization as well, multiplied by a unique exponential function: $\mathbf{f}(\mathbf{x}) = \mathbf{p} \exp P(\mathbf{x})$ with a constant \mathbf{p} . However, in order to get an approximation of order q of the equation $\mathbf{L}\mathbf{f} = 0$, the terms of the Taylor expansion of each component of $\mathbf{L}\mathbf{f}$ need to be canceled, and therefore this choice for \mathbf{f} leads to an overdetermined system for the polynomial coefficients. To avoid this problem, we propose to look for basis functions with a polynomial

polarization: $\mathbf{f}(\mathbf{x}) = \mathbf{A}(\mathbf{x}) \exp P(\mathbf{x})$.

In [2–5], GPWs have a constant amplitude equal to one and so the design process requires to find only one type of unknowns, that are the coefficients of the polynomial P . If we want to use a polynomial polarization, we introduce a new kind of unknowns in the design process, that are the coefficients of \mathbf{A} . We will introduce geometric optics expansions to split the design process in two, and accordingly solve one system for each type of unknowns involved in the process.

4 Geometric Optics twist

The WKB approximation method for linear partial differential equations with variable coefficients relies on asymptotic expansions with respect to the wave number. Consider the equation $\mathcal{L}_H u = 0$. An approximated solution is sought in the form $\varphi(\mathbf{x}) = A(\mathbf{x}) \exp i\kappa S(\mathbf{x})$, so that

$$\begin{aligned} \mathcal{L}_H \varphi(\mathbf{x}) &= \\ &= \left[\kappa^2 A(\mathbf{x}) \left(|\nabla S(\mathbf{x})|^2 - n(\mathbf{x}) \right) \right. \\ &\quad - i\kappa \left(A(\mathbf{x}) \Delta S(\mathbf{x}) + \nabla A(\mathbf{x}) \cdot \nabla S(\mathbf{x}) \right) \\ &\quad \left. - \kappa^0 (\Delta A(\mathbf{x})) \right] e^{i\kappa S(\mathbf{x})}. \end{aligned}$$

The WKB method provides an approximated solution to $\mathcal{L}_H \varphi = 0$ in the high frequency regime by neglecting the $O(\kappa^0)$ terms and considering separately the $O(\kappa^1)$ and $O(\kappa^2)$ terms as follows:

- solving first the so-called eikonal equation $|\nabla S(\mathbf{x})|^2 - n(\mathbf{x}) = 0$ for S ,
- solving the so-called transport equation $\nabla \cdot (A(\mathbf{x}) \nabla S(\mathbf{x})) = 0$ for A .

In order to obtain an approximation valid for any frequency κ , we do not want to neglect the $O(\kappa^0)$ terms in the design of GPWs with variable amplitude. We therefore propose to separate first the eikonal equation for the phase function S , then to gather the $O(\kappa^1)$ and $O(\kappa^0)$ terms to solve the following equation

$$i\kappa \left(A(\mathbf{x}) \Delta S(\mathbf{x}) + \nabla A(\mathbf{x}) \cdot \nabla S(\mathbf{x}) \right) + \Delta A(\mathbf{x}) = 0$$

for the amplitude A . Approximated solutions to these two equations can be constructed using again a Taylor expansion and canceling the terms of order lower than q .

In this presentation we will discuss the application of these ideas for vector valued operators, as well as corresponding interpolation properties.

References

- [1] B. Després, (1994) Sur une formulation variationnelle de type ultra-faible, *C. R. Acad. Sci. Paris Sér. I Math.* **318** no. 10, 939–944.
- [2] L.-M. Imbert-Gérard, Generalized plane waves for varying coefficients, *The 12th International Conference on Mathematical and Numerical Aspects of Wave Propagation Book of abstracts* (2015).
- [3] L.-M. Imbert-Gérard, Interpolation properties of generalized plane waves *Numerische Mathematik* (2015) doi:10.1007/s00211-015-0704-y.
- [4] L.-M. Imbert-Gerard, & B. Després, A generalized plane-wave numerical method for smooth nonconstant coefficients, *IMA Journal of Numerical Analysis*, (2014) **34** (3): 1072–1103.
- [5] L.-M. Imbert-Gerard, & P. Monk, Numerical simulation of wave propagation in inhomogeneous media using Generalized Plane Waves. *To appear in M2AN*.

**Fourth order explicit scheme for dissipative wave problems
based on modified equation technique**

Juliette Chabassier¹, Julien Diaz¹, Alain Ha¹, Sébastien Imperiale^{2,*}

¹MAGIQUE 3D - Inria Bordeaux Sud-Ouest and Université de Pau et des Pays de l'Adour

²M3DISIM - Inria and Paris-Saclay University

*Email: sebastien.imperiale@inria.fr

Abstract

In this talk we present an original numerical scheme for the explicit fourth order time discretization of linear dissipative wave equation. This scheme is based on the modified equation technique which, in general, gives implicit time discretization when dissipation is present in the propagating medium. We discuss the construction of the scheme, its stability properties and present some space/time convergence results. The scheme is shown to be more efficient for the considered cases than the fourth order explicit Runge-Kutta scheme *RK4*.

Keywords: Time discretization, Dissipative wave equation, Explicit schemes

1 Introduction

We consider the construction of efficient explicit high order time discretization for dissipative wave equation. The model PDE we consider is

$$\partial_{tt}u - \Delta u + r(\mathbf{x})\partial_tu = 0, \quad \mathbf{x} \in \Omega, \quad t \in [0, T], \quad (1)$$

where $\Omega \subset \mathbb{R}^d$ and $u(t) \in H_0^1(\Omega)$ with $u(0)$ and $\partial_tu(0)$ given. The damping function $r(\mathbf{x})$ is non negative. A typical spatial discretization in a finite element space gives the following ODE

$$d_{tt}U_h + A_h U_h + B_h d_tU_h = 0.$$

where U_h is the vector of unknowns, the stiffness matrix A_h is symmetric positive definite and B_h is the symmetric and semi-definite positive dissipation matrix. The matrix A_h is sparse and B_h is easily invertible if conforming finite elements with mass lumping or discontinuous Galerkin methods are used. In such case the Leap-Frog scheme, *LF*, gives an explicit second order in time fully-discrete approximation of (1)

$$\begin{aligned} & \frac{U_h^{n+1} - 2U_h^n + U_h^{n-1}}{\Delta t^2} + A_h U_h^n \\ & + B_h \frac{U_h^{n+1} - U_h^{n-1}}{2\Delta t} = 0. \end{aligned} \quad (2)$$

To improve the accuracy of the time discretization, the so-called modified equation technique, *ME*, can be used, following [1]. It reads

$$\begin{aligned} & \tilde{I}_h \frac{U_h^{n+1} - 2U_h^n + U_h^{n-1}}{\Delta t^2} + \tilde{A}_h U_h^n \\ & + (B_h + \Delta t^2 C_h) \frac{U_h^{n+1} - U_h^{n-1}}{2\Delta t} = 0, \end{aligned} \quad (3)$$

with $\tilde{I}_h = I_h + \Delta t^2 B_h^2 / 12$, where I_h is the identity matrix, $\tilde{A}_h = A_h - \Delta t^2 A_h^2 / 12$ and finally $C_h = (B_h A_h - A_h B_h) / 12$. The efficiency of the *ME* is deteriorated since the matrix C_h (which in general is no longer block diagonal or diagonal) has to be taken into account in the system that is solved at each time step: the scheme is no longer explicit. In what follows we suggest a variant of the *ME* that restores its efficiency by being explicit, stable and formally fourth order.

2 Explicit scheme construction

The idea is to replace the term C_h in equation (3) by an approximation \tilde{C}_h that should at least be a formal second order approximation in time. Such approximation is sought under the form

$$\Delta t^2 \tilde{C}_h := D_h(I_h + (I_h - \Delta t^2 D_h^{-1} C_h)^{-1}). \quad (4)$$

Where D_h is a symmetric positive definite and diagonal (or block diagonal) matrix yet to be defined. It can be shown, using a Neumann series that, if $\varepsilon_h := \Delta t^2 \|D_h^{-1} C_h\|_2 < 1$, the definition (4) is a formal second order approximation of C_h . After algebraic manipulations one can see that the choice

$$D_h := B_h + 2\tilde{I}_h/\Delta t$$

gives the explicit modified equation *EME* scheme

$$\begin{aligned} U_h^{n+1} &= U_h^{n-1} + 2\Delta t (D_h^{-1} - \Delta t^2 D_h^{-1} C_h D_h^{-1}) \\ &\times \left(2\tilde{I}_h \frac{U_h^n - U_h^{n-1}}{\Delta t^2} - \tilde{A}_h U_h^n \right). \end{aligned} \quad (5)$$

3 Stability analysis

Energy technique. From the *EME* scheme, one can deduce the energy identity

$$\frac{1}{\Delta t} \left(\mathcal{E}_h^{n+\frac{1}{2}} - \mathcal{E}_h^{n-\frac{1}{2}} \right) = - \left(B_h + \Delta t^2 \tilde{C}_h \right) V_h^n \cdot V_h^n$$

where $V_h^n = 2(U_h^{n+1} - U_h^{n-1})/\Delta t$ and $\mathcal{E}_h^{n+\frac{1}{2}}$ is a semi-norm for the solution if the CFL condition for the modified equation is satisfied (see [2])

$$\eta_h := \Delta t^2 \|A_h\|_2 / 12 \leq 1. \quad (6)$$

Because of the approximation (4), the matrix $B_h + \Delta t^2 \tilde{C}_h$ has, in general, indefinite sign. However one can show that

$$(B_h + \Delta t^2 \tilde{C}_h) V_h \cdot V_h \geq -\alpha \varepsilon^2 \|D_h\|_2 (\mathcal{E}_h^{n+\frac{1}{2}} + \mathcal{E}_h^{n-\frac{1}{2}})$$

where α is a constant independent of R and Δt and $\varepsilon^2 \|D_h\|_2 \sim \Delta t$. Hence, using discrete Gronwall's lemma one shows that the solution's energy grows with n at most as an exponential function whose exponent is of order $n \Delta t^2$.

Eigenvalues analysis. Numerical applications suggest that this estimate is not sharp if $r(\mathbf{x})$ is small. Therefore, writing $r(\mathbf{x}) = R \hat{r}(\mathbf{x})$ where $\hat{r}(\mathbf{x})$ is a normalized dissipation profile we write the scheme equation (5) as

$$(U_h^{n+1}, U_h^n)^T = \mathcal{A}_h(R) (U_h^n, U_h^{n-1})^T$$

and investigate the eigenvalues $\lambda_h(R)$ of the parametrized matrix $\mathcal{A}_h(R)$. We show that if the CFL condition (6) is satisfied then all the eigenvalues of $\mathcal{A}(0)$ are complex conjugate, have a module exactly 1, are semi-simple, hence continuous w.r.t. R and differentiable at $R = 0$. Moreover we can show that

$$\lambda_h(R) = \lambda_h(0)(1 + R \mu_h) + o(R)$$

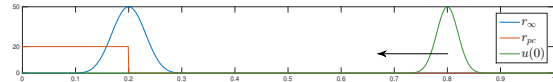
with, for some β independent of R and Δt ,

$$\mu_h := -\beta \Delta t \inf_{\phi_h \in \Sigma_h} \phi_h^T B_h \phi_h,$$

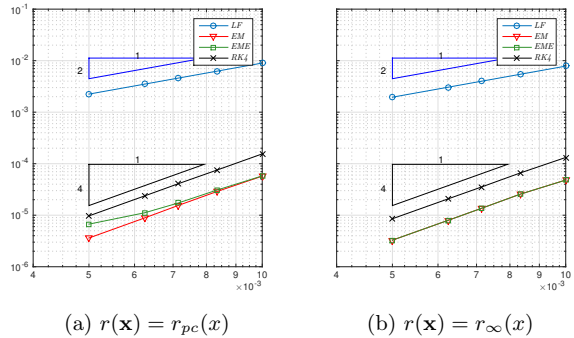
where Σ_h is the set of normalized eigenvectors of A_h . For standard finite element approximation, we can verify numerically, in 1D, that $\mu_h < 0$, meaning that for small values of R the solution's L^2 norm can not grow since $|\lambda_h(R)| < 1$.

4 Space/Time convergence in 1D

We consider a spatial discretization of problem (1) with $\Omega = [0, 1]$ and $T = 2$. We use spectral finite elements of order 4 on a uniform mesh. We consider the *LF*, *ME*, *EME* and *RK4* schemes. Being given a space step, the time step is chosen such as the maximum time step allowed when there is no dissipation (for *EM* and *EME*, it is (6)). We choose two dissipation functions $r_{pc}(x)$ or $r_\infty(x)$.



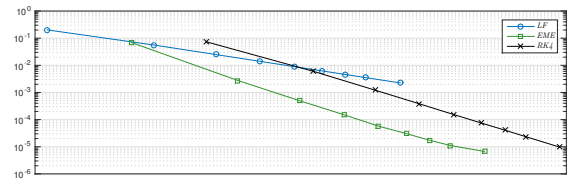
The convergence below are computed with a relative error computed in $C^0(0, T; L^2(\Omega))$ -norm



(a) $r(\mathbf{x}) = r_{pc}(x)$

(b) $r(\mathbf{x}) = r_\infty(x)$

The efficiency of the different explicit schemes can be compared. We assume that an iteration of *LF* have a cost of 1, 3 for the *EME* and 4 for the *RK4* (i.e. the number of mult. by A_h or C_h per it.). We see below that at a fixed cost the *EME* is ten times more accurate than *RK4*.



Estimated Cost / Relative Error ($r(\mathbf{x}) = r_{pc}(x)$)

References

- [1] M. A. Dablain, *The application of high order differencing for the scalar wave equation*, Geophysics, 1986, **1**, 51, pp. 54–66.
- [2] J.C. Gilbert and P. Joly, *Higher order time stepping for second order hyperbolic problems and optimal CFL conditions*, P. D. E.: Modeling and Numerical Simulation, 2008.

Acoustic Metamaterials in Moving Inhomogeneous Media

Wonju Jeon^{1,*}, Hyeonbin Ryoo¹

¹Department of Mechanical Engineering, Korea Advanced Institute of Science and Technology, 34141 Daejeon, South Korea

*Email: wonju.jeon@kaist.ac.kr

Abstract

During the past 10 years, most of acoustic metamaterial research has been done within a theoretical frame in which the medium is at rest. However, such acoustic metamaterials cannot preserve their unique properties or functions in the presence of flow. Therefore, in this study, we propose a theoretical framework to examine the effect of non-uniform mean flow on acoustic metamaterials for the purpose of understanding the physics of acoustic metamaterials within flow and designing a new concept of acoustic metamaterial.

Keywords: Acoustic metamaterial, scattering pattern, non-uniform flow, compressible fluid

1 Introduction

For a decade, the cloaking metamaterials have been attracting many researchers with high feasibility [1–3]. This concept, hiding an object optically or acoustically, is based on transformation optics or transformation acoustics. The acoustic cloak has been developed rapidly based on its analogy with the optical cloak, but there are clear limitations due to different physical properties between acoustics and electromagnetism [2, 3]. In this work, we focus on the presence of medium convection, which is a clear difference between acoustics and electromagnetism. Most of the acoustic metamaterial research have been done within a stationary medium, but the medium convection is important in acoustics unlike in electromagnetism. Thus, to be applied on a realistic situation, the research of acoustic cloaking metamaterials in flow field is important.

Recently, only a few researchers attempted to consider the acoustic cloak in the flow field. Huang *et al.* [3] introduced an analytic framework, which can consider the acoustic cloak in the flow field by taking the effect of non-uniform flow as equivalent sources. But, more of the real flow effects need to be considered theoretically [4–6]. Thus, in this study, we propose

a theoretical framework for an analysis of the flow effect on cloaking performance, by which we can get physical understandings and conceptual ideas for designing a new acoustic cloaks.

In Section 2, a formulation to study the acoustic cloaks in non-uniform and compressible flow field is summarized. In Section 3, the results of numerical simulation are illustrated and discussed with physical explanation.

2 Formulation

In this section, we propose a formulation to study scattering patterns of acoustic cloaks impinged by an acoustic wave in a moving medium. We derive a convective wave equation as an improved version of previous work [3] by including the non-uniform velocity in differential wave operator and taking the effect of compressibility in fluid into account.

$$\frac{D_0^2 p'}{D_0 t^2} - c^2 \nabla^2 p' = S_{eq}(\mathbf{x}, t) = S_{comp}(\mathbf{x}, t) + S_{non}(\mathbf{x}, t) \quad (1)$$

where $S_{comp}(\mathbf{x}, t) =$

$$\begin{aligned} & -\rho_0 c^2 [\mathbf{u}' \cdot \nabla + \frac{D_0}{D_0 t} (\frac{\gamma p'}{\rho_0 c^2}) + \frac{\gamma p'}{\rho_0 c^2} \frac{D_0}{D_0 t}] (\nabla \cdot \mathbf{u}_0) \\ & -\rho_0 c^2 \frac{D_0}{D_0 t} [\frac{1}{\gamma \rho_0} (\mathbf{u}' \cdot \nabla) \rho_0 + \frac{1}{\gamma c^2} (\mathbf{u}' \cdot \nabla) c^2] \\ & -c^2 \frac{D_0 p'}{D_0 t} (\mathbf{u}_0 \cdot \nabla) \frac{1}{c^2} \\ & -\rho_0 [\frac{D_0 p'}{D_0 t} (\mathbf{u}_0 \cdot \nabla) + \rho_0 c^2 \nabla p' \cdot \nabla] (\frac{1}{\rho_0}), \end{aligned} \quad (2)$$

$$\begin{aligned} S_{non}(\mathbf{x}, t) = & \\ & \nabla \cdot [2(\mathbf{u}' \cdot \nabla) \mathbf{u}_0 + \frac{\rho'}{\rho_0} ((\mathbf{u}_0 \cdot \nabla) \mathbf{u}_0)], \end{aligned} \quad (3)$$

where $D_0/D_0 t$ denotes the total derivative defined by $\partial/\partial t + \mathbf{u}_0 \cdot \nabla$, ρ is density, t is time, \mathbf{u} is velocity, p is pressure, c is speed of sound, and γ is ratio of specific heats.

As shown in Eq. (1), the non-uniform velocity is included in the differential operator. $S_{eq}(\mathbf{x}, t)$

indicates the equivalent source terms that can be interpreted as a coupled effect of background flow with incident wave. Such mathematically abstruse terms are divided into two parts with their own physical meanings, $S_{comp}(\mathbf{x}, t)$ for compressibility in fluid and $S_{non}(\mathbf{x}, t)$ for non-uniformity of flow.

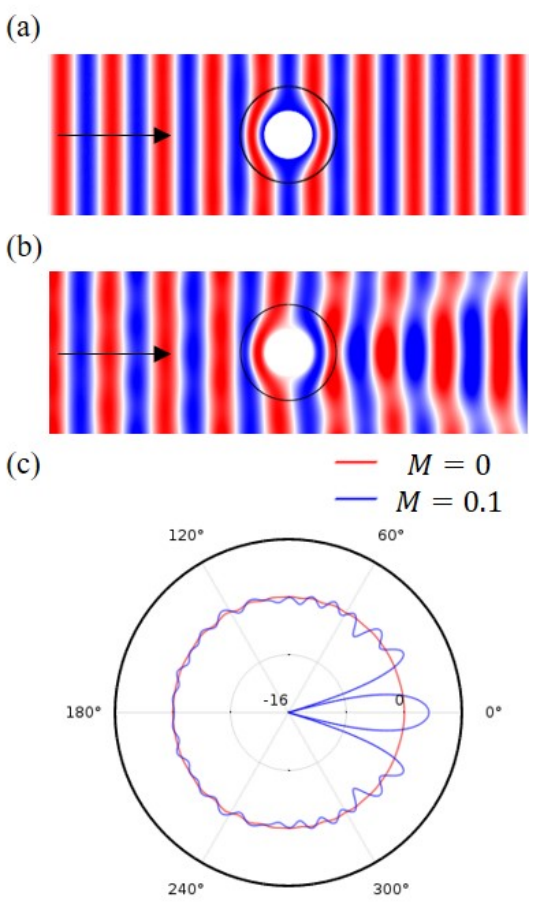
3 Results and Discussions

In this section, by solving Eq. (1) of present formulation with FEM, the numerical results are illustrated and discussed briefly. In numerical simulations, we used the existing acoustic cloak which was designed in a stationary medium [2]. The plane wave is impinging on acoustic cloak with Helmholtz number of $kR_1 = 3$. The background flow has a subsonic Mach number of $M=0.1$.

Figure 1 shows the numerical results of acoustic pressure around the acoustic cloak in the flow field for $M = 0$ and 0.1 by using the present formulation. As shown in Fig. 1(a), the acoustic cloak can hide the object almost perfectly. However, as shown in Fig. 1(b), the acoustic cloak loses its unique property to make an object acoustically invisible in presence of background flow. As compared in Fig. 1(c), the existing acoustic cloak clearly shows the unwanted scattering near the geometrical zone of shadow.

In this study, we proposed a theoretical framework to examine the scattering pattern of acoustic cloak in the presence of non-uniform mean flow. In numerical simulations, the existing cloak could not make an object acoustically invisible within flow. In order to understand the scattering from the acoustic cloak within flow, the equivalent source terms were divided into two terms with their own physical meanings. The proposed theoretical framework is expected to accurately predict the scattering from the acoustic cloak in a moving medium and give us an idea to design a new acoustic cloak.

References

- 
- Figure 1: Acoustic pressure scattered from the acoustic cloak; (a) Contour of acoustic pressure for $M = 0$, (b) Contour of acoustic pressure for $M = 0.1$, and (c) Comparison of directivity patterns in dB scale
- [1] J. B. Pendry, D. Schrig and D. R. Smith, Controlling electromagnetic fields, *Science* 312 (2006), pp. 1780-1782.
 - [2] S. A. Cummer and Schurig, D., One path to acoustic cloaking, *New J. Phys.* 9 (2007), pp. 45.
 - [3] X. Huang, S. Zhong and O. Stalnov, Analysis of scattering form an acoustic cloak in a moving fluid, *J. Acoust. Soc. Am.* 135 (2014), pp. 2571-2580.
 - [4] O. M. Phillips, On the generation of sound by supersonic turbulent shear layers, *J. Fluid Mech* 9 (1960), pp. 1-28.
 - [5] G. M. Lilley, On the noise from jets, *Agard cp-131* 13 (1974), pp. 12.
 - [6] M. E. Goldstein, *Aeroacoustics*, McGraw-Hill, 1976.

Wave Diffraction by Random Surfaces: Uncertainty Quantification via Sparse Tensor Boundary Elements

Paul Escapil-Inchauspé¹, Carlos Jerez-Hanckes^{1,*}

¹Institute for Mathematical and Computational Engineering, Pontificia Universidad Católica de Chile, Santiago, Chile

*Email: cjerez@ing.puc.cl

Abstract

We consider the numerical solution of time-harmonic scattering of acoustic and electromagnetic waves from obstacles with uncertain geometries. Using first-order shape derivatives, we derive deterministic boundary integral equations for the mean field and the two-point correlation function of the random solution for a soft-obstacle Dirichlet problem. Sparse tensor Galerkin discretizations of these equations are implemented with the so-called *combination technique*. We generalize the method to non-nested meshes using a nodal transfer operator. Similar discretization errors for the covariance is achieved with $\mathcal{O}(N \log N)$ degrees of freedom instead of $\mathcal{O}(N^2)$. Performance comparison of our approach to classic Monte-Carlo Galerkin formulation is given for different shapes. Finally, we verify the robustness of the sparse tensor approximation and compare it to low-rank approximations techniques.

Keywords: uncertainty quantification, sparse tensor approximation, boundary integral equations

1 Introduction

Let a nominal scatterer $D_0 \in \mathbb{R}^3$ be an open bounded perfect conducting/soft C^2 -domain with simply connected boundary $\Gamma_0 := \partial D_0$ and set $D_0^c = \mathbb{R}^3 \setminus \overline{D}_0$. We seek to model diffracted fields by small amplitude random shape variations of the nominal domain D_0 . For this, let $(\Omega, \mathbb{P}, \Sigma)$ be a probability space and, for simplicity, consider perturbations of the form:

$$(\mathbf{x}, \omega) := \kappa(\mathbf{x}, \omega) \mathbf{n}_0(\mathbf{x}), \quad \omega \in (\Omega, \mathbb{P}, \Sigma), \quad (1)$$

with $\mathbf{x} \in \Gamma_0$, and \mathbf{n}_0 the exterior unit normal vector to the reference domain D_0 . The amplitude $\kappa(\mathbf{x}, \omega)$ is such that it belongs to the Bochner space $L^\infty(\Omega, \mathbb{P}; C^2(\Gamma_0; \mathbb{R}))$, i.e.

$$\sup_{\omega \in \Omega} \|\kappa(\cdot; \omega)\|_{C^2(\Gamma_0; \mathbb{R})} < \infty.$$

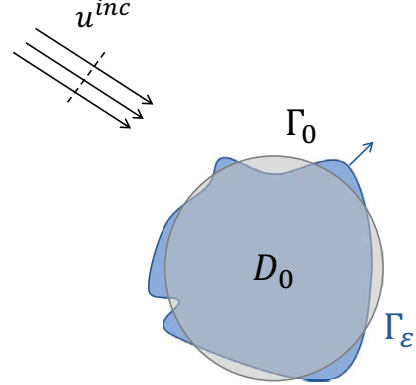


Figure 1: Nominal and perturbed domains

Furthermore, we assume the distribution κ to be centered at zero. For sufficiently small $\varepsilon > 0$, we define families of randomly perturbed boundaries by:

$$\Gamma_\varepsilon(\omega) := \{\mathbf{x} + \varepsilon \Psi(\mathbf{x}, \omega)\} : \mathbf{x} \in \Gamma_0\}, \quad (2)$$

defining interior and exterior domains $D_\varepsilon(\omega)$ and $D_\varepsilon^c(\omega)$, accordingly. The transformation (2) defines an isomorphism with Γ_0 .

Assuming a time-harmonic regime and an incident plane wave U^{inc} , we seek a total acoustic field $U_\varepsilon := U^{\text{inc}} + U_\varepsilon^s$ satisfying the following boundary value problem:

$$\Delta U_\varepsilon(\mathbf{x}) + k_0^2 U_\varepsilon(\mathbf{x}) = 0 \quad \mathbf{x} \in \mathbb{R}^3 \setminus D_\varepsilon(\omega), \quad (3)$$

$$\gamma_D U_\varepsilon^s(\mathbf{x}) = -\gamma_D U^{\text{inc}} \quad \mathbf{x} \in \Gamma_\varepsilon(\omega), \quad (4)$$

$$\left| \frac{\partial U_\varepsilon^s}{\partial r} - ik_0 U_\varepsilon^s \right| = o(r^{-1}) \quad r \rightarrow \infty, \quad (5)$$

with $k_0 \in \mathbb{R}_+$ a given wavenumber, $r = \|\mathbf{x}\|_2$ where $\|\cdot\|_2$ denotes the Euclidean norm and γ_D the Dirichlet trace. The above problem (3)-(5) is well posed [5] as well as its electromagnetic counterpart. Since U_ε is Fréchet differentiable on $D_\varepsilon^c(\omega)$ [4], for each realization $\omega \in (\Omega, \mathbb{P}, \Sigma)$, we can derive the shape-Taylor expansion:

$$U_\varepsilon(\mathbf{x}, \omega) = U_0(\mathbf{x}) + \varepsilon U'_0(\mathbf{x}, \omega) + \mathcal{O}(\varepsilon^2), \quad (6)$$

for $\mathbf{x} \in D_0^c \cap D_\varepsilon^c$, with U_0 being the solution in the nominal domain and U'_0 the shape derivative defined as

$$U'_0(\mathbf{x}, \omega) := \lim_{\varepsilon \rightarrow 0} \frac{1}{\varepsilon} (U_\varepsilon(\mathbf{x}, \omega) - U_0(\mathbf{x})).$$

Moreover, by analogy with [1], its local shape derivative U'_0 solves the following Dirichlet Problem over D_0^c :

$$\Delta U'_0(\mathbf{x}) + k_0^2 U'_0(\mathbf{x}) = 0 \quad \mathbf{x} \in D_0^c, \quad (7)$$

$$\gamma_D U'_0(\mathbf{x}) = -\kappa(\mathbf{x}, \omega) \gamma_N U_0 \quad \mathbf{x} \in \Gamma_0, \quad (8)$$

along with radiation conditions as in (5) and $\gamma_N U_0$ being the Neumann trace of the nominal solution. A similar problem holds for the electromagnetic case [3].

2 Deterministic solvers and sparse tensor approximation

Our goal is to estimate the statistical first and second moments:

$$\mathbb{E}[U_\varepsilon](\mathbf{x}) := \int_{\Omega} U_\varepsilon(\mathbf{x}, \omega) d\mathbb{P}(\omega)$$

and $\text{corr}_{U_\varepsilon}(\mathbf{x}, \mathbf{y}) := \mathbb{E}[U_\varepsilon(\mathbf{x}, \cdot) U_\varepsilon(\mathbf{y}, \cdot)]$. Based on the expansion (6), we can prove that

$$\mathbb{E}[U_\varepsilon](\mathbf{x}) = U_0(\mathbf{x}) + \mathcal{O}(\varepsilon^2)$$

and $\text{var}_{U_\varepsilon}(\mathbf{x}) = \varepsilon^2 \mathbb{E}[U'_0(\mathbf{x}, \cdot)^2] + \mathcal{O}(\varepsilon^3)$, with the first term deduced from

$$\text{corr}_{U'_0}(\mathbf{x}, \mathbf{y}) := \mathbb{E}[U'_0(\mathbf{x}, \cdot) U'_0(\mathbf{y}, \cdot)],$$

which is the unique solution of a suitably defined tensorized problem [6]. We can represent U_0 and U'_0 using single layer potentials. Thus, for each one, surface densities must solve the following boundary integral equations [5]:

$$\mathcal{V} \gamma_N U_0 = U^{inc} \quad \text{on } \Gamma_0, \quad (9)$$

$$(\mathcal{V} \otimes \mathcal{V}) \Theta = C \quad \text{on } \Gamma_0 \times \Gamma_0, \quad (10)$$

where \mathcal{V} is the single layer boundary integral operator with its corresponding tensor form for the covariance, $\Theta := \text{corr}_{\gamma_N U'_0}$ and $C(\mathbf{x}, \mathbf{y}) := \text{corr}_\kappa(\mathbf{x}, \mathbf{y}) \gamma_N U_0(\mathbf{x}) \gamma_N U_0(\mathbf{y})$.

By applying the program defined in [6] over nested meshes along with combination technique developed [2], we can obtain approximations of the second moments using $\mathcal{O}(N \log N)$ degrees of freedom with convergence rates as shown in Figure 2. By coercivity of \mathcal{V} , a minimum refinement level L_0 is required to observe convergence. Moreover, we will show that these results also hold for non-nested meshes by using nodal transfer operators.

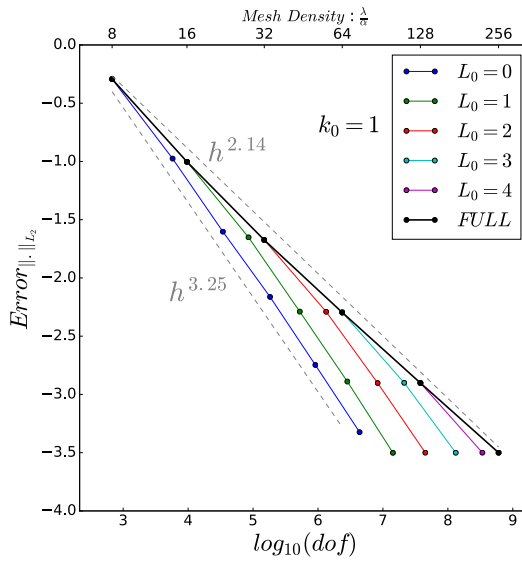


Figure 2: Convergence results for $k_0 = 1$.

References

- [1] H. Harbrecht, R. Schneider, and C. Schwab, *Sparse second moment analysis for elliptic problems in stochastic domains*, Numerische Mathematik, 109 (2008), pp. 385–414.
- [2] H. Harbrecht, M. Peters and M. Siebenmorgen, *Combination technique based k -th moment analysis of elliptic problems with random diffusion*, Journal of Computational Physics, 252 (2013), pp. 128–141.
- [3] C. Jerez-Hanckes and C. Schwab, Electromagnetic wave scattering by random surfaces: Uncertainty quantification via sparse tensor boundary elements, *IMA Journal of Numerical Analysis* (2016).
- [4] R. Potthast, *Frechet differentiability of boundary integral operators in inverse acoustic scattering*, Inverse Problems, 10 (1994), p. 431.
- [5] S. Sauter and C. Schwab, *Boundary Element Methods*, Springer Series in Computational Mathematics, Springer Berlin Heidelberg, 2010.
- [6] T. von Petersdorff and C. Schwab, *Sparse finite element methods for operator equations with stochastic data*, Applications of Mathematics, 51 (2006), pp. 145–180.

Nonlinear models of lasers, noise, and the SALT equations**Steven Johnson^{1,*}**¹Mathematics Department, Massachusetts Institute of Technology

*Email: stevenj.mit@gmail.com

Abstract

Nonlinear models of lasers, noise, and the SALT equations Although the theoretical description of lasing has been studied for many decades, only recently has it become practical to accurately model the lasing process in complex microstructured lasers, such as random lasers or photonic-crystal laser cavities. A key enabling factor is the SALT (steady state ab-initio laser theory) description pioneered by Tureci, Stone, and others starting in 2006, which reduces the complex time-dependent Maxwell-Bloch equations to a much simpler frequency-domain nonlinear eigenproblem for steady-state lasing modes. The SALT equations themselves resisted general solution for several years, but recently we have developed efficient numerical approaches to solving SALT for complex 3d structures. We can even exploit existing linear Maxwell solvers, simply performing a sequence of linear solves in an Anderson-accelerated loop to solve the nonlinear problem. Moreover, given this numerical foundation, a whole host of new analytical and semi-analytical results become possible, via perturbation theory around the SALT modes. This includes a new understanding of degenerate lasing modes, and a new generalized theory of the laser linewidth and relaxation sidebands arising from quantum fluctuations in the laser. In this talk, we review the mathematical description of lasing and explain why a nonlinear eigenproblem results above threshold, and outline several new developments in laser theory that have been enabled by SALT.

Transparent Boundary Conditions for the Wave Propagation in Fractal Trees

Patrick Joly^{1,*}, Maryna Kachanovska¹, Adrien Semin²

¹POEMS, ENSTA ParisTech-INRIA-CNRS, Université Paris-Saclay, Palaiseau, France

²Technische Universität Berlin, Berlin, Germany

*Email: patrick.joly@inria.fr

Abstract

This work is dedicated to an efficient resolution of the wave equation in self-similar trees (e.g. wave propagation in a human lung). In this case it is possible to avoid computing the solution at deeper levels of the tree by using the transparent boundary conditions. The corresponding DtN operator is defined by a functional equation in the frequency domain. In this work we propose and compare two approaches to the discretization of this operator in the time domain. The first one is based on the multistep convolution quadrature, while the second one stems from the rational approximations.

Keywords: fractal tree, wave equation, convolution quadrature, rational approximations

1 Introduction

Given a compact self-similar p -adic tree \mathcal{T} consisting of a countable set of edges and vertices, we study the wave equation defined on its edges

$$\mu\partial_{tt} - \partial_x(\mu\partial_x u) = 0 \quad (1)$$

equipped with condition $u(M^*, t) = f(t)$ at the root vertex M^* of \mathcal{T} . The function μ is constant along every edge Σ . If the length of Σ is ℓ , the length of each of its p children Σ_j , $j = 0, \dots, p-1$ is $\alpha_j \ell$ with $0 < \alpha_j < 1$. Moreover the value of μ along Σ_j is μ_j times its value along Σ , with $\mu_j > 0$. The problem (1) is completed with vertex conditions explained in Figure 1. The problem (1) is equipped with Neumann or Dirichlet boundary conditions at 'infinity' (notice however that the tree is compact), incorporated into the variational formulation of the problem. E.g., for Neumann:

$$\begin{aligned} \frac{d^2}{dt^2}(\mu u, v)_{\mathcal{T}} + (\mu \partial_x u, \partial_x v)_{\mathcal{T}} &= 0, \\ v \in H_{\mu}^1, \quad u \in C^1(0, T; L_{2,\mu}) \cup C^0(0, T; H_{\mu}^1). \end{aligned} \quad (2)$$

For a precise definition of the spaces and scalar products see [1]. We restrict ourselves to the

case

$$\sum_i \mu_i \alpha_i < 1, \quad \sum_i \mu_i / \alpha_i > 1 \quad (3)$$

so that Dirichlet and Neumann problem differ and the embedding $H_{\mu}^1 \subset L_{\mu}^2$ is compact.

In order to perform the computation, we truncate the tree at a certain level using a transparent boundary condition at each end point M :

$$\partial_x u(M) = \sum_{i=0}^{p-1} \mu_i \Lambda_i(\partial_t) u(M, \cdot)$$

where $\Lambda_i(\partial_t) = \alpha_i^{-1} \ell^{-1} \Lambda(\alpha_i \ell \partial_t)$, $\Lambda(\partial_t)$ is the DtN operator associated with a reference tree (whose root edge has length 1) and ℓ the length of the edge terminating at M . $\Lambda(\partial_t)$ is a convolution operator whose symbol $\Lambda(\omega)$ (through $\partial_t \leftrightarrow -i\omega$) is not known explicitly. However, this function satisfies

$$\begin{aligned} \Lambda(\omega) \cos(\omega) - \omega \sin \omega &= \\ \left(\cos \omega + \Lambda(\omega) \frac{\sin \omega}{\omega} \right) \left(\sum_{i=0}^{p-1} \frac{\mu_i}{\alpha_i} \Lambda(\alpha_i \omega) \right). \end{aligned} \quad (4)$$

A meromorphic solution $\Lambda(\omega)$ to the above problem is unique, provided the value $\Lambda(0)$ (which depends whether the Dirichlet or the Neumann problems are solved). In [1] the authors exploited this property to propose transparent BCs based on the Laurent expansion of $\Lambda(\omega)$ near $\omega = 0$. However, this requires truncating the tree at the level where $|\ell\omega| \ll 1$. The goal of this work is to relax this condition.

2 Approach 1: Convolution Quadrature

We suggest to apply a trapezoid convolution quadrature [2] for the approximation of $\Lambda(\partial_t)$. For the discretization of the volumetric terms in time we use an explicit leap-frog scheme. More precisely, denoting by \mathcal{T}_i the subtree for which the computation is done using FEM (for simplicity we assume that all end edges have same

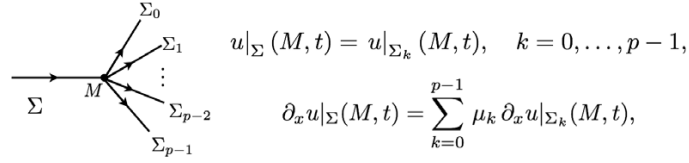


Figure 1: Edge transmission conditions

length ℓ), and by $\mathcal{T}_e = \mathcal{T} \setminus \mathcal{T}_i$, we rewrite (2) as:

$$\begin{aligned} & \frac{d^2}{dt^2}(\mu u, v)_{\mathcal{T}_i} + (\mu \partial_x u, \partial_x v)_{\mathcal{T}_i} \\ & + \frac{d^2}{dt^2}(\mu u, v)_{\mathcal{T}_e} + (\mu \partial_x u, \partial_x v)_{\mathcal{T}_e} = 0, \quad v \in H_\mu^1. \end{aligned} \quad (5)$$

After space discretization along \mathcal{T}_i (not along \mathcal{T}_e) we discretize in time, with constant Δt , $u|_{\mathcal{T}_i}$ with leapfrog and $u|_{\mathcal{T}_e}$ with the trapezoidal rule:

$$\begin{aligned} & \left(\mu \frac{u_{n+1} - 2u_n + u_{n-1}}{\Delta t^2}, v \right)_{\mathcal{T}_i} + (\mu \partial_x u_n, \partial_x v)_{\mathcal{T}_i} \\ & + \left(\mu \partial_x \frac{u_{n+1} + 2u_n + u_{n-1}}{4}, \partial_x v \right)_{\mathcal{T}_e} = 0. \end{aligned}$$

Denoting $u_{\Delta t} = (u_n)$ the semi-discrete solution, this can be rewritten in an equivalent way, $\{M_k\}$ being the set of end nodes of \mathcal{T}_e ,

$$\begin{aligned} & \left(\mu \frac{u_{n+1} - 2u_n + u_{n-1}}{\Delta t^2}, v \right)_{\mathcal{T}_i} + (\mu \partial_x u_n, \partial_x v)_{\mathcal{T}_i} \\ & + \sum_k \sum_{j=0}^{p-1} \mu_j (\Lambda_j(\partial_t^{\Delta t}) u_{\Delta t})_{n+1} v(M_k) = 0. \end{aligned}$$

Here $\Lambda_j(\partial_t^{\Delta t})$ are the discrete DtN operators with symbol $\Lambda_{j,\Delta t}(\omega) := \ell^{-1} \Lambda(\alpha_j \ell \Omega_{\Delta t}(\omega))$, where

$$\Omega_{\Delta t}(\omega) = \frac{2 \sin \omega \Delta t}{\Delta t (1 + \cos \omega \Delta t)}.$$

Therefore the operator $\Lambda_j(\partial_t^{\Delta t})$ reads

$$(\Lambda_j(\partial_t^{\Delta t}) u_{\Delta t})_n = \sum_{q=0}^n \lambda_j^{n-q}(\Delta t) u_q(M_k),$$

$$\text{where } \Lambda_{j,\Delta t}(\omega) = \sum_{n=0}^{+\infty} \lambda_j^n(\Delta t) e^{in\omega \Delta t}.$$

The computation of the convolution weights $\lambda_j^n(\Delta t)$, $n \geq 0$, requires a procedure of the evaluation of $\Lambda(\omega)$ in the complex plane; one way to do so is described in [1]. The stability of the scheme can be shown by energy techniques.

3 Approach 2: Rational Approximations

Using the coercivity properties of a DtN operator, one can show that $\omega^{-1} \Lambda(\omega)$ is a Herglotz function (i. e. an analytic map from the upper complex half-space into itself). Moreover, $\Lambda(\omega)$ is of the form

$$\Lambda(\omega) = \Lambda(0) + \sum_{p=0}^{\infty} \frac{a_p \omega^2}{\omega^2 - \Omega_p^2},$$

with $\Omega_p \neq 0$, $a_p > 0$ and $\Lambda(0) \geq 0$. The idea is to look for rational approximations of $\Lambda(\omega)$ in a class of rational Herglotz functions. For example, such an approximation $\Lambda^N(\omega)$ can be obtained by truncating at order N the above sum. In this case (5) becomes: for all $v \in H_{\mu,0}(\mathcal{T})$,

$$\begin{aligned} & \frac{d^2}{dt^2}(\mu u, v)_{\mathcal{T}_i} + (\mu \partial_x u_n, \partial_x v)_{\mathcal{T}_i} \\ & + \sum_k \sum_{j=0}^{p-1} \mu_j \Lambda_j^N(\partial_t) u(M_k, \cdot) v(M_k) = 0, \end{aligned} \quad (6)$$

where the operator $\Lambda_i^N(\partial_t)$ is given by

$$\begin{aligned} \Lambda_i^N(\partial_t) \varphi &= \alpha_i^{-1} \ell^{-1} (\Lambda_i(0) \varphi + \sum_{p=0}^N a_p \partial_t^2 \psi_{i,p}), \\ \partial_t^2 \psi_{i,p} + (\ell \alpha_i)^{-2} \Omega_p^2 \psi_{i,p} &= \varphi, \quad 0 \leq p \leq N. \end{aligned}$$

Then the volumetric terms in (6) can be semidiscretized in time with the help of the explicit leapfrog scheme, and the terms related to the boundary equations with the help of the implicit trapezoid rule, similarly to how it is done for the Maxwell equations in dispersive media.

References

- [1] P. Joly and A. Semin, Wave Propagation in Fractal Trees. Mathematical and Numerical Issues. Submitted.
- [2] C. Lubich, Convolution Quadrature and Discretized Operational Calculus. I. Numer. Math. 52, 129-145 (1988).

A Discontinuous Galerkin Difference Discretization of the Wave Equation

Fritz Juhnke^{1,*}, Thomas Hagstrom¹

¹Department of Mathematics, Southern Methodist University, Dallas, TX, U.S.A.

*Email: kjuhnke@smu.edu

Abstract

High-order finite difference (FD) methods for evolving simulated waves in time typically permit larger time steps than discontinuous Galerkin (DG) methods of equal order and degrees of freedom. This gap in efficiency widens as the order increases. If, however, one uses finite-difference-style basis functions within a Galerkin formulation, one can enjoy the stability benefits of a built-in discrete energy and upwinding without sacrificing the efficiency of large time steps. We call this new approach the discontinuous Galerkin difference (DGD) method.

Keywords: high-order, upwind, finite difference, discontinuous Galerkin

1 Introduction

The most popular method for simulating electromagnetic waves is the Yee scheme, a second-order-accurate finite difference method. Inexorably advancing computing power is gradually forcing practitioners to abandon the Yee scheme in favor of methods with a higher order of accuracy. The more wavelengths within the domain, the more the accuracy of a second-order method lags behind that of, say, a sixth-order method.

One thorny drawback of higher-order FD methods is the difficulty of achieving stable boundary closures. Stability issues in FD methods have been a strong impetus in the adoption of Galerkin methods. A Galerkin discretization of the continuous wave equation automatically translates the physically conserved energy into a discrete conserved energy. A discontinuous Galerkin discretization allows in addition the stabilizing influence of upwind fluxes.

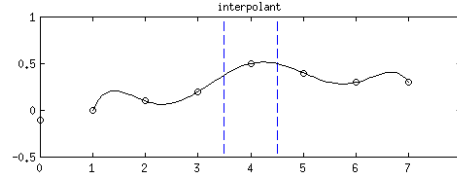
The stability of high-order DG methods has, however, historically required the sacrifice of some of the fabulous efficiency of high-order FD methods. The true solution on each DG cell is interpolated with high-degree polynomials which have large derivatives near the cell boundaries. As the degree of the polynomials increases, so do their derivatives, which inherently limits the size of the time step one can take when evolving

the discretized system of equations.

The innovation of the discontinuous Galerkin difference method is to approximate the true solution with the same polynomials that a high-order FD method would use, in particular using data from outside each cell to interpolate within the cell. This forestalls the problem of large derivatives near cell boundaries, thus large time steps are once again feasible [1].

2 DGD basis functions

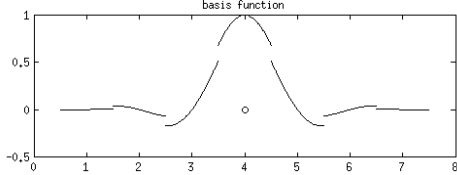
We illustrate in one dimension; higher-dimensional basis functions are tensor products of the one-dimensional basis functions. Also we illustrate with a degree-six polynomial interpolant although the method may be of arbitrary order. We use a uniform grid with a single node at the center of each cell.



The Lagrange interpolant is formed from the data at the center of seven different cells, but is used to approximate the solution only in the middle cell, between the dashed lines in the above figure. Note that high derivatives apparent at the edges of the interpolant are irrelevant because the interpolant is not used outside of the middle cell. Each other cell is interpolated across the seven nodes centered across that cell.

Conversely, the data at each node influences the interpolant in its own cell and in each of the three neighboring cells to each side. We can thus form a nodal basis with basis functions as illustrated below.

The discontinuity of the basis functions is a feature, not a bug. Insofar as the true solution can be approximated by a degree six polynomial, a linear combination of our basis functions will match it exactly, with no discontinu-



ties in the sum. If there are any discontinuities in our approximation, they must be due to “higher frequencies” that can’t be represented by polynomials of degree six. Such jumps on cell boundaries may be penalized by upwind fluxes, which dissipate (non-resolvable) high-frequency modes, thus enhancing numerical stability.

As this is simply a basis, we can use any DG formulation that can be applied to the partial differential equation of interest. In this work we focus on the scalar wave equation and employ the upwind DG method from [2]. However we could equally well have used IPDG [3], SIPDG [4], or LDG [5].

3 Boundary closures

DGD basis functions are identical up to translation, except near the domain boundaries. Outside the domain, we extend the grid with enough “ghost nodes” (e.g. three for degree six polynomials) so that the cells on the edge of the domain can be interpolated.

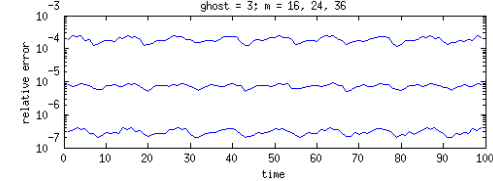
Values at the ghost nodes may be simply evolved as additional degrees of freedom in the discretization. Alternatively, one may choose to evolve only interior degrees of freedom, and obtain values at the ghost nodes by extrapolating interior nodes. In practice, we have had good results from evolving the one ghost node nearest the domain and extrapolating to the rest. It is important to note that regardless of whether ghost values are evolved or extrapolated, the Galerkin formulation remains energy-stable.

We impose boundary conditions by means of fluxes at the domain boundaries, just as with any DG method.

4 A numerical example

We discretized the two-dimensional scalar wave equation on a unit square with DGD basis functions and the formulation of [2] with 16, 24, and 36 grid points in each dimension. The basis polynomials were degree seven in position and degree six in velocity. The true solution had wavelengths around one half. Domain bound-

ary fluxes were calculated from outside states given by the true solution.



Simulations were stable to time 100 with a “CFL” of 0.5. The observed order of convergence was 7.6.

5 Acknowledgements

This work was supported by the U.S. Department of Energy ASCR Applied Math Program and NSF Grant DMS-1418871. Any opinions, findings, and conclusions or recommendations expressed in this material are those of the authors and do not necessarily reflect the views of the Department of Energy or the National Science Foundation.

References

- [1] J. W. Banks and T. Hagstrom, On Galerkin Finite Difference Methods, *J. Comput. Phys.* **313** (2016), pp. 4367–4382.
- [2] D. Appelö and T. Hagstrom, A New Discontinuous Galerkin Formulation for Wave Equations in Second Order Form, *SIAM J. Num. Anal.* **53** (2015), pp. 2705–2726.
- [3] B. Rivière and M. Wheeler, Discontinuous Finite Element Methods for Acoustic and Elastic Wave Problems, *Contemp. Math.* **329** (2003), pp. 271–282.
- [4] M. Grote, A. Schneebeli and D. Schötzau, Discontinuous Galerkin Finite Element Method for the Wave Equation, *SIAM J. Num. Anal.* **44** (2006), pp. 2408–2431.
- [5] C.-S. Chou, C.-W. Shu and Y. Xing, Optimal Energy Conserving Local Discontinuous Galerkin Methods for Second-Order Wave Equation in Heterogeneous Media, *J. Comput. Phys.*, **272** (2014) 88–107.

Analytic solutions to the extended Korteweg – de Vries equation

Anna Karczewska^{1,*}, **Piotr Rozmej**², **Eryk Infeld**³, **George Rowlands**⁴

¹Faculty of Mathematics, Computer Science and Econometrics, University of Zielona Góra, Poland

² Faculty of Physics and Astronomy, University of Zielona Góra, Poland

³National Centre for Nuclear Research, Warszawa, Poland

⁴Department of Physics, University of Warwick, Coventry, UK

*Email: A.Karczewska@wmie.uz.zgora.pl

Abstract

Over the last few decades, the KdV equation has been extended to include higher order effects. Although this equation has only one conservation law, exact periodic and solitonic solutions are shown to exist.

Keywords: 02.30.Jr, 05.45.-a, 47.35.Bb

1 Introduction

The KdV equation is one of the most ubiquitous physical equations. It consists of the mathematically simplest possible terms representing the interplay of the nonlinearity and dispersion. This simplicity may be one of the reasons for success. We investigate this equation improved as derived from the Euler inviscid and irrotational water equations.

Just as for conventional KdV, two small parameters are assumed: wave amplitude/depth (a/H) and depth/wavelength squared (H/l)². These dimensionless expansion constants are called α and β . We take the expansion one order higher. The new terms will then be of second order. This procedure limits considerations to waves for which the two parameters are comparable.

The next approximation to Euler's equations for long waves over a shallow riverbed is (η is the elevation above a flat surface divided by H)

$$\begin{aligned} \eta_t + \eta_x + \frac{3}{2}\alpha\eta\eta_x + \frac{1}{6}\beta\eta_{3x} - \frac{3}{8}\alpha^2\eta^2\eta_x \\ + \alpha\beta\left(\frac{23}{24}\eta_x\eta_{2x} + \frac{5}{12}\eta\eta_{3x}\right) + \frac{19}{360}\beta^2\eta_{5x} = 0. \end{aligned} \quad (1)$$

In (1) and subsequently we use low indexes for derivatives ($\eta_{nx} \equiv \frac{\partial^n\eta}{\partial x^n}$). This second order equation was called by Marchant and Smyth [1] the *extended KdV*. It was also derived in a different way in [2, 3]. We call it **KdV2**. It is not integrable. However, by keeping the same terms but changing one numerical coefficient we can

obtain an integrable equation [4]. Not only is KdV2 non integrable, it only seems to have one conservation law (volume or mass). A simple derivation of adiabatically conserved quantities can be found in [4].

2 Periodic solutions for KdV2

We look for periodic nonlinear wave solutions of KdV2 equation (1). Introduce $y := x - vt$. Then $\eta(x, t) = \eta(y)$, $\eta_t = -v\eta_y$ and equation (1) takes the form of the ODE

$$\begin{aligned} (1-v)\eta_y + \frac{3}{2}\alpha\eta\eta_y + \frac{1}{6}\beta\eta_{3y} - \frac{3}{8}\alpha^2\eta^2\eta_y \\ + \alpha\beta\left(\frac{23}{24}\eta_y\eta_{2y} + \frac{5}{12}\eta\eta_{3y}\right) + \frac{19}{360}\beta^2\eta_{5y} = 0. \end{aligned} \quad (2)$$

Now assume that periodic solutions exist in the same form as solutions of the KdV equation

$$\eta(y) = A \operatorname{cn}^2(By, m) + D, \quad (3)$$

where A, B, D are as yet unknown constants (m is the elliptic parameter). The constant D ensures that the volume of water is the same for all m .

Insertion of (3) into (2) leads to a set of three coupled equations for four unknowns A, B, D, v . The fourth equation, volume conservation condition completes the set. Then all unknowns can be calculated as functions of the elliptic parameter m and KdV2 parameters α and β .

One of the equations of this set is a quadratic equation for B^2 . Then there are two roots:

$$(B^2)_1 = \frac{A\alpha}{m\beta} z_1 \quad \text{and} \quad (B^2)_2 = \frac{A\alpha}{m\beta} z_2,$$

where

$$z_1 = \frac{43 - \sqrt{2305}}{152} \quad \text{and} \quad z_2 = \frac{43 + \sqrt{2305}}{152}.$$

A particular solution of this set of equations is obtained for $m = 1$. In this case $\operatorname{cn}^2(By, 1) \rightarrow \operatorname{Sech}^2(By)$ and $A > 0$, therefore only z_2 assures

real-valued B . Then A, B, v are expressed by z_2, α, β . This particular soliton solution was found by us in [3, Sec. IV].

For periodic solutions situation is more complex. There are two branches of solutions. In one branch, connected to z_2 , real-valued B are obtained for $m \in (m_s, 1)$, where $m_s \approx 0.9611495$ is the root of equation expressed by Jacobi elliptic functions. For this branch amplitudes A are always positive, that is, the wave profile are 'normal' cnoidal functions where crests are larger than troughs. The parameters A, B, D, v of solutions together with the wavelength λ and the period T for this branch are shown in figure 1 for $\alpha = \beta = 0.1$.

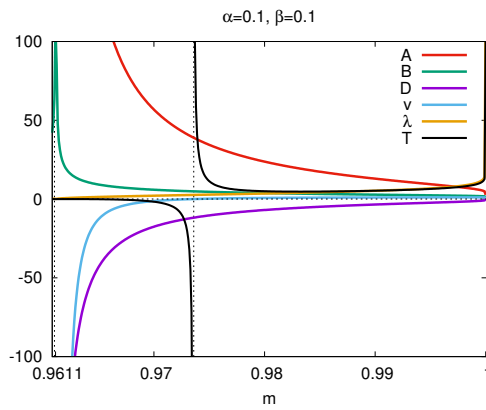


Figure 1: Parameters of the solution as functions of m for the branch related to $z = z_2$. Case $\alpha = \beta = \frac{1}{10}$.

The second branch of solutions is connected to z_1 . Then real values for B are obtained for $m \in (0, m_s)$, with amplitudes $A < 0$. This means that the wave profiles have the form of **inverted** cnoidal functions. For $m \rightarrow 0$ these solutions tend to a cosine functions with vanishing amplitude. Figure 2 display results for parameters of solutions of the second branch.

The most important difference of these exact solutions and KdV solutions is the fact that KdV2 admisses solutions of the form of inverted cnoidal function. The complexity shown in figures 1 and 2 is the result of imposing the condition of volume conservation.

In both branches of solutions there exist values of m for which solutions do not move $v = 0$. Positions of m values for such 'frozen' solutions are marked by thin dotted vertical lines in figures 1 and 2. Such a property appears in KdV

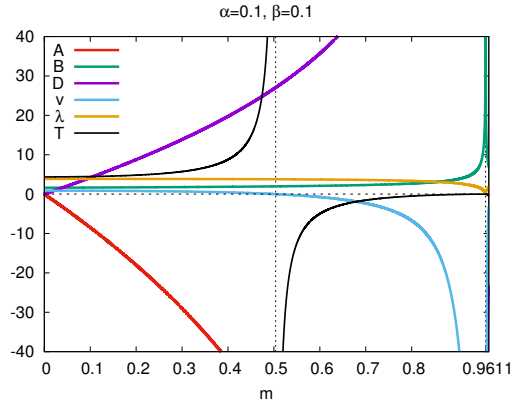


Figure 2: Parameters of the solution as functions of m for the branch related to $z = z_1$. Case $\alpha = \beta = \frac{1}{10}$.

solutions but with a single branch.

The details of the derivation of exact solutions to KdV2 and their properties will be published soon [5]. Numerical tests confirming the properties of analytic solutions are contained in this paper, as well.

References

- [1] T.R. Marchant, N.F. Smyth, *The extended Korteweg-de Vries equation and the resonant flow of a fluid over topography*, J. Fluid Mech., **221**, 263-288 (1990).
- [2] G.I. Burde, A. Sergyeyev, *Ordering of two small parameters in the shallow water wave problem*, J. Phys. A: Math. Theor., **46**, 075501 (2013).
- [3] A. Karczewska, P. Rozmej, E. Infeld, *Shallow-water soliton dynamics beyond the Korteweg-de Vries equation*, Physical Review E, **90**, 012907 (2014).
- [4] A. Karczewska, P. Rozmej, E. Infeld and G. Rowlands *Adiabatic invariants of the extended KdV equation*, Physics Letters A, in press. arXiv:1512.01194.
- [5] E. Infeld A. Karczewska, G. Rowlands and P. Rozmej, *Solutions to extended KdV equation for water surface waves*, submitted.

High Frequency Acoustic Scattering in Isogeometric Analysis

Tahsin Khajah^{1,*}, Xavier Antoine², Stéphane P.A. Bordas³

¹Department of Mechanical Engineering, University of Texas at Tyler, Tyler, USA

²Institut Elie Cartan de Lorraine, Université de Lorraine, Inria Nancy-Grand Est, SPHINX team, F-54506, Vandoeuvre-lès-Nancy Cedex, France.

³Université du Luxembourg, Legato-Team, Institute of Computational Engineering

*Email: tkhajah@uttyler.edu

Abstract

There is an emerging need to perform high frequency scattering analysis on high-fidelity models. Conventional Finite Element analysis suffers from irretrievable loss of the boundary accuracy as well as pollution error. Man-made geometries can be represented exactly in Isogeometric Analysis (IGA) with no geometrical loss even with very coarse mesh. The aim of this paper is to analyze the accuracy of IGA for exterior acoustic scattering problems. The numerical results show extremely low pollution error even for very high frequencies.

Keywords: Acoustic scattering, high-frequency, Isogeometric analysis, pollution error

1 Introduction

The pollution error is a limiting factor when analyzing high-frequency scattering problems with a conventional Finite Element Method. In order to achieve a prescribed upper bound for the error, it is necessary to increase the mesh density $n_\lambda = \lambda/h$ faster than the wavenumber k where λ is the wavelength ($\lambda = 2\pi/k$) and h is the element size. Another limitation in using conventional FEM is the loss of geometrical representation of the domain boundaries of the discretized model. The domain discretization in IGA however has no affect on the geometrical accuracy. In fact, the discretization of the IGA model is a result of its parametric definition. As a result the boundaries of the domain are presented exactly in IGA with no artificial facets. In addition, refinement in IGA can be performed without changing the geometry of the domain. To solve an unbounded exterior problem in the context of finite elements it is necessary to truncate the domain artificially. Constructing Absorbing Boundary Conditions (ABCs) and Perfectly Matched Layer (PML) are among the common methods of domain truncation. The truncation of the domain mimics the infinite space in a fi-

nite domain at the cost of introducing the truncation error to the numerical solution. In order to study the performance of any numerical scheme for exterior scattering problems it is necessary to separate the pollution error from the truncation error.

2 Problem formulation

Let us consider Ω^- as a two-dimensional circular cylinder $R_0 = 1$ centered at the origin with boundary $\Gamma := \partial\Omega^-$. The associated exterior (i.e. unbounded) domain of propagation is $\Omega^+ := \mathbb{R}^2/\overline{\Omega^-}$. Solving the scattering problem leads to computing the wave field u as the solution to the following Boundary-Value Problem (BVP): given an incident plane wave field u^{inc} , find u such that

$$\begin{aligned} \Delta u + k^2 u &= 0, \quad \text{in } \Omega^+, \\ \partial_{\mathbf{n}_\Gamma} u &= g := -\partial_{\mathbf{n}_\Gamma} u^{\text{inc}}, \quad \text{on } \Gamma, \\ \lim_{|\mathbf{x}| \rightarrow +\infty} |\mathbf{x}|^{(d-1)} \left(\nabla u \cdot \frac{\mathbf{x}}{|\mathbf{x}|} - iku \right) &= 0, \end{aligned} \quad (1)$$

where Δ is the Laplacian operator, ∇ the gradient operator and \mathbf{n}_Γ is the outward-directed unit normal vector to Ω^- . The spatial variable is $\mathbf{x} = (x, y)$. We consider the sound-hard case and apply the Neumann boundary conditions on Γ at $R = 1$ as stated in the second equation of system (1). The Sommerfeld's radiation condition at infinity is applied in the last equation of system (1) which presents the outgoing wave to the domain. We consider an incident plane wave $u^{\text{inc}}(\mathbf{x}) = e^{ik\mathbf{d} \cdot \mathbf{x}}$, with incidence direction $\mathbf{d} = (1, 0)^T$. To truncate the computational domain, the second-order Bayliss-Turkel ABC is applied on the circle with radius $R_1 = 2$ and is given by [1]:

$$\partial_{\mathbf{n}_\Sigma} u + \left(-ik + \frac{\kappa}{2} - \frac{\kappa^2}{8(\kappa - ik)} \right) u - \frac{1}{2(\kappa - ik)} \partial_s^2 u = 0,$$

where \mathbf{n}_Σ is the outward directed unit normal to Σ , $\partial_{\mathbf{n}_\Sigma} := \partial_r$ is the normal derivative, $\kappa =$

$1/R_1$ is the curvature and $\partial_s^2 := R_1^{-2} \partial_\phi^2$ is the second-order curvilinear derivative on the fictitious boundary at $R = 2$. The domain truncation error was included in the exact solution making it suitable to analyze the pollution and approximation errors and avoid domain truncation error. [2].

3 Numerical results

We generated the crown mesh between $R = 1$ and $R = 2$ by four identical patches in IGA. A Matlab® code was prepared to obtain the numerical results. The real part of the numerical solution is shown in Fig.1 where $k = 100$, degree $p = 4$ in IGA and $n_\lambda = 5$ points per wavelength. The error $|u_h - u^{\text{ex}}|$ is shown in Fig. 2. To examine the performance of IGA for higher k , the evolution of the L_2 -norm error vs. k is given in Fig. 3. No pollution error is visible even for k up to 100 for $p = 3$ and higher in IGA.

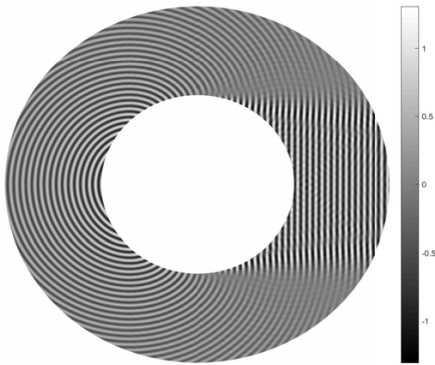


Figure 1: Real part of the numerical IGA solution u_h , $k = 100$, $p = 4$, $n_\lambda = 5$.

4 Conclusion

We studied the performance of IGA in solving high frequency scattering problems. By considering the truncation error in the exact solution, we separated the pollution error from the truncation error. Numerical results show no noticeable pollution error even for high k for basis functions of order $p = 3$ and higher. The possibility of exactly presenting domain boundaries in IGA even with very coarse meshes and its convenient refinement makes it an attractive platform for scattering problems.

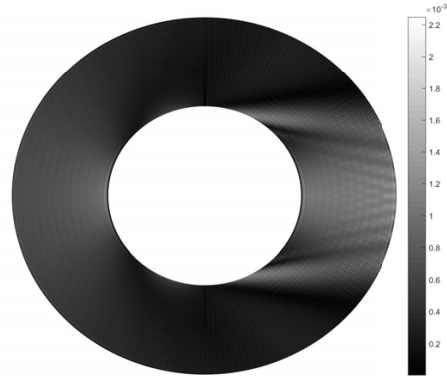


Figure 2: Absolute error $|u_h - u^{\text{ex}}|$.

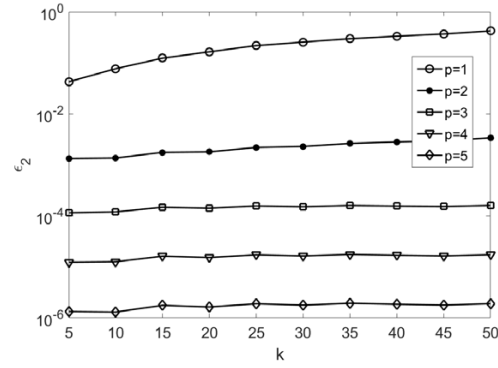


Figure 3: L_2 error vs. k ($p = 1 \cdots 5$).

References

- [1] T. Khajah, X. Antoine and S.P.A. Bordas, Isogeometric finite element analysis of time-harmonic exterior acoustic scattering problems, in *arXiv:1610.01694* .
- [2] X. Antoine and C. Geuzaine, Phase reduction models for improving the accuracy of the finite element solution of time-harmonic scattering problems I: General approach and low-order models, *Journal of Computational Physics* **228** (2009), pp. 3314–3136.

Complete radiation boundary conditions for the Helmholtz equation in waveguides

Seungil Kim^{1,*}

¹Department of Mathematics, Kyung Hee University, Seoul, Korea

*Email: sikim@khu.ac.kr

Abstract

We introduce a high-order absorbing boundary condition, called a complete radiation boundary condition (CRBC), for numerical computation of radiating solutions to the Helmholtz equation in waveguides. The CRBC is defined on an artificial boundary resulting from domain truncation by a certain recursive formula of auxiliary variables involving damping parameters, which can be tuned to minimize reflected waves from the fictitious boundary. We show that the solution to the problem supplemented with the CRBC converges exponentially to the exact radiating solution and present numerical experiments illustrating the convergence theory.

Keywords: complete radiation boundary condition, Helmholtz equation, waveguide

1 Introduction

We introduce a complete radiation boundary condition [1] for a domain truncation technique to numerically solve radiating solutions to the Helmholtz equation in waveguides. We consider the model problem

$$\begin{aligned} \Delta u + k^2 u &= f \text{ in } \Omega_\infty, \\ \frac{\partial u}{\partial \nu} &= 0 \text{ on } \partial \Omega_\infty \end{aligned}$$

with the radiation condition at infinity, where the semi-infinite waveguide Ω_∞ with boundary $\partial \Omega_\infty$ satisfies $\Omega_\infty \cap \{x > -\delta\} = (-\delta, \infty) \times \Theta$ for some $\delta > 0$. Further, we assume that $\Omega_\infty \cap \{x < -\delta\}$ is bounded and Θ is a Lipschitz bounded domain in \mathbb{R}^{d-1} , $d = 2$ or 3. The radiating solution is characterized by the series representation

$$u(x, y) = \sum_{n=0}^{\infty} A_n e^{i\mu_n x} Y_n(y)$$

for $(x, y) \in (-\delta, 0) \times \Theta$, where (λ_n^2, Y_n) for $n = 0, 1, \dots$, are Neumann eigenpairs of $-\Delta_y$ in Θ and $\mu_n^2 = k^2 - \lambda_n^2$. Noting that there exists N such that $\lambda_n^2 \leq k^2$ for $n \leq N$ and $\lambda_n^2 > k^2$ for $n > N$, the solution is composed of propagating modes $\sum_{n=0}^N A_n e^{i\mu_n x} Y_n$ and evanescent

mode $\sum_{n>N} A_n e^{-\tilde{\mu}_n x} Y_n$ with $i\mu_n = -\tilde{\mu}_n < 0$. Possibly, it may include a cutoff mode corresponding to $n = N$ with $\mu_N = 0$.

For numerical computation of the radiation solution domain truncation, for example at $x = 0$, needs to precede application of discretization techniques such as FEM or FDM, and we denote the resulting finite domain by $\Omega = \Omega_\infty \cap \{x < 0\}$ and the artificial boundary at $x = 0$ by Γ_E . The complete radiation boundary condition of order (n_p, n_e) to be imposed on Γ_E for an approximate radiation condition is defined in terms of auxiliary variables ϕ_j for $j = 0, 1, \dots, n_p + n_e$ satisfying the Helmholtz equation and the recurrence relations

$$\phi_0 = u, \quad (1)$$

$$(\partial_x + a_j)\phi_j = (-\partial_x + \tilde{a}_j)\phi_{j+1} \quad (2)$$

for $j = 0, 1, \dots, n_p + n_e - 1$ near the boundary Γ_E , and the terminal condition

$$\partial_x \phi_{n_p+n_e} = 0 \text{ on } \Gamma_E, \quad (3)$$

where a_j and \tilde{a}_j are damping parameters given by

$$\begin{aligned} a_j &= \begin{cases} -ikc_j & \text{for } j = 0, 1, \dots, n_p - 1, \\ \sigma_j & \text{for } j = n_p, \dots, n_p + n_e - 1 \end{cases} \\ \tilde{a}_j &= \begin{cases} -ik\tilde{c}_j & \text{for } j = 0, 1, \dots, n_p - 1, \\ \tilde{\sigma}_j & \text{for } j = n_p, \dots, n_p + n_e - 1 \end{cases} \end{aligned}$$

with the conditions

$$0 < c_j, \tilde{c}_j \leq 1 \text{ and } 0 < \sigma_j, \tilde{\sigma}_j. \quad (4)$$

It is easy to see that if a_j is chosen to be $-i\mu_n$ for some j then the CRBC serves as the exact radiation condition for the n -th mode. In general cases, it can be shown that the reflection coefficient ρ_n of the n -th mode is given by $\rho_n = |Z_n|$,

$$Z_n = \prod_{j=0}^{n_p+n_e-1} \frac{(a_j + i\mu_n)(\tilde{a}_j + i\mu_n)}{(a_j - i\mu_n)(\tilde{a}_j - i\mu_n)} \quad (5)$$

for non-cutoff modes and $\rho_N = 0$ (due to the terminal condition (3)) for the cutoff mode. The application of the CRBC to a time-harmonic wave propagation problem can be found in [3,4].

2 Parameter selection

The CRBC can be optimized by choosing parameters a_j and \tilde{a}_j minimizing the reflection coefficients for most important modes. In practice, if the distribution of eigenvalues of $-\Delta_y$ in Θ is known such as the smallest axial frequencies μ_{min} of propagating modes and the smallest decay rate $\tilde{\mu}_{min}$ of evanescent modes, then the parameters are taken to be a solution to the min-max problem

$$\rho_p \equiv \min_{a_j, \tilde{a}_j} \max_{\mu \in [\mu_{min}, k]} \prod_{j=0}^{n_p-1} \left| \frac{(a_j + i\mu)(\tilde{a}_j + i\mu)}{(a_j - i\mu)(\tilde{a}_j - i\mu)} \right|,$$

$$\rho_e \equiv \min_{a_j, \tilde{a}_j} \max_{\mu \in [\tilde{\mu}_{min}, \tilde{\mu}_{max}]} \prod_{j=n_p}^{n_p+n_e-1} \left| \frac{(a_j - \mu)(\tilde{a}_j - \mu)}{(a_j + \mu)(\tilde{a}_j + \mu)} \right|.$$

Here $\tilde{\mu}_{max}$ is an upper bound of decay rates of evanescent modes whose reflection would not be ignorable without the absorbing boundary condition. It is established (see e.g., [2]) that the reflection coefficients $\rho_{n,p}$ and $\rho_{n,e}$ with optimally selected parameters decay exponentially

$$\rho_p \leq e^{-Cn_p/\ln(k/\mu_{min})} \leq e^{-Cn_p},$$

$$\rho_e \leq e^{-Cn_e/\ln(\tilde{\mu}_{max}/\tilde{\mu}_{min})}$$

and the parameters of the min-max problems can be obtained numerically by the Remez algorithm.

3 Approximate the DtN operator

The exact radiation condition can be interpreted based on the Dirichlet-to-Neumann(DtN) operator

$$T : H^{1/2}(\Gamma_E) \rightarrow H^{-1/2}(\Gamma_E)$$

$$u = \sum_{n=0}^{\infty} u_n Y_n \mapsto T(u) = \sum_{n=0}^{\infty} i\mu_n u_n Y_n.$$

The CRBC is also associated with the approximate DtN operator

$$T_{crbc}(u) = \sum_{n=0}^{\infty} i\mu_n \left(\frac{1 - Z_n}{1 + Z_n} \right) u_n Y_n,$$

which converges to the DtN operator in the sense that for $M > N$ and for $\phi \in H^{1/2+s}(\Gamma_E)$, $s > 0$, it holds that

$$\frac{\|(T - T_{crbc})\phi\|_{H^{-1/2}(\Gamma_E)}^2}{\|\phi\|_{H^{1/2+s}(\Gamma_E)}^2}$$

$$\leq C \left(e^{-Cn_p} + e^{-Cn_e/\ln(\tilde{\mu}_M/\tilde{\mu}_{min})} + (1 + \lambda_M^2)^{-s} \right)$$

This convergence result of T_{crbc} plays a crucial role in the analysis on well-posedness of the truncated problem and convergence of approximate solutions.

4 Numerical experiments

We conduct numerical tests with the CRBC of different orders when $k = 20$, $\Theta = (0, 1)$ in \mathbb{R} and the source includes only propagating modes. As expected from the convergence theory, it is observed from the error plot that the accuracy of the CRBC is improved as the order n_p increases as long as the mesh size h is fine enough.

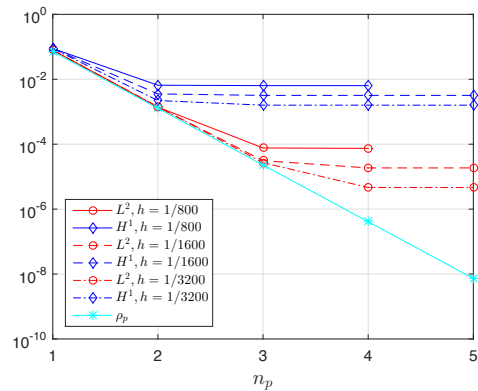


Figure 1: Relative errors in propagating modes

References

- [1] T. Hagstrom and S. Kim, Complete radiation boundary conditions for the Helmholtz equation I: Waveguides. *Manuscript*
- [2] P. Petrushev and V. Popov. *Rational Approximation of Real Functions*, Cambridge University Press, Cambridge, 1987.
- [3] S. Kim and H. Zhang, Optimized Schwarz method with complete radiation transmission conditions for the Helmholtz equation in waveguides , *SIAM J. Numer. Anal* **53**(3) (2015) pp. 1537–1558.
- [4] S. Kim and H. Zhang, Optimized double sweep Schwarz method by complete radiation boundary conditions, *Comput. and Math. Appl.* **72**(6) (2016) pp. 1573–1589.

On the efficiency of an ADI splitting combined with a discontinuous Galerkin discretization

Marlis Hochbruck¹, Jonas Köhler^{1,*}

¹Institute for Applied and Numerical Mathematics, Karlsruhe Institute of Technology, Germany

*Email: jonas.koehler@kit.edu

Abstract

We consider the alternating direction implicit (ADI) method for the time-integration of Maxwell's equations with linear, isotropic material properties on a cuboid. The main advantage of this method is unconditional stability, while only being of linear complexity if combined with finite differences on a Yee grid.

In this paper we combine the ADI method with a discontinuous Galerkin (dG) discretization in space. We show that for regular meshes consisting of cuboids the method can be implemented with optimal (linear) complexity. Our work in progress consists of proving error bounds which are uniform in the mesh discretization parameter.

Keywords: alternating direction implicit, discontinuous Galerkin, Maxwell's equations, second order scheme, unconditional stability

1 Introduction

The source-free linear Maxwell's equations with perfectly conducting boundary conditions on a cuboid domain $\Omega \subset \mathbb{R}^3$ are stated as

$$\begin{aligned}\partial_t E &= \frac{1}{\varepsilon} \operatorname{curl} H, & (0, T) \times \Omega, \\ \partial_t H &= -\frac{1}{\mu} \operatorname{curl} E, & (0, T) \times \Omega, \\ E(0) &= E^0, \quad H(0) = H^0, & \Omega, \\ n \times E &= 0, & (0, T) \times \partial\Omega.\end{aligned}$$

Here, $\varepsilon, \mu : \Omega \rightarrow \mathbb{R}$ denote the electric permittivity and the magnetic permeability, respectively. For the sake of readability, we set $\varepsilon = \mu = 1$ in the following.

Choosing a suitable function space and defining $u = (E, H)$, we can write this system as the abstract Cauchy problem

$$\partial_t u = \mathcal{M}u, \quad u(0) = u^0,$$

where the Maxwell operator \mathcal{M} is defined as

$$\mathcal{M} = \begin{pmatrix} 0 & \operatorname{curl} \\ -\operatorname{curl} & 0 \end{pmatrix}.$$

2 Discretization

The ADI scheme for Maxwell's equations was proposed in [2,3]. It is a splitting scheme, where the curl operators are split into a positive part \mathcal{C}_1 and a negative part \mathcal{C}_2 given by

$$\mathcal{C}_1 = \begin{pmatrix} 0 & 0 & \partial_y \\ \partial_z & 0 & 0 \\ 0 & \partial_x & 0 \end{pmatrix}, \quad \mathcal{C}_2 = \begin{pmatrix} 0 & \partial_z & 0 \\ 0 & 0 & \partial_x \\ \partial_y & 0 & 0 \end{pmatrix}.$$

Accordingly, the Maxwell operator is split into $\mathcal{M} = \mathcal{A} + \mathcal{B}$ with

$$\mathcal{A} = \begin{pmatrix} 0 & \mathcal{C}_1 \\ \mathcal{C}_2 & 0 \end{pmatrix}, \quad \mathcal{B} = \begin{pmatrix} 0 & -\mathcal{C}_2 \\ -\mathcal{C}_1 & 0 \end{pmatrix}. \quad (1)$$

The time-integration is then carried out via the so-called Peaceman–Rachford scheme, which is defined as

$$\begin{aligned}(\mathcal{I} - \frac{\tau}{2}\mathcal{A})u^* &= (\mathcal{I} + \frac{\tau}{2}\mathcal{B})u^n, \\ (\mathcal{I} - \frac{\tau}{2}\mathcal{B})u^{n+1} &= (\mathcal{I} + \frac{\tau}{2}\mathcal{A})u^*. \end{aligned} \quad (2)$$

It is well known, that the Peaceman–Rachford scheme is unconditionally stable and of classical (non-stiff) order two.

We combine the ADI scheme with a central flux dG discretization in space on a regular grid consisting of cuboids. This yields space-discretized versions of the operators \mathcal{C}_1 and \mathcal{C}_2 and – by composing them according to (1) – of the operators \mathcal{A} and \mathcal{B} .

3 Efficiency

The complexity of the method is mainly governed by the cost of solving the linear systems occurring in the Peaceman–Rachford scheme. The efficiency mainly depends on the sparsity pattern of the corresponding matrices resulting from the space discretization. We present two ways to achieve a scheme of optimal (linear) complexity, both yielding matrices with a bandwidth bounded independently of the number of elements in the mesh.

3.1 Second order formulation

The second order formulation follows the idea in [2, 3]. Here, in the first halfstep of (2), the unknown H -field is plugged into the equation for the E -field:

$$\begin{aligned} (\mathcal{I} - \frac{\tau^2}{4}\mathcal{C}_1\mathcal{C}_2)E^* &= (\mathcal{I} - \frac{\tau^2}{4}\mathcal{C}_1^2)E^n + \frac{\tau}{2}\operatorname{curl} H^n, \\ H^* &= H^n - \frac{\tau}{2}\mathcal{C}_1E^n + \frac{\tau}{2}\mathcal{C}_2E^*. \end{aligned}$$

This requires the solution of a linear problem for E^* .

Proceeding analogously for the spatially discretized version of (2) and numbering the degrees of freedom appropriately, we end up with matrix structures of the discretized operators \mathcal{C}_1 , \mathcal{C}_2 , and $\mathcal{I} - \frac{\tau^2}{4}\mathcal{C}_1\mathcal{C}_2$ as shown in Fig. 1. Since the latter matrix is banded with a bandwidth being independent of the number of elements, the above linear system for E^* can be solved in linear complexity. The second halfstep follows completely analogously by interchanging the roles of \mathcal{C}_1 and \mathcal{C}_2 .

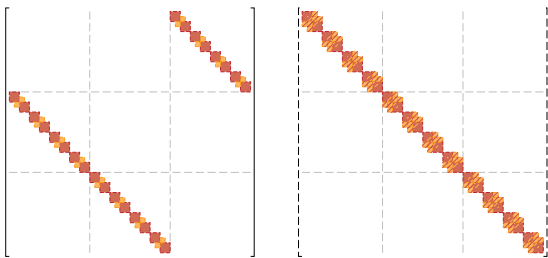


Figure 1: Structure of the matrices corresponding to \mathcal{C}_1 , \mathcal{C}_2 (left) and $\mathcal{I} - \frac{\tau^2}{4}\mathcal{C}_1\mathcal{C}_2$ (right) after reordering. Red: inner element coupling, orange: coupling between elements.

3.2 First order formulation

As an alternative to changing into the equivalent scheme above, we propose a suitable numbering of the degrees of freedom. This leads again to an implementation of the original Peaceman–Rachford scheme (2) which is of linear complexity. The numbering is motivated by noting that in the operators \mathcal{A} and \mathcal{B} only two components, one from the electric and one from the magnetic field, are actually coupled via only one spatial derivative, e.g. in \mathcal{A} , the E_1 component is only coupled to the H_3 component via ∂_y . By intertwining the degrees of freedom of these

coupled components and ordering them elementwise according to the spatial derivative applied to them, we end up with matrices of the structure displayed in Fig. 2. As the bandwidth of this matrix is again bounded independently of the number of elements, linear systems involving this matrix can be solved in linear time.

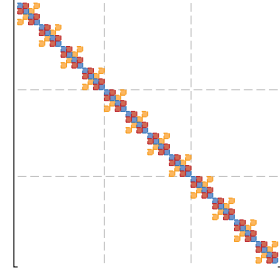


Figure 2: Structure of the matrix corresponding to $\mathcal{I} - \frac{\tau}{2}\mathcal{A}$ after reordering. Red: inner element coupling, orange: coupling between elements, blue: identity.

4 Error analysis

Currently, we investigate the error analysis of the full discretization of the ADI scheme. The aim is to prove error bounds of optimal order in space and time with constants being uniform in the mesh parameter of an admissible sequence of spatial meshes.

Our analysis is based on [1], where the abstract Cauchy problem is analyzed in a variational framework which fits nicely to the dG discretization. Nevertheless, it is considerably more involved, in particular for upwind fluxes.

References

- [1] Hochbruck, M., Jahnke, T., Schnaubelt, R., 2015. Convergence of an ADI splitting for Maxwell's equations. *Numer. Math.* 129, 535–561.
- [2] Namiki, T., 1999. A new FDTD algorithm based on alternating-direction implicit method. *IEEE Trans. Microwave Theory Tech.* 47, 2003–2007.
- [3] Zhen, F., Chen, Z., Zhang, J., 2000. Toward the development of a three-dimensional unconditionally stable finite-difference time-domain method. *IEEE Trans. Microwave Theory Tech.* 48, 1550–1558.

Application of the Floquet-Transform to Scattering Problems from Locally Perturbed Bi-periodic Structures in \mathbb{R}^3

Alexander Konschin^{1,*}, Armin Lechleiter¹

¹Center for Industrial Mathematics, University of Bremen, Bremen, Germany

*Email: alexk@uni-bremen.de

Abstract

We consider time-harmonic scattering problems of acoustic waves from either a bi-periodic inhomogeneous medium which is absorbing on an open set or a bi-periodic sound-soft obstacle in \mathbb{R}^3 , both with a local perturbation. For this, the Floquet-transform is used to reformulate the problem as an equivalent system of coupled variational problems on a bounded domain. This system possesses a unique solution for both scattering problems. Furthermore, we calculate the Fréchet derivative of the operator, which maps the perturbation to the solution.

Keywords: Scattering, Floquet-transform, Fréchet derivative

1 Introduction

Scattering problems from bi-periodic inhomogeneous medium or bi-periodic sound-soft obstacle are occurring for example during non-destructive testing methods for, e.g., nano-gras. The setting for the scattering problem from inhomogeneous medium is close to the setting analyzed in [1].

For simplicity, we consider here the simplest setting where functions are 1-periodic with respect to x_1 and x_2 , and set for $j \in \mathbb{Z}^2$

$$W_j := \{\omega + j : \omega \in (-1/2, 1/2)^2\}$$

and

$$I := \{\omega : \omega \in (-\pi, \pi)^2\}.$$

2 Problem formulation

The first problem that we investigate is the scattering problem from an inhomogeneous medium, which is formulated as follows: Let $n \in L^\infty(\mathbb{R}^3)$ be a 1-periodic function with respect to the first two coordinates and $\operatorname{Im}(n) > 0$ on an open set in \mathbb{R}^3 . Moreover, we choose $q \in L^\infty(\mathbb{R}^3)$ with $\operatorname{supp}(q) \subseteq W_0 \times (-R_0, R_0)$, $R_0 > 0$, and the wave number $k > 0$. Then find a function $u \in H_{loc}^1(\mathbb{R}^3)$ with $u \in H^1(\mathbb{R}^2 \times (-R, R))$ for all $R \geq R_0$ such that

$$\Delta u + k^2(n^2 + q)u = g \text{ in } \mathbb{R}^3, \quad (1)$$

where $g \in L^2(\mathbb{R}^2 \times (-R_0, R_0))$. Additionally, the function should fulfill the radiation condition

$$u(\tilde{x}, x_3) = \frac{1}{2\pi} \int_{\mathbb{R}^2} (\widehat{\gamma_{\Gamma^{\pm R}} u})(\xi) e^{i\xi \cdot \tilde{x} \pm i\sqrt{k^2 - |\xi|^2}(x_3 \mp R)} d\xi \quad (2)$$

for $\tilde{x} \in \mathbb{R}^2$ and $|x_3| > R \geq R_0$, where $\gamma_{\Gamma^{\pm R}}$ is the trace operator on $\Gamma^{\pm R} := \mathbb{R}^2 \times \{\pm R\}$ and \widehat{f} is the Fourier-transform of a function $f \in L^2(\mathbb{R}^2)$.

We define for $\alpha \in \bar{I}$ the space $H_\alpha^1(W_0 \times (-R, R))$ as the closure with respect to the $H^1(W_0 \times (-R, R))$ norm of α -quasi-periodic C^∞ -functions in \mathbb{R}^3 with respect to 1-periodicity in the first two coordinates. After applying the isomorphic Floquet-transform \mathcal{J} to the corresponding variational formulation we get the problem: Find a function $\tilde{u} \in L^2(I; H_\alpha^1(W_0 \times (-R, R)))$ such that for all $R \geq R_0$ and for all $\alpha \in \bar{I}$ the equation

$$\Delta \tilde{u}(\alpha, \cdot) + k^2 n^2 \tilde{u}(\alpha, \cdot) + \frac{1}{2\pi} k^2 q \mathcal{J}^{-1} \tilde{u} = \mathcal{J}g \quad (3)$$

holds in $W_0 \times (-R, R)$. This time the functions $\{\tilde{u}(\alpha, \cdot)\}_{\alpha \in \bar{I}}$ should fulfill Rayleigh's radiation condition.

The scattering problem from a sound-soft obstacle can be introduced analogously since it mainly differs in the following two things: The function n^2 is 1 everywhere and instead of \mathbb{R}^3 we introduce a domain Ω^R such that

$$\mathbb{R}^2 \times (R_0, R) \subseteq \Omega^R \subseteq \mathbb{R}^2 \times (0, R)$$

and

$$x \in \Omega^R \Rightarrow x + \begin{pmatrix} j_1 \\ j_2 \\ 0 \end{pmatrix} \in \Omega^R \quad \forall j \in \mathbb{Z}^2.$$

These changes enforce the perturbation to be in the parametrization of the domain instead in the parameter n^2 . Thus, let $\zeta : \mathbb{R}^3 \rightarrow \mathbb{R}^3$ be a function, which is the identity function in $\mathbb{R}^2 \times [R_0, \infty)$, and define $\Omega^R = \zeta(\mathbb{R}^2 \times (0, R))$,

$\Gamma := \zeta(\mathbb{R}^2 \times 0)$, and $\Omega := \bigcup_{R>0} \Omega_R$. Moreover, we choose a C^2 -function $q : \mathbb{R}^3 \rightarrow \mathbb{R}^3$ with $\text{supp}(q) \subseteq W_0 \times (-R_0, R_0)$ and define the perturbed domain Ω_s^R as $\Omega_s^R = (\zeta + q)(\mathbb{R}^2 \times (0, R))$. Since we have to fulfill the periodicity condition for the domain to apply the Floquet-transform, we use the transformation theorem to get the formulation: Find $u \in H_{loc}^1(\Omega)$ such that $u \in H^1(\Omega^R)$ for all $R > R_0$ satisfies the equations

$$\begin{aligned} \operatorname{div}(C_{\zeta+q} \nabla u) + k^2 c_{\zeta+q} u &= c_{\zeta+q} g \text{ in } \Omega, \\ \gamma_\Gamma u &= 0 \text{ on } \Gamma, \end{aligned} \quad (4)$$

and fulfills the radiation condition (2), with certain functions $C_{\zeta+q} \in C^1(\mathbb{R}^3, \mathbb{R}^3)$ and $c_{\zeta+q} \in C^1(\mathbb{R}^3, \mathbb{R})$. It is important that $\text{supp}(C_{\zeta+q} - I_3)$ and $\text{supp}(c_{\zeta+q} - 1)$ are included in $\zeta(W_0 \times (0, R))$.

Applying the Floquet-transform gives us the formulation:

Find a function $\tilde{u} \in L^2(I; H_\alpha^1(\zeta(W_0 \times (0, R))))$ such that for all $R \geq R_0$ and for all $\alpha \in \bar{I}$ the equation $\tilde{u}(\alpha, \cdot) = 0$ holds on $\Gamma_0^R := W_0 \times \{R\}$ and

$$\begin{aligned} \Delta \tilde{u}(\alpha, \cdot) + k^2 \tilde{u}(\alpha, \cdot) + \frac{1}{2\pi} k^2 (c_{\zeta+q} - 1) \mathcal{J}^{-1} \tilde{u} \\ + \frac{1}{2\pi} \operatorname{div}(C_{\zeta+q} - I_3) \nabla \mathcal{J}^{-1} \tilde{u} = \mathcal{J}g \end{aligned}$$

holds in $\zeta(W_0 \times (0, R))$. Again, the functions $\{\tilde{u}(\alpha, \cdot)\}_{\alpha \in \bar{I}}$ should fulfill Rayleigh's radiation condition.

3 Existence theory

If we assume to have $q = 0$, then the existence of a solution to the problem (3) pointwise in $\alpha \in \bar{I}$ follows from Fredholm-theory under further assumptions that $\operatorname{Im}(n^2) \geq 0$ and $\operatorname{Im}(n^2) > 0$ on a open set in \mathbb{R}^3 . With the help of a Neumann series argument we get uniform continuity of the solution operator with respect to $\alpha \in \bar{I}$. From this we conclude that the function $\tilde{u}, \tilde{u}(\alpha, \cdot) := \tilde{u}_\alpha$ with the solution \tilde{u}_α to the pointwise problem, lies in $L^2(I; H^1(\mathbb{R}^2 \times (-R, R)))$.

Thus, after considering the problem without a perturbation, we are able to use Fredholm-theory to conclude the existence of a solution to the perturbed problem.

Theorem 1 *Under the assumptions for $\operatorname{Im}(n^2)$ and $\operatorname{Im}(q) \geq 0$ there exists a unique solution $\tilde{u} \in L^2(I; H_\alpha^1(W_0 \times (-R, R)))$ for the problem*

(3) *such that*

$$\begin{aligned} \|\tilde{u}\|_{L^2(I; H_\alpha^1(W_0 \times (-R, R)))} \\ \leq c \|\mathcal{J}g\|_{L^2(I \times W_0 \times (-R, R))}. \end{aligned}$$

In consequence, there exists a solution to (1) under the same conditions.

For existence theory for the scattering problem from a sound-soft obstacle, e.g., see [2].

4 Fréchet derivatives

Apart from existence theory, the previously sketched framework also serves to, e.g., compute Fréchet derivatives for the solution operators $\mathbb{F}_{1,2}$ that map the perturbation q to the solution $u_q^{(1),(2)}$ of the corresponding perturbed scattering problem. These derivatives can be computed for both scattering problems and represented by the Floquet-transform on the bounded domain $I \times W_0 \times (-R_0, R_0)$ for the medium scattering problem and $I \times \zeta(W_0 \times (0, R_0))$ for the sound-soft scattering problem.

Theorem 2 *The operator $\mathbb{F}_1 : \mathcal{D}(\mathbb{F}_1) \rightarrow H^1(\mathbb{R}^2 \times (-R, R))$ has in $q \in \mathcal{D}(\mathbb{F}_1)$ the Fréchet derivative $\mathbb{F}'_q : L^\infty(W_0 \times (-R_0, R_0)) \rightarrow H^1(\mathbb{R}^2 \times (-R, R))$, $h \mapsto w_h$, where $w_h \in H^1(\mathbb{R}^2 \times (-R, R))$ is the solution to (1) with the right-hand side $g = k^2 h u_q^{(1)}$.*

Theorem 3 *The operator $\mathbb{F}_2 : \mathcal{D}(\mathbb{F}_2) \rightarrow H^1(\Omega^R)$ has in $q \in \mathcal{D}(\mathbb{F}_2)$ the Fréchet derivative $\mathbb{F}'_q : \mathcal{D}(\mathbb{F}_2) \rightarrow H^1(\Omega^R)$, $h \mapsto w_h$, where $w_h \in H^1(\Omega^R)$ is the solution to (4) in Ω^R with the right-hand side $-A(g)[h](u_q^{(2)}, \cdot)$, and $A(g)$ is the Fréchet derivative of the sesquilinear form of the corresponding variational problem with respect to q .*

References

- [1] H. Haddar and T.-P. Nguyen, A volume integral method for solving scattering problems from locally perturbed infinite periodic layers, *Applicable Analysis* (2016), pp. 1–29.
- [2] S. N. Chandler-Wilde and P. Monk, Existence, Uniqueness, and Variational Methods for Scattering by Unbounded Rough Surfaces, *SIAM Journal on Mathematical Analysis* **37** (2005), pp. 598–618.

Wave energy delivery to multiple subsurface targets using time-reversal method

Seungbum Koo^{1,*}, Loukas F. Kallivokas¹

¹Department of Civil, Architectural and Environmental Engineering
The University of Texas at Austin, Austin, TX 78712, USA

*Email: seungbum.koo@utexas.edu

Abstract

We discuss the applicability of a time-reversal concept to the focusing of wave energy to multiple subsurface targets embedded within an arbitrarily heterogeneous three-dimensional elastic host. The motivation stems from an interest in facilitating oil ganglia mobility in support of enhanced oil recovery (EOR) methods. We quantify the focusing by a suitable motion metric, and provide numerical evidence supportive of the method's efficacy in illuminating the targets even when embedded within randomized media.

Keywords: wave energy focusing, time-reversal, subsurface targets, EOR, fracking

1 Introduction

There are a few engineering applications, where there is interest in focusing wave energy to targets embedded within heterogeneous hosts. Lithotripsy, i.e., the breaking of kidney stones, has been a long-standing application of wave focusing in therapeutics; similarly motivated applications can be found in cancer treatment. In therapeutics, the typical setting involves a closed-cavity, or equivalently, the surrounding of the target with sources/receivers that direct energy to the target. Here, we are interested in exploring wave focusing to select targets embedded within the subsurface, i.e., hosted by a semi-infinite heterogeneous elastic domain, which poses challenges not encountered in closed-cavity or waveguide settings. The application is motivated by enhanced oil recovery needs, where there is interest in facilitating the mobility of oil ganglia in reservoir subregions typically bypassed by primary modes of recovery.

To this end, we numerically evaluate the potential of the application of a time-reversal concept to illuminate the targets, and assess its effectiveness by computing suitable motion metrics. Specifically, we consider the setting depicted in Fig. 1: we assume that there are multiple targets embedded within an arbitrarily

heterogeneous semi-infinite host, with, in general, contrasting properties with the host. We assume further that a single source (or more) is present within each target: the sources are triggered, and a time-reversal (TR) mirror (e.g., geophones) records the response on the surface of the half-space. The receiver signals are time-reversed and the interest is in assessing the wave energy refocusing potential to the targets, given the presence of multiple challenges, which include the limited extent of the mirror, the unboundedness of the host, the lack of a sink, and others.

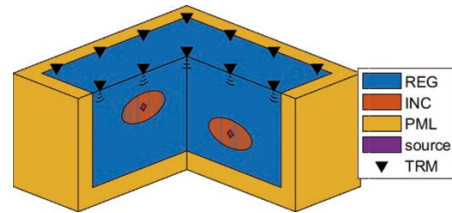


Figure 1: Model configuration: REG, INC, and PML stand for host (regular) domain, inclusions (targets), and perfectly-matched-layers, respectively; the sources are located within the targets, and TRM stands for the time-reversal mirror

2 Mathematical background

To numerically simulate the refocusing experiment, we consider the two steps typically involved in a time-reversal application. In a first, or forward step, the sources are triggered, and the receiver array (the TR mirror) records. This phase is governed by the Navier equations of motion, i.e.,

$$\nabla \cdot [\mu(\nabla \mathbf{u} + \nabla \mathbf{u}^\top) + \lambda \{(\nabla \cdot \mathbf{u}) \mathbf{I}\}] - \rho \ddot{\mathbf{u}} = \mathbf{f} \quad (1)$$

where $\mu(\mathbf{x})$ and $\lambda(\mathbf{x})$ are the Lamé parameters, and $\rho(\mathbf{x})$ denotes mass density; $\mathbf{u}(\mathbf{x}, t)$ is the displacement field and $\mathbf{f}(\mathbf{x}, t)$ denotes the source/force vector ($\mathbf{x} \in \Omega_{\text{REG}}$). To properly account for the unboundedness of the domain,

the physical domain is truncated through the introduction of perfectly-matched-layers (PMLs); the PMLs form the buffer zone Ω_{PML} around Ω_{REG} , per Fig. 1. The details of the numerical treatment for the forward step are given in [2].

Following the forward step, the recorded response at the mirror is time-reversed. If the domain of interest were a closed cavity, if the mirror were to envelope the domain, and if the forcing term in (1) were to be also time-reversed (sink), then perfect refocusing to the original source locations within the targets is expected [1] (for an infinite aperture and for the continuous problem). Due to practical limitations, the aforementioned ideal conditions are impossible to attain, and, consequently the focusing is expected to degrade. In addition: while the receivers record Dirichlet data (displacements), equipment limitations allow only the application of Neumann data (tractions), which could further degrade the focusing. With the above conditions, the time-reversal phase is numerically simulated using (1), without the forcing term, and subject to the free-surface mirror conditions, i.e., applied tractions implemented by time-reversing the recorded Dirichlet data. Mathematically, the time-reversal of recorded Dirichlet data as Neumann data resembles steps in subsurface imaging processes; however, the difference in the illumination zone between a migration approach and the inclusion-originating data would likely not allow for the imaging of the targets using a migration method.

To quantify the focusing, we introduce the time-averaged kinetic energy for $\mathbf{x} \in \Omega_{\text{REG}}$ [3]:

$$\text{KE}^{\text{TA}}(\mathbf{x}) = \frac{1}{2T} \int_0^T \mathbf{u}^\top(\mathbf{x}, t) \rho(\mathbf{x}) \mathbf{u}(\mathbf{x}, t) dt. \quad (2)$$

3 Numerical experiment

The model is 80m \times 80m \times 40m (depth), with a 6.25m-thick PML buffer enveloping all sides except the top surface. The model is divided into two layers, with the interface at 20m depth. Two spheroidal, relatively soft, targets (semi-axes 7.5m, 7.5m, and 3.75m), are placed at two different depths, with one centered at (-15m, -15m, -20m) and the other at (15m, 15m, -30m), respectively. The physical properties are summarized in table 1; in order to introduce further heterogeneity, the values of table 1 were spatially randomized; c_p and c_s indicate P- and S-wave speed, respectively; the shear wave map is

shown in Fig. 2. The resulting time aver-

	c_p (m/s)	c_s (m/s)
targets	387.30	223.61
top layer	670.82	387.30
bottom layer	866.03	500.00

Table 1: Model physical properties

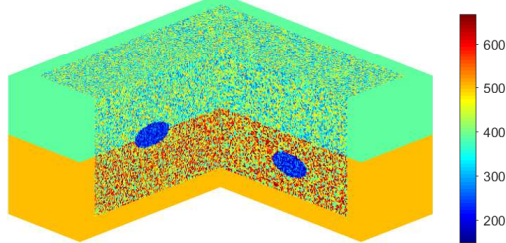


Figure 2: Shear wave speed distribution

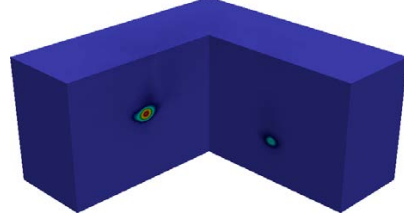


Figure 3: Time-averaged kinetic energy KE^{TA}

ged kinetic energy is shown in Fig. 3: despite the various limitations, the targets are clearly illuminated.

4 Conclusion

We quantified and demonstrated the applicability of time-reversal in the focusing of wave energy at multiple subsurface targets embedded within heterogeneous elastic hosts, without resolution loss of practical significance. The approach is a good candidate for EOR.

References

- [1] M. Fink, "Time-reversed acoustics," *Scientific American*, 1999, 281(5), 91–97
- [2] A. Fathi, B. Poursartip, and L.F. Kallivokas. "Time-domain hybrid formulations for wave simulations in three-dimensional PML-truncated heterogeneous media," *International Journal for Numerical Methods in Engineering*, 2015, 101 (3), 165–198
- [3] S. Koo, P.M. Karve, and L.F. Kallivokas, "A comparison of time-reversal and inverse-source methods for the optimal delivery of wave energy to subsurface targets," *Wave Motion*, 2016, 67, 121–140

Sobolev-dG: a class of dG methods with tame CFL numbers

Daniel Appelö¹, Thomas Hagstrom², Adeline Kornelus^{1,*}

¹Department of Mathematics and Statistics, University of New Mexico, Albuquerque, USA

²Department of Mathematics, Southern Methodist University, Dallas, USA

*Email: kornelus@unm.edu

Abstract

A new class of discontinuous Galerkin method with tame CFL numbers is presented.

Keywords: Discontinuous Galerkin, CFL.

Introduction

Discontinuous Galerkin methods has emerged as a highly flexible and accurate tool for numerical solution of wave propagation problems arising in many areas of engineering and science, [1]. A drawback with traditional dG methods is the strong reduction of the CFL number as the order of the spatial discretization increases. There are some alternatives for relaxing or taming the CFL, e.g. by the use of staggered approximations, [2, 3], mappings [1] or by careful modification of the numerical fluxes [4].

Below we present a different approach based on modifying the variational statement itself in a way so that we give up precise control of the L_2 -norm of the solution in favor of control of a semi-norm. As we will illustrate below our modification allows us to balance increased CFL numbers against an increase in the rate of the long term error growth. When paired with Taylor series method, the most aggressive version of Sobolev-dG (SOB-dG) is able to *time march with CFL numbers that increase with order*.

Sobolev discontinuous Galerkin

We introduce SOB-dG by considering the scalar transport equation, $u_t + u_x = 0$, on the periodic domain $x \in \Omega = [0, 2]$ and with initial data $u = \sin(\pi x)$. We discretize the spatial domain into K elements $\Omega_k = [x_{k-1}, x_k]$ with $x_k = 2(k/K)$. On each element we approximate the solution by a degree N polynomial $u \approx u_h^k = \sum_{j=0}^N \hat{u}_j^k(t) \phi_j(z)$, where $z \in [-1, 1]$ is a local co-

ordinate on each element and, for simplicity, we choose $\phi_j = z^{j-1}$.

Let $\Pi_a^b(z)$ be the polynomial space spanned by $\{z^a, z^{a+1}, \dots, z^b\}$, then SOB-dG is defined by the element-wise variational statements (2).

Note that the standard strong dG formulation (see [1]) is obtained with the “stride” $s = N + 1$ resulting in $\phi \in \Pi_0^N$ and $r \in \{0\}$. Also note that for $r > 0$, some of the equations for that r will be reduced to identities $0 = 0$ but that the total number of equations is always $N + 1$. Finally note that the choice of s is constrained to $(N + 1)/s$ being an integer.

The numerical fluxes are chosen as a straightforward generalization of the standard central or upwind flux ($\alpha = 1$ and $\alpha < 1$)

$$\left(\frac{\partial^r u}{\partial x^r} \right)^* = \left\{ \left\{ \frac{\partial^r u_h}{\partial x^r} \right\} \right\} + \frac{1 - \alpha}{2} \left[\left[\frac{\partial^r u_h}{\partial x^r} \right] \right]. \quad (1)$$

Here $\{\cdot\}$ and $[\cdot]$ are the standard definitions of trace average and jump, [1]. With this choice of numerical flux we have the following

Theorem 1 *Let u_h be the global solution composed of element solutions u_h^k satisfying (2) and (1) then*

$$\frac{d}{dt} \left\| \frac{\partial^{r_M} u_h}{\partial x^{r_M}} \right\|_{\Omega, h}^2 = -(1 - \alpha) \sum_{k=1}^K \left[\left[\frac{\partial^r u_h}{\partial x^r} \right] \right]^2.$$

Numerical Experiments

We first consider the case $N = 11$ and vary the stride $s = 1, 2, 3, 4, 6, 12$. We use an upwind flux with $\alpha = 0$. To the right in Figure 1 we plot the spectrum (scaled by the element size) of the discrete operator with 40 elements. As can be seen, the spectral radius

$$\begin{aligned} \int_{\Omega^k} \frac{\partial^r \phi}{\partial x^r} \left(\frac{\partial^r}{\partial x^r} \left(\frac{\partial u_h^k}{\partial t} + \frac{\partial u_h^k}{\partial x} \right) \right) dx &= \left[\frac{\partial^r \phi}{\partial x^r} \left(\frac{\partial^r u_h^k}{\partial x^r} - \left(\frac{\partial^r u}{\partial x^r} \right)^* \right) \right]_{\partial \Omega_k}, \\ \forall \phi \in \Pi_0^{r+s-1}, \quad r \in \{0, s, 2s, \dots, r_M \leq N\}. \end{aligned} \quad (2)$$

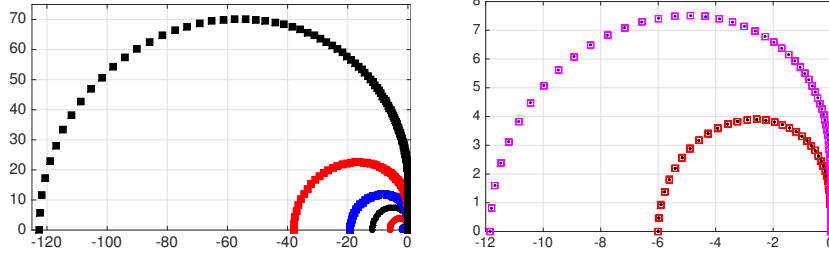


Figure 1: **Left:** the spectra for methods using $N = 11$ and strides from $s = 1$ to $s = 12$ (standard dG). The increase in the spectral radii is monotone with s . **Right:** For fixed strides the **spectrum remains identical** independent of N . The figure displays (s, N) for: (2,11), red squares, (2,9), black dots, (3,11), purple squares, and (3,5), blue dots.

Table 1: Maximum errors over space and time.

(s, K)	$\mathcal{E}(t = 1)$	$\mathcal{E}(t = 10)$	$\mathcal{E}(t = 100)$
(2,14)	9.18(-8)	1.07(-4)	6.14(-1)
(2,28)	5.76(-11)	2.05(-9)	1.98(-4)
Rate	10.6	15.7	11.6
(6,8)	3.47(-9)	3.73(-9)	5.96(-9)
(6,16)	1.14(-12)	1.56(-12)	2.51(-12)
Rate	11.6	11.2	11.2
(12,5)	2.13(-8)	2.09(-8)	2.09(-8)
(12,10)	5.12(-12)	7.02(-12)	3.01(-11)
Rate	12.0	11.5	9.4

increases drastically with the stride. In fact, when marching the solution with a 12th order Taylor series method we can use CFL numbers 2.5, 0.9, 0.45, 0.3, 0.15 for $s = 1, 2, 3, 4, 6$. Compared this to 0.04 for standard dG.

We also consider the case where the stride is kept fixed and the degree of the approximation, N , is varied. The results for stride $s = 2$ and $N = 9, 11$; and $s = 3$ and $N = 5, 11$ are displayed to the right in Figure 1. The spectra reveals an interesting property of SOB-dG, for a fixed stride the spectra is identical for all N . The explanation for this can be gleaned from the variational statement whose structure will result in mass matrices that are block triangular with $(N + 1)/s$ blocks with of size $s \times s$ on the diagonal. These blocks are similar and thus share eigenvalues.

Finally, Table 1 reports maximum errors (over space and time) for $N = 11$ and $s = 2, 6, 12$ (standard dG). The number of elements have

been scaled so that each method has the same computational cost. The method $s = 6$ gives the smallest errors for all times, outperforming standard dG, while $s = 2$ has rapid growth in time and is competitive only for short times.

Acknowledgement

DA & AK was supported in part by NSF Grant DMS-1319054. TH was supported in part by NSF Grant DMS-1418871. Any conclusions or recommendations expressed in this paper are those of the author and do not necessarily reflect the views of NSF.

References

- [1] J. S. Hesthaven and T. Warburton. Nodal Discontinuous Galerkin Methods: Algorithms, Analysis, and Applications. Springer, New York, 2008.
- [2] Y. Liu, C.-W. Shu, E. Tadmor and M. Zhang. Central discontinuous Galerkin methods on overlapping cells with a nonoscillatory hierarchical reconstruction. *SIAM J. Num. Anal.*, 45(6):2442–2467, 2007.
- [3] T. Warburton and T. Hagstrom. Taming the CFL number for discontinuous Galerkin methods on structured meshes. *SIAM J. Num. Anal.*, 46(6):3151–3180, 2008.
- [4] N. Chalmers, L. Krivodonova and R. Qin. Relaxing the CFL Number of the Discontinuous Galerkin Method. *SIAM J. Sci. Comp.*, 36(4):2047–2075, 2014.

Estimating the Error Distribution of Recovered Changes in Earth Properties with Full-Waveform Inversion

Maria Kotsi^{1,*}, Alison Malcolm¹

¹Memorial University of Newfoundland

*Email: mkotsi@mun.ca

Abstract

Multiple seismic data sets are often recorded to monitor changes in Earth properties. We test a method for imaging those changes, Alternating Full-Waveform Inversion (AFWI), to determine how errors in the model translate into errors in the final image. The results appear to follow a normal distribution, which opens up the possibility of quantifying these errors.

Keywords: full waveform inversion, time lapse seismic, uncertainty, noise

1 Introduction

Monitoring of an oil field for changes in reservoir parameters during production is important for efficient oil recovery. The technique most commonly used to do this is time-lapse (4D) seismic. In 4D seismic multiple surveys are acquired over a region and their differences used to detect changes in fluids (Lumley, 2001). The first survey acquired over a field is called a baseline survey and subsequent surveys are called monitor surveys. Full Waveform Inversion (FWI) is a promising tool for 4D analysis. The objective of FWI is to deliver a velocity model of the subsurface by iteratively matching modelled and recorded data (Virieux et al., 2009). FWI iteratively updates the Earth model, and 4D changes can then be related to changes in elastic properties (e.g. pressure, fluid saturation, density). Uncertainty is a key component of any measurement, especially in 4D monitoring where we are often looking for small changes in localized regions. Based on previous work (Yang 2014, Maharramov and Biondi, 2014), we try to understand the best way to quantify uncertainty following a more rigorous statistical approach, by understanding the main contributors to uncertainty. In seismic images, the main sources of uncertainty are usually velocity model uncertainty and coherent noise. The former will be considered for this project.

2 The Method

Because FWI is a nonlinear optimization problem, it is solved iteratively. In Alternating Full Waveform Inversion (AFWI), we use the differences in how baseline and monitor models converge to determine a set of weights. These weights are then used to constrain the final joint inversion for the change in the material properties, highlighting areas that have been identified as having the highest probability of changes. The objective function to be minimized is:

$$\begin{aligned} E(m_0, m_1) = & \frac{1}{2} \|F(m_0) - d_0\|^2 \\ & + \frac{1}{2} \|F(m_1) - d_1\|^2 \\ & + \frac{1}{2} \left\| \frac{m_0 - m_1}{\beta} \right\|^2 \end{aligned} \quad (1)$$

where m_0 and d_0 are the baseline model and data, m_1 and d_1 are the monitor model and data, and β is the set of weights calculated by AFWI.

3 Numerical Example

We use a simple 2D model of two reflectors, where the position of the top reflector is shifted to introduce a change between the baseline and monitor models. One hundred different gaussian noise realizations are created and added to the model. For each model realization, AFWI is applied to create a set of weights (Figure 1), and the time lapse velocity change is recovered by minimizing the objective function given in equation (1) (Figure 2 shows the recovered time lapse change for the same model used in Figure 1). For each time lapse change image the distance between the two reflectors Δ_z is calculated for each column of the resulting image, and then averaged. Figure 3 shows a histogram of the averaged Δ_z for all the noise realizations. As expected, the recovered Δ_z are approximately normally distributed. Most of the results are near the true Δ_z which is 16. The errors in Δ_z seem to be symmetric with small

errors occurring more frequently than large errors.

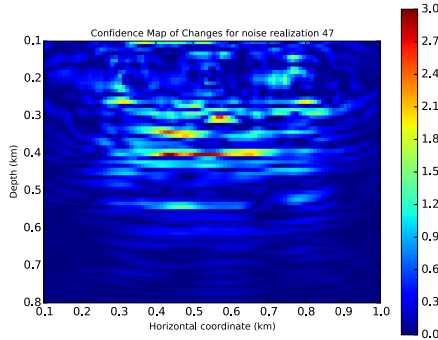


Figure 1: Map of probable changes in one of the models; areas with higher values represent areas where there is the highest probability of change.

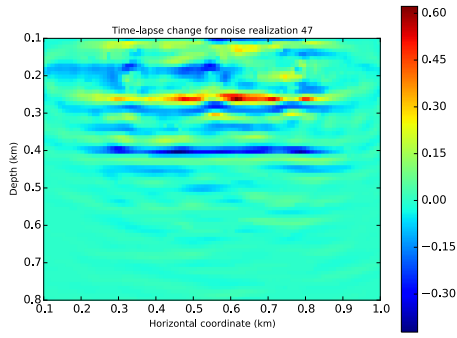


Figure 2: Recovered time lapse velocity change for the same noise realization as in Figure 1. Both top reflectors have been recovered accurately even though the noise artifacts are quite strong.

4 Discussion and Conclusion

We showed that errors in our recovered time lapse change are approximately normally distributed. The key remaining question is, can we go beyond this and provide an algorithm that calculates absolute errors? Current and future work to address this question is focusing on Bayesian statistics and the potential application of Monte Carlo methods.

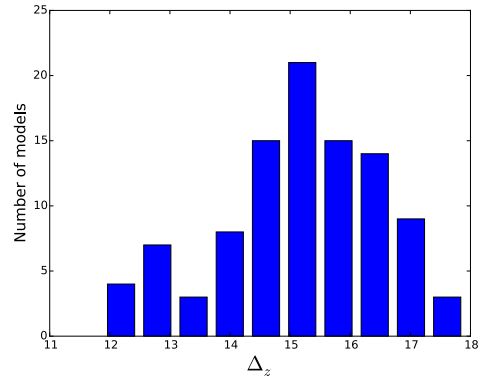


Figure 3: Histogram of the Δ_z from the recovered time lapse changes of the different noise realizations models

5 Acknowledgements

This work is supported by Chevron and with grants from the Natural Sciences and Engineering Research Council of Canada Industrial Research Chair Program and the Research and Development Corporation of Newfoundland and Labrador and by the Hibernia Management and Development Corporation.

References

- [1] Lumley, D., E., Time-lapse reservoir monitoring, *Geophysics* (2001), Vol. 66, No. 1, pp. 50–53.
- [2] Maharramov, M., and Biondi, B., Joint full waveform inversion of time-lapse seismic data sets, in *SEG Denver annual meeting* (2014), pp. 1–5.
- [3] Virieux, J., Operto, S., An overview on full waveform inversion in exploration geophysics, *Geophysics* (2009) **44**, WCC1–WCC26.
- [4] Yang, D., Malcolm, A., and Fehler, M., Time-lapse full waveform inversion and uncertainty analysis with different survey geometries, in *76th EAGE Conference and Exhibition* (2014).

Modelling and design of nano-structures: multilayer nanoplasmatics configurations

H. Kurkcu^{1,*}

¹Gulf University for Science and Technology, Mishref, Kuwait

*Email: kurkcu@math.umn.edu

Abstract

Nanoplasmatics forms a major part of the field of nanophotonics, which explores how electromagnetic fields can be confined over dimensions on the order of or smaller than the wavelength. Here, we present an integral-equation formulation of the mathematical model that delivers accurate solutions in small computational times for surface plasmons coupled by periodic corrugations of flat surfaces an extension of single layer configurations to a more challenging case; multilayered configurations. The new configuration is composed of a thin layer of a metal (gold, silver, etc.) with depth larger than skin depth of the material, buried into different epoxies on top (glass/polymer substrate) and the bottom (liquid/water/blood).

Keywords: plasmons, integral equations, high-order solvers

1 Introduction

Nanoplasmatics forms a major part of the field of nanophotonics, which explores how electromagnetic fields can be confined over dimensions on the order of or smaller than the wavelength. Initiated in 1902 by R.W. Wood [1] with the discovery of grating anomalies, this phenomenon has attracted significant attention over the last hundred years [2,3]. Mie in 1908 gave a mathematical description of light scattering from spherical particles of sizes comparable to the wavelength [2], describing an effect that would come to be known as localized surface plasmons in the context of nanoplasmatics. It is based on interaction processes between electromagnetic radiation and conduction electrons at metallic interfaces or in small metallic nanostructures, leading to an enhanced optical near-field at sub-wavelength dimension. In 1899, Sommerfeld had described surface waves (waves propagating at the surface of metals) mathematically, and in 1902 Wood observed anomalous drops in the intensity of light reflected by a metallic grating [2]. But theory and observation would not be linked until 1941, by Fano [4]. Further exper-

imental validation came in 1968, when Kretschmann and Raether used prism coupling to excite surface waves with visible light [5]. Other forms of coupling to surface plasmons have been thoroughly investigated since then. All of the phenomena mentioned above are based entirely on classical electromagnetics, and thus can be mathematically described by Maxwell's equations. In this paper, an integral-equations formulation is given for multilayered an infinitely periodic metal configuration whose period d is on the nanometer scale. This configuration is composed of a thin layer of metal with depth larger than skin depth of the material, buried into different epoxies on top (glass/polymer substrate) and the bottom (liquid/water/blood) both extend infinitely above and below the surface. Some details of the numerical implementation and the results of a few numerical experiments are also given in Sec. 2 and 3.

2 Formulation and Algorithm

In this section, a system of integral equations for the total exterior fields u_i ($u_i = E_z$ in Transverse Electric -TE- and $u_i = H_z$ in Transverse Magnetic -TM- polarizations) and its normal derivative $\frac{\partial u_i}{\partial n}$ on the surface Γ_i for $i = 1 \dots n$ are given. The metal surface Γ_i are periodic and satisfies $f_i(x + d_i, y) = f_i(x, y)$. For the sake of the completeness and for experimental setting, we look into 3 layer settings; glass/polymer substrate on the upper surface, epoxy in the lower one and metal in between.

As $x \rightarrow \Gamma_i$ and using the boundary conditions, the surface integral equations become:

$$\left(A_1 + [A_{21}|A_{22}] \right) \begin{bmatrix} u_1(x) \\ \frac{\partial u_1(x)}{\partial n(x)} \\ u_2(x) \\ \frac{\partial u_2(x)}{\partial n(x)} \\ \vdots \\ u_n(x) \\ \frac{\partial u_n(x)}{\partial n(x)} \end{bmatrix} = \begin{bmatrix} u^{\text{inc}}(x) \\ 0 \\ \frac{\partial u^{\text{inc}}(x)}{\partial n(x)} \\ 0 \\ \vdots \\ 0 \end{bmatrix}$$

where

$$A_1 = \begin{pmatrix} 1 & 0 & 0 & 0 \\ 0 & 0 & -1 & 0 \\ 0 & \frac{1+\nu_1}{2} & 0 & 0 \\ 0 & 0 & 0 & -\frac{1+\nu_2}{2} \end{pmatrix}$$

$$A_{21} = \begin{pmatrix} D_m^1 - D_e^1 & S_e^1 - \nu_1 S_m^1 \\ -D_m^1 & \nu_1 S_m^1 \\ -(N_e^1 - N_m^1) & D_e^{*1} - \nu_1 D_m^{*1} \\ -N_m^1 & \nu_1 D_m^{*1} \end{pmatrix}$$

$$A_{22} = \begin{pmatrix} D_m^2 & -S_m^2 \\ D_i^2 - D_m^2 & S_m^2 - \nu_2 S_i^2 \\ N_m^2 & -D_m^{*2} \\ -(N_m^2 - N_i^2) & D_m^{*2} - \nu_2 D_i^{*2} \end{pmatrix}$$

and the operators are

$$S_a^i(\mu) = \int_{\Gamma_i} G_a(x, y) \mu(y) dy$$

$$D_a^i(\mu) = \int_{\Gamma_i} \frac{\partial G_a(x, y)}{\partial n(y)} \mu(y) dy$$

$$D_a^{*i}(\mu) = \int_{\Gamma_i} \frac{\partial G_a(x, y)}{\partial n(x)} \mu(y) dy$$

$$N_a^i(\mu) = \int_{\Gamma_i} \frac{\partial^2 G_a(x, y)}{\partial n(x) \partial n(y)} \mu(y) dy$$

and $G_a(x, y)$ is the quasi periodic Green's function. Here $u^{\text{inc}}(r)$ denotes the incoming incident wave and $\nu = 1$ for TE polarization and $\nu = k_i/k_e$ for TM polarization.

Our numerical algorithm depends on seeking the unknowns on the surface of the grating, and the matrix elements are evaluated through the derivation of a careful decomposition that allows for explicit evaluation of the singular and non-singular parts of the kernels [7].

3 Numerical Results

In this section, we provide numerical experiments for the algorithm described above implemented in MATLAB. The test cases in the simulations that follow correspond to (“two-dimensional”) infinitely periodic metal gratings that invariant in the z direction. To investigate the existence of plasmonic resonances, we concentrate on the analysis at length scales where these do appear, namely

$$h \ll \lambda \sim d$$

where d is the period, h is the height of the rough surface and λ is the wavelength.

Here we present results of the integral solver for convergence, and display a specific verification against the high-order perturbation method introduced in [6] (See Fig. 1).

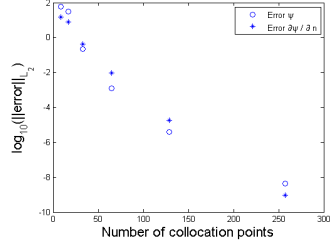


Figure 1: The error in the total field and its normal derivative as a function of the number of collocation points for the sinusoidal grating. The error is shown on a logarithmic scale for where a plasmon is generated.

References

- [1] R. W. Wood, *On a remarkable case of uneven distribution of light in a diffraction grating spectrum*, Philos. Mag. 4, 396-402, 1902.
- [2] G. Mie, *Contributions to the optics of turbid media, particularly of colloidal metal solutions*, Annalen der Physik, 377–445, 1908.
- [3] M. I. Stockman, *Nanoplasmonics: The physics behind the applications*, Physics Today, vol. 64.
- [4] Fano U., *The theory of anomalous diffraction gratings and of quasi-stationary waves on metallic surfaces*, JOSA, 213-222 1941.
- [5] Colton D. and Rainer K., *Inverse Acoustic and Electromagnetic Scattering Theory*, Springer-Verlag, 1992.
- [6] D. P. Nicholls, F. Reitich, T. Johnson, S.-H. Oh, *Fast High-Order Perturbation of Surfaces (HOPS) Methods for Simulation of Multi-Layer Plasmonic Devices and Metamaterials*, JOSA, 1820-1831 (2014).
- [7] Kurkcu H., F. Reitich and A. Ortan, *An efficient integral equation solver for two-dimensional simulations in nanoplasmonics*, Waves, 2015.

Sparse modal spectral-element methods for binary neutron stars

Stephen R. Lau^{1,*}

¹Department of Mathematics and Statistics, University of New Mexico, Albuquerque, NM USA

*Email: lau@math.unm.edu

Abstract

Adopting a post-Minkowski approximation for the Einstein-matter equations, we describe work towards numerical construction of helically symmetric spacetimes representing binary neutron stars. Established methods for solving the constraints of general relativity, thereby producing initial data for the Einstein-matter equations, start with trial data. We seek trial data without conformal flatness which gives rise to “junk radiation”. Our work relies on sparse, modal, spectral-element methods and 2-center domain decompositions. We gratefully acknowledge NSF DMS 1216866 for supporting most of this work.

Keywords: Spectral methods; neutron stars; gravitational waves.

1 Problem statement

Our efforts toward the construction of binary neutron star (BNS) initial data are based on the Landau-Lifschitz (LL) formulation of the Einstein equations. This formulation views the (densitized, contravariant) spacetime metric as

$$\mathbf{g}^{\mu\nu} \equiv (-\eta)^{1/2}(\eta^{\mu\nu} - \bar{h}^{\mu\nu}), \quad \eta = \det(\eta^{\mu\nu}), \quad (1)$$

where $\eta^{\mu\nu}$ is the (flat) Minkowski metric and $\bar{h}^{\mu\nu}$ the deviation from the flatness. The overbar is standard notation. We enforce the “harmonic gauge” (HG) condition $\partial\mathbf{g}^{\mu\nu}/\partial x^\mu = 0$, assuming the Einstein summation convention. For blackholes systems harmonic coordinates will not penetrate horizons, and so not cover the whole spacetime. We assume that a BNS spacetime (which, free of strong internal gravity, possesses no internal horizons) may be covered entirely by a harmonic coordinate system.

The HG Einstein equations in LL form are

$$\begin{aligned} \square\bar{h}^{\mu\nu} &= S_{\tau\phi\gamma\alpha}^{\mu\nu\kappa\beta}(\mathbf{g})\bar{h}^{\tau\phi},_{\kappa}\bar{h}^{\gamma\alpha},_{\beta} \\ &+ \bar{h}^{\alpha\beta}\bar{h}^{\mu\nu},_{\alpha\beta} - 16\pi|g|T^{\mu\nu}, \end{aligned} \quad (2)$$

where a comma denotes differentiation and density weights $(-\eta)^{1/2}$ are assumed unit. \square is the ordinary wave operator, and $S_{\tau\phi\gamma\alpha}^{\mu\nu\kappa\beta}(\mathbf{g})$ is a tensor

depending on the metric, but not its derivatives. The perfect-fluid stress energy tensor,

$$T^{\mu\nu} = (e + p)U^\mu U^\nu + pg^{\alpha\beta}, \quad (3)$$

depends on the velocity U^μ , energy density e , and pressure p . Our description of the fluid follows [1]. Define the enthalpy $h = (e+p)/(m_B n)$, where n is the baryon number density and m_B the mean baryon mass. Assume a cold matter equation of state: $n = n(h)$, $e = e(h)$, $p = p(h)$.

We also assume helical symmetry, in particular corotation $U^\alpha = (-\xi_\beta\xi^\beta)^{-1/2}\xi^\alpha$, where ξ^α is a Killing vector field which is timelike in the fluid. Covariant conservation of $T^{\mu\nu}$ then yields

$$h(-\xi_\beta\xi^\beta)^{1/2} = \text{constant in the fluid}, \quad (4)$$

to be enforced with (2) subject to nonlocal boundary conditions not discussed here.

For a scalar problem helical symmetry stems from $\partial_t \rightarrow -\Omega\partial_\varphi$, since the field depends on time through $\varphi \equiv \phi - \Omega t$, where ϕ is an azimuthal angle and Ω the rotation rate. This replacement converts \square into the mixed-type helically reduced wave operator (HRWO) $L = \nabla^2 - \Omega^2\partial_\varphi^2$. For a metric theory imposition of helical symmetry requires care, since it assumes a helical Killing vector ξ^μ . Price and coworkers have introduced helical scalars $\tilde{\Psi}^A$ [2], where the tilde means “corotation” and A runs over ten tensor-spherical-harmonic labels. The $\tilde{\Psi}^A$ are coefficients in an expansion of $\bar{h}^{\mu\nu}$ with respect to a basis of corotating tensor spherical harmonics. Although this formalism is a key aspect of our work, we ignore all details here.

2 Post-Minkowski (PM) approximation

Our PM approximation starts with expansions of $\bar{h}^{\mu\nu}$ and the fluid variables. Based on Kepler’s law and other considerations, we assume

$$\begin{aligned} \bar{h}^{tt} &\sim \bar{h}_1^{tt} + \bar{h}_2^{tt}, \quad \bar{h}^{tj} \sim \bar{h}_{1.5}^{tj}, \quad \bar{h}^{jk} \sim \bar{h}_2^{jk} \\ e &\sim e_1 + e_2, \quad p \sim p_1 + p_2, \quad \Omega \sim \Omega_{0.5} \end{aligned} \quad (5)$$

We seek variables which are accurate only through order 2, and consider the corresponding expansions/truncations of (2) and (4). One significant simplification is then $S_{\tau\phi\gamma\alpha}^{\mu\nu\kappa\beta}(\mathbf{g}) \rightarrow S_{\tau\phi\gamma\alpha}^{\mu\nu\kappa\beta}(\boldsymbol{\eta})$.

3 Numerical methods

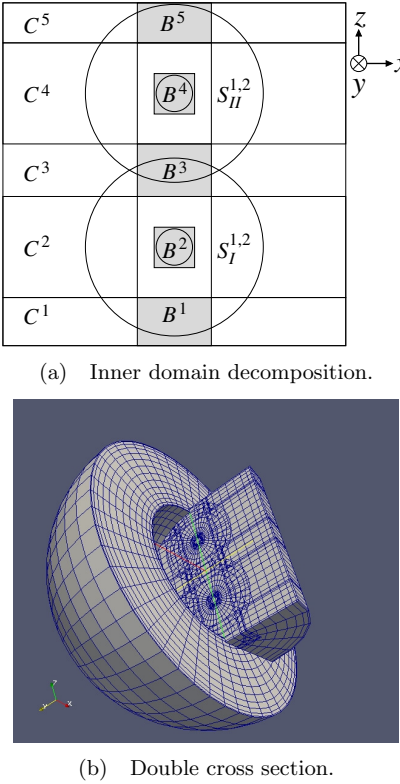


Figure 1: 2-CENTER DOMAIN.

Helically symmetric solutions are equilibrium configurations; whence we do not solve the above equations as an evolution problem. Instead, we use a version of the self-consistent field method [3], an iterative scheme. Linear problems encountered in the process are solved by preconditioned GMRES. Ours is a multidomain spectral-element approach, with a sparse representation of the HRW_O L achieved on subdomains through integration matrices [4]. We have shown that conditioning issues can be surmounted through the use of further preconditioning on top of the sparsification [5, 6]. The problem domain \mathcal{D} is a “2-center domain” split into a collection of (overlapping or conforming) subdomains. Here we consider the minimal configuration with 15 subdomains: blocks B^1, B^2, B^3, B^4, B^5 ; cylinders C^1, C^2, C^3, C^4, C^5 ; inner shells S_I^1, S_I^2 around star I ; inner shells S_H^1, S_H^2 around star H ; and an outer shell S_{out}^1 . Figure 1 depicts the decomposition. Such decompositions were pioneered by Pfeiffer et al. [7] and are used in the `EllipticSolver` of SpEC [8]. Our approach features (i) sparse representation of L on subdo-

mains, (ii) “gluing” of conforming and overlapping subdomains, (iii) modal-based preconditioning of subdomain solves, (iv) standard global preconditioning, (v) low-rank treatment of stellar surfaces, (vi) exact domain reduction.

References

- [1] E. Gourgoulhon, P. Grandclément, K. Taniguchi, J.-A. Marck, and S. Bonazzola, Quasiequilibrium sequences of synchronized and irrotational binary neutron stars in general relativity: Method and tests, *Phys. Rev. D* **63** (2001) 064029.
- [2] C. Beetle, B. Bromley, N. Hernández, and R. H. Price, Periodic standing-wave approximation: Post-Minkowski computations, *Phys. Rev. D* **76** (2007) 084016.
- [3] J. P. Ostriker and J. W.-K. Mark, Rapidly Rotating Stars I. The Self-Consistent Field Method, *Astrophys. J.* **151** (1968) pp. 1075–1088.
- [4] E. A. Coutsias, T. Hagstrom, J. S. Hesthaven, and D. Torres, Integration preconditioners for differential operators in spectral τ -methods, *Special Issue Houston J. Math.* **21** (1996) pp. 21–38.
- [5] S. R. Lau and R. H. Price, Sparse spectral-tau method for the three-dimensional helically reduced wave equation on two-center domains, *J. Comp. Phys.* **231** (2012) pp. 7695–7714.
- [6] S. R. Lau, Stellar surface as low-rank modification in iterative methods for binary neutron stars, 29 page preprint, November 2016. Submitted to *J. Comp. Phys.*
- [7] H. P. Pfeiffer, L. E. Kidder, M. A. Scheel, and S. A. Teukolsky, A multidomain spectral method for solving elliptic equations, *Comput. Phys. Commun.* **152** (2003) pp. 253–273.
- [8] Spectral Einstein Code (SpEC): <http://www.black-holes.org/SpEC.html>

Inverse Random Source Scattering Problems

Gang Bao¹, Chuchu Chen², Peijun Li^{3,*}

¹School of Mathematical Sciences, Zhejiang University, Hangzhou, China

²Department of Mathematics, Michigan State University, East Lansing, USA

³Department of Mathematics, Purdue University, West Lafayette, USA

*Email: lipeijun@math.purdue.edu

Abstract

This paper concerns the inverse random source scattering problem for the acoustic wave propagation. The goal is to reconstruct the statistical properties of the source from the boundary measurement of the radiated random wave field. Using multiple frequency data, we propose a regularized Kaczmarz method to solve the ill-posed Fredholm integral equations which arise from the mild solution for the direct problem. Numerical results are presented to show the efficiency of the proposed method.

Keywords: inverse source scattering, Helmholtz equation, stochastic differential equation

1 Introduction

Motivated by medical applications, the inverse source scattering problems have been investigated extensively in the literature [4]. There is a lot of information available concerning its solution mathematically and numerically. For instance, there exist an infinite number of sources that radiate fields which vanish identically outside their supported domain so that the inverse source problem does not have a unique solution at a fixed frequency. To overcome the obstacle, one may either seek the minimum energy solution, which represents the pseudo-inverse of the problem, or use multi-frequency scattering data to ensure uniqueness and gain increased stability of the solution [3].

In many applications the source and hence the radiated field may not be deterministic but rather are modeled by random processes. Their governing equations are stochastic differential equations and their solutions are random functions. It is more important to study their statistical characteristics such as mean, variance, and even higher order moments. The inverse stochastic source scattering problem is to deduce the mean and variance of the random source function from measurements of the random radiated fields [2, 5]. Although the deterministic

problem has been extensively investigated, little is known for the stochastic case, especially its computational aspects.

2 Problem formulation

Consider a model problem of the two-dimensional stochastic Helmholtz equation in a homogeneous medium:

$$\Delta u + \kappa^2 u = f \quad \text{in } \mathbb{R}^2,$$

where $\kappa > 0$ is the wavenumber, u is the radiated random wave field, and the electric current density f is assumed to be a random function driven by an additive white noise:

$$f(\mathbf{x}) = g(\mathbf{x}) + \sigma(\mathbf{x})\dot{W}_{\mathbf{x}}, \quad \mathbf{x} \in \mathbb{R}^2.$$

Here g and σ are two deterministic real functions which have compact supports contained in the rectangular domain $D \subset \mathbb{R}^2$, $W_{\mathbf{x}}$ is a Brownian sheet or a two-parameter Brownian motion, and $\dot{W}_{\mathbf{x}}$ denotes the white noise which can be roughly thought as the derivative of the Brownian sheet $W_{\mathbf{x}}$. In this random source model, the functions g , σ , and σ^2 can be viewed as the mean, standard deviation, and variance of the function f , respectively. As usual, the Sommerfeld radiation condition is required for the wave field:

$$\lim_{r \rightarrow \infty} r^{\frac{1}{2}} (\partial_r u - i\kappa u) = 0, \quad r = |\mathbf{x}|.$$

Let $B_R = \{\mathbf{x} \in \mathbb{R}^2 : |\mathbf{x}| = R\}$, where $R > 0$ is sufficiently large such that $D \subset B_R$. Denote by ∂B_R the boundary of B_R . Given the random source function f , i.e., given g and σ , the direct problem is to determine the random wave field u . The inverse problem is to reconstruct g and σ^2 simultaneously from the measured wave field on ∂B_R at a finite number of wavenumbers $\kappa_j, j = 1, \dots, m$.

3 Reconstruction formulas

We have proposed in [1] a new approach for solving the stochastic inverse source scattering

problem in higher dimensions. We show that there exists a unique mild solution to the stochastic direct scattering problem by constructing a sequence of regular processes approximating the white noise.

Theorem 1 *Let $\Omega \subset \mathbb{R}^2$ be a bounded domain. Assume that $g \in L^2(D)$, $\sigma \in L^p(D) \cap C^{0,\eta}(D)$, where $\eta \in (0, 1]$ and $p \in (p_0, \infty]$ if $\frac{3}{2} \leq p_0 \leq 2$ or $p \in (p_0, \frac{3p_0}{3-2p_0})$ if $1 \leq p_0 < \frac{3}{2}$. Then there exists almost surely a unique continuous stochastic process $u : \Omega \rightarrow \mathbb{C}$ satisfying*

$$\begin{aligned} u(\mathbf{x}, \kappa) = & \int_D G(\mathbf{x}, \mathbf{y}; \kappa) g(\mathbf{y}) d\mathbf{y} \\ & + \int_D G(\mathbf{x}, \mathbf{y}; \kappa) \sigma(\mathbf{y}) dW_{\mathbf{y}}, \end{aligned} \quad (1)$$

where $G(\mathbf{x}, \mathbf{y}; \kappa)$ is the fundamental solution for the Helmholtz equation.

Taking the expectation on both sides of (1) and using properties of stochastic integrals yields a Fredholm integral equation to reconstruct g :

$$\begin{aligned} \mathbf{E}(u(\mathbf{x}, \kappa_j)) = & \int_D G(\mathbf{x}, \mathbf{y}; \kappa_j) g(\mathbf{y}) d\mathbf{y}, \\ j = 1, \dots, m. \end{aligned} \quad (2)$$

Taking the variance on both side of (1) and using the Itô isometry for stochastic integrals, we derive another Fredholm integral equation can be derived to reconstruct σ^2 :

$$\begin{aligned} \mathbf{V}(\text{Re}u(\mathbf{x}, \kappa_j)) - \mathbf{V}(\text{Im}u(\mathbf{x}, \kappa_j)) \\ = \frac{1}{16} \int_D (Y_0^2(\kappa_j |\mathbf{x} - \mathbf{y}|) - J_0^2(\kappa_j |\mathbf{x} - \mathbf{y}|)) \\ \sigma^2(\mathbf{y}) d\mathbf{y}, \quad j = 1, \dots, m, \end{aligned} \quad (3)$$

where J_0 and Y_0 are the Bessel function of the first and the second kind with order zero, respectively.

It is known that Fredholm integral equations of the first kind are ill-posed. Using multi-frequency scattering data, the PI has proposed a regularized Kaczmarz method to overcome the challenge of solving the ill-posed integral equations (2) and (3). The Kaczmarz algorithm is an iterative method for solving linear systems of algebraic equations. The idea is to project the current approximation solution at each frequency successively onto the hyperplanes spanned by the solutions at other frequencies. It is only required to solve a small scale linear system with size equal to the number of measurement at each iteration.

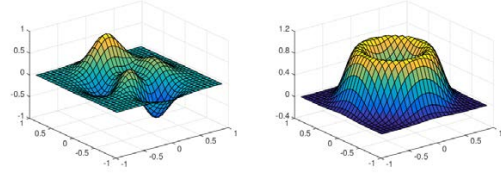


Figure 1: (left) The exact mean g ; (right) The exact variance σ^2 .

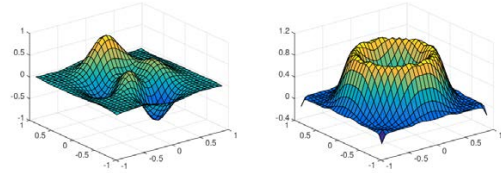


Figure 2: (left) The reconstructed mean g ; (right) The reconstructed variance σ^2 .

4 Numerical results

As a numerical example, Figure 1 shows the exact mean g and variance σ^2 ; Figure 2 shows the reconstructed mean g and σ^2 . The scattering data is obtained by the numerical solution of the stochastic Helmholtz equation via the Monte Carlo method, which allows us to simulate the actual process of measuring data. The mean and variance in (2) and (3) are approximated by taking the average of the solutions after a certain number of realizations are done for the randomness.

References

- [1] G. Bao, C. Chen, and P. Li, *SIAM/ASA J. Uncertainty Quantification* **4** (2016), pp. 1263–1287.
- [2] G. Bao, S.-N. Chow, P. Li, and H.-M. Zhou, *Math. Comp.* **83** (2014), pp. 215–233.
- [3] G. Bao, P. Li, J. Lin, and F. Triki, *Inverse Problems* **31** (2015), 093001.
- [4] V. Isakov, *Inverse Source Problems*, AMS, Providence, RI, 1989.
- [5] P. Li, *Inverse Problems* **27** (2011), 035004.

Numerical Study of Fracture Connectivity Effect on Seismic Wave Propagation

Mikhail Novikov¹, Vadim Lisitsa^{2,*}

¹Novosibirsk State University, Novosibirsk, Russia

²Institute of Petroleum Geology and Geophysics, Novosibirsk, Russia

*Email: lisitsavv@ipgg.sbras.ru

Abstract

According to theoretical study seismic wave propagating in a model with fluid-filled fractures structure may lead to the wave-induced fluid flow. Moreover, these flows are expected to depend on the connectivity of the fractures. However, this effect is expected at high frequencies where scattering may dominate. In this paper we perform numerical study of this effect. We show that in case of connected fractures the wave velocity is lower than in the case of the nonintersected fractures. However, energy dissipation is mainly connected with the scattering and effect of fracture connectivity can not be estimated from full waveform simulation.

Keywords: poroelasticity, wave induced fluid flow, attenuation, finite difference simulation.

1 Introduction

Problems of seismic wave propagation in media with mesoscopic heterogeneities (fractures) are of great interest in reservoir geophysics. Recently, it was shown that if the fractures are interconnected then wave propagating in such media causes wave-induced fluid flows (WIFF) inside the fracture system, whereas disconnected fractures do not support WIFF [1]. This causes seismic energy dissipation and opens a possibility to characterize the fracture system connectivity and reservoir permeability from the seismic waves.

However, previous numerical studies of this physical effect are performed using quasi-static approximation of poroelastic models, assuming that the wavelength is much greater than the fractures but the effect is observed at frequencies close to 10 kHz. It is clear that quasi-static approximation leads to high error at these frequencies, moreover the size of fractures is comparable with the wavelength which makes the scattering effect dominating. To observe the WIFF and estimate its influence on wave propagation in this paper we present numerical simulations of seismic wave propagation in poro-

elastic media with highly permeable fluid-filled fracture systems with different orientation and connectivity.

2 Numerical Simulation

Wave propagation in fluid-filled poroelastic media is described by the dynamic Biot equations [2]:

$$\begin{aligned} \rho_f \frac{T}{\phi} \frac{\partial \mathbf{q}}{\partial t} + \frac{\eta}{k_0} \mathbf{q} &= -\nabla p - \rho_f \frac{\partial \mathbf{v}}{\partial t}, \\ \rho \frac{\partial \mathbf{v}}{\partial t} &= \nabla \cdot \boldsymbol{\sigma} - \rho_f \frac{\partial \mathbf{q}}{\partial t}, \\ \frac{\partial \boldsymbol{\sigma}}{\partial t} &= (\lambda_u \nabla \cdot \mathbf{v} + \alpha M \nabla \cdot \mathbf{q}) \mathbf{I} + \mu \left[\nabla \mathbf{v} + (\nabla \mathbf{v}^T) \right], \\ -\frac{\partial p}{\partial t} &= M(\alpha \nabla \cdot \mathbf{v} + \nabla \cdot \mathbf{q}). \end{aligned}$$

Here \mathbf{v} and \mathbf{q} are solid and fluid particle velocities, $\boldsymbol{\sigma}$ is stress tensor, p is fluid pressure; T is tortuosity, ϕ is porosity, η is fluid viscosity, k_0 is permeability; ρ_f and ρ are fluid density and bulk density of the porous fluid-saturated material; M and α are auxiliary variables, λ_u and μ are Lame constants of undrained material.

For the numerical approximation of the presented model we use the standard staggered grid scheme with the second order of approximation in time and space [3].

We simulate plane wave propagation in four types of models: (a) fractures parallel to the wave propagation direction, (b) perpendicular fractures, (c) 50% of fractures are parallel to the wave propagation direction and 50% of them are perpendicular to the wave propagation direction with no conditions on the fracture intersection, (d) same as (c) but we require each fracture to intersect with at least one other fracture, Fig. 1.

For each mode, we simulated plane wave propagation using Ricker pulse with central frequencies from 250 Hz to 25 kHz, in total 28 different simulations. In addition, we varied permeability of the fracture filling material from 10^{-17} to 10^{-8} m². This particular parameter

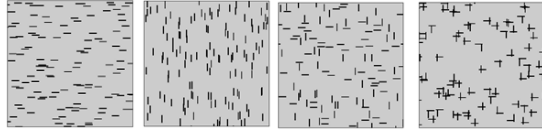


Figure 1: Sketches of the models types, left to right parallel, perpendicular, nonintersected, intersected

defines the transport property of the material and governs the fluid flow intensity.

We use periodic boundary conditions at the top and bottom of the domain and PML at the sides. We record the field at two lines and then, using deconvolution of these signals, we estimate velocity and attenuation of the seismic wave at frequencies around the central one.

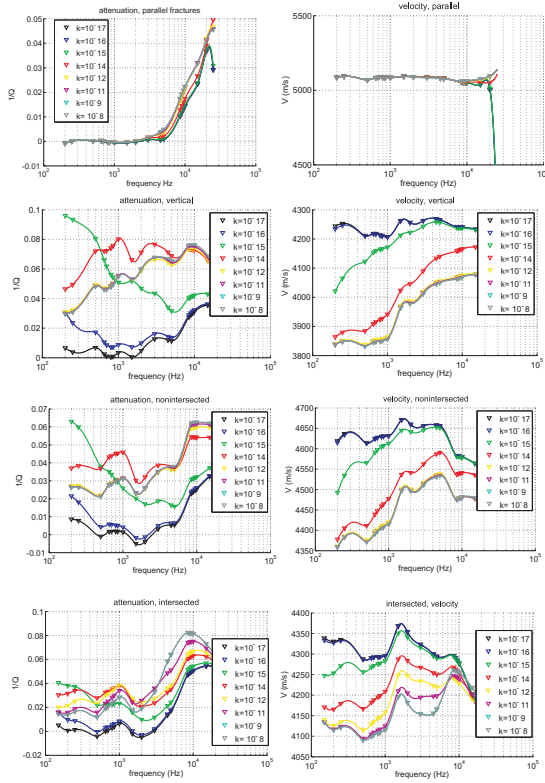


Figure 2: Attenuation (left) and phase velocity (right) for parallel, perpendicular, nonintersecting, and intersecting (from top to bottom).

3 Discussions

According to the plots presented in Fig. 2 if the signal frequency exceeds 10 kHz the scattering

of the seismic waves by the fractures dominates over all other physical attenuation mechanisms. Which is reasonable according to general wave scattering theory because at this frequency the wavelength is about 0.4 m whereas the fracture length is 0.04 m. At the same time no attenuation peaks [1] connected to the WIFF can be reliably determined. Meanwhile, the main result is that we can clearly see that in case of connected fractures the velocity of wave propagation is lower than that in the case of nonintersected fractures. This effect can be used to estimate the a degree of fracture network connectivity from seismic and acoustic data.

4 Acknowledgements

This research was partially financially supported by the RFBR grants no. 17-05-00250, 17-05-00579, 16-05-00800.

References

- [1] Rubino, J. German and Muller, Tobias M. and Guaracino, Luis and Milani, Marco and Holliger, Klaus, Seismoacoustic signatures of fracture connectivity, *Journal of Geophysical Research: Solid Earth* **119** (2014), pp. 2252–2271.
- [2] Masson, Y. J. and Pride, S. R. and Nihei, K. T., Finite difference modeling of Biot's poroelastic equations at seismic frequencies, *Journal of Geophysical Research: Solid Earth* **111**, (2006), B10305.
- [3] Virieux, J., P-SV wave propagation in heterogeneous media: Velocity-stress finite-difference method, *Geophysics* **51**, (1986), pp. 889–901.

Numerical modeling of a time-fractional Burgers equation

Bruno Lombard^{1,*}, Denis Matignon²

¹LMA, CNRS, UPR 7051, Aix-Marseille Univ., Centrale Marseille, 13453 Marseille, France

²ISAE-Supaéro, University of Toulouse, BP 54032, 31055 Toulouse, France

*Email: lombard@lma.cnrs-mrs.fr

Abstract

A fractional time derivative is introduced into Burgers equation to model losses of nonlinear waves arising in acoustics. A diffusive representation of the fractional derivative replaces the nonlocal operator by a continuum of memory variables that satisfy local ordinary differential equations. A quadrature formula yields a system of local partial differential equations. The quadrature coefficients are computed by optimization with a positivity constraint. One resolves the hyperbolic part by a shock-capturing scheme, and the diffusive part exactly. Extensive details can be found in [3].

Keywords: fractional derivatives, diffusive representation, nonlinear acoustics, Strang splitting

1 Introduction

We investigate Burgers equation with a fractional time derivative D_t^α ($\varepsilon \geq 0$, $0 < \alpha < 1$):

$$\frac{\partial u}{\partial t} + \frac{\partial}{\partial x} \left(a u + b \frac{u^2}{2} \right) = -\varepsilon D_t^\alpha u, \quad (1)$$

For a causal function $u(t)$, $D_t^\alpha u$ refers to the Caputo fractional derivative in time of order α :

$$D_t^\alpha u = \frac{1}{\Gamma(1-\alpha)} \int_0^t (t-\tau)^{-\alpha} \frac{\partial u}{\partial \tau}(x, \tau) d\tau, \quad (2)$$

where Γ is the Gamma function. The l.h.s. of (1) is a standard transport equation, with linear advection at constant speed a and a nonlinear quadratic term with coefficient b . The r.h.s. of (1) models linear losses and memory effects along the propagation. Since $\alpha < 1$, the hyperbolic nature of Burgers equation is preserved.

Various physical configurations are described by (1). Particular values of ε and α enable to recover Chester's equation describing propagation of finite-amplitude sound waves in tubes, up to $\mathcal{O}(\varepsilon^2)$ terms. This equation is widely used to model brass instruments (trombones, trumpets): the transport terms describe the steepening of waves, yielding the typical "brassy"

effect, and the fractional term models the viscothermal losses at the wall of the duct. Moreover, the linear Lokshin equation can be seen as the superposition of two one-way fractional transport equations of this type [1]. Other applications of (1) concern viscoelasticity, propagation in elastic-walled tubes, or more generally wave propagation in media with memory and complex rheological properties.

2 Diffusive approximation

The convolution product (2) can be recast as

$$D_t^\alpha u = \int_0^{+\infty} \phi(x, t, \theta) d\theta, \quad (3)$$

with the diffusive variable ϕ given by

$$\phi(x, t, \theta) = \gamma_\alpha \theta^{2\alpha-1} \int_0^t \frac{\partial u}{\partial \tau}(x, \tau) e^{-(t-\tau)\theta^2} d\tau, \quad (4)$$

with $\gamma_\alpha = \frac{2\sin(\pi\alpha)}{\pi} > 0$. From equation (4), ϕ satisfies the following first-order ordinary differential equation (ODE):

$$\frac{\partial \phi}{\partial t} = -\theta^2 \phi + \gamma_\alpha \theta^{2\alpha-1} \frac{\partial u}{\partial t}. \quad (5)$$

The integral in (3) is approximated by a quadrature formula on L points, where the diffusive variables ϕ_ℓ satisfy an ODE deduced from (5):

$$\begin{cases} D_t^\alpha u(x, t) \approx \sum_{\ell=1}^L \mu_\ell \phi(x, t, \theta_\ell) \equiv \sum_{\ell=1}^L \mu_\ell \phi_\ell(x, t), \\ \frac{\partial \phi_\ell}{\partial t} = -\theta_\ell^2 \phi_\ell + \gamma_\alpha \theta_\ell^{2\alpha-1} \frac{\partial u}{\partial t}, \quad \ell = 1, \dots, L. \end{cases} \quad (6)$$

An adequate choice of the weights μ_ℓ and nodes θ_ℓ is crucial for the efficiency and accuracy of the diffusive approximation, see e.g. [3] and references therein. Injecting (6) into (1) yields

$$\frac{\partial}{\partial t} \mathbf{U} + \frac{\partial}{\partial x} \mathbf{F}(\mathbf{U}) = \mathbf{S} \mathbf{U}, \quad (7)$$

with $\mathbf{U}(x, t) = (u, \phi_1, \dots, \phi_L)^T$. The energy of \mathbf{U} decreases if $\mu_\ell > 0$ and $\theta_\ell > 0$. A Strang

splitting is used to solve (7). The propagative part is solved by a finite-volume scheme with flux-limiters [2], whereas the diffusive part is solved exactly. The CFL condition of stability is the same as for the inviscid Burgers equation.

3 Numerical experiments

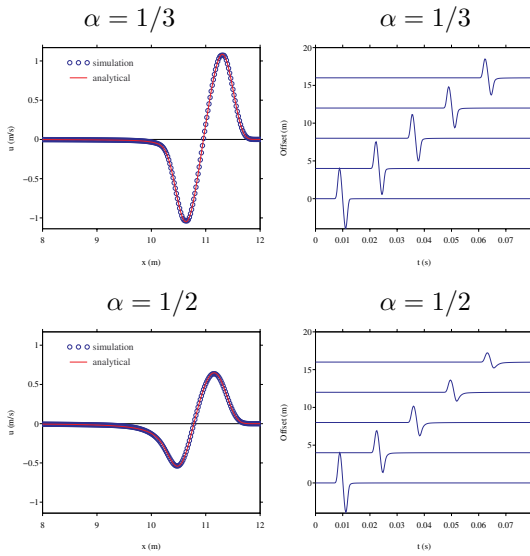


Figure 1: linear fractional advection, for various fractional order α . Left row: snapshots of the numerical and exact solutions. Right row: seismograms.

First, we consider linear advection ($b = 0$). A smooth truncated sinusoid is injected at the left boundary of the domain. Closed-form analytical solutions are known for $\alpha = 1/3$ and $\alpha = 1/2$. These cases are illustrated in figure 1. In the left row, one compares snapshots of the numerical and exact solutions. Greater values of α yield a greater attenuation and a slower propagation, as predicted by the dispersion analysis [3]. The right row illustrates the time and space evolution of the waves.

Second, we consider both nonlinear propagation and fractional attenuation (figure 2). The initial data is a rectangular pulse. Without attenuation, classical phenomena are observed: the pulse splits into a left rarefaction wave and a right shock (a), which collide (b). With attenuation, the right-going shock smears and even disappears for sufficiently large ε .

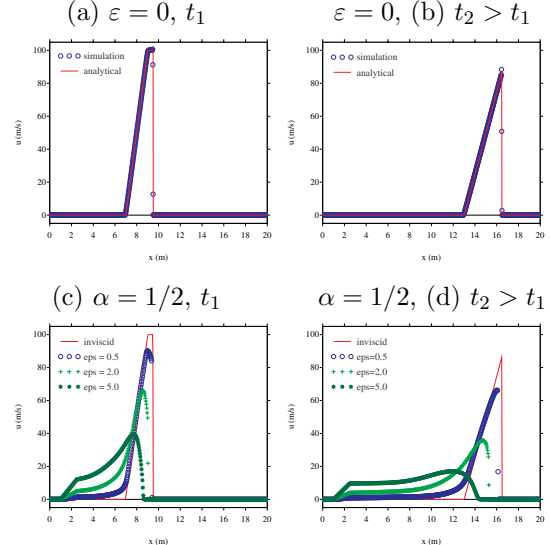


Figure 2: nonlinear advection and fractional attenuation. (a-b): numerical and exact solutions without attenuation. (c-d): numerical solutions for $\alpha = 1/2$ and various values of ε .

4 Conclusion

This article is an attempt for better understanding the competition between nonlinear effects and nonlocal relaxation. Many theoretical questions remain to be addressed. In particular, it seems that the emergence of shocks is conditional (unlike the inviscid Burgers equation). This question requires a deeper analysis to confirm / infirm the numerical observations.

References

- [1] T. Hélie and D. Matignon, Diffusive representations for the analysis and simulation of flared acoustic pipes with visco-thermal losses, *Math. Models Meth. Appl. Sci.* **16** (2006), pp. 503–536.
- [2] R. J. LeVeque, *Finite Volume Methods for Hyperbolic Problems*, Cambridge University Press, 2002.
- [3] B. Lombard and D. Matignon, Diffusive approximation of a time-fractional Burgers equation in nonlinear acoustics, *SIAM J. Appl. Math.* **76-5** (2016), pp. 1765–1791.

Modeling Gravitational Waves with Numerical-Relativity Simulations

Carlos O. Lousto¹, Manuela Campanelli, Yosef Zlochower

¹Center for Computational Relativity and Gravitation, School of Mathematical Sciences, Rochester Institute of Technology, 85 Lomb Memorial Drive, Rochester, New York 14623

Abstract

We report here on the calculation of gravitational radiation and strong-field dynamics from spinning black-hole binaries (BHB). This research is crucial not only for interpreting the data gathered by ground-based interferometric gravitational wave (GW) detectors such as advanced LIGO, VIRGO, and other similar detectors under construction, but it is also important for understanding the astrophysical and cosmological implications of the final kick, mass, and spin of the BHB merger remnant.

Keywords:

Binary Black Holes. Numerical Relativity Simulations. Gravitational Waves.

1 Introduction

In 2005, Campanelli, Lousto, Marronetti and Zlochower pioneered a major breakthrough in the area of numerical relativity (NR): the moving puncture method for numerically solving General Relativity's field equations [1]. This technique¹ has become one of the two dominant methods for simulating the inspiral, merger, and ringdown of binary black holes. It has allowed analysis of the rich physics of black-hole mergers, from the gravitational radiation produced by quasi-circular binary black holes [3] to the discovery of large gravitational recoils from generic binary mergers [4] and spin precessional dynamics [5]. We have studied the distributions of the spins, remnant mass, and recoil velocity of generic binaries during inspiral and merger [?, 6] and simulated binaries with large mass ratios [7].

2 Research summary

The main objective of this research program is to cover the physical 7-dimensional parameter space of a BHB system, i.e. arbitrary mass ratios $q = M_1/M_2$ and arbitrary individual spins (magnitude and direction) of the holes in an

efficient way. This program faces several important challenges. First, simply sampling the 7-dimensional parameter space in an efficient manner to extrapolate the behavior of generic BHBs from a small set of simulations is a task in itself. Second, the regions of parameter space that are directly relevant to current detectors like aLIGO/VIRGO as well as future detectors such as eLISA, KAGRA, and the Einstein Telescope, which encompass intermediate-mass and supermassive BHBs, respectively, require very high resolution near the horizons and have proven to be extremely computationally demanding.

The current generation of GW detectors are expected to identify many coalescing BHBs per year, over a broad range of (redshifted) masses between $20M_\odot$ and $100M_\odot$. These generally spinning and precessing moderate-mass BHBs should have a short but rich, multimodal signal. In much of this mass region, numerical relativity and hybrids are immediately actionable, with durations and frequency content comparable to relevant data. The signal brevity – relatively few cycles are available – also insures a broad posterior distribution, comparable to inter-simulation spacing. For this reason, numerical relativity has an extremely significant role to play in the interpretation of these kinds of events, both as synthetic signals used to validate existing search and parameter estimation algorithms, as well as parameter estimation templates, directly compared to the data itself.

One of the most remarkable results that came from breakthroughs of 2005 in numerical relativity is that the merger remnant of a BHB merger can recoil at thousands of kilometers per second .

As $\sim 93\%$ of the astrophysically interesting supermassive BHB merger recoil occur in the mass ratio range $1/10 < q < 1$, we need to model the mass ratio dependence accurately. Over the last few years we completed a set of several hundred high-recoil runs where one BH was spinning and the other non-spinning. These extensive runs allowed us to begin the model-

¹The method was also simultaneously and independently developed by the numerical relativity group at NASA/GSFC [2].

ing of the unequal-mass dependence of the recoil. However, because we had one BH non-spinning, our runs all obeyed the symmetry that $\vec{S} = \vec{S}_1 + \vec{S}_2$ and $\vec{\Delta} = m(\vec{S}_2/m_2 - \vec{S}_1/m_1)$ were collinear. To complete our modeling, we need to remove this symmetry. Similarly, all of our previous runs had spins $S_i/m_i^2 < 0.9$. Here too, we will need to use our new highly-spinning data to model the recoil for the astrophysically relevant case of $0.9 \lesssim S_i/m_i^2 \lesssim 0.998$.

One of the outstanding problems in numerical relativity is the simulation of nearly extremal (spin) binaries. Very high spins are thought to be common in nature. On the other hand, we have strong evidence from analysis of Kerr geodesic, particle-limit calculations of recoils, and perturbation theory that the dynamics of highly spinning black holes (BHs) cannot be elucidated with any degree of certainty using lower spin simulations.

The study of mergers of highly-spinning binaries started in earnest with the work of Lovelace and collaborators with their development of initial data that could represent binaries with high spins. Previously, initial data constructions were based on conformally flat backgrounds which are limited to spins of about $\alpha = S/M^2 \lesssim 0.92$. While spins of 90% the maximum may seem large enough, a more accurate measure of the spin would be the parameters $1/(1 - \alpha)$ (see the discussion in concerning spin-induced *turbulence* in black-hole perturbations), making $\alpha = 0.9$ very far calculations of the physical upper limit of BH spins $\alpha \sim 0.998$ (for thin-disk accretion).

Moving-punctures-based codes [1,2] have not been able to Evolve highly spinning holes. Importantly, this includes the international Einstein Toolkit consortium, which includes researchers at RIT and over 50 other institutions.

To overcome this limitation, our group developed a new initial data solver, HiSPID, that uses the single domain spectral method developed by Ansorg *et al.* for Bowen-York data to solve the nonlinear coupled system of elliptical PDEs for superimposed boosted Kerr BHs with arbitrary momenta and spins. Unlike the data introduced by Lovelace and collaborators, we use puncture based initial data, and thus our new data are manifestly compatible with the moving puncture approach. We are in the process of fine-tuning the algorithm for highly-

spinning binaries with arbitrary spin-orientations and have already produced waveforms for highly-spinning binaries with specific spin orientations.

Our initial data is based on a superposition of boosted conformally Kerr black holes (each in a puncture gauge) metrics and associated extrinsic curvatures. The free data we extract from this are the conformal metric and trace-free extrinsic curvature, as well as the trace of the extrinsic curvature. We intend to make this available to the whole NR community.

References

- [1] M. Campanelli, C. O. Lousto, P. Marronetti, and Y. Zlochower, “Accurate evolutions of orbiting black-hole binaries without excision,” *Phys. Rev. Lett.*, vol. 96, p. 111101, 2006.
- [2] J. G. Baker, J. Centrella, D.-I. Choi, M. Koppitz, and J. van Meter, “Gravitational wave extraction from an inspiraling configuration of merging black holes,” *Phys. Rev. Lett.*, vol. 96, p. 111102, 2006.
- [3] M. Campanelli, C. O. Lousto, and Y. Zlochower, “The last orbit of binary black holes,” *Phys. Rev.*, vol. D73, p. 061501(R), 2006.
- [4] M. Campanelli, C. O. Lousto, Y. Zlochower, and D. Merritt, “Large merger recoils and spin flips from generic black-hole binaries,” *Astrophys. J.*, vol. 659, pp. L5–L8, 2007.
- [5] C. O. Lousto and J. Healy, “Flip-flopping binary black holes,” *Phys. Rev. Lett.*, vol. 114, no. 14, p. 141101, 2015. [gr-qc].
- [6] M. Campanelli, C. O. Lousto, Y. Zlochower, and D. Merritt, “Maximum gravitational recoil,” *Phys. Rev. Lett.*, vol. 98, p. 231102, 2007.
- [7] C. O. Lousto and Y. Zlochower, “Orbital Evolution of Extreme-Mass-Ratio Black-Hole Binaries with Numerical Relativity,” *Phys. Rev. Lett.*, vol. 106, p. 041101, 2011.

Scattering from a row of aligned cylinders of arbitrary cross-section; tail-end asymptotics for efficient evaluation of the periodic Green's function

Georgia Lynott^{1,*}, William Parnell¹, David Abrahams², Mike Simon¹

¹School of Mathematics, University of Manchester, Oxford Road, Manchester, M13 9PL, UK

²Isaac Newton Institute, University of Cambridge, 20 Clarkson Road, Cambridge, CB3 0EH, UK

*Email: georgia.lynott@manchester.ac.uk

Abstract

The problem of wave scattering from a periodic row of parallel cylinders, of arbitrary cross-section, is studied via the boundary element method (BEM). The standard procedure of introducing the periodic Green's function is followed to give rise to a simplified integral equation. However, in general this requires the computation of an infinite sum that is slow to converge. Here a novel method is presented in order to approximate this infinite sum via a finite sum and asymptotic corrections; the scheme is rapidly convergent and straightforward to implement for cylinders of arbitrary cross-section. Numerical results for the transmission and reflection coefficients from arrays with different cross sections are obtained.

Keywords: Acoustic scattering, periodic Green's function, BEM.

1 Introduction

The problem of scattering from arrays of cylinders or gratings has been studied previously in acoustics e.g. [1], [3], and for elastic waves [2]. Following the approach of [1], we seek a solution via boundary element methods (BEMs). This requires the determination of the periodic Green's function (and its normal derivative) which is generally non-standard to compute. Here we present a novel approach to tackle this difficulty via an asymptotic correction to truncating the infinite series in the case of an infinite array. Results are given for arrays of cylinders of various cross sections.

2 Problem formulation

We consider an acoustic plane wave scattered by an infinite row of aligned, parallel cylinders, as illustrated in Fig. 1. The total field, which is written as the sum of the incident and scattered fields

$$\phi(\mathbf{x}) = \phi^{\text{in}}(\mathbf{x}) + \phi^{\text{sc}}(\mathbf{x}),$$

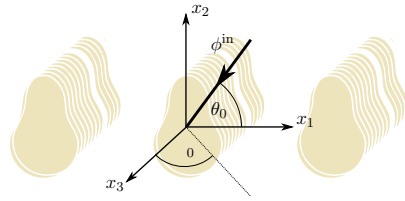


Figure 1: Time-harmonic plane wave, with incident angle (ψ_0, θ_0) , scattering from a periodic array of parallel cylinders with spacing d and cross section V_m .

satisfies the Helmholtz equation

$$(\nabla^2 + k^2)\phi = 0.$$

The case of rigid scatterers is considered so that a Neumann boundary condition is imposed on the surfaces of scatterers ∂V_m . Reformulating as a boundary integral equation and taking advantage of the periodicity in the domain, we may rewrite the problem as an integral over a single reference cylinder ∂V^0

$$\phi(\mathbf{x}^0) = \phi^{\text{in}}(\mathbf{x}^0) + \int_{\partial V^0} \phi(\boldsymbol{\xi}^0) \frac{\partial G^P(\mathbf{x}^0, \boldsymbol{\xi}^0)}{\partial n} dS(\boldsymbol{\xi}^0).$$

The kernel of this integral contains the periodic Green's function G^P , which for this problem takes the form of an infinite sum of Hankel functions and is not straightforward to compute. An important summary of current methods to evaluate the Green's function is given in [4].

3 The periodic Green's function

In order to efficiently compute G^P , we truncate the infinite sum at some integer M , and expand asymptotically, for large m , the remaining ‘tail-ends’ of the sum for $m \geq M$ and $m \leq -M$ so that

$$\begin{aligned} \frac{\partial G^P}{\partial n}(\mathbf{x}, \boldsymbol{\xi}) &= -\frac{i\bar{k}}{4} \sum_{m=-(M-1)}^{M-1} \left(e^{ikdm \sin \psi_0 \cos \theta_0} \right. \\ &\quad \times H_1^{(1)}(\bar{k}r_m) \left. \frac{(u + dm)n_1 + vn_2}{r_m} \right) + \sigma_+ + \sigma_-, \end{aligned}$$

where $u = x_1^0 - \xi_1^0$, $v = x_2^0 - \xi_2^0$ and

$$r_m = \sqrt{(u + dm)^2 + v^2}.$$

Also $\bar{k} = k\sqrt{1 - \cos(\psi_0)^2}$, as a result of factoring out the x_3 dependence in the problem. Expanding for large m , defining

$$\alpha_{\pm} = d(\bar{k} \pm k \sin \psi_0 \cos \theta_0),$$

and using the Lerch transcendent [5] allows us to replace the infinite sums that arise in the ‘tail-ends’ σ_{\pm} by the asymptotic form

$$\begin{aligned} \sigma_{\pm} = -\frac{i\bar{k}}{4} \sqrt{\frac{2}{\pi \bar{k} d}} e^{i(\pm \bar{k} u - \frac{3\pi}{4})} & \frac{e^{iM\alpha_{\pm}}}{\sqrt{M}(1 - e^{i\alpha_{\pm}})} \\ & \times \left(\pm n_1 + \frac{C'_{\pm}}{M} + \frac{D'_{\pm}}{M^2} \right), \end{aligned}$$

where C'_{\pm} and D'_{\pm} depend on the coordinates u, v , the surface normal \mathbf{n} , the dimensionless wavenumber, kd , and the angle of the incident wave.

4 Results

Recalling the periodic behaviour of the Green’s function in the x_1 direction, we can compare to what extent our approximations satisfy this condition by taking the largest difference between any two peaks in the function over a range $(-\frac{3d}{2}, \frac{3d}{2})$, say, as a measure of the error, as shown in Fig. 2. As can be seen, the sum with correction is more accurately periodic than the truncated sum alone. We employ this evalua-

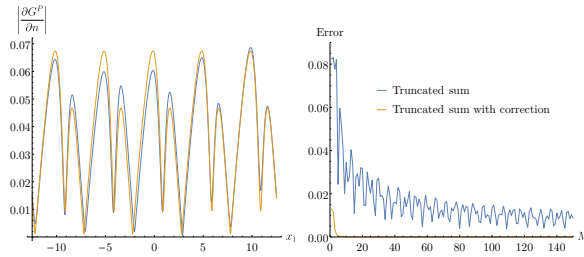


Figure 2: Left, the value of the derivative of G^P over x_1 for the truncated sum with (orange) and without (blue) correction term at $M = 150$. Right, a comparison of the error as M increases.

tion of G^P in a BEM scheme, in order to calculate reflection and transmission coefficients for infinite arrays. Given the excellent convergence of the corrected sum even at $M = 50$, a truncation point of $M = 200$ was chosen to ensure sufficiently accurate results, though this may not

be optimal. We have calculated results for a variety of cross sections, including the “gourd”-shaped cylinders as seen in Fig. 4. The results for circular cylinders shown in Fig. 3 display good agreement with [1].

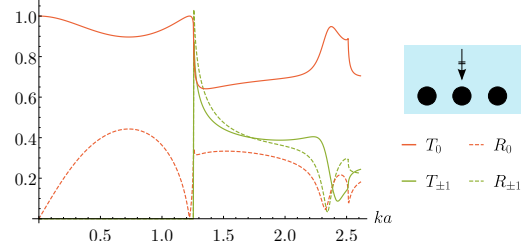


Figure 3: Reflection and transmission coefficients of the first two propagating modes for an array of circles, incident angle $(\psi_0, \theta_0) = (\frac{\pi}{2}, \frac{\pi}{2})$.

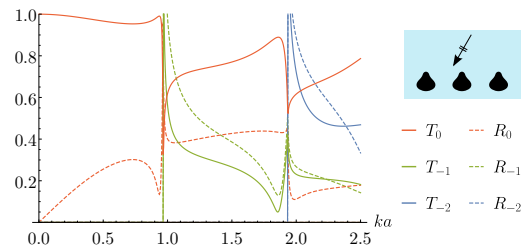


Figure 4: Reflection and transmission coefficients of the first three propagating modes for an array of gourds, incident angle $(\psi_0, \theta_0) = (\frac{\pi}{3}, \frac{\pi}{3})$.

References

- [1] J.D. Achenbach, Y.C. Lu, M. Kitahara, *Journal of Sound and Vibration* **125**(3) (1988), pp. 463–476.
- [2] J.D. Achenbach, M. Kitahara, *Journal of the Acoustical Society of America* **80** (4) (1986), pp. 1209–1214.
- [3] V. Twersky, *IRE Trans. on Antennas and Propagation* 4 pp. 330–345.
- [4] C.M. Linton, I. Thompson, *Wave Motion* **44**, pp. 165–175
- [5] A. Erdélyi, W. Magnus, F. Oberhettinger and F. G. Tricomi, *Higher Transcendental Functions Vol. I*, McGraw-Hill Book Company, New York-Toronto-London, 1953

Adaptive finite-element simulation of surface-plasmon polaritons on 2D materials

Matthias Maier^{1,*}, Dionisios Margetis², Mitchell Luskin¹

¹School of Mathematics, University of Minnesota, Minneapolis, Minnesota 55455, USA

²Department of Mathematics, University of Maryland, College Park, Maryland 20742, USA

*Email: msmaier@umn.edu

Abstract

We formulate a finite element framework for the observation of surface plasmon-polaritons (SPP) on 2D materials, such as graphene. The 2D material is modeled as an idealized hypersurface with an effective complex-valued conductivity. The simulation of the scattering process uses a perfectly matched layer. A good resolution of the SPP structures on the hypersurface is achieved by using goal-oriented adaptive local mesh refinement utilizing the *Dual-Weighted Residual* (DWR) method.

Keywords: Finite element method, surface plasmon-polariton, discontinuity on hypersurface, time-harmonic Maxwell's equations

1 Introduction

In the terahertz frequency range, the effective (complex-valued) surface conductivity of atomically thick 2D materials such as graphene has a positive imaginary part that is considerably larger than the real part. This feature allows for the propagation of slowly decaying electromagnetic waves, called surface plasmon-polaritons (SPPs), that are confined near the material interface with wavelengths much shorter than the wavelength of the free-space radiation. SPPs are promising ingredients in the design of novel optical applications promising “subwavelength optics” beyond the diffraction limit. There is a compelling need for controllable numerical schemes which, placed on firm mathematical grounds, can reliably describe SPPs in a variety of geometries.

We introduce a finite-element framework suitable for the treatment of electromagnetic wave propagation along conducting sheets embedded in spaces of arbitrary dimensions. The use of *higher-order conforming* elements is well suited for the numerical problem at hand. The weak discontinuity across the interface can be aligned with the triangulation and the regularity of the solution away from the interface leads to high convergence rates. For overcoming the two-scale

character with much finer SPP structures close to the interface, an adaptive, local refinement strategy based on a-posteriori error estimates is used.

2 Variational formulation and finite element approximation

Let Ω be a bounded domain. The effect of a surface conductivity σ_r^Σ on an interface Σ enters the time-harmonic Maxwell equations as a jump condition. After rescaling $k_0 = \omega\sqrt{\varepsilon_0\mu_0} \rightarrow 1$ the corresponding variational equation reads [3]

$$A(\mathbf{E}, \boldsymbol{\varphi}) = F(\boldsymbol{\varphi}) \quad \forall \boldsymbol{\varphi} \in \mathbf{X}(\Omega), \quad (1)$$

where the bilinear form

$$\begin{aligned} A(\mathbf{E}, \boldsymbol{\varphi}) := & \int_{\Omega} (\mu_r^{-1} \nabla \times \mathbf{E}) \cdot (\nabla \times \bar{\boldsymbol{\varphi}}) \, dx \\ & - \int_{\Omega} \tilde{\varepsilon}_r \mathbf{E} \cdot \bar{\boldsymbol{\varphi}} \, dx - i \int_{\Sigma} (\sigma_r^\Sigma \mathbf{E}_T) \cdot \bar{\boldsymbol{\varphi}}_T \, do_x \\ & - i \int_{\partial\Omega} \sqrt{\mu_r^{-1} \tilde{\varepsilon}_r} \mathbf{E}_T \cdot \bar{\boldsymbol{\varphi}}_T \, do_x, \end{aligned} \quad (2)$$

and the right hand side

$$F(\boldsymbol{\varphi}) := i \int_{\Omega} \mathbf{J}_a \cdot \bar{\boldsymbol{\varphi}} \, dx \quad (3)$$

are defined on a space

$$\mathbf{X}(\Omega) = \left\{ \boldsymbol{\varphi} \in \mathbf{H}(\text{curl}): \boldsymbol{\varphi}_T|_{\Sigma \cup \partial\Omega} \in L^2 \right\}. \quad (4)$$

$\tilde{\varepsilon}_r$ and μ_r denote relative permittivity and permeability, respectively. \mathbf{E} is the electric field and \mathbf{J}_a denotes a Hertzian dipole source.

Let $\mathbf{X}_h(\Omega) \subset \mathbf{X}(\Omega)$ be a finite-element space spanned by curl-conforming Nédélec-elements on a quadrilateral mesh [1] and define a finite-element approximation $\mathbf{E}_h \in \mathbf{X}_h(\Omega)$ of \mathbf{E} as the solution of (1) with $\mathbf{X}(\Omega)$ replaced by $\mathbf{X}_h(\Omega)$.

3 Local mesh refinement and adaptivity

The desired SPP has a wavelength much smaller than the one manifested by the dipole free-space radiation field. This two-scale character that the electromagnetic wave exhibits in the spatial

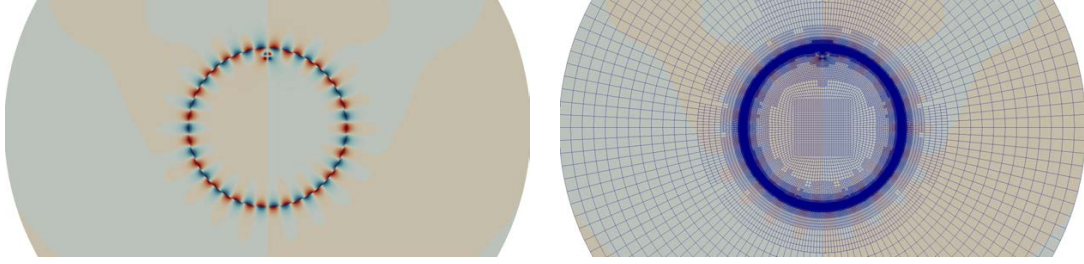


Figure 1: A resonating SPP excited on a ring of conducting material due to a Hertzian dipole located in the interior close to the material. Resonance of the SPPs changes the radiation characteristics of the dipole.

resolution creates a challenge for finite-element simulations. A much finer minimal mesh refinement is necessary near the interface Σ in order to resolve the highly oscillatory SPP. An efficient method for *a posteriori* error control is the *dual weighted residual* (DWR) method [2]. It constructs estimates of local error contributions in terms of a target functional \mathcal{J} with the help of a “dual problem.” More precisely, let $\mathcal{J}(\mathbf{E})$ be a quantity of interest given by a possibly non-linear Gâteaux-differentiable function

$$\mathcal{J} : \mathbf{H}(\operatorname{curl}; \Omega) \rightarrow \mathbb{C}.$$

The corresponding dual problem is to find a solution $\mathbf{Z} \in \mathbf{X}(\Omega)$ such that

$$A(\varphi, \mathbf{Z}) = D_{\mathbf{E}}\mathcal{J}(\mathbf{E})[\varphi] \quad \forall \varphi \in \mathbf{X}(\Omega). \quad (5)$$

Here, $D_{\mathbf{E}}[\varphi]$ denotes the Gâteaux derivative in direction φ with respect to \mathbf{E} . Let \mathbf{E}_H and \mathbf{Z}_H be finite-element approximations of \mathbf{E} and \mathbf{Z} . Then [2, 3] up to a term R of higher order

$$|\mathcal{J}(\mathbf{E}) - \mathcal{J}(\mathbf{U})| \leq \sum_{Q \in \mathbb{T}_H} \eta_Q + R, \text{ with}$$

$$\eta_Q := \frac{1}{2} \left| \rho_Q(\mathbf{E}_H, \mathbf{Z} - \mathbf{Z}_H) + \rho_Q^*(\mathbf{Z}_H, \mathbf{E} - \mathbf{E}_H) \right|.$$

Here, ρ_Q and ρ_Q^* denote the primal and dual cell-wise residual, respectively, associated with variational equations (1) and (5). The local indicators η_Q can be approximated efficiently and are used in an *estimate, mark, refine* cycle [2] for local mesh adaptivity. A good choice for a quantity of interest for SPPs is

$$\mathcal{J}(\mathbf{E}) = \int_{\Sigma} \|\mathbf{E}_T\|^2 \, d\sigma_x.$$

Figure 1 shows a solution and the corresponding locally refined mesh for a SPP on a circle excited by a Hertzian dipole close to the circle.

4 Outlook

The numerical framework that was presented admits several generalizations and extinctions, e.g., to waveguides that contain a few graphene layers. Although our numerical results focused on 2D thus far, our underlying choice of local adaptivity can lead to a significant reduction of computational cost in higher spatial dimension.

References

- [1] W. Bangerth, D. Davydov, T. Heister, L. Heltai, G. Kanschat, M. Kronbichler, M. Maier, B. Turcksin, D. Wells, The deal.II Library, Version 8.4. *Journal of Numerical Mathematics* **24**(3):135–141, 2016.
- [2] R. Becker, R. Rannacher, An Optimal Control Approach to A Posteriori Error Estimation in Finite Element Methods, *Acta Numerica* **10**:1–102 (2001).
- [3] M. Maier, D. Margetis, M. Luskin, Dipole excitation of surface plasmon on a conducting sheet: finite element approximation and validation, *arXiv:1605.08456 [math.NA]* (2016).
- [4] M. Maier, D. Margetis, M. Luskin, Generation of surface plasmon-polaritons by edge effects *arXiv:1702.00848 [physics.comp-ph]* (2017).
- [5] D. Margetis, M. Maier, M. Luskin, On the Wiener-Hopf method for surface plasmons: Diffraction from semi-infinite metamaterial sheet, *arXiv:1701.02784 [math-ph]* (2017).

An Algorithm for Vector data Full Waveform Inversion

Mostafa Akrami^{1,*}, Alison Malcolm¹

¹Department of Earth Sciences, Memorial University of Newfoundland, St. John's, Canada

*Email: mostafa.akrami@mun.ca

Abstract

In exploration seismology constructing an accurate velocity model is imperative. One of the algorithms which can lead to an accurate velocity model is Full Waveform Inversion (FWI). Standard FWI uses only scalar data such as pressure to construct a velocity model and does not provide any directivity information about the wavefields. Extending FWI to vector data allows us to use both pressure and velocity components at the same time, giving directivity information about the wavefields. By extending FWI to vector data and thus improving the input data to FWI, we obtain both improved resolution and directivity information.

Keywords: Wave propagation, Seismic inversion, FWI, Broadband data

1 Introduction

Recently, there have been some advances in marine seismology regarding data acquisition. Instead of recording only conventional seismic data (scalar ones), one can record both scalar and vector data (pressure and velocity components) at the same time [2]. This has led to various techniques in seismic acquisition as well as wavefield separation and ghost removal [1].

The main difference between the vector and scalar data is that for the vector data we know the pressure and particle velocity whereas for the scalar case we know only the pressure.

In spite of the fact that the standard FWI algorithm takes advantage of the large amount of scalar data contained in the seismic traces, it fails to provide directivity information about the wavefields.

In this study, we present an extension of the algorithm proposed by [3] to FWI of vector acoustic data. Thus we are able to gain complete information about the wavefields namely, directionality and because of this, better lateral resolution to estimate velocities. In this approach, we use dipole sources as well as monopole sources in different orientations and our wave solver for a complete acoustic wave equation to

generate vector acoustic data. We then derive and test an FWI algorithm with synthetic data.

2 Methodology and Results

Generally in Full Waveform Inversion we try to reconstruct model parameter m which can be defined by

$$m = \frac{\rho}{\kappa}, \quad (1)$$

from displacement data $u = \mathcal{F}m$, where \mathcal{F} is forward modelling operator. κ and ρ are the compressibility and mass density, respectively.

For the vector-acoustic system we denote source \mathcal{S} which denotes both pressure and point-force sources as

$$\mathcal{S} = \begin{pmatrix} q \\ f \end{pmatrix},$$

and also total wavefields

$$u_{q,f} = \begin{pmatrix} P_{q,f} \\ V_{q,f} \end{pmatrix},$$

where $P_{q,f}$ and $V_{q,f}$ are pressure and velocity and subscripts p and f refer to pressure and point-force source respectively. Now we can construct a set of equations for vector-acoustic system in terms of our model parameter m (Eq. 1), gives

$$\begin{cases} P_{q,f} + m\nabla \cdot V_{q,f} = q, \\ \ddot{V}_{q,f} + \nabla P_{q,f} = f. \end{cases} \quad (2)$$

Where $\ddot{\cdot}$ means second derivative with respect to time. In order to generate vector data and solve the wave equation of our system in the time domain, we use a two-dimensional constant density acoustic solver from PySIT [5]. The receivers in our system are the usual point receivers meaning they record pressure.

After generating vector data, the next step is the calculation of the objective function:

$$\begin{aligned} \mathcal{J}(m) = & \frac{w_s}{2} \int_{\mathbb{T}} \int_{\mathbb{R}} w_r [u_q(m; r, t) - d_q(r, t)]^2 + \\ & w_r [u_f(m; r, t) - d_f(r, t)]^2 dt dr \end{aligned}$$

Where w_s and w_r are the source and receiver linear weighting operators. d_q and d_f are

the recorded data from pressure and point-force source respectively. Minimization of the objective function requires computing the gradient and finally optimization; we use the l-BFGS method to do this optimization [4].

In order to verify our VFWI algorithm, we

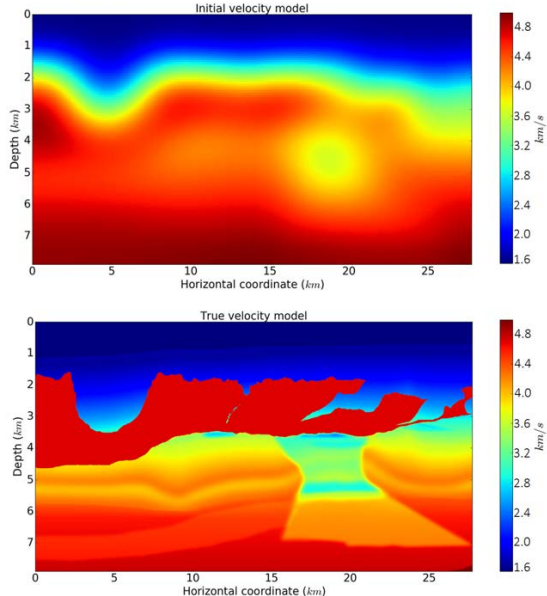


Figure 1: A sub-sampled initial and true BP velocity model (with %12 of samples remaining).

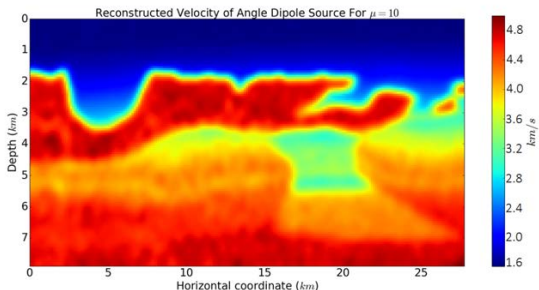


Figure 2: Reconstruction of a sub-sampled BP velocity model by using angle dipole source with regularization.

present a BP velocity model (Fig. 1) reconstruction. This model is consist of salt flanks and irregular shapes and discretized using 115 nodes in the z direction and 205 nodes in the x direction. The inverse crime is committed by using the same solver for generating the 'true' data and the 'synthetic' data. Here we only show the estimated BP velocity by using angle dipole source (Fig. 2). Reconstruction of velocity in the case of BP model is very hard as the model is

so complicated. In order to obtain a good recovery and remove the artefacts, we performed regularization process. we used 50 sources and 50 receivers are placed all the way across the top of the computational domain and also 30 l-BFGS iterations to estimate this model. As can be seen from Fig. 2, recording vector acoustic data in the case of angle dipole source results in getting sharp edges on some of the smaller features especially near the edges of the model. Therefore VFWI gives reasonable resolution and edge preservation.

References

- [1] Sun, D. and Jiao, K. and Vigh, D., Compensating for source and receiver ghost effects in full waveform inversion and reverse time migration for marine streamer data, *Journal of Geophysical Research*, 2015, 201, 3, pp. 1507–1521.
- [2] Robertsson, J. O. A. and Moore, I. and Vassallo, M. and Kemal, O. and van Manen, D.-J. and Ozbek, A., On the use of multicomponent streamer recordings for reconstruction of pressure wavefields in the crossline direction, *Journal of Geophysical Research*, 2008, 73, 5, pp. A45–A49.
- [3] Fleury, C. and Vasconcelos, I., Adjoint-state reverse time migration of 4C data:Finite-frequency map migration for marine seismic image, *Geophysical Journal International*, 2013, 78, 2, pp. WA159–WA172.
- [4] Nocedal,, J. and Wright, S. J., *Numerical Optimization*, Springer, Library of Congress Control Number, 2006.
- [5] Russell J. Hewett and Laurent Demanet, *an open source toolbox for seismic inversion and seismic imaging*, Imaging and Computing Group in the Department of Mathematics at MIT, <http://pysit.bitbucket.org/>.

Discrete exterior calculus for electromagnetic scattering by massive particle clusters

Jukka Räbinä^{2,1}, Sanna Mönkölä¹, Tuomo Rossi¹, Johannes Markkanen², Antti Penttilä², Karri Muinonen^{2,3}

¹University of Jyväskylä, Department of Mathematical Information Technology, P.O. Box 35
(Agora), FI-40014 University of Jyväskylä, Finland

²University of Helsinki, Department of Physics, P.O. Box 64, FI-00014 University of Helsinki, Finland

³Finnish Geospatial Research Institute, P.O. Box 15, FI-02431 Masala, Finland

Abstract

We consider multiple scattering of electromagnetic waves by randomly distributed, densely packed, spherical particles. For space discretization, we use the discrete exterior calculus (DEC). The time-dependent problem is solved by a wave frequency -corrected time-stepping scheme, and the time-harmonic solution is obtained by the exact controllability method.

Keywords: computational electromagnetics, light scattering, multiple particle scattering, discrete exterior calculus, exact controllability

1 Introduction

Randomly distributed spherical obstacles are used for modeling massive particle clusters, e.g., dust particles, aerosols, and regolith structures. Three-dimensional simulations considering multiple scattering of electromagnetic waves, by such obstacles, is modeled by the Maxwell equations,

$$\varepsilon \frac{\partial \mathbf{E}}{\partial t} - \nabla \times \mathbf{H} = -\mathbf{J}, \quad (1)$$

$$\mu \frac{\partial \mathbf{H}}{\partial t} + \nabla \times \mathbf{E} = -\mathbf{J}^*, \quad (2)$$

where \mathbf{E} and \mathbf{H} are the electric and magnetic fields, ε is the electric permittivity, μ is the magnetic permeability, and \mathbf{J} and \mathbf{J}^* are the source functions. Recently, e.g., the discrete dipole approximation and T-matrix methods are used for solving the problem (see, e.g. [5, 6]). In this paper, we consider discrete exterior calculus (DEC) [3] as a generalization of finite difference schemes.

2 Methods

For spatial discretization, we employ a pair of primal and dual mesh. The primal 1-cells (edges) \mathcal{E}_j and 2-cells (faces) \mathcal{F}_j are assigned with orthogonal dual 2-cells \mathcal{F}_j^* and dual 1-cells \mathcal{E}_j^* , respectively.

We consider electric and magnetic fields, respectively, as discrete primal and dual 1-forms.

Those are column vectors \mathbf{e} and \mathbf{h} , where each term is $\mathbf{e}_j := \int_{\mathcal{E}_j} \mathbf{E}$ and $\mathbf{h}_j := \int_{\mathcal{E}_j^*} \mathbf{H}$. The Maxwell system (1)-(2) is spatially discretized as

$$\star_1 \frac{d}{dt} \mathbf{e} - \mathbf{d}_1^T \mathbf{h} = -\mathbf{j}, \quad (3)$$

$$\star_2^{-1} \frac{d}{dt} \mathbf{h} + \mathbf{d}_1 \mathbf{e} = -\mathbf{j}^*, \quad (4)$$

where right-hand side are the source terms $\mathbf{j}^{(*)} := \int_{\mathcal{F}_j^{(*)}} \mathbf{J}^{(*)}$. Matrix \mathbf{d}_1 , built of values -1, 0, and 1, is the incidence matrix expressing the relative orientation between faces and edges [7]. The discrete Hodge stars \star_1 and \star_2 are diagonal matrices defined as

$$\star_{1,j,j} := \frac{\int_{\mathcal{F}_j^*} \varepsilon \mathbf{E}_0}{\int_{\mathcal{E}_j} \mathbf{E}_0}, \quad \star_{2,j,j} := \frac{\int_{\mathcal{E}_j^*} \mathbf{H}_0}{\int_{\mathcal{F}_j} \mu \mathbf{H}_0},$$

where \mathbf{E}_0 and \mathbf{H}_0 are fields of possible solution. The time integration and Hodge approximation are optimized for time-harmonic problems of single frequency, which also eliminates the eliminates the pollution effect, which is traditionally caused by systematic error in simulated wavelength [8]. Elimination of this cumulative error source improves accuracy especially in large scale problems, where domain diameter include dozens of wavelengths.

The time-harmonic solution is obtained by the exact controllability method [2]. That is, we steer a dynamical system from an initial state to a particular state by using an appropriate control mechanism realized by the conjugate gradient (CG) method. Essentially, we minimize a quadratic error functional, which is the squared energy norm of the system. At the discrete stage, the functional is spanned by a diagonal mass matrix, and the algorithm operates in L^2 -type Hilbert space without preconditioning. At each CG iteration, the state equation, advancing forward in time, and the corresponding adjoint state equation, advancing backward in time, are solved. Only the current and previous

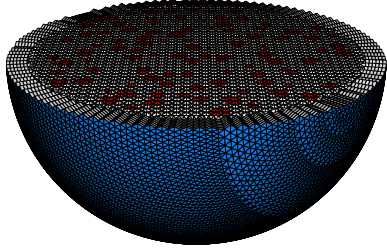


Figure 1: The spherical domain is filled with C15 structure and surrounded by perfectly matched layer layer. Existence of a particle in at any cell is marked by colors.

gradient and search vectors and scalar-valued weights are needed to be stored at each iterations.

3 Numerical experiments

A spherical domain is filled with N randomly distributed spherical particles of radius $0.28\lambda_0$, and the particle cluster is exposed by an electromagnetic plane wave of wavelength $\lambda_0 = 1$. Inside each particle, $\varepsilon = 2.25\varepsilon_0$, where ε_0 is the vacuum permittivity, and $\mu = 1$. The domain is discretized with a C15-type tetrahedral close-packed [9] grid with 6000 unknowns per λ_0^3 and cut by a structured spherical boundary (see, Fig. 1). The boundary elements are duplicated and stretched to apply radial perfectly matched layer [4] for truncating the domain. Existence of a particle at any position is marked by flags and the permittivity is changed element-wise, such that outside the particles $\varepsilon = \varepsilon_0$ and $\mu = 1$. We consider, for $N = 73$, 582, 1966, and 19992, the far-field Mueller matrix [1] components. The total scattering intensities (phase function S_{11}) are presented in Fig. 2 as a function of the phase angle.

References

- [1] C. F. Bohren, D. R. Huffman, *Absorption and Scattering of Light by Small Particles*, Wiley & Sons, New York (1983).
- [2] M. O. Bristeau, R. Glowinski, J. Périault, Controllability methods for the computation of time-periodic solutions; Application to scattering, *J. Comput. Phys.* 147 (2) (1998) 265–292.
- [3] M. Desbrun, A. N. Hirani, M. Leok, J. E. Marsden, Discrete exterior calculus, preprint, arXiv:math/0508341v2 [math.DG] (2005).
- [4] S. D. Gedney, An anisotropic perfectly matched layer-absorbing medium for the truncation of FDTD lattices, *IEEE Trans. Antennas Propag.* 44 (12) (1996) 1630–1639.
- [5] A. Karlsson, T. Yi, P.-E. Bengtsson, Absorption and scattering of light from ensembles of randomly oriented aggregates, *JOSA A* 30.3 (2013) 316–324.
- [6] M. I. Mishchenko, L. Liu, D. W. Mackowski, B. Cairns, G. Videen, Multiple scattering by random particulate media: exact 3D results, *Opt. Express* 15 (6) (2007) 2822–2836.
- [7] J. Räbinä, On a Numerical Solution of the Maxwell Equations by Discrete Exterior Calculus, Dissertation (Ph.D.), University of Jyväskylä, <http://urn.fi/URN:ISBN:978-951-39-5951-7> (2014).
- [8] J. Räbinä, S. Mönkölä, T. Rossi, Efficient time integration of Maxwell’s equations by generalized finite-differences, *SIAM J. Sci. Comput.* 37 (6) (2015) B834–B854.
- [9] J. M. Sullivan, New tetrahedrally close-packed structures, in: *Foams, emulsions and applications; Eurofoam 2000*, Verlag MIT, Bremen, (2000) 111–119.

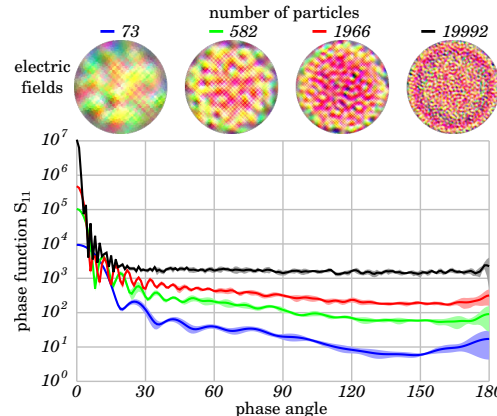


Figure 2: Far-field scattering by densely packed particle clusters.

Acoustic Scattering by Spheres and Spheroids in the Time Domain

P. A. Martin^{1,*}

¹Department of Applied Mathematics and Statistics, Colorado School of Mines, Golden, USA

*Email: pamartin@mines.edu

Abstract

The title problems are treated using Laplace transforms and separation of variables. This approach has been used for spheres since the 1950s. When applied to spheroids, we encounter new questions, such as how do spheroidal wavefunctions behave for complex parameters? We describe our recent work in this direction.

Keywords: acoustics, scattering, time domain

1 Introduction

We consider acoustic scattering of a sound pulse by a bounded three-dimensional obstacle with smooth boundary S . The scattered field $u(\mathbf{r}, t)$ solves an initial-boundary value problem (IBVP) for the wave equation

$$\nabla^2 u = c^{-2} \partial^2 u / \partial t^2 \quad \text{in } B \text{ for } t > 0,$$

where B is the unbounded exterior of S and c is the constant speed of sound. In addition, there are zero initial conditions

$$u = 0 \quad \text{and} \quad \partial u / \partial t = 0 \quad \text{in } B \text{ at } t = 0 \quad (1)$$

and a boundary condition on S for $t > 0$.

The word “acoustic” in the title is important: we always assume that u is a velocity potential, so that $\mathbf{v} = \operatorname{grad} u$ is the fluid velocity and $p = -\rho \partial u / \partial t$ is the (excess) pressure, where ρ is the constant background density.

Problems of physical interest often involve incident pulses, with moving wavefronts across which p or normal velocity v_n is discontinuous. However, in most cases, it can be arranged that u is continuous across wavefronts, even though p or v_n is not. Consequently, it is advantageous to solve for u , assumed to be continuous and piecewise-smooth; assuming too much smoothness may exclude interesting physical problems. Also, seeking weak solutions must be done with care: such solutions may not respect the proper jump conditions across wavefronts, conditions that stem from the underlying continuum mechanics. See [4] for details and references.

2 Use of Laplace transforms

The textbook method for solving IBVPs is to use Laplace transforms. Thus, define

$$U(\mathbf{r}, s) = \mathcal{L}\{u\} = \int_0^\infty u(\mathbf{r}, t) e^{-st} dt.$$

U satisfies the modified Helmholtz equation,

$$\nabla^2 U - (s/c)^2 U = 0 \quad \text{in } B. \quad (2)$$

Here, we have used the continuity of u and the initial conditions (1).

We solve (2) using the Laplace transform of the boundary condition and a mild growth condition as $|\mathbf{r}| \rightarrow \infty$, and then we invert using

$$u(\mathbf{r}, t) = \frac{1}{2\pi i} \int_{\text{Br}} U(\mathbf{r}, s) e^{st} ds,$$

where Br is a Bromwich contour in the s -plane.

For an incident sound pulse, we know that, for any fixed \mathbf{r} , $u(\mathbf{r}, t) = 0$ for sufficiently large t . Consequently $U(\mathbf{r}, s)$ is an analytic function of s for $\operatorname{Re} s > 0$. When $U(\mathbf{r}, s)$ is continued analytically into the other half-plane, $\operatorname{Re} s \leq 0$, singularities will be encountered. These singularities are poles and they occur in complex-conjugate pairs (unless they are real and negative). The singularities are known as *natural frequencies*. Once they have been located, we can contemplate moving the Bromwich contour to the left, picking up residue contributions.

3 The sphere

For scattering by a sphere of radius a , we use spherical polar coordinates, r , θ and ϕ . Separation of variables leads to

$$U = \sum_{m=0}^{\infty} \sum_{n=m}^{\infty} k_n(sr/c) P_n^m(\cos \theta) A_n^m(\phi, s), \quad (3)$$

$$A_n^m = A_n^m(s) \cos m\phi + B_n^m(s) \sin m\phi. \quad (4)$$

Here k_n is a modified spherical Bessel function, P_n^m is an associated Legendre function, and A_n^m and B_n^m are to be determined using the boundary condition. We note two things about the

form of expansion (3). First, the angular functions $P_n^m(\cos \theta) \sin m\phi$ do not depend on s . Second the radial function, $k_n(sr/c)$, does not depend on the mode number m . This structure is lost when we consider scattering by a spheroid.

As an example, suppose we have a Dirichlet boundary condition, $u(a, \theta, \phi, t) = d(\theta, \phi, t)$, a given function satisfying $d(\theta, \phi, 0) = 0$; this constraint ensures that u is continuous. Suppose that $D = \mathcal{L}\{d\}$ has the expansion

$$D(\theta, \phi, s) = \sum_{m=0}^{\infty} \sum_{n=m}^{\infty} P_n^m(\cos \theta) \mathcal{D}_n^m(\phi, s), \quad (5)$$

where $\mathcal{D}_n^m = D_{mn}^c(s) \cos m\phi + D_{mn}^s(s) \sin m\phi$ and D_{mn}^c and D_{mn}^s are coefficients. Then the boundary condition yields

$$U = \sum_{m=0}^{\infty} \sum_{n=m}^{\infty} \frac{k_n(sr/c)}{k_n(sa/c)} P_n^m(\cos \theta) \mathcal{D}_n^m(\phi, s). \quad (6)$$

This formula shows that the natural frequencies are those values of s for which $k_n(sa/c) = 0$. There may be additional singularities arising from the form of $D_{mn}^c(s)$ and $D_{mn}^s(s)$.

All this is well known; the method outlined above was first used by J. Brillouin in 1950. See [5] for details and references.

4 The prolate spheroid

We use prolate spheroidal coordinates ξ , η and ϕ , defined by $x = h\sqrt{(\xi^2 - 1)(1 - \eta^2)} \cos \phi$, $y = h\sqrt{(\xi^2 - 1)(1 - \eta^2)} \sin \phi$, $z = h\xi\eta$, where h is a positive constant. The foci are at $(x, y, z) = (0, 0, \pm h)$. The surface $\xi = \xi_0 > 1$ is a prolate spheroid with semi-major axis of length $a = h\xi_0$ and semi-minor axis of length $b = h\sqrt{\xi_0^2 - 1}$. The exterior of the spheroid corresponds to $\xi > \xi_0$, $-1 \leq \eta \leq 1$ and $-\pi \leq \phi < \pi$.

To solve (2), we write

$$U = \sum_{m=0}^{\infty} \sum_{n=m}^{\infty} R_{mn}^{(3)}(ip, \xi) S_n^m(ip, \eta) \mathcal{A}_n^m(\phi, s) \quad (7)$$

for $\xi > \xi_0$. Here $p = sh/c$, \mathcal{A}_n^m is defined by (4), $R_{mn}^{(3)}$ is an outgoing radial spheroidal wavefunction (SWF) and S_n^m is an angular SWF [1]. Comparing (7) with (3), we see that the radial part $R_{mn}^{(3)}(ip, \xi)$ depends on both m and n , and the angular part $S_n^m(ip, \eta)$ depends on s .

For the Dirichlet boundary condition, $u = d$ on $\xi = \xi_0$, we expand $D = \mathcal{L}\{d\}$ as

$$D(\eta, \phi, s) = \sum_{m=0}^{\infty} \sum_{n=m}^{\infty} S_{mn}(ip, \eta) \mathcal{D}_n^m(\phi, s),$$

see (5), whence

$$U = \sum_{m=0}^{\infty} \sum_{n=m}^{\infty} \frac{R_{mn}^{(3)}(ip, \xi)}{R_{mn}^{(3)}(ip, \xi_0)} S_n^m(ip, \eta) \mathcal{D}_n^m(\phi, s).$$

This formula should be compared with (6).

The natural frequencies are determined by the zeros of $R_{mn}^{(3)}(ish/c, \xi_0)$ in the complex s -plane. It turns out that the relevant properties of radial SWFs are not in the literature on special functions, so we have developed some new asymptotic approximations that can be used to estimate the natural frequencies. There is literature on computing SWFs numerically [2, 3]; comparisons between asymptotics and numerics are being made.

References

- [1] M. Abramowitz & I.A. Stegun (eds), *Handbook of Mathematical Functions*, Dover, New York, 1965.
- [2] R. Adelman, N.A. Gumerov & R. Duraiswami, Semi-analytical computation of acoustic scattering by spheroids and disks, *J. Acoust. Soc. Amer.* **136** (2014), pp. EL405–EL410.
- [3] B.E. Barrowes, K. O'Neill, T.M. Grzegorczyk & J.A. Kong, On the asymptotic expansion of the spheroidal wave function and its eigenvalues for complex size parameter, *Stud. Appl. Math.* **113** (2004), pp. 271–301.
- [4] P.A. Martin, The pulsating orb: solving the wave equation outside a ball, *Proc. Royal Society A* **472** (2016) 20160037 (20 pages).
- [5] P.A. Martin, Acoustic scattering by a sphere in the time domain, *Wave Motion* **67** (2016), pp. 68–80.

Transmission Conditions for Non-Overlapping Schwarz Domain Decomposition Methods Applied to Time-Harmonic Elastic Waves

V. Mattesi¹, M. Darbas², C. Geuzaine¹

¹University of Liège, Department of Electrical Engineering and Computer Science

²Université de Picardie Jules Verne, LAMFA UMR CNRS 7352

Abstract

We focus on the construction of transmission conditions for optimized Schwarz domain decomposition methods applied to time-harmonic elastic wave scattering problems solved numerically with finite element methods. In particular, we investigate different local approximations of the Dirichlet-to-Neumann map, and compare their impact on the convergence rate of the domain decomposition algorithm.

Keywords: Scattering, 2D elastic waves, optimized Schwarz method, approximate DtN map

1 Introduction

The aim of this ongoing work is to solve time-harmonic elastodynamic scattering problems for which the scatterer is inhomogeneous. As is well-known, direct sparse solvers do not scale well for such problems and iterative solvers exhibit poor convergence or even diverge, especially in the high-frequency regime. Domain decomposition methods provide an alternative, combining direct sparse solvers on subproblems of smaller sizes with an iterative Krylov solver. In this paper we investigate the impact of the transmission conditions used between the subdomains on the convergence of the iterative algorithm.

2 Problem statement

2.1 Mono-domain time-harmonic elastic wave problem

Let us consider $\Omega^- := \{\mathbf{x} \in \mathbb{R}^2 : |\mathbf{x}| \leq r_{int}\}$ with boundary Γ and its complementary $\Omega^+ := \mathbb{R}^2 \setminus \Omega^-$. When illuminated by a time-harmonic incident wave \mathbf{u}^{inc} , the scattering problem is formulated as follows: find the displacement \mathbf{u} in Ω^+ solution to the Navier equation

$$\operatorname{div}\sigma(\mathbf{u}) + \rho\omega^2\mathbf{u} = 0, \quad (1)$$

with

$$\sigma(\mathbf{u}) = \lambda(\operatorname{div}\mathbf{u})I + 2\mu\epsilon(\mathbf{u}), \quad (2)$$

$$\epsilon(\mathbf{u}) = \frac{1}{2}([\nabla\mathbf{u}] + [\nabla\mathbf{u}]^T), \quad (3)$$

such that

$$\mathbf{u} = -\mathbf{u}^{inc}, \quad \text{on } \Gamma, \quad (4)$$

and satisfying the Kupradze radiation conditions at infinity. The coefficients λ and μ in (2) are the Lamé coefficients. In view of a finite element discretization, Ω^+ is truncated by an artificial boundary Γ^∞ , which delimits the bounded domain Ω under study.

2.2 Domain decomposition

We split the domain Ω into N_{dom} sub-domains Ω_i without overlap. Let us denote $\Gamma_i := \Gamma \cap \Omega_i$, $\Gamma_i^\infty := \Gamma^\infty \cap \Omega_i$ and $\Sigma_{ij} := \overline{\Omega_i \cap \Omega_j}$ the transmission boundary. At iteration $n+1$ for a sub-domain Ω_i , the classical additive Schwarz domain decomposition method can be described as follows. First, find the volume solution \mathbf{u}_i^{n+1} such that

$$\begin{cases} \operatorname{div}\sigma(\mathbf{u}_i^{n+1}) + \rho\omega^2\mathbf{u}_i^{n+1} = 0, & \text{on } \Omega_i, \\ \mathbf{u}_i^{n+1} = -\mathbf{u}^{inc}, & \text{on } \Gamma_i, \\ \sigma(\mathbf{u}_i^{n+1})n_i + \mathcal{B}\mathbf{u}_i^{n+1} = 0, & \text{on } \Gamma_i^\infty, \\ \sigma(\mathbf{u}_i^{n+1})n_i + \mathcal{T}\mathbf{u}_i^{n+1} = g_{ij}^n, & \text{on } \Sigma_{ij}, \end{cases} \quad (5)$$

where n_i is the outgoing normal of Ω_i , \mathcal{B} is the operator describing boundary conditions at infinity, \mathcal{T} is the transmission operator and g_{ij}^n is the surface field given by the previous iteration. Then update the interface unknowns g_{ji}^{n+1} as follows

$$g_{ji}^{n+1} = -g_{ij}^n + 2\mathcal{T}\mathbf{u}_i^{n+1}, \quad \text{on } \Sigma_{ij}. \quad (6)$$

Considering the vector $\mathbf{g} = [g_{ij}]^T$ containing the interface unknowns for all ij pairs, one step of the above algorithm can be summarized as

$$\mathbf{g}^{n+1} = \mathcal{A}\mathbf{g}^n + \mathbf{b}, \quad (7)$$

for some right-hand side b . This is a fixed point iteration, the solution of which satisfies the linear system

$$\mathcal{F}g = (\mathcal{I} - \mathcal{A})g = b. \quad (8)$$

3 Transmission operators

Multiple choices are possible for the transmission operator \mathcal{T} , the optimal operator being the Dirichlet-to-Neumann map associated to the complementary of the subdomain. This operator being nonlocal (and thus computationally expensive), we investigate four approximations:

- Zeroth order condition:

$$\mathcal{T}_0\mathbf{u} = -i[(\lambda + 2\mu)k_p\mathbf{u}_p + \mu k_s\mathbf{u}_s], \quad (9)$$

with k_p and k_s the wavenumbers associated with \mathbf{u}_p (the longitudinal pressure wave with a vanishing curl), and \mathbf{u}_s (the transverse shear wave with a vanishing divergence) respectively.

- Padé-localized, split square-root condition:

$$\begin{aligned} \mathcal{T}_1\mathbf{u} = -i[(\lambda + 2\mu)k_p(\frac{\Delta_\Sigma}{k_{p,\epsilon}^2} + I)^{1/2}\mathbf{u}_p \\ + \mu k_s(\frac{\Delta_\Sigma}{k_{s,\epsilon}^2} + I)^{1/2}\mathbf{u}_s], \end{aligned}$$

with Δ_Σ the tangential Laplacian operator and $k_{\alpha,\epsilon} := k_\alpha + 0.39ik_\alpha^{1/3}\mathcal{H}^{2/3}$, $\alpha = s, p$ (\mathcal{H} being the mean curvature of Σ). This condition is then localized using complex Padé approximants [2, 3].

- Padé-localized, combined square-root condition [1]:

$$\mathcal{T}_2\mathbf{u} = -[(I + \Lambda_2)^{-1}\Lambda_1\mathbf{u} + 2\mu\mathcal{M}\mathbf{u}], \quad (10)$$

with the tangential Günter derivative \mathcal{M} ,

$$\Lambda_1 := i\rho\omega^2[(\Delta_\Sigma + k_{p,\epsilon}^2)^{-1/2}\mathbf{I}_n + (\Delta_\Sigma + k_{s,\epsilon}^2)^{-1/2}\mathbf{I}_t)],$$

and

$$\begin{aligned} \Lambda_2 := -i[\nabla_\Sigma(\Delta_\Sigma + k_{s,\epsilon}^2 I)^{-1/2}\mathbf{n} \cdot \mathbf{I}_n \\ - n(\Delta_\Sigma + k_{p,\epsilon}^2 I)^{-1/2}\operatorname{div}_\Sigma\mathbf{I}_t], \end{aligned}$$

where $\mathbf{I}_n = \mathbf{n} \otimes \mathbf{n}$, $\mathbf{I}_t = \mathbf{I} - \mathbf{I}_n$ with \mathbf{n} the outgoing normal, and $\operatorname{div}_\Sigma$ the tangential divergence operator. The square-roots are also implemented thanks to Padé approximants.

- Perfectly matched layers: the transmission operator is constructed by appending a volume layer to the transmission interface, in which a PML transformation with absorption profile is applied.

4 Preliminary results

We consider an annulus-shaped domain Ω , split into two concentric subdomains with $\rho = 1 \text{ kg.m}^{-3}$, $\omega = 2\pi \text{ s}^{-1}$ and $\lambda = \mu = 1 \text{ Pa}$. Figure 1 displays the eigenvalues of the iteration operator \mathcal{F} for the two transmission conditions \mathcal{T}_0 and \mathcal{T}_1 for a given finite element discretization. These spectra lead respectively to 49 and 23 GMRES iterations in the domain decomposition algorithm as implemented in [2].

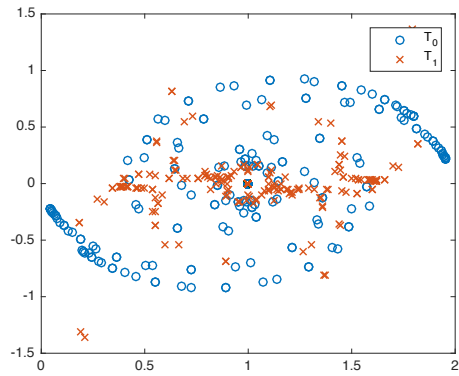


Figure 1: Spectrum of the iteration operator \mathcal{F} for transmission conditions \mathcal{T}_0 and \mathcal{T}_1

References

- [1] S. Chaillat, M. Darbas and F. Le Louer, *Approximate local Dirichlet-to-Neumann map for three-dimensional time-harmonic elastic waves*, Computer Methods in Applied Mechanics and Engineering, Elsevier, **297** (1) (2015), pp. 62-83.
- [2] B. Thierry, A. Vion, S. Tournier, M. El Bouajaji, D. Colignon, N. Marsic, X. Antoine and C. Geuzaine, *GetDDM: An open framework for testing optimized Schwarz methods for time-harmonic wave problems*, Computer Physics Communications, Elsevier, **203** (2016) pp. 309-330.
- [3] F.A. Milinazzo, C.A. Zala and G.H. Brooke, *Rational square-root approximations for parabolic equation algorithms*, Acoustical Society of America, 1997.

A Dispersion Optimized Mimetic Finite Difference Method for Maxwell's Equations in Metamaterials

Vrushali A. Bokil¹, Vitaliy Gyrya², Duncan McGregor^{3,*}

¹Department of Mathematics, Oregon State University, Corvallis, OR, USA

²Applied Mathematics and Plasma Physics, Los Alamos National Laboratory, Los Alamos, NM, USA

³Computational Multiphysics, Sandia National Laboratory, Albuquerque, NM, USA

*Email: damcgre@sandia.gov

Abstract

We present a numerical method for a Drude metamaterial model in two dimensions that is discretized using a mimetic finite difference (MFD) method in space and staggered exponential time discretization (ETD). The MFD spatial discretization on rectangular elements produces a three parameter family of mimetic schemes. By optimizing within the family for the lowest numerical dispersion error we identify the optimal ET-MFD method with fourth order dispersion error. The ETD was essential to the success of the optimization procedure.

Keywords: Maxwell's equations, Drude Metamaterial, Mimetic Finite Difference, Exponential Time Discretization.

1 Introduction

Mimetic finite difference methods for Maxwell's equations can be viewed as extensions of the famous Yee scheme in computational electromagnetics to polygonal and polyhedral meshes. The spatial discretization allows for the construction of a parameterized family of compatible discretizations for Maxwell's equations that, like the Yee scheme, preserve important continuum properties of the Maxwell system, such as exact preservation of the divergence conditions and energy conservation or decay (under a suitable stability condition) [1]. Here, we construct MFD discretization for a metamaterial model and exploit the parameterization on rectangular meshes to develop a method with low numerical dispersion error.

2 Maxwell-Drude Model

We consider the two dimensional (2D) Transverse Electric (TE) mode of Maxwell's curl equa-

tions in a Drude metamaterial given as

$$\begin{cases} \epsilon \frac{\partial}{\partial t} \mathbf{E} = -\mathbf{J} + \mathbf{curl} H, \\ \mu \frac{\partial}{\partial t} H = -K - \mathbf{curl} \mathbf{E}, \end{cases} \quad (1)$$

along with the constitutive laws

$$\begin{cases} \frac{\partial}{\partial t} \mathbf{J} = -\gamma_e \mathbf{J} + \epsilon \omega_{p,e}^2 \mathbf{E}, \\ \frac{\partial}{\partial t} K = -\gamma_m K + \mu \omega_{p,m}^2 H. \end{cases} \quad (2)$$

Here \mathbf{E} and H are the electric and magnetic fields; \mathbf{J} and K are the polarization, and magnetization current densities. The parameters ϵ and μ are the permittivity and permeability, $\omega_{p,e}$ and $\omega_{p,m}$ are the electric and magnetic plasma frequencies, and γ_e, γ_m are electric and magnetic damping frequencies, respectively. The operators \mathbf{curl} and \mathbf{curl} are the 2D vector and scalar curl operators, respectively. The system is completed by adding initial conditions, perfect conducting boundary conditions, and divergence constraints.

3 Exponential Time Discretization

Rewrite Maxwell's curl equations (1) and constitutive laws (2) in a matrix form

$$\frac{\partial}{\partial t} \begin{pmatrix} \mathbf{E} \\ \mathbf{J} \end{pmatrix} = \mathbb{X} \begin{pmatrix} \mathbf{E} \\ \mathbf{J} \end{pmatrix} + \begin{pmatrix} \epsilon^{-1} \mathbf{curl} H \\ 0 \end{pmatrix}, \quad (3)$$

$$\frac{\partial}{\partial t} \begin{pmatrix} H \\ K \end{pmatrix} = \mathbb{Y} \begin{pmatrix} H \\ K \end{pmatrix} - \begin{pmatrix} \mu^{-1} \mathbf{curl} \mathbf{E} \\ 0 \end{pmatrix}, \quad (4)$$

$$\mathbb{X} = \begin{pmatrix} 0 & -\epsilon^{-1} \\ \epsilon \omega_{p,e}^2 & -\gamma_e \end{pmatrix}, \quad \mathbb{Y} = \begin{pmatrix} 0 & -\mu^{-1} \\ \mu \omega_{p,m}^2 & -\gamma_m \end{pmatrix}.$$

A second order ETD method has the following staggered form ($m = n - \frac{1}{2}$):

$$\begin{pmatrix} \mathbf{E}^{n+1} \\ \mathbf{J}^{n+1} \end{pmatrix} = e^{\Delta t \mathbb{X}} \begin{pmatrix} \mathbf{E}^n \\ \mathbf{J}^n \end{pmatrix} + \mathbb{X}^{-1} (e^{\Delta t \mathbb{X}} - \mathbb{I}) \begin{pmatrix} \epsilon^{-1} \mathbf{curl} H^{m+1} \\ 0 \end{pmatrix},$$

$$\begin{pmatrix} H^{m+1} \\ K^{m+1} \end{pmatrix} = e^{\Delta t \mathbb{Y}} \begin{pmatrix} H^m \\ K^m \end{pmatrix} - \mathbb{Y}^{-1} (e^{\Delta t \mathbb{Y}} - \mathbb{I}) \begin{pmatrix} \mu^{-1} \mathbf{curl} \mathbf{E}^n \\ 0 \end{pmatrix}.$$

4 Mimetic Finite Difference Discretization is Space

MFD discretization can be viewed as a generalization of finite elements to general polygonal elements. However, here, we are interested only in the case of rectangular elements.

In the discrete form the electric field \mathbf{E} and the polarization current density \mathbf{J} will be represented by degrees of freedom (DoF) which are averages of tangential components along each of the mesh edges. The magnetic field H and the magnetization current density K will be represented by DoF that are the average values on the element, see Fig. 1. Computing these DoF for a smooth field defines an interpolant.

We construct the discrete (*primary*) scalar curl operator to be exact, in the sense that interpolant and curl operators commute. The vector **curl** operator is defined as dual to curl.

Next, each discrete space (edge space for \mathbf{E} and \mathbf{J} and face space for H and K) has to be equipped with an appropriate inner product, which is built based on the inner products local to individual elements. The inner product for face space for H and K is rather straightforward and is defined uniquely. It is in the construction of the local inner product for edge space for \mathbf{E} and \mathbf{J} that we encounter non-uniqueness that can be described by a set of three parameters.

To deal with computational efficiency issues and to preserve the parameters in the inner product matrices, \mathbb{M} , we use a generalized mass-lumping method. Instead of simply lumping all non-diagonal elements to diagonal, $\mathbb{M} \approx \mathbb{D}$, we use an approximation $\mathbb{M}^{-1} \approx \mathbb{D}^{-1}\mathbb{M}\mathbb{D}^{-1}$.

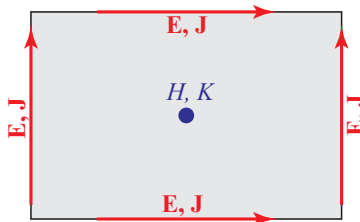


Figure 1: Illustration of DoF for unknown quantities \mathbf{E}, \mathbf{J} and H, K .

5 Dispersion Reduction

We express the numerical dispersion error for a general member of fully discrete ET-MFD family and for a general harmonic wave using generalized eigenvalues of the spatial and temporal discrete operators, which we refer to as in-

dexes. The problem of minimizing the numerical dispersion reduces to the problem of matching the indexes of these discrete operators at highest orders of accuracy by selecting appropriate parameters in the inner product matrices. A general member of the ET-MFD family is second order accurate both in space and time. On the other hand, the optimal ET-MFD achieves fourth order of accuracy by canceling the second order error coming from space and time discretizations. In Figure 1, we illustrate the dramatic increase in accuracy in the optimal ET-MFD method compared to the Yee scheme with ETD in the special case, $K = 0$, when the Drude model reduces to the cold isotropic plasma model [2].

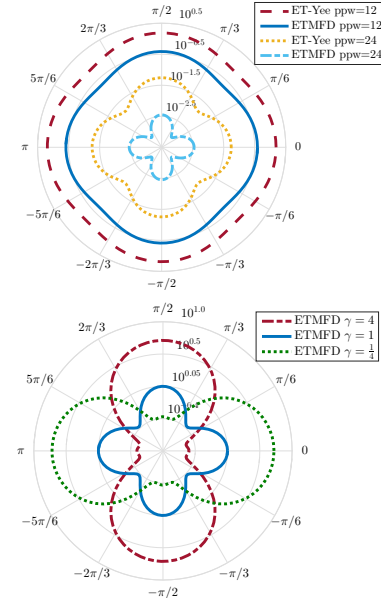


Figure 2: Numerical Dispersion error in a log polar plot for wave resolution measured in points per wavelength (ppw), $\omega_{p,e} = 1 = \gamma_e$, $\epsilon_\infty = 1$, aspect ratio of an element $\gamma = \frac{\Delta y}{\Delta x}$.

References

- [1] V. A. BOKIL, N. L. GIBSON, V. GYRYA, AND D. A. MCGREGOR, *Dispersion reducing methods for edge discretizations of the electric vector wave equation*, JCP, 287 (2015), pp. 88–109.
- [2] V. A. BOKIL, V. GYRYA, AND D. A. MCGREGOR, *A Dispersion Minimized Mimetic Method for Cold Plasma*, Proceedings of ECCOMAS Congress 2016, VII European Congress on Computational Methods in Applied Sciences and Engineering, (2016).

Time harmonic acoustic radiation in a circular flow

Jean-Francois Mercier^{1,*}, Antoine Bensalah², Patrick Joly¹

¹POEMS (CNRS-INRIA-ENSTA), ENSTA ParisTech, 828 Boulevard des Maréchaux, 91762
Palaiseau Cedex, France

²Airbus Group Innovation, 12 rue Pasteur, 92150 Suresnes, France

*Email: jean-francois.mercier@ensta.fr

Abstract

We aim at determining the acoustic field radiated in 2D by a time-harmonic source in a fluid in flow. We use Goldstein's equations, well-adapted to describe the complex coupling between the radiation of acoustic waves and the transport of acoustic vortices. These involve a vectorial harmonic transport equation which is proved to be well-posed outside a spectrum of frequencies corresponding to resonant streamlines. Then the full model is shown to be well-posed under a coercivity condition, implying a subsonic flow with a small enough vorticity.

Keywords: aeroacoustics, harmonic transport equation, Fredholm alternative

1 Introduction

We consider acoustic propagation in a general flow \mathbf{v}_0 , vortical which corresponds to $\omega_0 \equiv \mathbf{curl}(\mathbf{v}_0) \neq 0$. To describe the propagation of small acoustic and hydrodynamic perturbations, we have chosen Goldstein's equations [3]. In the potential areas $\omega_0 = \mathbf{0}$, corresponding to the velocity $\mathbf{v}_0 = \nabla\varphi_0$ where φ_0 is the velocity potential, the Goldstein equations reduce to a classical convected scalar wave equation [1]. Here we consider the more complicated case of non-potential flows, for instance the Lamb-Chaplygin dipole vortex [2], whose streamlines are represented in Fig. 1. The streamlines di-

vide in two families: closed streamlines corresponding to recirculation rolls and infinite streamlines. For the unclosed streamlines, we are able to prove that the Goldstein equations are well-posed. Here we focus on the recirculation areas, for instance on the one surrounded by a black line on Fig. 1. More precisely we will consider a circular flow, to simplify the presentation and to get explicit results.

2 Geometry and equations

We consider Ω a disc of radius $R > 0$ and a given circular flow $\mathbf{v}_0 = v_0(r)\mathbf{e}_\theta$ with $v_0/r \in C^1([0, R])$ and with $0 < v_- \leq v_0$. In polar coordinates, the Goldstein equations read in Ω :

$$\begin{aligned} p_0 c_0^{-2} D_\omega^2 \varphi &= \operatorname{div} [\rho_0 (\nabla \varphi + \boldsymbol{\xi})] + \rho_0 f(1) \\ D_\omega \boldsymbol{\xi} + B(r) \boldsymbol{\xi} &= \omega_0 \mathbf{curl} \varphi. \end{aligned} \quad (2)$$

We have introduced:

$$D_\omega \equiv -i\omega + \frac{v_0}{r} \frac{\partial}{\partial \theta}, \quad B(r) \equiv \begin{pmatrix} 0 & -2v_0/r \\ \omega_0 & 0 \end{pmatrix}.$$

$\omega_0(r) = v_0(r)/r + v'_0(r)$ and f is an acoustic source. $\varphi(r, \theta)$ is the acoustic potential and the vector $\boldsymbol{\xi}(r, \theta)$ is the hydrodynamic unknown. $\rho_0(r)$ and $c_0(r)$ are the given density and sound speed of the flow. Once the Goldstein equations are solved, the velocity perturbation is given by $\mathbf{v} = \nabla\varphi + \boldsymbol{\xi}$ and the pressure by $p = -\rho_0 D_\omega \varphi$. To close Eq. (1)-(2), we take $(\varphi, \boldsymbol{\xi})$ θ -periodic and we add a radiation condition:

$$\partial\varphi/\partial r + \xi_r = i(\omega/c_0)\varphi \quad \text{at } r = R.$$

Our aim is to study the well-posedness of Eq. (1)-(2). Our strategy is

- to determine the integral form of the solution $\boldsymbol{\xi}(\varphi)$ of the transport equation (2),
- to introduce $\boldsymbol{\xi}(\varphi)$ in the wave equation (1) and to prove that the resulting scalar problem is well-posed.

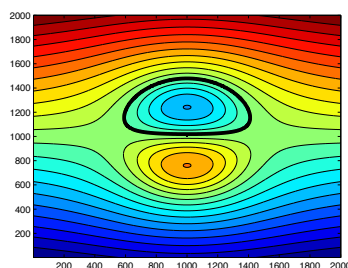


Figure 1: The Lamb-Chaplygin flow

3 Solution of the transport equation

We focus first on the transport equation (2) and we consider the following problem: for $\omega \geq 0$, find $\xi \in (L^2(\Omega))^2$ such that

$$\begin{cases} D_\omega \xi + B(r) \xi = f, \\ \forall r \in [0, R], \quad \xi(r, 0) = \xi(r, 2\pi), \end{cases} \quad (3)$$

where $f \in (L^2(\Omega))^2$ is a source term 2π -periodic in the variable θ . In the following we will consider $2\omega_0 v_0 / r > 0$: it corresponds to a stable flow profile and we can show that when $2\omega_0 v_0 / r < 0$, the time-harmonic regime doesn't exist. Then the eigenvalues of $B(r)$ are $\pm i\lambda(r)$ where $\lambda(r) := \sqrt{2\omega_0 v_0 / r}$ is real. We introduce the spectrum of resonance frequencies:

$$\mathcal{K}_{res}(v_0) := \left\{ \omega_{\pm,n}(r), n \in \mathbb{Z}, r \in [0, R] \right\}, \quad (4)$$

where $\omega_{\pm,n}(r) = (v_0/r)n \pm \lambda(r)$, and we have

Theorem 1

- If $\omega \notin \mathcal{K}_{res}(v_0)$, then (3) has a unique solution and $\exists C(\omega) > 0$ such that:

$$\|\xi\|_{L^2(\Omega)^2} \leq C(\omega) \|f\|_{L^2(\Omega)^2} \quad (5)$$

- If $\omega \in \mathcal{K}_{res}(v_0)$, (3) is ill-posed in $(L^2(\Omega))^2$.

The proof consists simply in determining explicitly the solution as a convolution integral.

$\mathcal{K}_{res}(v_0)$ is represented in blue in Fig. 2 for a velocity $v_0 = br + cr^2$ with $b = 1$ and $c = 0.5$, in a disc of radius $R = 1$. The spectrum is found continuous for large frequencies (here $\omega \gtrsim 2$) and band gaps exist at low frequencies. The frequency $\omega = 1.2$, represented as a red

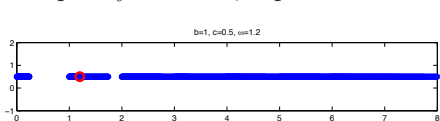


Figure 2: Spectrum $\mathcal{K}_{res}(v_0)$. The particular frequency $\omega = 1.2$ is represented in red.

circle, is in the spectrum since it corresponds to two resonant frequencies: $\omega_{+, -1}(r_1) = \omega = \omega_{-, 3}(r_2)$ with $r_1 = 0.27$ and $r_2 = 0.78$. On Fig. 3 is represented the quantity $\Re(\xi_x)$ obtained numerically for $\omega = 1.2$. We see that two lines are found resonant in the sense that the solution takes large values on these streamlines. These lines are found located at the values $r = r_1$ and $r = r_2$ obtained theoretically.

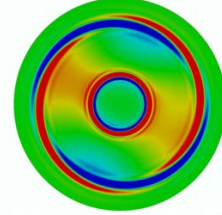


Figure 3: $\Re(\xi_x)$ obtained numerically.

4 Well-posedness of the Goldstein equations

Now we consider the coupled problem Eq. (1)-(2). Eq. (2) corresponds to Eq. (3) with $f = \omega_0 \operatorname{curl} \varphi$. The final result is

Theorem 2 *If $\omega \notin \mathcal{K}_{res}(v_0)$, then the Goldstein equations Eq. (1)-(2) are well-posed under the condition*

$$1 - [\min_{\Omega}(v_0/c_0)]^2 - C(\omega) \|\omega_0\|_{L^\infty} > 0, \quad (6)$$

with $C(\omega)$ introduced in (5).

This condition implies a subsonic flow $\min_{\Omega}(v_0/c_0) < 1$ and a vorticity of the flow $|\omega_0|$ small enough. The proof follows from:

- using a variational formulation, the problem (1)-(2) is proved to be of Fredholm type under the coercivity condition (6),
- using a Fourier decomposition in θ , the homogeneous problem for $f = 0$ is proved to have no other solution than 0.

References

- [1] D. Blokhintzev, The propagation of sound in an inhomogeneous and moving medium I., *J. Acoust. Soc. Am.* **18**(2), 322-328 (1946).
- [2] H. Lamb, Hydrodynamics, 6th ed., Cambridge Univ. Press, Cambridge, (1932).
- [3] M. E. Goldstein, Unsteady vortical and entropic distortion of potential flows round arbitrary obstacles, *J. Fluid Mech.* **89**(3), 433-468 (1978).

Stochastic Boundary Integral Equations in Electromagnetic Scattering

B.L. Michielsen^{1,*}

¹Onera, Toulouse, France

*Email: Bastiaan.Michielsen@Onera.fr

Abstract

We show how boundary integral equations on an uncertain boundary can be replaced by volume integral equations with a stochastic kernel but on a fixed support. This is advantageous for applications because with the volume integral equation, the Galerkin discretisation can be defined on a fixed domain instead of on (sample) realisations of the stochastic boundary.

Keywords: Stochastic Boundary integral equations

1 Introduction

We are studying electromagnetic scattering problems with boundary integral equations and want to account for uncertainties in the geometry of the boundary. This leads to define a probabilistic model for the uncertain boundary (see section 2) and, as a consequence, to study stochastic boundary integral equations. The numerical solution of stochastic boundary integral equations suffers from the fact that each realisation of the integral equation concerns the construction of a distribution on a new support and hence a numerical solution would require a new mesh, a new operator discretisation etc. For small geometrical fluctuations, it is possible to reduce the problem, via asymptotic expansions around a nominal (or average) surface, to an integral equation with only a stochastic kernel, on this fixed nominal boundary (see [1]). For geometrical fluctuations beyond asymptotically small variations we propose, in section 3, a volume integral equation equivalent to the stochastic boundary integral equation. In section 4, the weak formulation of the volume integral equation is defined showing how the deformation mappings are used in a concrete construction of stochastic Galerkin matrices.

2 Stochastic deformation

The nominal boundary surface, Γ_0 , is represented as a generic manifold, Γ , with charts, $\{U_p\}$, and a (chart-wise) embedding, $\mu \circ \varphi$, in \mathbb{R}^3 .

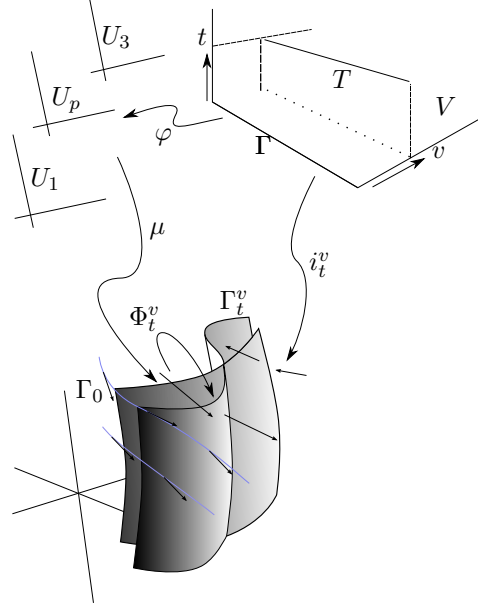


Figure 1: The mappings defining the stochastic kernel

To define deformations of Γ_0 , we use normalised finite stochastic linear combination of smooth vector fields on \mathbb{R}^3

$$v_\alpha = \sum_p \alpha_p v_p$$

with α_p centered random reals and $\|v_\alpha\| = 1$, spanning a vector space V . For each $v \in V$, the flow $\Phi^v : \mathbb{R}^3 \times T \rightarrow \mathbb{R}^3$, defined by

$$t \in T \quad \partial_t \Phi^v(x, t) = v(\Phi^v(x, t)),$$

defines a stochastic deformation of Γ_0 . We choose a probability density on T and take the flow coordinate, t , to be statistically independent of v . We put sufficient constraints on the vector fields (e.g., zero divergence) such that the set of deformations be a family of diffeomorphisms.

The Electric Field Integral Equation (EFIE), which is often used in electromagnetic scattering models, is given by

$$\left[\int_{y \in \Gamma_t^v} G_x^{eh}(y) \wedge H(y) \right]_{\Gamma_t^v} = -[E^i]_{\Gamma_t^v}(x)$$

on the deformed surfaces $\Gamma_t^v = \Phi_t^v[\Gamma_0]$. This integral equation can be “pulled back” to Γ via the embeddings $i_t^v = \Phi_t^v \circ \mu$. First, the integrand on the LHS is rewritten

$$\begin{aligned} \int_{y \in \Gamma_t^v} G_x^{eh}(y) \wedge H(y) &= \\ \int_{y \in \Gamma} G_x^{eh}(i_t^v(y)) \wedge H(i_t^v(y)) \end{aligned}$$

and, secondly, the equation itself

$$\begin{aligned} \int_{y \in \Gamma} G_x^{eh}(i_t^v(x), i_t^v(y)) \wedge H(i_t^v(y)) \\ = -E^i(i_t^v(x)) \end{aligned}$$

(We use differential forms for all the fields, such that the pull-back with f is simply the composition with f .)

3 The volume integral equation

The flow interval can be considered as a third dimension extending the manifold Γ into an abstract volume $\Gamma \times T$ where the line element on the flow interval T contributes to the volume element. On this volume, we obtain an integral equation with a “stratified” kernel

$$K((x, t), (y, s)) = \delta_{(s-t)} G(i_t^v(x), i_s^v(y))$$

parameterised by the normalised vector fields.

We can use the embedding map for any normalised vector field $v \in V$

$$i^v : \Gamma \times T \ni (x, t) \mapsto i_t^v(x) \in \mathbb{R}^3$$

to push forward differential forms on $\Gamma \times T$ via

$$i_*^v : T^*(\Gamma \times T) \ni (\xi, \tau) \mapsto i_{t*}^v(\xi, \tau) \in T^*\mathbb{R}^3$$

to differential forms on \mathbb{R}^3 . The “stratified” kernel of the integral equation over $\Gamma \times T$ is therewith transformed into a kernel on \mathbb{R}^3 with (v, t) -dependent weights. For a given probability distribution on $T \times V$, the kernel is actually a stochastic kernel on

$$\Omega = \bigcup_{(t, v) \in T \times V} \Gamma_t^v \subset \mathbb{R}^3$$

with a “surely 0” extension to any environment of Ω .

4 Weak formulation

In order to be able to solve the above defined integral equation numerically, we study the construction of the stochastic Galerkin matrix. For this, we define a finite dimensional approximation space for 2-form distributions on (an environment of) Ω

$$FES = \{j_k \in \bigwedge^2 T^*\mathbb{R}^3 : k = 1, \dots, N\}$$

(In addition, we define interpolators on the probability space $P = T \times V$ allowing for a discretisation of vector-valued functions on P , but we do not elaborate this here.) The current distribution, $J \in \bigwedge^2 T^*\mathbb{R}^3$, solution of the stochastic boundary integral equation is then represented as a function over the probability space $P \ni p \mapsto J(p) = \sum_n j_n I^n(p)$. The discretised integral equation, for any $p \in P$, is a linear algebra problem: find the coefficients $I^n(p)$ such that

$$\forall m \sum_n G_{p;mn}^{eh} I^n(p) = e_{p,m}$$

where

$$G_{p;mn}^{eh} = \int_{x \in \Omega} j_m(x) \wedge A_p j_n(x)$$

and

$$A_p j_n(x) = \int_{y \in \Omega} G_p^{eh}(x, y) \wedge j_n(y)$$

$$\text{with } G_{(t,v)}^{eh} = i_{t*}^v \times i_{t*}^v K.$$

5 Conclusion

We are studying the nature of stochastic boundary integral equations via mathematically equivalent stochastic volume integral equations. Because the volume integral equations are defined on a fixed domain, they are more convenient both for numerical computations and for the study of the convergence of numerical approximations, at least point-wise over the probability space. We will present a numerical implementation of a simplified 2-dimensional case for which we are able to compare exact solutions to numerical results.

References

- [1] B.L. Michelsen, First order estimates in integral equations on stochastic boundaries, *Waves 2015*, Karlsruhe (2015)

A nodal discontinuous Galerkin method with high-order absorbing boundary conditions and corner/edge compatibility

Axel Modave^{1,*}, Andreas Atle², Jesse Chan³, Tim Warburton⁴

¹Team POEMS (CNRS-ENSTA-INRIA), Palaiseau, France

²TOTAL E&P, Houston, TX, USA

³Rice University, Houston, TX, USA

⁴Virginia Tech, Blacksburg, VA, USA

*Email: axel.modave@ensta-paristech.fr

Abstract

We present the coupling of a nodal discontinuous Galerkin (DG) scheme with high-order absorbing boundary conditions (HABCs) for the simulation of transient wave phenomena. The HABCs are prescribed on the faces of a cuboidal domain in order to simulate infinite space. To preserve accuracy at the corners and the edges of the domain, novel compatibility conditions are derived. The method is validated using 3D computational results.

Keywords: Transient waves, Discontinuous finite element, Absorbing boundary condition

1 Introduction

DG schemes are widely used for large-scale simulations of transient waves in complex media. For many applications, these schemes must be coupled with nonreflective boundary techniques in order to limit the size of the computational domain without losing accuracy or computational efficiency. In this context, PMLs and local HABCs are attractive since they provide high-fidelity solutions at reasonable computational cost. Nevertheless, HABCs have received far less attention than PMLs, and very few couplings with DG schemes have been proposed.

Local HABCs involve the computation of auxiliary fields governed by differential equations on the boundary (see *e.g.* [1, 2]), and require specific treatments at the corners of the domain. Hagstrom and Warburton [2] proposed compatibility conditions that preserve accuracy, but that are difficult to devise for complicated problems. In this work, we derive simpler compatibility conditions in the acoustic case by using a different representation for the HABCs.

2 HABC and compatibility conditions

Let the field $p(\mathbf{x}, t)$ governed by the wave equation $\partial_{tt}p - \Delta p = 0$ in the cuboidal domain

$$\Omega = \{\mathbf{x} \in \mathbb{R}^3 : |x| < L_x, |y| < L_y, |z| < L_z\}.$$

For each face, we consider HABCs derived using the $(2N+1)^{\text{th}}$ Padé approximation of the square root in the exact nonreflective condition [1]. On the face belonging to the plane $x = L_x$, we write the condition as

$$\partial_t p + \partial_x p = \frac{2}{M} \sum_{i=1}^N a_i \partial_t (p_i^x - p), \quad (1)$$

where N auxiliary fields p_i^x are governed by

$$\partial_{tt} [b_i(p_i^x - p)] - \Delta_\perp^x p_i^x = 0, \quad \forall i \in [1, N], \quad (2)$$

with $a_i = \tan^2(i\pi/M)$, $b_i = a_i + 1$, $\Delta_\perp^x = \Delta - \partial_{xx}$ and $M = 2N + 1$. This HABC is nearly identical to the one proposed by Collino [1]. It is equivalent to a special case of the one considered in [2], but the specific structure of Eqs. 1-2 leads to simpler compatibility conditions.

Additional relations must be defined on the border of each face (*i.e.* on the edges) because of the operator Δ_\perp^x in Eq. 2. Following [2], they are devised to ensure the compatibility of the system. On the edge belonging to the line $(x, y) = (L_x, L_y)$, the fields p_i^x and p_j^y defined on the adjacent faces then verify the boundary conditions

$$\begin{aligned} \partial_t p_i^x + \partial_y p_i^x &= \frac{2}{M} \sum_{j=1}^N a_j \partial_t (p_{ij}^{xy} - p_i^x), \quad \forall i, \\ \partial_t p_j^y + \partial_x p_j^y &= \frac{2}{M} \sum_{i=1}^N a_i \partial_t (p_{ij}^{xy} - p_j^y), \quad \forall j, \end{aligned}$$

where N^2 auxiliary fields p_{ij}^{xy} are governed by

$$\begin{aligned} \partial_{tt} [(1 + a_i + a_j)p_{ij}^{xy} - b_i p_j^y - b_j p_i^x] \\ - \partial_{zz} p_{ij}^{xy} = 0, \quad \forall i, j. \end{aligned} \quad (3)$$

Similarly, relations close to Eq. 2 are prescribed on the corners to give boundary conditions for the auxiliary fields defined on the edges. They involve N^3 auxiliary fields that are governed by algebraic relations on the corners.

3 Scheme and computational procedure

The scheme is written for the pressure-velocity system and based on the variational form

$$\begin{cases} ((\partial_t p + \nabla \cdot \mathbf{u}), \phi)_{\Omega_k} = \langle \mathbf{n} \cdot (\mathbf{u}^{\text{in}} - \mathbf{u}^*), \phi \rangle_{\Gamma_k} \\ ((\partial_t \mathbf{u} + \nabla p), \psi)_{\Omega_k} = \langle \mathbf{n} \cdot (\mathbf{u}^{\text{in}} - \mathbf{u}^*), \psi \rangle_{\Gamma_k} \end{cases} \quad (4)$$

with test functions ϕ and ψ , a mesh cell Ω_k , its boundary Γ_k , and the external unit normal \mathbf{n} . Upwind fluxes are defined by taking

$$p^* = (r^+)^{\text{in}} + (r^-)^{\text{ex}} \quad (5)$$

$$\mathbf{n} \cdot \mathbf{u}^* = (r^+)^{\text{in}} - (r^-)^{\text{ex}} \quad (6)$$

where $r^\pm = p \pm \mathbf{n} \cdot \mathbf{u}$ are the outgoing (+) and incoming (-) characteristics. The subscripts ⁱⁿ and ^{ex} denote interior and exterior values on Γ_k .

The HABC is incorporated in the scheme by rewriting Eq. 1 with characteristics. On the face belonging to the plane $x = L_x$, one has

$$r^- \stackrel{\text{(def.)}}{=} p - \mathbf{e}_x \cdot \mathbf{u} \stackrel{\text{(Eq. 1)}}{=} \frac{2}{M} \sum_{i=1}^N a_i (p_i^x - p).$$

This incoming characteristic is used in the upwind fluxes (Eqs. 5-6) on the domain boundary. Since the auxiliary fields are governed by 2D and 1D wave-like equations (Eqs. 2-3) on the faces and the edges, we use 2D and 1D versions of the variational form (Eq. 4). HABCs are prescribed on the auxiliary fields by using the same strategy. The procedure then consists in 3D/2D/1D solvers on the domain/faces/edges. For each mesh node of the edges and for each corner, the incoming characteristics are computed by solving systems with $2N$ and $3N^2$ unknowns. See [3] for the detailed procedure and GPU computational performance results.

4 Numerical results

We consider the propagation of a spherical wave in the cuboidal domain $\Omega = [-0.5, 0.5]^3$. The wave is generated using a point source at the position $(0, 0.1, 0.2)$ with a Ricker wavelet. We use a mesh composed of 70,895 tetrahedra, third-degree basis functions and a fourth-order Runge-Kutta scheme. Simulations are performed with HABCs of different orders. For each case, Figure 1 shows the time-evolution of the error

$$\sqrt{\frac{\|p - p_{\text{ref}}\|_{L_2(\Omega)}^2 + \|\mathbf{u} - \mathbf{u}_{\text{ref}}\|_{L_2(\Omega)}^2}{\sup_{t>0} (\|p_{\text{ref}}\|_{L_2(\Omega)}^2 + \|\mathbf{u}_{\text{ref}}\|_{L_2(\Omega)}^2)}},$$

where p_{ref} and \mathbf{u}_{ref} correspond to the solution of the free-space problem defined on \mathbb{R}^3 .

At the beginning, the error is dominated by the numerical error (the same in all the cases) generated when the wavefront is travelling inside Ω and has not reached the boundary yet. Later, a modeling error is generated because of the spurious reflection of waves at the boundary. The higher the order of the HABC, the smaller the error, which validates the method for short times. For long times, the error converges towards the same value for all the orders, except for $N = 0$ where the error remains decreasing. This is due to the poor long-time behaviour of Padé-type HABCs, which has been observed in 2D in [2]. We plan to extend the method for long-time simulations and other physical waves.

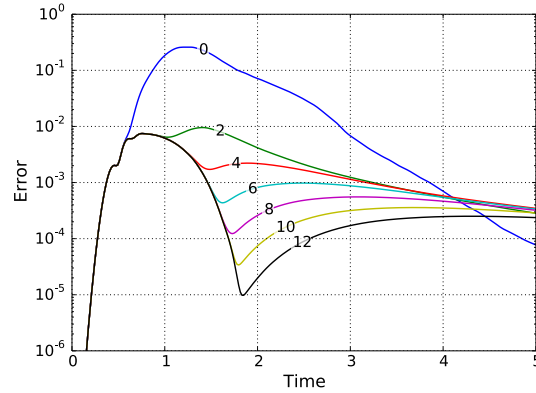


Figure 1: Error with HABCs having N additional fields ($N = 0, 2, \dots, 12$). The main spherical wavefront is travelling in Ω when $t \in [0, 2]$.

This work was funded by a grant from TOTAL E&P Research and Technology USA.

References

- [1] F. Collino (1993). “High-order absorbing boundary conditions for wave propagation models. Straight line boundary and corner cases”. *Proceedings of WAVES 1993*.
- [2] T. Hagstrom and T. Warburton (2004). “A new auxiliary variable formulation of high-order local radiation boundary conditions: corner compatibility conditions and extensions to first-order systems”. *Wave motion* **39**(4), 327-338.
- [3] A. Modave, A. Atle, J. Chan and T. Warburton (2016). “A GPU-accelerated nodal discontinuous Galerkin method with high-order absorbing boundary conditions and corner/edge compatibility”. Preprint [arXiv/abs/1610.05023](https://arxiv.org/abs/1610.05023).

Time dependent inverse scattering in a waveguide

Peter Monk^{1,*}, Virginia Selgas²

¹Department of Mathematical Sciences, University of Delaware, Newark DE 19716, USA.

²Departamento de Matemáticas, Universidad de Oviedo, EPIG, 33203 Gijón, Spain.

*Email: monk@udel.edu

Abstract

We study the inverse problem of determining the shape of sound soft inclusions in a sound hard waveguide using time domain data. We prove existence and uniqueness for the forward problem, and derive a numerical method using time domain integral equations. For the inverse problem we suggest to use a time domain version of the Linear Sampling Method. After analysis of the time domain inversion scheme, we provide numerical examples.

Keywords: Inverse scattering, Waveguide, Qualitative method, Time domain.

1 Introduction

The inverse problem of using the Linear Sampling Method to detect sound soft objects in a sound hard acoustic waveguide was studied in [1] and for penetrable scatterers was studied by us in [4]. This paper concerns the analogous problem using time domain data [2, 5], but unlike [2] we propose to use the time domain data directly in the time domain LSM (the TDLSM). An important contribution from [2] was the design of incident waves that have fast decay in time, limiting the need for long time computations. Here, we present numerical tests using the TDLSM with the new incident field and show promising results.

2 Forward Problem

Let $P := \mathbb{R} \times (0, H)$, $H > 0$ denote the infinite waveguide that forms the background domain for our study. Then $D \subset P$ denotes a bounded and smooth impenetrable sound soft obstacle in P . We assume that the incident field is due to a point source at $\mathbf{x}_0 \in P \setminus \overline{D}$ with time dependence $\xi(t)$ (a smooth causal function). Then, if $u_{\mathbf{x}_0}^i$ denotes this incident wave, it satisfies the wave equation in $P \setminus \{\mathbf{x}_0\}$ with vanishing initial conditions. The forward problem is to find

$u_{\mathbf{x}_0} \equiv u_{\mathbf{x}_0}(t, \mathbf{x})$, the scattered field, that satisfies

$$\begin{cases} \partial_{tt}^2 u_{\mathbf{x}_0} - \Delta u_{\mathbf{x}_0} = 0 & \text{in } P \setminus \overline{D}, \text{ for } t > 0 \\ \partial_\nu u_{\mathbf{x}_0} = 0 & \text{on } \partial P, \text{ for } t > 0 \\ u_{\mathbf{x}_0} = -u_{\mathbf{x}_0}^i & \text{on } \partial D, \text{ for } t > 0 \\ u_{\mathbf{x}_0} = \partial_t u_{\mathbf{x}_0} = 0 & \text{in } P, \text{ for } t \leq 0 \end{cases}$$

Here ν is the unit outward normal to P . There is no need of any radiation condition on u because $u_{\mathbf{x}_0}^i$ is causal and the wave speed is finite.

Using the Fourier-Laplace transform, in [3] we prove that this problem is wellposed, and show how the forward problem can be approximated using a time domain integral equation on ∂D . This requires a careful implementation of the fundamental solution for the waveguide. The use of a time domain integral equation obviates the need for a mesh truncation condition.

3 Inverse Problem

For the inverse problem we suppose that there is a measurement line $\Sigma = L \times (0, H)$ at $x = -L$ such $\overline{D} \cap \Sigma = \emptyset$ (of course the interesting case is when Σ is far from D). Then for every source point $\mathbf{x}_0 \in \Sigma$ we suppose that it is possible to record the scattered field $u_{\mathbf{x}_0}(t, \mathbf{x})$, $t > 0$, $\mathbf{x} \in \Sigma$. From this data we wish to find the shape of the unknown scatterer D . In practice the data will only be known for a finite number of measurement and source locations and at discrete times.

The TDLSM rests on the study of the time domain near field operator. This is defined for $g \in L^2((0, T) \times \Sigma)$ by

$$Ng(t, \mathbf{x}) = \int_{\Sigma} \int_0^{\infty} u_{\mathbf{x}_0}(t-\tau-\eta, \mathbf{x}) g(\eta, \mathbf{x}_0) d\eta ds_{\mathbf{x}_0}$$

where τ is a parameter. This is the time domain analogue of the near field operator in time harmonic scattering.

We prove that N is injective with dense range and then consider the near field equation of finding $g_{\mathbf{z}} \in L^2((0, T) \times \Sigma)$ such that

$$Ng_{\mathbf{z}}(t, \mathbf{x}) = u_{\mathbf{z}}^i(t, \mathbf{x}) \quad t > 0, \mathbf{x} \in \Sigma, \quad (1)$$

where $u_{\mathbf{z}}^i$ is the solution of the wave equation in the waveguide P due to a point source at

the auxilliary point $\mathbf{z} \in P$ and time modulation $\xi(t)$.

Again using Fourier-Laplace transform techniques, show that there is an approximate solution to the near field equation (1) that can be used as an indicator function for the scatterer D (but as usual for the TDLSM or time harmonic LSM we cannot prove that a regularized version of the solution of (1) is this solution).

In Fig. 1 we show results of a numerical experiment in the case $H = 1$ with $L = -2$ and $L = -5$ using the incident field from [2] with five terms:

$$\xi(t) = \sum_{n=1}^5 \xi_n(t)$$

where

$$\xi_n(t) = \frac{d}{dt} \left(\sin(A_n t) e^{-B_n(t-C_n)^2} \right)$$

and $A_n, B_n, C_n \in \mathbb{R}$ are fixed to select the mean frequency and the support of the signal in the Fourier domain. We use: $B_n = \frac{\pi^2}{200}$, $C_n = \frac{5}{\sqrt{2B_n}}$, and

$$A_n = \pi(n - 0.5) - \frac{4B_n}{\pi(n - 0.5)}$$

The advantage of this choice is that it decreases the amplitude of the modes in the waveguide at the cutoff frequencies, so the scattered wave decays rapidly in time.

The scatterer is a disk of radius 0.2 centered at $\mathbf{x} = (0, 0.6)$. The results show that the left hand side of the circular scatterer is detected by the algorithm (sources and measurements are to the left) and the reconstruction is rather insensitive to the Tikhonov regularization parameter.

4 Conclusion

We have demonstrated theoretically and numerically that the TDLSM can be used to solve a time domain inverse scattering problem in a waveguide. Interesting future work includes testing the method on scatterers that are invisible at a selected frequency.

Acknowledgement

The research of PM is partially supported by a grant from AFOSR.

References

- [1] L. Bourgeois, E. Lunéville, *The Linear Sampling Method in a waveguide: a modal*

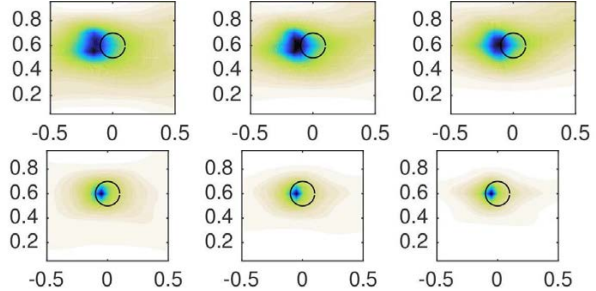


Figure 1: Reconstructions of a circular scatterer using measurements near (top row, $L = -2$) or far (bottom row, $L = -5$) from the obstacle. We show density plots of the indicator function derived from the regularized solution of the near field equation (1) see [5]. Different columns correspond to different Tikhonov regularization parameters (smaller to larger).

formulation, Inv. Prob. **24**(1) (2008), pp. 015018.

- [2] V. Baronian, L. Bourgeois, A. Recoquillay, *Imaging an acoustic waveguide from surface data in the time domain*, Wave Motion **66** (2016), pp. 68-87.
- [3] L. Fan, P. Monk, V. Selgas, *Time dependent scattering in an acoustic waveguide via convolution quadrature and the Dirichlet-to-Neumann map*, Trends in Differential Equations and Applications (SEMA-SIMAI Springer Series) **8** (2016), pp. 321-337.
- [4] P. Monk, V. Selgas, *Sampling type methods for an inverse waveguide problem*, Inverse Problems and Imaging **6**(4) (2012), pp. 709-747.
- [5] P. Monk, V. Selgas, *An inverse acoustic waveguide problem in the time domain*, Inverse Problems **32** (2016), pp. 055001.

Asymptotic stability of the linearised Euler equations with long-memory impedance boundary condition

Florian Monteghetti^{1,*}, Denis Matignon², Estelle Piot¹, Lucas Pascal¹

¹ONERA – The French Aerospace Lab, Toulouse, France

²Department of Applied Mathematics, ISAE-SUPAERO, Toulouse, France

*Email: florian.monteghetti@onera.fr

Abstract

This work focuses on the well-posedness and stability of the linearised Euler equations (1) with impedance boundary condition (2,3). The first part covers the *acoustical* case ($\mathbf{u}_0 = \mathbf{0}$), where the complexity lies solely in the chosen impedance model. The existence of an asymptotically stable C_0 -semigroup of contractions is shown when the passive impedance admits a dissipative realisation; the only source of instability is the time-delay τ . The second part discusses the more challenging *aeroacoustical* case ($\mathbf{u}_0 \neq \mathbf{0}$), which is the subject of ongoing research. A discontinuous Galerkin discretisation is used to investigate both cases.

Keywords: impedance boundary condition, diffusive representation, stability, discontinuous Galerkin

Introduction

This work focuses on the (dimensionless) homentropic linearised Euler equations (LEEs)

$$\begin{cases} \partial_t p + \nabla \cdot \mathbf{u} + \mathbf{u}_0 \cdot \nabla p + \gamma p \nabla \cdot \mathbf{u}_0 = 0 \\ \partial_t \mathbf{u} + \nabla p + [\mathbf{u}_0 \cdot \nabla] \mathbf{u} + [\mathbf{u} \cdot \nabla] \mathbf{u}_0 + p[\mathbf{u}_0 \cdot \nabla] \mathbf{u}_0 = \mathbf{0}, \end{cases} \quad (1)$$

defined on $(0, \infty) \times \Omega$, where $\Omega \subset \mathbb{R}^n$ is a bounded Lipschitz open subset, $p(\mathbf{u})$ is the acoustical pressure (velocity), $\mathbf{u}_0 \in \mathcal{C}^\infty(\bar{\Omega})^n$ is the (given) base flow, and $\gamma > 1$ is the specific heat ratio. On the boundary $\Gamma := \partial\Omega$ (with outward normal \mathbf{n}), a so-called acoustical *impedance boundary condition* is prescribed :

$$p(t, x) = [z * \mathbf{u} \cdot \mathbf{n}(\cdot, x)](t) \quad (x \in \Gamma := \partial\Omega), \quad (2)$$

where the *impedance* ($z \in \mathcal{D}'_+(\mathbb{R}) \cap \mathcal{S}'(\mathbb{R})$, causal convolution kernel) models a mono-dimensional medium as a continuous linear time-invariant system.

A recent analysis of acoustical models in the time domain [6] has shown that a wide range of sound absorbing materials and ground layers, assumed locally-reacting, can be modelled by kernels such as (“’” is the weak derivative, $a_0, a_1 \geq 0$):

$$z = a_0 \delta + a_1 \delta' + D_2' + D_3(\cdot - \tau), \quad (3)$$

where $\tau \geq 0$ and $D_i \in L^1_{\text{loc}}(0, \infty)$ is a causal oscillatory-diffusive kernel ($I_i \subset \mathbb{Z}$ countable, poles $\Re[s_{n,i}] < 0$, $r_{n,i} > 0$, μ_i positive Borel measure):

$$D_i(t) = \underbrace{\sum_{n \in I_i} r_{n,i} e^{s_{n,i} t}}_{\text{oscillatory}} + \underbrace{\int_0^\infty e^{-\xi t} d\mu_i(\xi)}_{\text{diffusive}}, \quad (4)$$

which models resonances and visco-thermal losses (e.g. fractional kernel $D_2 \propto t^{-1/2}$). A key feature of such *positive real* kernels is that they can be realised (in the sense of systems theory) by a *diagonal, dissipative*, infinite-dimensional dynamical system. Note that, if $\tau > 0$ in (3), then (2) is a *delayed* boundary condition, which models wave reflections. The two sources of instability in (1,2) are the base flow \mathbf{u}_0 and the impedance z .

1 Acoustical case

The acoustical assumption ($\mathbf{u}_0 = \mathbf{0}$) removes hydrodynamic instabilities, but leaves room for purely acoustical ones triggered by the impedance boundary condition (2,3). Below, the delayed ($\tau = 0$) and undelayed ($\tau > 0$) cases are successively investigated by recasting the PDE (1,2) into a Cauchy problem on a Hilbert space \mathcal{H} :

$$\dot{\mathbf{X}}(t) = \mathcal{A} \mathbf{X}(t), \quad \mathbf{X}(0) = \mathbf{X}_0 \in \mathcal{D}(\mathcal{A}). \quad (5)$$

To express \mathcal{A} , a time-domain realisation of z in a state-space Θ is needed. The given asymptotic stability results (see Thms. 3 and 5), crucially rely on the *dissipativity* of this realisation.

1.1 Undelayed impedance ($\tau = 0$)

Impedances z of increasing complexity can be considered, with Θ either finite or infinite-dimensional: proportional ($z = a_0 \delta$), for which no realisation is required; derivative ($z = a_1 \delta'$), for which $\Theta = \mathbb{C}$. For the sake of brevity and clarity, only two simplified examples (compared with (3)) are given below before the statement of the general result.

Example 1. Let $\hat{z}(s)$ be a real rational function, bounded for $\Re[s] \geq 0$. If $\Re[\hat{z}(s)] \geq 0$ (passivity), then it can be realised by a dissipative ODE

in $\Theta = \mathbb{R}^N$, with a suitable energy norm (positive real lemma, see [4, § 3.1]). Eq. (5) is then defined on $\mathcal{H} = L^2(\Omega) \times (L^2(\Omega))^n \times L^2(\Gamma; \Theta)$.

Example 2. Let $z = a_0\delta + D_2$ (*not* D'_2), and define the weighted spaces $\Phi_{\alpha(\xi)} = L^2(0, \infty; \alpha(\xi) d\mu_2)$. The diagonal, dissipative, infinite-dimensional realisation of D_2 in $\Theta = \Phi_1$ leads to $\mathcal{H} = L^2(\Omega) \times (L^2(\Omega))^n \times L^2(\Gamma; \Phi_1)$, and (5) then reads:

$$\begin{aligned} \mathcal{A}X &= \mathcal{A} \begin{pmatrix} p \\ \mathbf{u} \\ \varphi \end{pmatrix} = \begin{pmatrix} -\nabla \cdot \mathbf{u} \\ -\nabla p \\ A\varphi + B\mathbf{u} \cdot \mathbf{n} \end{pmatrix} \\ V &= H^1 \times (H^1(\text{div}) \cap (H^{1/2})^n) \times L^2(\Gamma; \Phi_{1+\xi}) \\ \mathcal{D}(\mathcal{A}) &= \left\{ X \in V \mid \begin{array}{l} [A\varphi + B\mathbf{u} \cdot \mathbf{n}] \in L^2(\Gamma; \Phi_1) \\ p|_\Gamma = a_0\mathbf{u} \cdot \mathbf{n} + C\varphi \text{ (in } L^2(\Gamma)) \end{array} \right\}, \end{aligned}$$

where, formally, $(A\varphi)(x, \xi) = -\xi\varphi(x, \xi)$ (state operator), $(B\mathbf{u} \cdot \mathbf{n})(x, \xi) = \mathbb{1}(\xi)\mathbf{u} \cdot \mathbf{n}(x)$ (control), and $(C\varphi)(x) = \int_0^\infty \varphi(x, \xi) d\mu_2(\xi)$ (observation).

Theorem 3. Assume that $\tau = 0$ in (3). If $\Re[a_0] > 0$, $a_1 \geq 0$, $\Re[s_{n,i}] < 0$, $r_{n,i} > 0$ and μ_i is a positive Borel measure, then z admits a dissipative realisation, and (5) has a unique strong solution X , such that $\|X(t)\| \leq \|X_0\|$ for $t \geq 0$ and $\|X(t)\| \xrightarrow{\infty} 0$.

Proof (Sketch). We follow [4]. The dissipativity of the realisation of z implies that of \mathcal{A} . Well-posedness follows from the m -dissipativity of \mathcal{A} . With the Fredholm alternative, we show that $\rho(\mathcal{A}) \supset i\mathbb{R}^*$ (we use that $H^s(\Omega) \subset L^2(\Omega)$, $s > 0$, is a compact embedding). Since $0 \notin \sigma_p(\mathcal{A})$, asymptotic stability then follows from the Arendt-Batty theorem. \square

Remark 4. With an infinite-dimensional realisation of z , the embedding $\mathcal{D}(\mathcal{A}) \subset \mathcal{H}$ may not be compact, hence the need to finely inspect $\rho(\mathcal{A})$, as the pre-compactness condition of LaSalle's invariance principle is not straightforward to verify.

1.2 Delayed impedance ($\tau > 0$)

The delayed case ($\tau > 0$) can also be recast into (5) using a *hyperbolic* realisation of the delay through a transport equation, which leads to an additional extension: $\tilde{\mathcal{H}} = \mathcal{H} \times L^2(\Gamma; L^2(0, \tau; \Theta))$. Asymptotic stability then becomes delay-dependent, which is typical of time-delayed linear systems (see [5] and references therein). The energy method of Thm. 3 leads to a sufficient stability condition for the *pure* delay case (i.e. $D_3 = a_\tau\delta$, *not* a diffusive kernel).

Theorem 5. Let $a_\tau \in \mathbb{C}$ and $a_1 > 0$. If $\Re[a_0] > |a_\tau|$, then the result of theorem 3 extends to the case $z = a_0\delta + a_1\delta' + D'_2 + a_\tau\delta(\cdot - \tau)$.

Proof (Sketch). Similar to Thm. 3. The energy norm on the hyperbolic variables, $\|\cdot\|_{L^2(\Gamma; L^2(0, \tau; \mathbb{C}))}$ (here, $\Theta = \mathbb{C}$), is tuned so that \mathcal{A} is dissipative. [5] \square

2 Aeroacoustical case

The aeroacoustical assumption is $\mathbf{u}_0 \neq 0$ in (1). In the case of a subsonic base flow ($|\mathbf{u}_0| < 1$), and under stringent assumptions on \mathbf{u} and \mathbf{u}_0 (which must be, in particular, potential), the energy functional of Cantrell and Hart [1, Eq. (64)] can be used to construct a contraction C_0 -semigroup. Without these assumptions, however, there is no energy balance, and the dissipativity of \mathcal{A} is lost: well-posedness can only be achieved in a space like “ $e^{-\mu t} L^2(\Omega)$ ”, for some $\mu > \omega_0(\mathcal{A}) > 0$, where $\omega_0(\mathcal{A})$ is the growth rate of \mathcal{A} . (This constitutes a difficulty of the LEEs, compared to e.g. the Galbrun equation, see [1].) Current research focuses on the identification of instabilities with (2,3), see e.g. [3].

3 Numerical method

Insights into the stability of (5) can be gained by a numerical approximation of the temporal growth rate $\omega_0(\mathcal{A})$. A nodal discontinuous Galerkin method [2] is used to formulate $\dot{X}^h = \mathcal{A}^h X^h + \mathcal{B}^h X(\cdot - \tau)$, with $X^h = (p^h, \mathbf{u}^h, \varphi^h)$. The time-domain impedance boundary condition (2,3) is enforced through a centred numerical flux that couples the acoustical unknowns (p^h, \mathbf{u}^h) with the memory variables φ^h . If $\tau > 0$, finite-dimensional criteria, which rely on e.g. linear matrix inequalities (LMIs) or spectral conditions, are used to assess stability.

Acknowledgment This research is supported jointly by ONERA and DGA.

References

- [1] J.-Ph. Brazier. “Derivation of an exact energy balance for Galbrun equation in linear acoustics”. In: *J. Sound Vib.* 330.12 (2011).
- [2] J. S. Hesthaven and T. Warburton. *Nodal discontinuous Galerkin methods*. Springer, 2008.
- [3] D. Khamis and E. J. Brambley. “Acoustic boundary conditions at an impedance lining in inviscid shear flow”. In: *J. Fluid Mech.* 796 (June 2016).
- [4] D. Matignon and C. Prieur. “Asymptotic stability of Webster-Lokshin equation”. In: *Math. Control Relat. F.* 4.4 (2014).
- [5] F. Monteghetti, G. Haine and D. Matignon. “Stability of Linear Fractional Differential Equations with Delays: a coupled Parabolic-Hyperbolic PDEs formulation”. In: *IFAC 20th World Congress*.
- [6] F. Monteghetti, D. Matignon, E. Piot and L. Pascal. “Design of broadband time-domain impedance boundary conditions using the oscillatory-diffusive representation of acoustical models”. In: *J. Acoust. Soc. Am.* 140.3 (2016).

Gravitational Waves from Core-Collapse Supernovae

Bernhard Müller^{1,*}

¹Astrophysics Research Centre, School of Mathematics and Physics, Belfast, UK

*Email: b.mueller@qub.ac.uk

Abstract

Gravitational waves (GWs) could directly probe the multi-dimensional flow during the first second of core-collapse supernova explosions. We outline the structure of the predicted GW signal from neutrino-driven supernovae of non-rotating progenitors and quantitative dependencies governing the amplitudes of this signal and its evolution in the time-frequency domain.

Keywords: supernovae, gravitational waves

1 Introduction

Core-collapse supernovae [1] are the explosions of stars that begin their life with a mass of $\gtrsim 8M_{\odot}$. At the end of their lives, such massive stars build up an iron core at their centre, which eventually collapses due to electron capture reactions and photodisintegration of heavy nuclei. After reaching supranuclear densities, the core rebounds, and a shock wave is launched into the infalling outer shells. The shock initially stalls, and is later revived on a time scale of hundreds of milliseconds, likely by neutrino heating, or in rare cases of rapidly rotating progenitors by magnetohydrodynamic effects.

Observations and theory have shown that these explosions typically exhibit strong asymmetries [2]. In the more generic case of slowly spinning progenitors, these asymmetries arise naturally during the first second as neutrino heating drives convective overturn behind the shock or from the large-scale “standing accretion shock instability” (SASI) [2].

The electromagnetic signatures from the explosion are determined at later times, and thus only provide indirect clues about the multi-D character of the supernova “engine” in the first second(s) after collapse. Gravitational waves (GWs) could provide a more direct way to probe the dynamics in the supernova core. Sophisticated data analysis methods could help to discriminate between different supernova mechanisms or at least facilitate GW detection by using predicted waveforms from simulations (see, e.g., [3]). We here sketch some of the physics

that determines properties of the GW signal from convection and the SASI in neutrino-driven explosions,

2 GW Emission from Supernovae

The GW amplitudes h (often expressed as invariant amplitudes $A = hD$ by factoring out the distance D of the source) are determined by the temporal variation of the mass quadrupole moment of a system, which can occur in supernova for several reasons.

In the classical scenario of GW emission during rotational collapse, the quadrupole moment is non-zero from the outset because of the rotational deformation of the core and changes during the collapse and bounce. This case is sufficiently well understood [4] to allow quantitative measurements of the angular momentum of the core for a Galactic supernova with Advanced LIGO [5].

In the absence of rotation, aspherical mass motions in the neutrino heating layer (or “gain layer”) also lead to GW emission in the later post-bounce phase due to temporal variations in the mass quadrupole moment. Recent 2D simulations [6, 7] show several distinct phases: Shock ringing after prompt convection leads to a low-frequency signal around 100 Hz for about 50 ms, followed by a signal at several hundred Hz with stochastic amplitude modulations, and a “tail” due to asymmetric shock expansion in the explosion phase. There are still few 3D models, which show lower amplitudes by a factor of ~ 10 [8, 9], but these have already revealed a new low-frequency component from the SASI at 100–200 Hz [9, 10].

3 The Typical GW Frequency

Because of the stochastic character of GW emission due to SASI and convection, the relation of the waveforms to the physical parameters of the accretion flow onto the proto-neutron star (PNS) is less obvious, but a closer analysis of the waveforms in the time-frequency domain still reveals systematic patterns. For example, the high-frequency component of the signal has

been shown to originate from the deceleration of downflows at the boundary of the gain region [6], which stochastically excites an $\ell = 2$ surface g -mode. The typical frequency f_g of the GW signal traces that of the g -mode, and can be related [7] to the PNS mass M and radius R , to the electron antineutrino mean energy $\langle E_{\bar{\nu}_e} \rangle$, and to the nucleon mass m_n as

$$f_g \approx \frac{1}{2\pi} \frac{GM}{R^2} \sqrt{1.1 \frac{m_n}{\langle E_{\bar{\nu}_e} \rangle}} \left(1 - \frac{GM}{Rc^2} \right). \quad (1)$$

In 3D [9], this relation still holds, although the excitation of surface oscillations from the gain region is less efficient, and the excitation of by *PNS convection* plays a relatively greater role.

4 Estimate of GW Amplitudes

The relation of the GW amplitudes to the violence of convection and SASI has only been studied qualitatively so far. Here we sketch a crude physical model that roughly explains qualitative dependencies seen in simulations.

Using dimensional analysis, the GW amplitude from oscillatory motions in the PNS surface layer can be related to the potential energy E_g stored in the $\ell = 2$ surface g -mode [9]:

$$A = hD \sim \frac{G}{c^4} \int \delta\rho_2 \frac{GM}{r} dV \sim \frac{GE_g}{c^4}. \quad (2)$$

One can estimate E_g by relating the g -mode energy flux to the convective luminosity in the adjacent region [11] and assuming that excitation is coherent over one convective overturn timescale, which results in $E_g \sim \alpha Ma E_{\text{conv}}$ in terms of the kinetic energy in convection E_{conv} , the convective Mach number Ma , and an additional factor $\alpha \lesssim 1$ quantifying the overlap of the forcing with the spatial dependence and frequency of the $\ell = 2$ mode visible in GWs.

For excitation by convection in the gain region, we can estimate the maximum amplitude A_{max} around shock revival by expressing E_{conv} in terms of the mass M_{gain} of the gain region and the typical convective velocity. By using $c_s = (GM/3r_{\text{sh}})^{1/2}$ [12], (where r_{sh} is the shock radius) and relating the mass in the gain region to the explosion energy E_{expl} via the nucleon recombination energy ϵ_{rec} [13], we obtain

$$A_{\text{max}} \sim \frac{G}{c^4} \alpha \frac{E_{\text{expl}}}{\epsilon_{\text{rec}}} \frac{GM}{3r_{\text{sh}}} Ma^3 \sim 9 \text{ cm} \times \alpha \times \left(\frac{E_{\text{expl}}}{10^{51} \text{ erg}} \right) \quad (3)$$

for typical values of $Ma^2 = 0.3$ [12] and $r_{\text{sh}} \approx 200 \text{ km}$ at shock revival. This estimate is close to the GW amplitudes from the 3D models of [9] for $\alpha \lesssim 1$ and qualitatively reproduces the trend towards stronger GW signals from more energetic explosions in 2D models [7].

For the excitation of oscillation modes by PNS convection, we can estimate E_{conv} by equating the convective luminosity and the diffusive core neutrino luminosity L_{core} . This leads to $E_{\text{conv}} \sim L_{\text{core}}^{2/3} \Delta R^{2/3} \Delta M^{1/3}$ in terms of the mass $\Delta M \approx 1M_{\odot}$ and width $\Delta R \approx 10 \text{ km}$ of the PNS convection zone during the pre-explosion phase. With typical values of $L_{\text{core}} = 10^{53} \text{ erg s}^{-1}$ and $Ma = 0.05$, we obtain $A \sim 1 \text{ cm} \times \alpha$, again roughly in line with [9]. Since L_{core} , ΔR , and ΔM do not vary strongly across progenitors, one expects smaller variations than for g -mode excitation by convection in the gain region.

References

- [1] H.-T. Janka, ARNPS **62**, 407 (2012).
- [2] T. Foglizzo *et al.*, PASA **32**, e009 (2015).
- [3] S. E. Gossan *et al.*, PRD **93**, 042002 (2016).
- [4] H. Dimmelmeier, C. D. Ott, H.-T. Janka, A. Marek, and E. Müller, PRL **98**, 251101:1 (2007).
- [5] E. Abdikamalov *et al.*, ApJ **808**, 70 (2015).
- [6] J. W. Murphy, C. D. Ott, and A. Burrows, ApJ **707**, 1173 (2009).
- [7] B. Müller, H.-T. Janka, and A. Marek, ApJ **766**, 43 (2013).
- [8] E. Müller, H.-T. Janka, and A. Wongwathanarat, A&A **537**, A63 (2012).
- [9] H. Andresen, B. Müller, E. Müller, and H.-T. Janka, ArXiv e-prints (2016), 1607.05199.
- [10] T. Kuroda, K. Kotake, and T. Takiwaki, ApJL **829**, L14 (2016).
- [11] P. Goldreich and P. Kumar, ApJ **363**, 694 (1990).
- [12] B. Müller and H.-T. Janka, MNRAS **448**, 2141 (2015).
- [13] L. Scheck, K. Kifonidis, H.-T. Janka, and E. Müller, A&A **457**, 963 (2006).

DPG Methodology for Wave Propagation in Optical Fibers

Sriram Nagaraj^{1,*}, Leszek Demkowicz², Jacob Grosek³

¹Institute for Computational Engineering and Sciences, UT Austin, Austin TX, USA

²Institute for Computational Engineering and Sciences, UT Austin, Austin TX, USA

³Airforce

*Email: sriram@ices.utexas.edu

Abstract

The DPG methodology with its attractive properties of uniform mesh independent stability, automatic adaptivity and parallelizability is studied in the context of wave propagation in optical fibers. In this application, we are interested in pulse propagation and laser amplification. Both these tasks present mathematical and numerical challenges: stability of the variational formulation, interaction with heating effects and transverse mode instability. We show how the DPG methodology offers an effective solution strategy to address these issues.

Keywords: Discontinuous Petrov-Galerkin method, electromagnetic waves, fiber optics

Introduction

Accurate modeling of wave propagation in nonlinear media is an important task in a variety of application areas including nonlinear optics, nonlinear elastic wave propagation and femtosecond laser spectroscopy. Our interest will be in modeling electromagnetic pulse propagation and laser amplification in optical fibers. These two applications are governed by the same set of Maxwell equations, but have different modelling ansatzes that account for different optical phenomena of interest. We briefly highlight both models.

Pulse Propagation via Schrödinger Equation

Nonlinear, dispersive Maxwell equations in the context of optical fibers have been studied extensively in the past [1]. Early approaches to the analysis of the dispersive, intensity-dependent nonlinearities in the model were based on several simplifying approximations. These approximations include: a slowly varying pulse envelope, the optical field being quasi-monochromatic and maintaining a specific polarization along the fiber length, and the nonlinear terms being a perturbation of the purely linear case. With these assumptions, the full Maxwell equations

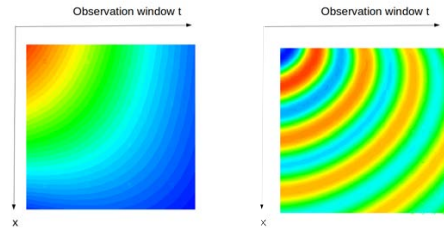


Figure 1: Plots of two different solutions

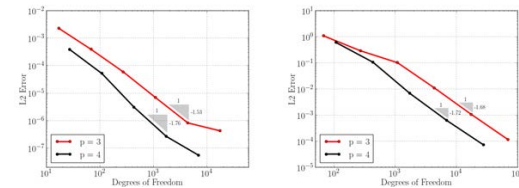


Figure 2: Convergence rate curves

were reduced to a nonlinear Schrödinger (NLS) type equation in the variable A , a complexified amplitude [1]:

$$i \frac{\partial A}{\partial z} - \frac{\beta}{2} \frac{\partial^2 A}{\partial T^2} + \gamma |A|^2 A = 0, \quad (1)$$

where T is an observation window (time), z is the propagation direction, and β, γ are material constants. Applying the DPG method to the above equation is non-trivial: as shown in [2], any reasonable first order reformulation of (1) results in an L^2 unstable variational formulation. This is overcome by developing a generalized boundary operator and proving L^2 stability of the resulting 2nd order variational formulation. In addition, non-standard energy spaces call for an operator-specific approximability theorem to guarantee convergence with optimal rates. Our theoretical results in this analysis are corroborated by numerical studies (shown in figures 1 and 2).

Transverse Mode Instability

Consider the coupled set of Maxwell equations with no free charges:

$$\begin{aligned}\nabla \times \mathbb{E} &= -\frac{\partial \mathbb{B}}{\partial t}, \\ \nabla \times \mathbb{H} &= \frac{\partial \mathbb{D}}{\partial t} + \mathbb{J}, \\ \nabla \cdot \mathbb{E} &= 0, \\ \nabla \cdot \mathbb{H} &= 0,\end{aligned}$$

As usual, upon eliminating the magnetic field \mathbb{H} , we get the following *curl – curl* equation for the electric field \mathbb{E} :

$$\nabla \times \nabla \times \mathbb{E} = \frac{-1}{c^2} \frac{\partial^2}{\partial t^2} \mathbb{E} - \mu_0 \frac{\partial^2}{\partial t^2} \mathbb{P}.$$

We assume the following model for the polarization vector $\mathbb{P}(\mathbb{E})$:

$$\mathbb{P}(\mathbb{E}) = \mathbb{P}_{\text{background}}(\mathbb{E}) + \mathbb{P}_{\text{gain}}(\mathbb{E}) + \mathbb{P}_{\text{thermal}}(\mathbb{E}).$$

The background polarization can then be written as:

$$\mathbb{P}_{\text{background}}(\mathbb{E}) = \epsilon_0 (\mathbf{n}_{\text{eff}}^2 - I) \mathbb{E},$$

where ϵ_0 is the free space dielectric constant, \mathbf{n}_{eff} is the effective refractive index tensor, and I is the identity tensor. The gain polarization is:

$$\mathbb{P}_{\text{gain}}(\mathbb{E}) = \frac{-i\epsilon_0 \mathbf{n}_{\text{eff}} c}{\omega_s} g \mathbb{E}.$$

where ω_s is the source frequency, c is the speed of light, and g is the population gain function. Finally, the thermal polarization is given as:

$$\mathbb{P}_{\text{thermal}}(\mathbb{E}) = 2\epsilon_0 (\delta n) \mathbf{n}_{\text{eff}} \mathbb{E}.$$

Here, we define the thermally perturbed refractive index $\delta n := n_\Theta \theta(x, y, z, t)$, where n_Θ is the experimentally calculated thermo-optic coefficient for silica (a uniform material constant) and the variable θ satisfies the following heat equation:

$$\begin{aligned}\frac{\partial \theta}{\partial t} &= \frac{\kappa_{\text{thermal}}}{\rho_0 C_{\text{fiber}}} \Delta \theta + Q(\mathbb{E}), \\ \theta(|\mathbf{r}| = r_0) &= 0.\end{aligned}$$

Here, the Dirichlet condition $\theta(|\mathbf{r}| = r_0) = 0$ is applied on the radial boundary $\sqrt{x^2 + y^2} = |\mathbf{r}| = r_0$ of the fiber. Also, $C_{\text{fiber}} = C_{\text{fiber}}(x, y, z)$ is the specific heat capacity of the material, ρ_0 is the background material density and $\kappa_{\text{thermal}} =$

$\kappa_{\text{thermal}}(x, y, z)$ is the thermal conductivity of the material. The heat source $Q(x, y, z, t)$ is a function that depends nonlinearly on \mathbb{E} as $\nabla(|\mathbb{E}|^2) \cdot \mathbf{n}_z$ and \mathbf{n}_z is the unit normal in the $+z$ direction.

Our final electromagnetic equation is thus:

$$\nabla \times \nabla \times \mathbb{E} = \left(\frac{\omega_s^2}{c^2} \mathbf{n}_{\text{eff}}^2 + \frac{2}{c} \frac{\partial g}{\partial t} \mathbf{n}_{\text{eff}} - i \frac{\omega_s}{c} g \mathbf{n}_{\text{eff}} + 2(\delta n) \frac{\omega_s^2}{c^2} \mathbf{n}_{\text{eff}} \right) \mathbb{E}.$$

Given that the electromagnetic phenomenon happens at a much smaller time scale than the heating effects, we assume a time-harmonic relation for the electric field:

$$\mathbb{E}(x, y, z, t) = \mathbb{E}_0(x, y, z) \cdot e^{-\omega_s t},$$

where the beam propagates with frequency ω_s , the signal (seed) frequency. Our solution scheme is as follows. We have a coupled system with three different time-scales: The time-harmonic Maxwell (time scale in nanoseconds), the time-independent population gain (time scale in microseconds) and the time dependent heat equation (time scale in milliseconds).

The primal DPG method is used with an implicit Euler time-stepping scheme for the heat equation (with \mathbb{E} dependent load) under radial Dirichlet conditions. The population gain is an algebraic update. The time harmonic Maxwell system is then solved with the ultraweak DPG formulation (effective in high-frequency wave propagation problems) with polarization values obtained from the previous heat equation solution. We iterate the process updating the relevant quantities until convergence. The time step is chosen corresponding to the largest time scale of the coupled system, i.e., the heat equation, and is updated with h/hp adaptive refinements. The use of DPG adaptivity for the heat/Maxwell systems along with the guaranteed discrete stability of the ultraweak/primal formulations is critical for a numerically stable and tractable method which allows us to effectively simulate the TMI phenomenon.

References

- [1] G.P. Agrawal, *Nonlinear Fiber Optics, Fifth Edition*, Academic Press, 2012
- [2] L. Demkowicz, J. Gopalakrishnan, S. Nagaraj and P. Sepulveda, *A spacetime DPG method for the Schrodinger equation*, submitted to SIAM J. Num. Anal. (also arXiv 1610.04678)

Two scale Hardy space infinite elements

Lothar Nannen^{1,*}, Martin Halla²

¹Institute for Analysis and Scientific Computing, TU Wien, Austria

²Institute for Analysis and Scientific Computing, TU Wien, Austria

*Email: lothar.nannen@tuwien.ac.at

Abstract

This paper deals with the efficient numerical simulation of time-harmonic scattering and resonance problems in open systems, which exhibit wavenumbers on different scales. One example are waves for which the geometry causes a dispersion effect, i.e. waves can propagate with different speed levels. In order to overcome the performance issues of standard non-modal methods, we present a two scale variant of the Hardy space method. It allows to optimize the method to two different wavenumbers on different scales.

Keywords: resonance problems, Hardy space infinite element method, Wood's anomaly

Introduction

For given frequency $\omega > 0$ let u be a radiating solution to the scalar Helmholtz equation

$$-\Delta u - \omega^2 u = 0 \quad (1)$$

on a cylindrical waveguide $\Omega := \mathbb{R}_+ \times \Upsilon$ with a bounded cross-section $\Upsilon \subset \mathbb{R}^d$. Then u is a superposition of the waveguide modes

$$u_n(x, y) := \exp(i\kappa_n(\omega)x)\varphi_n(y), (x, y) \in \Omega, \quad (2)$$

with wavenumbers $\kappa_n(\omega) := \sqrt{\omega^2 - \lambda_n}$. (λ_n, φ_n) are the eigenpairs of $-\Delta$ on Υ . In the vicinity of a so-called cut-off frequency $\omega_{n_0} := \sqrt{\lambda_{n_0}}$ (also referred to as Wood's anomaly), there exist wavenumbers on highly different scales, i.e. $|\kappa_{n_0}(\omega)| \ll |\kappa_n(\omega)|$, $n \neq n_0$. This leads to performance issues for non-modal methods like the perfectly matched layer or the Hardy space infinite element method, since they are typically adjusted to one specific wavenumber.

PML convergence results

For a linear complex scaling $\hat{x}(x) := \sigma x$ with $\sigma \in \mathbb{C}$ and $\Im(\sigma) > 0$ in longitudinal direction of the waveguide, the complex scaled functions $\hat{u}_n(x, y) := u_n(\hat{x}(x), y)$ decay exponentially for $\omega \neq \sqrt{\lambda_n}$. Therefore, the unbounded waveguide is typically truncated to a bounded layer

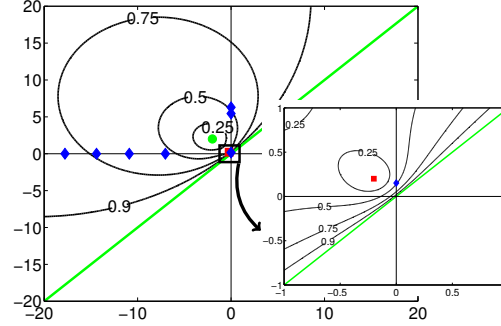


Figure 1: Level sets of g_{s_0, s_1} for $s_0 = -2 + 2i$ (green dot) and $s_1 = s_0/10$ (red square) with corresponding $\Gamma := \{s : g_{s_0, s_1}(s) = 1\}$ (green line). The blue diamonds are the poles $i\kappa_n(\omega)$ of U_n for $\omega = 6.285$ and $\lambda_n := (n\pi)^2$

of thickness L leading to a truncation error of the form $|\exp(i\sigma\kappa_n(\omega)L)|$ (see [1, 2]). Nevertheless, in the vicinity of cut-off frequencies this exponential convergence degenerates due to a very small wavenumber κ_{n_0} . In [3] a hybrid perfectly matched layer/modal based method was proposed for these cases. However, this hybrid method cannot be applied easily to resonance problems, where ω is the sought resonance.

HSM convergence results

In [2, 4] the Hardy space method is presented and analyzed for scattering and resonance problems in scalar waveguides. The method relies on a Laplace transform in longitudinal direction leading to meromorphic functions

$$U_n(s, y) := \mathcal{L}\{u_n(\cdot, y)\}(s) = \frac{\varphi_n(y)}{s - i\kappa_n(\omega)}, s \in \mathbb{C}. \quad (3)$$

See Fig. 1 for a location of the poles $i\kappa_n$ for a $\omega > 0$ in the vicinity of a cut-off frequency.

There are two complex parameters $s_0, s_1 \in \mathbb{C}$ in the two scale Hardy space method. In some sense, the method can be related to a complex scaling method where two linear complex scalings with $\sigma_j = 1/s_j$ are used simultaneously. The discretization error of the method with re-

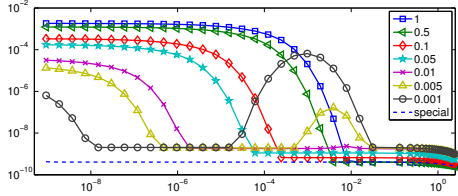


Figure 2: Discretization error with respect to $\delta_\omega > 0$ corresponding to frequencies $\omega = \sqrt{\lambda_2} + \delta_\omega$ for $N = 60$, $s_0 = -2 + 2i$ and $s_1 = cs_0$ with varying constants c .

spect to the number of unknowns N in longitudinal direction is bounded by

$$g_{s_0, s_1}(i\kappa_n(\omega))^N, \quad n \in \mathbb{N}, \quad (4)$$

with $g_{s_0, s_1}(s) := \left| \frac{s-s_0}{s+s_0} \frac{s-s_1}{s+s_1} \right|$, $s \in \mathbb{C}$.

If $\omega > 0$ with $\omega \neq \sqrt{\lambda_n}$, $\Re(s_0) < 0$, $\Im(s_0) > 0$ and $s_1 \in s_0\mathbb{R}$, than $g_{s_0, s_1}(i\kappa_n(\omega)) < 1$ for all $n \in \mathbb{N}$ and the Hardy space method converges exponentially up to an arbitrary small threshold. Fig. 1 indicates, that a scaling of the parameters s_0 and s_1 with respect to the wavenumbers improves the convergence rate considerably.

Numerical experiments

For the first numerical test we use a given reference solution consisting of 7 waveguide modes $U := \sum_{n=0}^6 c_n U_n$ with some $c_n \in \mathbb{C}$. Fig. 2 shows, that the optimal parameter choice for s_1 is related to the magnitude of the wavenumber $\kappa_2(\omega) \approx \sqrt{\lambda_2}\sqrt{\delta_\omega}$ for small δ_ω . Note, that there exists for scattering problems an extremely efficient version of the Hardy space method (labeled in Fig. 2 with 'special') using an implicit mode matching for the critical waveguide mode. Unfortunately, this version cannot be used for resonance problems.

But the two scale HSM can be used for resonance problems and leads to linear Matrix eigenvalue problems. So for the second numerical test we solve two resonance problems with resonances near $2\pi = \sqrt{\lambda_2}$. In Figures 3 and 4 the absolute value of a resonance functions for two slightly different domains are given. On the curved left part, on top and at the bottom of the domain we have used homogeneous Neumann boundary conditions. On the right the two scale HSM is used with fixed s_0 and dif-

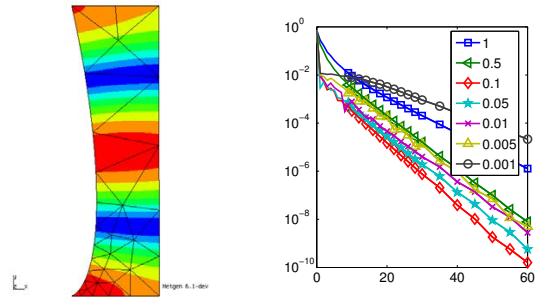


Figure 3: Resonance function (left) and corresponding discretization error (right) for a resonance ω with $|\omega - 2\pi| \approx 10^{-2}$ w.r.t. to N for $s_0 = -2 + 2i$ and $s_1 = cs_0$ with varying constants c .

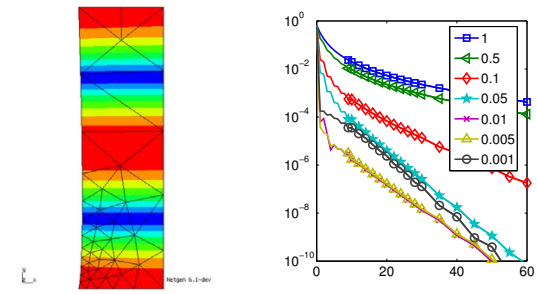


Figure 4: As in Fig. 3 with $|\omega - 2\pi| \approx 10^{-4}$

ferent s_1 and number of longitudinal unknowns N . The optimal values of s_1 correspond almost exactly to the values indicated by Fig. 2 for the scattering problem. With decreasing distance of ω to $\sqrt{\lambda_2}$ the HSM with smaller values for c becomes more and more efficient and outperforms the standard HSM and a standard linear PML substantially.

References

- [1] É. Bécache, A.-S. Bonnet-BenDhia, and G. Legendre, Perfectly matched layers for the convected Helmholtz equation, *SIAM Journal on Numerical Analysis*, **42** (2004), pp. 409–433.
- [2] T. Hohage and L. Nannen, Convergence of infinite element methods for scalar waveguide problems, *BIT Numerical Mathematics*, **55** (2015), pp. 215–254.
- [3] A.-S. Bonnet-BenDhia, C. Chambeyron, and G. Legendre, On the use of perfectly matched layers in the presence of long or backward propagating guided elastic waves, *Wave Motion*, **51** (2014), pp. 266 – 283.
- [4] M. Halla and L. Nannen, Two scale Hardy space infinite elements for scalar waveguide problems, *ASC Preprint, TU Wien*, **17** (2016).

Existence and Computation of a Weak Solution to the Hasegawa-Mima Equation in Periodic Sobolev Spaces

Nabil Nassif^{1,*}, Hagop Karakazian²

¹Department of Mathematics, American University of Beirut, Beirut, Lebanon

²Department of Mathematics, American University of Beirut, Beirut, Lebanon

*Email: nn12@aub.edu.lb

Abstract

In this paper, we first represent the non-linear Hasegawa-Mima Partial Differential Equations (PDE's) as a coupled two linear Elliptic-Hyperbolic system of PDE's. We then apply the Petrov-Galerkin method to obtain a sequence of fixed-point approximate solutions that converge weakly to a solution of the Hasegawa-Mima problem that is simulated using a Finite Element method.

Keywords: Plasma Confinement, Drift Waves, Hasegawa-Mima, Periodic Sobolev Spaces, Petrov-Galerkin approximations

1 Introduction

Magnetic plasma confinement is one of the most promising ways in future energy production. To understand the phenomena related to energy production through plasma confinement, several mathematical models can be found in literature (see [1–3]), of which the simplest and powerful 2D turbulent system model is the Hasegawa-Mima equation, which describes the time evolution of drift waves. Although it was originally derived by Akira Hasegawa and Kunioki Mima in [2], it can be extended [4, 5] and put as

$$-\Delta u_t + u_t = \{u, \Delta u\} + ku_y \quad (1)$$

where $\{u, v\} = u_x v_y - u_y v_x$ is the Poisson bracket, $u(x, y, t)$ describes the electrostatic fluctuations, $k = \partial_x \ln \frac{n_0}{\omega_{ci}}$ is a constant depending on the background particle density n_0 and the ion cyclotron frequency ω_{ci} , which in turn depends on the initial magnetic field

2 The Formulation

Let a square domain $\Omega = (0, L)^2$ with boundary $\Gamma = \partial\Omega$, a function $u_0 \in H^2(\Omega)$, and a temporal bound $T > 0$ be given. We consider the following Hasegawa-Mima problem: seek $u : \bar{\Omega} \times [0, T] \rightarrow \mathbb{R}^2$

such that

$$\begin{cases} -\Delta u_t + u_t = \{u, \Delta u\} + ku_y & \text{on } \Omega \times (0, T) \\ \text{PBCs on } u \text{ and } \vec{\nu} \cdot \nabla u & \text{on } \Gamma \times (0, T) \\ u(x, y, 0) = u_0(x, y) & \text{on } \bar{\Omega} \end{cases} \quad (2)$$

where $\vec{\nu}$ is a unit outward pointing normal vector to Γ and PBC stands for periodic boundary conditions. Since handling the non-linearity of the Poisson bracket is both theoretically and computationally expensive, we formulate (2) as a coupled system of linear equations as follows. Let $w = -\Delta u + u$, then the PDE of (2) can be put in the form of the following Elliptic-Hyperbolic coupled system problem: Seek $\{u, w\} : \bar{\Omega} \times [0, T] \rightarrow \mathbb{R}^2$ such that:

$$\begin{cases} -\Delta u + u = w & \text{on } \Omega \times (0, T) \\ w_t + \vec{V}(u) \cdot \nabla w = ku_y & \text{on } \Omega \times (0, T) \\ \text{PBCs on } u \text{ and } \vec{\nu} \cdot \nabla u & \text{on } \Gamma \times (0, T) \\ u(x, y, 0) = u_0(x, y) & \text{on } \bar{\Omega} \end{cases} \quad (3)$$

where $\vec{V}(u) = \langle -u_y, u_x \rangle$ is a divergence-free vector field. We begin with an existence result for the first PDE in (3) on Periodic Sobolev Spaces $H_P^1(\Omega)$, using the Petrov-Galerkin method, after which we formulate the system (3) as a sequence of fixed-point problems and obtain approximate solutions using the Hilbert basis $\{\phi_i\}_{i=1}^\infty$ of $H_P^1(\Omega)$ of eigenvectors of the (periodic) Laplacian operator with increasing eigenvalues $\lambda_i > 0$ and $E_N = \text{span } \{\phi_1, \phi_2, \dots, \phi_N\}$ the N -dimensional subspace of $H_P^1(\Omega)$.

3 Results

- We construct a sequence $\{u_N, w_N\}$ that converges weakly to a weak solution $\{u, w\}$ of (3).
- Based on this approach, we implement a numerical simulation based on Finite-element space semi-discretization of (3) followed by a semi-implicit Crank-Nicolson semi-discretization.

References

- [1] in *Nuclear Fusion*, vol. 39, num. 12, 1999, pp. 2175–2249.
- [2] A. Hasegawa, and K. Mima, *Physics of Fluids*, vol. 21, num. 1, 1978, pp. 87-92, American Institute of Physics.
- [3] A. Hasegawa, and M. Wakatani, *Phys. Rev. Lett.*, vol. 50, issue 9, 1983, pp. 682-686, American Physical Society.
- [4] Shivamoggi, B.K., Charney-Hasegawa-Mima Equation *Physics Letters A*, vol. 138, issue 1-2, 1989, pp. 37-42, Elsevier Science Publishers B.V.
- [5] F. A. Hariri, M.S. Thesis, American University of Beirut, 2010.
- [6] H. Karakazian M.S. Thesis, American University of Beirut, 2016.

A-stable high-order implicit time schemes

Hélène Barucq¹, Marc Durufle², Mamadou N'Diaye^{1,*}

¹Magique-3D INRIA Bordeaux Sud-Ouest, LMA-UPPA, Pau, France

²Magique-3D INRIA Bordeaux Sud-Ouest, IMB, Bordeaux, France

*Email: mamadou.ndiaye@inria.fr

Abstract

We address the problem of constructing high-order implicit schemes for wave equations. We considered two classes of one-step schemes adapted to linear Ordinary Differential Equations, one based upon Padé approximant of exponential, other one requiring the inversion of a unique linear system such as SDIRK (Singly Diagonally Implicit Runge Kutta) schemes.

Keywords: forward problem, implicit time integration, Runge-Kutta schemes, Padé schemes

Construction of diagonal Padé schemes

Let us consider the following linear ODE:

$$y'(t) = Ay(t) + F(t), \quad t \in (0, T] \quad (1)$$

where A is a given matrix, coming from spatial discretization, and F the term source. After each step $\Delta t = t_{n+1} - t_n$ the analytical solution to (1) reads

$$y(t_{n+1}) = e^{\Delta t A} y(t_n) + \int_0^{\Delta t} e^{-uA} F(n\Delta t + u) du \quad (2)$$

The diagonal Padé approximant [1] of the exponential function e^z is a rational function

$$R_m(z) = \frac{P_m(z)}{Q_m(z)}, \quad z \in \mathbb{C},$$

where $P_m(z) = \sum_{i=0}^m \frac{m! (2m-i)!}{(2m)! i! (m-i)!} (z)^i$ and $Q_m(z) = P_m(-z)$. R_m is the stability function and the stability region is defined as

$$S = \{z \in \mathbb{C} \text{ such that } |R_m(z)| \leq 1\}.$$

R_m satisfies the A-stability condition which requires that $S \supset \mathbb{C}^- = \{z \in \mathbb{C}, \operatorname{Re}(z) \leq 0\}$ [2].

Herein, we assume that $Q_m(\Delta t A)^{-1}$ is well defined. Solution (2) can then be written as

$$Q_m(\Delta t A)y(t_{n+1}) = P_m(\Delta t A)y(t_n) + \phi, \quad (3)$$

where

$$\phi = P_m(\Delta t A) \int_0^{\Delta t} e^{-uA} F(n\Delta t + u) du + O(\Delta t^{2m+1}). \quad (4)$$

By using the Taylor expansion of $y(t_n)$ and $y(t_{n+1})$ around $t_n + \frac{\Delta t}{2}$ in (3) we obtain the approximation ϕ_n of ϕ :

$$\phi_n = \sum_{r=1}^m A^{r-1} \Delta t^r \sum_{i=0}^{2m-r} \omega_i^r F(t_n + \Delta t c_i)$$

where c_i are quadrature points and ω_i^r are the weights. We then end up with the following numerical scheme:

$$Q_m(\Delta t A)y_{n+1} = P_m(\Delta t A)y_n + \phi_n. \quad (5)$$

The obtained scheme is the diagonal Padé scheme of order $2m$. It is implicit and A-stable. Its stability function is the same as that of the Gauss-Runge-Kutta (Gauss RK) schemes [1]. However, Gauss RK schemes which are used also to solve non-linear ODE, are too expensive in practice. The Padé schemes presented here can be seen as a simplification of Gauss RK schemes in the case of linear ODE. In fact with these diagonal Padé schemes we need to solve $m/2$ complex linear system if m is even, $(m-1)/2$ complex and one real linear system if m is odd.

Numerical dispersion and dissipation

To study the dispersion and dissipation properties of the scheme, we consider the following linear test equation

$$y'(t) = i\lambda y(t), \quad y(t_0) = y_0 \text{ and } \lambda \in \mathbb{R},$$

which analytical solution is approximated by

$$y(t_{n+1}) = e^{iz} y(t_n) \approx R_m(iz) y_n = y_{n+1}.$$

The dispersion and dissipation errors can be measured by considering the ratio between e^{iz} and $R_m(iz)$. We then define the dissipation error as $\psi(z) = |R_m(iz)| - 1$ and the dispersion error as $\Phi(z) = z - \arg[R_m(iz)]$. Since $|P_m(iz)| = |Q_m(iz)|$, the diagonal Padé schemes are not dissipative: $\psi(z) = 0$. Furthermore, we show in Figure 1 the relative dispersion errors, for $m = 1, \dots, 5$, which is much smaller with high-order schemes. We choose z/m in the x -axis because m represents the computational complexity of the schemes.

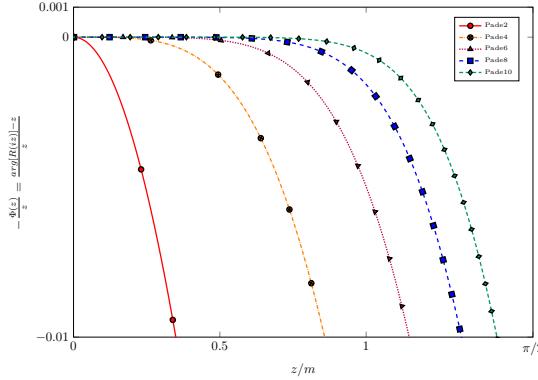


Figure 1: Relative dispersion error

Efficiency in terms of computational time

We consider the acoustic wave equation

$$\begin{cases} \rho \partial_t u - \operatorname{div} v = 0, & \forall (x, t) \in \Omega \times \mathbb{R}^+ \\ \mu^{-1} \partial_t v - \nabla u = 0, & \forall (x, t) \in \Omega \times \mathbb{R}^+ \\ u = f_D, & x \in \Gamma_D \\ \mu \partial_n u = f_N, & x \in \Gamma_N \end{cases} \quad (6)$$

Equation (6) is solved in 1-D with $\rho = \mu = 1$ in $\Omega = [0, 500]$ using the finite element solver Montjoie. We choose $[0, 1000]$ for the time interval. We used Dirichlet condition on the left

$$u(x = 0, t) = e^{-i\omega t} \exp \left(-\frac{1}{2} \left(\frac{t - T}{\tau} \right)^2 \right).$$

where

$$\omega = 2\pi, \quad \tau = \frac{20}{2\sqrt{2 \log 2}}, \quad T = 100$$

and a homogeneous Neumann condition is set on the right extremity. The analytical solution reads

$$u(x, t) = e^{i\omega(x-t)} \exp \left(-\frac{1}{2} \left(\frac{t - T - x}{\tau} \right)^2 \right).$$

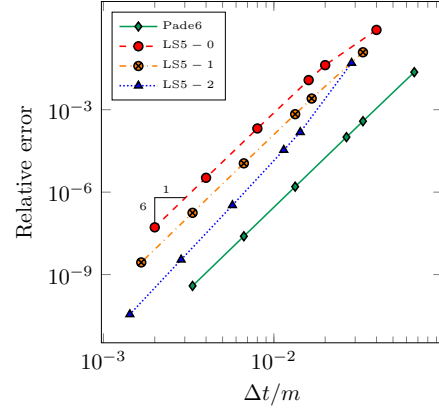
Since Padé schemes can be used only for linear ODE, their comparison with classical SDIRK [1] which solve also non-linear ODE may not be fair. So, to get a comparable scheme, we consider the case:

$$R_s^l(z) = \frac{N(z)}{(1 + \gamma z)^{s+l}}, \quad s \in \mathbb{N}, l \in \mathbb{N}. \quad (7)$$

The numerator $N(z)$ and γ are computed such that R_s^l satisfies the A-stability condition and

represents an approximation of order $s+1$ to the exponential function. The obtained schemes are new and we called them Linear-SDIRK schemes ($LSs-l$) since they share the same property as SDIRK.

In Figure 2 we show the convergence curves of Linear-SDIRK and Padé schemes of order 6. We choose $\Delta t/m$ to take into account the complexity of each scheme ($m = s + l$ for $LSs-l$).

Figure 2: Convergence curves at $t = 200$

In Table 1, we present the computational times needed for Linear-SDIRK and Padé schemes to reach 1% of relative L^2 error computed at $t = 1000$ between the numerical solution and the analytical solution. The results show that the Padé schemes are more efficient than the Linear-SDIRK schemes. The obtained results in 1-D

Padé	Pade4	Pade6	Pade8
Nb time step	33333	8360	3875
Times	1mn36	37s	24s
Linear-SDIRK	LS3-1	LS5-2	LS7-3
Nb time step	25960	7355	3700
Times	1mn48	53s	38s

Table 1: Computational time after imposing 1% of relative errors at $t = 1000$.

and 2-D confirmed the efficiency of Padé schemes. The next step is to combine Padé schemes with optimized high-order explicit schemes we are developing to construct locally implicit schemes.

References

- [1] J. C. Butcher, “Numerical Methods for ODE 2nd edition”, *John Wiley*, 2008
- [2] E. Hairer and G. Wanner, “Solving ODE II”, *Springer*, 2010

Electromagnetic Wave Diffraction of Perfect Electric Conducting Wedges with Arbitrary Linear Polarization

Matthew Nethercote^{*}, **Raphael Assier**¹, **David Abrahams**²

¹School of Mathematics, University of Manchester, Oxford Road, Manchester, UK

²INI, University of Cambridge, Clarkson Road, Cambridge, UK

^{*}Email: matthew.nethercote@manchester.ac.uk

Abstract

This paper focuses on finding the electromagnetic (EM) field and the time-averaged Poynting vector produced after a time harmonic EM plane wave of an arbitrary fixed (linear) polarization is incident on an infinite perfect electric conducting (PEC) wedge. The aim is to find out how the polarization of this incident EM wave impacts the solution to diffraction by perfectly conducting wedges.

We use the z invariance of the scatterer and the PEC boundary conditions to rewrite the EM field governed by Maxwell's equations in terms of two uncoupled scalar potentials or Debye potentials. These potentials will be functions of an arbitrary polarization angle and respectively solve the acoustic (or scalar) wedge problem with Dirichlet or Neumann boundary conditions.

Keywords: Electromagnetic Wave Diffraction, PEC Wedge, Arbitrary Linear Polarization, Debye Potential, Sommerfeld-Malyuzhinets Technique

1 Introduction

The focus of this paper is the diffraction of a time harmonic EM plane wave of any polarization by a PEC infinite wedge. To solve this, we follow techniques in [5], [4] and [9] to rewrite the EM field for Maxwell's equations in terms of two uncoupled scalar potentials called the Debye potentials. These potentials will both solve the scalar infinite wedge problem with perfect boundary conditions, i.e. Dirichlet or Neumann boundary conditions. We find these scalar solutions by the Sommerfeld-Malyuzhinets technique outlined in [1]. We check the scalar wedge solutions by comparing with results and plots obtained in [1] and [3]. The most comparable paper is [6] which studies an inhomogeneous (or evanescent) EM plane wave of arbitrary polarization diffracted by a PEC wedge at skew incidence expanding on a simpler problem in [7].

Introduced in 1909 by P. Debye in [2], Debye potentials have mostly been used for problems involving conical or spherical domains, for example [10] and [8]. These same methods can also be applied to wedge problems.

2 Formulation

Let the region exterior to the wedge be $-\pi < -\theta_w < \theta < \theta_w < \pi$, where $\theta = \pm\theta_w$ are the wedge faces. The incident wave is a time-harmonic EM plane wave with time factor $e^{-i\omega t}$, wavenumber k , amplitude \mathcal{A} , polarization angle α and incident angle $\theta = \theta_I$. The governing equations are Maxwell's equations. We assume that the domain is linear, isotropic, homogeneous and source free so that the electric permittivity ϵ and the magnetic permeability μ can be assumed to be constant scalars. The electric and magnetic phasors, \underline{E} and \underline{H} , are defined from the electric and magnetic intensity, $\hat{\underline{E}}$ and $\hat{\underline{H}}$, by,

$$\hat{\underline{E}} = \operatorname{Re} \left\{ \frac{\underline{E} e^{-i\omega t}}{\sqrt{\epsilon}} \right\}, \quad \hat{\underline{H}} = \operatorname{Re} \left\{ \frac{\underline{H} e^{-i\omega t}}{\sqrt{\mu}} \right\}. \quad (1)$$

Noting that the wave speed is $c = \frac{\omega}{k} = \frac{1}{\sqrt{\epsilon\mu}}$, Maxwell's equations can be rewritten in terms of the two phasors,

$$\begin{aligned} \nabla \times \underline{H} + ik\underline{E} &= 0, & \nabla \cdot \underline{E} &= 0, \\ \nabla \times \underline{E} - ik\underline{H} &= 0, & \nabla \cdot \underline{H} &= 0. \end{aligned} \quad (2)$$

The PEC boundary conditions are,

$$\underline{E} \times \underline{n}|_{\theta=\pm\theta_w} = 0, \quad (3)$$

$$\underline{H} \cdot \underline{n}|_{\theta=\pm\theta_w} = 0, \quad (4)$$

where \underline{n} is the unit normal to the wedge faces,

$$\underline{n}|_{\theta=\pm\theta_w} = \pm \underline{e}_\theta. \quad (5)$$

These boundary conditions imply that the electric field has no tangential component on the wedge faces and that both the magnetic field and the Poynting vector,

$$\hat{\underline{S}} = \hat{\underline{E}} \times \hat{\underline{H}}, \quad (6)$$

have no normal component on the wedge faces. We also define the time-averaged Poynting vector in terms of the phasors as,

$$\underline{S} = \frac{1}{2} c \Re \{ \underline{E} \times \underline{H}^* \}. \quad (7)$$

3 The Electromagnetic Field

The EM field satisfying (2)-(4) can be written in terms of an electric and a magnetic vector potential which are both independent of z and fixed in the z direction requiring us to construct two scalar potentials. These two scalar potentials are proportional to the total field solutions to the acoustic wedge problem with Dirichlet and Neumann boundary conditions, denoted $\Phi^{(D)}$ and $\Phi^{(N)}$ respectively. This EM field is,

$$\underline{E} = \begin{pmatrix} -\frac{\sin(\alpha)}{ikr} \frac{\partial}{\partial \theta} \Phi^{(N)} \\ \frac{\sin(\alpha)}{ik} \frac{\partial}{\partial r} \Phi^{(N)} \\ \cos(\alpha) \Phi^{(D)} \end{pmatrix}, \quad (8)$$

$$\underline{H} = \begin{pmatrix} \frac{\cos(\alpha)}{ikr} \frac{\partial}{\partial \theta} \Phi^{(D)} \\ -\frac{\cos(\alpha)}{ik} \frac{\partial}{\partial r} \Phi^{(D)} \\ \sin(\alpha) \Phi^{(N)} \end{pmatrix}. \quad (9)$$

where α is the polarization angle and denotes the angle that the incident electric field makes with the z -axis. $\Phi^{(D)}$ and $\Phi^{(N)}$, obtained from [1], in integral form are,

$$\Phi^{(D)} = \frac{\mathcal{A}}{2\pi i} \int_{\gamma_+ + \gamma_-} \frac{\delta \cos(\delta\theta_I) e^{-ikr \cos(\hat{z})}}{\sin(\delta(\theta + \hat{z})) - \sin(\delta\theta_I)} d\hat{z} \quad (10)$$

$$\Phi^{(N)} = \frac{\mathcal{A}}{2\pi i} \int_{\gamma_+ + \gamma_-} \frac{\delta \cos(\delta(\theta + \hat{z})) e^{-ikr \cos(\hat{z})}}{\sin(\delta(\theta + \hat{z})) - \sin(\delta\theta_I)} d\hat{z} \quad (11)$$

where $\delta = \frac{\pi}{2\theta_w}$ and γ_+ , γ_- are the usual Sommerfeld contours.

4 Conclusion

The EM field can be approximated as $kr \rightarrow \infty$ for a high frequency or far-field approximation. This is used to determine $\underline{E} \cdot \underline{H}$ and \underline{S} . We find that the problem is \underline{E} -polarized if $\alpha = 0$ or π and is \underline{H} -polarized if $\alpha = \pm\frac{\pi}{2}$. In both cases the total EM field is orthogonal and the Poynting vector is confined to the x - y plane. If α is not equal to a multiple of $\frac{\pi}{2}$ then the total EM field is not orthogonal and the Poynting vector is not confined to the x - y plane.

References

- [1] V. M. Babich, M. A. Lyalinov, and V. E. Grikurov. *Diffraction Theory: The Sommerfeld-Malyuzhinets Technique*. Alpha Science, 2007.
- [2] P. Debye. Der Lichtdruck auf Kugeln von beliebigem material. *Annals of Physics*, 335(11):57–136, 1909.
- [3] F. Hacivelioglu, L. Sevgi, and P. Y. Ufimtsev. Electromagnetic Wave Scattering from a Wedge with Perfectly Reflecting Boundaries : Analysis of Asymptotic Techniques. *IEEE Antennas and Propagation Magazine*, 53(3):232–253, 2011.
- [4] G. L. James. *Geometrical Theory of Diffraction for Electromagnetic Waves*. Peter Peregrinus, The Institution of Engineering and Technology, London, third edition, 1986.
- [5] D. S. Jones. *The Theory of Electromagnetism*. Pergamon Press, London, 1964.
- [6] R. G. Kouyoumjian, T. Celardroni, G. Manara, and P. Nepa. Inhomogeneous electromagnetic plane wave diffraction by a perfectly electric conducting wedge at oblique incidence. *Radio Science*, 42(6):295–304, 2007.
- [7] R. G. Kouyoumjian, G. Manara, P. Nepa, and B. J. E. Taute. The Diffraction of an Inhomogeneous Plane Wave by a Wedge. *Radio Science*, 31(6):1387–1397, 1996.
- [8] M. A. Lyalinov. Electromagnetic scattering by a plane angular sector : I . Diffraction coefficients of the spherical wave from the vertex. *Wave Motion*, 55:10–34, 2015.
- [9] M. A. Lyalinov and N. Y. Zhu. *Scattering of Waves by Wedges and Cones with Impedance Boundary Conditions*. Scitech, Edison, New Jersey, 2013.
- [10] V. P. Smyshlyaev. The High Frequency diffraction of Electromagnetic Waves by Cones of Arbitrary Cross Sections. *SIAM Journal of Applied Mathematics*, 53(3):670–688, 1993.

Reconstructing the geometry of a local perturbation in periodic layers

T-P.Nguyen^{1,*}, H. Haddar¹

¹INRIA Saclay, CMAP Ecole Polytechnique, Palaiseau, France

*Email: tpnguyen@cmap.polytechnique.fr

Abstract

We investigate a sampling method to recover the support of a local perturbation in a periodic layer from measurements of scattered waves at a fixed frequency without knowledge of the geometry of the periodic background media. We analyze the method in a simplified case where the infinite domain is truncated using periodic boundary conditions (which would correspond with the semi-discretized version of the continuous model with respect to the Floquet-Bloch (FB) variable [2]). As a data for the inverse problem, (propagative and evanescent) plane waves are used to illuminate the structure and measurements of the scattered wave at a parallel plane to the periodicity directions are performed. We introduce the near field operator and the near field operator associated with single FB-mode measurements then exploit them to built an indicator function of the defect. Numerical validating results are provided for synthetic data in dimension 2.

Keywords: Inverse scattering, locally perturbed period layer, sampling methods

1 The direct problem

Let $L > 0$ and M be a positive number, $M > 1$. For simplicity, we present the problem only in \mathbb{R}^2 but the results remain valid in dimension 3. In what follows periodicity is understood to hold only with respect to the first space coordinate. We consider the ML -periodic Helmholtz equation for which the total field u is an ML -periodic (with respect to the first variable) function and satisfies

$$\Delta u + k^2 n u = 0 \quad \text{in } \mathbb{R}^2 \quad (1)$$

where the wavenumber k is positive and real valued. We assume that the index of refraction $n \in L^\infty(\mathbb{R}^2)$ has a non negative imaginary part and is ML -periodic. Moreover, we assume in addition that $n = n_p$ outside a compact domain Ω where $n_p \in L^\infty(\mathbb{R}^2)$ is L -periodic and there exists $h > 0$ such that $n = 1$ for $|x_d| > h$. We denote by $D := \text{supp}(n - 1)$ (respectively

$D_p := \text{supp}(n_p - 1)$) such that $D = D_p \cup \bar{\Omega}$. Let u^i be an ML -periodic incident wave satisfying $\Delta u^i + k^2 n u^i = 0$ in \mathbb{R}^2 . Then the scattered wave $u^s := u - u^i$ is ML -periodic, verifies

$$\Delta u^s + k^2 n u^s = -k^2(n - 1)u^i \quad \text{in } \mathbb{R}^2 \quad (2)$$

and is assumed to satisfy the Rayleigh radiation condition

$$u^s = \sum_{\ell \in \mathbb{Z}} \hat{u}^{s,\pm}(\ell) e^{i\alpha_\#(\ell) \cdot \bar{x} + i\beta_\#(\ell)(x_d \mp h)}, \forall \pm x_2 \geq h$$

where $\alpha_\#(\ell) := \frac{2\pi\ell}{ML}$, $\beta_\#(\ell) := \sqrt{k^2 - \alpha_\#(\ell)^2}$ with non negative imaginary part, $\{\hat{u}^{s,\pm}(\ell)\}_{\ell \in \mathbb{Z}}$ are the Rayleigh sequences at $x_d = \pm h$ and $h > 0$ is such that $D \subset \{|x_2| \leq h\}$.

Assumption 1 We assume that n and k are such that for all $u^i \in L^2(D)$, problem (2)-(1) has a unique solution $u^s \in H^1(|x_2| \leq h, |x_1| \leq ML)$ for all $h > 0$.

2 The inversion algorithm

The main goal is to build an indicator function for Ω without reconstructing D or D_p . We use incident plane waves defined as

$$u^i(x; j) = \frac{-i}{2\beta_\#(j)} e^{i\alpha_\#(j)\bar{x} + i\bar{\beta}_\#(j)(x_d - h)}, j \in \mathbb{Z}.$$

We then consider the near field operator $N : \ell^2(\mathbb{Z}) \rightarrow \ell^2(\mathbb{Z})$ defined by

$$[Na]_\ell = \sum_{j \in \mathbb{Z}} a(j) \hat{u}^{s,+}(\ell, j), \forall a = \{a(j)\}_{j \in \mathbb{Z}} \in \ell^2(\mathbb{Z})$$

where $\hat{u}^{s,+}(\cdot, j)$ are the Rayleigh coefficients associated with the scattered field generated by the incident field $u^i(\cdot, j)$.

We shall also consider a single FB near field operator. We remark that an ML -periodic function has decomposition into the sum of M quasi-periodic functions with period L and quasi-periodicity factors $\alpha_q := 2\pi q/(ML)$, with $q = 0, \dots, M - 1$. This can be seen by arranging the Fourier coefficients modulo M so that

$$u = \frac{1}{M} \sum_{q=0}^{M-1} u_q$$

where u_q has a Fourier expansion only on $q+Mj$ Fourier modes. Let $a \in \ell^2(\mathbb{Z})$, we define for $q = 0, \dots, M-1$, the element $a_q \in \ell^2(\mathbb{Z})$ by $a_q(j) = a(q+Mj)$. We then define the operator $I_q : \ell^2(\mathbb{Z}) \rightarrow \ell^2(\mathbb{Z})$ which transforms a to \tilde{a} such that $\tilde{a}_q = a$ and $\tilde{a}_{q'} = 0$ if $q \neq q'$. We then remark that the dual of I_q , $I_q^*a = a_q$. The single FB near field operator is defined as $N_q = I_q^*NI_q$. The justification of the sampling method introduced below relies on the solvability of the so-called *interior transmission problem* defined as: Seek $(u, v) \in L^2(D) \times L^2(D)$ such that $u - v \in H_0^2(D)$ and

$$\begin{cases} \Delta u + k^2 n u = 0 & \text{in } D, \\ \Delta v + k^2 v = 0 & \text{in } D, \\ u - v = \varphi & \text{on } \partial D, \\ \partial(u - v)/\partial\nu = & \text{on } \partial D, \end{cases} \quad (3)$$

for given $(\varphi, \psi) \in H^{3/2}(\partial D) \times H^{1/2}(\partial D)$ where ν denotes the outward normal on ∂D . In the following q is a fixed number between 0 and $M-1$. We assume that $\mathbb{R}^2 \setminus D$ is connected, Ω does not intersect D_p and Ω lies within a period of size L . Moreover, we recall that M should be greater than 1 meaning in particular that there exists one period of size L that does not contain Ω .

Our algorithm uses the framework of the Generalized Linear Sampling Method [1, 3] to built an indicator function for identifying the domain Ω (we also provide indicator functions for D and D_p). We introduce two functionals $J_\alpha(\phi, \cdot)$ and $J_{\alpha,q}(\phi, \cdot) : \ell^2(\mathbb{Z}) \rightarrow \mathbb{R}$ defined by

$$J_\alpha(\phi, a) := \alpha(N_\sharp a, a) + \|Na - \phi\|^2,$$

$$J_{\alpha,q}(\phi, a) := \alpha(N_\sharp I_q a, I_q a) + \|I_q^* NI_q a - \phi\|^2$$

where $N_\sharp := |\Re N| + |\Im N|$. Let us denote by ϕ^z and ϕ_q^z the Rayleigh sequences of respectively $\Phi(\cdot, z)$ and $\Phi_q(\cdot, z)$, which are respectively to the ML -periodic and α_q -quasiperiodic fundamental solutions of $\Delta v + k^2 v = -\delta_z$ satisfying the Rayleigh radiation condition. We then consider $a^{\alpha,z}, a_q^{\alpha,z}$ and $\tilde{a}_q^{\alpha,z}$ in $\ell^2(\mathbb{Z})$ verifying

$$J_\alpha(\phi^z, a^{\alpha,z}) \leq \inf_{a \in \ell^2(\mathbb{Z})} J_\alpha(\phi^z; a) + c(\alpha)$$

$$J_\alpha(\phi_q^z, a_q^{\alpha,z}) \leq \inf_{a \in \ell^2(\mathbb{Z})} J_\alpha(\phi_q^z; a) + c(\alpha)$$

$$J_{\alpha,q}(I_q^* \phi_q^z, \tilde{a}^{\alpha,z}) \leq \inf_{a \in \ell^2(\mathbb{Z})} J_{\alpha,q}(I_q^* \phi_q^z; a) + c(\alpha)$$

with $c(\alpha)/\alpha \rightarrow 0$ when $\alpha \rightarrow 0$. We introduce

$$I_\alpha(z) = (N_\sharp a^{\alpha,z}, a^{\alpha,z}) \left(1 + \frac{(N_\sharp a^{\alpha,z}, a^{\alpha,z})}{D(a_q^{\alpha,z}, \tilde{a}_q^{\alpha,z})} \right)$$

where for a and b in $\ell^2(\mathbb{Z})$

$$D(a, b) = (N_\sharp(a - I_q b), (a - I_q b)).$$

Theorem 2 Assume that Assumption 1 holds, that (3) defines a well posed problem and that $\Re(n) - 1$ or $1 - \Re(n)$ is positive definite in a neighborhood of ∂D . Then,

- $z \in D$ iff $\lim_{\alpha \rightarrow 0} (N_\sharp a^{\alpha,z}, a^{\alpha,z}) < \infty$
- $z \in D_p$ iff $\lim_{\alpha \rightarrow 0} (N_\sharp a_q^{\alpha,z}, a_q^{\alpha,z}) < \infty$
- $z \in \Omega$ iff $\lim_{\alpha \rightarrow 0} I_\alpha(z) < \infty$.

3 A numerical example

We here present a numerical example that shows how one can reconstruct Ω even though the reconstruction of D is not accurate. The parameters setting is:

$k = \pi/3.14$, $n_p = 2$ in D_p , and $n = 4$ in Ω ; set $\lambda = 2\pi/k$ and choose $L = 2\pi$. Index of incident waves: $\mathbb{Z}_{inc} := \{j = q + M\ell, 0 \leq q \leq M-1, -N_{min} \leq N_{max}\}$ with $N_{min} = N_{max} = 5$.

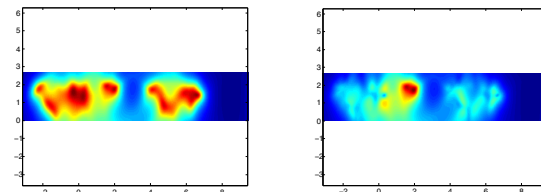
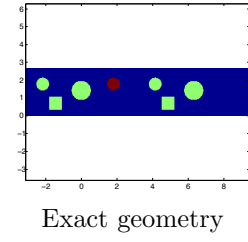


Figure 1: Reconstruction of D (left) and reconstruction Ω (right).

References

- [1] F. Cakoni, D. Colton and H. Haddar, *SIAM, CBMS Series* **88** (2016).
- [2] H. Haddar and Thi-Phong Nguyen, *Applicable Analysis*, 2016
- [3] L. Audibert and H. Haddar, *Inverse Problems*, 2014

An Efficient Monte Carlo Transformed Field Expansion Method for Electromagnetic Wave Scattering by Random Rough Surfaces

Xiaobing Feng¹, Junshan Lin², David P. Nicholls^{3,*}

¹Department of Mathematics, The University of Tennessee, Knoxville, TN, U.S.A.

²Department of Mathematics and Statistics, Auburn University, Auburn, AL, U.S.A.

³Dept. of Mathematics, Stat., and Comput. Sci., University of Illinois, Chicago, IL, U.S.A.

*Email: davidn@uic.edu

Abstract

We develop an efficient and accurate numerical method for the computation of linear waves scattered by random rough surfaces. The method is based upon a combination of the Transformed Field Expansion method, which represents the solution as a provably convergent power series, and the Monte Carlo technique for sampling the probability space. The compelling aspect of the proposed method is that, at each perturbation order and every sample, the governing Transformed Field Expansion equations share the same deterministic Helmholtz operator on a deterministic domain. Thus, an LU factorization of the matrix discretization of this single operator can be employed repeatedly for every perturbation order and every random sample. The computational complexity of the whole algorithm is significantly reduced as a result.

Keywords: Grating scattering; Linear Waves; High-Order Spectral Methods; Transformed Field Expansions; Monte Carlo Simulation.

1 Introduction

The scattering of linear waves from random rough surfaces has long been a subject of interest due to its significant applications in seismology, remote sensing, oceanography, and surface plasmonics to name just a few. The simplest approach is to use the Monte Carlo (MC) method where a set of numerical solutions are obtained for independent identically distributed (i.i.d.) sample surface profiles which are subsequently utilized to calculate the statistics of the scattered waves [2]. An alternative approach is to transform the scattering problem on a random domain into a stochastic problem on a deterministic domain, which is then solved with either Monte Carlo simulations [1] or stochastic Galerkin methods [3]. Both of these methods become computationally intractable when a large number of degrees of freedom is required

for the spatial discretization.

We propose an efficient Monte Carlo Transformed Field Expansion (MC-TFE) method for the simulation of electromagnetic wave scattering by random rough surfaces. To be more precise, our algorithm begins with the TFE approach: A change of variables which flattens the problem domain, followed by expansion of the scattered field in a Taylor series. This generates a Helmholtz problem at every perturbation order with deterministic coefficients and random sources posed on a deterministic domain. We then employ a Monte Carlo method to sample the relevant probability space and compute statistics.

An important observation is that for every perturbation order and every surface realization, the same deterministic Helmholtz operator must be inverted. For this we apply a High-Order Spectral Legendre–Galerkin method, and the resulting discretization matrix is factored (e.g., by the LU factorization algorithm) and stored. In this way we can efficiently solve at every perturbation order and every sample with simple forward and backward substitutions, thereby significantly reducing the computational cost.

2 The Model

We consider the simplified problem of scalar linear waves propagating in two dimensional, constant-density layers, scattered by a random periodic interface shaped by $y = g(\omega; x)$, $g(\omega; x+d) = g(\omega; x)$, where ω is the random sample and (x, y) are the spatial variables. As we have a perturbative method in mind we let $g = \varepsilon f$ (where initially $\varepsilon \ll 1$), and we assume that f is a stationary process with a continuous and bounded covariance function $c(x - y)$.

2.1 Governing Equations

The well-known time-harmonic governing equations for the reflected, $v^+(\omega; x, y)$, and transmit-

ted, $v^-(\omega; x, y)$, fields generated by plane-wave incidence $v^i(x, y) = \exp(ik^+(\sin(\theta)x - \cos(\theta)y))$, can be stated generically as

$$\mathcal{L}[v^\pm] = 0, \quad \text{in } S_g^\pm, \quad (1a)$$

$$\mathcal{B}[v^\pm] = \mathcal{Q}[v^i], \quad \text{at } \partial S_g^\pm, \quad (1b)$$

posed on the truncated domains

$$S_g^+ := \{g < y < a\}, \quad S_g^- := \{-a < y < g\}.$$

The operator \mathcal{L} contains Helmholtz operators, while the boundary operator \mathcal{B} incorporates not only the transmission conditions at the layer interface (continuity of the total field and its normal derivative), but also transparent boundary conditions using DtN maps at $y = \pm a$.

To model the stationary random surface we appeal to the Karhunen–Loéve expansion. If the covariance operator $K\varphi(x) := \int_0^d c(x-s)\varphi(s) ds$, has singular values λ_j and eigenfunctions $\varphi_j(x)$ the Karhunen–Loéve expansion of $f(\omega; x)$ is given by $f(\omega; x) = \bar{f}(x) + \sum_{j=1}^{\infty} \sqrt{\lambda_j} \xi_j(\omega) \varphi_j(x)$, where \bar{f} is deterministic while the ξ_j are i.i.d. Gaussian random variables with zero mean and unit variance.

2.2 The MC-TFE Method

The Transformed Field Expansions (TFE) method was devised by the author and Reitich to overcome severe cancellations in classical High-Order Perturbation of Surfaces algorithms applied to (1). In brief, a domain flattening change of variables, e.g., in $\{g < y < a\}$,

$$x' = x, \quad y' = a(y - g)/(a - g),$$

is affected which transforms (1) into

$$\begin{aligned} \mathcal{L}'[u^\pm] &= \mathcal{F}'(u^\pm, g), & \text{in } S_0^\pm, \\ \mathcal{B}'[u^\pm] &= \mathcal{Q}'[u^i] + \mathcal{R}'(u^\pm, g) & \text{at } S_0^\pm. \end{aligned}$$

for transformed fields, u^\pm , on “trivial” domains.

The right-hand-sides \mathcal{F}' and \mathcal{R}' are $\mathcal{O}(g)$ so that, upon setting $g = \varepsilon f$ and expanding u^\pm in a Taylor series in ε , one realizes a linear, constant coefficient Helmholtz equation with known source for each correction u_n^\pm :

$$\begin{aligned} \mathcal{L}'[u_n^\pm] &= \mathcal{F}'_n(u_{n-1}^\pm, \dots, f), \\ \mathcal{B}'[u_n^\pm] &= \mathcal{Q}'[u_n^i] + \mathcal{R}'_n(u_{n-1}^\pm, \dots, f). \end{aligned}$$

It is this last observation which reveals the strength of our new approach: Once a single solver for inverting the differential operator \mathcal{L}' and boundary conditions \mathcal{B}' is constructed, it can be reused not only for every perturbation order, but also for every realization in a Monte Carlo simulation, greatly reducing the cost of the algorithm.

3 Preliminary Results

Using this computational strategy we can compute statistics of quantities of interest, e.g., the reflectivity, R (the sum of the efficiencies in the upper layer), which we display in Figure 1 for a selection of incidence angles θ between 0 and 60 degrees for four values of ε .

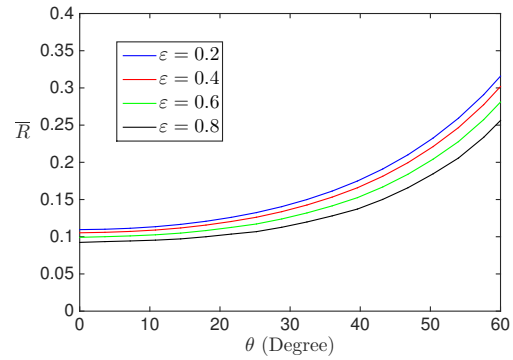


Figure 1: Mean reflectivity for $\theta \in [0, 60^\circ]$ and $\varepsilon = 0.2, 0.4, 0.6, 0.8$.

References

- [1] M. Deb, I. Babuška, and J. Oden, “Solution of stochastic partial differential equations using Galerkin finite element techniques,” *Comput. Methods Appl. Mech. Engrg.*, **190** 6359–6372 (2001).
- [2] N. Garcia and E. Stoll, “Monte Carlo calculation for electromagnetic-wave scattering from random rough surfaces,” *Phys. Rev. Lett.* **52** 1798 (1984).
- [3] D. Xiu and G. Karniadakis, “Modeling uncertainty in steady state diffusion problems via generalized polynomial chaos,” *Comput. Methods Appl. Math. Engrg.*, **191** 4927–4948 (2002).

Singular solutions of cold plasma Maxwell's equations.

Martin Campos Pinto¹, Bruno Després², Anouk Nicolopoulos^{3,*}

¹CNRS and Laboratoire Jacques-Louis Lions

²Institut Universitaire de France and Laboratoire Jacques-Louis Lions

³Laboratoire Jacques-Louis Lions, UPMC-Paris 6, 4 place Jussieu, 75005 Paris, France

*Email: nicolopoulos@ljll.math.upmc.fr

Abstract

Well-posed variational formulations for resonant time-harmonic Maxwell's equations are an important matter as they are convenient for finite element methods and they help understand the resonant heating in tokamaks. Still, the limit of the viscous system when $\nu \rightarrow 0$ is ill-posed and the difficulty is that the solution has singularities of type $\frac{1}{x}$. We consider the cold plasma model to study the influence of a radio-frequency (RF) electromagnetic wave sent in a tokamak plasma for heating purpose. Combining the vanishing viscosity principle with some well defined manufactured solution leads to a well-posed variational formulation of the equations in the case of a normal incidence heating wave.

Keywords: Maxwell's equations, hybrid resonance, resonant heating, singular solutions, manufactured solutions, finite element method

1 Propagation of a RF heating wave

We consider that the electromagnetic phenomena related to the RF heating wave are described by the linear current Maxwell equations combined with the Newton law for the electrons

$$\begin{cases} -\frac{1}{c^2} \partial_t \mathbf{E} + \nabla \wedge \mathbf{B} = \mu_0 \mathbf{J} \\ \partial_t \mathbf{B} + \nabla \wedge \mathbf{E} = 0 \\ \mathbf{J} = -q_e N_e \mathbf{u}_e \\ m_e N_e (\partial_t \mathbf{u}_e + \mathbf{u}_e \cdot \nabla \mathbf{u}_e) = -q_e N_e (\mathbf{E} + \mathbf{u}_e \wedge \mathbf{B}) \end{cases}$$

A viscous term $m_e N_e \nu \mathbf{u}_e$ in the source term of the Newton law can be considered. We then want to pass to the limit $\nu \downarrow 0$ as ν shall be of order 10^{-7} in ITER. Considering the bulk magnetic field is much more intense than the one associated to the RF heating, after the Fourier transform $\partial_t \leftarrow -i\omega$, and introducing $\mathbf{B}' = \nabla \wedge \mathbf{E}'$, the viscous system rewrites at the first order

$$\nabla \wedge \mathbf{B}' - \left(\frac{\omega}{c}\right)^2 \underline{\epsilon}' \mathbf{E}' = 0$$

with $\underline{\epsilon}' = \underline{\epsilon} + i\nu I$, $\underline{\epsilon}$ being the hermitian tensor of the plasma. The plasma is supposed uniform

in the y and z directions, so $\underline{\epsilon} = \underline{\epsilon}(x)$ and is of the form

$$\left(\frac{\omega}{c}\right)^2 \underline{\epsilon} = \begin{pmatrix} \alpha & i\delta & 0 \\ -i\delta & \alpha & 0 \\ 0 & 0 & \gamma \end{pmatrix} \text{ with } \begin{cases} \alpha(0) = 0 \\ \alpha'(0) \neq 0 \\ \delta, \gamma > 0 \end{cases} .$$

We also consider that the electric component of the RF wave is a plane wave $\mathbf{E}(\mathbf{x}) = \mathbf{e} \exp(i\mathbf{k} \cdot \mathbf{x})$ with $\mathbf{k} = (k_x, 0, k_z)$, so that we can consider the problem for $\nabla = (\partial_x, 0, ik_z)$ and functions $(\mathbf{E}', \mathbf{B}')$ depending only on $x \in \Omega = [-1, 1]$. The solution to this regularized problem has been studied in [2], and the x component of the electric field \mathbf{E}' admits a singular part composed of a principal value of $\frac{1}{\alpha}$ and of a Dirac mass. Introducing some manufactured solutions which verify the symmetrized system

$$\begin{cases} \nabla \wedge \mathbf{C}' - \left(\frac{\omega}{c}\right)^2 (\underline{\epsilon}')^t \mathbf{F}' = \mathbf{g}' \\ \mathbf{C}' = \nabla \wedge \mathbf{F}' + \mathbf{q}' \end{cases}$$

and such that F'_x admits a similar singularity as E'_x , we observe that for $\varphi \in C_0^1(\Omega)$

$$\int_{\Omega} (\mathbf{E}' \wedge \mathbf{C}' - \mathbf{F}' \wedge \mathbf{B}')|_x \varphi' = \int_{\Omega} (\mathbf{E}' \cdot \mathbf{g}' - \mathbf{B}' \cdot \mathbf{q}') \varphi .$$

The goal is now to build such fields so that we will be able to pass to the limit and therefore obtain information on (\mathbf{E}, \mathbf{B}) that could complete the ill-posed variational formulation

Find $(e_y, b_z) \in L^2(\Omega) \times L^2(\Omega)$ such that

$$\begin{cases} \int_{\Omega} (e_y \varphi'_1 + b_z \varphi_1) = 0, \forall \varphi_1 \in H_0^1(\Omega) \\ \int_{\Omega} (b_z \varphi'_2 + e_y (\frac{\delta^2}{\alpha} - \alpha) \varphi_2) = 0, \forall \varphi_2 \in H_{0,0}^1(\Omega) \end{cases}$$

and

$$b_z(\pm 1) \mp i\lambda e_y(\pm 1) = f_{\pm} .$$

With $H_{0,0}^1(\Omega)$ the space $\{v \in H_0^1(\Omega), v(0) = 0\}$.

2 Normal incidence case: numerical simulations

We first consider the case $k_z = 0$, which allows us to separate the study of E_z (O-mode) of the

study of the other components (X-mode) since $\nabla \wedge \nabla \wedge \mathbf{E} = (0, -E_y'', E_z'')$. For any $\varphi \in C_0^1(\Omega)$ such that $\varphi(0) \neq 0$, the well-posedness of the formulation

$$\begin{aligned} \text{Find } (e_y, b_z) \in L^2(\Omega) \times L^2(\Omega) \text{ such that} \\ \left\{ \begin{array}{l} \int_{\Omega} (e_y \varphi'_1 + b_z \varphi_1) = 0, \forall \varphi_1 \in H_0^1(\Omega) \\ \int_{\Omega} (b_z \varphi'_2 + e_y (\frac{\delta^2}{\alpha} - \alpha) \varphi_2) = 0, \forall \varphi_2 \in H_{0,0}^1(\Omega) \\ \int_{\Omega} (b_z (F_y^+ \varphi' - q_z^+ \varphi) + e_y (g_y^+ \varphi - C_z^+ \varphi')) = 0, \end{array} \right. \end{aligned}$$

and
 $b_z(\pm 1) \mp i\lambda e_y(\pm 1) = f_{\pm}$.

for any $\lambda > 0$ and $(f_-, f_+) \in \mathbb{C}^2$ has been established in [3]. And the solution to this problem has been shown to be the same as the vanishing viscosity limit solution for $\nu > 0$.

A finite element method discretization enforcing the boundary conditions in the equations leads to a linear system $AX = B$ of dimension $4N + 1$ for $2N + 1$ equidistant nodes in the domain $[-1, 1]$ to solve. The mass matrix A is composed of two band matrix blocks, and of one line corresponding to the integral relation and compensating the fact that the second equation is verified for test functions that do not vanish at 0. This method leads to efficient numerical

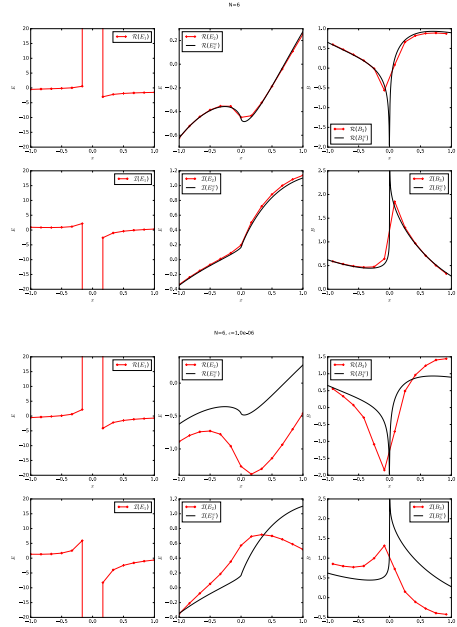


Figure 1: FEM with manufactured solutions (above) and with a friction regularizing term (below) for 13 nodes on the Whittaker test case.

schemes compared to methods involving a small

regularizing friction term, see Figure 1.

Another result from the analysis made in [3] is the identification of the singular parts of the fields in function of the manufactured solutions $(\mathbf{E}, \mathbf{B}) = k(\mathbf{F}^+, \mathbf{C}^+) + (\mathbf{E}_r, \mathbf{B}_r)$ with the regular part $(\mathbf{E}_r, \mathbf{B}_r) \in H_{v(0)=0}^1(\Omega) \times H^1(\Omega)$. A finite element method discretization leads to similar results as the ones of the previous method. These results prove the utility of a well posed variational formulation on the limit of the $(\mathbf{E}'', \mathbf{B}'')$ fields.

3 Oblique incidence case

Now if k_z is not necessarily 0, the major difference is that the z component of the electric field is no more decoupled from the x and y components. This is called mode coupling in plasma physics. The singularity of E_x might have a greater influence on the system as the equation on E_z'' now writes

$$E_z'' + \gamma E_z' = ik_z E_x''$$

with E_x'' expected to be as singular as $\frac{1}{x}$. However we will show that the manufactured functions method can be modified to fit this problem. These results shall be illustrated by numerical simulations.

References

- [1] J.-M. Rax, Physique des Tokamaks, Les Éditions de l’École Polytechnique (2011).
- [2] B. Després, L.-M. Imbert-Gérard and R. Weder, Hybrid Resonance of Maxwell’s Equations in Slab Geometry, *Journal de Mathématiques Pures et Appliquées* **101** (2014), pp. 623–259.
- [3] M. Campos Pinto and B. Després, Constructive Formulations of Resonant Maxwell’s Equations (2016).
- [4] C. Caldini-Queiros, B. Després, L.-M. Imbert-Gérard and M. Kachanovska, A Numerical Study of the Solution of X-mode Equations Around the Hybrid Resonance, *ESAIM: Proceedings ans Surveys*, **53** (2016), pp. 1–21.

Eigenvalue computation with the boundary element method and the contour integral method for periodic boundary value problems for Helmholtz' equation in 3D

Takaya Yamamoto¹, Kazuki Niino^{1,*}, Naoshi Nishimura¹

¹Graduate School of Informatics, Kyoto University

*Email: niino@acs.i.kyoto-u.ac.jp

Abstract

A numerical method for eigenvalue computations in periodic boundary value problems for Helmholtz' equation in 3D with the boundary element method (BEM) and the Sakurai-Sugiura method (SSM) is proposed. The SSM is one of numerical methods for non-linear eigenvalue problems. This method obtains eigenvalues inside a fixed contour in the complex plane by calculating an integral along the contour. In this paper, we extend integral operators in the BEM to complex phase factor in order to calculate the contour integral. With this calculation, we develop an eigenvalue analysis for Helmholtz' equation in 3D with the BEM and the SSM.

Keywords: BEM, Sakurai-Sugiura method, contour integral method, eigenvalue analysis

1 Introduction

We consider eigenvalue analyses of problems in which waves are scattered by a periodic array of scatterers. Eigenvalues of these problems are called Wood's anomalies (also called Rayleigh's anomalies). One of the promising numerical methods for analysing Wood's anomaly is the combination of the boundary element method(BEM) and the Sakurai-Sugiura method (SSM) [1, 2]. Although eigenvalue problems formulated with the BEMs result in non-linear eigenvalue problems, the SSM can solve non-linear eigenvalue problems efficiently.

The combination of the BEM and the SSM has been applied to periodic boundary value problems in 2D [3] and non-periodic problems in 3D [4]. In this paper, we develop a numerical method of analysis for periodic boundary value problems for Helmholtz' equation in 3D with the BEM and the SS method.

2 Formulation

We deal with periodic boundary value problems for Helmholtz' equation in 3D. The unit domain $(-\infty, \infty) \times (-L/2, L/2) \times (-L/2, L/2)$ is denoted by D . For simplicity, we consider a

single scatterer whose domain D_2 is simply connected and finite. The exterior domain D_1 is defined by $D_1 = D \setminus \overline{D_2}$ and the surface between D_1 and D_2 is denoted by Γ . We consider the wave scattering problems for Helmholtz' equation: find a function u satisfying Helmholtz' equation $\Delta u + k_i^2 u = 0$ in each domain D_i , boundary conditions

$$u := u_i = u_j, \quad q := \frac{1}{\varepsilon_i} \frac{\partial u_i}{\partial n} = \frac{1}{\varepsilon_j} \frac{\partial u_j}{\partial n}$$

on Γ and periodic conditions

$$\begin{aligned} u(x_1, L/2, x_3) &= e^{i\beta_2} u(x_1, -L/2, x_3), \\ u(x_1, x_2, L/2) &= e^{i\beta_3} u(x_1, x_2, -L/2), \\ \frac{\partial u}{\partial x_2}(x_1, L/2, x_3) &= e^{i\beta_2} \frac{\partial u}{\partial x_2}(x_1, -L/2, x_3), \\ \frac{\partial u}{\partial x_3}(x_1, x_2, L/2) &= e^{i\beta_3} \frac{\partial u}{\partial x_3}(x_1, x_2, -L/2), \end{aligned}$$

where u_i is the limit value of u from domain D_i to ∂D_i , k_i is the wave number in D_i , β_j ($j = 2, 3$) is the phase factor along x_j directions, ε_i is a constant defined in each subdomain D_i and n is the normal vector defined on ∂D_i and the direction of n is fixed. We also assume that the scattered wave $u^s = u - u^{\text{inc}}$ satisfies the radiation condition in D_1 .

One of boundary integral equations corresponding to this problem is written as follows:

$$\begin{aligned} &\int_{\Gamma} (\varepsilon_1 G_1^p + \varepsilon_2 G_2^p) q dS_y \\ &- \int_{\Gamma} \left(\frac{\partial G_1^p}{\partial n_y} + \frac{\partial G_2^p}{\partial n_y} \right) u dS_y = u^{\text{inc}}(\mathbf{x}), \end{aligned} \quad (1)$$

$$\begin{aligned} &\int_{\Gamma} \left(\frac{\partial G_1^p}{\partial n_x} + \frac{\partial G_2^p}{\partial n_x} \right) q dS_y \\ &- \int_{\Gamma} \left(\frac{1}{\varepsilon_1} \frac{\partial^2 G_1^p}{\partial n_x \partial n_y} + \frac{1}{\varepsilon_2} \frac{\partial^2 G_2^p}{\partial n_x \partial n_y} \right) u dS_y \\ &= \frac{1}{\varepsilon_1} \frac{\partial u^{\text{inc}}}{\partial n}(\mathbf{x}). \end{aligned} \quad (2)$$

G_i^p is the periodic Green function defined by

$$G_i^p(\mathbf{x} - \mathbf{y}) = \sum_{\xi \in \mathcal{L}} e^{i\frac{\beta_i \xi}{L}} G_i(\mathbf{x} - \mathbf{y} - \xi) \quad (3)$$

where \mathcal{L} is the lattice points defined by $\mathcal{L} = \{(0, \xi_2, \xi_3) | \xi_2 = pL, \xi_3 = qL, p, q \in \mathbb{Z}\}$, $\beta = (0, \beta_2, \beta_3)$ and G_i is the Green function of Helmholtz' equation with the wave number k_i . (1) and (2) are known as the PMCHWT formulations.

By an appropriate discretisation method, e.g. Galerkin's method, the integral equations in (1) and (2) can be reduced to a linear equation $A(\beta_2)\mathbf{x} = \mathbf{b}$ where $A(\beta_2)$ is a given matrix, \mathbf{x} is an unknown vector and \mathbf{b} is a given vector. We use the notation $A(\beta_2)$ in order to emphasize that the coefficient matrix A depends on the phase factor β_2 while β_3 is fixed. In this paper, we consider an eigenvalue problem as follows; find β_2 such that $A(\beta_2)\mathbf{x} = 0$ has a non-trivial solution.

3 Eigenvalue analysis

The non-linear eigenvalue problem defined in the previous section can be solved with the SSM. This method finds eigenvalues inside a fixed contour C in the complex plane by reducing the non-linear eigenvalue problem to a generalised eigenvalue problem [1].

For applying the SSM to the integral equations in (1) and (2), we have to calculate $A(\beta_2)$ along the contour C . The periodic Green function in (3), however, cannot be calculated as is for complex β_2 since the summation in (3) diverges if β_2 has a imaginary part. This problem is solved by the Fourier analysis for calculating the lattice sums in the periodic fast multipole method. We found that this technique gives the analytic continuation of (3) with respect to β_2 though this technique was first proposed for accelerating the calculation of (3) [5].

4 Numerical results

We consider spherical scatterers arranged periodically along x_2 and x_3 directions with period $L = 1$. The radius of each sphere is 0.35. We first solve the periodic boundary value problem with these scatterers for several β_2 and observe the behaviour of the solution. Figure 1 shows the absolute values of the solution \mathbf{u} at $\mathbf{x} \approx (0.097, -0.157, 0.298)$. In this figure, the absolute value of the solution \mathbf{u} diverges at $\beta_2 \approx 3.00$ and it implies that an eigenvalue of this problem is expected to be around this point. According to this result, we apply the SSM with the contour $C = \{z | z = 3 + 0.05e^{i\theta}, 0 \leq \theta < 2\pi\}$ and obtain one eigenvalue $(3.004, -4.156 \times 10^{-6})$ in

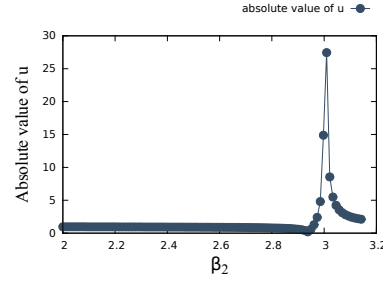


Figure 1: The absolute value of the solution \mathbf{u} at $\mathbf{x} \approx (0.097, -0.157, 0.298)$.

this contour as is expected in Figure 1.

5 Conclusion

We developed a numerical method of eigenvalue analysis for periodic boundary value problems with the BEM and the SSM.

References

- [1] Tetsuya Sakurai and Hiroshi Sugiura. A projection method for generalized eigenvalue problems using numerical integration. *Journal of computational and applied mathematics*, 159(1):119–128, 2003.
- [2] Wolf-Jürgen Beyn. An integral method for solving nonlinear eigenvalue problems. *Linear Algebra and Its Applications*, 436(10):3839–3863, 2012.
- [3] Taichiro Nose and Naoshi Nishimura. Calculation of eigenvalues with the sakurai-sugiura method and periodic fast multipole method in 2 dimensional periodic boundary value problems for helmholtz' equation. *Transactions of the Japan society for industrial and applied mathematics*, 24(3):185–201, 2014.
- [4] Haifeng Gao, Toshiro Matsumoto, Toru Takahashi, and Hiroshi Isakari. Eigenvalue analysis for acoustic problem in 3d by boundary element method with the block sakurai-sugiura method. *Engineering Analysis with Boundary Elements*, 37(6):914–923, 2013.
- [5] Y. Otani and N. Nishimura. A periodic FMM for Maxwell's equations in 3D and its applications to problems related to photonic crystals. *Journal of Computational Physics*, 227(9):4630–4652, 2008.

Performances of the boundary integral equations for transmission problems and the distributions of the complex fictitious eigenvalues

Ryota Misawa¹, Naoshi Nishimura^{1,*}

¹Department of Applied Analysis and Complex Dynamical Systems, Kyoto University, Kyoto, Japan

*Email: nchml@i.kyoto-u.ac.jp

Abstract

Boundary Integral Equations (BIEs) for scattering problems are usually designed not to have real fictitious eigenvalues. However, they may still have complex fictitious eigenvalues with small imaginary parts which may cause inaccurate solutions. This paper discusses the performances of BIEs for transmission problems based on the distributions of complex fictitious eigenvalues. Numerical examples suggest that a properly formulated Single Integral Equation (SIE) has fictitious eigenvalues with larger imaginary parts and are more accurate than other BIEs tested.

Keywords: transmission problems, single integral equations, fictitious eigenvalues

1 BIEs and fictitious eigenvalues

Fictitious eigenvalues of a BIE for wave problems are the frequencies ω 's at which the BIE is irregular although the original problem has a unique solution. BIEs are usually designed not to have real valued fictitious eigenvalues, although they may have complex ones. In [1], we have proposed a simple method to distinguish true and fictitious complex eigenvalues in transmission problems. Also, we have presented numerical examples in [1] which indicate that BIEs may have almost real fictitious eigenvalues, which may result in inaccuracies of the solutions. These results motivate us to find desirable BIEs for transmission problems whose fictitious eigenvalues have large imaginary parts.

We first formulate transmission problems governed by the Helmholtz' equation in 2D with $e^{-i\omega t}$ time dependence. The scatterer is denoted by $\Omega_2 \in \mathbb{R}^2$ whose boundary is $\Gamma = \partial\Omega_2$ and whose exterior domain is $\Omega_1 = \mathbb{R}^2 \setminus \overline{\Omega_2}$. Our problem is to find u which satisfies $\Delta u + k_i^2 u = 0$ in Ω_i ($i = 1, 2$) subject to boundary conditions $u^+ = u^- (= u)$, $\frac{1}{\epsilon_1} \frac{\partial u^+}{\partial n} = \frac{1}{\epsilon_2} \frac{\partial u^-}{\partial n} (= q)$ on Γ and outgoing radiation condition for $u^{\text{sca}} = u - u^{\text{inc}}$. In this statement, ϵ_i is a constant ($\epsilon_i > 0$) in Ω_i , k_i is the wavenumber given by $k_i = \omega\sqrt{\epsilon_i}$, the superscript + (-) stands for the trace to

the boundary from Ω_1 (Ω_2), $\partial/\partial n$ stands for the normal derivative (the normal is directed towards Ω_1) and u^{inc} is the incident wave, respectively. True eigenvalues for this problem are defined as those $\omega \in \mathbb{C}$ at which the homogeneous problem has non-trivial solutions.

To solve this problem, we consider the following boundary integral equations:

$$\begin{pmatrix} \frac{\alpha-\beta}{2} I - (\alpha D_1 + \beta D_2) \\ -(\gamma N_1 + \delta N_2) \\ (\alpha \epsilon_1 S_1 + \beta \epsilon_2 S_2) \\ \frac{\gamma \epsilon_1 - \delta \epsilon_2}{2} I + (\gamma \epsilon_1 D'_1 + \delta \epsilon_2 D'_2) \end{pmatrix} \begin{pmatrix} u \\ q \end{pmatrix} = \mathbf{b} \quad (1)$$

where I is the identity, \mathbf{b} is the incident wave term, S_i and D_i ($i = 1, 2$) stand for single and double layer potentials and D'_i and N_i represents their normal derivatives, respectively. The kernel functions G_i ($i = 1, 2$) for S_i are given by $G_1(x, y) = (i/4)H_0^{(1)}(k_1|x-y|)$ and $G_2(x, y) = (-i/4)H_0^{(2)}(k_2|x-y|)$ where $H_n^{(m)}$ stands for the n -th Hankel function of m -th kind. With this non-standard choice of kernel functions one can distinguish true and fictitious eigenvalues easily because the true (fictitious) ones appear in the lower (upper) half of the complex plane (see [1]).

The constants $(\alpha, \beta, \gamma, \delta)$ in (1) are chosen either $(1, 1, 1/\epsilon_1, 1/\epsilon_2)$ or $(1/\epsilon_1, -1/\epsilon_2, 1, -1)$ or $(\epsilon_1, -\epsilon_2, 1, -1)$. We call the equations thus obtained as PMCHWT, Müller 1 and Müller 2, respectively. The complex fictitious eigenvalues of the PMCHWT and Müller formulations are those of certain transmission problems [1] and those of Müller 2 and PMCHWT are identical. Also, it is known that complex eigenvalues of some transmission problems may have very small imaginary parts. Therefore, the fictitious eigenvalues of (1) may have very small imaginary parts which results in inaccurate BIE solutions for real frequencies if ω is close to one of fictitious eigenvalues.

We next consider the following Single Inte-

gral Equation (SIE) proposed in section 5 of [2]:

$$\begin{aligned} \epsilon_2 S_2 \left(\frac{1}{\epsilon_1} M_1 \mu \right) - \left(\frac{I}{2} + D_2 \right) L_1 \mu \\ = \frac{1}{2} u^{\text{inc}} + D_2 u^{\text{inc}} - \epsilon_2 S_2 \left(\frac{1}{\epsilon_1} \frac{\partial u^{\text{inc}}}{\partial n} \right). \quad (2) \end{aligned}$$

where μ is the unknown density function, a, b are constants and L_1, M_1 are defined as follows:

$$\begin{aligned} L_1 \mu &= a S_1 \mu + b \left(\frac{I}{2} + D_1 \right) \mu \\ M_1 \mu &= a \left(-\frac{I}{2} + D'_1 \right) \mu + b N_1 \mu. \end{aligned}$$

The SIE is a promising candidate for our desirable BIEs, because its fictitious eigenvalues are not those of the transmission problems. Indeed, one can show that fictitious eigenvalues of (2) are those of the exterior Dirichlet problem with incoming radiation condition, and those of the interior impedance problem with the boundary condition given by $av^- + b\partial v^-/\partial n = 0$. We can adjust the constants a, b so that the latter eigenvalues have sufficiently large imaginary parts. In this paper, we choose $a = 1, b = -i/k_1$ because this choice is expected to separate fictitious eigenvalues farther from real axis than other choices [3]. Note that $\text{Im}(a/b) > 0$ holds, thus ensuring that the related fictitious eigenvalues have positive imaginary parts. The exterior Dirichlet eigenvalues also have positive imaginary parts because of the choice for G_2 . Finally, we note that the operator of the SIE in (2) is a compact perturbation of a non-zero constant, hence the corresponding discretized equation converges fast with iterative solvers.

2 Numerical examples

We consider a single circular scatterer with the radius of 1.0 for Ω_2 , in which case we can calculate eigenvalues and solutions analytically. We set $\epsilon_1 = 4, \epsilon_2 = 1$. The upper figure of Fig. 1 shows the eigenvalues. (See [1] for the numerical method to obtain them.) We see that fictitious eigenvalues of the SIE have larger imaginary parts than those of the PMCHWT and Müller formulations. The middle three figures show the averaged error of the solutions u and q vs (real) relative to the exact solutions vs (real) ω . We see that the SIE is more accurate than other formulations which become inaccurate at frequencies near fictitious eigenvalues with small imaginary parts. We also see that the PMCHWT is

more accurate than the Müller 2 although their eigenvalues are identical to each other. In addition, the SIE converges faster than other formulations with GMRES (the lower of Fig. 1).

Acknowledgement: This work is supported by JSPS KAKENHI Grant Number 14J03491.

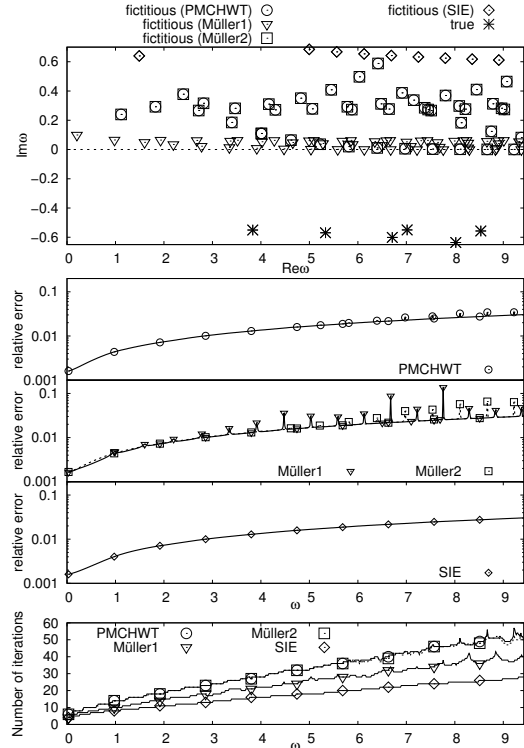


Figure 1: Eigenvalues of the BIEs (upper), error of the BIEM solutions for $u^{\text{inc}} = e^{ik_1 x_2}$ relative to the exact solutions (middle) and number of iterations (lower) with GMRES.

References

- [1] R. Misawa, K. Niino, and N. Nishimura, arXiv:1608.00500[math.NA] (2016) (preprint, accepted for publication in *SIAM Journal on Applied Mathematics*).
- [2] R.E. Kleinman and P.A. Martin, *SIAM Journal on Applied Mathematics*, **48** (1988), pp. 307–325.
- [3] C.-J. Zheng, H.-F. Gao, L. Du, H.-B. Chen, and C. Zhang, *Journal of Computational Physics*, **305** (2016), pp. 677–699.

Dispersive Quantization of Linear and Nonlinear Waves

Peter J. Olver^{1,*}

¹ School of Mathematics University of Minnesota

*Email: olver@umn.edu

Abstract

The evolution, through spatially periodic linear dispersion, of rough initial data leads to surprising quantized structures at rational times, and fractal, non-differentiable profiles at irrational times. Similar phenomena have been observed in optics and quantum mechanics, and lead to intriguing connections with exponential sums arising in number theory. Ramifications and recent progress on the analysis, numerics, and extensions to nonlinear wave models will be discussed.

Keywords: Dispersive wave models, Talbot effect, fractal, quantized, optics, quantum mechanics, integrable system.

In the early 1990's, Michael Berry and collaborators, [2–4], discovered a fascinating and unexpected phenomenon that they named the *Talbot effect* after an experimental observation of William Henry Fox Talbot, [24], the inventor of the photographic negative. This remarkable phenomenon was first observed in the fundamental equations of geometric optics and quantum mechanics on periodic domains. Early analytical investigations can be found in [12, 20, 21].

Unaware of this work, in the course of writing my undergraduate text on partial differential equations, [19], I posed the following "elementary" exercise: find and graph the solution to the *linearized Korteweg-deVries* or *Airy equation*

$$u_t = u_{xxx}, \quad (1)$$

the "simplest" model of linearly dispersive waves, with periodic boundary conditions on $[-\pi, \pi]$ and Riemann-problem-type initial data:

$$u(0, x) = \sigma(x) = \begin{cases} 1, & 0 < x < \pi, \\ 0, & -\pi < x < 0. \end{cases}$$

Plotting the evident Fourier series solution

$$u(t, x) = \frac{1}{2} + \frac{2}{\pi} \sum_{j=0}^{\infty} \frac{\sin((2j+1)x - (2j+1)^3 t)}{2j+1}, \quad (2)$$

at times uniformly spaced by $\Delta t = .1$, produced surprising non-differentiable, fractal-like profiles, as plotted in Figure 1. Even more remarkably, at times spaced by $\Delta t = \pi/30 \approx .10472$, the *same* solution has a piecewise constant profile, as illustrated in Figure 2.

Indeed, it can be proved that, at "rational" (relative to the length of the interval) times $t = \pi p/q$, for $p, q \in \mathbb{N}$, the solution (2) is constant on subintervals of length π/q , [18], whereas, at irrational times, it is a non-differentiable fractal function, [20], [8]. Differentiation confirms the remarkable result that, at rational times, the fundamental solution to the periodic initial-boundary value problem is a linear combination of delta functions. Consequently, given *any* solution $u(t, x)$ to the initial value problem, its value $u(\pi p/q, x)$ at rational time $t = \pi p/q$ and position x depends on only *finitely many values* of the initial data! Berry and Klein, [3], use the latter behavior to explain the phenomenon of *quantum revival*, in which an initially concentrated wave function, representing, say, an electron in an atomic orbit, at first spreads out but later relocates. Indeed, relocation occurs at all rational times, the number of localization sites depending upon the size of the denominator. Experimental confirmations of the Talbot effect in both optics and atomic physics are described in [4].

As shown in [18], these same phenomenon arise in all one-dimensional linear evolution equations with integral polynomial (meaning a constant multiple of a polynomial with all integer coefficients) dispersion relation [18], including the Airy equation (1) and the free space linear Schrödinger equation $i u_t = u_{xx}$. In fact, the Fourier series representation of the integrated fundamental solutions of such dispersive partial differential equations are known as *Gauss sums* or, more generally, *Weyl sums*, of great importance in modern number theory, [26]. Indeed, one route to proving the celebrated Riemann Hypothesis, initiated by Hardy and Littlewood, [11], would be to establish the best

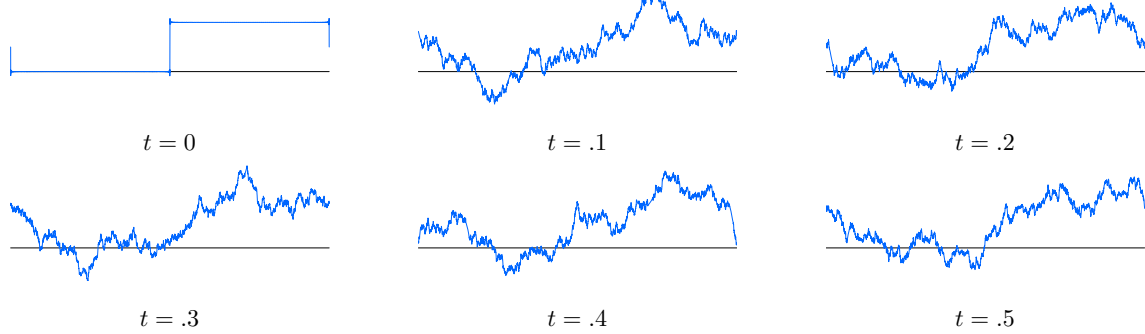


Figure 1: Fractal solution profiles to the Airy equation on a periodic domain at irrational times.

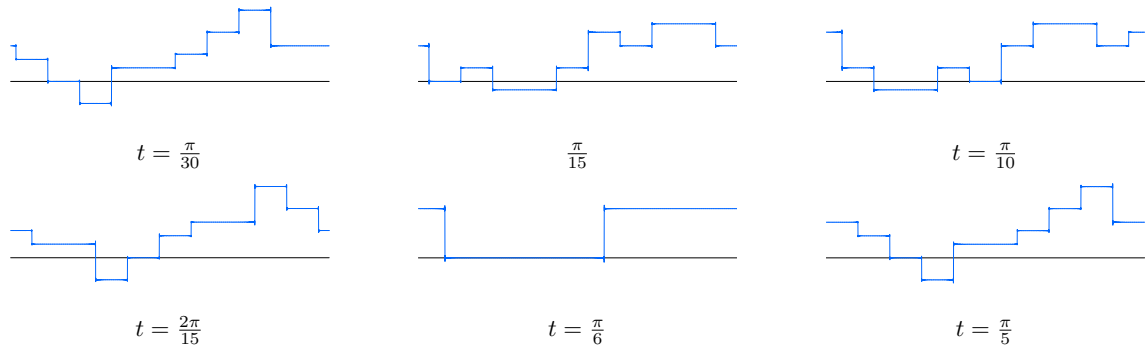


Figure 2: Piecewise constant solution profiles to the Airy equation on a periodic domain at irrational times.

conjectured estimates on such slowly convergent Fourier series, although the modern consensus is that this proof strategy is too difficult to carry out, and so the million dollar Clay Prize remains out of reach.

Subsequent investigations, [6], revealed that the dynamic evolution of linearly dispersive waves on periodic domains with discontinuous initial profiles is strongly dependent upon the large wave number asymptotics of the dispersion relation. In particular, asymptotically linear or sublinear dispersion, such as that in the Benjamin-Bona-Mahoney (BBM) equation, [1], the regularized Boussinesq equation, [23], or the full water wave problem, [27], eventually produces slowly changing waves, in which the solution has assumed what looks like a slightly fractal wave form superimposed over a slowly oscillating ocean, similar to small scale ripples on a swelling sea that moves up and down while gradually changing form. If the dispersion relation is superlinear but subquadratic, the waves

start out oscillatory, eventually becoming fractal, having an overall unidirectional motion while small scale features vary rapidly and seemingly chaotically. For dispersion relations exhibiting polynomial asymptotics, such as the Schrödinger, Korteweg-deVries, Benjamin-Ono, and integrable Boussinesq equations, [9], we observe dispersive quantization at rational times and fractalization at irrational times. As above, if the dispersion relation is exactly polynomial, it can be rigorously proved that the solution quantizes into piecewise constant profiles. In the asymptotically polynomial case the quantized profile is an unknown non-constant form between jumps, in some case possibly with some small fractalization superimposed (although this may be a numerical artifact). Finally, if the dispersion relation is superquadratic but asymptotic to a non-integer power of k , only fractal solution profiles are observed. Apart from the case when the dispersion relation is polynomial, all such results are currently based on numeri-

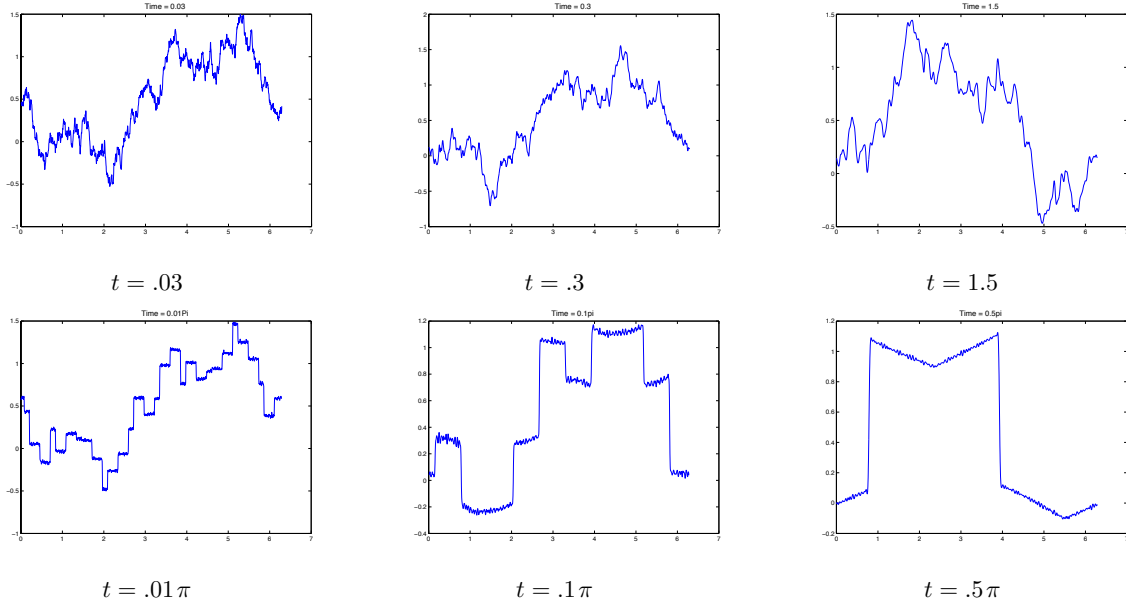


Figure 3: Solution profiles to the Korteweg–deVries equation on a periodic domain.

cal observations through explicit summation of the rather elementary, slowly decaying Fourier series.

Further numerical experiments strongly indicate that the dispersive quantization and fractalization effects persist into the nonlinear regime, for both integrable and non-integrable systems [6], including equations of both generalized Korteweg–deVries and nonlinear Schrödinger type. In Figure 3 we display samples of our numerical calculations of the solution to the periodic Korteweg–deVries equation with step function initial data. Again, at irrational times the solution appears to be a continuous fractal, non-differentiable function, whereas at rational times it is evidently quantized, although the profiles between jumps are no longer constant, and may include some fractal “foam”. Our numerics are based on an elementary operator splitting scheme combined with FFT for both the linear and nonlinear components; a convergence analysis, sadly not quite complete, is outlined in [7]. Subsequently, Chousionis, Erdogan, and Tzirakis, [8,10], rigorously established some of our numerical observations, including estimates on the fractal dimension of the solution graphs. Their proofs rely on functional analytic Besov space estimates combined with subtle number-theoretic cancel-

lations in the slowly convergent series.

Finally, let me remark on some well known history. The revolutionary discovery of the *soliton* was sparked by the original movie of Zabusky and Kruskal, [28], that displayed a numerical simulation of the solution to the periodic initial-boundary value problem for the Korteweg–deVries equation with small nonlinearity. Indeed, in our numerical simulations in Figure 3, we used the *same* parameter values as in the original Zabusky–Kruskal experiments. (In contrast, the celebrated studies of Lax, Levermore, and Venakides, [14, 15, 25], are concerned with the small dispersion regime and convergence to shock wave solutions of the limiting nonlinear transport equation.) Because Zabusky and Kruskal’s selected initial data was a smoothly varying cosine, no Talbot fractalization effect was observed. (And, technically, the elastically interacting waves that emerge from the initial cosine profile are not true solitons, in that these only exist for the full line problem, but, rather, cnoidal waves embedded in a hyperelliptic finite gap solution to the periodic initial-boundary value problem, [13,16].) It is fascinating to speculate how the history of solitons and integrable systems might have differed were Zabusky and Kruskal to have chosen a discontinuous initial profile instead!

One evident consequence of these studies is that, contrary to the conventional wisdom, when dealing with nonlinear wave models on bounded intervals, the principal source of analytic difficulty may be, counterintuitively, not the nonlinear terms, but rather the poorly understood behavior of linearly dispersive partial differential equations. Our investigations imply that the qualitative behavior of the solution to the periodic problem depends crucially on the large wave number asymptotics of the dispersion relation, reinforcing Benjamin et. al.'s critique, [1], that, for example, the Korteweg–deVries equation is an unsatisfactory model for surface waves because its cubic dispersion relation effectively transmits the high frequency modes in the wrong direction, with unboundedly negative phase velocity and group velocity, inciting unphysical interactions with other solution components. And indeed, in the periodic problem, this shortcoming is observed as the number-theoretic resonant interaction of high frequency modes spawned by the initial data serve to produce a-physical fractalization and quantization effects in the engendered solution.

The elementary but surprising results described in this presentation raise many more questions than they answer. Beyond the analytical challenges of rigorously proving some of our experimental observations, here are a few possible directions for further research.

- We have concentrated on the periodic boundary value problem for linearly dispersive wave equations. The behavior under other boundary conditions, e.g. $u(t, -\pi) = u_x(t, -\pi) = u(t, \pi) = 0$ in the case of the Airy equation, is not evident because, unlike the Schrödinger equation, these boundary value problems are not naturally embedded in the periodic version.
- Another important direction would be to extend our analysis to dispersive equations in higher space dimensions. With the appropriate integrality hypothesis on the dispersion relation, the periodic problem on a rectangle whose initial data is constant on rational subrectangles will result in a solution that is quantized at rational times and fractalized at irrational times. An interesting question is whether similar phe-

nomena arise on more general domains. The case of dispersive waves on a sphere, e.g. the earth, is particularly deserving of further investigation. Other important examples include the integrable Kadomtsev–Petviashvili (KP) and Davey–Stewartson equations, [9], and a variety of non-integrable three-dimensional surface wave models found, for example, in [5, 17].

- How does this subtle analytic behavior impact numerical solution techniques? The fact that different time steps (rational versus irrational) result in radically different solution profiles indicates that the design of numerical solution schemes that accurately capture the phenomena will be a significant challenge.
- As noted above, the Talbot effect has been experimentally observed in both optics and atoms. Can one design experiments that exhibit such behavior in other dispersive media?

References

- [1] T.B. Benjamin, J.L. Bona and J.J. Mahony, Model equations for long waves in nonlinear dispersive systems, *Phil. Trans. Roy. Soc. London A*, **272** (1982), 47–78.
- [2] M.V. Berry, Quantum fractals in boxes, *J. Phys. A*, **29** (1996), 6617–6629.
- [3] M.V. Berry and S. Klein, Integer, fractional and fractal Talbot effects, *J. Mod. Optics*, **43** (1996), 2139–2164.
- [4] M.V. Berry, I. Marzoli and W. Schleich, Quantum carpets, carpets of light, *Physics World*, **14** (2001), 39–44.
- [5] J.L. Bona, M. Chen, and J.-C. Saut, Boussinesq equations and other systems for small-amplitude long waves in nonlinear dispersive media. I. Derivation and linear theory, *J. Nonlinear Sci.*, **12** (2002), 283–318.
- [6] G. Chen and P.J. Olver, Dispersion of discontinuous periodic waves, *Proc. Roy. Soc. London*, **469** (2012), 20120407.

- [7] G. Chen and P.J. Olver, Numerical simulation of nonlinear dispersive quantization, *Discrete Cont. Dyn. Syst. A*, **34** (2013), 34.
- [8] V. Chousionis, M.B. Erdoğan and N. Tzirakis, Fractal solutions of linear and nonlinear dispersive partial differential equations, *Proc. London Math. Soc.*, **110** (2015), 543–564.
- [9] P.G. Drazin and R.S. Johnson, *Solitons: An Introduction*, Cambridge University Press, Cambridge, 1989.
- [10] M.B. Erdoğan and N. Tzirakis, Talbot effect for the cubic nonlinear Schrödinger equation on the torus, *Math. Res. Lett.*, **20** (2013), 1081–1090.
- [11] G.H. Hardy and J.E. Littlewood, Some problems of Diophantine approximation. II. The trigonometric series associated with the elliptic ϑ -functions, *Acta Math.*, **37** (1914), 193–238.
- [12] L. Kapitanski and I. Rodnianski, Does a quantum particle know the time?, in: *Emerging Applications of Number Theory*, D. Hejhal, J. Friedman, M. C. Gutzwiller and A. M. Odlyzko, eds, IMA Volumes in Mathematics and its Applications, vol. 109, Springer, New York, 1999, pp. 355–371.
- [13] P.D. Lax, Periodic solutions to the KdV equation, *Commun. Pure Appl. Math.*, **28** (1975), 141–188.
- [14] P.D. Lax and C.D. Levermore, The small dispersion limit of the Korteweg–deVries equation I, II, III, *Commun. Pure Appl. Math.*, **36** (1983), 253–290, 571–593, 809–829.
- [15] P.D. Lax, C. D. Levermore and S. Venakides, The generation and propagation of oscillations in dispersive initial value problems and their limiting behavior, in: *Important Developments in Soliton Theory*, A. S. Fokas and V. E. Zakharov, eds., Springer–Verlag, Berlin, 1993, pp. 205–241.
- [16] H.P. McKean and P. van Moerbeke, The spectrum of Hill’s equation, *Invent. Math.*, **30** (1975), 217–274.
- [17] O. Nwogu, Alternative form of Boussinesq equations for nearshore wave propagation, *J. Waterway Port Coastal Ocean Eng.*, **119** (1993), 618–638.
- [18] P.J. Olver, Dispersive quantization, *Amer. Math. Monthly*, **117** (2010), 599–610.
- [19] P.J. Olver, *Introduction to Partial Differential Equations*, Undergraduate Texts in Mathematics, Springer, New York, 2014
- [20] K.I. Oskolkov, A class of I.M. Vinogradov’s series and its applications in harmonic analysis, in: *Progress in Approximation Theory*, Springer Ser. Comput. Math., vol. 19, Springer, New York, 1992, pp. 353–402.
- [21] K.I. Oskolkov, Schrödinger equation and oscillatory Hilbert transforms of second degree, *Fourier Anal. Appl.*, **4** (1998), 341–356.
- [22] I. Rodnianski, Fractal solutions of the Schrödinger equation, *Contemp. Math.*, **255** (2000), 181–187.
- [23] A.C. Scott, Soliton oscillations in DNA, *Phys. Rev. A*, **31** (1985), 3518–3519.
- [24] H.F. Talbot, Facts related to optical science. No. IV, *Philos. Mag.*, **9** (1836), 401–407.
- [25] S. Venakides, The zero dispersion limit of the Korteweg–deVries equation with periodic initial data, *Trans. Amer. Math. Soc.*, **301** (1987) 189–225.
- [26] I.M. Vinogradov, *The Method of Trigonometrical Sums in the Theory of Numbers*, Dover Publ., Mineola, NY, 2004.
- [27] G.B. Whitham, *Linear and Nonlinear Waves*, John Wiley & Sons, New York, 1974.
- [28] N.J. Zabusky and M.D. Kruskal, Interaction of “solitons” in a collisionless plasma and the recurrence of initial states, *Phys. Rev. Lett.*, **15** (1965) 240–243.

Computational complexity of artificial boundary conditions for Maxwell's equations in the FDTD method

Mikhail Osintcev^{1,*}, Semyon Tsynkov¹

¹Department of Mathematics, North Carolina State University, Raleigh, USA

*Email: mishaosintsev@gmail.com

Abstract

We compare several approaches for handling the artificial outer boundaries that can be implemented with the standard FDTD method in 3D. Our goal is to obtain the asymptotic estimates of computational complexity for each class of methods and corroborate those with numerical results so as to show the advantages and disadvantages of the various methodologies.

Keywords: computational electromagnetics, unbounded domains, numerical efficiency.

1 Local artificial boundary conditions

There is a number of established artificial boundary conditions (ABCs) for Maxwell's equations that are derived using asymptotic considerations. The low-order ABCs (e.g., Sommerfeld, Higdon, Betz-Mittra, or Mur) are widely used in FDTD methods since 1970's [1]. These ABCs are easy to implement (independently at each boundary node), but their accuracy is not satisfactory in most cases. Furthermore, these ABCs may suffer from a deterioration of performance in long-time computations [2]. The overall complexity is

$$C_0(N) = N^3 a, \quad (1)$$

where N is the grid dimension in one direction and $a = \text{const}$ depends on the implementation.

A number of more accurate local high-order ABCs (e.g., Givoli-Neta or Hagstrom-Warburton [3]) have also been proposed, but in most cases the treatment of corners is difficult and no 3D implementation has been described by the authors. The exception is the recent development of double absorbing boundaries (DAB) by LaGrone and Hagstrom [4]. It provides a nearly uniform theoretical accuracy over long time intervals, yet in our experiments we observed a rapid growth of the error for the magnetic field when the solution was driven by a non-solenoidal current. The algorithm of DAB is rather sophisticated, but we assume that the

computational complexity can still be estimated in the form similar to (1).

2 Perfectly matched layer

Another group of popular and efficient approaches for truncating the unbounded regions in EM simulations are perfectly matched layers (PMLs). A PML is an absorbing layer that surrounds the computational domain. The PML and the computational domain are usually discretized on the same grid, hence the computational complexity of a FDTD/PML implementation is as follows:

$$C_{\text{PML}}(N) = (1 + 2\nu)^3 N^3 a, \quad \nu = P/N, \quad (2)$$

where P is the number of nodes in the PML. The value of ν may be relatively small for large grid dimensions N . The PMLs usually provide a low level of spurious reflections and their implementation is straightforward in FDTD. Yet they may be prone to error growth in long-time simulations [5, 6]. In particular, our computations show that the performance depends on the type of the source (antenna current) that drives the EM field. For solenoidal currents the solution with a PML is usually stable yet for non-solenoidal currents it may deteriorate rapidly.

3 Lacunae-based time marching

The lacunae-based time marching can be used to mitigate the long-time deterioration of the PML [6, 7]. This approach is based on the following property of Maxwell's equations in vacuum (the Huygens' principle): provided that the currents are compactly supported in both space and time, the propagating electromagnetic waves have sharp aft fronts. The original problem is decomposed into a series of partial subproblems driven by compactly supported partial currents. The latter are obtained by a smooth partition of the original currents. The computational complexity of this algorithm is

$$C_{\text{Lac-PML}} = \frac{(1 + 2\nu)^3}{(1 - \mu)} N^3 a, \quad (3)$$

where $0 < \mu < 1$ is the overlap between the consecutive partial currents. If the overlap is small, then the computational complexity (3) tends to (2). The original lacunae-based time marching requires divergence-free sources [6]. Its extension based on quasi-lacunae [7] removes this limitation yet keeps the asymptotic complexity (3) unchanged. The most recent work [8] reduces quasi-lacunae to classical lacunae, which improves the performance and enables the proof of a temporally uniform error bound.

The lacunae-based time marching can also be used as a standalone closure at the artificial outer boundary [9]. The idea is to take a sufficiently large auxiliary domain beyond the actual computational domain so that the reflections off the outer boundary of this auxiliary domain won't reach the computational domain by the time the latter falls into the lacuna. This algorithm is considerably more expensive than the lacunae-based algorithm with PML. Its complexity is given by the same expression (3) but with the quantity $(1+2\nu)^3$ replaced with a large constant, on the order of 150. The advantage of this algorithm, however, is that it does not require any special treatment of the artificial outer boundary per se. The outgoing waves propagate into the auxiliary region and then get canceled there once the main computational domain falls inside the lacuna. As such, this algorithm is provably free from any error associated with the domain truncation.

4 Computational results

We use our serial FORTRAN FDTD code to compare the computational complexity of the various boundary conditions numerically. Consider a cubic domain with side $l = 10$ and the propagation speed $c = 1$. Take a $100 \times 100 \times 100$ grid for the FDTD scheme, with the spatial size $h = 0.1$ and the time step $\Delta t = 0.03(3)$. We compute on a 16-core Linux server, Intel Xeon CPU E5-2698 v3 with 2.30 GHz. Table 1 shows the time T for an update of one time step, the value of a , and the maximum relative error ε for each ABC. Note that for more accurate ABCs the value of ε is dominated by the discretization error rather than reflections. Finally, we include the data for the original implementation of the DAB [4], which is written in C++ and therefore does not allow for a direct comparison.

ABC	T (sec)	a	ε
1	0.657	6.565×10^{-7}	17.08×10^{-2}
2	0.667	6.665×10^{-7}	5.44×10^{-2}
3	0.805	4.656×10^{-7}	3.56×10^{-2}
4	1.301	1.506×10^{-7}	3.56×10^{-2}
5	26.709	3.459×10^{-8}	3.56×10^{-2}
6	0.6669	8.551×10^{-7}	3.56×10^{-2}

Table 1: Comparison of the various boundary conditions in a serial implementation. The ABC types: 1 - Sommerfeld ABC, 2 - Higdon ABC, 3 - Uniaxial 10-point PML, 4 - Lacunae with Uniaxial 10-points PML, 5 - Lacunae without PML, 6 - DAB with 4 recursions.

Acknowledgment

Work supported by US ARO, grants W911NF-16-1-0115 and W911NF-14-C-0161, and US-Israel BSF, grant 2014048.

References

- [1] S. D. Gendey, *Introduction to the finite-difference time-domain (FDTD) method for electromagnetics*. Morgan & Claypool Publishers, San Rafael, CA, 2011.
- [2] O. M. Ramahi, *IEEE Trans. Antennas Propagat.*, 47:593-599, 1999.
- [3] D. Givoli, *Wave Motion*, 39:319-326, 2004.
- [4] J. LaGrone and T. Hagstrom, *J. Comput. Phys.*, 326:650-665, 2016.
- [5] S. Abarbanel, D. Gottlieb, and J. Hesthaven, *J. Sci. Comput.*, 17(14):405-422, 2002.
- [6] H. Qasimov and S. Tsynkov, *J. Comput. Phys.*, 227:7322-7345, 2008.
- [7] S. V. Petropavlovsky and S. V. Tsynkov, *J. Comput. Phys.*, 231:558-585, 2012.
- [8] S. V. Petropavlovsky and S. V. Tsynkov, *J. Comput. Phys.*, 336C:1-35, 2017.
- [9] S. V. Tsynkov *J. Comput. Phys.*, 199(1):126-149, 2004.

Using gravitational waves to understand the physics of neutron stars

Benjamin J. Owen¹

¹Department of Physics & Astronomy, Texas Tech University, Lubbock, Texas, USA

Abstract

Neutron stars are complicated objects, touching on all ten volumes of the famous Landau-Lifschitz textbook series on theoretical physics. They can emit several types of gravitational wave signals, from ringdowns of normal modes lasting a fraction of a second to continuous waves lasting longer than human civilization. I summarize the possible signals and describe how they can be used in the future to learn about the physics of matter under the most extreme conditions in the modern universe.

Keywords: Gravitational waves, astrophysics, neutron stars

The first gravitational wave detections were from binary black holes, but neutron stars have more to tell us in the long run [1]. Neutron star mergers can produce “chirps” like those from black hole mergers, but longer and carrying more information. Single neutron stars can also emit gravitational waves from the ringdown of their fundamental modes, excited by the same events that produce giant gamma-ray flares. Single or binary neutron stars can produce continuous wave signals lasting thousands of years. The latter two types of signals are only possible with matter, and we can use all three to probe the properties of the matter, which cannot be reproduced under terrestrial conditions.

First the mergers, which are a safe bet to detect in the next few years: Chirping means the amplitude and frequency both rise with time, entering the LIGO band at tens of Hz and ending minutes later above a kHz, followed by an exponentially damped sinusoid. The precise amplitude and frequency chirp rates are determined for most of the signals’ duration by the evolution of the orbit, which is well approximated by point particles moving in their mutual gravitational field. But in the later orbits and first stages of the merger the frequency evolution is slightly accelerated by the tidal deformability of the neutron stars—their tides induce quadrupoles on each other, which change their gravitational fields [2]. Matched filtering is capable of picking up this small acceleration (on top of the basic

chirp rate due to the masses) and determining it via the response to filtering with waveform templates of varying parameters.

As the stars merge, numerical simulations show power spectra with peaks at a frequency dependent on tidal deformability, and peaks at two more characteristic frequencies related to the mean densities of the stars and their relativistic compactness parameters (roughly the Newtonian gravitational potentials at the stellar surfaces) [3]. The compactness frequency corresponds to the point at which the stars begin to touch and hydrodynamical forces significantly alter the point particle motion; and the density-related frequency is related to *f*-mode acoustic oscillations of the merged star. All three frequencies can tell us about the equation of state of bulk matter at densities higher than in atomic nuclei, and thus give insight into a poorly constrained sector of nuclear physics. The bad news is that it requires combining 100 events or so to get all this detail [4], so if neutron star merger rates are low we may wait beyond 2020 for the whole picture.

Fundamental modes (*f*-modes) of neutron stars have frequencies of a few kHz and damping times of hundreds of ms [5]. The main damping mechanism is gravitational radiation, in fact: the large pressure and density oscillations are extremely effective at producing gravitational waves rather than losing energy to viscous and other damping mechanisms. The biggest excitations of *f*-modes of single neutron stars likely are associated with “giant gamma-ray flares,” which are observed every few years in our galaxy and nowadays thoroughly searched for gravitational waves, mainly with time-frequency techniques rather than matched filtering [6]. An *f*-mode frequency is a good measurement of the mean density of the star, not surprisingly since the mode is a global acoustic wave. The damping time relates somewhat to the total mass of the neutron star, although the connection is less clean and robust.

Continuous gravitational waves are amplitude and frequency modulated by the daily and

yearly motions of the detectors as they move with the Earth. Since these modulations depend on the sky location of the signal source, searches for such signals benefit from knowing the location, for instance from radio observations. Conversely, detection of a new continuous gravitational wave source will yield an accurate sky location. These most sensitive of these searches (for known targets) have been variations on the coherent integration techniques of heterodyning and matched filtering; while all-sky searches have used various semi-coherent techniques to produce candidates for coherent follow-up. The latter methods are necessary due to the impossible computational costs of coherently searching years of data, the whole sky, and wide frequency bands.

The amplitude of a continuous wave signal will yield information on the source. Combined with radio measurements of the distance, the gravitational wave amplitude tells us the non-axisymmetry of the neutron star, which in turn tells us about the internal magnetic field or elastic stresses in the star. For example, searches without detections already have placed upper limits on the internal magnetic fields of some neutron stars [7]. An extremely strong signal could provide evidence for a stellar composition including particles more exotic than neutrons [8].

The ratio of continuous gravitational wave frequency to the star's spin frequency (as indicated by radio pulses) tells us about the emission mechanism. The ratio is expected to be 2, possibly with some admixture of 1: This tells us emission is from a static deformation of the neutron star, and tells us how close the star's rotation axis is to a principal axis [9]. A ratio about 4/3 means the emission mechanism is rotational modes or *r*-modes, whose mere existence could reveal some complicated physics [10], and the correction from 4/3 is a robust measurement of the neutron star's compactness [11].

References

- [1] B. J. Owen, Probing Neutron Stars with Gravitational Waves, in *New Words, New Horizons in Astronomy and Astrophysics, a report on the Astro2010 Decadal Survey*, National Academies Press, Washington, 2010.
- [2] E. E. Flanagan and T. Hinderer, Constraining neutron star tidal Love numbers with gravitational wave detectors, *Physical Review D* **77** (2008), 021502.
- [3] K. Takami, L. Rezzolla, and L. Baiotti, Spectral Properties of the Post-merger Gravitational-wave Signal from Binary Neutron Stars, *Physical Review D* **91** (2015), 064001.
- [4] M. Agathos *et al.*, Constraining the Neutron Star Equation of State with Gravitational Wave Signals from Coalescing Binary Neutron Stars, *Physical Review D* **92** (2015), 023012.
- [5] V. Ferrari and L. Gualtieri, Quasi-Normal Modes and Gravitational Wave Astronomy, *General Relativity and Gravitation* **40** (2008), 945–970.
- [6] J. Abadie *et al.*, Search for Gravitational Wave Bursts from Six Magnetars, *Astrophysical Journal Letters* **734** (2011), L35–L42.
- [7] J. Aasi *et al.*, Gravitational-waves from Known Pulsars: Results from the Initial Detector Era, *Astrophysical Journal* **785** (2014), 119–135.
- [8] B. J. Owen, Maximum Elastic Deformations of Compact Stars with Exotic Equations of State, *Physical Review Letters* **95** (2005), 211101.
- [9] D. I. Jones, Parameter Choices and Ranges for Continuous Gravitational Wave Searches for Steadily Spinning Neutron Stars, *Monthly Notices of the Royal Astronomical Society* **453** (2015), pp. 53–66.
- [10] K. D. Kokkotas and K. Schwenzer, *R*-mode astronomy, *European Physical Journal A* **52** (2016), 38.
- [11] A. Idrisy, B. J. Owen, and D. I. Jones, *R*-mode frequencies of slowly rotating relativistic neutron stars with realistic equations of state, *Physical Review D* **91** (2015), 024001.

Spectral analysis of cavities partially filled with a negative-index material

Sandrine Paolantoni^{1,*}, Christophe Hazard¹

¹POEMS, CNRS / ENSTA ParisTech / INRIA, Palaiseau, France

*Email: sandrine.paolantoni@ensta-paristech.fr

Abstract

The purpose of this talk is to investigate the spectral effects of an interface between a usual dielectric and a negative-index material (NIM), that is, a dispersive material whose electric permittivity and magnetic permeability become negative in some frequency range. We consider here an elementary situation, namely, 1) the simplest existing model of NIM : the Drude model (for which negativity occurs at low frequencies); 2) a two-dimensional scalar model derived from the complete Maxwell's equations; 3) the case of a simple bounded cavity: a camembert-like domain partially filled with a portion of non dissipative Drude material. Because of the frequency dispersion (the permittivity and permeability depend on the frequency), the spectral analysis of such a cavity is unusual since it yields a nonlinear eigenvalue problem. Thanks to the use of an additional unknown, we show how to linearize the problem and we present a complete description of the spectrum.

Keywords: Maxwell's equations, metamaterials, spectral theory

1 Formulation of the problem

In [1], it is proved that the time-harmonic transmission problem between a dielectric material and a NIM may be ill-posed for particular ratios of the refraction index across the interface. On the one hand, for a smooth interface, this occurs when this ratio is equal to -1 . On the other hand, when the interface contains a corner, this occurs for a whole interval of ratios, which is related to a *black hole* effect at the corner. We propose here to study the spectral counterpart of these properties.

We consider a circular cavity C of radius R , divided into two angular sectors V and D defined by an angle $\theta_1 \in (0, \pi)$, as shown in figure 1. The domains V and D respectively contain vacuum and a NIM described by a non dissipative Drude model. This leads us to define two functions $\varepsilon_\omega(\theta)$ and $\mu_\omega(\theta)$ of the polar angle

$\theta \in (-\pi, \pi]$ by

$$\frac{\varepsilon_\omega(\theta)}{\varepsilon_0} = 1 - \frac{\Omega_e^2}{\omega^2} \chi(\theta) \text{ and } \frac{\mu_\omega(\theta)}{\mu_0} = 1 - \frac{\Omega_m^2}{\omega^2} \chi(\theta),$$

where Ω_m and Ω_e are constants linked with the NIM, and χ is the indicator function of $(-\theta_1, \theta_1)$ (so that $\varepsilon_\omega(\theta) = \varepsilon_0$ and $\mu_\omega(\theta) = \mu_0$ if $|\theta| > \theta_1$).

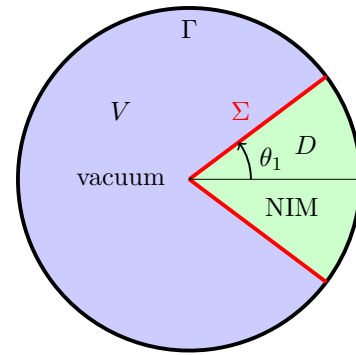


Figure 1: The cavity

We consider the following eigenvalue problem : find $\omega \in \mathbb{C}$ and a nonzero $\varphi \in H_0^1(C)$ such that

$$\omega^2 \varepsilon_\omega \varphi + \operatorname{div} \left(\frac{1}{\mu_\omega} \operatorname{grad} \varphi \right) = 0, \quad (1)$$

which implicitly contains transmission conditions at the interface Σ between V and D : the continuity of φ and $\mu_\omega^{-1} \partial \varphi / \partial n$.

This problem is clearly non-linear (with respect to ω^2). It can be linearized by using an augmented formulation approach, which consists in introducing a new unknown u , only defined in D . We denote by R the operator of restriction to D of functions defined on the whole cavity C and by Π the operator of extension by 0 in V of functions defined in D . It is readily seen that if $\omega^2 \notin \{0, \Omega_m^2\}$, problem (1) is equivalent to find $(\varphi, u) \in H_0^1(C) \times L^2(D)$ such that

$$A \begin{pmatrix} \varphi \\ u \end{pmatrix} = \omega^2 \begin{pmatrix} \varphi \\ u \end{pmatrix}$$

$$\text{with } A = \begin{pmatrix} -\frac{1}{\varepsilon_0\mu_0}\Delta + \Omega_e^2 \mathbf{1}_D & -\frac{1}{\varepsilon_0\mu_0} \operatorname{div} \Pi \\ \Omega_m^2 R \operatorname{grad} & \Omega_m^2 \end{pmatrix}.$$

The implicit transmission conditions across Σ are now the continuity on φ and $(\operatorname{grad} \varphi + \Pi u) \cdot \mathbf{n}$.

Consider the Hilbert space $H = L^2(C) \times L^2(D)^2$. By defining the domain of operator A by $D(A) = \{(\varphi, u) \in H, \varphi \in H_0^1(C), \operatorname{div}(\operatorname{grad} \varphi + \Pi u) \in L^2(C)\}$, we can show that A is self-adjoint and non negative if we choose the inner product

$$((\varphi, u), (\varphi', u'))_H = \varepsilon_0 \mu_0 \int_C \varphi \bar{\varphi}' + \frac{1}{\Omega_m^2} \int_D u \cdot \bar{u}'.$$

Its spectrum thus belongs to \mathbb{R}^+ .

2 The essential spectrum

Contrarily to the case of a cavity filled by a usual dielectric (for which the spectrum is always purely discrete), the presence of the interface of the Drude material is responsible for a component of essential spectrum $\sigma_{ess}(A)$.

Theorem 1 $\sigma_{ess}(A) = \{\Omega_m^2\} \cup \{0\} \cup I$ where $I = \left[\frac{\Omega_m^2}{2} \left(1 - \frac{|\pi - 2\theta_1|}{\pi} \right), \frac{\Omega_m^2}{2} \left(1 + \frac{|\pi - 2\theta_1|}{\pi} \right) \right]$.

Each point $\lambda = \omega^2$ of the essential spectrum is characterized by the existence of a so-called Weyl sequence, that is, a sequence $(\varphi_n, u_n) \in D(A)$ such that $\|(\varphi_n, u_n)\| = 1$, $(A - \lambda I)(\varphi_n, u_n)$ strongly tends to 0 in H and (φ_n, u_n) weakly tends to 0. We will show how to construct such Weyl sequences. Their construction depends on the various parts of $\sigma_{ess}(A)$ which are respectively related to different phenomena.

First of all, Ω_m^2 is an artifact of the augmented formulation. Indeed, it is easily seen that for any $\psi \in H_0^1(D)$, the pair $(0, \operatorname{curl}_{2D}(\psi))$ is an eigenfunction of A associated with Ω_m^2 , which shows that Ω_m^2 is an eigenvalue of infinite multiplicity of A (any Hilbertian basis of the associated eigenspace is thus a Weyl sequence of A).

The remainder of the essential spectrum is related to various *resonance* phenomena.

The value $\omega^2 = 0$ is linked with a *bulk resonance* in the Drude material. Indeed, as $\omega^2 \varepsilon_\omega \mu_\omega$ tends to ∞ as $\omega^2 \rightarrow 0$, we can build a Weyl sequence which represents low frequency oscillations confined in D , that is, (φ_n, u_n) with $\varphi_n = 0$ in V .

Then, $\omega^2 = \frac{\Omega_m^2}{2}$ is associated with a *surface resonance* on the interface between V and D , which occurs when the ratio $\mu_\omega|_V/\mu_\omega|_D$ is equal to -1 . Indeed, we can construct a Weyl sequence which corresponds to highly oscillating vibrations which are localized near any point of Σ different from the corner.

Finally, if $\theta_1 \neq \pi/2$, then $I \setminus \{\Omega_m^2/2\}$ is non-empty and any ω^2 in this set is associated with a *corner resonance* related to the *black hole* effect highlighted in [2]. A possible Weyl sequence represents a family of waves which propagate towards the corner. As the distance from the corner tends to 0, they become more and more oscillating and their group velocity tends to 0, so that their energy accumulates near the corner.

There is no other point in the essential spectrum of A . This follows from the fact that if $\omega^2 \notin \{0; \Omega_m^2\} \cup I$, the operator $A - \omega^2 I$ is semi-Fredholm (that is, of closed range and finite dimensional kernel), which can be deduced from [1]. The complementary part of the spectrum, that is, the discrete spectrum of A (composed of isolated eigenvalues of finite multiplicity), is thus located in $\mathbb{R}^+ \setminus (\{0, \Omega_m^2\} \cup I)$. These eigenvalues accumulate at ∞ (since A is unbounded) as well as at 0, since 0 belongs to $\sigma_{ess}(A)$ without being an eigenvalue of A .

References

- [1] A.S. Bonnet-Ben Dhia, L. Chesnel and P. Ciarlet Jr, T-coercivity for scalar interface problems between dielectrics and metamaterials, *Math. Mod. Num. Anal.* **46** (2012), pp. 1363–1387.
- [2] A.-S. Bonnet-Ben Dhia, C. Carvalho, L. Chesnel and P. Ciarlet , Plasmonic cavity modes: black-hole phenomena captured by Perfectly Matched Layers, *PIERS, Stockholm, August 2013* .

Imaging with intensities only

George Papanicolaou^{1,*}

¹Mathematics Department, Stanford University

*Email: papanicolaou@stanford.edu

Abstract

High frequency imaging with optical, infrared or microwave systems must be done with only intensities because phases, or time resolved signals, cannot be recorded. Phase retrieval methods have been developed over a long time and are flexible and effective but depend on prior information about the image and can give uneven results. When, however, multiple illuminations of the object to be imaged are available then it may be possible to recover the missing phase information. I will present some recent results that use multiple illuminations and I will discuss associated imaging methods, their resolution and their robustness. I will also present the results of numerical simulations using these methods in optical and microwave imaging.

An Efficient Flux-Lumped Discontinuous Galerkin Scheme for the 3D Maxwell Equations on Nonconforming Cartesian Grids

Matthieu Patrizio^{1,*}, Bruno Fornet¹, Vincent Mouysset², Xavier Ferrieres²

¹NUCLETUDES, 3 avenue du Hoggar -Les Ulis -CS 70117- 91978 Courtabœuf Cedex, France

²Onera, The French Aerospace Lab, F-31055, Toulouse, France

*Email: matthieu.patrizio@gmail.com

Abstract

The Discontinuous Galerkin in Time Domain Method (DGTD) is one of the most promising methods to simulate multiscale phenomena. It combines high order precision (p) with flexible geometries (h) resulting in inhomogeneous hp -approximation spaces. In a cartesian framework we show that some parts of the numerical scheme, namely heterogeneous flux terms, can lead to an outburst of computational cost on nonconforming meshes. A new scheme devoid of this bottleneck and proved to be stable is presented along with numerical results.

Keywords: Discontinuous Galerkin, nonconforming approximation, computational cost

1 Introduction

DG methods build an approximate solution which is piecewise polynomial (p) over the mesh (h). It shows various attractive properties, especially flexibility to multiscale geometries, allowing high precision modelling. However, DG-TD solvers have performance bottlenecks which limit its use for industrial purpose, compared to Finite Difference in Time Domain for instance.

One can notice that, in a hp -conforming context, increasing correlatively the approximation order and the mesh size is a powerful strategy to reduce numerical cost. However, in complex geometries, the presence of low-scale inner elements can constrain the mesh, leading to hp -nonconforming configurations (Fig. 1). As shown in the sequel, the latter create extra computational costs, due to nonconforming fluxes, which can invalidate the interest of hp -expansion strategies.

We present here a new numerically efficient DGTD scheme based on lumped fluxes for nonconforming cartesian grids. A stability result is provided, as well as a numerical example on electromagnetic wave propagation.

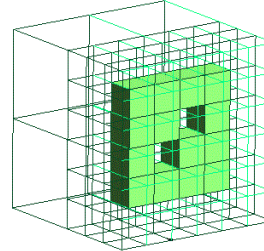


Figure 1: Usual h -nonconforming mesh. The front part is refined to fit with a drilled dielectric plate, the back one is relaxed.

2 DG Scheme and Performance Issues

We consider 3D time-dependent Maxwell's equations on a cavity Ω , with metallic boundary conditions on $\partial\Omega$:

$$\begin{aligned} \partial_t U + A(\partial)U &= 0 && \text{in } (0, T) \times \Omega, \\ B(n_b)U &= 0 && \text{in } (0, T) \times \partial\Omega, \\ U(0, \cdot) &= U_0 && \text{in } \Omega, \end{aligned}$$

where $U = (E, H)^T$ is the electromagnetic field, $A(\partial) : (E, H) \mapsto (-\nabla \wedge H, \nabla \wedge E)^T$ the Maxwell differential operator, $B(n_b) : (E, H)^T \mapsto (0, -n_b \wedge E)^T$ the boundary condition operator, n_b the unit outward normal, and U_0 the initial data. This problem is well-posed in $\mathfrak{U} = \mathcal{C}^0((0, T); H_{curl}(\Omega)^2)$. Denoting by T_h the mesh, F_{int} and F_{bound} the sets of interior and boundary faces, and \mathfrak{U}_{hp} the approximation space of \mathfrak{U} , DG usual variational formulation holds:

$$\begin{aligned} \text{For all } t \in (0, T), \text{ find } (u(t, \cdot), \phi) \in (\mathfrak{U}_{hp})^2, \text{ such as:} \\ \sum_{K \in T_h} \left[\underbrace{\langle \partial_t u, \phi \rangle_K}_{\text{mass}} + \underbrace{\langle A(\partial)u, \phi \rangle_K}_{\text{stiffness}} + \sum_{\substack{f \subset \partial K \\ f \in F_{bound}}} \underbrace{\langle B(n_b)u, \phi \rangle_f}_{\text{bound. flux}} \right. \\ \left. \sum_{\substack{f \subset \partial K \\ f \in F_{int}}} \underbrace{\langle [M(n_f)u]_f, \phi^- \rangle_f - \langle [M(-n_f)u]_f, \phi^+ \rangle_f}_{\text{int. fluxes}} \right] = 0, \end{aligned} \quad (1)$$

where $M(n_f) = A(n_f) - \beta N(n_f)$, is the flux matrix accross a given face f with arbitrary unit normal n_f , $A(n_f)$ and $N(n_f)$ the centered and upwind parts, and $\beta \in [0, 1]$ an upwinding parameter. ϕ^\pm stands for the trace of ϕ on both sides of f , $[\cdot]$ is the jump accross f and $\langle \cdot, \cdot \rangle_K$ is the usual $L^2(K)^6$ scalar product. Discretization of (1) is led using Line-Based method [1]

in space and Leapfrog integration in time. This DGTD scheme uses Gauss-Lobatto basis functions with a lumping method to compute mass, stiffness and conforming flux terms. Table 1 shows the numerical costs for three different configurations giving the same level of accuracy:

Config.	CPU-time (w.r.t. Q^1)	Dofs ($\times 10^3$)
Q^1	1.0	93
Q^2	0.13	10
Q^1/Q^2	52	47

Table 1: *Comput. costs on 12^3 mesh with Q^1 functions, 4^3 with Q^2 , and related Q^1/Q^2 hybrid config.*

One can notice that CPU-time on hybrid configuration (t) is about 50 times more important than on the Q^1 refined mesh (t_{ref}), while expected to be $\frac{t_{ref}}{2} \leq t \leq t_{ref}$. A cost tracking led on this computation revealed this is due to nonconforming fluxes involved in Q^1/Q^2 coupling, computed with standard exact surface quadratures. Thus, a new handling of these terms is developed, so-called flux-lumping, to recover a satisfactory level of performance.

3 The Flux-Lumped (FL) DG Approach

The idea is to consider the flux term across a nonconforming surface S_{nc} as one global quantity, instead of several local fluxes. Each interior flux in (1) is splitted into 4 terms, corresponding to homogeneous (\pm, \pm) and heterogeneous (\pm, \mp) centered and upwind parts. Homogeneous terms are treated as before, nonconforming heterogeneous ones can be lumped but have to be rebalanced to ensure scheme stability. Given Γ^\pm , the trace spaces of u on S_{nc}^\pm , we define two reconstruction operators $\Pi_{S_{nc}}^\pm : \Gamma^\mp \rightarrow \Gamma^\pm$, by:

$$\Pi_{S_{nc}}^\pm(A^\mp u^\mp) = \sum_{j=1}^{N_{dof}^\pm} \hat{\pi}_j^\pm(u^\mp) \mathcal{P}_{f(j)}(\hat{A}^\pm \hat{L}_j^\pm) \mathbf{1}_{f(j)},$$

where $A^\pm = A(\mp n)$, $\hat{\pi}_j^\pm(u^\mp) \in \mathbb{R}$, $f(j)$ is the sub-face containing dof j , $\mathcal{P}_{f(j)}$ is the $(H_{curl})^2$ surface-conforming transformation, \hat{A} and $(\hat{L}_j)_j$ are the matrix A and basis functions expressed in the reference element $[-1, 1]^3$. Finally, the heterogeneous nonconforming flux-lumping holds:

$$\langle \Pi_{S_{nc}}^\pm(A^\pm u^\mp), \phi^\pm \rangle_{S_{nc}}^\pm = \sum_{j=1}^{N_{quad}^\pm} \omega_j^\pm \Pi_{S_{nc}}^\pm(A^\pm u^\mp)(\sigma_j^\pm) \cdot \phi^\pm(\sigma_j^\pm), \quad (2)$$

where $(\omega_j^\pm, \sigma_j^\pm)_j$ are surface quadrature weights and points, fulfilling the following conditions:

- **(C1) Consistency:** $\forall u^\pm \in \Gamma^\pm$,

$$\langle \Pi_{S_{nc}}^-(A^+ u^+), u^- \rangle_{S_{nc}}^- = \langle \Pi_{S_{nc}}^+(A^- u^-), u^+ \rangle_{S_{nc}}^+,$$

and either

$$\langle A^- u^-, A^- u^- \rangle_{S_{nc}}^- = \langle \Pi_{S_{nc}}^+(A^- u^-), \Pi_{S_{nc}}^+(A^- u^-) \rangle_{S_{nc}}^+,$$

or the same identity switching signs + and -.

- **(C2) Positivity:**

$$\forall u^\pm \in \Gamma^\pm, \langle A^\pm u^\pm, A^\pm u^\pm \rangle_{S_{nc/c}}^\pm \geq 0.$$

We thus proved the following stability result:

Theorem 1 *Given $u \in \mathfrak{U}_{hp}$, if $(\omega_j^\pm, \sigma_j^\pm)_j$ in (2) are satisfying (C1) and (C2), then the semi-discrete energy associated to the Gauss-Lobatto Flux-Lumped DG approach decreases: $\forall t \in (0, T)$,*

$$\frac{de}{dt}(t) \leq 0, \text{ with } e(t) = \frac{1}{2} \sum_{K \in T_h} \langle u, u \rangle_K.$$

4 Numerical Example

Computing propagation of 1-modes using flux-lumping approach on the hybrid configuration, the expected numerical efficiency is reached, see Fig. 2 and Table 2.

Config.	CPU-time (w.r.t. Q^1)	Dofs ($\times 10^3$)
FL Q^1/Q^2	0.86	47

Table 2: *Computational costs with FLDGTD scheme on the hybrid configuration (same accuracy).*

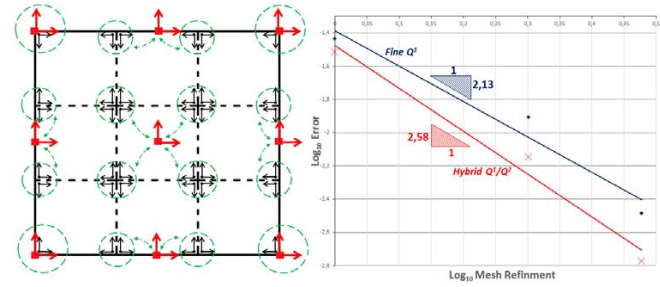


Figure 2: Left: Nonconforming surfaces and reconstruction operators used in the example. Right: L^2 -space/ L^1 -time error w.r.t. mesh isotropic refinement factor.

References

- [1] P. Persson, *High-Order Navier-Stokes Simulations using a Sparse Line-Based Discontinuous Galerkin Method*, AIAA 2012-0456 (2012).

Acknowledgements This work is financially supported by The French Ministry of Defence-DGA.

Acoustic scattering by inhomogeneous media with piecewise smooth material properties

Jagabandhu Paul^{1,*}, B. V. R. Kumar¹, Akash Anand¹

¹Department of Mathematics and Statistics, Indian Institute of Technology Kanpur, Kanpur, India

*Email: bondhu.paul@gmail.com

Abstract

We provide a generalization, in both two and three dimensions, of the volume-surface integral equation formulation given in [SIAM J. Appl. Math., 297-308, 2003], for acoustic scattering by inhomogeneous media to the case where the material properties have jump discontinuities within the scattering inhomogeneity. We also discuss a Nyström numerical solution methodology that relies on analytic resolution of singularities to achieve rapidly convergent integration scheme while employing an FFT based interpolation strategy for accurate approximations of differential operators.

Keywords: Wave Scattering, Bergmann's Equation, Integral Equation, High-Order Method.

1 Introduction

We consider an open bounded set Ω , representing the scattering inhomogeneity, that is a union of a finite number J of open connected domains Ω_j of class C^2 , $j = 1, \dots, J$, such that $\Omega_i \cap \Omega_j = \emptyset$ for $i \neq j$, and $\Omega_0 = \mathbb{R}^d \setminus \cup_{j=1}^J \bar{\Omega}_j$ for $d = 2, 3$, to be the homogeneous exterior. We further assume that no more than two different Ω_j s interface at any given point. The density and wave number inside Ω_j , denoted by ρ_j and κ_j , respectively, are smooth within Ω_j .

The interaction of the incident field ψ_{inc} with the inhomogeneity Ω induces a field ψ_j in Ω_j that satisfies the Bergmann's equation

$$\rho_j \cdot \nabla \left[\frac{1}{\rho_j(\mathbf{x})} \nabla \psi_j(\mathbf{x}) \right] + \kappa_j^2(\mathbf{x}) \psi_j(\mathbf{x}) = 0, \quad (1)$$

for $j = 0, 1, \dots, J$. As ρ_0 is constant, equation (1) reduces to the Helmholtz equation for $j = 0$. The scattered field $\psi_s = \psi_0 - \psi_{inc}$, being outgoing, satisfies the Sommerfeld radiation condition. Moreover, across the interface Γ_{jk} between Ω_j and Ω_k , the following transmission

conditions are satisfied

$$j - \psi_k = 0, \quad (2)$$

$$\frac{1}{\rho_j} \frac{\partial \psi_j}{\partial \mathbf{n}_{jk}} - \frac{1}{\rho_k} \frac{\partial \psi_k}{\partial \mathbf{n}_{jk}} = 0, \quad (3)$$

where \mathbf{n}_{jk} is the unit normal to the surface Γ_{jk} .

It can be shown that the field ψ_ℓ in Ω_ℓ for $\ell = 0, \dots, J$ can be obtained as the solution of the integral equation given by

$$\psi_\ell = \psi_{inc} + \sum_{j=1}^J \mathcal{K}_j V_j \psi_j + \sum_{(j,k) \in \mathcal{I}} \mathcal{S}_{jk} F_{jk} \psi_j$$

where $\mathcal{I} := \{(j, k) : j > k \text{ and } \Gamma_{jk} \text{ is an interface between } \Omega_j \text{ and } \Omega_k\}$,

$$(\mathcal{K}_j V_j \psi_j)(\mathbf{x}) = \int_{\Omega_j} G_0(\mathbf{x}, \mathbf{x}') (V_j \psi_j)(\mathbf{x}') d\mathbf{x}',$$

$$(\mathcal{S}_{jk} F_{jk} \psi_j)(\mathbf{x}) = \int_{\Gamma_{jk}} G_0(\mathbf{x}, \mathbf{x}') (F_{jk} \psi_j)(\mathbf{x}') d\mathbf{s}',$$

$V_j \psi_j = (\kappa_0^2 - \kappa_j^2) \psi_j + \rho_j^{-1} (\nabla \rho_j) \cdot \nabla \psi_j$, $F_{jk} \psi_j = (\rho_k / \rho_j - 1) \partial \psi_j / \partial \mathbf{n}'$, and $G_0(\mathbf{x}, \mathbf{x}')$ is the Green's function of the Helmholtz equation. The corresponding integral equation for $J = 1$ can be found in [3].

2 Numerical method and results

While the method we propose below can be applied, with minor adaptations, for solution of the three dimensional problem, in this text, we restrict our presentation to the two dimensional case.

To compute the integral $\mathcal{K}_j V_j \psi_j$, we begin by decomposing $\bar{\Omega}_j$ into P_B number of *boundary patches* and P_I number of *interior patches*, where boundary patches are homeomorphic to $(0, 1) \times (0, 1]$ and interior patches are homeomorphic to $(0, 1) \times (0, 1)$ via a smooth invertible parametrization $\mathbf{x}_p = \mathbf{x}_p(s, t)$ for $p = 1, \dots, P$. Then, by employing a partitions of unity $\{\omega_p(\mathbf{x}) : p = 1, \dots, P_B, P_B + 1, \dots, P = P_B + P_I\}$, we rewrite the volume integral operator as $(\mathcal{K}_j V_j \psi_j)(\mathbf{x})$

$= \sum_{p=1}^P (\mathcal{K}_{j,p} V_{j,p} \psi_{j,p})(\mathbf{x})$, where $(\mathcal{K}_{j,p} V_{j,p} \psi_{j,p})(\mathbf{x}) =$
 $\iint_{00}^{11} G_0(\mathbf{x}, \mathbf{x}'_p) V_{j,p} \psi_{j,p}(\mathbf{x}'_p) ds' dt'$, $V_{j,p} \psi_{j,p} = (\kappa_0^2 - \kappa_j^2(\mathbf{x}'_p))$
 $_j(\mathbf{x}'_p) + \rho_j(\mathbf{x}'_p)^{-1} (\nabla \rho_j(\mathbf{x}'_p)) \cdot \nabla \psi_j(\mathbf{x}'_p) w_p(\mathbf{x}'_p) J_p(\mathbf{x}'_p)$,
 $\mathbf{x}'_p = \mathbf{x}_p(s', t')$ and J_p is the Jacobian of the transformation \mathbf{x}_p . We observe that $\{\omega_p(\mathbf{x}|_{t=1}), p = 1, \dots, P_B\}$ serves as a partitions of unity for Γ_{jk} , which enable us to rewrite the surface integral operator as $(\mathcal{S}_{jk} F_{jk} \psi_j)(\mathbf{x}) = \sum_{p=1}^{P_B} (\mathcal{S}_{jk,p} F_{jk,p} \psi_{j,p})(\mathbf{x})$, where $(\mathcal{S}_{jk,p} F_{jk,p} \psi_{j,p})(\mathbf{x}) = \int_0^1 G_0(\mathbf{x}, \mathbf{x}') F_{jk,p} \psi_{j,p}(\mathbf{x}') ds'$, and $F_{jk,p} \psi_{j,p} = (\rho_k / \rho_j - 1) \partial \psi(\mathbf{x}'_p) / \partial \mathbf{n}_{jk}(\mathbf{x}'_p)$
 $w_p(\mathbf{x}'|_{t=1}) J_p^S(\mathbf{x}'_p)$, where J_p^S is the surface Jacobian.

We place the computational grid in such a way that it simultaneously conforms to the requirements of the high order quadratures for approximations of volume and surface integral operators. Before discussing the approximation of integral operators, we briefly describe our approach for the computation of differential operators.

Differential Operators: We employ an FFT based efficient and accurate two dimensional interpolation scheme for off-grid evaluation of the discrete data. This allows us to obtain derivatives using, for instance, a finite difference scheme with a very small step size, yielding accurate approximations in an efficient manner.

Surface Integral: For computing $S_{jk,p} F_{jk,p} \psi_{j,p}$ when $\mathbf{x} \in \Gamma_{jk}$ or is close to the interface Γ_{jk} , we adopt an approach similar to the one discussed in [1]. As a first step, the singularity in the kernel is localized using a floating partition of unity. In this region, a change of integration variable centered around the point of singularity with vanishing derivatives at the origin, analytically resolves the logarithmic singularity of the kernel. We then use a high-order quadrature rule to integrate accurately.

Volume Integral: To integrate over an interior patch, we adopt the methodology similar to the one introduced in [2]. The singular integral is handled by changing to polar variables centered around the point of singularity followed by an application of trapezoidal rule for accurate approximation of the integral. Our methodology to integrate over boundary patches, on the other hand, follows closely the steps prescribed in [1] where the numerical approach utilizes a

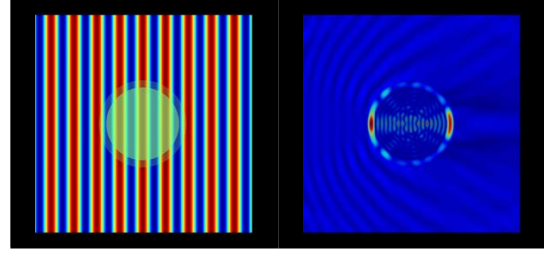


Figure 1: Concentric disc of radius units 1 and annulus of thickness 0.2. Inside the annulus $\kappa_1/\kappa_e = \sqrt{8}$ and $\rho_1/\rho_e = 10$. Inside the disc $\kappa_2/\kappa_e = \sqrt{2}$ and $\rho_2/\rho_e = 20$. Acoustic size of the scatterer is $\kappa_e a = 24$. In the left, we display the real part of the incident field and in the right, we display the absolute value of the total field.

change of variable in s' variable that not only resolve the kernel singularity, but also helps overcome the near singular behavior of the integrand. We refer the readers to [1] for a more detailed discussion on this methodology.

References

- [1] A. Anand. *An efficient high-order algorithm for scattering from penetrable thin structures*. PhD thesis, University of Minnesota, 2006.
- [2] O.P. Bruno and L.A. Kunyansky. A fast, high-order algorithm for the solution of surface scattering problems: Basic implementation, tests, and applications. *Journal of Computational Physics*, 169:80–110, 2001.
- [3] P. A. Martin. Acoustic scattering by inhomogeneous obstacles. *SIAM Journal of Applied Mathematics*, 64:297–308, 2003.

Table 1: $\kappa_1 = \sqrt{2}/2$, $\rho_1 = 2$, $\kappa_2 = \sqrt{3}/2$, $\rho_2 = 4$ and acoustic size of the obstacle $\kappa_e a = 4$. 3-point Newton-Cotes quadrature is used for integration in the t -direction over the boundary patches.

N_2	N_1	Iter.	Rel. Err.	Order
202	612	2	3.18e-01	—
722	2244	4	8.30e-02	1.94e+00
2722	8580	5	2.49e-02	1.74e+00
10562	33540	6	2.03e-03	3.61e+00
41602	132612	8	1.72e-04	3.56e+00

Gravitational waves from inflation at interferometer scales

Marco Peloso^{1,*}

¹School of Physics and Astronomy and Minnesota Institute for Astrophysics, University of Minnesota

*Email: peloso@physics.umn.edu

Abstract

We discuss how to test the late stages of cosmic inflation through the measurement of the stochastic gravitational wave (GW) background at terrestrial and space interferometers, as well as at pulsar timing array experiments.

Keywords: Gravitational waves, Inflation

1 Detection of GW from inflation

The current standard cosmological paradigm requires a stage of accelerated expansion that took place well within the first second of life of our universe. This accelerated expansion was driven by an unconventional source that is commonly denoted as the “inflaton field”. Inflation explains why the observed universe is nearly homogeneous and isotropic at large scale, why it is nearly spatially flat, and why it has few or none topological defects. Inflation also explains the generation of primordial energy density density perturbations, that gave rise to temperature anisotropies in the Cosmic Microwave Background (CMB) radiation, and acted as the seed of structures in the universe (galaxies, and clusters of galaxies) [1].

We do not know at what energy scale inflation took place, and we do not know how long it lasted. We conventionally measure the inflationary expansion in terms of e-folds. During inflation, the scale factor $a(t)$ of the universe (a quantity proportional to how physical lengths expand; loosely speaking, one can think of it as the radius of the universe) expanded according to the law

$$\begin{aligned} a(t) &\simeq a_0 e^{H(t-t_0)} , \quad t \leq t_0 \\ &\equiv a_0 e^{-N} , \quad N \geq 0 \end{aligned} \quad (1)$$

In this expression, t is cosmic time, and t_0 denotes the value of time at the end of inflation. The quantity a_0 denotes the value of the scale factor at this time. The quantity H is nearly constant (and its value is related to the energy scale of inflation), so that the expansion during inflation is nearly exponential. The quantity N

is called “e-folds”, and inflation ends at $N = 0$. We denote by t_N the time corresponding to the e-fold N , and by a_N the value of the scale factor at this time (we thus see that it is appropriate to denote by t_0 the time at the end of inflation, when $N = 0$). Greater values of N correspond to earlier times. We do not know at which value of N inflation started.

The primordial energy density perturbations can be understood as the sum of many modes of different wavelength. Modes of larger wavelength \equiv smaller frequencies were produced earlier during inflation, so at greater values of N . The largest modes in our sky were produced at $N \simeq 60$ (this number differs for different models of inflation, but typical models of inflation give $N \simeq 60$, so we will keep this number fixed in our discussion). We cannot observe greater modes, and so we cannot experimentally probe inflation at times [1].

CMB measurements are extremely precise, and they have provided us with %-accurate knowledge of cosmological parameters. However, the CMB only measures modes of the density perturbations of cosmic-size, produced in the interval $53 \leq N \leq 60$. As we mentioned, modes produced at earlier times are too large to be observed in our sky. Modes produced at later times are too small to affect CMB measurement. All the final stages of inflation, from $N \simeq 53$ to $N = 0$ are currently essentially unexplored, apart from constraints related to the requirement that the density perturbations are small enough so that they do not produce too many primordial black holes.

Inflation also produced GW. These GW are also present in our sky as a superposition of waves of all possible wavelengths. GW produced at $53 \leq N \leq 60$ also leave an imprint on the CMB (they have an effect that is subdominant with respect to that of the density perturbations; this effect has not been measured yet, and it is the object of a very intensive experimental program [2]). GW produced in the later stages of inflation (smaller values of N) have

smaller wavelength, and they can be probed through interferometers (either on earth, or on space) and pulsar array experiments [3]. This opens new potential observational windows on inflation.

There can be different sources of GW in act during inflation. The most common one is simply the production from the inflationary expansion itself (the space-time expansion, excites all fields in the universe to some extent). This signal is universal, but it is unfortunately too weak to be observed at the current and the next generation interferometers. There are however well motivated models of inflation, belonging to the so called class of axion inflation [4], that can potentially result in a larger GW signal [5–8]. This signal is extremely characteristic, as it has a blue spectrum (it grows with frequency), it is polarized [6,9], and it has large non-gaussianity [10, 11]. All these properties differ from those of the universal GW signal from the expansion, and from the GW background produced by astrophysical sources. Therefore, such a signal could be clearly characterized, if above observational threshold. Our talk is mostly based on Ref. [3], which discusses the status of this field. Additionally, we will also mention other possible cosmological sources of GW, both within and outside the inflationary paradigm.

References

- [1] A. D. Linde, *Contemp. Concepts Phys.* **5**, 1 (1990) [hep-th/0503203].
- [2] K. N. Abazajian *et al.* [CMB-S4 Collaboration], arXiv:1610.02743 [astro-ph.CO].
- [3] J. Garcia-Bellido, M. Peloso and C. Unal, *JCAP* **1612**, no. 12, 031 (2016) doi:10.1088/1475-7516/2016/12/031 [arXiv:1610.03763 [astro-ph.CO]].
- [4] E. Pajer and M. Peloso, *Class. Quant. Grav.* **30**, 214002 (2013) doi:10.1088/0264-9381/30/21/214002 [arXiv:1305.3557 [hep-th]].
- [5] N. Barnaby and M. Peloso, *Phys. Rev. Lett.* **106**, 181301 (2011) doi:10.1103/PhysRevLett.106.181301 [arXiv:1011.1500 [hep-ph]].
- [6] L. Sorbo, *JCAP* **1106**, 003 (2011) doi:10.1088/1475-7516/2011/06/003 [arXiv:1101.1525 [astro-ph.CO]].
- [7] J. L. Cook and L. Sorbo, *Phys. Rev. D* **85**, 023534 (2012) Erratum: [Phys. Rev. D **86**, 069901 (2012)] doi:10.1103/PhysRevD.86.069901, 10.1103/PhysRevD.85.023534 [arXiv:1109.0022 [astro-ph.CO]].
- [8] N. Barnaby, E. Pajer and M. Peloso, *Phys. Rev. D* **85**, 023525 (2012) doi:10.1103/PhysRevD.85.023525 [arXiv:1110.3327 [astro-ph.CO]].
- [9] S. G. Crowder, R. Namba, V. Mandic, S. Mukohyama and M. Peloso, *Phys. Lett. B* **726**, 66 (2013) doi:10.1016/j.physletb.2013.08.077 [arXiv:1212.4165 [astro-ph.CO]].
- [10] J. L. Cook and L. Sorbo, *JCAP* **1311**, 047 (2013) doi:10.1088/1475-7516/2013/11/047 [arXiv:1307.7077 [astro-ph.CO]].
- [11] M. Shiraishi, A. Ricciardone and S. Saga, *JCAP* **1311**, 051 (2013) doi:10.1088/1475-7516/2013/11/051 [arXiv:1308.6769 [astro-ph.CO]].

Bounds on the Helmholtz equation in heterogeneous and random media

Owen R. Pembery^{1,*}, Ivan G. Graham¹, Euan A. Spence¹

¹Department of Mathematical Sciences, University of Bath, Bath, UK

*Email: O.R.Pembery@bath.ac.uk

Abstract

We prove bounds on the heterogeneous Helmholtz equation $\nabla \cdot (A \nabla u) + k^2 n u = -f$ that are explicit in k , A , and n , and then extend these to the case when A and n are random fields.

Keywords: Helmholtz equation, heterogeneous, random

1 Introduction

There is a long history of proving bounds on the solution of BVPs involving the homogeneous Helmholtz equation

$$\Delta u + k^2 u = -f, \quad (1)$$

where $k > 0$. In particular:

1. The argument introduced by Vainberg [10] proves a sharp k -explicit bound on the solution of (1) under conditions on the propagation of singularities. In the case of the exterior Dirichlet and Neumann problems, these propagation of singularities results hold when the obstacle is nontrapping by the results of Melrose and Sjöstrand [6].
2. Identities introduced by Morawetz [7] prove k -explicit bounds on the solution of (1); these arguments work best on the exterior Dirichlet problem when the domain is star-shaped.

In this talk we consider proving bounds on the heterogeneous Helmholtz equation.

$$\mathcal{L}_{A,n} u := \nabla \cdot (A \nabla u) + k^2 n u = -f \quad (2)$$

where $k > 0$, A is a symmetric real-valued positive definite $d \times d$ matrix, and n is a real-valued function bounded away from zero (when this equation is posed on an unbounded domain we assume that $I - A$ and $1 - n$ have compact support, so equation (2) becomes (1) near infinity). Our goal is for these bounds to be explicit in k , A , and n .

Note that the arguments in point 1 above prove a sharp k -explicit bound on the solution of (1) under a nontrapping condition. However, the constant in the bound is not explicit in A or n , and it is not straightforward to check if

a given A and n satisfy the nontrapping condition.

Having proved bounds on the heterogeneous Helmholtz equation we then convert them into bounds on the Helmholtz equation where A and n are random fields – this is motivated by the body of work on uncertainty quantification for the equation (2) when $k = 0$, and on the work by Feng, Lin, and Lorton [5] on the interior impedance problem when $A = I$ and n is a random perturbation of a constant (with the magnitude of this perturbation decreasing with k).

2 Main results

We consider 4 problems:

1. The *exterior Dirichlet problem*; i.e. equation $\mathcal{L}_{A,n} u = -f$ is posed in the exterior of a bounded obstacle, with Dirichlet boundary conditions on the obstacle and the Sommerfeld radiation condition at infinity.
2. The *truncated exterior Dirichlet problem*; i.e. equation $\mathcal{L}_{A,n} u = -f$ is posed in the exterior of a bounded obstacle, with Dirichlet boundary conditions on the obstacle, but the radiation condition is approximated by truncating the (unbounded) exterior domain and applying an impedance boundary condition on the artificial boundary.
3. The *transmission problem*; i.e. equation $\mathcal{L}_{A,n} u = -f$ is posed in \mathbb{R}^d , with the Sommerfeld radiation condition at infinity.
4. The *truncated transmission problem*; i.e. equation $\mathcal{L}_{A,n} u = -f$ is posed in \mathbb{R}^d , but the radiation condition is approximated by truncating the (unbounded) exterior domain and applying an impedance boundary condition on the artificial boundary; this problem is therefore the *interior impedance problem*.

Problem 3 can be considered as a special case of Problem 1 when the obstacle is the empty set, and similarly Problem 4 can be considered as a special case of Problem 2.

We use appropriate generalisations of the identities introduced by Morawetz to prove bounds

on these problems that are explicit in k , A , and n , under the condition that the domains are either star-shaped or star-shaped with respect to a ball and under certain conditions on A and n . (These bounds are quite involved, and so we do not have space to state them here.) We note that the conditions on A and n allow them to be sufficiently small (but independent of k) perturbations of constants.

Some bounds on these problems that are explicit in k , A , and n already exist in the literature; these are summarised in §3 below. The main differences between our bounds and this previous work are:

1. To our knowledge, our bounds are the only ones that cover the case when both A and n vary.
2. We show how the conditions on A and n that arise from the Morawetz-multiplier argument are equivalent to a non-trapping condition on the rays.

Furthermore, to our knowledge, the only existing bound in the literature when one of A or n are random fields is the one in [5] mentioned above.

3 Previous bounds in the heterogeneous case

We now outline the previous work on bounds on the four problems above that are explicit in k , A , and n . We highlight, however, that there is also a large body of work on proving analogous bounds for the Helmholtz equation posed above an infinite rough surface, and the Helmholtz transmission problem through an infinite rough layer.

Bounds on the transmission problem when $A = I$ and n is variable were obtained in [9].

Bounds on the exterior Dirichlet problem when $A = I$ and n is variable were obtained in [2], and when A is variable and $n = 1$ in [1].

Bounds on the interior impedance problem when $A = I$ and n is variable were obtained in [3] and [4] and when A is variable and $n = 1$ in [8].

References

- [1] C.O. Bloom, Estimates for solutions of reduced hyperbolic equations of the second order with a large parameter, *Journal of Mathematical Analysis and Applications*, **44**(2) (1973), pp. 310–332.
- [2] C. O. Bloom and N.D. Kazarinoff, A priori bounds for solutions of the Dirichlet problem for $[\Delta + \lambda^2 n(x)]u = f(x, \lambda)$, *Journal of Differential Equations* **24**(3) (1977), pp. 437–465.
- [3] D. L. Brown, D. Gallistl and D. Peterseim, Multiscale Petrov-Galerkin Method for High-Frequency Heterogeneous Helmholtz Equations, *arXiv preprint arXiv:1511.09244*, (2015).
- [4] T. Chaumont Frelet, Approximation par éléments finis de problèmes d’Helmholtz pour la propagation d’ondes sismiques, *PhD Thesis*, INSA, Rouen, 2015.
- [5] X. Feng, J. Lin and C. Lorton, An efficient numerical method for acoustic wave scattering in random media, *SIAM/ASA Journal on Uncertainty Quantification* **3**(1) (2015), pp. 790–822.
- [6] R. B. Melrose and J. Sjöstrand, Singularities of boundary value problems. I, *Communications on Pure and Applied Mathematics*, **31**(5) (1978), pp. 593–617.
- [7] C. S. Morawetz, Decay for solutions of the exterior problem for the wave equation, *Communications on Pure and Applied Mathematics* **28**(2) (1975), pp. 229–264.
- [8] M. Ohlberger and B. Verfürth, Analysis of multiscale methods for the two-dimensional Helmholtz equation with highly heterogeneous coefficient. Part I. Homogenization and the Heterogeneous Multiscale Method, *arXiv preprint arXiv:1605.03400*, 2016.
- [9] B. Perthame and L. Vega, Morrey–Campanato estimates for Helmholtz equations, *Journal of Functional Analysis* **164**(2) (1999), pp. 340–355.
- [10] B. R. Vainberg, On the short wave asymptotic behaviour of solutions of stationary problems and the asymptotic behaviour as $t \rightarrow \infty$ of solutions of non-stationary problems, *Russian Mathematical Surveys* **30**(2) (1975), pp. 1–58.

Reliable and efficient a posteriori error estimate for EFIE in electromagnetism

M. Bakry¹, S. Pernet^{2,*}, F. Collino³

¹INRIA Saclay Ile de France

²The French Aerospace Lab, Toulouse, France

³CERFACS, Toulouse, France

*Email: Sebastien.Pernet@onera.fr

Abstract

We construct a new reliable, efficient and local a posteriori error estimate for the Electric Field Integral Equation (EFIE). It is based on a new localization technique depending on the choice of a generic operator which is used to transport the residual into L^2 -type space. Under appropriate conditions on the construction of this operator, we show that it is asymptotically exact with respect to an energy norm of the error.

Keywords: *a posteriori* error, integral equations, electromagnetism

1 Introduction

The Boundary Element Method (BEM) is a widely used tool, based on boundary integral formulations, for the resolution of wave propagation problems (Acoustics, Electromagnetism ...). Nevertheless, for these BEM which are used for oscillating problems, we lack efficient, reliable and automatic tools for the control of the error. Such tools are called *a posteriori* error estimates η and are ideally reliable and efficient *i.e.* $C_{eff}\eta \leq \|u - u_l\| \leq C_{rel}\eta$ thus ensuring complete control over the norm of the error. Moreover, they must be local in the sense that η can be decomposed as the sum of local contributions computed over each element of a mesh \mathcal{T}_l . Such η can be included in an auto-adaptive refinement algorithm to ensure the quality of numerical simulations.

The main difficulties in the context of BEM are the non-local character of the norms and operators. Consequently, localization techniques must be used to derive an indicator η but the standard ones do not yield to an explicit information on the constants C_{rel} and C_{eff} and by consequence, can lead to inaccurate measure of the error.

Recently, we have proposed for acoustic problem a new localization technique which enables a full control over these constants [1]. In this abstract, we propose an extension of the technique

to electromagnetism problems. In the section 2, we present an abstract setting larger than the electromagnetism in order to explain the methodology. In the next sections, we apply it to the EFIE.

2 Abstract setting

Let $\mathcal{A} : H \rightarrow H^*$ be a linear operator from some Hilbert space H to its topological dual H^* such that $\mathcal{A} = \mathcal{A}_0 + \mathcal{K}$ where \mathcal{A}_0 is a continuous and T -coercive operator *i.e* there exists $T \in \mathcal{L}(H, H)$ some bijective operator such there exists $\alpha > 0$, $\langle \mathcal{A}_0 \mathbf{v}, T \mathbf{v} \rangle \geq \alpha \|\mathbf{v}\|_H^2$ and $\langle \mathcal{K} \cdot, T \cdot \rangle$ is a compact bilinear form where $\langle \cdot, \cdot \rangle$ is the duality bracket.

We are interested in the Galerkin approximation of the problem $\mathcal{A} u = b$ in a sequence of nested discrete spaces $(V_l)_{l \in \mathbb{N}}$ *i.e* $V_l \subset V_{l+1} \subset H$: find $u_l \in V_l$ such that $\langle \mathcal{A} u_l, v_l \rangle = \langle b, v_l \rangle$, for all $v_l \in V_l$. We assume that this discrete problem is well-posed and $\lim_{l \rightarrow +\infty} u_l = u$ in H .

We have the following fundamental result:

Theorem 1 Let $\Lambda : H^* \rightarrow V \subset [L^2(\Gamma)]^d$ be an isomorphism where V is a closed subspace of $[L^2(\Gamma)]^d$. Then the *a posteriori* error estimate defined by $\eta_\Lambda := \|\Lambda r_l\|_{0,\Gamma}$ where $r_l := b - \mathcal{A} u_l$ is reliable, efficient and local.

Moreover, if there exists Λ such that the identity $\Lambda^* \Lambda \mathcal{A}_0 = T + \mathcal{K}_1$ holds where Λ^* is the adjoint operator of Λ and \mathcal{K}_1 is a compact perturbation, then η_Λ is asymptotically exact with respect to the norm of the error $\|u - u_l\|^2 = \langle \mathcal{A}_0(u - u_l), T(u - u_l) \rangle$.

Remarks:

1. The first part of the theorem is trivial. Actually, since Λ is an isomorphism, we have $\|\Lambda^{-1}\|_{op} \|r_l\|_{H^*} \leq \eta_\Lambda \leq \|\Lambda\|_{op} \|r_l\|_{H^*}$. We conclude by using the fact that $\|r_l\|_{H^*}$ is equivalent to $\|u - u_l\|_H$ when the continuous problem is well-posed.

2. The second part comes from the following property: $\lim_{l \rightarrow +\infty} u_l = u$ in H implies $\bar{e}_l := (u - u_l)/\|u - u_l\|_H \rightharpoonup 0$ weakly in H when $l \rightarrow +\infty$ and consequently, for any compact operator $\tilde{\mathcal{K}} : H \rightarrow W$, $\tilde{\mathcal{K}}\bar{e}_l \rightarrow 0$ strongly in W , in other words, $\tilde{\mathcal{K}}(u - u_l)$ tends to zero faster than $\|u - u_l\|_H$.

3 Application to the Electric Field Integral Equation

We consider the scattering by a perfectly conductor object in a non-bounded homogeneous media of an electromagnetic wave. This object is represented by a Lipschitz bounded domain with simply connected and connected boundary Γ whose outward unit normal is \mathbf{n} . We use the well-known EFIE to solve this problem. This integral equation can be written in the previous abstract setting in this way (see for example [2]): $H = H^{-1/2}(\operatorname{div}_\Gamma, \Gamma)$,

$$\mathcal{A}\mathbf{u} = \mathbf{S}_k\mathbf{u} + \frac{1}{k^2}\nabla_\Gamma S_k \operatorname{div}_\Gamma \mathbf{u} \quad (1)$$

where S_k and \mathbf{S}_k are the scalar and the vector single layer potentials respectively, k is the wavenumber and ∇_Γ is the surface gradient.

The operator T is defined from the Helmholtz decomposition of every vector field of H : $\forall \mathbf{v} = \Pi_{loop}\mathbf{v} + \Pi_{star}\mathbf{v} = \mathbf{n} \times \nabla_\Gamma \psi + \nabla_\Gamma \varphi \in H^{-1/2}(\operatorname{div}_\Gamma, \Gamma)$, $T\mathbf{v} = \Pi_{loop}\mathbf{v} - \Pi_{star}\mathbf{v}$. Finally, the T-coercive operator \mathcal{A}_0 is defined by (see [2])

$$\mathcal{A}_0\mathbf{v} = \mathbf{S}_0\mathbf{v} + \frac{1}{k^2}\nabla_\Gamma S_0 \operatorname{div}_\Gamma \mathbf{v} - 2\Pi_{star}^*\mathbf{S}_0\mathbf{v}. \quad (2)$$

The construction of a candidate for Λ is based on pseudo-differential calculus. Therefore, in order to use this tool, the surface Γ is assumed to be smooth for the construction. Moreover, the Helmholtz decomposition allows us to handle any vectorial boundary operator M as a 2×2 matrix of scalar boundary operators M_{ij} :

$$M = [\mathbf{n} \times \nabla_\Gamma \nabla_\Gamma] \begin{bmatrix} M_{11} & M_{12} \\ M_{21} & M_{22} \end{bmatrix} \begin{bmatrix} \Pi_{loop} \\ \Pi_{star} \end{bmatrix}$$

We propose to find Λ as a pseudodifferential operator such that the principal symbol $\sigma_p(\Lambda^* \Lambda \mathcal{A}_0) = \sigma_p(\Lambda)^2 \sigma_p(\mathcal{A}_0) = \sigma_p(T)$. In this context, we have

$$\sigma_p(\mathcal{A}_0) = \begin{bmatrix} \frac{1}{2\|\xi\|} & 0 \\ 0 & -\frac{\|\xi\|}{2k^2} \end{bmatrix}, \quad \sigma_p(T) = \begin{bmatrix} 1 & 0 \\ 0 & -1 \end{bmatrix}$$

where ξ is a parameter being a cotangent vector on Γ .

The structure of these principal symbols suggests to find Λ in the form

$$\Lambda = [\mathbf{n} \times \nabla_\Gamma \nabla_\Gamma] \begin{bmatrix} \Lambda^+ & 0 \\ 0 & \Lambda^- \end{bmatrix} \quad (3)$$

with $\sigma_p(\Lambda^+) = 1/\sqrt{2\|\xi\|}$ and $\sigma_p(\Lambda^-) = k\sqrt{2/\|\xi\|}$

Finally, we construct the candidates for Λ^\pm by using the Laplace-Beltrami operator:

$$\Lambda^\pm = \sqrt{2k} \left(I - \frac{\Delta_\Gamma}{k^2} \right)^{\mp 1/4} \quad (4)$$

In fact, $\sigma_p(\Delta_\Gamma) = -\|\xi\|^2$ and we have added the identity I to obtain an isomorphism.

Remarks:

1. The operator Λ defined by (3) and (4) is an isomorphism [3] onto $L_t^2(\Gamma) = \{\mathbf{v} \in [L^2(\Gamma)]^3 : \mathbf{v} \cdot \mathbf{n} = 0\}$ for Lipschitz surface.
2. By construction, η_Λ is asymptotically exact for smooth surface but as for the acoustic case, we expect that the efficiency constant is close to one in presence of some geometrical singularities.
3. The implementation of η_Λ is based on the use of the algorithm proposed in [4] to compute efficiently the operators (4).

4 References

References

- [1] M. Bakry, *Fiabilité et optimisation des calculs obtenus par des formulations intégrales en propagation d'onde*, phd of university Paris Saclay, 2016.
- [2] A. Buffa and, R. Hiptmair, *Galerkin Boundary Element Methods for Electromagnetic Scattering*, In Topics in computational wave propagation, pp. 85–126. Springer Berlin Heidelberg, 2003.
- [3] F. Gesztesy, I. Mitrea, D. Mitrea, and M. Mitrea, *On the nature of the laplace-beltrami operator on Lipschitz manifolds*, Journal of Mathematical Sciences, 172(3) :279–346, 2010.
- [4] N. Hale, N. J. Higham, and L. N. Trefethen, *Computing A^α , $\log(A)$, and Related Matrix Functions by Contour Integrals*, SIAM Journal on Numerical Analysis, 46(5) :2505–2523, 2008.

A hybrid method combining boundary elements and ray tracing for high frequency diffraction. Application to NDT.

M.Bonnet¹, F. Collino², E. Demaldent³, A. Imperiale³, L. Pesudo^{1,3,*}

¹POEMS, ENSTA ParisTech, Palaiseau, France

²Freelance, Paris, France

³DISC, CEA LIST, Saclay, France

*Email: laure.pesudo@ensta-paristech.fr

Abstract. We propose a new hybrid strategy between the boundary element method (BEM) and ray tracing in order to allow the accurate and quick simulation of high frequency Non Destructive Testing (NDT) configurations involving diffraction phenomena. Results from its implementation to 2D acoustic NDT-like diffraction configurations are presented. The strategy proposed is however generic, and can be extended to three-dimensional configurations and elastodynamic wave propagation.

Keywords: Hybrid method, BEM, Ray tracing, High frequency scattering

1. Motivations. Aiming at the computational modeling of ultrasonic NDT experiments, we consider the simulation of the diffraction of an ultrasonic wave by a small object whose characteristic diameter r_Γ is similar to the characteristic wavelength λ ($r_\Gamma = O(\lambda)$) and embedded in a spatially large medium ($L \gg \lambda$, see Fig. 1). Neither discretization-based numerical methods (FEM, FDM, BEM...) nor asymptotic methods, if applied in isolation to such configurations, allow for fast or accurate enough simulation: numerical methods are precise but expensive at high frequencies, while asymptotic methods are well-suited for long-distance propagation simulations but inaccurate for diffraction. This leads us to propose a hybrid strategy coupling BEM and ray tracing. The latter is a Lagrangian formulation of geometrical optics, based on a WKB ansatz [3]

$$u(x) = A(x)e^{i\omega\phi(x)}$$

for the primary field variable u . The amplitude A , phase ϕ , and direction of propagation $\hat{d}(x)$ at point $x \in \Omega$, which characterise the ansatz, are evaluated by solving the ray tracing system composed of the eikonal and transport equations, see [3].

We focus here on the implementation of the hybrid strategy to the model problem of 2D

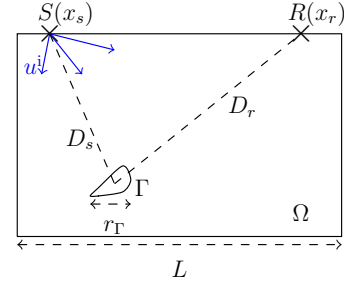


Figure 1: Geometrical setting.

acoustic diffraction.

2. The Hybrid method. The hybrid method relies on a multi-scale approach to solve the scattering problem whereby propagation and diffraction phenomena are treated separately. Its framework is based on the conditions under which far field asymptotics is valid, expressed in terms of two parameters $\alpha := r_\Gamma / \min(D_s, D_r)$ and $\beta := k \min(D_s, D_r)$. In its far field zone, i.e seen from points for which $\alpha \ll 1$, $\beta \gg 1$, and $\alpha\beta = O(1)$, the probed defect can be modelled by a moderate number P of well-chosen points y_c^p , $1 \leq p \leq P$ on its boundary Γ (or by its centroid y_c for sufficiently small r_Γ/λ), as follows. Incident and diffracted waves are approximated as rays $(A_{i/r}, \phi_{i/r}, \hat{d}_{i/r})$ received or emitted by these points. Then, to take the diffraction effect into account by BEM, we first approximate the incident field on the defect as a superposition of plane waves locally defined in the vicinity of each point y_c^p from the incident ray. Using a partition of unity $(\eta_p)_p$ of the boundary we write on the defect $y \in \Gamma$,

$$\begin{aligned} u^i(y) \approx \sum_{p=1}^P \eta_p(y) A_i(y_c^p; x_s) e^{i\omega\phi_i(y_c^p; x_s)} \\ \times e^{i\omega\hat{d}_i(y_c^p) \cdot (y - y_c^p)}. \end{aligned}$$

By linearity of the diffraction problem, we then solve P problems for unknown densities ψ^p supported on Γ , with the Brakhage-Werner indirect

integral equation,

$$\frac{p}{2}(x) + \int_{\Gamma} \left(\frac{\partial G}{\partial \nu(y)} - ikG \right)(x, y)\psi^p(y)ds(y) \\ = -\eta^p(x) e^{i\omega \hat{d}_i(y_c^p) \cdot (x - y_c^p)}, \quad x \in \Gamma, p \in [1, P].$$

Finally, resorting to the far field (relative to defect size r_{Γ}) asymptotics allows to approximate the diffracted wave at a sufficiently-remote receiver x_r as

$$u(x_r) = \sum_{q=1}^P \sum_{q=1}^P A_r(x_r; y_c^q) A_i(y_c^q; x_s) \\ \times e^{i\omega(\phi_r(x_r; y_c^q) + \phi_i(y_c^q; x_s))} \mathcal{R}_p^q(\hat{d}_r(y_c^q), \hat{d}_i(y_c^q)),$$

i.e. a superposition of diffracted rays emitted by each modelization point y_c^q , propagated in the direction $\hat{d}_r(y_c^q)$ and weighted by a diffraction coefficient \mathcal{R}_p^q defined by

$$\mathcal{R}_p^q(\hat{d}_r, \hat{d}_i) = -ik \int_{\Gamma} e^{-ik(\hat{d}_r \cdot (y - y_c^q))} \eta^q(y) \\ \times (1 + \hat{d}_r \cdot \nu(y)) \psi^p(y; \hat{d}_i) ds(y).$$

3. Online-Offline acceleration. Additionally, we have developed an online-offline procedure to reduce the computational cost of the diffraction coefficient evaluation (most expensive operation in the method) to allow a fast treatment of multi-source and multi-receiver configurations which involve large numbers of pairs of incident and diffraction directions. Offline, we evaluate the matrix of the diffraction coefficients for predefined incident and diffraction directions, and compute its truncated low rank approximation using a SVD [4]. Online, we evaluate a polynomial interpolation of the singular matrices in the direction of interest and compute from them an approximation of the diffraction coefficients in the same directions. The acceleration was found in 2D numerical tests to be effective if the number of directions exceeds about 200, and is expected to perform even better under 3D conditions.

4. Numerical experiment. We tested the coupling strategy (in conjunction with the CIVA platform [1]) on the computation of the time response for the diffraction of an ultrasonic plane wave by a small circular hole in a solid rectangular slab immersed into water (Fig. 2). Using (i) CIVA's ray tracing solver to propagate the rays in the media and through their interfaces

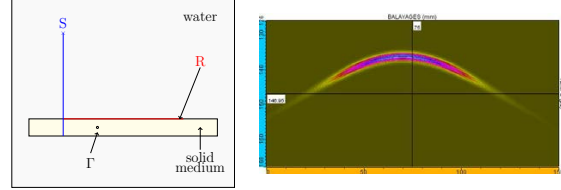


Figure 2: Configuration (left), computed echo for a cylindrical flaw (right).

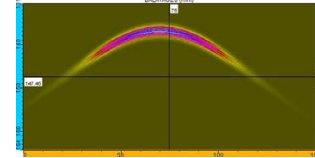


Figure 3: Computed echo for a kite-shaped flaw.

and (ii) a home-made BEM solver to evaluate the diffraction coefficients for a suitable sample of frequencies, and then performing an inverse Fourier transform, we computed the transient diffracted field at points located on a line of receivers (labelled 'R' in Fig.2). We checked that the time reconstruction of our solution coincides with CIVA's obtained from the harmonic analytic evaluation of diffracted field for cylindrical cavities. Besides, we point out that this hybrid strategy brings flexibility in NDT simulations. For the same configuration in CIVA, one can compute the diffraction echo of any flaw geometry of same size, just by changing the diffraction coefficient in CIVA. For the configuration of Fig. 2, we present in Fig. 3 the time response of a kite-shaped flaw in the solid material at the points on the line of receivers.

5. Ongoing work and outlook. Current work aims at extending the presented approach to cases where the defect is close to a boundary. We will then develop its extensions to 3D acoustics before elastodynamics.

References

- [1] <http://www.extende.com>.
- [2] D. Colton, R. Kress, *Inverse acoustic and electromagnetic scattering theory*, Springer, 1998.
- [3] O. Runborg, Mathematical models and numerical methods for high frequency waves, *Comm. In Comp. Physics*, 2:827-880, 2007.
- [4] N. Yarvin, V. Rokhlin, Generalized Gaussian quadratures and singular value decomposition of integral operators, *SIAM J. Sci. Comput.*, 20:699–718, 1998.

An Adaptive DPG Method for High Frequency Time-harmonic Wave Propagation Problems

Socratis Petrides^{1,*}, Leszek F. Demkowicz¹

¹Institute for Computational Engineering and Sciences, UT Austin, Austin, TX, USA

*Email: socratis@ices.utexas.edu

Abstract

In this paper we discuss the discontinuous Petrov-Galerkin (DPG) method for high frequency wave propagation problems. The DPG method offers uniform pre-asymptotic stability for any wave number, and this allows for a fully automatic hp -adaptive algorithm. In addition, being a minimum residual method, DPG always delivers a Hermitian positive definite matrix. We introduce a new iterative solution scheme which benefits from these attractive properties. This novel solver is integrated within the DPG adaptive procedure by constructing a two-grid-like preconditioner for the Conjugate Gradient (CG) method. We demonstrate our results using a 2D acoustics problem and show convergence in terms of iterations at a rate independent of the mesh and the wavenumber.

1 Introduction - Overview of DPG

As a model problem we consider linear acoustics in a bounded domain Ω .

$$\begin{cases} i\omega u + \nabla p = 0, & \text{in } \Omega \\ i\omega p + \operatorname{div} u = 0, & \text{in } \Omega \\ p - u \cdot n = g, & \text{on } \partial\Omega \end{cases} \quad (1)$$

1.1 Different variational formulations

Depending on which norm one seeks to measure convergence, the equations in (1) give rise to four different formulations: the *trivial* or *strong*, the *classical*, the *mixed* and the *ultraweak* [2]. Using methods similar to those in [1], it can be shown that the four formulations are simultaneously well or ill posed.

1.2 Optimal test functions

Discretizing (1) leads in a well posed problem if and only if Babuška's *discrete inf-sup* condition holds. An arbitrary choice of the discrete test space often leads to lack of stability. On the contrary, in the case of the DPG method, one computes on the fly the *optimal test functions* which realize the supremum of the *inf-sup*

condition. We thus obtain a Petrov-Galerkin scheme for which discrete stability is guaranteed even in the pre-asymptotic region.

1.3 Minimum residual method

DPG can also be viewed as a minimum residual method, wherein one minimizes the residual in the norm dual to the test space norm. Consequently, the resulting stiffness matrix is always Hermitian and positive definite, making the use of CG ideal.

1.4 Mixed method

DPG can be interpreted as a mixed method where one solves simultaneously for the solution and the Riesz representation of the residual. The existence of a built-in error indicator and the aforementioned stability properties suggest the use of automatic hp -adaptivity, starting from very coarse meshes.

2 Gaussian beam (resonating cavity)

For reasons outlined in [2] the ultraweak formulation is preferred. The DPG ultraweak formulation of (1) reads:

$$\begin{cases} u \in (L^2(\Omega))^d, \quad p \in L^2(\Omega) \\ \widehat{u \cdot n} \in H^{-1/2}(\Gamma_h), \quad \hat{p} \in H^{1/2}(\Gamma_h) \\ \hat{p} - \widehat{u \cdot n} = g, \quad \text{on } \partial\Omega \\ (i\omega u, v) - (p, \operatorname{div}_h v) + \langle \hat{p}, v \cdot n \rangle = 0 \\ (i\omega p, q) - (u, \nabla_h q) + \langle \widehat{u \cdot n}, q \rangle = 0 \\ \forall v \in H(\operatorname{div}, \Omega_h), \quad q \in H^1(\Omega_h) \end{cases} \quad (2)$$

We demonstrate the adaptive DPG technology by solving a problem that is characterized by a solution with localized behavior. In particular, we use (2) to simulate a Gaussian beam in free space with a cavity in the middle of the domain. The angular frequency is 500π (approximately 350 wavelengths along a 45° angle). Note that the initial mesh is far away from satisfying the Nyquist criterion. In Figures (1, 2) we show the evolution of the mesh and the corresponding numerical solution of the pressure. The mesh is

built along with the solution. The DPG method avoids unnecessary computations in areas of the domain where the wave does not exist.

Figure 1: Meshes

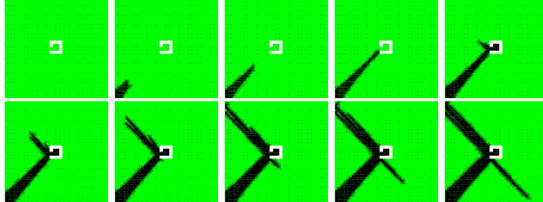
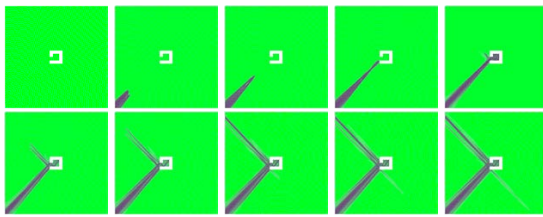


Figure 2: Pressure



3 Solver

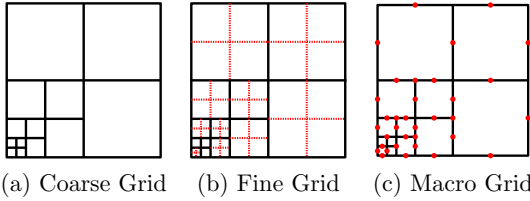
In practice, we are not interested in a fully converged solution at every adaptive step, but only in a solution which is accurate enough to perform reliable refinements. Consequently, an iterative solver would be preferable provided that it is combined with a good preconditioner.

3.1 Two-grid-like solver outline

Direct solver on the coarse grid. We fix an arbitrary mesh throughout the adaptive refinements and solve the problem using a direct solver. We define this to be our *coarse* grid, and we store the Cholesky decomposition of the global stiffness matrix. The Cholesky decomposition is used later in the coarse grid correction.

Macro-element. We now choose a *fine* grid. The *fine grid* is the mesh obtained after arbitrary many adaptive *hp*-refinements applied to the coarse grid.

Figure 3: Macro Grid Definition



We define the *macro* grid to be the resulting mesh after we eliminate all the new degrees of

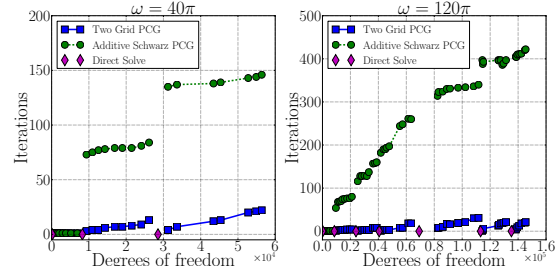
freedom which do not lie on the skeleton of the coarse mesh (Fig.3).

Symmetric two-grid cycle. We perform the symmetric two grid cycle between the coarse and the macro grid and use it as a preconditioner for the CG method. We use the additive Schwarz smoother with patches defined to be the support of a coarse grid vertex basis function. Note that for the coarse grid correction the construction of restriction and prolongation operators reduces to a 1D interpolation problem since the macro grid and the coarse grid have the same topology.

3.2 Results

In Fig 4, we compare the two-grid-like preconditioner with the additive Schwarz. For the two-grid-like preconditioner, we follow a simple strategy, where the coarse grid is redefined every 10 refinements. We show results for angular frequencies $\omega = 40\pi$ and 120π .

Figure 4: Iterations vs dof



The number of iterations for the two-grid-like preconditioner remains bounded and appears to be independent of the frequency and the mesh.

4 Current/future work

Our current work focuses on some theoretical convergence analysis to support our results. Ultimately, we are aiming to build a solver suitable for larger problems arising from 3D computations (3D Maxwell).

References

- [1] Demkowicz, L. and Gopalakrishnan, J., Discontinuous Petrov-Galerkin (DPG) Method. *ICES Report 15-20* (2015).
- [2] Petrides S. and Demkowicz, L., An Adaptive DPG Method for High Frequency Time-harmonic Wave Propagation Problems. *ICES Report 16-20* (2016).

A study of the numerical robustness of single-layer method with Fourier basis for multiple obstacle scattering in homogeneous media

Hélène Barucq^{1,*}, Juliette Chabassier¹, Ha Pham^{1,*}, Sébastien Tordeux¹

¹Inria Magique3D, Pau, France.

*Email: ha.howard@inria.fr

Abstract

We investigate efficient methods to simulate multiple scattering (MS) of obstacles in homogeneous media. With a large number of small obstacles, optimized softwares based on Finite Element Method (FEM) lose their robustness. As an alternative, we work with an integral equation method, which uses single-layer potentials and truncation of Fourier series to describe the scattered field. We limit our numerical experiments to disc-shaped obstacles. We first compare our method with Montjoie (a FEM-based software); secondly, we investigate the efficiency of different solver types (direct and iterative) in solving the dense linear system generated by the method. We observe that the optimal choice depends on the distance between obstacles, their size and number, and applications.

Keywords: small obstacles, acoustic scattering, single layer, GMRES preconditioning.

1 Introduction

This project is part of a program studying direct and inverse problem for acoustic wave in strongly inhomogeneous media. As a first step, we consider inhomogeneities created by a great number of small non-overlapping obstacles. The following discussion are based on our report [1].

The method we use is in the family of Galerkin Boundary Integral Equations; for convenience, we call it Fourier Series - Single Layer (FS-SL). For N_{Obs} non-overlapping obstacles with boundary $\{\Gamma_J\}_{1 \leq J \leq N_{\text{Obs}}}$, the scattered wave is described as a superposition of single-layer potentials with density $V_J \in \mathcal{C}(\Gamma_J)$,

$$u_{\text{scatt}} = \sum_{J=1}^{N_{\text{Obs}}} \int_{\Gamma_J} \frac{i}{4} H_0^{(1)}(\kappa |x - y|) V_J(y) d\sigma(y).$$

The continuous densities are approximated by truncation of their Fourier Series. We choose the single-layer Ansatz, since it gives rise to the simplest integral equations. Generally, acceptable precision ($\sim 10^{-7}$) can be obtained with low approximation order (< 4). As a result, the

linear system (LS) generated by FS-SL, however dense, is small. Moreover, the intrinsic problem regarding invertibility does not arise with small obstacles. We limit our numerical experiments to soft scattering of disc-shaped obstacles. In this geometry, a SL potential can be written as a superposition of multipoles; as a result, the resulting LS-s have explicit expressions.

The use of integral equation, in particular single-layer, in MS problems is not new. In particular, the authors of [3] also used this Ansatz for low and high frequencies. Our numerical experiments can be considered as a complement to their work. On the other hand, our collaboration with the acoustic lab I2M at Université de Bordeaux necessitates the development of robust ‘in-house’ codes, which can be evolved according to our needs. Our codes are written in Fortran 90 with double precision and use a parallel architecture¹. Users can select among the Direct Solvers (Mumps, Lapack and Scalapack), and the iterative GMRES solvers [2] with various preconditioners.

2 Numerical Comparison with FEM

The comparison is done at precision 10^{-3} between Montjoie (MJ) Q6 and FS-SL order 2.

Parameters : Angle of incidence of plane wave (PL) = 90.0 ; Wavenumber $\kappa = 10.0$; Number of obstacles = 200; $\frac{\text{Obs. Rad.}}{\text{Wavelength}} \sim 0.048$; $\frac{\text{Obs. Rad.}}{\text{Obs Dist.}} = 0.1$; $\frac{\text{Obs. Dist.}}{\text{Wavelength (WL)}} \sim 0.48$.

With small linear system, the pre-processing time of FS-SL is small compared to that of MJ.

Time comparison for Pre-processing	FS-SL Order 2	Montjoie CG Q6
Size of linear system (LS)	1000	842677
Task		Duration of time (in secs)
Construction of LS	$5.46e-2$	1.97
Factorization of Coeff mat	0.44	29.8
Resolution (by Mumps)	$2.91e-3$	0.35
Total time	0.498	32.12

For post-processing, one can either evaluate the Hankel function exactly or use a cubic Hermite interpolation. The relative difference in L^2 norm

¹Our tests were run on the cluster Plafrim (www.plafrim.fr).

between two evaluation methods is of order 10^{-5} .

Evaluation on 400 × 400 points	Exact Eval	Inter- polation	Montjoie
Post-pro. time (secs)	26.2	4.30	0.72
Pre + Post time (secs)	26.70	4.80	33.82

Despite the time cost for post-processing, for the final solution, FS-SL is still faster than MJ.

3 Solver comparison

We investigate the efficiency of different solver types in solving the dense LS generated by FS-SL. For iterative solvers, we study the preconditioners associated to Jacobi and Gauss-Seidel, c.f. [1, Appendix C] for definitions.

Numerical Result 2 For closely-spaced obstacles, we observe that the direct solvers outperform the iterative ones. We note the prominent robustness of the Lower-upper Symmetric Gauss-Seidel (LU-SGS) and Symmetric Gauss-Seidel (SGS) among other preconditioners.

Parameters : Method order =2; Angle of incidence = 90.0; Wavenumber = 10.0; $\frac{\text{Obs. Rad.}}{\text{Wavelength}} \sim 0.048$; $\frac{\text{Obs. Rad.}}{\text{Obs Dist.}} = 0.1$; $\frac{\text{Obs. Dist.}}{\text{Wavelength}} \sim 0.48$; Size matrix = $10^4 \times 10^4$. GMRES parameters : Error Tol= 10^{-6} , Iter Max = 5000, Restart = 400.

Solver	Rel diff of density in $H^{1/2}$	# Iter	Time (secs)
Mumps	$3.07E - 10$	n/a	$2.42E + 02$
Lapack	0.0	n/a	8.04E+01
Right LU-SGS	$1.44E - 01$	1146	$5.73E + 02$
Right SGS	$1.47E - 01$	1151	$5.98E + 02$
Scalapack (-n16)	$3.22E - 10$	n/a	3.46E+01

The optimal choice is Scalapack and Hermite interpolation, taking 1 min 10 secs on 16 processors for visualization on a 800×800 grid.

Numerical Result 3 When the obstacles are further apart, GMRES with LU-SGS and SGS regain in performance.

The parameters are the same as above except $\frac{\text{Obs. Rad.}}{\text{WL}} \sim 0.016$, $\frac{\text{Obs. Rad.}}{\text{Obs Dist.}} = 0.005$, $\frac{\text{Obs. Dist.}}{\text{WL}} \sim 3.18$. GMRES parameters : Error Tol= 10^{-7} , Iter Max = 5000, Restart = 500.

Solver	Rel diff of density in $H^{1/2}$	# Iter	Time (secs)
Mumps	0.0	n/a	$2.51e + 02$
Lapack	$4.04e - 12$	n/a	$7.99E + 01$
Right LU-SGS	$2.89e - 04$	57	3.75E+01
Right SGS	$3.50E - 04$	56	3.70E+01
Scalapack (-n16)	$9.27E - 12$	n/a	3.49E+01

For the current configuration, GMRES with LU-SGS is faster than Lapack, and is head-to-head with Scalapack run on 16 processors. We also note that the distance between obstacles has small impact on the direct solvers.

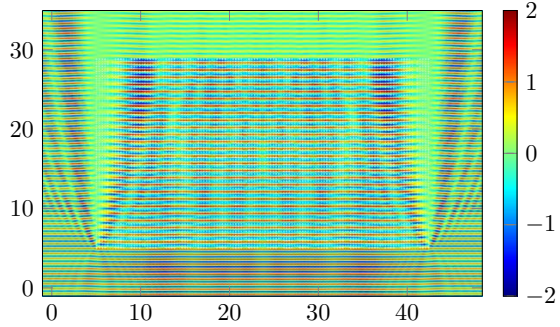


Figure 1: Soft scattering of a planewave coming from the south by 10^4 obstacles, by FS-SL + Scala.+ Hermit inter. Size matrix = 50000×50000 .

Numerical Result 4 Currently, the only solver that can handle very large number of obstacles is Scalapack. For 10000 obstacles with the same parameters as in Experiment 2, FS-SL with Scalapack takes 24 mins 40 secs on 48 processors, see Figure 1.

4 Conclusion

When the obstacles are far-way, under low precision, one can either use Scalapack or GMRES with LUSGS or SGS as preconditioners. When the obstacles are close together, direct solvers are more efficient. Regarding application to inverse problems using full wave inversion technique, direct solvers provide an attractive choice, with higher precision and the feature to resolve linear systems with multiple right hand sides. We are currently extending this work to solid obstacles.

References

- [1] H. Barucq, J. Chabassier, H. Pham, and S. Tordeux. A study of the numerical robustness of single-layer method with Fourier basis for multiple obstacle scattering in homogeneous media. Research Report 8988, Inria Bordeaux, December 2016.
- [2] V. Frayssé, L. Giraud, S. Gratton, and J. Langou. A set of gmres routines for real and complex arithmetics on high performance computers. Technical report, CERFACS, 1997. TR/PA/03/3.
- [3] B. Thierry, X. Antoine, C. Chniti, and H. Alzubaidi. μ -diff: an open-source matlab toolbox for computing multiple scattering problems by disks. *Computer Physics Communications*, 192:348–362, 2015.

Generalized linear sampling method for active imaging of subsurface fractures

Fatemeh Pourahmadian^{1,*}, Bojan B. Guzina², Houssem Haddar³

¹Department of Civil, Environmental and Architectural Engineering, University of Colorado, Boulder, USA

²Department of Civil, Environmental and Geo- Engineering, University of Minnesota, Minneapolis, USA

³INRIA Saclay Ile de France and Ecole Polytechnique (CMAP) Route de Saclay, F-91128, Palaiseau, France

*Email: fatemeh.pourahmadian@colorado.edu

Abstract

A theoretical foundation is developed for active seismic reconstruction of fractures endowed with spatially-varying interfacial condition (e.g. hydraulic fractures). The proposed indicator functional carries a superior localization property with no significant sensitivity to the fracture's contact condition, measurement errors, and illumination frequency. This is accomplished through the paradigm of the F_\sharp -factorization technique and the recently developed Generalized Linear Sampling Method (GLSM) applied to elastodynamics. The analysis of the well-posedness of the forward problem leads to an admissibility condition on the fracture's (linearized) contact parameters. This in turn contributes toward establishing the applicability of the F_\sharp -factorization method, and consequently aids the formulation of a convex GLSM cost functional whose minimizer can be computed without iterations. Such minimizer is then used to construct a robust fracture indicator function, whose performance is illustrated through a set of numerical experiments.

Keywords: inverse scattering, elastic-wave imaging, partially-closed fractures

1 Problem statement

With reference to Fig. 1(a), consider the elastic-wave sensing of a partially closed fracture $\Gamma \subset \mathbb{R}^3$ embedded in a homogeneous, isotropic, elastic solid endowed with mass density ρ and Lamé parameters μ and λ . The fracture is characterized by a heterogeneous contact condition synthesizing the spatially-varying nature of its rough and/or multi-phase interface. Next, let Ω denote the unit sphere centered at the origin. For a given triplet of vectors $\mathbf{d} \in \Omega$ and $\mathbf{q}_p, \mathbf{q}_s \in \mathbb{R}^3$ such that $\mathbf{q}_p \parallel \mathbf{d}$ and $\mathbf{q}_s \perp \mathbf{d}$, the obstacle is illuminated by a combination of compressional

and shear plane waves

$$\mathbf{u}^f(\xi) = \mathbf{q}_p e^{ik_p \xi \cdot \mathbf{d}} + \mathbf{q}_s e^{ik_s \xi \cdot \mathbf{d}} \quad (1)$$

propagating in direction \mathbf{d} , where k_p and $k_s = k_p \sqrt{(\lambda+2\mu)/\mu}$ denote the respective wave numbers. The interaction of \mathbf{u}^f with Γ gives rise to the scattered field $\mathbf{v} \in H_{loc}^1(\mathbb{R}^3 \setminus \Gamma)^3$, solving

$$\begin{aligned} \nabla \cdot (\mathbf{C} : \nabla \mathbf{v}) + \rho \omega^2 \mathbf{v} &= \mathbf{0} && \text{in } \mathbb{R}^3 \setminus \Gamma, \\ \mathbf{n} \cdot \mathbf{C} : \nabla \mathbf{v} - \mathbf{K}(\xi)[\mathbf{v}] - \mathbf{t}^f &= 0 && \text{on } \Gamma, \end{aligned} \quad (2)$$

where $\omega^2 = k_s^2 \mu / \rho$ is the frequency of excitation; $[\mathbf{v}] = [\mathbf{v}^+ - \mathbf{v}^-]$ is the jump in \mathbf{v} across Γ , hereon referred to as the fracture opening displacement (FOD); $\mathbf{C} = \lambda \mathbf{I}_2 \otimes \mathbf{I}_2 + 2\mu \mathbf{I}_4$ is the fourth-order elasticity tensor; \mathbf{I}_m ($m=2, 4$) denotes the m th-order symmetric identity tensor; $\mathbf{t}^f = \mathbf{n} \cdot \mathbf{C} : \nabla \mathbf{u}^f$ is the free-field traction vector; $\mathbf{n} = \mathbf{n}^+$ is the unit normal on Γ , and $\mathbf{K} = \mathbf{K}(\xi)$ is a *symmetric* and possibly *complex-valued* matrix of specific stiffness coefficients mapping the displacement jump to surface traction. The far-field patterns of the scattered waveforms i.e. $\mathbf{v}^\infty := \mathbf{v}_p^\infty \oplus \mathbf{v}_s^\infty$ – defined based on the asymptotic expansion of \mathbf{v}

$$\mathbf{v}(\xi) = \frac{e^{ik_p r}}{4\pi(\lambda+2\mu)r} \mathbf{v}_p^\infty(\hat{\xi}) + \frac{e^{ik_s r}}{4\pi\mu r} \mathbf{v}_s^\infty(\hat{\xi}) + O(r^{-2}),$$

as $r := |\xi| \rightarrow \infty$, are then recorded over the unit sphere of observation directions $\hat{\xi}$.

Theorem (well-posedness). Assume that $\mathbf{t}^f \in H^{-1/2}(\Gamma)^3$ and that $\mathbf{K} \in L^\infty(\Gamma)^{3 \times 3}$ is symmetric such that $\Im \mathbf{K} \leq \mathbf{0}$ on Γ , i.e. that $\bar{\theta} \cdot \Im \mathbf{K}(\xi) \cdot \theta \leq 0$, $\forall \theta \in \mathbb{C}^3$ and a.e. on Γ . Then problem (2) has a unique solution that continuously depends on $\mathbf{t}^f \in H^{-1/2}(\Gamma)^3$.

proof. see [1, Theorem 3.2].

2 Elements of the inverse solution

For given compressional and shear wave densities $\mathbf{g}_p(\mathbf{d}) \parallel \mathbf{d}$ and $\mathbf{g}_s(\mathbf{d}) \perp \mathbf{d}$, $\mathbf{d} \in \Omega$, the elastic Herglotz wave function is defined as

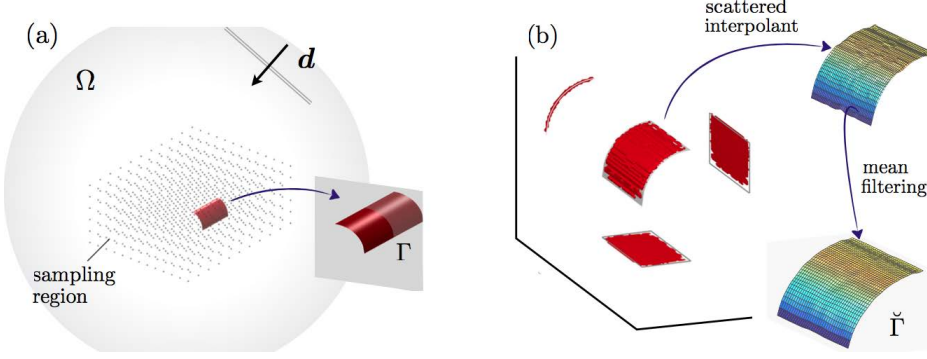


Figure 1: Elastic-wave imaging of a heterogeneous fracture Γ : (a) sensing configuration, and (b) 3D GLSM indicator thresholded at 10% and thus-recovered fracture surface $\tilde{\Gamma}$.

$$\mathbf{u}_g(\xi) := \int_{\Omega} \left\{ \mathbf{g}_p(d) e^{ik_p d \cdot \xi} \oplus \mathbf{g}_s(d) e^{ik_s d \cdot \xi} \right\} dS_d,$$

where $\xi \in \mathbb{R}^3$. In this setting, the far-field operator $F : L^2(\Omega)^3 \rightarrow L^2(\Omega)^3$ is defined by

$$F(\mathbf{g}) = \mathbf{v}_{g_\Omega}^\infty, \quad (3)$$

where $\mathbf{v}_{g_\Omega}^\infty$ is the far-field pattern of $\mathbf{v} \in H_{\text{loc}}^1(\mathbb{R}^3 \setminus \Gamma)^3$ solving (2) with data $\mathbf{u}^f = \mathbf{u}_g$. Based on this, the self-adjoint operator $F_\sharp : L^2(\Omega)^3 \rightarrow L^2(\Omega)^3$ is defined by

$$F_\sharp := |\Re F| + \Im F, \quad (4)$$

$$\Re F = \frac{1}{2}(F + F^*), \quad \Im F = \frac{1}{2i}(F - F^*).$$

It is then shown that both F and F_\sharp possess the following decompositions

$$F = \mathcal{H}^* T \mathcal{H}, \quad F_\sharp = \mathcal{H}^* T_\sharp \mathcal{H}. \quad (5)$$

Here, the Herglotz operator $\mathcal{H} : L^2(\Omega)^3 \rightarrow H^{-1/2}(\Gamma)^3$ is given by

$$\mathcal{H}(\mathbf{g}) := \mathbf{n} \cdot \mathbf{C} : \nabla \mathbf{u}_g \quad \text{on } \Gamma, \quad (6)$$

whose adjoint operator $\mathcal{H}^* : \tilde{H}^{1/2}(\Gamma)^3 \rightarrow L^2(\Omega)^3$ is shown to be compact and injective; The middle operator $T : H^{-1/2}(\Gamma)^3 \rightarrow \tilde{H}^{1/2}(\Gamma)^3$ (resp. T_\sharp) is governed by the contact law at the fracture interface, and given by

$$T(\mathbf{t}^f)(\xi) := [\mathbf{v}(\xi)], \quad \xi \in \Gamma, \quad (7)$$

(resp. [1, Remark 4]). Now, the following properties form the bedrock of the GLSM's theorem and its affiliated indicator, namely: (i) the ranges of \mathcal{H}^* and $F_\sharp^{1/2}$ coincide, and (ii) both operators T and T_\sharp are continuous and coercive i.e.

$$\begin{aligned} (\varphi, T_\sharp(\varphi))_{H^{-\frac{1}{2}}(\Gamma)} &\geq c \|\varphi\|_{H^{-\frac{1}{2}}(\Gamma)}^2, \\ |\langle \varphi, T(\varphi) \rangle| &\geq c \|\varphi\|_{H^{-\frac{1}{2}}(\Gamma)}^2, \quad \forall \varphi \in H^{-1/2}(\Gamma)^3 \end{aligned}$$

where $c, c > 0$ are independent of φ .

3 GLSM criteria for imaging

The essential idea behind GLSM stems from the particular nature of an approximate solution \mathbf{g} to the far-field equation

$$F^\delta \mathbf{g} = \Phi_L^\infty, \quad \|F^\delta - F\| \leq \delta, \quad (8)$$

where $\delta > 0$ is a measure of noise in data, and Φ_L^∞ is the far-field pattern of a trial radiating field, see [1, Definition 2]. In this setting, the behavior of \mathbf{g} in the sampling region is exposed by characterizing the range of \mathcal{H}^* , which then forms the basis for approximating the characteristic function of a hidden fracture. In this vein, let us define the GLSM cost functional by

$$\mathfrak{J}_\alpha(\Phi_L^\infty; \mathbf{g}) := \|F^\delta \mathbf{g} - \Phi_L^\infty\|^2 + \quad (9)$$

$\alpha(|(\mathbf{g}, B^\delta \mathbf{g})| + \delta \|\mathbf{g}\|^2)$, $\mathbf{g} \in L^2(\Omega)^3$, where $\alpha > 0$ and B^δ denotes either F^δ or F_\sharp^δ .

Assuming that B^δ is compact, \mathfrak{J}_α has a minimizer $\mathbf{g}_{\alpha,\delta}^L \in L^2(\Omega)^3$ satisfying

$$\lim_{\alpha \rightarrow 0} \limsup_{\delta \rightarrow 0} \mathfrak{J}_\alpha(\Phi_L^\infty; \mathbf{g}_{\alpha,\delta}^L) = 0. \quad (10)$$

In the case where $B^\delta = F_\sharp^\delta$, the cost functional (9) is convex and that its minimizer is obtained non-iteratively.

Theorem (main). $\Phi_L^\infty \in \text{Range}(\mathcal{H}^*) \iff \left\{ \limsup_{\alpha \rightarrow 0} \limsup_{\delta \rightarrow 0} (|(\mathbf{g}_{\alpha,\delta}^L, B^\delta \mathbf{g}_{\alpha,\delta}^L)| + \delta \|\mathbf{g}_{\alpha,\delta}^L\|^2) < \infty, \right. \quad \iff \quad \left. \liminf_{\alpha \rightarrow 0} \liminf_{\delta \rightarrow 0} (|(\mathbf{g}_{\alpha,\delta}^L, B^\delta \mathbf{g}_{\alpha,\delta}^L)| + \delta \|\mathbf{g}_{\alpha,\delta}^L\|^2) < \infty \right..$

Based on this, a robust GLSM criterion

$$I^G(L) := [|(\mathbf{g}_{\alpha,\delta}^L, B^\delta \mathbf{g}_{\alpha,\delta}^L)| + \delta \|\mathbf{g}_{\alpha,\delta}^L\|^2]^{-1/2}$$

is designed for the reconstruction of heterogeneous fractures, as illustrated in Fig. 1 (b).

References

- [1] F. Pourahmadian and B. B. Guzina and Houssem Haddar, Generalized linear sampling method for elastic-wave sensing of heterogeneous fractures, *Inverse Problems*, **33(5)** 055007.

Adiabatically propagating phase boundaries in non-linear chains with twist and stretch

Prashant K. Purohit^{1,*}

¹Department of Mechanical Engineering and Applied Mechanics, University of Pennsylvania,
Philadelphia, PA 19104, USA.

*Email: purohit@seas.upenn.edu

Abstract

Mass-spring chains with only extensional degrees of freedom have for long provided insights into the behavior of crystalline solids. Here we add rotational degrees of freedom to the masses in a chain and study the dynamics of phase boundaries across which both twist and stretch can jump. Surprisingly, for some combinations of parameters characterizing the energy landscape of our springs we find propagating phase boundaries for which the rate of dissipation, as calculated using isothermal expressions for the driving force, is negative. This suggests that we cannot neglect the energy stored in the oscillations of the masses in the interpretation of the dynamics of mass-spring chains. Thus, we define a local temperature of our chain and show that it jumps across phase boundaries, but not across sonic waves. Hence, impact problems in our mass-spring chains are analogous to those on continuum thermoelastic bars with Mie-Gruneisen type constitutive laws.

Keywords: Phase transitions, non-linear lattices, elastic rods

1 Introduction

Chains of masses and springs (see figure 1) have been used as models to understand thermal properties and phonons in crystalline solids for a long time. When the potentials characterizing the springs have multiple wells then the dynamics of mass-spring chains has been shown to be similar to that of one-dimensional bars capable of phase transitions [1, 2]. This insight has been utilized to extract kinetic relations for moving phase boundaries by comparing solutions of impact and Riemann problems in continuum bars to those in the bistable chains [2].

In this paper we go beyond mass-spring chains in which each mass has just a translational degree of freedom – each of our masses translates and rotates about the line connecting them. The continuum analogue of this mass-spring chain is a rod that can stretch and twist (but not bend).

The dynamics of phase boundaries in such a rod is described by a kinetic relation which connects the thermodynamic driving force across the phase boundary with its velocity. We show that the appropriate kinetic relation is one in which the phase boundary propagates adiabatically.

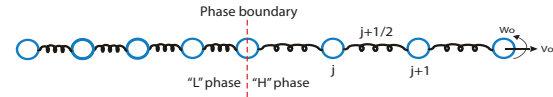


Figure 1: Mass-spring chain in which each mass has an extensional and rotational degree of freedom. A phase boundary separates regions of the chain in which springs are in different phases. Springs in the ‘H’ phase have high strains and those in the ‘L’ phase have low strains. We specify extensional velocity v_0 and rotational velocity w_0 on the masses at the boundary.

2 Thermomechanics of 1-D chain

Let us begin by considering phase boundaries propagating in a one-dimensional continuum representing our chain in the interval $0 \leq x \leq L$. At each reference point we have two variables – the deformed position $z(x, t)$ of the rod cross-section located at x at time t , and $\alpha(x, t)$ the angle through which that cross-section has rotated at time t . We require that $z(x, t)$ and $\alpha(x, t)$ be continuous at all x and t so that the rod does not break. We do not allow bending deformations of the rod. The stretch of the rod is $\lambda(x, t) = \frac{\partial z}{\partial x}$ and the twist is $\kappa(x, t) = \frac{\partial \alpha}{\partial x}$. These quantities are allowed to jump at a finite number of points in our continuum. If one such jump is located at $x = s(t)$ then let us denote $x > s(t)$ as the + side, $x < s(t)$ as the - side. For any quantity $y(x, t)$ we denote $y(x_+, t) - y(x_-, t)$ by $[y]$ and $\frac{y(x_+, t) + y(x_-, t)}{2}$ by $\langle y \rangle$. From continuity of the deformed material we have $[z] = 0$ and $[\alpha] = 0$. Differentiating these two equations with respect to time we get the kinematic

jump conditions

$$\dot{s}[\lambda] + [\dot{z}] = 0, \quad (1)$$

$$\dot{s}[\kappa] + [\dot{\alpha}] = 0. \quad (2)$$

The equation for balance of linear momentum for a portion of the rod in the interval (x_1, x_2) in the absence of body forces is $\frac{d}{dt} \int_{x_1}^{x_2} \rho \dot{z} dx = T|_{x_1}^{x_2}$, where $\rho(x, t)$ is the mass per unit length and $T(x, t)$ is the tension in the rod [1,2]. If we localize this equation to a discontinuity $s(t)$ (with $x_1 \leq s(t) \leq x_2$) then we get the linear momentum jump condition

$$[T] + \dot{s}[\rho v] = 0, \quad (3)$$

with $v(x, t) = \dot{z}$. The equation for the balance of angular momentum for a portion of the rod in the interval (x_1, x_2) in the absence of body moments is $\frac{d}{dt} \int_{x_1}^{x_2} \rho r_g^2 \dot{\alpha} dx = M|_{x_1}^{x_2}$, where r_g is the radius of gyration of the cross-section and $M(x, t)$ is the torque in the rod. If we localize this equation to a discontinuity $s(t)$ (with $x_1 \leq s(t) \leq x_2$) then we have

$$[M] + \dot{s}[\rho r_g^2 w] = 0, \quad (4)$$

where $w(x, t) = \dot{\alpha}$. Starting from the balance laws given above one can derive an expression for the isothermal driving force across a discontinuity which is given by

$$f_{driving} = [W] - \langle T \rangle [\lambda] - \langle M \rangle [\kappa], \quad (5)$$

where $W(\lambda, \kappa)$ is the Helmholtz free energy per unit length of our continuum. We imagine that $W(\lambda, \kappa)$ has two wells located at different points on the $\lambda - \kappa$ plane. The phase corresponding to low (high) values of λ and κ is denoted as $j = L(j = H)$, and in each phase $W(\lambda, \kappa)$ assumes a quadratic form.

3 Results

Our major result is that the use of eqn. (5) gives *negative* dissipation rates that violate the second law of thermodynamics. To re-examine the negative dissipation rate cases, we introduce a temperature in our analysis defined locally at mass j through

$$k\Theta_j(t) = KE_j(t) + PE_{j+\frac{1}{2}}(t) - E_j^{cont}. \quad (6)$$

Here, $KE_j(t)$ is the kinetic energy of the j^{th} mass at time t , $PE_{j+\frac{1}{2}}(t)$ is the potential energy

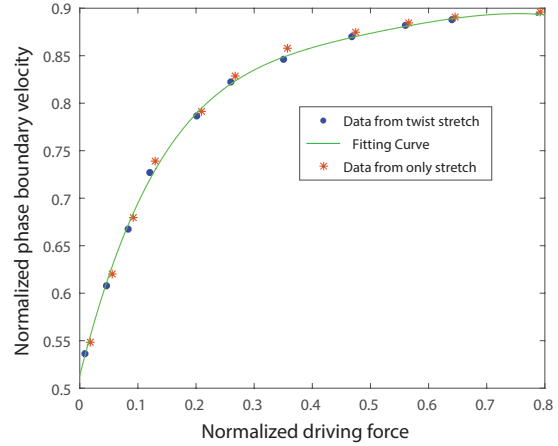


Figure 2: Adiabatic driving force as a function of phase boundary velocity in a chain.

of the spring between mass j and mass $j + 1$ at time t and E_j^{cont} is the sum of kinetic energy at mass j and potential energy in spring $j + \frac{1}{2}$ computed using the average values of the velocities and strains that satisfy the continuum jump conditions, $E_j^{cont} = \frac{1}{2}m_j\langle \dot{u}_j \rangle^2 + \frac{1}{2}I_j\langle \dot{\theta}_j \rangle^2 + \phi_1(\langle z_j - z_{j-1} \rangle, \langle \alpha_j - \alpha_{j-1} \rangle)$, where $\langle y \rangle$ is the temporal average of y over a time corresponding to few periods and ϕ_1 is the potential energy of one spring. k is proportional to a specific heat in the continuum theory. So, our definition of the local temperature captures the ‘thermal’ portion of the energy in the chain that is neglected in a purely mechanical continuum theory. The appropriate expression for the driving force across a phase boundary in such a situation is

$$f_{driving} = -E \log(1 + \frac{[\Theta]}{\Theta_-}), \quad (7)$$

where we treat Θ_- and E as constants. This driving force gives non-negative dissipation rates and is plotted in figure 2.

References

- [1] Q. Zhao and P.K. Purohit, (Adiabatic) phase boundaries in a bistable chain with twist and stretch, *J. Mech. Phys. Solids* **92** (2016), pp. 176–194.
- [2] R. Abeyaratne and J.K. Knowles *Evolution of phase transitions: A continuum theory*, Cambridge University Press, New York, 2006.

Imaging defects in an elastic waveguide using time-dependent surface data

Vahan Baronian¹, Laurent Bourgeois², Arnaud Recoquillay^{12,*}

¹CEA, LIST, Gif-sur-Yvette, France

²Laboratoire POEMS, ENSTA ParisTech, Palaiseau, France

*Email: arnaud.recoquillay@ensta-paristech.fr

Abstract

We are interested here in using the Linear Sampling Method [1] in its modal form [2] to image defects in an elastic waveguide by using realistic scattering data, that is data coming from sources and receivers on the surface of the waveguide in the time domain, as it has already been done in the acoustic case [3].

Keywords: Linear Sampling Method, surface data, waveguide, elasticity, time domain

1 The Linear Sampling Method: a modal formulation

Let the space dimension be 2. We consider a waveguide $W = \Sigma \times \mathbb{R}$ of transverse section Σ and boundary Γ . This waveguide is made of an isotropic material of density ρ and Lamé constants (λ, μ) . Let be denoted \mathbf{u} the displacement, σ the stress tensor associated with \mathbf{u} following $\sigma(\mathbf{u}) = \lambda(\operatorname{div} \mathbf{u}) I + \mu(\nabla \mathbf{u} + \nabla \mathbf{u}^T)$, and let us decompose

$$\mathbf{u} = \begin{pmatrix} \mathbf{u}_S \\ u_3 \end{pmatrix}, \quad \sigma \cdot \mathbf{e}_3 = \begin{pmatrix} \mathbf{t}_S \\ -t_3 \end{pmatrix},$$

where the subscripts S and 3 denote the components of a vector along the transverse section and along the axis, respectively. We introduce the mixed variables \mathbf{X}, \mathbf{Y} defined by:

$$\mathbf{X} = \begin{pmatrix} \mathbf{t}_S \\ u_3 \end{pmatrix}, \quad \mathbf{Y} = \begin{pmatrix} \mathbf{u}_S \\ t_3 \end{pmatrix}.$$

The guided modes are the solutions with separated variables to $\operatorname{div}\sigma(\mathbf{u}) + \rho\omega^2 \mathbf{u} = 0$ in W with boundary condition $\sigma(\mathbf{u}) \cdot \nu = 0$ on Γ , where ν is the exterior normal to W . They are given for $n \in \mathbb{N}$ by

$$\begin{pmatrix} \mathbf{X}_n^\pm(x) \\ \mathbf{Y}_n^\pm(x) \end{pmatrix} = \begin{pmatrix} \pm \mathcal{X}_n(\mathbf{x}_S) \\ \mathcal{Y}_n(\mathbf{x}_S) \end{pmatrix} e^{\pm i\beta_n x_3},$$

with $(\mathcal{X}_n, \mathcal{Y}_m)_\Sigma = \delta_{mn}$, where $(\cdot, \cdot)_\Sigma$ is a scalar product over $L^2(\Sigma)$ without complex conjugation.

For a given frequency ω , β_n is real for only a finite number of guided modes, which are named propagating modes. The other ones are either inhomogenous or evanescent. Because we only consider far fields, thoses modes will not be taken into account.

The assumption is then made that any elastic field, written in the (\mathbf{X}, \mathbf{Y}) variables, can be decomposed as follows:

$$\mathbf{X}|_\Sigma = \sum_n (\mathbf{X}, \mathcal{Y}_n)_\Sigma \mathcal{X}_n, \quad \mathbf{Y}|_\Sigma = \sum_n (\mathcal{X}_n, \mathbf{Y})_\Sigma \mathcal{Y}_n.$$

We then consider a defect D inside the waveguide which lies between two sections Σ_\pm and denote $\Omega = W \setminus \overline{D}$. The scattered field $\mathbf{u}_n^{s\pm}$ (and its \mathbf{Y} extension $\mathbf{Y}_n^{s\pm}$) associated to the incident propagating mode \mathbf{u}_n^\pm is solution of the following forward problem for a given frequency ω :

$$\left\{ \begin{array}{ll} \operatorname{div}\sigma(\mathbf{u}_n^{s\pm}) + \rho\omega^2 \mathbf{u}_n^{s\pm} = 0 & \text{in } \Omega, \\ \sigma(\mathbf{u}_n^{s\pm}) \cdot \nu = 0 & \text{on } \Gamma, \\ \mathbf{u}_n^{s\pm} = -\mathbf{u}_n^\pm & \text{on } \partial D, \end{array} \right. \quad (RC),$$

with (RC) a radiation condition. The data in this case are the components of the scattering matrix \mathcal{S} , namely the projections $\mathcal{S}_{mn}^{\pm\pm}$ along the \mathcal{X}_m on the two sections Σ_\pm of the scattered fields $\mathbf{Y}_n^{s\pm}$, the number of lines and columns being limited to $2P$. The Linear Sampling Method consists in solving the following system for all sampling points $z = (z_S, z_3)$:

$$\left\{ \begin{array}{l} \sum_{n=0}^{P-1} \mathcal{U}_{mn}^{+-} h_n^- + \mathcal{U}_{mn}^{--} h_n^+ = e^{i\beta_m(R+z_3)} \mathcal{Y}_m(z_S) \cdot \mathbf{p}, \\ \sum_{n=0}^{P-1} \mathcal{U}_{mn}^{++} h_n^- + \mathcal{U}_{mn}^{-+} h_n^+ = e^{i\beta_m(R-z_3)} \mathcal{Y}_m(z_S) \cdot \mathbf{p}, \end{array} \right.$$

$m = 0, \dots, P-1$, where

$$\mathcal{U} = \mathcal{S} \begin{pmatrix} K & 0 \\ 0 & K \end{pmatrix},$$

K is the $P \times P$ diagonal matrix the components of which are $e^{i\beta_n R} / 2i\beta_n$, $\pm R$ is respectively the

x_3 coordinate of the section Σ_{\pm} and \mathbf{p} is a polarisation parameter. If, roughly speaking, a solution $H = (h^-, h^+)$, with $h^{\pm} = (h_1^{\pm}, \dots, h_P^{\pm})$, is found, then $z \in D$ according to a classical result related to the LSM [2].

2 The case of surface solicitations and measurements

The method shown above needs data within the waveguide, which is not realistic in the context of Non Destructive Evaluation. We write $\Gamma = \Gamma_0 \cup \Gamma_d$, d being the height of the waveguide and Γ_0 and Γ_d being respectively its lower and upper boundary. A family of source functions $(\mathbf{g}_i^{\pm}(x))_{1 \leq i \leq M} = (\mathbf{g}(x - x_i^{\pm}))_{1 \leq i \leq M}$ is defined for an even and compactly supported function \mathbf{g} defined on \mathbb{R} with $x_i^{\pm} = \pm(R + i\delta)$. The diffraction problem satisfied by the total field \mathbf{u} is:

$$\left\{ \begin{array}{ll} \operatorname{div}\sigma(\mathbf{u}) + \rho\omega^2\mathbf{u} = 0 & \text{in } \Omega, \\ \sigma(\mathbf{u}) \cdot \nu = \mathbf{g}_i^{\pm} & \text{on } \Gamma_d \\ \sigma(\mathbf{u}) \cdot \nu = 0 & \text{on } \Gamma_0, \\ \mathbf{u} = 0 & \text{on } \partial D, \\ (\mathcal{RC}). \end{array} \right. \quad (1)$$

The corresponding scattered field \mathbf{u}^s is $\mathbf{u} - \mathbf{u}^i$, where \mathbf{u}^i solves the same problem (1) as \mathbf{u} in W without the boundary condition $\mathbf{u} = 0$ on ∂D . Our data are the components of a matrix \mathcal{M} of general term defined by a single component of the scattered fields measured at points $(d, x_j^{\pm})_{1 \leq j \leq M}$ for all sources $(\mathbf{g}_i^{\pm})_{1 \leq i \leq M}$. The measurement matrix \mathcal{M} is related to the LSM matrix \mathcal{U} by the relationship

$$\mathcal{M} = -\mathcal{R}\mathcal{U}\mathcal{E}^T, \quad (2)$$

where \mathcal{R} and \mathcal{E} are some reception and emission matrices. The conditioning of these matrices can be rigorously analyzed and optimized: it strongly depends on the number $2M$ of sources and receivers and on the minimal distance δ between them. Inverting the system (2) enables to compute \mathcal{U} and then to apply the modal LSM as in section 1.

The above method can be extended to the 3D case by considering one or several lines of source and measurement points.

3 The case of data in the time domain

In the time domain, we consider the following problem:

$$\left\{ \begin{array}{ll} \rho\partial_t^2\mathbf{u} - \operatorname{div}\sigma(\mathbf{u}) = 0 & \text{in } \Omega \times (0, +\infty), \\ \sigma(\mathbf{u}) \cdot \nu = \mathbf{g}_i^{\pm}(x)\chi(t) & \text{on } \Gamma \times (0, +\infty), \\ \mathbf{u} = 0 & \text{on } \partial D \times (0, +\infty), \\ \mathbf{u} = \partial_t\mathbf{u} = 0 & \text{on } \Omega \times \{0\}. \end{array} \right.$$

The data consist of the corresponding scattered fields measured at the same points as before in the time interval $(0, +\infty)$. Here, $\chi(t)$ is suitably chosen so that the frequencies for which the group velocity vanishes are avoided. By applying a Fourier transform to our data, we recover the previous system (1) at a given frequency ω . We now have multi-frequencies data, which allows us to image the defect with a better accuracy than in the frequency domain. In the figure below, the reconstruction is done using multiple frequencies which correspond to a number of propagating modes P ranging from 8 to 14.

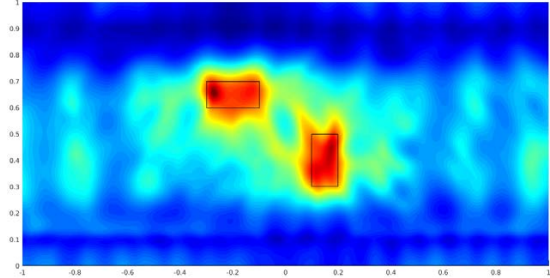


Figure 1: Defect identification with artificial data using multiple frequencies, $M = 42$

References

- [1] D. Colton, A. Kirsch: A simple method for solving inverse scattering problems in the resonance region, in *Inverse Problems* **12** (1996) pp. 383-393.
- [2] L. Bourgeois, F. Le Louër, E. Lunéville: On the use of Lamb modes in the linear sampling method for elastic waveguides, in *Inverse Problems* **27** (2011).
- [3] V. Baronian, L. Bourgeois, A. Recoquillay: Imaging an acoustic waveguide from surface data in the time domain, in *Wave Motion* **66** (2016) pp. 66-87.

Localized time-periodic solutions of nonlinear wave equations

Wolfgang Reichel^{1,*}

¹Department of Mathematics, Karlsruhe Institute of Technology, Karlsruhe, Germany

*Email: wolfgang.reichel@kit.edu

Abstract

We collect some results obtained recently for time-periodic solutions of nonlinear wave equations. The model problem arises from Maxwell's equations in the presence of nonlinear material responses. The emphasis will be on the aspect of *localization*, i.e., the effect of having solutions that decay to zero in the (unbounded) spatial directions.

Keywords: nonlinear wave equation, breathers, calculus of variations, polychromatic solutions

1 The problem

Our problem consists in finding suitable conditions on the coefficient $V : \mathbb{R}^3 \rightarrow \mathbb{R}$ and the nonlinear function $f : \mathbb{R}^3 \times \mathbb{R} \rightarrow \mathbb{R}$ such that spatially localized, time-periodic solutions $E : \mathbb{R}^3 \times \mathbb{R} \rightarrow \mathbb{R}^3$ exists either for the quasilinear problem

$$\nabla \times \nabla \times E + \partial_t^2 (V(x)E + f(x, |E|^2)E) = 0 \quad (1)$$

or the semilinear problem

$$\nabla \times \nabla \times E + V(x)\partial_t^2 E + f(x, |E|^2)E = 0. \quad (2)$$

(1) arises, e.g., from a nonlinear Maxwell model without charges and currents

$$\begin{aligned} \nabla \times E + \partial_t B &= 0, & \nabla \cdot D &= 0, \\ \nabla \times H - \partial_t D &= 0, & \nabla \cdot B &= 0 \end{aligned}$$

and with Kerr-type nonlinear material laws

$$B = \mu_0 H, \quad D = \epsilon_0(1 + \chi_1(x) + \chi_3(x)|E|^2)E.$$

2 Time harmonic solutions of (1)

The ansatz: $E(x, t) = U(x)e^{i\omega t}$ reduces (1) to the stationary problem

$$\nabla \times \nabla \times U + \tilde{V}(x)U = \tilde{f}(x, |U|^2)U \text{ in } \mathbb{R}^3 \quad (3)$$

with $\tilde{V} = -\omega^2 V$ and $\tilde{f} = \omega^2 f$. Our results are based on the variational characterization of solutions of (3) as critical points of the functional

$$J[U] = \int_{\mathbb{R}^3} |\nabla \times U|^2 + \tilde{V}(x)|U|^2 - \tilde{F}(x, |U|^2) dx$$

where $\tilde{f}(x, s) = \partial_s \tilde{F}(x, s)$. For the following three theorems, cf. [1], [3], we make the assumption of cylindrical symmetry $\tilde{V} = \tilde{V}(r, x_3)$, $\tilde{f} = \tilde{f}(r, z, s)$, $r = \sqrt{x_1^2 + x_2^2}$. We denote by $\sigma(L)$ the spectrum of a selfadjoint linear operator $L = \nabla \times \nabla \times + \tilde{V}(x)$.

Theorem 1 (Defocusing case) *Let $\tilde{f}(x, s) = \tilde{\Gamma}(x)|s|^{\frac{p-1}{2}}$. If $\tilde{V}, \tilde{\Gamma}$ satisfy*

$$(i) \quad \tilde{\Gamma}(x) \leq -C(1 + |x|^\alpha), \quad \alpha > \frac{3}{2}(p-1), \quad p > 1,$$

$$(ii) \quad \tilde{V} \in L^\infty(\mathbb{R}^3), \quad \sup \tilde{V} < 0$$

then (3) has a ground-state.

Theorem 2 (Focusing case) *Let $\tilde{f}(x, s) = \tilde{\Gamma}(x)|s|^{\frac{p-1}{2}}$ with $1 < p < 5$ and let $\tilde{V}, \tilde{\Gamma} \in L^\infty(\mathbb{R}^3)$ be 1-periodic with $\inf \tilde{\Gamma} > 0$. If $0 \notin \sigma(L)$ then (3) has a ground-state.*

Additionally, examples of cylindrically symmetric coefficients \tilde{V} are constructed with $0 \notin \sigma(L)$.

Theorem 3 (Positive definite case) *Let L have positive spectrum and assume*

$$(i) \quad \tilde{V}(r, z) \text{ is reverse Steiner-symmetric in } z,$$

$$(ii) \quad 0 \leq \tilde{f}(r, z, s) \leq C(1 + s^{\frac{p-1}{2}}), \quad 1 < p < 5,$$

$$(iii) \quad \tilde{f}(r, z, s) = o(1) \text{ as } s \rightarrow 0 \text{ unif. in } r, z,$$

$$(iv) \quad s \mapsto \tilde{f}(r, z, s) \text{ strictly increasing in } s,$$

$$(v) \quad \tilde{F}(r, z, s)/s \rightarrow \infty \text{ as } s \rightarrow \infty \text{ unif. in } r, z,$$

$$(vi) \quad \phi_\sigma(r, z, s) := \tilde{f}(r, z, (s + \sigma)^2)(s + \sigma)^2 - \tilde{f}(r, z, s^2)s^2 \text{ is symmetrically decreasing in } z \text{ for all } s \geq 0, \sigma \geq 0.$$

Then (3) has a ground-state.

Examples of nonlinearities satisfying (i)–(vi) are given.

3 Real-valued breathers for (2)

Except for the sine-Gordon breather and [2] very few examples of real-valued breather solutions for nonlinear wave equations are known. However, for the vector-valued semilinear problem (2) with $f(x, s) = q(x) \pm \Gamma(x)|s|^{\frac{p-1}{2}}$ the following result was proven in [4].

Theorem 4 Let $T = 2\pi\sqrt{\frac{V(0)}{q(0)}}$ and $p > 1$. Assume V, q and Γ are positive radially symmetric and C^2 with $\sup \frac{q}{\Gamma} < \infty$ and $T\sqrt{\frac{q(r)}{V(r)}} \leq 2\pi$ on $\mathbb{R}^3 \setminus \{0\}$. Assume further that

$$\left| 2\pi - T \sqrt{\frac{q(r)}{V(r)}} \right|^{\frac{1}{p-1}} = \begin{cases} O(e^{-\alpha r}) & \text{as } r \rightarrow \infty, \\ o(1) & \text{as } r \rightarrow 0. \end{cases}$$

Then (2) has a non-zero T -periodic, real-valued, exponentially decaying solution.

The idea is to reduce (2) via the ansatz $E(x, t) = \psi(r, t)\frac{x}{r}$, $r = |x|$ to an ODE in time with $r = |x|$ as a parameter and to discuss the ODE in phase space. Under exactly the same assumptions on q, V, Γ also complex-valued exponentially decaying solutions $E(x, t) = e^{i\frac{2\pi}{T}t}\psi(r)\frac{x}{r}$ exist.

Our final example illustrates how real-valued breathers can be constructed via the calculus of variations. Here we consider $f(x, s) = \Gamma(x)|s|$ and polarized solutions $E(x, t) = (0, u(x_1, t), 0)^T$ with a real valued time-periodic profile $u : \mathbb{R} \times \mathbb{R} \rightarrow \mathbb{R}$. With V, Γ depending only on x_1 and writing x instead of x_1 the wave equation (2) becomes

$$V(x)u_{tt} - u_{xx} = \Gamma(x)u^3 \text{ in } \mathbb{R} \times \mathbb{R}.$$

Our special choice is

$$V(x) = \delta(x), \quad V(x) = \alpha + \beta\delta^{per}(x), \quad \alpha, \beta > 0,$$

i.e., Γ is the delta-distribution centered at 0 and V is made from a 1-periodic extension of the delta-distribution centered at 1/2. (2) will be solved by an even-in- x function $u(-x, t) = u(x, t)$ satisfying the nonlinear Neumann problem

$$\begin{cases} V(x)u_{tt} - u_{xx} &= 0 \text{ in } (0, \infty) \times \mathbb{R}, \\ -2\partial_x u(0, t) &= u(0, t)^3, \\ u(x, t) &\rightarrow 0 \text{ as } x \rightarrow \infty \\ u(x, t+T) &= u(x, t) \end{cases} \quad (4)$$

Theorem 5 Let $\alpha > 0$, $\beta > 4\alpha/\pi$. Then (4) has infinitely many real-valued breathers which are even in x and $T/2$ -antiperiodic in t with $T = 4\sqrt{\alpha}$.

The variational framework comes into play as follows. We use a Fourier-decomposition in time

$$u(x, t) = \sum_{k \text{ odd}} a_k \phi_k(x) e^{ik\omega t}, \quad a_{-k} = \bar{a}_k$$

with normalized Bloch-modes ϕ_k which are exponentially decaying as $x \rightarrow \infty$ and $\phi_k(0) = 1$. The nonlinear Neumann boundary condition

$$-2\partial_x u(0, t) = u(0, t)^3$$

becomes for odd $k = 2l + 1$

$$\pi|k|(-1)^l a_k + O(1)a_k = (a * a * \bar{a})_k. \quad (5)$$

In the suitable sequence Hilbert-space solutions of (5) can be found as critical points of a strongly indefinite functional $J : H \rightarrow \mathbb{R}$.

Concluding remarks. By construction we get polychromatic waves $\sum_k a_k \phi_k(x) e^{ik\omega t}$ with $a_k \neq 0$ for infinitely many k . Here even the ground-states are polychromatic.

References

- [1] Th. Bartsch, T. Dohnal, M. Plum, and W. Reichel. Ground states of a nonlinear curl-curl problem in cylindrically symmetric media. *NoDEA Nonlinear Differential Equations Appl.*, 23(5):23:52, 2016.
- [2] C. Blank, M. Chirilus-Bruckner, V. Lescarret, and G. Schneider. Breather solutions in periodic media. *Comm. Math. Phys.*, 302(3):815–841, 2011.
- [3] A. Hirsch and W. Reichel. Existence of cylindrically symmetric ground states to a nonlinear curl-curl equation with non-constant coefficients. arXiv:1606.04415[math.AP]. To appear in *Z. Anal. Anwend.*
- [4] M. Plum and W. Reichel. A breather construction for a semilinear curl-curl wave equation with radially symmetric coefficients. arXiv:1610.09203[math.AP]. To appear in: *J. Elliptic Parabol. Equ.*

Non-linear Tikhonov Regularization for Inverse Scattering from Anisotropic Media

Marcel Rennoch^{1,*}, Armin Lechleiter¹

¹Center for Industrial Mathematics, University of Bremen, Germany

*Email: mrennoch@math.uni-bremen.de

Abstract

Considering time-harmonic inverse scattering of either electromagnetic or acoustic waves from an inhomogeneous anisotropic medium, we provide Tikhonov and sparsity-promoting regularization techniques in Banach spaces. To this end we analyze the dependence of the scattered fields and their derivatives on material parameters of an admissible set equipped with L^p -topology. Therewith we first show convergence of non-linear Tikhonov regularization against a minimum-norm solution and second extend that method to a sparsity-promoting one.

Keywords: inverse medium scattering, regularization, sparsity

1 The scattering problem

We consider a penetrable and anisotropic inhomogeneous medium $D \subset \mathbb{R}^d$ ($d = 2, 3$ in the acoustic and $d = 3$ in the electromagnetic case), which is either described by a matrix-valued contrast $Q \in \mathbb{C}^{d \times d}$ in the acoustic case or by the inverse of relative permittivity $\varepsilon_r \in \mathbb{C}^{3 \times 3}$ in the case of electromagnetic scattering, where D is additionally assumed to be non-magnetic. To simplify notation both material parameters will be named ρ in the sequel, an element of a bounded subset \mathcal{P} of $L^p = L^p(B, \mathbb{C}^{d \times d})$ for $p \in [1, \infty]$ in the acoustic and $p = \infty$ in the electromagnetic case on a ball B containing \overline{D} . Roughly speaking \mathcal{P} provide some bounds for the real and imaginary parts of ρ , such that the underlying solution approach as well as basic concepts of scattering theory are applicable, using Meyers' bounds [1, 2] in the acoustic case.

The propagation of acoustic scattered waves u^s in \mathbb{R}^d generated by an incident field u^i is governed by

$$\operatorname{div}((\operatorname{Id} + \rho) \nabla u^s) + k^2 u^s = -\operatorname{div}(\rho \nabla u^i), \quad (1)$$

and the scattered magnetic field H^s in \mathbb{R}^3 by

$$\operatorname{curl}(\rho \operatorname{curl} H^s) - k^2 H^s = \operatorname{curl}((\operatorname{Id} - \rho) \operatorname{curl} u^i). \quad (2)$$

Note that the scattered fields are radiating, i.e. u^s satisfies Sommerfeld's radiation condition

$$\lim_{|x| \rightarrow \infty} |x|^{(d-1)/2} \left(\frac{\operatorname{du}^s}{\operatorname{d}|x|}(x) - ik u^s(x) \right) = 0,$$

and H^s the Silver-Müller radiation condition

$$\lim_{|x| \rightarrow \infty} \operatorname{curl} H^s(x) \times \hat{x} - ik H^s(x) = 0,$$

both uniformly in all directions $\hat{x} = x/|x|$ of the unit sphere \mathbb{S}^{d-1} .

2 The solution operator

Because we require u^s to be locally H^1 and accordingly $H^s \in H_{\operatorname{loc}}(\operatorname{curl}, \mathbb{R}^3)$, the solutions of (1) and (2) have to be understood in the weak sense, i.e. partially integrated against test functions gain sesquilinear forms, with corresponding solution operators $\mathbf{L}(\rho, u^i)$.

Under the assumption of unique solvability for all parameters $\rho \in \mathcal{P}$, one can show that existence and continuous dependence of this solution follows from uniqueness due to the theory of Riesz-Fredholm. Since we will handle perturbations ρ' of ρ , we therefore assume that ρ' is small enough such that $\rho + \rho' \in \mathcal{P}$. Then we have that the solution operator is continuous and differentiable in the following sense:

Theorem 1 For $\{\rho'_n\}_{n \in \mathbb{N}}$ such that $\rho + \rho'_n \in \mathcal{P}$ for all $n \in \mathbb{N}$ and $\|\rho'_n\|_{L^p} \xrightarrow{n \rightarrow \infty} 0$, it holds that

$$\frac{\|\mathbf{L}(\rho + \rho'_n, u^i) - \mathbf{L}(\rho, u^i) - \mathbf{L}'(\rho, u^i)[\rho'_n]\|_{H^1}}{\|\rho'_n\|_{L^p}} \rightarrow 0.$$

3 The forward operator

From now on, we rely on incident fields u^i in form of Herglotz wave functions

$$v_g(x) = \int_{\mathbb{S}^{d-1}} e^{ikx \cdot \theta} g(\theta) \operatorname{d}S(\theta), \quad \text{for } x \in \mathbb{R}^d$$

and for $g \in L^2(\mathbb{S}^{d-1})$ (or rather for square-integrable tangential vector fields $g \in L_t^2(\mathbb{S}^2)$), that solve the homogeneous Helmholtz equation or Maxwell's equations.

Since the scattered field $L(\rho, v_g)$ (representative for the acoustic or rather the electromagnetic problem) has an asymptotic behavior as a spherical function for $|x| \rightarrow \infty$, its far field pattern $(L(\rho, v_g))^\infty$ defines the well-known far field operator F_ρ on $L^2_{(t)}(\mathbb{S}^{d-1})$ such that $F_\rho g = (L(\rho, v_g))^\infty$. Now, for $q \in [1, \infty)$ we denote the q th Schatten class by \mathcal{S}_q , a Banach space of compact operators on $L^2_{(t)}(\mathbb{S}^{d-1})$. Then using a trace class operator, which—roughly speaking—maps the total field $L(\rho, v_g) + v_g$ to the corresponding far field pattern, allows to define a contrast-to-far field mapping

$$F : \mathcal{P} \times L^2_{(t)}(\mathbb{S}^{d-1}) \rightarrow \mathcal{S}_q, \quad q \geq 1,$$

which becomes the forward operator of our problem. Note that F_ρ is compact and belongs to the set \mathcal{S}_1 of trace class operators on $L^2_{(t)}(\mathbb{S}^{d-1})$, as the integral kernel $(L(\rho, v_g))^\infty : \mathbb{S}^{d-1} \times \mathbb{S}^{d-1} \rightarrow \mathbb{C}$ of $F(\rho)$ is analytic in both variables. Due to the embedding $\ell^p \subset \ell^q$ for $1 \leq p < q \leq \infty$, it even belongs to \mathcal{S}_q .

Since the forward operator F is linked to the solution operator L , its properties of continuity and differentiability can be transferred.

4 Regularization results

For the inverse problem we consider the stable approximation of ρ_{exa} from perturbed measurements of its far field operator $F(\rho_{\text{exa}})$. In detail, we seek to approximate ρ for noisy measurements F_{meas}^δ such that

$$\|F(\rho_{\text{exa}}) - F_{\text{meas}}^\delta\|_{\mathcal{S}_q} \leq \delta.$$

Therefore for a convex regularization functional \mathcal{R} we minimize the Tikhonov functional

$$\mathcal{J}_{\alpha, \delta}(\rho) := \frac{1}{2} \|F(\rho) - F_{\text{meas}}^\delta\|_{\mathcal{S}_q}^2 + \alpha \mathcal{R}(\rho).$$

4.1 The acoustic case

In the acoustic case we can benefit from the compact embedding of W^{1,p_*} into L^p , where $p_* = \frac{dp}{p+d} \in (1, d)$, such that a classical non-linear Tikhonov regularization result, e.g. see [3], is derived for $\mathcal{R}(\rho) = \|\rho\|_{W^{1,p_*}}^{p_*}$.

A sparsity-promoting alternative is based on a wavelet basis of W^{1,p_*} , such that

$$\mathcal{R}(\rho) = \frac{1}{r} \sum_j \omega_j |\rho_j|^r \geq C(r) \|\rho\|_{W^{1,p_*}}^r,$$

for $r \in [1, p_*]$ and wavelet coefficients ρ_j (e.g. Daubechies or Meyer wavelets).

Recall that ρ^\dagger is called a \mathcal{R} -minimizing solution to $F(\rho^\dagger) = F(\rho_{\text{exa}})$, if

$$\mathcal{R}(\rho^\dagger) = \min_{\mathcal{R}(\rho)} \{\rho \in \mathcal{P} \cap W^{1,p_*}, F(\rho) = F_{\text{exa}}\}.$$

Thus we gain a statement of sparsity regularization:

Theorem 2 $\mathcal{J}_{\alpha, \delta}$ possesses a minimizer in $\mathcal{P} \cap W^{1,p_*}$. If $\delta_n \rightarrow 0$ and $\alpha_n = \alpha_n(\delta_n)$ such that

$$0 < \alpha_n \rightarrow 0 \quad \text{and} \quad 0 < \delta_n^2 / \alpha_n \rightarrow 0,$$

then every sequence of minimizers of $\mathcal{J}_{\alpha_n, \delta_n}$ contains a subsequence, weakly converging to an \mathcal{R} -minimizing solution ρ^\dagger in \mathcal{S}_q .

4.2 The electromagnetic case

Somewhat weaker results compared to Theorem 2 can also be stated in the electromagnetic case via the following approach:

Let ρ_j be coefficients of a wavelet basis in L^2 such that all basis functions are also in L^∞ . Thus a weighted ℓ^p -norm then gives an appropriate penalty term,

$$\mathcal{R}(\rho) = \frac{1}{p} \sum_j \omega_j |\rho_j|^p, \quad p \in (1, 2],$$

for weights $(\omega_j)_j$ satisfying $\|\rho\|_{L^\infty} \leq \mathcal{R}(\rho)$

To avoid Hölder continuous spaces one can otherwise handle functions of bounded variation. Therefore we restrict the parameter set such that also the total variation of $\rho \in \mathcal{P}$ is bounded and thus the penalty term becomes

$$\mathcal{R}(\rho) = \|\rho\|_{BV} = \|\rho\|_{L^1} + TV(\rho).$$

References

- [1] N. G. Meyers, An L^p -estimate for the gradient of solutions of second order elliptic divergence equations, *Annali della Scuola Norm. Sup. Pisa* **17** (1963), pp. 189–206.
- [2] A. Lechleiter and M. Rennoch, Non-linear Tikhonov Regularization in Banach Spaces for Inverse Scattering from Anisotropic Penetrable Media, *Inverse Problems and Imaging*, **11** (2017), pp. 151–176.
- [3] T. Schuster, B. Kaltenbacher, B. Hofmann, and K. S. Kazmierski, *Regularization Methods in Banach Spaces* De Gruyter, 2012

Searching for a stochastic background of gravitational radiation

Joseph D. Romano¹, Neil J. Cornish²

¹Department of Physics, University of Texas Rio Grande Valley, Brownsville, TX, USA

²Department of Physics, Montana State University, Bozeman, MT, USA

Abstract

We give a brief introduction to stochastic gravitational-wave backgrounds and discuss the standard detection methods used to search for them.

Keywords: gravitational radiation, stochastic backgrounds, detection methods

1 Introduction

The direct detection of gravitational waves (GWs) by the Laser Interferometric Gravitational-Wave Observatory (LIGO) [1] has opened a radically new way of observing the universe. The first detected event (GW150914) was observed on Sep 14th, 2015 by the two LIGO detectors [2]. The observed signal consisted of the final inspiral and merger of a pair of black holes (roughly $30 M_{\odot}$ each) at a distance of ~ 1.3 billion light-years from Earth. The energy in the GWs emitted by this system was approximately $3M_{\odot}c^2$, corresponding to a peak luminosity of more than 10 times the combined luminosity of all the stars in all the galaxies in the visible universe! The second event (GW151226), observed on Dec 26th 2015, also consisted of the inspiral and merger of a pair of black holes, this time with component masses of approximately $14 M_{\odot}$ and $7 M_{\odot}$, at a distance of ~ 1.4 billion light years from Earth [3]. The fact that such energetic events were observed only in terms of the GWs they emitted illustrates the potential for new discoveries that comes with the opening of this new window onto the universe.

2 Stochastic gravitational waves

GW150914 and GW151226 were single events, observable with both template-based and burst searches with relatively high significance [2, 3]. But in addition to these “loud” events, we expect there to be many more “quiet” events (at larger distances from Earth or with smaller component masses), which cannot be *individually* detected. The combined signal from the final mergers of binary black holes from the population that gave rise to GW150914 and GW151226

is “popcorn-like”, in the sense that the duration of an individual signal is small compared to the separation in time between successive signals. Since the individual arrival times are randomly distributed, the combined signal is itself random—i.e., an example of a *stochastic background* of gravitational radiation.

More generally, a stochastic background of gravitational radiation is *any* random signal produced by a large number of weak, independent, and unresolved sources. A stochastic background can be popcorn-like (described above) or it can be a *confusion noise*, produced by signals that overlap in time or frequency. It can be either astrophysical or cosmological in origin. In many ways, a stochastic GW background is analogous to the cosmic microwave background (CMB)—a stochastic background of *electromagnetic* radiation, produced roughly 400,000 years after the Big Bang.

Given the weakness of the gravitational interaction, cosmological GWs are expected to decouple from matter in the very early universe much earlier than any other form of radiation. The detection of a cosmological background would thus allow us to study the physics of the earliest times and highest energy scales, unachievable in standard laboratory experiments. On the other hand, the detection of a stochastic background of astrophysical origin, such as that from the population of binary black holes, would provide information about the spatial distribution and formation rate of this source.

3 Characterizing stochastic GWs

The simplest type of stochastic background is *Gaussian, stationary* (in time), *unpolarized*, and *isotropic* (GW power on the sky equal from all directions). Such a background is characterized by a single quantity $S_h(f)$, which is the GW strain *power spectral density* (units strain²/Hz) summed over both polarizations and integrated over the sky. It is related to the fractional en-

ergy density spectrum $\Omega_{\text{gw}}(f)$ via

$$\Omega_{\text{gw}}(f) \equiv \frac{1}{\rho_c} \frac{d\rho_{\text{gw}}}{d \ln f} = \frac{2\pi^2}{3H_0^2} f^3 S_h(f), \quad (1)$$

where $\rho_c = 3c^2 H_0^2 / 8\pi G^2$ is the critical energy density needed to close the universe. For an *anisotropic* distribution of GWs, the background is described by a function $\mathcal{P}(f, \hat{n})$, which specifies the GW power coming from direction \hat{n} . It is related to $S_h(f)$ via $S_h(f) = \int d^2\Omega_{\hat{n}} \mathcal{P}(f, \hat{n})$.

4 Distinguishing signal from noise

Detecting a stochastic background is challenging because a stochastic signal is effectively another source of noise in a single detector. As such, one must either construct null combinations of the data (which act as an instrumental noise monitor), or use instrumental noise modeling to help distinguish the GW signal component from instrumental noise. Better yet, with two or more detectors, one can *cross-correlate* the data, taking advantage of the *common* GW signal incident on all detectors. Cross-correlation is a robust method for searching for a stochastic background, provided the instrumental and environmental noise are not also correlated across the detectors.

5 Detection methods

To claim detection of a stochastic GW background, one needs to show that the observed data are more consistent with a model \mathcal{M}_1 that consists of a stochastic signal plus instrumental noise than with a model \mathcal{M}_0 that consists of instrumental noise alone. This can be done [4] using either *frequentist statistics* or *Bayesian inference*, both of which are typically based on a *likelihood function* $p(d|\vec{\theta}_\alpha, \mathcal{M}_\alpha)$, which gives the probability of the observed data d , given a model \mathcal{M}_α having parameters $\vec{\theta}_\alpha$. From the likelihood function, one can construct the (frequentist) *maximum-likelihood ratio* statistic

$$\Lambda_{\text{ML}}(d) \equiv \frac{\max_{\vec{\theta}_1} p(d|\vec{\theta}_1, \mathcal{M}_1)}{\max_{\vec{\theta}_0} p(d|\vec{\theta}_0, \mathcal{M}_0)}, \quad (2)$$

or *Bayes' factor* (for Bayesian inference)

$$\mathcal{B}_{10}(d) \equiv \frac{\int d\vec{\theta}_1 p(d|\vec{\theta}_1, \mathcal{M}_1)p(\vec{\theta}_1|\mathcal{M}_1)}{\int d\vec{\theta}_0 p(d|\vec{\theta}_0, \mathcal{M}_0)p(\vec{\theta}_0|\mathcal{M}_0)}, \quad (3)$$

where $p(\vec{\theta}_\alpha|\mathcal{M}_\alpha)$ is the prior probability distribution for the parameters $\vec{\theta}_\alpha$ associated with

model \mathcal{M}_α . A large value of $\Lambda_{\text{ML}}(d)$ or $\ln \mathcal{B}_{10}(d)$ is evidence in favor of model \mathcal{M}_1 over \mathcal{M}_0 .

6 Observational results

To date, a stochastic background of gravitational radiation has not been detected, but there are constraints on the strength of both isotropic and anisotropic backgrounds using data from a variety of detectors spanning the GW spectrum. Figure 1 shows current and projected bounds on $\Omega_{\text{gw}}(f)$ for an isotropic background from CMB measurements, pulsar timing observations (PTA), and ground-based interferometers [5].

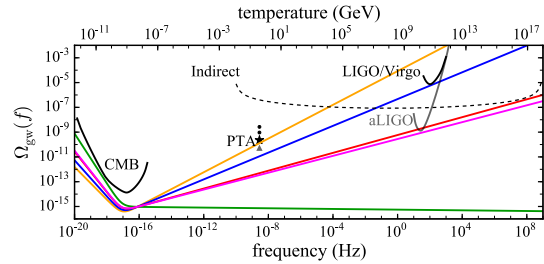


Figure 1: Current and projected bounds on $\Omega_{\text{gw}}(f)$. The colored lines are different theoretical predictions for a cosmological background.

References

- [1] J. Aasi et al., “Advanced LIGO.” *Class. Quantum Grav.*, **32**, 074001 (2015).
- [2] B.P. Abbott et al., “Observation of Gravitational Waves from a Binary Black Hole Merger,” *Phys. Rev. Lett.*, **116**(6), 061102 (February 2016).
- [3] B.P. Abbott et al., “GW151226: Observation of Gravitational Waves from a 22-Solar-Mass Binary Black Hole Coalescence,” *Phys. Rev. Lett.*, **116**(24), 241103 (June 2016).
- [4] J.D. Romano and N.J. Cornish, “Detection methods for stochastic gravitational-wave backgrounds: A unified treatment,” *Living Reviews in Relativity* (to appear) (2017).
- [5] P.D. Lasky et al., “Gravitational-wave cosmology across 29 decades of frequency,” *Phys. Rev.*, **X6**(1), 011035 (2016).

Adiabatic invariants of the extended KdV equation

Piotr Rozmej^{1,*}, Anna Karczewska², Eryk Infeld³, George Rowlands⁴

¹ Faculty of Physics and Astronomy, University of Zielona Góra, Poland

²Faculty of Mathematics, Computer Science and Econometrics, University of Zielona Góra, Poland

³National Centre for Nuclear Research, Warszawa, Poland

⁴Department of Physics, University of Warwick, Coventry, UK

*Email: P.Rozmej@if.uz.zgora.pl

Abstract

When higher order, beyond KdV, shallow water equations are considered, momentum and energy are no longer exact invariants. However, adiabatic invariants (AI) can be found. Their existence results from the general theory of near-identity transformations (NIT) which allow us to transform higher order nonintegrable equations to asymptotically equivalent (when small parameters tend to zero) integrable form. The exactness of these adiabatic invariants is shown in numerical tests.

Keywords: 02.30.Jr, 05.45.-a, 47.35.Bb

1 Introduction

It is a well known fact that the Korteweg – de Vries equation (KdV) possesses an infinite number of invariants, see, e.g. [1, 2], also known as *integrals of motion*. The lowest order invariant assures volume conservation of the fluid (as the fluid is assumed to be incompressible this is equivalent to mass conservation). The second invariant is related to the conservation of the fluid momentum. The third order KdV invariant is related to the energy. This relation is not so obvious. As shown in [3, 4] the energy of the fluid has an invariant form only in a particular reference frame moving with the velocity of sound. In the fixed frame energy has a noninvariant form. However, it varies only by a small fraction, particularly when collisions of solitons occur, see [4].

Several authors have extended the KdV to second order (KdV2). Here the term **second order** means the order of perturbation expansion with respect to small parameters. However, this improved form is short of exactly conserved entities other than the ubiquitous mass law.

2 Extended KdV equation

We consider the second order KdV equation [4, Eq. (1)], (α and β are small expansion param-

eters, $\alpha = a/h$, $\beta = (h/l)^2$, where a, h, l are wave amplitude, water depth and average wavelength, respectively)

$$\begin{aligned} \eta_t + \eta_x + \frac{3}{2}\alpha\eta\eta_x + \frac{1}{6}\beta\eta_{3x} - \frac{3}{8}\alpha^2\eta^2\eta_x \\ + \alpha\beta\left(\frac{23}{24}\eta_x\eta_{2x} + \frac{5}{12}\eta\eta_{3x}\right) + \frac{19}{360}\beta^2\eta_{5x} = 0, \end{aligned} \quad (1)$$

called by Marchant and Smyth [5, Eq. (2.8)] the "extended KdV". We call it KdV2.

It is well known, see, e.g. [2, Ch. 5], that an equation of the form

$$\frac{\partial T}{\partial t} + \frac{\partial X}{\partial x} = 0, \quad (2)$$

where neither T (an analog to density) nor X (an analog to flux) contain partial derivatives with respect to t , corresponds to some *conservation law*. It can be applied, in particular, to the KdV equations and to the equations of KdV type like (1). If both functions T and X_x are integrable on $(-\infty, \infty)$ and $\lim_{x \rightarrow \pm\infty} X = \text{const}$ (soliton solutions), then integration of equation (2) yields

$$\frac{d}{dt} \left(\int_{-\infty}^{\infty} T dx \right) = 0 \quad \text{or} \quad \int_{-\infty}^{\infty} T dx = \text{const}. \quad (3)$$

$$\text{since } \int_{-\infty}^{\infty} X_x dx = X(\infty, t) - X(-\infty, t) = 0. \quad (4)$$

The same conclusion applies for periodic solutions (cnoidal waves), when in the integrals (3), (4) limits of integration $(-\infty, \infty)$ are replaced by (a, b) , where $b - a = \Lambda$ is the space period of the cnoidal wave (the wave length).

In [4], we noted that $I^{(1)} = \int_{-\infty}^{\infty} \eta dx$ is an invariant of equation (1) and represents the conservation of mass.

The second invariant of KdV, $I^{(2)} = \int_{-\infty}^{\infty} \eta^2 dx$ is *not* an invariant of KdV2, since upon multiplication of equation (1) by η one obtains

$$0 = \frac{\partial}{\partial t} \frac{\eta^2}{2} + \frac{\partial}{\partial x} F(\eta, \eta_x, \dots, \eta_{4x}) + \frac{1}{8}\alpha\beta\eta\eta_x\eta_{2x}. \quad (5)$$

Since the last term in (5) cannot be expressed as $\frac{\partial}{\partial x} X(\eta, \eta_x, \dots)$, $\int_{-\infty}^{+\infty} \eta^2 dx$ is not a conserved quantity. There are no exact higher order invariants of (1).

3 Near-identity transformation (NIT)

In [7] we derived an AI for KdV2 using mainly a direct method consisting in an approximate elimination of nonintegrable terms in equations like (5). In this paper we stress another method based on NIT introduced in 1985 by Kodama [8]. NIT allows us to transform a given second order KdV type equation into Hamiltonian form if one neglects higher (third) order terms in the resulting equation. Introduce a near-identity transformation of the following form

$$\eta = \eta' + \alpha a \eta'^2 + \beta b \eta'_{xx} + \dots \quad (6)$$

[In the following we use the sign +. The inverse transformation, up to second order terms, is $\eta' = \eta - \alpha a \eta^2 - \beta b \eta_{xx} + \dots$].

When (6) is inserted into KdV2 (1) and third order terms neglected the resulting equation for η' has the same form as (1) but with some coefficients altered. This property allows us to choose the parameters a, b of NIT such that the transformed KdV2 equation takes a Hamiltonian form. This condition implies

$$\frac{\beta}{\alpha} a - 3b = -\frac{1}{8} \frac{\beta}{\alpha}. \quad (7)$$

Then there exist exact invariants of the transformed KdV2 equation which under inverse NIT transformation become adiabatic invariants of original equation (1). The general form of the second invariant is then

$$\int_{-\infty}^{\infty} \eta'^2 dx \int_{-\infty}^{\infty} [\eta^2 - 2\alpha a \eta^3 + 2\beta b \eta_x^2] dx. \quad (8)$$

The third invariant is

$$\begin{aligned} I_{\text{ad}}^{(3)} = & -\frac{1}{4} \int_{-\infty}^{\infty} \left\{ \left(\eta^3 - \frac{1}{12} \frac{\beta}{\alpha} \eta_x^2 \right) \right. \\ & + \alpha \left[\left(-\frac{5}{2} a - \frac{1}{8} \right) \eta^4 + \left(\frac{19}{180} + \frac{2}{3} b \right) \frac{\beta^2}{\alpha^2} \eta_{2x}^2 \right. \\ & \left. \left. - \frac{\beta}{\alpha} \left(\left(\frac{5}{6} - 6b \right) \eta \eta_x^2 + \frac{4}{3} a \eta \eta_{2x}^2 \right) \right] \right\} dx. \end{aligned} \quad (9)$$

In (8)-(9) a, b have to fulfil relation (7). Our numerical studies [7] confirmed that relative deviations of these AI from constant values are indeed very small (of the order of 10^{-5} – 10^{-4}) for several multisoliton waves evolving according to the KdV2.

References

- [1] R.M. Miura, C.S. Gardner, M.D. Kruskal, *KdV equation and generalizations II. Existence of conservation laws and constants of motion*, J. Math. Phys., **9** 1204-1209 (1968).
- [2] P.G. Drazin, R.S. Johnson, *Solitons: An Introduction*, Cambridge University Press, Cambridge, 1989.
- [3] A. Ali, H. Kalisch, *On the formulation of mass, momentum and energy conservation in the KdV equation*, Acta Appl. Math., **133**, 113-131 (2014).
- [4] A. Karczewska, P. Rozmej, E. Infeld, *Energy invariant for shallow-water waves and the Korteweg-de Vries equation: Doubts about the invariance of energy*, Physical Review E, **92**, 053202 (2015).
- [5] T.R. Marchant, N.F. Smyth, *The extended Korteweg-de Vries equation and the resonant flow of a fluid over topography*, J. Fluid Mech., **221**, 263-288 (1990).
- [6] A. Karczewska, P. Rozmej, E. Infeld, *Shallow-water soliton dynamics beyond the Korteweg-de Vries equation*, Physical Review E, **90**, 012907 (2014).
- [7] A. Karczewska, P. Rozmej, E. Infeld and G. Rowlands *Adiabatic invariants of the extended KdV equation*, Physics Letters A, **381**, in press. arXiv:1512.01194.
- [8] Y. Kodama, *On integrable systems with higher order corrections* Phys. Lett. A, **107**, 245-249 (1985); *Normal forms for weakly dispersive wave equations*, Phys. Lett. A, **112**, 193-196 (1985).

Mathematical Analysis of Plasmonic Nanoparticles

Habib Ammari¹, Pierre Millien², Francisco Romero¹, Matias Ruiz^{3,*}, Hai Zhang⁴

¹Seminar for Applied Mathematics, ETH, Zurich, Switzerland

²Institut Langevin, Paris, France

³Department of Mathematics and Applications, Ecole Normale Supérieure, Paris, France

⁴Department of Mathematics, HKUST, Hong Kong, China

*Email: matias.ruiz@ens.fr

Abstract

Using layer potential techniques we explore the plasmon resonance phenomenon for nanoparticles. We give asymptotic formulas on the size of the particle for: the shift in the resonances as the size of the particles increases, the far and inner field at the plasmonic resonances and the heat generated by them.

Keywords: plasmonic resonances, layer potentials, Neumann-Poincaré operator

1 Introduction

Plasmon resonant nanoparticles are particles whose size range in the order of a few to a hundred nanometers and whose material has a negative permittivity and permeability. These properties give them unique capabilities of enhancing the brightness and directivity of light, confining strong electromagnetic fields, and outcoupling of light into advantageous directions, when illuminated at the right frequency [3]. Plasmonic nanoparticles find their use, among many, as labels in molecular biology and thermotherapy as nanometric heat-generators.

As the size of the nanoparticles increases, the resonance frequency shifts. This was observed in, for instance, [2]

In this paper we present results concerning their mathematical analysis using layer potential and asymptotic analysis techniques. We precisely quantify the shift phenomenon and give asymptotic formulas for the far field, inner far field and heat generation.

2 Layer potential formulation

Let u^i be the incident wave of frequency ω and D be the particle of size δ . The scattering problem for a TM polarized wave can be modeled by

the following Helmholtz equation

$$\begin{aligned} \nabla \cdot \frac{1}{\mu_D} \nabla u + \omega^2 \varepsilon_D u &= 0 \quad \text{in } \mathbb{R}^2 \setminus \partial D, \\ u_+ - u_- &= 0 \quad \text{on } \partial D, \\ \left. \frac{1}{\mu_m} \frac{\partial u}{\partial \nu} \right|_+ - \left. \frac{1}{\mu_c} \frac{\partial u}{\partial \nu} \right|_- &= 0 \quad \text{on } \partial D, \end{aligned} \tag{1}$$

and $u - u^i$ satisfies the Sommerfeld radiation condition. Here

$$k_m = \omega \sqrt{\varepsilon_m \mu_m}, \quad k_c = \omega \sqrt{\varepsilon_c \mu_c},$$

and

$$\varepsilon_D = \varepsilon_m \chi(\mathbb{R}^3 \setminus \bar{D}) + \varepsilon_c \chi(\bar{D}), \quad \mu_D = \varepsilon_m \chi(\mathbb{R}^3 \setminus \bar{D}) + \varepsilon_c \chi(D),$$

We assume that ε_m and μ_m are real and strictly positive and that $\Re \mu_c < 0$ and $\Im \mu_c > 0$. Let $G(x, y, k)$ be the green function for the Helmholtz equation. By using the following single-layer potential and Neumann-Poincaré integral operator

$$\begin{aligned} \mathcal{S}_D^k[\psi](x) &= \int_{\partial D} G(x, y, k) \psi(y) d\sigma(y), \quad x \in \mathbb{R}^2, \\ (\mathcal{K}_D^k)^*[\psi](x) &= \int_{\partial D} \frac{\partial G(x, y, k)}{\partial \nu(x)} (y) d\sigma(y), \quad x \in \partial D, \end{aligned}$$

we can represent the solution u in the following form

$$u(x) = \begin{cases} u^i + \mathcal{S}_D^{k_m}[\psi], & x \in \mathbb{R}^2 \setminus \bar{D}, \\ \mathcal{S}_D^{k_c}[\phi], & x \in D, \end{cases}$$

where $\psi, \phi \in H^{-\frac{1}{2}}(\partial D)$ satisfies the following system of integral equations on ∂D :

$$\begin{cases} \mathcal{S}_D^{k_m}[\psi] - \mathcal{S}_D^{k_c}[\phi] = u^i, \\ \frac{1}{\mu_m} \left(\frac{1}{2} Id + (\mathcal{K}_D^{k_m})^* \right)[\psi] + \frac{1}{\mu_c} \left(\frac{1}{2} Id - (\mathcal{K}_D^{k_c})^* \right)[\phi] \\ = \frac{\partial u^i}{\partial \nu}, \end{cases} \tag{2}$$

In what follows we note $\mathcal{K}_D^* := (\mathcal{K}_D^0)^*$ and $\mathcal{S}_D = \mathcal{S}_D^0$.

3 Main results

We write system (2) as $\mathcal{A}(\delta, \omega)[\psi, \phi] = [u^i, \frac{\partial u^i}{\partial \nu}]$.

The plasmonic resonances occur when an eigenvalue of $\mathcal{A}(\delta, \omega)$ approaches zero. In the limit where the size of the particle is going to zero (or quasi-static limit), the resonance occurs at the frequencies where $\lambda_\mu := \frac{\mu_c + \mu_m}{2(\mu_c - \mu_m)}$ is very close to one of the eigenvalues of the Neumann-Poincare operator \mathcal{K}_D^* . We note this eigenvalues by $\lambda_0, \lambda_1, \lambda_2, \dots$ and by $\varphi_0, \varphi_1, \varphi_2, \dots$ the associated eigenfunctions.

Using asymptotic analysis in system (2) we have the following theorem, which confirms the quasi-static approximation for plasmonic resonances and quantifies the shift in the resonances as the particles size increases.

Theorem 1 *Let $\tau_0, \tau_1, \tau_2, \dots$ be the eigenvalues of $\mathcal{A}(\delta, \omega)$. The following asymptotic expansion hold*

$$\tau_j(\omega) = \lambda_\mu - \lambda_j + (\omega\delta)^2 \log(\omega\delta)\tau_{j,1} + O((\omega\delta)^2),$$

where

$$\tau_{j,1} = -(\mathcal{A}_{D,1}[\varphi_j], \mathcal{S}_D[\varphi_j])_{L^2},$$

and $\mathcal{A}_{D,1}$ is a compact operator on $L^2(\partial D)$.

Finding asymptotic solutions to system (2) gives asymptotic expansion in the far field and inner field.

Theorem 2 *The solution u to (1), for x away from the domain D , centered at the origin, has the following asymptotic uniformly in x*

$$\begin{aligned} u(x) &= u^i(x) + \nabla_y G(x, 0, k_m) \cdot M(\lambda_\mu, D) \nabla u^i(0) \\ &\quad + O\left(\frac{\delta^4}{\text{dist}(\lambda_\mu, \sigma(\mathcal{K}_D^*))}\right), \end{aligned}$$

where $\sigma(\mathcal{K}_D^*)$ denotes the spectrum of \mathcal{K}_D^* in $L^2(\partial D)$ and $M(\lambda_\mu, D) := \int_{\partial D} (\lambda_\mu Id - \mathcal{K}_D^*)^{-1}[\nu] x d\sigma(x)$.

Theorem 3 *The solution u to (1), inside the domain D , centered at the origin, has the following asymptotic in $L^2(D)$*

$$\begin{aligned} u &= u^i(0) + \left(\delta x + \mathcal{S}_D(\lambda_\mu Id - \mathcal{K}_D^*)^{-1}[\nu] \right) \cdot \nabla u^i(0) \\ &\quad + O\left(\frac{\delta^3}{\text{dist}(\lambda_\mu, \sigma(\mathcal{K}_D^*))}\right), \end{aligned}$$

where ν is the outward-going normal to D .

The inner field enhancement translates into a change of temperature governed by the heat equation

$$\left\{ \begin{array}{l} \rho C \frac{\partial \tau}{\partial t} - \nabla \cdot \gamma \nabla \tau = \frac{\omega}{2\pi} \Im(\varepsilon) |u|^2, \quad \text{in } (\mathbb{R}^2 \setminus \bar{D}) \times (0, T) \\ \tau_+ - \tau_- = 0 \quad \text{on } \partial D, \\ \gamma_m \frac{\partial \tau}{\partial \nu} \Big|_+ - \gamma_c \frac{\partial \tau}{\partial \nu} \Big|_- = 0 \quad \text{on } \partial D, \\ \tau(x, 0) = 0, \end{array} \right. \quad (3)$$

where $\rho = \rho_c \chi(D) + \rho_m \chi(\mathbb{R}^2 \setminus \bar{D})$ is the mass density, $C = C_c \chi(D) + C_m \chi(\mathbb{R}^2 \setminus \bar{D})$ is the thermal capacity, $\gamma = \gamma_c \chi(D) + \gamma_m \chi(\mathbb{R}^2 \setminus \bar{D})$ is the thermal conductivity and $T \in \mathbb{R}$ is the final time of measurements.

Theorem 4 *Let u be the solution to (1). The solution τ to (3), in the boundary of a plasmonic particle occupying a domain D , has the following asymptotic, uniformly in $(x, t) \in \partial D \times (0, T)$*

$$\begin{aligned} \tau &= F_D + \mathcal{V}_D^{b_c}(\lambda_\gamma Id - \mathcal{K}_D^*)^{-1} \left[\frac{\partial F_D}{\partial \nu} \right] \\ &\quad + O\left(\frac{\delta^4 \log \delta}{\text{dist}(\lambda_\mu, \sigma(\mathcal{K}_D^*))^2}\right). \end{aligned}$$

where $\mathcal{V}_D^{b_c}$ is the single layer heat potential, ν is the outward-going normal to D , $\lambda_\gamma := \frac{\gamma_c + \gamma_m}{2(\gamma_c - \gamma_m)}$, $b_c := \frac{\rho_c C_c}{\gamma_c}$ and

$$F_D := \frac{\omega}{2\pi\gamma_c} \Im(\varepsilon_c) \int_0^t \int_D \frac{e^{-\frac{|x-y|^2}{4b_c(t-t')}}}{4\pi b_c(t-t')} |u|^2(y) dy dt'.$$

4 References

References

- [1] H. Ammari, P. Millien, M. Ruiz, Hai Zhang, “Mathematical analysis of plasmonic nanoparticles: the scalar case.” submitted.
- [2] R. Giannini, C.V. Hafner, and J.F. Löffler, Scaling behavior of individual nanoparticle plasmon resonances, *J. Phys. Chem. C*, 119 (2015), 6138–6147.
- [3] D. Sarid and W. A. Challener, *Modern Introduction to Surface Plasmons: Theory, Mathematical Modeling, and Applications*, Cambridge University Press, New York, 2010.

Wave Attenuation Along a Rough Floating Elastic Beam

Sebastian Rupprecht^{1,*}, Luke G. Bennetts², Malte A. Peter¹

¹Institute of Mathematics, University of Augsburg, Germany

²School of Mathematical Sciences, University of Adelaide, Australia

*Email: sebastian.rupprecht@math.uni-augsburg.de

Abstract

Semi-analytical and numerical methods are presented to describe the attenuation of water waves in a two-dimensional fluid domain, which has its surface covered by a rough thin elastic beam and is of finite depth. Roughness of the beam is incorporated via a random process describing the variations in the properties of the beam's mass and rigidity. The semi-analytical method is based on a multiple-scale expansion of the velocity potential, from which an equation can be derived describing the attenuation of the effective wave field. The numerical results, which are obtained via a step-approximation method, validate the multiple-scale approach for small-amplitude beam roughness.

Keywords: random media, wave attenuation, effective wave field, multiple-scale approach

Introduction

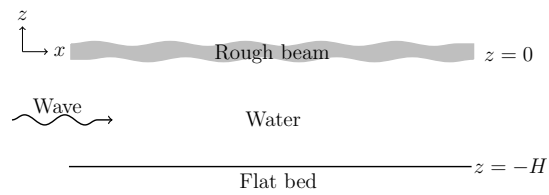
Scattering and wave-localisation phenomena occur in many branches of wave science for incident waves propagating through rough (randomly disordered) media. However, models for wave propagation along elastic plates floating on water are often based on homogeneous plate assumptions, i.e. constant material properties and constant thickness. This assumption may not hold and the wave-propagation characteristics over large distances may be affected by the plate roughness causing attenuation of the waves.

Here, we extend the work of Rupprecht et al. [1] who considered wave propagation along a rough thin-elastic beam in vacuo to a model of a rough thin-elastic beam floating on water of finite depth. This extension introduces a vertical dimension to the problem, and a 5th-order boundary condition at the interface of water and the elastic beam has to be satisfied. The beam roughness is modelled by small-amplitude, continuous variations in beam mass and rigidity.

A semi-analytical multiple-scale approximation for the velocity potential is used to describe the attenuation of the effective wave field, i.e. the mean wave field with respect to realisations of the random medium. We compare the results with those obtained from a random sampling approach, which is based on a step approximation of the roughness profile.

Mathematical model

We consider an infinitely long thin-elastic beam of negligible draught floating on water of constant depth H . The equilibrium fluid surface coincides with $z = 0$, where the coordinate z denotes the vertical axis pointing upwards. The beam extends to infinity in both horizontal directions (with horizontal coordinate x) and is modelled using Euler–Bernoulli theory. The schematic is shown in the figure below.



Under the usual assumptions of linear water-wave theory (i.e. fluid incompressible, inviscid and its flow irrotational) the velocity potential is described by Laplace's equation. Furthermore, the sea-floor is assumed to be impermeable. Using the linearised version of Bernoulli's beam equation and the linearised kinematic surface condition at the interface between beam and water, the following PDE system is obtained for $x \in (-\infty, \infty)$,

$$\Delta\phi = 0, \quad z \in (-H, 0), \quad (1a)$$

$$\partial_z\phi = 0, \quad z = -H, \quad (1b)$$

$$(\partial_x^2(b\partial_x^2) - \alpha g + 1)\partial_z\phi - \alpha\phi = 0, \quad z = 0, \quad (1c)$$

where α is the angular frequency squared over the gravitational acceleration, g the beam mass and b its rigidity (both functions of x). For the varying mass and the varying rigidity

problem, respectively, the beam roughness is modelled as a (continuous) Gaussian autocorrelated random process with correlation length l_G and small roughness amplitude ε .

Random sampling step approximation

We consider a monochromatic wave of unit-amplitude propagating in positive x -direction. For a given roughness realisation on a long, finite interval $(0, L)$ for the varying mass and the varying rigidity problem (quantities constant outside of this interval), the roughness profile is approximated by a piece-wise constant function.

Whereas the solution in the work of Rupprecht et al. [1] only consists of one travelling and one evanescent wave mode in both directions and each subinterval, the full linear solution of the velocity potential here contains one travelling, two damped-travelling and an infinite number of evanescent wave modes in both directions and each subinterval. For numerical computations, the full linear solution has to be approximated with a finite number of wave modes and an iterative algorithm is used to obtain the solution in the rough interval.

The beam deflections η , which can be obtained via $\partial_t \eta = \partial_z \phi$ for $z = 0$, are calculated for large ensembles containing approximately 1500 samples of randomly generated beam realisations, which share the same roughness amplitude, ε , and correlation length, l_G . The effective attenuation rate, Q , is extracted from the effective wave field, $\langle \eta \rangle$, where $\langle \cdot \rangle$ denotes the ensemble average of the included quantity with respect to realisations, i.e. the effective attenuation rate is defined via

$$|\langle \eta \rangle| \propto e^{-Qx} \quad (0 < x < L). \quad (2)$$

Multiple-scale approximation

The semi-analytical approach to approximate the wave attenuation considers two scales: the local scale l (coordinate denoted by x), which is of the order of the wave length and roughness correlation length, and the observation scale L (coordinate denoted by x_2), over which attenuation is observed. It is assumed that the scales are related by $L = \varepsilon^{-2}l$ for small $\varepsilon \ll 1$. Applying a multiple-scale expansion of the complex, time-harmonic potential $\phi(x, z)$ gives

$$\phi(x) = \phi_0(x, x_2) + \varepsilon \phi_1(x, x_2) + \varepsilon^2 \phi_2(x, x_2) + \dots,$$

where $x_2 = \varepsilon^2 x$. Applying this expansion to the underlying PDE system (1) and separating

the resulting equations with respect to orders of ε provides systems of order $O(1), O(\varepsilon), O(\varepsilon^2)$.

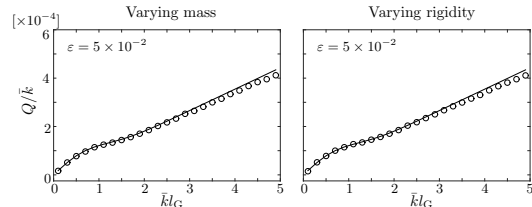
Solving the systems of orders $O(\varepsilon)$ and $O(\varepsilon^2)$ using the stationarity of the random processes which describe the varying mass and varying rigidity over $(-\infty, \infty)$, respectively, leads to the evolution equation of the leading-order-wave amplitude, $A(x_2)$, from which the attenuation coefficient

$$Q = \text{Im} \left[\frac{\bar{k}^3 \zeta}{4\bar{b}\bar{k}^5 \tanh(\bar{k}H) + \alpha(1 + \frac{2\bar{k}H}{\sinh(2\bar{k}H)})} \right] \quad (3)$$

can be derived, where \bar{k} corresponds to the travelling wave mode for a beam with averaged mass and mean rigidity \bar{b} . ζ is a complex-valued integral, which is evaluated numerically.

Results

The figure below shows non-dimensional attenuation rates predicted by the numerical simulations (circles) and multiple-scale approximation (solid line) as functions of non-dimensional correlation length, for the varying mass (left-hand panel) and the varying rigidity problem (right-hand panel).



We can observe good agreement between the two solution approaches for both varying mass and varying rigidity problem in the small correlation length regime. The agreement of the multiple-scale approach in both cases suggests that varying mass and varying rigidity produce same attenuation. Results for the phase changes will be shown at the conference.

Acknowledgements

SR acknowledges funding from the Australian government, through an Endeavour Research Fellowship in 2016/2017.

References

- [1] S. Rupprecht, L. G. Bennetts, and M. A. Peter, Effective wave propagation along a rough thin-elastic beam, *Wave Motion* (2016), in press.

Coupling High-Frequency methods and Boundary Element Techniques for scattering problems with several obstacles.

Marc LENOIR¹, Eric LUNÉVILLE¹, Nicolas SALLÉS^{1,*}

¹POEMS, ENSTA ParisTech, CNRS, Inria, Université Paris-Saclay, Palaiseau, France

*Email: nicolas.salles@ensta-paristech.fr

Abstract

We are interested in solving sound-hard scattering problems by two obstacles with a large obstacle subject to high-frequency regime relatively to the wavelength and a small one subject to low-frequency regime. The iterative method presented allows to decouple the two obstacles and to use Geometric Optics for the large obstacle and Boundary Element Method for the small obstacle.

Keywords: Helmholtz equation, High-frequency problems, Boundary Element Method, Multiple scattering.

1 Introduction

Literature provides a lot of interest and techniques for multiple scattering problems and high-frequency problems, see for example [1–3].

In this talk, we want to solve multiple scattering problems with two obstacles (or more): a large obstacle Ω_1 subjects to high-frequency techniques (Geometric Optics) and a small one Ω_2 , see Figure 1. We used disks for simplicity but the shapes can be more complicated.

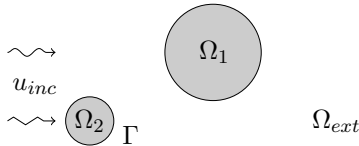


Figure 1: Geometric configuration : a large obstacle (Ω_1) and a small one (Ω_2).

Geometrics Optic (G.O.) is really interesting for high-frequency problems but has several drawbacks like: **i)** difficulty to evaluate the normal derivative of the solution on the boundary of Ω_2 , **ii)** difficulty to find enough rays going from Ω_1 to the small obstacle Ω_2 and, **iii)** when Ω_2 has a complicated shape, difficulty to obtain an accurate solution in the vicinity of Ω_2 .

The iterative method presented tackles these difficulties by coupling Galerkin Boundary Element Method and Geometrics Optic using an

iterative method where both obstacles can be considered independently (see Section 2). Then, instead of solving an integral equation with Neumann boundary condition on $\partial\Omega_2$, we define an equivalent problem just with the knowledge of the trace of the G.O. solution on an additional boundary. This equivalent problem is introduced in Section 3.

Notations

Let Ω_1 be the large obstacle, Ω_2 the small one and $\Gamma = \partial\Omega_2$. Finally, we denote the exterior domain by $\Omega_{ext} = \mathbb{R}^2 \setminus (\bar{\Omega}_1 \cup \bar{\Omega}_2)$, the incident field is u_{inc} and the outgoing normal is ν . The initial Helmholtz problem to solve is

$$\begin{cases} -\Delta u(x) - k^2 u(x) = 0, x \in \Omega_{ext} \\ \frac{\partial u}{\partial \nu}(x) = -\frac{\partial u_{inc}}{\partial \nu}(x), x \in \partial(\bar{\Omega}_1 \cup \bar{\Omega}_2) \end{cases} \quad (1)$$

Radiation condition at infinity.

2 The iterative method

The iterative method decouples the obstacles and allows to solve iterative problems where interactions between obstacles are taken into account by the boundary conditions that are updated at each iteration [1]. We denote by u_1 and u_2 the scattered fields produced respectively by Ω_1 and Ω_2 .

Each step of the iterative method consists in solving two problems: **i)** the scattering by Ω_1 using G.O. with an incident field that is the sum of $\frac{\partial u_{inc}}{\partial \nu} + \frac{\partial u_2}{\partial \nu}$ the normal derivative of the scattered field by Ω_2 (initialized to zero) and **ii)** the scattering problem for Ω_2 with boundary condition on Γ : $\frac{\partial u_{inc}}{\partial \nu} + \frac{\partial u_1}{\partial \nu}$. The total scattered field by these two obstacles is then $u_1 + u_2$.

Convergence of this iterative process was studied and proved under distance condition between the obstacles (depending on the frequency) by Balabane [1].

In our case, we want to use a G.O. code for Ω_1 and XLiFE++ a C++ library providing FEM and BEM solvers (XLiFE++ [4]) for Ω_2 .

3 Coupling Integral equations with high-frequency methods

The difficulty with the evaluation of the normal derivative of the G.O. solution on Γ and the influence of the shape of Ω_2 on the accuracy are withdrawn using a total field integral equation on Γ with an additional arbitrary artificial boundary, denoted by Σ , around Ω_2 where we enforce the coupling by using the trace of the solution from the G.O. problem, see Figure 2. There is no condition on the shape of Σ , we will use a circle in the sequel. Instead of solving an integral equation (with Neumann boundary condition) on Γ , we introduce a system of two integral equations on Γ and Σ to get a total field integral equation without Neumann boundary condition.

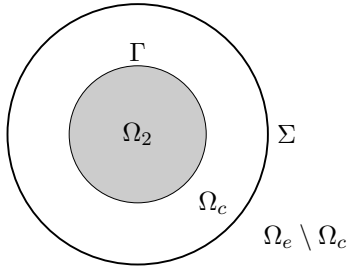


Figure 2: The small obstacle Ω_2 , its boundary $\Gamma = \partial\Omega_2$, the additional boundary Σ and Ω_c .

We introduce $\mathcal{V}_\Sigma, \mathcal{K}_\Gamma$ respectively the single layer and double layer potential operators for the Helmholtz equation and we add in index the boundary where it operates then an integral representation of the solution of the scattering by Ω_2 can be given by

$$u_2(x) = \begin{cases} (\mathcal{K}_\Gamma p)(x) - (\mathcal{V}_\Sigma q)(x) & \text{in } \Omega_c \\ (\mathcal{K}_\Gamma p)(x) & \text{in } \Omega_e \setminus \Omega_c \end{cases}$$

The additional potential $\mathcal{V}_\Sigma q$ will enforce the boundary condition. The related boundary integral system is:

$$\begin{aligned} \gamma_1^{(\Gamma)}(\mathcal{K}_\Gamma p)(x) - \gamma_1^{(\Gamma)}(\mathcal{V}_\Sigma q)(x) &= 0, \text{ on } \Gamma \\ \gamma_0^{(\Sigma)} \mathcal{V}_\Sigma q &= \gamma_0^\Sigma \tilde{u}, \text{ on } \Sigma, \end{aligned}$$

where γ_0^Θ and γ_1^Θ are the trace and the normal trace on Θ and $\tilde{u} = u_{inc} + u_1$, the sum of the traces on Σ of the incident field and the solution from the large obstacle problem using G.O.

This formulation is not eigenfrequency-free but using a Brakhage-Werner formulation for

the p and by reconstructing the normal derivative of u_1 on Σ with an additional problem, we can obtain an eigenfrequency-free formulation that will be presented in the talk.

4 Conclusion

We have presented a method to couple a high-frequency code with a boundary element code to solve multiple scattering problems. This method based on an iterative method and a total field integral equation tackles the difficulties induced by the G.O. (normal derivative, accuracy, limitation for the shape of the small obstacle). Figure 3 presents a preliminary result after one iteration using BEM on $\partial\Omega_1$ and G.O. on $\partial\Omega_1$. The first iteration provides a quite good result except in the shadow area. We need to write a G.O. code able to iterate to continue.

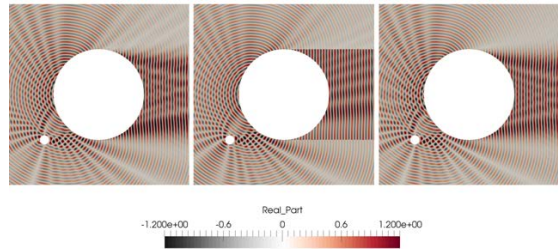


Figure 3: The scattered field after 1 iteration with the total field I.E on Γ, Σ and on $\partial\Omega_1$ i) BEM (left), ii) G.O. (center), and iii) the reference solution (one I.E on $\Gamma \cup \partial\Omega_1$) (right).

References

- [1] M. Balabane, Boundary Decomposition for Helmholtz and Maxwell equations 1: disjoint sub-scatterers, *Asymptotic Analysis*, **38** (2004).
- [2] C. Geuzaine, O. Bruno and F. Reitich, On the $O(1)$ solution of multiple-scattering problems, *IEEE transactions on magnetics*, **41** (2005).
- [3] X. Antoine, C. Chniti and K. Ramdani, On the numerical approximation of high-frequency acoustic multiple scattering problems by circular cylinders, *Journal of Computational Physics*, **227** (2008).
- [4] eXtended Library of Finite Elements in C++ (XLiFE++), <http://uma.ensta-paristech.fr/soft/XLiFE++>

FEM-BEM coupling for transient acoustic scattering by thermoelastic obstacles

Tonatiuh Sánchez-Vizuet^{1,*}, George Hsiao², Francisco-Javier Sayas², Richard Weinacht²

¹Courant Institute of Mathematical Sciences, New York University, USA

²Department of Mathematical Sciences, University of Delaware, USA

*Email: tonatiuh@cims.nyu.edu

Abstract

We present a combined field and boundary integral equation method for solving time-dependent scattering of acoustic waves by thermoelastic obstacles. The approach is geared towards a finite element discretization in the interior of the scatterer and a boundary element approximation of the acoust field. Using an integral representation of the solution in the infinite exterior domain occupied by the fluid, the problem is reduced to one defined only over the finite region occupied by the solid, with nonlocal boundary conditions. The resulting non local boundary problem is analized using the Laplace transform in terms of time-domain data. Existence and uniqueness results are established in the Laplace domain where Galerkin semi-discretization approximations are derived and error estimates are obtained. Full space-time discretization and time-domain error estimates based on the Convolution Quadrature method are also presented.

Keywords: Fluid-structure interaction, Coupling BEM-FEM, Time-domain boundary integral equation, Wave scattering, Convolution quadrature.

Introduction

We are concerned with a time-dependent direct scattering problem in fluid-thermoelastic solid interaction, which can be simply described as follows: an acoustic wave propagates in a fluid domain of infinite extent in which a bounded thermoelastic body is immersed. We denote Ω_- the bounded domain occupied by the thermoelastic body with a Lipschitz boundary Γ and we let $\Omega_+ := \mathbb{R}^3 \setminus \overline{\Omega}_-$ be its exterior. The problem is then to determine the scattered velocity potential V in the fluid domain, the deformation of the solid \mathbf{U} and the variation of the temperature Θ in the obstacle with respect to the equilibrium temperature Θ_0 .

In the linear small displacement regime, the

governing equations are [3] :

$$\begin{aligned} c^{-2} \partial_{tt} V - \Delta V &= 0 \quad \text{in } \Omega_+ \times (0, T), \\ \rho_\Sigma \partial_{tt} \mathbf{U} - \Delta^* \mathbf{U} + \zeta \nabla \Theta &= \mathbf{0} \quad \text{in } \Omega_- \times (0, T), \\ \kappa^{-1} \partial_t \Theta - \Delta \Theta + \eta \partial_t (\nabla \cdot \mathbf{U}) &= 0 \quad \text{in } \Omega_- \times (0, T), \end{aligned}$$

where ρ_Σ is the density of the solid, κ is the thermic difussivity, η is a constant proportional to the thermal expansion coefficient ζ . As usual the symbol Δ^* is the Lamé operator defined by

$$\Delta^* \mathbf{U} := \mu \Delta \mathbf{U} + (\lambda + \mu) \nabla (\nabla \cdot \mathbf{U}).$$

On the interface Γ between the solid and the fluid we have the transmission conditions

$$\begin{aligned} (\mathbf{C}\boldsymbol{\varepsilon}(\mathbf{U}) - \zeta \Theta \mathbf{I}) \mathbf{n} &= -\rho_f \partial_n (V + V^{inc}) \mathbf{n}, \\ \partial_t \mathbf{U} \cdot \mathbf{n} &= -\partial_n (V + V^{inc}) \\ \partial_n \Theta &= 0 \end{aligned}$$

where \mathbf{n} is the exterior unit normal to Ω_- , and V^{inc} denotes the given incident field. We assume the causal initial conditions

$$\begin{aligned} \mathbf{U}(x, t) &= \frac{\partial \mathbf{U}(x, t)}{\partial t} = \mathbf{0}, \quad \Theta(x, t) = 0, \\ V(x, t) &= \frac{\partial V}{\partial t}(x, t) = 0. \end{aligned}$$

An integro-differential system

Following the ideas introduced in the seminal work of Bamberger and Ha-Duong [1] the system is transformed into the Laplace domain and recast as an integro-differential problem making use of a layer potential representation of the acoustic field.

The resulting non-local system below involves the operators of the Calderón projector for the acoustic field but retains the weak PDE formulation for the elastic and thermal unknowns. It can be represented in matrix operator form as

$$\mathbf{L}(\mathbf{u}, \theta, \phi, \lambda) = (d_1, d_2, d_3, d_4),$$

where the data (d_1, d_2, d_3, d_4) is given by

$$\begin{aligned} d_1 &= -s \rho_f \gamma' (\gamma^+ v^{inc} \mathbf{n}), \quad d_2 = 0, \\ d_3 &= \partial_n^+ v^{inc}, \quad d_4 = 0, \end{aligned}$$

and the matrix of integral and differential operators is given by

$$\mathbf{L} := \begin{pmatrix} \mathbf{A}_s & -\zeta(\operatorname{div})' & s\rho_f \gamma^{-'} \mathbf{n} & 0 \\ s\eta \operatorname{div} & \mathbf{B}_s & 0 & 0 \\ -s\mathbf{n}^\top \gamma^- & 0 & \mathbf{W}(s) & -\left(\frac{1}{2}\mathbf{I} - \mathbf{K}(s)\right)' \\ 0 & 0 & \frac{1}{2}\mathbf{I} - \mathbf{K}(s) & \mathbf{V}(s) \end{pmatrix}.$$

Above $s \in \mathbb{C}_+$ is the Laplace parameter and

$$\begin{aligned} \mathbf{A}_s : \mathbf{H}^1(\Omega_-) &\rightarrow (\mathbf{H}^1(\Omega_-))', \\ \mathbf{B}_s : H^1(\Omega_-) &\rightarrow (H^1(\Omega_-))' \end{aligned}$$

are the operators associated with the elastic and thermal bilinear forms

$$\begin{aligned} a(\mathbf{u}, \cdot; s) &:= (\mathbf{C}\boldsymbol{\varepsilon}(\mathbf{u}), \boldsymbol{\varepsilon}(\cdot))_{\Omega_-} + s^2 \rho_\Sigma(\mathbf{u}, \cdot)_{\Omega_-}, \\ b(\theta, \cdot; s) &:= (\nabla\theta, \nabla(\cdot))_{\Omega_-} + (s/\kappa)(\theta, \cdot)_{\Omega_-}. \end{aligned}$$

Continuous and discrete well posedness

We study the conforming Galerkin discretization of the system on arbitrary closed subspace of the solution space endowed with the appropriate energy norm. The well posedness of the discrete problem is done by reformulating this equations in terms of an exotic transmission problem and showing the coercivity of the resulting operator. This technique is similar to the one discussed in [4] for purely acoustic/elastic interaction.

Error estimates for the semidiscretization are obtained by observing that an appropriate elliptic projection of the error term satisfies equations with the same structure as the ones satisfied by the unknowns, to which all of the above machinery can be applied.

Bounds are established explicitly in terms of the laplace parameter s and its real part σ . This enables to translate the estability estimates into the time-domain while mantaiing explicit knowledge of the behaviour of the bounding constants with respect to time. The fact that the analysis is carried out in arbitrary closed subspaces implies that, by taking the discrete space to be the entire solution space, the well posedness of the continuous problem is obtained as a by-product.

A fully discrete system

The linear system arising from the discretization has a structure that can be depicted by the block matrix

$$\begin{bmatrix} \mathbf{FEM}(s) & s\rho_f(\mathbf{N}\Gamma)_h^t \\ -s\rho_f(\mathbf{N}\Gamma)_h & \mathbf{BEM}(s) \end{bmatrix} \begin{bmatrix} \begin{bmatrix} \mathbf{u}^h \\ \theta^h \\ \lambda^h \\ \phi^h \end{bmatrix} \end{bmatrix} = \begin{bmatrix} \begin{bmatrix} -s\rho_f \Gamma_h^t \beta^h \\ \eta^h \\ 0 \\ \rho_f \alpha^h \end{bmatrix} \end{bmatrix},$$

where the sparse Finite Element block contains mass and stiffness matrices as well as first order terms related to the elastic and thermal unknowns. The boundary element block $\mathbf{BEM}(s)$ contains the Galerkin discretization of the operators of the acoustic Calderón calculus and the coupling trace matrix $(\mathbf{N}\Gamma)_h$ is the discretization of the bilinear form arising from the duality pairing $\langle \mathbf{u}^h \cdot \boldsymbol{\nu}, \chi^h \rangle_\Gamma$.

The system is discretized in time using BDF2 Convolution Quadrature [5] for the integral equation block and BDF2 time-stepping for the finite element block. As pointed out in [2], this approach is equivalent to an application of BDF2-CQ to the entire discrete matrix. This fact is used to derive error estimates for the discretization by considering a global CQ approximation resulting in a second order accurate scheme. Numerical convergence studies and simulations for the 2D case are carried out.

References

- [1] A. Bamberger and T. Ha-Duong. Formulation Variationnelle Espace-Temps pour le Calcul par Potentiel Retardé de la Diffraction de d'une Onde Acoustique (I). *Math. Meth. Appl. Sci.*, 8(3): 405–435, 1986.
- [2] M. E. Hassell and F.-J. Sayas. A fully discrete BEM-FEM scheme for transient acoustic waves. *Comput. Methods Appl. Mech. Engrg.*, 309:106 – 130, 2016.
- [3] G. Hsiao, T. Sánchez-Vizuet, F.-J Sayas, and R. Weinacht, A wave-thermoelastic solid interaction. 2016, *submitted*.
- [4] G. Hsiao, T. Sánchez-Vizuet, and F.-J. Sayas, Boundary and coupled boundary-finite element methods for transient wave-structure interaction, *IMA J. Numer. Anal.*, 37(1):237–265, 2016.
- [5] Ch. Lubich . On the multistep time discretization of linear initial-boundary value problems and their boundary integral equations. *Numer. Math.*, 67(3): 365–389, 1994.

BEM with variable time step size for absorbing boundary conditions

Stefan A. Sauter¹, Martin Schanz^{2,*}

¹Institut für Mathematik, University of Zurich, Zurich, Switzerland

²Institute of Applied Mechanics, Graz University of Technology, Graz, Austria

*Email: m.schanz@tugraz.at

Abstract

In room acoustics, sound absorbing materials are often used. The mathematical description is done with the wave equation and absorbing boundary conditions. The numerical treatment can be done with Boundary Element methods, where the absorbing boundary results in a Robin boundary condition. This boundary condition connects the Neumann trace with the Dirichlet trace of the time derivative.

Here, an indirect formulation in combination with the generalized convolution quadrature method is applied. This allows, first, to have a simple formulation of the Robin boundary condition in the Laplace domain and, second, to have a variable time step size. The latter allows to discretise right hand sides with a non-smooth behavior. Convergence studies of a pure time dependent problem show the expected rates. The computation of the sound pressure level in a staircase of the University of Zurich, show the suitability of this approach in determining the indoor acoustics.

Keywords: indirect BEM, generalized CQ, absorbing BC

1 Governing equations

Let $\Omega^- \subset \mathbb{R}^3$ be a bounded Lipschitz domain with boundary $\Gamma := \partial\Omega$ and let $\Omega^+ := \mathbb{R}^3 \setminus \overline{\Omega^-}$ denote its unbounded complement. Let n denote the unit normal vector to Γ pointing into the exterior domain Ω^+ . We consider the homogeneous wave equation (with constant sound speed c in the medium) for $\sigma \in \{+, -\}$

$$\begin{aligned} \partial_{tt} u - c^2 \Delta u &= 0 && \text{in } \Omega^\sigma \times \mathbb{R}_{>0}, \\ u(x, 0) = \partial_t u(x, 0) &= 0 && \text{in } \Omega^\sigma, \\ \gamma_1^\sigma(u) - \sigma \frac{\alpha}{c} \gamma_0^\sigma(\partial_t u) &= f(x, t) && \text{on } \Gamma \times \mathbb{R}_{>0}, \end{aligned} \quad (1)$$

where $\gamma_1^\sigma = \partial/\partial n$ is the normal derivative applied to a sufficiently smooth function in Ω^σ and γ_0^σ denotes the trace operator to Γ applied to a sufficiently smooth function in Ω^σ . In (1), α denotes the non-negative admittance, which is

the inverse of the specific impedance of the surface Γ . This specific impedance is scaled by the density and the wave velocity. The mathematical analysis allows any non-negative finite value for α , however, realistic values are in the range $0 \leq \alpha \leq 1$. The lower limit models a sound hard wall and the upper limit is a totally absorbing surface. Further, measured values show a frequency dependence and are listed in national design codes like the ÖNORM in Austria (ÖNORM EN 12354-6).

We employ layer potentials to express the solution in terms of retarded potentials (cf. [1]). The ansatz for the solution u as a single layer potential is given by

$$u(x, t) = (\mathcal{S} * \varphi)(x, t) := \int_{\Gamma} \frac{\varphi(y, t - \frac{\|x-y\|}{c})}{4\pi \|x-y\|} d\Gamma_y \quad \forall (x, t) \in \Omega^\sigma \times \mathbb{R}_{>0},$$

which satisfies the first two equations in (1). The density φ then is determined via the third equation. The application of the trace γ_0 and normal trace γ_1 to u involves the usual integral operators of acoustics. It holds for $\sigma \in \{+, -\}$

$$\begin{aligned} \gamma_0^\sigma(\mathcal{S} * \varphi) &= (\mathcal{V} * \varphi) \\ \gamma_1^\sigma(\mathcal{S} * \varphi) &= -\left(\sigma \frac{\varphi}{2} - \mathcal{K}' * \varphi\right), \end{aligned}$$

where these equations hold almost everywhere on $\Gamma \times \mathbb{R}_{>0}$.

The third equation in (1) leads to the boundary integral equation for the single layer ansatz

$$-\left(\sigma \frac{\varphi}{2} - \mathcal{K}' * \varphi\right) - \sigma \frac{\alpha}{c} (\mathcal{V} * \dot{\varphi}) = f \quad \text{a.e. in } \Gamma \times \mathbb{R}_{>0}. \quad (2)$$

Certainly, also an integral equation using the double layer potential is possible.

The integral equation (2) is discretized in space and time. The spatial discretization follows the standard procedure. The geometrical discretization is done with linear triangles

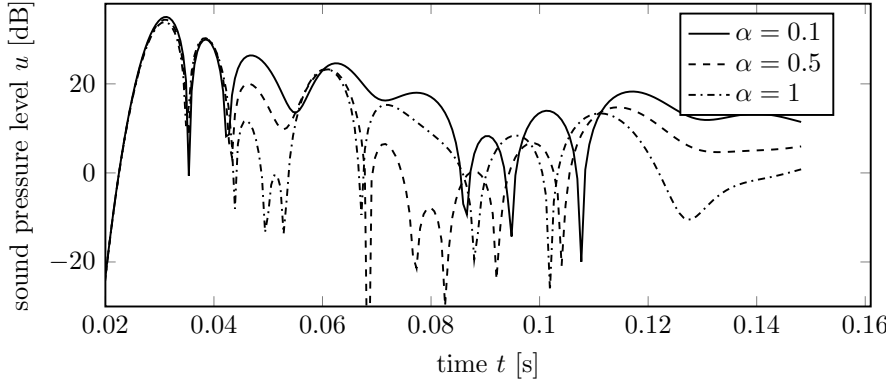


Figure 1: Sound pressure level in dB versus time in the upper left part of the observation screen

and the data are approximated by piecewise linear shape functions. The temporal discretization uses the generalized convolution quadrature method (gCQ) [3]. This allows an easy realization of the time derivative in (2) as a simple multiplication by the Laplace variable.

All computations are done in 3-D and a normal BE formulation without any fast techniques is used. All regular integrals are performed with Gaussian quadrature formulas. The singular integrals are treated with the formulas of Erichsen and Sauter [2]. For the solution a direct solver is used. All implementations are done within the BE-library HyENA [4].

2 Numerical examples

The numerical behavior of the proposed method and the advantage of using the gCQ will be presented in the talk. Here, due to space restrictions, only the industrial example is shown. The influence of absorbing layers in room acoustics is studied. In 2010/11, the atrium of the “Institut für Mathematik” at the University Zurich has been acoustically improved by installing absorber panels at the ceilings. This action has been successful and the following numerical model tries to model this effect. The material data from air resulting in a wave speed $c = 343 \text{ m/s}$ are assumed. In Fig. 1, the sound pressure level is depicted over time. Note, the sound pressure level is given in dB and negative values indicate sound below the threshold of hearing. Further, the initial phase where the pressure is zero, i.e., the time until the wave arrives, is truncated as in this case the dB measure gives very large negative values. In this plot two things can be observed. First, the peaks with the negative val-

ues show the wave reflections, which arrive for the different damping cases at different times. Second, the sound pressure for $\alpha = 0.1$, i.e. no mounted damping material, has in the mean the larger pressure values. The two other cases show that the damping material can reduce the sound pressure level as reported from the real building, where it is claimed that the atrium is no longer such noisy.

References

- [1] A. Bamberger and T. Ha-Duong. Formulation variationnelle espace-temps pour le calcul par potentiel retardé d'une onde acoustique. *Math. Meth. Appl. Sci.*, 8:405–435 and 598–608, 1986.
- [2] S. Erichsen and S. A. Sauter. Efficient automatic quadrature in 3-d Galerkin BEM. *Comput. Methods Appl. Mech. Engrg.*, 157(3–4):215–224, 1998.
- [3] Maria Lopez-Fernandez and Stefan A. Sauter. Generalized Convolution Quadrature with Variable Time Stepping. *IMA J. Numer. Anal.*, 33(4):1156–1175, 2013.
- [4] Ma. Messner, Mi. Messner, F. Rammerstorfer, and P. Urthaler. Hyperbolic and elliptic numerical analysis BEM library (HyENA). <http://www.mech.tugraz.at/HyENA>, 2010. [Online; accessed 22-January-2010].

Inverse scattering with iterative determination of the regularization parameter

Nick Schenkels^{1,*}, Wim Vanroose¹

¹Department of Mathematics and Computer Science, University of Antwerp, Antwerp, Belgium

*Email: nick.schenkels@uantwerpen.be

Abstract

Many applications can be described by a PDE model with a set of unknown parameters that we wish to calibrate based on measurements related to its solution. This can be seen as a constrained minimization problem where we want to minimize the mismatch between the observed data and our model prediction, including an extra regularization term, and use the PDE as a constraint. Often, a suitable regularization parameter is determined by solving the problem for a whole range of parameters – e.g. using the L-curve – which is computationally very expensive. In this work we present an iterative way to find a good regularization parameter based on the discrepancy principle.

Keywords: Inverse scattering, iterative regularization, constrained minimization

1 Problem description

We consider the Helmholtz equation on a square domain $\Omega \subseteq \mathbb{R}^2$ and write the solution u as the sum of an incoming and a resulting scattered wave:

$$(\Delta + k^2)(u_{in} + u_{sc}) = 0. \quad (1)$$

In order to simulate outgoing waves, we use ECS boundary conditions. We now wish to reconstruct the space dependent wave number k on Ω based on measurements of the scattered waves u_{sc} on the boundary $\delta\Omega$ for different incoming waves u_{in} . We use $u_{in}, \tilde{u}_{sc} \in \mathbb{C}^n$ to denote the vectors that contain all the incoming waves and the measurements of the resulting scattered waves respectively and $u_{sc}(k) \in \mathbb{C}^n$ for our model predictions. This results in the following constrained minimization problem:

$$\min_{k \in \mathbb{R}^m} \mathcal{J}(k) = \underbrace{\|u_{sc}(k) - \tilde{u}\|_2^2}_{=: \mathcal{D}(u_{sc}(k))} + \alpha \underbrace{\|k^2\|_2^2}_{=: \mathcal{R}(k)} \quad (2)$$

such that $H(k)(u_{in} + u_{sc}(k)) = 0$.

Here, $H(k) \in \mathbb{R}^{mn \times mn}$ is the discrete version of the Helmholtz operator from (1), applied to all the different waves at the same time.

2 Iterative regularization

In [1] Gazzola and Nagy derive an iterative way to determine a suitable regularization parameter for the classical Tikhonov problem for linear problems of the form $\|Ax - b\|_2^2 + \alpha \|x\|_2^2$, with $x, b \in \mathbb{R}^n$, $A \in \mathbb{R}^{n \times n}$ and $\alpha \in \mathbb{R}_0^+$. The approach they used can be generalized to non-square linear problems [3] and even non-linear problems as we shall describe next.

Assume we can solve (2) for a fixed value of α using some iterative method. We then define the discrepancy $\mathcal{D}_i(\alpha) = \mathcal{D}(u_{sc}(k_\alpha))$, i.e. the residual after i iterations for a fixed regularization parameter. If ε is an estimate for the norm of the noise, then the discrepancy principle proposes to choose α such that for large i $\mathcal{D}_i(\alpha) \approx \eta\varepsilon$, with $1 \lesssim \eta$ a small tolerance value.

If we approximate the discrepancy linearly as $\mathcal{D}_i(\alpha) \approx a\alpha + b$, then $b = \mathcal{D}_i(0)$, i.e. the residual if no regularization. Furthermore, if α_{i-1} is our current best estimate for the regularization parameter, then a can be approximated by:

$$a = \frac{\mathcal{D}_i(\alpha) - b}{\alpha} \approx \frac{\mathcal{D}_i(\alpha_{i-1}) - \mathcal{D}_i(0)}{\alpha_{i-1}}.$$

Using the discrepancy principle as a stopping criterion, i.e. $\mathcal{D}_i = \eta\varepsilon$, we find the following update formula for the regularization parameter:

$$\alpha_i = \left| \frac{\eta\varepsilon - \mathcal{D}_i(0)}{\mathcal{D}_i(\alpha_{i-1}) - \mathcal{D}_i(0)} \right|. \quad (3)$$

The absolute value is added in order to assure that the regularization parameter stays positive in the first few iterations. From (3), it follows that we can update the regularization parameter based on the residual without regularization and the residual with our current estimate.

3 Numerical experiment

We performed a numerical experiment, where we wished to reconstruct k on a regular 100×100 grid based on measurements of the scattered waves for incoming waves hitting the domain at 50 different angles. We added Gaussian noise to simulate a noise level of approximately 35%.

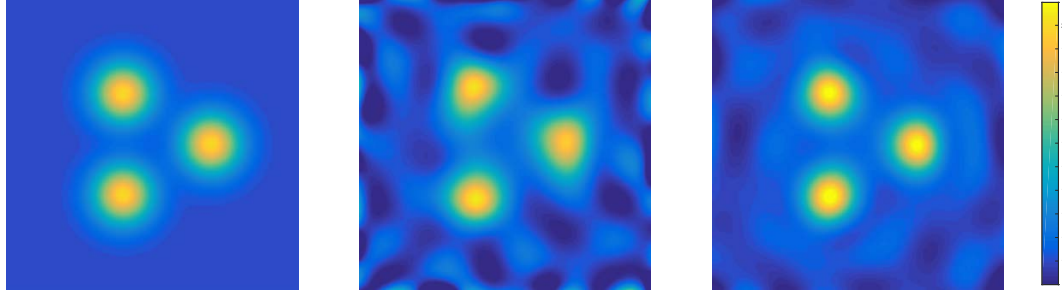


Figure 1: From left to right: the exact wave number, which is the sum of three Gaussian functions, and the reconstructed wave number without and with regularization.

Figure 1 shows the reconstruction and figure 2 the evolution of the relative error and the regularization parameter. Clearly, the regularization suppresses some of the oscillations that occur due to the noise in the measurements. We also forced the algorithm to perform 25 iterations, even though the discrepancy principle was already satisfied after 8.

4 Conclusion and remarks

From our numerical experiments we see that the method proposed in [1] can be adapted to non-linear problems. We used a Newton-CG solver for the minimization, but the update for the regularization parameter doesn't depend on this. The biggest difference is that the original method is a Krylov method, where in each iteration a new basis vector is added to the solution space. These vectors turn out to be independent of the regularization parameter, hence the same basis can be used to solve both the regularized and the non-regularized system for any regularization parameter. In the non-linear context this will generally not be the case any more and in order to calculate $\mathcal{D}_i(\alpha_{i-1})$, i Newton steps have to be performed. Even though this is computationally very expensive, typically only a few iterations are needed before the discrepancy principle is satisfied. Hence the method can still be more efficient than calculating a full L-curve for example [2]. Furthermore, we can drastically decrease the computational cost by only recalculating the last few Newton iterations or not recalculating anything at all.

References

- [1] S. Gazzola and J. G. Nagy, Generalized Arnoldi-Tikhonov Method for Sparse Re-

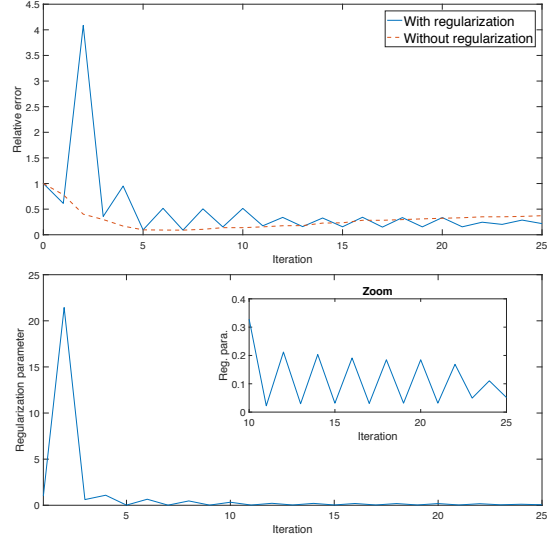


Figure 2: The relative error (top) and the regularization parameter α (bottom). The initial spike is typical for the method as $\mathcal{D}_i(0)$ is initially very far away from $\eta\varepsilon$.

construction, *SIAM Journal on Scientific Computing* **36**(2) (2014), pp. B255–B247.

- [2] F. Bruckner and Claas Abert et al., Solving Large-Scale Inverse Magnetostatic Problems using the Adjoint Method, *arXiv preprint arXiv:1609.00060* (2016).
- [3] N. Schenckels, J. Sijbers, W. van Aarle and W. Vanroose, A Generalized Bidiagonal-Tikhonov Method Applied To Differential Phase Contrast Tomography, *arXiv preprint arXiv:1510.03233* (2015).

The Unified Transform Method in Dispersive Quantization

Natalie E. Sheils^{1,*}, Peter J. Olver²

¹Institute for Mathematics and Its Applications, Minneapolis, USA

²School of Mathematics, University of Minnesota, Minneapolis, USA

*Email: nesheils@umn.edu

Abstract

Unified Transform Method (UTM) [8, 10], alternatively called the Fokas Method, has recently advanced the understanding of boundary value problems (BVPs) in the case of linear and nonlinear integrable equations. This method provides significant advantages computationally and allows for the study of many equations with various boundary conditions using a unified conceptual framework.

The surprising phenomenon of “dispersive quantization” describes the solutions to a wide range of dispersive wave models for rough initial data on bounded domains exhibiting fractal profiles at irrational times and quantized, meaning discontinuous but otherwise smooth, at rational times. This is an example of an observed, but as yet poorly understood, dynamical behaviors that depend crucially upon the large wave number asymptotics of the dispersion relation. The UTM will enable a better understanding of the effects of the boundary conditions in linear and nonlinear dispersive models with various boundary conditions and new numerical methods.

Keywords: Unified Transform Method, Boundary Value Problems, Dispersive Quantization

BVPs have been shown to possess an interesting property known as dispersive quantization or the “Talbot effect.” Chen and Olver [5, 6] numerically study fractalization and quantization in linear and nonlinear systems. For linear systems with nonpolynomial dispersion relations as well as for nonlinear systems, they are unable to attain rigorous theoretical results. Chousionis, Erdogan, and Tzirakis [7, 9] provide a rigorous confirmation of some of their numerical observations but are unable to go beyond periodic boundary conditions. Olver also attained theoretical results in the case of periodic boundary conditions for specific linear equations [12]. Figure 1 shows graphs of the solution to the periodic initial-boundary value problem on $0 \leq x \leq 2\pi$ for $u_t = u_{xxx}$ with a

step function initial condition (see [12] for details).

The current restriction to periodic boundary conditions will be eliminated using the UTM since in this method using different boundary conditions has only a minor effect appearing in calculational details. Further, using the UTM, one can find solutions to third order PDEs on the finite interval such as the linear KdV equation. This is a case where classical series solutions do not exist.

Applying the UTM to these problems allows for a deeper understanding of this phenomenon and its relation to boundary conditions and dispersion relation at least in the case of linear problems. Numerically, this phenomenon is very difficult to capture and a greater understanding of this analytically will aid in the creation of appropriate and useful numerical methods. Indeed, the design of appropriate numerical methods is a significant challenge.

The Talbot effect or dispersive quantization, so named in honor of an optical experiment by Talbot [13], was first discovered in the early 1990’s in the contexts of optics and quantum mechanics by Berry and collaborators [1, 2, 3, 4, 11]. Dispersive quantization is one of a class of phenomena involving the extreme coherent interference of waves that also helps to illustrate the structure of limits in physics [4]. The Talbot effect has been investigated for periodic BVPs for both integrable nonlinear equations as well as non-integrable models of a similar nature [5, 6, 7, 9, 12].

References

- [1] M. V. Berry. Quantum fractals in boxes. *J. Phys. A*, 29(20):6617–6629, 1996.
- [2] M. V. Berry and E. Bodenschatz. Caustics, multiply-reconstructed by Talbot interference. *J. Modern Opt.*, 46:349–365, 1999.
- [3] M. V. Berry and S. Klein. Integer, fractional and fractal Talbot effects. *J. Modern*

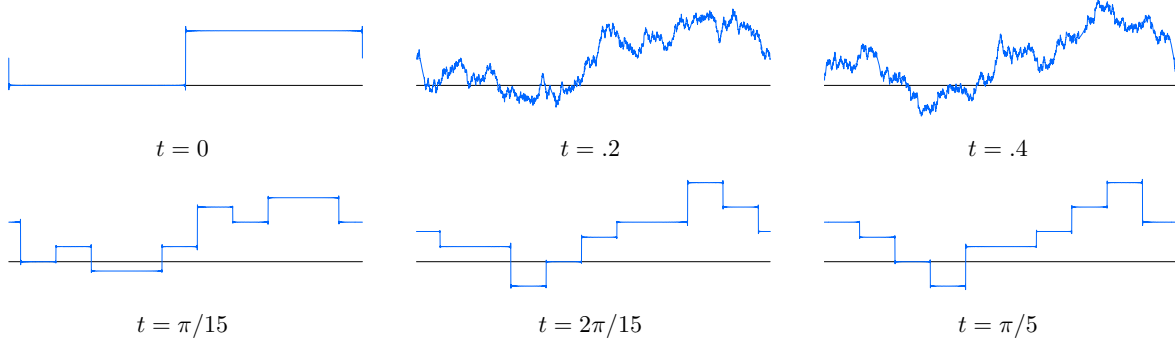


Figure 1: Solutions to the most basic linearly dispersive wave equation on a periodic domain exhibits fractal-like profile for rational times and piecewise constant behavior when time is a rational multiple of π [12].

- Opt.*, 43(10):2139–2164, 1996.
- [4] M. V. Berry, I. Marzoli, and Schleich W. Quantum carpets, carpets of light. *Physics World*, 14(6):39–44, 2001.
 - [5] G. Chen and P.J. Olver. Dispersion of discontinuous periodic waves. *Proc. R. Soc. Lond. Ser. A Math. Phys. Eng. Sci.*, 469(2149):20120407, 21, 2013.
 - [6] G. Chen and P.J. Olver. Numerical simulation of nonlinear dispersive quantization. *Discrete Contin. Dyn. Syst.*, 34(3):991–1008, 2014.
 - [7] V. Chousionis, M. B. Erdogan, and N. Tzirakis. Fractal solutions of linear and nonlinear dispersive partial differential equations. *Proc. Lond. Math. Soc.*, 110(3):543–564, 2015.
 - [8] B. Deconinck, T. Trogdon, and V. Vasan. The method of Fokas for solving linear partial differential equations. *SIAM Rev.*, 56(1):159–186, 2014.
 - [9] M.B. Erdogan and N. Tzirakis. Talbot effect for the cubic nonlinear Schrödinger equation on the torus. *Math. Res. Lett.*, 20(6):1081–1090, 2013.
 - [10] A.S. Fokas. *A unified approach to boundary value problems*, volume 78 of *CBMS-NSF Regional Conference Series in Applied Mathematics*. Society for Industrial and Applied Mathematics (SIAM), Philadelphia, PA, 2008.
 - [11] J. H. Hannay and M. V. Berry. Quantization of linear maps on a torus-Fresnel diffraction by a periodic grating. *Phys. D*, 1(3):267–290, 1980.
 - [12] P.J. Olver. Dispersive quantization. *Amer. Math. Monthly*, 117(7):599–610, 2010.
 - [13] H.F. Talbot. Facts related to optical science. no. IV. *Philos. Mag.*, 9:401–407, 1836.

Timelike Surfaces and the Wave Equation

Barbara A. Shipman^{1,*}, Patrick D. Shipman²

¹Department of Mathematics, University of Texas at Arlington, Arlington, TX, USA

²Department of Mathematics, Colorado State University, Fort Collins, CO, USA

*Email: bshipman@uta.edu

Abstract

Solutions of the wave equation produce Lorentz-holomorphic functions that generate timelike surfaces via generalized Weierstrass-Enneper representations. These solutions can be naturally extended to non-smooth functions, allowing for variants of timelike surfaces with non-smooth features. In this context, we investigate families of isometric timelike surfaces arising from semi-rigid motions, which differ only in the directions of principal curvatures.

Keywords: timelike surface, Weierstrass representation, Lorentz-holomorphic mapping

1 Weierstrass-Enneper representations

The paper [2] gives a unified Lie-algebraic structure for conformal parametrizations of general Euclidean, spacelike, and timelike surfaces via Weierstrass-Enneper representations. These representations are expressed through pairs of generating functions of a complex or hyperbolic variable, where features of the geometry of the surface are expressed in terms of properties of the generating functions.

In $\mathbb{R}^{1,2}$ with metric $-dr_1^2 + dr_2^2 + dr_3^2$, we parametrize a timelike surface by a simply connected region Ω in $\mathbb{R}^{1,1}$ with metric $-dx^2 + dy^2$. Rather than introducing a complex structure on (x, y) as for Euclidean and spacelike surfaces, we use, for compatibility with the Lorentz metric, the hyperbolic structure $z = x + \tau y$, where $\tau^2 = 1$ and $\bar{z} = x - \tau y$. Then $z\bar{z} = x^2 - y^2$ and $\bar{\partial} = \frac{\partial}{\partial \bar{z}} = \frac{1}{2}(\frac{\partial}{\partial x} - \tau \frac{\partial}{\partial y})$. Functions $f(z) = u(x, y) + \tau v(x, y)$ where $\bar{\partial}f = 0$ are Lorentz-holomorphic; they satisfy the Lorentz-Cauchy-Riemann equations

$$u_x = v_y, \quad u_y = v_x. \quad (1)$$

Consequently, u and v satisfy the wave equation: $u_{xx} - u_{yy} = 0$ and $v_{xx} - v_{yy} = 0$.

It is shown in [2] that for mappings Ψ_1 and Ψ_2 of a hyperbolic variable that satisfy the in-

tegrability conditions

$$\begin{aligned} \operatorname{Im}(\psi_1 \bar{\partial} \psi_2 - \psi_2 \bar{\partial} \psi_1) &= 0 \\ \bar{\psi}_1 \bar{\partial} \psi_1 - \bar{\psi}_2 \bar{\partial} \psi_2 &= 0, \end{aligned} \quad (2)$$

the following formulas give conformal parametrizations of timelike surfaces:

$$\begin{aligned} r_1(x, y) &= \operatorname{Re} \int_{z_0}^z (\psi_1^2 + \psi_2^2) d\zeta \\ r_2(x, y) &= \operatorname{Re} \int_{z_0}^z \tau(\psi_1^2 - \psi_2^2) d\zeta \\ r_3(x, y) &= 2\operatorname{Re} \int_{z_0}^z \psi_1 \psi_2 d\zeta. \end{aligned} \quad (3)$$

These are generalized Weierstrass-Enneper representations for timelike surfaces, determined up to a translational constant. When ψ_1 and ψ_2 are Lorentz holomorphic, they satisfy (2) automatically and yield timelike surfaces with mean curvature zero.

2 Lorentz-holomorphic maps

Lorentz-holomorphic functions appear as solutions of the Lorentz-Cauchy-Riemann equations (1), taking the form

$$(u, v) = \quad (4)$$

$\frac{1}{2}(h(x+y) - k(-x+y), h(x+y) + k(-x+y))$, where h and k have partial derivatives of at least first order. Lorentz-holomorphic maps are plentiful since they constitute an infinite-dimensional Lie group.

The form of the expression (4) shows how Lorentz-holomorphic functions are immediately generalized by removing conditions of smoothness on h and k . We refer to these non-smooth functions also as Lorentz-holomorphic. The paper [1] motivates and constructs general Lorentz-holomorphic maps and studies them from a geometric perspective.

3 Special constructions

The present study makes use of the work in [1] and [2] to construct families of timelike surfaces.

Equation (4) with smooth h and k produces Lorentz-holomorphic functions ψ_1 and ψ_2 given

as

$$2\psi_i(x + \tau y) = \quad (5)$$

$$h_i(x+y) - k_i(-x+y) + \tau[h_i(x+y) + k_i(-x+y)].$$

These functions yield smooth timelike surfaces with mean curvature zero by means of (3).

One may consider extensions of the Weierstrass representation (3) where we relax smoothness conditions on h_i and k_i in (5) in such a way that the integrals in (3) are independent of path. We refer to these also as timelike surfaces. Given a curve in the $x + \tau y$ plane with certain prescribed properties, the paper [1] shows how to construct a Lorentz-holomorphic function $x + \tau y \rightarrow u + \tau v$ so that the given curve is a constant- u or constant- v contour of the function. In this way, a curve in the Lorentz plane (which need not be smooth) gives rise to a timelike surface.

We also construct timelike surfaces that are related in that they arise from different Lorentz-holomorphic functions $\psi_i : x + \tau y \mapsto u + \tau v$ whose constant- u and v contour plots in the $x + \tau y$ plane appear identical when the coloring that distinguishes the constant- u curves from the constant- v curves is removed. The contour plots of these functions have different symmetries under the dihedral group D_4 (see [1]). Those with larger symmetry groups are built from functions h and k that have a lower degree of invertibility.

Any of the surfaces thus constructed give rise to a family of isometric timelike surfaces with mean curvature zero by the transformation $(\psi_1, \psi_2) \rightarrow (e^{\tau\theta}\psi_1, e^{\tau\theta}\psi_2)$, where $\theta \in [0, \frac{\pi}{4}]$. This is analogous to the Bonnet transformations of Euclidean minimal surfaces, that transform, for example, the catenoid to the helicoid. The surfaces in any such family have more in common than simply the mean curvature and metric and therefore the Gaussian curvature. Across any such family, the composition of the Gauss map with the coordinate chart is identical, as well as the principal curvatures. Transformations between surfaces in one family simply change the directions of principal curvature. We refer to these deformations as semi-rigid motions, one step away from a rigid motion. The question of finding non-trivial isometries that preserve principal curvatures but allow the directions of principal curvature to vary is the

classic problem of Bonnet, which is solved in [3] for isothermally parametrized Euclidean surfaces.

References

- [1] B.A. Shipman, P.D. Shipman, and S.P. Shipman, Lorentz-Conformal Transformations in the Plane, *Expositiones Mathematicae* doi: 10.1016/j.exmath.2016.07.003 (2016)
- [2] B.A. Shipman, P.D. Shipman, D. Packard, Generalized Weierstrass-Enneper Representations of Euclidean, Spacelike, and Timelike Surfaces: A Unified Lie-Algebraic Formulation, *Journal of Geometry* doi: 10.1007/s00022-016-0358-7 (2016)
- [3] Z. Soyuçok, The Problem of Non-trivial Isometries of Surfaces Preserving Principal Curvatures. *Journal of Geometry* 52:173–188 (1995)

Robin spectrum of quantum trees and orthogonal polynomials

Stephen P. Shipman^{1,*}, Zhaoxia Wang¹

¹Department of Mathematics, Louisiana State University, Baton Rouge, USA

*Email: shipman@math.lsu.edu

Abstract

We investigate the spectrum of regular quantum trees through a relation to orthogonal polynomials of two variables. For self-adjoint Robin vertex conditions, the behavior of the low eigenvalues is analyzed through the interlacing property of the roots of orthogonal polynomials. The spectrum approaches a band-gap structure as the length of the quantum tree increases. The lowest band becomes negative for large negative derivative-to-value ratio, and there emerge two isolated eigenvalues below the bands.

Keywords: quantum graph, Robin spectrum, orthogonal polynomials

1 A quantum tree and its spectrum

For a metric tree graph as in Fig. 1, we investigate the spectrum of a Schrödinger operator with Robin-type vertex conditions. The graph Γ_n is finite with n branching levels and the same degree $b + 1$ at each vertex; b is the branching number. It is known that the eigenvalues approach those of the Neumann vertex conditions as the spectral variable tends to infinity. The aim of this investigation is to compute the lower Robin spectrum.

The graph can be viewed as a model for photons in a tree structure with high optical density compared with the surrounding medium. The eigenvalues of Γ_n correspond to the frequencies of the free standing waves in the structure.

Each edge of Γ_n is identified with the x -interval $[0, 1]$. The quantum-graph operator A_n acts on each edge by

$$-\frac{d^2}{dx^2} + q(x).$$

The domain $\mathcal{D}(A_n)$ consists of all continuous functions $f \in L^2(\Gamma_n)$ whose restriction to any edge e is in $H^2(e)$ and that satisfy the Robin vertex condition

$$\sum_{e \in \mathcal{E}(v)} f'_e(v) - \alpha f(v) = 0, \quad (1)$$

in which $\mathcal{E}(v)$ is the edge set of a vertex v and $f'_e(v)$ is the derivative of f at v along the edge e .

directed away from v . A_n is self-adjoint on its domain [1, Theorem 1.4.4]. Neumann vertex conditions correspond to $\alpha = 0$.



Figure 1: A quantum graph tree Γ_n with $n = 3$ branching levels, each with branching number $b = 3$.

In this communication, we take $q(x) = 0$ and consider only eigenfunctions that are totally symmetric, that is, invariant under all symmetries of the graph. This allows one to reduce the spectral problem to a tree with no branching (Fig. 2). The vertex conditions (1) become, for the reduced graph, the Robin condition

$$-f'_i(1) + bf'_{i+1}(0) - \alpha f_{i+1}(0) = 0. \quad (2)$$



Figure 2: The totally symmetric eigenfunctions of the quantum tree in Fig. 1 are the eigenfunctions of this reduced graph with vertex conditions (2) depending on the branching numbers of the tree.

The eigenvalue problem $A_n f = \lambda f$ is equivalent to a matrix system $M_n(\mu)(c_{1i}, c_{2i})_{i=1}^n = 0$, with $M_n(\mu)$ a square matrix of size $2n$, $\lambda = \mu^2$, and $f_i(x) = c_{1i} \cos(\mu x) + c_{2i} \sin(\mu x)$. Let $D_n = h_n(\mu) \det M_n$ denote the determinant of M_n multiplied by an appropriate non-vanishing scalar function of μ . The roots of D_n as a function of μ are the square roots of the eigenvalues λ of A_n . We take $\mu > 0$ if $\lambda > 0$ and $i\mu < 0$ if $\lambda < 0$. Figure 3 shows the graphs of D_{19} for various values of α .

By choosing $h_n(\mu)$ appropriately, the sequence $\{D_n\}$ satisfies the recurrence relation

$$\begin{aligned} D_{n+1} &= [(b+1)x + \alpha z] D_n - b D_{n-1}, \\ D_{-1} &= x^2 - 1, \quad D_0 = -\alpha z, \\ (x &= \cos \mu, \quad z = \mu^{-1} \sin \mu). \end{aligned}$$

Observe that $\lambda = \mu^2$ is an eigenvalue of A_n whenever the curve $(x = \cos \mu, z = \mu^{-1} \sin \mu)$ in the (x, z) -plane intersects the zero-set of D_n as a polynomial in x and z , as shown in Fig. 4.

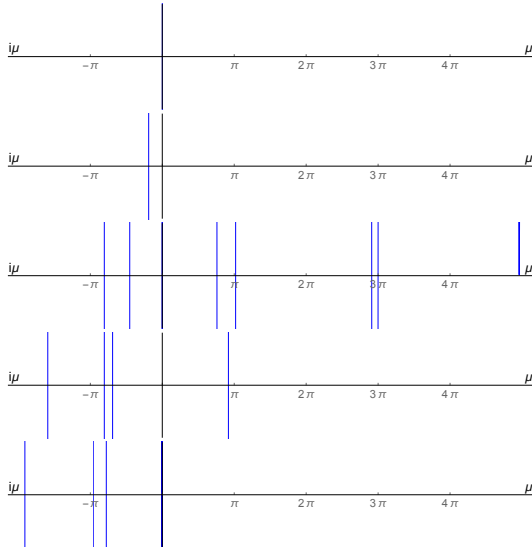


Figure 3: Graph of $D_{19}(\mu)$. The roots mark the square-root eigenvalues $\mu = \sqrt{\lambda}$ for the totally symmetric eigenfunctions of the quantum tree in Fig. 1 with 19 levels. In each case, the branching number is 2, and, from top to bottom, the Robin constant α is 2, 0 (Neumann case), -2.5 , -5 , and -6 .

2 Spectrum and orthogonal polynomials

By defining two sequences of polynomials in the variable $v = (b + 1)x + \alpha z$,

$$\begin{aligned} P_n &= vP_{n-1} - bP_{n-2}, & P_{-1} &= 0, & P_0 &= 1, \\ Q_n &= vQ_{n-1} - bQ_{n-2}, & Q_{-1} &= 1, & Q_0 &= 0, \end{aligned}$$

one can write

$$D_n = (x^2 - 1)Q_n - \alpha z P_n.$$

Because of Favard's Theorem [2, Theorem 4.4], $\{Q_n\}$ and $\{P_n\}$ are sequences of orthogonal polynomials. Their roots are symmetric about $v = 0$, and for each n , the roots of P_n and Q_n interlace and the roots of P_n and P_{n+1} interlace.

The zero set of P_n in the (x, z) -plane consists of the straight lines $(b + 1)x + \alpha z = v_{nk}$ ($k = 1, \dots, n$), and for Q_n one has $(b + 1)x + \alpha z = \tilde{v}_{nk}$ ($k = 1, \dots, n - 1$). Using the signs of αz and $x^2 - 1$ and the interlacing property of $\{v_{nk}\}_k$ and $\{\tilde{v}_{nk}\}_k$, one can prove that the zero set of D_n consists of curves separated by the zero sets of P_n and Q_n and that they cross those of Q_n when $z = 0$ and those of P_n when $x = \pm 1$, as shown in Fig. 5. The two rightmost zero-curves of D_n are unrestricted for $x > 1$ and $z > 0$.

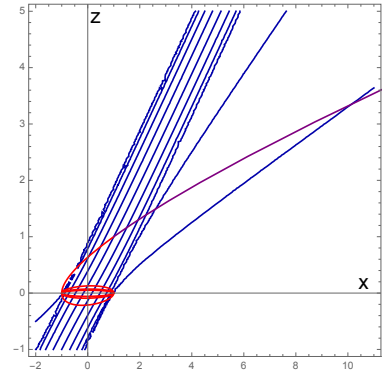


Figure 4: The blue curves form the zero-set of the polynomial $D_9(x, z)$. Their intersection with the spiral curve $(x = \cos \mu, z = \mu^{-1} \sin \mu)$ determine the eigenvalues $\lambda = \mu^2$ of A_n .

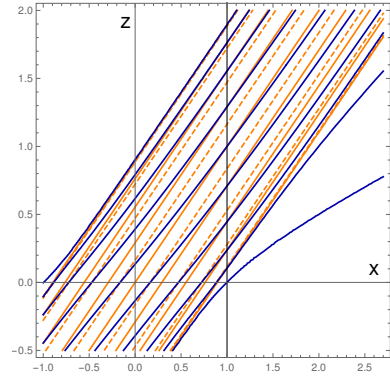


Figure 5: Solid straight lines: level sets of P_n . Dashed straight lines: level sets of Q_n . Solid curves: level sets of D_n .

One deduces the following facts:

- (a) The eigenvalues of A_n gather in spectral bands as $n \rightarrow \infty$, and each but the first band lies in an interval $\pi^2(n^2, (n + 1)^2)$ for $n \geq 1$.
- (b) If $\alpha < -2(b + 1)$, then the first band of eigenvalues is negative. This band tends to $-\infty$ and its width tends to 0 as $\alpha \rightarrow -\infty$.
- (c) Two negative eigenvalues appear to the left of the first band for sufficiently negative α .

References

- [1] G. Berkolaiko and P. Kuchment, *Introduction to Quantum Graphs*, AMS Publications, Vol. 186, 2013.
- [2] T. S. Chihara, *An Introduction to Orthogonal Polynomials*, Dover Publications, Mineola, New York, 2011.

Trefftz-DG approximation for elasto-acoustics

Elvira Shishenina^{1,*}, Hélène Barucq¹, Henri Calandra², Julien Diaz¹

¹Team-Project Magique-3D, Inria, Pau, France

²Total S.A., Houston, USA

*Email: elvira.shishenina@inria.fr

Abstract

Discontinuous finite element methods have proven their numerical accuracy and flexibility, but they are still criticized for high number of degrees of freedom used for computation. The Trefftz approach provides a way to overcome these difficulties. The particularity of Trefftz-type methods is in special choice of basis functions: they represent the local solutions of the initial equations. Thus in case of time-dependent problems it requires a space-time mesh.

This approach has been widely used with time-harmonic formulations [1,2], while the studies are still limited for reproducing temporal phenomena [3].

In the present work we develop the theory for coupled elasto-acoustic systems and we present results for the first-order acoustic wave propagation system.

Keywords: Elasto-acoustic system, Trefftz-DG method, space-time formulation

1 Acousto-elastic system

We consider an initial boundary value problem in elasto-acoustic media. Given a space domain $\Omega = \Omega_F \cup \Omega_S \subset R^n$, a bounded Lipschitz polytope, and a time domain $I = [0, T]$, we set $Q_F := \Omega_F \times I$, $Q_S := \Omega_S \times I$ and $Q = Q_F \cup Q_S$.

Wave propagation in elastic media can be described in terms of velocity $v_s \equiv v_s(x, t)$ and stress tensor $\sigma \equiv \sigma(x, t)$:

$$A\partial_t\sigma - \varepsilon(v_s) = 0 \text{ in } Q_S, \quad (1)$$

$$\rho_s\partial_tv_s - \nabla \cdot \sigma = 0 \text{ in } Q_S.$$

and in acoustic media in terms of velocity $v_f \equiv v_f(x, t)$ and pressure $p \equiv p(x, t)$:

$$\partial_tp + c_f^2\rho_f\nabla \cdot v_f = f \text{ in } Q_F, \quad (2)$$

$$\rho_f\partial_tv_f + \nabla p = 0 \text{ in } Q_F,$$

Here $A \equiv C^{-1}$, ρ_s , c_f , ρ_f are piecewise constant medium parameters.

Continuity of velocity and stress normal components through the fluid-solid interface $\Gamma :=$

$\Omega_F \cap \Omega_S$ is guaranteed by natural transmission conditions:

$$\begin{aligned} v_f \cdot n_\Gamma &= v_s \cdot n_\Gamma \text{ on } \Gamma, \\ \sigma n_\Gamma &= -pn_\Gamma \text{ on } \Gamma, \end{aligned} \quad (3)$$

where $n_\Gamma \in \Omega$ is a normal vector to Γ .

We also consider Dirichlet boundary conditions on $\partial\Omega$, and initial conditions v_{f0} , p_0 , v_{s0} , σ_0 at time $t = 0$. In the following, in order to simplify the formulations, we set the source function $f \equiv 0$.

2 Trefftz-DG formulation

We preliminary introduce a mesh \mathcal{T}_h on $Q := Q_F \cup Q_S$. We consider a particular mesh whose elements are right rectangular-sided prisms with vertical faces parallel to the time axes. We suppose evenly that all discontinuities of media parameters lie on the inter-element boundaries. We denote by $\mathcal{F}_h := \cup_{K \in \mathcal{T}_h} \partial K$ the mesh skeleton, which can be decomposed into the subsets:

\mathcal{F}_h	description
$\mathcal{F}_h^{\Omega_F}, \mathcal{F}_h^{\Omega_S}$	internal Ω -like faces $t = const.$
$\mathcal{F}_h^{I_F}, \mathcal{F}_h^{I_S}$	internal I -like faces $x = const.$
$\mathcal{F}_h^{0_F}, \mathcal{F}_h^{0_S}$	$\Omega_F \times \{0\}, \Omega_S \times \{0\}$
$\mathcal{F}_h^{T_F}, \mathcal{F}_h^{T_S}$	$\Omega_F \times \{T\}, \Omega_S \times \{T\}$
$\mathcal{F}_h^{D_F}, \mathcal{F}_h^{D_S}$	$(\partial\Omega_F \setminus \Gamma) \times I, (\partial\Omega_S \setminus \Gamma) \times I$
\mathcal{F}_h^{FS}	$\Gamma \times I$

We define Trefftz space:

$$\mathbf{T}(\mathcal{T}_h) := \left\{ (\omega_f, q, \omega_s, \xi) \subset H^1(\mathcal{T}_h)^4 \text{ s.t.} \right. \quad (4)$$

$$\left. \partial_t q + c_f^2 \rho_f \nabla \cdot \omega_f = \rho_f \partial_t \omega_f + \nabla q = 0, \forall K_F \in \mathcal{T}_h, \right.$$

$$\left. A\partial_t \xi - \varepsilon(\omega_s) = \rho_s \partial_t \omega_s - \nabla \cdot \xi = 0, \forall K_S \in \mathcal{T}_h \right\}.$$

Multiplying equations (1-2) by the test functions of Trefftz space, integrating by parts in space and time, we obtain the Trefftz-DG formulation for coupled elasto-acoustic system:

Search $(v_{fh}, p_h, v_{sh}, \sigma_h) \subset H^1(\mathcal{T}_h)^4$ such that, for all $K_F, K_S \in \mathcal{T}_h$ and for all $(\omega_f, q, \omega_s, \xi) \subset$

$H^1(\mathcal{T}_h)^4$ it holds:

$$\begin{aligned} \int_{\partial K_S} \left[(A \sigma_h : \xi + \rho_s v_{sh} \cdot w_s) \cdot n_K^t \right. \\ \left. - (v_{sh} \xi + \hat{\sigma}_h \omega_s) \cdot n_K \right] ds = 0, \\ \int_{\partial K_F} \left[\left(\frac{1}{c_f^2 \rho_f} \hat{p}_h q + \rho_f v_{f_h} \cdot \omega_f \right) \cdot n_K^t \right. \\ \left. + (\hat{p}_h \omega_f + v_{f_h} q) \cdot n_K \right] ds = 0. \end{aligned} \quad (5)$$

The numerical fluxes v_{f_h} , \hat{p}_h , v_{sh} , $\hat{\sigma}_h$ are defined on the mesh skeleton \mathcal{F}_h as following:

\mathcal{F}_h	v_{f_h}	\hat{p}_h
$\mathcal{F}_h^{I_F}$	$\{v_{f_h}\} + \beta [\![p_h]\!]_x$	$\{p_h\} + \alpha [\![v_{f_h}]\!]_x$
$\mathcal{F}_h^{\Omega_F}$	$v_{f_h}^-$	p_h^-
$\mathcal{F}_h^{T_F}$	v_{f_h}	p_h
$\mathcal{F}_h^{0_F}$	v_{f_0}	p_0
$\mathcal{F}_h^{D_F}$	g_{D_F}	$p_h + \alpha(v_{f_h} - g_{D_F}) \cdot n_K$
\mathcal{F}_h^{FS}	$v_{f_h} \cdot n_K^t = v_{sh} \cdot n_K^t$	$p_h + \alpha(v_{f_h} - v_{sh}) \cdot n_K^t$

\mathcal{F}_h	v_{sh}	$\hat{\sigma}_h$
$\mathcal{F}_h^{I_S}$	$\{v_{sh}\} - \delta [\![\sigma_h]\!]_x$	$\{\sigma_h\} - \gamma [\![v_{sh}]\!]_x$
$\mathcal{F}_h^{\Omega_S}$	v_{sh}^-	σ_h^-
$\mathcal{F}_h^{T_S}$	v_{sh}	σ_h
$\mathcal{F}_h^{0_S}$	v_{s_0}	σ_0
$\mathcal{F}_h^{D_S}$	$v_{sh} - \delta(\sigma_h - g_{D_S})n_K$	g_{D_S}
\mathcal{F}_h^{FS}	$v_{sh} - \delta(\sigma_h - p_h)n_K^t$	$\sigma_h n_K^t = -p_h n_K^t$

Here α , β , γ , δ are positive penalty parameters, $(n_K, n_K^t) \in Q$ the outward pointed unit normal vectors to $\partial K \subset \mathcal{F}_h$, and superscript “ $-$ ” represents the flux taken from neighbour element with lower time.

Coercivity and continuity of the bilinear and linear forms in (5) are based on $L^2(\mathcal{T}_h)$ norm estimations. They confirm well-posedness of Trefftz-DG variational problem.

3 Numerical results

To test the performances of our formulation, we have decided to solve the acoustic equation first. For that purpose many choices of basis functions are possible. The main condition to be satisfied is the Trefftz property (4) inside each element. We have computed a wave polynomial basis using the Taylor expansions of generating exponential functions, which are the exact solutions of the initial acoustic system (2). In the one-dimensional case, we need eight polynomial functions for each unknown, velocity and pressure, to achieve approximation of order 3.

The results of convergence of the numerical velocity as a function of cell size h for different approximation orders are represented in Figure 1.

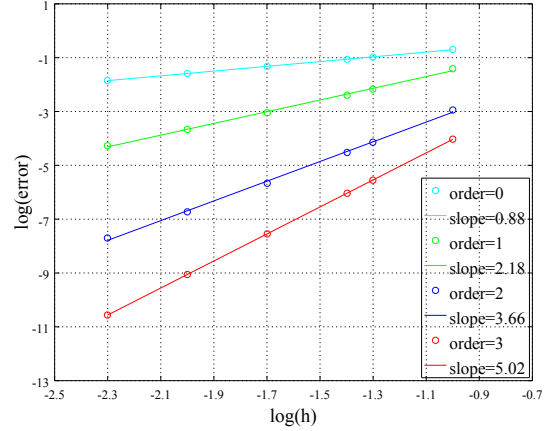


Figure 1: Convergence of $v_f(x, t)$ as a function of cell size h

The obtained convergence order is higher than the order of polynomial basis used for computation. Moreover it requires less number of degrees of freedom compared to the classical DG method in order to achieve the same accuracy. In higher-dimension cases, polynomials are similarly computed using Taylor expansions of generating exponential functions, the exact solutions of the system in 2D plus time and 3D plus time. The accuracy of wave simulations in coupled acoustic-acoustic media shows a high sensitivity to the handling of transmission conditions.

References

- [1] G. Gabard, A Discontinuous Galerkin Methods and Plane Waves for Time-Harmonic Problems, *Journal of Computational Physics* **255** (2007), pp. 1961–1984.
- [2] R. Hiptmair, A. Moiola and I. Perugia, Plane Wave Discontinuous Galerkin Methods for the 2D Helmholtz Equation: Analysis of the p-version, *SIAM Journal of Numerical Analysis* **49** (2011), pp. 264–284.
- [3] F. Kretzschmar, A. Moiola, I. Perugia and S. Schnepp, A priori Error Analysis of Space-Time Trefftz-DG Method for Wave Problems, *IMA Journal of Numerical Analysis* **36(4)** (2015).

On the dynamic features of discrete lattices with nonlinear local resonators

Priscilla B. Silva^{1,*}, Varvara G. Kouznetsova¹, Marc G. D. Geers¹

¹Department of Mechanical Engineering, Eindhoven University of Technology, Eindhoven, The Netherlands

*Email: p.brandao.silva@tue.nl

Abstract

The possibility of designing structures able to manipulate and control wave propagation — the so-called metamaterials — has attracted a lot of interest in different fields, from optics to mechanics. With respect to mechanical metamaterials, most of the works up to now have been limited to linear material behavior. In this paper, the dynamic behavior of local resonant metamaterials with nonlinear oscillators is investigated. The harmonic balance method is used to derive approximate expressions for the dispersion relations of these materials. The key idea here is to account for the effects of sub/superharmonic terms which have been neglected so far. Direct numerical simulations are also performed in order to verify the approximate solutions. From these analyses, unique features of this class of nonlinear metamaterials are revealed, such as: tunability, multiple stable wave modes and multiple band gap generation. Moreover, the possibility of designing non-reciprocal devices is demonstrated.

Keywords: wave propagation, nonlinearity, metamaterials, lattice system

1 Introduction

Metamaterials are engineered structures in which the design of a meta-atom with specific properties gives rise to on-demand and unusual macroscopic effective behavior. Herein, the interest lies in the possibility of manipulating wave propagation by making use of local resonance phenomenon [1], typical of so-called acoustic metamaterials. Most of the works up to now in acoustic metamaterials have been limited to linear material models [2]. This work intends to show that fascinating and unrevealed phenomena are yet to be discovered when nonlinearities, proper of many real materials, as for instance, rubber-like materials, are taken into account (see Figure 1(a)).

The interest in investigating new features emerging from geometric or material nonlineari-

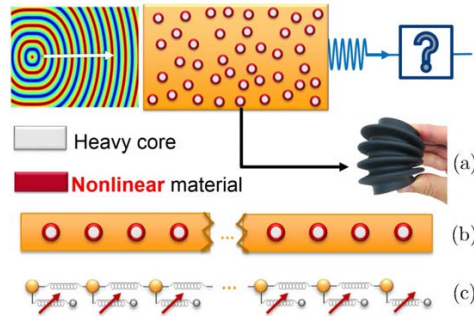


Figure 1: (a) Problem overview, i.e., revealing the effects of nonlinear metamaterials on wave propagation, (b) corresponding 1D continuum model, and (c) corresponding 1D lattice model investigated in this paper.

ties within the framework of local resonant metamaterials and phononic crystals has evolved as a natural consequence of the fast development in the area in the recent years. Among the promising features associated with nonlinearity in periodic systems are solitary wave propagation [3], nonreciprocal wave propagation [4], amplitude-dependent dispersion relation [5], bistability and multistability [3].

Within the framework of local resonant metamaterials, Lazarov and Jensen [6] were the first to investigate the effect of nonlinear local resonators on the propagation of waves through a 1D lattice system. They showed that due to the nonlinearity, the dispersion relation of the system becomes amplitude-dependent, which induces a frequency shift of the local resonant band gap. In the present paper, a chain with **nonlinear cubic resonators**, as shown in Figure 1(c), is studied in more detail. In particular, **sub/superharmonic generation** has been considered and revealed the possibility of generating multiple band gaps.

2 Methodology

The harmonic balance method was used to analyze the oscillatory motion of the nonlinear peri-

odic system. Direct numerical simulations were also performed in order to verify the approximating solutions.

3 Results and Discussion

The analysis of the dispersion relations derived for the considered nonlinear local resonant metamaterial (LRMM) shows that multiple stable wave solutions may exist, as depicted in Figure 2. This occurs because each local resonator attached to the chain acts as a forced duffing oscillator. In damped nonlinear systems, **multiple stable waves** occur only for sufficiently large values of the nonlinear parameter Γ , which encompasses both the degree of nonlinearity and excitation wave amplitude. In this case, one wave mode (wave 1 in Figure 2) is associated with the main chain and its interaction with local oscillators and it is typical in linear LRMMs; the second one (wave 2 in Figure 2) has low propagation speed (group velocity) and it is responsible for large displacements of oscillators. This second wave mode contributes to the reduction of the effectiveness of the attenuation zone due to local resonance phenomenon.

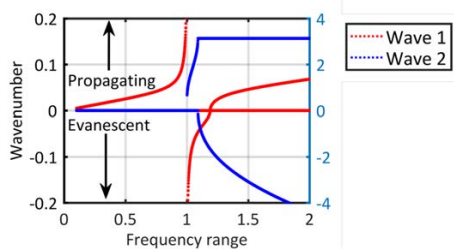


Figure 2: Multiple stable wave modes in a discrete cubic LRMM.

Up to now, the few works in the literature concerned with nonlinear LRMMs neglected the contribution of sub/superharmonics. In this work, sub/superharmonic generation has been considered within the framework of the harmonic balance formulation and revealed a new phenomenon proper of nonlinear LRMMs: the possibility of the existence of **multiple band gaps** around sub/superharmonic resonances. This opens new possibilities for passive vibration control.

Due to the generation of multiple harmonics, nonlinear LRMMs can be used in the design of devices whose dynamic behavior depends on the wave propagation direction [7]. By sequen-

tially coupling two chains of LRMMs, one with linear resonators and another one with nonlinear resonators, a system with **asymmetric behavior** is constructed (see Figure 3).

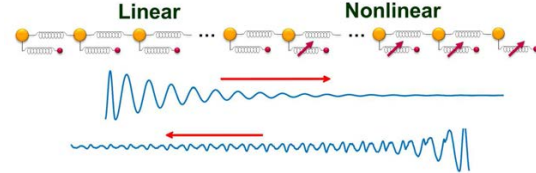


Figure 3: Nonreciprocal behavior of a system comprising connected linear and nonlinear lattices.

4 Conclusions and Future Prospects

It was shown that cubic metamaterials exhibit multiple stable wave modes, multiple band gap generation and nonreciprocity. Such features make them promising for applications in sensor technology, damage detection, imaging, energy harvesting, among others. In the future, the effect of other nonlinear material models in the dynamic behavior of metamaterials will be investigated.

References

- [1] Z. Liu et al., *Science* **289**(5485) (2000), pp. 1734–1736.
- [2] J. Christensen et al., *M R S Communications* **5**(3) (2015), pp. 453–462.
- [3] N. Nadkarni et al., *Physical Review E* **90** (2014), pp. 023204.
- [4] S. Lepri and A. Pikovsky, *Chaos* **24** (2014), pp. 043119.
- [5] R. Khajehtourian and M. I. Hussein, *AIP Advances* **4** (2014), pp. 124308.
- [6] B.S. Lazarov and J.S. Jensen, *International Journal of Non-Linear Mechanics* **42**(10) (2007), pp. 1186–1193.
- [7] J.M. Manimala, *Ph.D. Thesis*, Purdue University (2014).

Uncertainty Quantification for Electromagnetic Scattering by 1D Perfect Electric Conducting Gratings

Rubén Aylwin¹, Patrick Fay², Carlos Jerez-Hanckes¹, Gerardo Silva-Oelker^{1,2,*}

¹School of Engineering, Pontificia Universidad Católica de Chile, Santiago, Chile

²Department of Electrical Engineering, University of Notre Dame, South Bend, Indiana, United States

*Email: gsilva@nd.edu

Abstract

A novel deterministic method capable to compute the first two statistical moments of electric fields scattered by a perfect electric conducting grating with stochastic surface perturbations was developed and implemented. The resulting electric field integral equations are solved via the boundary elements method with discretization based on piecewise hierarchical constant basis, e.g. Haar's wavelets, and a sparse approximation.

Keywords: Uncertainty quantification, gratings, scattering

Introduction

One dimensional periodic gratings are ubiquitous in electromagnetic technologies due to their remarkable properties, generating a vast literature devoted to their analysis and simulation. Yet, most works assume an ideal deterministic shape, oblivious to the effect of roughness or *uncertainty* that the surface in reality may portray. Roughness can be produced, for example, by manufacturing processes or operating conditions. Though generally small, these distortions can undermine the gratings performance. To provide an efficient and robust tool to accurately account these uncertainties motivates the present work.

Due to the random nature of the perturbations, it is necessary to formulate the scattering problem in terms of stochastic parameters. The well-known Monte-Carlo simulation is generally used to quantify these uncertainties. However, this method requires high computational effort. Alternative methods for solving stochastic partial differential equations (SPDEs) have been proposed, calculating the statistical moments (mean, variance, and so on) based on a deterministic approach [1, 2], and avoiding the calculation of a set of samples. By using a first-order shape Taylor expansion, valid for small

perturbations, the statistical moments are deterministically obtained, which produces a fast and reliable numerical algorithm.

In this work, we seek to compute the expected value and variance of the scattered field by a perfect electric conducting (PEC) grating with random surface perturbations. As customary, we reduce the volume problem to one over the boundary by means of a suitable Green's function, establishing an integral equation. This dimension reduction considerably reduces the number of degrees of freedom (DOFs) required to solve the problem. Furthermore, by using hierarchical basis or Haar wavelets, we can naturally implement a sparse approximation.

Mathematical Modeling

We consider a PEC grating with surface $\tilde{\Gamma} \times \mathbb{R}$, where $\tilde{\Gamma} \in \mathbb{R}$ is parametrized by a Λ -periodic mapping $\mathbb{R} \ni t \rightarrow (t, y(t))$ i.e. $y(t + \Lambda) = y(t)$. This defines the infinite, z -invariant open and periodic domain of propagation $\tilde{D} \times \mathbb{R} \subset \mathbb{R}^3$. We denote the restriction to a period by D with boundary Γ .

Decomposing the electric field E and the magnetic field H in their cartesian components, it is possible to define the transverse electric (TE) polarization, where $E_x = E_y = H_z = 0$. Moreover, we assume a time-harmonic wave ($e^{i\omega_0 t}$) with angular frequency ω_0 . The total polarized electric field u is defined as $u(\mathbf{r}) := E_z(\mathbf{r})$ with $\mathbf{r} \in \tilde{D} \subset \mathbb{R}^2$, and parallel to the grooves of the grating. We consider incident plane waves $u^i = e^{i\mathbf{k} \cdot \mathbf{r}}$, where $\mathbf{k} = k(\cos \theta_i, \sin \theta_i) = (k_x, k_y)$ is the wave-vector with module $2\pi/\lambda$, and angle of incidence θ_i . By linearity, the total wave is given by $u(\mathbf{r}) = u^i(\mathbf{r}) + u^s(\mathbf{r})$, where u^s is the scattered field. Moreover, the incident field satisfies Helmholtz's equation; therefore, we aim to calculate the scattered one. For TE polarization, a PEC surface leads to a Dirichlet boundary condition, given by the trace operator γ_0 .

With this setting, it is possible to condense the scattering problem over one period through the restricted domain D with boundary Γ , and the appropriate radiation condition:

$$(\Delta + k^2)u^s = 0 \quad \text{in } D, \quad (1)$$

$$\gamma_0 u^s = -\gamma_0 u^i \quad \text{on } \Gamma, \quad (2)$$

$$u^s(x + \Lambda, y) = e^{ik_x \Lambda} u^s(x, y), \quad (3)$$

$$y^{1/2} (\partial_y - ik) u^s = 0 \quad \text{as } y \rightarrow \infty. \quad (4)$$

Our numerical method is based on the electric field integral equation (EFIE) [3]:

$$(\nabla \mathcal{J})(\mathbf{r}) = -\gamma_0 u^i(\mathbf{r}), \quad \mathbf{r} \in \Gamma. \quad (5)$$

In this formulation, the density $\mathcal{J} : \Gamma \rightarrow \mathbb{C}$ is the surface current density, and ∇ is the weakly singular (WS) operator. This operator is given by the Dirichlet trace of the Single Layer (SL) potential \mathcal{S} , so that $\nabla := \gamma_0 \mathcal{S}$. Since the scattering problem is defined over a periodic domain, the SL potential is given in terms of a periodic Green's function.

To introduce shape randomness, a standard probability space $(\Omega, \Sigma, \mathbb{P})$ is set. Specifically, we define small random perturbations from a reference nominal deterministic boundary Γ_0 as

$$\Gamma_\epsilon(\omega) := \{\mathbf{r} + \epsilon \kappa(\mathbf{r}, \omega) \mathbf{n}_0(\mathbf{r}) : \mathbf{r} \in \Gamma_0\},$$

with $\omega \in \Omega$, and the bounded amplitude $\kappa \in \mathbb{R}$. This defines an infinite open perturbed domain $D_\epsilon \subset \mathbb{R}^2$ wherein solutions of (1)-(4) are denoted by $u_\epsilon(\omega)$.

To approximate the statistical moments, a first order shape-Taylor expansion is considered:

$$u_\epsilon^s(\mathbf{r}, \omega) = u_0^s + \epsilon \dot{u}^s[\kappa(\omega) \mathbf{n}_0] + O(\epsilon^2), \quad (6)$$

where \dot{u}^s is the shape derivative of u^s at D_0 given the perturbation field $\kappa(\omega) \mathbf{n}_0$ [1].

We aim to obtain deterministically the expected value and the variance of the scattered field u_ϵ^s over D_ϵ . According to (6), the mean field can be computed as $\mathbb{E}[u_\epsilon^s](\mathbf{r}) = u_0^s + O(\epsilon^2)$, where u_0^s can be obtained directly from (1)-(4) on the nominal domain D_0 via (5). On the other hand, for $\epsilon \ll 1$, the variance can be obtained from [1]

$$\text{Var}[u_\epsilon^s](\mathbf{r}) = \epsilon^2 \mathbb{E}[\dot{u}^s(\mathbf{r}, \cdot)^2] + O(\epsilon^3).$$

Hence, we need to calculate

$$\text{Cor}[\dot{u}^s] = (\mathcal{S} \otimes \mathcal{S})M, \quad (7)$$

where $M : \Gamma_0 \times \Gamma_0 \rightarrow \mathbb{C}$ is a bivariate unknown surface density. To compute M , we must solve the tensorized volume problem for \dot{u}^s through the integral representation [1]:

$$(\nabla \otimes \nabla)M = \text{Cor}[\kappa](\mathcal{J} \otimes \mathcal{J}), \quad \text{on } \Gamma_0 \times \Gamma_0. \quad (8)$$

Direct tensorization increases the number of DOFs from N to N^2 . Nevertheless, by using hierarchical constant basis or Haar wavelets, we can perform a sparse approximation thereby reducing DOFs from N^2 to $\mathcal{O}(N \log N)$. With this, (5) and (8) are solved via the Boundary Element Method.

Numerical Results

For the implemented algorithm, we obtain rates of convergence of 0.50 and 0.67 for the dense and sparse approximations considering $k = 42$, respectively. While, the obtained convergence rate for the first moment is equal to 1.0 for $k = 6, 13$, and 42 (Fig.1).

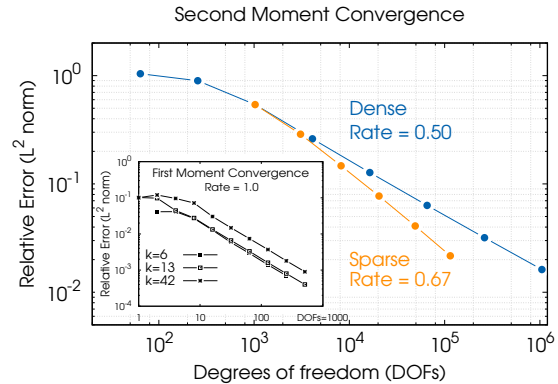


Figure 1: Method convergence

References

- [1] Harbrecht, H., Schneider, R., and Schwab, C., Sparse second moment analysis for elliptic problems in stochastic domains, *Seminar für Angewandte Mathematik Eidgen 2007-02* (2007)
- [2] Petersdorff, T. von, and Schwab, C., Sparse finite element methods for operator equations with stochastic data. *Applications of Mathematics*, **51(2)** (2006), pp. 145–180.
- [3] Jin, J.-M., *Theory and Computation of Electromagnetic Fields*, 1st edition, John Wiley & Sons, New Jersey, 2010.

Low-Rank Properties in Schur Complements of Discretized Helmholtz Equations

Sergey Solovyev^{1,*}, Martin J. Gander²

¹Institute of Petroleum Geology and Geophysics SB RAS, Novosibirsk, Russia

²Section of Mathematics, University of Geneva, Switzerland

*Email: solovevs@ipgg.sbras.ru

Abstract

We study numerically the ϵ -rank of subblocks arising in Schur complement matrices of discretized three dimensional Helmholtz problems. A small ϵ -rank is the key ingredient for \mathcal{H} -matrix techniques, and while Laplace-like problems have this property, the ϵ -rank for the Helmholtz case is growing with increasing wave number. We study here the growth rate in the case of a heterogeneous Helmholtz problem with a checker board wave speed distribution, and compare it to the constant wave number case.

Keywords: Heterogeneous Helmholtz Equation, Schur Complements, ϵ -Rank

1 Introduction

In contrast to Laplace-like problems, effective iterative methods for solving Helmholtz problems are rare and expensive, for an overview, see [4, 6] and references therein. Direct methods are thus attractive for such problems, and a significant effort has gone into combining reordering techniques and LU-decompositions using multifrontal methods, where additional savings are sought through compression techniques using low rank properties of subblocks arising in the factorization. While there are some theoretical results on the potential low rank property for the constant wave number case [1–3], and also comprehensive numerical experiments [5], much less is known about the case of variable wave numbers. We study here numerically the specific case of a checker board wave speed distribution.

2 Problem Setting

We study numerically the Helmholtz equation

$$\begin{aligned} \Delta u + \frac{(2\pi\nu)^2}{V^2} u &= \delta(\bar{r} - \bar{r}_s) f \quad \text{in } \Omega := (0, L)^3, \\ u &= 0 \quad \text{on } \partial\Omega, \end{aligned} \tag{1}$$

where ν is the frequency, V is the velocity, \bar{r}_s are the coordinates of the source f , and the wave number is $k := \frac{(2\pi\nu)}{V(x,y,z)}$, chosen such that we

have a well posed problem with Dirichlet conditions.

We discretize the Helmholtz equation (1) using a standard seven point finite difference discretization with mesh spacing $h := \frac{1}{n}$, which leads to a sparse linear system $A\mathbf{u} = \mathbf{f}$. If we partition the system matrix into a first block A_1 corresponding to the first x - y plane of discretization points, and denote the remaining diagonal block by A_2 , the linear system becomes

$$\begin{pmatrix} A_1 & A_{12} \\ A_{21} & A_2 \end{pmatrix} \begin{pmatrix} \mathbf{u}_1 \\ \mathbf{u}_2 \end{pmatrix} = \begin{pmatrix} \mathbf{f}_1 \\ \mathbf{f}_2 \end{pmatrix}. \tag{2}$$

We are interested in the Schur complement matrix $S := A_1 - A_{12}A_2^{-1}A_{21} \in \mathbb{C}^{N \times N}$, $N = (n-1)^2$. We apply the singular value decomposition to the matrix subblock $S_m := S(1 : m, N-m+1 : N)$ and study the decay of its singular values σ_j as a function of h and k . We will compute for a large subblock, $m = \frac{(n-1)^2-1}{2}$, its ϵ -rank, which is defined as the smallest number r_ϵ such that $\frac{\sigma_j}{\sigma_1} < \epsilon$ for all $j > r_\epsilon$.

3 Numerical Experiments

We simulate on the cube with dimension $L = 1200m$, and frequency $\nu = 4Hz, 8Hz, 16Hz$ using the corresponding number of grid points $n = 20, 40, 80$ with velocity $V_1(x, y, z) = 2400m/s$ for 10 points per wavelength (ppw), and velocity $V_1(x, y, z) = 1200m/s$ for 5 ppw. We see in Table 1 that with 5 ppw the ϵ -rank is substantially larger than with 10 ppw. We then consider a Checker Board (ChB) type case with five fields in each direction and velocity $V_1 = 2400m/s$ in the white fields using 10 ppw, and $V_2 = \frac{V_1}{c}$ in the black fields using $10/c$ ppw, where c is a contrast parameter. We see in Table 1 that the ϵ -rank grows in the ChB case with $c = 2$ for larger ϵ more like for ν const and 10ppw, while for small ϵ the growth is more like for ν const and 5 ppw. For $c = 4$ the ϵ -rank is then much larger, while for $c = 8$ it suddenly drops, probably because the waves in the black fields are now not at all resolved any more with 1.25 ppw. We

n	ϵ	1e-2	1e-4	1e-6	1e-2	1e-4	1e-6	1e-2	1e-4	1e-6	1e-2	1e-4	1e-6	1e-2	1e-4	1e-6
n	ν	V=const, ppw=10			V=const, ppw=5			V=ChB, $c = 2$			V=ChB, $c = 4$			V=ChB, $c = 8$		
20	4	27	46	59	19	50	67	34	55	73	50	102	138	20	38	50
40	8	6	68	110	96	154	198	89	148	198	108	227	326	44	66	91
80	16	32	180	276	84	417	547	35	296	449	94	497	749	86	124	176

Table 1: ϵ -rank for a large matrix subblock S_m for a constant velocity and checker board cases with contrast c and 10 ppw in the white fields, and under-resolution in the black fields

n	ϵ	1e-2	1e-4	1e-6	1e-2	1e-4	1e-6	1e-2	1e-4	1e-6	1e-2	1e-4	1e-6	1e-2	1e-4	1e-6
n	ν	V=const, ppw=10			V=const, ppw=20			V=ChB, $c = 1/2$			V=ChB, $c = 1/4$			V=ChB, $c = 1/8$		
20	4	27	46	59	24	44	56	27	47	62	9	29	47	24	46	58
40	8	6	68	110	53	94	120	53	98	126	50	88	121	55	103	127
80	16	32	180	276	110	201	249	125	210	292	113	201	280	111	199	278

Table 2: ϵ -rank in 3d for a large matrix subblock S_m for a constant velocity and checker board cases with contrast c and 10 ppw in the white fields, and over-resolution in the back fields

next show in Table 2 the corresponding results for the over-resolved case. We see that now in all cases the ϵ -rank is growing comparably to the constant wave number case at resolution of 10 ppw in the first column (which is the same as in Table 1), which indicates that it is the lower resolution of 10 ppw in the white fields which dictates the ϵ -rank growth. The growth is $O(k^{4/3})$, like in the constant wave number case, see [5], where it was also noticed that increasing the resolution does not influence the ϵ -rank once the waves are well resolved.

4 Conclusion

We studied numerically how the ϵ -rank is growing in subblocks of Schur complement matrices arising from discretized heterogeneous Helmholtz problems. We found that the growth for a checker board situation is comparable to the homogeneous case, provided the resolution in all fields of the checker board is at least as good as the resolution of the homogeneous case, and there are no under-resolved fields of the checker board. The growth in 3d for a planar Schur complement is then also $O(k^{4/3})$, like in the constant and random wave number case studied in [5].

This research was partially supported by RFBR grants 16-05-00800, 17-01-00399 and the Russian Academy of Sciences Program "Arctic".

References

- [1] L. Banjai and W. Hackbusch. Hierarchical matrix techniques for low- and high-frequency Helmholtz problems. *IMA J. Numer. Anal.*, 28:46–79, 2008.

- [2] S. Börm and J. M. Melenk. Approximation of the high-frequency Helmholtz kernel by nested directional interpolation. *arXiv preprint arXiv:1510.07189*, 2015.
- [3] B. Engquist and H. Zhao. Approximate separability of Green's function for high frequency Helmholtz equations. Technical report, DTIC Document, 2014.
- [4] O. G. Ernst and M. J. Gander. Why it is difficult to solve Helmholtz problems with classical iterative methods. In *Numerical analysis of multiscale problems*, pages 325–363. Springer, 2012.
- [5] M. J. Gander and S. Solov'yev. A numerical study on the compressibility of subblocks of Schur complement matrices obtained from discretized Helmholtz equations. In *Proceedings of the 7th International Conference, NAA 2016, Lozenetz*. Springer Verlag, 2016.
- [6] M. J. Gander and H. Zhang. Iterative solvers for the Helmholtz equation: Factorizations, sweeping preconditioners, source transfer, single layer potentials, polarized traces, and optimized Schwarz methods. *submitted*, 2016.

Domain-decomposition preconditioning for high-frequency Helmholtz and Maxwell problems with absorption

**Euan A. Spence^{1,*}, Marcella Bonazzoli², Victorita Dolean³, Ivan G. Graham¹,
Pierre-Henri Tournier⁴, Eero Vainikko⁵**

¹Department of Mathematical Sciences, University of Bath, Bath, UK

²Laboratoire J.A. Dieudonné, Université de Nice Sophia-Antipolis, Nice, France

³Department of Mathematics and Statistics, University of Strathclyde, Glasgow, UK

⁴Laboratoire Jacques-Louis Lions, Université Pierre et Marie Curie, Paris, France

⁵Institute of Computer Science, University of Tartu, Tartu, Estonia

*Email: E.A.Spence@bath.ac.uk

Abstract

When applied to the Helmholtz or time-harmonic Maxwell equations with absorption, classical-additive-Schwarz domain-decomposition preconditioning works well if the absorption is large enough.

Keywords: Helmholtz equation, time-harmonic Maxwell equations, domain decomposition, absorption, iterative solvers, preconditioning, GMRES

1 Introduction

This talk is about domain-decomposition preconditioners for the Helmholtz and time-harmonic Maxwell equations with absorption. The main message is that, when applied to the Helmholtz or time-harmonic Maxwell equations with absorption, the classical additive-Schwarz domain-decomposition preconditioner works well if the absorption is large enough. How large the absorption needs to be is quantified in theorems, and illustrated in numerical results.

This talk is based on the recent paper [5] and the upcoming paper [1].

2 The Helmholtz equation

We consider the Helmholtz interior impedance problem,

$$\begin{cases} -\Delta u - (k^2 + i\varepsilon)u = f & \text{in } \Omega, \\ \partial u / \partial n - iku = g & \text{on } \partial\Omega, \end{cases} \quad (1)$$

where $k, \varepsilon > 0$ and Ω is a 2-d convex polygon. We assume that $\varepsilon \lesssim k^2$.

We denote by A_ε the system matrix arising from continuous piecewise linear ($P1$) Galerkin finite element approximations of (1).

We consider the classical two-level additive-Schwarz preconditioner, where zero Dirichlet boundary conditions are imposed on the subdomains

(observe that, since $\varepsilon > 0$, these subdomain problems have a unique solution for every k); we denote the action of this preconditioner by $B_{\varepsilon,AS}^{-1}$ (see [5, Equations 3.1 and 3.7] for the precise definition). We let H_{sub} denote the subdomain diameter, H the coarse-grid diameter, and δ the overlap parameter.

We work with the euclidean vector norm, weighted by the matrix $D_k := S + k^2 M$, where S is the matrix corresponding to the discretisation of the $\nabla u \cdot \bar{\nabla v}$ term in the variational formulation, and M is the mass matrix (and thus A_ε equals $S - (k^2 + i\varepsilon)M$ plus a term corresponding to an integral over $\partial\Omega$). We denote the weighted norm and inner-product by $\|\cdot\|_{D_k}$ and $\langle \cdot, \cdot \rangle_{D_k}$ respectively.

Theorem 1 (Main result for left preconditioning)

$$(i) \quad \|B_{\varepsilon,AS}^{-1} A_\varepsilon\|_{D_k} \lesssim \left(\frac{k^2}{|\varepsilon|} \right) \quad \text{for all } H, H_{\text{sub}}.$$

Furthermore, there exists a constant C_1 such that

$$(ii) \quad |\langle \mathbf{V}, B_{\varepsilon,AS}^{-1} A_\varepsilon \mathbf{V} \rangle_{D_k}| \gtrsim \left(1 + \frac{H}{\delta} \right)^{-1} \left(\frac{\varepsilon}{k^2} \right)^2 \|\mathbf{V}\|_{D_k}^2,$$

for all $\mathbf{V} \in \mathbb{C}^n$, when

$$\begin{aligned} & \max \left\{ k H_{\text{sub}}, k H \left(1 + \frac{H}{\delta} \right) \left(\frac{k^2}{|\varepsilon|} \right)^2 \right\} \\ & \leq C_1 \left(1 + \frac{H}{\delta} \right)^{-1} \left(\frac{|\varepsilon|}{k^2} \right). \end{aligned} \quad (2)$$

Combining this result with the analogue in the D_k norm of the Elman estimate for GMRES (see [5, Theorem 5.1]) we obtain:

Corollary 2 (GMRES convergence for left preconditioning) Consider the weighted GMRES method where the residual is minimised in the norm induced by D_k (see, e.g., [6]). Let \mathbf{r}^m denote the m th iterate of GMRES applied to the system A_ε , left preconditioned with $B_{\varepsilon,AS}^{-1}$. Then

$$\frac{\|\mathbf{r}^m\|_{D_k}}{\|\mathbf{r}^0\|_{D_k}} \lesssim 1 - \left(1 + \frac{H}{\delta}\right)^{-2} \left(\frac{\varepsilon}{k^2}\right)^6^{m/2}, \quad (3)$$

provided condition (2) holds.

The bound (3) shows that, if $\varepsilon \sim k^2$, $\delta \sim H$, and both kH and kH_{sub} are sufficiently small, then GMRES converges in a k -independent number of iterations (and this is confirmed by numerical experiments). The bound (3) has the number of iterations growing severely when $\varepsilon \ll k^2$, but numerical experiments show that this bound is pessimistic in this regime [5, §6.1].

Our main motivation for studying this problem is so-called ‘‘shifted Laplacian’’ preconditioning; i.e. preconditioning A_0 (the discretisation of the problem (1) with $\varepsilon = 0$) with an approximation of A_ε^{-1} (such as $B_{\varepsilon,AS}^{-1}$), and the natural question of how best to choose ε .

This question of how to choose ε is discussed further (in conjunction with the results in [3]) in [5, §1]. With the preconditioner $B_{\varepsilon,AS}^{-1}$ defined above, the theory is not yet able to justify rigorously the choice of ε for $B_{\varepsilon,AS}^{-1}$ to be a good preconditioner for A_0 . Nevertheless, this situation can be improved if the Dirichlet boundary conditions on the subdomains are replaced by impedance boundary conditions – this will be discussed in the talk by Ivan Graham.

3 The time-harmonic Maxwell equations

Analogues of Theorem 1 and Corollary 2 can be obtained for the PEC problem for the time-harmonic Maxwell equations [1]; i.e. (1) is replaced by

$$\begin{cases} \nabla \times (\nabla \times \mathbf{E}) - (k^2 + i\varepsilon)\mathbf{E} = \mathbf{f} & \text{in } \Omega, \\ \mathbf{E} \times \mathbf{n} = \mathbf{0} & \text{on } \partial\Omega, \end{cases}$$

where now Ω is a 3-d convex polyhedra. Note the PEC boundary condition means that this is not the exact analogue of the Helmholtz problem (1) (the main obstacle to translating the Helmholtz results across to the Maxwell impedance problem is that the appropriate function space for the latter problem is not $H(\text{curl}; \Omega)$).

4 How these results were obtained

The Helmholtz theory in [5] was inspired by the results in [2], where non-self-adjoint problems that are ‘‘close to’’ self-adjoint coercive problems were considered. Although the Helmholtz problem (1) is not close to a self-adjoint coercive one, and our technical tools are very different, [2] provided a framework that we were able to adapt into the above results.

The paper [4] provides, in some sense, the Maxwell analogue of [2]; our Maxwell results, therefore, both follow this framework and use some specific results from [4].

References

- [1] M. Bonazzoli, V. Dolean, I. G. Graham, E.A. Spence, and P.-H. Tournier. Domain decomposition preconditioning for the high-frequency time-harmonic Maxwell equations with absorption. *in preparation*.
- [2] X-C. Cai and O. B. Widlund. Domain decomposition algorithms for indefinite elliptic problems. *SIAM Journal on Scientific and Statistical Computing*, 13(1):243–258, 1992.
- [3] M. J. Gander, I. G. Graham, and E. A. Spence. Applying GMRES to the Helmholtz equation with shifted Laplacian preconditioning: What is the largest shift for which wavenumber-independent convergence is guaranteed? *Numerische Mathematik*, 131(3):567–614, 2015.
- [4] J. Gopalakrishnan and J. Pasciak. Overlapping Schwarz preconditioners for indefinite time harmonic Maxwell equations. *Mathematics of Computation*, 72(241):1–15, 2003.
- [5] I. G. Graham, E. A. Spence, and E. Vainikko. Domain decomposition preconditioning for high-frequency Helmholtz problems with absorption. *arXiv preprint arXiv:1507.02097*, to appear in *Math. Comp.*, 2016. .
- [6] S. Güttel and J. Pestana. Some observations on weighted GMRES. *Numerical Algorithms*, 67(4):733–752, 2014.

Boundary elements with mesh refinements for the wave equation

Heiko Gimperlein¹, Fabian Meyer², Ceyhun Oezdemir³, David Stark^{4,*}, Ernst P. Stephan⁵

¹Maxwell Institute for Mathematical Sciences and Department of Mathematics, Heriot-Watt University, Edinburgh, EH14 4AS, United Kingdom

²Institute of Applied Analysis and Numerical Simulation, Universität Stuttgart, Pfaffenwaldring 57, 70569 Stuttgart, Germany

³Institute of Applied Mathematics, Leibniz University Hannover, 30167 Hannover, Germany

⁴Maxwell Institute for Mathematical Sciences and Department of Mathematics, Heriot-Watt University, Edinburgh, EH14 4AS, United Kingdom

⁵Institute of Applied Mathematics, Leibniz University Hannover, 30167 Hannover, Germany

*Email: ds221@hw.ac.uk

Suggested members of the Scientific Committee

Simon Chandler-Wilde, Patrick Joly, Peter Monk

Abstract

We discuss time domain boundary element methods for singular geometries, in particular graded meshes and adaptive mesh refinements. First, we discuss edge and corner singularities for a Dirichlet problem for the wave equation. Time independent graded meshes lead to efficient approximations, as confirmed by numerical experiments for wave scattering from screens. We briefly discuss adaptive mesh refinement procedures based on a posteriori error estimates. A modified MOT scheme provides an efficient preconditioner (or stand-alone solver) for the space-time systems obtained for the Galerkin discretisations.

Keywords: Time-domain boundary element method, adaptive mesh refinements, graded meshes.

Efficient and accurate computational methods to simulate sound emission in space and time are of interest from the modeling of environmental noise to acoustic scattering. Galerkin time domain boundary element methods prove to be stable and accurate in long-time computations and are competitive with frequency domain methods for realistic problems [2].

In this talk we discuss recent work on adaptive mesh refinements and graded meshes for singular geometries, as motivated by the sound emission on tires [1].

We consider the wave equation outside a scatterer Ω^- in \mathbb{R}^3 , where Ω^- is a bounded polygon or a screen with connected complement

$\Omega = \mathbb{R}^3 \setminus \overline{\Omega^-}$. The acoustic sound pressure field u due to an incident field or sources on $\Gamma = \partial\Omega$ satisfies the linear wave equation for $(t, \mathbf{x}) \in \mathbb{R} \times \Omega$:

$$\partial_t^2 u(t, \mathbf{x}) - \Delta u(t, \mathbf{x}) = 0$$

with Dirichlet boundary conditions $u(t, \mathbf{x}) = f(t, \mathbf{x})$ for $\mathbf{x} \in \Gamma$, and $u(t, \mathbf{x}) = 0$ for $t \leq 0$.

A single-layer ansatz for u ,

$$u(t, \mathbf{x}) = \int_{\Gamma} \frac{\phi(t - |\mathbf{x} - \mathbf{y}|, \mathbf{y})}{4\pi|\mathbf{x} - \mathbf{y}|} ds_y,$$

results in an equivalent weak formulation as an integral equation of the first kind in space-time anisotropic Sobolev spaces [2, 5]:

Find $\phi \in H_{\sigma}^1(\mathbb{R}^+, \tilde{H}^{-\frac{1}{2}}(\Gamma))$ such that for all $\psi \in H_{\sigma}^1(\mathbb{R}^+, \tilde{H}^{-\frac{1}{2}}(\Gamma))$

$$\begin{aligned} & \int_0^\infty \int_{\Gamma} (V\phi(t, \mathbf{x})) \partial_t \psi(t, \mathbf{x}) ds_x d_{\sigma} t \\ &= \int_0^\infty \int_{\Gamma} f(t, \mathbf{x}) \partial_t \psi(t, \mathbf{x}) ds_x d_{\sigma} t , \end{aligned} \quad (1)$$

where $d_{\sigma} t = e^{-2\sigma t} dt$ and

$$V\phi(t, \mathbf{x}) = \int_{\Gamma} \frac{\phi(t - |\mathbf{x} - \mathbf{y}|, \mathbf{y})}{4\pi|\mathbf{x} - \mathbf{y}|} ds_y .$$

A theoretical analysis requires $\sigma > 0$, but practical computations use $\sigma = 0$.

We study time dependent boundary element methods to solve (1) and related boundary integral equations for a half-space, based on approximations by tensor products of piecewise polynomials in space and time.

We present three types of results:

1) If Γ is a screen, the density ϕ exhibits edge and corner singularities. Motivated by recent work by Müller and Schwab for 2d FEM, in [3] we adapt a classical analysis by von Petersdorff for time-independent problems and obtain the precise singular behaviour of ϕ near $\partial\Gamma$: $\phi(t, \mathbf{x}) \sim \text{dist}(\mathbf{x}, \partial\Gamma)^{-1/2}$ near an edge, $\phi(t, \mathbf{x}) \sim \text{dist}(\mathbf{x}, \partial\Gamma)^{-0.703}$ near a right-angled corner.

Time-independent graded meshes provide a quasi-optimal approximation of these singularities. The numerical experiment depicted in Figure 1 compares the convergence in energy norm on graded and uniform meshes for $\Gamma = [0, 1]^2 \times \{0\}$ and illustrates the theoretically predicted convergence of order DOF^{-1} , resp. $\sim DOF^{-1/2}$. We present

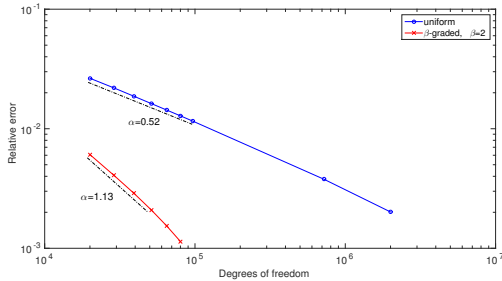


Figure 1: Energy convergence for graded vs. uniform meshes.

an application to the singular horn geometry between a vibrating tire and the road.

2) We use provably reliable residual error indicators, as well as heuristic ZZ and hierarchical indicators to steer adaptive mesh refinements. Figure 2 shows that the residual indicators converge at the same rate as the energy error for an example problem with $\Gamma = S^2$. We briefly recall the theoretical results on reliability and (weak) efficiency of the residual error indicators (see [2]) and compare the adaptive methods obtained from the different error indicators.

3) To obtain provably stable methods and a rigorous error analysis, we require conforming Galerkin discretisations. In general, the discretization of (1) leads to a lower Hessenberg linear system in space-time, with one band above the diagonal. Motivated by adaptivity and C^∞ temporal basis functions, there has been much recent interest in works by Sauter-Veit, Merta et al., Schanz and others in efficient solvers. We present an approximate time-stepping scheme [4], based on extrapolation, which becomes ex-

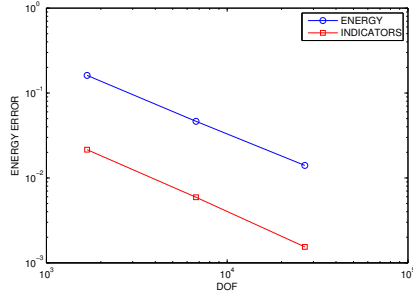


Figure 2: Energy convergence vs. residual error indicators for model problem on $\Gamma = S^2$.

Geometry	DOF	Energy	MOT	Error
sphere	320	8.5692	8.5470	.26%
	1280	8.6059	8.6059	$\ll 1\%$
icosahed.	320	20.538	21.480	4.6%
	1280	19.879	20.143	1.3%
screen	288	0.4233	0.4497	6.2%
	1250	0.4589	0.4716	2.8%

Table 1: relative errors in energy: modified MOT vs. GMRES with residual 10^{-9} .

act for $\Delta t \rightarrow 0$. It may be used as either a preconditioner or standalone solver. Table 1 compares one step of this method to the (essentially exact) solution of the space-time system as obtained from GMRES.

References

- [1] L. Banz, H. Gimperlein, Z. Nezhi, E. P. Stephan, *Time domain BEM for sound radiation of tires*, Comput. Mech. **58** (2016), 45–57.
- [2] H. Gimperlein, M. Maischak, E. P. Stephan, *Adaptive time domain boundary element methods and engineering applications*, survey, Journal of Integral Equations and Applications, to appear (2016).
- [3] H. Gimperlein, F. Meyer, C. Özdemir, D. Stark, E. P. Stephan, *Boundary elements with mesh refinements for the wave equation*, in preparation (2016).
- [4] H. Gimperlein, D. Stark, *Extrapolation as preconditioner for time domain boundary element methods*, preprint (2016).
- [5] F.-J. Sayas, *Retarded Potentials and Time Domain Boundary Integral Equations: a road-map*, Springer Series in Comp. Math. 50, Springer, 2016.

Upwind discontinuous Galerkin space discretization and locally implicit time integration for Maxwell's equations

Marlis Hochbruck¹, Andreas Sturm^{1,*}

¹Institute for Applied and Numerical Mathematics, Karlsruhe Institute of Technology, Karlsruhe, Germany

*Email: andreas.sturm@kit.edu

Abstract

We consider the efficient numerical approximation of Maxwell's equations in a spatial domain with complex geometry.

For the space discretization discontinuous Galerkin (dG) methods are well-suited since they easily allow to use unstructured, possibly locally refined meshes. For the time integration standard explicit or implicit methods perform sub-optimal. The former suffer from a constraint on the time step size (CFL condition). The latter require the solution of a large linear system in each time step.

If the geometry of the problem requires a grid with only a few tiny elements, a combination of an explicit and an implicit time integrator provides a promising alternative. These so-called locally implicit methods have been considered in [1–3] for central fluxes dG discretizations.

We present an error analysis for the full discretization of Maxwell's equations with the locally implicit scheme [3] and show how this method can be extended to an upwind fluxes dG discretization.

Keywords: Maxwell equations, locally implicit schemes, error analysis, full discretization, discontinuous Galerkin methods

1 Linear Maxwell's equations

Let $\Omega \subset \mathbb{R}^3$ be a bounded domain and T be a finite time. The time evolution of electromagnetic phenomena in linear, isotropic materials with magnetic permeability $\mu(x)$ and electric permittivity $\varepsilon(x)$ are described by Maxwell's equations

$$\begin{aligned} \mu \partial_t \mathbf{H} &= -\operatorname{curl} \mathbf{E}, & \text{in } (0, T) \times \Omega, \\ \varepsilon \partial_t \mathbf{E} &= \operatorname{curl} \mathbf{H} - \mathbf{J}, & \text{in } (0, T) \times \Omega. \end{aligned} \quad (1)$$

Here, the unknowns $\mathbf{H}(t, x)$ and $\mathbf{E}(t, x)$ are the magnetic and the electric field, respectively, and $\mathbf{J}(t, x)$ is a given electric current density. The

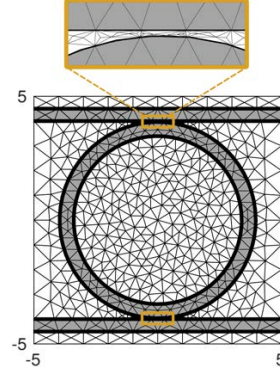


Figure 1: Locally refined mesh.

equations (1) are complemented with initial conditions $\mathbf{H}^0(x), \mathbf{E}^0(x)$ and metallic boundary conditions $(n \times \mathbf{E})|_{\partial\Omega} = 0$.

2 Space discretization

We discretize (1) in space by employing a dG method with polynomial order k . This leads to the semidiscrete problem

$$\begin{aligned} \partial_t \mathbf{H}_h &= -\mathcal{C}_{\mathbf{E}} \mathbf{E}_h - \alpha \mathcal{S}_{\mathbf{H}} \mathbf{H}_h, & \text{in } (0, T), \\ \partial_t \mathbf{E}_h &= \mathcal{C}_{\mathbf{H}} \mathbf{H}_h - \alpha \mathcal{S}_{\mathbf{E}} \mathbf{E}_h - \mathbf{J}_h, & \text{in } (0, T), \end{aligned} \quad (2)$$

where $\mathcal{C}_{\mathbf{H}}$ and $\mathcal{C}_{\mathbf{E}}$ denote the discretized curl-operators and $\mathcal{S}_{\mathbf{H}}$ and $\mathcal{S}_{\mathbf{E}}$ are stabilization operators. For $\alpha = 0$ we obtain a central fluxes dG method and for $\alpha \in (0, 1]$ we use an upwind fluxes dG scheme. It is well-known that central fluxes dG methods are convergent of order k whereas upwind fluxes dG methods are convergent of order $k + 1/2$.

3 Time discretization

In order to obtain a fully discrete scheme we further have to integrate (2) in time. Explicit time integration schemes, such as the Verlet (or

leap frog) method,

$$\begin{aligned}\mathbf{H}_h^{n+1/2} - \mathbf{H}_h^n &= -\frac{\tau}{2} \mathcal{C}_{\mathbf{E}} \mathbf{E}_h^n, \\ \mathbf{E}_h^{n+1} - \mathbf{E}_h^n &= \tau \mathcal{C}_{\mathbf{H}} \mathbf{H}_h^{n+1/2} - \frac{\tau}{2} \bar{\mathbf{J}}_h^n, \\ \mathbf{H}_h^{n+1} - \mathbf{H}_h^{n+1/2} &= -\frac{\tau}{2} \mathcal{C}_{\mathbf{E}} \mathbf{E}_h^{n+1},\end{aligned}$$

where $\bar{\mathbf{J}}_h^n = \mathbf{J}_h^{n+1} + \mathbf{J}_h^n$, require a severe restriction on the time step size τ in order to guarantee stability. In fact, we are forced to use step sizes $\tau \sim h_{\min}$, where h_{\min} denotes the diameter of the smallest mesh element (CFL condition).

This constraint can be overcome by using an implicit time integrator, for instance the *Crank–Nicolson* method,

$$\begin{aligned}\mathbf{H}_h^{n+1/2} - \mathbf{H}_h^n &= -\frac{\tau}{2} \mathcal{C}_{\mathbf{E}} \mathbf{E}_h^n, \\ \mathbf{E}_h^{n+1} - \mathbf{E}_h^n &= \frac{\tau}{2} \mathcal{C}_{\mathbf{H}} (\mathbf{H}_h^{n+1} + \mathbf{H}_h^n) - \frac{\tau}{2} \bar{\mathbf{J}}_h^n, \\ \mathbf{H}_h^{n+1} - \mathbf{H}_h^{n+1/2} &= -\frac{\tau}{2} \mathcal{C}_{\mathbf{E}} \mathbf{E}_h^{n+1}.\end{aligned}$$

However, this requires the solution of a large linear system for \mathbf{E}_h^{n+1} in each time step.

4 Locally implicit scheme

We consider the case where the spatial mesh contains only a small number of fine elements, see Figure 1 for an example. Unfortunately, even one single fine element requires using a very tiny time step when applying an explicit time integrator. One remedy to this problem is to apply a locally implicit time integrator. These schemes employ an implicit time integrator for the fine elements while retaining an explicit time integration method on the coarse elements. In [1] Verwer proposed such a scheme for central fluxes dG methods ($\alpha = 0$) by blending the Crank–Nicolson scheme with the Verlet method. We adapted Verwer’s idea in [3] which results in the following *locally implicit scheme*,

$$\begin{aligned}\mathbf{H}_h^{n+1/2} - \mathbf{H}_h^n &= -\frac{\tau}{2} \mathcal{C}_{\mathbf{E}} \mathbf{E}_h^n, \\ \mathbf{E}_h^{n+1} - \mathbf{E}_h^n &= \tau \mathcal{C}_{\mathbf{H}}^e \mathbf{H}_h^{n+1/2} \\ &\quad + \frac{\tau}{2} \mathcal{C}_{\mathbf{H}}^i (\mathbf{H}_h^{n+1} + \mathbf{H}_h^n) - \frac{\tau}{2} \bar{\mathbf{J}}_h^n, \\ \mathbf{H}_h^{n+1} - \mathbf{H}_h^{n+1/2} &= -\frac{\tau}{2} \mathcal{C}_{\mathbf{E}} \mathbf{E}_h^{n+1}.\end{aligned}\tag{3}$$

Here, the operators $\mathcal{C}_{\mathbf{H}}^e$, $\mathcal{C}_{\mathbf{H}}^i$ constituting the blending of both methods are given as

$$\mathcal{C}_{\mathbf{H}}^i = \mathcal{C}_{\mathbf{H}} \circ \chi_i, \quad \mathcal{C}_{\mathbf{H}}^e = \mathcal{C}_{\mathbf{H}} \circ \chi_e,$$

where χ_i and χ_e are cut-off functions assigning the mesh elements to the implicitly and explicitly integrated part, respectively. It turns out that besides all fine elements we have to treat their neighbors implicitly. All remaining elements can be integrated explicitly.

As mentioned above the scheme (3) is limited to a central fluxes dG discretization. We extended this scheme to the upwind fluxes case resulting in the method

$$\begin{aligned}\mathbf{H}_h^{n+1/2} - \mathbf{H}_h^n &= -\frac{\tau}{2} \mathcal{C}_{\mathbf{E}} \mathbf{E}_h^n - \frac{\tau}{2} \alpha \mathcal{S}_{\mathbf{H}}^e \mathbf{H}_h^n, \\ \mathbf{E}_h^{n+1} - \mathbf{E}_h^n &= \tau \mathcal{C}_{\mathbf{H}}^e \mathbf{H}_h^{n+1/2} \\ &\quad + \frac{\tau}{2} \mathcal{C}_{\mathbf{H}}^i (\mathbf{H}_h^{n+1} + \mathbf{H}_h^n) \\ &\quad - \tau \alpha \mathcal{S}_{\mathbf{E}}^e \mathbf{E}_h^n - \frac{\tau}{2} \bar{\mathbf{J}}_h^n, \\ \mathbf{H}_h^{n+1} - \mathbf{H}_h^{n+1/2} &= -\frac{\tau}{2} \mathcal{C}_{\mathbf{E}} \mathbf{E}_h^{n+1} - \frac{\tau}{2} \alpha \mathcal{S}_{\mathbf{H}}^e \mathbf{H}_h^n,\end{aligned}\tag{4}$$

where $\mathcal{S}_{\mathbf{H}}^e$, $\mathcal{S}_{\mathbf{E}}^e$ are appropriate modifications of the full stabilization operators $\mathcal{S}_{\mathbf{H}}$, $\mathcal{S}_{\mathbf{E}}$.

Our main result is the following.

Theorem 1 *The locally implicit schemes (3), (4) are stable under a CFL condition depending only on the coarse part of the mesh. Both schemes converge with order two in time. Moreover, the scheme (3) is convergent of order k in space. The method (4) is convergent of order $k + 1/2$ on the coarse part of the mesh and of order k in the fine part.*

References

- [1] J. G. Verwer, Component splitting for semi-discrete Maxwell equations, *BIT*, 51(2), pp. 427–445, 2011.
- [2] S. Descombes, S. Lanteri, and L. Moya, Locally implicit time integration strategies in a discontinuous Galerkin method for Maxwell’s equations, *J. Sci. Comput.*, 56(1), pp. 190–218, 2013.
- [3] M. Hochbruck, and A. Sturm, Error analysis of a second-order locally implicit method for linear Maxwell’s equations, *SIAM J. Numer. Anal.*, 54(5), 3167–3191, 2016.

Surface water waves over bathymetry

Walter Craig¹, Catherine Sulem²

¹Department of Mathematics, McMaster University, Canada

²Department of Mathematics, University of Toronto, Canada

Abstract

We examine the effect of a periodic bottom on the free surface of a fluid linearized near the stationary state, and we develop a Bloch theory for the linearized water wave system. This analysis takes the form of a spectral problem for the Dirichlet – Neumann operator of the fluid domain with periodic bathymetry.

Keywords: water waves, bottom topography, shallow water regime, Bloch spectral decomposition.

1 Introduction

The motion of a free surface of fluid propagating over a variable topography is a problem of significance for ocean dynamics in coastal regions where waves are strongly affected by the bathymetry. There is an extensive literature devoted to the effect of variable depth over surface waves and there are many scaling regimes of interest, including long-wave scaling regimes where the typical wavelength of surface waves is assumed to be much longer than the typical lengthscale of the variations of the bottom depth. In Section 2, we report on the evolution of waves in the shallow water regime in the presence of a periodic bottom varying rapidly with respect to the typical surface wavelength, a regime fitting the context of homogenization theory [5]. Our analysis brings out a resonance phenomenon between nonlinear surface waves and the periodic bottom. The need for new tools to address the dynamics of these resonant situations motivated our recent work on a Bloch theory for the linearized water wave equations [4].

Bloch decomposition is a classical tool to study wave propagation in periodic media. In the setting of the Schrödinger operator with a periodic potential, known as Hill's equation, the problem has been studied in great detail, see reference [6] for example. In another setting, Allaire, Palombaro and Rauch [1] studied the problem of propagation of waves packets through a slightly perturbed periodic medium, where

the period is assumed small compared to the size of the wave packet, and constructed solutions in the form of slowly modulated Bloch plane waves.

Here, we develop a Bloch theory in the context of surface water waves in the form of a spectral problem for the Dirichlet - Neuman operator of the fluid domain. We find that the presence of the bottom results in the splitting of double eigenvalues near such points of multiplicity, creating a spectral gap. Thanks to the explicit expansion of the Dirichlet-Neuman operator in powers of the bottom variations [2], we compute the gap opening for a bottom of the form $b(x) = \beta \tilde{b}(x)$ perturbatively in β and we quantify bounds on spectral gap openings.

In a numerical study of Bloch waves, Yu and Howard [9] considered linear waves propagating over a periodic bottom for various examples of bottom profiles. Using a conformal map that transforms the original fluid domain to a uniform strip, they computed numerically Bloch eigenfunctions and identified spectral gaps. Our work provides a theoretical framework and a rigorous analytic basis for these numerical computations. In addition we provide a systematic perturbation method that describes the splitting of multiple eigenvalues and the formation of intervals of forbidden energies, or energy gaps. We consider the case $b(x) = \beta \cos(x)$ in analogy with the Mathieu equation for the Schrödinger operator. We calculate the asymptotic behavior of the first several spectral gaps and their centres. In particular, we observe a distinct difference between the behavior of spectral gaps in the theory of Hill's operator and with the Dirichlet - Neumann operator.

2 Shallow water scaling regime

The fluid domain consists of the region ($d = 1, 2$)

$$\Omega(b, \eta) = \{(x, z) \in \mathbb{R}^{d+1}, -h_0 + b(x) < z < \eta(x, t)\}$$

where the dependent variable $\eta(x, t)$ denotes the surface elevation and $b(x)$ is the variation of the

bottom of the fluid domain from its mean value, assumed to be periodic. Our starting point is the Hamiltonian formulation (Zakharov [10]) phrased in terms of the Dirichlet-Neumann operator [3] which takes the form of a coupled system for the surface elevation η and the trace of the velocity potential at the surface $\xi = \varphi|_{z=\eta}$:

$$\begin{cases} \partial_t \eta - G[\eta, b]\xi = 0 , \\ \partial_t \xi + g\eta + \frac{1}{2}|\nabla \xi|^2 - \frac{(G[\eta, b]\xi + \nabla \eta \cdot \nabla \xi)^2}{2(1 + |\nabla \eta|^2)} = 0 . \end{cases} \quad (1)$$

The quantity $G[\eta, b]$ is the Dirichlet-Neumann operator, defined by

$$G[\eta, b]\xi = \sqrt{1 + |\nabla \eta|^2} \partial_n \varphi|_{z=\eta} , \quad (2)$$

where φ is the solution of the elliptic boundary value problem

$$\begin{cases} \Delta \varphi + \partial_z^2 \varphi = 0 & \text{in } \Omega(b, \eta) , \\ \varphi|_{z=\eta} = \xi , \quad \partial_n \varphi|_{z=-h_0+b} = 0 . \end{cases} \quad (3)$$

In order to identify the various scaling asymptotic regimes, we define the parameters

$$\mu = \frac{h_0^2}{\lambda^2}, \varepsilon = \frac{A}{h_0}, \beta = \frac{B}{h_0}, \gamma = \frac{\ell}{\lambda},$$

where A and B are the amplitude of surface waves and the bottom variations respectively and λ , and ℓ their respective typical wavelength.

We consider relatively large amplitude surface waves, setting $\varepsilon = 1$ and assuming

$$\beta = \sqrt{\mu} = \gamma \ll 1 . \quad (4)$$

The condition $\beta = \gamma$ expresses a small bathymetry slope, while the roughness strength is

$$\rho := \sqrt{\mu}/\gamma = 1 .$$

The first step consists of the construction of an approximate solution and a consistency analysis. The latter refers to an estimate on how well the approximate solution satisfies the original water wave system. We look for an approximate solution of the form

$$\eta_a = \eta_0(X, t) + \gamma \eta_1(X, X/\gamma, t/\gamma) \quad (5)$$

$$\xi_a = \xi_0(X, t) + \gamma^2 \xi_1(X, X/\gamma, t/\gamma) . \quad (6)$$

where ($\tau = t/\gamma, Y = X/\gamma$) are fast variables. The following system of equations is derived in [5].

Theorem 2.1. *Setting $V_0 = \nabla \xi_0$ and $h = 1 + \eta_0$, the leading term $(\eta_0, V_0 = \nabla \xi_0)$ satisfies the classical shallow water system ($h = -1 + \zeta_0$)*

$$\begin{cases} \partial_t \eta_0 + \nabla \cdot (h V_0) = 0 , \\ \partial_t V_0 + (V_0 \cdot \nabla) V_0 + \nabla \eta_0 = 0 . \end{cases} \quad (7)$$

The corrector term (η_1, ξ_1) satisfies the linear nonlocal coupled system ($D_Y = \frac{1}{i} \partial_Y$)

$$\begin{cases} \partial_\tau \eta_1 + V_0 \cdot \nabla_Y \eta_1 - |D_Y| \tanh(h|D_Y|) \xi_1 \\ \qquad \qquad \qquad = V_0 \cdot \nabla_Y \operatorname{sech}(h|D_Y|) b , \\ \partial_\tau \xi_1 + V_0 \cdot \nabla_Y \xi_1 + \eta_1 = 0 . \end{cases} \quad (8)$$

The system (7) represents the *effective* or *homogenized* surface wave dynamics, while the system (8) for the corrector terms has the form of the linearized water wave equations in a domain of depth $h(x, t)$, with a background flow given by the velocity $V_0(x, t)$. Here, the functions (η_1, ξ_1) are periodic in the fast variables Y , while the variables (X, t) are to be treated as parameters. The source term in the rhs of the evolution equation for η_1 is due to the scattering of the background flow from the variable bottom.

Theorem 2.2. *The functions (η_a, ξ_a) are approximate solutions of the Euler equations, i.e. they satisfy the Euler equations up to a ‘small’ error term E_a*

$$|E_a|_{H_e} < C_a \gamma^{3/4} ,$$

where $|\cdot|_{H_e}$ is an energy norm defined as :

$$|E_a|_{H_e} = |E_{a1}|_{L^2} + \gamma^{-3/8} |E_{a2}|_{H^{1/2}}$$

and $E_a = (E_{a1}, E_{a2})$ (corresponding to the equations for (η, ξ)). The constant C_a depends upon various norms of the data $(\eta_0, \xi_0, \eta_1, \xi_1)$.

The principal difficulty in the analysis is that the shallow water limit and the homogenization process must be performed simultaneously. We prove that (η_1, ξ_1) are bounded uniformly on time intervals $\tau \in [-T/\gamma, T/\gamma]$. This result is valid for the natural time scale $t = \mathcal{O}(1)$ associated to the shallow water equation only if the free surface does not resonate with the rapidly varying bottom. Such a resonance occurs if there exists (X, t) such that

$$(k \cdot V_0(X, t))^2 = |k| \tanh(h(X, t)|k|)$$

for some $k \in \mathbb{Z}$ corresponding to a nonzero mode of the Fourier decomposition of b . This condition can be viewed as a nonlinear generalization of the classical Bragg resonance. When such resonances occur, it induces secular growth effects that destroy the accuracy of the approximation, which is then valid on a much smaller time scale, $t = o(1)$ and the dynamics of the leading term (η_0, V_0) will likely be affected. A quantitative measure of nonresonance is then necessary. The k^{th} Fourier modes $(\hat{\eta}_{1,k}, \hat{\xi}_{1,k})$ are nonresonant at (X, t) with respect to the homogenized solution $(\eta_0(\cdot, t), \xi_0(\cdot, t))$ and the bottom topography $b(Y)$ if $\hat{b}_k \neq 0$ and

$$|\omega_k(X, t)^2 - (k \cdot V_0(X, t))^2| > \frac{1}{B_k}.$$

Resonances are however not exceptional. When resonances occur, secular growth of the corrector terms takes place, and it compromises the validity of the approximation. In this way, a small amplitude, rapidly oscillating bathymetry will affect the free surface at leading order.

3 Bloch Theory

Motivated by the limitations of the above study, we are interested in analytical tools that may be useful to address the dynamics of these resonant situations. As a first step, we considered the two-dimensional water wave system with a periodic bottom profile, linearized near the stationary state, and we develop a Bloch theory for the linearized water wave evolution [4]. This analysis takes the form of a spectral problem for the Dirichlet – Neumann operator in a fluid domain with periodic bathymetry and flat upper surface elevation. We restrict here to the two-dimensional water wave problem.

The system (1) linearized about the stationary solution $(\eta(x), \xi(x)) = (0, 0)$ is

$$\begin{cases} \partial_t \eta - G[b] \xi = 0 \\ \partial_t \xi + g \eta = 0, \end{cases} \quad (9)$$

where we denote $G[0, b]$ by $G[b]$. This is an analog of the wave equation, with the usual Laplacian replaced by the nonlocal operator $G[b]$ with 2π -periodic dependence on the horizontal spatial variable x :

$$\partial_{tt} \eta + g G[b] \eta = 0. \quad (10)$$

In analogy with the classical case of partial differential operators with periodic coefficients, we

construct the Bloch eigenvalues and eigenfunctions of the spectral problem

$$G[b] \Phi(x, \theta) = \Lambda(\theta) \Phi(x, \theta), \quad (11)$$

with boundary conditions $(-\frac{1}{2} \leq \theta < \frac{1}{2})$

$$\Phi(x + 2\pi, \theta) = \Phi(x, \theta) e^{2\pi i \theta}. \quad (12)$$

It is convenient in Bloch theory to define

$$\psi(x, \theta) = e^{i\theta x} \Phi(x, \theta) \quad (13)$$

to transform the original problem to an eigenvalue problem with periodic boundary conditions. Indeed, condition (12) implies that $\psi(x, \theta)$ is periodic in x of period 2π . The spectral problem is now rewritten in conjugated form

$$e^{-i\theta x} G[b] e^{i\theta x} \psi(x, \theta) = \Lambda(\theta) \psi(x, \theta) \quad (14)$$

$$\psi(x + 2\pi, \theta) = \psi(x, \theta). \quad (15)$$

When the bottom is flat ($b = 0$), the Bloch eigenvalues $\Lambda_n^{(0)}(\theta)$ are given explicitly in terms of the dispersion relation for water waves over a constant depth h and labeled in order of increasing amplitude (see Figure 1). Denoting $g_n(\theta) = g(n + \theta) \tanh(h(n + \theta))$,

$$\text{for } -\frac{1}{2} \leq \theta < 0, \quad \Lambda_{2n}^{(0)}(\theta) = g_{-n}(\theta)$$

$$\text{for } 0 \leq \theta \leq \frac{1}{2}, \quad \Lambda_{2n}^{(0)}(\theta) = g_n(\theta)$$

while

$$\text{for } -\frac{1}{2} \leq \theta < 0, \quad \Lambda_{2n-1}^{(0)}(\theta) = g_n(\theta)$$

$$\text{for } 0 \leq \theta \leq \frac{1}{2}, \quad \Lambda_{2n-1}^{(0)}(\theta) = g_{-n}(\theta),$$

where $n \in \mathbb{N}$ and the Bloch parameter $\theta \in \mathbb{T}^1$, i.e. the parameter is assumed to be periodic of period 1.

Eigenvalues are simple for $-\frac{1}{2} < \theta < 0$ and $0 < \theta < \frac{1}{2}$. For half-integer values of θ , namely $\theta = 0, \frac{1}{2}, 1, \dots$, eigenvalues $\Lambda_n^{(0)}(\theta)$ have multiplicity two. As in the case of Bloch theory for other problems, the presence of the bottom results in the splitting of double eigenvalues near such points of multiplicity, creating a spectral gap.

An illustration of eigenvalues as functions of θ is given in Figure 1. The left hand side shows the unperturbed first five eigenvalues in the case of a flat bottom, labelled in order of

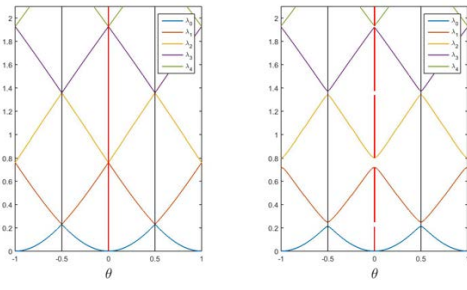


Figure 1: First five eigenvalues in order of magnitude: (left) flat bottom; (right) in the presence of a small generic bottom perturbation. The spectrum is represented by the vertical red lines.

magnitude. The right hand side shows these eigenvalues in the presence of a small generic bottom perturbation and the gap openings.

The spectrum of the Dirichlet-Neumann operator $G[b]$ on the line, namely on $L^2(\mathbb{R})$, is the union of the ranges of the Bloch eigenvalues $\Lambda_n(\theta)$:

$$\sigma_{L^2(\mathbb{R})}(G[b]) = \cup_{n=0}^{+\infty} [\Lambda_n^-, \Lambda_n^+]$$

where

$$\Lambda_n^- = \min_{\theta \in \mathbb{T}^1} \Lambda_n(\theta), \quad \Lambda_n^+ = \max_{\theta \in \mathbb{T}^1} \Lambda_n(\theta).$$

It is the analog of the structure of spectral bands and gaps of the Hill's operator [6].

Theorem 3.1. *For all $\theta \in (-\frac{3}{8}, -\frac{1}{8}) \cup (\frac{1}{8}, \frac{3}{8})$, the L^2 -spectrum of $G^\theta[b] := e^{-i\theta} G[b] e^{i\theta x}$ on the domain $\mathcal{D} = H^1(\mathbb{T}^1)$ is composed of an increasing sequence of eigenvalues $\Lambda_n(\theta)$ that are simple, and analytic in θ and $b \in B_R(0) \subset H^1[0, 2\pi]$. The corresponding eigenfunctions $\Psi_n(x, \theta)$ are 2π -periodic in x , and analytic in θ and $b \in B_R(0)$.*

The result in Theorem 3.1 can be seen a direct consequence of the general theory of perturbation of self-adjoint operators (Rellich [8]). An alternate proof using the implicit function theorem in a functional form (see [7]) is presented in [4] which in turn, can be extended to prove the following result.

Theorem 3.2. *In the neighbourhood of the crossing points $\theta = 0, \pm\frac{1}{2}$, i.e for $\theta \in [-\frac{1}{2}, -\frac{5}{16}] \cup$*

$(-\frac{3}{16}, \frac{3}{16}) \cup (\frac{5}{16}, \frac{1}{2}]$, the spectrum of $G_\theta[b]$ is composed of an increasing sequence of eigenvalues $\Lambda_n(\theta)$ which are continuous in θ . For $\frac{-3}{16} < \theta < \frac{3}{16}$, the lowest eigenvalue $\Lambda_0(\theta)$ is simple, and it and the eigenfunction $\Psi_0(x, \theta)$ are analytic in θ and b .

Both Theorems 3.1 and 3.2 are local in θ . Their domains of definition overlap on the intervals $\theta \in (-\frac{3}{8}, -\frac{5}{16}) \cup (-\frac{1}{8}, -\frac{3}{16}) \cup (\frac{1}{8}, \frac{3}{16}) \cup (\frac{5}{16}, \frac{3}{8})$. By uniqueness, in these intervals the eigenvalues and eigenfunctions agree.

4 The example of $b(x) = \beta \cos(x)$

We now examine the classical example of $b(x) = \beta \cos(x)$ corresponding to the Matthieu equation for the Schrödinger operator.

A perturbation calculation using the expansion of $G[b]$ in powers of b [2] shows that the first gap occurs for $\theta = \pm 1/2$ and is of order $O(\beta)$

$$\Lambda_1^- - \Lambda_0^+ = \frac{1}{4} \operatorname{sech}^2\left(\frac{h}{2}\right) \beta.$$

The second gap occurs at $\theta = 0$. We find that, unlike the case of the Matthieu operator, the second gap opens only at order $O(\beta^4)$.

$$\Lambda_2^- - \Lambda_1^+ = \frac{1}{12} \beta^4 \operatorname{sech}^2(h) \tanh(2h). \quad (16)$$

In general the n^{th} gap satisfies

$$\Lambda_n^- - \Lambda_{n-1}^+ \leq C(n) \beta^n.$$

We see in Figure 2b of [9] that the second gap is indeed much smaller in size than the first one.

We are also able to calculate analytically the deviation of the centre. Denoting

$$s_n(\theta) = (n + \theta) \operatorname{sech}((n + \theta)h)$$

we find that

$$\frac{1}{2}(\Lambda_1^- + \Lambda_0^+) = -\beta^2 \frac{s_0^2(\frac{1}{2})(g_0^2(\frac{1}{2}) - \frac{9}{4})}{4(g_0(\frac{1}{2}) - g_1(\frac{1}{2}))}. \quad (17)$$

It is straightforward to check that this quantity is negative. More generally, one can prove that this is the case for gaps of higher index. Namely, $\frac{1}{2}(\Lambda_n^- + \Lambda_{n-1}^+) < 0$, i.e., the deviation of the centers of the gap from its unperturbed position is negative. Hence for increasing β all of the gap centers are transposed, or downshifted, to lower frequency. This is an analytical verification of Figure 2b of reference [9].

On the other hand, when $b(x) = \beta(\cos(x) + \cos(3x))$, the second gap opens at order $O(\beta^2)$

$$\Lambda_2^- - \Lambda_1^+ = \beta^2 \operatorname{sech}^2(h) \frac{4 - 2 \tanh(h) \tanh(2h)}{\tanh(h) - 2 \tanh(2h)}.$$

We are currently working on the construction of slowly modulated Bloch plane waves assuming the bottom variations are significantly shorter than the long surface modulations. We are examining how the presence of the bottom modifies the effective coefficients of the derived Nonlinear Schrödinger equation.

Acknowledgments

W.C. is partially supported by the Canada Research Chairs Program and NSERC through grant number 238452–16. C.S. is partially supported by NSERC through grant number 46179–13.

References

- [1] G. Allaire, M. Palombaro, J. Rauch. Diffractive geometric optics for Bloch wave packets, *Arch. Rat. Mech. Anal.*, **202**, 2011, 373–426.
- [2] W. Craig, P. Guyenne, D. Nicholls, C. Sulem, Hamiltonian long-wave expansions for water waves over a rough bottom, *Proc. R. Soc. Lond. Ser. A* **461** (2005), pp. 839–873.
- [3] W. Craig, C. Sulem, Numerical simulation of gravity waves, *J. Comp. Phys.* **108** (1993), 73–83.
- [4] W. Craig, M. Gazeau, C. Lacave, C. Sulem, Bloch theory and spectral gaps for linearized water waves, 2017, preprint.
- [5] W. Craig, D. Lannes, C. Sulem. Water waves over a rough bottom in the shallow water regime, *Annales de l'Institut H. Poincaré, Analyse nonlinéaire*, **29** (2012), 233–259.
- [6] H. McKean, E. Trubowitz. *Hill's operator and hyperelliptic function theory in the presence of infinitely many branch points*, Comm. Pure Appl. Math. **29** (1976), no. 2, 143–226.
- [7] L. Nirenberg. *Topics in Nonlinear Functional Analysis*, Courant Lecture Notes Series, Vol. 6, 2001.
- [8] F. Rellich. *Perturbation theory of eigenvalue problems*, New-York, Gordon and Breach, 1969.
- [9] J. Yu, L. N. Howard, Exact Floquet theory for waves over arbitrary periodic topographies, *J. Fluid Mech.* **712** (2012), 451–470.
- [10] V.E. Zakharov, Stability of periodic waves of finite amplitude on the surface of a deep fluid, *J. Appl. Mech. Tech. Phys.* **2** (1968), 190–194.

Polarized Uncertainty Principles for the Inverse Source Problem

John Sylvester^{1,*}

¹Department of Applied Mathematics, University of Washington

*Email: sylvest@uw.edu

Abstract

I plan to discuss recent work (joint with Roland Griesmaier) on the fixed frequency inverse source problem, emphasizing how we adapted uncertainty principles from the work of Donoho-Stark [1] to the far field splitting and data completion problems.

Keywords: Polarized uncertainty principle, inverse source problem

The far field radiated by a source f , at wavenumber k , is the asymptotic description of the outgoing solution to the Helmholtz equation

$$(\Delta + k^2) u = k^2 f$$

which has asymptotics

$$u \sim \frac{e^{ikr}}{(kr)^{\frac{d-1}{2}}} k^d \widehat{f}(k\Theta)$$

where \widehat{f} denotes the Fourier transform of f and Θ is a point on the unit sphere. Thus the data for the inverse source problem is the restricted Fourier transform of the source. We cannot recover f from this data, but we can say something about a lower bound for the convex hull of the support of f [2, 6]. In particular, if a far field is radiated from the union of two disjoint domains (i.e. by a sum of sources, each of which is supported in one component), unique continuation tells us that the far field can be split uniquely into the fields radiated from each component. We focus on the question of how far apart these sets must be so that the splitting is reasonably well-conditioned. Because the problem is linear, it makes sense to estimate the condition number of this splitting operator. We bound the condition number by $(1 - \tau^2)^{-\frac{1}{2}}$, where τ is the dimensionless parameter $\frac{kd_1 kd_2}{k|c|}$ in \mathbb{R}^2 , and $\frac{(kd_1 kd_2)^{3/2}}{k|c|}$ in \mathbb{R}^3 , where d_1 and d_2 are the diameters of the connected components and $|c|$ is the distance between them. We show by example that the bound is sharp in \mathbb{R}^2 .

I think the most interesting feature is that we can obtain these estimates as a simple application of an uncertainty principle. Perhaps the simplest example of an uncertainty principle (from [1]) is the following, where f is a function on \mathbb{Z}^N and \widehat{f} is its N -point discrete Fourier transform.

Theorem 1 (Donoho-Stark). *Let $\text{supp } f \subset T$ and $\text{supp } \widehat{f} \subset W$, then*

$$|T| |W| \geq N$$

Theorem 1 implies that, if $|T| |W| < N$, the subspaces V_T of functions supported on T , and X_W of functions with DFT's supported on W have empty intersection. Donoho and Stark combined this principal with other arguments to do data completion. They showed that if $f \in X_W$, then the values of f on T could be recovered from its values on the complement, and they described L^2 and L^1 based algorithms to carry this out.

We call the theorem below a polarized uncertainty principle.

Theorem 2 (Griesmaier, S.). *Let $\text{supp } f \subset T$ and $\text{supp } \widehat{g} \subset W$, then*

$$|(f, g)| \leq \sqrt{\frac{|T| |W|}{N}} \|f\| \|g\|$$

Where theorem 1 implies that $V_T \cap X_W$ is empty if $|T| |W| < N$, the polarized principle in theorem 2 explicitly bounds the cosine of the angle between the two subspaces by $\sqrt{\frac{|T| |W|}{N}}$. A direct consequence is that the splitting operator that maps the sum $f + g$ into its components has a condition number no greater than the cosecant of that angle.

A more general version replaces the Fourier transform with an operator A :

Theorem 3 (Griesmaier, S.). *Suppose that*

$$A : L^2 \rightarrow L^2, \quad A^{-1} : L^1 \rightarrow L^\infty, \\ c_A := \|A\|_{2,2} \|A^{-1}\|_{1,\infty}$$

and that $\text{supp } f \subset T$ and $\text{supp } Ag \subset W$, then

$$|(f, g)| \leq c_A \sqrt{|T| |W|} \|f\| \|g\|$$

The relevant subspaces for our application to the inverse source problem are dictated by the phenomenon of evanescence, which tells us that, if f is supported in the ball of radius R , then its far field is very close to the subspace V_{kR} . In 2D, V_{kR} is the subspace of $L^2(S^1)$ spanned by $e^{in\theta}$ with $|n| \leq kR$, and in 3D it is the span of the spherical harmonics of index n , such that $n(n+1) \leq kR$.

The role of A is played by the far field translation operator T_c , which maps a far field $\alpha(\Theta)$ to $e^{ic\cdot\Theta}\alpha(\Theta)$. If α is the restricted Fourier transform of f , then $T_c\alpha$ is the restricted Fourier transform of $f(\cdot + c)$. Once we show that T_c has the required mapping properties, the polarized uncertainty principle estimates the cosine of the angle between V_{R_1} and $T_c V_{R_2}$ and gives us the bound on the condition number referred to in the first paragraph. Similar analysis applies to splitting for more than two disjoint domains, as well simultaneous splitting and data completion.

Examples in 2D show that the dependence on wavenumber, diameter, and separation distance in $\frac{kd_1 kd_2}{k|c|}$ is sharp, at least when the separation distance is large compared to the diameters. A corollary is that increasing resolution (by increasing k) also increases the condition number. This is not the case for the linearized inverse scattering problem or for the splitting of point sources, where increasing the wavenumber does not adversely affect the conditioning.

References

- [1] D. L. Donoho and P. B. Stark, Uncertainty principles and signal recovery, *SIAM J. Appl. Math.*, **49** (1989), 906–931, <http://dx.doi.org/10.1137/0149053>.
- [2] S. Kusiak and J. Sylvester, The scattering support, *Comm. Pure Appl. Math.*, **56** (2003), 1525–1548, <http://dx.doi.org/10.1002/cpa.3038>.
- [3] R. Griesmaier and J. Sylvester, Far field splitting by iteratively reweighted ℓ^1 minimization, *SIAM J. Appl. Math.*, **76** (2016), 705–730, <http://dx.doi.org/10.1137/15M102839X>.
- [4] R. Griesmaier and J. Sylvester, Uncertainty principles for inverse source problems, far field splitting and data completion, *SIAM J. Appl. Math.*, **77** (2017) 154–180, <http://dx.doi.org/10.1137/16M1086157>.
- [5] R. Griesmaier and J. Sylvester, Uncertainty principles for three-dimensional inverse source problems, *preprint*, <http://www.math.washington.edu/~sylvest/papers/uncertainty3D.pdf>.
- [6] J. Sylvester, Notions of support for far fields, *Inverse Problems*, **22** (2006), 1273–1288, <http://dx.doi.org/10.1088/0266-5611/22/4/010>.

Local Time-Stepping for the Solution of the Helmholtz Equation via Controllability Methods

M. J. Grote¹, J. H. Tang^{1,*}

¹Department of Mathematics and Computer Science, University of Basel, Switzerland

*Email: jet.tang@unibas.ch

Abstract

When the Helmholtz equation is discretized by standard finite difference or finite element methods, the resulting linear system is notoriously difficult to solve, in fact increasingly so at higher frequencies [1, 2]. Instead of solving the Helmholtz equation in the frequency domain, we thus reformulate it in the time domain and seek a time-periodic solution of the wave equation via Controllability Method (CM) [3, 4]. Although straightforward time integration of the wave equation can actually be used to reach the asymptotic time-periodic limit, its convergence is usually too slow in practice. The CM approach greatly speeds up convergence to the time-periodic solution by using the (unknown) initial conditions as control variables.

At each iteration the Controllability Method requires only the solution of a forward and backward time-dependent wave equation and that of a positive definite elliptic problem; hence, it is inherently parallel. To overcome the bottleneck from the stringent CFL condition due to local mesh refinement, we use local time-stepping (LTS) methods based on explicit Runge-Kutta schemes [5].

Keywords: time-harmonic waves, controllability method, local time-stepping, scattering problems

1 Introduction

We consider a time-harmonic acoustic scattering problem outside a sound-soft bounded obstacle Γ_D :

$$\begin{aligned} -\nabla \cdot (c^2 \nabla u) - \omega^2 u &= f \quad \text{in } \Omega, \\ u &= g_D \quad \text{on } \Gamma_D, \\ c \frac{\partial u}{\partial n} - i\omega u &= g_S \quad \text{on } \Gamma_S. \end{aligned} \quad (1)$$

Here, $\Omega \subset \mathbb{R}^d$ is a bounded region, Γ_S is an artificial boundary, ω is the time frequency, c is the speed of propagation and f, g_D and g_S are given sources.

If u solves (1), the function

$$y(x, t) := \operatorname{Re}(u(x)\psi(t)), \quad (t) = \exp(-i\omega t),$$

is the time-periodic solution of the corresponding wave equation with period $T = 2\pi/\omega$:

$$\begin{aligned} y_{tt} - \nabla \cdot (c^2 \nabla y) &= \tilde{f} \quad \text{in } \Omega \times (0, T), \\ y &= \tilde{g}_D \quad \text{on } \Gamma_D \times (0, T), \\ c \frac{\partial y}{\partial n} + y_t &= \tilde{g}_S \quad \text{on } \Gamma_S \times (0, T), \end{aligned} \quad (2)$$

where $\tilde{f} = \operatorname{Re}(f\psi)$, $\tilde{g}_D = \operatorname{Re}(g_D\psi)$ and $\tilde{g}_S = \operatorname{Re}(g_S\psi)$. The (unknown) initial values are denoted by

$$y(\cdot, 0) = e_0, \quad y_t(\cdot, 0) = e_1 \quad \text{in } \Omega. \quad (3)$$

Once e_0 and e_1 have been determined, the sought time-harmonic solution of (1) is given by

$$u = e_0 + \frac{i}{\omega} e_1. \quad (4)$$

2 Controllability Method

Instead of solving the Helmholtz equation (1) directly, we look for initial values $\mathbf{e} = (e_0, e_1)$ such that the time-dependent solution $y(x, t)$ of (2) is T -periodic. To do so, we minimize the functional

$$J(\mathbf{e}) = \frac{1}{2} \int_{\Omega} |c\nabla(y(T; \mathbf{e}) - e_0)|^2 + |y_t(T; \mathbf{e}) - e_1|^2,$$

where $y(\cdot; \mathbf{e})$ solves (2), (3), by using the preconditioned conjugate gradient method (PCG) [3, 4].

3 Spatial Discretization

We discretize the weak formulation of (2), (3) in space with conforming \mathcal{P}^3 finite elements with order preserving “mass lumping”. Next, we let $\mathbf{z}(t) = \mathbf{M}^{\frac{1}{2}}\mathbf{y}(t)$ and $\mathbf{Z} = (\mathbf{z}, \dot{\mathbf{z}})^T$, which yields the system of ordinary differential equations:

$$\dot{\mathbf{Z}}(t) = \mathbf{B}\mathbf{Z}(t) + \mathbf{R}(t) \quad t > 0$$

with $\mathbf{A} = \mathbf{M}^{-\frac{1}{2}}\mathbf{K}(c^2)\mathbf{M}^{-\frac{1}{2}}$, $\mathbf{D} = \mathbf{M}^{-\frac{1}{2}}\mathbf{S}(c)\mathbf{M}^{-\frac{1}{2}}$,

$$\mathbf{B} = \begin{bmatrix} \mathbf{0} & \mathbf{I} \\ -\mathbf{A} & -\mathbf{D} \end{bmatrix} \quad \text{and} \quad \mathbf{R} = \begin{bmatrix} \mathbf{0} \\ \mathbf{M}^{-\frac{1}{2}} \mathbf{F} \end{bmatrix}.$$

Here, \mathbf{M} is the (diagonal) mass matrix, \mathbf{K} is the stiffness matrix, \mathbf{S} is a mass matrix restricted to Γ_S , and \mathbf{F} is the right-hand side.

4 Time-Discretization

For the time discretization of (2), we use the Runge-Kutta based local time-stepping method (LTS-RK4) [5]. Hence, we split the mesh into fine and coarse part and then advance inside each subregion with a different time step, Δt and $\Delta\tau = \Delta t/p$, respectively. As shown in [5], the LTS-RK4 method is fully explicit and fourth-order accurate.

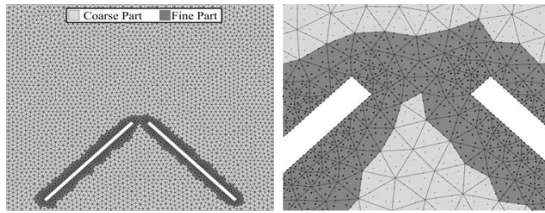


Figure 1: The FE mesh (Left: computational domain; Right: zoom of the refined mesh)

5 Numerical Results

First, we consider (1) in $\Omega = (0, 1) \times (0, 1)$ with the exact solution

$$u(x) = \exp(i d^\top x), \quad d = (\cos(3\pi/4), \sin(3\pi/4))^\top.$$

The mesh inside Ω is locally refined near the upper left corner. The local mesh refinement ratio p is given by $p \approx h_{\text{coarse}}/h_{\text{fine}}$. For the time integration of (2) we either use a standard RK4 method or the LTS-RK4 method from [5]. In Figure 2 we observe that the LTS-RK4 method results in a comparable number of iterations yet at a smaller cost. Moreover, the number of PCG-iterations is essentially independent of p .

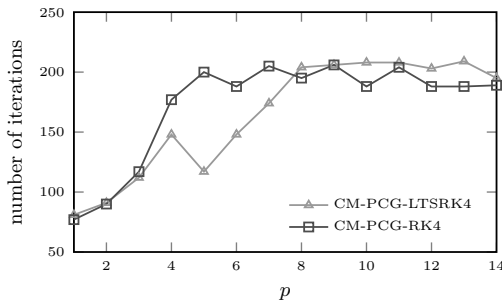


Figure 2: Number of PCG-iterations vs. local mesh refinement ratio $p \approx h_{\text{coarse}}/h_{\text{fine}}$

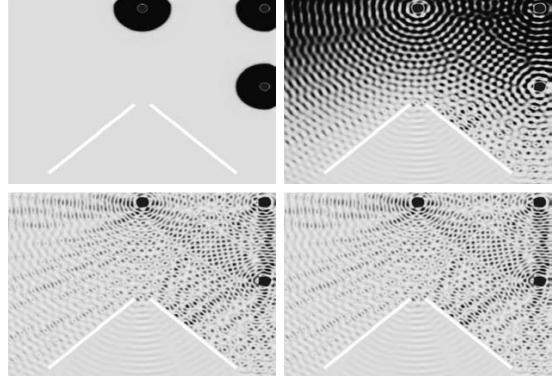


Figure 3: Controllability Method: e_ℓ at iterations $\ell = 1$ (top left), $\ell = 100$ (top right) and $\ell = 600$ (bottom left). Solution of the Helmholtz equation (bottom right).

Next, we compare the solution of (1) by using the Controllability Method (CM-PCG) and the standard direct solution of (1). Again, we use \mathcal{P}^3 -FE with LTS-RK4 integration. The wave number is $k = \omega/c = 128\pi$ ($\omega = 32\pi$, $c = 0.25$). As shown in Figure 3, the iterative solution of the CM-PCG converges to the solution of the Helmholtz equation.

References

- [1] O. G. Ernst and M. J. Gander, Why it is Difficult to Solve Helmholtz Problems with Classical Iterative Methods, in Numerical Analysis of Multiscale Problems, I. G. Graham et al., Eds., *LNCSE Springer 83*, pp. 325-116, 2012.
- [2] M. Bollhöfer, M. J. Grote and O. Schenk, Algebraic Multilevel Preconditioner For the Helmholtz Equation In Heterogeneous Media, *SIAM J. Sci. Comput.*, 31(5), 3781–3805, 2009.
- [3] M.-O. Bristeau, R. Glowinski and J. Périaux, Controllability Methods for the Calculation of Time-Periodic Solutions. Application to Scattering, *J. Comput. Phys.* 147 (2), 265-292, 1998.
- [4] E. Heikkola, S. Mönkölä, A. Pennanen and T. Rossi, Controllability method for acoustic scattering with spectral elements, *J. Comput. Appl. Math.*, 204(2), 344-355, 2007.
- [5] M. J. Grote, M. Mehlin and T. Mitkova, Runge-Kutta Based Explicit Local Time-Stepping Methods for Wave Propagation, *SIAM J. Sci. Comput.*, 37(2), 747-775, 2015.

Accuracy and Pollution Errors of HDG Methods for the Helmholtz equation involving point sources

Matthias Taus^{1,*}, Leonardo Zepeda-Núñez², Laurent Demanet¹

¹Department of Mathematics, Massachusetts Institute of Technology, USA

²Department of Mathematics, University of California at Irvine, USA

*Email: mattthias.taus@gmail.com

Abstract

The pollution error of Hybridizable Discontinuous Galerkin (HDG) methods is studied for problems involving non-smooth solutions. A quasi-optimal HDG method for problems involving point sources is designed for which quadratic accuracy is proved in the L^2 -error. It is shown that even for non-smooth solutions, if the order p of the HDG discretization is slightly increased with the frequency ω , the pollution error can be eliminated. In particular, it is proved that the order should be chosen such that $p = O(\log \omega)$. Results are derived for constant wave-speeds but can be directly extended to piecewise smooth wave-speeds, albeit with a slightly more aggressive scaling for p . Numerical examples are provided to corroborate the claims.

Keywords: first, second, third

1 Introduction

Solving the time-harmonic wave equation for heterogeneous wave-speeds in the high-frequency regime is an ubiquitous problem, in particular in geophysical exploration. This problem is still open in the context of numerical analysis, both from the points of view of efficiency and accuracy.

In view of accuracy, several advances have been made following mostly two fronts: (*i*), methods using basis functions adapted to the problem, *e.g.*, plane-waves, and (*ii*), new stabilized formulations relying on polynomials basis.

Within the second front, Hybridizable Discontinuous Galerkin (HDG) methods provide an accurate discretization technique, especially for heterogeneous media. Further, HDG methods can be seamlessly combined with state-of-the-art solvers resulting not only in an accurate but also efficient method (*c.f.* [2]). Alas, it is well-known that HDG methods suffer from the pollution error. In practice, this means that even if the number of degrees of freedom per wavelength is kept constant, the numerical so-

lution deteriorates as the frequency increases. However, if the order of the polynomial approximation is increased logarithmically with the frequency, the pollution error can be entirely eliminated for smooth problems.

Several applications, however, rely on problems involving point sources or discontinuous wave-speeds, which produces non-smooth solutions. Unfortunately, for non-smooth problems there is few methods treating this case.

In the present work, we design a quasi-optimal HDG method with a quadratic accuracy in the L^2 -error for problems involving point sources. We focus on problems involving constant wave-speeds but all results can be easily extended to piecewise smooth wave-speeds.

2 Method

Let $\Omega = [0, 1]^2$. We solve the constant density acoustic Helmholtz equation given by

$$-\Delta u - \omega^2 u = \delta_x \quad \text{in } \Omega, \quad (1)$$

with Robin boundary conditions on the boundary $\partial\Omega$

$$u + i\omega \frac{\partial u}{\partial n} = g \quad \text{on } \partial\Omega; \quad (2)$$

here, ω is the frequency and δ_x is the Delta distribution centered at $x \in \Omega$ modeling a point source at x .

Note that the solution u of this problem will in general not be smooth. Nevertheless, it can be decomposed as $u = \tilde{u} + G_\Delta(x, \cdot)$ where G_Δ is the fundamental solution of Laplace's equation and \tilde{u} can be proved to be in $H^2(\Omega)$. The unknown part \tilde{u} can be obtained from equations (1)-(2) with appropriately adjusted right-hand sides.

We discretize the model problem for \tilde{u} using an HDG method based on the ultra-weak formulation previously considered in [1].

For appropriately chosen basis functions of order p defined on elements T of a mesh \mathcal{T}_h with

mesh-size h , we can prove that the corresponding HDG solution \tilde{u}_h approximating \tilde{u} satisfies the optimal error estimate

$$\|\tilde{u} - \tilde{u}_h\|_{L^2(\Omega)} \leq C(\omega) \sum_{T \in \mathcal{T}_h} \left(\frac{h}{p} \right)^2 |\tilde{u}|_{H^2(T)},$$

as long as $h = O(1/\omega)$. Here, $C(\omega)$ is independent of h and p and depends linearly on ω . This linear dependence determines the pollution error.

3 Numerical Examples

Numerical examples verifying the quadratic accuracy can be found in [1]. Here, we concentrate on the assessment of the pollution error. To this end, we place a point source at $(1/\pi, 1/\pi) \in \Omega$ and choose the boundary data g in such a way that the exact solution \tilde{u} is the fundamental solution of Helmholtz' equation centered at $(1/\pi, 1/\pi)$.

To assess the pollution error, we compute the approximation \tilde{u}_h of \tilde{u} defined over a uniform partitioning of Ω into squares. Then, $C(\omega)$ can be estimated as the ratio $C^h(\omega)$ of the error of the HDG solution and the best approximation error:

$$C(\omega) \approx C^h(\omega) = \frac{\|\tilde{u} - \tilde{u}_h\|_{L^2(\Omega)}}{\inf_{v_h} \|\tilde{u}_h - v_h\|_{L^2(\Omega)}}$$

We computed numerical solutions \tilde{u}_h on sev-

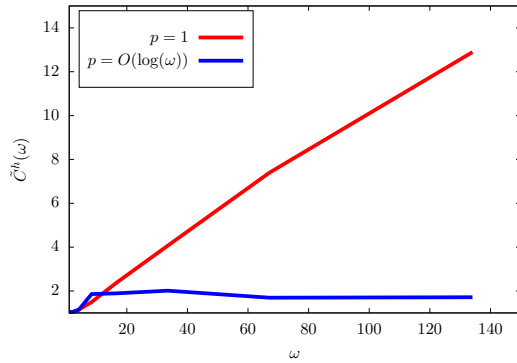


Figure 1: Estimates for $C^h(\omega)$ for different choices of p . For each choice, there are 6 (uniform) elements per wavelength.

eral uniform meshes. For each mesh, the problem is defined so that the frequency depends on the mesh-size. In particular, for each mesh we chose the frequency ω so that there are 6 elements per wavelength. In Figure 1 for each

mesh, we compare the effect of polynomial refinement on $C^h(\omega)$. We see that $C(\omega) = C\omega$ for $p = 1$ and therefore that mere mesh refinement is not sufficient to attenuate the pollution error. However, if the polynomial degree p is increased as $\omega^{0.25}$, the pollution error is eliminated.

4 Future work

We would like to explore adaptive refinement techniques in order to increase the efficiency of the approach. We believe that this might lead to a numerical method that allows for an almost optimal choice of degrees of freedom per wavelength while preserving the elimination of the pollution error and the quadratic accuracy in the L^2 -error.

5 Acknowledgement

The authors thank Total SA for the generous support. LD is also supported by AFOSR, ONR, and NSF.

References

- [1] R. Griesmaier and P. Monk, Error analysis for a hybridizable discontinuous Galerkin method for the Helmholtz equation, *J.Sci.Comput.* **49** (2011), no. 3, pp. 291–310.
- [2] M. Taus, L. Demanet, and L. Zepeda-Núñez, A short note on a fast and high-order hybridizable discontinuous Galerkin solver for the 2D high-frequency Helmholtz equation *SEG Technical Program Expanded Abstracts* (2016), pp. 3835–3840.

The Half-Space Matching Method for the diffraction by polygonal scatterers

Anne-Sophie Bonnet-Ben Dhia¹, Sonia Fliss¹, Yohanes Tjandrawidjaja^{1,*}, Antoine Tonnoir²

¹POEMS (CNRS-INRIA-ENSTA ParisTech-Université Paris Saclay), Palaiseau, France

²INSA, Rouen, France

*Email: yohanes.tjandrawidjaja@ensta-paristech.fr

Abstract

In this work, we want to solve a scattering problem outside a convex polygonal scatterer for a general class of boundary conditions using the Half-Space Matching Method. This method has been introduced in [1] and consists in replacing the problem by a system of coupled integral equations whose unknowns (whose definition depends on the boundary conditions) live on the lines supported by each edge of the polygon. Using the Mellin Transform, we are able to show that this system is coercive + compact in presence of dissipation. Compared to integral methods, this method can be applied for some anisotropic elastic problems where calculating the green function might be expensive or impossible.

Keywords: scattering problem, integral operators, Fourier transform

1 The model problem

The problem that we are interested in is the Helmholtz equation in a 2D infinite plane minus a compactly supported non-penetrable convex polygonal scatterer \mathcal{O}

$$\begin{cases} \Delta p + \omega^2 p = 0 & \text{in } \Omega = \mathbb{R}^2 \setminus \mathcal{O}, \\ \alpha p + \beta \frac{\partial p}{\partial n} = g & \text{on } \partial \mathcal{O}, \end{cases} \quad (1)$$

for a given $g \in L^2(\partial \mathcal{O})$ and where n is the outgoing normal to \mathcal{O} . We consider the dissipative case ($\text{Im}(\omega^2) > 0$) and look for a solution p decaying at infinity. Without loss of generality, we suppose that $\beta \in \{0, 1\}$.

- If $\beta = 1$, the problem is coercive in $H^1(\Omega)$ if $\text{Im}(\alpha) \geq 0$. Let us remark that one classically consider $g \in H^{-\frac{1}{2}}(\partial \mathcal{O})$ but our formulation requires $g \in L^2(\partial \mathcal{O})$.
- If $\beta = 0$ and $\alpha \neq 0$, in contrast to the previous case, the classical framework would lead to take $g \in H^{\frac{1}{2}}(\partial \mathcal{O})$ but our approach allows to consider more general data.

As a consequence, the solution may not be in $H^1(\Omega)$ up to the boundary (see [2] for a similar problem).

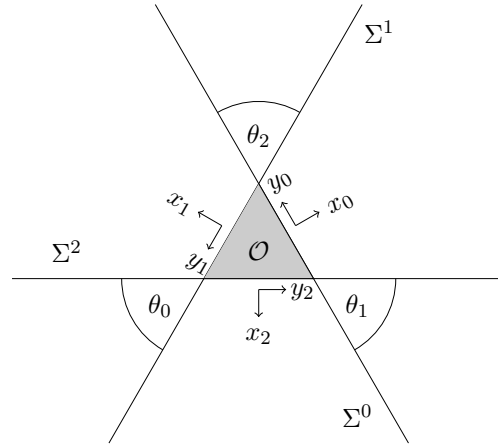


Figure 1: Multi-domain representation

2 The Half-Space Matching formulation

The Half-Space Matching Method consists in coupling several analytical representations of the solution in half-planes surrounding the obstacle. To simplify the presentation, we will suppose that $\partial \mathcal{O}$ is a triangle, as represented in Figure 1. If we denote

$$\phi^j = \alpha p + \beta \frac{\partial p}{\partial n} \text{ on } \Sigma^j,$$

applying the Fourier transform in the y^j direction, the solution in each half-space Ω^j is given by

$$p(x^j, y^j) =$$

$$\frac{1}{\sqrt{2\pi}} \int_{\mathbb{R}} \frac{\hat{\phi}^j(\xi) d\xi}{\alpha + i\beta\sqrt{\omega^2 - \xi^2}} e^{i\sqrt{\omega^2 - \xi^2}x^j} e^{i\xi y^j} \quad (2)$$

in $\Omega^j = \{(x^j, y^j), x^j > 0\}, j \in \mathbb{Z}/3\mathbb{Z}$, where $\text{Im} \sqrt{\omega^2 - \xi^2} \geq 0$ (see Figure 1 for the notations). We assume that $\beta \text{Im}(\alpha) \geq 0$ so that the denominator does not vanish.

The representations have to coincide in the infinite intersections of the half-planes. Since $\text{Im}(\omega^2) > 0$, we can show that this will be satisfied if and only if the representations match on the boundaries of these intersections. These relations, completed with the boundary conditions on $\partial\mathcal{O}$, give

$$\begin{cases} \phi^j = D_{\alpha,\beta}^{j,j\pm 1} \phi^{j\pm 1} & \text{on } \Sigma^{j\pm 1} \cap \Omega^j, \\ \phi^j = g & \text{on } \Omega^j \cap \partial\mathcal{O}, \end{cases} \quad (3)$$

for $j \in \mathbb{Z}/3\mathbb{Z}$, where

$$\begin{aligned} D_{\alpha,\beta}^{j,j\pm 1} : L^2(\Sigma^j) &\rightarrow L^2(\Sigma^{j\pm 1} \cap \Omega^j) \\ \psi &\rightarrow \alpha p^j(\psi) + \beta \frac{\partial p^j(\psi)}{\partial n^{j\pm 1}}. \end{aligned}$$

This leads to a system of coupled integral equations whose unknowns are $\phi_{\pm}^j = \phi_{\Sigma^j \cap \Omega^{j\pm 1}}^j$:

$$\begin{aligned} \forall j \in \mathbb{Z}/3\mathbb{Z}, \\ \phi_+^j &= D_{\alpha,\beta}^{j,j+1} \phi_+^{j+1} + D_{\alpha,\beta}^{j,j+1} \phi_-^{j+1} + D_{\alpha,\beta}^{j,j+1} g^{j+1}, \\ \phi_-^j &= D_{\alpha,\beta}^{j,j-1} \phi_+^{j-1} + D_{\alpha,\beta}^{j,j-1} \phi_-^{j-1} + D_{\alpha,\beta}^{j,j-1} g^{j-1}, \end{aligned} \quad (4)$$

where $g^j = g|_{\Sigma^j \cap \partial\mathcal{O}}$. This system can be rewritten as

$$[\mathbb{I} + \mathbb{D}][\phi] = [\mathbb{G}]. \quad (5)$$

The operator \mathbb{D} is not compact because of the cross points. However, it has been shown in [1] that in the case of a square, we can decompose the operator by using the Laplace transform into

$$\mathbb{D} = \mathbb{D}_0 + \mathbb{K},$$

where $\|\mathbb{D}_0\| < 1$ and \mathbb{K} is a compact operator. For a general polygon, this result can be extended by using the Mellin transform and we get the

Proposition 1. Problem (4) can be written as

$$[\mathbb{A} + \mathbb{K}][\phi] = [\mathbb{G}], \quad (6)$$

where \mathbb{A} is coercive and \mathbb{K} is compact. Moreover, since $\mathbb{A} + \mathbb{K}$ is injective, problem (4) is well-posed.

The injectivity of $\mathbb{A} + \mathbb{K}$ can be deduced from the uniqueness property of the initial problem. Let us mention that when one of the angle of the polygon tends to 0 or π , the norm of \mathbb{D}_0 tends to 1 and the formulation (6) becomes ill-conditioned.

3 Numerical results

For the simulation, we truncate each Σ^j and discretize the formulation by Lagrange finite elements. To compute the Fourier integrals, we introduce also a truncation and a quadrature formula. Note finally that once we obtain the ϕ^j , we can reconstruct the solution in Ω by using the formula (2).

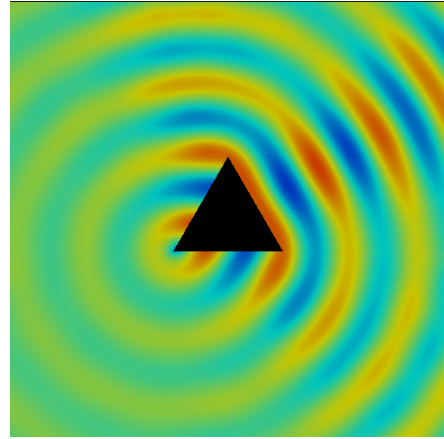


Figure 2: Real part of p with $\alpha = 1, \beta = 0, \omega = 1$, and $g = -\exp(i\omega(\sqrt{3}/2x + 1/2y))$.

Remark that, even if the theoretical results are established only for $\text{Im}(\omega^2) > 0$, the numerical method works for the case without dissipation, provided that we use the representation of the outgoing solution in (2) for each half space. One numerical result, obtained using XLiFE++ [3], is shown in Figure 2.

Acknowledgement: preliminary results have been obtained during the internship of Pablo Alonso.

References

- [1] A. Tonnoir, Transparent conditions for the diffraction of elastic waves in anisotropic media. *Ecole Polytechnique, PhD Thesis*, (2015).
- [2] T. Apel, S. Nicaise, J. Pfefferer, Discretization of the Poisson equation with non-smooth data and emphasis on non convex domains, *arXiv*, (2015).
- [3] N. Kielbasiewicz and E. Lunéville, User documentation of XLiFE++, *POEMS, ENSTA*, (2016).

Analysis of an observers strategy for initial state reconstruction in unbounded domains

S. Fliss¹, S. Impériale², P. Moireau², Antoine Tonnour^{3,*}

¹POEMS (CNRS/ENSTA ParisTech / Inria), Palaiseau, France

²Inria Saclay-Ile de France, Team MÉDISIM, France

³Normandie Université, INSA Rouen Normandie, LMI, 76000 Rouen, France

*Email: antoine.tonnour@insa-rouen.fr

Abstract

In this work, we are interested in the problem of recovering a compactly supported initial state of the wave equation in unbounded domain (such as the whole plane, a waveguide...). To this purpose, we assume that the velocity is known in a bounded observation region surrounding the support of the initial state. We consider an iterative algorithm of reconstruction based on back and forth nudging and prove the exponential convergence of this algorithm and its robustness with respect to noisy measures, at the continuous level. We also study the effect of the discretization process on the algorithm convergence.

Keywords: Initial state recovery, Geometrical Control Condition, Observers, Unbounded domain

1 The Observers strategy

Let us consider the problem of recovering (u_0, v_0) the initial state of the wave equation

$$\begin{cases} \partial_{tt}u - \Delta u = 0 & \text{in } \mathcal{D}, \\ u = 0 & \text{on } \partial\mathcal{D}, \\ (u, \partial_t u)_{t=0} = (u_0, v_0) & \text{in } \mathcal{D}, \end{cases}$$

given the partial measures $z = \partial_t u$ during time $[0, T]$, $T > 0$, in the observation domain \mathcal{D}_{Obs} (see Figure 1). Following the ideas of [1], let

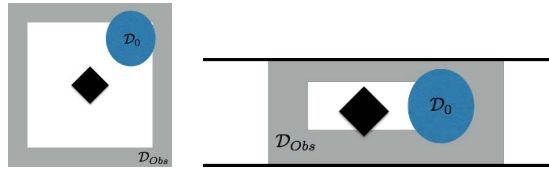


Figure 1: Notations and examples of unbounded domains: on the left $\mathcal{D} = \mathbb{R}^2 \setminus \mathcal{O}$ and on the right $\mathcal{D} = \mathbb{R} \times [0, 1] \setminus \mathcal{O}$, where \mathcal{O} is a bounded obstacle represented in black.

us introduce the sequence of observers $\{\hat{u}^n, \hat{u}_b^n\}$

where:

$$\begin{cases} \partial_{tt}\hat{u}^n - \Delta\hat{u}^n + \gamma(\partial_t\hat{u}^n - z)|_{\mathcal{D}_{Obs}} = 0 & \text{in } \mathcal{D}, \\ \hat{u}^n = 0 & \text{on } \partial\mathcal{D}, \\ (\hat{u}^n, \partial_t\hat{u}^n)_{t=0} = \mathcal{P}(\hat{u}_b^{n-1}, \partial_t\hat{u}_b^{n-1})_{t=0} & \text{in } \mathcal{D}, \end{cases}$$

and

$$\begin{cases} \partial_{tt}\hat{u}_b^n - \Delta\hat{u}_b^n - \gamma(\partial_t\hat{u}_b^n - z)|_{\mathcal{D}_{Obs}} = 0 & \text{in } \mathcal{D}, \\ \hat{u}_b^n = 0 & \text{on } \partial\mathcal{D}, \\ (\hat{u}_b^n, \partial_t\hat{u}_b^n)_{t=T} = (\hat{u}^n, \partial_t\hat{u}^n)_{t=T} & \text{in } \mathcal{D}, \end{cases}$$

and $\gamma > 0$ is a gain parameter. The *forward* observer is initialized with an arbitrary initial condition compactly supported in \mathcal{D}_0 . The *backward* observer \hat{u}_b^n is initialized at final time T and is solved indeed backward in time. The *forward* observer is initialized at $t = 0$ via a projection step with the linear operator \mathcal{P} defined from $\mathcal{Y} = H^1(\mathcal{D}) \times L^2(\mathcal{D})$ into itself and that satisfies

- $\mathcal{P}(u, v) = (u, v)$ if $\text{Supp}(u, v) \subset \mathcal{D}_0$
- and $\|\mathcal{P}(u, v)\|_{\mathcal{Y}} \leq \|(u, v)\|_{\mathcal{Y}}$

In this iterative algorithm, we expect the sequence of initial state error $(\tilde{u}_0^n = \hat{u}_{t=0}^n - u_0, \tilde{v}_0^n = \partial_t\hat{u}_{t=0}^n - v_0)$ to converge to $(0, 0)$ as n grows.

2 The reconstruction operator

Let Π_γ denotes the operator from \mathcal{Y} into itself defines by $(\tilde{u}_0^{n+1}, \tilde{v}_0^{n+1}) = \Pi_\gamma(\tilde{u}_0^n, \tilde{v}_0^n)$. We can show that $\forall Y \in \mathcal{Y}$

$$\Pi_\gamma Y = Y - 2\gamma \int_0^T \mathcal{S}^*(0, s) \mathcal{S}(0, s) Y ds.$$

The operator $\mathcal{S}(0, s)$ is defined by $\mathcal{S}(0, s)(\tilde{u}_0, \tilde{v}_0) = (\tilde{u}, \partial_t\tilde{u})_{t=s}$ where \tilde{u} is solution to the damped wave equation:

$$\begin{cases} \partial_{tt}\tilde{u} - \Delta\tilde{u} + \gamma\partial_t\tilde{u}|_{\mathcal{D}_{Obs}} = 0 & \text{in } \mathcal{D}, \\ \tilde{u} = 0 & \text{on } \partial\mathcal{D}, \\ (\tilde{u}, \partial_t\tilde{u})_{t=0} = (\tilde{u}_0, \tilde{v}_0) & \text{in } \mathcal{D}. \end{cases} \quad (1)$$

With the above form of Π_γ , we are able to prove

Theorem 1 *The operator Π_γ is symmetric and positive. Moreover, if the observability inequality*

$$\int_0^T \|\partial_t u\|_{L^2(\mathcal{D}_{Obs})}^2 dt \geq \kappa \| (u_0, v_0) \|_{\mathcal{Y}}^2, \quad (2)$$

is satisfied for any initial state (u_0, v_0) compactly supported in \mathcal{D}_0 , then Π_γ is a contraction and the algorithm converges. Furthermore, if we consider noisy data $z = \partial_t u + \eta$ with $\eta \in L^1([0, T], L^2(\mathcal{D}_{Obs}))$ we have the error bound

$$\| \tilde{u}_0^n, \tilde{v}_0^n \|_{\mathcal{Y}} \leq \alpha^n \| \tilde{u}_0^0, \tilde{v}_0^0 \|_{\mathcal{Y}} + \frac{2\gamma}{1-\alpha} \int_0^T \| \eta \|_{L^2(\mathcal{D}_{Obs})}$$

where $0 < \alpha < 1$.

Let us point out that the projection step is necessary to ensure the convergence of the algorithm. Indeed, if at step n $\text{Supp}(\tilde{u}^n, \partial_t \tilde{u}^n)_{t=0} \not\subset \mathcal{D}_0$, then we cannot ensure that Π_γ is a contraction.

A classical way to prove observability inequalities consists in using the so-called Geometrical Control Condition (GCC) [2,3]. In our case, the difficulty is that the domain \mathcal{D} is unbounded whereas the observation area \mathcal{D}_{Obs} is bounded. Therefore, we cannot expect the inequality (2) to be true for initial states with support outside the domain surrounded by \mathcal{D}_{Obs} . Let \mathcal{D}_{ext} denotes this exterior domain. To prove (2), we show

Theorem 2 *Under the GCC on $\mathcal{D}_{ext} \cup \mathcal{D}_{Obs}$ and recalling that \mathcal{D}_{Obs} surround \mathcal{D}_0 , there exists a time T s.t. the observability inequality (2) is satisfied for initial data supported in \mathcal{D}_0 .*

In some sense, Theorem 2 is a GCC restricted to a class compactly supported initial data. To prove this result, we proceed in two steps : first we show that the energy in \mathcal{D}_{ext} is controlled by the observations in \mathcal{D}_{Obs} (this holds only because \mathcal{D}_{Obs} surrounds \mathcal{D}_0), then we apply the result on the GCC on the union $\mathcal{D}_{ext} \cup \mathcal{D}_{Obs}$.

3 Discretization aspects

From a numerical point of view, we need to bound the computational domain by introducing an artificial boundary and imposing an absorbing boundary condition. Because this condition is not exact, the problem in the bounded domain is not equivalent to the original one set

on the unbounded domain. As a consequence, because of this approximation added to the discretization one, we cannot deduce directly from Theorem 1 the convergence of the associated discrete algorithm.

Following the same approach as for the continuous level, we are able to construct the discrete equivalent of the operator Π_γ which is the matrix Π_γ^h that reads

$$\Pi_\gamma^h = I - 2\gamma \sum_{j=0}^{N-1} (\mathbb{S}^t)^j \mathbb{S}^j$$

where N is the number of time-step, \mathbb{S} is the matrix s.t. $\tilde{\mathbb{U}}^{j+1} = \mathbb{S} \tilde{\mathbb{U}}^j$ and $\tilde{\mathbb{U}}^j$ is the approximation of \tilde{u} solution to (1) at step j . Then, we can show with the expression of Π_γ^h that the discretized algorithm ensures, at least, that the error decreases (provided there is no measure noise). More importantly, we can also formulate the discrete observability inequality that $\tilde{\mathbb{U}}^j$ should satisfy to ensure the exponential convergence of the algorithm at the discrete level.

Acknowledgement: This work is supported by M2NUM project which is co-financed by the European Union with the European regional development fund (ERDF, HN0002137) and by the Normandie Regional Council.

References

- [1] K. Ramdani, M. Tucsnak and G. Weiss, Recovering the initial state of an infinite-dimensional system using observers, *Automatica* **46** (2010), pp. 1616–1625.
- [2] C. Bardos, G. Lebeau and J. Rauch, Sharp sufficient conditions for the observation, control, and stabilization of waves from the boundary, *SIAM journal on control and optimization* **30** (1992) pp. 1024–1065.
- [3] N. Burq and R. Joly, Exponential decay for the damped wave equation in unbounded domains, *Communications in Contemporary Mathematics* (2014).
- [4] S. Ervedoza and E. Zuazua, Uniformly exponentially stable approximations for a class of damped systems, *Journal De Mathématiques Pures Et Appliquées* **91** (2009), pp. 20–48.

A Trefftz method whose shape functions are constructed thanks to a high-order DG finite element method

Hélène Barucq¹, Abderrahmane Bendali², Julien Diaz¹, Sébastien Tordeux^{1,*}

¹Team-Project Magique 3D, INRIA Bordeaux Sud-Ouest, LMAP UMR CNRS 5142, Université de Pau et Pays de l'Adour

²INSA-Toulouse, Institut de Mathématiques de Toulouse UMR CNRS 5219

*Email: sebastien.tordeux@inria.fr

Abstract

We investigate the feasibility of constructing local solutions to the Helmholtz equation thanks to high-order DG finite element approximations of the Dirichlet-to-Neumann operator. This is then used in a Trefftz Discontinuous Galerkin method in place of a boundary element method that was successfully applied in [1] to solve the Helmholtz problem in very large domains. We perform comparisons between the two approaches by considering large domains of propagation including heterogeneities.

Keywords: Helmholtz equation; time-harmonic elastic equation; pollution effects; discontinuous approximation; Dirichlet-to-Neumann

Introduction

When the Helmholtz equation is set in very large domains, the finite element solution may suffer from *pollution effect*. Maintaining a given level of accuracy requires increasing the density of nodes which rapidly exceeds the capacities in storage and computational times even in the framework of massively parallel computer platforms (cf., for example, [2]). Discontinuous Galerkin (DG) methods have demonstrated a stronger durability than standard FEMs, also called Continuous Galerkin (CG) methods (cf., for example, [3]). Trefftz methods for which the local shape functions are wave functions (cf., for example, [4]) have also proved to be a good alternative with its pioneering example called Ultra Weak Variational Formulation (UWVF) devised by Després [5]. In the other hand Boundary Integral Equations (BIE) seem to resist better to “*pollution effect*” than FEMs. and the idea of building a FEM in which local shape functions are obtained as BIE solutions has been recently investigated in [1,6,7]. [1] uses DG framework and the key feature of this work is the construction of an improved approximation of the Dirichlet-to-Neumann (DtN) operator for

matching the local solutions at the interfaces of the mesh. It is thus possible to see the method, called in [1] BEM Symmetric Trefftz DG method (BEM-STDG), globally as a DG method at the level of the DG formulation mesh and locally as a BIE at the element level. Actually, BIEs are used only to compute the DtN operator within each element of the DG formulation mesh. Obviously the quality of the overall solution strongly depends on the accuracy of the approximation of the DtN operator. The symmetry yields an important gain too. The storage of the boundary integral operators involved in the formulation is indeed avoided, the contribution of the BIEs being element-wise only. Moreover the degrees of freedom of the discrete problem to be solved are located on the boundaries of the elements and the approximations are ultimately performed in terms of piecewise polynomial functions on a BEM mesh. In contrast then to usual Trefftz methods, h or p refinements are as simple and efficient as in a standard FEM or DG. In [1], several numerical experiments with BEM-STDG show very good performance as compared to standard FEM.

Regarding the very good performance of BEM-STDG for solving Helmholtz problems in very large domains, we propose here to extend the approach of [1] to solve time harmonic elastic equations. Nevertheless, since at the end we want to consider problems with variable coefficients, we propose to approximate the DtN operator with FEM instead. By this way, we can benefit from the high level of flexibility of FEM. BEM-STDG does resist to the pollution effect because the approximation of the Neumann trace is discontinuous. This can not be achieved with a standard FEM. We could think about using mixed finite elements but it turns out that using mixed FEM for the elasticity contributes to breaking the symmetry of the stress tensor. There is thus a need in introducing a

Lagrange multiplier which pertubs the inf-sup conditions making them unstable. This is why we propose to build a DG approximation of the DtN operator and to plug it into the solver that we have developed for BEM-STG.

The considered problem

We consider the numerical solution of the time-harmonic elastic problem that is supposed to be well-posed

$$\begin{cases} \frac{\lambda+2\mu}{\omega^2\rho}\nabla\nabla\cdot\mathbf{u} + \frac{2\mu}{\omega^2\rho}\nabla\times\nabla\times\mathbf{u} + \mathbf{u} = 0 \text{ in } \Omega, \\ \Sigma\mathbf{n} = \mathbf{g}(\mathbf{x}) \text{ on } \partial\Omega \end{cases}$$

posed on the two dimensional domain Ω . The constraint tensor Σ is given by the Hooke's law

$$\Sigma(\mathbf{u}) = \lambda\text{div}(\mathbf{u})\mathbf{I} + \mu(\nabla\mathbf{u} + \mathbf{u}^T)$$

and \mathbf{n} is the outward unit normal.

The global Trefftz DG numerical method

The domain Ω can be partitioned into a mesh \mathcal{T} composed of polygons T : $\Omega = \cup_{T \in \mathcal{T}} T$. Every edge E of the mesh is either a part of the exterior boundary $\partial\Omega$ or an interior edge $E \in \mathcal{E}_{\text{int}}$. The interior edges are shared by two polygons $T_{E,+}$ and $T_{E,-}$.

Moreover, we denote by \mathbf{u}_T and \mathbf{v}_T the restrictions to the polygon T of the trial and test functions \mathbf{u} and \mathbf{v} . The linear space V consists of the functions such that $\mathbf{u}_T \in (H^1(T))^2$ satisfies the elastic equation on every polygon T . The finite dimensional subset V_h of V is composed of functions such that \mathbf{u}_T is a piecewise polynomial on every edge of T .

The variational formulation takes the form:
Find $\mathbf{u} \in V_H$ such that for all $\mathbf{v} \in V_h$

$$\begin{aligned} \sum_{E \in \mathcal{E}_{\text{int}}} \int_E \mathbf{u}_{T_{E,+}} \bar{\mathbf{q}}_{T_{E,-}} + \mathbf{u}_{T_{E,-}} \bar{\mathbf{q}}_{T_{E,+}} \\ + \mathbf{p}_{T_{E,-}} \bar{\mathbf{v}}_{T_{E,+}} + \mathbf{p}_{T_{E,+}} \bar{\mathbf{v}}_{T_{E,-}} \\ + \int_E \alpha [\mathbf{u}] [\bar{\mathbf{v}}] = \int_{\partial\Omega} \mathbf{g} \bar{\mathbf{v}}. \end{aligned}$$

where we have denoted by $\mathbf{p}_T = \Sigma(\mathbf{u}_T)\mathbf{n}_T$ and $\mathbf{q}_T = \Sigma(\mathbf{v}_T)\mathbf{n}_T$ the Neumann traces of \mathbf{u}_T and \mathbf{v}_T . The penalization coefficient α is a strictly positive number.

The local numerical method

On every polygon T , the traces \mathbf{u}_T , resp. \mathbf{v}_T , and \mathbf{p}_T , resp. \mathbf{q}_T , are related by a Dirichlet-to-Neumann operator:

$$\mathbf{p}_T = DtN_T \mathbf{u}_T \text{ and } \mathbf{q}_T = DtN_T \mathbf{v}_T.$$

The auxiliary method (here a high-order DG method) computes an approximation of the Neumann traces on a set of quadrature points. It allows to compute the first four integrals of the variation formulation. In order to ensure no loss of accuracy, these local computations should be achieved with a higher polynomial degree than the given traces u_T and p_T .

References

- [1] Barucq, Bendali, Fares, Mattesi, Tordeux, A Symmetric Trefftz-DG Formulation based on a Local Boundary Element Method, J. Comp. Phys. **330** (2017) 1069-1092
- [2] Ihlenburg, Babuška, Finite element solution of the Helmholtz equation with high wave number Part I: The h-version of the FEM. Computers & Mathematics with Applications, **30**(9) (1995) pp. 9-37.
- [3] Ainsworth, Monk, Muniz, Dispersive and dissipative properties of discontinuous Galerkin finite element methods for the second-order wave equation. Journal of Scientific Computing, **27**(1-3) (2006) 5-40.
- [4] Hiptmair, Moiala, Perugia, A survey of Trefftz methods for the Helmholtz equation, Springer Lecture Notes on Computational Science and Engineering (to appear).
- [5] Després, Sur une formulation variationnelle ultra-faible, Comptes Rendus de l'Académie des Sciences Série I **318** (1994) 939–944.
- [6] Hofreither, A non-standard Finite Element Method using Boundary Integral Operators, Ph.D. thesis, J. Kepler University, Linz (2012)
- [7] Hofreither, Langer, Weisser, Convection-adapted BEM-based FEM, ZAMM, **92** (2016) pp. 1467-1481

Vector solitons for elastic waves in architected soft solids

Bolei Deng^{1,*}, Jordan R. Raney^{2,*}, Vincent Tournat^{3,*}, Katia Bertoldi^{1,*}

¹John A. Paulson School of Engineering and Applied Science, Harvard University, Cambridge 02139, MA, USA.

²Department of Mechanical Engineering and Applied Mechanics, University of Pennsylvania, Philadelphia, PA 19104, USA.

³LAUM UMR-CNRS 6613, CNRS, Université du Maine, Av. O. Messiaen, 72085 Le Mans, France.

*Email: boleideng@g.harvard.edu, raney@seas.upenn.edu, vincent.tournat@univ-lemans.fr, bertoldi@seas.harvard.edu

Abstract

In this work, we theoretically and experimentally study nonlinear elastic wave propagation in architected soft solids. Different PDMS structures are considered based on a "rotating squares" geometry, known to exhibit an auxetic behavior upon unidirectional quasi-static loading. The nonlinear dynamics of these structures is modeled with a discrete model, accounting for both the translational and rotational degrees of freedom of the rigid square masses as well as their elastic coupling exhibiting geometrical nonlinearity. Vector soliton solutions are predicted and observed experimentally. We also demonstrate that managing the nonlinearity of these structures over a range of different nonlinearity types and amplitudes is quantitatively feasible.

Keywords: Nonlinear elastic waves, architected soft solids, vector solitons, nonlinearity management

1 Introduction

Soft architected solids have recently attracted a significant attention, because of the exotic effective mechanical properties that can be assessed from the careful design of their geometries [1], and their various applications, such as in robotics [3]. While the vast majority of reported results deal with their quasi-static mechanical properties, or with the tuning of the linear wave dispersion properties [4–6], we here focus on the propagation of nonlinear waves in a soft structure composed of "rotating squares", known to exhibit a negative Poisson Ratio [7]. The main goal we pursue is to understand and model the relation between the dynamic elastic nonlinearity experienced by nonlinear waves during their propagation and the geometrical structure of the architected soft solid metama-

terial. We expect these results will contribute to the design of advanced elastic wave devices, complementary to what has been achieved with granular structures, with applications for instance in pulse mitigation or nonlinear wave control [8–10].

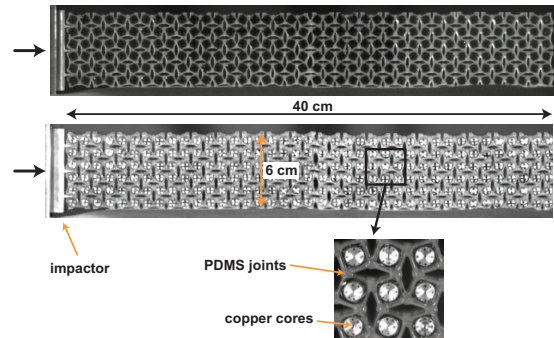


Figure 1: Pictures of the architected soft solid samples that have been tested. Unit cells of the periodic arrangement consist of square masses connected to the neighbors with PDMS joints. In the presented designs, squares are alternatively rotated by a static angle $\theta_0 = 25^\circ$. Masses can be modified by adding copper cores.

2 Description of the problem

We consider the propagation of plane pulse elastic waves in a high symmetry direction of a soft solid structure as shown in Fig. 1. Modeling of nonlinear plane waves propagating in the horizontal direction is proposed, based on discrete square masses, arranged periodically and connected together at their corners by longitudinal and torsional linear springs. Each mass has two degrees of freedom, an horizontal displacement and a rotation, and the nonlinearity of the system comes from the nonlinear relations between these degrees of freedom and the

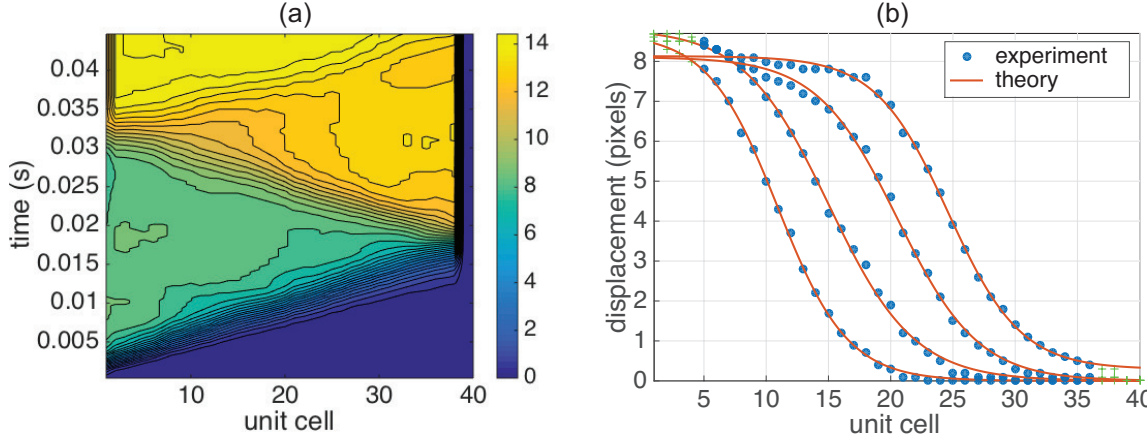


Figure 2: (a) Spatio-temporal diagram of a displacement pulse propagating along the soft metamaterial structure. (b) Spatial profiles of the displacements at four times of the experiment before the first reflexion at the right boundary. Experimental results are in circles and fits with the analytical soliton solution are the lines.

elongations of the coupling springs, i.e. it is a geometrical nonlinearity. A system of coupled nonlinear equations is derived and can be numerically solved or, applying several approximations, transformed into a single nonlinear Klein-Gordon equation. Classical solitary wave solution forms can therefore be obtained [11].

3 Results

We experimentally realize several tests for the propagation of pulses in the presented samples. For some of the excitation parameters, we are able to observe propagation of stable pulses of elastic wave (see Fig. 2(a)), composed of both rotation and displacement motions. These pulses exhibit shapes that show quantitative agreement with the analytical solitary wave solution, Fig. 2(b). In the linear approximation, there exists two modes of propagation with different dispersion properties. In the nonlinear case analyzed here, both modes act together to form a stable solitary wave pulse with a defined velocity, and thus qualifies as a vector solitary wave. Analytical results have also been derived for a wide range of other geometrical parameters and show that these soft solid structures represent an interesting platform for quantitative nonlinearity management of elastic waves.

References

- [1] S. Shan *et.al.*, *Adv. Mater.* **27**, 42964301 (2015).
- [2] D. Restrepo, N. D. Mankame, and P. D. Zavattieri, *Extreme Mechanics Letters* **4**, 52 (2015).
- [3] R. F. Shepherd *et.al.*, *PNAS* **108**, 20400 (2011).
- [4] K. Bertoldi and M. C. Boyce, *Phys. Rev. B* **77**, 052105 (2008).
- [5] S. Rudykh and M. Boyce, *Phys. Rev. Lett.* **112**, 034301 (2014).
- [6] P. Wang, F. Casadei, S. Shan, J. C. Weaver, and K. Bertoldi, *Phys. Rev. Lett.* **113**, 014301 (2014).
- [7] K. Bertoldi, P.M. Reis, S. Willshaw, T. Mullin, *Advanced Materials* **22**, 361-366 (2010).
- [8] N. Boechler, G. Theocharis, and C. Daraio, *Nature Mater.* **10**, 665 (2011).
- [9] T. Devaux, V. Tournat, O. Richoux, V. Pagneux, *Phys. Rev. Lett.* **115**, 234301 (2015).
- [10] A. Spadoni, C. Daraio, *PNAS* **107**, 7230-7234 (2010).
- [11] B. Deng, J. R. Raney, V. Tournat, K. Bertoldi, *Phys. Rev. Lett.*, submitted (2017).

An efficient numerical algorithm for the 3D wave equation in domains of complex shape

S.V. Petropavlovsky¹, S.V. Tsynkov^{2,*}, E. Turkel³

¹National Research University Higher School of Economics, Moscow 101000, Russia

²Department of Mathematics, North Carolina State University, Raleigh, NC, USA

³School of Mathematical Sciences, Tel Aviv University, Tel Aviv, Israel

*Email: tsynkov@math.ncsu.edu

Abstract

We propose an efficient finite difference algorithm for the 3D wave equation in domains with curvilinear boundaries. Our approach combines the method of difference potentials for handling the complex geometries on regular grids and the Huygens' principle for time marching.

Keywords: method of difference potentials, Huygens' principle, wave equation

1 Introduction

We consider an initial boundary value problem (IBVP) for the 3D wave equation:

$$u_{tt} = c^2 \Delta u, \quad (\mathbf{x}, t) \in \Omega \times [0, T], \quad (1a)$$

$$\text{B.C. on } \partial\Omega \times [0, T], \quad \text{I.C. at } t = 0, \quad (1b)$$

where c is the speed of light and Δ is the Laplacian. The boundary conditions set on the walls of the curvilinear cylinder $\Gamma = \partial\Omega \times [0, T]$ may depend on time. The computational domain Ω may have a complex shape in 3D in the sense that its boundary $\partial\Omega$ does not have conform to the (regular) discretization grid, see Fig. 1.

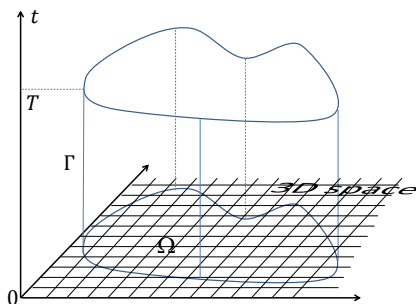


Figure 1: Computational domain (schematic).

The approaches to solving IBVPs of type (1) include various discretizations over Ω (e.g., finite volumes, DG) that have to exercise a case-by-case care for the geometry and specific boundary conditions (BCs) in (1b), as well as

the time-dependent BEM that becomes progressively more costly as the time elapses and is also sensitive to the type of boundary conditions.

We propose an easy to implement finite difference time domain algorithm capable of handling complex non-conforming boundaries and arbitrary boundary conditions on regular grids with no loss of accuracy. Moreover, for the governing PDEs that admit the diffusionless propagation of waves (i.e., satisfy the Huygens' principle), *the proposed algorithm has a provably better asymptotic complexity in long runs than even the plain explicit time marching over Ω regardless of the type of discretization* (finite differences, finite volumes, FEM, DG). The reason is that the original 3D problem is efficiently reduced from the domain to its boundary only.

Our approach employs the method of difference potentials (MDP) [1] that has previously been used for steady-state problems, e.g., the Helmholtz equation [2]. The novel contribution of this paper is the time marching algorithm that is particularly efficient for Huygens' PDEs as it exploits the lacunae in their solutions. In our prior work, we have used lacunae for handling the artificial outer boundaries [3, 4].

2 Method

The MDP equivalently reduces the PDE (1a) from its domain $\Omega \times [0, T]$ to the operator equation at the boundary $\Gamma = \partial\Omega \times [0, T]$:

$$\mathbf{P}_\Gamma \boldsymbol{\xi}_\Gamma = \boldsymbol{\xi}_\Gamma, \quad (2)$$

where \mathbf{P}_Γ is a Calderon's projection and $\boldsymbol{\xi}_\Gamma \equiv (\xi_0, \xi_1)$ is the density of a generalized Calderon's potential. The functions ξ_0 and ξ_1 can be interpreted as traces of the solution u and its normal derivative on Γ , respectively. The boundary equation (2), which is equivalent to (1a), is solved as a system along with the BC from (1b), which can be arbitrary as long as the overall formulation (1) is well-posed. In simple cases, the BC explicitly provides some component of $\boldsymbol{\xi}_\Gamma$,

e.g., ξ_0 in the case of a Dirichlet BC and ξ_1 in the case of a Neumann BC. The remaining component is then obtained as a solution to (2).

The MDP enables an efficient solution of the boundary equation (2). It also allows one to easily restore the solution u on the entire Ω at T_{final} using ξ_Γ . The solution of (2) requires solving a number of inhomogeneous auxiliary problems (APs) for equation (1a) formulated on a larger domain Ω_0 that has simple shape, see Fig. 2. The boundary $\partial\Omega_0$ conforms to the grid and as such, the APs can be easily integrated by any appropriate finite difference scheme.

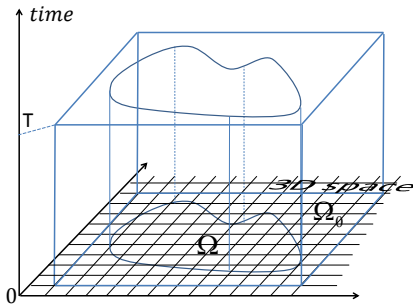


Figure 2: Computational domain for the AP.

The key component of our time marching algorithm is the use of the Huygens' principle, which implies that for a finite domain in space, the extent of the domain of dependence of equation (1a) in time is also finite. This property allows one to solve (2) over long computational times $T_{\text{final}} \gg T$ sequentially, updating the density ξ_Γ by “chunks” of size T , see Fig. 3.

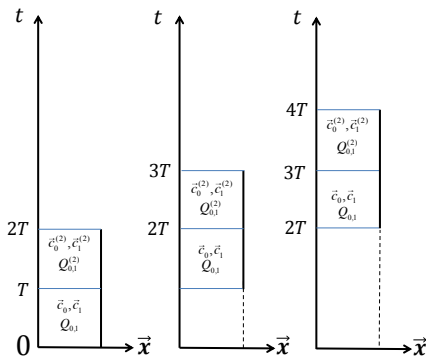


Figure 3: Time marching by “chunks” of size T .

In doing so, the time marching is done only along the boundary Γ , which effectively reduces the space dimension of the evolution scheme for ξ_Γ by one compared to the conventional time

marching of the solution over the entire 3D domain Ω . The solution u on Ω is computed only once, at the final moment $t = T_{\text{final}}$. Due to the reduced dimension and the special choice of an economical basis on Γ , the proposed method appears more efficient in long runs than the standard explicit time marching over Ω .

3 Numerical simulations

We have tested the proposed method for a variety of IBVPs (1) where the domain Ω was a ball while the discretization grid was Cartesian. In all the cases, we have obtained stable performance over long times and the design rate of grid convergence that corresponds to that of the core scheme used in MDP (second order for our current simulations). In Fig. 4, we are showing the convergence for a Robin BC in (1b).

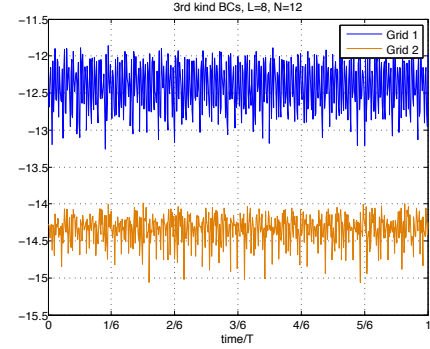


Figure 4: Grid convergence for a Robin BC.

4 Future work

In the future, we will consider exterior problems and high order accurate schemes.

Acknowledgment

Work supported by US ARO, grants W911NF-16-1-0115 and W911NF-14-C-0161, and US-Israel BSF, grant 2014048.

References

- [1] V.S. Ryaben'kii, *Method of Difference Potentials and Its Applications*, Springer-Verlag, Berlin, 2002.
- [2] M. Medvinsky, S. Tsynkov, E. Turkel, *J. Sci. Comput.* **53** (2012), pp. 150–193.
- [3] S. V. Petropavlovsky, S. V. Tsynkov, *J. Comput. Phys.* **231** (2012), pp. 558–585.
- [4] S. V. Petropavlovsky, S. V. Tsynkov, *J. Comput. Phys.* **336C** (2017), pp. 1–35.

High-order numerical solution of the Helmholtz equation for domains with reentrant corners

S. Magura^{1,*}, S. Petropavlovsky², S. Tsynkov¹, E. Turkel³

¹Department of Mathematics, North Carolina State University, Box 8205, Raleigh, NC 27695, USA

²National Research University Higher School of Economics, Moscow 101000, Russia

³School of Mathematical Sciences, Tel Aviv University, Ramat Aviv, Tel Aviv 69978, Israel

*Email: srmagura@ncsu.edu

Abstract

Standard numerical methods often fail to solve the Helmholtz equation accurately near reentrant corners, since the solution may become singular. The singularity has an inhomogeneous contribution from the boundary data near the corner and a homogeneous contribution determined by boundary conditions far from the corner. We present a regularization algorithm that uses a combination of analytical and numerical tools to distinguish between these two contributions and ultimately subtract the singularity. We then employ the method of difference potentials to numerically solve the regularized problem with high-order accuracy on a domain with a curvilinear boundary. Our numerical experiments show that the regularization successfully restores the design rate of convergence.

Keywords: singular solutions, regularization, difference potentials

We consider the constant coefficient homogeneous Helmholtz equation on a bounded 2D domain with a reentrant corner, see Figure 1. The PDE is supplemented with Dirichlet boundary conditions on each segment of the boundary:

$$\Delta u + k^2 u = 0 \quad \text{on } \Omega, \quad (1a)$$

$$u|_{\Gamma_1} = \varphi_1, \quad u|_{\Gamma_2} = \varphi_2, \quad u|_{\Gamma_3} = \varphi_3. \quad (1b)$$

Problems with reentrant corners are hard because the solution may become singular near the corner, i.e., the derivatives of the solution become unbounded. Standard numerical methods perform poorly near singularities, so they must be modified before use on singular problems. Wave problems with reentrant corners may arise, for instance, when analyzing the scattering of radar waves near an air–ocean–sea ice interface. Marin et al. [1] have solved several Helmholtz-type equations on domains with reentrant corners using BEM and the method of fundamental solutions.

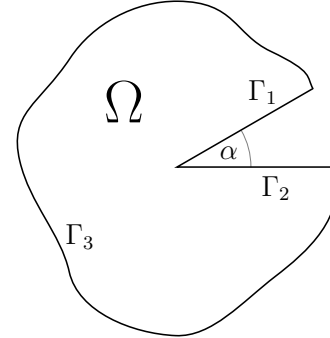


Figure 1: A schematic for the domain Ω with a reentrant corner.

We use regularization (i.e., singularity subtraction) and the method of difference potentials [3] to achieve high-order accuracy near a corner. Singular solutions to the boundary value problem that are expected to hamper numerical convergence are first subtracted out to produce a regularized problem, whose solution is known ahead of time to be smooth enough to be solved numerically without loss of accuracy. The regularized problem is then solved numerically with the method of difference potentials.

The key difficulty with this problem is that there may be two contributions to the singularity which must be handled individually. If we temporarily ignore the boundary condition on the outer boundary Γ_3 , we can write the solution u to the Helmholtz equation over the domain Ω as $u = v + w$, where v is a particular solution that satisfies the boundary conditions on the sides of the wedge and

$$w(r, \theta) = \sum_{m=1}^{\infty} a_m J_{m\nu}(kr) \sin(m\nu(\theta - \alpha))$$

is an arbitrary linear combination of solutions that satisfy the homogeneous boundary conditions. Both the particular solution v and the Fourier–Bessel series w may be singular, and we refer to these two components of the singularity

as the inhomogeneous contribution and homogeneous contribution, respectively. The inhomogeneous contribution is local, in the sense that it is determined by the boundary conditions in the vicinity of the corner. We use the methodology of Fox and Sankar [2] to derive an asymptotic series for v near the corner:

$$v(r, \theta) \sim \sum_{m=1}^{\infty} v^{(m)}(r, \theta) \quad (r \rightarrow 0).$$

The work [2] provides a constructive procedure for determining the terms $v^{(m)}$ from the Helmholtz equation and boundary conditions near the corner. These terms have increasing regularity, as do the Bessel functions $J_{m\nu}$, so we propose the regularization

$$\begin{aligned} u = & u^{(\text{reg})} + v^{(1)} + \dots + v^{(M_v)} \\ & + \sum_{m=1}^{M_w} a_m J_{m\nu}(kr) \sin(m\nu(\theta - \alpha)), \end{aligned} \quad (2)$$

where the fixed integers M_v and M_w are chosen large enough to guarantee that $u^{(\text{reg})}$ has a certain number of bounded derivatives.

Unlike the inhomogeneous contribution, the homogeneous contribution is nonlocal, since the unknown intensity factors (a_m) that characterize w are determined by the boundary condition on Γ_3 , far from the corner. To compute the leading intensity factors a_1, \dots, a_{M_w} for use in the regularization (2), we must know what portion of the boundary data on Γ_3 is from w , and what portion is from v . When both v and w are nonzero, “splitting” the data on Γ_3 becomes a challenging issue. In this way, our work is more general than that of Marin et al. [1], who have considered problems with only homogeneous contributions to the singularity. Once the leading intensity factors are computed, the original boundary value problem (1) is recast in terms of the sufficiently smooth function $u^{(\text{reg})}$ to form the regularized problem.

The method of difference potentials [3] uses the discrete counterparts of Calderon’s operators to accommodate general curvilinear boundaries while leveraging the accuracy and efficiency of high-order finite difference schemes. This way, the method of difference potentials overcomes a primary limitation of finite difference methods, their inability to accurately handle boundaries that do not conform to the

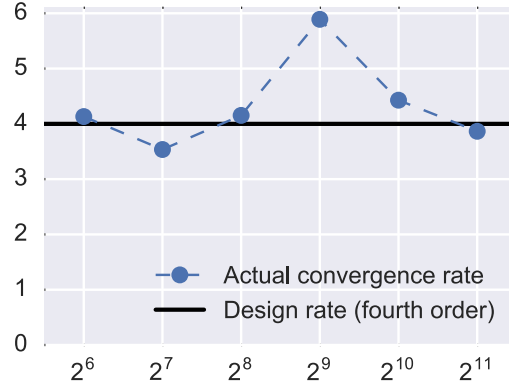


Figure 2: Convergence rate vs. grid dimension.

discretization grid. The method of difference potentials has the same asymptotic complexity as finite difference schemes on regular structure grids. In FEM, on the other hand, high-order accurate approximations can be built for arbitrarily shaped boundaries only in fairly sophisticated and costly algorithms with isoparametric elements.

We have applied the method of difference potentials to the regularized problem for several different configurations of the boundary and data. In all cases we found that the regularization restored the design fourth order convergence; see Figure 2 for the results from one such experiment. Future work could extend our methodology to more difficult cases, such as time-dependent waves, or reentrant corners that lay on the interface between two materials.

This work was supported by the US Army Research Office (ARO) under grants # W911NF-11-1-0384 and # W911NF-16-1-0115, and by the US-Israel Binational Science Foundation (BSF) under grant # 2014048.

References

- [1] L. Marin, D. Lesnic, and V. Mantič, *J. Sound Vibration* **278** (1–2) (2004), pp. 39–62.
- [2] L. Fox, R. Sankar, *J. Inst. Math. Appl.* **5** (1969), pp. 340–350.
- [3] M. Medvinsky, S. Tsynkov, and E. Turkel, *Journal of Scientific Computing* **53** (1) (2012), pp. 150–193.

The Doppler Effect for SAR

Mikhail Gilman¹, Semyon Tsynkov^{1,*}

¹Department of Mathematics, North Carolina State University, Raleigh, NC 27695, USA

*Email: tsynkov@math.ncsu.edu

Abstract

We present a mathematical analysis of the start-stop approximation that is routinely used in synthetic aperture radar (SAR) imaging. The objective is to quantify the effect of those factors that the start-stop approximation neglects. They include the displacement of the antenna during the pulse round-trip time between the radar platform and the target and the Doppler frequency shift. We show that both phenomena can be accounted for by appropriately correcting the signal processing algorithm. This, in turn, requires computing the emitted and scattered field with the help of the Lorentz transform. If the correction is done, then the effect of the antenna motion on the image becomes negligibly small. Otherwise, the image gets shifted and also distorted. For some imaging settings, the distortions due to the start-stop approximation may become substantial, which is not commonly discussed in the SAR literature.

Keywords: synthetic aperture radar (SAR), start-stop approximation, Lorentz transform, correction for antenna motion.

We analyze the Doppler effect in the context of synthetic aperture radar (SAR) imaging, following up and expanding on our earlier results [1]. Understanding of the Doppler effect is critical for evaluating and then mitigating the effect of the start-stop approximation on the image. The start-stop approximation is a common tool in SAR signal processing. It simplifies the analysis by assuming that the radar antenna is motionless during the transmission and reception of the interrogating signals.

The two important effects ignored under the start-stop approximation are the displacement of the antenna during the time the signal travels back and forth between the antenna and the Earth's surface and the Doppler frequency shift. The latter appears because the antenna actually moves when the pulse is emitted and the reflected signal received. Our main objective is to provide a quantitative analysis of the impact

of these two effects on SAR imaging.

The role of the start-stop approximation can be analyzed by having the standard retarded potential

$$P\left(t - \frac{2r}{c}\right)$$

replaced with the new propagator

$$P\left(t\left(1 + 2\frac{\mathbf{v}}{c} \cos \gamma\right) - \frac{2r}{c}\left(1 + \frac{\mathbf{v}}{c} \cos \gamma\right)\right) \quad (1)$$

derived using the Lorentz transform, which preserves the governing wave equation in the case of moving transmitters/receivers. Formula (1) takes into account both the frequency shift and antenna displacement. The quantity \mathbf{v} in (1) is the platform velocity, γ is the angle between the velocity and the direction to the target, and $2r$ is the round-trip distance, see Figure 1.

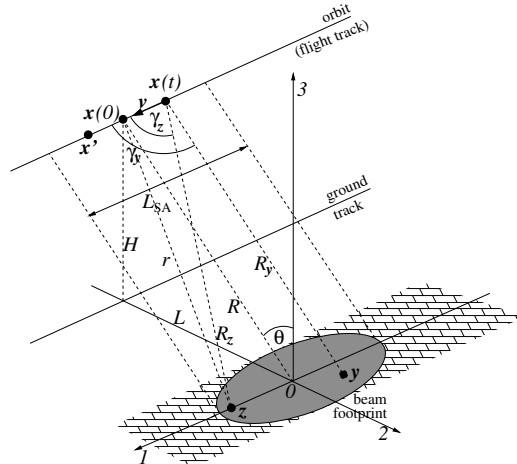


Figure 1: Monostatic stripmap SAR.

The new propagator (1) helps one correct the SAR signal processing algorithm and compensate for the adverse effect of the start-stop approximation on the image. In doing so, implementing the correction is relatively easy because it does not require any additional information besides the geometric quantities (angles and distances, see Figure 1) and the platform velocity \mathbf{v} . This is in contradistinction, say, to the corrections aimed at mitigating the distortions due

to the Earth's ionosphere, see [2] and [3, Chapter 3], for which one first needs to reconstruct the unknown characteristics of the ionosphere.

Our analysis is based on representing the image as a convolution of the ground reflectivity $\nu(\mathbf{z})$ that characterizes the target with the imaging kernel $W(\mathbf{y}, \mathbf{z}) = W(\mathbf{y} - \mathbf{z})$ that characterizes the radar system:

$$I(\mathbf{y}) = \int \nu(\mathbf{z}) W(\mathbf{y}, \mathbf{z}) d\mathbf{z}. \quad (2)$$

The effect of the Doppler correction is quantified by studying the properties of the corresponding kernel W . Representation (2) allows for a rigorous consideration of all the effects and robust prediction of the system performance.

If, on the other hand, the SAR signal processing procedure is not corrected to account for the motion of the radar platform, then the resulting SAR image becomes shifted in the azimuthal direction and may also be distorted (blurred). In many cases, the foregoing distortions will be small. Yet for certain imaging scenarios, the distortions of the image caused by the start-stop approximation may appear significant. The type of SAR imaging systems that may be particularly prone to this kind of distortions are those that exploit the interrogating waveforms (chirps) with low rate of frequency modulation, i.e., the so-called frequency modulated continuous waves (FMCW). These systems are actually contemplated and built in practice (see, e.g., [4, 5], as well as the new ViSAR project by DARPA), because the FMCW waveforms seem to present fewer hardware limitations for airborne or spaceborne SAR platforms. At the same time, to the best of our knowledge the possibility of image deterioration caused by the start-stop approximation did not receive a proper attention in the SAR literature, with the exception of [3, Chapter 6]. Other relevant publications include [6].

Let us also note that some existing books on SAR, e.g., [7, 8], treat the Doppler effect with notable inaccuracies, erroneously attributing to it the mechanism of azimuthal resolution. Hence, we find it important to clearly demonstrate the role of both the actual physical Doppler effect, which is due to the antenna velocity \mathbf{v} and is referred to as the Doppler effect in fast time, as well as that of the so-called Doppler effect in slow time. The latter is a linear variation of the local wavenumber along the

synthetic array, and it is this phenomenon that enables the signal compression in the azimuthal direction and yields the azimuthal resolution.

Acknowledgment

This material is based upon work supported by the US Air Force Office of Scientific Research under award number FA9550-14-1-0218.

References

- [1] S. V. Tsyrkov. *SIAM J. on Imaging Sciences*, 2(2):646–669, 2009.
- [2] Mikhail Gilman, Erick Smith, and Semyon Tsyrkov. *Inverse Problems*, 29(5):054005 (35pp), April 2013.
- [3] Mikhail Gilman, Erick Smith, and Semyon Tsyrkov. *Transitionospheric Synthetic Aperture Imaging*. Birkhäuser, New York, 2017. (To appear).
- [4] A. Meta, P. Hoogeboom, and L. P. Ligthart. *IEEE Transactions on Geoscience and Remote Sensing*, 45(11):3519–3532, Nov 2007.
- [5] Angel Ribalta. *IEEE Geoscience and Remote Sensing Letters*, 8(3):396–400, 2011.
- [6] Pau Prats-Iraola, Rolf Scheiber, Marc Rodriguez-Cassola, Josef Mittermayer, Steffen Wollstadt, Francesco De Zan, Benjamin Bräutigam, Marco Schwerdt, Andreas Reigber, and Alberto Moreira. *IEEE Transactions on Geoscience and Remote Sensing*, 52(10):6003–6016, 2014.
- [7] Giorgio Franceschetti and Riccardo Lanari. *Synthetic Aperture Radar Processing*. Electronic Engineering Systems Series. CRC Press, Boca Raton, FL, 1999.
- [8] Ian G. Cumming and Frank H. Wong. *Digital Processing of Synthetic Aperture Radar Data. Algorithms and Implementation*. Artech House, Boston, 2005.

Boundary integral equations for scattering problems with mixed boundary conditions

Catalin Turc^{1,*}, Oscar Bruno²

¹Department of Mathematics New Jersey Institute of Technology, Newark, USA

²Computing and Mathematical Sciences Department, Caltech, Pasadena, USA

*Email: catalin.c.turc@njit.edu

Abstract

We present boundary integral equation formulations of scattering problems with mixed boundary conditions that rely on smooth blendings of the different types of boundary conditions.

Keywords: Scattering, mixed boundary conditions

1 Introduction

We consider a scalar scattering problem with mixed Dirichlet and Neumann boundary conditions, for which we present a blending strategy via smooth cutoff functions. Specifically, we solve for the scattered field u^s that satisfies the Helmholtz equation

$$\begin{aligned} \Delta u^s + k^2 u^s &= 0 \text{ in } \mathbb{R}^3 \setminus D \\ u^s &= -u^i \text{ on } \Gamma_D \\ \partial_n u^s &= -\partial_n u^i \text{ on } \Gamma_N \\ \lim_{|r| \rightarrow \infty} r^{-1} (\partial u^s / \partial r - iku^s) &= 0, \end{aligned} \quad (1)$$

where D is a bounded domain in \mathbb{R}^3 whose boundary is a closed surface Γ such that $\Gamma_D \cup \Gamma_N = \Gamma$. We use a smooth family of partitions of the unity parametrized by the parameter δ consisting of a pair of cut-off functions $(\chi_D^\delta, \chi_N^\delta)$ such that (i) $\chi_D^\delta + \chi_N^\delta = 1$ on Γ and (ii) χ_D^δ is supported in a δ -neighborhood of Γ_D in Γ and χ_N^δ is supported in a δ -neighborhood of Γ_N in Γ , that is $\chi_D^\delta(x) = 1$ for all $x \in \Gamma_D$ such that $d(x, \Gamma_N) \geq \delta$ and $\chi_D^\delta(x) = 0$ for all $x \in \Gamma_N$ such that $d(x, \Gamma_D) \geq \delta$ where the distances are measured on the surface Γ —and similar properties for χ_N^δ . Given this family of partitions of unity we consider the following family of scattering problems parametrized by δ : find $u^{s,\delta}$ radiative solutions of Helmholtz equation with *blended* impedance boundary conditions

$$\begin{aligned} \Delta u^{s,\delta} + k^2 u^{s,\delta} &= 0 \text{ in } \Omega^+ \\ Z\chi_D^\delta u^{s,\delta} + \chi_N^\delta \partial_n u^{s,\delta} &= -Z\chi_D^\delta u^i - \chi_N^\delta \partial_n u^i, \end{aligned} \quad (2)$$

on Γ , where the impedance Z is such that $\Im Z > 0$. It can be easily shown that equations (2) are

well posed. We retrieve the solution u^s of equations (1) as the limit when $\delta \rightarrow 0$ of the solutions $u^{s,\delta}$ of equations (2). The blending strategy can be easily extended to the case of penetrable scattering when the interior of D is filled with a material with corresponding wavenumber k_- , and the same Dirichlet boundary conditions are imposed on Γ_D while the classical transmission conditions are imposed on Γ_N (i.e. D is partially coated).

2 Numerical Results

Using regularization strategies introduced in [2], well-conditioned boundary integral equation formulations of the blended equations (2) can be readily obtained. More importantly, Nyström solvers based on these formulations [1] can be applied without the need to directly address the nature of discontinuity of their solutions at the junction between Γ_D and Γ_N . We present in Figures 1 and 2 scattering experiments for both impenetrable and penetrable cases that illustrate the convergence in the far-field of the blended solutions $u^{s,\delta}$ in the limit as the overlap parameter δ approaches 0.

References

- [1] O. Bruno, T. Elling, and C. Turc, *Regularized integral equations and fast high-order solvers for sound-hard acoustic scattering problems*, J. Num. Meth. Eng., **91** (2012), 1045-1072.
- [2] Y. Boubendir, V. Dominguez, D. Levadoux, and C. Turc, *Regularized combined field integral equations for acoustic transmission problems*, SIAP, **75** (2015), 929-952.

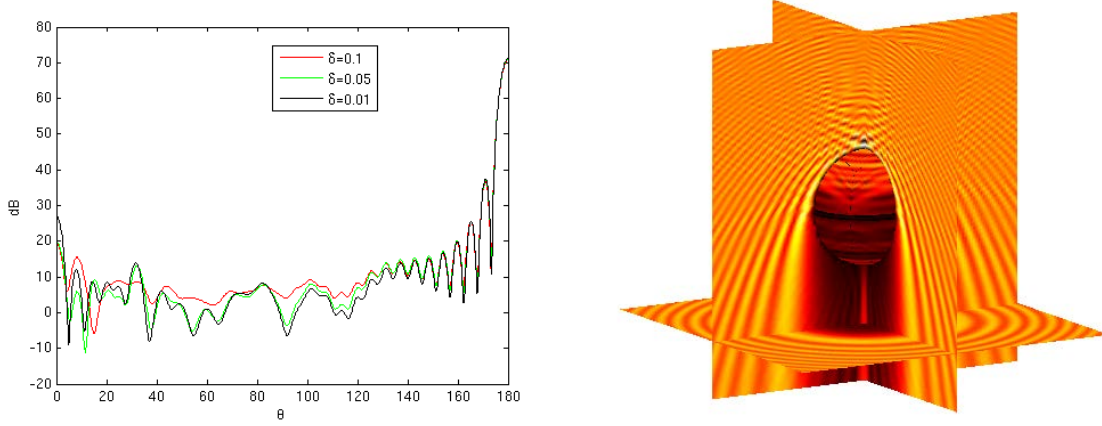


Figure 1: Scattering experiments in the case of a unit sphere with Dirichlet boundary conditions in the northern hemisphere and Neumann boundary conditions in the southern hemisphere, and wavenumber $k = 32$. Left: plots of the radar cross section as a function of the azimuthal angle θ for $\phi = 0$ for various values of the parameter δ in the *blended* boundary conditions. We computed RCS for 1024 values of the angle θ from 0° to 180° . Right: plots of the total fields in the near field in the case $\delta = 0.01$.

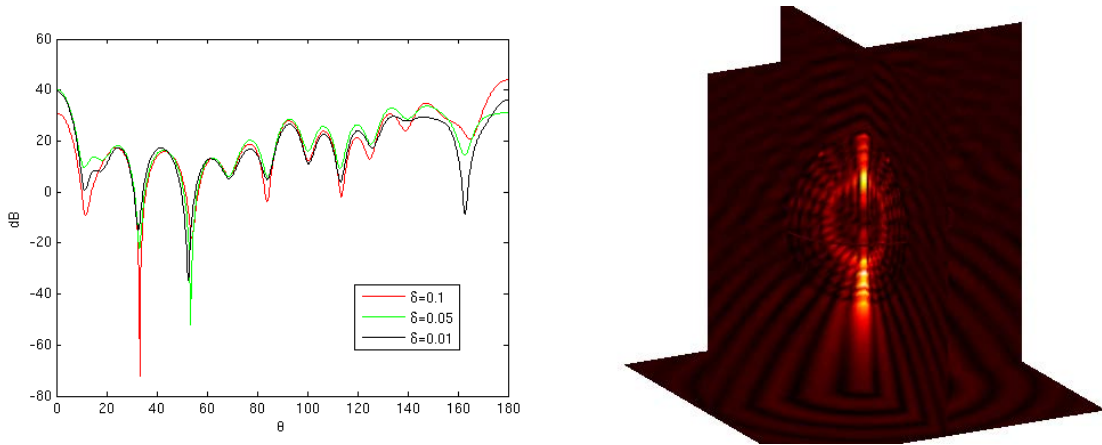


Figure 2: Scattering experiments in the case of a unit sphere with $k_+ = 16$ and $k_- = 32$, when the northern hemisphere is coated. Left: plots of the radar cross section as a function of the azimuthal angle θ when the longitudinal angle $\phi = 0$ for various values of the parameter δ in the *blended* boundary conditions. We computed RCS under broadsight incidence, for 1024 values of the angle θ from 0° to 180° . Right: plots of the total fields in the near field in the case $\delta = 0.01$.

Solution of the focusing Davey-Stewartson equations and the reconstruction of complex-valued conductivities

E. Lakshtanov¹, B. Vainberg^{2,*}

¹Department of Mathematics, Aveiro University, Aveiro , Portugal

²Department of Mathematics and Statistics, UNCC, Charlotte, USA

*Email: brvainbe@uncc.edu

Abstract

We will solve the Cauchy problem for the focusing Davey-Stewartson II equations (that model the shallow-water limit of evolution of weakly nonlinear water waves) in the presence of exceptional points (and/or curves). We also provide a method of reconstruction of complex-valued once differentiable conductivities in the inverse impedance tomography problem.

Both results are based on the inverse scattering problem for the Dirac equation, which is solved without restrictions that guarantee the absence of exceptional points. Below we will mostly discuss the latter result (see [1-3] for more details and applications).

Keywords: $\bar{\partial}$ -equation, inverse Dirac problem, conductivity, Davey-Stewartson equations

1 Main results

I. Let $z = x + iy \in \mathbb{C}$, $\bar{\partial} = \frac{1}{2} \left(\frac{\partial}{\partial x} + i \frac{\partial}{\partial y} \right)$. Consider the Dirac equation

$$\bar{\partial}\psi = Q\bar{\psi}, \quad Q(z) = \begin{pmatrix} 0 & Q_{12}(z) \\ Q_{21}(z) & 0 \end{pmatrix} \quad (1)$$

where $Q_{ij} \in L^p_{com}(\mathbb{C})$, $p > 4$.

Let ψ be the (2×2) -matrix solution of (1) that depends on parameter $k \in \mathbb{C}$ and has the following behavior at infinity:

$$\psi(z, k)e^{-i\bar{k}z/2} \rightarrow I, \quad z \rightarrow \infty. \quad (2)$$

Note that the plane waves $\varphi_0(k, z) := e^{i\bar{k}z/2}$, $k \in \mathbb{C}$, are growing at infinity exponentially in some directions, and the same is true for the elements of the matrix $\psi(z, k)$.

Problem (1),(2) is equivalent to the Lippmann-Schwinger equation:

$$\begin{aligned} \psi(z, k) &= e^{i\bar{k}z/2}I \\ &+ \int_{\mathcal{O}} G(z - z', k)Q(z')\bar{\psi}(z', k)dx'dy', \end{aligned} \quad (3)$$

where $G(z, k) = \frac{1}{\pi} \frac{e^{i\bar{k}z/2}}{z}$ and $\mathcal{O} \subset \mathcal{C}$ is a bounded domain containing the support of Q . Equation (3) is Fredholm in $L^q(\mathcal{O})$, $q > 2p/(p - 2)$. After ψ is found in \mathcal{O} , the right-hand side of (3) defines ψ for all $z \in \mathcal{C}$. Solutions ψ of (3) are called the *scattering solutions*, and the values of k such that the homogeneous equation (3) has a non-trivial solution are called *exceptional points*. The set of exceptional points will be denoted by \mathcal{E} .

The matrix

$$h(\varsigma, k) = \frac{1}{(2\pi)^2} \int_{\partial\mathcal{O}} e^{-i\bar{\varsigma}z/2} \bar{\psi}(z, k) dz,$$

where $\varsigma \in \mathbb{C}$, $k \notin \mathcal{E}$, is called the *(generalized) scattering data*.

Following Sung, we will work with matrix v (instead of ψ) defined as follows

$$v = \begin{pmatrix} \overline{\mu_{11}}(z, k) & \mu_{12}(z, k)e^{i\Re(\bar{k}z)} \\ \mu_{21}(z, k)e^{i\Re(\bar{k}z)} & \overline{\mu_{22}}(z, k) \end{pmatrix}, \quad (4)$$

where $\mu_{ij} = \psi_{ij}(z, k)e^{-i\bar{k}z/2}$. Matrix-function v is defined for $k \notin \mathcal{E}$ and satisfies

$$\frac{\partial}{\partial \bar{k}} v(z, k) = e^{i(\bar{k}z + \bar{z}k)/2} \bar{v}(z, k) h^o(k, k) =: \mathcal{T}v, \quad (5)$$

where $h^o := \Pi^o h$ is the off-diagonal part of h obtained by replacing the diagonal entries by zeros.

If $\mathcal{E} = \emptyset$, then equation (5) holds in the whole plane and can be solved. After v (and therefore, ψ) is found, the potential Q can be found from (1): $Q = \bar{\partial}\psi(\bar{\psi})^{-1}$.

We use the following method to recover Q if $\mathcal{E} \neq \emptyset$. It is known that the set \mathcal{E} is bounded. We choose A large enough so that the disk

$$D = \{k \in \mathbb{C} : |k| < A\}$$

contains \mathcal{E} and a non-exceptional point k_0 . Let $\psi^+(z, k)$ be the solution of the Lippmann-Schwinger equation (3) with the argument k in

the function G being fixed and equal to k_0 . Such a solution exists and is analytic in k . Moreover, one can show that $\frac{\partial v^+}{\partial k} = 0$, $k \in D$, where v^+ is defined by (4) with ψ replaced by ψ^+ .

Let $v' = v$ for $k \notin D$ and $v' = v^+$ for $k \in D$. Then $\frac{\partial v'}{\partial k} = \mathcal{T}'v'$, where $\mathcal{T}' = \mathcal{T}$ outside of D and $\mathcal{T}' = 0$ in D . The above construction allows one to express the jump of v' on ∂D as an integral operator applied to $v^+|_{\partial D}$ and reduce the above equation for v' to a Fredholm integral equation of the form

$$(I + T_z)w = -T_z I, \quad w = v' - I. \quad (6)$$

Operator T_z is defined on the space

$$\mathcal{H}^s = \left\{ u \in L^s(\mathbb{R}_k^2) \cap C(D) \right\}, \quad s > 2,$$

of functions of k . It depends on parameter z and is given by

$$\begin{aligned} T_z \phi(k) &= \frac{1}{\pi} \int_{\mathbb{C} \setminus D} e^{i(\bar{\zeta}z + \bar{z}\zeta)/2} \overline{\phi}(\zeta) h^o(\zeta, \zeta) \frac{d\zeta_R d\zeta_I}{\zeta - k} \\ &+ \frac{1}{2\pi i} \int_{\partial D} \frac{d\zeta}{\zeta - k} \int_{\partial D} \left(e^{i/2(\bar{\zeta}\bar{z} + \bar{\zeta}'z)} \overline{\phi^-(\zeta')} \Pi^o \right. \\ &\left. + e^{i/2(\zeta - \zeta')\bar{z}} \phi^-(\zeta') \Pi^d \mathcal{C} \right) \left[\ln \frac{\bar{\zeta}' - \bar{\zeta}}{\zeta' - k_0} h(\zeta', \zeta) d\zeta' \right], \end{aligned}$$

where $\phi \in \mathcal{H}^s$, ϕ^- is the boundary trace of ϕ from the interior of D , \mathcal{C} is the operator of complex conjugation, $\Pi^o M = M^o$ is the off-diagonal part of a matrix M , $\Pi^d M = M^d$ is the diagonal part, and $h^o = \Pi^o h$.

Let $S_{\varepsilon,p}$ be the space of potentials Q with support in \mathcal{O} such that $Q \in L_{\text{comp}}^p(\mathcal{C})$, $p > 4$, and $\mathcal{F}Q \in L^{2-\varepsilon}(\mathcal{C})$, $\varepsilon > 0$ (\mathcal{F} is the Fourier transform).

Theorem 1 Let $Q_{12}, Q_{21} \in S_{\varepsilon,p}$. Then for each $\tilde{s} > \max(\frac{2p}{p-4}, \frac{4}{\varepsilon} - 2)$ the following statements are valid.

- Operator T_z is compact in $\mathcal{H}^{\tilde{s}}$ for all $z \in \mathbb{C}$ and depends continuously on z .
- Let us fix $z_0 \in \mathbb{C}$. Then, for generic potentials Q_{12}, Q_{21} in $S_{\varepsilon,p}$, the equation

$$(I + T_z)w = -T_z I \quad (7)$$

is uniquely solvable in $\mathcal{H}^{\tilde{s}}$ for all z in some neighborhood of z_0 (the neighborhood may depend on Q).

- For $k \notin \mathcal{E}$, the function $\psi = [e^{ikz/2} \mathcal{C} \Pi^d + e^{-izk/2} \Pi^o](w + I)$, where $w(\cdot)$ is the solution of (7), satisfies the equation $\bar{\partial}\psi = Q\bar{\psi}$ in \mathcal{O} .

- From (1), (2) it follows that $Q = \bar{\partial}\psi(\bar{\psi})^{-1}$, $|k| \gg 1$.

II. Consider the Davey-Stewartson II equations

$$q_t = 2iq_{xy} \pm 4q(\bar{\varphi} - \varphi),$$

$$\bar{\partial}\varphi = \bar{\partial}|q|^2, \quad q(z, 0) = q_0(z),$$

where the choice of the sign corresponds to the defocusing/focusing case. Let

$$Q^0(z) = \begin{pmatrix} 0 & q_0(z), \\ \pm q_0(z) & 0 \end{pmatrix}, \quad z \in \mathbb{C}.$$

Let h be the scattering data for the Dirac equation (1) with $Q = Q^0$. We define the time dependent scattering data $h(\zeta', \zeta, t)$ as

$$e^{-t(\zeta^2 - \zeta'^2)/2} \Pi^o h(\zeta', \zeta) + e^{-t(\bar{\zeta}^2 - \bar{\zeta}'^2)/2} \Pi^d h(\zeta', \zeta),$$

and use Theorem 1 to find the potential $q = q(t, z)$ that corresponds to this data. The potential satisfies the Davey-Stewartson II equations (see [2] for details).

III. We find the complex-valued conductivity γ via the Dirichlet-to-Neumann map on $\partial\mathcal{O}$ for the equation

$$\operatorname{div}(\gamma \nabla u(z)) = 0, \quad z \in \mathcal{O}. \quad (8)$$

Theorem 1 allows one to recover γ assuming that $\gamma \in W^{1,p}(\mathcal{O})$, $p > 4$, $\mathcal{F}(\nabla \gamma) \in L^{2-\varepsilon}(\mathbb{R}^2)$, $\varepsilon > 0$, (here $\nabla \gamma$ is extended by zero in $\mathbb{R}^2 \setminus \mathcal{O}$). The results, under weaker conditions, have been known for real-valued γ .

References

- [1] E. Lakshtanov, R. Novikov, B. Vainberg, A global Riemann-Hilbert problem for two-dimensional inverse scattering at fixed energy, to appear in Rendiconti dell'Istituto di Matematica dell'Università di Trieste (2016).
- [2] E. Lakshtanov, B. Vainberg, On reconstruction of complex-valued once differentiable conductivities, to appear in J. of Spectral Theory (2016).
- [3] E. Lakshtanov, B. Vainberg, Solution of the initial value problem for the focusing Davey-Stewartson II system, (2016), arXiv:1604.01182.

Breathers and Passive Wave Redirection in Forced Ordered Granular Networks

Yijing Zhang¹, Keegan J. Moore¹, D. Michael McFarland², Alexander F. Vakakis^{1,*}

¹Department of Mechanical Science & Engineering, University of Illinois at Urbana-Champaign, USA

²Department of Aerospace Engineering, University of Illinois at Urbana-Champaign, USA

*Email: avakakis@illinois.edu

Abstract

We study passive pulse redirection in a granular network of two semi-infinite, ordered homogeneous granular chains mounted on linear elastic foundations and coupled by weak linear stiffnesses. A series of repetitive half-sine pulses is applied to an “excited chain”, whereas the “absorbing” chain is initially at rest. Passive pulse redirection from the excited to the absorbing chain can be achieved by macro-scale realization of the Landau-Zener quantum tunneling effect, induced by a stratification of the elastic foundation of the excited chain. Irreversible wave redirection in the forced network happens through sustained 1:1 resonance capture, whereas recurring nonlinear beats between the two chains occur in the absence of resonance capture.

Keywords: Breathers, granular media

1 Introduction

Uncompressed ordered granular networks exhibit rich nonlinear behavior [1, 2]. The absence of linear acoustics and the zero speed of sound in these media led to their characterization as “sonic vacua” [1]. Their strongly nonlinear acoustics are fully tunable with energy, so they can support a variety of interesting wave phenomena [3, 4], including discrete standing or propagating breathers, *i.e.*, oscillating wavepackets with localized envelopes [5, 6]. Hasan *et al.* [7] considered an impulsively forced granular network and showed irreversible wave redirection in the form of propagating breathers. This phenomenon was governed by the macroscopic analog of the Landau-Zener quantum tunneling effect [8], and its practical realization was by spatial stratification of the coupling of the network. Here we extend these results to a periodically forced network.

2 Propagating Breathers and Recurring Energy Transfers

We consider the forced granular network of Figure 1 of two semi-infinite, weakly coupled (with

linear stiffnesses) and weakly damped, uncompressed, homogeneous granular chains of identical PDMS beads with radius $R = 4.75 \times 10^{-3}$ m mounted on linear elastic foundations. The foundation stiffness and the coupling stiffness for each bead have parameters $\tilde{k}_1 = 4115 \text{ N m}^{-1}$ and $\tilde{k}_2 = 402 \text{ N m}^{-1}$, respectively. The force applied to the “excited” chain is a series of half-sines, $\tilde{F}_0 \sin(2\pi ft)H[\sin(2\pi ft)]$, where $H[\cdot]$ denotes the Heaviside function, whereas the “absorbing” chain is unforced. In Figure 2 we show propagating breathers in the network for $\tilde{F}_0 = 23.1 \text{ N}$ and $f = 51.52 \text{ Hz}$. Intense and recurring energy exchanges are noted, as well as synchronization of each applied pulse with a generated breather, indicating *1:1 resonance* in the acoustics.

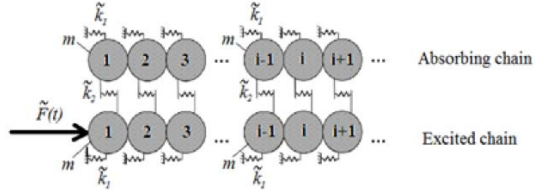


Figure 1: The two-dimensional weakly coupled granular network under periodic excitation.

3 Targeted Energy Transfer and Passive Wave Redirection

By stratifying the elastic foundation of the excited chain we can induce a macroscopic analogue of the Landau-Zener quantum tunneling effect in space. This stratification is given by $(1 - s_i)\tilde{k}_1$ for $i = 1, 2, \dots$, where $s_i = (i - 1)s$ for $i = 1, 2, 3$, and $s_i = 3s$ for $i \geq 4$. In Figure 3 we present the resulting wave redirection for $s = 27\%$. We deduce passive breather redirection from the excited to the absorbing chain. This is due to sustained 1:1 resonance captures between dominant frequency components of the responses of the excited and absorbing chains as explained in [9]. In fact, for fixed excitation such wave redirection can occur only if the stratification parameter is above the critical thresh-

old $s \approx 26\%$ [9]. These results pave the way for designing nonlinear acoustic metamaterials with features of passive wave redirection.

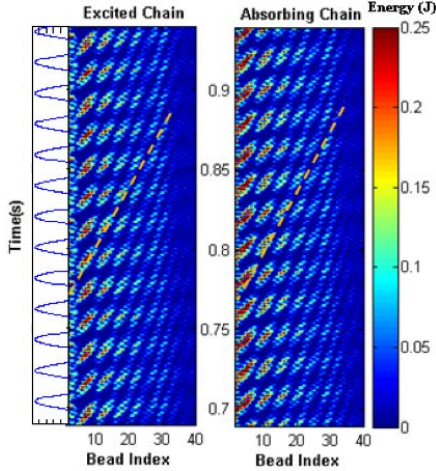


Figure 2: Spatio-temporal evolutions of the instantaneous kinetic energies of the leading beads showing recurring energy exchanges between propagating breathers.

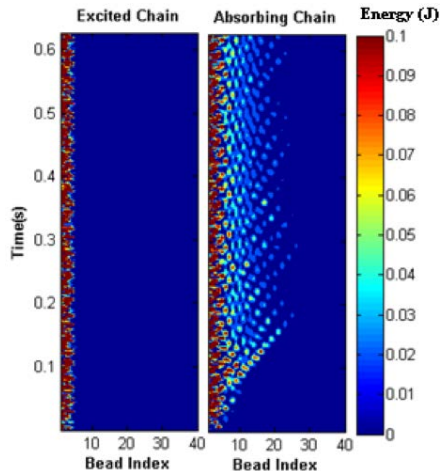


Figure 3: LZT effect leading to wave redirection: Spatio-temporal evolutions of instantaneous kinetic energies of the leading 40 beads of the excited and absorbing chains for $s = 27\%$.

References

- [1] V. Nesterenko, *Dynamics of Heterogeneous Materials*, Springer Verlag, 2001.
- [2] C. Daraio, V. Nesterenko, B. Herbold, and S. Jin, Tunability of Solitary Wave Properties in One-dimensional Strongly Nonlinear Phononic Crystals, *Phys. Rev. E* **73** (2006), 026610.
- [3] K. Jayaprakash, Y. Starosvetsky, A.F. Vakakis, A New Family of Solitary Waves in Granular Dimmer Chains with No Pre-compression, *Phys. Rev. E* **83** (2011), 036606.
- [4] M. Hasan, S. Cho, K. Remick, A.F. Vakakis, D.M. McFarland, and W.M. Kriven, Experimental Study of Nonlinear Acoustic Bands and Propagating Breathers in Ordered Granular Media Embedded in Matrix, *Granular Matter* **17** (2015), pp. 49–72.
- [5] N. Boechler, G. Theocharis, S. Job, P.G. Kevrekidis, M.A. Porter and C. Daraio, Discrete Breathers in One-Dimensional Diatomic Granular Crystals, *Phys. Rev. Lett.* **104** (2010), 244302.
- [6] G. James, Nonlinear Waves in Newton's Cradle and the Discrete p -Schrödinger Equation, *Math. Models Meth. Appl. Sci.* **21** (2011), pp. 2335–2377.
- [7] M. Hasan, Y. Starosvetsky, A.F. Vakakis and L.I. Manevitch, Nonlinear Targeted Energy Transfer and Macroscopic Analog of the Quantum Landau-Zener Effect in Coupled Granular Chains, *Physica D* **252** (2013), pp. 46–58.
- [8] C. Zener, Non-Adiabatic Crossing of Energy Levels, *Proc. Royal Soc. London A* **137** (1932), pp. 696–702.
- [9] Y. Zhang, K. Moore, D.M. McFarland, and A.F. Vakakis, Targeted Energy Transfers and Passive Acoustic Wave Redirection in a Two-dimensional Granular Network Under Periodic Excitation, *J. Appl. Phys.* **118** (2015), 234901.

Parallel preconditioned boundary element methods for wave scattering problems

Elwin van 't Wout^{1,*}

¹School of Engineering and Faculty of Mathematics, Pontificia Universidad Católica de Chile,
Santiago, Chile

*Email: e.wout@uc.cl

Abstract

The Boundary Element Method (BEM) is a powerful numerical method for the computational simulation of wave scattering problems in acoustics and electromagnetics. Because of the surface integral representation, the number of degrees of freedom scales favourably compared to volumetric methods. However, solving the dense set of linear equations poses severe limitations on the maximum frequency that can be used on present-day computing platforms. This paper presents the combined use of parallelisation, preconditioning, and compression techniques to achieve large-scale BEM simulations.

Keywords: boundary element methods, high-performance computing, parallelisation

1 Introduction

Wave scattering phenomena play an important role in many engineering problems. Here, we will consider acoustic scattering at rib cages for the design of ultrasound medical devices and electromagnetic scattering at telescope mirrors used in astronomy. For both applications, the physical model is given by time-harmonic wave scattering at a bounded object embedded in free space. Then, using a boundary integral formulation will be effective because the radiation conditions are automatically satisfied and discretisation with the Boundary Element Method (BEM) will only need a grid density that scales quadratically with the frequency. However, the resulting linear system is dense and, therefore, requires a large storage capacity and efficient algorithms to solve it. This becomes all the more important when considering high-frequency scattering at large-scale objects, as is the case in our targeted engineering applications. Standard BEM will be unfeasible to obtain accurate results for large-scale simulations without the use of acceleration techniques, such as matrix compression, preconditioning, and parallelisation. Where the use of only one or two of these is sufficient for moderately high frequencies [2,3], for numerical

simulations at larger scale, all three will have to be used simultaneously, as will be presented in this paper. All techniques are implemented in the open-source library BEM++ [1].

2 Background

The present research in high-performance computing for BEM is inspired by two different applications in engineering. Both have the challenge that scattering of high-frequency waves have to be computed at a large-scale object consisting of smaller, disjoint parts.

The first target application is within medical treatment planning. Computational experiments are important prediction tools in the development of surgery with non-invasive modalities. For instance, High-Intensity Focused Ultrasound (HIFU) uses a focusing of acoustic rays to locally destroy tissue with ablation. In the case of liver cancer, the reflection of rib bone has to be computed at a frequency of 1 MHz.

The other target application is in the area of astronomical instrumentation. The mirrors of large telescopes typically consist of a constellation of many bended plates that reflect the signals from the universe to the feed. These mirrors can be adaptively perturbed to improve the quality of the image. Numerical simulation of which requires the computation of electromagnetic scattering at a reflector with a size of several thousand wavelengths across.

3 Formulation

Time-harmonic acoustic and electromagnetic scattering can be modelled with the Helmholtz and Maxwell equations, respectively, reformulated into boundary integral equations. Here, for the acoustic model, the rib cage is considered to be a rigid object and we will use a Burton-Miller formulation since it is free of spurious resonances. For the electromagnetic model, the metal mirror is a perfect electrical conductor modelled by a sheet, so the Electric Field Integral Equation (EFIE) will be used.

3.1 Matrix compression

The memory footprint of a BEM scales quadratically with the number of degrees of freedom and, therefore, becomes prohibitively expensive at high frequencies. Acceleration methods that reduce the memory footprint are the fast multipole method and \mathcal{H} -matrix compression, among others. Here, we will use \mathcal{H} -matrix compression because it is readily available in the open-source BEM++ library, it is very effective for moderately high frequencies and it will be advantageous for future research into simulation of multiple right-hand sides.

3.2 Preconditioning

Iterative linear solvers typically require an increased number of iterations for larger simulations, leading to longer compute times. Here, the OSRC preconditioner will be used, which is based on high-frequency approximations of the Neumann-to-Dirichlet map.

3.3 Parallelisation

The trend of modern computer architecture is to include more and more compute cores in a single system, instead of faster cores. Here, we will use the special structure of the targeted engineering applications having disjoint objects. This allows for a high-level parallelisation approach of the block structure, which can be combined with \mathcal{H} -matrix compression and OSRC-preconditioning.

4 Numerical results

For the HIFU problem, a human rib cage model will be excited by an array of ultrasound piston elements at 1 MHz, which yields an object of 135 times the wavelength. The surface mesh covers the wavelength with at least 8 triangular elements, resulting in a BEM with 479 124 degrees of freedom. The use of \mathcal{H} -matrix compression for the assembly of the boundary operators reduced the memory requirement from 7 TB to 194 GB. Solving the system with OSRC preconditioning took 19 iterations and 7 minutes only, where the result is depicted in Fig. 1.

5 Conclusions and outlook

Computational simulation of high-frequency wave scattering at large-scale objects with BEM is

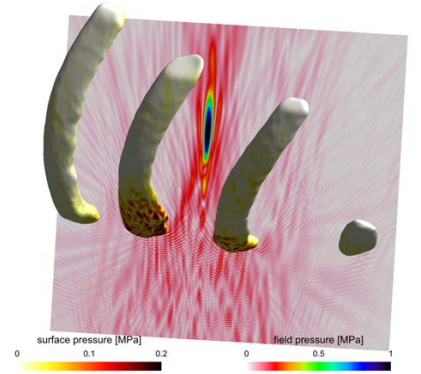


Figure 1: The acoustic pressure at the surface of and exterior to a human rib cage model.

only feasible when acceleration algorithms are being used. Here, parallelisation, preconditioning and compression are combined to achieve efficient numerical simulations. Current research consists of computational experiments at objects of larger scales and the design of fast BEM techniques that employ a tighter connection between parallelisation, preconditioning and compression.

References

- [1] W. Śmigaj, T. Betcke, S. Arridge, J. Phillips, M. Schweiger, “Solving Boundary Integral Problems with BEM++,” *ACM TOMS* **41** (2016) pp. 6:1–6:40.
- [2] E. van ’t Wout, P. Gélat, T. Betcke, and S. Arridge, “A fast boundary element method for the scattering analysis of high-intensity focused ultrasound,” *JASA* **138** (2015), pp. 2726–2737.
- [3] T. Betcke, E. van ’t Wout, and P. Gélat, “Computationally Efficient Boundary Element Methods for High-Frequency Helmholtz Problems in Unbounded Domains,” chapter to appear in *Modern solvers for Helmholtz problems*, Geosystems Mathematics, Springer, 2017.

Minimum-Uncertainty Squeezed States for the Simple Harmonic Oscillator

José M. Vega Guzmán^{1,*}

¹Department of Mathematics, Lamar University, Beaumont, TX-USA

*Email: jose.vegaguzman@lamar.edu

Abstract

We elaborate on a class of solutions to the time-dependent Schrödinger equation for the simple harmonic oscillator in one dimension. They are derived by the action of the corresponding maximal kinematical invariance group on the standard ground state solution. We show that the product of the variances attains the required minimum value only at the instances that one variance is a minimum and the other is a maximum, when the squeezing of one of the variances occurs. The generalized coherent states are explicitly constructed and their Wigner function is studied. The overlap coefficients between the squeezed, or generalized harmonic, and the Fock states are explicitly evaluated in terms of hypergeometric functions and the corresponding photon statistics are discussed. Some applications to quantum optics, cavity quantum electrodynamics and superfocusing in channelling scattering are mentioned. Explicit solutions of the Heisenberg equations for radiation field operators with squeezing are found.

Keywords: harmonic oscillator, squeezing, quantum optics

1 Introduction

From the very beginning, nonclassical states of the linear Planck oscillator, in particular the coherent and squeezed states, have been a subject of considerable interest in quantum physics [1]. They occur naturally on an atomic scale and, possibly, can be observed among the vibrational modes of crystals and molecules. A single mono-chromatic mode of light also represents a harmonic oscillator system for which nonclassical states can be generated very efficiently by using the interaction of laser light with nonlinear optical media. Generation of squeezed light with a single atom has been experimentally demonstrated. On a macroscopic scale, the squeezed states are utilized for the detection of gravitational waves below the so-called vacuum noise level and without violation of the uncertainty relation. The past decades' progress

in the generation of pure quantum states of motion of trapped particles provides not only a clear illustration of basic principles of quantum mechanics, but it also manifests the ultimate control of particle motion. These states are of interest from the standpoint of quantum measurement concepts and facilitate other applications including quantum computation

It is well known that the harmonic quantum states can be analyzed through the dynamics of a single, two-level atom which radiatively couples to the single-mode radiation field in the Jaynes-Cummings(-Paul) model extensively studied in the cavity QED. Creation and detection of thermal, Fock, coherent and squeezed states of motion of a single ion confined in an rf Paul trap where the state of atomic motion had been observed through the evolution of the atom's internal levels (e.g., collapse and revival) under the influence of a Jaynes-Cummings interaction realized with the application of external (classical) fields [8, 9]. The distribution over the Fock states is deduced from an analysis of Rabi oscillations. Moreover, Fock, coherent and squeezed states of motion of harmonically bound cold cesium atoms were experimentally observed in a 1D optical lattice. This method gives a direct access to the momentum distribution.

Experimental recognitions of the nonclassical harmonic states of motion have been achieved through the reconstruction of the Wigner function in optical quantum state tomography, from a Fourier analysis of Rabi oscillations of a trapped atom, and/or by a direct observation of the square of the modulus of the wavefunction for a large sample of cold cesium atoms in a 1D optical lattice [6, 8]. Our theoretical consideration complements all of these advanced experimental techniques by identifying the state quantum numbers from first principles. This approach may provide a guidance for engineering more advanced nonclassical states.

2 Aims

The aim of this work is to show how to construct the minimum-uncertainty squeezed states for quantum harmonic oscillators, which are important in the above applications, in the most simple closed form. Our approach reveals the quantum integrals of motion of the squeezed states in terms of solution of a certain *Ermakov-type* system [1–3]. As a result, the probability amplitudes of these nonclassical states of motion are explicitly evaluated in terms of hypergeometric functions. Their experimental observations in cavity QED and quantum optics are briefly reviewed. Moreover, the radiation field operators of squeezed photons, which can be created from the QED vacuum, are introduced by second quantization with the aid of hidden symmetry of the harmonic oscillator problem [5, 7] in the Heisenberg picture.

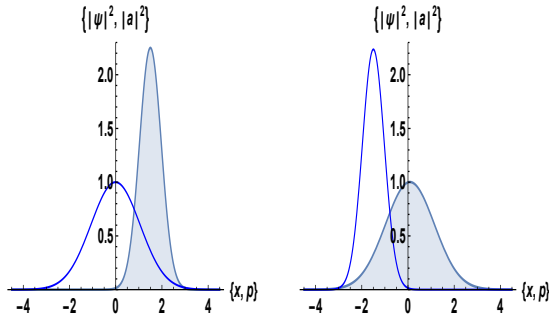


Figure 1: Snapshot of the oscillating electron density of the dynamic harmonic state of (1).

3 Methods

First, the minimum-uncertainty squeezed states for the time-dependent linear harmonic oscillator

$$2i\psi_t + \psi_{xx} - x^2\psi = 0 \quad (1)$$

in coordinate representation, with the help of transformation

$$\psi = \sqrt{\frac{\beta(t)}{\sqrt{\pi}}} e^{i[\alpha(t)x^2 + \delta(t)x + \kappa(t) + \gamma(t)]} e^{-(\beta(t)x + \kappa)^2/2} \quad (2)$$

is discussed. Then, the generalized coherent, or TCS states are constructed. The Wigner and Moyal functions of the squeezed states are evaluated directly from the corresponding wavefunctions and their classical time evolution is verified with the help of *Mathematica*. The

eigenfunction expansions of the squeezed (or generalized harmonic) states in terms of the standard Fock ones are derived.

References

- [1] S.I. Kryuchkov, S.K. Suslov and J.M. Vega Guzmán, The minimum-uncertainty squeezed states for atoms and photons in a cavity. *Journal of Physics B: Atomic, Molecular and Optical Physics* **46** (2013), pp. 104007.
- [2] R. Lopez, S.K. Suslov and J.M. Vega Guzmán, On a hidden symmetry of quantum harmonic oscillators. *Journal of Difference Equations and Applications* **19** (2013), pp. 543–554.
- [3] R. Lopez, S.K. Suslov and J.M. Vega Guzmán, Reconstructing the Schrödinger Group. *Physica Scripta* **87** (2013), pp. 038112.
- [4] M.E. Marhic, Oscillating Hermite–Gaussian wave functions of the harmonic oscillator. *Lettore Al Nuovo Cimento* **22** (1978), pp. 376–378.
- [5] E. Suazo, S.K. Suslov and J.M. Vega Guzmán, The Riccati equation and a diffusion-type equation. *New York Journal of Mathematics* **17a** (2011), pp. 225–344.
- [6] V.V. Dodonov, I.A. Malkin and V.I. Man’ko, Integrals of motion, green functions, and coherent states of dynamical systems. *International Journal of Theoretical Physics* **14** (1975), pp. 37–54.
- [7] U. Niederer, The maximal kinematical invariance group of the harmonic oscillator. *Helvetica Physica Acta* **46** (1973), pp. 191–200.
- [8] A.I. Lvovsky and J. Mlynek, Quantum-optical catalysis: generating nonclassical states of light beams of linear optics. *Physics Review Letters* **88** (2002), pp. 250401.
- [9] D.F. Walls and G.J. Milburn *Quantum Optics*, 2nd edition, Berlin, Springer, 2008.

Criteria for opening band gaps in periodic media

Robert Lipton¹, Robert Viator Jr.^{2,*}

¹Department of Mathematics, Louisiana State University, Baton Rouge, United States

²Institute for Mathematics and its Applications, University of Minnesota, Minneapolis, United States

*Email: rviator@umn.edu

Abstract

We identify explicit conditions on geometry and material contrast for creating band gaps in acoustic and 2-d photonic crystals. The approach here makes use of the electro-static and quasi-periodic source free resonances of the crystal, which deliver a representation for solution operators associated with propagation of waves inside the periodic high contrast medium. This, together with the Dirichlet spectrum and an auxiliary spectrum associated with the inclusions, delivers conditions for opening band gaps at finite contrast for a given inclusion geometry.

Keywords: band gaps, PDE, photonics, spectral theory

1 Introduction

We identify new explicit conditions on geometry and material contrast for creating band gaps in certain periodic media. We consider waves in a periodic medium in \mathbb{R}^d , $d = 2, 3$ composed of two materials. One material is in the form of disjoint inclusions, while the other acts as a “host” for the inclusions. The inclusions are surrounded by the host and do not touch the boundary of the period cell. The union of the inclusions D_1, \dots, D_n inside each period is denoted by D . The crystal occupies all of \mathbb{R}^d and has fundamental period cell $Y = (0, 1]^d$.

The material coefficient is $a(x) = k(1 - \chi_\Omega(x)) + \chi_\Omega(x)$, where $\chi_\Omega(x)$ is the indicator on the inclusions $\Omega = \cup_{m \in \mathbb{Z}^d} (D + m)$. Wave propagation in the crystal at frequency ω is described by

$$-\nabla \cdot (a(x)\nabla u(x)) = \omega^2 u(x), \quad x \in \mathbb{R}^d \quad (1)$$

The self-adjoint operator $L_k = -\nabla \cdot a(x)\nabla$ is defined by the quadratic form in $L^2(\mathbb{R}^d)$

$$\int_{\mathbb{R}^d} a(x)|\nabla u(x)|^2 dx \quad (2)$$

whose domain is the Sobolev Space $W^{1,2}(\mathbb{R}^d)$. Equation 1 describes both waves in acoustic crystals as well as (transverse) waves in 2-d photonic

crystals. For acoustic crystals, the coefficient $(a(x))^{-1} = \rho(x)$ describes the medium's mass density, while for photonic crystals, $(a(x))^{-1} = \epsilon(x)$ describes the dielectric coefficient of a non-magnetic isotropic medium.

By Floquet Theory ([2]), the spectrum of the operator L_k has the band structure

$$\sigma(L_k) = \cup_{j \in \mathbb{N}} S_j \quad (3)$$

where S_j are the spectral bands associated with Bloch waves propagating inside the crystal. The Bloch waves $h(x)$ satisfy equation 1 with the quasi-periodicity condition

$$h(x + p) = h(x)e^{i\alpha \cdot p}, \quad x \in \mathbb{R}^d, \quad p \in \mathbb{Z}^d \quad (4)$$

where the wave vector α lies in the first Brillouin zone $Y^* = (-\pi, \pi]^d$ and ω^2 is an associated Bloch eigenvalue $\lambda_j(\alpha, k)$ for $j \in \mathbb{N}$. The spectral bands S_j can then be described by

$$S_j = [\min_{\alpha \in Y^*} \lambda_j(k, \alpha), \max_{\alpha \in Y^*} \lambda_j(k, \alpha)]. \quad (5)$$

A band gap is an interval (ω_-, ω_+) such that

$$\sigma(L_k) \cap (\omega_-^2, \omega_+^2) = \emptyset \quad (6)$$

2 Analyticity of Bloch Eigenvalues in k

The main result relies on a representation of solution operators for the form

$$B_k[u, v] = \int_Y a(x)\nabla u(x) \cdot \nabla \overline{v(x)} dx \quad (7)$$

This form is defined on the Sobolev space

$$H_\alpha^1(Y) = \{u \in H^1(Y) : u(x)e^{-i\alpha \cdot x} \text{ is } Y\text{-periodic}\} \quad (8)$$

for $\alpha \neq 0$, and $H_\#^1(Y)/\mathbb{C}$ for $\alpha = 0$. In both cases, the inner product is

$$\langle u, v \rangle = \int_Y \nabla u(x) \cdot \nabla \overline{v(x)} dx \quad (9)$$

so that the operator T_k^α can be defined

$$\langle T_k^\alpha u, v \rangle = B_k[u, v] \quad (10)$$

This operator has a spectral representation in terms of the eigenvalues $\{\mu_i\}_{i \in \mathbb{N}}$ of the Neumann-Poincaré operator

$$K_D^\alpha \rho(x) = \text{p.v.} \int_{\partial D} \frac{\partial G^\alpha(x, y)}{\partial n(y)} \rho(y) d\sigma(y), \quad x \in \partial D. \quad (11)$$

where $G^\alpha(x, y)$ is the (quasi)-periodic Green's function for the Laplacian on Y .

This representation is used to show that, for fixed α , the Bloch eigenvalues $\lambda_j(\alpha, k)$ are analytic in a neighborhood of $k = \infty$ by following [1]. When the ∂D is smooth enough, and when D belongs to the class of “buffered geometries”, i.e. geometries for which there is a minimum distance t between each inclusion (and from the inclusions to the cell wall), there is an α -independent lower bound $\mu^* > -\frac{1}{2}$ on $\sigma(K_D^\alpha)$. For these geometries and each $j \in \mathbb{N}$, one obtains a radius of convergence $r_j^*(\alpha)$ such that, for $|k^{-1}| < r_j^*(\alpha)$, the power series in k^{-1} for $\lambda_j(\alpha, k)$ converges uniformly (see [4]).

3 Main Result: Band Gaps for Finite Contrast

We now state the main theorem. We consider only the class of “buffered” inclusions with $C^{1,\gamma}$ boundary for $\gamma > 0$.

Let $\sigma(-\Delta_D)$ denote the Dirichlet spectrum of the Laplacian on D , and let $\{\delta_j^*\}_{j \in \mathbb{N}} \subset \sigma(-\Delta_D)$ denote the eigenvalues with nonzero mean eigenfunctions. Set $\{\delta'_j\}_{j \in \mathbb{N}} = \sigma(-\Delta_D) \setminus \{\delta_j^*\}_{j \in \mathbb{N}}$. Let

$$S(\nu) = \nu \sum_{j \in \mathbb{N}} \frac{a_j^2}{\nu - (\delta_j^*)^2} - 1, \quad (12)$$

where a_j is the mean of the eigenfunction of δ_j^* , and let $\{\nu_j\}_{j \in \mathbb{N}}$ be the roots of 12. Finally, set

$$\sigma_N = \{\delta'_j\}_{j \in \mathbb{N}} \cup \{\nu_j\}_{j \in \mathbb{N}} \quad (13)$$

No longer distinguishing between the components of σ_N , we write $\sigma_N = \{\nu_j\}_{j \in \mathbb{N}}$. Combining the analyticity of the Bloch eigenvalues and an interlacing theorem relating $\sigma(-\Delta_D)$ and σ_N ([3], Prop. 3.4), we obtain the main result, which establishes the existence of band gaps in $\sigma(L_k)$ for finite contrast ratio k :

Theorem 1 *Opening a band gap*

Consider any “buffered” crystal geometry such that the inclusions D have $C^{1,\gamma}$ boundary with

$\gamma > 0$. Suppose $\delta_j^* \in \sigma(-\Delta_D)$ is simple, so that $\delta_j^* < \nu_{j+1}$. Set

$$d_j = \frac{1}{2} \text{dist} \left(\{\nu_{j+1}^{-1}\}, \sigma_N \setminus \{\nu_{j+1}^{-1}\} \right)$$

where σ_N is given by equation (13), and

$$\bar{r}_j = \frac{\pi^2 d_j (1/2 + \mu^*)}{1 + \pi^2 d_j (1/2 - \mu^*)}. \quad (14)$$

Then one has the band gap

$$\sigma(L_k) \cap \left(\delta_j^*, \nu_{j+1} \left(1 - \frac{\nu_{j+1} d_j}{k \bar{r}_j - 1} \right) \right) = \emptyset \quad (15)$$

if

$$k > \bar{k}_j = \bar{r}_j^{-1} \left(1 + \frac{d_j \nu_{j+1}}{1 - \frac{\delta_j^*}{\nu_{j+1}}} \right). \quad (16)$$

The proof for this theorem can be found in [5]. Equation 15 shows the existence of band gaps for the medium, as well as estimates on the gaps' size and location, so long as the contrast k exceeds the threshold \bar{k}_j in equation 16. 14 and 16 show explicitly the dependence of \bar{k}_j on the spectral parameters μ^* , $\sigma(-\Delta_D)$, and σ_N , all given by the inclusion geometry. This theorem provides mathematically sound guidance for prescribing material parameters to open band gaps in acoustic and photonic crystals, and could be used to engineer band gap structures in a wide variety of frequency ranges.

References

- [1] T. Kato, *Perturbation Theory for Linear Operators*, Springer, Berline Heidelberg, Germany, 1995.
- [2] P. Kuchment, *Floquet Theory for Partial Differential Equations*, Birkhauser Verlag, Basel, 1993.
- [3] R. Hempel and K. Lienau, Spectral properties of periodic media in the large coupling limit, *Communications in Partial Differential Equations* **25** (2000), pp. 1445-1470.
- [4] R. Lipton and R. Viator Jr., Bloch waves in crystals and periodic high contrast media, *ESAIM M2AN* Accepted June 16, 2016. doi:10.1051/m2an/2016046
- [5] R. Lipton and R. Viator Jr., Creating band gaps in periodic media, *arXiv:1607.02365* 2016.

Detecting Low-Frequency Gravitational Waves with Pulsar Timing Arrays

Sarah J. Vigeland^{1,*}, The NANOGrav Collaboration

¹Department of Physics, University of Wisconsin–Milwaukee, Milwaukee, Wisconsin, USA

*Email: vigeland@uwm.edu

Abstract

Efforts are currently underway to detect gravitational waves with $f \sim 10^{-7} - 10^{-9}$ Hz using pulsar timing arrays by collaborations around the world, and detection is expected within the next few years. One such group is the North American Nanohertz Observatory for Gravitational Waves (NANOGrav). I will discuss how pulsar timing arrays are used to detect gravitational waves and what sources we expect to find in the low-frequency regime, with an emphasis on supermassive black hole binaries.

Keywords: astrophysics, cosmology, black holes, gravitational waves, pulsars

1 Introduction

General relativity predicts orbiting black holes produce gravitational waves (GWs), as was confirmed by the LIGO detection in 2015 [1]. Supermassive black hole binaries (SMBHBs), which form in galaxy mergers, produce GWs with $f \sim 10^{-7} - 10^{-9}$ Hz. These can be detected through long-term timing observations of millisecond pulsars (MSPs) in pulsar timing arrays (PTAs).

2 Pulsar Timing

MSPs are rapidly spinning ($P \sim 1 - 10$ ms) neutron stars whose radio emission is observed as a series of periodic pulses. Pulsar timing involves fitting the observed pulse times of arrival (TOAs) to complex models that account for the pulsar's spin evolution and the pulse propagation from the pulsar to Earth [2]. The differences between the observed and predicted TOAs are called the residuals.

Low-frequency GWs induce changes in the residuals which can be detected by timing pulsars over many years [3, 4]. Since this effect is correlated between different pulsars, analyzing the residuals from an array of pulsars allows the effect of GWs to be separated from other systematic effects [5, 6]. PTAs have been formed by the Parkes Pulsar Timing Array (PPTA) [7], the European Pulsar Timing Array (EPTA) [8], and the North American Nanohertz Observa-

tory for Gravitational Waves (NANOGrav) [9], and these groups also share data and collaborate as part of the International Pulsar Timing Array (IPTA) [10]. Currently, more than ten years of timing observations have been made.

3 Stochastic Background Detection

SMBHBs form a GW stochastic background that can be detected by PTAs. Assuming circular binaries that evolve solely due to GW emission, the GW strain is [11]

$$h_c(f) = A_{\text{gw}} \left(\frac{f}{f_{1\text{yr}}} \right)^\alpha, \quad (1)$$

where $f_{1\text{yr}} \equiv (1 \text{ yr})^{-1}$, A_{gw} is the dimensionless GW amplitude at $f = f_{1\text{yr}}$, and $\alpha = -2/3$. A_{gw} depends on the black hole mass distribution, the co-evolution of galaxies and black holes, and the galaxy merger rate [12–16]. In addition, gas and stars around SMBHBs may accelerate the orbital decay, changing the frequency-dependence of $h_c(f)$ [13, 17]. The current limits from PTAs are already being used to constrain astrophysical models (see Fig. 1) [11]. Based on current PTA sensitivities and source modeling, a detection is expected soon.

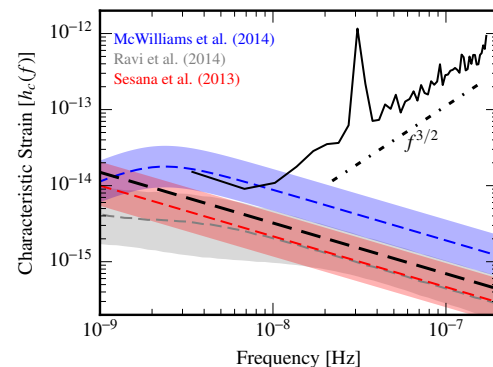


Figure 1: Limit on the GW stochastic background from the NANOGrav 9-yr data release [11]. Predictions from theoretical models [12–14] are shown for comparison.

4 Continuous Wave Detection

GWs from individual SMBHBs are also detectable for nearby massive sources. The GW strain from a circular SMBHB with black hole masses M_1 and M_2 is given by [18]

$$h(f) = \sqrt{\frac{32}{5}} \frac{\mathcal{M}^{5/3}}{D_L} (\pi f)^{2/3}, \quad (2)$$

where $\mathcal{M} \equiv (M_1 M_2)^{3/5}/(M_1 + M_2)^{1/5}$ is called the “chirp mass,” and D_L is the luminosity distance. While no detection has been made yet, pulsar timing has been used to put constraints on the black hole masses of the nearby galaxy 3C 66B [19].

References

- [1] Abbott, B. *et al.*, Observation of Gravitational Waves from a Binary Black Hole Merger, *Phys. Rev. Lett.* **6** (2016), p. 061102.
- [2] R. T. Edwards, G. B. Hobbs, and R. N. Manchester, TEMPO2, a new pulsar timing package - II. The timing model and precision estimates, *MNRAS* **372** (2006), pp. 1549–1574.
- [3] M. V. Sazhin, Opportunities for detecting ultralong gravitational waves, *Soviet Astronomy* **22** (1978), pp. 36–38.
- [4] S. Detweiler, Pulsar timing measurements and the search for gravitational waves, *ApJ* **234** (1979), pp. 1100–1104.
- [5] R. W. Hellings and G. S. Downs, Upper limits on the isotropic gravitational radiation background from pulsar timing analysis, *ApJ* **265** (1983), pp. L39–L42.
- [6] R. S. Foster and D. C. Backer, Constructing a pulsar timing array, *ApJ* **361** (1990), pp. 300–308.
- [7] G. Hobbs, The Parkes Pulsar Timing Array, *Classical and Quantum Gravity* **30** (2013), p. 224007.
- [8] M. Kramer and D. J. Champion, The European Pulsar Timing Array and the Large European Array for Pulsars, *Classical and Quantum Gravity* **30** (2013), p. 224009.
- [9] M. A. McLaughlin, The North American Nanohertz Observatory for Gravitational Waves, *Classical and Quantum Gravity* **30** (2013), p. 224008.
- [10] G. Hobbs *et al.*, The International Pulsar Timing Array project: using pulsars as a gravitational wave detector, *Classical and Quantum Gravity* **27** (2010), p. 084013.
- [11] Z. Arzoumanian *et al.*, The NANOGrav Nine-year Data Set: Limits on the Isotropic Stochastic Gravitational Wave Background, *ApJ* **821** (2016), p. 13.
- [12] A. Sesana, Systematic investigation of the expected gravitational wave signal from supermassive black hole binaries in the pulsar timing band, *MNRAS* **433** (2013), L1–L5.
- [13] S. T. McWilliams, J. P. Ostriker, and F. Pretorius, Gravitational Waves and Stalled Satellites from Massive Galaxy Mergers at $z <= 1$, *ApJ* **789** (2014), p. 156.
- [14] V. Ravi *et al.*, Prospects for gravitational-wave detection and supermassive black hole astrophysics with pulsar timing arrays, *MNRAS* **447** (2015), pp. 2772–2783.
- [15] A. Sesana *et al.*, Selection bias in dynamically measured supermassive black hole samples: consequences for pulsar timing arrays, *MNRAS* **463** (2016), L6–L11.
- [16] L. Z. Kelley, L. Blecha, L. Hernquist, Massive black hole binary mergers in dynamical galactic environments, *MNRAS* **464** (2017), pp. 3131–3157.
- [17] V. Ravi *et al.*, Binary supermassive black hole environments diminish the gravitational wave signal in the pulsar timing band, *MNRAS* **442** (2014), pp. 56–68.
- [18] P. C. Peters and J. Mathews, Gravitational Radiation from Point Masses in a Keplerian Orbit, *Physical Review* **131** (1963), pp. 435–440.
- [19] Jenet, F. A. *et al.*, Constraining the Properties of Supermassive Black Hole Systems Using Pulsar Timing: Application to 3C 66B, *ApJ* **606** (2004), pp. 799–803.

High Order Farfield Expansions Absorbing Boundary Condition Coupled with High Order Finite Difference Methods

Vianey Villamizar^{1,*}, Otilio Rojas², Sebastian Acosta³

¹Department of Mathematics, Brigham Young University, Provo, Utah, USA

²CASE Department, Barcelona Supercomputing Center, Barcelona, Spain

³Department of Pediatrics-Cardiology, Baylor College of Medicine, Houston, TX, USA

*Email: vianey@mathematics.byu.edu

Abstract

Time-harmonic acoustic scattering problems originally defined on unbounded regions are numerically solved. This is done by coupling the authors' recently developed high order local absorbing boundary condition (ABC) with high order finite difference methods. As a result, high order numerical methods with an overall order of convergence equal to the methods employed in the interior of the computational domain are obtained. These methods are compared in terms of their implementation, complexity, computational cost, and their convergence on several numerical experiments.

Keywords: Acoustic scattering, High order local absorbing boundary condition, High order methods, Helmholtz equation

1 Introduction

In a recent work [1], we developed a new high order local ABC based on exact series representation of the outgoing waves in the exterior region to a circle in two-dimensions (2D) or a sphere in three dimensions (3D) of radius R enclosing a scattering or radiating region. We used the acronym FFE-ABCs to refer to them. Our construction of the FFE-ABCs proceeded in the opposite direction of many previously defined ABCs. Instead of defining local differential operators which progressively annihilate the first terms of a series representation of the solution in the exterior of the artificial boundary, we used a truncated version of an exact series representation of the solution in the exterior, directly. As a result, we were able to construct the ABC without defining special differential operators at the boundary. This derivation of the absorbing condition is extremely simple. Moreover, the order of the error at the artificial boundary induced by this novel ABC can be easily reduced to reach any accuracy within the limits of the computational resources. This is accomplished

by simply adding as many terms as needed to the truncated series without moving the artificial boundary farther out.

We showed in [1] that the error introduced by using the FFE-ABC at the artificial boundary can be made negligible in comparison with the error made using the second order finite difference method in the computational domain. As a consequence, a second order convergent method was obtained on the whole domain. This was achieved with relatively few terms in the expansions (5 terms in 2D and 8 terms in 3D). This is a good performance. However, the full potential of the FFE-ABCs can be achieved by combining them with higher order methods of discretization for the computational domain to produce overall high order methods. In this work, we consider high order finite difference methods, such as those described in the next sections, for the discretization of the computational domains. Then, we show that we can easily maintain, over the whole domain, the magnitude of the error made by an appropriate high order method used in the interior, employing the truncated FFE-ABC with enough terms at the boundary. As a result, a method with an overall order of convergence equal to the method employed in the interior of the computational domain is obtained.

2 High order finite difference methods

We consider the scattering of a time-harmonic plane wave from a circular obstacle in an unbounded two-dimensional region. Therefore, the equation to be discretized is the Helmholtz equation in polar coordinates:

$$\Delta u + k^2 u = \frac{1}{r} \partial_r u + \frac{1}{r^2} \partial_\theta^2 u + k^2 u = 0. \quad (1)$$

We choose as an artificial boundary a circle of radius R at which the following Karp FFE-ABC

is imposed:

$$\begin{aligned} u(R, \theta) &= H_0(kR) \sum_{l=0}^{L-1} \frac{F_l(\theta)}{(kR)^l} + H_1(kR) \sum_{l=0}^{L-1} \frac{G_l(\theta)}{(kR)^l}, \\ \partial_r u(R, \theta) &= \partial_r \left. H_0(kr) \sum_{l=0}^{L-1} \frac{F_l(\theta)}{(kr)^l} + H_1(kr) \sum_{l=0}^{L-1} \frac{G_l(\theta)}{(kr)^l} \right|_{r=R}, \\ \partial_r^2 u(R, \theta) &= \partial_r^2 \left. H_0(kr) \sum_{l=0}^{L-1} \frac{F_l(\theta)}{(kr)^l} + H_1(kr) \sum_{l=0}^{L-1} \frac{G_l(\theta)}{(kr)^l} \right|_{r=R}, \\ 2lG_l(\theta) &= (l-1)^2 F_{l-1}(\theta) + d_\theta^2 F_{l-1}(\theta), \\ 2lF_l(\theta) &= -l^2 G_{l-1}(\theta) - d_\theta^2 G_{l-1}(\theta), \quad \text{for } l = 1, \dots, L-1. \end{aligned}$$

Our computational domain is the circular annular domain $r_0 \leq r \leq R$. The number of grid points in the radial direction is N and in the angular direction is $m+1$. Therefore, the step sizes in the radial and angular directions are $\Delta r = (R - r_0)/(N - 1)$ and $\Delta\theta = 2\pi/m$, respectively. Also, $r_i = (i-1)\Delta r$, $\theta_j = (j-1)\Delta\theta$ and $u_{i,j}$ is the approximation to $u(r_i, \theta_j)$, where $i = 1, \dots, N$ and $j = 1, \dots, m+1$.

We employ various high order finite difference methods to discretize the Helmholtz equation (1) in polar coordinates and modify them, nearby and at the artificial boundary points, to incorporate the above FFE-ABC.

The first method is the standard fourth order centered finite difference method in polar coordinates. After substitution of the discretized first and second order derivatives into (1), we arrive to the discrete equation

$$\begin{aligned} \alpha_i^{++} u_{i+2,j} + \alpha_i^+ u_{i+1,j} + \alpha_i^- u_{i,j} + \alpha_i^- u_{i-1,j} \\ + \alpha_i^{--} u_{i-2,j} + \beta_i u_{i,j+1} + \beta_i u_{i,j-1} \\ + \gamma_i u_{i,j+2} + \gamma_i u_{i,j-2} = 0, \end{aligned} \quad (2)$$

where

$$\begin{aligned} \alpha_i^{++} &= -\frac{1}{12} \left(\frac{1}{\Delta r^2} + \frac{1}{\Delta r} \right), \quad \alpha_i^+ = \frac{1}{3} \left(\frac{4}{\Delta r^2} + \frac{2}{r_i \Delta r} \right), \\ \alpha_i &= \frac{-30}{12 \Delta r^2} - \frac{30}{12 \Delta \theta^2 r_i^2} + k^2, \quad \alpha_i^- = \frac{1}{3} \left(\frac{4}{\Delta r^2} - \frac{2}{r_i \Delta r} \right), \\ \alpha_i^{--} &= -\frac{1}{12} \left(\frac{1}{\Delta r^2} - \frac{1}{r_i \Delta r} \right), \quad \beta_i = \frac{4}{3 \Delta \theta^2 r_i^2}, \\ \gamma_i &= \frac{1}{12 \Delta \theta^2 r_i^2}. \end{aligned}$$

This is a classical fourth order 9-point scheme for the Helmholtz equation in polar coordinates. It requires special treatment at several nodes near the boundaries where the FFE-ABC must be included. We applied it to the scattering of a plane wave of frequency $k = 2\pi$ from a soft circular obstacle of radius $r_0 = 1$. An order of convergence fourth for the farfield pattern approximation was obtained with $L=8$ terms in Karp's expansion. Also, the L^2 -norm relative error made with only 12 points per wavelength

(ppw) was 2.09×10^{-3} while the error made using a second order centered scheme with 24 ppw was 2.59×10^{-3} . Thus, the extra computations made using the fourth order method compared with the second order one were negligible considering the greater accuracy achieved on a coarser grid.

A drawback of this 4th order method is the modifications needed at several points close to the boundary and the complex discrete formulas that result. In an attempt to remedy this, we also explored the application of a fourth order *deferred corrections* method. It consists of a standard centered second order method with a 5-points stencil which includes the truncation error given by

$$\begin{aligned} \tilde{\nabla}_5^2 u_{i,j} + k^2 u_{i,j} - \tau_{i,j} &= 0, \quad \text{where} \\ \tau_{i,j} &= \left[\frac{\Delta r^2}{12} \left(\partial_r^4 u + \frac{2}{r} \partial_r^3 u \right) + \frac{\Delta \theta^2}{12 r^2} \partial_\theta^4 u \right] (r_i, \theta_j) \end{aligned}$$

This computation proceeds in two steps. First, a second order approximation is obtained from the application of a second order difference scheme for the Helmholtz equation and the FFE-ABC. Secondly, the derivatives in $\tau_{i,j}$ are calculated using the approximations $u_{i,j}$ obtained in step 1 and employing second order difference. Then, the second order centered scheme is applied again with the approximated $\tau_{i,j}$ as forcing term. This implementation is based on a smaller stencil than the standard fourth order technique and produce similar results. We also considered compact finite difference schemes with 9-point stencils for fourth and sixth order techniques called *equation based* schemes which are described in [2] and other papers cited there. Results and comparison of the various methods will be discussed in the presentation.

References

- [1] V. Villamizar, S. Acosta and B. Dasttrup, High order local absorbing boundary conditions for acoustic waves in terms of farfield expansions, *J. Comput. Phys.* **333** (2017) 331-351.
- [2] S. Britt, S. Tsynkov and E. Turkel, A Compact Fourth Order Scheme for the Helmholtz equation polar coordinates, in *J. Sci. Comput.*, **45** (2010) pp. 26–47.

Approximate models for transmission problems between homogeneous and homogenized half-planes

Xavier Claeys¹, Sonia Fliss², Valentin Vinoles^{3,*}

¹Laboratoire Jacques-Louis Lions, Université Pierre and Marie Curie, Paris, France

²POEMS (CNRS–ENSTA Paristech–Inria), Palaiseau, France

³SB MATHAA CAMA, École Polytechnique Fédérale de Lausanne, Lausanne, Switzerland

*Email: valentin.vinoles@epfl.ch

Abstract

We study approximate models for transmissions problem between homogeneous and periodic half-planes when the period is small regarding to the wavelength. In a previous work, using matched asymptotic expansions techniques, we derived high order transmission conditions. Here, we study an approximate model associated to these high order transmission conditions which consists in replacing the periodic media by an effective one but the transmission conditions are not classical. We establish well-posedness for the approximate problem and error estimates and show some numerical results.

Keywords: homogenization, periodic media, high order transmission conditions

A transmission problem between an homogeneous and a periodic half-plane. We look for $(\mathbf{x} = (x_1, x_2) \in \mathbb{R}^2)$:

$$\nabla \cdot \left[a \left(\frac{\mathbf{x}}{\varepsilon} \right) \nabla u_\varepsilon(\mathbf{x}) \right] + \omega^2 u_\varepsilon(\mathbf{x}) = f(\mathbf{x}) \quad (1)$$

where $\varepsilon > 0$ is a small parameter, $\operatorname{Im} \omega^2 > 0$, $f \in L^2(\mathbb{R}^2)$ such that $\operatorname{supp} f \subseteq \Omega^- := \{x_1 < 0\}$, and a is an uniformly bounded and coercive function such that, in Ω^- , a is a constant $a_0 > 0$, and in $\Omega^+ := \{x_1 > 0\}$, a is 1-periodic in the two directions.

Matched asymptotic expansions and high order transmission conditions. In [1,2], we used different asymptotic expansions far from the interface and near the interface. By matching these expansions, we can derive a problem at order 0 ($\Gamma := \partial\Omega^\pm$):

$$\begin{cases} \nabla \cdot (A_0^* \nabla u_0) + \omega^2 u_0 = f & \text{on } \mathbb{R}^2 \setminus \Gamma \\ [u_0]_\Gamma = 0, [A_0^* \nabla u_0 \cdot \mathbf{e}_1]_\Gamma = 0 \end{cases} \quad (2)$$

where $A_0^* = a_0$ on Ω^- and $A_0^* = A^*$ on Ω^+ with $A^* = (a_{ij}^*)$ the homogenized tensor [3].

At the next order, we obtain

$$\begin{cases} \nabla \cdot (A_0^* \nabla u_1) + \omega^2 u_1 = 0 & \text{on } \mathbb{R}^2 \setminus \Gamma \\ [u_1]_\Gamma = \mathcal{P}(u_0) \\ [A^* \nabla u_1 \cdot \mathbf{e}_1]_\Gamma = \mathcal{Q}(u_0) \end{cases} \quad (3)$$

where \mathcal{P} and \mathcal{Q} are defined by

$$\begin{cases} \mathcal{P}(u) := C_1 \partial_{x_1} \langle u \rangle_* + C_2 \partial_{x_2} \langle u \rangle \\ \mathcal{Q}(u) := C_3 \partial_{x_1 x_2}^2 \langle u \rangle_* + C_4 \partial_{x_2 x_2}^2 \langle u \rangle. \end{cases} \quad (4)$$

with $\langle \cdot \rangle$ the average over Γ and $\langle \cdot \rangle_*$ the weighted average $\langle u \rangle_* := (a_0 u|_{\Gamma^-} + a_{11}^* u|_{\Gamma^+})/2$.

The constants C_j are defined from *profile functions*, which are solution of problems posed in the infinite strip $\mathcal{B} := \mathbb{R} \times (0, 1)$:

$$\nabla \cdot [a(\mathbf{y}) \nabla U] = g \quad \text{on } \mathcal{B} \quad (5)$$

Due to the matching conditions, the functional framework for (5) is non-standard because U must be allowed to grow polynomially when $y_1 \rightarrow \pm\infty$ (weighted Sobolev spaces). The constants C_j are defined from the behaviours at $y_1 = \pm\infty$ of the profile functions (see Figure 1).

“Naive” approximate model. In order to construct a approximate model, setting $u_\varepsilon^1 := u_0 + \varepsilon u_1$ and neglecting the $\mathcal{O}(\varepsilon^2)$ terms, we get a first approximate model:

$$\begin{cases} \nabla \cdot (A_0^* \nabla u_\varepsilon^1) + \omega^2 u_\varepsilon^1 = f & \text{on } \mathbb{R}^2 \setminus \Gamma \\ [u_\varepsilon^1]_\Gamma = \varepsilon \mathcal{P}(u_\varepsilon^1) \\ [A_0^* \nabla u_\varepsilon^1 \cdot \mathbf{e}_1]_\Gamma = \varepsilon \mathcal{Q}(u_\varepsilon^1) \end{cases} \quad (6)$$

But this is not possible to show that this problem is well-posed (or even Fredholm) because the constants C_j can have the wrong sign.

Geometric shift. The idea is to “open” the interface Γ into a small strip of order ε so that the jumps and means over Γ are now taken over the two boundaries $\Gamma_\varepsilon^\pm := \{\pm\alpha^\pm\varepsilon\} \times \mathbb{R}$ where

$\alpha^\pm > 0$ are two constants chosen carefully. We also define $\Omega_{\alpha\varepsilon}^\pm := \{x_1 \gtrless \pm \alpha^\pm \varepsilon\}$. Denoting $[\cdot]_{\alpha\varepsilon}$ and $\langle \cdot \rangle_{\alpha\varepsilon}$ such jump and mean, we look for the shifted transmission problem

$$\begin{cases} \nabla \cdot (A_0^* \nabla u_{\alpha\varepsilon}^1) + \omega^2 u_{\alpha\varepsilon}^1 = f & \text{on } \Omega_{\alpha\varepsilon}^\pm \\ [u_{\alpha\varepsilon}^1]_{\alpha\varepsilon} = \varepsilon \mathcal{P}_{\alpha\varepsilon}(u_{\alpha\varepsilon}^1) \\ [A_0^* \nabla u_{\alpha\varepsilon}^1 \cdot \mathbf{e}_1]_{\alpha\varepsilon} = \varepsilon \mathcal{Q}_{\alpha\varepsilon}(u_{\alpha\varepsilon}) \end{cases} \quad (7)$$

where $\mathcal{P}_{\alpha\varepsilon}$ and $\mathcal{Q}_{\alpha\varepsilon}$ are defined as in (4) but with $[\cdot]_{\alpha\varepsilon}$ and $\langle \cdot \rangle_{\alpha\varepsilon}$ for the jumps and means instead and with new constants C_j^α instead of the C_j . One can prove that for α^\pm large enough, the constants C_j^α have the correct sign thus we have the following result: it exists $\alpha_0 > 0$ such that (7) is well-posed for all $\alpha^\pm > \alpha_0$.

Error estimates. When adding an oscillating part to the approximate solution $u_{\alpha\varepsilon}^1$ in the homogenized medium (the so-called correctors in homogenization [3]), one can show that if $\alpha^\pm > \alpha_0$ and under regularity assumptions on a , one has

$$\|u_\varepsilon - (u_{\alpha\varepsilon}^1 + \varepsilon \nabla u_{\alpha\varepsilon}^1 \cdot \mathbf{w}(\cdot/\varepsilon) + \varepsilon^2 \nabla \cdot (\Theta(\cdot/\varepsilon) \nabla u_{\alpha\varepsilon}^1)\|_{H^1(\Omega)} = \mathcal{O}(\varepsilon^2)$$

on any open set Ω such that $\overline{\Omega} \cap \Gamma = \emptyset$, where $\mathbf{w} = (w_j)$ and $\Theta = (\theta_{ij})$ are the solutions of the cell problems of first and second order [3] (considered zero for $x_1 < 0$).

Numerical methods. For solving the exact problem (1), we use a Floquet-Bloch transform in the x_2 direction so (1) reduces to a family of problems in $\mathbb{R} \times (0, \varepsilon)$ indexed by $\xi \in (0, 2\pi/\varepsilon)$. For the x_1 direction, we use Dirichlet-to-Neumann (DtN) operators adapted to periodic media [4]. The parameter ξ is discretized using a trapezoidal rule. We use the same treatment for the homogenized problems (2) and (7) (*i.e.* the homogenized medium is considered as a periodic one).

For computing the profile functions solutions of (5), it is possible to use such DtN operators to reduce (5) to a problem on the interface $\{0\} \times (0, 1)$ with a right-hand side that depends on the behaviour at infinity of others profile functions. Moreover these operators can be used to reconstruct such profile functions in the whole strip \mathcal{B} and give use their behaviour at $y_1 = \pm\infty$. Then this is used to compute the C_j^α .

Numerical results. We use $a_0 = 1$, $a(\mathbf{y}) = (2 + \sqrt{2} \sin 2\pi y_1)(4 + \sqrt{2} \sin 2\pi y_2)$, $\omega = 2 + 0.01i$ and f a Gaussian centred at $(-0.2, 0.5)$. The figure 1 confirms the efficiency of our approximate model (7) compared to (2) and shows a profile function.

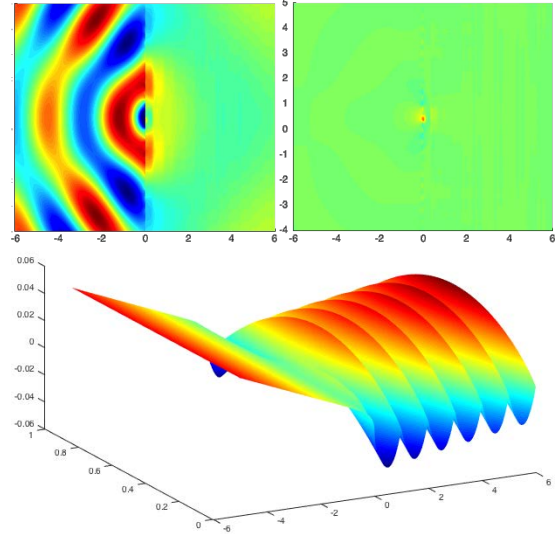


Figure 1: Top: Difference between u_ε and u_0 (left) and between u_ε and $u_{\alpha\varepsilon}^1$ (right), both with correctors of first and second order ($\varepsilon = 0.25$). Bottom: a typical profile function.

References

- [1] V. Vinoles, *Problèmes d'interface en présence de métamatériaux : modélisation, analyse et simulations*, PhD thesis, Université Paris-Saclay, 2016
- [2] X. Claeys, S. Fliss and V. Vinoles, *Homogenization of transmission problems between homogeneous and periodic half-planes. Part 1: asymptotic expansions*, To be submitted.
- [3] G. Papanicolaou, A. Bensoussan and J. L. Lions, *Asymptotic analysis for periodic structures*, Elsevier, 1978.
- [4] P. Joly, J.R. Li and S. Fliss, *Exact boundary conditions for periodic waveguides containing a local perturbation*, Commun. Comput. Phys. 1(6) 945-973, 2006.

An energy based discontinuous Galerkin method for acoustic-elastic waves

Daniel Appelö¹, Siyang Wang^{2,*}

¹Department of Mathematics and Statistics, University of New Mexico, USA

²Department of Information Technology, Uppsala University, Sweden

*Email: siyang.wang@it.uu.se

Abstract

We consider wave propagation in a media with both fluid and solid. In the fluid, the problem is modeled by the acoustic wave equation in terms of a velocity potential. In the solid, the elastic wave equation in displacement form is used. To couple the two regions, suitable physical conditions are imposed on the interface. We are interested in the numerical treatment of those interface conditions. The equations are discretized directly on second-order form by a discontinuous Galerkin method. We derive stable energy-conserving and upwind discretizations. The talk will present numerical experiments illustrating the accuracy and robustness of the proposed method.

Keywords: discontinuous Galerkin, fluid-solid coupling, acoustic wave equation, elastic wave equation.

1 Introduction

Problems with fluid-solid interfaces can be found, in marine seismic or offshore seismic surveying. There pressure waves are mechanically generated from a sound source in the water, and propagate from the water (fluid) to the seafloor (solid). Coupling the fluid and solid region in a stable and accurate manner is crucial for numerical simulations of such wave phenomena.

Discontinuous Galerkin methods have been used to solve acoustic-elastic coupling problems in different forms of the governing equations. In [5], the first-order velocity-strain formulation is used, whereas in [4] the discretization is performed on the first-order velocity-stress form.

In this work, we propose a discontinuous Galerkin method for the governing equations on the second-order form. The same form is used in [3] with a spectral element method.

2 The continuous problem

We consider wave propagations in the fluid Ω^f satisfying the acoustic wave equation in terms

of velocity potential ψ and its time derivative p

$$\frac{\partial \psi}{\partial t} = p, \quad \frac{1}{c^2} \frac{\partial p}{\partial t} = \nabla \cdot \nabla \psi, \quad (1)$$

where c is the wave speed, and p is the pressure scaled by density.

In the solid Ω^s , the problem is modeled by the elastic wave equation governing time evolution of displacement vector $\mathbf{u} = [u_1, u_2]^T$ and velocity vector $\mathbf{v} = [v_1, v_2]^T$

$$\frac{\partial u_i}{\partial t} = v_i, \quad \rho \frac{\partial v_i}{\partial t} = \nabla \cdot \boldsymbol{\sigma}_i, \quad (2)$$

for $i = 1, 2$. Here, ρ is the density, and $\boldsymbol{\sigma} = [\boldsymbol{\sigma}_1, \boldsymbol{\sigma}_2]$ is the stress tensor.

At the interface $\Gamma = \Omega^f \cap \Omega^s$, we first ensure the continuity of the velocity in the normal direction

$$\nabla \psi \cdot \mathbf{n} = \mathbf{v} \cdot \mathbf{n}, \quad (3)$$

where $\mathbf{n} = \mathbf{n}^S = -\mathbf{n}^F$ denotes the outward-pointing normal of the interface for the solid region. Next, we also ensure balance of tractions

$$p\mathbf{n} = \boldsymbol{\sigma} \cdot \mathbf{n}. \quad (4)$$

Therefore, the fluid-solid coupling problem is modeled by equations (1), (2) and interface conditions (3), (4).

3 The discretized problem

We use the discontinuous Galerkin method developed in [1, 2] to discretize the equations in space. Let the finite element mesh

$$\Omega^f = \bigcup_i \Omega_i^f, \quad \Omega^s = \bigcup_j \Omega_j^s,$$

be a discretization of the domain consisting of geometry-conforming and non-overlapping mesh elements with piecewise smooth boundaries. On each element, we require that the unknown

$$\int_{\Omega_j^f} \nabla \phi_\psi \cdot \nabla \left(\frac{\partial \psi^h}{\partial t} - p^h \right) = \int_{\partial \Omega_j^f} (\nabla \phi_\psi \cdot \mathbf{n}^F) (p^* - p^h), \quad \forall \phi_\psi \in (\Pi(q))^2, \quad (5)$$

$$\int_{\Omega_j^f} \frac{1}{c^2} \phi_p \frac{\partial p^h}{\partial t} + \nabla \phi_p \cdot \nabla \psi^h = \int_{\partial \Omega_j^f} \phi_p (\nabla \psi^* \cdot \mathbf{n}^F), \quad \forall \phi_p \in (\Pi(q))^2, \quad (6)$$

$$\int_{\Omega_j^s} \boldsymbol{\sigma}_i^{\phi_{ui}} \cdot \nabla \left(\frac{\partial u_i^h}{\partial t} - v_i^h \right) = \int_{\partial \Omega_j^s} (\boldsymbol{\sigma}_i^{\phi_{ui}} \cdot \mathbf{n}^S) (v_i^* - v_i^h), \quad \forall \phi_{ui} \in (\Pi(q))^2, \quad i = 1, 2, \quad (7)$$

$$\int_{\Omega_j^s} \phi_{vi} \rho \frac{\partial v_i^h}{\partial t} + \nabla \phi_{vi} \cdot \boldsymbol{\sigma}_i^h = \int_{\partial \Omega_j^s} (\boldsymbol{\sigma}_i^* \cdot \mathbf{n}^S) \phi_{vi}, \quad \forall \phi_{vi} \in (\Pi(q))^2, \quad i = 1, 2. \quad (8)$$

variables in (2) are approximated by piecewise tensor product polynomials of degree q in the broken space $(\Pi(q))^2$. The approximations are denoted by a superscript h .

Let ϕ be a basis function from the same space as the approximation to the solution, with a subscript indicating its associated unknown. We write the Galerkin variational formulation:

Problem. *On each element in the fluid, the variational formulation (5)-(6) holds together with moments against the null vector of the acoustic energy, [1], on each element in the solid, the variational formulation (7)-(8) holds with moments against the null vectors of the elastic energy, [2]. Above $\boldsymbol{\sigma}_i^{\phi_{ui}}$ is $\boldsymbol{\sigma}_i$ with argument u_i replaced by ϕ_{ui} . The variables with an asterisk in the superscript are numerical fluxes.*

Numerical fluxes for inter-element interfaces and outer boundaries can be found in [1,2]. The following theorem presents the numerical fluxes for an element boundary that is on the interface between the fluid Ω^f and solid Ω^s .

Theorem. *For the element boundary at the fluid-solid interface Γ , the following numerical fluxes*

$$\mathbf{v}^* \cdot \mathbf{n} = \nabla \psi^* \cdot \mathbf{n} = \tau (\mathbf{v}^h \cdot \mathbf{n}) \quad (9)$$

$$+ (1 - \tau) (\nabla \psi^h \cdot \mathbf{n}) - \alpha (\boldsymbol{\sigma}^h \cdot \mathbf{n} - p^h \mathbf{n}) \cdot \mathbf{n},$$

$$\mathbf{v}^* \cdot \mathbf{m} = \mathbf{v}^h \cdot \mathbf{m}, \quad (10)$$

$$\begin{aligned} p^* \mathbf{n} &= \boldsymbol{\sigma}^* \cdot \mathbf{n} = \tau p^h \mathbf{n} + (1 - \tau) (\boldsymbol{\sigma}^h \cdot \mathbf{n} \cdot \mathbf{n}) \mathbf{n} \\ &- \beta ((\mathbf{v}^h - \nabla \psi^h) \cdot \mathbf{n}) \mathbf{n}, \end{aligned} \quad (11)$$

lead to a stable discretization if $\alpha, \beta \geq 0$, where $\mathbf{v}^* = [v_1^*, v_2^*]^T$ and \mathbf{m} is the tangential vector satisfying $\mathbf{m} \cdot \mathbf{n} = 0$. In particular, the discretization is energy-conserving when $\alpha = \beta = 0$ and dissipates the energy when $\alpha, \beta > 0$ by

$$-\int_{\partial \Omega_j^f} \alpha ((\boldsymbol{\sigma}^h \cdot \mathbf{n}) \cdot \mathbf{n} - p^h)^2 + \beta (\mathbf{v}^h \cdot \mathbf{n} - \nabla \psi^h \cdot \mathbf{n})^2.$$

Acknowledgement

DA was supported in part by NSF Grant DMS-1319054. Any conclusions or recommendations expressed in this paper are those of the author and do not necessarily reflect the views of NSF.

References

- [1] D. APPELÖ AND T. HAGSTROM, *A new discontinuous Galerkin formulation for wave equations in second-order form*, SIAM J. Numer. Anal., 53(2015), 2705–2726.
- [2] D. APPELÖ AND T. HAGSTROM, *An energy-based discontinuous Galerkin discretization of the elastic wave equation in second order form*, submitted.
- [3] D. KOMATITSCH, C. BARNES AND J. TROMP, *Wave propagation near a fluid-solid interface: A spectral-element approach*, Geophysics, 65(2000), 623–631.
- [4] M. KÄSER AND M. DUMBSER, *A highly accurate discontinuous Galerkin method for complex interfaces between solids and moving fluids*, Geophysics, 73(2008), pp. T23–T35.
- [5] L. C. WILCOX, G. STADLER, C. BURSTEDDE AND O. GHATTAS, *A high-order discontinuous Galerkin method for wave propagation through coupled elastic-acoustic media*, J. Comput. Phys., 229(2010), pp. 9373–9396.

Discrete resonances of the complex scaled Helmholtz equation

M. Wess^{1,*}, L. Nannen²

¹Institute for Analysis and Scientific Computing, TU Wien

²Institute for Analysis and Scientific Computing, TU Wien

*Email: markus.wess@tuwien.ac.at

Abstract

Complex scaling is a popular method for treating scattering and resonance problems in open domains. For solving scattering problems it is common to use frequency dependent scaling parameters. Using similar ideas for resonance problems leads to non-linear eigenvalue problems. In this talk we analyze the discrete resonances of both, the frequency independent and the frequency dependent complex scaled Helmholtz equation.

Keywords: Helmholtz resonance problem, perfectly matched layer, spurious solution

Introduction

We are concerned with the approximation of eigenpairs $(\omega, u) \in \mathbb{C} \times H_{loc}^1(\mathbb{R}^n) \setminus \{0\}$ of the Helmholtz equation

$$-\Delta u(x) - \omega^2(1 + p(x))^2 u(x) = 0, \quad (1)$$

in \mathbb{R}^n . The function p is a given potential function such that there exists an open and simply connected interior domain $\Omega_{int} \subset \mathbb{R}^n$, with $\text{supp } p \subset \Omega_{int}$. As radiation condition, we demand, that u satisfies

$$u(x) = \sum_{\nu=0}^{\infty} \sum_{k=0}^{l_{\nu}} c_{\nu,k} \mathcal{H}_{\nu}^{(1)}(\omega \|x\|) \Phi_{\nu,k}^n \left(\frac{x}{\|x\|} \right) \quad (2)$$

for $x \in \mathbb{R}^n \setminus \overline{\Omega_{int}}$, where $\mathcal{H}_{\nu}^{(1)}$ are the (spherical) Hankel functions of the first kind, and $\Phi_{\nu,k}^n$ are the circular (spherical) harmonics.

To realize the radiation condition we use complex scalings of the form

$$\hat{x}(x) = x - d(x) + \tau_{\omega}(\|d(x)\|) d(x), \quad (3)$$

for some continuous and piecewise smooth distance function $d : \mathbb{R}^n \rightarrow \mathbb{R}^n$ such that

$$d(x) = 0, \quad x \in \overline{\Omega_{int}}, \quad (4)$$

$$x - d(x) \in \partial \Omega_{int}, \quad x \in \mathbb{R}^n \setminus \Omega_{int}, \quad (5)$$

and some continuous and piecewise smooth scaling function $\tau_{\omega} : \mathbb{R}^+ \cup \{0\} \rightarrow \mathbb{C}$, such that

$$\lim_{t \rightarrow \infty} \text{Im } \tau_{\omega}(t) > 0, \quad \lim_{t \rightarrow \infty} \frac{\text{Im } \tau_{\omega}(t)}{\text{Re } \tau_{\omega}(t)} > 0. \quad (6)$$

It can be shown, that for any given eigenpair (ω, u) of (1), the pair (ω, \hat{u}) , with the scaled function $\hat{u}(x) := u(\hat{x}(x)) \in H^1(\mathbb{R}^n)$ is an eigenpair of the complex scaled equation

$$-\hat{\Delta} \hat{u}(x) - \omega^2(1 + p(x))^2 \hat{u}(x) = 0, \quad (7)$$

where $\hat{\Delta} := J_{\hat{x}}^T \nabla \cdot J_{\hat{x}}^T \nabla$ and $J_{\hat{x}}(x)$ is the Jacobian of the scaling $\hat{x}(x)$.

The essential Spectrum of the unbounded problem

The simplest scaling is an affine, linear and frequency independent radial complex scaling, i.e. $\Omega_{int} := B_{R_0}(0)$ for some $R_0 > 0$ and

$$\hat{x}(x) := x + \chi_{\Omega_{int}^c}(x)(\sigma - 1)(\|x\| - R_0) \frac{x}{\|x\|} \quad (8)$$

for $\sigma \in \mathbb{C}$, with $\text{Im } \sigma > 0$. It can be shown, that the set

$$\Sigma_{ess} := \{\omega \in \mathbb{C} : \omega \sigma \in \mathbb{R}^+ \}, \quad (9)$$

is the essential spectrum of the complex scaled problem (7). Moreover the eigenvalues of the initial problem (1) and the complex scaled problem (7) coincide if they are located in the sector bounded by the positive real axis and Σ_{ess} (cf. [1]). For large $\|x\|$, the complex scaled resonance functions are approximately given by (2) where the argument of the Hankel functions is replaced by $\omega \sigma \|x\|$, indicating an exponential decay for $\|x\| \rightarrow \infty$.

Choosing a frequency dependent complex slope $\sigma(\omega)$ in (8) changes the shape of the essential spectrum of the resulting complex scaled problem. Particularly notable is the fact that for

$$\sigma(\omega) := \sigma_0 \omega^{-1}, \quad \sigma_0 \in \mathbb{C}, \quad \text{Im } \sigma_0 > 0 \quad (10)$$

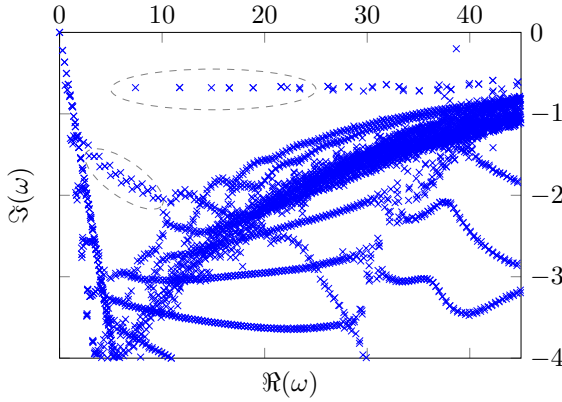


Figure 1: Computed resonances of a two dimensional resonance problem using $\sigma(\omega) \equiv 1 + 3i$.

the argument of the Hankel functions becomes asymptotically $\sigma_0 \|x\|$. The problem has no essential spectrum in the lower complex half plane and the decay of the resonance functions is almost independent of the resonance ω .

In general, choosing a frequency dependent scaling function τ_ω leads to a non-linear eigenvalue problem. In case of a frequency scaled affine linear scaling however, the problem can be reduced to a polynomial eigenvalue problem.

Asymptotic results

The complex scaled problem (7) is discretized on a sufficiently large computational domain $\Omega_T := B_T(0)$ using high order finite element spaces $V_{h,p,T}$ of order p and meshsize h . Spectral convergence can be shown using results from [3] and [4] for sufficiently good discretizations. Hence, for all $h < h_\omega$ and $T > T_\omega$, there are no spurious eigenvalues in a small neighborhood of a resonance ω , and the error of the approximated eigenvalues decays with h^{2p} and exponentially with T . Nevertheless solving one eigenvalue problem on a too coarse discrete space might result in discrete eigenvalues, which are neither an approximation to the essential spectrum, nor approximations to the desired eigenvalues of (1), since the approximation quality of the discrete spaces to the complex scaled eigenfunctions \hat{u} depends heavily on the frequency w .

Discretization resonances

Figures 1 and 2 show resonances of a discretized two dimensional transmission problem with piecewise constant potential function

$p(x) := p_0 \chi_{[-r,r] \times [-r,r]}(x)$, affine, linear complex scaling (8).

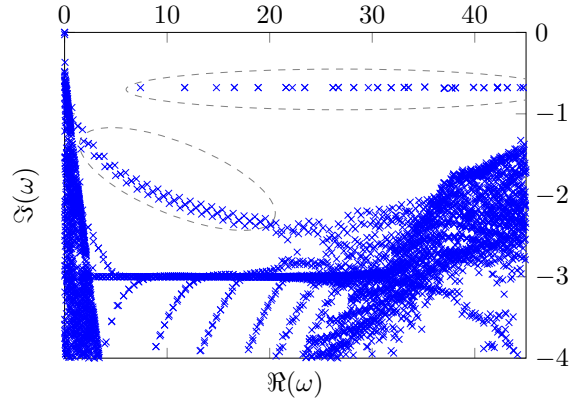


Figure 2: Computed resonances of a two dimensional resonance problem using $\sigma(\omega) := \frac{9+9i}{\omega}$.

The set of discrete resonances can be separated into the approximated sought for outgoing resonances of (1) (marked by the dashed ellipses), the approximation of the essential spectrum and the aforementioned spurious resonances. Even though the unbounded problem in the frequency dependent case does not have an essential spectrum in the lower complex half-plane, due to truncation a corresponding set of discrete resonances appears, located on a horizontal line. An analysis of some easy accessible examples and numerical experiments in [2] show, that these spurious resonances, can be categorized into interior and exterior spurious resonances induced by the discretization errors of the interior and exterior domain respectively. The exterior spurious resonances depend heavily on the choice of the parameters of the complex scaling. Choosing a frequency dependent scaling (10) however, reduces this dependency as mentioned above. As Figures 1 and 2 indicate a clear improvement in the number of well approximated resonances it might pay off to invest into solving the polynomial eigenvalue problem arising from a frequency dependent scaling for more evolved examples, e.g. by using the contour integration method.

References

- [1] Kim, S. and Pasciak, J. E., The computation of resonances in open systems using a perfectly matched layer, *Math. Comp.*, **78** (2009), pp. 1375–1398.
- [2] Nannen, L. and Wess M., Spurious modes of the complex scaled Helmholtz Equation, *ASC Report, TU Wien*, **15** (2016).
- [3] Karma, O., Approximation in eigenvalue problems for holomorphic Fredholm operator functions. I, *Numer. Funct. Anal. Optim.*, **17** (1996), pp. 365–387.
- [4] Karma, O., Approximation in eigenvalue problems for holomorphic Fredholm operator functions. II, *Numer. Funct. Anal. Optim.*, **17** (1996), pp. 389–408.

Probing Extreme Gravity with Gravitational Waves from Binary Black Hole Coalescences

Kent Yagi¹, Nicolás Yunes², Frans Pretorius¹

¹Department of Physics, Princeton University, Princeton, New Jersey 08544, USA.

²eXtreme Gravity Institute, Department of Physics, Montana State University, Bozeman, MT 59717, USA.

Abstract

General Relativity has passed all Solar System experiments and binary pulsar observations with flying colors. Recent direct detections of gravitational waves from binary black hole coalescences offer us unique testbeds of gravity in the regime where the field is both strong and dynamical. Based on a Fisher analysis, we derive constraints on parameterized deviations in the gravitational waveform from General Relativity. We then map such constraints to those on fundamental pillars of General Relativity, such as the equivalence principle, Lorentz/parity invariance and the dispersion relation of the massless graviton. We find that one can only place relatively weak constraints on generation mechanisms of gravitational waves due to our lack of knowledge of the modified gravitational waveform in the merger regime. On the other hand, one can place relatively strong constraints on modified propagation mechanisms of gravitational waves that are complementary to the existing bounds.

Keywords: Gravitational Waves, General Relativity, Black Holes

1 Introduction

A century after their prediction, gravitational waves (GWs) have finally been detected directly with Advanced LIGO (aLIGO) [1, 2]. These GWs were generated from binary black hole (BH) coalescences. Such a historic discovery not only opens an era of GW astronomy, but also offers us unique testbeds to probe gravity in the extreme regime [3].

Figure 1 presents the amount of gravitational potential and curvature of systems that have been used to probe GR. The top right corner of this figure, where the GW sources live, corresponds to the strong-field regime. Observe also that such sources are shown by lines instead of points, which means that these sources are highly dynamical. Thus, such GW systems

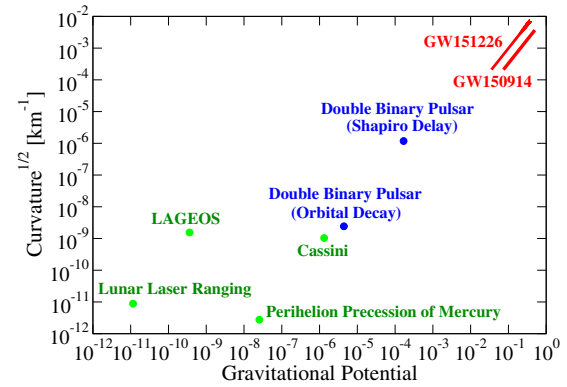


Figure 1: Phase diagram showing the amount of gravitational potential and curvature for systems used to probe gravity. We classify such systems into the Solar System (green), the double binary pulsar (blue) and the binary BH coalescences (red). Observe that the field of the GW sources are not only strong but also dynamical. This figure is taken and edited from [3].

are in the *extreme* gravity regime, where the field is not only strong but also dynamical.

One can use these new GW sources to probe fundamental pillars of GR, including the strong equivalence principle, Lorentz invariance, parity invariance, four dimensionality of the spacetime and the massless graviton. In this article, we summarize the results presented in [3].

2 Analysis and Results

We carry out a Fisher analysis and derive parameterized deviations from GR in the waveform. Such deviations are introduced following the parameterized post-Einsteinian (ppE) formalism [4], in which the modified waveform in the Fourier domain is given by

$$\tilde{h}(f) = \tilde{h}_{\text{GR}}(f) e^{i\beta v^{2n-5}}. \quad (1)$$

Here \tilde{h}_{GR} is the GR waveform, β is the ppE parameter representing the magnitude of the non-GR deviation and v is the relative velocity of

the binary constituents. The above correction enters at n th post-Newtonian (PN) order.

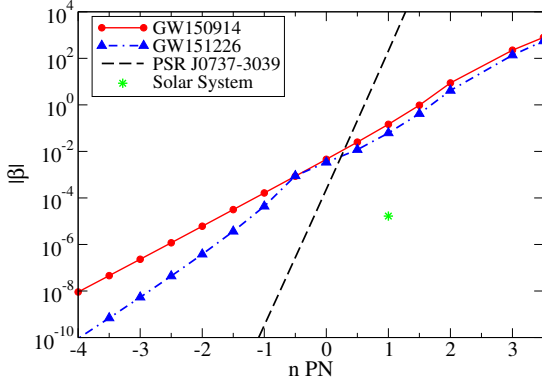


Figure 2: Upper bounds on the ppE parameter β in Eq. (1) with GW150914 and GW151226 entering at different PN orders. We also present bounds from binary pulsar observations and Solar System experiments. This figure is taken and edited from [3].

Regarding non-GR corrections to generation mechanisms of GWs, we include the ppE correction in the waveform only in the inspiral part of the waveform as a good modeling of the non-GR waveform in the merger-ringdown part is currently unavailable. Figure 2 presents upper bounds on the ppE parameter β with GW150914 and GW151226 at various PN orders. Observe that the latter places stronger constraints than the former, especially in the negative PN region. This is because (i) the velocity of the binary constituents is smaller for GW151226 at a fixed frequency and (ii) the observed frequency range is larger that helps breaking the degeneracy between β and other parameters. Comparing these GW bounds with those from binary pulsar observations and Solar System experiments, we see that the former are stronger for positive PN corrections where the strong-field effect becomes important.

One can then map these constraints on β to those on various GR pillars. For example, -4PN correction allows us to probe the existence of extra dimensions and the strong equivalence principle via a time variation of gravitational constant, while 0PN (2PN) correction can be used to probe a violation of Lorentz (parity) invariance. Doing so, we found that the GW sources either do not place stronger constraints

than weak-field bounds or the GW bounds are too weak that one cannot say anything meaningful. Though, such weak GW bounds are distinct from other existing ones as the former come directly from the extreme gravity regime.

Regarding non-GR corrections to propagation mechanisms of GWs, one can include ppE corrections to all of the inspiral, merger and ringdown parts. Similar to the generation mechanism case, one can carry out a Fisher analysis to derive bounds on β and map such constraints to those on the modified dispersion relation of the graviton. We found that the new bounds from the GW sources are complementary to the existing bounds from cosmic ray observations and give unique constraints on some regions in the non-GR parameter space.

3 Discussions

The bounds on fundamental pillars in GR will only increase in the near future as (i) the detector sensitivity improves, (ii) one combines signals from multiple events, (iii) one finds GWs from different sources such as neutron star binaries, (iv) multi-band ground- and space-based tests maybe possible. The bounds on generation mechanisms will further increase as the non-GR waveform modeling becomes available including the merger and ringdown phases. To achieve this, numerical relativity simulations in various modified theories of gravity are necessary.

One can also probe extreme gravity by studying whether final objects after merger are consistent with the Kerr BH. For example, we derived bounds on an effective viscosity of the remnant and also placed constraints on the amplitude of the higher order ringdown modes that are useful to probe the BH no-hair property [3].

References

- [1] B. P. Abbott *et al.*, Phys. Rev. Lett. **116**, 061102 (2016).
- [2] B. P. Abbott *et al.*, Phys. Rev. Lett. **116**, 241103 (2016).
- [3] N. Yunes, K. Yagi and F. Pretorius, Phys. Rev. D **94**, 084002 (2016).
- [4] N. Yunes and F. Pretorius, Phys. Rev. D **80**, 122003 (2009).

Shape reconstruction of nanoparticles from plasmonic resonances

Habib Ammari¹, Mihai Putinar², Matias Ruiz³, Sanghyeon Yu^{1,*}, Hai Zhang⁴

¹Department of Mathematics, ETH Zürich, Zürich, Switzerland

²Department of Mathematics, University of California at Santa Barbara, Santa Barbara, USA

³Department of Mathematics and Applications, Ecole Normale Supérieure, Paris, France

⁴Department of Mathematics, HKUST, Kowloon, Hong Kong

*Email: sanghyeon.yu@sam.math.ethz.ch

Abstract

We prove by means of a couple of examples that plasmonic resonances can be used on one hand to classify shapes of nanoparticles with real algebraic boundaries and on the other hand to reconstruct the separation distance between two nanoparticles from measurements of their first collective plasmonic resonances. To this end, we explicitly compute the spectral decompositions of the Neumann-Poincaré operators associated with a class of quadrature domains and two nearly touching disks. Numerical results are included in support of our main findings.

Keywords: plasmonic resonance, algebraic domain, Neumann-Poincaré operator

1 Introduction

The present paper is a part of an ample and recent effort to understand the mathematical structure of inverse problems arising in nanophotonics. Although very classical, the spectral analysis of the Neumann-Poincaré (NP) operator emerges as the main theme of investigation. Consider a domain Ω with $C^{1,\eta}$ boundary in \mathbb{R}^2 for $\eta > 0$. Let ν denote the outward normal to $\partial\Omega$. The NP operator \mathcal{K}_Ω^* associated with Ω is defined as follows: for $x \in \partial\Omega$,

$$\mathcal{K}_\Omega^*[\varphi](x) = \frac{1}{2\pi} \int_{\partial\Omega} \frac{\langle x - y, \nu_x \rangle}{|x - y|^2} \varphi(y) d\sigma(y).$$

Using the quasi-static limit of electromagnetic fields, plasmonic resonances are associated with the set of eigenvalues λ_j of the Neumann-Poincaré operator \mathcal{K}_Ω^* for which $\langle \varphi_j, x_i \rangle_{L^2(\partial\Omega)} \neq 0$, for either $i = 1$ or $i = 2$, where φ_j is an eigenfunction associated to λ_j . We refer the reader to [3, 4] for the mathematical theory of plasmonic resonances for nanoparticles.

In our paper [2], we prove that based on plasmonic resonances we can on one hand classify the shape of a class of domains with real

algebraic boundaries and on the other hand recover the separation distance between two components of multiple connected domains. These results have important applications in nanophotonics. They can be used in order to identify the shape and separation distance between plasmonic nanoparticles having known material parameters from measured plasmonic resonances, for which the scattering cross-section is maximized [3, 4].

2 Plasmonic resonance for algebraic domains

Let us first explain the algebraic domains. Let D be the unit disk in \mathbb{C} . For $m \in \mathbb{N}$ and $a \in \mathbb{R}$, define $\Phi : \mathbb{C} \setminus \overline{D} \rightarrow \mathbb{C}$ by

$$\Phi_{m,a}(\zeta) = \zeta + \frac{a}{\zeta^m}.$$

Assume that Φ is injective on $\mathbb{C} \setminus \overline{D}$. We introduce the class \mathcal{Q} as the collection of all bounded domains $\Omega \subset \mathbb{C}$ bounded by the curves

$$\partial\Omega = \{\Phi(\zeta) : |\zeta| = r_0\}$$

for some $r_0 > 1$, $m \in \mathbb{N}$ and $a \in \mathbb{R}$. Note that Φ is a conformal mapping from $\{|\zeta| > r_0\}$ onto $\mathbb{C} \setminus \overline{\Omega}$. We introduce the parameter δ defined by $a = e^{(m+1)\rho_0}\delta$. Then the shape of Ω is determined by the two parameters m and δ , while the size by the parameter ρ_0 .

The far field response of nanoparticle Ω is determined by the *generalized polarization tensors* [1]:

$$M_{\alpha\beta} = \int_{\partial\Omega} y^\beta (\lambda I - \mathcal{K}_\Omega^*)^{-1} \left[\frac{\partial x^\alpha}{\partial \nu} \right] (y) d\sigma(y),$$

for $\alpha, \beta \in \mathbb{N}^d$. Here, λ is given by

$$\lambda = \frac{\epsilon + 1}{2(\epsilon - 1)},$$

where ϵ is the permittivity of the nanoparticle. It is more convenient to use special linear combinations of GPTs, M_{mn}^{cc} , M_{mn}^{cs} and M_{mn}^{ss} for $m, n \in \mathbb{N}$. See [1] for details.

If δ is small enough, then the shape of $\partial\Omega$ is close to a circle. By investigating the asymptotic behavior of the NP operator and its spectrum for small δ , we derive asymptotic expansions of M_{11}^{cc} and M_{22}^{cc} :

$$M_{11}^{cc} = \frac{\pi}{2} e^{2\rho_0} \left(\frac{1}{\lambda - \lambda_+} + \frac{1}{\lambda - \lambda_-} \right),$$

$$M_{22}^{cc} = \frac{\pi e^{4\rho_0} (\frac{1}{2} - \lambda'_+)}{(\frac{1}{2} + \lambda'_+) (\lambda - \lambda'_+)} + \frac{\pi e^{4\rho_0} (\frac{1}{2} + \lambda'_-)}{(\frac{1}{2} - \lambda'_-) (\lambda - \lambda'_-)},$$

up to order δ^2 . Here, λ_\pm and λ'_\pm are given by

$$\lambda_+ = \frac{1}{2}\delta\sqrt{m}, \quad \lambda'_+ = \frac{1}{2}\delta\sqrt{2(m-1)}.$$

In fact, λ_\pm and λ'_\pm are (asymptotically) eigenvalues of the NP operator and characterize the plasmonic resonances of the algebraic domains.

The identification of the parameters ρ_0 and m is now straightforward. Suppose that we can obtain the values of $\lambda_\pm, \lambda'_\pm$ approximately from M_{11}^{cc} and M_{22}^{cc} . Then the parameters m and δ can be reconstructed by the following formulas:

$$m = \frac{\lambda_+^2}{\lambda_+^2 - (\lambda'_+)^2/2}, \quad \delta = 2\sqrt{\lambda_+^2 - (\lambda'_+)^2/2}.$$

In Figure 1, we provide a numerical example for $m = 4$ and $\delta = 0.05$. By assuming the Drude model for ϵ , we measure λ_+, λ'_+ and then reconstruct the target shape.

3 Two separated nanoparticles and their plasmonic resonances

We now consider two circular disks of radius r separated by a distance $\epsilon > 0$. We find that the eigenvalues $\lambda_{\epsilon,n}^\pm$ of the corresponding NP operator are given by

$$\lambda_{\epsilon,n}^\pm = \pm \frac{1}{2} e^{-2|n|s}, \quad n \neq 0,$$

where $s = \sinh^{-1}(\alpha/r)$ and $\alpha = (\epsilon(r+\epsilon/4))^{1/2}$. By using the spectral decomposition of the NP operator, we derive M_{11}^{cc} as follows:

$$M_{11}^{cc} = \sum_{n \neq 0} \frac{4\pi\alpha^2|n|e^{-2|n|s}}{\lambda - \lambda_{\epsilon,n}^+}.$$

Suppose that the first eigenvalue $\lambda_{\epsilon,1}^+ = \frac{1}{2}e^{-2s}$ is measured. Then we immediately find the value of s . The distance ϵ can be determined by the following formula: $r \cosh s = \epsilon/2 + r$.

Recently, the plasmonic resonance of two 3D spheres is analytically investigated and the hybrid numerical scheme is developed [5].

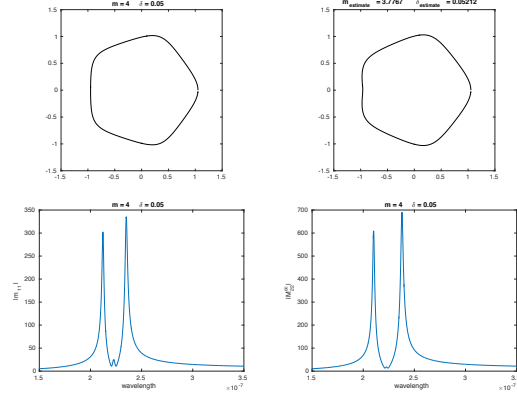


Figure 1: From top to bottom and left to right: initial shape, reconstructed shape, $|M_{11}^{cc}|$ and $|M_{22}^{cc}|$ with respect to the wavelength for $m = 4$, $\delta = 0.05$.

References

- [1] H. Ammari, J. Garnier, H. Kang, M. Lim, and S. Yu, Generalized polarization tensors for shape description, *Numer. Math.*, 126 (2014), 199–224.
- [2] H. Ammari, M. Putinar, M. Ruiz, S. Yu and H. Zhang, Shape reconstruction of nanoparticles from their associated plasmonic resonances, submitted, arXiv:1602.05268.
- [3] H. Ammari, P. Millien, M. Ruiz, and H. Zhang, Mathematical analysis of plasmonic nanoparticles: the scalar case, submitted, arXiv:1506.00866.
- [4] H. Ammari, M. Ruiz, S. Yu, and H. Zhang, Mathematical analysis of plasmonic resonances for nanoparticles: the full Maxwell equations, *J. Differ. Equat.*, 261 (2016), 3615–3669.
- [5] S. Yu and H. Ammari, Plasmonic interaction between nanospheres, submitted, arXiv:1604.02624.

Quasi-Stable Dynamics of a Mode-Locked Laser

YiMing Yu^{1,*}, Richard O. Moore¹

¹Department of Mathematical Sciences, NJIT, Newark, USA

*Email: yy286@njit.edu

Abstract

We study the quasi-stable dynamics of a mode-locked laser with active feedback and noise due to amplified spontaneous emission. We show that, in a distinguished small-noise limit, an effective boundary can be drawn in parameter space for quasi-stability that is distinct from the deterministic stability boundary. We consider the probability that a mode-locked laser with active feedback will experience a transition between stable equilibria in a potential well when subjected to amplified spontaneous emission noise generated by the gain medium. To investigate the influence of noise on quasi-stability, we reduce the infinite-dimensional model to a finite-dimensional system of stochastic ordinary differential equations and compute the quasi-stable state by evaluating the action functional via the geometric minimum action method. This computation shows how and to what extent noise effectively destabilizes the system, and producing a region of quasi-stability in its parameter space that is smaller than that of the deterministic system.

Keywords: Mode-locked lasers; large deviation theory; stochastic perturbation; rare events.

1 Mathematical Model

We consider the following model of a mode-locked fiber laser with a nonlinear gain element that controls the pulse amplitude and active phase modulation that controls the pulse position, ie.,

$$\begin{aligned} iu_t + \frac{1}{2}u_{xx} + |u|^2u &= -b\cos(\omega x)u - ic_1u \\ &+ ic_2u_{xx} + id_1|u|^2u - id_2|u|^4u + i\epsilon f(x, t), \end{aligned} \quad (1)$$

where u is the electric field envelope, u_{xx} represents filtering, $\cos(\omega x)u$ is the active phase modulation, and $-ic_1u + id_1|u|^2u - id_2|u|^4u$ represents linear loss and saturable gain. The noise process $f(x, t)$ is assumed to derive from spontaneous emission noise and assumed to be mean-zero Gaussian white noise, delta-correlated in x and t [1]. Eqn.(1) with trivial right-hand side has a soliton solution of the following form:

$$u_s(x, t) = A(t) \operatorname{sech}[A(t)(x - X(t))] \exp[i\phi], \quad (2)$$

where $\phi = \varphi(t) + (x - X(t))\Omega(t)$. A, X, φ and Ω represent amplitude, position, phase and frequency.

To approximate the dynamics of optical pulses in this model, we assume slow adiabatic changes in the pulse parameters with the above ansatz. We obtain a set of four stochastic ordinary differential equations(SODE) for the four soliton parameters through a variational approach, using an extended version of Rayleigh-Ritz process for the non-variational part of the PDE [2]. Following the above procedure, we have the following corresponding SODE

$$dU = F(U)dt + \epsilon\sigma(U)dW, \quad (3)$$

where $U = (A, \Omega, X)^T$ and

$$F(U) = \begin{pmatrix} -2c_1u_1 + (\frac{4}{3}d_1 - \frac{2}{3}c_2)u_1^3 - \frac{16}{15}d_2u_1^5 - 2c_2u_1u_2^2 \\ -\frac{4}{3}c_2u_1^2u_2 - \frac{\pi bw^2}{2u_1^3} \operatorname{csch}(\frac{\pi w}{2u_1}) \sin(wu_3) \\ u_2 \end{pmatrix} \quad (4)$$

and

$$\sigma(U) = \begin{pmatrix} \sqrt{u_1} & 0 & 0 \\ -\frac{u_2}{\sqrt{u_1}} & \sqrt{\frac{u_1}{3} + \frac{u_2^2}{u_1}} & 0 \\ 0 & 0 & \frac{\pi}{\sqrt{12u_1^3}} \end{pmatrix}. \quad (5)$$

The phase evolution is not included in the above dynamical system since it does not affect the above dynamics.

2 Linearization and Stability

Considering $\epsilon = 0$, the fixed points of $F(U)$ are

$$U_n = (A_0, 0, n\pi/\omega),$$

$n \in \mathbb{Z}$ and $A_0^2 = \frac{5}{16d_2}[2d_1 - c_2 + \sqrt{(2d_1 - c_2)^2 - \frac{96}{5}c_2d_2}]$, provided $(2d_1 - c_2)^2 - \frac{96}{5}c_2d_2 > 0$. Recalling that all the physical parameters of Eqn.(1) are positive, the fixed points are stable if n is even, otherwise they are unstable. The stable fixed points are nodes if $(\frac{4}{3}c_2A_0^2)^2 > \frac{2\pi bw^3}{A_0^3} \operatorname{csch}(\frac{\pi w}{2A_0})$; otherwise, they are spirals. The eigenvalues of the fixed points are given by

$$\lambda_{U_1} = 8c_1 - \frac{4}{3}(2d_1 - c_2)A_0^2$$

$$\lambda_{U_2} = \frac{1}{2}(M_{22} - \sqrt{M_{22}^2 + 4M_{23}})$$

$$\lambda_{U_3} = \frac{1}{2}(M_{22} + \sqrt{M_{22}^2 + 4M_{23}})$$

where $M_{22} = -4/3c_2A_0^2$, and

$$M_{23} = (-1)^{n+1}\pi b\omega^3/(2A_0^3) \operatorname{csch}(\pi\omega/(2A_0)).$$

To examine the effect of noise on quasi-stability of the mode-locked laser we focus on the active feedback parameters (ω, b) and we fix the parameters of $(c_1, c_2, d_1, d_2) = (0.01, 0.002, 0.034, 0.02)$, which imply large gain, dispersion and pulse power. The fixed points with even n are stable in the first quadrant of parameter plane (ω, b) . Notice that when $b \rightarrow 0$ we have $\lambda_{U_2} = \lambda_{U_3} \rightarrow 0$. Meanwhile as $\omega \rightarrow \infty$, $U_n = (A_0, 0, n\pi/\omega) \rightarrow (A_0, 0, 0)$. These limits confirm the intuition that the susceptibility of the state to undergo a transition is affected by b and ω .

3 Quasi-stability and large deviation theory

In presence of noise $\epsilon > 0$, any trajectory that starts at stable fixed point $(A_0, 0, 0)$, will almost surely exit the basin of attraction and enter the basin of attraction of $(A_0, 0, \pm 2\pi/\omega)$. Large deviation theory[3] states that the probability of exiting the basin of attraction G from a stable fixed point before finite T is given by

$$\lim_{\epsilon \rightarrow 0} \epsilon^2 \ln P(t \leq T) \sim - \inf_{\phi(T) \notin G} S_T(\phi) \quad (6)$$

and that the mean first exit time τ is given by

$$\lim_{\epsilon \rightarrow 0} \epsilon^2 \ln E\tau \sim - \inf_{\phi(\tau) \notin G} S_\infty(\phi) \quad (7)$$

where

$$S_T(\phi) = \frac{1}{2} \int_0^T |\sigma^{-1}(\phi)(\dot{\phi} - F(\phi))|^2 dt. \quad (8)$$

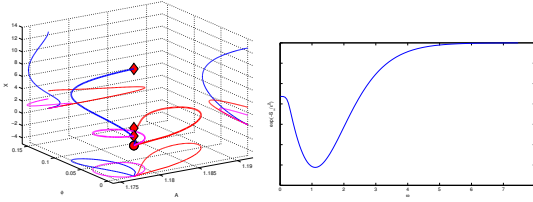


Figure 1: Three different optimal paths corresponding to three different values of ω (left). There is a unique ω that minimizes the transition rate, i.e., maximizes the mean exit time (right).

Eqn.(6) and Eqn.(7) suggest that as $T \rightarrow \infty$, $P(t \leq T) \rightarrow 1$ almost surely. Meanwhile, for any T and $\epsilon = 0$, the transition event does not occur. By choosing $T_\epsilon = \exp(A/\epsilon^2)(B + O(\epsilon))$, where $A, B > 0$ and $\tau \sim \nu \exp(S/\epsilon^2)$, the probability of an exit before T_ϵ is given by

$$\begin{aligned} P &\sim 1 - \exp(-T_\epsilon/\tau) \\ &= 1 - \exp(-\exp((A - S)/\epsilon^2) \frac{B}{\nu}). \end{aligned}$$

If $A = S$, we have that P remains bounded away from 0 and 1 as $\epsilon \rightarrow 0$. If $A > S$, we have $P \rightarrow 1$ as $\epsilon \rightarrow 0$. If $A < S$, we have $P \rightarrow 0$ as $\epsilon \rightarrow 0$. Thus, in a manner related to the finite-temperature astroids studied for magnetic materials in [4], this distinguished limit of vanishing noise strength provides a quasi-stable region with a boundary inside the deterministic stability boundary.

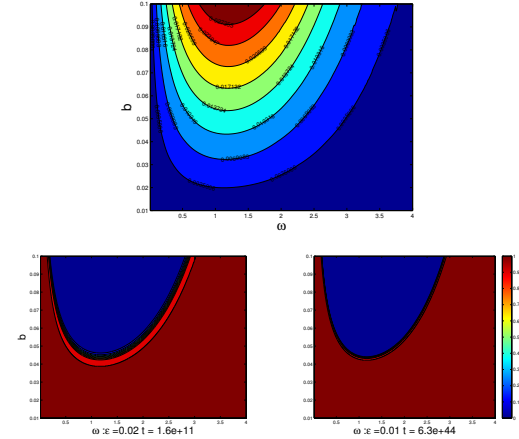


Figure 2: Top: Contours of the action functional (8). Bottom: Quasi-stable region determined by choosing $T(\epsilon)$ with $A = 0.010316$. For small ϵ , the transition region shrinks to a narrow band, which converges to one of contours in top figure.

References

- [1] Richard O. Moore. Trade-off between linewidth and slip rate in a mode-locked laser model. *Opt. Lett.*, 39(10):3042–3045, May 2014.
- [2] D. Anderson, M. Lisak, and A. Berntson. A variational approach to nonlinear evolution equations in optics. *Pramana*, 57(5):917–936, 2001.
- [3] Mark I Freidlin and Alexander D Wentzell. *Random Perturbations of Dynamical Systems*. Springer Berlin Heidelberg, Berlin, Heidelberg, 2012.
- [4] R. V. Kohn, M. G. Reznikoff, and E. Vandenberg-Eijnden. Magnetic elements at finite temperature and large deviation theory. *Journal of Nonlinear Science*, 15(4):223–253, 8 2005.